Vladimir P. Kolotov
Natalia S. Bezaeva *Editors*

Advances in Geochemistry, Analytical Chemistry, and Planetary Sciences

75th Anniversary of the Vernadsky Institute of the Russian Academy of Sciences

Springer

Advances in Geochemistry, Analytical Chemistry, and Planetary Sciences

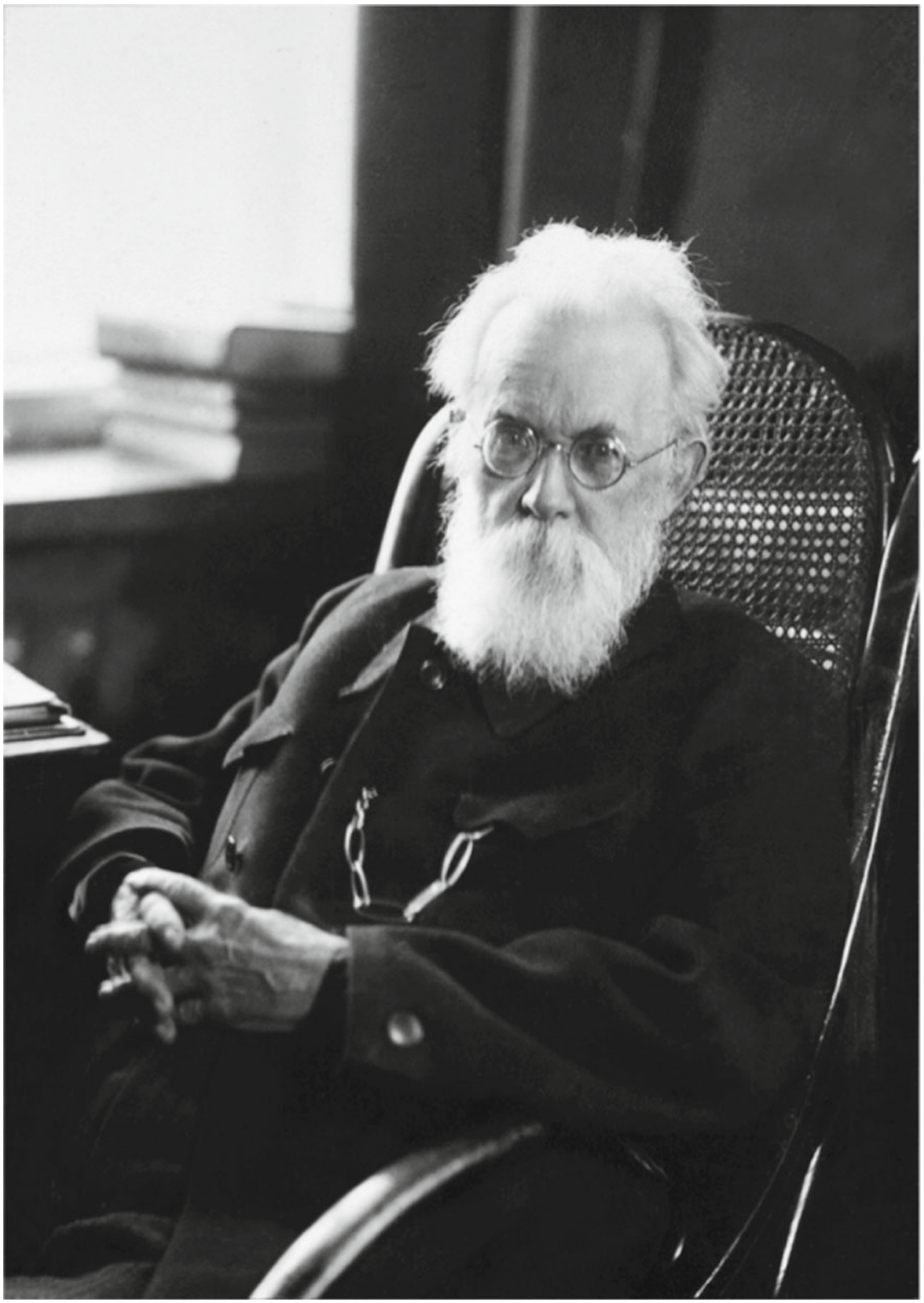

Academician Vladimir I. Vernadsky (1863–1945), after whom the institute was named (photographed 1940)

Vladimir P. Kolotov •
Natalia S. Bezaeva
Editors

Advances in Geochemistry, Analytical Chemistry, and Planetary Sciences

75th Anniversary of the Vernadsky Institute of the Russian Academy of Sciences

Springer

Editors
Vladimir P. Kolotov
Vernadsky Institute of Russian
Academy of Sciences
Moscow, Russia

Natalia S. Bezaeva
Vernadsky Institute of Russian
Academy of Sciences
Moscow, Russia

ISBN 978-3-031-09882-6 ISBN 978-3-031-09883-3 (eBook)
https://doi.org/10.1007/978-3-031-09883-3

Cover illustration:
Panoramic view of the Vernadsky Institute in late autumn

This Springer imprint is published by the registered company Springer Nature Switzerland AG
The registered company address is: Gewerbestrasse 11, 6330 Cham, Switzerland

Dedicated with reverence and gratitude
to
those who had been before us,
the late scientists, who made a major contribution
to the formation and development
of the Vernadsky Institute

Preface

Dear Readers!

The publication commemorates the 75th anniversary of the Vernadsky Institute of Geochemistry and Analytical Chemistry of the Russian Academy of Sciences (Vernadsky Institute RAS). The diamond jubilee of the institute is being celebrated in 2022, and this publication represents the scientific portfolio of the institute today.

The volume comprises selected articles written by the leading researchers of the Vernadsky Institute RAS. The institute came into being in 1947 and since has made immense contributions to the development of Earth and planetary sciences, biogeochemistry, cosmochemistry, analytical chemistry, and radiochemistry and is currently the leading research center in Russia in these areas.

The collection of 41 articles covers the main areas of modern research, focusing on the recently obtained critical results. The articles are grouped into four broad categories: (1) geochemistry, (2) meteoritics, cosmochemistry, lunar and planetary sciences, (3) biogeochemistry and ecology, and (4) analytical chemistry, radiochemistry, and radioecology. The articles divulge into the evolution of scientific ideas and the emergence of new promising areas of scientific research.

Besides its extensive brand-new research content, this volume includes an extended introduction with information about the history of the Vernadsky Institute, its main goals and achievements, description of published journals, i.e. *Geochemistry International*, and *Journal of Analytical Chemistry*, in both Russian and English, which welcome submissions by international authors. It also comprises a list of organized conferences, including the upcoming ones, which also welcome international participation. All the departments and the laboratories of the institute are presented with contact details, as the Vernadsky Institute is open to new international collaborations.

The articles are followed by an annex, which gives brief information about the life and work of Soviet and Russian scientist and philosopher V. I. Vernadsky, whose ideas, to a great extent, foreshadowed the development of science and society. In the future, the plan is to publish his major works in English. The annex also includes information about A. P. Vinogradov, founder of the institute, and other famous late scientists who contributed majorly to the formation and development of the Vernadsky Institute.

The collection of scientific articles and historical materials will be of interest to scientists and graduate students working in the fields of geochemistry, biogeochemistry, meteoritics and planetary sciences, analytical chemistry, and radiochemistry.

We wish you an enjoyable reading and looking forward to receiving your feedback!

Moscow, Russia

Vladimir P. Kolotov
Natalia S. Bezaeva

Acknowledgements The editors express their deepest gratitude to Vladimir E. Kulikovsky (Vernadsky Institute RAS) for his invaluable contribution to the preparation of the materials on the history of the institute, his work on the processing of photographic materials, and the cover design.

Contents

About the Editors

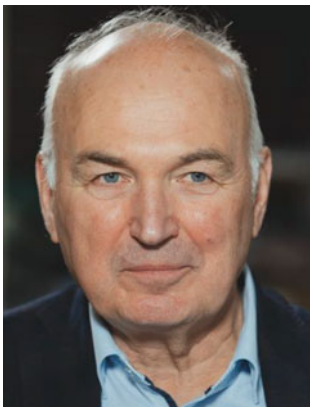

Vladimir P. Kolotov is Corresponding Member of the Russian Academy of Sciences, Professor, Doctor of Chemistry, former (deputy) Director, and current Scientific Advisor (Analytical Chemistry Branch) of the Vernadsky Institute of the Russian Academy of Sciences. Currently, he is also heading the Laboratory of Methods for Research and Analysis of Substances and Materials and simultaneously acts as Editor-in-Chief of the *Journal of Analytical Chemistry*. For the period 1995–2005, he worked at the International Union of Pure and Applied Chemistry (chairman of the Commission on Radiochemistry, titular member of the division on Analytical Chemistry), International Committee on Activation Analysis, and was involved as Expert in different projects by the International Atomic Energy Agency, etc.

His research interests are as follows: development of models and computer programs for processing activation analysis data (semiconductor gamma-ray spectrometry, autoradiographic images, database handling, etc.), development of theoretical and practical approaches to the development of a new class of environmentally friendly structural materials for nuclear power, characterized by accelerated decay of induced radioactivity, and mass spectrometry for ultra-trace analysis of various materials. V. P. Kolotov was awarded the G. Hevesy International Medal for his achievements in the field of radioanalytical chemistry and the Russian Academy of Sciences Khlopin Prize for his work in radiochemistry.

Natalia S. Bezaeva is Leading Scientist at the Vernadsky Institute of the Russian Academy of Sciences (Moscow, Russia). She graduated from the Faculty of Physics, Lomonosov Moscow State University, in 2005 and received a Ph.D. in Physics and Mathematics from the same University in 2007. She completed a second Ph.D. in Environmental Geosciences from Aix-Marseille University (Aix-en-Provence, France) in 2008 and was awarded a D.Sc. title in Physics and Mathematics from Lomonosov Moscow State University in 2016. Her primary research interests are in geosciences, meteoritics and planetary sciences with a particular emphasis on extraterrestrial and planetary magnetism, rock magnetism along with the effects of pressure, shock, and particle radiation on the magnetic properties of extraterrestrial materials, and their synthetic analogs. She is Member of the editorial board of Impact Studies Book Series (Springer) since 2017 and Editor-in-Chief of Springer Proceedings in Earth and Environmental Sciences Book Series since 2019.

Introduction

Vladimir P. Kolotov and Natalia S. Bezaeva

Summary In the first part of this section, we briefly describe the history of the Vernadsky Institute of Geochemistry and Analytical Chemistry of the Russian Academy of Sciences (further referred to as Vernadsky Institute RAS), its main scientific goals and achievements. In the second part of this section, we present information about its departments, laboratories, and museums. The introduction is supplied with numerous illustrations. Provided figures are numbered consecutively and illustrate lab descriptions. They are combined with photos of the interiors and exteriors of the Vernadsky Institute, which have a separate numbering.

1 Geochemistry, Cosmochemistry and Planetary Sciences, Analytical Chemistry, and Radiochemistry at the Vernadsky Institute RAS

The decision of the Presidium of the USSR Academy of Sciences organized Vernadsky Institute RAS in the year 1947 and bore the name of the great Russian scientist Vladimir I. Vernadsky, naturalist, philosopher, founder of geochemistry and biogeochemistry, radiogeology, and cosmochemistry. V. I. Vernadsky's scientific ideas about the development of the cosmos, the regular chemical evolution of the planet and its biosphere, and the increasing influence of human activity on its development determined the main directions for the institute's scientific research (see also a separate article about V. I. Vernadsky in Annex I).

The founder and first director of the institute was Academician A. P. Vinogradov, one of Vernadsky's closest disciples (see also a separate article about A. P. Vinogradov in Annex I). From 1975 to 1992, the institute was headed by Academician V. L. Barsukov. Between 1992 to 2015, the institute was headed by Academician E. M. Galimov, and from 2015 to May 2021, the institute was headed by Academician Yu. A. Kostitsyn. Then, from May to October 2021, Corresponding Member of RAS V. P. Kolotov was appointed as the Acting Director, and since the end of October 2021, Corresponding Member of RAS R. Kh. Khamizov has been the Acting Director of the institute.[1]

The institute is associated with a pleiad of outstanding scientists who contributed to the development of geochemistry, cosmochemistry, analytical chemistry, and radiochemistry. These are members of the Russian Academy of Sciences (further referred to as RAS), both those who worked at the institute earlier (academicians of RAS I. P. Alimarin, V. L. Barsukov, E. M. Galimov, A. B. Ronov, L. V. Tauson, V. S. Urusov, corresponding members of RAS L. A. Gribov, B. Ya Spivakov, D. I. Ryabchikov, A. I. Tugarinov, G. B. Udintsev, N. I. Khitarov, corresponding member of the Soviet Academy of Agricultural Sciences V. V. Kovalvsky, see Annex I for details) and current scientists (academicians of RAS V. A. Zolotov, L. N. Kogarko, Yu. A. Kostitsyn, M. Ya. Marov, B. F. Myasoedov, A. V. Sobolev, M. A. Fedonkin and corresponding members of RAS F. V. Kaminsky, V. P. Kolotov, R. Kh. Khamizov, O. L. Kuskov, T. I. Moiseenko). Most of the leading scientists of the institute are presented in this book as authors of the articles published in this collection. At the end of the book (see Annex I), we have also listed late scientists who enlightened us with their work.

Since its establishment, the institute has been actively developing fundamental and applied research important to the country. 24 employees have received Lenin and State Prizes for outstanding scientific achievements, and 20

V. P. Kolotov (✉) · N. S. Bezaeva
Vernadsky Institute of Russian Academy of Sciences,
Moscow, Russia
e-mail: kolotov@geokhi.ru

N. S. Bezaeva
e-mail: bezaeva@geokhi.ru

[1] Here and further in the text we use Dr. for Doctors of Sciences (D. Sc.) and Ph.D. for the so-called Candidates of Sciences.

V. P. Kolotov and N. S. Bezaeva (eds.), *Advances in Geochemistry, Analytical Chemistry, and Planetary Sciences*,
https://doi.org/10.1007/978-3-031-09883-3_1

scientists have been awarded personal prizes from the Academy of Sciences. The institute was awarded the Orders of Lenin and the October Revolution for its contribution to solving problems of national importance.

In the early years after the Second World War, the institute was involved in problems of nuclear power engineering. It was involved in supporting production processes at the radiochemical plants of the plutonium complex. Here fundamental questions of radiochemistry, separation of transuranic and rare-earth elements, and the search for uranium raw materials were solved. The institute actively worked on the development of various methods of ultrasound elemental analysis, on the search for new methods of separation and concentration of substances, and on searching for strategic metals in nature and methods of their extraction.

The institute was the birthplace of the national school of isotope geochemistry.

Isotope studies play a key role in creating new geological and cosmological concepts, understanding geochemical and cosmochemical processes, and their dating in geological time. The institute was at the origin of this method and contributed to the development of the theory of isotope effects and the creation of new methods in isotope geochronology. Academician A. P. Vinogradov organised the country's first laboratory to study the behaviour of isotopes in natural processes.

The thermodynamic isotope factors of organic compounds have been calculated for the first time. The concept of intramolecular isotope effects has been introduced. The method of isotopic bonding numbers has been developed, which allowed the theoretical estimation of isotopic characteristics of complex organic compounds and biopolymers, including lipids, carbohydrates, peptides. The theory of biological isotope fractionation has been developed. In addition, the geochemistry of isotopes of carbon, oxygen, and sulfur has been classically studied. New data characterising the main stages of evolution of the Earth's crust in various regions have been obtained with the help of radioisotope dating methods. In stable isotope fractionation studies, new methods have recently been developed to estimate equilibrium isotope separation constants based on the use of thermodynamic perturbation theory.

Vernadsky viewed the Earth as a planetary body to be studied in connection with cosmic phenomena. With the advent of the space age, the institute was at the forefront of lunar and planetary matter exploration. The **foundations of cosmochemistry, geochemistry, and comparative planetology** were laid down at Vernadsky Institute**.** The role of cosmic rays and nucleogenesis processes, chemical and mineralogical composition of meteorites, the phenomenon of impact cratering on the planetary surface were studied in detail. The institute provided scientific instruments for the study of extraterrestrial matter (gamma-ray spectrometers, X-ray spectrometers, mass spectrometers, neutron detectors, gas analyzers, etc.), which were installed on the first spacecrafts heading for the Moon and Venus. For the first time in the world, the chemical composition of the rocks of the Moon (1966), Mars (1975, 1988), the atmosphere and rocks of Venus (1967, 1972) was determined at the institute; the institute compiled the world's first atlas of the surface of Venus (1991). Samples of the lunar soil, delivered by the Soviet automatic interplanetary stations Luna 16, Luna 20, and Luna 24, have been transferred to the institute and are still being stored under special conditions.

The institute has a Committee on Meteorites of the RAS and holds the oldest collection of meteorites, comprising over 3250 unique species and more than 20000 samples. There is permanent ongoing work to increase the collection through organising expeditions and outreach programs.

New methods have been developed for the **reconstruction of chemical composition, mineral structure, and thermal regime of planets** based on a set of geochemical, petrological, and geophysical data. Geochemical and geophysical models of the internal structure of the Earth, Mars, the Moon, Io and the ice satellites of Jupiter's Europa, Ganymede, and Callisto have been constructed. Using data on the seismic sounding of the Moon, received in the Apollo expedition, it was possible to model the chemical-mineralogical structure of the Moon's lower mantle and to estimate the size of the Moon's core ($\sim$300–320 km).

Original algorithms based on which the numerical simulation of the internal structure of spatially inhomogeneous dust fractal clusters as a basis for the formation of primary solids have been developed. Growth of such bodies under collisions taking into account the kinetic energy of interactions and elasticity up to the size of planetesimals is studied. Migration of the matter in the modern Solar System and the forming Solar System, in comparison with the planetary systems of the single stars, has been simulated. The formation of satellite systems embryos, including the Earth and Moon embryos, at the stage of sparse condensations, has been studied.

Together with scientists from the USA, the **geological structure of Venus, Mars, and small bodies of the Solar System** was investigated, based on geological and morphological analysis of TV images of these planets and infrared spectrometry data. Traces of geological processes on the surface of Mars involving water were revealed.

The determination of long-lived ^{54}Mn, ^{22}Na, ^{26}Al isotopes in meteorites resulting from the influence of hard galactic cosmic rays has established patterns of change in the density of this radiation in circumsolar space.

The institute has created **a new geochemical concept of the Earth's formation** and the initial stages of its evolution, ideas about the multistage nature of the formation of the Earth's core and its influence on the chemical differentiation

of the Earth, the redox state of the mantle, and the composition of degassed products of the planet. The concept reconstructs the geochemical environment of the origin of life in the early stages of the Earth's evolution.

A significant place in the institute's work is occupied by **research on ocean geochemistry and the ocean floor**. Numerous marine expeditions have yielded important data on ocean floor structure, geochemical and biogeochemical processes taking place in marine waters and sediments, and generalised extensive material on seabed geomorphology, isotope organic geochemistry, and sediment metallogeny.

Studies of the crystalline basement of the ocean floor are aimed at determining the composition of the oceanic mantle and learning the underlying processes of formation and movement of the Earth's matter, **conditions of magma formation and magmatic differentiation in complex dynamic conditions of mantle convection**, movement of lithospheric plates, and exchange of matter in the crust-mantle Earth system under the influence of hot mantle jets. The significance of recycled oceanic crust in mantle magmatism has been proved, compositions and models of mantle magma formation over subduction zones have been established, and P–T conditions for metamorphism of oceanic crust rocks have been revealed.

The quantitative side of crustal recycling is still poorly understood. Together with foreign colleagues, the presence of young crustal material of Phanerozoic age in the mantle sources of the Hawaiian magmas was established. This made it possible to estimate the **rate of crustal material recycling** in the Earth's mantle, which was 1–3 cm/year.

A series of ecological voyages to the northern seas revealed patterns of man-made radionuclide distribution in marine and coastal waters and bottom sediments. A peculiarity of the **radioecology of the Russian Arctic** is that the Arctic waters of the Kara Sea, the Ob, and Yenisei rivers, in the hydrographic network of which the giants of the Russian radiochemical industry are located, flow into the Arctic. In addition, nuclear tests have been carried out on Novaya Zemlya island. Radioecological mapping of the Kara Sea was carried out on several expeditions. The peculiarity and uniqueness of this work was that the mapping was carried out simultaneously with biogeochemical research. It was shown that radionuclides in the Kara Sea does not exceed permissible values. This is important in connection with the concerns voiced in the press about the dangerous contamination of the Russian Arctic.

A new concept of development and growth of alkaline magmatism in the Earth's history is proposed. Its emergence at the turn of 2.5–3 billion years is associated with a change in the geodynamic regime of the planet, determined by the change of plume tectonics to plate tectonics, mantle oxidation and activation of large-scale mantle metasomatism. Geochemical studies of alkaline and carbonatite magmatism of the Earth have led to a theory of formation of related rare-metal deposits. At the quantitative level, the **potential of strategic metals of alkaline complexes of East Fennoscandia and Polar Siberia was established** and the complexity of rare-earth ores for their industrial use was evaluated. Rare earth elements, the connection of carbonatites with the African zone of generation of deep plumes at the core-lower mantle interface, were shown for the first time using a modern model of absolute paleotectonic reconstructions.

The institute has contributed to the development of a new direction in geochemistry related to the elucidation of the **dependence of geochemical processes on changes in the redox state of planetary matter** during its chemical differentiation. Evidence of significant variations in mantle fluid compositions has been obtained as a reflection of changes in oxygen balance during formation of the Earth's metallic core, melting, and the evolution of the planet's geodynamic regime.

Fundamental, experimental, and theoretical studies of **chemical differentiation of magmas** during their crystallization, liquation of silicate fluids, and formation of fluids were carried out. Models of magma formation during adiabatic decompression of deep rocks were developed, processes of magma degassing during their ascent and crystallization were studied. For the first time, data on the influence of fluids on physical and chemical properties of magmatic melts, magmatic and metamorphic rocks of the lithosphere (viscosity, density, electrical conductivity, elastic wave velocity) at high temperatures and pressures were obtained.

Consideration of the **evolution of the Earth's geochemical reservoirs**, its geosphere in an interconnected dynamic relationship is the starting point of several concepts developed at the institute. These include ideas on the regularities of the structure and geochemical evolution of the Earth's sedimentary shell, the evolution of the composition of the Earth's crust, the ocean, and the atmosphere.

For the first time, **lithological and paleogeographic maps** at 1:20,000,000 scale have been produced for the Neo- and Eopleistocene of Eurasia, including the Russian Arctic. Quantitative parameters were obtained for the evolution of sedimentation of plain and mountain areas, including important genetic types of continental sediments.

Scientists of the institute contributed significantly to **the creation of experimental and thermodynamic foundations of hydrothermal processes**, to the elucidation of physical and chemical conditions for the concentration of ore elements in the lithosphere, in the formation of magmatic fluids, and in the transformation of sedimentary rock containing kerogen.

The institute is the country's leader in the **geochemistry of organic matter and the geochemistry of carbon,** whose behaviour most profoundly reflects the interaction of living

and non-living nature. A theory of biological isotope fractionation was created, and molecular isotope criteria for the study of processes in organic and petroleum geochemistry were developed. Regularities of carbon isotope distribution in diamonds have been revealed, and models of diamond formation have been developed. Patterns of changes in the carbon isotope balance of the biosphere during various geological epochs have been established. The isotope balance of carbon in the biosphere at various geological epochs has been determined. A new concept of origin and evolution of life has been proposed, according to which the key role in the transition from the primary organic compounds to the pre-biological and then to the biological evolution was played by the adenosine triphosphate (ATP) molecule. These processes are thought to have required a highly reductive environment in the early stages of Earth's evolution.

Biogeochemical studies started by Vernadsky led to the development of the theory of formation and evolution of biogeochemical provinces, the creation of geochemical ecology, the teachings on the interaction of organisms and their communities with the geochemical environment, on the material and energy interaction of the structural parts of the planetary ecosystem of the biosphere.

Fundamental studies of evolutionary processes in the biosphere in the modern period of anthropogenic loads and climate warming, including mechanisms of self-organization of landscapes, biogeochemical adaptation of organisms and ecosystems both in the period of increasing and decreasing pollution, are developed. The state of small lakes in a wide range of natural zones (from tundra to steppe) as an indicator of global dispersion of elements and substances has been proposed. The processes of eutrophication and acidification, forms of elements migration, their bioavailability, and ecotoxicity in natural environments were studied.

Regularities of formation of different-scale fields of technogenic radionuclide contamination in different natural zones have been established. Landscape mechanisms of transformation of contamination fields and migration of chemical elements in the composition of micro- and nanoparticles are determined.

The institute was actively involved in setting up and conducting **radiation, radiogeochemical, and radioecological studies** at nuclear disposal sites, studying the consequences of nuclear tests and radiation accidents in the South Urals and at the Chernobyl NPP, developing methods of landscape geochemical and radioecological mapping, radioecological monitoring of contaminated areas and water areas, modelling of behaviour and prediction of radionuclide migration in the environment and food chains, decision-making support methods.

The institute works on justification and support of **technological processes at nuclear fuel cycle facilities, radioactive waste management**, and the **development of new radiopharmaceutical forms**.

The behaviour of several transuranic elements in unusual oxidation states has been investigated, which has enabled the development of new methods for their isolation, separation, and determination. The scientific basis for new technologies of spent nuclear fuel reprocessing was developed, including separation of fissile uranium and plutonium for their return into the fuel cycle, fractionation of resulting radioactive waste for separate handling of their components. New materials are proposed: aluminous-iron-phosphate glass matrix and mineral-like magnesium-potassium-phosphate matrix for radioactive waste immobilization. Their effectiveness and manufacturability for the long-term storage of solidified wastes are shown. The prospects of using carbon nanomaterials (nanodiamonds, nanotubes) for immobilization of some radionuclides without carriers for the purposes of nuclear medicine have been shown. Scientific bases of the creation of a new class of structural materials for nuclear power engineering, low-activated or with accelerated decay of induced radioactivity, have been developed.

The foundations of the post-war national school of analytical chemistry were laid within the walls of the institute with the participation of academicians A. P. Vinogradov and I. P. Alimarin and its principles and objectives were formulated. The institute became the leading organisation in the country in **analytical chemistry, development of new analytical methods for the study of chemical composition and transformation of substances of various nature** (extraterrestrial, natural, artificial, and industrial materials). The first Russian mass-spectrometer (1948) which allowed to carry out pioneer work in isotope geochemistry, **the first studies on neutron activation analysis**, one of the first studies on **voltammetry**, new solutions in the field **of spectral methods of analysis**, developed efficient **methods of concentration and separation** of substances enabling to improve selectivity and accuracy of determinations of chemical elements and compounds in a wide range of concentrations and thermodynamic states. Efficient **arsenazo-II and III** reagents successfully used for the determination of uranium, thorium, plutonium, and other elements have been synthesised. Theoretical studies in **molecular spectroscopy and quantum chemistry** have led to the creation of the new scientific area of mathematical chemistry. Theoretical statements were implemented as expert systems, which were widely spread. The general theory of chemical reactions of complex molecules has been developed. Based on the created methods for the calculation of spectra, a general theory for the analysis of substances by their spectra without the use of samples of standard composition has been proposed. The principal importance of the multiplicity of isomeric structures of molecules in the formation of the molecular world has been shown.

New sorption methods of **metals extraction from seawater and separation of rare earth elements from concentrated phosphoric acid** based on the original acid retention method are proposed. Technological systems for wastewater treatment, including the organisation of stationary self-sustaining processes of softening—desalination of saline water, have been developed. Efficient methods for determining **gas-forming impurities** in metals and inorganic materials have been developed.

Theoretical approaches to the description of the equilibrium and kinetics of adsorption and ion exchange processes have been proposed and **computer programmes** for the modelling of high-performance gas and ion chromatography with the prediction of optimal solutions have been created.

New extraction **methods for concentrating, separating non-ferrous, rare, noble metals, and** combined methods for their determination have been proposed. New methods of synthesis, including microwave methods, of magnetic nanosorbents, including those modified with functional components, have been developed.

Methods for the concentration of a wide range of substances (inorganic, organic, and biological) using solid-phase extraction, carbon nanomaterials, and magnetic nanosorbents have been proposed.

New complex approaches to the problem of studying the **chemical composition, transformation, and migration of nanoparticles** and mobile forms of elements in the environment (urban dust, industrial impact zones, volcanic ashes) using the methods of step ultrafiltration, rotating spiral columns, etc. are proposed.

New sample preparation and analysis methods have been developed for a wide range of analysed matrices (rocks, ores, environmental samples, oil and petrochemical products, biological and medical samples).

A group of highly sensitive (tens of femtograms) high **resolution mass spectrometric methods of analysis of organic compounds** based on soft laser ionization (without decomposition) of the compounds being detected using semiconductors with inducing electron transfer as a matrix (SALDI, LETDI) has been developed.

New sources of atomisation and excitation based on electrolyte cathode discharges have been developed: droplet-spark discharge and in-channel boiling. They require low energy to excite the emission spectrum, which implies a miniaturised and mobile design. The device is designed for medical diagnostic purposes.

A multi-sensor oxythermographic unit was developed with the possibility of simultaneously recording oxygen consumption and carbon dioxide emission. The unit has been used to monitor the condition of river waters.

Today the research work at the Vernadsky Institute is concentrated in 25 laboratories, forming five departments: Geochemistry, Analytical Chemistry, Biogeochemistry and Ecology, Planetary Sciences, and Marine Research (for more details, see the second part of the introduction).

The research is carried out in the following areas:

- Isotopic geochemistry and geochronology;
- Cosmochemistry, cosmogony, meteoritics, lunar and planetary sciences, comparative planetology, and the development of tools and methods for the investigation of extraterrestrial matter along with tektites, impactites, and terrestrial impact craters;
- Experimental and theoretical modelling of geochemical processes in the Earth's deep zones, the geochemistry of magmatism and metamorphism;
- Origin and evolution of the biosphere, organic geochemistry, biogeochemistry, carbon geochemistry;
- Geoecological and biogeochemical studies; ecological-geochemical studies of aquatic and terrestrial ecosystems, oceanographic and marine geochemical and geophysical studies, pollution monitoring, environmental analysis, and forecasting;
- Geochemistry of sedimentary cover, hydrochemistry; geochemical ecology; geological-geochemical and eco-geochemical studies of the world ocean floor;
- Geochemistry of mineral deposits (ore elements, precious metals, oil and gas, diamonds) and the development of prospecting methods;
- Analytical chemistry, chemometrics and mathematical modelling of chemical processes, new physical, physico-chemical methods of analysis of substances of different nature, methods of separation and concentration; new reagents and sorbents for analysis, extraction of valuable components from industrial and natural media;
- Analytical chemistry of radioactive, rare, and noble elements, radioecological monitoring methods, radioactive waste management, improvement of various stages of the nuclear fuel cycle, creation of novel forms of radiopharmaceuticals;
- Development and prototyping of analytical instruments, sensors for various applications;
- The institute is a co-founder of two international scientific journals, which are published in both Russian and English languages: The Journal of Analytical Chemistry and Geochemistry International (see below);
- The institute constantly organizes national and international conferences, seminars, and workshops open to international participation (see below).

The **Journal of Analytical Chemistry** (since 1946, Photo 1) is an international peer-reviewed journal that covers theoretical and applied aspects of analytical chemistry; it informs the reader about new achievements in analytical methods, instruments, and reagents. Ample space is devoted

to problems arising in the analysis of vital media, such as water and air. Consideration is given to the detection and determination of metal ions, anions, and various organic substances. The journal is indexed in Scopus and Web of Science and welcomes manuscripts from all countries in the English or Russian language.

Geochemistry International (since 1956, Photo 2) is a peer-reviewed journal that publishes articles on fundamental problems in cosmochemistry; geochemistry of magmatic, metamorphic, hydrothermal, and sedimentary processes; experimental geochemistry; isotope geochemistry; organic geochemistry; biogeochemistry; and chemistry of the environment. The journal publishes regular articles, reviews (normally solicited by the editors), short communications, letters to the editor, and replies to them. The journal is indexed in Scopus and Web of Science and welcomes manuscripts from all countries in the English or Russian language.

National and international conferences, workshops, and seminars organized by the institute include (Photo 3 and 4):

- Annual conference **Vernadsky Readings** takes place on March 12 every year (over 60 meetings have been held).
- All-Russia **Annual Seminar on Experimental Mineralogy, Petrology, and Geochemistry** (named **Khitariada** after and in memory of N.I. Khitarov, see Annex I) is held annually (56 meetings have been organized since 1960).
- The conference **Biogeochemistry Readings in memory of V. V. Kovalsky** is held annually.
- **Congress of Russian Analytical Chemists** is held every four years. The IV Congress took place from September 25 through October 1, 2022.
- **Symposium on Isotope Geochemistry named after A. P. Vinogradov** is held once per 4 years (22 symposiums have been organized since 1966).
- **Conference on Physico-Chemical and Petrophysical Research in Earth Sciences** is regularly organized (it was annual in the past).
- Series of conferences on **Magmatism of the Earth and related deposits of strategic metals** had been regularly organized (35 meetings have been held).
- **Simposium on Separation and Concentration in Analytical Chemistry and Radiochemistry** is held once per 2–3 years.
- **The 81st Annual Meeting of the Meteoritical Society (MetSoc)** was hosted in Moscow on July 22–26, 2018, and united over 300 international participants.

In the next part of the introduction, the readers will find detailed information on the laboratories and departments of the institute. The introduction preceeds the collection of articles, divided into four broad categories. This collection gives a fairly complete picture of the research currently being carried out at the Vernadsky Institute and may be of interest to a wide range of specialists. Photos 5, 6 illustrate a range of exterior views of the Vernadsky Institute RAS.

Photo 1 Cover of the Journal of Analytical Chemistry

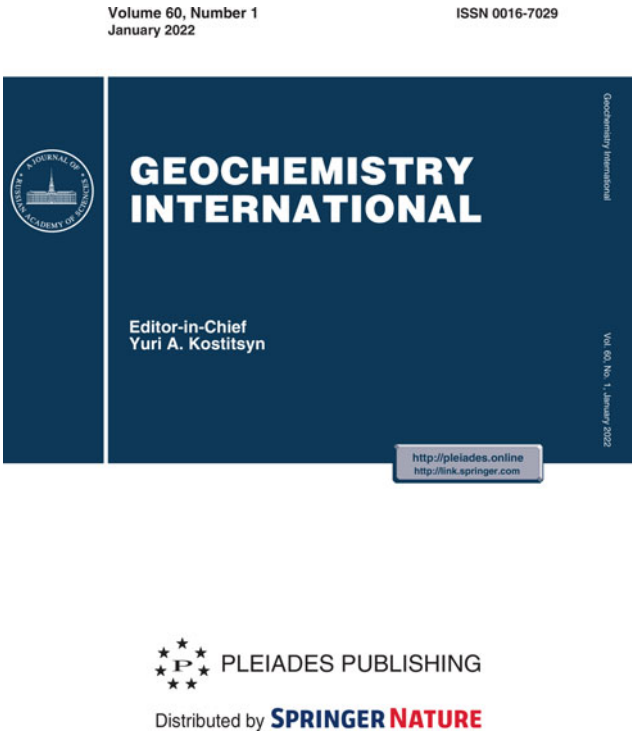

Photo 2 Cover of Geochemistry International

Photo 3 Academician Valery L. Barsukov during a meeting in his office of the director of the institute

Photo 4 Academician Erik M. Galimov during a press conference in the conference hall of the Vernadsky Institute, dedicated to the Chelyabinsk meteorite fall (2013)

2 Departments and Laboratories of the Vernadsky Institute

Photo 5 The main entrance of the Vernadsky Institute

Department of Geochemistry

Head of the Department
Petr S. Fedotov
Doctor of Chemistry,
Deputy Director of Research for the Vernadsky Institute RAS
Email: fedotov_ps@mail.ru

The department of geochemistry currently includes nine laboratories:

- Laboratory of Geochemistry and Analytical Chemistry of Noble Metals
- Laboratory of Geochemistry of Magmatic and Metamorphic Rocks
- Laboratory of Geochemistry and Ore Content of Alkaline Magmatism
- Laboratory of Isotope Geochemistry and Geochronology
- Laboratory of Modeling of Hydrogeochemical and Hydrothermal Processes
- Laboratory of Geochemistry of the Earth's Mantle
- Laboratory of Geochemistry of Nanoparticles
- Laboratory of Crystal Chemistry
- Laboratory of Carbon Geochemistry.

In the department of geochemistry, research is carried out on the following directions:

- chemical differentiation of the early Earth's mantle during its melting, segregation of the metallic core, and formation of silicate and outer, volatile component enriched, envelopes of the planet;
- geochemistry of magmatic and metamorphic processes, their role in the formation and evolution of the oceanic and continental lithosphere, the relationship of magmatism with the geodynamic regime of the Earth's deep zones;
- geochemistry of isotopes, their prevalence and behavior in the processes of formation of terrestrial and extraterrestrial matter; determination of the isotopic age of rocks and ores, the oldest rocks of the Earth's crust;
- origin, evolution, and ore content of alkaline magmas in different geotectonic settings of oceans and continents, geochemistry of rare and disseminated elements during differentiation of alkaline and carbonatite magmas, formation of supergiant rare-metal and phosphate deposits;
- geochemistry of carbon and organic geochemistry, processes of diamond formation, prevalence and forms of fossil organic matter in the Earth's interior, oil and gas formation;
- experimental and thermodynamic modeling of geochemical processes in hydrochemical and ore-forming water-rock-gas systems, mineralogical and thermobarogeochemical studies of hydrothermal deposits;
- geochemistry and analytical chemistry of platinum group elements (PGEs) and gold, their migration behaviour in natural systems, deposition mechanisms on geochemical barriers, the role of PGEs and other toxic elements in eco-geochemical processes.

Photo 6 Memorial plaque in honor of the memory of Academician A.P. Vinogradov, founder and first director of the institute. The plaque is installed on the left side from the main entrance to the institute

Laboratory of Geochemistry and Analytical Chemistry of Noble Metals

Head of the Laboratory
Irina V. Kubrakova
Doctor of Chemistry
Email: kubrakova@geokhi.ru
Website: http://portal.geokhi.ru/sites/eng/lab11
Articles by lab members in this volume: Chapters 4 and 35

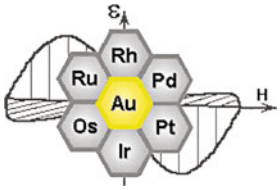

The laboratory was established in 1996. Its first head Professor, Doctor of Chemistry G. M. Varshal, created the direction to study the interaction of organic substances of humic nature with metal ions and the role of this interaction in geochemical processes. Since 2004 the laboratory has been headed by Dr. I. V. Kubrakova. Currently, the laboratory consists of 7 employees, including 1 Doctor of Sciences and 3 Ph.D.'s.

Main areas of research:

- contents, forms of occurrence, and geochemical behavior of noble metals (NM) in natural and natural-technogeneous environments;
- role of organic matter in transport and accumulation of platinum group elements (PGE) and gold;
- environmental aspects of the development of NM deposits;
- new methods for studying contents and speciation of trace elements in natural objects.

Methods:

Study of the composition of natural objects by ICP-AES, ICP-MS, ETAAS, UV-vis-spectrophotometry, chromatography; determination of the initial forms of elements by selective leaching; model sorption experiments with individual forms of elements and synthesized and/or isolated rock components (iron and manganese oxyhydroxides, fractions of dissolved and sedimentary organic matter, natural colloids, individual sedimentary layers, etc.); calculation of the distribution of dissolved and sorbed forms of elements; static and dynamic experiments on the kinetics of leaching of elements from rocks.

Equipment:

- IRIS Intrepid Duo ICP-AES spectrometer (Thermo Electron, USA); ETAAS Solaar MQZ spectrometer (Thermo Electron, USA); EXPEC 6500 ICP-AES spectrometer (China, a demonstration device of Labtest company).
- Microwave systems for sample preparation and synthesis of new materials (MARS 6, Discover, etc., CEM Corp. (USA) within the demonstration center organized by GC "Interanalyt" in the lab). Spectrophotometric (UV 1800), spectrometric (atomic absorption) (AA7000), and chromatographic (LC 20) equipment from Shimadzu Corp. (Japan) is also present in the center.

Main achievements:

- A methodology has been developed to investigate the geochemical behavior of PGE and gold in oceanic and freshwater settings. The migration ability of PGE was shown to be determined by the stable ($lgK_{st} \sim 6–9$) compounds with the humic matter, hydroxyl, and thiosulfate ions, as well as by nanosized species of PGE.
- Nanosized NM stabilized by humic substances possess the greatest sorption affinity in relation to components of

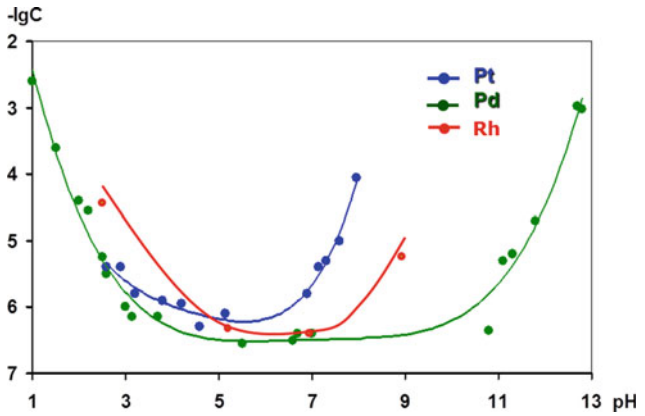

Fig. 1 The effect of acidity of aqueous solution on solubility of noble metal hydroxides

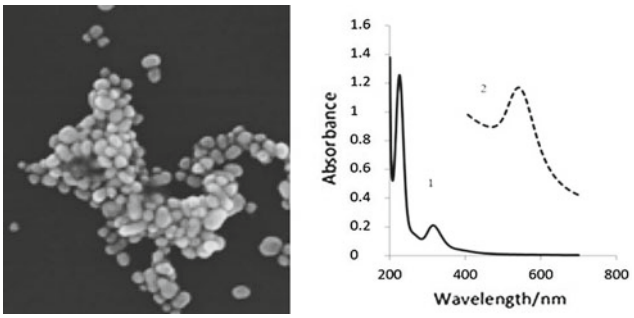

Fig. 2 TEM image of AuNPs and absorption spectra of molecular (1) and nanosized (2) forms of gold, stabilized with asphaltenes

geochemical barriers and are efficiently concentrated by them. The regularities of PGE transfer by marine, river, and technogeneous suspended matter are established. Significant differences in migration behavior of individual PGE, which determine the fractionation of PGE in natural conditions (Pd > Pt > > Rh), are revealed. A qualitative model of Pt transport and coprecipitation in oceanic conditions is proposed.

- Formation of NM nanoparticles resulting from redistribution of chlorides between aqueous saline solutions and the immiscible organic phase, followed by metal reduction at $\geq$160 °C, was experimentally confirmed on the example of gold. Model nanosized Au, Pd, Pt, stable up to T $\geq$ 200 °C, were synthesized in the presence of geopolymers. The possibility of separate determination of complex and nanosized forms of NM in organic systems by their chromatographic separation and spectrometric detection was shown.

The obtained results allow considering nanosized NM, which provide the most efficient mass transfer of NM, and complex compounds of NM with organic ligands as the main transfer forms of these metals in carbon-containing fluids and hydrocarbons—as their important transporting agent.

- Based on experimental and calculated data on the water-rock interaction in conditions of the oxidative dissolution of sulfides, the forecast of accumulation of toxic elements and environmental danger of technogenic pollution in the zones of development of some NM deposits were made.
- New efficient methods of instrumental investigation of waters, rocks, technogenic solutions, and bio-objects for the content of a broad spectrum of elements in the range of 0.00n-n μg/g were proposed for analytical support of environmental studies. Highly dispersed magnetic sorption materials, promising for the determination of traces of toxic components in aqueous media, were synthesized, investigated, and applied (Figs. 1, 2 and 3).

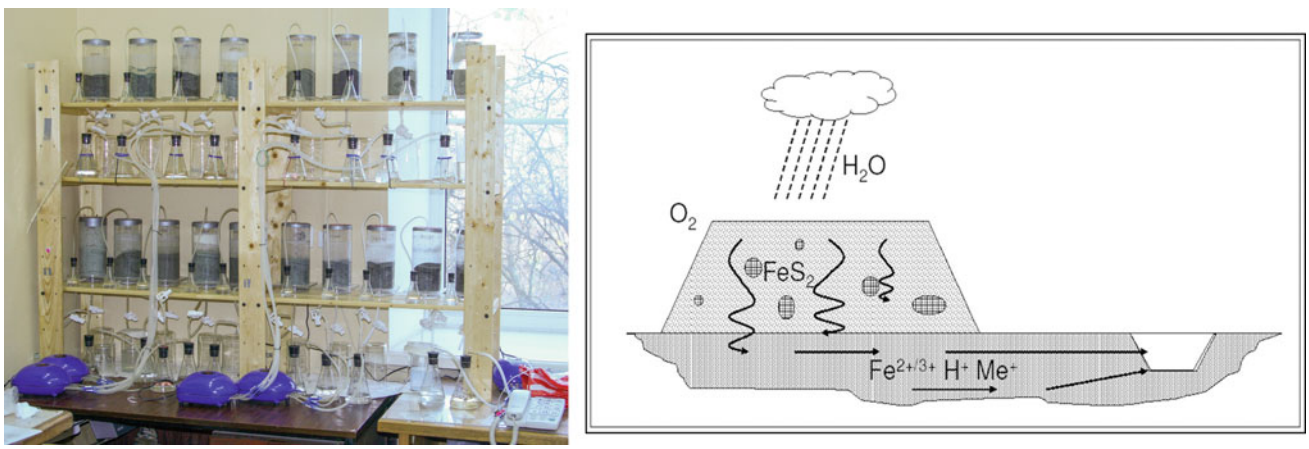

Fig. 3 Acid rock drainage in nature (scheme) and in a laboratory experiment (photo)

Laboratory of Geochemistry of Magmatic and Metamorphic Rocks

Head of the Laboratory
Sergey A. Silantyev
Doctor of Geological and Mineralogical Sciences
Email: silantyev@geokhi.ru
Website: http://portal.geokhi.ru/sites/eng/lab12
Articles by lab members in this volume: Chapter 2

The laboratory was established in 1952 by Professor V. I. Gerasimovsky. From 1979 to 2005, it was headed by Professor L. V. Dmitriev. From 2006 to 2017, the laboratory was headed by Academician A. V. Sobolev. Currently, 21 research workers work at the laboratory, including 5 Doctors of Sciences, 6 Ph.D.'s, 3 Ph.D. students, and 3 engineers.

Alexander V. Sobolev,
Academician of RAS

Main objects of study

The whole range of geodynamic settings realized during the formation of the Earth's lithosphere (Fig. 4).

Research methods

Geological exploration of the key objects; the use of highly accurate chemical and isotopic data; high-precision local microanalysis of rocks and minerals; application of physical and chemical methods of process description and mathematical modeling; studies of inclusions in minerals.

Interdisciplinary studies

The research is conducted at the interface between geochemistry, petrology, geodynamics, and geophysics.

International cooperation

Joint research and publications with scientists from the USA, Canada, France, Germany, England, Italy, Serbia, Australia, and Japan; Participation in major international projects: Deep Carbon Observatory, InterRidge.

Main achievements in recent years

It was found that Archean komatiite melts are significantly enriched in Cl and H_2O relative to the elements of similar incompatibility with source mantle (Sobolev et al. 2016, 2019; Asafov et al. 2020). The recycled Cambrian oceanic crust in the mantle source of the Hawaiian magmas was established (Sobolev et al. 2011a). A model of rapid destruction of the lithosphere leading to the formation of the Siberian Trap Province and the Upper Permian mass extinction was developed (Sobolev et al. 2011b). The main factors controlling magmatic events and associated nickel-sulfide mineralization in the Norilsk region (Russian Federation) have been reconstructed (Krivolutskaya 2016). The structure of the lithosphere section below the volcanic centers of Zhokhov and Vilkitsky Islands (Eastern Arctic Basin) from the surface to a mantle depth of about 60 km has been reconstructed (Silantyev 2019).

Investigations of geochemical peculiarities of volcanic glasses from proximal pyroclastics belonging to the largest explosive volcanic eruptions in Kamchatka have been made. The unique database includes about 300 explosive eruptions, which occurred in Kamchatka from the Miocene up to recent times (Portnyagin et al. 2020). A unique technique has been developed to homogenize melt inclusions in olivine at high H_2O pressure to estimate the initial volatiles content in island-arc magmas (Mironov et al. 2015). The origin conditions of ultramafic rocks of different ophiolitic and non-ophiolitic massifs were established (Bazylev et al. 2013; Batanova et al. 2014).

The main factors determining the structure and composition of the Oceanic Core Complexes and affecting the geochemical specific of oceanic hydrothermal systems have been established (Silantyev et al. 2016). The composition of magmatic melts related to the evolution of Mesozoic mantle plumes, which initiated the split of Gondwana, was reconstructed (Sushevskaya et al. 2009, 2021); The new

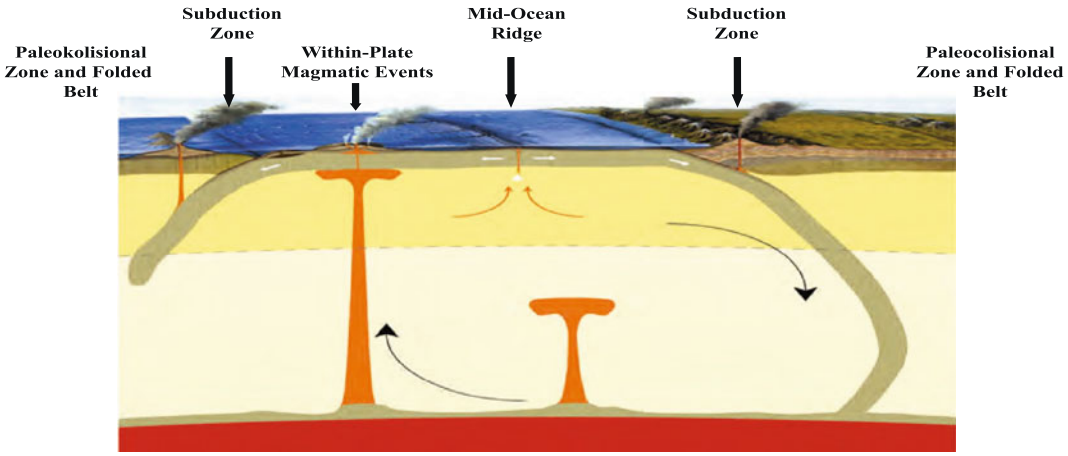

Fig. 4 Scheme of geodynamic settings of the Earth, studied by the laboratory

ultra-precise electron microprobe analytical method and international reference material of olivine have been developed (Batanova et al. 2015, 2020).

A new oxybarometer for island-arc basalts based on the distributions of Vanadium between Olivine and melt has been developed (Shishkina et al. 2018);

From 2010 to 2020, the laboratory published 120 papers, including 5 in Nature, 1—in Nature Communications, 1—in Nature Geosciences.

Publications:

E.V. Asafov, A.V. Sobolev, V.G. Batanova, M.V. Portnyagin (2020) Chlorine in the Earth's Mantle as an Indicator of the Global Recycling of Oceanic Crust. *Russian Geology and Geophysics*, 61, 937-950.

V.G. Batanova, Z.E. Lyaskovskaya, G.N. Savelieva, A.V. Sobolev (2014) Peridotites from the Kamchatky Mys: Evidence of Oceanic Mantle Melting near a Hotspot. *Russian Geology and Geophysics*, 55, 1395-1403.

V.G. Batanova, A.V. Sobolev, D.V. Kuzmin (2015) Trace element analysis of olivine: High precision analytical method for JEOL JXA-8230 electron probe microanalyser. *Chemical Geology*, 419, 149–157.

V.G. Batanova, J.M. Thompson, L.V. Danyushevsky, M.V. Portnyagin, D. Garbe-Schönberg, E. Hauri, J.-I. Kimura, Q. Chang, R. Senda, K. Goemann, C. Chauvel, S. Campillo, D.A. Ionov, A.V. Sobolev (2019) New Olivine reference material for in-situ microanalysis. *Geostandards and Geoanalytical Research*, 43 (3), 453-473.

B.A. Bazylev, G.V. Ledneva, Ya.V. Bychkova, N.N. Kononkova, T.G. Kuz'mina, T.V. Romashova (2019) Estimation of the Content and Composition of Trapped Melt in Dunite, *Geochemistry International*, 57(5), 509-523.

B.A. Bazylev, G.V. Ledneva, A. Ishiwatari (2013) High-pressure ultramafics in the lower crustal rocks of the Pekul'ney complex, central Chukchi Peninsula. 2. Internal structure of blocks and ultramafic bodies, geologic and geodynamic setting of rock formation, *Petrology*, 21(4).

N.A. Krivolutskaya (2016) Siberian Traps and Pt-Cu-Ni Deposits in the Noril'sk Area. Springer-Cham, Heidelberg, New York, Dordrecht. London, 364 pp.

N. Mironov, M. Portnyagin, R. Botcharnikov, A. Gurenko, K. Hoernle, F. Holtz. (2015) Quantification of the CO_2 budget and H_2O-CO_2 systematics in subduction-zone magmas through the experimental hydration of melt inclusions in olivine at high H_2O pressure. *Earth and Planetary Science Letters*, 425, 1-11.

M.V. Portnyagin, V.V. Ponomareva, E.A. Zelenin, L.I. Bazanova, M.M. Pevzner, A.A. Plechova, A.N. Rogozin, D. Garbe-Schönberg (2020) TephraKam: geochemical database of glass compositions in tephra and welded tuffs from the Kamchatka volcanic arc (northwestern Pacific). *Earth System Science Data*, 12, 469-486.

T.A. Shishkina, M.V. Portnyagin, R.E. Botcharnikov, R.R. Almeev, A.V. Simonyan, D. Garbe-Schönberg, S. Schuth, M. Oeser, F. Holtz (2018) Experimental calibration and implications of olivine-melt vanadium oxybarometry for hydrous basaltic arc magmas. *American Mineralogist*, 103, 369-383.

S.A. Silantyev, N.S. Bortnikov, K.N. Shatagin, V.E. Bel'tenev, N.N. Kononkova, Ya.V. Bychkova, E.A. Krasnova (2016) Petrogenetic Conditions at 18°–20° N MAR: Interaction between Hydrothermal and Magmatic Systems. *Petrology*, 24 (4), 336-366.

S. Silantyev (2019) Neogene within-plate magmatism of De Long Islands: Footprint of young mantle plume of the Eastern Arctic Basin. Large Igneous Provinces trough Earth history: mantle plumes, supercontinents, climate change, metallogeny and oil-gas, planetary analogues (LIP—2019). *Abstract volume of the 7 International Conference, Tomsk, Russia,* 128-129.

A.V. Sobolev, E.V. Asafov, A.A. Gurenko, N.T. Arndt, V.G. Batanova, M.V. Portnyagin, D. Garbe-Schönberg, S.P. Krasheninnikov (2016) Komatiites reveal a hydrous Archaean deep-mantle reservoir. *Nature*, 531, 628–632.

A.V. Sobolev, E.V. Asafov, A.A. Gurenko, N.T. Arndt, V.G. Batanova, M.V. Portnyagin, D. Garbe-Schönberg, A.H. Wilson, G.R. Byerly (2019) Deep hydrous mantle reservoir provides evidence for crustal recycling before 3.3 billion years ago. *Nature*, 571, 555–559.

N.M. Sushchevskaya, B.V. Belyatsky, G.L. Leichenkov, and A.A. Laiba (2009) Evolution of the Karoo–Maud Mantle Plume in Antarctica and Its Influence on the Magmatism of the Early Stages of Indian Ocean Opening. *Geochemistry International*, 47(1), 1–17.

N.M. Sushchevskaya, A.V. Sobolev, G.L. Leitchenkov, V.G. Batanova, B.V. Belyatsky, A.V. Zhilkina (2021) Role of Pyroxenite Mantle in the Formation of the Mesozoic Karoo Plume Melts: Evidence from the Western Queen Maud Land, East Antarctica. *Geochemistry International*, 59(4), 357–376.

Laboratory of Geochemistry and Ore Content of Alkaline Magmatism

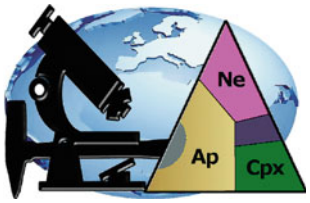

Head of the Laboratory
Lia N. Kogarko
Academician RAS,
Doctor of Geological and Mineralogical Sciences
Email: kogarko@geokhi.ru
Website: http://portal.geokhi.ru/sites/eng/lab14

Articles by lab members in this volume: Chapter 6

The laboratory was established based on the Laboratory of Magmatic Rocks Geochemistry in 1982. Currently, the laboratory has 17 researchers, including 1 Academician of RAS, 1 Corresponding Member of RAS, 3 D.Sc. and 7 Ph.D.'s.

The main task of the laboratory is to identify the conditions for the accumulation of strategic and noble metals (PGE, REE, Nd, Ta, Zr, Hf, U, Th) in the processes of differentiation of alkaline-carbonatite magmatism for the growth of the raw material base of Russia.

The most important results include:

- Based on the created data bank, the emergence of alkaline and carbonatite magmatism of the Earth somewhere around 3 billion years, and its activity, kept increasing during the evolution of the Earth. This is associated with a global change in the geodynamic regime and oxygen potential of the Earth, as well as the activation of large-scale mantle metasomatism. The proposed concept explains the growth of kimberlitic magmatism and the decline of its diamondiferous content during the evolution of the Earth.
- A model of the genesis of potassic magmatism was developed. It is shown experimentally that melting of subduction material with volatile components at 6–8 GPa (180–240 km) as a result of coesite or stishovite fractionation may result in melting of undersaturated alkaline melts. Preservation of jadeite pyroxene in the restite zone leads to forming melts with a high K/Na ratio. This mechanism allows us to explain the formation of alkaline rocks of island arcs.
- Based on the geological, petrological, and isotopic data (systems Rb–Sr, Sm–Nd, Lu–Hf, U, Th-Pb), geochemical models of the formation of superlarge deposits of strategic metals were developed. The principle of early cotectic saturation of alkaline magmas concerning an ore mineral as a necessary condition for forming magmatic deposits of strategic metals was developed. The new geochemical criterion of rare-metal loparite and eudialyte mineralization of the Lovozero superlarge deposit (Kola Peninsula) was proposed based on the change in the forms of these minerals separation (Fig. 5), and the patent was obtained.
- A quantitative model of concentration, fractionation of valuable strategic metals Zr and Hf- in the final products of differentiation of alkaline magmatic systems considered as a new source of rare-metal raw materials are constructed.
- The geochemistry of metasomatized mantle-source deposits of alkaline magmatism was investigated.
- It has been shown that the criterion of potential noble-metal specialization of alkaline-ultrabasic magmatic complexes of Polar Siberia is high values of oxygen fugacity, which provided accumulation of platinoids and gold in melting alkaline melts and their occurrence in the native state (Fig. 6).
- Based on experimental studies, several fundamental for geochemistry and ore formation of alkaline magmatism phase diagrams are constructed; distribution ratios of some strategic metals in the equilibrium mineral-alkali-carbonatite melt at high temperatures and pressures are determined.
- Stability fields of the chromium, titanium, and sodium concentration phases in the Earth's mantle (garnet,

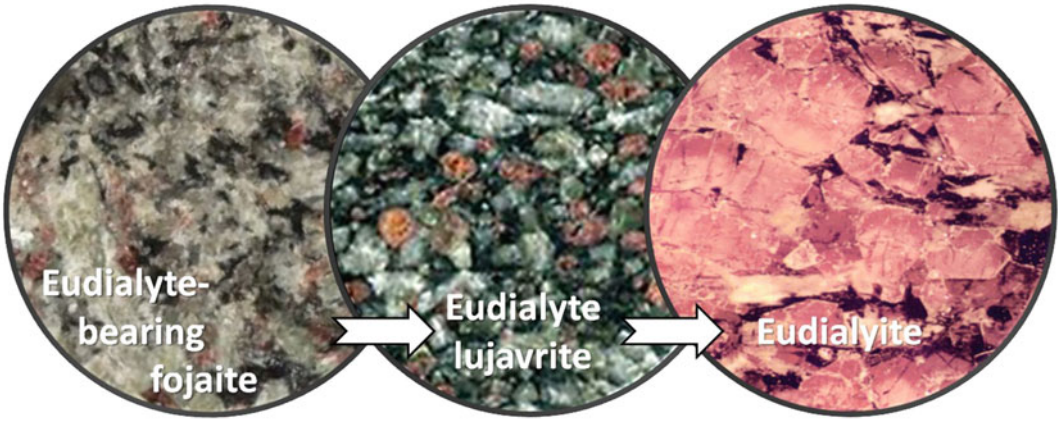

Fig. 5 Evolution of eudialyte crystal forms in alkaline rocks of Lovozero deposit

$MgSiO_3$ akimotoite/bridgmanite, high titanium bridgmanite, $MgCr_2O_4$ with post-spinel structure) are experimentally established; mechanisms of chromium, sodium, and titanium incorporation into the deep minerals are suggested, and the pressure dependence of their composition is shown.

- The new peculiarity of the geodynamic regime of the Earth has been established. Absolute paleotectonic reconstructions for Phanerozoic carbonatites have shown their connection with the global African region of mantle decompaction at the boundary between the lower mantle and core (Tuzo). The majority of kimberlites and large magmatic provinces are confined to the same area. This fact confirms the genetic connection of considered formations. The closest connection with the mentioned mantle heterogeneity is observed for ancient carbonatites as compared to young ones.
- 90 new mineral species have been discovered. Bases of genetic crystallochemistry and classification of important geochemistry agpaitic rocks and pegmatites containing groups of eudialyte, labuntsovite, hilairite, lamprophyllite, etc., minerals were developed based on the study of titano- and zirconosilicates, including new minerals.
- During the last 5 years, 500 papers have been published by the laboratory staff, 199 of which are published in leading Russian and international journals of VAK list and the editions indexed in Web of Science or Scopus databases.
- In recent years, 11 monographs have been published.

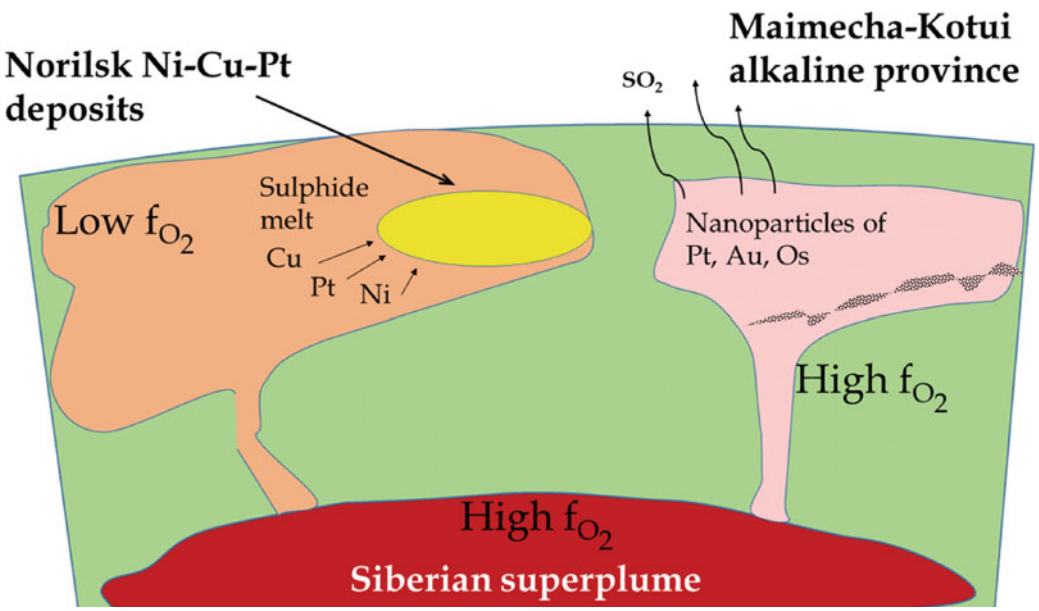

Fig. 6 Oxigen fugacity is the leading factor of native metal behaviour in the plume-related magmas

Laboratory of Isotope Geochemistry and Geochronology

Head of the Laboratory
Yuri A. Kostitsyn
Academician of RAS, Doctor of Geological and Mineralogical Sciences,
Former Director and current Scientific Advisor of the Vernadsky Institute
E-mail: kostitsyn@geokhi.ru
Website: http://portal.geokhi.ru/sites/eng/lab15

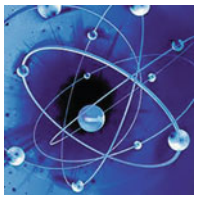

The laboratory was founded in 1949. The heads of the laboratory were A. V. Trofimov (1950–1954), A. P. Vinogradov (1954–1975), A. I. Tugarinov (1975–1977), Yu. A. Shukolyukov (1979–2001). Since 2002, the laboratory has been headed by Yu. A. Kostitsyn.
Currently, the laboratory consists of 18 employees, including 1 Academician of RAS, 1 Doctor of Sciences and 6 Ph.D.'s.

Main research directions include: Chemical and isotopic composition of the Earth mantle and the causes of its isotopic heterogeneity; rocks' and ores sources material origin and their formation processes; geochronology of the oldest rocks of the Earth's crust; thermal and impact history of meteorite parent bodies; geochemistry of noble gases, nitrogen, and carbon of extraterrestrial material; stable isotopes fractionation in natural systems; theory of stable isotope fractionation; simulation of isotope fractionation processes; assessment of isotope fractionation factors using the methods of γ-resonance scattering and inelastic neutron scattering; development of instruments and techniques for isotopic studies; a new direction—precise dating of magmatic, metasomatic, and metamorphic events.

Research methods

Geochemical and geochronological studies using Rb–Sr, Sm–Nd, U-Th-Pb, K–Ar isotopic systems of various rocks, minerals, and meteorites; multi-element chemical analysis by ICP-MS and laser ablation technique for U–Pb dating and in situ studies of the chemical composition of minerals; multi-isotopic (He–Ne–Ar–N_2–CO_2–H_2O) analysis of a fluid phase from rocks and minerals using the stepwise crushing method; a combination of stepwise crushing and stepwise oxidation techniques for studies of meteorites gas phase.

International cooperation

The laboratory collaborated with various organizations and individual scientists from different countries for many years. As the result of joint research with GEMOC ARC National Key Centre (Macquarie University, Sydney, Australia), the dynamics of continental crust growth throughout the Earth's history have been established. In cooperation with the Swedish Museum of Natural History (Stockholm), the investigations of the early Earth history, formation, and stabilization processes of the ancient crust were performed. In cooperation with the Institute of Earth Sciences of the University of Heidelberg (Germany), ^{40}Ar-^{39}Ar dating of meteorites and terrestrial rocks and study of noble gases isotope geochemistry and cosmochemistry were provided. Collaboration with The Open University (Milton Keynes, UK) resulted in isotopic studies of carbon, nitrogen, and noble gases in the terrestrial and extraterrestrial matter.

Main achievements

- Yu. A. Kostitsyn compared the results of studies of short-lived ^{182}Hf-^{182}W isotope systems with data on long-living U–Pb isotope systems for meteorites and terrestrial material and concluded that the formation of the Earth core could be long, lasting hundreds of millions of years. Based on the analysis of abundant isotopic data ($^{143}Nd/^{144}Nd$, $^{87}Sr/^{86}Sr$, $^{176}Hf/^{177}Hf$) for mantle rocks, Yu. A. Kostitsyn has established that the composition of the primitive Earth mantle differed from the composition of chondrites (Fig. 7). He also found that isotopic heterogeneity of the mantle rocks in Rb–Sr, Sm–Nd, Lu–Hf, U-Th-Pb systems statistically agrees with their chemical heterogeneity, which in turn is caused by magmatic processes in the crust-mantle system.
- E. V. Bibikova and collaborators have analyzed the results of own and published studies of the ancient Earth rocks and showed that there were at least three types of cratons with distinct age boundaries in Archean history.

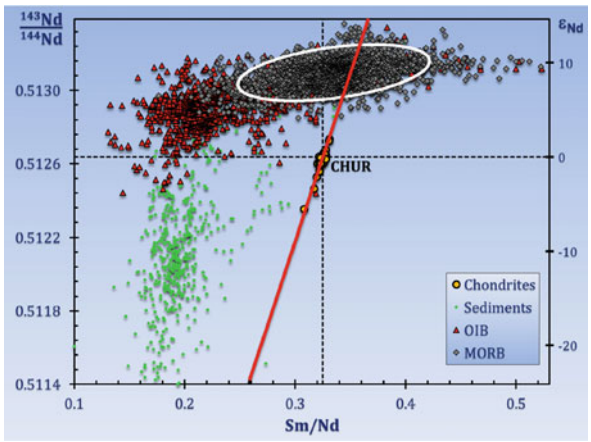

Fig. 7 The plot shows the present difference in Nd isotopic composition of chondrites and Earth-mantle rocks, that reflect the difference in Sm/Nd ratio between their sources

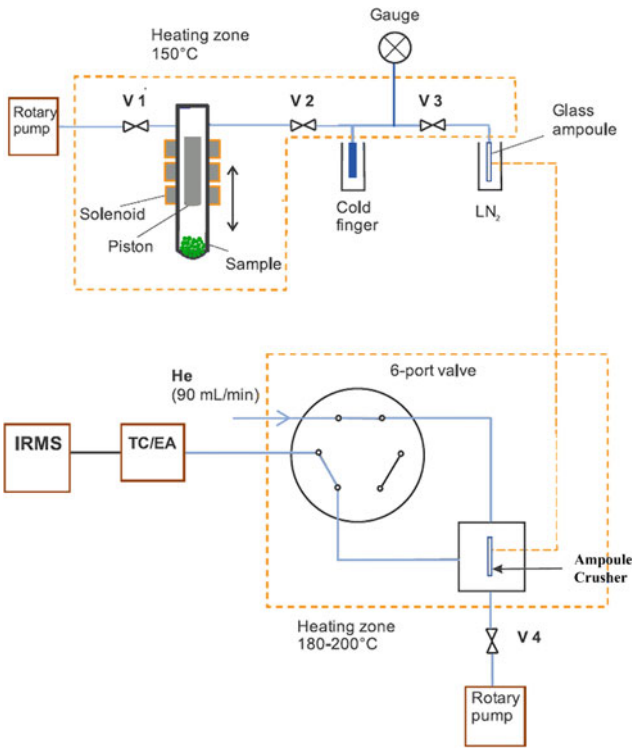

Fig. 8 A simplified scheme (modified after Buikin et al., 2020) of the instrumental complex for analysis of micro-quantities of gases from fluid/gas inclusions (H_2O, CO_2, N_2 and noble gases) in rocks and minerals using stepwise crushing. The complex consists of Gas Extraction System (top) and device for injection of micro-quantities of water into the high-temperature conversion elemental analyzer isotope ratio mass spectrometry (TC-EA/IRMS) system in a continuous helium flow (bottom)

According to these data, the Ukrainian Shield is similar in its evolution to the Pilbara and Kaapwala cratons, while the Baltic Shield is closer in evolution to the Superior Province (Canada).

- V. B. Polyakov has developed a technique for measuring the equilibrium isotopic fractionation from γ-resonance scattering data and estimated the scale of equilibrium fractionation of iron and tin isotopes on this basis.
- M. O. Anosova was the first who performed the in situ age determination of the lunar meteorite Dhofar-1442 using the U–Pb technique on zircon.
- A. I. Buikin and Yu. A. Nevinny created an original instrumental complex and techniques for analysis of micro-quantities of gases from fluid/gas inclusions (H_2O, CO_2, N_2, and noble gases) in rocks and minerals using stepwise crushing (Fig. 8).
- E. V. Korochantseva and A. I. Buikin obtained the most precise age of the catastrophic event (470 ± 6 Ma) on the L-chondrite parent body. The age of the asteroid breakup is fully consistent with the refined stratigraphic age of the Middle Ordovician fossil meteorites (467.3 ± 1.6 Ma), which were transferred from the asteroid belt to the Earth within a few million years after the L-chondrite parent body destruction. This is the first direct geochronological proof of a causal link between two events that occurred on two different large cosmic bodies in the Solar system. The argon trapped on an asteroid (the parent body of L-chondrites) during a large-scale impact event was identified for the first time. Later the trapped extraterrestrial argon was also found in other meteorites from different asteroids (Fig. 9).

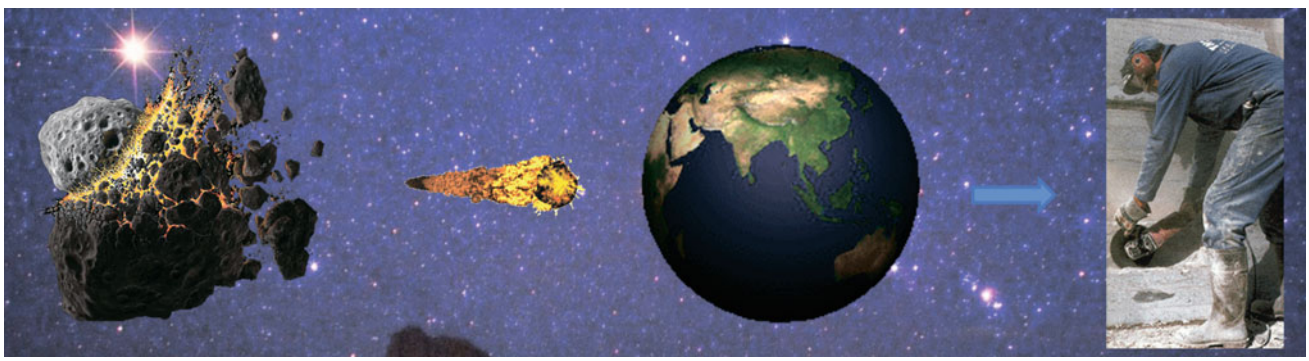

Fig. 9 Age of L chondrite parent body disruption determined by Ar-Ar chronology at 470 ± 6 Ma coincides with the stratigraphic age of fossil extraterrestrial material (Korochantseva et al. 2007) rapidly transferred from the asteroid belt (<1 Ma; Heck et al. 2004). This is the first direct geochronological proof of a causal link between two events on two different cosmic bodies in our Solar System

Laboratory of Modeling Hydrogeochemical and Hydrothermal Processes

Head of the Laboratory
Evgeniya S. Sidkina
Ph.D. in Geological and Mineralogical Sciences
Email: sidkinaes@geokhi.ru
Website: http://portal.geokhi.ru/sites/eng/lab16
Articles by lab members in this volume: Chapters 8, 9, 10

The laboratory was founded in 1992 on the initiative of Academician V. L. Barsukov during the reorganization of the Laboratory of Theoretical Foundations of Applied Geochemistry. Initially, the laboratory included B. N. Ryzhenko (Head of the Laboratory till 2016), V. A. Alexeev, L. A. Bannikova, Viktor L. Barsukov, A. R. Erokhin, S. N. Knyazeva, N. I. Kovalenko, S. R. Kraynov, N. T. Sokolova, N. I. Prisyagina, L. S. Medvedeva, M. Yu. Spasennykh, T. M. Suschevskaya. Later E. V. Cherkasova, B. I. Oleinik, O. A. Limantseva, N. N. Baranova, V. S. Karpukhina, N. N. Kolpakova, L. N. Kochnova, V. V. Fadeev, A. A. Konyshev, E. S. Sidkina, I. A. Bugaev, O. S. Naimushina, M. V. Mironenko, V. B. Naumov, O. F. Mironova, S. S. Vorobei, E. A. Soldatova joined the laboratory. From 2015 to 2017, the laboratory was headed by M. V. Mironenko. Currently, the Head of the Laboratory is E. S. Sidkina.
Today the laboratory consists of 13 employees, including 2 Doctors of Sciences and 7 Ph.D.'s.

Boris N. Ryzhenko
Doctor of Chemistry,
Ph.D. in Geological and
Mineralogical Sciences

Laboratory objectives/research areas

- computer modeling geochemical processes in the "water-rock-gas-organic matter" systems,
- software development and database replenishment for computer modeling,
- experimental study of hydrothermal systems,
- mineralogical and geochemical studies of ore-forming hydrothermal systems.

Methods developed

- thermodynamic and equilibrium-kineticmodeling,
- laboratory physicochemical experiment,
- mineralogical studies and the study of fluid inclusions.

Interdisciplinary research

Research is conducted at the interface of chemical thermodynamics, kinetics, computational mathematics, hydrogeochemistry, geochemistry of hydrothermal processes, geoecology, and planetology.

The main results of research in recent years

- The GEOCHEQ_Isotope software package for the simultaneous calculation of chemical and isotopic (carbon and oxygen) equilibria with the Gibbs energy minimization method was developed. According to the proposed approach, the Gibbs energy G*(P, T) of formation of rare isotopologues is calculated through the Gibbs energies of formation of basic and rare isotopologues, taking into account the values of β-factors of these substances and the ratio of masses of rare and basic isotopes of a chemical element. The research has been conducted in cooperation with Lab of isotopic geochemistry and geochronology.
- The process of spontaneous distillation of aqueous solution in a closed system is experimentally discovered and

investigated. The distillation is initiated by evaporation of a thin film of solution at the wall-water-vapor boundary and is enhanced in the presence of a hydrophilic rough wall. It causes the redeposition of minerals at the liquid-vapor interface and the renewal of the solvent power of the solution.

- The equilibrium-kinetic model for assessing the efficiency of underground iron and manganese removal from water on the example of the Tunguskoye field (Khabarovsk) was developed.
- The GEOCHEQ database was replenished with information on the thermodynamic properties of a wide range of hydrocarbons. Thermodynamic modeling of hydrothermal transformation of sedimentary rock containing kerogen in the temperature range of 50–400 ºC was carried out under gradually increasing pressure. Calculations reproduce the chemistry of kerogen transformation, oil formation, and metamorphism of mineral rock components.
- Generalization of physical and chemical parameters of the formation of hydrothermal mineral deposits of various elements was carried out based on the minerals' fluid and melt inclusion database.
- Prospective assessments of the impact of ore deposits development on natural waters were made using the Pavlovskoye polymetallic deposit, the Udokan copper deposit. Models of formation of acid drainage of sulfide-bearing gold ore deposits were developed.
- The chemical composition of bedrock, dumps, and natural waters of several historical mines of the Pitkyaranta ore district (Karelia) has been studied. Currently, the assessment of the impact of these objects on the environment is carried out. Thermodynamic and equilibrium-kinetic modeling is being applied in the evaluation.
- New statements on the geochemistry of brines of the Siberian platform were formulated. The relations of brine' genesis and chemical composition and the distribution patterns of different brine types were revealed. The formation features of the brine chemical composition were highlighted based on the comparative analysis of brines of two major hydrogeological structures: the Tunguska artesian and Olenek cryoartesian basins.
- The formation of geochemical barriers in the water-rock system within the wetlands of Western Siberia (Russia) and Poyang Lake basin (China) was studied using thermodynamic modeling. The formation of sorption barrier in the soil cross-section and the influence of sewage discharge on the geochemical barrier formation within wetlands was also investigated. *Photo 7 illustrates an exterior view of the Vernadsky Institute RAS.*

Photo 7 Vernadsky Institute in late autumn

Laboratory of Geochemistry of the Earth's Mantle

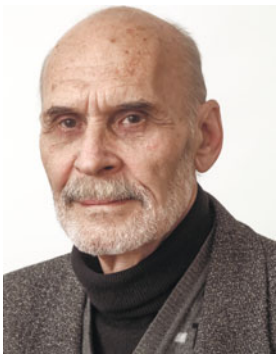

Head of the Laboratory
Oleg A. Lukanin
Doctor of Geological and Mineralogical Sciences
Former Deputy Director of the Vernadsky Institute RAS
Email: lukanin@geokhi.ru
Website: http://portal.geokhi.ru/sites/eng/lab17
Articles by lab members in this volume: Chapter 7

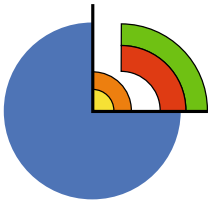

The laboratory was founded in 1953 by N. I. Khitarov, Corresponding Member of the USSR Academy of Sciences, for experimental and theoretical studies of geochemical processes at high pressure and temperature. From 1985 to 2016, the laboratory was headed by Doctor of Geological and Mineralogical Sciences, Professor A. A. Kadik.
At present, the laboratory consists of 15 people, including 4 Doctors of Sciences and 4 Ph.D.'s.

The Scientific and Educational Center "*Experimental Modeling of Magmatic and Mineral Equilibria, Mineral Synthesis*" was organized at the laboratory together with the Department of Petrology of the MSU Faculty of Geology to train undergraduate and graduate students in modern methods of studying mineral equilibria at high pressure and temperature.

The Laboratory co-organizes *the All-Russian Annual Seminar on Experimental Mineralogy, Petrology, and Geochemistry* (held since 1960*)* and *the International Conference on Physicochemical and Petrophysical Investigations in the Earth Sciences* (held since 1999*)*.

Main directions of experimental and theoretical research

- Behavior of volatile components like C, N, H, O, etc., at the early stages of the Earth's evolution at its melting and segregation of the metal core of the planet.
- Influences of impact processes on the chemical differentiation of planetary matter.
- Study of mechanisms of the silicate melt, sulfide, and metallic phases segregation in the zones of the partial melting leading to the forming of the Earth, Moon, and other planetary bodies metal core
- Fractionation of volatile, lithophilic, and ore elements at degassing magmas
- Study of phase equilibria in the mantle with the participation of high-baric mineral phases.

Equipment and research methods

The laboratory has the following equipment for experimental studies: (1) high-pressure solid compression setups for experiments up to 25 kbar and 1500 °C as well as up to 70 kbar and 1700° C (Fig. 10); (2) high-temperature oxygen and hydrogen controlled setup to study redox reactions in silicate systems at 1 atm and temperatures up to 1450 °C; (3) high-temperature installation with solid electrochemical cells to measure the intrinsic fO_2 of mineral phases; (4) high-temperature centrifuge to study the dynamic separation of silicate melts, crystals, metal, and sulfide phases (Fig. 11).

Main achievements of the laboratory in recent years

It has been shown experimentally that large-scale melting and segregation of the metallic core of the planet is accompanied by the formation of CH_4, NH_3, H_2 molecules, and complexes in silicate melt with subordinate amounts of H_2O, N_2, CO_2. This allows us to consider the early magmatic transport of C–N–H volatile components of the planet as an endogenous source of gas components of the early reduced atmosphere of the Earth (*Sci. supervisor Prof. A. A. Kadik, D.Sc. O. A. Lukanin*).

A model for impact melting and evaporation influence on the redox state of the Earth's silicate matter and its water content has been proposed (*Sci. supervisor D.Sc. O. A. Lukanin*).

The possibility of segregation of iron and sulfide phases during partial melting and deformation of protomancy of the Moon in conditions of low values of oxygen fugacity has

been established using methods of high-temperature centrifugation (*Sci. supervisor D.Sc. E. B. Lebedev*).

A computer model for volatile (H_2O, CI), ore (Zn, Pb) and rare-earth elements behavior in the process of degassing of granitoid magmas, during their rise to the surface and crystallization has been developed. This allows quantitatively estimate scales of these elements removal from magmatic melts during their degassing at different depths (*Sci. supervisor D.Sc. O. A. Lukanin*).

Criteria of diamond-forming efficiency of mantle melts have been developed. For the first time, in world practice, the synthesis of sodium-rich majorite, ringwoodite, and bridgmanite has been carried out, and conditions of their magmatic crystallization have been established. The ranges of conditions and compositions for several water-bearing phases—potential concentrators of alkalis (Egg, X, and B phases), have been revealed at parameters of the upper mantle and transition zone of the Earth. For the first time, the stability of iron-bearing bridgmanite in the whole range of depths of the Earth's lower mantle has been proved (*Sci. supervisor D.Sc., Prof. A. V. Bobrov*). *Photo 8 illustrates an exterior view of the Vernadsky Institute RAS.*

Fig. 10 Solid compression high-pressure apparatus for experiments up to 70 kbar and 1500–1700 °C

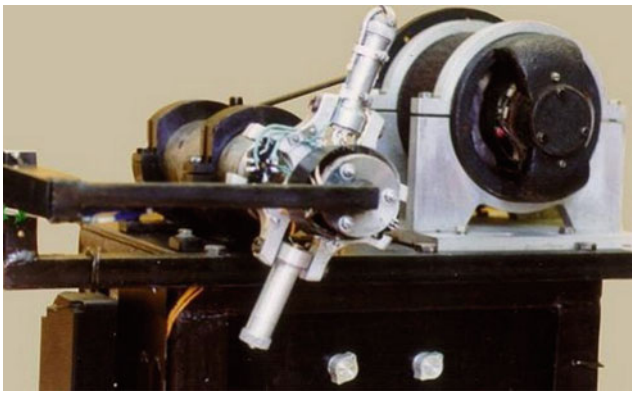

Fig. 11 High-Temperature Centrifuge for the Study of Dynamic Phase Separation in Magmatic Systems

Photo 8 Courtyard of Vernadsky Institute through the arch in late autumn on a sunny day

Laboratory of Geochemistry of Nanoparticles

Head of the Laboratory
Petr S. Fedotov
Doctor of Chemistry
Deputy Director of Research for the Vernadsky Institute RAS
Email: fedotov_ps@mail.ru
Website: http://portal.geokhi.ru/sites/eng/lab18
Articles by lab members in this volume: Chapter 5

The laboratory was established in 2019 by P. S. Fedotov to solve the problems of a new scientific discipline: nanogeochemistry.
At present, there are 11 researchers in the laboratory, including 3 Doctors of Sciences, 4 Ph.D.'s, and 2 postgraduate students.

Main areas of research

- development of new combined methods for fractionation, characterization, and analysis of nano/microparticles and soluble components of environmental samples to solve problems of geochemistry, soil science, and environmental monitoring;
- study of the size, morphology, and chemical composition of nanoparticles and nanoinclusions in rocks and environmental samples;
- study of stability and mobility of nanoparticles in aqueous systems;
- development of standard samples of natural nanoparticles;
- study of regularities of distribution of elements between different mineral-organic phases of soils of various types;
- study of the role of impact events in the formation and evolution of the substance of the Earth and the Moon by high-local electron microscopy methods.

Research methods

- methods of particle fractionation (field-flow fractionation, membrane filtration, sedimentation);
- dynamic fractionation of elements in soils and sediments using rotating coiled columns and micro-columns;
- dynamic and static light scattering;
- capillary electrophoresis;
- inductively coupled plasma mass spectrometry (including single-particle mode);
- scanning electron microscopy.

Interdisciplinary studies

Research is conducted at the frontiers of geochemistry, soil science, and analytical chemistry.

International cooperation

Petr S. Fedotov is a member of the Bureau and the Division of Chemistry and the Environment of the International Union of Pure and Applied Chemistry (IUPAC). Laboratory staff conducts joint research with foreign colleagues and has multiple publications with scientists from France, Germany, and Spain.

Main achievements of the laboratory in recent years

- A combined approach to the study of nanoparticles of polydisperse environmental samples such as dust and volcanic ash has been developed (Ermolin et al., *Journal of Analytical Chemistry* 2017, Vol. 72, No. 5, pp. 448–461);
- Volcanic ash nanoparticles were isolated and quantitatively analyzed for the first time; the concentration of toxic and potentially toxic metals and metalloids in volcanic ash nanoparticles was shown to be tens to hundreds of times higher than their total concentration in ash (Ermolin et al., *Chemosphere* 2018, V. 200, 16–22);
- It has been found that toxic and potentially toxic elements in volcanic ash nanoparticles can be both adsorbed on pyroclastic nanoparticles and present as individual nanoparticles (Ermolin et al., *Chemosphere* 2021, V. 281);
- Volcanic ash nanoparticles have been shown to have high aggregation stability in model surface waters and hence a higher potential for long-range transport of toxic and nutrient elements in aquatic ecosystems (Ermolin et al.,

Environmental Chemistry Letters 2021, V. 19, P. 751–762);

- It has been shown for the first time that nanoparticles of urban dust can accumulate toxic and potentially toxic elements whose content in nanoparticles can be tens or hundreds of times higher than their total content in the dust (Fedotov et al., *Talanta* 2014, V. 130, P. 1–7);
- It has been found that the contribution of nanoparticles to the pollution of urban wastewater by heavy metals is comparable to that of water-soluble fractions of heavy metals (Ermolin et al., *Chemosphere* 2018, V. 210, P. 65–75);
- Metal–organic complexes have been shown to play a major role in the binding of rare earth elements in soils (Fedotov et al., *Environmental Chemistry* 2019, V. 16, P. 323–332);
- 105 mineral phases of the Moon have been discovered, of which 43 were found under natural conditions for the first time (Mokhov et al., *Crystallography* 2021, Vol. 66, No. 4, pp. 610–618) (Figs. 12, 13, 14 and 15).

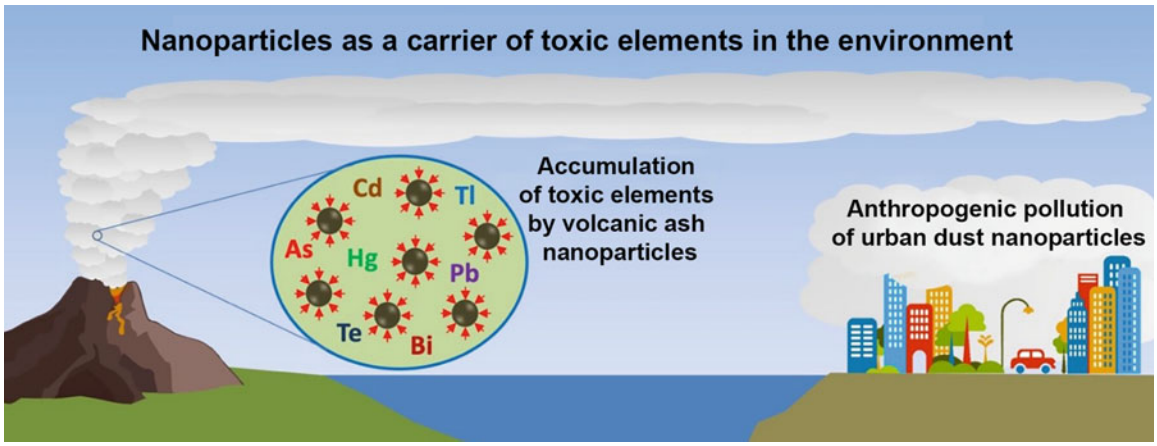

Fig. 12 Nanoparticles as a carrier of toxic elements in the environment

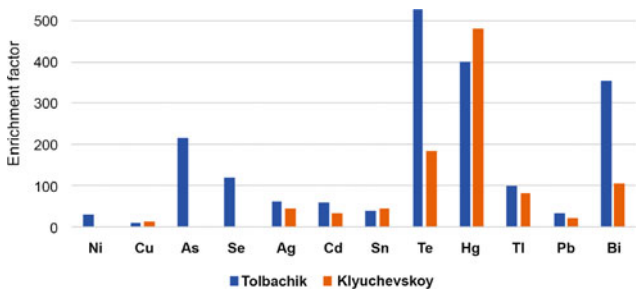

Fig. 13 Enrichment of volcanic ash nanoparticles by toxic metals and metalloids

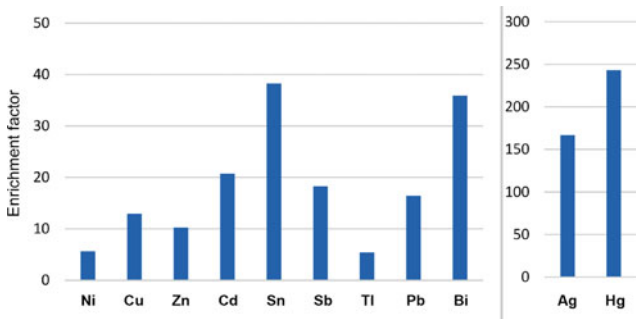

Fig. 14 Enrichment of road dust particles by heavy metals

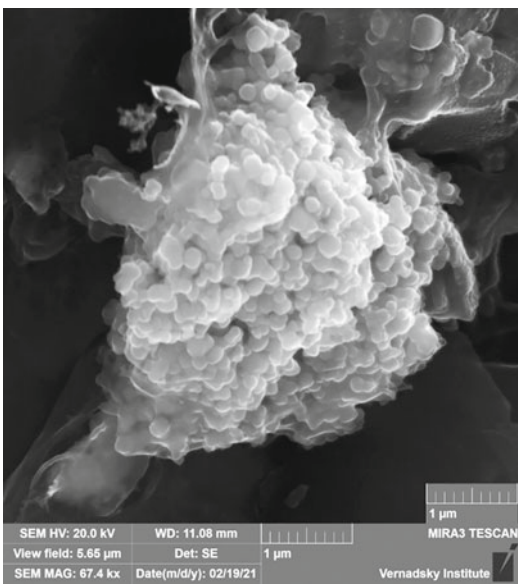

Fig. 15 Impact. Condensate glass

Laboratory of Crystal Chemistry

Head of the Laboratory
Artem R. Oganov
Professor of RAS, Doctor of Physics and Mathematics
Email: a.r.oganov@mail.ru
Website: http://portal.geokhi.ru/sites/eng/lab19
http://uspex-team.org

The laboratory of crystal chemistry was part of the Vernadsky Institute in the period 1956–2008. It was founded and headed by Dr. E. S. Makarov (from 1957) and then by Academician of RAS V. S. Urusov (from 1981), see Annex I. It reopened in 2021 and since then is headed by Prof. A. R. Oganov, Doctor of Physics and Mathematics, Hab., Professor RAS, Member of Academia Europaea, Fellow of the Royal Society of Chemistry, American Physical Society, Mineralogical Society of America.
Currently the laboratory consists of 4 employees including 1 Professor RAS and 3 Ph.D.'s. Key personnel include Senior Researchers, Ph.D. in Physics and Mathematics S. V. Lepeshkin and V. S. Baturin.

Research objectives

Prediction of the structure and properties of molecules, nanoparticles, and crystalline phases (also at high pressures) to elucidate the geochemical behavior of elements and understand the composition, structure, and evolution of planetary interiors. To tackle these problems, we are developing new simulation techniques, which can also be applied to predict new materials with desired properties.

Methods

- Quantum-mechanical calculations (in particular, based on density functional theory).
- Artificial intelligence methods (evolutionary algorithms for structure prediction, machine learning methods).
- Molecular dynamics and lattice dynamics methods.
- We are actively developing new methods—especially methods for predicting the structure of molecules, nanoparticles, and crystals (USPEX program). These methods require the use of powerful supercomputers.

The main results achieved in recent years:

- Refinement of concepts of classical crystal chemistry, in particular, a new scale of electronegativity was created (Tantardini, Oganov, Nature Communications, 2021). We have also defined the electronegativity of the elements under pressure, and for several elements, we found a dramatic change in the chemical and geochemical properties (Dong, Oganov, et al., Proc. Natl. Acad. Sci. USA, 2022). Recently, we have also deciphered the physical meaning of the so-called "Mendeleev numbers" of the elements (Allahyari, Oganov, J. Phys. Chem. C, 2020)
- We have developed a new method for predicting the structure and composition of stable nanoparticles and molecules and introduced the concept of stability maps of molecules (Lepeshkin et al., J. Phys. Chem. Lett., 2019). Different types of chemical systems have different topologies of stability maps—it is often possible to distinguish seas of instability, stability ridges and stability islands. Often molecules with unexpected compositions turn out to be stable
- We have developed the AICON (Ab Initio CONductivities) code to calculate the thermal conductivity of crystalline substances (Fan, Oganov, Computer Physics Communications, 2020, 2021). In particular, it was shown that minerals of the Earth's lower mantle have low thermal conductivities, which allows maintaining a huge temperature gradient near the core-mantle boundary
- The behavior of the C–N–H–O system was theoretically studied at pressures present in the interiors of the planets Uranus and Neptune (Naumova et al., J. Phys. Chem. A., 2021). We have demonstrated that the formation of diamonds on these planets is unavoidable. Predicted phase diagram of the C–N–H–O system at high pressures (Figs. 16, 17 and 18).

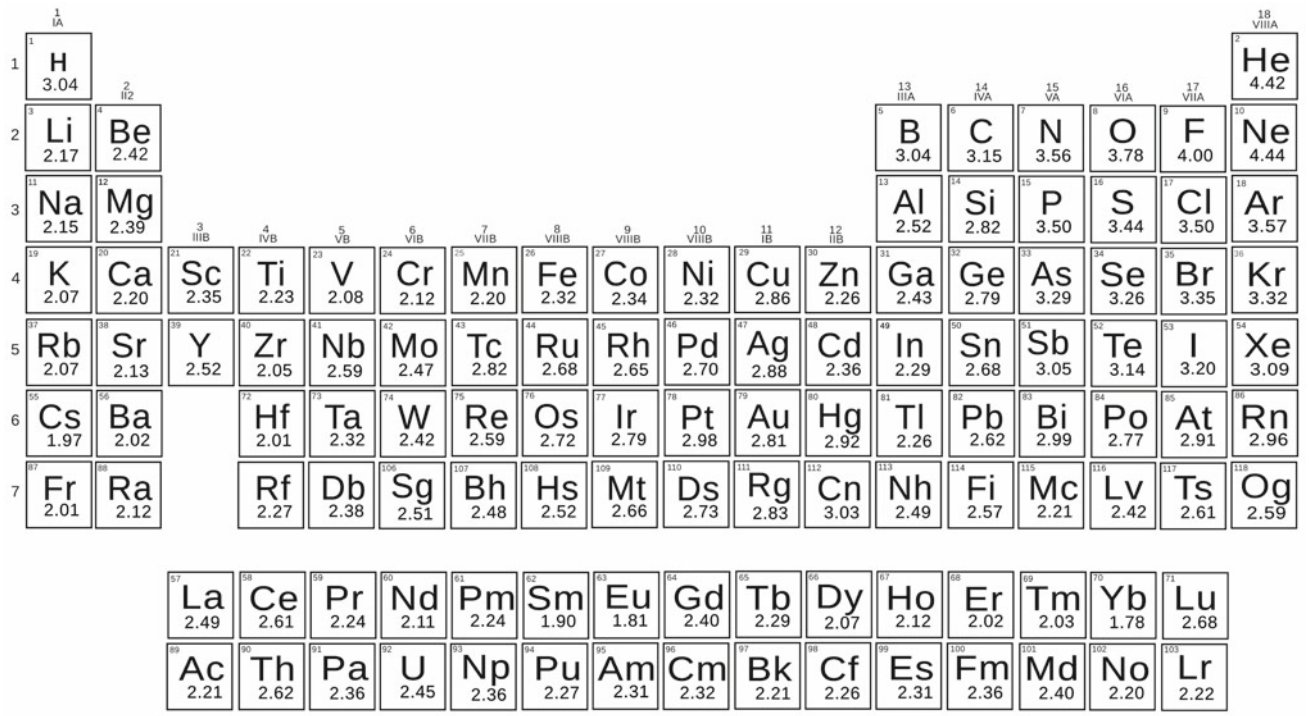

Fig. 16 Tantardini-Oganov electronegativity scale

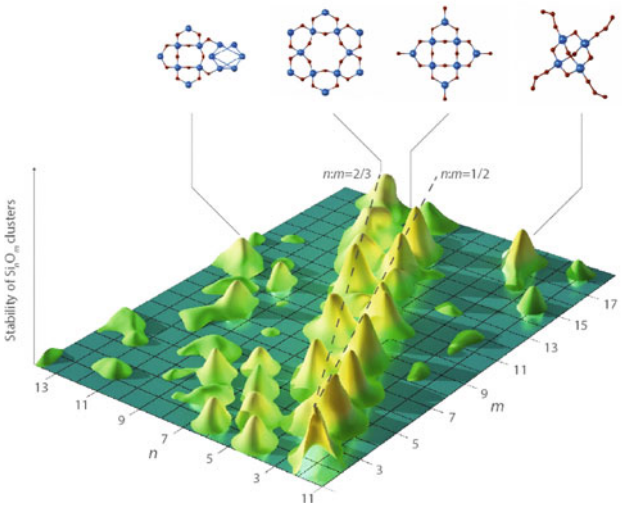

Fig. 17 Stability map of Si–O molecules

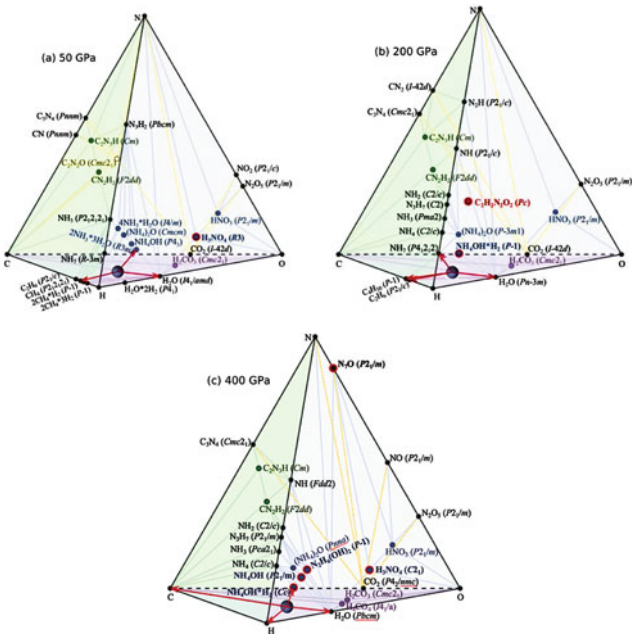

Fig. 18 Predicted phase diagram of the C–N–H–O system at high pressures

Laboratory of Carbon Geochemistry

Head of the Laboratory
Vyacheslav S. Sevastyanov
Doctor of Technical Sciences
Email: vsev@geokhi.ru
Website: http://portal.geokhi.ru/sites/eng/lab51
Articles by lab members in this volume: Chapter 20

The laboratory was established in 1973 by Academician E. M. Galimov of the Russian Academy of Sciences. Since February 1, 2017, it has been headed by Doctor of Technical Sciences V. S. Sevastyanov. The laboratory consists of 16 researchers, including 1 corresponding member of the Russian Academy of Sciences, 1 Doctor of Sciences, 5 Ph.D.'s.

The main research directions are:

The genesis of carbon-containing natural substances—oil, gases, diamonds, graphite, etc.; geochemistry of carbon isotopes; the theory of biological and organic fractionation of isotopes; the laws of transformation of organic matter from living to fossil forms; marine research; the evolution of the biosphere; the origin of life and the early history of the Earth. The methodological basis of the research is the study of matter at the isotopic and molecular levels. The isotopic approach allows us to study substances so remote in nature and origin as diamonds, oil, carbonates, meteorites in an interconnected way. The molecular level allows us to understand the chemical history of complex complexes that represent biogenic organic matter and its derivatives in nature.

The methods of research are:

- Mass spectrometry of isotope ratios;
- gas and liquid chromatography-mass spectrometry;
- gas and liquid chromatography;
- CHNO-elemental analysis and pyrolysis;

The most important results include:

- The experiments conducted on the spherical-symmetric collapses of cavitation bubbles in aqueous solutions of isopropyl alcohol using a water hammer confirmed the possibility of cavitation synthesis of diamonds in natural fluids. It is shown that during cavitation, the formation of nanoscale diamond grains coated with fcc-carbon occurs when initiated by a water hammer. In a short time (2–3 ns), it is possible to achieve an increase in the temperature in the cavitation cavity to 2–3 thousand degrees Celsius and an increase in the pressure to 5 GPa, which provides thermodynamic conditions for the genesis of the diamond phase from carbon-containing molecular fragments.
- As part of the experimental verification of the dynamic model of the formation of the Moon and the Earth as a binary system from a common cloud of evaporating particles developed by Academician E. M. Galimov, the isotopic compositions of iron samples of the Soviet lunar missions Luna 16, 20, and 24 were analyzed. It is shown that samples from the Luna 24 landing region, represented by basalts with a sparse titanium content (very low-titanium basalts), have δ^{57} Fe = 0.08 ± 0.04%. This isotopic composition, reflecting the least differentiated melt of the lunar magmatic ocean, is identical to the Earth's gross isotopic composition of iron, which confirms the model of a common reservoir of primary matter.
- A general model of diamond formation in nature has been created. It is shown that diamond is a polygenic mineral. It can crystallize both as a result of high temperatures and pressures realized during the formation of kimberlites and lamproites and in metastable conditions other than the equilibrium thermodynamic parameters. In particular, the recently discovered micro-diamonds of the Tolbachik volcano in Kamchatka were formed during an eruption, under conditions of pressures close to that of the atmosphere, during the implementation of the mechanism of chemical deposition from the gas phase (Figs. 19 and 20).
- The main regularities of the distribution of hydrocarbon gases (CH_4, C_2H_4, C_2H_6, C_3H_6, C_3H_8, C_4H_8, n-C_4H_{10},

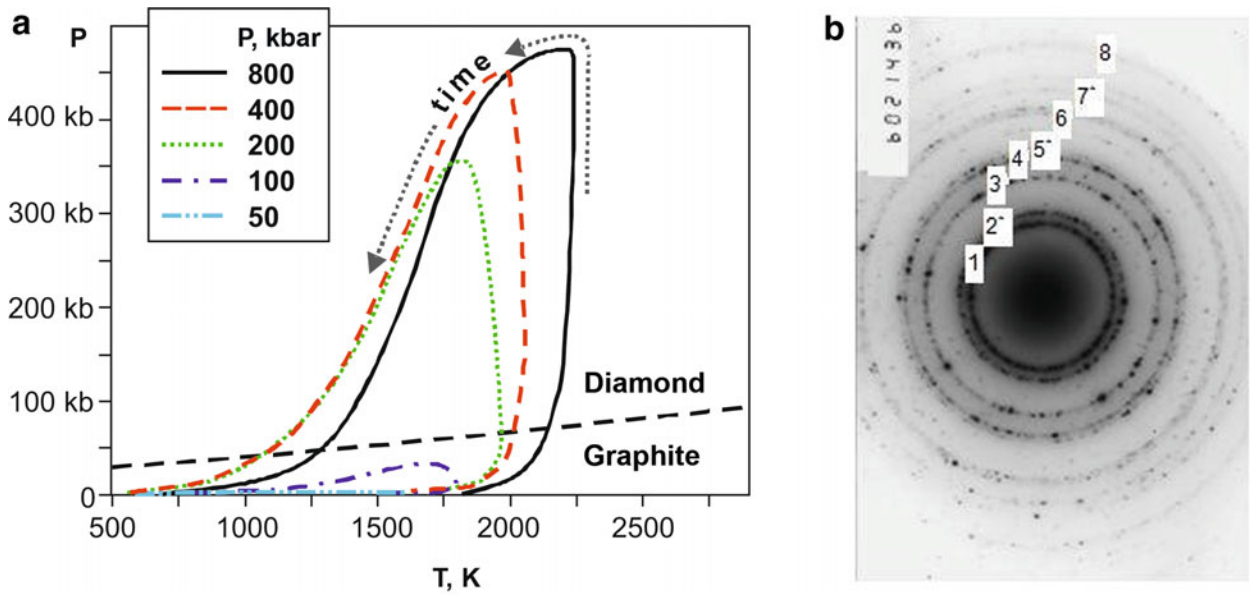

Fig. 19 **a** thermodynamic conditions for the genesis of the diamond phase from carbon; **b** electronic diffractogram with reflections of the crystal lattice

i-C_4H_{10}, n-C_5H_{12}, i-C_5H_{12}, neo-C_5H_{12}), CO_2, H_2S, CH_3SCH_3, COS in the vertical section of the Laptev Sea and the Kara Sea are studied. It is shown that the content of hydrocarbon gases depends on the degree of transformation of organic matter(s) in marine sediments. The concentration of HC gases increased in the area of an increased concentration of CH_3SCH_3, and the concentration of COS decreased. It was concluded that the sips are formed as a result of the migration of hydrocarbon gases of thermogenic (catagenetic) genesis from great depths in the area of the junction of the Laptev Sea Rift system with the Khatanga-Lomonosov fault zone.

- The hydrothermal transformation of OM can be considered as one of the main methods of modelling catagenesis. It was found that after several successive cycles of hydrothermal extraction of "synthetic" oil (thermolysate) from the oil-producing rock of the Domanic sediment of the Middle Fran tier of the upper Devonian system, the total carbon isotope composition shifts towards an increase in δ13C. Simultaneously, the similarity of the IFX between the obtained synthetic oils and bitumoids from the rock is preserved, along with the IFX of oil of the reference section of the Domanic formation.

Interdisciplinary research includes:

- Work within the agreement on scientific and technical cooperation was signed between Vernadsky Institute RAS and the State Historical Museum.
- Joint work with the Department of Planetary Research and Cosmochemistry under the Russian Academy of Sciences grant "Genesis and Geochemistry of lunar matter and prospects for the use of lunar resources".
- Joint work with the Russian Register Association on developing a new method for synthesizing carbon nanoparticles.
- Work within the Agreement on scientific and technical cooperation with the Institute of natural and technical systems for conducting field research on the synthesis of protein microspheres in the waters. *Photos* 9, 10 *and* 11 *illustrate a range of interiors and exteriors of the Vernadsky Institute RAS*.

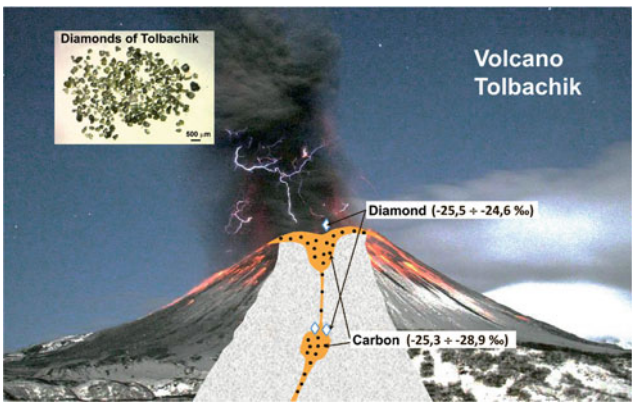

Fig. 20 Genesis of microdiamonds during volcano eruption

Photo 9 Entrance to the conference hall of the institute. On the right side above the entrance, there is a bas relief of Sergey I. Konenkov, a famous Russian sculptor of the XX century

Photo 10 The main conference hall of the institute

Department of Analytical Chemistry

Head of the Department
Sergey E. Vinokurov
Doctor of Chemistry,
Deputy Director of Research for the Vernadsky Institute RAS
Email: vinokurov@geokhi.ru

The department of analytical chemistry currently includes seven laboratories:

Laboratory of Instrumental Methods and Organic Reagents

Preconcentration Laboratory

Laboratory of Molecular Modeling and Spectroscopy

Laboratory of Methods for Research and Analysis of Substances and Materials

Laboratory of Radiochemistry

Laboratory of Sorption Methods

Laboratory of Chemical Sensors and Determination of Gas-Forming Impurities.

The basic and applied research is aimed at:

- development of theoretical foundations of analytical chemistry and radiochemistry;
- search and development of fundamentally new approaches for chemical analysis, methods of separation and determination of substances of organic and inorganic nature, including radionuclides;
- development of new instruments, methods of analysis, distinguished by high metrological characteristics;
- extended application of computational mathematics and statistical methods to enhance the informativeness of chemical analysis and predictive modeling;
- conducting the analysis without the use of reference materials;
- ensuring metrological validity of the results of chemical analysis;
- intellectualization of chemical analysis systems and developing expert systems of chemical analysis.

In the laboratories, both bulk and local analysis are successfully developed. Great attention is paid to the issues of substantial analysis, new methods of determination of organic compounds for biomedical tasks, environmental control, etc.

The focus is on problems of analysis and processing of strategic raw materials (nuclear materials, rare-earth raw materials, etc.).

Successfully developing technical areas: safe storage and disposal of radioactive waste, reprocessing of spent nuclear fuel, production of concentrated liquid fertilizers, reprocessing of oil raw materials, etc.

Photo 11 The arch between two buildings of the institute

Laboratory of Instrumental Methods and Organic Reagents

Head of the Laboratory
Alexander A. Grechnikov
Doctor of Chemistry
Email: grechnikov@geokhi.ru
Website: http://portal.geokhi.ru/sites/eng/lab01
Articles by lab members in this volume: Chapter 33

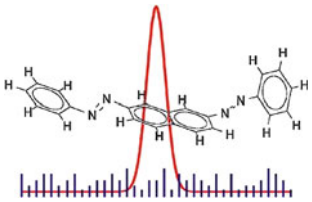

The laboratory was established in 2009 by merging the Laboratory of Precision Analytical Instrumentation and the Laboratory of Organic Reagents. Continuing traditional and developing new scientific directions, the laboratory solves problems of the development of instrumental methods for obtaining and processing analytical signals in various fields of chemical analysis.Currently, the laboratory employs 10 researchers, including 1 D.Sc. and 5 Ph.D.'s.

Main areas of research

- Development of novel approaches for mass spectrometric determination of organic and bioorganic compounds using pulsed laser radiation, and on this basis creating analytical equipment for highly sensitive determination of biologically active compounds.
- Development of methods for determining metal ions by reactions with organic reagents on the solid phase and the creation of new analytical systems for multi-element determination of metals by spectrophotometric and mass spectrometric methods.
- Development of a luminescent method for the determination of trace amounts of actinides in environmental samples.

The following methods of analysis are being developed in the laboratory

- Laser mass spectrometry
- Diffuse reflectance spectrophotometry
- Luminescence of crystallophosphors activated by actinides
- Piezosorption method.

Interdisciplinary research

The laboratory conducts researches in the fields of analytical chemistry, bioorganic chemistry, laser physics, and physical chemistry.

Main achievements in recent years

- A methodology for the quantitative determination of organic compounds by silicon surface -assisted laser desorption ionization mass spectrometry has been developed. New emitters of ions have been proposed, and simple methods have been developed for their formation, which provides high reproducibility of ionization properties and high sensitivity of the analysis. A technology for mass spectrometric determination of volatile organic compounds based on a combination of laser desorption/ionization with the thermal desorption method and gas chromatography has been worked out. The developed technique has been successfully applied to quantify clinically relevant concentrations of pharmaceutical drugs in biological liquids.
- A new method of mass spectrometric determination of chemical compounds based on laser-induced electron transfer desorption/ionization (LETDI) on specially prepared surfaces of metal oxides has been developed (Fig. 21). The method has been tested for determination and identification of metal complexes with organic reagents and bioligands.
- A new method of ionizing organic compounds affected by laser-plasma radiation at atmospheric pressure has been developed. The method applies to the analysis of gaseous, liquid, and solid substances, including mass spectrometry imaging, without sample preparation.

- The analyzer of neptunium in soils and natural waters with the limit of detection at sub picogram level was created. The principle of operation of the analyzer is based on the use of neptunium-activated luminescence of crystal phosphors. The analyzer can be used to control leakage of neptunium at large distances from long-term storage sites (Figs. 22 and 23).
- The portable and compact vapor micro-stream generator based on quartz crystal microbalance was created. The generator intends to create a continuous vapor stream of low volatile chemical compounds in a range of 0.01–10 ng/sec.
- Several simple express methods of determining metal ins (Zr, Ni, W, Mo, Ti, Cr, Vi, Cu, and some others) by diffuse reflectance spectrometry have been developed. The determination of metal cations is based on color reactions with organic reagents on the solid phase of porous polyacrylonitrile fiber filled with ion exchangers.

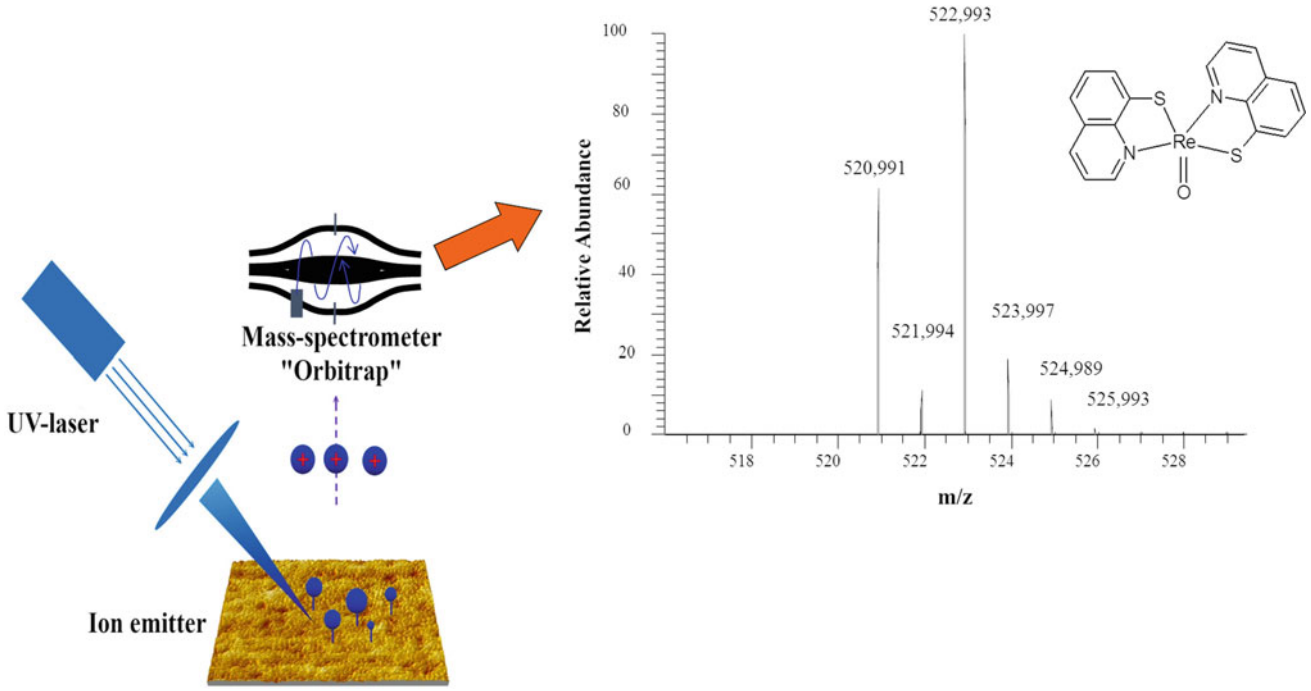

Fig. 21 Scheme of analysis by laser-induced electron transfer desorption/ionization (LETDI)

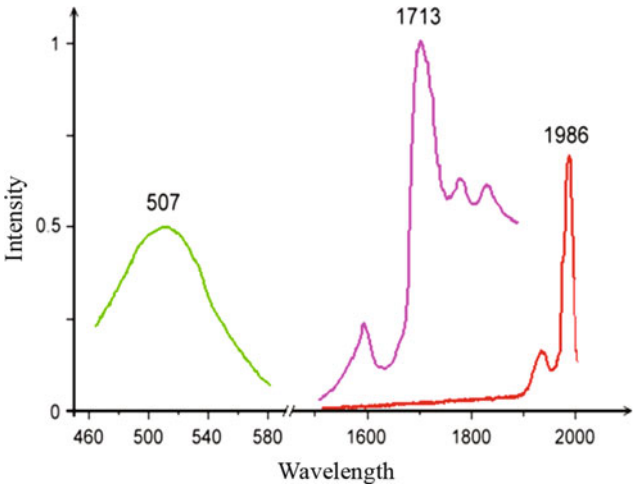

Fig. 22 Luminescence spectra of uranium, neptunium and plutonium. Lead molybdate was used as crystal phosphor matrix

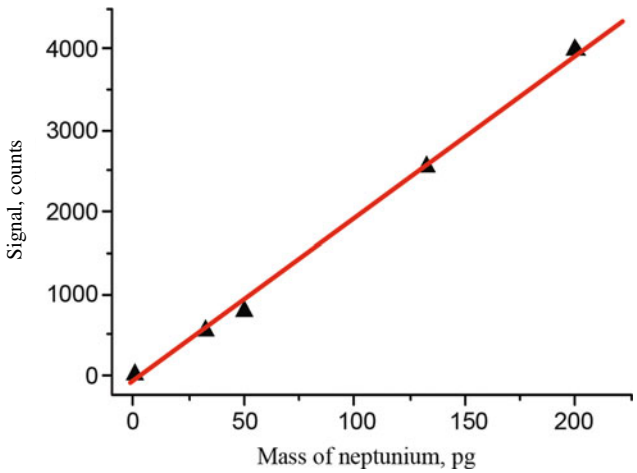

Fig. 23 Calibration curve for the determination of neptunium in groundwater

Preconcentration Laboratory

Head of the Laboratory
Tatiana A. Maryutina
Doctor of Chemistry
E-mail: maryutina@geokhi.ru
Website: http://portal.geokhi.ru/sites/eng/lab02
Articles by lab members in this volume: Chapters 32 and 34

The Laboratory of Extraction Methods (later renamed the Preconcentration Laboratory) was established in 1971 by Corresponding Member and later Academician of RAS Yu. A. Zolotov. From 1990 to 2016 the laboratory was headed by Doctor of Chemistry, then a Corresponding Member of RAS B. Ya. Spivakov. Since 2016 the laboratory has been headed by Dr. T. A. Maryutina.
Currently, the laboratory consists of 19 researchers, including 1 Corresponding Member of RAS, 3 Doctors of Sciences and 7 Ph.D.'s.

Yuri A. Zolotov
Academician of RAS

Methods of metal ions separation based on the formation and distribution of their complexes in two-phase systems have been developed in the laboratory, which made a significant contribution to the development of the general theory of the extraction of neutral chelates, ion associates and coordination-solvated complexes. The phenomenon of suppression of extraction of one element by another was discovered. Theoretical foundations and practical applications of extraction with sulfur-containing extractants and macrocyclic reagents, development of various original sorbents, new organic reagents were performed.

For the first time in Russia, the laboratory began the studies on flow-injection analysis, liquid chromatography of metal complexes, and capillary electrophoresis. The greatest progress in capillary electrophoresis was achieved in the research of metal-containing anticancer agents and metal-containing nanomaterials for medical purposes, in addition to inorganic analysis of seawater and biological fluids.

The main directions of the laboratory's research are related to the development of the theory of methods of separation and preconcentration of substances and their optimal combination with various methods of determination. Special attention is paid to the development of extraction, chromatographic, membrane, and other methods of substances separation. A new class of organometallic extractants for anions, in which the complexing atom is not oxygen, nitrogen, or sulphur, but the metal (tin) atom interacting with oxygen atoms of the anions has been proposed and studied. Aqueous biphasic systems (ABSs) have been proposed for the extraction of metal complexes. The chemistry of metal extraction in polymer-salt-water and polymer–polymer-water systems was investigated. The use of ABBs significantly expanded the range of extraction reagents and allowed them to work in the absence of conventional organic solvents.

The laboratory was the first in the world to develop the theory and application of counter-current chromatography realized in rotating coiled columns (RCC) for the separation of inorganic substances. The prospects of RCC application are shown as a sample preparation method for various analytical tasks, from the determination of trace elements in natural and anthropogenic samples to fractionation and analysis of nanoparticles.

Membrane methods, together with separation methods based on the use of physical fields (ultrasonic, magnetic,

centrifugal), are currently being developed in the laboratory. Novel extraction systems based on ionic liquids, deep eutectic solvents, ABSs have been proposed for recovery and separation of bioorganic compounds and metals including platinum group metals. Special attention has recently been paid to the synthesis of nano- and microparticles of iron and zinc oxides for their analytical use.

Methods of preconcentration of trace elements from oil media using liquid–liquid and supercritical fluid extraction for their subsequent instrumental analysis have been offered. In addition, studies on the separation of water–oil emulsions into separate fractions using wave impacts are also being carried out. Several analytical pieces of research of oil raw materials have found continuation in the development of bases of technological processes of oil refining (Figs. 24 and 25).

Numerous researches of the laboratory are carried out with the support of various scientific funds and industrial partners. The laboratory closely cooperates with Russian and foreign research institutes and universities. The works of the laboratory researchers are published in highly ranked journals. The high level of work carried out in the laboratory was also noted at many international conferences.

Selected publications:

1. Spivakov B., Shkinev V. Membrane techniques—ultrafiltration. In: Encyclopedia of analytical science: Second edition. 2004. p 524–530.
2. Timerbaev, A.R., Foteeva, L.S., Rudnev, A.V., … Jarosz, M., Keppler, B.K. Probing the stability of serum protein-ruthenium(III) drug adducts in the presence of extracellular reductants using CE //Electrophoresis, 2007, 28(13), pp. 2235–2240.
3. Berthod A., Maryutina T., Spivakov B., Shpigun O., Sutherland I.A. Countercurrent chromatography in analytical chemistry (IUPAC technical report). Pure Appl Chem 2009;81(2):355–87.
4. Fedotov P.S., Vanifatova N.G., Shkinev V.M., Spivakov B.Ya. Fractionation and characterization of nano- and microparticles in liquid media. Anal Bioanal Chem 2011;400(6):1787–804.
5. Romanova, Y.N., Maryutina, T.A., Musina, N.S., Yurtov, E.V., Spivakov, B.Y. Demulsification of water-in-oil emulsions by exposure to magnetic field // Journal of Petroleum Science and Engineering, 2019, 179, pp. 600–605.
6. Magomedov, R.N., Pripakhaylo, A.V., Dzhumamukhamedov, D.S., Maryutina, T.A. Solvent deasphalting of vacuum residue using carbon dioxide-toluene binary mixture // Journal of CO2 Utilization, 2020, 40, 101,206.
7. Maryutina, T.A., Savonina, E.Y., Fedotov, P.S., Smith, R.M., Siren, H., Hibbert, D.B. Erratum: Terminology of separation methods //Pure and Applied Chemistry, 2021, 93 (3), p. 405.
8. Mokhodoeva O.B., Maksimova V.V., Dzhenloda R.Kh., Shkinev V.M. Magnetic nanoparticles modified by ionic liquids in environmental analysis. J Anal Chem 2021;76 (6):675–84.
9. Katasonova O.N., Savonina E.Y., Maryutina T.A. Extraction methods for removing sulfur and its compounds from crude oil and petroleum products. Russ J Appl Chem 2021;94(4):411–436.

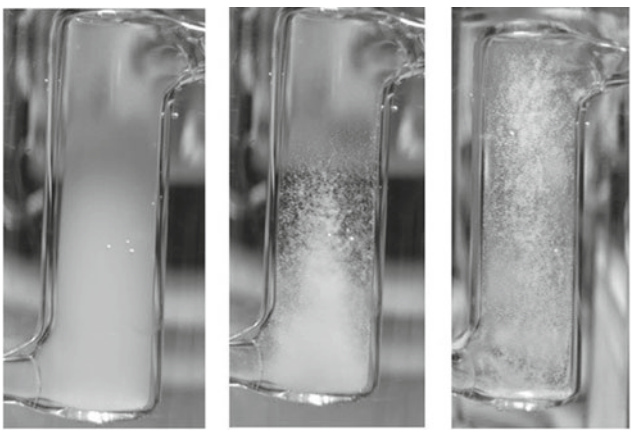

Fig. 24 Suspension column in an ultrasonic field

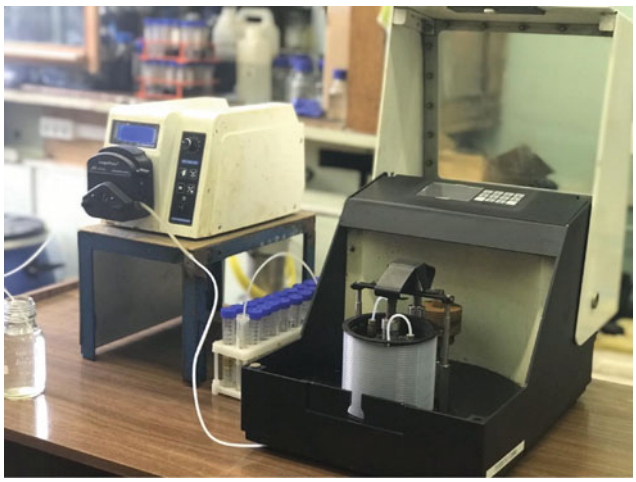

Fig. 25 Planetary centrifuge for separation of soluble components in a rotating coiled column

Laboratory of Molecular Modelling and Spectroscopy

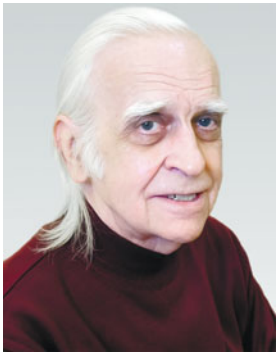

Head of the Laboratory
Victor I. Baranov
Doctor of Physics and Mathematics
E-mail: baranov@geokhi.ru
Website: http://portal.geokhi.ru/sites/eng
Articles by lab members in this volume: Chapters 28, 37 and 38

Laboratory of Molecular Modelling and Spectroscopy was established in 1975 by Professor (further Corresponding Member of RAS) L. A. Gribov.
The laboratory consists of 7 employees, including 5 Doctors of Sciences and 1 Ph.D.

The main objective of the research

Creation based on the quantum theory of computer forecasting tools for a wide range of properties and characteristics of complex molecules and nano-objects (geometry, spectra, types of chemical bonds, etc.) and processes (chemical transformations, energy storage, reception, transmission, transformation of input information, etc.), as well as the use of computational methods for solving analytical problems.

Areas of work

- Development of the quantum theory of structure and properties of complex molecules and polymers and computational methods suitable for mass calculations and prediction of desired characteristics with high reliability.
- Formalization and creation of software for solving the general problem of determining the structures of molecules based on measurements of their spectra.
- Development of the general quantum theory of chemical reactions in complex molecular systems.
- Development of the general theory of spectral methods for the analysis of substances to create new approaches and methods for solving analytical problems.
- The problem of the origin of life and the formation of the biosphere, formulation, and study of general questions related to the possibility of the appearance of properties in the molecular world that provide the emergence and existence of the phenomenon of life itself.
- The primary importance of these studies is determined by the fact that exploration of the infinite number of objects and variety of properties of the molecular world becomes impossible without advanced theoretical analysis and engineering calculations, especially in areas where the accumulated chemical empirical rules and recommendations turn out to be insufficient.

Some of the most important results

- The foundations of a new scientific direction, mathematical chemistry, were created. The theoretical developments have been implemented in expert systems that are widely used (Elyashberg M. E. et al. Contemporary Computer-Assisted Approaches to Molecular Structure Elucidation, Cambridge, RSC Publishing, 2012; Elyashberg M. E. et al. Computer-based structure elucidation from spectral data. The art of solving problems. Heidelberg: Springer, 2015). The results of the studies have international recognition, which have been included in textbooks and monographs (see, e.g., Gribov L. A., Orville-Thomas W. J. Theory and methods of calculation of molecular spectra. Chichester, New York: John Wiley and Sons. 1988.; Gribov L. A., Baranov V. I. Theory and methods of computing molecular processes: spectra, chemical transformations, and molecular logic. Moscow: ComKniga. 2006.; Gribov, L. A. Oscillations of molecules. Moscow: KOMKNIGA. 2008).
- A general theory for chemical reactions of complex molecules was developed. Rules suitable for practical use were formulated to predict the probability and course of chemical transformations based on given structures of reacting objects. For the first time in the world, it was possible to predict the quantum yields of several photochemical reactions (Gribov L. A., Baranov V. I.,

Mikhailov I. V. Physical theory of chemical reactions. Moscow: Rusaens, 2018).

- The basic principles of quantum chemistry were revised, new ways of formulation and algorithms for solving the problems were proposed, and methods for calculating the properties of molecular objects with heavy elements were developed.
- Based on the developed methods for calculating the spectra that quantitatively correlate with the experiment, a general theory of the analysis of substances by their spectra without using samples of standard composition was proposed. This fundamentally expands the possibilities of the practical application of spectroscopic methods for the qualitative and quantitative analysis of pure substances and mixtures. Special methods for processing experimental results for analytical purposes under conditions of indistinct experimental and theoretical data were developed.
- For the first time, the fundamental importance of the multiplicity of isomeric structures of molecules in the formation of the molecular world, the complementarity (according to N. Bohr) of randomness and determinism, the phenomena of birth and destruction (life and death) was shown. The factors leading to the emergence of biological rhythms and a decrease in the level of the entropic barrier during self-organization of matter, as a consequence of the surrounding world objects diversity, were elucidated. The main sign of life—the effect of replication, the transfer of hereditary traits from father to son, and the appearance of the arrow of time—found its explanation based on developed concepts of processes in molecules.
- The scientific results are summarized in 64 original monographs (38 from 2000 to 2021).

The recognition of the importance of this direction for the development of molecular science resulted in the 2013 Nobel Prize in Chemistry for the development of molecular modelling methods.

Leading former and current members of the laboratory (L. A. Gribov, V. I. Baranov, V. A. Dementiev, and M. E. Eliashberg) were awarded the State Prize of the Russian Federation in the field of science and technology for "The development of the theory and methods for molecular spectra computation and creation of expert systems" (1999) (Fig. 26).

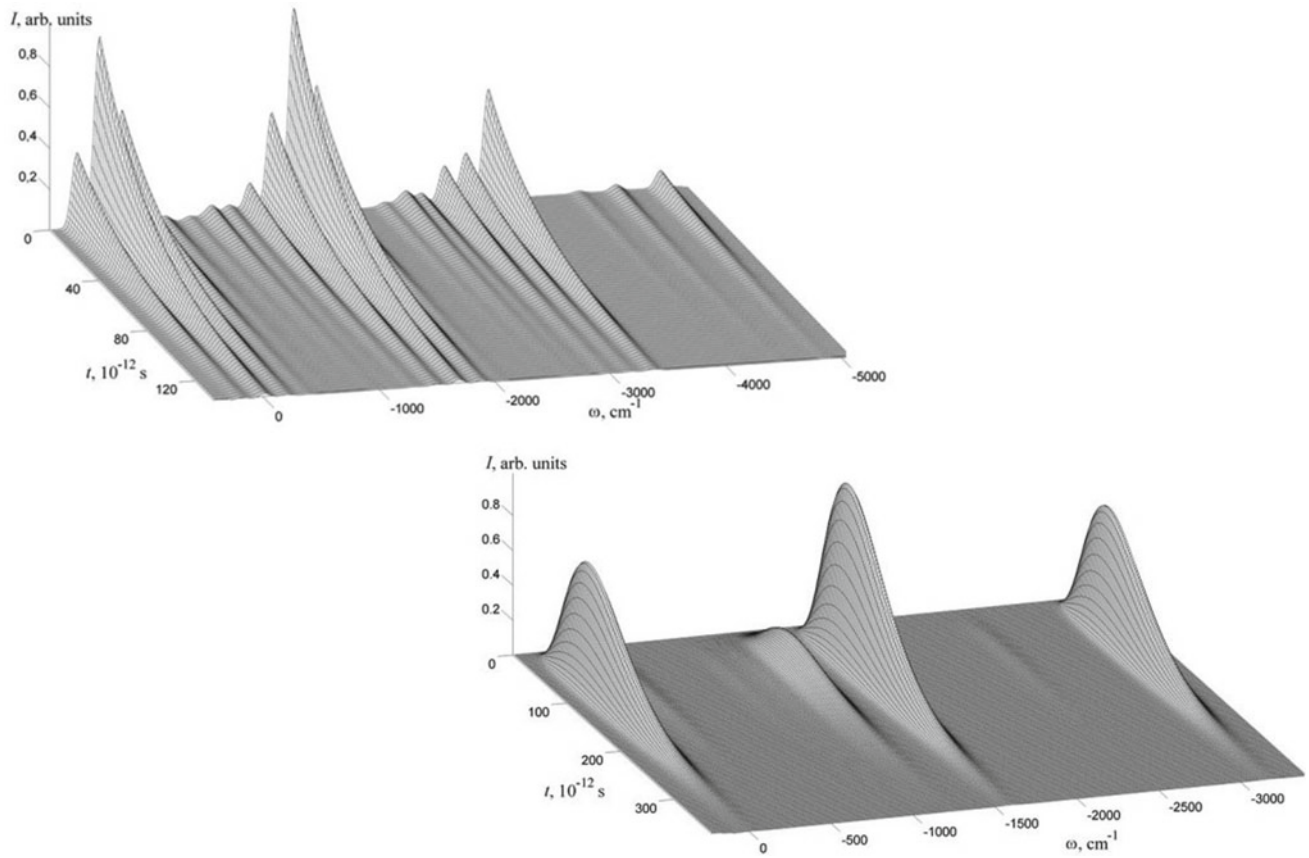

Fig. 26 Time-dependent spectra of a mixture of substances (initial data for analysis)

Laboratory of Methods for Research and Analysis of Substances and Materials

Head of the Laboratory
Vladimir P. Kolotov
Corresponding Member of RAS,
Doctor of Chemistry,
Former Director and current Scientific Advisor of the Vernadsky Institute RAS (Analytical Chemistry Branch)
Email: kolotov@geokhi.ru
Website: http://portal.geokhi.ru/sites/eng/lab04
http://www.wssradel.org
Articles by lab members in this volume: Chapter 36

The laboratory was organised on the 30th of December 2013, as a result of the merger of two laboratories: the Laboratory of Radioanalytical and Electrochemical Methods and the Central Laboratory for Substance Analysis. The Laboratory of Radioanalytical and Electrochemical Methods was established in 1949. The first head was Academician I. P. Alimarin, who successfully managed the laboratory for 40 years. Under his guidance, a galaxy of leading analytical chemists emerged from the laboratory. Since 1987, V. P. Kolotov became head of the laboratory. Central Laboratory for Substance Analysis was founded in 1976 by Academician V. L. Barsukov and was headed by Yu. I. Belyaev (1976–1979), G. M. Varshal (1979–1986), N. M. Kuzmin (1986–1997), G. M. Kolesov (1997–2012). Today the laboratory consists of 18 employees, including 1 Doctor of Sciences and 8 Ph.D.'s.

The equipment of the laboratory currently includes:

ICP-MS: X Series2 (Thermo Scientific); ICP-AES: iCAP6500 (Thermo Scientific) and iCAP9000 (Thermo Jarell Ash); X-ray fluorescent analysis: Axious Advanced PW 4400/04 (Philips); Electron probe microanalysis: SX-100 X-ray (Cameca); mercury atomic absorption detection (Lumex); gamma-ray spectrometers equipped with high-resolution detectors (Canberra and GreenStar).

Laboratory tasks

- Development and improvement of analytical methods for the study of substances and materials (bulk and local analysis; methods of analysis: X-ray fluorescent analysis (wavelength dispersive spectrometry), electron probe microanalysis (EPMA), atomic emission spectrometry, quadrupole mass-spectrometry, radioanalytical methods;
- Development of an intelligent data processing system to improve the metrological level of analysis results, mathematical and computer solutions to resolve interferences when performing analysis, processing of large data sets, consolidation of analytical data obtained by different methods listed above;
- Improvement of sample preparation for the analysis of different types of samples, development of new systems for sample decomposition, development of concentration methods to determine ultralow elements concentrations;
- Analysis of real substances and materials of various origins, rocks, extraterrestrial matter, industrial samples, certification of candidates for reference materials;
- Development of electronic internet systems to support research in analytical chemistry;
- Development of low activation structural materials for nuclear power industry and related tasks.

Key research findings

- Development of methodology and software for comprehensive processing of ICP-MS data by means of relational database management system. The results are presented as a multidimensional data set, including element concentrations, measurement uncertainty, detection limits, analysis quality control, different normalizations, and other information (Fig. 27);
- Algorithms for computer processing of different types of measured data. Gamma-ray spectrometry (deconvolution of multiplets, compensation of the effect of true coincidences when measuring bulk sources, isotope identification, etc.), ICP-AES (accounting for mutual interference when determining the whole range of REEs in ores),

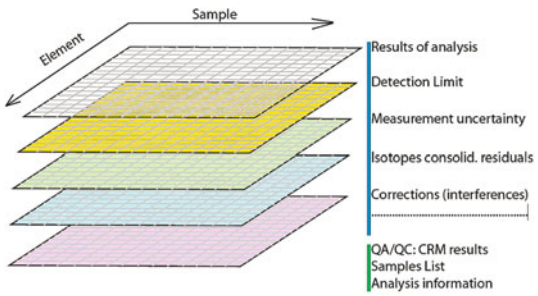

Fig. 27 Diagram of a multidimensional array of analysis results that are exported to MS Excel tabs

gamma activation digital autoradiography (to improve the selectivity of radionuclide distribution mapping);

- Original hardware for open system acid decomposition of different types of geological samples (Fig. 28), including low-mass samples in the MW system. Application of the sintering method in an inert argon atmosphere for the decomposition of some ores and rocks was implemented. Regulations have been developed for the decomposition of samples of various types in these systems for subsequent analysis by ICP-AES and ICP-MS methods, and it is supposed to be used both for direct analysis and for the concentration of target elements (for example, using carbon nanomaterials for the determination of ultralow REE concentrations in ultramafic rocks);
- Techniques for the X-ray spectral determination of petrogenic and trace elements in geological samples have been developed. To improve the accuracy of sulphide ores analysis it is suggested to use multivariate statistical (cluster) methods for selection the most adequate reference samples. Approaches have been developed to determine fluorine and iron (in various oxidation states) in geological samples. Techniques for analysis of plant materials, zeolites, etc. have been suggested.
- A method for the quantitative determination of carbon by secondary ion mass spectrometry (SIMS) has been

Fig. 28 Developed hardware for high productive acid decomposition of different types of geological samples (open system)

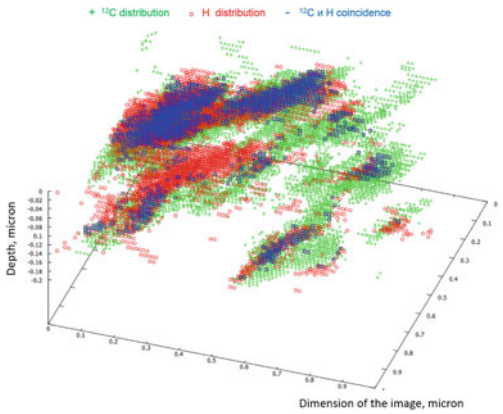

Fig. 29 3D distribution of carbon, hydrogen, and mixed zones for a silicate sample

developed. The dependence of the ionization coefficient of the determining element on the parameter NBO/T characterizing the composition and structure of the silicates understudy has been revealed. Software for visualization of three-dimensional distributions of an element obtained by SIMS, with the possibility of detecting areas of spatial coincidence of two or more elements has been released (Fig. 29);

- Method of electron probe microanalysis has been developed for simultaneous determination of more than 25 elements in silicate samples and minerals of complex multi-component composition (carbonatites, fluorapatite, ore minerals, extraterrestrial matter). By detecting and taking spectral interferences into account, the metrological characteristics of the analysis are considerably increased. It was found that fluorapatite and its substituting monazite-(Ce) are the main concentrators of P, Sr, Th, and REE. The microstructure and phase composition of meteorites have been investigated. These data allow us to understand the origin of the substance and to reconstruct its evolution. For example, the thermal history of the Elgin and Seymchan meteorites has been recovered recently;
- A new class of environmentally safer structural materials for nuclear power engineering (vanadium-based steels and alloys) with accelerated decay of induced radioactivity has been developed (jointly with IMET RAS);
- Consolidated thesaurus of terms on general issues and metrology of analytical chemistry has been launched. It is as a basis for creating an ontology and a hierarchical taxonomy for indexing documents of the various supported sites. Several Internet resources using modern information technologies have been developed.

Laboratory of Radiochemistry

Head of the Laboratory
Sergey E. Vinokurov
Doctor of Chemistry
Deputy Director of Research for the Vernadsky Institute RAS
Email: vinokurov@geokhi.ru
Website: http://portal.geokhi.ru/sites/eng/lab05
Articles by lab members in this volume: Chapters 39 and 40

The laboratory was established in 1949 as Special Laboratory No. 1–2 to provide analytical control of nuclear materials and technologies during the realization of the USSR Atomic Project. In 1960 the laboratory was renamed Laboratory of Radiochemistry.
The laboratory consists of 20 employees, including 2 Academician and 1 corresponding members of the Russian Academy of Sciences, 5 doctors of sciences, 2 Ph.D.'s and 4 Ph.D. students.

Boris F. Myasoedov,
Academician of RAS

The scientific activity of the laboratory is to investigate fundamental aspects of the chemistry of actinide and fission product elements for their use in solving problems of the nuclear fuel cycle, radioactive waste management, radiopharmaceutical chemistry, as well as providing radiation safety for the environment. Scientists who headed the laboratory for 40 years (since 1970) had a key influence on the development of the directions of scientific activity of the laboratory.

The main areas of research

- study of the chemical properties and behavior in various systems of actinide elements (plutonium, americium, and neptunium) in higher oxidation states;
- creation of effective methods of removal, separation, and determination of actinides and fission product elements and their application in the analysis of technogenic and natural samples, in radioactive waste fractionation, and for obtaining radioisotopes for medical purposes;
- development of scientific bases for innovative technologies of nuclear fuel generation and reprocessing of spent nuclear fuel;
- development and study of the behavior of natural and engineered safety barriers to the placement of radioactive waste storage facilities, including the development of new matrices for reliable immobilization of radionuclides and other waste components;
- development of new approaches to radioecological monitoring and renovation of objects contaminated with radionuclides and forecasting the radioecological situation.

Developing methods

The laboratory uses modern physicochemical methods, including radiometric alpha-, beta- and gamma-spectrometry, liquid scintillation spectrometry, spectroscopic, microscopic (SEM, TEM), and X-ray methods (XRD, XRF, EXAFS, XANES) in conducting research.

Interdisciplinary Studies

The laboratory participates in interdisciplinary research involving advances in radiochemistry, physical chemistry, geochemistry, radioecology, radiopharmaceutical chemistry, and nuclear medicine.

Scientific Connections

The laboratory cooperates with leading scientific, educational, and industrial organizations of Russia: institutes of the Russian

Academy of Sciences (IPCE RAS, IGEM RAS, IGIC RAS, etc.), universities: (Lomonosov Moscow State University, Mendeleev University of Chemical Technology, Moscow Engineering Physics Institute, etc.), enterprises of the State Atomic Energy Corporation ROSATOM (FSUE PA Mayak, FSUE Mining and Chemical Combine, JSC VNIINM, JSC ARRICT, V. G. Khlopin Radium Institute, FSUE Radon).

Since 2009 the Research and Education Center "Actinides: Properties, Behavior in anthropogenic and natural Processes" for high-level training in radiochemistry and radioecology has been successfully functioning based on the Radiochemistry Laboratory and the Radiochemistry Division of Chemistry Department of the Lomonosov MSU.

New methods developed by the laboratory are approbated at production enterprises under contracts of scientific and technical cooperation, including ELEMASH Machine-Building Plant (Elektrostal, Moscow region), Mining and Chemical Combine (Zheleznogorsk, Krasnoyarsk region), the Production Association Mayak (Ozersk, Chelyabinsk region) and others.

The laboratory maintains international relations in the field of radiochemistry and chemistry of transuranic elements with many scientific centers around the world, including the United States, Japan, France, the Czech Republic, and Germany.

Main results of laboratory research in recent years

- the highest degree of oxidation of plutonium has been discovered—Pu(VIII);
- new approaches to nuclear fuel production under microwave radiation have been developed;
- scientific basis for innovative technology for spent nuclear fuel reprocessing, including reprocessing of structural materials of fuel assemblies, has been created;
- methods of high-level waste fractionation with subsequent separation of americium and curium by conversion of americium to higher oxidation states have been developed;
- new technologies for immobilization of liquid radioactive waste using a mineral-like low-temperature magnesium-potassium-phosphate matrix and aluminum iron phosphate glass have been developed;
- The laboratory has published 5 monographs in the series "Analytical Chemistry of Elements": Actinium, Uranium, Plutonium, Protactinium, and Transplutonium Elements.

Photo 12 illustrates an exterior view of the Vernadsky Institute RAS.

Photo 12 Sculpture of the famous Soviet avant-garde sculptor Vadim Sidur installed next to the institute. More information about Vadim Sidur: https://en.wikipedia.org/wiki/Vadim_Sidur

Laboratory of Sorption Methods

Head of the Laboratory
Ruslan Kh. Khamizov
Corresponding Member of RAS
Doctor of Chemistry,
Director of the Vernadsky Institute RAS
Email: khamiz@geokhi.ru
Website: http://portal.geokhi.ru/sites/eng/lab06
Article by lab members in this volume: Chapters 29 and 30

The laboratory was organized in 1967 by D.Sc. (Chem.) Prof. M. M. Senyavin (1917–1989). D.Sc. (Chem.) Prof. B. A. Rudenko (1932–2013) led the laboratory from 1990 to 2002. Since 2002 it has been headed by Dr. R. Kh. Khamizov. The laboratory has played a vital role in developing the theory of ion-exchange and chromatography, establishing the REM separation technology in the country, and water preparation for thermal and nuclear power plants. The laboratory staff has taken part in the liquidation of the Chernobyl accident. M. M. Senyavin was awarded the State Prize of the USSR in 1972 and the State Prize of the Russian Federation in 1991.
The laboratory has 15 research associates, among them 4 Doctors of Sciences and 6 Ph.D.'s.

The main research directions

- Development of the theory of sorption and chromatographic processes, methods of their calculation and optimization, development of new methods of gas, liquid, and ion chromatography.
- Development of environment friendly and economically effective methods of processing technological solutions, natural and wastewaters with the aim of their purification and extraction of valuable components.
- Creation of new ion-exchange and sorption materials for technology and analysis.

Interdisciplinary studies

The preparation and application of nano-ion-exchangers in analytical chemistry and medicine.

The most important results

- Fundamental approaches to the theoretical description of equilibrium and dynamics of mass transfer in multicomponent heterophase systems with concentrated electrolytes in nanoporous polymeric media are developed.
- The technology of purification of industrial wet-process phosphoric acid (WPA) with simultaneous extraction of REE has been developed.
- Fundamental approaches to the theoretical description of intermolecular forces, adsorption, and dynamics of multicomponent sorption have been developed.
- The general theory of chromatography was developed, new methods of separation under isocratic and gradient conditions were proposed.
- The method for synthesizing nanocomposites with ion-exchange properties has been developed, and new highly effective analytical columns for ion chromatography have been obtained.
- Methods of preparation of nanosized ion-exchange resins and complexes on their basis for use in medicine have been developed.
- The modern prototypes of devices for highly sensitive X-ray fluorescence analysis of small samples (one micro-drop) of aqueous solutions using poly-capillary optics have been elaborated.
- The laboratory researchers have published 18 monographs and 8 chapters in foreign monographs. They have obtained more than 90 USSR inventor's certificates and patents in Russia and other countries (Figs. 30 and 31).

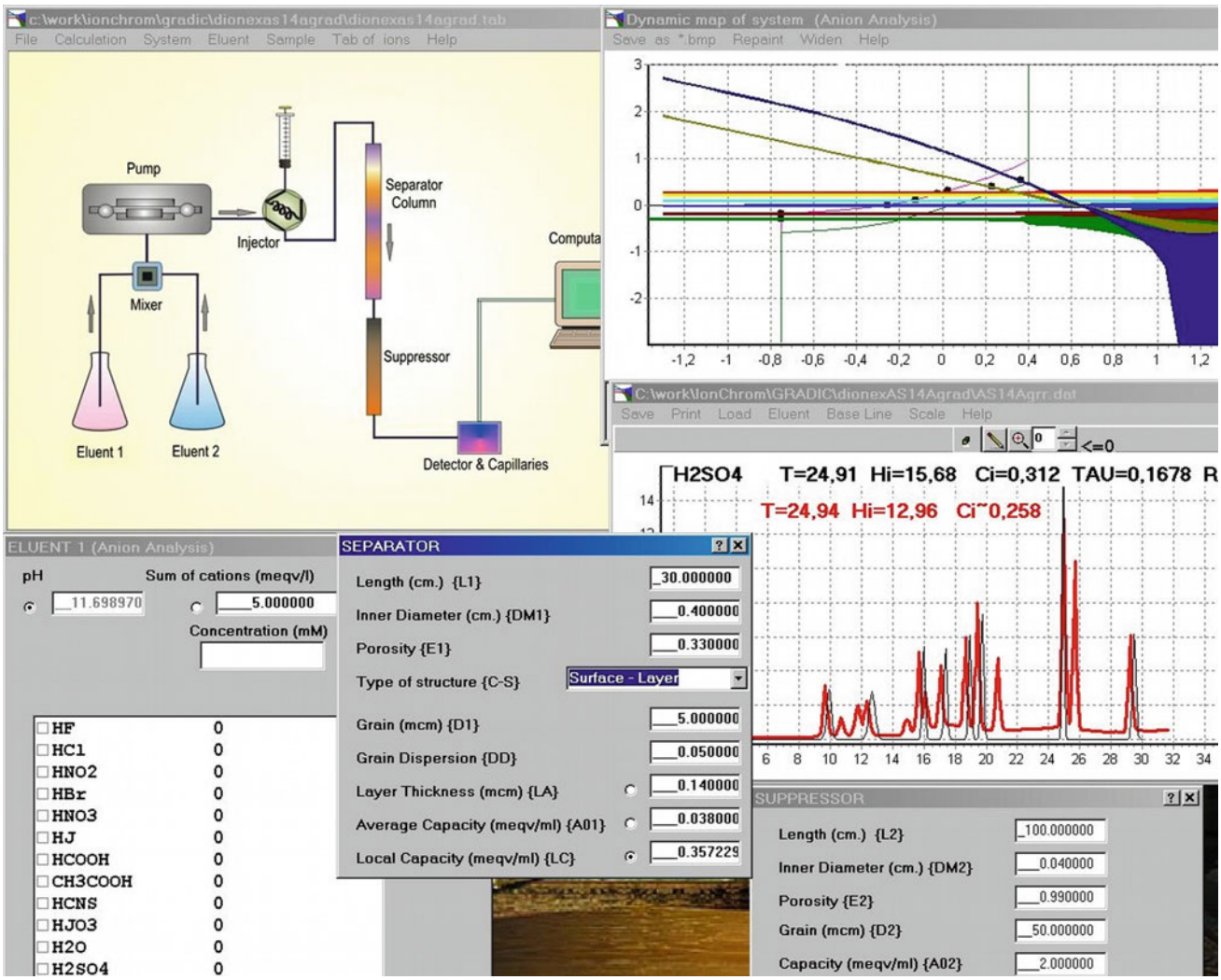

Fig. 30 The interactive interface of the IONCHROM program (left, top). The windows shown: composition of the eluent, separation column, suppression column, dynamic map of the system, chromatograms: calculated (in black), experimental (in red). The program solves: direct problem of calculating theoretical chromatograms; inverse problem of analyzing experimental ones, optimization for fast and complete separation of mixtures of ions

Fig. 31 Pilot plant for WPA purification and REE extraction using the technology developed in the laboratory jointly with NewChem Technology, LLC and Ya.V. Samoilov Institute NIUIF, JSC (PhosAgro). Tests were conducted at the Belorechensk Mineral Fertilizer Plant (BMU—EuroChem)

Laboratory of Chemical Sensors and Determination of Gas-Forming Impurities

Head of the Laboratory
Vladimir V. Yagov
Ph.D. in Chemistry
Email: vladvy65@yandex.ru
Website: http://portal.geokhi.ru/sites/eng/lab07
Articles by lab members in this volume: Chapter 31

The laboratory for the determination of gas-forming impurities was formed in 1967 and headed by Professor Dr. Lev L. Kunin until 1988. From 1988, the laboratory received its modern name and was led by Professor Dr. Boris K. Zuev. Since 2019, Senior Researcher, Ph.D. Vladimir V. Yagov is the acting head of the laboratory.
The laboratory has a staff of 12 researchers, including 2 Doctors of Science and 7 Ph.D.'s.

Boris K. Zuev
Doctor of Technical Sciences, Professor

Traditionally the task of the division is not only to study physical and chemical processes and underlying methods of chemical analysis but also to create analytical equipment and techniques. In a fundamental aspect, we are focused on the principles of optical and electrical signal formation during charge, substance, and energy transfer through gas/electrolyte and metal/spacer/electrolyte interfaces. The laboratory develops thermal oxidation spectroscopy, photoluminescence, plasmon resonance spectroscopy in organized media, cathodic electrochemiluminescence, and microplasma atomic emission spectroscopy with sources based on liquid electrode discharges. We are also interested in new sampling devices adapted to the combined methods of analysis of waters, some geological and biomedical objects.

The devices and methods developed in the laboratory are used in geochemical investigations to study the composition of seawater and bottom sediments; in cosmic investigations to study the chemical composition of meteorites and celestial bodies of the Solar System; in the development of hydrochemical technology processes; in clinical diagnostics; in the educational process (Department of Chemistry at Dubna State University and the Department of Analytical Chemistry at the Lomonosov Moscow State University).

The following main results have been obtained in recent years:

- Jointly with the Laboratory of Geochemistry of the Moon and Planets, a monopole mass spectrometer mounted on the descent vehicle was developed and manufactured (Phobos-Grunt Project).
- A new thermo-oxidative method of substance investigation—oxithermography—has been proposed. A prototype of a multi-sensor oxythermographic unit with the possibility of simultaneous measurement of oxygen and carbon dioxide content has been created. Original methods and sampling devices oriented to apply oxythermography in biomedical and geochemical studies have been developed. A combined membrane-oxythermographic method for determining the suspended and dissolved organic matter in natural waters was proposed.
- New sources of atomization and excitation based on pulsed discharges with liquid electrodes are proposed and studied. A thermal model of electrolyte cathode atomization is developed, which qualitatively explains the influence of several experimental parameters on the signal. The influence of metal type on its transfer from the solution to the discharge torch was investigated for some microplasma sources (see Fig. 32). The selective transfer of some heavy metals from the liquid anode, formed by concentrated salt solution in plasma, is discovered. A prototype of a drop-spark atomic emission spectrometer for solution analysis has been created. Express methods for the determination of Na, K, Ca, and Mg in

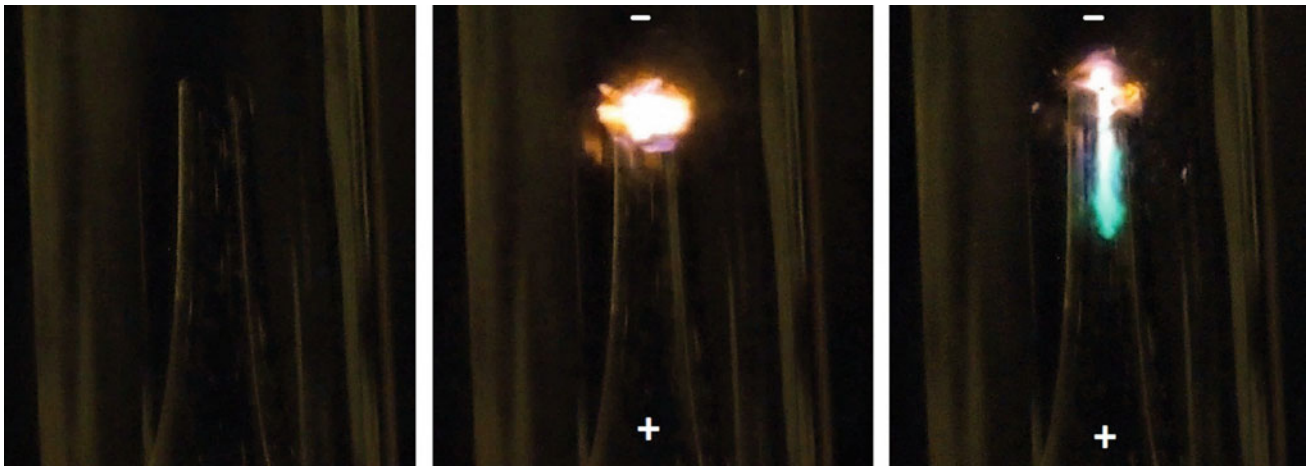

Fig. 32 Single-frame images captured from video of flow boiling discharge in a solution containing 8 mM NaCl and 4 μM Tl. Sodium D-line and green Tl emission are separated in time and space

some biological fluids were developed for clinical diagnostics.

- A new preparative technique for photochemical synthesis and targeted formation of the surface layer of silver nanoparticles of variable geometry and theoretical approaches to describe the mechanisms of their growth was developed. The silver nanoparticles with surface plasmon resonance enhance the fluorescence of the nearby molecules in the self-assembled supramolecular systems. This phenomenon was used for the fluorescence detection of polycyclic aromatic hydrocarbons.
- A method for the detection of some heavy metals and aromatic compounds by electrochemical excitation of luminescence at the oxide-covered aluminum electrode is proposed. The conditions of stable operation of the electrochemiluminescent (ECL) detector were determined. A possibility of ECL determination of organotin and organomercury compounds, along with some aromatic drugs, was shown. The cathodic ECL of 13 heavy metals in concentrated acidified salt solutions was discovered and studied. This type of ECL is sensitive to the matrix salt, similar to the photoluminescence of crystal phosphors. The cathodic nanophosphor effect is promising for the analysis of some inorganic materials.
- The method of analytical signal extraction on the changing background based on the original algorithm of partial curve matching using ordinate distribution was developed. The algorithm is implemented in the software of the instruments developed in the laboratory, including real-time measurements. *Photo 13 illustrates an interior view of the Vernadsky Institute RAS and Photo 14 introduces the Department of Planetary Sciences of the Vernadsky Institute.*

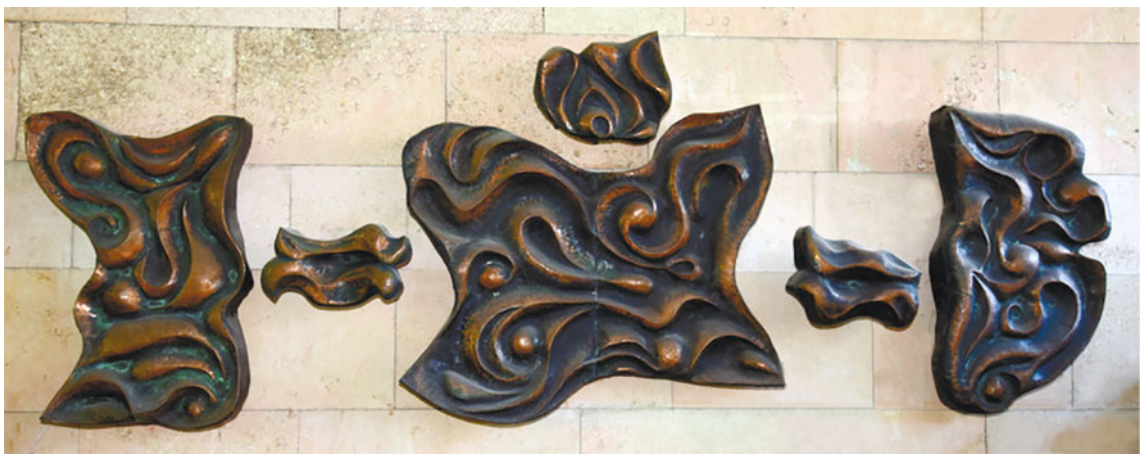

Photo 13 Wall panel made by unknown disciple of Vadim Sidur, decorating the interiors of the institute

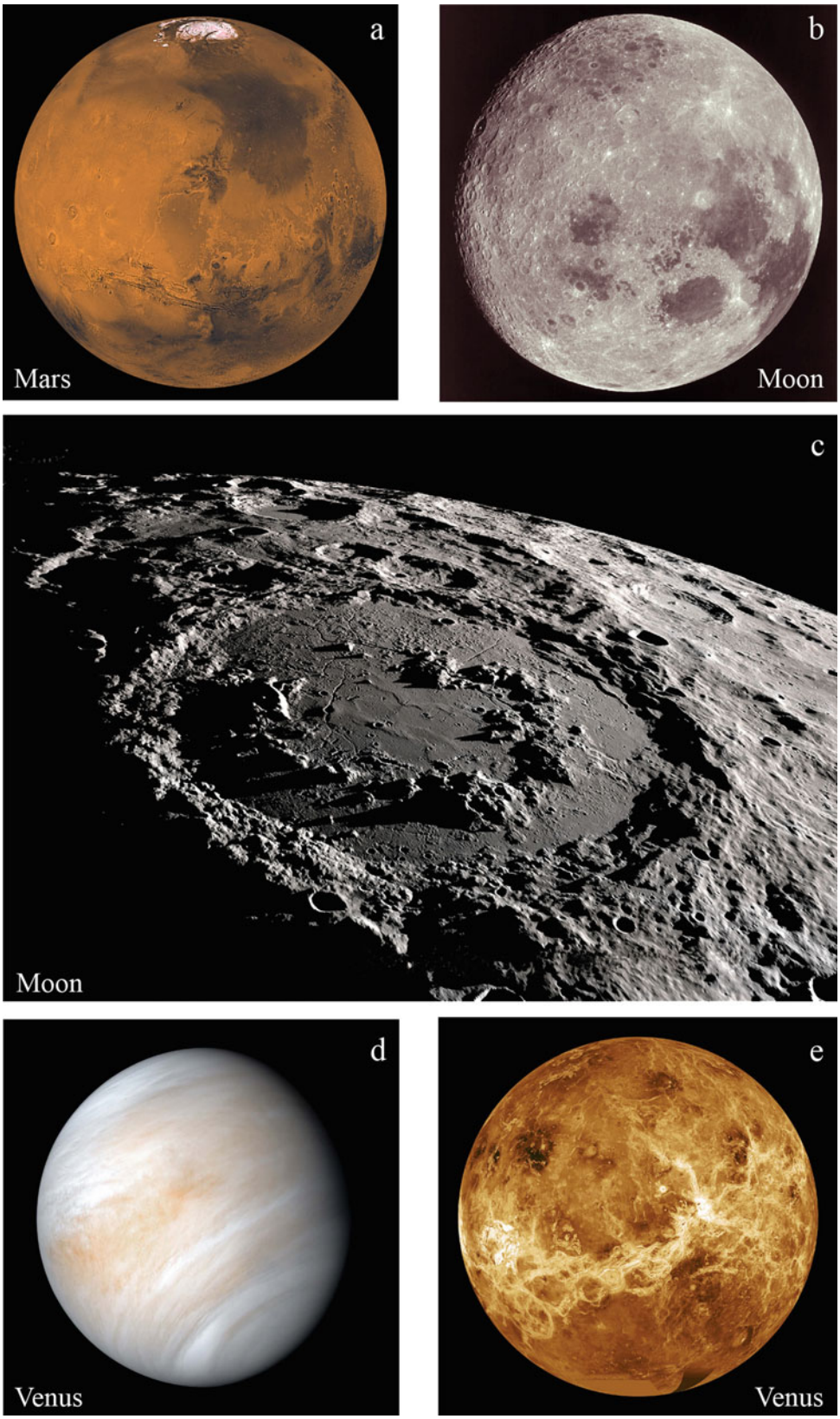

Photo 14 **a** Mosaic picture of Mars made of images by Viking orbiter. *Photo credit* NASA/JPL-Caltech/USGS; **b** MOSAIC picture of the Moon; **c** perspective view of schrodinger basin and the South Pole. *Source* NASA GSFC scientific visualization studio; **d** newly-processed views of Venus from mariner 10, obtained in 1974. *Source* NASA/JPL-Caltech; **e** computer simulated global view of Venus (Magellan synthetic aperture radar mosaics from the first cycle of Magellan mapping). *Source* NASA/Jet Propulsion Laboratory-Caltech

Department of Planetary Sciences

Head of the Department
Mikhail Ya. Marov
Academician of RAS,
Doctor of Physics and Mathematics,
Email: marovmail@yandex.ru

The Department of Planetary Sciences currently includes four laboratories and one museum:

- Laboratory of Geochemistry of the Moon and Planets
- Laboratory of Meteoritics and Cosmochemistry
- Laboratory of Comparative Planetology
- Laboratory of Thermodynamics and Mathematical Modeling of Natural Processes and curates one museum
- Museum of Extraterrestrial Matter.

The main activities of the department are the investigation of problems of origin and evolution of planets (Photo 14) and small bodies of the Solar System (asteroids, comets) and exoplanets based on the study of extraterrestrial samples (meteorites, lunar soil) and mathematical modeling of processes underlying their genesis and formation together with the study of cosmochemistry, planetary geology, and comparative planetology. Such an integrated approach provides unique opportunities to investigate problems of planetary cosmogony by model reconstruction of evolutionary processes and verification of results using a direct study of extraterrestrial matter, preserving in its composition the traces of these processes.

The department participates in the development of federal programs of space research, development of methodological justification and creation of scientific instruments for spacecraft and analysis of measurements, selection and geological-geochemical justification of spacecraft landing sites on the surface of the Moon (Photo 14), planets, and their satellites. One of the directions of cosmochemical research relates to studying long-periodic variations of galactic cosmic rays and solar activity based on studying tracks in microsamples of meteorites.

The Laboratory of Meteoritics and Cosmochemistry curates and replenishes the unique collection of meteorites and lunar soil of the Russian Academy of Sciences. Staff members of the laboratory are also involved in the examination of samples collected from the public to determine their possible extraterrestrial origin (Photos 15, 16 and 17).

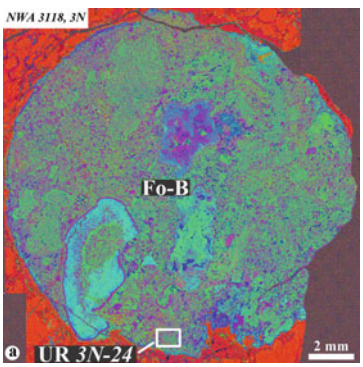

Photo 15 X-ray elemental map in Kα (Mg-red, Ca-green, Al-blue) of a compound CAI 3 N containing UR CAI 3 N-24 from the North West Africa 3118 CV3 chondrite (Ivanova et al. 2012, 2015, Meteorit. Planet. Sci.). CAI stands for calcium-aluminium-rich inclusion. With an age of 4567.30 ± 0.16 Ma, CAIs are the oldest known objects in the Solar System (Connelly et al. 2012, Science)

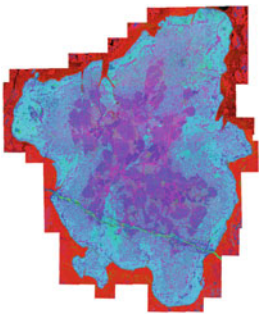

Photo 16 X-ray elemental map in Kα (Mg-red, Ca-green, Al-blue) of CAI 27cE of Type B from the Efremovka CV3 chondrite (Ivanova et al. 2021, Geochim. Cosmochim. Acta). CAI is calcium-aluminium-rich inclusion. With an age of 4567.30 ± 0.16 Ma, CAIs are the oldest known objects in the Solar System (Connelly et al. 2012, Science)

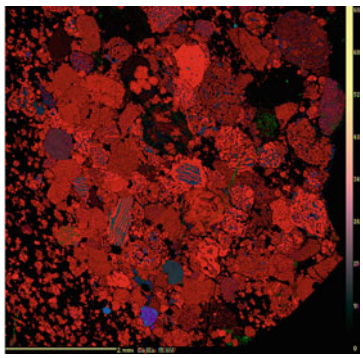

Photo 17 X-ray elemental map in Kα (Mg-red, Ca-green, Al-blue) of a metal-poor lithology on contact with a metal-rich lithology from the Isheyevo CH/CBb chondrite (Ivanova et al. 2008, Meteorit. Planet. Sci.)

Laboratory of Geochemistry of the Moon and Planets

Head of the Laboratory
Evgeny N. Slyuta
Ph.D. in Geological and Mineralogical Sciences
Email: slyuta@geokhi.ru
Website: http://portal.geokhi.ru/sites/eng/lab41
Articles by lab members in this volume:
Chapters 16, 21, 22 and 24

On the initiative of Academician A. P. Vinogradov, the laboratory was founded at the Vernadsky Institute in 1961 to develop scientific equipment for spacecraft to study the substance of the Moon and planets. The laboratory was headed by Professor Yu. A. Surkov and from 2006 to 2015 by Dr. L. P. Moskaleva. The laboratory has developed and manufactured more than 30 types of various scientific equipment for spacecraft for studying the Moon, Venus, Mars, and Phobos.
The laboratory currently employs 10 scientific and 11 engineering and technical staff, including 3 Ph.D.

The laboratory's instrumentation includes a lunar test bench, a clean room, a receiving chamber for lunar soil (Fig. 33), a laboratory complex for creating soil analogues, a soil laboratory for studying the physical and mechanical properties of soil (Fig. 34), and a cabinet of planetary cartography.

The main research directions of the laboratory are associated with the development, design, and creation of various types of scientific instruments and soil sampling devices for geological, geochemical, and geophysical research of the Moon, planets, and other small Solar System bodies.

The tasks of the laboratory also include:

- study of the physical–mechanical, thermophysical and electromagnetic properties of the lunar and Martian soil and the development of their analogues (Fig. 35) for testing scientific equipment and spacecraft;
- research and mapping of potential landing sites on the Moon, Mars, and Venus in order to create engineering models of the surface;
- experimental studies of the chemical differentiation of matter as a result of meteorite bombardment on the surface of the Moon and other bodies;
- study of implantation and enrichment of minerals and particles of regolith on the lunar surface with cosmogenic isotopes;
- analyze and mapping of various types of lunar and extraterrestrial resources, and the development of methods for their exploration and technology for extraction and enrichment;
- study of the observed transition between small and planetary bodies and the parameters of the gravitational deformation of small Solar System bodies, depending on their chemical and mineral composition.

Methods

The laboratory has developed and tested thermal desorption mass spectrometry methodology (Slyuta et al. 2017) for

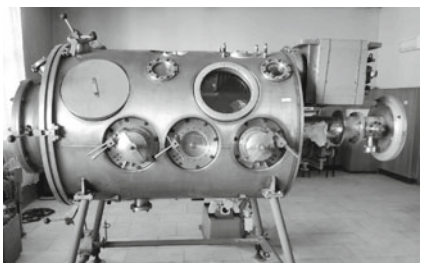

Fig. 33 General view of a receiving lunar chamber for lunar soil. At the top of the camera, there are small windows for lighting and large viewing windows, below are three glove devices, and to the right is a gateway

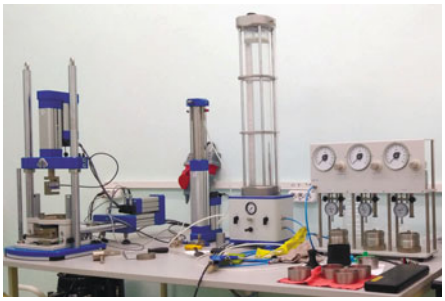

Fig. 34 Automated testing complex "ASIS Pro" for testing soil samples by compression, filtration tests, by a single-plane cut method, under triaxle compression etc

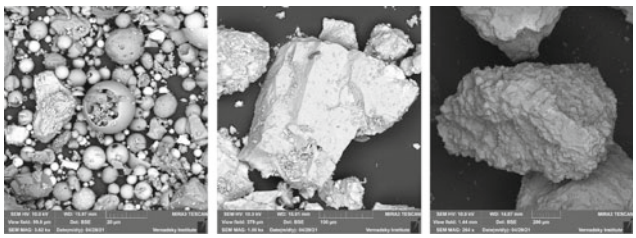

Fig. 35 SEM images of initial components of VI-75 lunar soil-analogue

studying implanted gases of the Earth and solar winds in lunar soil samples, depending on the depth of implantation and activation energy. A method for simulating micrometeorite bombardment using a pulsed laser to study the evaporative chemical differentiation of matter has been developed (Sorokin et al., 2020). The method of multiscale volumetric microscopy used in the laboratory makes it possible to study a particle of extraterrestrial matter with minimal impact on its structure while preserving its digital image for further petrological studies.

The most important results:

- The content of natural radionuclides in the lunar soil and the type of lunar rocks with the first gamma-spectrometer on the Luna-10 and Luna-12 spacecrafts was determined for the first time.
- The composition of Venus atmosphere with mass spectrometers and gas analyzers on spacecraft Venera-4, -5, -6 (1967–1969) and Venus-8, -9, -10 (1972–1975) was determined. The composition of the Venus cloud layer aerosol component has been determined for the first time using an X-ray fluorescence spectrometer on the Venera-12 spacecraft.
- The chemical composition of rocks from three regions of Venus with a soil sampling device and an X-ray fluorescence spectrometer on Venera-13, -14 (1981), and Vega-2 (1984) spacecrafts was determined.
- For the first time, data on the chemical composition of the Martian rocks were obtained with an orbital gamma-ray spectrometer on the Mars-5 (1973) and Phobos-2 (1989) spacecrafts.
- The cosmic dust detector METEOR-L for the lunar orbiting spacecraft Luna-26 has been developed (Fig. 36) (Slyuta et al. 2021).
- A deep logging probe to study the thermophysical, physicomechanical, and electromagnetic properties of the lunar soil for the TERMO-LR experiment on the Luna-27 landing spacecraft was developed (Fig. 37) (Slyuta et al. 2021).
- The first Russian lunar soil analogue VI-75 for experiments and testing of landing spacecraft has been developed (Slyuta et al. 2021).

Fig. 36 The cosmic dust detector METEOR-L for the lunar orbiting spacecraft Luna-26

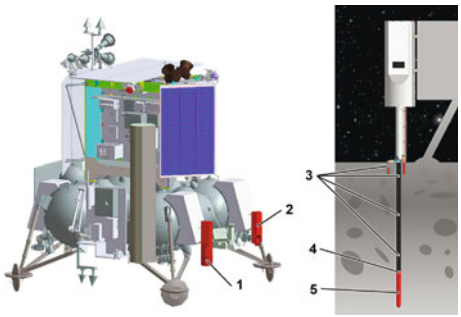

Fig. 37 Deep logging probe (DLP) to study the thermophysical, physicomechanical and electromagnetic properties of the lunar soil for TERMO-LR experiment on the Luna-27 landing spacecraft: 1—DLP; 2—block for thermal research on the surface; 3—DLP thermal sensors; 4—sensors of electromagnetic measurements of DLP; 5—DLP hammer-penetrator

Fig. 38 The concept of a new generation heavy lunar rover "Robot-Geologist" with a drilling rig for carrying out geological and geophysical surveys on the Moon

- The first Russian Martian soil analogue for testing the ExoMars landing spacecraft has also been developed.
- The laboratory has developed the concept of a new generation heavy lunar rover, "Robot-Geologist" (Fig. 38), with a drilling rig for carrying out geological and geophysical surveys on the Moon.
- A theory of gravitational deformation of small Solar System bodies has been developed (Slyuta and Voropaev 2015).

Laboratory of Meteoritics and Cosmochemistry

Head of the Laboratory
Dmitry D. Badyukov
Ph.D. in Geological and Mineralogical Sciences
Email: badyukov@geokhi.ru
Website: http://portal.geokhi.ru/sites/eng/lab43
http://www.meteorites.ru
Articles by lab members in this volume: Chapters 17, 18, 19 and 23

Committee on Meteorites RAS (Russian abbreviation: KMET) and the Laboratory of Comparative Planetology at the Vernadsky Institute RAS are historic predecessors of the Laboratory of Meteoritics. In 2019, the Laboratory of Cosmochemistry at the Vernadsky Institute RAS was joined with the Laboratory of Meteoritics and formed the Laboratory of Meteoritics and Cosmochemistry. Currently, the staff includes 25 scientists, including 2 Doctors of Sciences and 12 Ph.D.'s.

Following their scientific traditions and subjects of investigations, the scientific personnel researches in the following directions: formation and evolution of a solid matter in the Solar nebulae; mechanisms of formation and evolution of elemental and isotopic compositions; the radiation history of meteorites and cosmic rays; accretion, differentiation, metamorphic and exogenic history of cosmic bodies; geochemistry and petrology of impact processes; the magnetism of extraterrestrial matter, tektites and impactites.

The laboratory curates the Meteorite collection of the RAS and the national collection of lunar soil delivered by Soviet lunar missions Luna 16, 20, and 24. Meteorite samples (Figs. 39 and 40) can be loaned from the collection by requests only for scientific goals. Also, the laboratory examines stones suspected of extraterrestrial origin. The laboratory uses many modern geochemical, mineralogical, petrological, and geophysical methods applied to meteorites, lunar soil, and impactites, including different mathematical models of natural processes. Impact craters and tektites are also investigated.

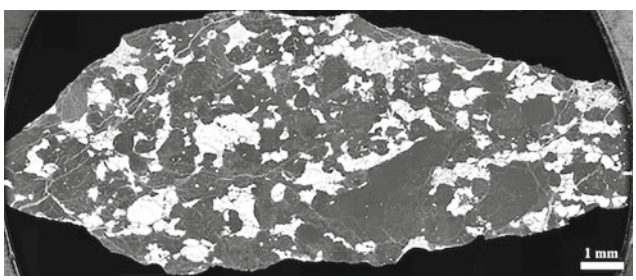

Fig. 39 Panoramic BSE image of Sierra Gorda 009 G chondrite from Chile (Ivanova et al. 2020, Meteoritics and Planetary Science)

Fig. 40 Chelyabinsk ordinary chondrite (fall of February 2013)

The laboratory has done some pioneering work in the field of lunar soil and unique meteorites. It was among the first ones to start a study of the Cretaceous-Tertiary impact event.

The main achievements of the laboratory of meteoritics

- Based on the investigation of the first solid material formed in the early Solar System—Ca, Al-rich refractory inclusions (CAIs) from carbonaceous chondrites, the Solar System age was determined (4567.30 ± 0.16 Ma). Ultrarefractory CAIs were found among the first solid material, and they record very high-temperature chemical and isotopic fractionation in the early Solar System and evolution of oxygen isotopic composition.
- A new mineral group of phosphorous sulfides of Fe and Ni was found in carbonaceous CM chondrites. It is suggested that they were formed in gas shells of carbon stars due to the s-process.

- New minerals—florenskite, hapkeite, and sodium sulfide—were found in the Kaidun meteorite. The Kaidun meteorite contains a unique association of various materials carrying signs of matter evolution of the Solar System, which encompass processes from condensation in the nebulae to water alteration and magmatic differentiation.
- A new subgroup (G) of metal-rich chondrites was established (Fig. 39). It may represent a unique metal-rich parent asteroid containing primitive and fractionated material from the inner Solar System. G chondrites may have formed by a planetesimal collision resulting in the lack of matrix in chondrites (Fig. 40).
- Placers of micrometeorites were found on glaciers of the Novaya Zemlya archipelago. Both common and unique types of micrometeorites are present in the micrometeorite collection (Fig. 41).
- The evaluation of the lunar meteorite flux on the Earth was made. Fragments of deep-seated rocks in lunar meteorites were discovered that were ejected from the lunar lower crust or even upper mantle. The native silicon and Fe silicides were described in lunar regolith breccias shock-induced evaporation, and condensation processes were considered for their formation.
- Analyzing radiation ages and orbits of ordinary chondrites allowed us to reveal the hierarchy of the most probable parent bodies of H- and L-chondrites. The method of calculating the depth distribution of radionuclides in cosmic bodies was developed. It allows not only monitoring the current radiation situation in the Solar System but also forecasting radiation safety in the near future.
- The application of tracking method applied to determine the energy of superheavy ($Z > 30$) galactic cosmic ray nuclei allowed the detection of transuranic element nuclei in the galactic rays.
- It was demonstrated that a layered (graphene-like) carbon phase can be a potential candidate for the carrier phase of trapped primary noble gases of planetary type (Q-gases) in meteorites and that the origin of xenon components in meteorite nanodiamonds can be limited to two astrophysical sources—one of type II supernovae and a molecular cloud.
- A scale of Maastrichtian-Danian (M/D) impact event is estimated. The work on impactites of the Kara and Boltysh impact structures shows their possible (with a probability of 80%) simultaneous formation, linking the events with the terminal Maastrichtian-Danian catastrophic impact event.
- In 2019, a new mineral nazarovite ($Ni_{12}P_5$) was named in honour of the former head of the Laboratory of Meteoritics (1998–2016), Dr. Mikhail A. Nazarov (see Annex I).

The laboratory supports a broad collaboration with various leading Russian and foreign scientific organizations. The high-grade professional skills of the scientists give a possibility to say that the Laboratory of Meteoritics and Cosmochemistry is the only scientific institute in Russia that carries out the study of extraterrestrial matter on a modern level (Fig. 42). In 2018 lab members organized the 81st Annual Meeting of the Meteoritical Society in Moscow (Russia).

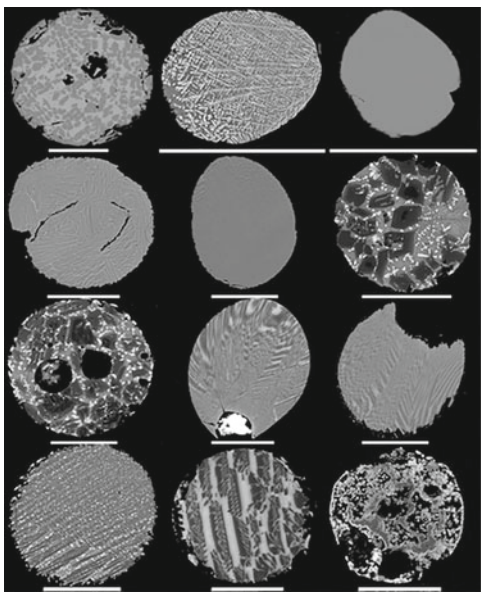

Fig. 41 Micrometeorites from Novaya Zemlya. The scale bar is 100 microns (see Chap. 17 for details)

Fig. 42 **a–b** The fall of Chelyabinsk ordinary chondrite (2013). *Photo credit* Marat Ahmetvaleev

Laboratory of Comparative Planetology

Head of the Laboratory
Mikhail A. Ivanov
Doctor of Geological and Mineralogical Sciences
E-mail: mikhail_ivanov@brown.edu
Website: http://portal.geokhi.ru/sites/eng/lab44
https://www.planetology.ru/
Articles by lab members in this volume: Chapters 15 and 23

The laboratory was founded in 1967 on the initiative of Academicians A. P. Vinogradov and G. I. Petrov as part of the USSR Academy of Sciences and was headed by Dr. K. P. Florensky. In 1975 the whole laboratory was transferred to Vernadsky Institute of the USSR Academy of Sciences.
At present, the laboratory staff includes 8 people, including 2 Doctors of Sciences and 4 Ph.D.'s.

Alexander T. Basilevsky.
Doctor of Geological and Mineralogical Sciences

From 1982 to 2016, the laboratory was headed by A. T. Basilevsky, Doctor of Geological and Mineralogical Sciences. In 1987 the extraterrestrial matter sector headed by Dr. M. A. Nazarov was organized as a part of the laboratory and subsequently separated into a separate Laboratory of Meteoritics, currently the Laboratory of Meteoritics and Cosmochemistry.

Since 2016 the laboratory has been headed by M. A. Ivanov, Doctor of Geological and Mineralogical Sciences.

Main research directions include studying the surface morphology, the geological structure of planets, satellites, and small Solar System bodies. Based on the developments of the laboratory, characterized landing sites were selected for automatic stations Luna 15–24. Carried out operational support of the work of Lunokhod 1 and 2 and the subsequent analysis of the information collected by them performed a geological and morphological analysis of optical images of the surface of Venus and Mars, obtained by soviet satellites Venus 9–14 and Mars 4–5. At the same time, studies of extraterrestrial matter were carried out in the laboratory. In recent years much attention has been paid to the geological analysis of the surface of Venus, Mars, and Moon, based on the analysis of radar images obtained by the spacecraft Venera 15 and 16 (USSR) and Magellan (USA) and optical images from Mars Surveyor, Mars Odyssey, Mars Reconceiver, Lunar Reconceiver Orbiter (USA), Mars Express, and Venus Express (European Space Agency). The laboratory has produced a global geological map of Venus at a scale of 1:10 000 000. For selection and characterization of Luna-Glob and Luna-Resurs spacecraft landing sites, the study of geological structure and relief of polar lunar surface areas is conducted. The laboratory has successfully implemented the Russian Science Foundation project "Reconstruction of the geological history of the lunar sub-polar regions on the base of new high-precision data for establishing sources, distribution, and accumulation of volatiles (water) on the Moon" (2017–2019). Studies are currently underway as part of the RSF project "Estimates of the rate of exogenous resurfacing on the Moon" (2021–2023). An important direction of this work is the study of geological and geochemical aspects of impact cratering.

The main directions of work include the study of the geological structure and geological history of Mars, Venus, Mercury, satellites of the planets, asteroids, and comets; analysis of observational data on the distribution of various forms of water in the upper layers of the Martian crust and theoretical modeling of this distribution; conducting experiments simulating the geochemical differentiation of matter in the impact process; selection and characterization of spacecraft landing sites on planets and satellites, development of engineering models of relief and soil; collection and storage of images and maps of planets and satellites of the Solar System; teaching on the subject of the laboratory.

Developed methods: photogeological analysis of images; compilation of geological maps of planets (for e.g., Fig. 43) and small bodies; analysis of remote sensing data and direct measurements on the surface of planets and small bodies; experimental and theoretical modeling of geological and geochemical processes on planets and small bodies.

The most important results: laboratory staff published 6 monographs in domestic and 3 in foreign languages; participated in soviet missions Lunokhod 1, 2, Luna 16, 20, 24, Mars 4, 5, Venus 9–16, Vega 1, 2, and Phobos 2 (selection and characterization of landing sites, analysis of data obtained); participated in foreign missions Voyager, Magellan, Mars Global Surveyor, Mars Odyssey, Mars Express, Venus Express, Lunar Reconnaissance Orbiter, and Mars Science Laboratory (analysis of data obtained).

From 1985 to 2010, the laboratory, together with Brown University (USA), conducted annually in Moscow and Houston an International Symposium on Comparative Planetary Science. Employees of the laboratory combine scientific work with teaching activities. 10 master's and 2 doctoral dissertations were prepared and defended in the laboratory. A. T. Basilevsky, G. A. Burba, and A. A. Pronin became the USSR State Prize laureates (1989) for creating surface maps of Venus and analysis of Venusian geology on their basis. A. T. Basilevsky has received international awards: Humboldt Research Award, Germany (1999); Runcorn-Florensky Medal of the European Geophysical Society (2000); Barringer Medal of the Meteoritical Society (2001); Masursky Award of the Division of Planetary Science (2004).

The laboratory actively cooperates with Brown University, Providence, USA; Free University of Berlin, Germany; Max-Planck Institute for Solar System Research, Göttingen, Germany; Institute of Planetology, Berlin, Germany; Institute of Planetology, Münster, Germany.

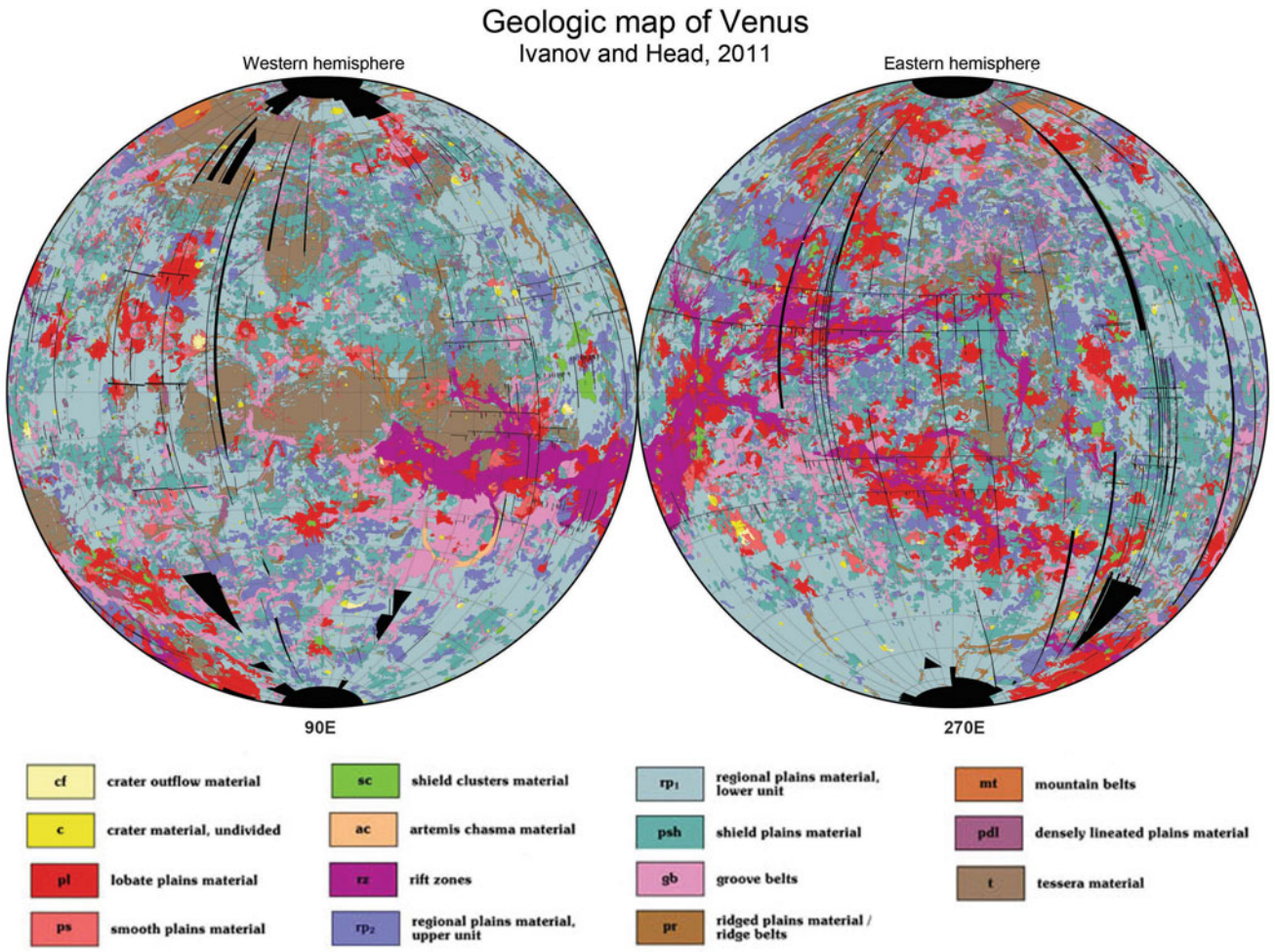

Fig. 43 Geologic map of Venus (Ivanov and Head 2011)

Laboratory of Thermodynamics and Mathematical Modeling of Natural Processes

Head of the Laboratory
Vera A. Dorofeeva
Doctor of Chemistry
Email: dorofeeva@geokhi.ru
Website: http://portal.geokhi.ru/sites/eng/lab45
Articles by lab members in this volume: Chapters 3 and 14

The laboratory was formed in 1977 and headed by Prof. I. L. Khodakovsky. From 1989 to 1991 the laboratory was led by M. Ya. Frenkel, Ph.D. From 1991 to 2016 the laboratory was headed by O. L. Kuskov, Corresponding Member of RAS, Doctor of Chemistry. Since 2016 Dr. V. A. Dorofeeva is the head of the laboratory.
The laboratory has 18 scientific employees, including 1 Academician of RAS, one Corresponding Member of RAS, 5 Doctors of Sciences and 6 Ph.D.'s.

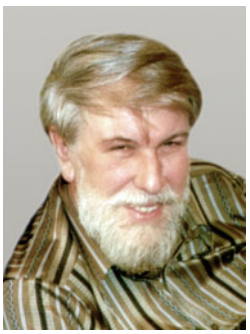

Oleg L. Kuskov
Corresponding Member of RAS

The subject of laboratory works *—the study of geochemical, cosmogonical, and cosmochemical processes with the help of mathematical modeling.*

This includes several directions of research

- Mathematical modeling of the processes of matter formation and evolution in the gas-dust medium of the early Solar System, the formation and growth of primary solids, and the formation of the embryos of planetary bodies in the Solar and exoplanetary systems. Supervisor: Academician of RAS, Doctor of Physics and Mathematics M. Ya. Marov
- Mathematical modeling of the evolution of matter of comets, the Moon, and ice satellites. Experimental obtaining of thermodynamic data. Supervisor: Corresponding Member of RAS, Doctor of Chemistry O. L. Kuskov
- The thermodynamic modeling of geochemical effects of chrome-spinelide and sulfide liquation during crystallization of mafic-ultramafic magmas. Supervisor: Doctor of Geological and Mineralogical Sciences A. A. Ariskin.

Main achievements of the laboratory in recent years

- Numerical studies of the growth of primary solids during mutual collisions of dust clusters in the protoplanetary gas-dust disk have been carried out. A mathematical model and software packages were developed to study the thermal and mechanical properties of heterogeneous fractal dust-ice clusters sized ~0.1–10 cm with different ratios of refractory and icy components at the water ice line. Peculiarities of decomposition, including dependency of porosity and density on fractal dimensionality, have been studied.
- Models of the migration of celestial bodies in the emerging and modern Solar System have been created, and the probabilities of their collisions with planets and satellites have been calculated. A scenario of the Moon origin, based on the multi-impact model, taking into account the constraints on the angular momentum value and isotopic relations of elements, was proposed, and estimates of the comparative growth of the Earth and Moon embryos due to the planetesimals precipitation on them were obtained. Quantitative estimates of the delivery of water and volatiles to the Earth, Moon, and Earth-group planets at different stages of the Solar System evolution have been made.
- Based on experimental data in the field of cosmochemistry, geochemistry, astrophysics, and geophysics, the following was investigated by methods of physical–chemical and mathematical modeling: the structures of Jupiter and Saturn accretion disks that satisfy the Galileo and Cassini-Huygens data and limitations on the main physical characteristics of protosatellite disks have been acquired; the processes of Earth-Moon system and Solar System bodies formation; models of the chemical composition, thermal regime, internal structure of the Moon, and giant planets satellites (Europe, Ganymede, Callisto, Titan,

Enceladus) have been constructed; conditions for the development of the Enceladus' water plumes and Titan's atmosphere were determined; dependences of comet coma composition on physical and dynamical parameters of comets' cores have been studied (Figs. 44 and 45).

- COMAGMAT-5 program has been developed to simulate crystallization of basaltic magmas under conditions of sulfide liquid saturation (Fe–Ni–Cu–S system), see Fig. 46. In the development of this model, the method of modeling behavior of noble metals (PGE + Au + Ag) and other chalcophile elements (Cd, Zn, Pn, Bi, Te) during fractionation of sulfide-silicate systems is proposed. The high-pressure version of the SPINMELT-2.0 model designed for thermodynamic equilibrium calculations of spinelide-melt at pressures of up to 15 kbar and adapted for COMAGMAT-5 program allows studying coupled effects of oxides and sulfides formation in a wide range of P–T-fO_2 parameters (Fig. 47).

Plans

- Continued research of the dust clusters behavior, taking into account the influence of fractal dimensionality and pore space inhomogeneity on the interaction with the disk environment; calculations of planetesimals migration in exoplanetary systems to assess the possibility of water delivery from behind the ice line to some exoplanets in the potential habitability zone.
- Studies of possible scenarios of the Moon formation, detailed development of mathematical models of the chemical composition, internal structure, and chemical differentiation of the satellites of the Earth, Jupiter, and Saturn, coordinated with the petrological, geochemical, and geophysical data.
- Development of the sulfide-spinel version of the COMAGMAT-5 computer model implies developing new methods to estimate the composition and crystallization conditions of mafic-ultramafic magmas in the context of their ore Cu-Ni-EPG potential in different geodynamic settings.
- The solution of these problems will make it possible to make a significant contribution to the solution of priority tasks in the development of mineral resources of Russia, as well as in the study of the chemical composition and internal structure of the bodies of the solar system carried out within the framework of the Russian federal projects.

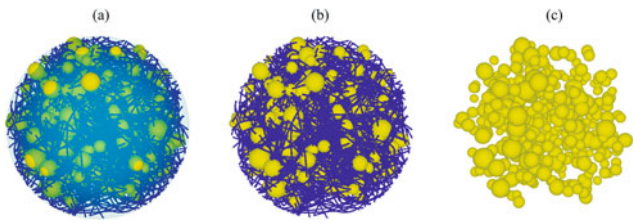

Fig. 44 Example of a model of a fractal dust-ice cluster in which refractory aggregates are an order of magnitude larger than ice aggregates: **a** covering volume, **b** cluster before ice sublimation, **c** after ice sublimation

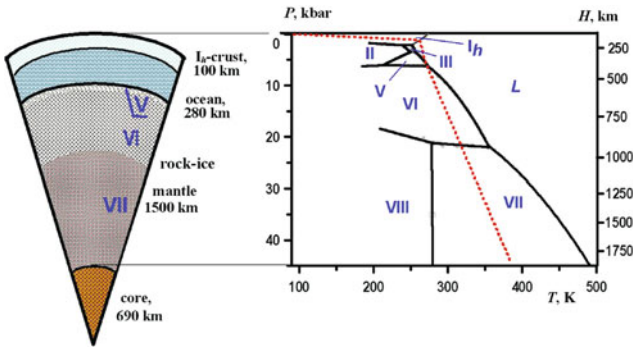

Fig. 45 Model of the internal structure of Titan at a heat flux of 5.8 mW/m^2 and corresponding temperature distribution (dotted line) and H_2O phases (water, ice I_h and high barrier ice II, III, V, VI, VII, VIII) with depth (H) in water–ice shell and rock-ice mantle composition

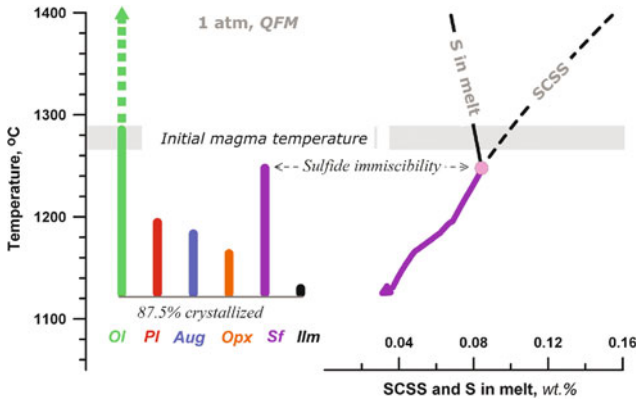

Fig. 46 Example of silicate-sulfide immiscibility modeling during fractionation of initial magma of the Bushveld complex in South Africa: left—order of crystallization of rock-forming minerals, right—variations of sulfur content and SCSS (sulfur concentration at sulfide saturation) in the melt

Fig. 47 Several important monographs by lab members

The Museum of Extraterrestrial Matter

Curator
of the Museum
Anna Ya. Skripnik
Research Associate at
the Vernadsky Institute RAS

Curator of the Meteorite
Collection of the RAS
Dmitry D. Badyukov
Ph.D. in Geological and
Mineralogical Sciences
Email: badyukov@geokhi.ru

The Museum of Extraterrestrial Matter of the Vernadsky Institute and the Meteorite Collection of the Russian Academy of Sciences are curated by the Laboratory of Meteoritics and Cosmochemistry of the Vernadsky Institute RAS. The museum opened at the Vernadsky Institute on April 3, 1997 on the initiative of Dr. Mikhail A. Nazarov (see Annex I).

The institute has been researching extraterrestrial matter and building instruments for space missions in the Solar System for several decades. Meteorites to date remain the only source of information about the protoplanetary and early planetary history of the Solar System.

The museum (Figs. 48 and 49) is organized to demonstrate the main types of extraterrestrial matter, the processes of its formation and evolution, catastrophic phenomena leading to the formation of giant meteorite craters, in addition to the history of extraterrestrial matter research in Russia.

The exposition was created based on the meteorite collection of the RAS, the archive of the Committee on Meteorites of the RAS, and the collection of lunar samples stored at the Vernadsky Institute RAS. The exhibition also presents instruments developed at the Vernadsky Institute RAS that were installed on spacecrafts for studying the different celestial bodies: Venus, Mars, the Moon, together with a model of the insertion probe penetrator for the Mars-96 mission (Fig. 50).

The meteorite collection of the Russian Academy of Sciences, stored at the Vernadsky Institute, is the largest collection of meteorites in Russia. It has been collected for over 270 years and is among the ten largest collections in the world. It contains more than 3250 unique species of all classes and types, including many rare and unique meteorites, and more than 20 000 samples. Among them—134 meteorites are from Russia (e.g. Figs. 51, 53 and 54). The collection includes impactites and tektites—rocks and glasses from meteorite craters.

Onboard spacecraft instruments developed at the Vernadsky Institute were used to determine the chemical and isotopic composition of the atmosphere, rocks of Venus and Mars, and to study the composition of the Moon (Fig. 50). The penetrator was designed for interplanetary station Mars-96.

The exposition of the Museum demonstrates the main types of meteorites, planetary matter, the processes of origin and evolution of extraterrestrial matter, historical falls, including the three largest falls in Russia: the Tunguska disaster (1908), the Sikhote-Alin (1947), and Chelyabinsk (2013) meteorites. The exhibition also describes the phenomena, which accompanied the meteorite fall, the catastrophes, which led to the formation of huge meteorite craters, and the surrounding rock types composed of different types of tektites and impactites. It

Fig. 48 The interior of the Museum of extraterrestrial matters (there are big pieces of Sikhote-Alin' iron meteorite)

Fig. 49 The interior of the museum

Fig. 50 Instruments developed at the Vernadsky Institute

Fig. 51 Sikhote-Alin iron meteorite

serves scientific and educational purposes for scientists and students interested in the extraterrestrial matter.

There are 323 items on display, out of which 177 specimens belong to various types of meteorites, 1 sample of the lunar soil delivered by the Luna 16 automatic station in 1970 (Fig. 52), 114 tektites from 11 strewn fields, 10 impactites from 7 meteorite craters, photographs, and drawings of witnesses together with 15 onboard instruments developed at the Vernadsky Institute RAS (Fig. 50)

Meteoritics and Cosmochemistry lab members organized the 81st Annual Meeting of the Meteoritical Society (MetSoc) in Moscow (July 22–27, 2018) with more than 300 international participants from all over the world. It was the first MetSoc meeting in Russia. *Photos* 18 and 19 *illustrate a range of interiors of the Vernadsky Institute RAS.*

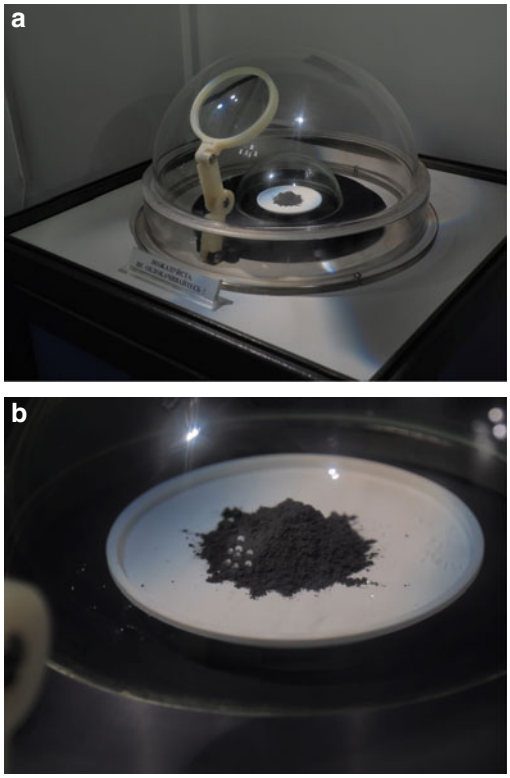

Fig. 52 Lunar soil probe delivered by the Soviet spacecraft Luna 16 in 1970

Fig. 53 Brahin pallasite

Fig. 54 Karakol ordinary chondrite

Photo 18 Poster hall of the Vernadsky Institute, where each of 25 laboratories is presented

Photo 19 The central hall of the institute with a temporary exhibition about the life and professional activities of Academician V. I. Vernadsky on the occasion of the annual conference Vernadsky Readings-2022 dedicated to the 159th anniversary of Vernadsky's birthday (March 12, 2022)

Department of Biogeochemistry and Ecology

Head of the Department
Tatiana I. Moiseenko
Corresponding Member of RAS,
Doctor of Biology,
Former Deputy Director of the Vernadsky Institute RAS
Email: moiseenko@geokhi.ru

The department of biogeochemistry and ecology currently includes three laboratories:

Laboratory of Environmental Biogeochemistry
Laboratory of Sedimentary Geochemistry
Laboratory of Evolutionary Biogeochemistry and Geoecology.

Development of biogeochemical direction at Vernadsky Institute RAS

In 1926 V. I. Vernadsky, in order to separate the biogeochemical investigations into an independent line of research, organized the Department of Living Matter at the Commission for Study of the Productive Forces of Russia (Russian abbreviation: KEPS). From 1928 to 1934, the department functioned as the Biogeochemical Laboratory (BIOGEL) at the Radium Institute of the USSR Academy of Sciences.

The scientific goal of BIOGEL was formulated by V. I. Vernadsky as cognition of life phenomena from the geochemical point of view. Its main objectives, according to V. I. Vernadsky, were as follows:

- determination of the chemical composition of living organisms, including for chemical characterization of species;
- elucidation of specificity of the isotopic composition of elements of living matter;
- determination of the geochemical energy of living matter;
- determination of radioactive elements in living organisms and investigation of the contribution of radioactivity to the geochemical energy of living matter.

In March 1943, BIOGEL was transformed into the Laboratory of Geochemical Problems of the USSR Academy of Sciences, and in March 1947, the Vernadsky Institute of Geochemistry and Analytical Chemistry was established and was directed by Academician A. P. Vinogradov.

The three laboratories develop the following research work:

Laboratory of Environmental Biogeochemistry

- genesis, formation, and evolution of natural-technogenic biogeochemical provinces;
- chemical composition of living matter and its biogeochemical parameters;
- geochemical ecology of organisms; ecological and biogeochemical normalization and zoning of biosphere taxa.

Laboratory of Sedimentary Geochemistry

- the study of the Earth's sedimentary mantle, which captures the former biosphere;
- creation of small-scale lithologic-facies maps of Mesozoic-Cenozoic continents and oceans to determine quantitative sedimentation parameters;
- global and regional studies of continental and oceanic sedimentary shell geochemistry.

Laboratory of Evolutionary Biogeochemistry and Geoecology

- anthropogenic-driven processes in the biosphere and its components, evolution in the period of technogenesis;
- the formation of stable substance and energy cycles in the course of evolution at the main stages of the Earth's history;
- the universality of the mechanisms of the Life phenomenon.

Laboratory of Environmental Biogeochemistry

Head of the Laboratory
Elena M. Korobova
Doctor of Geological and Mineralogical Sciences, Ph.D. in Geography
Email: korobova@geokhi.ru
Website: http://portal.geokhi.ru/sites/eng/lab21
Articles by lab members in this volume: Chapters 26 and 27.

The theoretical foundations of scientific research performed in the laboratory were laid by Academician V. I. Vernadsky in his laboratory BIOGEL at the beginning of the last century. In 1947 the Biogeochemical Laboratory was incorporated in the Vernadsky Institute and directed by Academician A. P. Vinogradov (from 1947 to 1954), followed by Prof. Dr. V. V. Kovalsky (from 1954 to 1983). In 1983 it was integrated with the Laboratory of Carbon Geochemistry and was headed by Academician E. M. Galimov until 1987. In 1987 it was restored as the Laboratory of Environmental Biogeochemistry and led by Prof. Dr. V. V. Dobrovolsky. From December 1989 to February 2020, the laboratory was headed by Prof. Dr. V. V. Ermakov. Now the laboratory is headed by Dr. E. M. Korobova.
The staff consists of 14 specialists, including four Doctors of Sciences and three Ph.D.'s.

Vadim V. Ermakov.
Doctor of Biology

The range of problems being solved by the staff included regularities of the chemical interaction of living organisms with the habitat; the geochemistry of organic matter; reactions of different organisms to changes in elements concentration in vivo and in vitro; analyzing food chains; studying biogeochemical provinces searching for minerals.

The laboratory contributed to the understanding of the genesis and the role of biogeochemical provinces in organic evolution (Vinogradov 1938, 1949, 1960, 1963), laid the foundations of the geochemistry of organic matter (Manskaya and Drozdova 1964; Drozdova, 1977) and biogeochemical principles and methods of prospecting for minerals (Malyuga 1963), created a new branch of the geochemical ecology, and established threshold concentrations of micronutrients (Cu, Co, Zn, I, Mo, B, etc.) in soils and fodder, causing adverse biological effects in animals (Kovalsky 1957, 1974, 1982; Kovalsky and Andrianova 1976). The laboratory constructed the first map of the USSR biogeochemical zoning and revealed reactions and adaptation of soil microorganisms, plants and animals living in various biogeochemical provinces (Kovalsky, 1957; Kovalsky and Petrunina, 1970; Petrunina, 1974; Ermakov and Kovalsky, 1974; Letunova and Kovalsky, 1978; Konova, 1987). The laboratory also expanded understanding of biochemical reactions of plants and animals and the possibilities of methods of biogeochemical indication (Ermakov 1978; Ermakov and Tyutikov 2008), studied the geochemical structure of biogeochemical provinces, and developed methods of revealing geochemical conditions leading to endemic diseases (Kovalsky and Korobova, 1978; Korobova 1992, 1999, 2016).

The main goal of current investigations is the further development of scientific knowledge in the field of biogeochemistry and geochemical ecology aimed at revealing processes and laws of interaction between living organisms and their environment.

The studies of the staff are devoted to the **solution of the following problems**:

- geochemical composition and structure of the modern noosphere formed by interaction of the living organisms with their environment;
- identification of biogeochemical provinces, their spatial structure, and evolution;
- criteria for assessing the ecological state and the risk of negative biological reactions;
- the principles of biogeochemical zoning and health risk mapping related to geochemical features of the environment at different levels of geosystems and territorial organization;
- new approaches to revealing, preventing, and eliminating microelementoses and endemic diseases of geochemical origin.

Fig. 55 Field measurements of ^{137}Cs and ^{90}Sr and soil core sampling along the transect in the head of the Eastern Urals radioactive trace (Chelyabinsk oblast')

To solve the above problems, a wide range of methods and techniques are used: comparative geographical method and biogeochemical indication; landscape, phyto- and soil-geochemical; radioecological approaches; analytical techniques (RFA, AES, AAS, ES, MS, HPLC, GC, ISE); methods of field and laboratory gamma and beta spectrometry (Fig. 55); geoinformation analysis; thermodynamic and mathematic modeling.

The main achievements for the last 5 years.

- Development of the original concept of a genetic, two-layer geochemical structure of the modern noosphere and biogeochemical provinces; the methodology for constructing risk maps to reveal and eliminate diseases of geochemical origin provoked by both natural and technogenic geochemical factors (Fig. 56).
- New chemical and biological approaches to biogeochemical indication, the establishment of the ecological and geochemical state of the environment (Fig. 57), and its geochemical optimum parameters for human health.
- Identification of critical geochemical factors in the development of the Urov endemic disease in Eastern Transbaikalia, fluorosis, thyroid gland diseases in the impact zone of the Chernobyl accident.
- Revealing regular (cyclic) features of ^{137}Cs and ^{90}Sr variation in soil and vegetation cover of the elementary landscape systems both undisturbed and cultivated believed to trace patterns of any other substance migration in such systems.
- Demonstration of the possibility to estimate the main parameters of a geochemical anomaly from the frequency histograms of element concentrations, depending on the position of the regular sampling area within the anomaly.

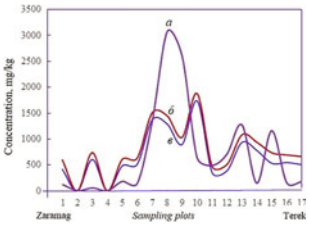

Fig. 57 Zn, Cd, Pb, and Cu content in soils (summed, **a**) in the Ardon River bed and the of thio-containing substances in *Hippophae rhamnoides L.* leaves (**b**) and the total content of glutathione (**c**). 1—Zaramag, 7–10—pulp tailings of the Mizur mining and processing plant in Unal, 17—Terek

The recent results are presented in three monographs devoted to oxidative stress and health of farm animals (Safonov and Nezhdanov 2016), the biogeochemical indication of microelement diseases (Ermakov et al. 2018), theoretical and methodological analysis of ecological and geochemical problems of the modern noosphere (Korobova 2019). Other publications include 66 scientific articles, out of which 31 are in journals registered in the WoS and Scopus databases. The intellectual results are also presented by three patents of the Russian Federation for the developed methodological approaches and four certificates for biogeochemical databases.

Organization activity

Since 1999, the laboratory has organized eleven conferences of the *All-Russian and International* ***school in biogeochemistry***. It annually organizes and hosts the ***readings*** established ***in memory of V. V. Kovalsky*** and continues to publish ***Transactions of the Biogeochemical Laboratory***, the first volume of which was published on the initiative of V. I. Vernadsky in 1930. Currently, this edition contains the most fascinating and promising results obtained by scientists from different institutions and countries.

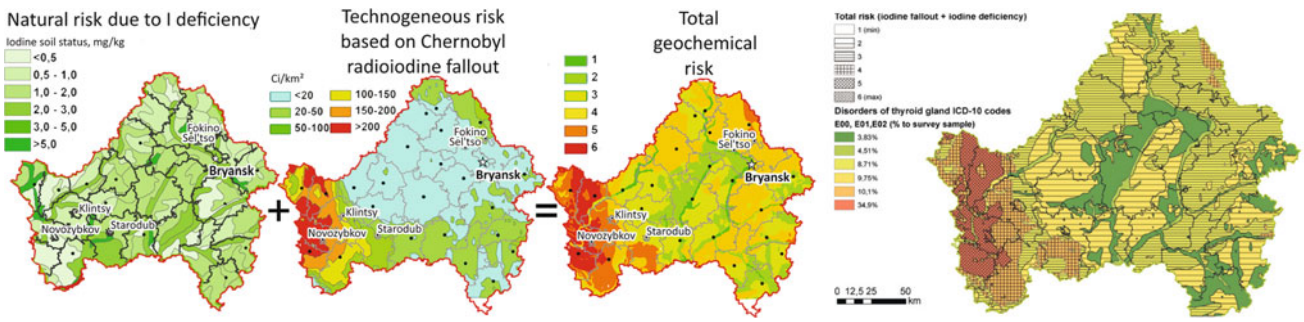

Fig. 56 Superposition of natural and anthropogenic risk zones of different configuration due to stable **iodine deficiency** and **radioiodine (^{131}I) contamination** and **medical verification** of the risk map (on the example of the Bryansk oblast' with an indication of its administrative regions and their centers, medical data was provided by the Bryansk clinical and diagnostic center)

Laboratory of Sedimentary Geochemistry

Head of the Laboratory
Mikhail A. Levitan
Doctor of Geological
and Mineralogical Sciences
Email: m-levitan@mail
Website: http://portal.geokhi.ru/sites/eng/lab22
Articles by lab members in this volume: Chapters 11 and 12

A. B. Ronov established the laboratory in 1950. Along with Academician A. B. Ronov, prominent experts such as Academician V. E. Khain, Professors A. A. Yaroshevsky, N. A. Yasamanov, A. Yu. Lein; A. A. Migdisov, A. P. Kazakov, Y. P. Girin, A. N. Balukhovsky, K. B. Seslavinsky, and many others worked here. Since 2004, the laboratory has been in its present form after merging with the Laboratory of Geochemistry and Lithology of World Ocean Sediments.
The staff consists of 10 people, including 2 Doctors of Sciences and 1 Ph.D.

Main areas of research

- Creation of overview of lithological-paleogeographical and lithological-facies maps of continents and oceans for Mesozoic-Quaternary using the volumetric method of Academician A. B. Ronov as a basis for the quantitative geochemical history of the stratisphere;
- Study of lithology and geochemistry of modern, Holocene, and Upper Pleistocene sediments of the Arctic Ocean and Subarctic seas.

Research Objects

- Triassic-Pliocene deposits of the Circum-Arctic belt (from 60 °N to the modern shelf break).
- Upper Quaternary sediments of the Kara, Laptev, East Siberian, and Chukchi Seas.
- Pleistocene deposits of the World Ocean (according to deep-sea drilling data).

Most important results

- Under the leadership of A. B. Ronov, more than 10 volumes of Atlases of lithologic-paleogeographic and paleotectonic maps of Eastern Europe, the USSR, and the World have been published. These show the evolution of sedimentation and volcanism from Precambrian to Pliocene. More than 10 monographs were published based on the materials of the maps. The World atlases, a series of monographs "Historical Geotectonics" Vol.1–3 and the monograph "Stratisphere or the Earth's sedimentary cover" were awarded the State Prize of the Russian Federation in 1994 (A. B. Ronov, V. E. Khain, A. N. Baluhovsky, K. B. Seslavinsky);
- A model of underwater hydrothermal-sedimentary lithogenesis was developed;
- A set of 26 overview of lithologic-facies maps for the Triassic-Pliocene of the Circum-Arctic region has been created. It has been established that the Mesozoic-Cenozoic sedimentation history (Fig. 58) is determined mainly by global patterns.
- The lithologic-paleogeographic maps for the Neo- and Eopleistocene of Eurasia at a scale of 1:20,000,000 have been created;
- Based on the created set of 54 overview lithological-facies maps for the Neo- and Eopleistocene of the World Ocean, weighted average lithological compositions of Pleistocene deposits for the main ocean basins are calculated (Fig. 59);
- Over the past 15 years, 6 monographs and proceedings have been published.

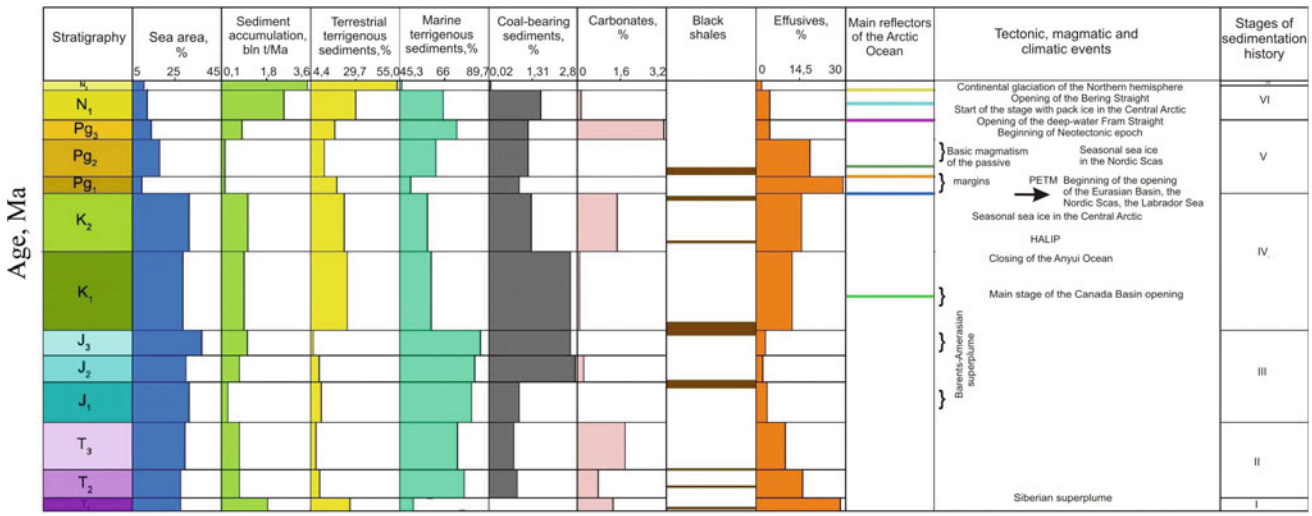

Fig. 58 Main regularities of Mz–Cz sedimentation in Circum-Arctic region

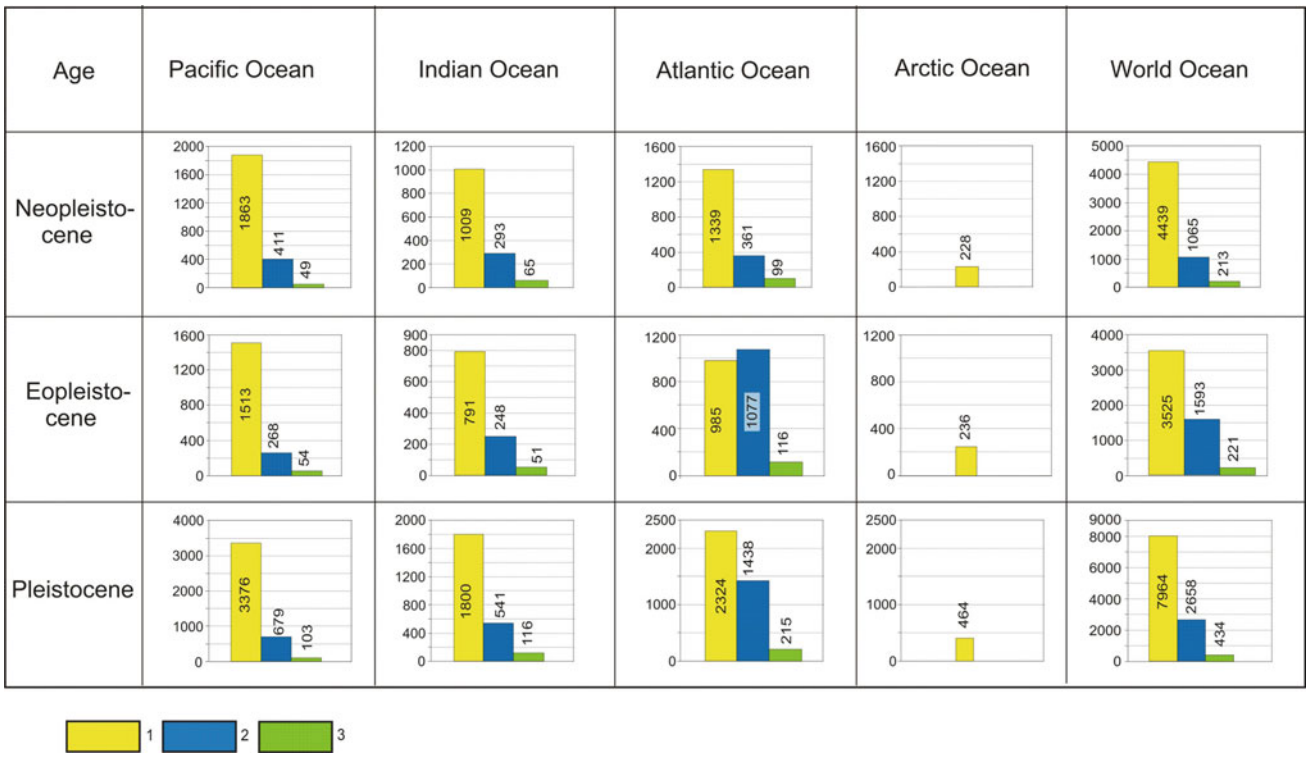

Fig. 59 Average weighted lithological composition of pleistocene sediments (in 10^{18} g). *Legend* 1—lithogenic matter; 2—$CaCO_3$; 3—biogenic opal

Laboratory of Evolutionary Biogeochemistry and Ecology

Head of the Laboratory
Tatiana I. Moiseenko
Corresponding Member of RAS,
Doctor of Biology
Former Deputy Director of the Vernadsky Institute RAS
Email: moiseenko@geokhi.ru
Website: http://portal.geokhi.ru/sites/eng/lab23
www.aquaticecology.ru
Articles by lab members in this volume:
Chapters 25 and 41

The laboratory was established in July 2008 to fulfill V. I. Vernadsky's scientific heritage regarding the biosphere and understanding its evolution in the past and present times in terms of anthropogenic transformations on the planet. The first head of the laboratory was Academician Mikhail A. Fedonkin. Since January 2010, the corresponding member of RAS Tatiana I. Moiseenko has been heading the laboratory.
The laboratory has 13 members, including 3 Doctors of Sciences and 4 Ph.D.'s.

Main scientific directions of the laboratory

- evolutionary processes in the biosphere in the modern period of anthropogenic loads and climate warming; mechanisms of self-organization of landscapes and aquatic ecosystems;
- forms of elements migration, their bioavailability, and ecotoxicity in environments, including radionuclides;
- biogeochemical processes in aquatic and terrestrial ecosystems; analysis of long-term changes in environments, including local and global changes;
- study of restoration and biogeochemical adaptation of ecosystems and organisms during the period of pollution reduction;
- study of landscape factors of biogeochemical migration using lateral and radial migration modeling as an example;
- Evolution and self-organization of landscapes under conditions of technogenic pollution; study of the multiscale structure of technogenic geochemical fields;
- Deterministic and stochastic processes of transformation of technogenic geochemical fields.

Scientific Achievements

- The factors and mechanisms of development of anthropogenic-induced processes in the biosphere, transformations of biogeochemical cycles, and pollution of natural environments under conditions of anthropogenic load and climate warming were determined (Fig. 60). The theory of critical anthropogenic loads on environments is developed, and algorithms of their calculations by pollution factors (T. I. Moiseenko);
- Regularities of formation of multiscale fields of technogenic radionuclide contamination in different natural

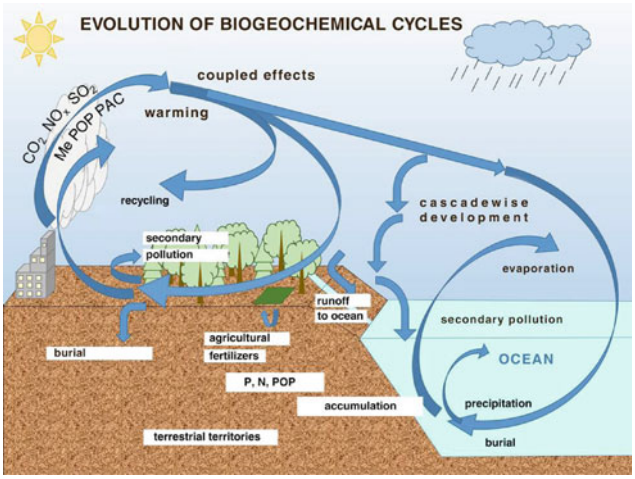

Fig. 60 Scheme of anthropogenic-introduced elements and substances cycle in Earth spheres: Me—metals with ecotoxic properties; POP—persistent organic pollutants (superecotoxicants); NOx, SO_2—acid-forming gases; P—phosphorus and N—nitrogen, biogenic elements stimulating eutrophication of water systems

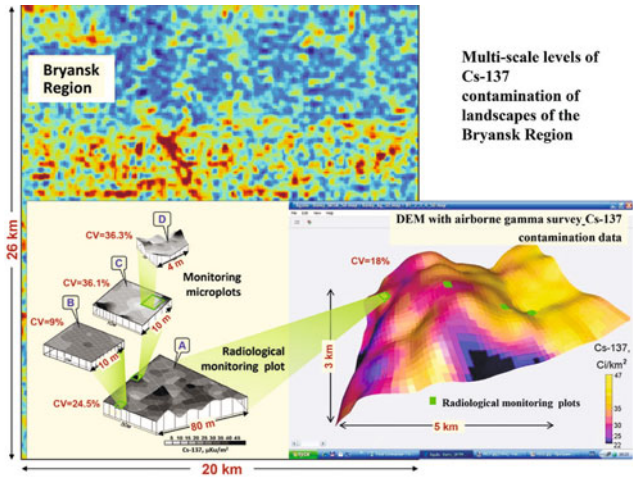

Fig. 61 Multi-scale levels of landscape-radioecological monitoring organization in the Bryansk region

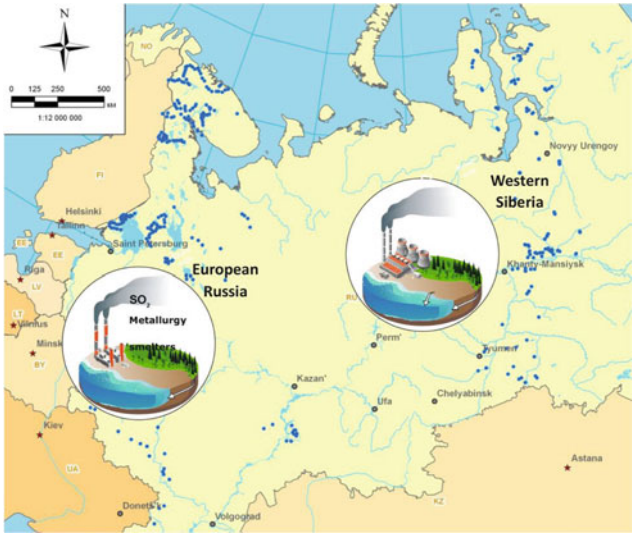

Fig. 62 Diagram of water quality survey points

zones have been established (Fig. 61). Landscape mechanisms of transformation of contamination fields and migration of radionuclides and chemical elements in the composition of micro-and nanoparticles have been determined (V. G. Linnik);

- Based on the analysis of mercury's behavior in technological processes of mercury and mercury manufactures, at the clearing of sewage and industrial emissions, the geochemical cycle of mercury in anthropogenic landscapes, cycle and influence on natural ecosystems and public health is established (Yu. G. Tatsiy);
- The tendencies of global transformations of the chemical composition of surface waters in the latitudinal geographical zonation (from tundra zone to arid and subtropical) under the conditions of changing climate and transboundary atmospheric transfer of pollutants in the European territory of Russia and Western Siberia have been revealed;
- The estimation of possible climate warming on the indicators of the chemical composition of waters is given;
- The regularities of metal accumulation in fish organisms as a reflection of geochemical background and anthropogenic load on water objects have been studied, which is of paramount importance for medical and geographical research (T. I. Moiseenko and N. A. Gashkina);
- Functional features of humus substances (HS) of soils and waters of three natural zones causing distinctions in the mechanism of the course of processes of their complexation with heavy metals are established;
- The calculation algorithm is applied to the theoretical definition of forms of metal presence in water objects;
- Certificates for the computer program for calculating the equilibrium forms of metal distribution in 140 small lakes of different natural and climatic zones (M. I. Dinu) are carried out;
- Peculiarities of biogeochemical migration of elements and organic substances in the system atmospheric precipitation—lysimeter water—lake water at the site Valday National Park" (cooperation with the State Hydrological Institute and the Valday National Park) were revealed;
- Mechanisms of elements distribution by forms depending on climatic season and anthropogenic influence were evaluated, and seasonal changes of organic substances protector properties were studied (Fig. 62) (M .I. Dinu, D. Yu. Baranov, Yu. G. Tatsiy).

The laboratory researches topics of Vernadsky Institute RAS, programs of the Presidium of the Russian Academy of Sciences, RFBR, and Russian Science Foundation projects. The laboratory is conducting a major project on the state budget topic: "Development of the theory of biogeochemical evolution of natural systems under changing anthropogenic pressures and climatic conditions: assessment of permissible impacts (2019–2023)", as well as under several other grants. The laboratory is involved in the international project (2007–present): International cooperative program on Assessment and Monitoring of Acidification of Rivers and Lakes (involving 22 countries). Employees participate in expert work for the Ministry of Science and Education of the Russian Federation, teaching activities, preparing scientific-methodical manuals for students and graduate students, and heading the Attestation Commission. *Photo 20 illustrates an interior view of the Vernadsky Institute RAS.*

Photo 20 Main stairs of the Vernadsky Institute. A large format wall panel (40 m^2) upstairs showing the inner structure of the Earth and volcanos on its surface was designed and painted by Yu. A. Ignat'ev, research scientist of the laboratory of geochemistry of the Earth's Mantle of the Vernadsky Institute

Department of Marine Research

Head of the Department
Victor N. Nosov
Doctor of Technical Sciences
Email: victor_nosov@mail.ru

Department of Marine Research, headed by Dr. V. N. Nosov, was established at the Vernadsky Institute RAS in January 2012.

Currently, the department includes two laboratories:

Laboratory of Physical and Chemical Processes and Ocean Surface Dynamics

Laboratory of Environmental Radiochemistry.

Besides preparation and carrying out sea expeditions within the frameworks of the department, the Marine Research Department actively participates in activities on preparing and carrying out sea expeditions carried out by other subdivisions of the Institute.

From 1984 to 2014, the Vernadsky Institute RAS had its research vessel "Akademik B. Petrov" (Photo 21). The research vessel named after Academician Boris Petrov was built in 1984 in Finland for the USSR Academy of Sciences. The ship is designed to study the hydrophysical and hydrochemical structure of the ocean, the structure of the ocean floor, and the layers of the atmosphere adjacent to the surface of the ocean. The complex is equipped with equipment and software for processing the received data with their presentation in the form of profiles of bottom sediments, bathymetric maps, three-dimensional images of the bottom, and archiving information. Over 70 scientific expeditions have been carried out on the ship in various regions of the World Ocean, including the Arctic and Antarctica.

Photo 21 Research vessel Akademik B. Petrov, named after Academician Boris Petrov, which was in possession of the institute till 2015. *Photo credit* Sergey Zhvansky

Laboratory of Physical and Chemical Processes and Ocean Surface Dynamics

Head of the Laboratory
Victor N. Nosov
Doctor of Technical Sciences
E-mail: viktor_nosov@mail.ru
Website: http://portal.geokhi.ru/sites/eng/lab32
Articles by lab members in this volume: Chapter 13

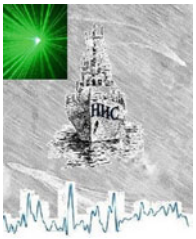

The laboratory was established on 11 May 2010, resulting from the reorganization of the Ocean Surface Dynamics Sector of Geo-Ecology.
The laboratory consists of 13 employees, including 5 Ph.D.'s and 3 Doctors of Sciences.

The research areas of the laboratory

- development of laser-optical methods and creation of ship and aircraft experimental setups for remote registration of the hydrodynamic processes (HDPs) in the ocean by their manifestations on the sea surface and in the near-surface layers of the marine environment and the driven atmosphere (Figs. 63 and 64);
- development of algorithms and software for signal processing methods of laser-optical equipment (LOE) under development for effective remote registration of the HDPs;
- development of methods of photogrammetry processing and their software to detect sea surface manifestations on the images obtained in the framework of the space experiment onboard the International Space Station (ISS) jointly with Vernadsky Institute RAS;
- theoretical studies of the mechanisms of formation of anomalous manifestations from the HDPs on the sea surface and in the near-surface layers of the marine environment and the atmosphere and assessment of their spatial and temporal characteristics;
- laboratory experimental studies of the effect of various hydrodynamic disturbances on the near-surface aerosol based on the method of elastic scattering of laser radiation.

The most important results of the research carried out by the laboratory

- development of an integrated approach to the application of the LOE used, allowing a significant increase in the efficiency of remote registration of the HDPs in the ocean;
- development and creation of setups of a scanning laser locator and a two-channel photometer for application from an aircraft carrier and carrying out full-scale experiments on remote registration of the HDPs from a helicopter and an aircraft;
- creation of software for solving the problem of investigation HDPs using LOE in real-time;
- application of machine learning neuromethods to solve the inverse problem of determining the parameters of the HDPs by water surface occurrences.

Main publications

1. Gorelov A.M., Zevakin E.A., Ivanov S.G., Kaledin S.B., Leonov S.O., Nosov V.N., Savin A.S. (2012) On a complex approach to remote registration of hydrodynamic disturbances of the marine environment by optical methods, *Physical Basis of Instrument Engineering*, **1** (№4), 58–64.

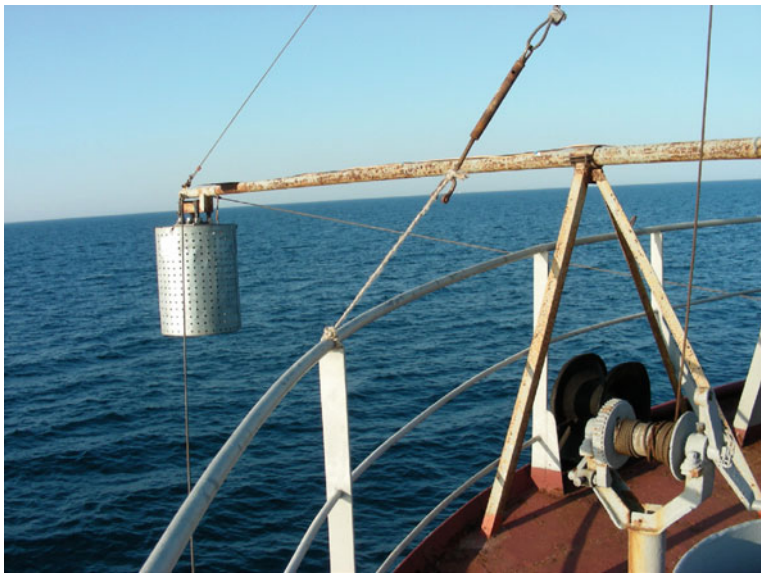

Fig. 63 Arrangement of the scanning laser locator setup in a windproof casing on board the research vessel in its forward section

2. Nosov V.N., Kaledin S.B., Ivanov S.G., Glebova T.V., Timonin V.I. (2016) On increase of efficiency of detection of anomalies excited by a sea underwater source at complex use of laser-optical methods of registration, *Processes in Geospheres*, №1(5), 85–94.
3. Nosov V.N., Kaledin S.B., Ivanov S.G., Timonin V.I. (2019) Remote Tracking to Monitor Ship Tracks at or near the Water Surface, *Optics and Spectroscopy*, **127**, 669–674.
4. Nosov V.N., Ivanov S.G. Kaledin S.B., Petukhov A.V., Savin A.S. (2021) Prospects of application of drones for laser sensing of sea surface, *Physical Basis of Instrument Engineering*, **10**, №1(39), 70–81.
5. Nosov V.N., Ivanov S.G., Timonin V.I., Podgrebenkov A.L., Plishkin A.N., Kaledin S.B., Glebova T.V., Yadrentsev A.N., Zakharov V.K. (2015) Joint space and sea experiment on integrated vessel trace registration using subsatellite measurements, *Fundamental and Applied Hydrophysics*, **8** (№4), 34–35.

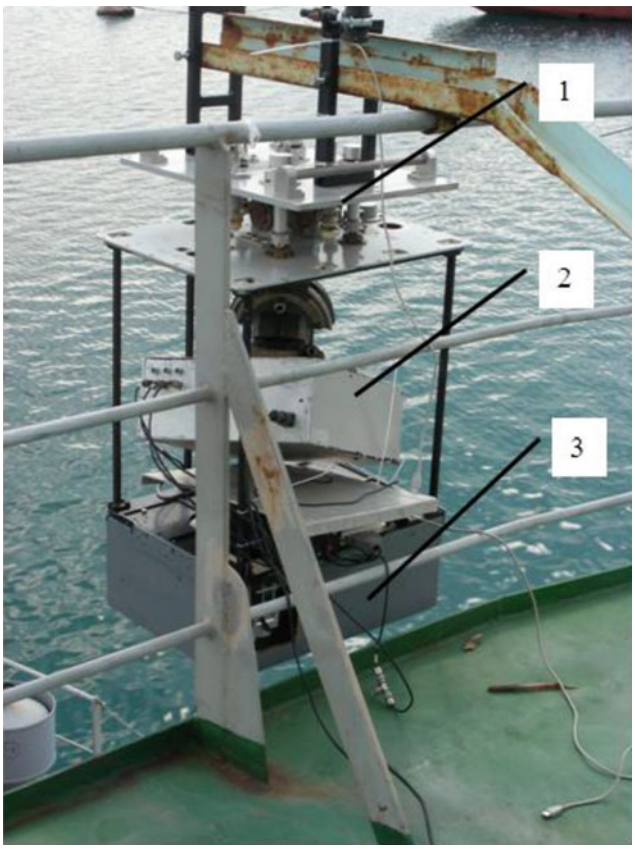

Fig. 64 Placement of sea brightness photometer (2) and aerosol lidar (3) setups onboard the research vessel in a rack with a stabilizing device (1)

Laboratory of Environmental Radiochemistry

Head of the Laboratory
Alexander P. Novikov
Doctor of Chemistry
Email: novikov@geokhi.ru
Website: http://portal.geokhi.ru/sites/eng/lab34
Articles by lab members in this volume: Chapter 42

The laboratory was founded based on the radiochemistry lab of the Vernadsky Institute of Geochemistry and Analytical Chemistry of the Russian Academy of Sciences. Initially called the radioecological monitoring group, founded by F. I. Pavlotskaya, the laboratory has been in its present form since 2011, led by A. P. Novikov.
Now the laboratory has 19 researchers, of which 5 are Ph.D.'s and 1 D.Sc. (Chemistry).

Main areas of research

- analysis of environmental objects for content and physicochemical forms of radionuclides;
- study of regularities and migration pathways of technogenic radionuclides in surface and underground biogeocenoses, including marine areas of the Russian Arctic;
- development of new, highly effective, and express methods for the radiochemical analysis of environmental objects;
- development of methods for control and purification of aquatic environments from radioactive substances and other ecotoxicants impurities.

Research Methods

- methods of radiochemical analysis;
- methods of fractionation of physicochemical forms of radionuclides;
- spectral and luminescent methods for the determination of physical and chemical forms of radionuclides.

Interdisciplinary Studies

physicochemical forms and migration of long-lived, man-made radionuclides in natural waters of different genesis taking into account biogeochemical factors (jointly with IPCE RAS and FIC RAS Biotechnology).

Key Achievements

- radioecological monitoring of NFC enterprise areas (Krasnoyarsk MCC, Kirovo-Chepetsk Chemical Complex, industrial nuclear explosion `Kraton-3') was conducted; true colloids of uranium, neptunium, and plutonium in formation waters of radioactive waste disposal site (FGUP SChK) were identified for the first time; mineralogical composition of natural pseudocolloids and soil particles accumulating actinides was determined; groups and fractions of soil organic matter that most firmly bind radionuclides were determined (Fig. 65);
- large-scale studies of the radioecological situation in the areas of the Arctic basin of Russia were carried out (Fig. 66); correlations in horizontal distribution of radionuclides in bottom sediments with parameters of lithological and mineral composition of sediments were revealed; the role of suspended material and dissolved organic matter on the transfer and behavior of radionuclides in seawater was assessed;
- for the first time, biological absorption coefficients of the most mobile and biologically important radionuclide—neptunium in the natural environment were measured;
- experimental models of devices for ecological and technological monitoring of water environments were created, which implement new principles of measurement that

allow real-time, prompt, automatic, and reagent-free monitoring (Fig. 67).

Marine Expeditionary Research

- Kara Sea, 2011, 2012; research vessel "Irresistible"; A. V. Travkina, E. M. Sizov.
- White Sea, 2013, 2014; research vessel "Ecologist"; V. D. Volodin.
- Kara Sea, Laptev Sea, 2016; the research vessel "Akademik Mstislav Keldysh"; E. M. Sizov.
- Kara Sea, Laptev Sea, East Siberian Sea, 2017; research vessel "Akademik Mstislav Keldysh"; V. D. Volodin.
- Kara Sea, Laptev Sea, East Siberian Sea, 2019; The research vessel "Akademik Mstislav Keldysh"; A. V. Travkina, V. D. Volodin.
- Kara Sea, Laptev Sea, East Siberian Sea, 2020; The research vessel "Akademik Mstislav Keldysh"; A. M. Emelyanov.

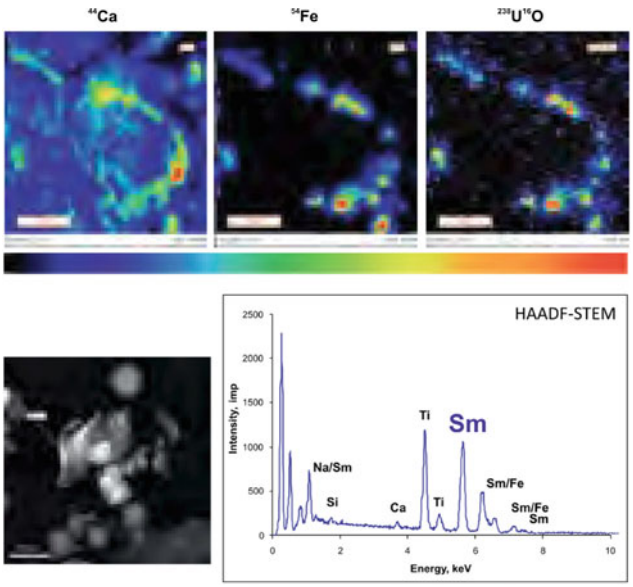

Fig. 65 Secondary-ion mass spectra of the colloidal particles with accumulated radionuclides

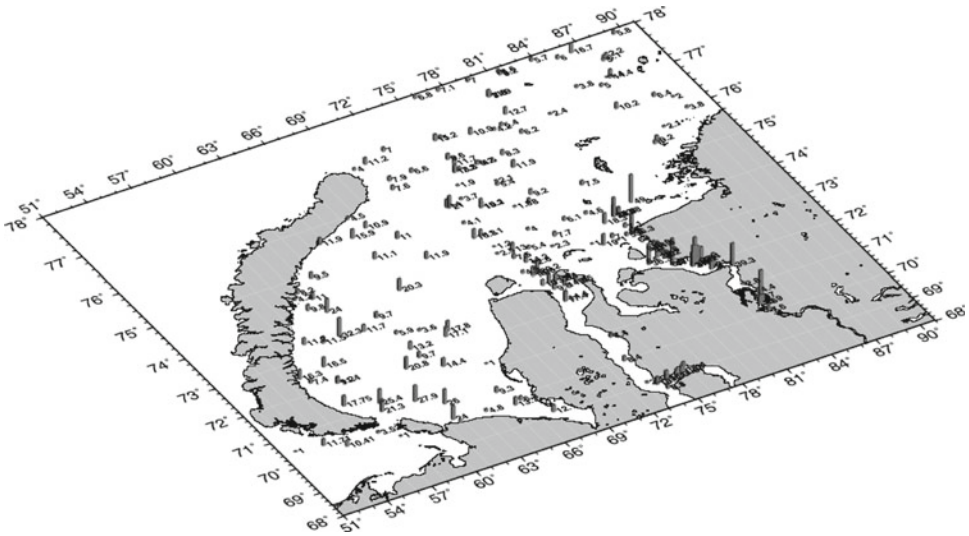

Fig. 66 Cesium-137 content in the surface layer Arctic basin sediments

Fig. 67 Radioactive control beacon

Geochemistry

The PGE-Cu-Ni Norilsk Deposits and Siberian Traps: Genetic Relationships

N. A. Krivolutskaya

1 Introduction. The Problems of Magmatic Ore Origin

1.1 Magmatic Deposits

Magmatic deposits related to ultrabasic-basic complexes are divided into three groups differing in ore composition and their genesis. They are represented (Fig. 1) by (1) Cr, V, Ti oxides (Bushveld, Great Dike, Panzhihua, etc.), (2) platinum group elements, PGE (Bushveld, Great Dyke, Norilsk), and (3) Cu-Ni sulfides (Sudbury, Norilsk, Jinchuan, Voisey's Bay, etc.). Since oxides are part of silicate melt, the formation of the first group of deposits is usually considered as a result of multistage fractionation of initial magma. Deposits of the second group are genetically correlated with the second and third groups in many respects. The formation of the third group deposits represented by sulfide minerals is the most complicated, taking into account a low sulfur solubility in melts. As a rule, for the explanation of their genesis, external sources of sulfur are involved.

It is well known that large and super large deposits of different genetic types play the main role in the world economy: they supply from 66 to 99% of raw materials to the world market despite consisting of only 5% of explored deposits [1–3]. Their formation is a unique geological problem, which attracts many researchers around the world [4, 5]. A special UNESCO project of the International Geological Correlation Program No. 354 was devoted to this topic "Industrial super concentrations of metals in the lithosphere" (1995–1999), and several symposia (St. Petersburg, 1996; Moscow, 2000; Adelaida, 2010; Beijing, 2017) were devoted to this topic. The origin of world-class deposits is regularly discussed at the Symposium of International Association on the Genesis of Ore Deposits (IAGOD, 1999, 2001, 2006). For example, the 13th Quadrennial IAGOD Symposium (Adelaida, 2010) had the title "Giant Ore Deposits Down-Under". The genesis of giant deposits is extremely important not only for discovering new and unique deposits but also in playing a fundamental role in a global problem of the origin of large geochemical anomalies in the Earth's crust where metal contents are several orders of magnitude higher than Clarke values. The mechanisms of these concentrations remain largely unclear.

1.2 Norilsk Deposits

The extra-large PGE-Cu-Ni Norilsk deposits located in the north of Eastern Siberia belong to the second and third groups of magmatic deposits at the same time [6–10]. As a rule, platinum and copper-nickel deposits are separated in space: the formers are localized as reefs in large layered plutons, and the latter ones occur in near-contact zones of intrusions. The Norilsk deposits are an exception to this rule where both types of ores take place within a single intrusive body: low-sulfide mineralization in its upper zone and Cu-Ni sulfide mineralization enriched in PGE in its lower zone. Norilsk ranks second after Sudbury in Ni reserves and second after Bushveld in PGE reserves (Fig. 2). The value of one ton of Norilsk ore exceeds the value of other deposits [10, 11]. Not only the chemical composition but also the mineral composition of these ores is unique. More than 100 mineral species were discovered in Norilsk, mostly belonging to PGM. [9]. They are also characterized by large size in contrast to similar minerals from other deposits; it is typical of sperrylite from the main ore body of the Oktyabr'sky deposit (Fig. 3).

These features of the Norilsk deposits attracted geologists from Russia and other countries since the mid-1960s when the thick sulfide veins in the Talnakh and Oktyabr'sky deposits were discovered. This event made the Norilsk area a

N. A. Krivolutskaya (✉)
Vernadsky Institute of Geochemistry and Analytical Chemistry, Russian Academy of Sciences, 19 Kosygin St, Moscow, 119991, Russia
e-mail: nakriv@mail.ru

V. P. Kolotov and N. S. Bezaeva (eds.), *Advances in Geochemistry, Analytical Chemistry, and Planetary Sciences*,
https://doi.org/10.1007/978-3-031-09883-3_2

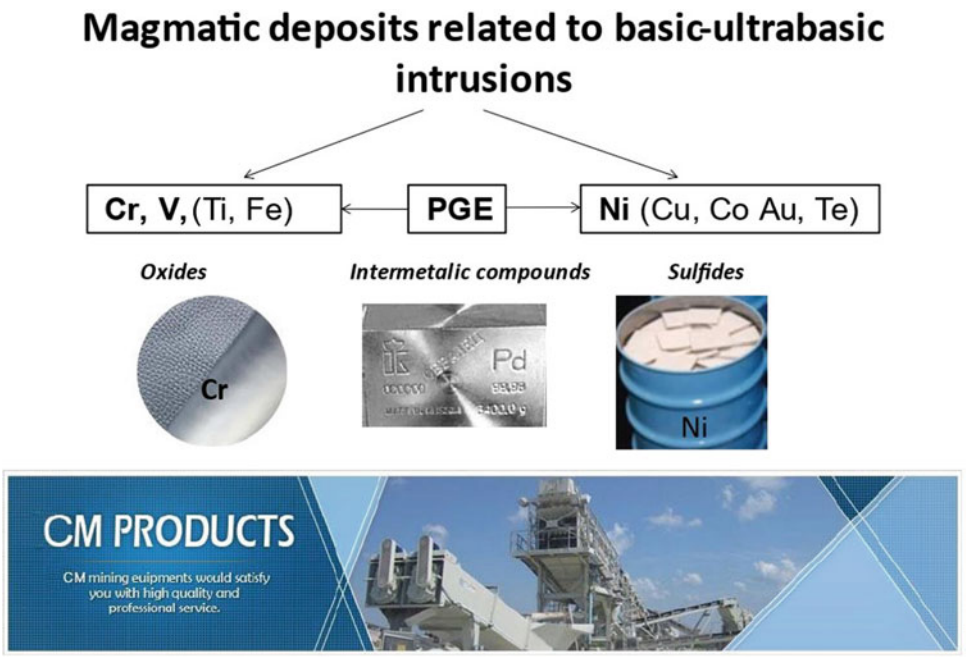

Fig. 1 The main types of magmatic deposits

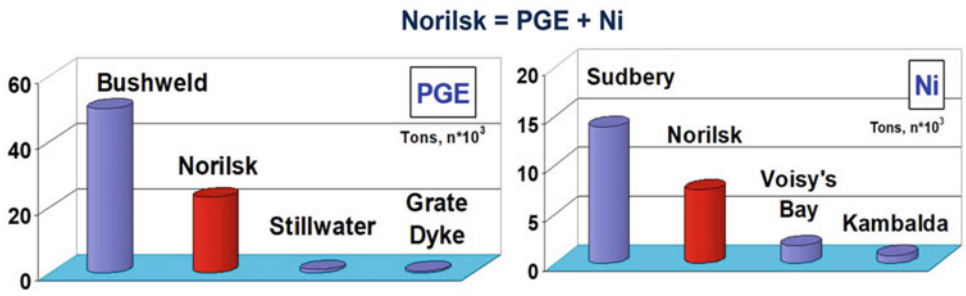

Fig. 2 Resources of the Norilsk deposits in comparison with the major PGE and Ni deposits in the world

geological phenomenon and brought Russia to a leading position in Ni and PGE (especially Pd) production in the world [12]. Numerous hypotheses have been proposed for ore formation in the Norilsk area (magmatic, metasomatic, hydrothermal, and others [6, 13–19 et ctr.]). Two main models dominate at this moment. The first one suggests the ore formation in a closed magmatic system from picritic magma enriched in metals and volatile components originating from an intermediate chamber [6, 8, 11]. The second one regards intrusions as horizontal parts of channels for lavas to the surface [20], where sulfides were formed in an open magmatic system due to assimilation of anhydrite by

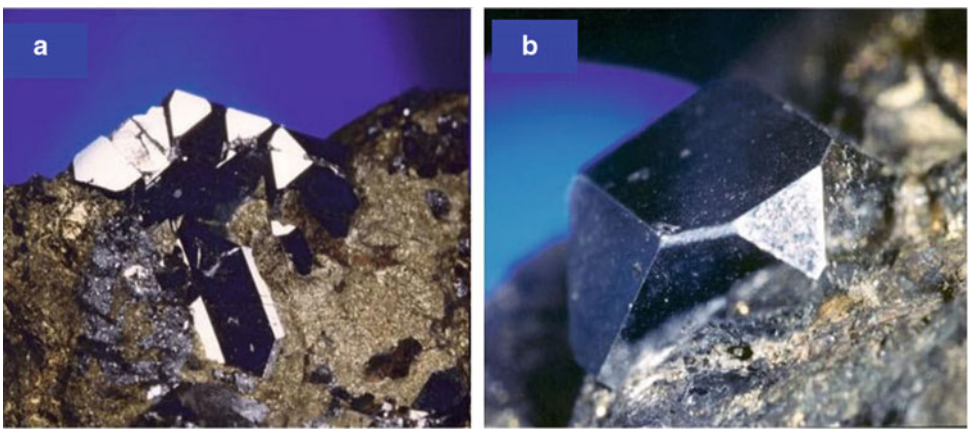

Fig. 3 Sperrylite ($PtAs_2$) crystals in chalcopyrite ore of the Oktyabr'sky deposit: **A**—aggregate, **B**—single crystal (frame is 3 cm). Photo M. Bogomolov, sample from collection of E. Sereda. After [25]

magma *in situ*. The latter model has been widely developed abroad [21–24]. In both cases, the main questions of ore genesis are the following: (1) relationships between intrusions and basalts, (2) composition of the parental magma for ore-bearing intrusions, and (3) scale of assimilation of host rocks by magmas.

The goal of our study is to clarify the genesis of the Norilsk deposits with a focus on these three points. This paper contains new information on the geological structure of the Talnakh and Oktyabr'sky deposits and the geochemistry of igneous rocks of the Siberian province. It comprises of results of our previous works [11, 14, 16, 19], carried out at the Laboratory of geochemistry of magmatic and metamorphic rocks of GEOCHI RAS from 2001 to 2021. We propose a new approach to deposits' genesis, considering their occurrence within the paleorift zones and the evolution of magmatism in the Arctic zone of the Siberian traps province.

2 Brief Geology of the Siberian Traps Province and Related Deposits

The Siberian traps province is the largest continental province on Earth. It is located in Eastern Siberia, covering the Middle Siberian Plateau and the Taimyr Peninsula (Fig. 4). The province consists of volcanic, plutonic, and pyroclastic rocks, with the ratios between them varying significantly in their different parts [26–31]. It is zoned, i.e., lavas dominate in the central part, they are framed by tuffs, and intrusive rocks are exposed at the periphery. The thickness of volcanic rocks is maximum in the northern regions (up to 3.5 km). The bulk of the rocks are tholeiitic basalts of normal alkalinity and sills of gabbro-dolerites, which are close in composition to lavas. Rocks of high alkalinity and high-Mg rocks are localized in the northern parts of the province. A subdivision of the volcanic sequence into formations was carried out during geological mapping in the 1960–1970s. Different formations are distinguished in different areas (Table 1) [27]. The intrusive rocks are subdivided into several complexes; the most widespread is the Katangsky complex (6–7 wt % MgO). Sills of this complex occur in the western, southern, and eastern rim of the Tunguska syneclise. Subalkaline, alkaline massifs, as well as ultrabasic intrusions are also present in the northern part of the province.

PGE-Cu-Ni sulfide deposits are related to intrusions with elevated MgO content (10-12 wt.%) in the Norilsk area [8, 32]. The largest ones are concentrated within the Talnakh and Norilsk ore junctions, in the periclinal parts of Kharaelakh and Norilsk trough (Fig. 5). The ore-bearing massifs are ribbon-like bodies with an average thickness of 100 m, 1–2 km in width, and 15–18 km in length. As a rule, they are

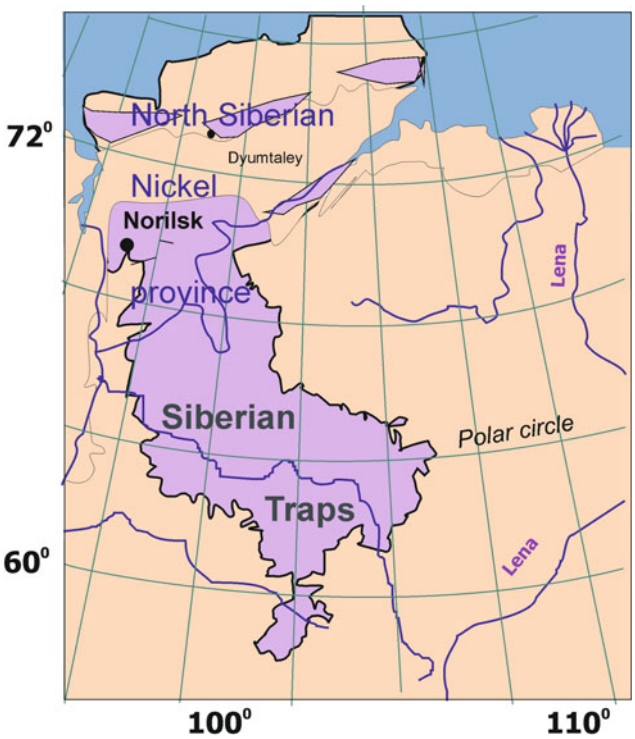

Fig. 4 Position of the Norilsk deposits within the Siberian traps province

situated within carbonate-terrigenous sediments of the Devonian-Permian age (the Kharaelak, Talnakh, Norilsk 1, Pyasino-Vologochansky intrusions), rarely cutting tuff-lava sequence forming dykes and pipe-like bodies (the Norilsk 2, Bolshaya Bariernaya, North- and South-Maslovsky intrusions). Intrusions are composed of gabbro-dolerites (from bottom to top): contact, taxitic, picritic, olivine, olivine-bearing, olivine-free [8, 33]. The upper zone consists of gabbro-diorites, leucogabbro, ferrogabbro, magmatic breccias; some horizons could be absent in it. The ores are represented by disseminated sulfides in picritic and taxitic gabbro-dolerites and the host rocks, as well as by massive sulfides at the intrusion contact with underlying rocks (Fig. 6). Low-sulfide mineralization was discovered in the upper part of the ore-bearing intrusions [34, 35].

3 Materials and Methods

To understand the genesis of the Norilsk deposits and their relationships with basalts in the Siberian traps province, we studied flank zones of the Talnakh and Oktyabr'sky deposits (Fig. 5) based on drillholes MK-10, MK-11, ZF-11, ZF-69, ZF-59. Magma composition of ore-bearing intrusions was studied using melt inclusions in olivines and pyroxenes from the olivine-bearing gabbro-dolerites of the Maslovsky deposit. Homogenization of melt inclusions was carried out

Table 1 Division of volcanic rocks in formations for the key areas of the Siberian traps province (after [27] with changes)

System	Noril'sk	Taimyr	Putorana	Tunguska	Maymecha-Kotuy
T_1	Lavas: Samoedsky Kumginsky Kharaelakhsky Mokulaevsky Morongovsky Nadezhdinsky Tuklonsky (Tuffs) Khakanchansky Gudchikhinsky Syverminsky	Lavas: Fadiykudinsky Ayatarinsky		Lavas: Yambukansky Kochechumsky Nidymsky	Lavas: Maymechinsky Delkansky Tyvankitsky/Onkuchaksky/ Arydzhangsky
		Lavas: Betlingsky Zverinsky	Lavas: Nerakarsky Honnamakitskyy Ayansky		
		Lavas: Labaksky Verkhnetamsky		Tuffs: KorvunchanskyTutonchansky	Tuffs: Pravoboyarsky Khardakhsky
P_3	Lavas: Ivakinsky	Lavas: Syradasaysky		Tuffs: Degalinsky Pelyatkinsky	Tuffs: Pelyatkinsky -

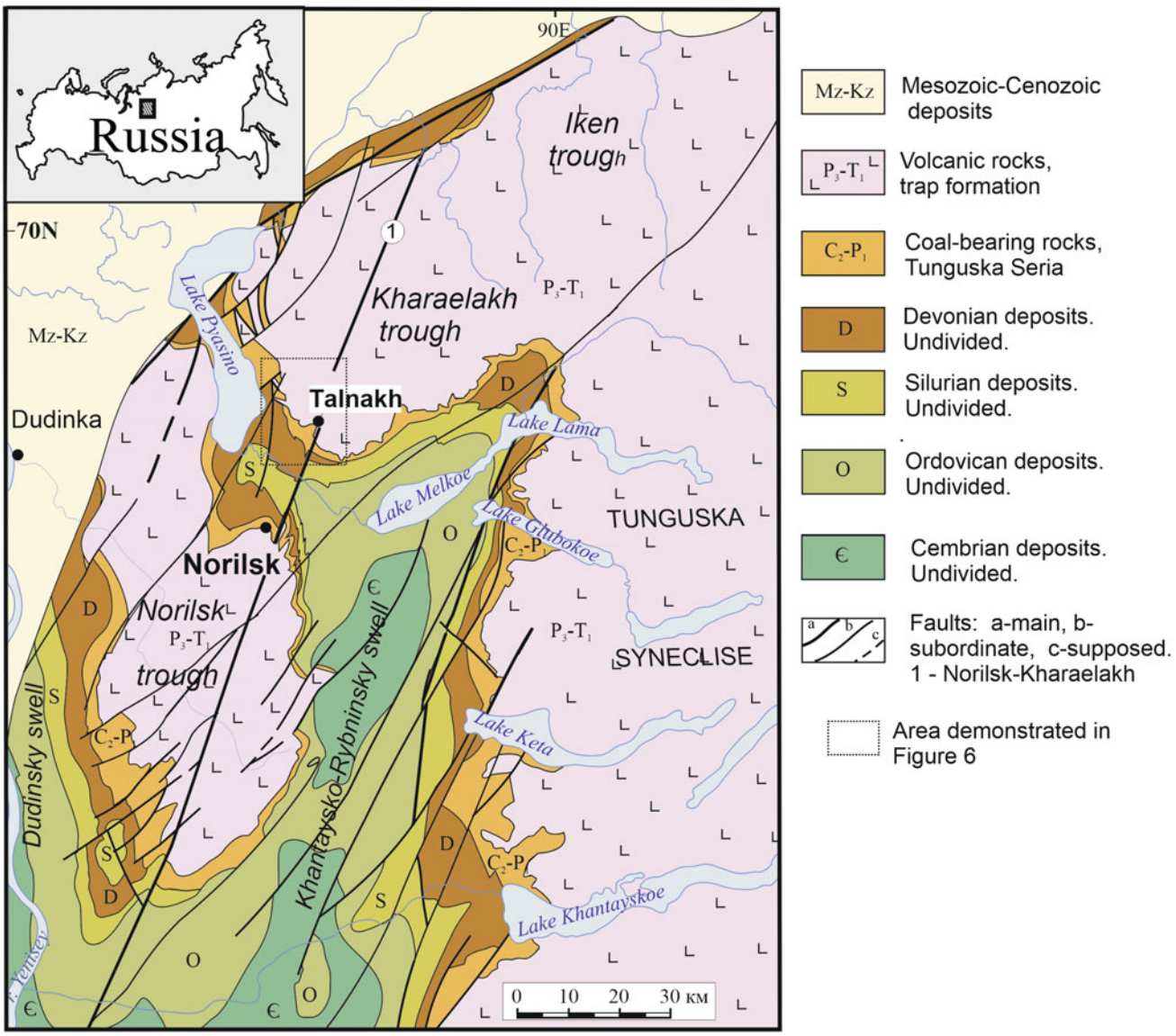

Fig. 5 Schematic geology map of the Norilsk area

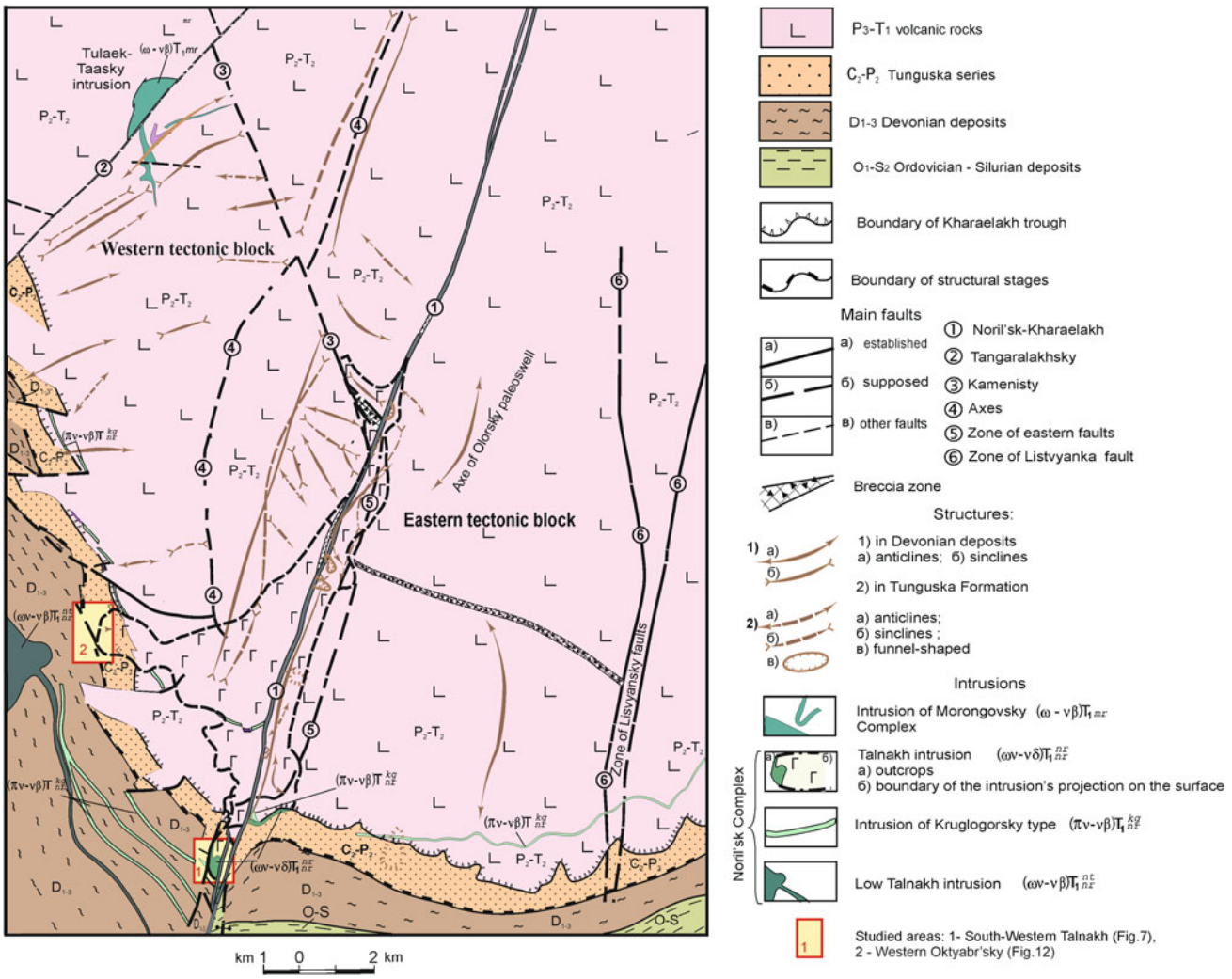

Fig. 6 Schematic geology map of the Talnakh ore junction (after Ltd. Norilskgeology data, with corrections)

in a high-temperature chamber with oxygen fugacity control at the Vernadsky Institute RAS. Specific geochemical features of the Norilsk igneous rocks were identified by comparing their composition with the composition of volcanic and intrusive rocks from the key areas of the province.

Major element concentrations in rocks were analyzed using X-ray fluorescence (XRF) at the Institute of Geology of Ore Deposits, Petrography, Mineralogy and Geochemistry of RAS on a sequenced-action vacuum spectrometer (with dispersion over the wavelength), and using an AxiosmAX model from PANalytical (Almelo, The Netherlands) (analyst A. I. Yakushev). This spectrometer is equipped with a 4 kW X-ray tube with an Rh-anode. The maximum voltage on the tube is 60 kV, and the maximum anode current is 160 mA. When the spectrometer is calibrated, the industry and state standard samples of the chemical composition of rocks and ores are used. The quality control of the results is carried out according to the analysis of rock standard samples from the US Geological Survey (USGS). The relative standard deviations (RSD) for major oxides are as follows (%): SiO_2—0.12; TiO_2—0.05; Al_2O_3—0.12; $Fe_2O_{3(total)}$—0.13; MnO—0.005; MgO—0.07; CaO—0.08; Na_2O—0.08; K_2O—0.03; and P_2O_5—0.01. Trace element concentrations in the rocks were determined using inductively coupled plasma mass spectrometry (ICP-MS) at the Institute of Microelectronics Technology and High Purity Materials of RAS (IMT RAS), Chernogolovka, Russia (analyst V.K. Karandashev). The procedure was described in [36]. Base and precious metal concentrations in disseminated and massive ores were analyzed at IGEM RAS (analyst V. A. Sychkova) and GEOKHI RAS (analysts I.V. Kubrakova and O.A. Tyutyunnik) according to the procedure published earlier [37]. Sr, Nd, and Pb isotopes were studied in representative samples from volcanic rocks at the A.P. Karpinsky Russian Geological Research Institute (VSEGEI), St. Petersburg, Russia (analyst B.V. Belyatsky). Chemical separation of

elements was carried out by chromatographic method on ion exchange columns, and the procedure of isotopes measurement was described in [38]. Minerals and glasses were analyzed using a CAMECA SX 100 (Cameca, Gennevilliers, France) at the Vernadsky Institute of Geochemistry and Analytical Chemistry of RAS (analyst N.N. Kononkova).

4 Results

4.1 Flank Zones of the Norilsk Deposits, the Talnakh Ore Junction

The Oktyabr'sky and Talnakh deposits are the largest deposits in the Norilsk district. They are situated in the south Kharaelakh trough (Fig. 6). The structure of flank zones of these deposits allows examination of the conditions of ore formation: whether they were formed in closed or open magmatic systems, as it is supposed in some works [23, 39]. To solve this problem, we studied the structure of the peripheral parts of the deposits, i.e., the southern part of the Talnakh and the western part of the Oktyabr'sky deposits (Fig. 6) using cores of drillholes of Norilskgeology Ltd. These areas have distinctive features compared to the central parts of the deposits and allow a representative view of the structure of the deposits, which is extremely important for solving the problems of ore genesis. The selected areas are similar to each other by the presence of thick sulfide veins in gabbro-dolerites, the composition of which is specific. The South-Western branch of the Talnakh deposit comprises very copper-rich ores that differ from the Oktyabr'sky deposit and other Norilsk deposits. We described these ores earlier [37, 40], but their unusual structure and composition deserve more attention.

The South-Western branch of the Talnakh deposit

The Talnakh deposit consists of two branches, the North-Eastern and South-Western [33]. The intrusion lies at the boundary of Devonian carbonate-terrigenous deposits (the Kalargonsky formation) and terrigenous rocks of the Tunguska series (C_2-P_2) in a highly fractured block of rocks (Fig. 6). The structure of the south-western branch is shown in some works [17, 33, 37]. Intrusive rocks of this branch are partly eroded (Fig. 7). In the vertical section, they are represented (from bottom to top) by fine-grained contact gabbro-dolerites (<1 m, out of scale, not shown in the section 7b), taxitic and picritic gabbro-dolerites, and gabbro-diorites, which occupy ½ of the section (Fig. 7, Table 2). Sulfides occur as droplets and aggregates in picritic and taxitic gabbro-dolerites and also form a vein of massive ores within the intrusive body, which is 15 m thick in drillhole MK-10 (Southern 2 orebody). Mineralized gabbro-dolerites present within the vein, splitting it into two branches.

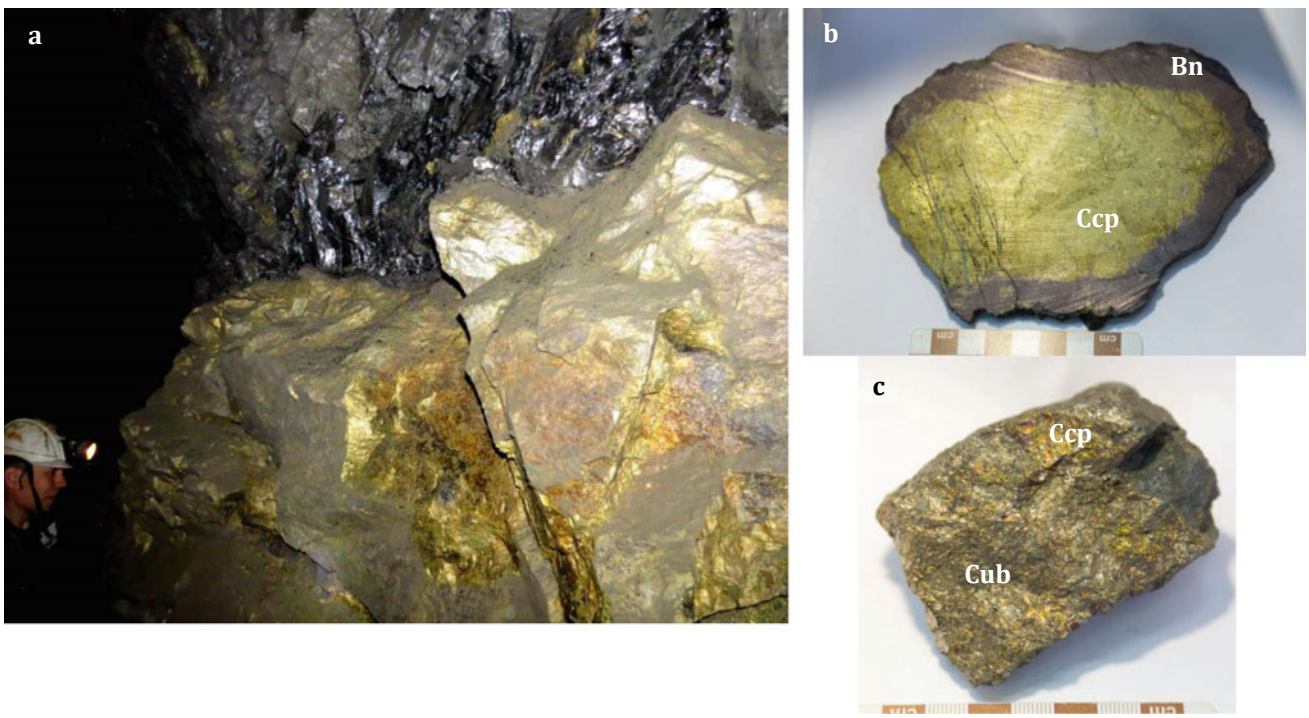

Fig. 7 Sulfide ores: a—chalcopyrite, mine Majak; b—bornite-chalcopyrite, Southern 2 orebody; c—cubanite-chalcopyrite ore. Ccp-chalcopyrite, Bn-bornite, Cub-cubanite

Table 2 Intrusive rock compositions in drillhole MK-10

Sample, No	49.6	62.0	80.1	91.0	91.8	92.3
SiO_2	49.31	49.10	45.30	37.39	42.70	39.73
TiO_2	1.12	1.07	0.89	0.49	0.93	0.85
Al_2O_3	14.62	15.12	16.43	7.76	10.84	12.05
Fe_2O_3	10.21	11.78	14.17	21.47	14.04	20.85
MnO	0.27	0.18	0.18	0.20	0.19	0.19
MgO	7.53	7.29	8.97	18.12	15.21	7.87
CaO	9.96	9.19	9.36	5.41	11.39	9.94
Na2O	3.48	2.71	2.20	0.89	1.44	1.62
K_2O	1.05	1.08	0.59	0.39	0.50	1.01
P_2O_5	0.19	0.14	0.19	0.14	0.02	0.18
LOI	3.05	3.06	2.98	6.69	2.74	4.62
Total	100.81	100.71	99.26	99.05	100.03	99.01

Note Sample No—depth in drillhole MK-10, m

The main ore minerals in both disseminated and massive ores are (in %): chalcopyrite tetragonal $CuFeS_2$ (75–85), pentlandite (Ni, Fe, Co)$_9S_8$ (10–25), cubanite $CuFe_2S_3$ (5–10), pyrrhotite Fe_{1-x} S (Figs. 8, 9). The major minerals are bornite Cu_5FeS_4, chalcocite Cu_2S, magnetite $FeFe_2O_4$, violarite $FeNi_2S_4$, millerite NiS, sphalerite ZnS, galena PbS, pyrrhotite FeS_2. The minerals of platinum group elements (MPG) are represented by zvyagintsevite Pd_3Pb, plumbopalladinite Pd_3Pb_2, polarite Pd (Pb, Bi), rustenburgite (Pt, Pd)$_3$Sn, atokite (Pd, Pt)$_3$Sn, taimyrite (Pd, Cu, Pt)$_3$Sn and other minerals [37, 40]. Cu-Au-Ag alloys are widespread. A large amount of bornite and chalcocite distinguishes ores of Southern 2 from other orebodies of the Norilsk deposits. The composition of chalcopyrite and pyrrhotite corresponds to stoichiometric, while pentlandite varies both in the content of the main components—Fe and Ni, and impurity elements, the main of which are Co and Cu (Fig. 10).

The chemical composition of the ores (Table 3, Fig. 11a-c) reflects their mineral composition. Thus, the dominance of chalcopyrite led to high concentrations of copper, which exceeded the nickel content by several times (Cu/Ni ratio varies on average from 2 to 5). The maximum Cu/Ni values are typical of disseminated ore between the vein bodies. This ratio is close to that studied in the samples taken in the underground and the EM-6 drillhole [40], although in the latter, it can reach 12. The PGE concentrations are also anomalously high (max ΣPt+Pd=131 ppm), although slightly lower than in the samples studied earlier by us, where it reaches 180 ppm [37], and even 220 ppm [40]. Palladium dominates in ore, Pd/Pt ratio reaches up to 13 (Fig. 11a)

The western flank of the Oktyabr'sky deposit

The Oktyabr'sky deposit is associated with the Kharaelakh intrusion [41, 42], which has a complex structure. The western flanks of the deposit are characterized by an occurrence of numerous small gabbro-dolerite bodies with disseminated and massive ores (Fig. 12), as well as disseminated mineralization in the surrounding sedimentary rocks (so-called "cuprous ores"). The thickest orebodies were penetrated by drillholes ZF-12 (two horizons, 6.1 and 12m), ZF-7 (6.1m), and ZF-11 (3.5m). The Ni content varies from 1.5 to 3 wt.%, Cu- from 0.6 to 3.0 wt.%, S- from 20 to 33 % wt, Pt+Pd from 1 to 7 ppm. The Cu/Ni ratio varies from 0.3 to 2, and Pd/Pt = 0.9 to 4.1. The ores have essentially pyrrhotite composition (>70 vol.%), the chalcopyrite content is usually 10–15 vol.%, and pentlandite—10 vol.%. Copper ores are 90% composed of chalcopyrite; they contain on average 8-10 wt.% Cu, 0.8 wt.% Ni, Pt + Pd=15 ppm.

The western part of the Oktyabr'sky deposit has some similarities with the southern zone of Talnakh described above—it also contains thick veins of massive ores (up to 12 m), associated with small gabbro-dolerite bodies (50–70 m). However, this massive ore essentially differs from the Southern 2 orebody due to lower concentrations of copper and platinum metals. We have described these ores earlier in drillholes ZF-10 and ZF-12 [43]. However, the western part of the deposit has a very complex structure, so we additionally investigated the structure of intrusive rocks and related ores in drillholes ZF-11, ZF-59, ZF-69.

Drillhole ZF-11 (Fig. 13) demonstrates the occurrence of several intrusive bodies separated by interlayers of Devonian sedimentary rocks as well as drillholes ZF-12 and ZF-10 [43]. A characteristic feature of this part of the deposit is the absence of high-magnesian rocks (picritic and taxitic gabbro-dolerites, Table 4), where disseminated ores are localized in the central part of the deposit. The rocks are mainly represented by gabbro-dolerites and olivine gabbro-dolerites, which have a weakly manifested taxitic texture in

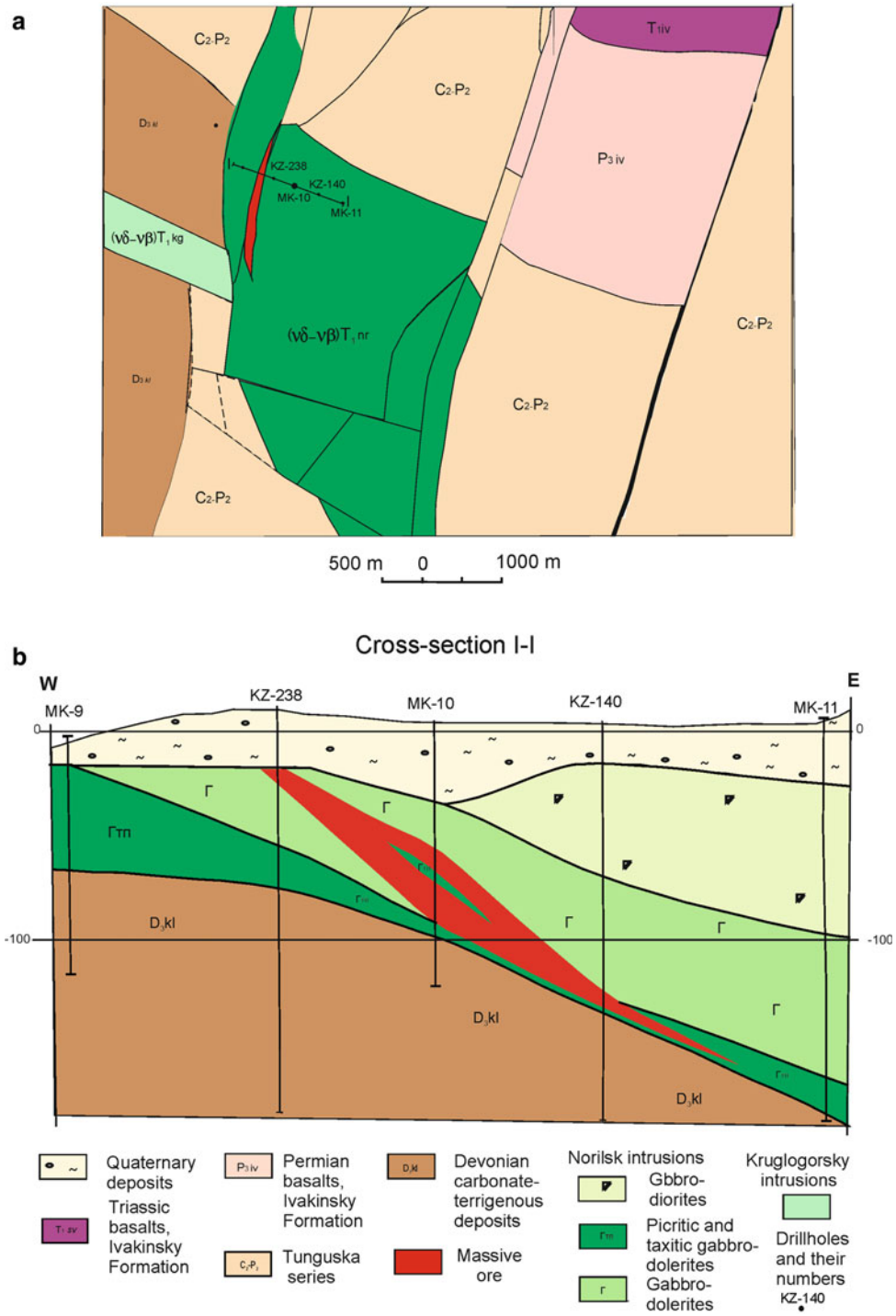

Fig. 8 Schematic geology map (a, Q sediment cover removed) and cross-section(b) of the southern part of the Talnakh deposit (after Ltd Norilskgeology data, with corrections)

the upper part of the section and are therefore called "taxitic-like". Their compositions are given in Table 3.

Veins of massive ore (0.2–03 m) are observed in the ZF-11 drillhole at depths (m): 448.2–448.5, 462.1–462.4, and 466.7–466.0. The thickest ores are located in the lower part of the section (491.1–495.5 m, Table 5) at the boundary of intrusive and sedimentary rocks (in hornblende). Mean concentrations of metals in them (wt.%): 1.6 Cu, 0.9 Ni, 0.1 Co; Pt+Pd—3.5 ppm. Sulfide minerals are represented by pyrrhotite (80%), pentlandite (10%), chalcopyrite (10%), and sometimes pyrite (less than 1%). Rare minerals are sphalerite, mackinawite, argentopentlandite, and valleriite. Among MPG, rustenburgite, moncheite, couperite, and isoferroplatinum were recognized. Au-Ag allows contain 85–90 wt.% Au, sometimes they are enriched in Pd (up to 5.6 wt.%).

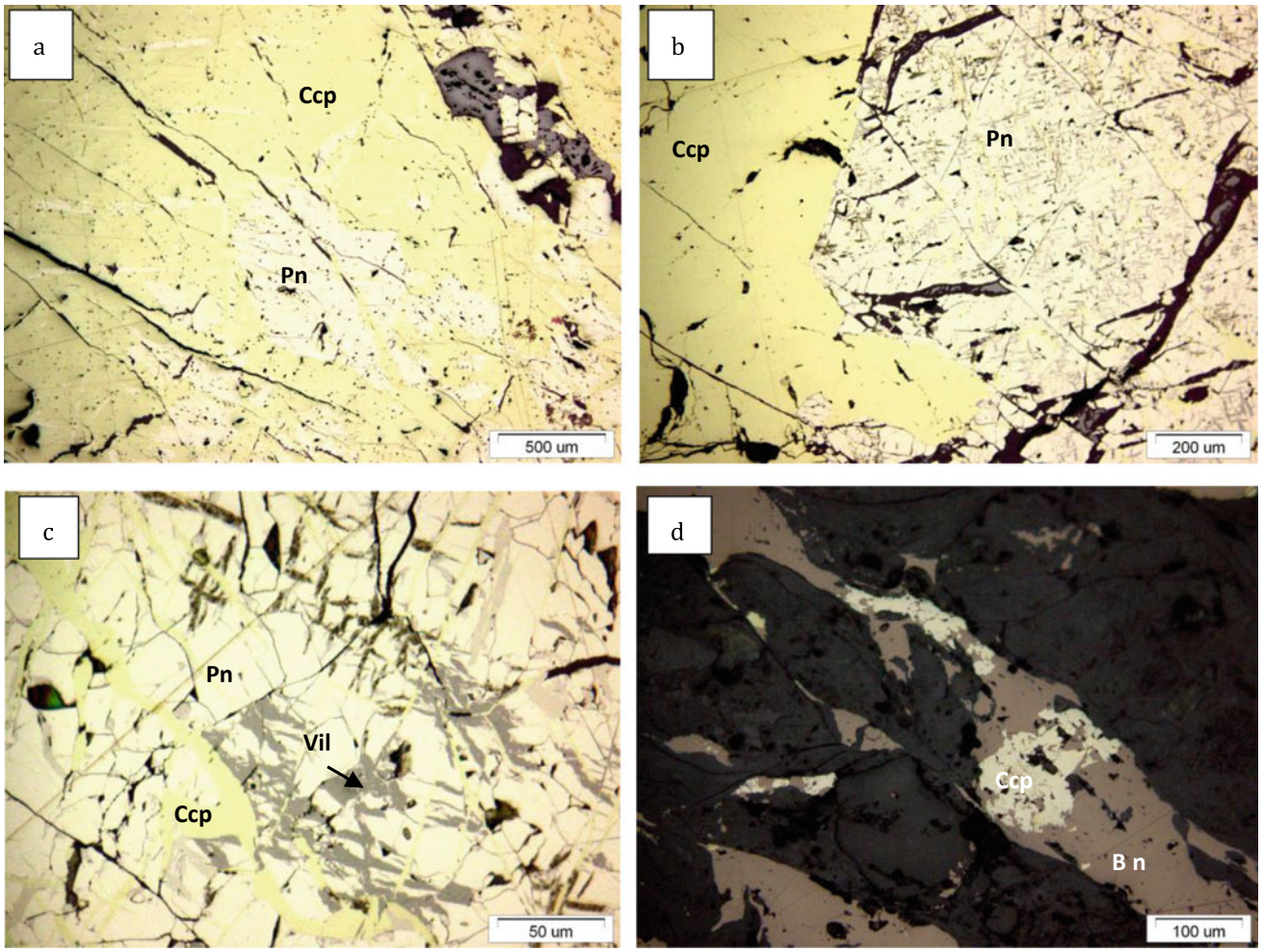

Fig. 9 Photomicrographs of sulfide ore from the Southern 2 orebody: **a** pentlandite grains in chalcopyrite, **b** pentlandite crystal in chalcopyrite, **c** replacement of pentlandite by chalcopyrite and violarite, **d** veinlets of bornite and chalcopyrite in silicate minerals. Reflected light. Minerlas: Ccp—chalcopyrite, Pn—pentlandite, Vil—violarite, Bn—bornite

Usually, massive orebodies of this area are described as a peripheral part of the main orebody of the Oktyabr'sky deposit, the central part of which is composed of chalcopyrite-cubanite ores. But the structure of the western part of the deposit does not support this idea since the structure is very complicated (Fig. 14). There are several intrusive bodies composed of poorly differentiated gabbro-dolerites: MgO concentrations vary from 6 to 19 wt.%. As is seen in Fig. 14, the bodies of ore-bearing gabbro-dolerites pinch out in the western direction and have no connections with lavas, which are assumed in many works [20–24].

4.2 Composition of Ore-Bearing Magmas

According to many publications [10, 17, 19], the composition of parental magma plays a critical role in ore formation. We determined magma compositions in several ways: (1) by calculating the average weighted composition of ore-bearing intrusions, taking into account insignificant alteration of rocks, (2) by geochemical thermometry using the "Comagmat" Software, and (3) by studying magmatic inclusions in early liquidus phases.

The average weighted composition of intrusions of the Norilsk Complex has been continuously determined by researchers over several years. The most adequate results were obtained using several boreholes, which take into account variations in thickness of separate horizons within intrusive bodies. Such work was carried out by M.N. Godlevsky for Norilsk 1 [6] and M.B. Dneprovskaya for Talnakh [44] (Table 6). We calculated weighted average compositions of multiple intrusive bodies using one or several drillholes [45, 46]. Such calculations reflect the composition of the whole intrusion only in the case of its sill-like morphology and constant thickness of all horizons. These data

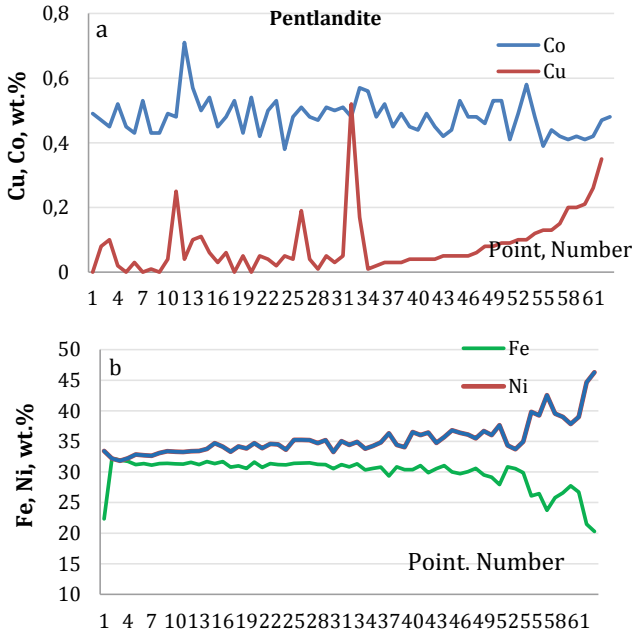

Fig. 10 Variations of pentlandite composition (**a**—Cu and Co, **b**—Fe and Ni) along the extension of the orebody Southern 2 (from south to north)

demonstrate a very similar compositions of ore-bearing intrusions belonging to the Norilsk Complex.

The composition of the initial magma for the Talnakh intrusion was also estimated by geochemical thermometry [47] on the basis of an assumption that the intruded magma consisted of melt and crystals. Calculated Talnakh magma contained 11 vol. % crystals (7 vol.% olivine and 4 vol.% plagioclase), and the composition of melt was close to the basalts of the Morongovsky-Mokulayevsky formations [48]. The calculated data testify to the closeness of the characteristics of ore-bearing magmas of the Norilsk region obtained by different methods (Table 6).

However, the methods used above do not allow us to estimate the content of volatile components in magmas. To this end, we have studied melt and fluid inclusions in olivine and pyroxene from several deposits—Talnakh, Norilsk 1, and barren intrusions—Lower Talnakh and Zelenogrivsky [49, 50]. The concentrations of volatiles were equally low (H_2O = 0.4–1.1 wt.%; Cl = 0.02-0.2 wt.%; F = 315 ppm on average), and the melt composition corresponded to tholeiitic basalts of slightly higher MgO content (8-9 wt.% MgO) (Table 7).

New data on melt inclusion in liquidus clinopyroxenes in the upper part of the Southern Maslovsky intrusion (Fig. 15)

Table 3 Chemical ore composition in drillhole MK-10

No sample	Cu	Ni	Co	Pt	Pd	Au	Ag
69.2	0.35	0.21	0.016	0.31	1.55	2.21	31.13
71.2	0.51	0.28	0.015	0.29	1.57	8.14	111.2
73.2	1.21	0.62	0.018	1.62	3.97	8.23	115.7
74.7	5.01	1.32	0.021	8.42	24.10	2.13	29.17
76.2	2.37	0.84	0.015	4.31	12.98	8.14	117.3
78.1	20.01	4.01	0.049	17.02	78.13	3.12	32.17
79.8	24.20	5.02	0.061	36.08	94.71	6.11	84.11
80.5	6.03	1.42	0.024	7.95	24.03	1.02	14.88
80.9	17.55	5.02	0.061	10.22	7.21	8.77	64.89
81.2	1.22	0.24	0.012	0.82	3.10	6.12	81.17
82.8	6.99	1.12	0.024	9.98	33.17	6.19	79.44
83.7	16.22	3.97	0.015	21.86	74.11	2.16	69.14
84.9	0.55	0.70	0.011	2.04	24.17	1.18	32.22
87.6	22.47	4.87	0.062	11.86	62.18	1.89	30.19
89.2	20.21	4.78	0.061	12.14	70.2	0.88	4.73
90.1	24.44	4.01	0.059	13.02	67.10	1.01	6.22
90.4	17.18	4.77	0.060	3.05	44.17	0.92	5.43
92.4	16.17	5.11	0.057	3.11	39.18	0.82	5.11
93.8	10.96	5.14	0.071	2.22	31.26	0.44	3.98
94.9	1.24	0.47	0.014	1.02	3.78	0.05	1.04

Note No sample = depth in drillhole MK-10 (m); Cu, Ni, Co are given in wt.%, Pt, Pd, Au, Ag—in ppm

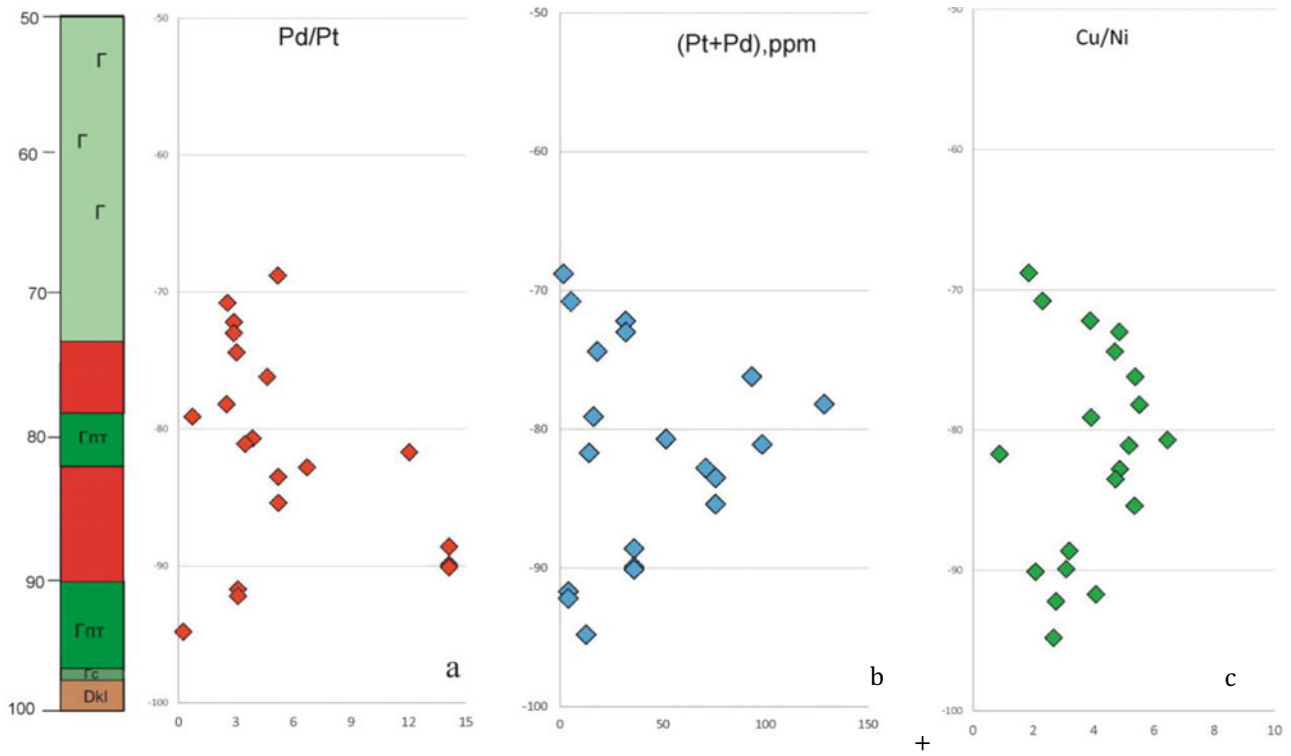

Fig. 11 Distribution of **a** Pd/Pt, **b** Pt + Pd and **c** Cu/Ni in vertical section of the Southern 2 orebody (drillhole MK-10). Data in Table 2. Gabbro-dolerites: Гпт—picrirtic-taxitic, Го—olivine. Г—olivine-free; red mark-massive ore; brown mark—Devonian rocks, Kalargonsky formation

demonstrate the composition of a fractionated melt containing elevated amounts of titanium, alkalis, and reduced amounts of MgO (Table 7).

Thus, our data indicate that the deposits were formed in a closed magmatic system, not in an open system. The composition of sulfide ore does not depend on the composition of silicate rocks (Tables 2–5). The composition of the parental magmas of ore-bearing intrusions did not differ from the compositions of magmas formed by barren intrusions. These magmas were close to magmas of within plate basalts, especially in terms of volatile contents [51]. They were characterized by elevated MgO in comparison to the basalts of platform magmatism within the Siberian traps province.

These results forced us to change an approach to solving genetic problems of the deposits. We turned to consider the peculiarities of the structure of the Norilsk ore district.

4.3 Geochemistry of Igneous Rocks Within the Siberian Traps Province

To elucidate the features of magmatism in the Norilsk region and determine the place of ore-bearing intrusions in the evolution of magmatism within the Siberian traps province, we studied the composition of volcanic and intrusive rocks in the key areas of the province (Fig. 16). The study of igneous rocks in Eastern Siberia is laborious due to the huge size of the territory, where many areas are remote. Consequently, they were studied by different organizations during systematic geological surveying (mostly 1:1000000 and 1:200000 scale mappings), and numerous legends appeared. Many formations and intrusive complexes were distinguished within the province. Their correlation and linking are some of the most important tasks at this moment. We used modern geochemical methods for this purpose. Firstly, we were interested in intrusive rocks that are an integral part of the trap formation and are widely distributed within the Siberian Platform. Most of them are combined in the Katangsky Intrusive Complex. Its massifs are widespread in the southern, western, and eastern parts of the Tunguska syneclise. They are represented by thick sills (up to 400 m) and length (10–100 km) in the south and small (5–50 m) sill-like bodies and sills in the west and east. Intrusions are poorly differentiated and composed of gabbro-dolerites, olivine gabbro-dolerites, and sometimes gabbro-diorites in the upper parts. We have studied them in the Viluy, Podkamennaya Tunguska, and Lower Tunguska (Fig. 17) river valleys. Their composition varies insignificantly (Table 8).

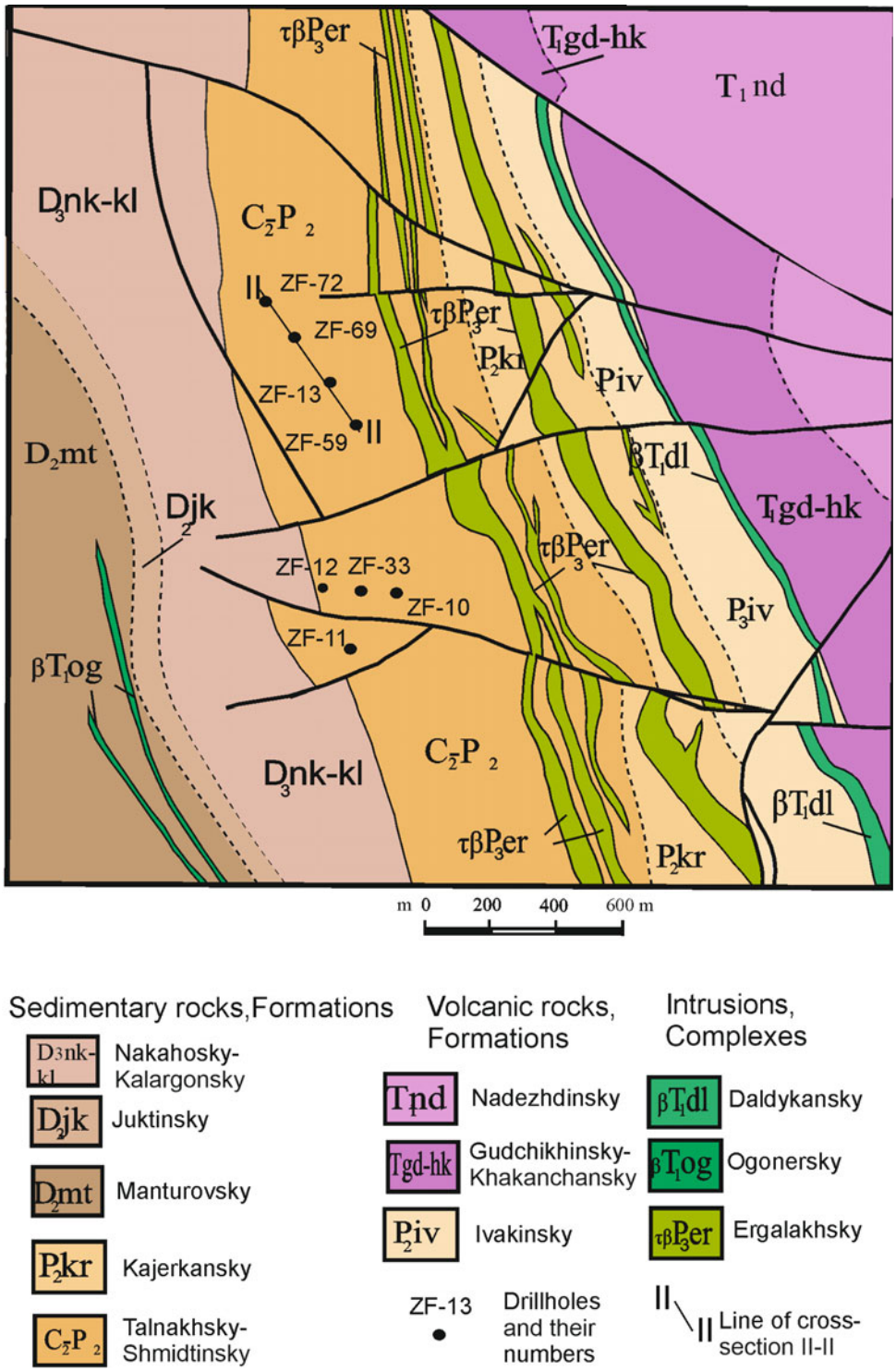

Fig. 12 Geology map of Western flank of the Oktyabr'sky deposit (after Ltd. Norilskgeology data, with corrections)

The composition of intrusive rocks varies within a wide range in the northern part of the province, i.e., in the Norilsk, Kulyumber, Maymecha-Kotuy areas, and Taimyr peninsula. Here have been established subalkaline, alkaline rocks, as well as massifs of basic and ultrabasic composition [26, 53]. We have studied massifs of the Ergalakh, Norilsk (including the Lower Talnakh, Kruglogorsky, and Zubovsky types), Morongovsky, and Daldykansky Intrusive Complexes in the Norilsk area and Kulyumber river valley [25, 54, 55], and many other complexes (Tarisimiseysky, Byrrangsky et ctr.). As a result, we discovered two new intrusive complexes. The first one was found in the southern part of the Norilsk trough. Its rocks are similar to the Ergalakh Complex, but they are enriched in TiO_2 up to 5.2 wt.% in comparison with

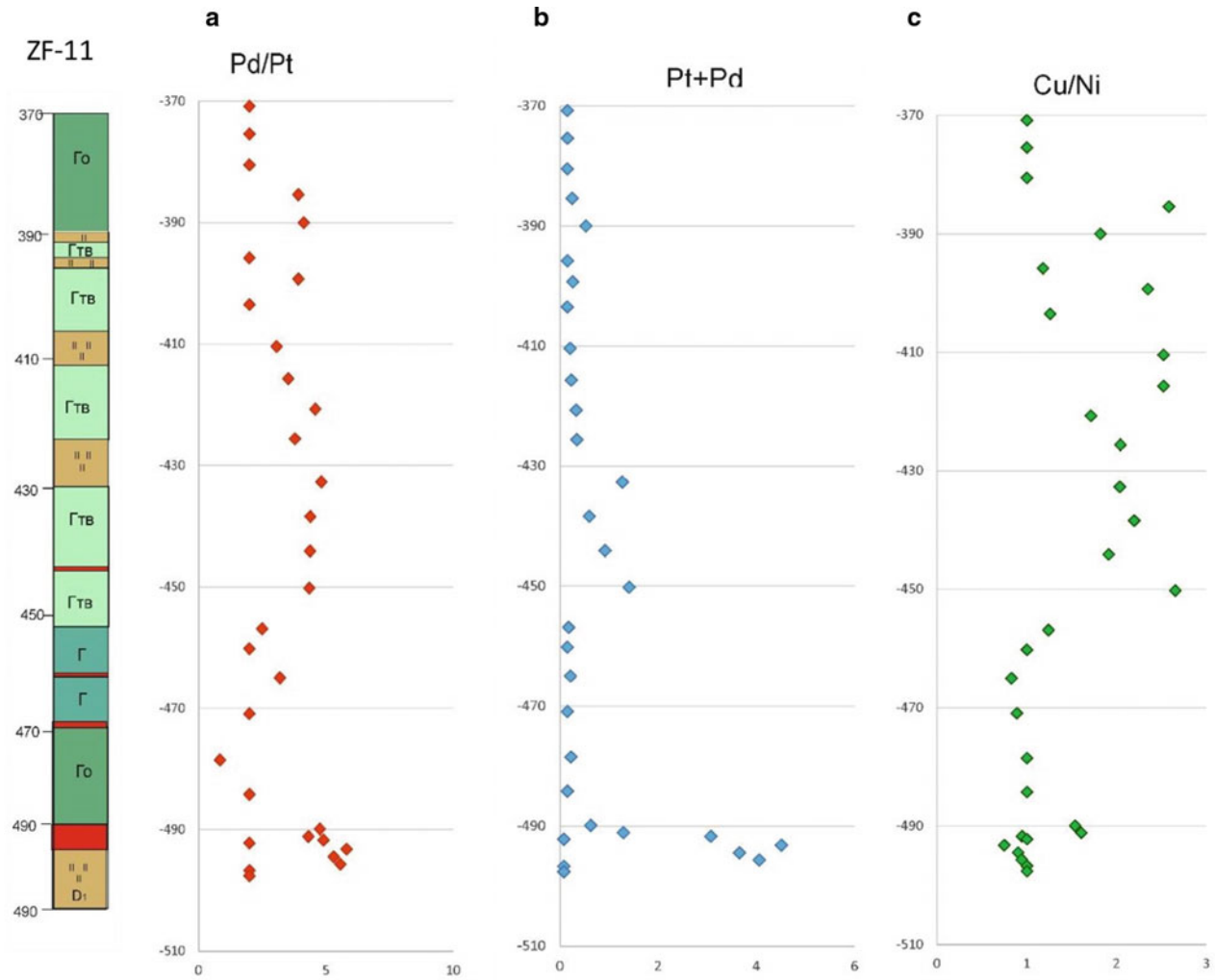

Fig. 13 The Pd/Pt **a**, Pd + Pt **b**, and Cu/Ni **c** ratios in drillhole ZF-11 of Gabbro-dolerites: Гтв—taxitic-like, Го—olivine, Г—olivine-free; red mark-massive ore, brown mark—Devonian rocks. Unpublished data

Table 4 Intrusive rock compositions in drillhole ZF-11

Sample, No	374	398	413	432	448	468	484
SiO_2	42.73	45.81	47.20	47.00	48.70	49.63	47.73
TiO_2	1.39	1.19	1.31	1.19	1.33	1.15	0.88
Al_2O_3	11.62	14.02	15.42	13.99	14.84	14.55	13.36
Fe_2O_3	15.94	12.61	12.47	12.90	13.14	11.45	11.24
MnO	0.14	0.21	0.19	0.20	0.22	0.19	0.21
MgO	10.90	7.21	6.88	7.72	7.21	6.87	12.02
CaO	6.12	9.96	9.99	9.98	10.39	10.94	9.48
Na2O	2.55	2.73	2.61	2.50	2.54	2.42	1.42
K_2O	0.44	0.97	0.78	0.79	0.80	1.01	0.79
P_2O_5	0.13	0.12	0.12	0.11	0.12	0.12	0.11
LOI	9.01	5.05	3.87	3.88	1.74	1.64	2.89
Total	100.96	99.86	100.83	100.26	101.03	99.97	100.12

Note Sample No—depth in drillhole ZF-11, m

Table 5 Chemical ore composition in drillhole ZF-11

No sample	Ni	Cu	Co	Pt	Pd	Au	Ag
490.5	1.68	1.59	0.094	0.52	2.55	0.06	1.56
492.0	0.05	0.05	0.006	0.03	0.05	0.01	0.50
493.0	2.94	2.21	0.153	0.66	3.85	0.07	1.59
494.0	2.09	1.88	0.109	0.58	3.07	0.06	1.40
495.0	1.86	1.74	0.097	0.62	3.44	0.06	1.40

Note Sample No—depth in drillhole ZF-11, m

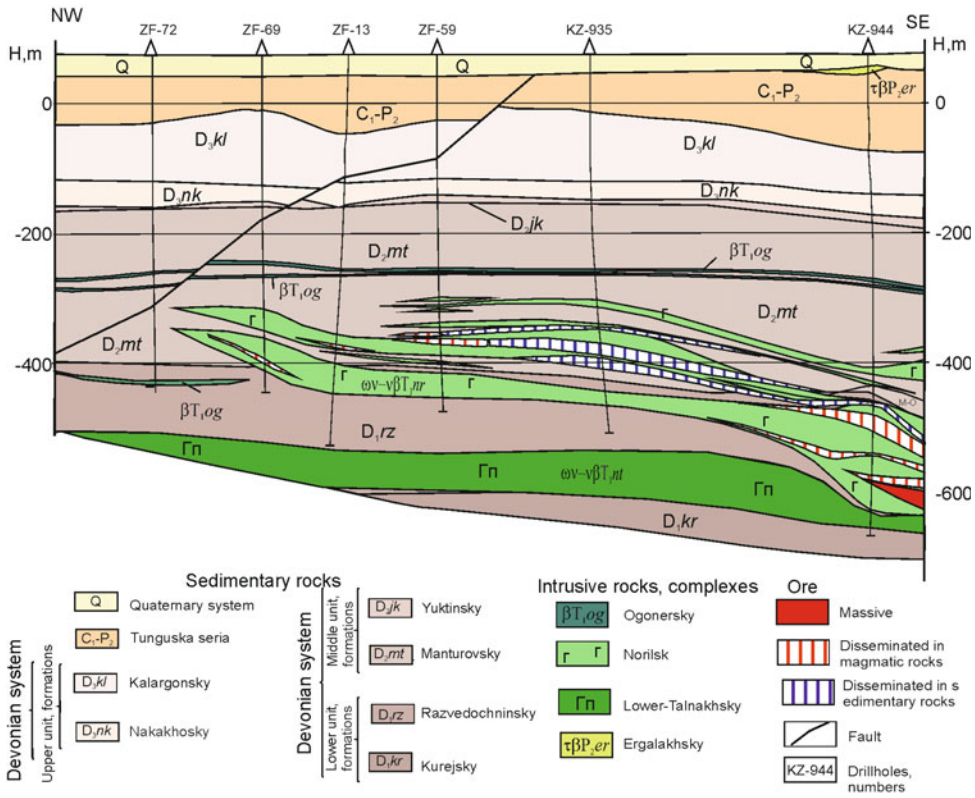

Fig. 14 Cross-section of the western part of the Oktyabr'sky deposit (line II-II in Fig. 12, after Ltd. Norilskgeology data, with changes)

Table 6 Average mean compositions of the ore-bearing intrusions in the Norilsk area

Oxide	1	2	3	4	5	6
SiO_2	48.20	46.19	47.71	47.2	49.18	47.29
TiO_2	0.85	0.74	0.91	0.61	0.90	1.67
Al_2O_3	15.30	15.53	13.30	16.7	14.95	14.95
FeO	12.32	13.44	12.66	9.91	10.92	13.73
MnO	0.19	0.15	0.18	0.16	0.21	0.21
MgO	9.98	11.36	13.42	11.64	11.66	7.50
CaO	10.43	10.33	9.47	11.40	9.64	11.52
Na_2O	1.86	1.32	1.79	1.85	1.91	2.11
K_2O	0.20	0.69	0.45	0.46	0.50	0.89
P_2O_5	0.10	0.25	0.10	0.07	0.12	0.12
Number of drillholes	29	54	1	1	1	

Note Intrusions, data after 1-Norilsk 1 [6], 2—Talnakh [44], 3—Mikchangdinsky [48], 4—Chernogorsky [46], 5—Vologochansky [45], 6—model melt [49]

Table 7 Composition of homogenized melt inclusions in pyroxenes, the Maslovsky deposit

SiO_2	TiO_2	Al_2O_3	FeO	MnO	MgO	CaO	Na_2O	K_2O	P_2O_5	S	Cl	H_2O	Mg# Cpx
49.5	1.78	12.68	14.08	0.26	5.732	10.23	3.04	0.74	0.19	0.12	0.19	0.43	76.1
49.76	1.78	12.21	15.25	0.26	5.541	10.27	2.95	0.67	0.21	0.14	0.2	–	74.6
47.98	1.61	10.61	16	0.26	7.18	12.14	1.43	0.49	0.18	0.06	0.12	–	74.6
50.26	1.64	12.75	14.2	0.24	5.468	10.13	2.89	0.66	0.19	0.1	0.13	0.33	75.3

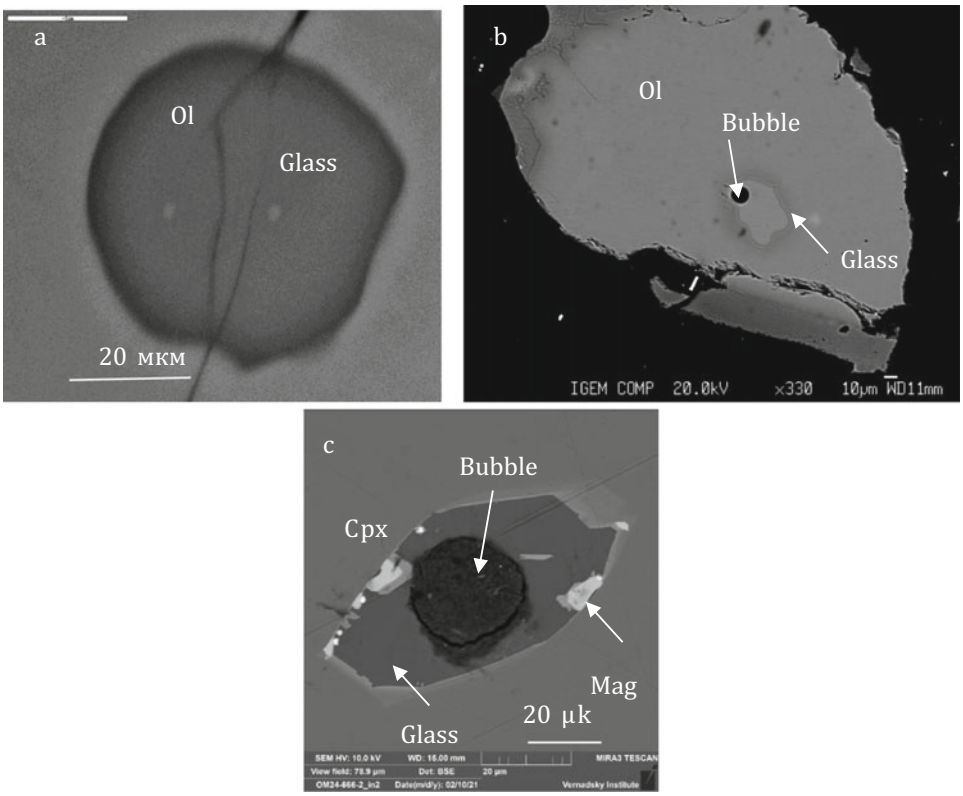

Fig. 15 BSE images of melt inclusions in olivine (homogenized at 1230 °C, **a**, **b**) and pyroxene **c**

the Ergalakh intrusions containing 3–3.5 wt.% TiO_2. The rocks attributed to this new Turumakitsky Complex differ in strontium and neodymium isotopes from the other rocks [55] (Fig. 18). According to studies of the U-Pb system in zircons and baddeleyites from these rocks, they are younger than rocks of all complexes mentioned above [54]. We established the second new intrusive complex 150 km south of Norilsk in the Kulyumber river valley. This complex has no analogues among known intrusive rocks of the province, and we called it the Kulyumbinsky Intrusive Complex, represented by olivine gabbro-dolerites. The concentrations of major elements are close to their concentrations in gabbro-dolerites of the Katangsky Complex. But the distribution of trace elements is fundamentally different from all complexes due to the low concentrations of heavy rare earths, indicating the presence of garnet in the source. The isotopic data also testify to the differences of the discovered rocks from other previously known intrusive rocks [55].

The large volume of analytical data obtained during last years (815 XRF+ICP analyses, 96 Sr, Nd, and Pb analyses) allowed us to compare the igneous rocks of the key areas of the Siberian Trap Province. Figure 19 shows the main patterns (normalized to primitive mantle after [56]) of intrusive rocks from the Norilsk area (Fig. 19a) and from the southern part of the province where only Katangsky intrusions occur (Fig. 19b). The latter is rather uniform in the southern and eastern parts of the province, while in the north, intrusions differ significantly in morphology and composition.

Geochemistry of the volcanic rocks from these areas (Fig. 20) proves that magmatic rocks of the Arctic Zone (i.e., Norilsk area) are characterized by the maximum diversity in comparison with the rocks from the southern part of the province. The greatest variations in the composition of volcanic rocks are typical of the Taimyr peninsula and Maymecha-Kotuy areas that were demonstrated earlier [57]. There are rocks with typical crustal marks (negative Ta-Nb,

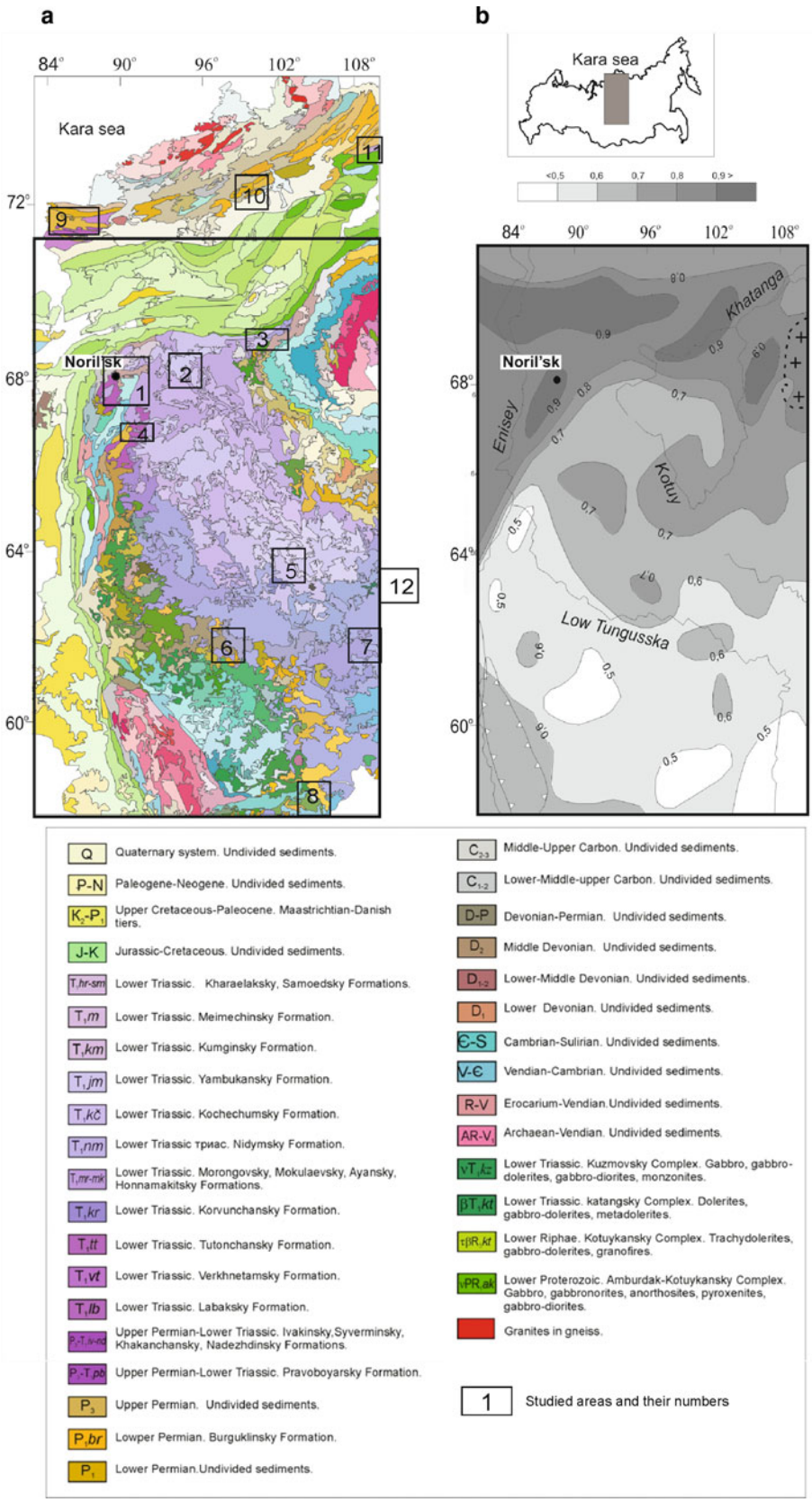

Fig. 16 Geological map of Eastern Siberia **a** and schema of Coefficient of crust basement (**b**, after [55]). Studied areas: 1-Norilsk, 2-Putorana, 3-Maymecha-Kotuy, 4–8, 12- river valleys: 4-Kulyumber, 5-Lower Tunguska, 6–7—Podkamennaya Tunguska, 8-Angara, 12-Viluy; 9–11-Taimyr peninsula: 9-western, 10-central, 11-eastern

Fig. 17 Gabbro-dolerite sill of the Katangsky complex, Lower Tunguska River

positive Pb anomaly; high La/Sm and low Gd/Yb ratio, $^{87}Sr/^{86}Sr$=0.705–0.710, ε_{Nd} =−7+1) and more rare products of mantle magmas without Ta-Nb and Pb anomalies with high Gd/Yb ratio indicating great depths of magma generations.

To interpret these results, we used geophysical data published in recent times with the aid of new methods of interpretation developed by A.S. Dolgal et co-author [58, 59]. Fig. 16 shows the geological structure of the Siberian Trap Province (a) and the map of the coefficient of the crustal basement (b) compiled by Erinchek [60]. This coefficient was calculated based on gravimetric and magnetic data carried out along the profiles where basic and ultrabasic rocks had been distinguished. The volume of these rocks to the volume of the whole crust was used as a coefficient of the basement of the crust. After that, the results were transformed into a map of the coefficient isolines. Despite some shortcomings, in our opinion, this schematic map reflects the deep structure of Eastern Siberia quite well. It demonstrates a high proportion of ultrabasic-basic rocks in its northern part compared to the southern part of the province. The ultrabasic-basic intrusions occur within the largest paleoritft structure, the Yenisei-Khatanga Trough, and its flanking smaller structures, i.e., in the Norilsk-Igarka paleorift zone.

5 Discussion

5.1 Testing of the Existing Models of the Norilsk Deposits

There are two main scenarios of the origin of the Norilsk deposits (Fig. 21). According to the first one, sulfides were formed in the intermediate chamber [6, 8, 13, 14] or in mantle [17, 19] and then were directly transported by magma into the modern chamber. In this model, intrusions are blind bodies representing the peripheral parts of a closed magmatic system. According to the second scenario, intrusions are horizontal parts of a single magmatic system, representing a way for magma from its source to the surface. In this case, sulfides crystallized directly in the modern intrusive chambers *in situ* due to a long flowing magma and its interaction with host anhydrite-bearing rocks. This model suggests that ore were formed in an open magmatic system because intrusions connect with channels and lavas [20–22, 60]. A combination of these models assumes that an open magmatic system occurred in the lower modern chamber where sulfides were formed in the channel due to the assimilation of host rocks as well [61]. Thus, intrusions have no link with basalts.

The most widespread is the second model of the origin of the Norilsk deposits, i.e., ore formation occurred in an open magmatic system where intrusions connected with depleted in Cu Nadezhdinsky lavas throw peripheral sills (Fig. 22a) [10]. Later this model was transformed into a two-step model (Fig. 22b). Very similar trace elements' compositions of volcanic rocks of the Mokulaevsky formation and ore-bearing intrusions led to suggestions on their connection [60]. However, the structure of the peripheral parts of the deposits, which was demonstrated (Fig. 14) earlier [43], rejects suggestions on direct links of ore-bearing intrusions with any volcanic rocks. Therefore, the model of an open magmatic system is untenable.

The second important aspect of this model is the assimilation of host rocks (mainly containing anhydrite) by

Table 8 Chemical composition of gabbro-dolerites from the Katangsky complex

No	NT-82	NT-83	NT-84	NT-86	NT-88	NT-90
SiO_2	49.78	48.88	47.88	48.8	48.57	48.97
TiO_2	1.7	1.38	1.6	1.96	1.55	1.86
Al_2O_3	14.13	15.26	14.45	14.59	14.86	15.11
Fe_2O_3	14.5	12.96	14.63	15.17	13.9	13.68
MnO	0.21	0.19	0.24	0.23	0.20	0.18
MgO	4.92	7.14	6.86	4.62	6.24	4.53
CaO	10.54	10.5	10.62	9.96	10.45	10.55
Na_2O	2.62	2.58	2.39	2.62	2.52	2.79
K_2O	0.55	0.46	0.53	1	0.52	0.59
P_2O_5	0.17	0.13	0.16	0.22	0.16	0.21
LOI	0.77	0.32	0.47	0.62	0.82	1.37
Li	7.17	5.96	16.04	21.65	9.77	9.07
Be	0.69	0.55	0.56	0.77	1.02	1.31
Sc	38.7	34.7	38.7	36.2	37.3	38.9
V	332	271	310	342	307	350
Cr	29	170	149	124	136	146
Co	40	46	48	40	48	41
Ni	36	110	96	45	73	47
Cu	174	125	189	225	167	251
Zn	110	102	157	162	266	110
Ga	21	20	21	23	20	22
Rb	14.3	12.4	14.1	29.8	12.8	14.0
Sr	227	208	187	309	201	212
Y	32	26	31	38	27	36
Zr	113	95	105	138	55	126
Nb	5.53	4.48	4.71	6.86	7.49	7.18
Ba	174	143	199	328	256	181
La	11.8	8.9	8.2	14.5	9.3	10.9
Ce	27.2	20.7	19.8	33.9	22.2	26.2
Pr	3.45	2.76	2.75	4.40	3.07	3.64
Nd	16.5	13.3	13.6	20.8	14.4	17.2
Sm	4.44	3.73	4.02	5.47	3.89	4.89
Eu	1.48	1.32	1.48	1.94	1.38	1.64
Gd	5.51	4.63	5.38	7.01	4.75	5.79
Tb	0.89	0.76	0.87	1.10	0.83	1.02
Dy	5.76	4.89	5.91	7.03	5.42	6.59
Ho	1.19	1.00	1.20	1.43	1.11	1.41
Er	3.54	3.01	3.57	4.32	3.10	4.01
Tm	0.50	0.42	0.50	0.58	0.45	0.59
Yb	3.45	2.85	3.37	3.94	3.00	3.73
Lu	0.53	0.43	0.49	0.59	0.44	0.53
Hf	3.18	2.58	2.83	3.85	1.43	3.37
Ta	0.49	0.32	0.30	0.46	1.38	1.18
Pb	2.25	3.02	3.96	4.22	2.78	3.08
Th	1.66	1.28	1.04	2.00	1.03	1.38
U	0.63	0.43	0.34	0.66	0.33	0.55

Note Oxides are given in wt.%, elements in ppm

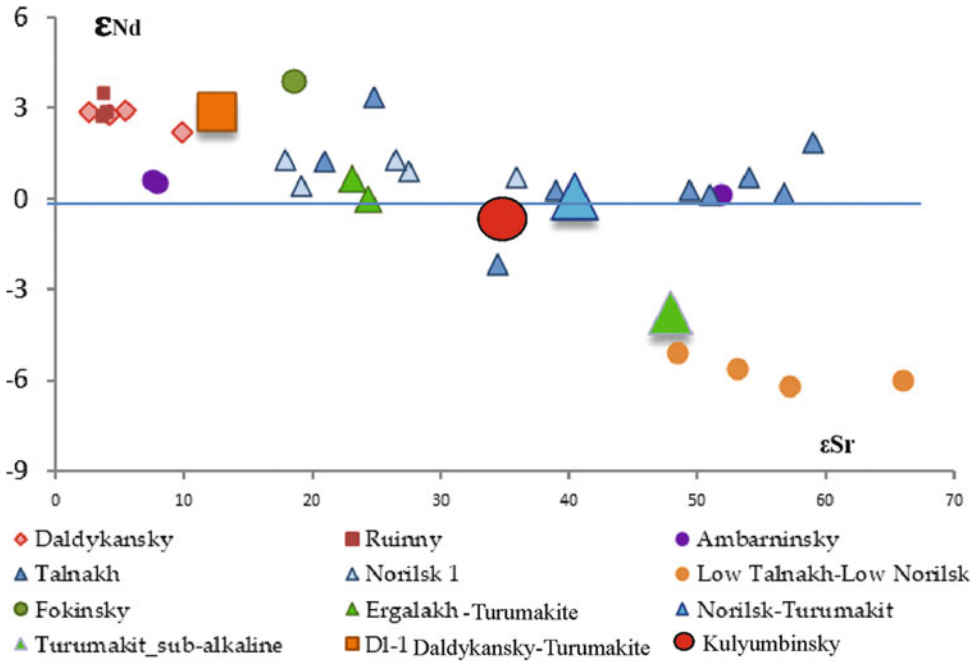

Fig. 18 Diagram ε_{Sr}- ε_{Nd} for intrusive rocks of the Norilsk area. Data in [54, 55]

magmas that formed ore-bearing intrusions. We have considered this question in detail earlier [25, 45, 62], therefore here we only briefly formulate the arguments rejecting anhydrite assimilation as the main process of ore formation: (1) the melting temperature of anhydrite is much higher (1450 °C) [63] than the temperature of the parental magma of the Norilsk intrusions (1200 °C) [49]; (2) supposed decomposition of anhydrite under the action of hot magma does not give significant SO_2 amount, and solubility of S-bearing gases is too small compared to the amount of sulfur in ores; (3) ore-bearing magmas do not intrude pure anhydrite (mentioned in publications stating that anhydrite xenoliths in intrusions are very rare [10, 64]), but intrude anhydrite-bearing rocks, therefore, assimilation should be accompanied with essential change of melt composition which is not registered in nature; (4) isotope composition of anhydrite (Pb, Sr) does not correspond to supposed contaminant [25]; (5) the bulk composition of different intrusions does not depend on the composition of host rocks and does not correlate with ore volume in intrusions [45]; (6) there are quenching zones with glass in rocks, glassy inclusions in rock-forming minerals (Fig. 15), and zoned minerals in upper parts of the intrusions; that evidence quick crystallization of ore-bearing magmas which prevent assimilation; (7) geochemical studies of rocks from the contact zones of several ore-bearing intrusions (Maslovsky, Talnakh, etc.), demonstrate the absence or limited assimilation of host rocks by parental magmas [62]; (8) mass-balance calculations reject supposed assimilation of anhydrite by magmas because the expected huge volume of calcium in rocks is absent [45].

The combined model of open and closed magmatic systems [61, 65], which assumes deep (3–5 km) assimilation of anhydrite and carbonates by magmas on their way to chambers, could be checked. These deep zones are well exposed in the western and southern regions of the Tunguska syneclise, where gabbro-dolerite sills intruded into various sedimentary rocks (carbonate-terrigenous with anhydrite and coal from the Cambrian to Late Permian). Assumed formation of sulfides at the contacts of intrusions with host rocks is completely absent.

The open system model rejects intra-chamber sulfide gravity and suggests sulfide transport to the surface due to gas bubbles [23, 24]. Gravitational accumulation of sulfides is well documented at the Norilsk deposits, especially within thick picritic horizons with disseminated ores. Two examples of this gravitation are shown in Fig. 23, where gradual enrichment of sulfide and their segregation at the bottom of the horizons are observed (drillholes RT-30 and RT-107). In addition, the size of sulfide droplets is often much larger than the size of bubbles (Fig. 24). The concentrations of volatile components in ore-bearing magmas in the Norilsk region are low (Sect. 4.2), so the assumed mechanism can act only in areas where basaltic melts contain high concentrations of water, i.e., in subduction zones. This was also noted in [66]. However, all Cu-Ni deposits, especially large and unique ones, are localized within ancient platforms and not in subduction zones. Thus, the proposed mechanism of the Norilsk deposits formation has no geological substantiation.

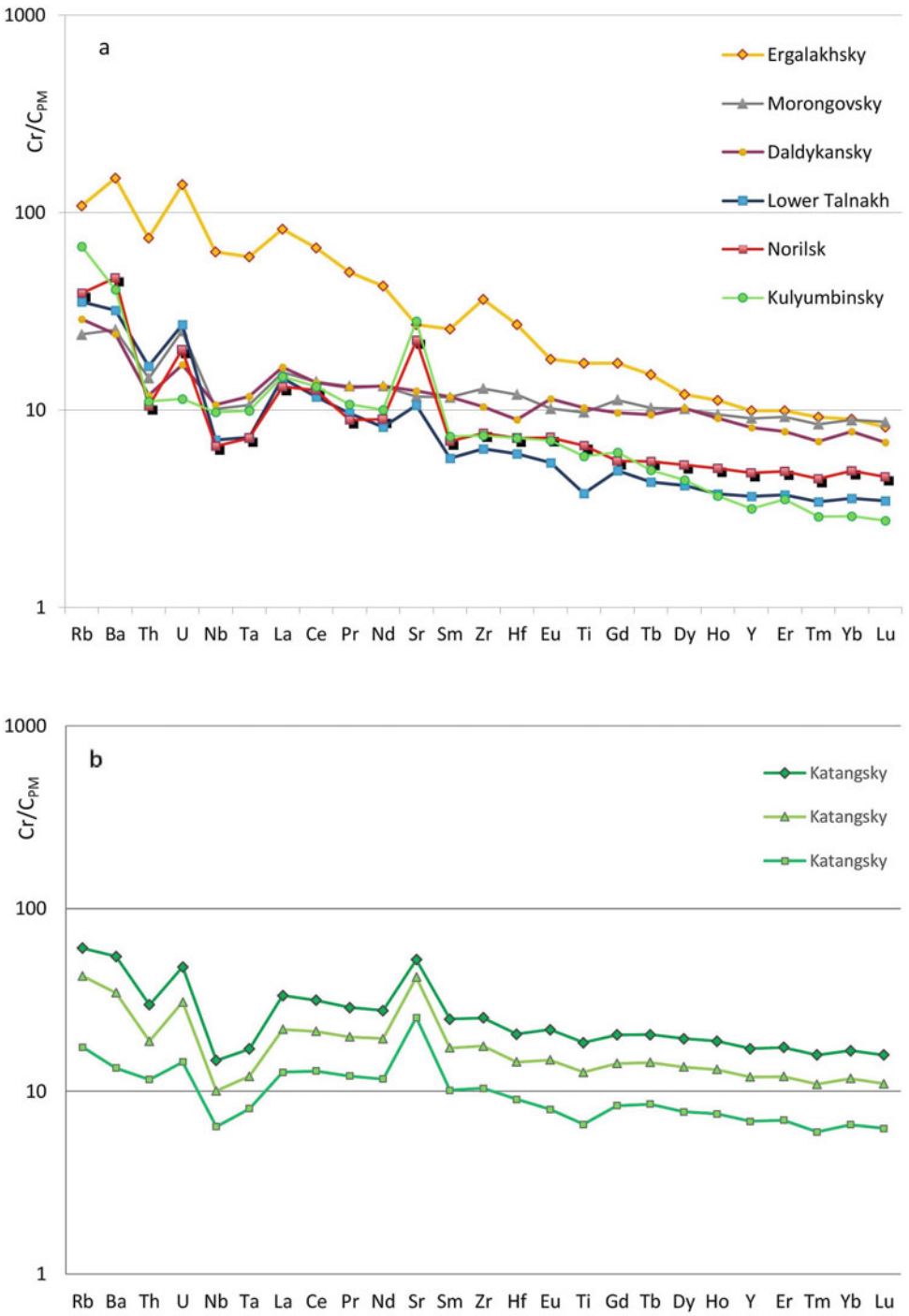

Fig. 19 Spider-diagrams for intrusive rocks in the Norilsk area **a** and in the Lower Tunguska river valley **b**. Normalized to primitive mantle after [59]. Data in Table 8 and after [25, 38, 45]

For many years, the formation of deposits in conditions of a closed magmatic system was assumed from special melts enriched in magnesium, volatile, and ore components [6, 67–69]; the same was suggested for the open system as well [70]. However, this assumption was not supported by data on volatile components in melt and fluid inclusions. Their concentrations in the parental magmas are low and correspond to the concentrations in typical within plate basalts [51] (Fig. 26).

5.2 A new Approach to the Deposits' Origin

The testing of the most widespread models of the formation of the Norilsk deposits has shown that none of them fully corresponds to the geological data. Obviosy, the ores were formed in a closed magmatic system (paragraph 4.1, [43]), but from ordinary tholeiitic magmas of slightly increased MgO content with low concentrations of volatile components (paragraph 4.2, [49]). Ore-bearing massifs of the Norilsk

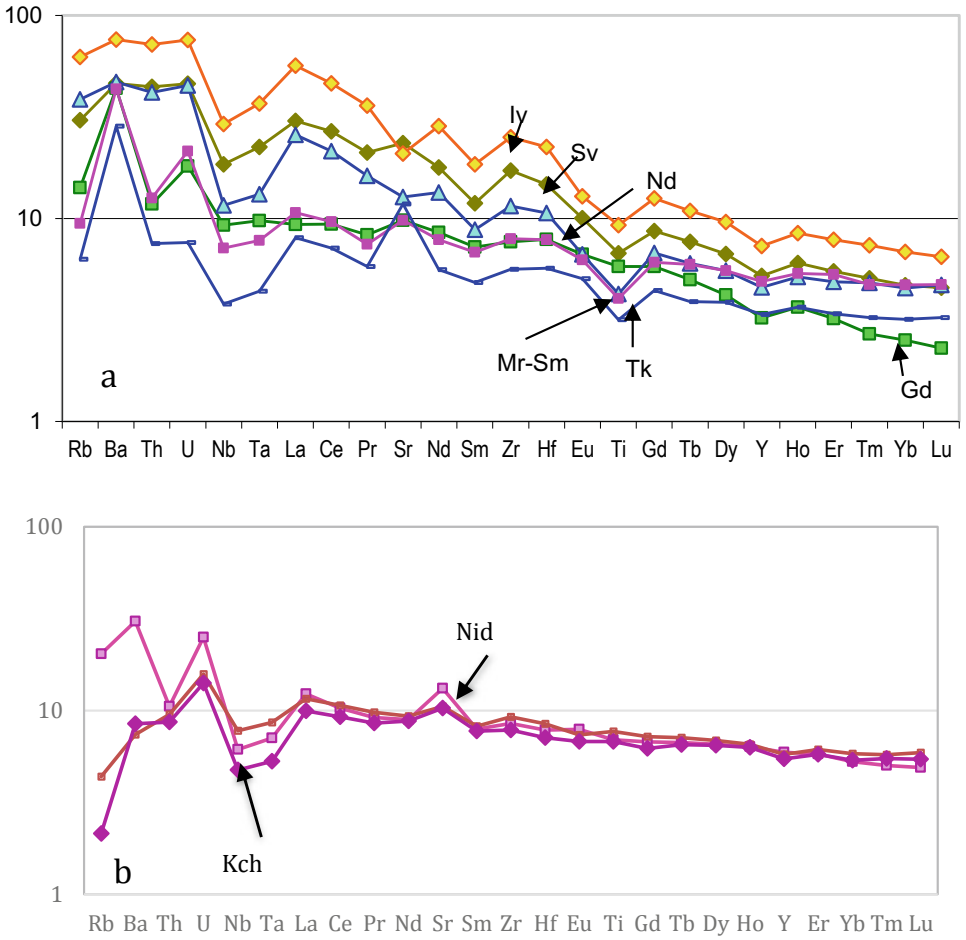

Fig. 20 Spider-diagrams of volcanic rocks in the Norilsk area **a** and Lower Tunguska river valley **b**. Data in [25]. Formations: Iv—Ivakinsky, Sv—Syverminsky, Gd—Gudchikhinsky, Tk—Tuklonsky, Nd—Nadezhdinsky, Mr-Sm—Morongovsky-Samoedsky, Nid—Nidymsky, Kch—Kochechumsky

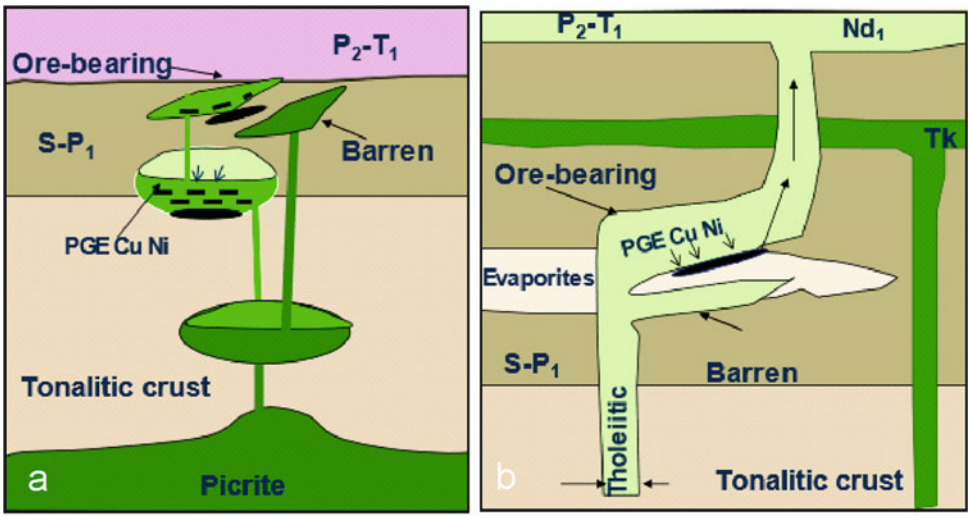

Fig. 21 Main models of the Norilsk deposits: **a**-closed magmatic system [8], **b**—open magmatic system [30]

complex have practically identical composition irrespective of the volume and composition of related ores [45, 46], which indicates the absence of the essential assimilation and its supposed important role in ore formation. Hence, what is the reason for elevated sulfide concentrations in magmas formed ore-bearing intrusions in NW Siberian province?

Undoubtedly, the uniqueness of the Norilsk region is largely determined by both its specific tectonic structure and

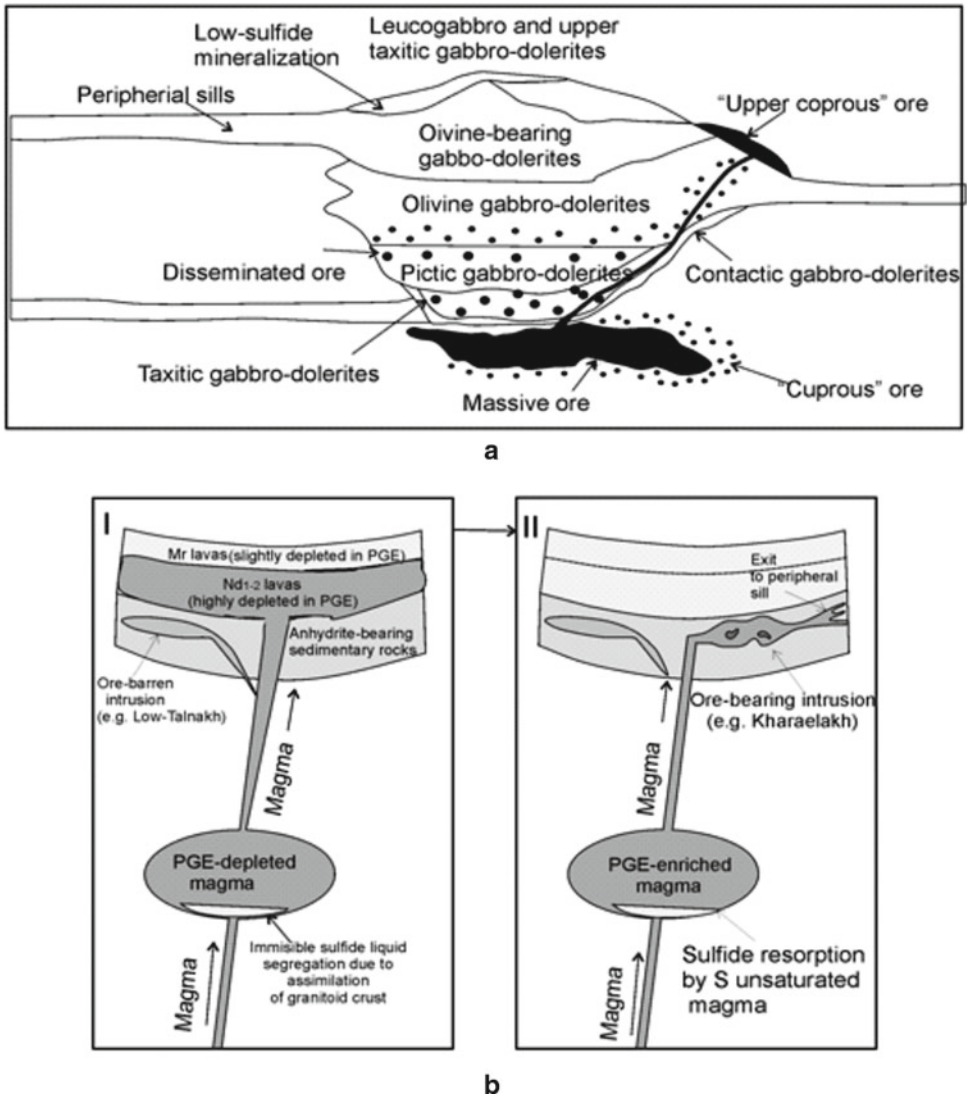

Fig. 22 Models of ore origin in open systems (after: **a** [10], **b** [22])

magmatic activity. Therefore, the reconstruction of tectonic-magmatic evolution in space and time in this area is the most important point in the deposits' origin. To understand the main features of this region, it is necessary to compare it with the other parts of the province where deposits are absent (Tunguska syneclise; Lower Tunguska, Podkamennaya Tunguska, Viluy, Angara river valleys).

The geophysical data and compositions of igneous rocks demonstrate that PGE-Cu-Ni deposits in Eastern Siberia (Norilsk and Taimyr) occur in tectonic zones with products of different magmas and are absent outside of them. These zones are characterized by active long-term magmatism. The main tectonic element is the Yenisey-Khatanga trough, which is flanked by smaller structures, including the Norilsk-Igarka paleorift zone (Fig. 20). Earlier it was suggested that the coupling of the deposits with these zones was caused by deep faults, penetrating the mantle and bringing mantle magmas to the upper crust [71, 72]. Later crustal characteristics of ore-bearing melts were established [29, 30], and therefore they could not derivate directly from a mantle source (Fig. 25).

New data on the geochemistry of rocks in the northern areas of the province shows the occurrence of magmas of different compositions at different depths of the lithosphere and the crust in contrast to southern areas, resulting from a long-term magmatic activity. New intrusive complexes detected by us confirm this conclusion. Products of these magmas were established both in Taimyr and in the Siberian platform along the North-Kharaelakh fault. Thus, we believe that a consistent series of geological processes led to the gradual accumulation of sulfides in the lower crust. Later the sulfides were carried to the surface by trap magmas, leading to the formation of the PGE-Cu-Ni deposits. Therefore, trap magmatism alone is not enough for the deposits' formation, as it must be combined with other processes. Large deposits could be discovered in areas with complex structures within

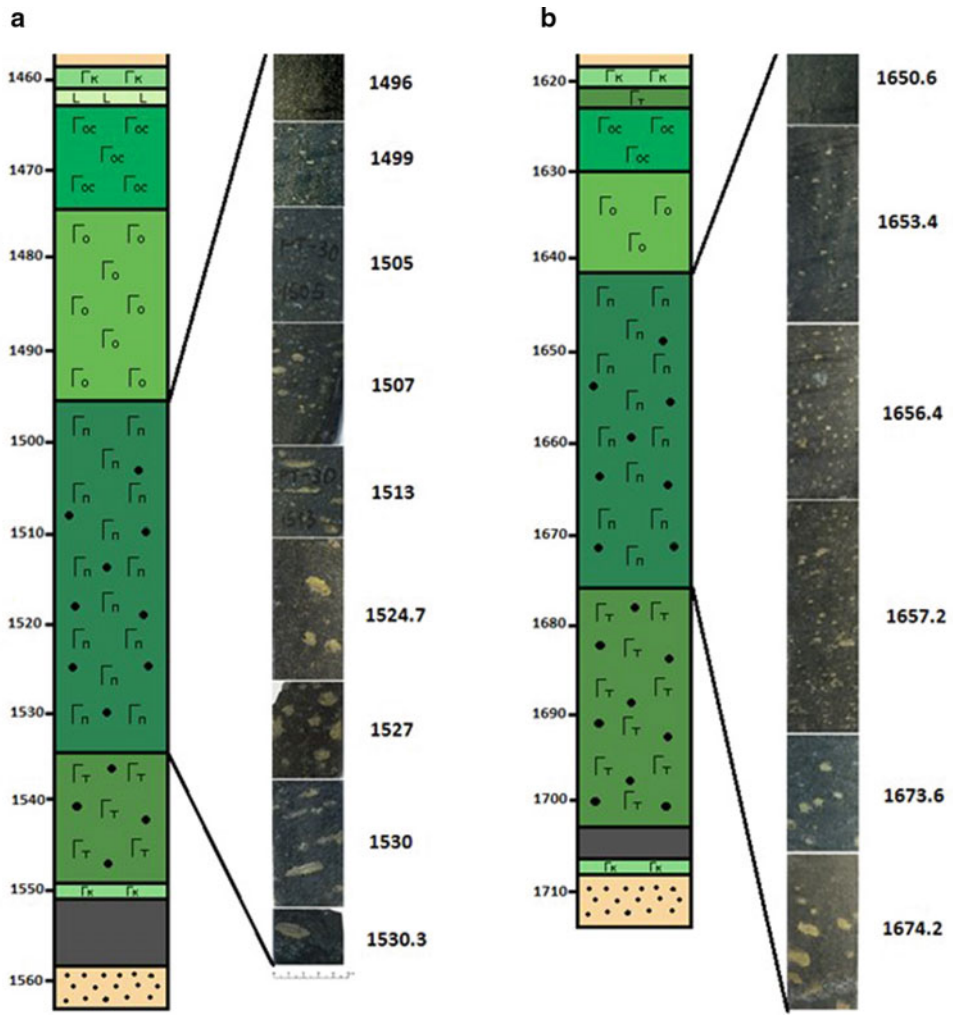

Fig. 23 Inner structure of the picritic gabbro-dolerite horizons in drillholes RT-30 **a** and RT-107 **b** with sulfide accumulation in their bottoms

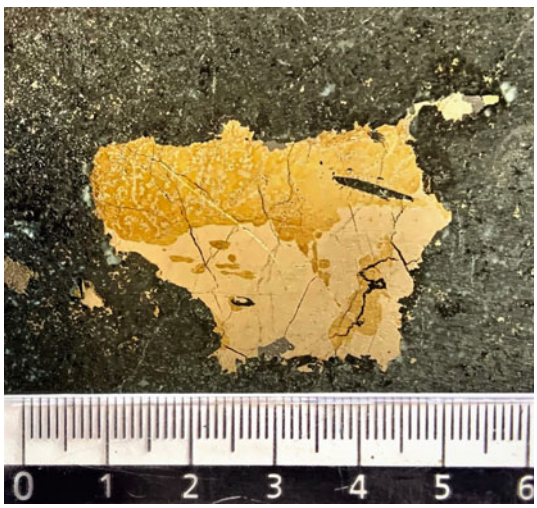

Fig. 24 Photo of disseminated ore of the Oktyabr'sky deposit

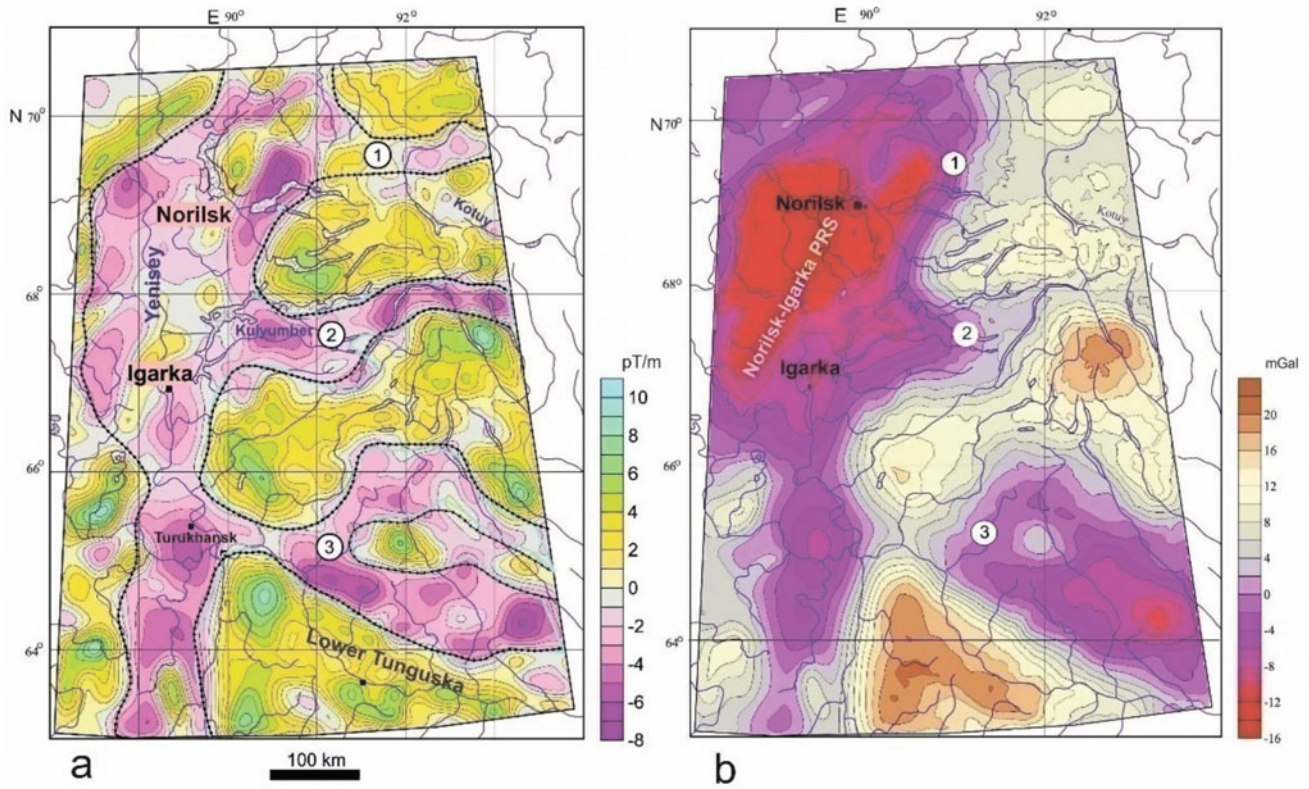

Fig. 25 The Noril'sk-Igarka paleorift on maps of the first vertical derivative of the anomalous magnetic field at an altitude of 20 km **a** and iso-anomalous of pseudo-gravitation field **b** The numbers refer to the branch of the paleo-rift system (PRS): 1—Bolsheavamsky; 2—Dyupkunsky; and 3—Lower Tunguska. After [61, 62]

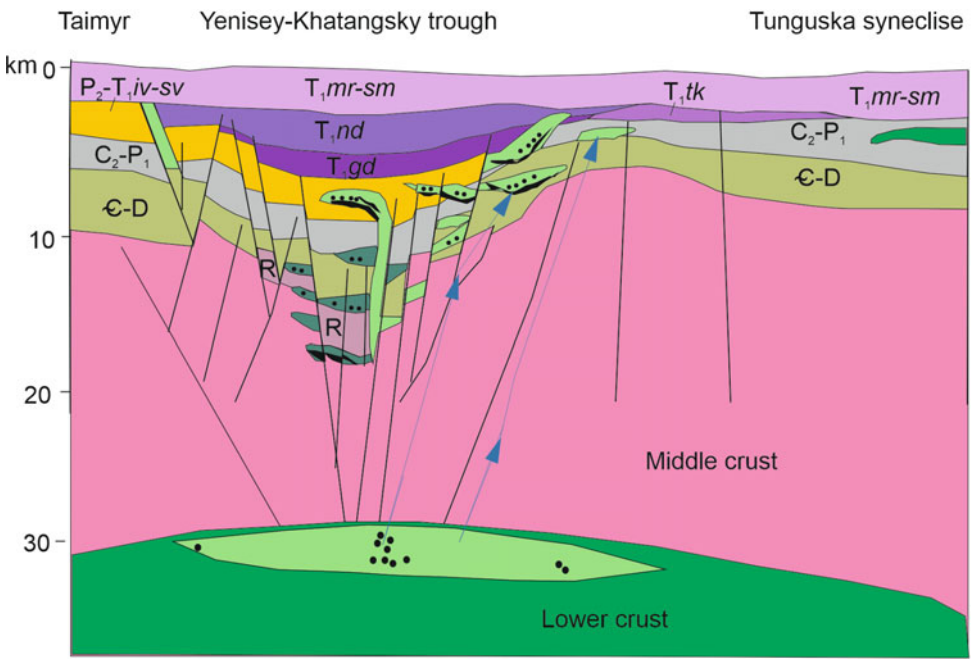

Fig. 26 Shema of the Norilsk deposits formation. After [48]

trap provinces around the world, but they could not be found there due to the stochastic nature of the ore-forming process.

The currently dominant studies of ore deposits using only local methods [73–77] provide information on the processes of crystallization of silicate and sulfide melts and their subsequent transformations in intra-chamber conditions that are not enough for our understanding of deposits genesis. Further progress in the theory of magmatic ore formation in the Arctic zone of Eastern Siberia should be based on knowledge of the geological evolution of this territory during the Late Permian-Early Triassic period.

Acknowledgements Author thanks geologists of the Ltd. Norilskgeology V. V. Kurgin, V. N. Mikhailov, I. A. Matveev, K. V. Shishaev, V. A. Teteryuk, Yu. B. Burmistrov, V. Yu. Van-Chan, L. I. Trofimova, I. N. Tushentsova, V. A. Rad'ko, G. I. Legezin, T. A. Taraskina, E. V. Kovaleva and many other people for their assistance in the field trips. This work was largely realized due to the help of Ya. V. Bychkova, B. V. Belyatsky, A. A. Ariskin, I. V. Kubrakova, O. A. Tutunnik, D. V. Kuzmin, V. A. Turkov, A. A. Konyshev, S. P. Krasheninnikov. My special thanks to B. I. Gongalsky and N. M. Svirskaya who helped in this work for all the years. Invaluable assistance was provided by A. V. Sobolev, who supported these studies for many years and provided an opportunity to conduct analytical research in the laboratories of Max-Plank Institute of Chemistry (Mainz, Germany) as part of the Wolfgang Paul Project. This work was financially supported by Russian Science Foundation (Project 22-27-00387).

References

1. Luznicka, P.: Giant ore deposits: a quantitative approach. Glob. Tect. Metall **2**(1,2), 41–63 (1983)
2. Large and extra large deposits. In: Rundkvist (eds.) V. 1. Global regularities of localization. IGEM, Moscow, 2006
3. Santosh, M., Groves, D.I.: Giant mineral deposits: introduction. Geosci. Front. **7**(3), 1–9 (2016)
4. Luznicka, P.: Giant metallic deposits. Future sources of industrial metals. Springer, Berlin (2010)
5. Schodde, R.: Role of Technology and Innovation for Identifying and Growing Economic Resources // https://minexconsulting.com/role-of-technology-and-innovation-for-identifying-and-growing-economic-resources/. Last accessed Oct 19 2021
6. Godlevsky, M.N.: Traps and Ore-Bearing Intrusions of the Noril'sk District. Gosgeoltekhizdat, Moscow (1959)
7. Vaulin, L.L., Sukhanova, E.N.: The Oktyabr'sky Copper-Nickel Deposit. Razvedka i Okhrana Nedr **4**, 48–52 (1970)
8. Dyuzhikov, O.A., Distler, V.V., Strunin, B.M., B.M. Mkrtychyan, A.K., Sherman, M.L., Sluzhenikin, S.F., Lurye, A.: Geology and Resource Potential of the Noril'sk Ore District. Nauka, Moscow (1988).
9. Genkin, A.D., Gladyshev, G.D., Grokhovskaya, T.L., Distler, V. V., Evstigneeva, T.L., Kovalenker, V.A., Laputina, I.P., Smirnov, Filimonova, A.A.: Sulfide copper–nickel ores of the Noril'sk deposits. Nauka, Moscow (1981)
10. Naldrett, A.J.: Magmatic Sulphide Deposits: Geology, Geochemistry and Exploration. Springer, Berlin/Heidelberg/New York (2004)
11. Bezhanova, M.P., Kyzina, L.V.: The World's Resources and Mining of the Most Important Mineral Deposits. VNIIZarubezhgeologiya, Moscow (2009)
12. Naldrett, A.J.: A history of our understanding of magmatic Ni–Cu sulfide deposits. Can. Mineral. **43**, 2069–2098 (2005)
13. Likhachev, A.P.: The role of leucocratic gabbro in the origin of Noril'sk differentiated intrusions. Izv Akad Nauk SSSR Ser. Geol. **12**, 50–66 (1965)
14. Distler, V.V., Grokhovskaya, T.L., Evstigneeva, T.L., et al.: Petrology of Magmatic Sulfide Ore Formation. Nauka, Moscow (1988)
15. Zotov, I.A.: Transmagmatic Fluids in Magmatism and Ore Formation. Nauka, Moscow (1989)
16. Zolotukhin, V.V.: Basaltic Pegmatoides of the Noril'sk Ore-Bearing Intrusions and the Problem of its Origin. Trudy IGG, Novosibirsk (1997)
17. Likhachev, A.P.: Platinum–Copper–Nickel and Platinum Deposits. Eslan, Moscow (2006)
18. Spiridonov, E.M.: Ore–magmatic systems of the Noril'sk ore field. Russian Geology Geophys. **51**, 1356–1378 (2010)
19. Likhachev, A.P.: Possibility of self-enrichment in heavy sulfur isotope and ore metals of mantle magmas and perspective areas of ore localization in the Norilsk district. Otechestvennaya Geologia **1**, 1–18 (2019)
20. Rad'ko, V.A.: Model of dynamic differentiation of intrusive traps at the northwestern Siberian trap. Geol Geophys **32**(11), 19–27 (1991)
21. Naldrett, A.J.: Model for the Ni–Cu–PGE ores of the Noril'sk region and its application to other areas of flood basalts. Econ. Geol. **87**, 1945–1962 (1992)
22. Li, C.S., Ripley, E.M., Naldrett, A.J.: A new genetic model for the giant Ni–Cu–PGE sulfide deposits associated with the Siberian flood basalts. Econ. Geol. **104**, 291–301 (2009)
23. Barnes, S.J., Mungall, J.E., Mungall, J.E., Le Vaillant, M., Godel, B., Lesher, C.M., Holwell, D., Lightfoot, P.C., Krivolutskaya, N., Wei, B.: Sulfide-silicate textures in magmatic Ni-Cu-PGE sulfide ore deposits: disseminated and net-textured ores. Am. Miner. **102**, 473–506 (2017)
24. Le Vaillant, M., Barnes, S.J., Mungall, J.E., Mungall, E.L.: Role of degassing of the Noril'sk nickel deposits in the Permian-Triassic mass extinction event. PNAS **114**, 2485–2490 (2017)
25. Krivolutskaya, N.A.: Siberian Traps and Pt-Cu-Ni Deposits in the Noril'sk Area. Springer, Cham/Heidelberg/New York/Dordrecht/London (2016)
26. Zolotukhin, V.V., Vasil'ev, Y.R., Dyuzhikov, O.A.: Diversity of traps and initial magmas: a case of the Siberian platform. Nauka, Novosibirsk (1978).
27. Zolotukhin, V.V., Vilensky, A.M., Dyuzhikov, O.A.: Basalts of the Siberian Platform. Nauka, Novosibirsk (1986)
28. Staroseltsev, V.S.: Tectonic of Lava Plateau. Nedra, Moscow (1989)
29. Nesterenko, G.V., Tikhonenkov, P.I., Romashova, T.V.: Basalts of plateau Putorana. Geokhimiya **10**, 1419–1425 (1991)
30. Wooden, J.L., Czamanske, G.K., Bouse, R.M., King, R.J., Siems, D.T.: Isotopic and trace-element constraints on mantle and crustal contributions to Siberian continental flood basalts, Norilsk area Siberia. Geochimica Cosmochimica Acta **57**, 3677–3704 (1993)
31. Lightfoot, P.C., Naldrett, A.J., Gorbachev, N.S., Fedorenko, V.A., Howkesworth, C.J., Hergt, J., Doherty, W.: Chemostratigraphy of Siberian trap lavas, Noril'sk district: implication for the source of flood basalt magmas and their associated Ni-Cu mineralization. In: Proceeding of the Sudbary—Noril'sk Symposium, spec **5**(22), 283–312, Geological Survey, Ontario, (1994)

32. Ryabov, V.V., Shevko, A.Ya., Gora, M.P.: Trap magmatism and ore formation in the Siberian Noril'sk region, **1**(2). Springer, Heidelberg/New York/Dordrecht/London (2014)
33. Geological map of the Norilsk ore district, scale 1:200000 In: Sherman, M.L. (ed) Committee of Russian Federation on geology and use of mineral resources, St. Petersburg (1994).
34. Dodin, D.A., Batuev, B.N., Mitenkov, G.A.: Atlas of the Rocks and Ores of the Noril'sk Copper–Nickel Deposits. Nedra, Leningrad (1971)
35. Sluzhenikin, S.F., Distler, V.V., Dyuzhikov, O.A., Kravtsov, V.F., Kunilov, V.E., Laputina, I.P., Turovtsev, D.M.: Low sulphide platinum mineralization of the Noril'sk differentiated intrusions. Geol. Ore Deposits **36**, 195–217 (1994)
36. Sluzhenikin, S.F., Yudovsksya, M.A., Barnes, S.J., Abramova, V.D., Le Vaillant M., Petrenko, D.B., Grigor'eva A.V., Brovchenlo V.D.: Low-sulfide platinum group element ores of the Norilsk-Talnakh Camp. Econ. Geology **115**(6), 1267–1303 (2020)
37. Karandashev, V.K., Khvostikov, V.A., Nosenko, S.V., Burmii, Z.: Stable highly enriched isotopes in routine analyses of rocks, soils, grounds, and sediments by ICP-MS. Inorg Mater **53**, 1432–1441 (2017)
38. Krivolutskaya N., Tolstykh N., Kedrovskaya T., Naumov K., Kubrakova I., Tutunnik O., Gongalsky B., Kovalchuk E., Magazina L, Bychkova Ya., Yakushev A.: World-class PGE-Cu-Ni Talnakh Deposit: New Data on the Structure and Unique Mineralization of the South-Western branch . minerals 2018-03-22 (2018).
39. Sereda, E., Belyatsky, B., Krivolutskaya, N.: Geochemistry and geochronology of Southern Norilsk intrusions. SW Siberian Traps. Minerals **10**, 165 (2020)
40. Naldrett, A.J., Lightfoot, P.C.: Ni-Cu-PGE deposits of the Noril'sk region, Siberia: their formation in conduits for flood basalt volcanism. Short Course Notes. Geological association of Canada, Ontario **13**, 195–250 (1999)
41. Likhachev, A.P.: Ore-bearing intrusions of the Noril'sk region. In: Proceeding of the Sudbury–Noril'sk Symposium, spec. **5**, pp. 185–201, Ontario Geol Surv (1994)
42. Likhachev, A.P.: The Kharaelakh Intrusion and Its PGM–Cu–Ni Ores. Rudy I Metally **3**, 48–62 (1996)
43. Malitch, K.N., Belousova, E.A., Griffin, W.L., Badanina, I.Y., Pearson, N.J., Presnyakov, S.L., Tuganova, E.V.: Magmatic evolution of the ultramafic–mafic Kharaelakh intrusion (Siberian Craton, Russia): insights from trace-element, U-Pb and Hf-isotope data on zircon. Contrib. Miner. Petrol. **159**, 753–768 (2010)
44. Krivolutskaya, N., Gongalsky, B., Kedrovskaya, T., Kubrakova, I., Tyutyunnik, O., Chikatueva, V., Bychkova, Y., Kovalchuk, E., Yakushev, A., Kononkova, N.: Geology of the Western Flanks of the Oktyabr'skoe deposit, Noril'sk District, Russia: evidence of a closed magmatic system. Mineralium Deposita **54**, 611–630 (2019)
45. Dneprovskaya, M.B., Frenkel', M.Y., Yaroshevsky, A.A.: A quantitative model for layering in the Talnakh intrusion, Noril'sk region. In: Simulating Systems of Ore Mineralization. Nauka, Novosibirsk, 96–106 (1987)
46. Krivolutskaya, N., Makvandi, S., Gongalsky, B., Kubrakova, I., Svirskaya, N.: Chemical characteristics of ore-bearing intrusions and origin of PGE–Cu–Ni mineralization in the Norilsk area. Minerals **11**(8), 819 (2021)
47. Krivolutskaya, N.A., Kuzmin, D.V., Gongalsky, B.I., Kubrakova, I.V., Tyutyunnik, O.A.: Mineralogical-geochemical characteristics of the ore-bearing Chernogorsky intrusion. Norilsk Area. Geochem. Int. **59**(7), 633–666 (2021)
48. Ariskin, A.A., Barmina, G.S.: Simulation of Phase Equilibria at Basalt Magma Crystallization. Nauka, Moscow (2000)
49. Krivolutskaya, N.A., Ariskin, A.A., Sluzhenikin, S.F., Turovtsev, D.M.: Geochemical thermometry of rocks of the Talnakh intrusion: assessment of the melt composition and the crystallinity of the parental magma. Petrology **9**(5), 389–414 (2001)
50. Krivolutskaya, N.A., Sobolev, A.V.: Magmatic inclusions in olivines from intrusions of the Noril'sk region, Northwestern Siberian platform: evidence for primary melts. Dokl. Earth Sci. **381**(3), 1047–1052 (2001)
51. Krivolutskaya, N.A., Sobolev, A.V., Sluzhenikin, S.F., Pokrovsky, B.G.: Olivine-hosted magmatic inclusions from the Noril'sk intrusions: application to origine of Pt-Cu-Ni deposits (Russia). In: Khanchuk, A.I., Gonevchuk, G.A., Mitrokhin, A.N., Simanenko, L.F., Cook, N.J., Seltmann, R. (eds.) Metallogeny of the Pacific Northwest: Tectonics, Magmatism and Metallogeny of Active Continental Margins. Dalnauka, Vladivostok 296–299 (2004)
52. Naumov, V.B., Dorofeeva, V.A., Girnis, A.V., Yarmolyuk, V.V.: Mean Concentrations of volatile components, major and trace elements in magmatic melts in major geodynamic environments on earth. I. Mafic Melts. Geochem. Int. **55**(7), 629–653 (2017)
53. Erinchek, Y.M., Milshtein, E.D., Kolesnik, N.N.: Deep structure and geodynamic of the Siberia platform kimberlite area. Reg. Geol. Metall. **10**, 209–228 (2000)
54. Zolotukhin, V.V., Vasil'ev, Y.: Problems of Platform Magmatism: Examples from the Siberian platform. Nauka, Novosibirsk, (1986)
55. Sereda, E., Belyatsky, B., Krivolutskaya, N.: Geochemistry and geochronology of southern Norilsk intrusions, SW Siberian Traps. Minerals **10**(2), 00165 (2020)
56. Krivolutskaya, N., Belyatsky, B., Gongalsky, B., Dolgal, A., Lapkovsky, A., Bayanova, T.: Petrographical and geochemical characteristics of magmatic rocks in the northwestern Siberian traps province, Kulyumber River Valley. Part I: rocks of the Kulyumber sites. Minerals **10**(415) (2020)
57. Hofmann, A.W.: Chemical differentiation of the earth: the relationship between mantle, continental crust and oceanic crust. Earth Planet Sci. Lett. **90**, 297–314 (1988)
58. Krivolutskaya, N., Latyshev, A., Dolgal, A., Gongalsky, B., Makareva, E., Makarev, A., Svirskaya, N., Bychkova, Ya., Yakushev, A., Asavin, A.: Unique PGE–Cu–Ni Noril'sk deposits, Siberian trap province: magmatic and tectonic factors in their origin. Minerals **9**(1) 66 (2019).
59. Dolgal, A.S.: Realization of V.N. Strakhov ideas in interpretation of geopotential fields. In: Academician V.N. Strakhov as Geophysics and Mathematic. Nauka, Moscow, 55–78 (2012)
60. Dolgal, A.S.: New mathematical forms of presenting the results of quantitative interpretation of geopotential fields. Gornoe Echo. **82** (1), 83–90 (2021)
61. Rad'ko, V.A.: Facies of intrusive and effusive magmatism of the Norilsk region. VSEGEI, St. Petersburg (2016)
62. Krivolutskaya, N.A., Plechova, A.A., Kostitsyn, Y.A., Belyatsky, B.V., Roshchina, I.A., Svirskaya, N.M., Kononkova, N.N.: Geochemical aspects of the assimilation of host rocks by basaltic magmas during the formation of the Noril'sk Cu–Ni ores. Petrology **22**, 110–128 (2014)
63. Yao, Z., Mungall, J.E.: Linking the Siberian flood basalts and giant Ni-Cu-PGE sulfide deposits at Norilsk. J. Geophys. Res.: Solid Earth **126**, e2020JB020823
64. Godovikov, A.A.: Mineralogy. Nedra, Moscow (1983)
65. Barnes, S.J., Robertson, J.C.: Time scales and length scales in magma flow pathways and the origin of magmatic Ni-Cu-PGE ore deposits. Geosci. Front. **10**, 78–87 (2019)
66. Yao, Z., Mungall, J.E.: Flotation mechanism of sulphide melt on vapour bubbles in partially molten magmatic systems. Earth Planetary Sci. Lett. **542**, 116298 (2020)
67. Yao, Z., Mungall J.E., Qin K.: A Preliminary model for the migration of sulfide droplets in a magmatic conduit and the

significance of volatiles. J. Petrology, 1–35. https://doi.org/10.1093/petrology/egaa0052020
68. Aplonov, V.S.: Fluid regime and platinum resource potential of differentiated basic intrusions. In: Platinum of Russia 102–106, Geoinformmark, Moscow (1995)
69. Distler, V.V., Sluzhenikin, S.S., Cabri, L.J., Krivolutskaya, N.A., Turovtsev, D.M., Golovanova, T.I., Oleshkevich, O.I.: Platinum ores of the Noril'sk layered intrusions: magmatic and fluid concentration of noble metals. Geol. Ore Deposits **41**(3), 214–237 (1999)
70. Neruchev, S.S., Prasolov, E.M.: Fluid geochemical model of platinum deposits related to trap magmatism. In: Platinum of Russia 94–101, Geoinformmark, Moscow (1995)
71. Tolstykh, N.D., Krivolutskaya, N.A., Safonova, M.O., Shapovalova, I.Yu., Zhitova L.M., Abersteiner A.: Unique Cu-rich sulphide ores of the Southern-2 orebody in the Talnakh Intrusion, Noril'sk area (Russia): geochemistry, mineralogy and conditions of crystallization. Ore Geol. Rev. **122**, 103525 (2020)
72. Le Barnes, S.J., Vaillant, M., Godel, B., Lesher, C.M.: Droplets and bubbles: solidification of sulphide-rich vapour-saturated orthocumulates in the Norilsk-Talnakh Ni–Cu–PGE ore-bearing Intrusions. J. Petrol. **60**(2), 269–300 (2019)
73. Malitch, N.S. (ed.): Geological Structure and Regularities of Mineral Deposits' Location, vol. 4. Siberian Platform. VSEGEI, Leningrad (1987)
74. Spiridonov, E.M., Belyakov, S.N., Korotaeva, N.N., Egorov, K.V., Ivanova, Y.A., Naumov, D.I., Serova, A.A.: Menshikovite $Pd_3Ni_2As_3$ and associating minerals of sulfide ores at the eastern flank of the oktyabrsky deposit (Norilsk Ore Field). Mosc. Univ. Geol. Bull. **75**(5), 472–480 (2020)
75. Chayka, I.F., Kamenetsky, V.S., Zhitova, L.M., Izokh, A.E., Tolstykh, N.D., Abersteiner, A., Lobastov, B.M., Yakich, T.Y.: Hybrid nature of the platinum group element chromite-rich rocks of the Norilsk 1 intrusion: genetic constraints from Cr spinel and spinel-hosted multiphase inclusions. Econ. Geol. **115**(6), 1321–1342 (2020)
76. Marfin, A.E., Ivanov, A.V., Abramova, V.D., Anziferova, T. N., Radomskaya, T.A., Yakich, T.Y., Bestemianova, K.V.A.: Trace element classification tree for chalcopyrite from oktyabrsk deposit, Norilsk-Talnakh Ore District, Russia: LA-ICPMS Study. Minerals, **10**(8) (2020)
77. Brovchenko, V.D., Sluzhenikin, S.F., Kovalchuk, E.V., Kovrigina, S.V., Abramova, V.D., Marina A. Yudovskay, M.A.: Platinum group element enrichment of natural quenched sulfide solid solutions, the Norilsk 1 deposit, Russia. Econ. Geol. **115**(6), 1343-1361 (2020)

Intrusive COMAGMAT: From Simple Magma Differentiation Models to Complex Algorithms Simulating the Structure of Layered Intrusions

A. A. Ariskin, G. S. Barmina, E. V. Koptev-Dvornikov, K. A. Bychkov, and G. S. Nikolaev

1 Introduction

Problems of differentiation of mafic-to-ultramafic magmas are of key importance in geochemistry and petrology of magmatism. This is due to the scales of occurrence of mafic rocks and the parental role of their basalt-komatiite precursors. Examples of such magmatic evolution are recorded in the compositions of volcanic suites ranging from basalts to dacites and rhyolites, and compound intrusions that include both relatively small sills (oceanic crust, continental traps) and large complexes of layered rocks, such as the Bushveld, Stillwater or Dovyren in South Siberia. The layered intrusions occupy a special place in this diversity and for a long time they have been considered as some kind of natural laboratories, at the example of which differentiation processes can be studied 'in their pure form', postulating closed magma chambers and insignificant role of additional injections. In this case, spatial variations in the composition of rocks and composing minerals can be considered as a genetic record of the direction of magmatic evolution, the corresponding physico-chemical conditions and mechanisms responsible for separation of crystallizing minerals and evolved melts originated in the chamber. Deciphering of such information in the form of specific thermodynamic and dynamic parameters is complicated by multi-factor character of differentiation processes which proceed as a result of interaction of a diversity of heat and mass transfer phenomena in crystallizing magmas and protocumulates systems (convection regimes, crystal settling, compaction of cumulates, infiltration of intercumulus melts, etc.). It is for this reason, when interpreting the structure of intrusive bodies, researchers use different, sometimes mutually exclusive petrogenetic schemes and concepts.

Challenging the problems of the multifactorial evolution involves the creation and investigation of petrological programs based on a mathematically formalized theory of transport phenomena in combination with magma crystallization models. Only in this case hypothetical scenarios presented as pictures with different differentiation schemes turn into real physical and chemical models that allow comparison with natural observations and have predictive capabilities concerning both model rock mineralogy and their geochemical characteristics [1–3]. The task to develop a multiparametric computer model, which could be used for simulating differentiation of basaltic magmas for the first time has been set at the Vernadsky Institute (Moscow, Russia) in the beginning of 70 s, and the first principle results were published in the series of papers of M. Ya. Frenkel with colleagues in 1976–1979 and summarized in the monograph [3], see also list of original articles in [4]. These works considered theoretical aspects of cooling and crystallization in magma chambers, proposed principles of modeling crystal settling/flotation, and studied the effect of thermal and chemical dynamics on the formation of cumulate layers in model intrusions. These studies laid a foundation for further development of the theory of crystallization differentiation, when the ideas about leading mechanisms of intra-chamber differentiation were combined with well calibrated models allowing for simulation of crystallization of basaltic magmas [5, 6], which later were named COMAGMAT [7]. With time, the development of magma crystallization models evolved into an independent area that led to the creation of new petrological techniques and tools used to estimate the composition of parental magmas and their crystallization conditions for volcanic series and cumulate rocks composing layered intrusions [8–10]. Simulation of the spatial structure of intrusive bodies was continued in parallel at the Department of Geochemistry

A. A. Ariskin (✉) · G. S. Barmina · G. S. Nikolaev
Vernadsky Institute of Geochemistry and Analytical Chemistry, Russian Academy of Sciences, 19 Kosygin St, Moscow, 119991, Russia
e-mail: ariskin@rambler.ru

A. A. Ariskin · E. V. Koptev-Dvornikov · K. A. Bychkov
Faculty of Geology, Lomonosov Moscow State University, 1 Leninskie Gory, Moscow, 119992, Russia

V. P. Kolotov and N. S. Bezaeva (eds.), *Advances in Geochemistry, Analytical Chemistry, and Planetary Sciences*,
https://doi.org/10.1007/978-3-031-09883-3_3

(Lomonosov Moscow State University, Russia), mainly for intrusions of the Olanga Group in Northern Karelia [11]. Our review presents the main stages and results of these studies and the latest models, including the relationships between the cooling rate of intrusive bodies and in situ crystallization, as well as the coupled effects of crystal accumulation from convecting magmas and compaction of protocumulate systems.

2 The Most Important Results of 1976–1979

In creating the computational basis for the first generation of 'intrusive models', a virtual 200 m thick basalt sill (assumed to be formed by solidification in the sedimentary rock strata at a depth of 1–2 km) was chosen as the modeling object. Such a choice implied subsequent comparisons with differentiated traps of East Siberia, most of which have a clear geological settings and simple geometry, removing questions concerning the influence of intrusion shape on intrachamber processes. It was postulated that the main condition for chemical differentiation of the magmatic reservoir is the presence of a heterogeneous medium composed of coexisting minerals and melt, compositional differences of which and possibility of their spatial separation serve as a thermodynamic precondition of magma differentiation. This implied the need to develop a model phase diagram approximating the crystallization sequence of three rock-forming minerals—olivine, plagioclase, and pyroxene. As a result, a simplified phase diagram of basalts based on a linearized representation of the *Di-An-Fo* system has been proposed, the main points of which (melting temperatures for cotectic and eutectic compositions) have been adjusted to the specifics of the Siberian magmas (Fig. 1a).

The formulation of the physical basis of the proposed model was reduced to the description of two types of transport phenomena including diffusion of melt components from in situ crystallization fronts and downward transport of specific minerals in the form of Stokes settling of crystals originated near the roof of the magma chamber. It was found that the diffusive transport of melt components is controlled by thermal flows and is fundamentally limited by the heat stock in the cooling chamber [3]. Taking into account low diffusion coefficients of the assumed components and high cooling rate of magmatic bodies, the simple in situ differentiation mechanism turned out to be ineffective. These results were similar to the conclusions of George Hess for the Stillwater intrusion [12]. Thus, the option accounting for diffusion mechanisms in the subsequent calculations of crystallization differentiation was disabled, focusing the main attention on the mechanisms of gravitational transport of crystals.

2.1 The Sedimentation Model

Initially, the mechanism of crystal settling was studied, termed *the* '*Sedimentation Model'*. This allowed for the relative movement of crystals and melt, assuming that mineral individuals of different species (olivine/plagioclase/pyroxene) sink at different velocities. A detailed description of the system of equations that characterize the thermal history of a tabular intrusion taking into account Stokes settling of crystals is given in [3]. The complete problem of cooling and differentiation of the model intrusion was solved using a finite-difference computational scheme, which included separation of a 200 m thick layer of intrusive magma into 100 intervals, in each of which the balance of incoming and outgoing flows of heat and substance was controlled. The time scale was divided into many stages, which allowed us to trace the evolution of temperature and magma composition along the vertical section of the chamber as the model intrusion solidified [4].

An important feature of this algorithm (used later when accounting for convection) was separation of a transition horizon that was adjacent to the upper crystallization front and simulated the existence of a boundary layer where the bulk (i.e., homogeneous, not heterogeneous!) nucleation of the solid minerals to occur. The boundary conditions of the studied models were not usually changed when solving the thermal problem, but the possibility of varying a number of initial parameters, including the composition and degree of crystallization of the parent magma, as well as the crystals settling velocities for different minerals were provided. Calculations were carried out using BESM-6 machines, which provided about 1 million operations per second. As a result, for 15 variants of 'trap magmas' and different crystal settling velocities the spatial configuration of temperature fields in solidifying intrusions at the current moment of time was presented [3, 4]. Crystallization of the latest portions of the residual melt (being the same as that trapped in the uppermost cumulates) corresponded to the complete solidification of the intrusive body; at this stage the solution of the thermal and dynamic problem was terminated. The results of these calculations were the mineral composition of the cumulate layers distributed along the vertical coordinate, which were compared with the structure of natural objects (Fig. 1c).

The most important results of these early works included (1) the formation of a basal horizon showing the olivine enrichment of the model rocks upward from the lower contact into the shrinking magma chamber, (2) olivine depletion during the formation of the main cumulate succession (considered as the 'Layered Series') and (3) a return to the initial olivine content in the system near the upper contact. These features of the model bodies manifested

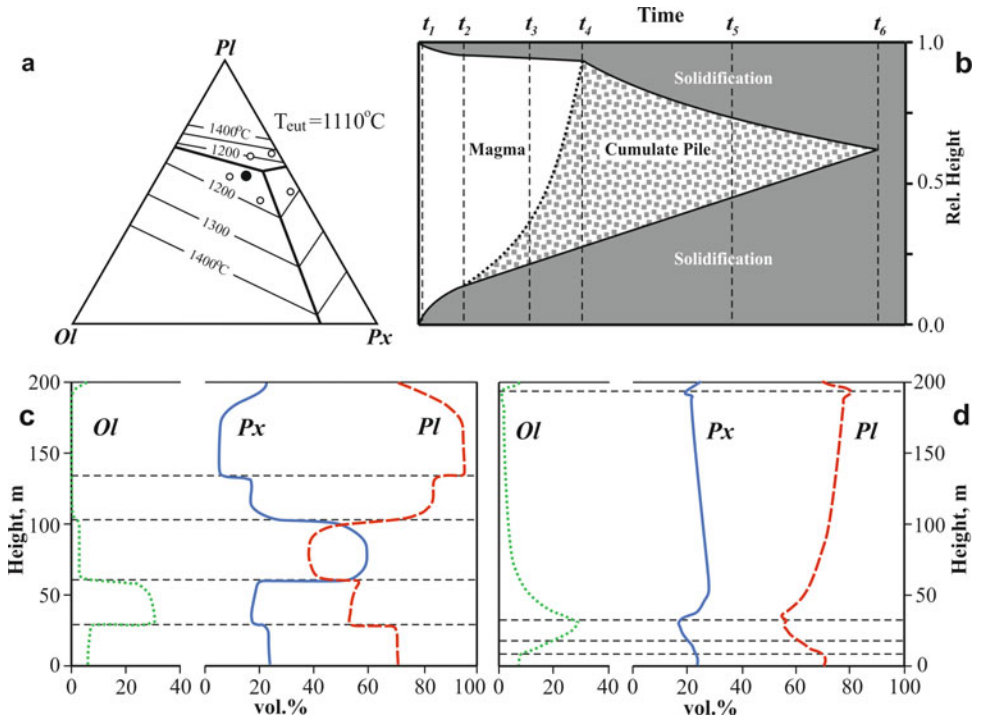

Fig. 1 Characteristics of early works on modeling the structure of sheet-like intrusions, from the review [4] with with modifications. **a** Diagram of the olivine-pyroxene-plagioclase system and compositions of the magmas used in developing the first models of intra-chamber differentiation of basaltic magmas [3] (the filled circle corresponds to the initial magma for the models shown in Fig. 1c and 1d); **b** main stages of cooling and differentiation of intrusive magmas: t_0–t_1—formation of quenching zones; t_1–t_2—counter-motion of the upper and lower crystallization fronts; t_2–t_3–t_4—stopping of the upper front and formation of protocumulate layers; t_4–t_5–t_6—final stage of cooling of the cumulate pile; (**c**–**d**) distribution of minerals along the section of the model intrusion formed by the sedimentation **c** and convection-accumulation **d** mechanisms. The absence of intratelluric minerals is assumed in both variants

themselves as a result of crystal settling at the upper crystallization front and crystal accumulation at the lower solidification front and are consistent with the asymmetry of the so-called the S-shaped profiles, which are characteristic of most layered intrusions and differentiated sills [13–15]. The obvious result was that upward changes in the main types of model cumulates were controlled by the crystallization order of the initial magma. In addition, these calculations revealed that crystal settling is a powerful mechanism of heat transport within crystallizing magma reservoirs.

Subsequent comparisons of these simulations with data on differentiated sills from the Siberian Platform showed that the Sedimentation Model qualitatively reproduced the main features of the structure of the intrusive traps, first of all, the olivine enrichment of the lower horizons, presence of the lower and upper reversible near-contact zones (‘basal and upper reversals’ in the terminology [15]), and enrichment in the lowest temperature eutectoid components of the upper portions of the model bodies, similar to the occurrence of the ‘sandwich horizon’ in the Skaergaard intrusion [16]. However, the model sills exhibited much more contrasting differentiation, which was expressed in abrupt step-like changes in the mineral compositions at the transition from one cumulate horizon to another (Fig. 1c). The solution to this problem was found in the consideration of the vigorous convection [3, 4].

2.2 The Convection-Accumulation Model

The physical cause of the vigorous compositional convection in intrusive magmas is density inversion, which occurs as a result of magma crystallization in boundary layers and leads to the appearance of convective currents relatively enriched and depleted in solids. This situation was first described qualitatively by Harry Hess [17] in his analysis of the origin of downward magmatic currents in the Stillwater magma. Taking into account that such phenomena required changes in the Sedimentation Model algorithm, two additional assumptions proved to be useful. The first postulated that the settling velocities of individual crystals (relative to the melt) are small compared to the average rate of heterogeneous masses composed of a mixture of crystals and melt. The second one resulted from a high efficiency of convective mixing of magma that assumes homogeneity of its

temperature and composition at arbitrary moment of time. In this case, modeling the chemical consequences of the vigorous convection at each time interval can be reduced to the calculation of weighted average parameters of the temperature and composition just for one chamber-thick convection layer, assuming that such efficient mixing does not prevent the transition of settling crystals from the convecting magma to the cumulate pile. The conjugation of in situ crystallization, compositional convection and crystal settling at the lower front of formation of cumulates underlies *the* '*Convection-Accumulation Model*' (herein after CAM) justified in [3, 4]. Thus, to simulate such combined processes we used an algorithm, which is very similar to the Sedimentation Model [3], supplemented with the procedure of averaging the physical and chemical characteristics of the crystallizing magma body after each cycle of nucleation of solids in the boundary layer and their partial transfer to the lower portions of the chamber.

The realism of the proposed model 'with convection' was confirmed by the first results of calculations. When compared with intrusive traps of Eastern Siberia, it turned out that the structure of virtual objects formed by the CAM mechanism is more consistent with natural observations than model bodies stratified by simple crystal sedimentation (compare Fig. 1c and 1d). In particular, accounting for magma mixing resulted in gradual and smooth transitions between different types of cumulates, similar to what is observed in differentiated sills [3]. The obtained results were of the pioneering nature and formed the basis for building the next generation of computer models allowing for approximations of the dynamics of crystal transport from convecting magmas combined with a new algorithm designed for modeling crystallization of basaltic magmas. These developments opened a new stage in studies of intrusive magma differentiation: comparison of alternative hypotheses was put on a quantitative basis for the first time [4].

3 COMAGMAT-3 and Modeling the Structure of Layered Intrusions (1985–2019)

Two circumstances stimulated further modeling the structure of layered intrusions. The first one is related to field work in Eastern Siberia: from 1969 to 1980 we carried out four expeditions to the areas of occurrence of intrusive traps exposed along the Podkamennaya Tunguska River and headwaters of the Vilyui River (Fig. 2). Purposeful search and detailed sampling of complete vertical sections of dolerite sills (usually with interval of 3–10 m) allowed construction of the structure of several intrusions from 90 to 160 m thick, which exhibit different degree of magma differentiation. Data on mineralogy, petrochemistry, and geochemistry of these dolerites [3] were the basis for comparisons with the results of calculations by an updated CAM [5, 6]. The second point was that these studies coincided with the development of the first models simulating crystallization of basaltic magmas. These models, initially called THOLEMAG, took into account the variable composition of rock-forming minerals and variations in their crystallization proportions for different cotectic assemblages [18–20].[1] The empirical basis for these programs was a set of mineral-melt geothermometers calibrated from experimental data on the partitioning of major and impurity components between rock-forming silicates (Ol, Pl, Cpx, pigeonite) and basic melt [24–26]. Using systems of such equations for a number of end-member minerals, it was shown that integral mineral models (i.e., including 4–5 end-members) allow calculations of mineral-melt equilibria with accuracy within 10–20 °C and can be applied to low-alkaline magmas, including oceanic and continental tholeiites. Calibrations of new more accurate geothermometers for plagioclase and olivine [27] and the construction of semi-empirical models for ilmenite and magnetite allowed us to present the first version of the COMAGMAT-3.0 program operating under DOS and coupling calculations of magma crystallization with dynamic equations approximating the CAM process [7].

Further development of the empiric basis of the COMAGMAT-3 program followed the path of calibrations that provide maximum accuracy of mineral-melt geothermometers in a wider range of magmas. In particular, COMAGMAT-3.5 version includes new equations for orthopyroxene, titanomagnetite and ilmenite which are better suited for modeling magmatic series ranging from high-Mg basalt to andesite and dacite [8, 28]. To model the structure of intrusive complexes, which exhibit a strong enrichment in iron and titanium, a special version of COMAGMAT-3.65 was developed, calibrated on experimental compositions including an extensive data set for ferrobasaltic systems [29, 30]. In the early 2000s, the first WINDOWS versions of COMAGMAT-3.5, from ver. 3.5*n* to more modern 3.7*n* were presented (https://comagmat.web.ru/apps-comagmat.html).

[1] The fundamentals of THOLEMAG were first presented in [21]; a rigorous thermodynamic justification for subsequent versions called COMAGMAT is given in [3, 7, 9, 10]. The main difference between our models and those of the popular MELTS family [22] is that American colleagues use algorithms of direct minimization of Gibbs potentials at given P–T parameters [23]. COMAGMAT allows solving thermodynamic equilibrium problems at a given degree of crystallization, when the equilibrium temperature is initially unknown. The solution is followed from a series of temperature-compositional iterations for each mineral using systems of non-linear mass-balance equations formulated in the form of the mass action law. Such an algorithm is convenient when combining crystallization models with heat and mass transfer calculations, when local data on the mineral and melt proportions and their compositions are needed [3, 6].

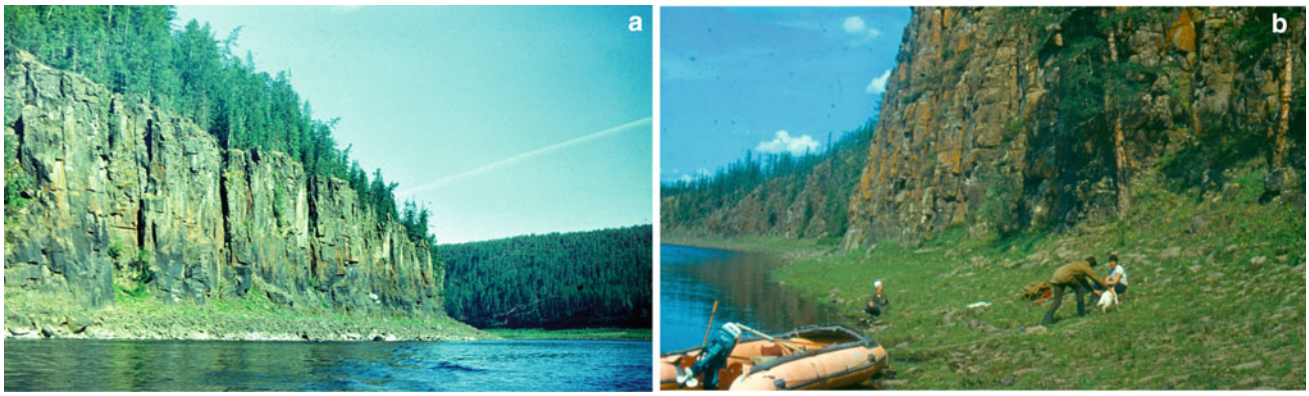

Fig. 2 Examples of differentiated traps from Eastern Siberia. **a** unnamed sill in the Podkamennaya Tunguska River valley, **b**—middle and upper part of the Vavukan intrusion in the upper Vilyui River

3.1 Approach to Model the CAM Dynamics of the Intra-Chamber Process

During the development of the new generation of intrusive models, the main emphasis was placed on simulations of a chemical diversity of cumulate rocks expressed as the chemostratigraphy of the model intrusions. To achieve the goal, in 1981, Frenkel [31] presented a system of analytical equations approximating the CAM dynamics and cooling of magma chambers. These equations connected the sequence of magma crystallization (followed from the COMAGMAT-3 modeling) with the convection-accumulation transport of crystals to the lower parts of the chamber. These relations described the dependences of thermodynamic and dynamic parameters on the heat fluxes through the crystallization fronts, including the rate of accumulation of crystals, initial temperature, mineral composition, and thickness of formed layers of protocumulates. The proposed model was consistent with the spatial and temporal structure of solidifying intrusions, which we call 'the dynamics of the CAM-model' (Fig. 1b). According to this scheme, three main stages of the intra-chamber process are distinguished, characterizing: (1) formation of chilling zones (short interval from magma emplacement to t_1), (2) short-lived oncoming movement of the upper and lower crystallization front (t_1–t_2) and (3) abrupt deceleration (almost stopping) of the upper front with simultaneous fast growth of the cumulate pile in the chamber (t_2–t_3–t_4). It was assumed that the final stages of cooling and solidification of the model protocumulates (t_4–t_5–t_6) are not of interest from the chemical point of view (Fig. 1b).

With respect to the scale of differentiation, the third stage, namely the convection-accumulation one, when the overwhelming part of the substance crystallizing near the roof enters the convecting magma and is gradually deposited at the lower front, as the convection subsides, is the most important. This is a stage of the most complete fractionation of the magmatic melt and formation of the Layered Series that compose the main part of the model intrusion. The algorithm linking the thermal history and dynamics of the convection-accumulation process is considered in [3, 4, 6]. The corresponding flowchart of the intrusive version of the COMAGMAT program is presented in [7, 9].

Petrological Postulates

The calculations assume that the initial state corresponds to a magma system approximating the tabular chamber of a sheet-like intrusion of arbitrary thickness H as the varying parameter. The chamber is filled with a heterogeneous magma (melt ± crystals), which spatially is equally distributed with respect to its composition and temperature; the latter is calculated using the thermodynamic options of the COMAGMAT model. It is suggested that the magma emplacement occurred instantaneously, after which the system is to be closed, so that only diffusive heat transfer is considered in the host rocks in the absence of any mass transfer. The system cools down due to temperature differences between the magma and the host rocks. Crystallization process starts assuming that crystals nucleation is homogeneous being occurred in a thin boundary layer below the upper boundary of solidification of the magma chamber. Because of rapid cooling, the first crystallizing minerals may be mechanically bound to the roof succession (early stage t_1–t_2 in Fig. 1b) but most of them remain as crystal-melt suspension. This results in the origin of the gravitationally driven downward suspension flows capable of delivering this heterogeneous mass to the bottom parts of the model chamber. At the same time, less dense grains, plagioclase in particular, can float. As a result, the formation of a cumulate pile below the main magma volume to occur, with the lowest cumulates capturing initial phenocrysts and increasing amount of settled crystals (t_1–t_2 in Fig. 1b), and overlying protocumulates composed of a bound framework of cumulus grains, the space between which is filled with intercumulus melt (the main stage t_2–t_3–t_4 in Fig. 1b).

Sequence of Calculations by Means of COMAGMAT-3.0
The first DOS version of this intrusive program was written in FORTRAN IV [7]. In accordance with the accepted assumptions and the proposed algorithm, simulations using the 'Intrusion' subroutine start with calculations of equilibrium crystallization of a virtual melt corresponding to the initial magma. These calculations are performed up to a given degree of crystallization, which corresponds to the assumed portion of intratelluric phenocrysts at the time of magma emplacement. At the same time, information on the equilibrium state (T, phase proportions, minerals and melt compositions) is first supplied to the intrusive block, where thermal parameters of the host rocks and the melt are specified to calculate heat fluxes at the upper and lower contacts. The heat fluxes determine the amounts of crystallizing minerals, as well as the time interval during which the mass of crystals is to be generated. The balance between the rate of nucleation of crystals and the rate at which they enter the main volume of the magma reservoir sets the composition and thickness of the near-contact horizons being formed. Correction of the composition and volume of residual magma is then performed; after that information on its current state is fed to the main module of the COMAGMAT program to continue crystallization calculations at the next step. Thus, the proposed equations of the differentiation dynamics are sequentially solved in the 'Intrusion' subroutine, which is activated periodically, as the main trajectory of magma fractionation is constructed. These iterations continue until the surface of the cumulate pile reaches the upper crystallization front or the amount of cumulate minerals in the model rock exceeds a given limit. At this point, the calculations stop, and model variations in the compositions of rocks, cumulate minerals, and melt become available for further petrological and geochemical considerations.

Initial Conditions and Fitting Parameters
Reconstruction of the structure of intrusive bodies using programs of the COMAGMAT-3 family includes the distribution of cumulate minerals and variable proportions of trapped melt, which determine variations in the contents of petrogenic oxides and 20 trace elements. Such work is an example of direct modeling, in which the response of the computational system to accepted initial conditions and model fitting parameters is investigated. Calculation results are compared with natural data, then corrections are made to the initial conditions and predicted parameters, and the calculations are repeated until the observed and model characteristics match (if possible). The initial conditions include the thickness of the model intrusion, the composition of its parental magma (estimated as the weighted average composition of the intrusion or using quenched varieties of rocks), the thermal and physical properties of the host rocks (temperature and melt density are calculated as crystallization proceeds), pressure, and the f_{O2} regime. The fitting parameters define the semi-empirical nature of the proposed model, including: (1) the portion of intratelluric phenocrysts, (2) some empirical coefficients for heat flux calculations at the roof and near the lower contact, (3) quenching duration, (4) maximum portion of the total amount of cumulate crystals in protocumulates, and (5) settling velocities for different minerals. The latter represent the effective characteristics, as the averaged integral result of the transfer of crystals from the convecting magma into the cumulate pile. Finally, optimum dynamic characteristics obtained as a result of these calculations for different sills are presented in [3, 6, 7, 9].

3.2 Modeling the Structure of Siberian Sills

Simulations of the structure of layered intrusions were first demonstrated in [5, 6], but the main cycle of such calculations is based on the use of an improved model of basalt magma crystallization [3]. The Kuzmovsky sill (Podkamennaya Tunguska River) and two intrusions from the upper Vilyui River ('B-304' and 'Vavukan') were selected for the modeling. In all cases, a good agreement between the observed and natural distributions of the major and trace elements was achieved, sometimes demonstrating a surprising coincidence of the observed and model chemical trends. It is important that the most realistic models include the entire list of major and trace elements: if we cannot replicate the distribution at least for one or two, it is not possible to find an optimum solution for the others. Figures 3 and 4 show the results of a series of calculations that were recently repeated for the Vavukan sill using the COMAGMAT-3.5 software. This sheet-like intrusion (Fig. 2b) is exposed in the valley of the Vilyui River and its right tributary Vavukan. Detailed sampling of two rock outcrops, 1.5 km distant and representing overlapping sequences, resulted in a complete cross-section of ~100 m thick, including the upper and lower endocontact zones, which are composed of fine-grained dolerites. In the main part of this section, the rocks change sequentially from a horizon of poikilophytic dolerites below to taxitoophytic varieties and trachytoid gabbrodolerites, which in places change to lens-like ferrogabbro above. At the same time, cryptic variations in the concentrations of major and trace elements along the vertical section of the intrusion were established.

The modeling calculations were carried out at a pressure of 1 atm and redox conditions close to the wustite-magnetite buffer (~10 wt. % oxidized iron). The weighted average composition of the Vavukan intrusion was taken as the initial magma, which corresponds to tholeiite with about 50 wt. % SiO_2 and 8 wt. % MgO (Table 1). The liquidus temperature of such a melt makes 1216 °C, and the calculated

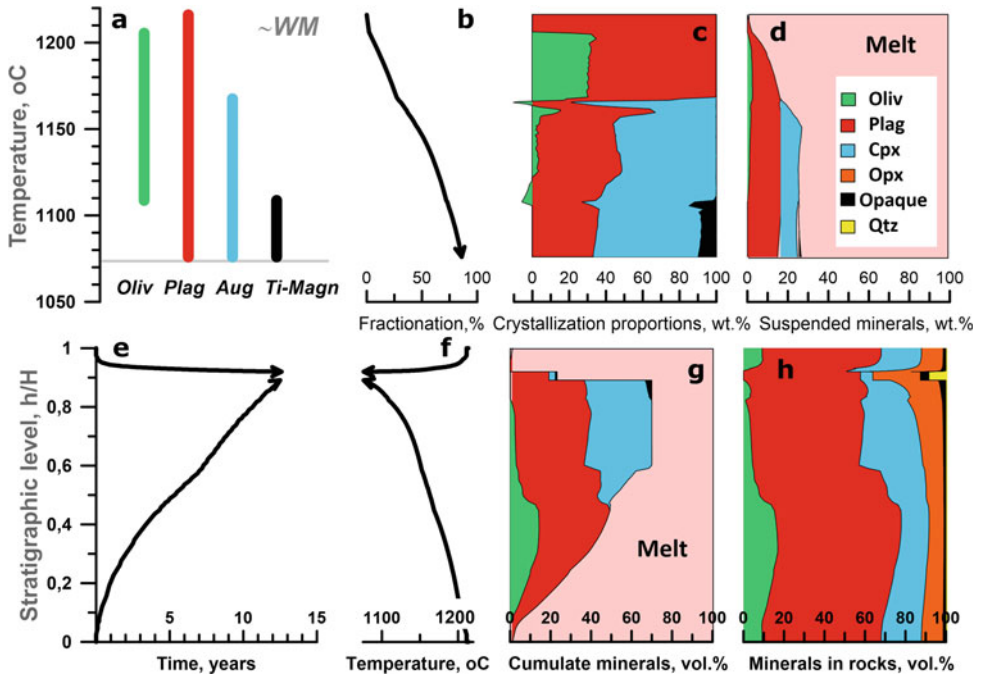

Fig. 3 Thermodynamic and dynamic parameters of the crystallization differentiation of magma corresponding to the average composition of the Vavukan intrusion (Table 1). **a–d** crystallization parameters of the Vavukan magma: **a** sequence of minerals crystallization, **b** dependence of the magma fractionation degree on temperature, **c** crystallization proportions of minerals for model cotectic assemblages, **d** evolution of the phase composition of residual magmas; **e–h** dynamic parameters consistent with different stratigraphic levels: **e** relative timing of the formation of solidified rocks and protocumulates (time scale counted from quenching), **f** temperatures of magma crystallization consistent with the formation of protocumulates, **g** the composition of the protocumulate mixtures of settled crystals and melt, where 'melt' represents trapped (at early stages) or intercumulus material, **h** normative composition of model rocks was calculated from modeling variations of whole-rock concentrations of the petrogenic oxides, see Fig. 4

Table 1 The compositions used for COMAGMAT-3 calculations

Intrusion	SiO_2	TiO_2	Al_2O_3	FeO	MnO	MgO	CaO	Na_2O	K_2O	P_2O_5
Vavukan*	49.48	1.16	15.85	11.00	0.28	7.86	11.77	2.12	0.35	0.13
Kivakka**	49.7	0.21	12.42	8.72	0.16	18.7	8.33	1.48	0.22	0.02
Virtual***	49.32	0.60	15.10	7.65	0.20	13.08	12.38	1.61	0.06	0.0

* Based on [3]; ** based on [11]; *** primitive MORB from [32] used for test calculations in the BLF mode (see text)

crystallization sequence ($Ol + Pl \rightarrow Ol + Pl + Aug \rightarrow Ol + Pl + Aug + Mt$) is typical for tholeiitic systems (Fig. 3a). In searching for optimum differentiation parameters, the degree of crystallization of the initial magma, the limiting portion of crystals in the cumulate pile, and the effective mineral settling velocities were varied. The work started with setting arbitrary parameters, which were adjusted as the model distribution of major and trace elements became more and more realistic. Figure 3 shows features of thermodynamics and dynamics of solidification at differentiation of the Vavukan magma—for the optimum model corresponding to the best fit with data of natural observations (Fig. 4).

The three upper graphs in Fig. 3a–c reflect the common features of crystallization of dolerite magmas [9, 10], with more important data shown in Fig. 3d. The phase proportions in the residual magmas are attributed here to the current volume of a magma reservoir between the upper crystallization and mineral accumulation fronts, thus characterizing the state of the convecting suspension of crystals and melt at each moment of time. As we see, plagioclase and clinopyroxene dominate in the composition of this convecting suspension, and in ratios different from cotectic proportions of crystallization (Fig. 3c). This is caused by given differences in the effective crystal settling velocities of olivine, pyroxene, and plagioclase, which determine the amount of minerals

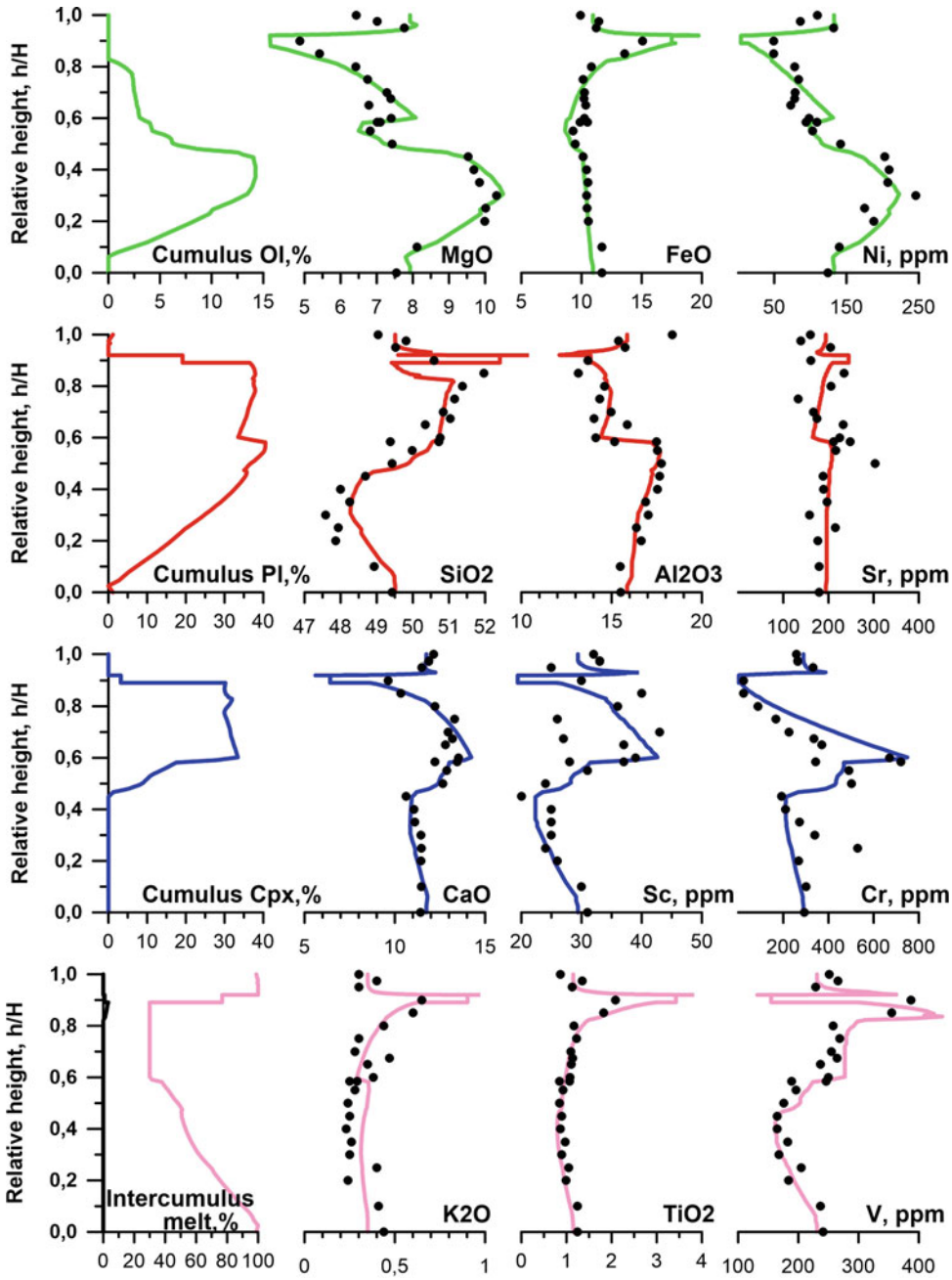

Fig. 4 Observed and modeled characteristics of the Vavukan trap intrusion. Circles—natural data, lines—results of calculations using 'Intrusion' subroutine in COMAGMAT-3.5.1 version: P = 1 atm, WM buffer, initial composition in Table 1

transferred from convecting magma to the cumulate pile, i.e., accumulation of femic minerals occurs more efficiently. At the final stages of magma differentiation, the amount of crystals suspended in the residual magma volume reaches as much as 30%. Thus, one of the main differences of the CAM model from the common perfect fractional crystallization is that our calculations provide possibility of incomplete separation of crystals of different sort in the magma chamber.

The dynamic characteristics in Fig. 3e–g give an idea of the course of the differentiation process on real space and time scales. In particular, Fig. 3e shows that variations in the mineral (Fig. 3h) and chemical composition of the model rocks (Fig. 4) are formed during 12–13 years from the moment of quenching the contacts; after that the whole cumulate pile cools down, followed with complete solidification of the magma chamber. Given the 100 m thickness of the Vavukan intrusion, the average rate of the formation of the cumulate pile is just under 10 m/yr. Figure 3f shows the profile of initial temperatures at the crystallization fronts and in the protocumulate systems formed at stratigraphic levels corresponding to the specific cooling time of the intrusion. The data in Fig. 3g characterize the portions of cumulate minerals in the protocumulates and the amount of the complementary intercumulus melt. By comparing these data

with the normative composition of the whole rocks in Fig. 3h, it becomes clear how the amounts of cumulate minerals and intercumulus melt predetermine the composition of finally forming cumulate rocks. A comparison of the observed and model chemical compositions of the Vavukan rocks is shown in Fig. 4.

3.3 Modeling the Structure of the Kivakka Intrusion

There are three main problems in applying the intrusive versions of COMAGMAT-3 to large layered massifs. The first two are of geological nature and are related to the fact that large intrusions (1) are usually irregular, often funnel-shaped, and in some cases (2) consist of several disintegrated blocks, where the presence of additional magma injections cannot be excluded. In this case, the possibility of modeling their structure using the sheet-like chamber approximation is questionable, primarily with respect to the relative volumes of cumulate rocks and solving the cooling problem. Dynamic parameters of such calculations should be treated as very approximate, in fact virtual ones. The third problem is due to the deterministic nature of the CAM itself, which postulates the absence of mass transfer in the mixtures of crystals and melt, excluding a number of phenomena like compaction of cumulate piles, infiltration of residual and intercumulus melts, and local re-equilibration of the infiltrates and hosting cumulus minerals [2, 33–35].

Accordingly, the modeling based on the CAM algorithm for large intrusions should be considered as a first approximation, which assumes the dominant role of vigorous convection coupled with downward crystal transport at the early stages of magma differentiation, but does not take into account possible mechanisms of transformation of the original protocumulates leading to the formation of rocks crystallized at the postcumulus stage. This necessitates abstracting from any superimposed processes and learning to divide into parts the mineralogical and geochemical characteristics, which could be attributed to the CAM signatures in the generalized structures of intrusive objects. The methodology proposed for challenging such problems is refined by examples of modeling several layered intrusions of the Olanga Group (Northern Karelia, Russia), with the main results being used currently in teaching students of the Faculty of Geology at the Lomonosov Moscow State University. These results were partly published in a companion paper [11], which is focused on the origin of late differentiates of the Kivakka magma. Below the results of modeling the structure of the Kivakka intrusion are considered in the light of relationships between the dynamic and chemical characteristics of the cumulate rocks.

Geological Settings of the Kivakka Intrusion

This layered massif is located in Northern Karelia and is part of the Olanga group of Paleoproterozoic peridotite-gabbronorite intrusions (known as Kivakka, Tsipringa and Lukkulujasvaara), which are well defined in the relief along the northwestern shore of Lake Pyaozero [36, 37], Fig. 5. Their age analogues (~2.44 Ga) can be traced sub-latitudinally in Finland, including the Tornio-Narankavaara belt group of ore-bearing intrusions (Tomio, Penikat, Kemi, Portimo, etc.) [38]. These magmatic events mark an important stage in evolution of the Karelian craton connected with local emplacement and differentiation of high-magnesia magmas, including comagmatic rocks which compose contemporaneous suites of mafic dykes, e.g. (Cleidon et al. 1997) [39]. The host rocks are represented by the migmatized biotite and amphibole gneisses, granitic to granodioritic gneisses of the Upper Archean. With respect to the host strata, all intrusions are discordant; they are well stratified demonstrating both modal and crypting magmatic layering.

The Kivakka intrusion dated at 2441–2443 Ma (U–Pb method [40, 41]) is an originally funnel-shaped body about 6.5 km in diameter, with the calculated axis height ~3.9 km, and the angle at the apex ~80º [37]. In the secondary settings, the axis is inclined 35° to 40° to the northwest (Fig. 6, left). The upper 2000 m of the vertical section is exposed by erosion, whereas the lower part of the cone, presumably composed of olivinite, is not exposed. Nevertheless, the layered series has been uncovered almost completely, which allowed for detailed sampling (87 samples from the main section) and reconstruction of the generalized structure of the Kivakka intrusion (Fig. 6, right). Such structure represents an idealized model of the massif, where all spatial coordinates (including average thicknesses of stratigraphic units and vertical coordinates of the used samples) were recalculated following relative volumes of corresponding rocks and geometric parameters of the original cone. These data were the basis for estimating the average weighted composition of the initial magma (Table 1) and subsequent calculations of the magma differentiation dynamics.

The Structure of the Kivakka Intrusion

According to Fig. 6, the vertical section of the Kivakka intrusion comprises the Lower and Upper boundary groups and the Layered Series, which composes the main volume of the intrusion. The principal units of the Layered Series are consistent with successive changes in the observed cumulus

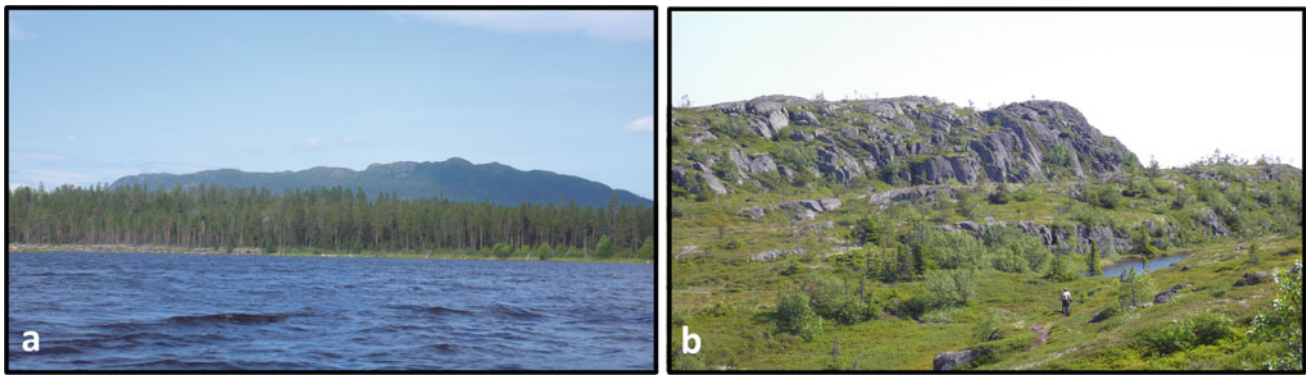

Fig. 5 The Kivakka intrusion in Northern Karelia (Russia). **a** general view of the Kivakka mountain from Lake Pyaozero, **b** outcrops of gabbronorite in mountain tundra near the top of the Kivakka mountain

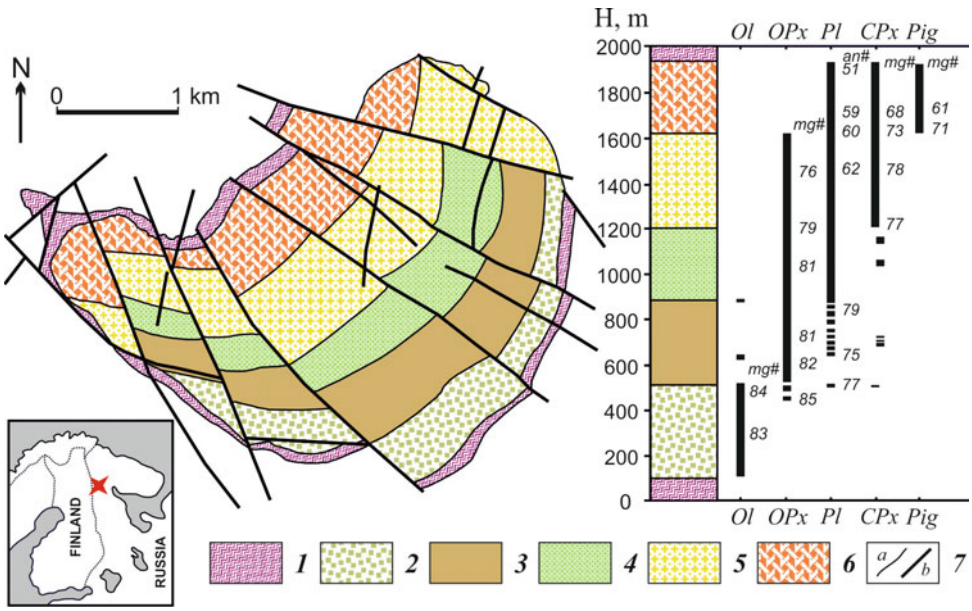

Fig. 6 Geological structure and reconstruction of the generalized section of the Kivakka intrusion, after [11] with modifications. 1—rocks of lower boundary group (LBG) and upper boundary group (UBG); 2–6—the layered series: 2—Olivinite zone (OZ); 3—subzone of bronzite-norite interlayering (SBNI); 4—Norite zone (NZ); 5—Gabbronorite zone (GZ); 6—gabbronorite zone with pigeonite (GZP); 7—geological boundaries; 8—fractures; 9—geological profiles; 10—geographical position of the Kivakka intrusion. Right panel. Mineral compositions in the rocks of the Kivakka intrusion: *Ol* is olivine; *Pl* is plagioclase; *Opx* is orthopyroxene; *C*px is clinopyroxene; *P*gt is pigeonite. 'H, m' is the visible thickness in meters

mineral assemblages, which represent (from bottom to top) the olivinite (cumulus Ol), norite (Opx + Pl), gabbonorite (Opx + Pl + high-Ca pyroxene), and gabbonorite with pigeonite (Pl + high-Ca pyroxene + Pgt). The Lower boundary group (LBG) is composed mainly of gabbronorite. Its average apparent thickness is about 50 m but reaches as much as 100 m in some places, including complex contacts with the Archean gneiss [11, 36]. In terms of the mineralogical and geochemical characteristics, LBG may be considered as the 'basal reversal' [15], demonstrating the upward enrichment in cumulus olivine and complementary depletion in the whole spectrum of major and trace elements, which are incompatible with olivine. These variations are reflected in changes in the mineral composition of near-contact rocks providing an illusion of the reverse order of the cumulate assemblages changing from gabbronorite to olivinite.

The olivinite zone (OZ) composes the base of the Layered Series, its apparent thickness is 460 m. The predominant mineral is olivine, but within the upper 50 m of the unit the relative role of cumulus bronzite is increased. The transition to the overlying norite zone (NZ) is proceeded through a 20–30 m thick horizon of small-scale intercalation of harzburgite and bronzitite, where decimeter-thick rock layers

predominate. The NZ reaches an apparent thickness of 540 m and is composed of norite differing in the proportions of orthopyroxene and plagioclase. In the lower part of NZ, the subzone of bronzitite-norite interlacing with apparent thickness of 285 m (SBNI, Fig. 6b) is distinguished. It clearly demonstrates rhythmic layering of bronzite and bronzite-plagioclase cumulates [37]. The gabbronorite zone (GZ) is located higher, being composed of bronzite-plagioclase-augite cumulates; it is about 440 m thick.

The uppermost unit of the Layered Series is the gabbronorite with pigeonite (GZP). It is 460 m thick and its rocks are slightly different in composition from the underlying gabbronorite. The main difference is that the cumulus orthopyroxene is replaced here by the inverted pigeonite. The upper 50 m of this zone are composed of specific rocks with increased amounts of titanomagnetite, biotite, potassium feldspar, apatite, i.e. minerals which commonly crystallize from the late residual melts as a result of mafic magma differentiation. These mineral assemblages are consistent with the lowest-temperature products of the crystallization and, by analogy with other large intrusions, can be classified as a 'Sandwich Horizon', which marks the boundary between the Layered Series and the lowest part of the Upper boundary group. The UBG rocks, approximately 50 m thick, are strongly altered, include large amounts of epidote, presenting no opportunity to reconstruct their original mineral compositions. However, their chemical characteristics meet the 'upper reversal' [15], indicating that the UBG rocks have crystallized from the roof downward. The data of aerial surveys confirm the proximity of their occurrences to the upper contact with the Archean gneiss. Indirect confirmation of the existence of this group are lenses of granophyre, which probably represent squeezed portions of the lowest-temperature and differentiated melts [11].

Calculations on Modeling the Structure of the Kivakka Intrusion

Taking into account the depth of occurrence of the overlying strata of about 8 km, the calculations were performed at a pressure of 2.6 kbar, assuming reduced magma crystallization conditions, as it has been done for the Vavukan sill. The weighted average composition of the Kivakka intrusion was taken as an approximation of its parental magma, using the relative volumes of all major types of cumulates (Fig. 6, Table 1). Similar to the calculations for the Siberian sills, the main calculated parameters are the time-varying amounts of crystallizing minerals originated near the roof of the model intrusion. At each time interval mass fluxes of these minerals were recalculated for the volume fractions in the convecting magma, which, due to the downward transfer of these crystals, controlled the mineral composition of model protocumulates and, ultimately, the compositions of newly forming rocks. In addition to the effective crystal 'settling velocities', different combinations of the probable portion of intratelluric crystals at the moment of magma emplacement were studied. Following the CAM restrictions, a maximum portion of crystals in the cumulate pile was given, above which the volume of the forming protocumulates (mean their thickness) was excluded from further calculations.

Consideration of multiple modeling results led to the conclusion that the optimum solution is provided by the emplacement of a picritic magma containing 21% olivine (Fo88.6) in equilibrium with a high-magnesia melt (10.8 wt. % MgO) at 1283 °C, see details in the Appendix to the paper [11]. This heterogeneous magma crystallized in the chamber with release of additional amounts of olivine, which was gradually replaced with orthopyroxene, followed by a cotectic assemblage *Opx* + *Pl* at 1226 °C (Fig. 7a). At 1198.4 °C augite began to crystallize.

Calculated changes in the crystallization proportions and the phase composition of residual magmas with the temperature are shown in Fig. 7cd. Interestingly, the total of suspended minerals in the latest derivate magmas is more than 30%. Figure 7e shows that it took about 3000 years to fill the virtual Kivakka chamber with cumulates; this estimate is nearly 300 times as that for the 100 m Vavukan intrusion (Fig. 3e). The lowest-temperature fractions correspond to ~ 1130 °C and were accumulated near the roof, at the distance 5–9 rel.% of the intrusion thickness (Fig. 7f). The composition of the modeled mixtures of accumulated minerals and intercumulus melt mixtures is shown in Fig. 7g. These data are consistent with the conclusion that it is the distribution of the cumulus minerals along the section that determines the final mineral composition of the forming rocks (Fig. 7h). A comparison of the observed and optimum model chemical compositions of the Kivakka rocks is shown in Fig. 8. These plots demonstrate how the behavior of compatible elements is controlled by the amounts of corresponding concentrating minerals, whereas the chemostratigraphy of incompatible elements (such as K, Ti, REE, and others) depends upon the porosity of cumulates and the degree of fractionation of the intercumulus melt.

4 Discussion

4.1 The Significance of the Convection-Accumulation Model

Examples of applications of the intrusive version of COMAGMAT-3 shown in Figs. 3, 4 and Figs. 7, 8 clearly show that understanding of the convectional nature of the intra-chamber differentiation and the capabilities of modern computational techniques allow modeling many features of the modal layering and geochemical structure of small to

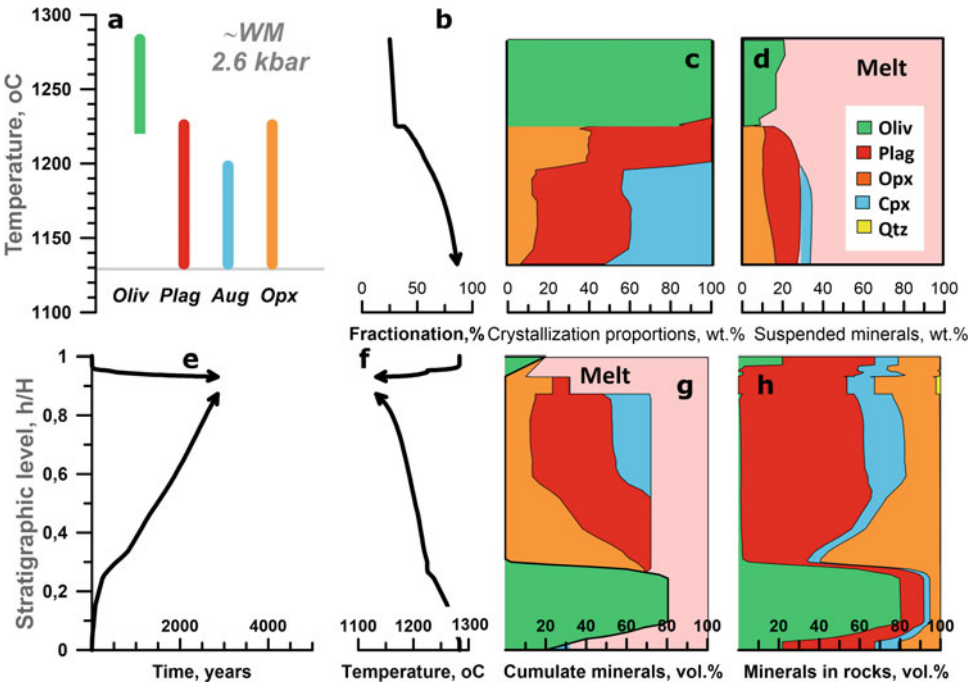

Fig. 7 Thermodynamic and dynamic parameters of the crystallization differentiation of magma corresponding to the average composition of the Kivakka intrusion (Table 1). (**a**–**d**) crystallization parameters of the Kivakka magma, (**e**–**h**) dynamic parameters of magma differentiation consistent with different stratigraphic levels (see additional notes to Fig. 3). The normative composition of model rocks was calculated from modeling variations of whole-rock concentrations of the petrogenic oxides, see Fig. 8

large layered intrusions. The CAM algorithm is unique in that it has no relation to primitive genetic schemes like 'crystal settling', as some authors write [42, 43]. In fact, it is a complex and physically grounded model that takes into account different regimes of thermal and chemical evolution of multiply-saturated magmatic systems, which solidify under a certain dynamics of in situ crystallization fronts coupled with accumulation of magma crystallization products. This conjugation is formalized as appropriate mass-balance equations, which describe the rates of inward movement of stratigraphic cumulate boundaries and the efficiency of capturing cumulus minerals, which crystallize in near-contact boundary layers and are transported to lower parts of the chamber by vigorous convection [3–7]. The relative role of these processes depends on the thickness of intrusive bodies and their cooling rate, so that the contribution of in situ crystallization is higher for smaller intrusions at initial stages of their solidification. In the case of large intrusions, their spatial structure is formed mostly as a response to mineral accumulation processes, with the formation of a strongly reduced 'basal reversal' followed a thick sequence of cumulates composing the Layered Series.

As can be seen in Fig. 4 and 8, regardless of the thickness of intrusive bodies, the chemostratigraphy of model objects is controlled by their cumulate structure, which, in turn, reflects the dynamics of cooling and filling of the magma chamber with crystallizing minerals. The conjugation of in situ crystallization and crystal accumulation is the main reason of the formation of S-shaped profiles of chemical elements in the rocks. Such an understanding of the observed asymmetry of differentiated intrusions was gained back in the 1980s [3, 5], long before the terminology of 'marginal reversals' was introduced into petrological usage [15]. In Fig. 4 and 8 these extrema are well traced on behavior of trace elements partitioned in femic minerals (Mg, Ni, Cr and Sc). The distribution of the lime, alumina, and strontium is controlled by the amount of cumulus plagioclase. In the case of incompatible elements, such alkalies, titanium, and REE, direct correlations with the original cumulate porosity are evident, as well with the fractionation degree of the intercumulus melt, particularly at upper stratigraphic levels. Thus, almost every maximum, minimum, or changing the direction of the concentration lines in the chemostratigraphic diagrams may be explained as a result of the evolution of the mineral composition of original cumulates, including the portion of the intercumulus melt. Note, that the smoothed character of geochemical trends for most of the model sections is dictated by the given condition of large-scale magma mixing in the chamber, which is the basis of the proposed Convection-Accumulation Model.

Criticism and Perspectives of the CAM Development

Despite almost 40 years have passed since the first quantitative models of intra-chamber magma differentiation were presented, no other similar algorithms have been developed in Russia or abroad so far. In the literature, there are no models that replicate all petrological functions of the intrusive COMAGMAT, which combines solving thermal problems and simulations of the intra-chamber dynamics with modeling the crystallization history of magmas parental to layered

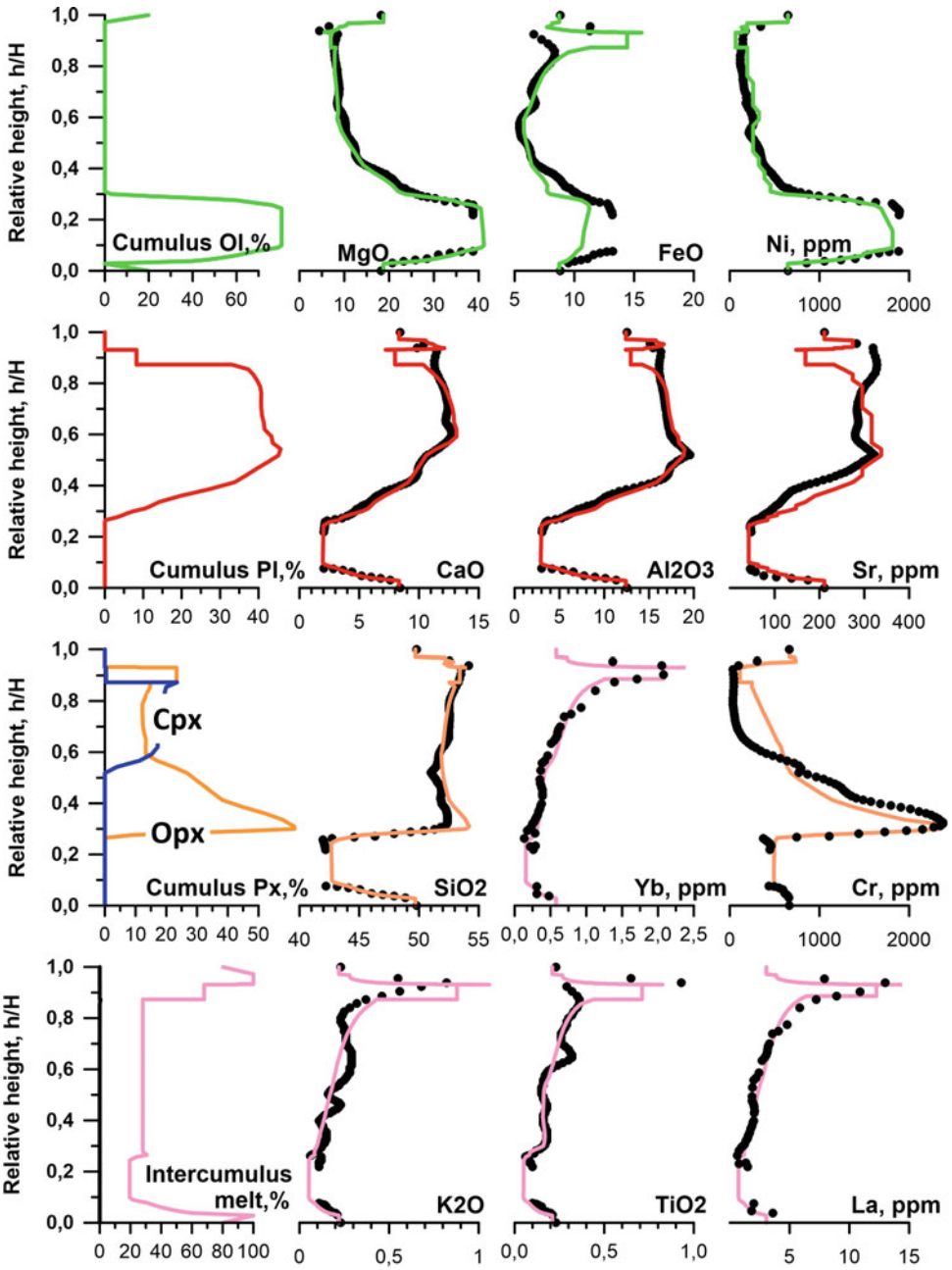

Fig. 8 Observed and model characteristics of the structure of the Kivakka intrusion in Northern Karelia (Russia). Circles are natural data representing the result of processing the observed whole-rock compositions by the 'sliding window method'; lines are the results of calculations using the Intrusion subroutine in COMAGMAT-3.5.1 version: P = 1 atm, WM buffer, initial composition in Table 1

intrusions. More often it is caused by the lack of experience in solving such complicated problems, sometimes—by the desire to substitute the fundamental physical and chemical considerations by verbal hypotheses. Such information mixture of quantitative and conceptual models is very eclectic, allowing to put strictly grounded multiparametric algorithms on a par with scenarios proposed according to geological intuition or natural quick-wittedness of this or that researcher. An illustration is a series of papers by Latypov and colleagues [15, 42, 43], where the authors even did not try to understand the reasons for the success in CAM simulations of the structure of layered intrusions. Instead, they focused on the search for any geological or mineralogical signature that could be used to negate the convection-accumulation mechanism in general. Such a doubtful 'petrological' approach gives rise to attempts to reanimate previous ideas on over-simplified in-situ crystallization of crystal-free magmas as a leading intra-chamber process [44].

Meanwhile, there is a need for further development of the CAM algorithm. First of all, it concerns the evolution of large magma chambers which inevitably pass through the stage of existence of crystal mush precursors of cumulates subjected to gravitational compaction and recrystallization [33–35]. These processes are accompanied by percolation of

residual melts, i.e. one more style of the compositional convection, possible geochemical consequences of which have been discussed in the literature [45, 46]. The most evident is the return of a portion of low-temperature intercumulus melts to the main volume of convecting magma leaving behind complementary adcumulates. This should lead to a specific magma fractionation known as 'Boundary Layer Fractionation' (*BLF* [45]). Towards the end of the last century, Kuritani [47, 48] tried to combine cooling calculations for a basaltic flow with modeling evolution of its boundary layers, including the BLF fractionation. This required the construction of a complex computational procedure resembling the early models of Frenkel [3], but including crystallization calculations using the MELTS [49, 50]. According to these calculations, the chemical effect of the BLF process was not high, in fact, following from fragmentary results which did not give a complete picture of crystallization and differentiation of considered magma bodies [47, 48]. A more consistent approach to understanding the role of compositional convection in protocumulates is demonstrated by modeling the structure of the Nosappumisaki sill in Northern Japan [51]. The ideology of the latter study is very similar to principles of updating the basic CAM algorithm, proposed to model the effects of compaction of cumulates and induced removal of their pore melts [52].

4.2 Introducing the First COMAGMAT-BLF Model

The geochemical effect of the BLF fractionation is due to the possibility of additional crystallization of original protocumulate systems, followed by separation of the newly formed lower temperature and more evolved melt from the cumulate pile. It is to occur regardless of whether this cumulate layer represents a zone of growing crystals or their mechanical accumulation. The mixing of the late melts from the boundary layer into the main volume of magma results in its evolving along a BLF pathway which differs from the ordinary trajectories of homogeneous fractional crystallization [45]. Using the subtraction-addition principle, Nielsen and DeLong [46] presented the expected signatures of the BLF processes, but their semi-quantitative estimates did not take into account any physical constraints on the phenomenon. To achieve the goal, we modified the intrusive block of the COMAGMAT model, so that now the program can account for the effects of additional equilibrium crystallization in the uppermost layer of the cumulate pile coupled with compaction of these protocumulates on a spatial and temporal grid dependent on the cooling rate of intrusive bodies. The technical aspect of the issue was to learn how to combine calculations of the homogeneous fractionation within the CAM algorithm with the results of modeling partial recrystallization and consolidation of cumulate layers against pushing away of some residual melt. The essence of the proposed computational scheme is illustrated by the flowchart in Fig. 9.

The Proposed Sequence of Calculations

The first stage is the same as in the original intrusive COMAGMAT, including modeling homogeneous crystallization of convecting magma and partial sedimentation of crystallization products with formation of a layer of cumulus minerals with fill factor F_1. This horizon is ascribed a sense of the uppermost boundary layer in the lower zone of accumulation of crystals, which initially has a bulk composition $X_{BL}(F_1)$. The difference from the CAM algorithm [7] is that the cumulate system is not closed in this case. On the contrary, the possibility of additional equilibrium crystallization within the boundary layer, which results in changes in the composition of cumulus minerals and the intercumulus melt $C_{BL}(F_1)$, is allowed. Thus, the second stage of computations begins with a temporary stop of the CAM-style dynamic modeling followed by re-activation of the thermodynamic module of the COMAGMAT program, where the current composition of the boundary layer $X_{BL}(F_1)$ is used as the initial composition, Fig. 9. The course of equilibrium crystallization in this layer is calculated up to the degree of crystallization $F_2 > F_1$. At that, the residual melt in quantity 1- F_2 acquires $C_{BL}(F_2)$ composition.

At the third calculation stage, a certain fraction of this new residual melt is mixed into the main magma reservoir. This has two consequences. First, the composition of the liquid part of the convecting magma and its bulk composition changes. Thus, the effect of the additional crystallization of original protocumulates on the direction of magma fractionation is quantified. Second, diminishing amount of the intercumulus melt is equivalent to the compaction of original protocumulates, which leads to a change in the bulk composition of cumulate rocks to solidify at the stratigraphic level. After the completion of mass-balance calculations for the current cumulate layer, the main module of the CAM calculations is switched on, so that the construction of the crystallization evolution of the whole magma system is continued. From the petrological point of view, this scheme means the transformation of original orthocumulate systems into meso- and adcumulates, a possibility that was previously absent in our intrusive models.

The presented modifications of the intrusive block of the COMAGMAT-3 program allowed us to develop the first version of the COMAGMAT-BLF model, which is still under debugging and is only being prepared for presentation to the petrological community. Nevertheless, herein we present some preliminary results of the BLF modeling, which are shown in Fig. 10 and quite clearly illustrate the

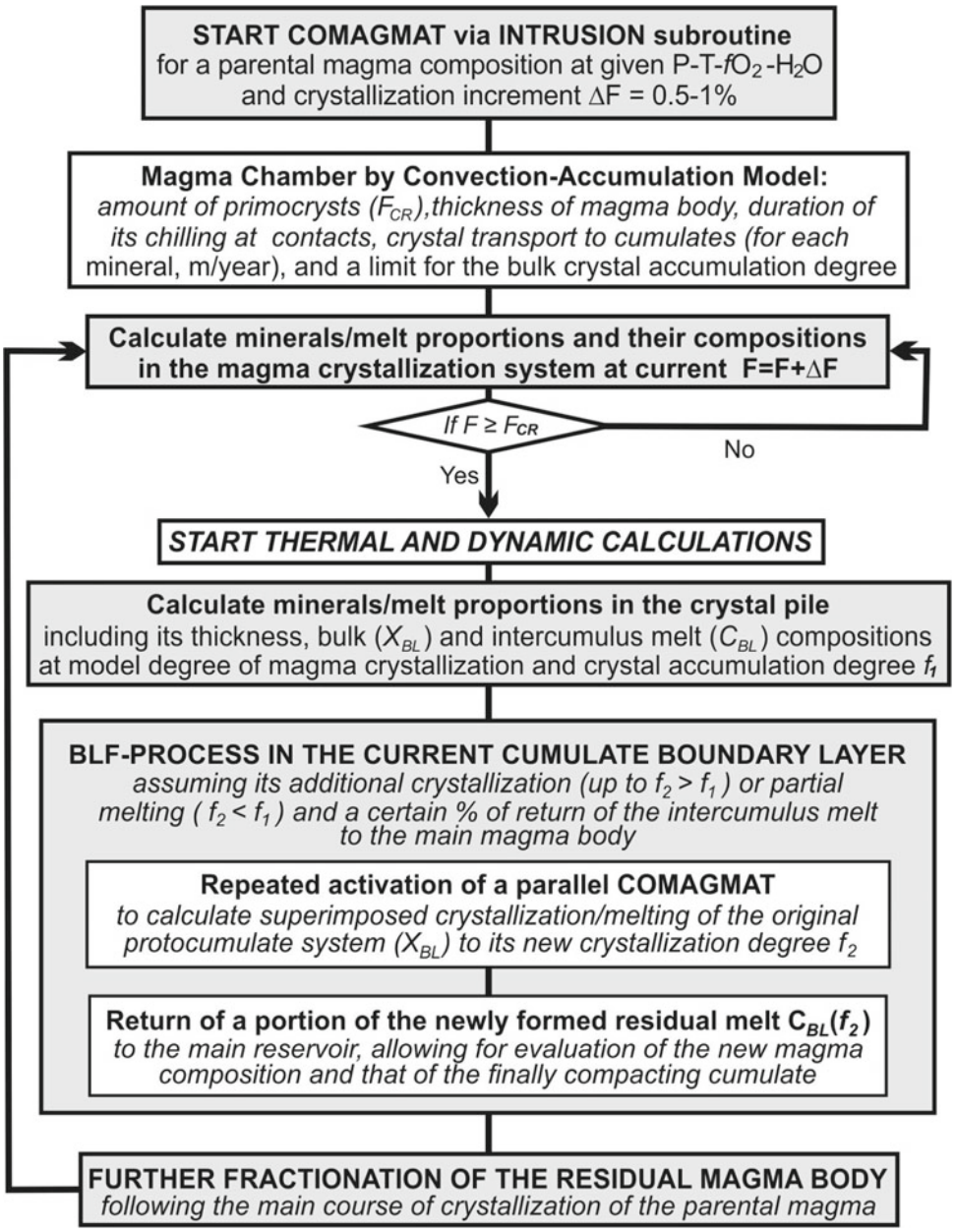

Fig. 9 Flowchart of modeling differentiation of intrusive magmas taking into account the boundary layer processes in the uppermost protocumulates, which is the basis of the development of the first version of the COMAGMAT-BLF program [52]

difference between the effects of the CAM and updated BLF models. For the test calculations, a high-magnesia magma corresponding to the primary MORB was chosen, according to melt inclusion studies in magnesian olivine [32] (Table 1). A 1 km thick virtual intrusion was proposed as a model object, and the absence of olivine intratelluric crystals in the initial magma was postulated.

Demonstration Results

The test calculations were carried out in three stage. The first one characterizes the chemostratigraphy of a model body, constructed assuming close to perfect magma fractionation and the convection-accumulation mechanism (Fig. 10a). At that, a high efficiency of crystal transfer from convecting magma to cumulate piles was postulated, assuming a maximum portion of cumulate crystals F_1 = 70%. The absence of any post-cumulus processes was suggested, so that the composition of the model protocumulates corresponds to the compositions of rocks that are formed at each stratigraphic level. The second variant assumes additional crystallization in the current uppermost protocumulate layers, from 70% to F_2 = 85% of crystals followed by the escape of 2/3 of the evolved melt into the main volume of the magma reservoir (Fig. 10b). The third variant is the most hypothetical,

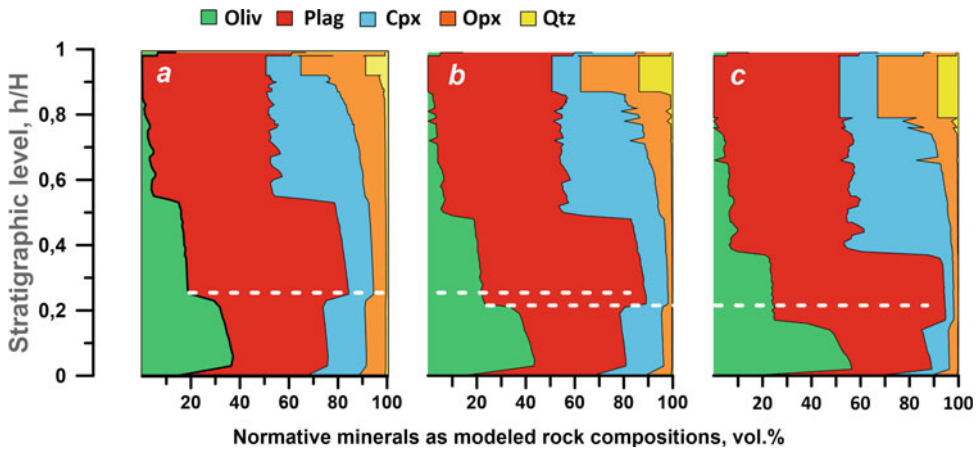

Fig. 10 Comparison of the sequence of model cumulates formed by the convection-accumulation mechanism **a** and taking into account possible compaction of cumulate piles **b**, **c** The calculations were performed using the first trial version of the COMAGMAT-BLF program [52]. The thickness of the model intrusion is 1000 m, the composition of the initial magma corresponds to high-magnesia MORB (Table 1)

allowing a partial melting of the initial protocumulate by 15% (F_2 = 55% < F_1 = 70%) and removal of the proposed 2/3 of the corresponding more primitive intercumulus melt (Fig. 10c).

As shown by the compositions of the model rocks in Fig. 10, this series of calculations reveals consistent olivine enrichment of the lower cumulate horizons and complementary decrease in the proportion of intercumulus melt, which is clearly visible in the amount of normative pyroxene. In addition, an increase in the relative volume of late products of magma differentiation is observed in the upper part of the model intrusion (see amounts of Opx and normative quartz). Thus, the superposition of the compaction induced removal of intercumulus melts on protocumulates formed by the CAM mechanism results in changes in the form of S-shaped profiles for olivine (respectively, Mg, Ni, etc.), even in the case of the same magma in the bodies of the same thickness. These results clearly show the large-scale effect of the BLF-processes on the mineral compositions of the model rocks and, obviously, the geochemical structure of the model intrusions.

5 Conclusions

The studies presented demonstrate the significance of physico-chemical approaches proposed to quantify a number of magma differentiation processes proceeding in small to large magma chambers. The basis of these works is the use of multiparametric models that combine the construction of basalt magma crystallization trajectories (using thermodynamic capabilities of the main COMAGMAT-3 code) with calculations of thermal and chemical dynamics of solidification of intrusive bodies, following the convection-accumulation mechanism and formalized in the INTRUSION subroutine. The uniqueness of the proposed algorithm is determined by its possibility to account for different modes of thermal and chemical evolution of magmatic systems, including coupling the movement of in situ crystallization fronts and stratigraphic location of cumulates originated due to mechanical accumulation of magma crystallization products. This is why the developed programs cannot be classified as an ‘in-situ crystallization model’ or ‘crystal settling model’, simply because those incorporate both factors that manifest themselves with different efficiencies at different stages of the magma chamber history.

The creation of such complex petrological instruments became possible due to the experience in numerical modeling the formation dynamics of small intrusions based on rigorous physical considerations and obtained at the Vernadsky Institute (Moscow, Russia) in the 1970s, followed by the introduction in these developments of magma crystallization models of the COMAGMAT family [3–7]. The successful modeling of the inner structure of differentiated sills from Eastern Siberia and the modal layering of the Olanga Group intrusions in Karelia [11] has shown that the intrusive version of COMAGMAT-3 has predictive abilities, providing a quantitative explanation of many features of apparent and cryptic layering of the differentiated intrusions. This is most obvious in modeling the behavior of compatible and incompatible elements in the rocks, including the occurrence of S-shaped profiles of their distribution along the vertical sections. The specific shape of such geochemical profiles depends on the thickness of intrusions and their cooling rate, thus, for small differentiated sills the relative contribution of in situ crystallization with the formation of

'basal reversals' is higher. In the case of large intrusions, their spatial structure reflects mostly large-scale accumulation of crystallizing minerals with the formation of a thick Layered Series and weakly pronounced inversion zones.

At the same time, analysis of data available on large layered intrusions shows that the capability to trace changes in the rate of movement of crystallization fronts against the capturing cumulus minerals at different stratigraphic levels is a necessary but insufficient condition for understanding the full picture of magma differentiation. The fact that the vigorous compositional convection in the form of suspension flows in magma reservoirs is the main factor of deposition of crystal-rich material does not mean that these phenomena define all features of the observed geochemical structure and types of rock stratification. The postcumulus history of original cumulate piles, including transport phenomena in the mixture of cumulate minerals and melt, is important. Cumulate layers tens to hundreds of meters thick inevitably show the effect of hydrodynamic instability which leads to gravitational compaction of cumulates and squeezing of the pore melt [34, 35]. Under these conditions, the upward infiltration and removal of intercumulus melts may be considered as the leading factor in the continued chemical evolution of the protocumulate systems.

Consistent accounting for these factors is a non-trivial problem from the physical point of view [35, 51], the solution of which requires repeated calls to the thermodynamic block of the COMAGMAT program on a time-grid. At this stage, as a first approximation, we followed the path of complication of the basic CAM algorithm by combining the calculations of the ordinary homogeneous fractionation of the convecting magma with modeling additional crystallization in related cumulates coupled with mixing of the evolved residual melt into the main magma volume [52]. These changes have been made in the first trial version of the COMAGMAT-BLF model, which allows the coupled effects of cumulate compaction and escaping the intercumulus melt to be investigated (Fig. 9). The mineralogical consequences of this transformation can be seen when comparing the results of simulations using the classical Convection-Accumulation Model and calculations using the BLF-fractionation mode (Fig. 10). The main result of the BLF processes is more contrasting pattern of olivine accumulation in the near-bottom horizons and a complementary increase in the volume of late differentiates in the upper part of the model intrusion.

Such relations confirm genetic conclusions of Frenkel [1, 2], who noted that almost all known features of the structure of layered intrusions may be quantitatively interpreted from the point of the interference of two main styles of compositional convection in magma chambers: (1) vigorous mixing due to occurrence of crystal-rich suspension flows in the magma reservoir and (2) pore migration of intercumulus melts due to compaction of original cumulate systems. The relative role of these processes depends on thermal fields in the host strata (which determine the cooling rates of intrusive bodies) and the amount of crystals suspended in parental magmas. Correspondingly, one or another type of stratification of cumulate rocks are formed, ranging from 'smoothed' distributions (such as shown in Figs. 3 and 4) to 'stepped profiles' (Figs. 7, 8, and 10). It is hoped that these fundamental conclusions will be appreciated by future generations of specialists in the intrusive magmatism, and that the material presented will be useful in constructing more efficient and sophisticated models of intra-chamber differentiation.

Acknowledgements This work as a synthesis of magma differentiation studies at the same time is a tribute to our teachers, friends and colleagues, with whom we once started and passed this long way of examinations of layered intrusions and building unique models simulating their inner structure. Blessed memory to Mikhail Yakovlevich Frenkel (1943–1993), Boris Sultanovich Kireev (1947–1999), Alexey Andreevich Yaroshevsky (1934–2017), Yana Vyacheslavovna Bychkova (1966–2020) and Denis Mikhailovich Khvorov (1971–2020). We also express our gratitude to many other colleagues from the Vernadsky Institute and Lomonosov Moscow State University, as well as undergraduate and graduate students who at different times were part of our team and contributed both to the field sampling and analytical studies of rocks from a number of layered intrusions in Russia.

References

1. Frenkel, M.Ya.: Thermodynamics, dynamics, and simulation of geochemical systems. Geochem. Int. **30**(5), 21–30 (1992)
2. Frenkel, M.Y.: Thermal and Chemical Dynamics of Differentiation of Mafic Magmas. Nauka, Moscow (1995) (in Russian)
3. Frenkel, M.Y., Yaroshevsky, A.A., Ariskin, A.A., Barmina, G.S., Koptev-Dvornikov, E.V., Kireev, B.S.: Dynamics of in situ Differentiation of Mafic Magmas. Nauka, Moscow (1988) (in Russian)
4. Ariskin, A.A., Yaroshevsky, A.A.: Crystallization differentiation of intrusive magmatic melt: development of a convection-accumulation model. Geochem. Int. **44**, 72–93 (2006)
5. Frenkel, M.Y., Yaroshevsky, A.A., Koptev-Dvornikov, Y.V., Ariskin, A.A., Kireyev, B.S., Barmina, G.S.: A crystallization mechanism for layering in stratifiedintrusions. Int. Geol. Rev. **27** (10), 1149–1165 (1985)
6. Frenkel, M.Y., Yaroshevsky, A.A., Ariskin, A.A., Barmina, G.S., Koptev-Dvornikov, E.V., Kireev, B.S.: Convective-cumulative model simulating the formation process of stratified intrusions. In: Magma-Crust Interactions and Evolution (ed. B. Bonin). Theophrastus Publications, Athens-Greece, pp. 3–88 (1989)
7. Ariskin, A.A., Barmina, G.S., Frenkel, M.Y., Nielsen, R.L.: COMAGMAT: a fortran program to model magma differentiation processes. Comput Geosci **19**(8), 1155–1170 (1993)
8. Ariskin, A.A.: Phase equilibria modeling in igneous petrology: use of COMAGMAT model for simulating fractionation of ferro-basaltic magmas and the genesis of high-alumina basalt. J. Volcanol. Geoth. Res. **90**, 115–162 (1999)
9. Ariskin, A.A., Barmina, G.S.: Modeling Phase Equilibria during the Crystallization of Basaltic Magmas. Nauka, Moscow (2000)

10. Ariskin, A.A., Barmina, G.S.: COMAGMAT: Development of a magma crystallization model and its petrologic applications. Geochem. Int. **42** (Supplementary 1), S1-S157 (2004)
11. Bychkova, Y.V., Mikliaeva, E.P., Koptev-Dvornikov, E.V., Borisova, A.Y., Bychkov, A.Y., Minervina, E.A.: Proterozoic Kivakka layered mafic-ultramafic intrusion, Northern Karelia, Russia: implications for the origin of granophyres of the upper boundarygroup. Precambr. Res. **331**, 105381 (2019)
12. Hess, G.: Heat and mass transport during crystallization of the Stillwater igneous complex. Geol. Soc. Am. Mem. **132**, 503–520 (1972)
13. Jaupart, C., Tait, S.: Dynamics of differentiation in magma reservoirs. J. Geophys. Res. **100**, 17615–17636 (1995)
14. Tait, S., Jaupart, C.: The production of chemically stratified and adcumulate plutonic igneous rocks. Mineral. Mag. **60**, 99–114 (1996)
15. Latypov, R.M.: The origin of in basic-ultrabasic sills with S-, D-, and I-shaped compositional profiles by in-situ crystallization of a single input of phenocryst-poor parental magma. J. Petrol. **44**, 1619–1656 (2003)
16. Wager, L.R., Brown, G.M.: Layered igneous rocks. Oliver and Boyd, Edinburgh and London (1968)
17. Hess, H.H.: Stillwater igneous complex, Montana: a quantitative mineralogical study. Geol. Soc. Am. Mem. **80**, 1–230 (1960)
18. Ariskin, A.A., Barmina, G.S., Frenkel, M.Y.: Computer simulation of basalt magma crystallization at a fixed oxygen fugacity. Geochem. Int. **24**(6), 85–98 (1987)
19. Ariskin, A.A., Barmina, G.S., Frenkel, M.Y.: Simulating low-pressure tholeiite-magma fractional crystallization. Geochem. Int. **25**(4), 21–37 (1988)
20. Ariskin, A.A., Frenkel, M.Ya., Tsekhonya, T.I.: High-pressure fractional crystallization of tholeiitic magmas. Geochem. Int. **27** (9), 10–20 (1990)
21. Frenkel, M.Ya., Ariskin, A.A.: Computer simulation of basalt-magma equilibrium and fractional crystallization. Geochem. Int. **22**(3), 73–84 (1985)
22. Ghiorso, M.S.: Modeling magmatic systems: thermodynamic relations. In: SE Carmichael, I. S. E., Eugster, H. P. (eds) Thermodynamic Modeling of Geological Materials: Minerals, Fluids and Melts, Reviews in Mineralogy 17, 443–465 (Washington, DC: Mineral. Soc. Am. 499 pp. (1987)
23. Ghiorso, M.S.: Algorithms for the estimation of phase stability in heterogeneous thermodynamic systems. Geochim. Cosmochim. Acta **58**, 5489–5501 (1994)
24. Roeder, P.L., Emslie, E.: Olivine-liquid equilibrium. Contrib. Miner. Petrol. **29**, 275–289 (1970)
25. Drake, M.J.: Plagioclase-melt equilibria. Geochim. Cosmochim. Acta **40**, 457–465 (1976)
26. Nielsen, R.L., Drake, M.J.: Pyroxene-melt equilibria. Geochim. Cosmochim. Acta **43**, 1259–1272 (1979)
27. Ariskin, A.A., Barmina, G.S.: Equilibria thermometry between plagioclases and basalt or andesite magmas. Geochem. Int. **27**(10), 129–134 (1990)
28. Ariskin, A.A., Barmina, G.S.: An empirical model for the calculation of spinel-melt equilibrium in mafic igneous systems at atmospheric pressure: II. Fe-Ti oxides. Contrib. Miner. Petrol. **134**, 251–263 (1999)
29. Barmina, G.S., Ariskin, A.A.: Estimation of chemical and phase characteristics for the initial magma of the Kiglapait troctolite intrusion, Labrador, Canada. Geochem. Int. 40(10), 972-983 (2002)
30. Ariskin, A.A.: The compositional evolution of differentiated liquids from the Skaergaard layered series as determined by geochemical thermometry. Russian J. Earth Sci. **5**(1), 1–29 (2003)
31. Frenkel, M.Y.: Geochemical structure of a stratiform intrusion. In: Dynamic Models in Physical Geochemistry. Nauka, Novosibirsk, pp. 19–30 (1981) (in Russian).
32. Dmitriev, L.V., Sobolev, A.V., Sushchevskaya, N.M., et al: Evolution of tholeiitic magmatism in oceanic rift zones. In: Proceedings of 27th International Geological Congress (Nauka, Moscow, 1984), vol. 6: Oceanic Geology, Part 1, pp. 147–154 (1984)
33. Irvine, T.N.: Magmatic infiltration metasomatism, double-diffusive fractional crystallization, and adcumulus growth in the Muskox intrusion and other layered intrusions. In: Physics of Magmatic Processes. Princeton University Press, Princeton, NJ, 325–384 (1980)
34. McKenzie, D.: The generation and compaction of partially molten rock. J. Petrol. **25**, 713–765 (1984)
35. McKenzie, D.: Compaction and crystallization in magma chambers: towards a model of the Skaergaard Intrusion. J. Petrol. **52**, 905–930 (2011)
36. Lavrov, M.M.: Precambrian Ultramafic Rocks and Layered Peridotite-Gabbronorite Intrusions of North Karelia. Nauka, Leningrad (1979)
37. Koptev-Dvornikov, E.V., Kireev, B.S., Pchelintseva, N.F., Khvorov, D.M.: Distribution of cumulative mineral assemblages, major and trace elements over thevertical section of the Kivakka intrusion, Olanga group intrusions. Northern Karelia. Petrology **9** (1), 1–24 (2001)
38. Maier, W.D., Hanski, E.J.: Layered mafic-ultramafic intrusions of Fennoscandia: Europe's treasure chest of magmatic metal deposits. Elements **13**, 415–420 (2017)
39. Vuollo, J., Huhma, H.: Paleoproterozoic mafic dikes in NE Finland. In: Lehtinen, M., Nurmi, P.A., Rämö, O.T. (eds.) Precambrian Geology of Finland: Key to the Evolution of the Fennoscandian Shield, pp. 195–236. Elsevier, Amsterdam (2005)
40. Semenov, V.S., Koptev-Dvornikov, E.V., Berkovskii, A.N., Kireev, B.S., Pchelintseva, N.F., Vasil'eva, M.O.: Layered troctolite-gabbro-norite Tsipringa intrusion, Northern Karelia: geologic structure and petrology. Petrology **3**, 645–668 (1995)
41. Revyako, N., Anosova, M., Kostitsyn, Yu.: U-Pb dating of zircon, Rb-Sr and Sm-Nd isotopic analysis of layered intrusion Kivakka (N. Karelia). In: Goldschmidt Conference Abstracts 2010, A864 (2010)
42. Latypov, R.M., Egorova, V.: Plagioclase compositions give evidence for in situ crystallization under horizontal flow conditions in mafic sills. Geology **40**, 883–161 (2012)
43. Latypov, R.M.: Basal reversals in mafic sills and layered intrusions. In: Charlier, B., Namur, O., Latypov, R., Tegner, C. (eds.), Layered Intrusions, 1st ed. Springer, pp. 259–293 (2015)
44. Latypov, R. M., Chistyakova, S. Yu, Namur, O., Barnes, S.: Dynamics of evolving magma chambers: textural and chemical evolution of cumulates at the arrival of new liquidus phases, Earth-Sci. Rev., 103388 (2020).
45. Langmuir, C.H.: Geochemical consequences of in situ crystallization. Nature **340**, 199–205 (1989)
46. Nielsen, R.L., DeLong, S.E.: A numerical approach to boundary layer fractionation: application to differentiation in natural magma systems. Contrib. Miner. Petrol. **110**, 355–369 (1992)
47. Kuritani, T.: Boundary layer fractionation constrained by differential information from the Kutsugara lava flow, Rishiri Volcano Japan. J. Geophy. Res. **104**(B12), 29401–29417 (1999)
48. Kuritani, T.: Thermal and compositional evolution of a cooling magma chamber by boundary layer fractionation: model and its application to primary magma estimation. Geophys. Res. Lett. **26**, 2029–2032 (1999)
49. Kuritani, T.: The relative roles of boundary layer fractionation and homogeneous fractionation in cooling basaltic magma chambers. Lithos **110**(1–4), 247–261 (2009)

50. Ghiorso, M.S., Sack, R.O.: Chemical mass transfer in magmatic processes IV. A revised and internally consistent thermodynamic model for the interpolation and extrapolation of liquid-solid equilibria in magmatic systems at elevated temperatures and pressures. Contrib. Miner. Petrol. **119**, 197–212 (1995)
51. Simura, R., Ozawa, K.: Magmatic fractionation by compositional convection in a sheet-like magma body: constraints from the Nosappumisaki Intrusion, Northern Japan. J. Petrol. **52**, 1887–1925 (2011)
52. Bychkov, K.A., Ariskin, A.A.: Modeling phase composition of adcumulates during the formation of layering of tabular intrusions. In: Mathematical Studies in Crystallography, Mineralogy and Petrography (collection of papers of All-Russian Scientific School). K&M, Apatity, 188–194 (1995)

Forms of Existence of PGE and Gold in Natural Systems and Their Geochemical Behavior

I. V. Kubrakova

1 Introduction

Research in chemistry, geochemistry, geology of PGE, processing technologies of platinum-metal raw materials traditionally occupies an important place in Russian science. The Russian Federation has significant reserves of these metals; together with the Republic of South Africa it controls more than 95.9% of the world's platinum metal resources [1], which are of strategic importance to the world economy. Among today's most urgent practical problems are the search for new deposits and alternative sources of raw materials; problems caused by technogenic pollution of the environment by platinum and other elements of the platinum group (PGE) in the zones of the development of ore deposits; biomedical applications using gold and PGE compounds. The solution of these applied problems is inextricably linked to the study of fundamental geochemical processes; their character is reflected, in particular, on the content, distribution, transport and accumulation of PGE in various natural environments. All these reasons cause necessity of development of methods of research of noble metals contents and obtaining of new data on their behavior in natural systems.

Study of behavior of trace quantities of elements in processes of their transfer and accumulation in geological conditions includes, on the one hand, study of forms of their existence (speciation) in various natural systems by modeling, on the other—identification of changes in the material composition of rocks and the nature of distribution of elements under the influence of certain factors. These approaches are used in this work for further investigation of geochemical behavior of PGE and gold.

I. V. Kubrakova (✉)
Vernadsky Institute of Geochemistry and Analytical Chemistry, Russian Academy of Sciences, 19 Kosygin St, Moscow, 119991, Russia
e-mail: kubrakova@geokhi.ru

2 Natural Abundances of PGE and Gold

Despite the existence of large deposits with high PGE content, these elements are present in natural objects mainly in ultratrace amounts. Study of mechanisms of dispersion and concentration of such amounts of metals is complicated by the problem of differentiation of sources of PGE input into natural systems, caused by increasing contribution of anthropogenic sources: over the past decades, background levels of PGE contents in soils, bottom sediments, and surface waters have increased significantly (Table 1). It concerns mainly the most important (dominating both in natural and natural-technogeneous systems) palladium, platinum and (to a lesser extent) rhodium. It is the importance of these PGE is caused by the prevalence of data on their behavior in the literature. In this paper, ruthenium, iridium and osmium also are practically not considered.

3 Processes Underlying the Migration Behavior of PGE in Liquid Media

The basis of the geochemical behavior of elements is the transformation of their dissolved forms and the sorption of these forms at the phase boundary. The course of these processes depends on the forms of element input, redox and acid–base properties of natural media, their composition, the presence of carbon-containing components (as a forming and/or transporting agent) or complexing substances. In the case of colloidal transport, sorption of elements on suspended matter and other surfaces, hydrodynamic characteristics of aqueous systems and many other factors play an important role.

The main part of PGE under consideration enters natural waters in the form of finely dispersed (up to nanosized) particles; the smaller one is in the form of dissolved (molecular) species. When the redox conditions of water system change, these forms undergo mutual transformations.

V. P. Kolotov and N. S. Bezaeva (eds.), *Advances in Geochemistry, Analytical Chemistry, and Planetary Sciences*,
https://doi.org/10.1007/978-3-031-09883-3_4

Table 1 PGE and gold abundances in natural systems [2–11]

	Gold	Palladium	Platinum	Rhodium	Ruthenium	Iridium	Osmium
Earth's crust (ng/g)	2.5	0.4–1.9	0.4–2.4	0.06–1.1	0.1–1	0.04–1	0.041
Chondrite (μg/g)	0.15	0.7	1.4	0.2	1.15	0.76	0.8
Ore (μg/g)	Up to 10 *n*	Up to 10 *n*	Up to 10 *n*	Up to 10 *n*	0.0 *n*	0.0 *n*	0.0 *n*
Surface water (ng/l)	0.001–1	0.02–40	0.04–190	0.04–0.1	0.001	< 0.001	0.005–0.040
Bottom sediments (ng/g)	Up to 1000 *n*	0.1–61	0.2–100	0.1–17	–	–	–
Road dust (ng/g)	–	1–500	0.3–680	5–110	–	–	–
Soils (ng/g)	1–1000 *n*	0.9–1760	0.03–500	0.2–26	1–66	2–21	–
Urban aerosols (pg/m3)	–	0.1–280	0.02–2700	0.3–27	–	–	–

The highly dispersed mineral phases of PGE partially or completely dissolve, forming compounds with inorganic anions or organic matter, and the mobility of elements increases. In turn, dissolved forms and nanosized particles interact with inorganic or organomineral phases of suspensions and sediments, providing colloidal transport of PGE. In addition, absorption of dissolved and nanosized forms of PGE by living organisms, subsequent binding of elements by suspended (sedimentary) matter, and reduction with the formation of mineral forms are also possible.

The main parameters of aqueous media, influencing a speciation of PGE, are values of pH and Eh. Calculated data on forms of occurrence depending on these parameters of natural solutions are received for many elements; for platinum they are given, for example, in [1]. From among anions defining inorganic composition of waters, only chloride- and in some cases thiosulfate-ions influence on composition of dissolved forms of PGE and gold. In addition, water systems contain dissolved and suspended organic matter and/or mineral phases with iron oxyhydroxides and aluminosilicates as the basis. Chloride (hydroxochloride) complex forms of PGE as well as their compounds with soluble humic substances are typical for surface and ocean waters [12]. The mobility of PGE in the zones of hypergenesis is associated with the weathering of PGE-incorporating sulfides and oxidative dissolution of natural intermetallic and other mineral forms of PGE. The bacterial oxidation of sulfides and reduction of sulfates (with formation of thiosulfate-ion and its compounds with PGE), as well as interaction of PGE with natural organic substances play an important role in these processes.

In magmatic and hydrothermal fluids the PGE mobility is determined by chloride, sulfide and bisulfide forms [1, 13–15], but is not limited to them. Thus, in high-temperature hydrothermal fluids the formation of stable organoelement compounds of PGE is possible under certain conditions [16, 17].

"Dry" CO–CO_2 and C–O–S fluids are considered as alternative (non-aqueous) media, which can provide the transport and subsequent concentration of noble metals [18, 19]. It was experimentally proved that the solubility of metals in carbon dioxide fluid can reach tens and hundreds ppm. In the same works possibility of formation of volatile carbonyl compounds of platinum $Pt_3(CO)_6$ as a form of its transfer in reducing conditions is confirmed.

Fluids containing various amounts of hydrocarbons (HC) are another example of a transporting carbon-containing medium [20, 21]. In real geological conditions, HC are produced by both mantle and crustal sources and are involved in magmatic and hydrothermal activity at different depth levels. Mantle fluids include naphthenic, paraffinic, and aromatic hydrocarbons, which are stable at great depths (over 300 km) in conditions of high temperatures and pressures (7000 MPa, 1000 °C) [17, 21, 22]; they can participate in the joint transport of metals and organic matter in mineral formation processes.

Metals in concentrations sufficient for participation in ore-forming processes enter the HC phase by dissolution [23]. Under the influence of kinetic factors (time increase and/or temperature increase) reduction of noble metals, first of all gold, and formation of Me^0 and nanosized phases is very probable. Their dimensions, shape and stability will be determined by properties and concentration of reducing and stabilizing agents (for example, organic matter or sulfides) [23, 24]. Reduction and secondary accumulation of metals, primarily gold, is also observed in technogeneous aquatic systems.

Thus, special attention should be paid to nanosized noble metals as a form, significant for transportation and accumulation of PGE and gold in various natural conditions.

A considerable part of the mentioned data was obtained in model experiments. Low natural contents of PGE (Table 1), coupled with analytical problems in determination of traces, essentially limit possibilities of studying of transport and accumulation of PGE in real conditions and thus hamper studying of behavior of PGE in natural settings. In this regard, of great importance for geochemistry of PGE is to obtain experimental data on the speciation and solubility of

compounds in solutions, as well as their redistribution between solution and solid phase, including modeling the behavior of elements using model forms of elements and individual sorption phases—components of geochemical barriers.

For comprehensive characterization of PGE behavior in complex natural systems, a wide range of studies can be used [12–15, 19, 24, 25], including: study of the composition of natural objects (the host environment) by ICP-AES, ICP-MS, ETAAS, UV–vis spectrophotometry, chromatography; determination of the initial soluble forms of elements by selective leaching methods; chemical phase analysis of organic matter and identification of its components; obtaining the individual forms of elements typical for different natural conditions, and determination of their physicochemical characteristics, in particular, stability constants (by methods of solubility, potentiometry, X-ray spectroscopy as XAS, XANES, EXAFS, etc.) and dimensions (by electron microscopy (SEM, TEM) and dynamic light scattering (DLS) methods); model sorption experiments using synthesized and/or separated by chemical phase analysis rock components (iron and manganese oxyhydroxides, fractions of dissolved and sedimentary natural organic matter, natural colloids and some layers of sediments, etc.); experimental evaluation of the kinetics of leaching of elements from rocks under different conditions (static and dynamic experiments); high-temperature experiments involving various solid and liquid phases; thermodynamic calculations of the distribution of dissolved and sorbed forms of elements, and other methods and approaches.

4 PGE Speciation in Natural Aqueous Solutions

In carbonate-chloride-sulfate systems with near-neutral pH and predominantly weakly oxidative properties, i.e. in conditions typical for natural waters–from meteoric waters to sea water and its derivatives—basic platinum metals (platinum, palladium, rhodium) exist as neutral or slightly negatively charged hydroxo- or hydroxochloride complexes [25–28]. The solubility of the hydroxocomplex forms of PGE (Fig. 1) varies in the series Pt > Rh > Pd, being 1.5 x 10^{-6} M [29], 4 x 10^{-7} M [30], and 3.5 x 10^{-8} M [31, 32], respectively. The ranges of noble metals contents in natural water systems are given in Table 1.

In a number of natural environments characterized by the formation of sulfoanions (under bacterial oxidation of sulfide minerals in waters of zones of the development of ore deposits, in anoxic sulfate-bearing zones), the migration of PGE may be affected by their interaction with thiosulfate-ion. Model studies of water–rock interaction have shown that even with sulfides content in the rock of less than

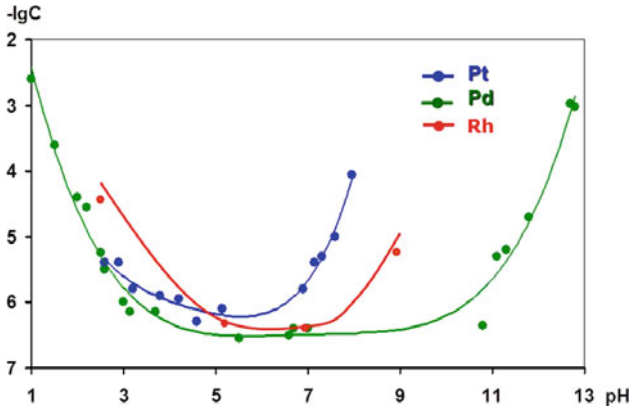

Fig. 1 The effect of acidity of aqueous solution on solubility of platinum, palladium and rhodium hydroxides

1% the thiosulfate-ion concentration in solutions can reach 0.35 mg/l. At the same time the resulting solutions contain up to 1 µg/l of dissolved gold (at its content in the rock ~75 ppb) [33]. Note that the same value was obtained for dissolved and colloidal species of gold in drainage flows of Novo-Ursky sulfide deposit (pH ~ 4.5) [34].

The study of the possibility of formation of thiosulfate forms of palladium in the conditions characteristic of natural-technogenic zones of sulfide oxidation allowed to establish the composition of these compounds and determine the stability constant of the complex in solution (K_{st} = $3.7 \cdot 10^9$ [33]), whose value was not known before. These species will be dominant under conditions of slow sulfide oxidation (for example, during the formation of the composition of waters of sulfide deposit dispersion flows in permafrost landscapes). At low content of suspended matter in such waters, the transfer of palladium thiosulfate compounds, like gold, can be carried out in the dissolved form.

The main natural complexing agent of surface waters are substances of humus nature. Humic and fulvic acids (irregular polymers containing fragments of aromatic oxycarboxylic acids, nitrogen-, sulfur-, and carbohydrate fragments) can exist in aqueous solutions up to 200 °C in a wide pH range, actively bind metal ions and increase the migration ability of elements, particularly PGE, by orders of magnitude [35–39]. As the pH increases, the molecules of these substances form associates of various sizes, some of which turn into colloidal particles. According to the data [12, 40] obtained by electron microscopy and dynamic light scattering methods, nanoparticles of humus substances and their aggregates in aqueous solutions can sometimes reach hundreds of nanometers. The binding of PGE ions can be considered both by carboxyl groups of the dissolved humus substance and by groups located on the surface of its colloidal particle. Based on the obtained data on the stability constants of hydroxo- and fulvate complexes, thermodynamic calculations were performed which confirmed the

dominance of hydroxofulvate forms in weakly acidic and neutral media [25]. The complexing properties of dissolved humic substances (fulvic acids) in relation to PGE and gold, stability, migration ability of noble metal coordination compounds, and their behavior in contact with natural sorption phases were described, in particular, in [12]. It has been shown that PGE and gold are able to form strong compounds (K_{st} 10^6–10^8) with N–, O–, S–containing groups of natural organic ligands which can be considered as a migration species of noble metals in aqueous media, which can serve as an effective form for transportation of these metals in aqueous media.

In contrast to gold, nanosized elemental forms of PGE have not been sufficiently investigated. The existance of their highly dispersed species, stabilized by natural organic matter, in natural waters was discussed in [12, 40–44]. These species are also formed in the hydrothermal process during the leaching of particles from rocks or are precipitated from solutions when the pH changes. In the migration process the particles can dissipate in the form of pseudocolloids in both aqueous and hydrocarbon media [21, 34, 45], to be sorbed at the interface and thus accumulate up to the formation of ore deposits. The formation of nanosized gold (AuNPs), stabilized by humic acids of brown coals, is described in [42, 46]. The model nanoscale platinum (PtNPs) and palladium (PdNPs), stabilized by fulvic acids, were obtained and characterized [43]. It was shown that the formation of PdNPs (as well as AuNPs) occurs even at room temperature (Figs. 2, 3). The formation of nanocomposites of gold and platinum with carbonaceous matter of black shales of Sukhoy Log was described in [45].

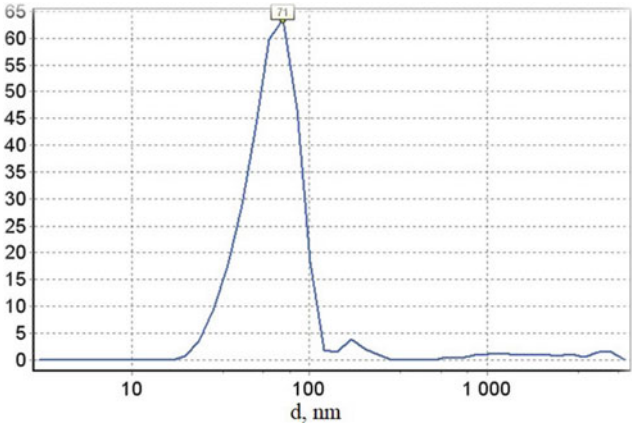

Fig. 3 Size distribution of hydrodynamic diameters of PdNPs stabilized with fulvic acids (DLS data) [12]

5 Interaction of PGE Species with Mineral Phases and Natural Slurries. Examples of the Behavior of Dissolved PGE in Natural Systems

As noted above, the main approach to the study of the geochemical behavior of PGE in natural conditions is experimental and computational modeling of the behavior of elements depending on various factors [27, 28, 37]. In this case, data on the forms of the elements and their stability, as well as the processes occurring at the interface of the sorption phases, most typical for a particular natural system, are taken into account.

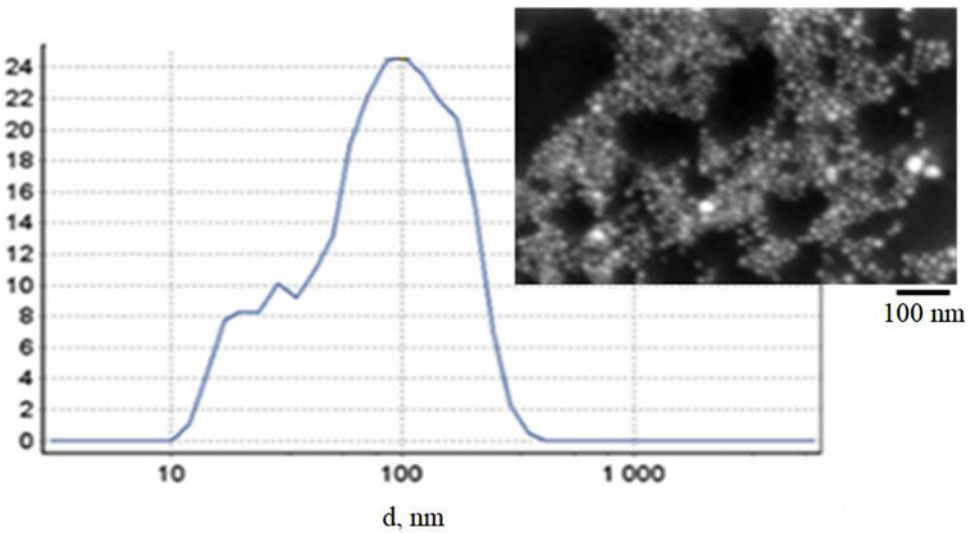

Fig. 2 Size distribution of hydrodynamic diameters of AuNPs stabilized with fulvic acids at room temperature (DLS data) [43] and their SEM image

One of the main components of natural geochemical barriers are iron oxyhydroxides. Many natural and technogeneous processes are associated with iron (II) oxidation accompanied by the formation of amorphous and colloidal oxyhydroxides with varied composition and high sorption capacity. Studying in model experiments the dynamics of interaction of hydroxochloride forms of gold, palladium, platinum and rhodium, typical for natural solutions, with freshly deposited iron oxyhydroxide forms [25, 30] showed that all PGE hydroxochlorides actively interact with this phase, especially rhodium. The thiosulfate species, as it was shown for palladium at pH 6.3, are quantitatively bound with iron oxyhydroxides during the first hours of the experiment [32], i.e., much more efficiently compared to the hydroxochloride forms. The same behavior is demonstrated by gold in weakly acidic media; in neutral and weakly alkaline media it is mainly in solution as thiosulfate.

The behavior of nanosized forms of noble metals, stabilized by natural organic matter, in contact with phase of ferrihydrite, and its comparison with the behavior of dissolved hydroxochlorides lead to conclusion about the more efficient binding of particles. Under natural conditions, this can facilitate the transfer of elements by suspended matter and their subsequent accumulation by precipitation. Thus, nanosized forms stabilized by humic substances (as well as ferrihydrite pseudocolloids) can be considered as the most important migration form of noble metals in the studied types of natural water media.

Another active participant of accumulation of elements, including noble ones, is sedimentary organic (humic) matter [47]. In this interaction very significant differences in the behavior of individual PGE and gold are observed. Figure 4 shows the binding of inorganic species of PGE and gold by natural organic matter (HA) depending on the acidity of the medium. It can be seen, that in specific natural environment, the transfer or accumulation of elements will prevail. Data on the predominant binding of noble metals by fractions of organic matter of different composition in natural conditions are given in [12]. For example, it was established for brown coals of Northern Urals, that gold and palladium are accumulated by humic acids fraction, whereas the most part of platinum is accumulated by bitumoids; it correlates well with data of model experiment (Fig. 4). Accumulation of gold and platinum by asphaltene fractions of bituminoids of black shales is described, in part, in [45].

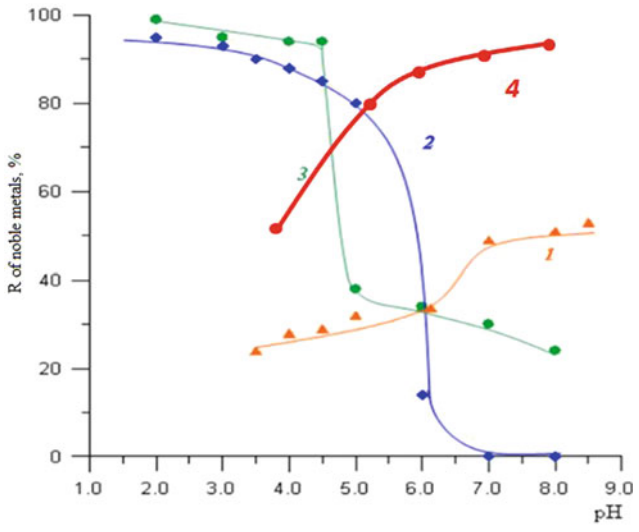

Fig. 4 Sorption of inorganic species of Pt (1), Pd (2), Au (3) and Rh (4) by humic acids versus the acidity of the medium

Thus, differences in the interaction with the components of geochemical barriers are observed both for individual noble metals, and for various forms of existence of each element. The behavior of forms of PGE in contact with individual natural sorption phases, as well as with living and inert organic matter, is considered in detail in [12, 39].

A special case of interaction of metals with natural sorption phases is the sorption by colloidal (suspended) matter. Due to high sorption activity and mobility, the highly dispersed substance is an effective carrier of trace elements in water flows and in the pore space, so the colloidal (or rather, pseudocolloidal) transport plays an important role in the transfer of elements in natural conditions.

Based on the data obtained in the model sorption experiments described above, the ratio of dissolved and bound forms of noble metals in contact with suspended matter of various nature was calculated (Table 2); this allows to predict qualitatively the transfer and accumulation of noble metals in water systems [12]. The potential ability of colloids to accumulate PGE at binding their dissolved forms was investigated in experiments with river, marine and technogeneous suspended matter.

The patterns revealed in the model experiments with individual sorption phases are traced on the example of colored river water samples containing suspended matter. Distribution of platinum and palladium, which were introduced into the water sample in the form of hydroxychloride forms, between the phases of solution and suspension, demonstrates the absence of sorbed forms of palladium and accumulation of platinum in the suspended phases [48]; similar conclusions about the nature of the distribution were made on the basis of calculated data [25]. Thus, in colored surface waters, the main form of palladium transport are dissolved molecular compounds, and for platinum the pseudocolloid transport and transfer of dissolved forms are the equivalent migration pathways. As for gold, its average content in river suspended matter exceeds the content in clay and shale by 7 times that indicates a high sorption affinity of this element in relation to surfaces of different nature and dominance of pseudocolloid transport as the main mode of transport of this element. It should be noted that river runoff,

Table 2 Dissolved forms of metals in surface waters (%)[a] [12]

Composition of suspended matter	Gold	Palladium	Platinum	Rhodium
$Fe(OH)_xFA$	6	12	6	2
Shale	No data	70	40	2
$Fe(OH)_x$	42	42	3	5
Humic acids	100	98	44	26

[a] Data are obtained under assumption that the water contains 6 mg/l of suspended solids consisting of one of the components

along with hydrothermal sources and extraterrestrial matter, is considered to be the main source of PGE delivery to the ocean. In spite of the fact that the content of noble metals in the ocean is extremely low, their circulation in natural aquatic environments amounts to tens of tons per year [1].

The behavior of individual PGEs in the sedimentary process in the ocean differs dramatically, which is caused by differences in the chemical properties of the elements, as well as by a different composition of oceanic suspensions (unlike river suspensions, oceanic ones consist mainly of organic matter). As a result, during arising of iron-manganese formations on the slopes of seamounts, abnormal accumulation (up to ore contens (ppm)) of only one PGE element—platinum—has been observed: according to Halbach, the Pt/Pd ratio in them is an order of magnitude higher than in sea water. This fact can be explained by assuming a significant role in the accumulation of platinum of organic matter [49], which is confirmed by the results of the model sorption experiments on interaction of inorganic forms of platinum with iron and manganese oxyhydroxides in the presence of low-molecular and high-molecular natural organic compounds. The obtained data were also confirmed in experiments with the use of marine colloidal fractions of different dimensions. These experiments made it possible to establish that at pH ~ 8 and salt concentration corresponding to the composition of sea water, platinum is extracted by marine suspended matter by 70%.

The chemical transformations of PGE also play a certain role during the low-temperature weathering (galmyrolysis) of the oceanic floor rocks at interaction of the oceanic crust with seawater and its derivates. A comparative study of palladium and platinum mobility in high-salt chloride media, close in composition to seawater derivatives, under dynamic conditions was considered on the example of interaction of model solutions containing chloride forms of palladium and platinum with oceanic serpentinites [50]. The composition of solutions and the kinetics of leaching demonstrate the palladium transfer and complete retention of platinum by serpentinites. It is supposed that palladium transport through the rock is realized by strong complex with thiosulfate-ion, which is formed during oxidation of sulfides of the rock [32]. These results confirm the increased mobility of palladium (in comparison with platinum) and the possibility of its transfer during serpentinization, i.e. the possibility of palladium and platinum fractionation in the hydrothermal process. This assumption is supported by the data on the change of noble metal content ratios in oceanic serpentinites [51].

The study of environmental pollution by platinum and related elements is also relevant for the zones of development of ore deposits and areas of processing of sulfide platinum-metal ores. Thus, according to the data [7], in the topsoil of some regions of the Kola Peninsula the platinum content exceeds 200 ppb, palladium—650 ppb. Getting into the soil in the form of nanosized particles, these metals in the environment undergo transformations determining their migration behavior: leaching by natural waters (surface and meteoric ones) with formation of soluble inorganic compounds, and also interaction with water and soil components with formation of modified particles and molecular compounds with organic ligands (the latter, according to calculations [25], can predominate in color surface waters typical for this region). Depending on the conditions, these transformations can promote both the transport of dissolved or pseudocolloidal PGE particles and their redeposition and accumulation on geochemical barriers.

The forms and ways of transfer of gold and silver by water flows in zones of development of ore deposits are studied in detail in works [34, 46].

Thus, the combination of data on the composition of aqueous solutions, the type of suspended matter, the forms of the studied elements and the behavior of their dominant forms in contact with sorption phases allow to predict the migration behavior and transport of PGE and gold in various natural environments, as well as to anticipate the possibility of environmental pollution due to technogenic accumulation of elements.

6 PGE and Gold Transfer by Carbon-Containing Media

The transport of ore material from its source to the ore deposition zone can be carried out with the participation of various migration forms of elements and fluids of different compositions. As noted above, hydrothermal transport of dissolved inorganic (chloride) forms of metals by acidic

NaCl water fluids is considered to be one of the possible mechanisms. In the presence of organic matter, the formation of organoelement and complex forms of PGE in fluids is possible. Fluid flows containing hydrocarbons can also serve as transporting medium for PGE and gold. In experiments [24, 52] the ability of natural organic media to mobilize (dissolve) the metals present in the host rocks associated with hydrocarbons, and transport them in concentrations sufficient for participation in ore-forming processes is proved.

The study of distribution of PGE chloride species between aqueous and organic phases shows that if organic substances (phases) are present in the system, complex chlorides can interact with them, forming compounds soluble in organic media. These transformations are well known for the transition of complex chlorides into organic media in the presence of low molecular weight substances (ketones, amines, organic sulfides). In natural conditions, such transferring compounds are, first of all, polyfunctional "geopolymers"—asphaltenes, as well as monomeric N–, O–, or S–containing compounds.

Under favorable physical and chemical conditions, for example, with an increase in temperature, organic compounds, including those mentioned above, can possess reducing properties. In liquid medium or at the interface of phases there will be reduction of dissolved forms of noble metals, especially gold, with formation of Me^0, clusters and nanosized particles, stable in hydrocarbon medium. Their dimensionality, shape and stability is determined by the properties and concentration of reducing and stabilizing agents, which can be, for example, organic matter or inorganic sulfides [53].

Reduction of noble metal compounds, followed by the formation of nanoparticles (NPs), in organic media is shown in [24]. When studying the behavior of gold in a solution obtained by extracting gold chlorides into octanol, it was found that at 160 °C, a characteristic pink coloration of the organic phase appears, that, in accordance with the plasmon resonance spectra (Fig. 5), indicates the formation of NPs. A similar spectrum of AuNPs obtained in other conditions is shown in Fig. 6. These experiments qualitatively confirm an important conclusion about the formation of noble metal NPs in organic media and the role of hydrocarbon transfer for both dissolved and nanosized forms. Under natural conditions, the kinetics of the process and the ratio of species will be determined by temperature, as well as the reactivity of organic compounds in natural fluid and the efficiency of NPs stabilization.

It should be emphasized that the mass transfer of metal particles is undoubtedly more efficient than the transport of dissolved forms, which is limited by the solubility of noble metal compounds. The important role of highly dispersed particles, the formation of which is characteristic of natural

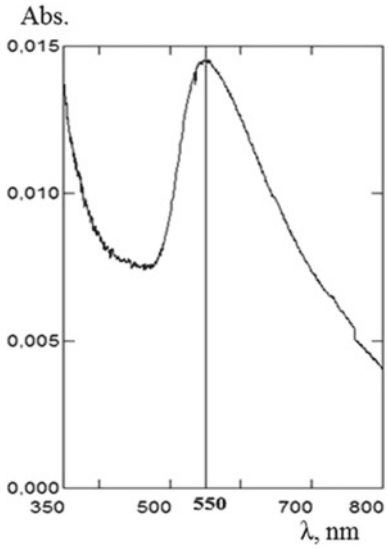

Fig. 5 Absorption spectrum of AuNPs formed in the organic phase at 160 °C

geological systems, in the dissipation and concentration of noble metals is discussed in a number of works [45, 54–56]. The concept of the role of colloidal gold in the formation of hydrothermal deposits has been recently developed especially actively [24, 57, 58].

Thus, organic matter of natural fluids plays a significant role in the transfer of noble metals under geological conditions. Various mechanisms are involved in this transport. Hydrocarbons and other organic compounds of different structure and composition (1) promote the transfer of noble metals halide forms from the aqueous phase to the organic phase coexisting with it in the fluid; (2) form strong mobile complex compounds with increased solubility; (3) participate in the formation and stabilization of nanosized PGE particles; (4) serve as a migration medium. Despite the progress in the development of instrumental methods, a significant place in the study of these processes is still occupied by experimental studies using synthesized model nanosized forms.

Although many works are devoted to the methods of noble metals (primarily gold) NPs synthesis, it follows from reviews [59, 60] that only a small part of them describes the preparation of these NPs in organic, especially nonpolar, media. In geochemical works, mainly AuNPs formed using low molecular weight organic compounds, citrate ion [58] and dodecantiol [61], have been used as models. To study the transport of PGE and gold by organic media, the NPs more typical for natural conditions, for example, AuNPs and PdNPs, stabilized by natural high-molecular weight compounds (geopolymers), are of interest.

In [62], in order to study the forms of transfer of noble metals by carbon-containing fluids, nanosized metals formed

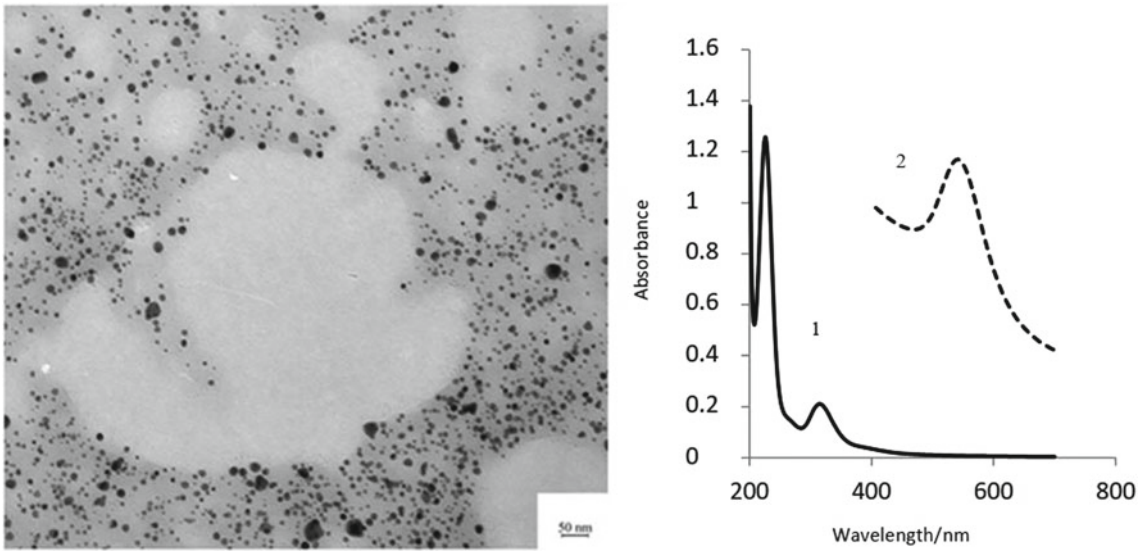

Fig. 6 TEM image and absorption spectra of molecular (1) and nanosized (2) forms of gold, stabilized with asphaltenes

in the presence of natural asphaltenes were obtained and investigated. Asphaltene molecules contain polycyclic structures with a large number of peripheral O–, N–, S–containing groups, are capable of forming strong covalent bonds and organized structures on the surface of NPs and therefore are effective stabilizers of noble metal NPs. The authors characterized the obtained NPs, studied their temperature and temporal stability, investigated the efficiency of noble metals transfer between the aqueous and organic phases with the aim of the subsequent use of nanosized forms for geochemical modeling of the processes of transfer and accumulation of PGE and gold.

NPs of noble metals in hydrocarbon media were obtained by the developed methods of two-phase synthesis. The size of PdNPs corresponds to the absorption wavelength of 542.5 nm (Fig. 6) and is 20–40 nm (spectrophotometry, TEM and DLS data). The problem of obtaining PdNPs lies in both the complexity of PdNPs formation and the difficulty in their identification because of similarity of optical characteristics of initial complex compounds of palladium (222–234 nm), PdNPs (230 nm) and natural organic substances (190–280 nm) in the UV region (Fig. 7). The synthesized PdNPs are single nanoparticles ranging in size from 5–7 nm and stable for at least several months.

Comparison of the properties of NPs stabilized with low- and high-molecular-weight model and natural ligands has shown that the most stable particles in organic media are formed in the presence of geopolymers—asphaltenes, which concentrate PGE and gold in natural conditions. This conclusion coincides with the data obtained earlier in the study of NPs in aqueous media. In [12], it was found that the colloidal stability of AuNPs obtained in the presence of a water-soluble high-molecular-weight ligand (FA), firmly covalently attached to the surface of NPs, was higher compared to particles modified with a low-molecular-weight citrate ion. The study of temperature stability of NPs, stabilized with natural asphaltenes, showed that they are stable up to temperatures of at least 200 °C. Thus, NPs of noble metals (palladium and gold) have sufficient temporal and temperature stability, which allows to assume the existence of these forms in natural conditions. On the other hand, this provides the possibility of their use as model phases in experimental modeling of the transport of noble metals by hydrocarbon liquids included in mantle fluids.

7 Conclusions

A promising approach to solving fundamental problems associated with the transfer and accumulation of PGE and gold is the study of the migration behavior of these metals in aqueous solutions and natural fluids through experimental modeling. The development of such an approach, which makes it possible to predict the behavior of these strategically important metals in natural and natural-technogeneous systems, is associated with the appearance and active use of modern means and methods of experimental research.

The difficulty of direct experimental study of PGE and gold in natural settings is due to the variety of forms of the occurrence of these elements in natural environments, their ultratrace contents in objects, the different nature of the interaction with the native sorption phases and a variety of transport mechanisms.

Modeling the transport of elements requires data on the stability, physico-chemical characteristics, transformations of the forms present in a specific natural system, their behavior

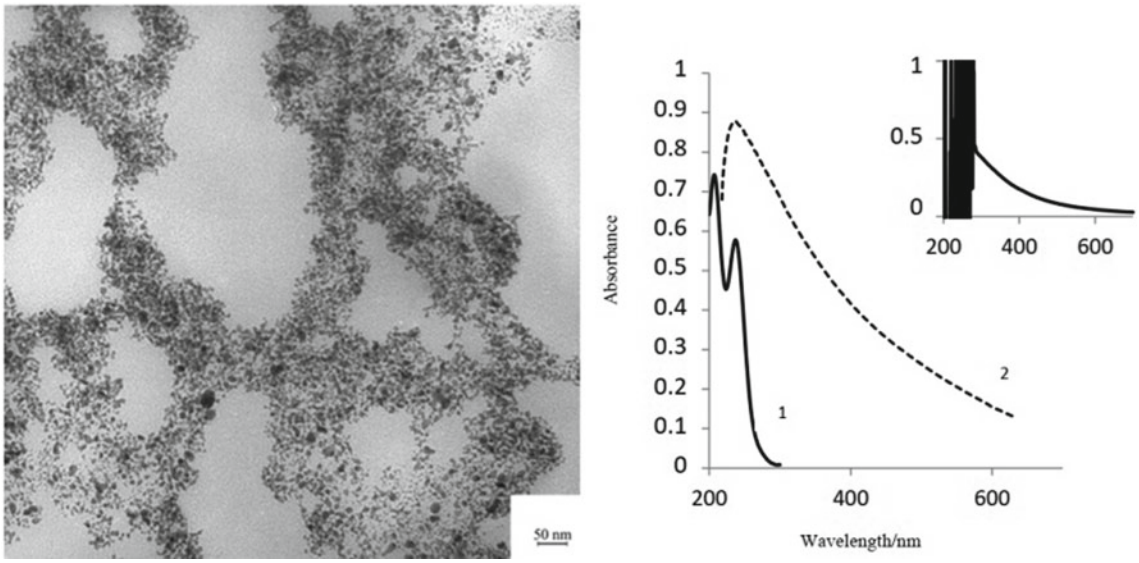

Fig. 7 TEM image and absorption spectra of molecular (1) and nanosized (2) forms of palladium stabilized by asphaltenes. Insert—spectrum of asphaltenes

at the interface, and transport pathways. Despite the large number of studies in this area, in particular those cited in this paper, the available information often incompletely characterizes the processes occurring in the system. Lack of data (related, for example, to the inability to determine thermodynamic characteristics) leads to distorted conclusions about the dominance of forms under specific conditions and the inability to calculate coexisting forms, predict transport, accumulation and/or fractionation of elements. An objective assessment of the efficiency of experimental modeling and the reliability of its results is the coincidence of modeling data with the results obtained for the real natural settings.

The directions of further development of studies of the geochemical behavior of PGE can include the following:

(1) Obtaining new data for poorly studied forms of PGE, first of all nanosized ones, capable to provide efficient mass transfer of metals and their accumulation at the level of tens and hundreds ppm (considered as sufficient for participation of PGE and gold in ore-forming processes).
(2) Development of methods for obtaining and characterization of the forms of elements promising for experimental modeling of their transfer with liquids included in mantle fluids. Development of experimental and computational ways to estimate the contribution of individual forms of noble metals in their distribution between immiscible or insoluble phases. Study of influence of environment and physicochemical (redox, temperature etc.) conditions on geochemical behavior of elements.
(3) Further exploration of the role of organic matter as a forming and transporting agent during transfer and accumulation involving different migration forms of elements and fluids of different composition.

Acknowledgements This work is conducted under the GEOKHI RAS state assignment.

References

1. Reith, F., Campbell, S.G., Ball, A.S., Pringe, A., Southam, G.: Platinum in earth surface environments. Earth Sci. Rev. **131**, 1–21 (2014)
2. Moldovan, M.: Origin and fate of platinum group elements in the environment. Anal. Bioanal. Chem. **388**(3), 537–540 (2007)
3. Ek, K.H., Morrison, G.M., Rauch, S.: Environmental routes for platinum group elements to biological materials-a review. Sci. Total Environ. **334–335**, 21–38 (2004)
4. Kabata-Pendias, A., Pendias, H.: Trace elements in soils and plants. CRC Press, Boca Raton (1986)
5. Ravindra, K., Bencs, L., Van Grieken, R.: Platinum group elements in the environment and their health risk. Sci. Total Environ. **318**, 1–43 (2004)
6. Hein, J.R., McIntyre B., Koschinsky, A.: The global enrichment of platinum group elements in marine ferromanganese crust // Ext. In: Abstract 10th international platinum symposium "platinum-group elements—from genesis to beneficiation and environmental impact". Oulu, Finland, pp 98–101 (2005)
7. Clemens, R., Heikki N.: Regional distribution of Pd, Pt and Au-emissions from the nickel industry on the Kola Peninsula, NW Russia, as seen in moss and humus samples. In: Zereini, F., Alt, F. (eds.) Palladium Emissions in the Environment: Analytical Methods, Environmental Assessment and Health Effects. Springer, Berlin–Heidelberg, p. 53 (2006)

8. Iavicoli, I., Bocca, B., Carelli, G., Caroli, S., Caimi, S., Alimonti, I., Fontana, L.: Biomonitoring of tram drivers exposed to airborne platinum, rhodium and palladium. Occupation. Environ. Health **81** (1), 109–114 (2007)
9. Dubiella-Jackowska, A., Kudłak, B., Polkowska Ż., Namieśnik J.: Environmental fate of traffic-derived platinum group metals. Crit. Rev. Anal. Chem. 39, 251–271 (2009)
10. Pilchin, A., Eppelbaum, L.: Concentration of platinum group elements during the early earth evolution: a review. Nat. Resour. **8**, 172–233 (2017)
11. Zereini, F., Skerstupp, B., Rankenburg, K., Dirksen, F., Beyer, J-M., Claus, T., Urban, H.: Anthropogenic emission of platinum-group elements (Pt, Pd and Rh) into the environment: concentration, distribution and geochemical behaviour in soils. J. Soils Sediments. **1**(I), 44 – 49 (2001)
12. Kubrakova, I.V., Tyutyunnik, O.A., Koshcheeva, I.Y., Sadagov, A.Y., Nabiullina S.N.: Migration behavior of platinum group elements in natural and technogeneous systems. Geochem. Int. **55** (1), 108–124 (2017)
13. Tagirov, B.R., Baranova, N.N., Zotov, A.V., Akinfiev, N.N., Polotnyanko, N.A., Shikina, N.D., Koroleva, L.A., Shvarov, Yu. V., Bastrakov, E.N.: The speciation and transport of palladium in hydrothermal fluids: experimental modeling and thermodynamic constraints. Geochim. Cosmochim. Acta. **117**, 348–373 (2013)
14. Tagirov, B.R., Trigub, A.L., Filimonova, O.N., Kvashnina, K.O., Nickolsky, M.S., Lafuerza, S., Chareev, D.A.: Gold transport in hydrothermal chloride-bearing fluids: insights from in-situ X-ray absorption spectroscopy and ab initio molecular dynamics. ACS Earth Space Chem. **3**(2), 240–261 (2019)
15. Tagirov, B.R., Filimonova, O.N., Trigub, A.L., Akinfiev, N.N., Nickolsky, M.S., Kvashnina, K.O., Chareev, D.A., Zotov, A.V.: Platinum transport in hydrothermal chloride-bearing fluids and melts: insights from in-situ X-ray absorption spectroscopy and thermodynamic modelling. Geochim. Cosmochim. Acta. **254**, 86–101 (2019)
16. Slobodskoy, R.M.: Organoelement compounds in magmatogenic and ore-forming processes. Novosibirsk: Nauka, 134 p. (1981) (in Russian)
17. Buslaeva, E.Y., Novgorodova, M.I.: Organoelement compounds in the problem of migration of ore matter. M.: Nauka, 152 p. (1989) (in Russian)
18. Simakin, A.G., Salova, T.P., Gabitov, R.I., Kogarko, L.N., Tyutyunnik, O.A.: Gold solubility in reduced carbon-bearing fluid. Geochem. Int. **57**(4), 400–406 (2019)
19. Simakin, A., Salova, T., Borisova, A.Y., Pokrovski, G.S., Shaposhnikova, O., Tyutyunnik, O., Bondarenko, G., Nekrasov, A., Isaenko, S.I.: Experimental study of Pt solubility in the CO-CO_2 fluid at low f_{O2} and subsolidus conditions of the ultramafic-mafic intrusions. Minerals **11**(2), 225 (2021)
20. Beskrovny, N.S.: Petroleum bitumen and hydrocarbon gases as satellites of hydrothermal activity. L.: Nedra, 209 p. (1967) (in Russian)
21. Zubkov, V.S., Razvozzhaeva, E.A.: Ore mineralization in naphtides and problems of its genesis. Geochem. Int. **50**(4), 309–318 (2012)
22. Kaminsky, F.V., Kulakova, I.I., Ogloblina, A.I.: Polycyclic aromatic hydrocarbons in carbonado and diamond. Trans. USSR Acad. Sci. **283**(4), 147–150 (1985)
23. Williams-Jones, A.E., Bowell, R.J., Migdisov, A.A.: Gold in solution. Elements **5**, 281–287 (2009)
24. Crede, L.-S., Liu, W., Evans, K.A., Rempel, K.U., Testemale, D., Brugger, J.: Crude oils as ore fluids: an experimental in-situ XAS study of gold partitioning between brine and organic fluid from 25 to 250 C. Geochim. et Cosmochim. Acta. **244**, 352–365 (2019)
25. Kubrakova, I.V., Fortygin, A.V., Lobov, S.G., Koshcheeva, I.Y., Tyutyunnik, O.A., Mironenko M.V.: Migration of platinum, palladium, and gold in the water systems of platinum deposits. Geochem. Int. **49**(11), 1072–1084 (2011)
26. Sassani, D.C., Shock, E.L.: Solubility and transport of platinum-group elements in supercritical fluids: summary and estimates of thermodynamic properties of ruthenium, rhodium, palladium and platinum solids aqueous ions, and complexes to 1000°C and 5 kbar. Geochim. Cosmochim. Acta **62**(15), 2643–2671 (1998)
27. Wood, S.A., Mountain, B.W., Pan, P.: The aqueous geochemistry of platinum, palladium and gold: recent experimental constraints and a reevaluation of theoretical predictions. Can. Mineral. **30**, 955–982 (1992)
28. Turner, A.: Particle-water interactions of platinum group elements estuarine condition. Mar. Chem. **103**, 103–111 (2007)
29. Kubrakova, I.V., Varshal, G.M., Pogrebnyak, Y.V., Kudinova, T. F.: Species of platinum and palladium migration in natural waters. In: Ostroumov, E. A. (ed.) Chemical Analysis of Marine Sediments. Nauka, Moscow, 103–119 (1988) (in Russian).
30. Koshcheeva, I.Y., Kubrakova, I.V., Korsakova, N.V., Tyutyunnik O.A.: Solubility and migration ability of rhodium in natural conditions: model experimental data. Geochem. Int. **54** (7), 624–632 (2016)
31. van Middlesworth, J.M., Wood, S.A.: The stability of palladium (II) hydroxide and hydroxyl–chloride complexes: an experimental solubility study at 25–85°C and 1 bar. Geochim. Cosmochim. Acta. **63**, 1751–1765 (1999)
32. Tyutyunnik, O.A., Kubrakova, I.V., Pryazhnikov, D.V.: Formation and sorption behavior of the palladium thiosulfate complexes under natural conditions (model experiments). Geochem. Int. **1**, 85–91 (2016)
33. Kubrakova I.V., Pryazhnikov D.V., Koshcheeva I.Ja., Tyutyunnik O.A., Korsakova N.V., Chkhetija D.N., Krigman L.V.: Formation and fate of gold tiosulfate under the leaching of sulphide rocks (experimental study) Vestn. Otd. Nauk Zemle RAN, 3 (2011). NZ6059. https://doi.org/10.2205/2011NZ000189
34. Myagkaya, I.N., Lazareva, E.V., Gustaytis, M.A., Zhmodik, S.M.: Gold and silver in a system of sulfide tailings. Part 1: migration in water flow. J. Geochem. Exploration 160, 16–30 (2016)
35. Varshal, G. M., Velyukhanova, T. K., Koshcheeva, I. Ya., Kubrakova, I. V., Baranova, N. N.: Complexation of noble metals with fulvic acids and its geochemical role. In: Analytical Chemistry of Trace Elements. Nauka, Moscow, pp. 112–145 (1988) [in Russian].
36. Morel, F. M. M., Milligan, A. J. , Saito, M. A.: Marine bioinorganic chemistry. The role of trace metals in the oceanic cycles of major nutrients. In: Holland H. D., Turekian, K. K. (eds.) Treatise on Geochemistry, vol. 6, pp. 113–143, Elsevier (2003)
37. Sobrova, P., Zehnalek, J., Adam, V., Beklova, M., Kizek, R.: The effects on soil/water/plant/animal systems by platinum group elements. Cent. Eur. J. Chem. **10**(5), 1369–1382 (2012)
38. Wood, S.A.: The interaction of dissolved Pt with fulvic acid and simple organic acids analogues in aqueous solution. Can. Mineral. **28**, 665–673 (1990)
39. Koshcheeva I.Ya., Korsakova N.V., Tyutyunnik O.A., Kubrakova I.V.: Interaction of Rh(III) with humic acids and components of natural adsorption phases. Geochem. Int. **56**(3). 711–718 (2018)
40. Baalousha, M., Motelica-Heino, M., Coustumer, P.L.: Conformation and size of humic substances: Effects of major cation concentration and type, pH, salinity, and residence time. Colloids Surf. A: Physicochem. Eng. Aspects **272**, 48–55 (2006)

41. Bratskaya, S.Y., Solk, V.A., Ivanov, V.V., Ustinov, A.Y., Barinov, N.N., Avramenko, V.A.: A new approach to precious metals recovery from brown coals: correlation of recovery efficacy with the mechanism of metal–humic interactions. Geochim. Cosmochim. Acta **73**, 3301–3310 (2009)
42. Avramenko, V. A., Bratskaya, S. Yu., Yakushevich, A. S., Voit, A. V., Ivanov, V. V., Ivannikov, S. I.: Humic acids in brown coals from the southern Russian far east: general characteristics and interactions with precious metals. Geochem. Int. 50 (5), 437–446 (2012)
43. Kubrakova, I.V., Kiseleva, M.S.: Microwave synthesis of nano-sized model substances and sorption materials. Appl. Geochem. Res. Geochem. Int. **54**(13), 1273–1281 (2016)
44. Zhmodik, S.M., Kalinin, Y.A., Roslyakov, N.A., Belyanin, D.K., Nemirovskaya, N.A., Nesterenko, G.V., Airiyants, E.V., Moroz, T. N., Bul'bak, T.A., Mironov, A.G., Mikhlin, Y.L., Spiridonov, A. M.: Nanoparticles of noble metals in a supergene environment. Geol. Ore Depos. **54**(2), 141–154 (2012)
45. Nemerov, V.K., Razvozzhaeva, E.A., Spiridonov, A.M., Sukhov, B.G., Trofimov, B.A.: Nanodispersed state of metals and their migration in carbonaceous natural media. Dokl. Earth Sci. **425**(2), 334–337 (2009)
46. Myagkaya, I.N., Lazareva, E.V., Gustaytis, M.A., Zhmodik S.M.: Gold and silver in a system of sulfide tailings. Part 2: reprecipitation on natural peat. J. Geochem. Exploration. 165, 8–22 (2016)
47. Varshal, G.M., Veliukhanova, T.K., Chkhetiya, D.N., Kholin, Yu. V., Shumskaya, T.V., Tyutyunnik, O.A., Koshcheeva, I.Ya., Korochantsev, A.V.: Sorption on humic acids as a basis for the mechanism of primary accumulation of gold and platinum group elements in black shales. Lithol. Miner. Resour. **35**(6), 538–545 (2000)
48. Kubrakova, I. V., Nikulin, A. V., Koshcheeva, I. Y., Tyutyunnik, O. A.: Platinum metals in environment: content, determination, and behavior in natural systems. Chem. Sustain. Deve. **20**(6), 593–603 (2012)
49. Kubrakova, I. V. Koshcheeva, I. Ya., Tyutyunnik, O. A. Asavin, A. M.: Role of Organic matter in the accumulation of platinum in oceanic ferromanganese deposits. Geochemistry Int. **48** (7), 655–663 (2010)
50. Kubrakova, I.V., Tyutyunnik, O.A., Silantyev, S.A.: Mobility of dissolved palladium and platinum species during the water-rock interaction in a chloride environment: modeling of pge behavior during interaction between oceanic serpentinites and seawater derivatives. Geochem. Int. **57**(3), 282–289 (2019)
51. Silantyev, S.A., Kubrakova, I.V., Tyutyunnik, O.A.: Distribution of siderophile and chalcophile elements in serpentinites of the oceanic lithosphere as an insight into the magmatic and crustal evolution of mantle peridotites. Geochem. Int. **54**(12), 1019–1034 (2016)
52. Migdisov, A.A., Guo, X., Xu, H., Williams-Jones, A.E., Sun, C.J., Vasyukova, O., Sugiyama, I., Fuchs, S., Pearce, K., Roback, R.: Hydrocarbons as ore fluids. Geochem. Persp. Let. **5**, 47–52 (2017)
53. Mikhlin, Y., Likhatski, M., Karacharov, A., Zaikovski, V., Krylov, A.: Formation of gold and gold sulfide nanoparticles and mesoscale intermediate structures in the reactions of aqueous $HAuCl_4$ with sulfide and citrate ions. Phys. Chem. Chem. Phys. **11** (26), 5445–5454 (2009)
54. Moiseenko, V.G.: From gold atoms through clusters, nano- and microscopic particles to precious metal nuggets. Blagoveshchensk: Institute of Geology and Environmental Management of the Russian Academy of Sciences, 187 p. (2007) (in Russian)
55. Seredin, V.V.: Distribution and formation conditions of noble metal mineralization in coal-bearing basins. Geol. Ore Deposits **49** (1), 1–30 (2007)
56. Vasil'eva, I.E., Shabanova, E.V., Goryacheva, E.M., Sotskaya, O. T., Labusov, V.A., Nekludov, O.A., Dzyuba, A.A.: Noble metals in black shales of the sukhoi log gold deposit (East Siberia): evidence from scintillation arc atomic-emission spectrometry. Russian Geol. Geophys. **59** (8), 997–1009 (2018)
57. Saunders, J.A., Burke, M.: Formation and aggregation of gold (electrum) nanoparticles in epithermal ores (review). Minerals. **7** (163), 11 (2017)
58. Liu, W., Chen, M., Yang, Yi., Mei, Yu., Etschmann, B., Brugger, J., Johannessen, B.: Colloidal gold in sulphur and citrate-bearing hydrothermal fluids: an experimental study. Ore Geol. Rev. 114, 103-142 (2019)
59. Saldan, I., Semenyuk, Y., Marchuk, I., Reshetnyak, O.: Chemical synthesis and application of palladium nanoparticles. J. Mater. Sci. **50**(36), 2337–2354 (2015)
60. Dykman, L.A., Khlebtsov, N.G.: Methods for chemical synthesis of colloidal gold. Russ. Chem. Rev. **88**(3), 229–247 (2019)
61. Crede, L.-S., Evans, K.A., Rempel, K.U., Grice, K., Sugiyama, I.: Gold partitioning between 1-dodecanethiol and brine at elevated temperatures: implications of Au transport in hydrocarbons for oil-brine ore systems. Chem. Geology **504**, 28–37 (2019)
62. Kubrakova, I.V., Nabiullina, S.N., Tyutyunnik, O.A.: Noble metal nanoparticles functionalized by natural asphaltenes as model phases for geochemical research. Mendeleev Commun. **30**, 815–816 (2020)

Study of Elemental Composition and Properties of Volcanic Ash and Urban Dust Nanoparticles

P. S. Fedotov, M. S. Ermolin, and A. I. Ivaneev

1 Introduction

Nanoparticles formed as a result of natural and anthropogenic processes are ubiquitous in the environment and are an integral component of terrestrial, air and aquatic ecosystems [1]. Depending on the source of origin, environmental nanoparticles are divided into two main groups: natural and anthropogenic ones. Natural nanoparticles exist on our planet since time immemorial and are components of the soil, dust, and volcanic ash. Volcanic eruptions are one of the main sources of natural nanoparticles in the environment. According to recent estimates, the annual flux of volcanic eruptions to the total amount of natural nanoparticles is about 22 million tons [1]. During an eruption, volcanic ash nanoparticles can be ejected to a height of tens of kilometers and reach the stratosphere, where they then spread around the entire globe, affecting different regions for years [2]. It is known that natural nanoparticles can play an important role in natural processes [1]. For example, it has been suggested that nanomineral surfaces were involved in the processes of protocell self-assembly and early evolution of bacterial cell walls [3, 4]. It has been shown that iron-containing nanoparticles as a source of nutrients can increase the bioproductivity of phytoplankton [5–7], influence the geochemical carbon cycle [8, 9] and, consequently, the climate change [1]. It has also been established that periods of active volcanism on our planet coincide with its global cooling [10], which was caused by the absorption and scattering of solar radiation by volcanic ash particles in the atmosphere [11].

Anthropogenic nanoparticles, in turn, are divided into two subgroups: engineered and incidental ones [12]. The rapid development of nanotechnology inevitably leads to the release of engineered nanoparticles, intentionally created by man, into the environment. Engineered nanoparticles have become part of people's everyday life as components of electronics (elements and coatings of electronic circuits and processors), cosmetic products, food additives, systems for drug delivery, sensors for bacterial recognition, etc. [13–17].

Incidental nanoparticles are a by-product of human activity. Industrial emissions, mining, wear of automobile and aircraft engine parts, use of fossil fuels in power stations, and many other anthropogenic processes are sources of formation of incidental nanoparticles. It should be noted that in the urban environment technogenic nanoparticles are mainly formed as a result of industrial and construction activities as well as a result of waste disposal and recycling [18–21].

Huge amounts of nanoparticles released into the environment can have adverse effects on human health. Mineral dust and volcanic ash nanoparticles are known to be toxic for living beings and may have carcinogenic effects [21–23]. The chemical composition of nanoparticles plays an important role [22, 23]. For example, it has been shown that volcanic ash with a high content of iron-containing nanoparticles can cause oxidative DNA damage in mononuclear cells of the human peripheral circulatory system [24] since iron promotes the formation of a harmful hydroxyl radical upon contact with hydrogen peroxide [24]. Anthropogenic nanoparticles also pose a threat to human health [19, 25, 26].

The study of environmental nanoparticles is of a fundamental geochemical significance. A new scientific area, nanogeochemistry, has been proposed [27, 28], the subject of which is geochemical reactions occurring in the nanometer size range, the features of nanostructure formation in geological systems and their influence on geochemical processes [27]. It should be noted that environmental nanoparticles have become the object of study only in the last two decades, which is associated with the development of new instrumental methods of analysis.

P. S. Fedotov · M. S. Ermolin (✉) · A. I. Ivaneev
Vernadsky Institute of Geochemistry and Analytical Chemistry, Russian Academy of Sciences, 19 Kosygin St, Moscow, 119991, Russia
e-mail: ermolin@geokhi.ru

V. P. Kolotov and N. S. Bezaeva (eds.), *Advances in Geochemistry, Analytical Chemistry, and Planetary Sciences*,
https://doi.org/10.1007/978-3-031-09883-3_5

2 Problems of Isolation and Quantitative Analysis of Environmental Nanoparticles

Until now there is a noticeable gap in the study of the chemical composition of natural nanoparticles and their behavior in the environment. One of the main reasons for this is the difficulty of isolating nanoparticles from polydisperse environmental samples for further study and quantitative analysis. The fraction of nanoparticles in polydisperse environmental samples, such as dust [29] and volcanic ash [30], can be only of the order of 10^{-2} wt. %, so isolating nanoparticle fractions sufficient for subsequent quantitative analysis is not an easy task. There are various methods for the isolation of nanoparticle fractions from environmental samples, among which membrane filtration, sedimentation, and field-flow fractionation in a rotating coiled column (RCC), or coiled tube field-flow fractionation should be particularly mentioned. The efficiency of these methods in the isolation of environmental nanoparticles, their advantages and limitations were studied in detail on the example of ash samples from the volcanoes Puyehue (Chile), Tolbachik and Klyuchevskoy (Kamchatka, Russia) [31].

As an example, Fig. 1 represents the particle size distribution of Klyuchevskoy volcanic ash fractions isolated by methods of fractionation in RCC, sedimentation, and membrane filtration. It is shown that using the methods of membrane filtration and fractionation in RCC fractions containing only particles smaller than 400 nm can be isolated from the original samples. In turn, the fractions separated by sedimentation, in addition to particles smaller than 400 nm, also contain submicron particles ranging in size from 400 to 900 nm ($\leq 5\%$) [31].

It is found that among the considered methods of nanoparticle separation, membrane filtration is characterized by the lowest separation efficiency. The mass of nanoparticles separated by the filtration method was an order of magnitude smaller than the mass of nanoparticles separated by sedimentation and fractionation in RCC (Table 1). In this connection, the concentrations of most trace elements in the nanoparticle fraction isolated by the membrane filtration method were below the detection limits [31].

The method of particle fractionation in RCC was shown to reduce the separation time down to 2 h as compared to the sedimentation method (48 h), but its application requires the use of special equipment (planetary centrifuge). The fractions of nanoparticles isolated in RCC contained the highest amount of nanoparticles compared to the fractions isolated by membrane filtration and sedimentation. In addition, the results of the analysis of the isolated fractions show that the particle fractionation method in RCC has the highest repeatability and can be successfully used to isolate nanoparticles from polydisperse environmental samples for their subsequent study. Nevertheless, the sedimentation method, along with the fractionation in RCC, can also be used for the isolation of environmental nanoparticle fractions for their further characterization and analysis.

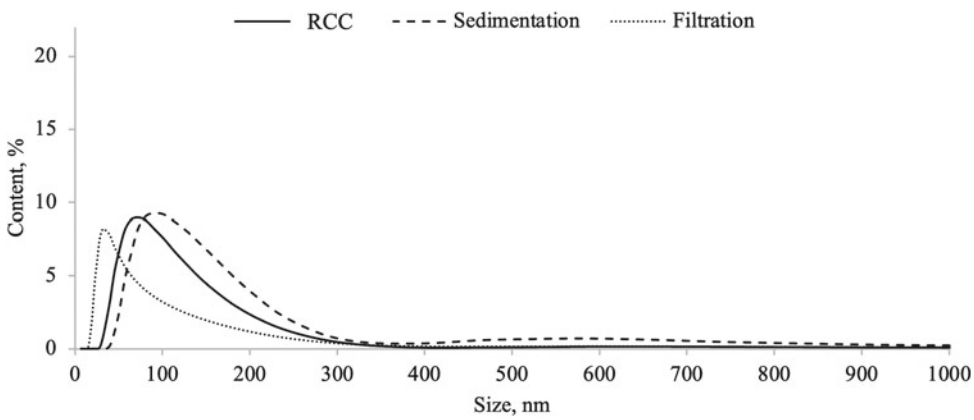

Fig. 1 Size distribution of nanoparticle fractions separated from Klyuchevskoy volcanic ash by field-flow fractionation in RCC, sedimentation, and membrane filtration; according to laser diffraction data [31]

Table 1 Calculated masses of nanoparticles separated from volcanic ash samples by filtration, sedimentation, and field-flow fractionation in RCC [31]

Sample	Calculated masses of nanoparticle fractions, mg		
	Filtration	Sedimentation	RCC
Puyehue	0.03 ± 0.01	0.22 ± 0.09	0.06 ± 0.02
Tolbachik	0.03 ± 0.01	0.38 ± 0.06	0.45 ± 0.07
Klyuchevskoy	–*	0.31 ± 0.03	0.51 ± 0.05

* Fraction mass was not calculated as concentrations of most macro elements were below the detection limits

One of the main parameters of environmental particles are their size as well as particle size distribution. In order to determine the morphology, size and particle size distribution of environmental particles, particularly nanoparticles, methods of field-flow fractionation, electron microscopy, light scattering and capillary electrophoresis are commonly used [25, 32, 33]. Nanoparticles should be characterized and analyzed by complementary methods of light scattering and electron microscopy. It should be noted that the size distribution of nanoparticles determined by light scattering methods may be distorted due to polydispersity of suspensions and non-sphericity of particles, which is typical for natural nanoparticles. In this case, the results obtained by light scattering methods need to be confirmed by electron microscopy. Characterization by microscopy provides accurate information on the morphology, shape and size of particles due to their visualization [34, 35].

Various analytical methods can be used to assess the elemental and mineral composition of environmental nanoparticles. They include X-ray spectroscopy (X-ray energy dispersive microanalysis, X-ray diffraction analysis), inductively coupled plasma mass spectrometry (ICP-MS), inductively coupled plasma atomic emission spectrometry (ICP-AES), atomic absorption spectrometry. To assess the results of elemental analysis, it is recommended to determine the concentrations of some elements in the studied environmental nanoparticles by two independent methods of analysis, which allows to control the accuracy of measurements by means of statistical comparison of the values of the concentrations of the corresponding elements obtained by two independent methods [25, 36]

3 Pre-concentration of Trace Elements by Nanoparticles of Urban Dust and Volcanic Ash

As has been noted earlier, determination of the chemical composition of environmental nanoparticles is directly related to the procedure of their separation from polydisperse samples, and the isolation of nanoparticles is complicated due to their low content in the initial polydisperse samples. For this, a comprehensive approach including isolation of nanoparticles by coiled tube field-flow fractionation and subsequent analysis of nanoparticles by ICP-AES and ICP-MS methods after acid decomposition was proposed [30, 37].

For the first time nanoparticles of the urban dust have been isolated and quantitatively analyzed using Moscow dust samples [38]. Uneven distribution of heavy metals between fractions of nano-, submicro- and microparticles of Moscow dust was revealed (Fig. 2). It is shown that the content of heavy metals in the dust particles increases with decreasing particle size. It has been demonstrated that the content of Zn, Cr, Ni, Cu, Cd, Sn, Pb, etc., in the Moscow dust nanoparticles can be tens and even hundreds of times higher than in the initial polydisperse dust samples [38].

In modern cities transport is one of the main sources of environmental pollution. Road dust is a composite sample containing anthropogenic particles, along with natural ones. Natural particles, as a rule, are mineral particles resulting from soil weathering. Anthropogenic particles can be sourced from asphalt wearing, vehicle brake pads and tires wearing, fuel combustion, etc. These anthropogenic particles

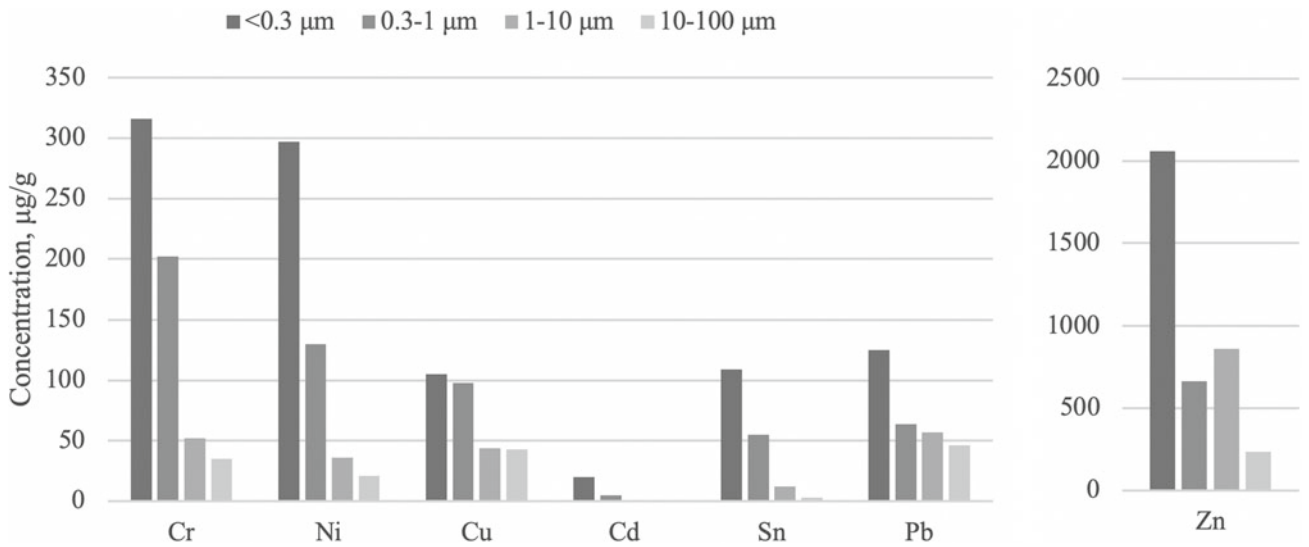

Fig. 2 Concentration of heavy metals in nano-, submicro- and microparticle fractions of Moscow urban dust [38]

contain toxic elements. For instance, particles sourced from the wear of car brake pads contain Ca, Ti, Fe, Cu, Ba, Sb [39–43]. Increased copper content is considered to be the main indicator of road dust contamination by brake pad particles [42]. The wear of tires is a source of particles containing Al, Si, S, Ca, Zn [39]. ZnO is applied in the production of tires, so increased Zn content in urban dust often indicates its contamination by the products of tire wear [41]. Cd may also be present in tire wear particles because it is containing in zinc oxide [44]. The tire wear also results in Sb pollution of urban dust because Sb_2S_5 is used as a colorant in the production of automobile rubber [45]. The wear of pavement is an important source of anthropogenic dust particles as well. For instance, Na, Mg, Al, K, Ca, Ti, Fe and to a lesser extent V, Cr, Co, Ni, Cu, Zn, Pb are characteristic for the particles resulting from asphalt wear [39, 40]. Besides, TiO_2 is used as a white colorant for road markings that results in the pollution of urban dust with Ti. Emissions of products of fuel combustion also lead to the pollution of urban dust. Ni and V are the main markers of this pollution [46]. It is known that automobile catalytic converters used to reduce emissions of carbon monoxide, nitrogen oxides and hydrocarbons resulting from incomplete fuel combustion [47, 48] are a source of Pt, Pd and Rh [48–50].

Studies of road dust on Moscow highways (the Third Ring Road and Leninsky Prospekt) have been carried out. It is revealed that nanoparticles of road dust accumulate toxic metals and metalloids (Ni, Cu, Zn, Cd, Ag, Sn, Sb, Hg, Tl, Pb, Bi) whose content is tens and hundreds of times higher than their total content in dust (Fig. 3) [29]. In addition, Pt (up to 0.7 μg/g) was found in the nanoparticles of road dust, the presence of which is caused by the wear of automotive catalysts.

Thus, it has been demonstrated that nanoparticles of dust can accumulate toxic elements from the environment and serve as their carriers. Taking into account the extremely high mobility of nanoparticles in the environment and their ability to penetrate into the human body during breathing, nanoparticles of urban dust can pose a serious threat to human health and therefore require special ecoanalytical control.

The study of volcanic ash nanoparticles is an important task in assessing the transport of chemical elements both regionally and globally. For the first time, the concentrations of major and trace elements in volcanic ash nanoparticles were estimated using ash from the Kamchatka volcanoes Tolbachik and Klyuchevskoy, as well as from the Chilean volcano Puyehue (Table 2) [51]. Field-flow fractionation in RCC was used to isolate nanoparticles.

It was shown that the concentration of toxic and potentially toxic metals and metalloids (Ni, Cu, As, Se, Ag, Cd, Sn, Te, Hg, Tl, Pb, and Bi) in volcanic ash nanoparticles significantly exceeds their total concentration in the initial polydisperse ash samples [51]. The concentration ratios of Ni, Cu, As, Se, Ag, Cd, Sn, Te, Hg, Tl, Pb, and Bi by volcanic ash nanoparticles relative to the bulk element content vary in the range from 10 to 500 (Fig. 4). Such elements as As, Se, Te, Hg, and Bi have the highest concentration factors (at the level of hundreds). For Ni, Ag, Cd, Sn, Tl, Pb also revealed high concentration factors in the range from 30 to 100.

It has been found that the accumulation of elements in nanoparticle fraction depends on volatility of elements. Thus, for example, the most volatile Hg, Te, As, Se are characterized by the highest concentration factors (Fig. 4). There are two main mechanisms of element concentration in

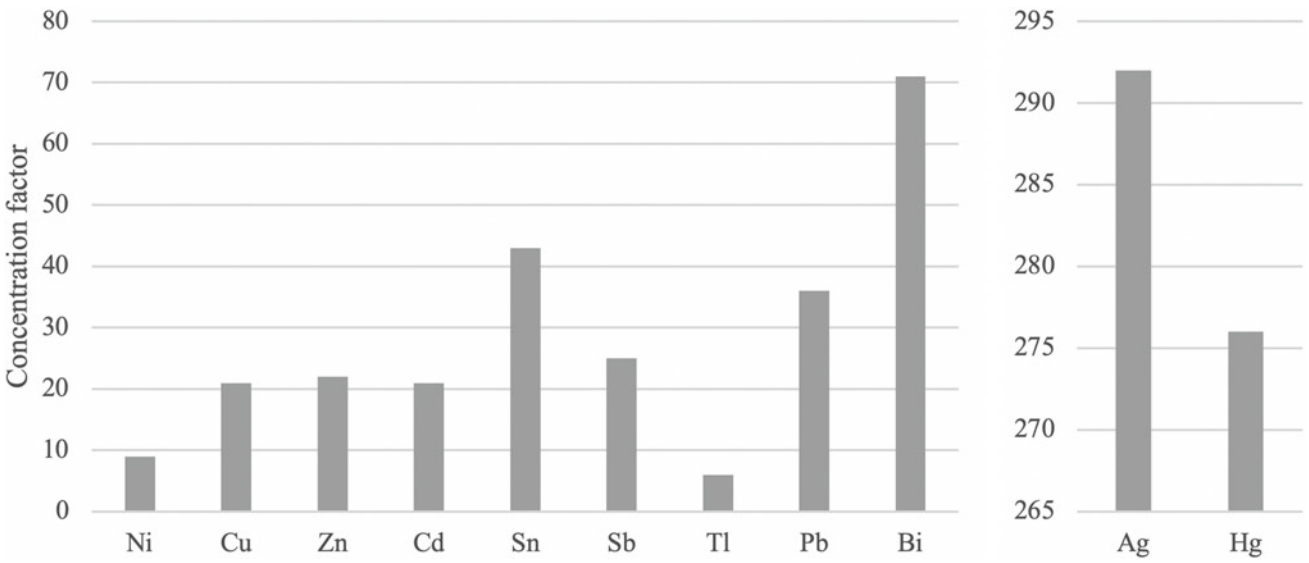

Fig. 3 Concentration factors of toxic metals and metalloids by Moscow road dust nanoparticles (relative to the total content) [29]

Table 2 Concentrations of elements in nanoparticles of Tolbachik, Klyuchevskoy and Puyehue volcanic ashes [51]

Element	Clark in the Earth's crust	Tolbachik		Klyuchevskoy		Puyehue	
		Total concentration	Concentration in nanoparticles	Total concentration	Concentration in nanoparticles	Total concentration	Concentration in nanoparticles
	%						
Na	2.4	2.8	1.0 ± 0.3	2.4	2.3 ± 0.3	3.6	3.1 ± 0.3
Al	8.2	8.4	6.5 ± 2.5	8.6	11.8 ± 0.9	7.4	8.3 ± 0.1
Si	28.2	–	20.6 ± 2.4	–	21.6 ± 1.8	–	29.6 ± 2.1
K	2.1	2.0	0.6 ± 0.1	0.8	0.5 ± 0.2	2.3	1.3 ± 0.1
Ca	4.2	5.1	2.8 ± 1.0	5.7	6.3 ± 0.9	1.6	4.9 ± 3.0
Fe	5.6	6.9	20.0 ± 6.0	6.2	10.1 ± 0.8	2.9	3.9 ± 0.3
	µg/g						
Ni	75	9	$(0.28 \pm 0.03) \times 10^3$	22	<26	0.7	49 ± 6
Cu	55	0.24×10^3	$(2.4 \pm 0.4) \times 10^3$	68	$(0.92 \pm 0.06) \times 10^3$	16.4	<47
As	1.8	3.4	$(0.7 \pm 0.1) \times 10^3$	0.6	<2	4.0	<17
Se	0.05	<2.5	$(0.3 \pm 0.1) \times 10^3$	<0.7	<34	1.6	<60
Ag	0.07	0.10	6.4 ± 1.2	0.07	3.1 ± 0.8	0.1	6 ± 4
Cd	0.2	<0.03	1.7 ± 0.8	0.1	3.3 ± 0.8	0.1	2.7 ± 0.6
Sn	2	1.6	65 ± 15	0.9	38 ± 9	2.6	29 ± 5
Te	–	<0.05	27 ± 9	<0.05	9.3 ± 3.6	<0.07	<1.6
Hg	0.08	0.07	29 ± 7	0.08	36 ± 4	<0.08	9 ± 7
Tl	0.45	0.19	19 ± 3	0.08	7 ± 1	0.5	11 ± 1
Pb	12.5	7	$(0.24 \pm 0.04) \times 10^3$	3	62 ± 12	23	$(0.16 \pm 0.03) \times 10^3$
Bi	0.17	0.10	35 ± 10	0.06	6.1 ± 0.4	0.22	35 ± 6
La	30	21	38 ± 7	7	13 ± 4	29	40 ± 2
Ce	60	51	95 ± 17	18	31 ± 10	66	84 ± 4
Pr	8.2	7.5	14 ± 2	2.8	4.5 ± 1.3	8.6	11 ± 1
Nd	28	33	63 ± 8	13	22 ± 4	37	48 ± 4
Y	33	40	51 ± 9	22	27 ± 3	53	59 ± 2
Gd	5.4	7.7	12 ± 2	3.9	6 ± 1	8.6	10 ± 1
Dy	3.0	7.2	10 ± 2	4.0	5.4 ± 0.4	8.8	10.4 ± 0.4
Ho	1.2	1.5	2.0 ± 0.3	0.9	1.1 ± 0.1	1.8	2.1 ± 0.1
Th	9.6	3.2	8 ± 1	0.6	1.5 ± 0.3	8.6	15 ± 2
U	2.7	1.7	1.8 ± 0.3	0.5	0.9 ± 0.1	2.3	3.3 ± 0.2

nanoparticle fraction: sorption and/or desublimation. Nanoparticles, due to their high specific surface and reactivity, can sorb the elements from the gaseous phase during eruption. On the other hand, a sharp drop in temperature at the crater outlet may result in desublimation of elements from the gaseous phase and the formation of individual nanoparticles of these elements. Studying the forms of elements in volcanic ash nanoparticles is a separate important task, the solution of which is necessary to assess the behavior of nanoparticles in the environment and their role in geochemical processes.

4 Study of Element Species in Volcanic Ash Nanoparticles

It is known that the mobility, bioavailability, and toxicity of chemical elements depend not only on their concentration, but also on their chemical species. The task of determining the species of metals and metalloids in volcanic nanoparticles can be partially solved by the method of single particle inductively coupled plasma mass spectrometry (SP-ICP-MS). The SP-ICP-MS method makes it possible to detect single

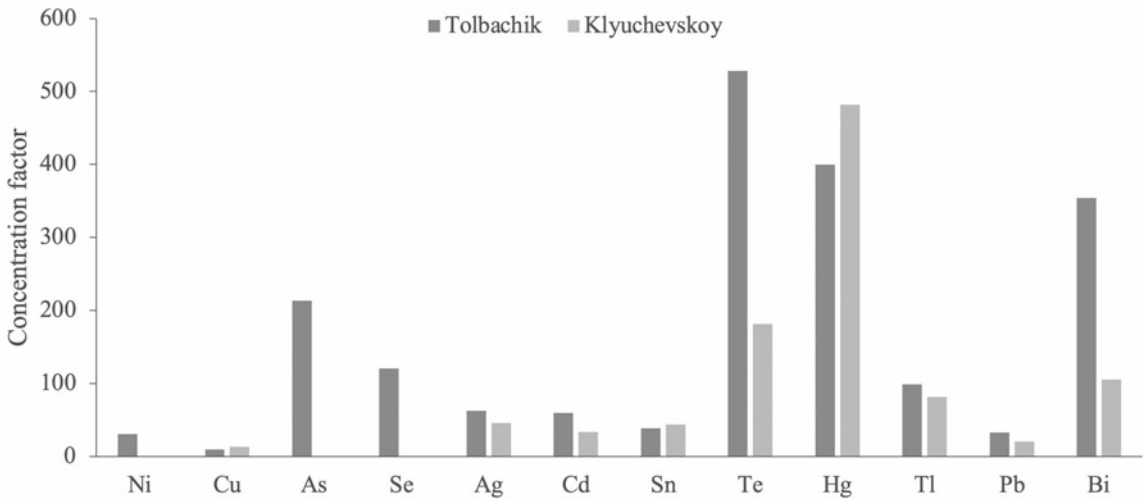

Fig. 4 Concentration factors of heavy metals by Tolbachik and Klyuchevskoy volcanic ash nanoparticles (relative to the total content) [51]

(individual) nanoparticles in highly diluted suspensions and obtain information on the concentration and size distribution of metal and metalloid nanoparticles [52–55].

As mentioned above, metals and metalloids can be present in volcanic ash nanoparticles either in sorbed form or as individual nanoparticles (e.g., oxides). If trace elements are sorbed on pyroclastic particles their content in these particles should be at trace level and their determination is impossible due to insufficient sensitivity of method. If metals and metalloids are in volcanic ashes in the form of separate nanoparticles, they behave as major components, and their determination by SP-ICP-MS becomes possible.

The results of the analysis of ash nanoparticle suspensions of Tolbachik and Klyuchevskoy volcanoes show that the concentrations of Ni, Zn, Ag, Cd, Tl, Pb, Bi, Te and Hg can be three orders of magnitude higher than in the corresponding suspension filtrates used as control samples (Fig. 5) [56]. Thus, we can conclude that these elements are found in the ash nanoparticles of Tolbachik in the form of individual nanoparticles. Analysis of nanoparticles of Klyuchevskoy volcano ash also showed that Ni, Zn, Ag, Cd, Tl, Pb, Bi, and Te are contained in nanoparticles in the form of individual nanoparticles [56].

Taking into account rather severe conditions of nanoparticles formation (high temperature and oxidizing environment), it can be assumed that these elements are in oxidized form. It should be noted that, for example, bismuth oxide nanoparticles were found in the upper stratosphere in 1985; the presence of these nanoparticles was attributed to large volcanic eruptions in the early 1980s [57]

The size distribution of metal and metalloid nanoparticles in the ashes of Tolbachik and Klyuchevskoy volcanoes was also estimated using SP-ICP-MS (Fig. 6) [56] It is found that the average size of detected metal and metalloid nanoparticles varies from 12 to 74 nm (depending on the element). As can be seen from the figure, Ag, Tl, Pb and Bi nanoparticles have the smallest size ranging from 12 to 28 nm. The average size of Ni, Zn, Cd and Hg nanoparticles varies from 34 to 55 nm. Te nanoparticles have the largest average size, about 70–74 nm. In SP-ICP-MS analysis, the nanoparticle size is calculated assuming that nanoparticles are spherical and monometallic. Obviously, due to the harsh conditions of formation, metallic nanoparticles of volcanic ash are not mono-elemental but represent some compounds. The density, for example, of element oxides is somewhat lower than the density of elements (about 1.1–1.6 times), so the true size of metal oxide nanoparticles may be somewhat underestimated.

Thus, it is shown that metals and metalloids are contained in volcanic ash as individual nanoparticles. However, metals and metalloids can also present as adsorbed species on pyroclastic nanoparticles [56]. To assess the relationship of the two forms, element concentrations in volcanic ash nanoparticles determined by both SP-ICP-MS and ICP-MS after acid decomposition were compared. The concentration of elements determined after acid decomposition is the total concentration of elements contained as individual nanoparticles and adsorbed on pyroclastic nanoparticles. Concentrations of Ni, Zn, Tl, As and Hg in nanoparticles of Tolbachik volcanic ash were found not to differ significantly. Thus, it is assumed that these elements present in the Tolbachik ash nanoparticles only in the form of individual nanoparticles and not in the adsorbed form [56]. The concentrations of Bi, Pb, Ag, Cd, and Te in nanoparticles of Tolbachik volcanic ash determined by SP-ICP-MS are 2–10 times lower (depending on the element) than their concentrations determined after acid decomposition. Thus, it can be assumed that Bi, Pb, Ag, Cd, and Te present in volcanic ash

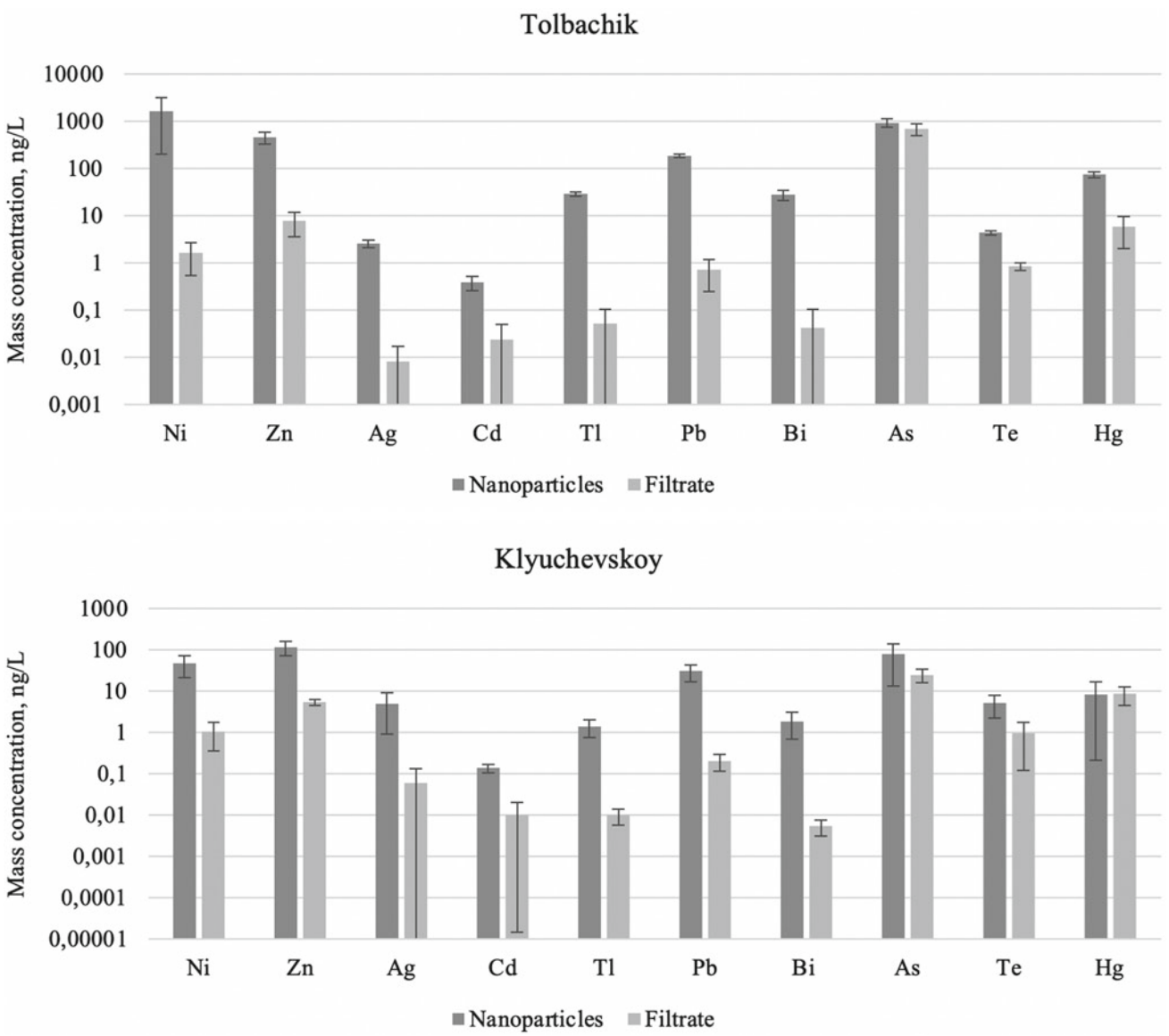

Fig. 5 Concentrations of trace elements in Tolbachik and Klyuchevskoy volcanic ash nanoparticles and in the corresponding control samples (filtrates) [56]

nanoparticles both as individual nanoparticles and in the adsorbed form [56]. The ratio of these elements contained as nanoparticles and in the adsorbed form decreases in the following order: Bi ≈ Pb > Ag > Cd > Te.

It should be noted metal and metalloid nanoparticles having a size below the detection limit cannot be detected by SP-ICP-MS in highly diluted suspensions. At the same time, these nanoparticles can be detected by ICP-MS after decomposition. This may be the reason for the lower concentration of metal and metalloid nanoparticles determined by SP-ICP-MS compared to ICP-MS data obtained after acid decomposition. Thus, it cannot be unequivocally stated that the studied metals and metalloids partially present as species adsorbed on pyroclastic nanoparticles; the fraction of individual nanoparticles (nanophases) of metals and metalloids can be higher.

5 Nanoparticles of Volcanic Ash and Urban Dust as a Carrier of Toxic Elements in Aquatic Environments

Natural mineral nanoparticles are widely spread in the oceans, groundwater and surface water [58]. Rivers carry approximately 10^3–10^4 million tons of natural nanoparticles annually [1]. In addition, glaciers and icebergs also provide a significant flow of nanoparticles [59–61]. In general, the fluxes of nanoparticles to the oceans are vast and have global

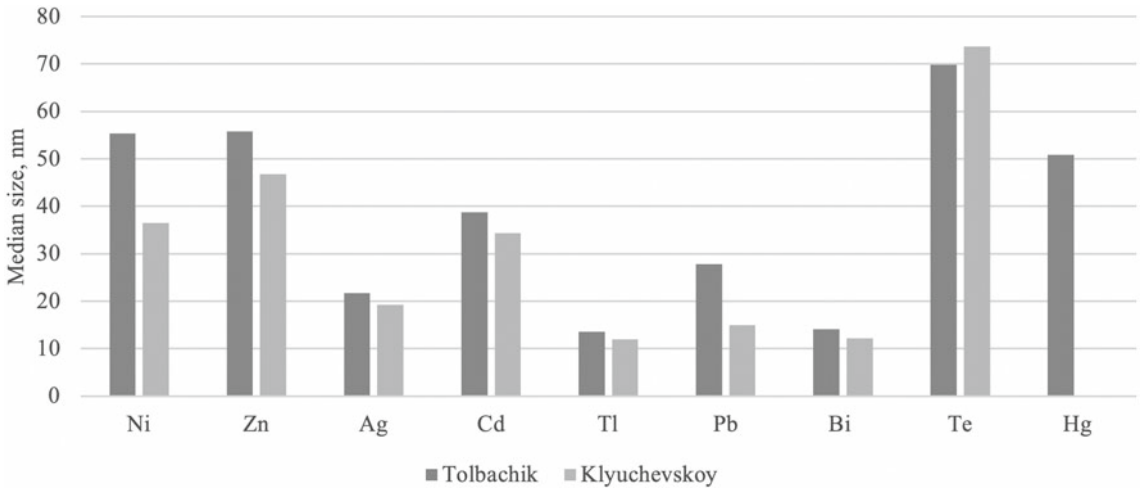

Fig. 6 Mean size of Tolbachik and Klyuchevskoy volcanic ash nanoparticles according to SP-ICP-MS data [56]

biogeochemical impacts [62, 63]. For example, the flux of iron delivered by nanoparticles from icebergs to the Southern Ocean is comparable to the flux of soluble bioavailable iron from aeolian dust [59]. Due to their bioavailability, Fe-containing nanoparticles may have a stronger biogeochemical impact than ionic species of Fe [64, 65].

The transport of particles in the environment directly depends on their size, and nanoparticles are the most mobile fraction. Studying the transport of nanoparticles in various environmental compartments is an important task of biogeochemistry because the transport of nanoparticles in the environment determines the transport of the associated chemical elements and the impact on the environment on both regional and global scales [1, 58]. The transport of nanoparticles in aquatic systems is depending on their aggregation and sedimentation stability [66]. When particles are stable, they can move in aqueous environment for a long period of time, whereas their aggregation results in their immobilization. The size of particles as well as zeta potential (or electrokinetic potential) are the important factors determining their stability. The aggregation stability of particles in aqueous medium highly depends on the ionic strength and pH. Typically, surface waters have pH in the range from 6.0 to 8.5 and seawater—from 7.4 to 8.5. It should be noted that seawater due to its extreme ionic concentration results in rapid aggregation of nanoparticles [67]. Surface waters (1–5 mM) can serve as a good carrier for nanoparticles in the environment.

Long-term stability of Klyuchevskoy volcano ash nanoparticles under conditions close to natural (ionic strength 2.5 mM, pH 7.2 and 8.5) was evaluated [68]. To assess the stability, the size distribution was measured after 2, 7, 14 and 28 days of storage of ash nanoparticles suspension. Volcanic ash nanoparticles were shown to have good long-term stability at both pH 8.5 and 7.2. During the storage, ash nanoparticles had bimodal size distribution consisting of 50–230 nm fraction and of 0.6–0.8 μm sub-fraction. The content of 0.6–0.8 μm particle fraction was <3%. The size distributions of volcanic ash nanoparticles at pH 8.5 and 7.2 did not practically differ, and minor differences in the size profiles of these distributions were of random nature and probably related to measurement errors.

Thus, volcanic ash nanoparticles are shown to have high long-term stability in aquatic environments under near-natural conditions and, therefore, have high potential for long-range transport of toxic and nutrient elements in fresh surface waters.

It is known that road dust particles are the main source of heavy metal pollution of wastewater and urban aquatic ecosystems during rainfall. At the same time, the pollution of urban wastewater by nanoparticles of road dust has not been previously studied. The contribution of road dust nanoparticles to the pollution of urban wastewater by heavy metals was assessed for the first time on the example of dust samples from a major highway in Moscow (the Third Ring Road) [69]. Despite the low content of nanoparticles in the dust, it was found that their contribution to pollution of wastewater by Cr, Co, Ni, Cu, Zn, Cd, Sn, Tl, Pb is very significant and comparable to the contribution of the fraction of water-soluble species of these metals (Fig. 7). It was found that Zn in suspensions of road dust nanoparticles is almost completely contained as nanoparticles. It is important to note that the fraction of water-soluble species of metals upon release into urban aquatic ecosystems is gradually diluted, whereas the dust nanoparticles are able to carry heavy metals in concentrated form over considerable distances before their entry into living organisms or sedimentation/immobilization. Thus, nanoparticles are characterized by long-term transport of associated heavy metals in urban aquatic ecosystems.

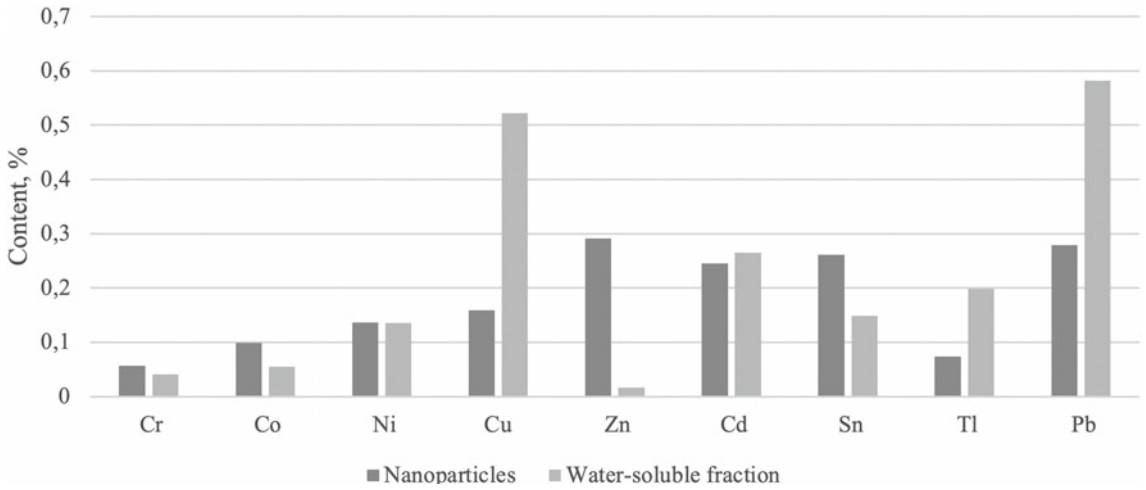

Fig. 7 Concentrations of heavy metals in nanoparticles and water-soluble fractions of elements relative to the total content of heavy metals in the bulk sample of Moscow road dust [69]

6 Conclusion

The data summarized in this paper show how important can be the role of natural nanoparticles in biogeochemical cycles. For example, volcanic ash nanoparticles are accumulators and carriers of toxic elements on a global scale. Assessment of the long-term aggregation stability of volcanic ash nanoparticles confirms their important role in the transport of elements in aquatic ecosystems (surface and groundwater), which are reservoirs of natural nanoparticles. It should be noted that a comprehensive study of natural nanoparticles is just beginning and requires further intensive research and application of a set of complementary methods of separation, quantitative analysis, and study of particle size, morphology and surface properties. Particularly relevant is the determination of element species in nanoparticles. Use of single particle inductively coupled plasma mass spectrometry seems promising for solving this problem. The development of standard samples of natural nanoparticles, without which it is impossible to compare the results obtained in different laboratories, remains an urgent need.

References

1. Hochella, M.F., Mogk, D.W., Ranville, J., Allen, I.C., Luther, G. W., Marr, L.C., McGrail, B.P., Murayama, M., Qafoku, N.P., Rosso, K.M., Sahai, N., Schroeder, P.A., Vikesland, P., Westerhoff, P., Yang, Y.: Natural, incidental, and engineered nanomaterials and their impacts on the Earth system. Science **363**(6434) (2019)
2. Taylor, D.A.: Dust in the wind. Environ. Health Perspect **110**(2) (2002)
3. Sahai, N., Kaddour, H., Dalai, P., Wang, Z., Bass, G., Gao, M.: Mineral surface chemistry and nanoparticle-aggregation control membrane self-assembly. Sci. Rep. **7**(1), 1–13 (2017)
4. Xu, J., Campbell, J.M., Zhang, N., Hickey, W.J., Sahai, N.: Did mineral surface chemistry and toxicity contribute to evolution of microbial extracellular polymeric substances? Astrobiology **12**(8), 785–798 (2012)
5. Lindenthal, A., Langmann, B., Pätsch, J., Lorkowski, I., Hort, M.: The ocean response to volcanic iron fertilisation after the eruption of Kasatochi volcano: a regional-scale biogeochemical ocean model study. Biogeosciences **10**(6), 3715–3729 (2013)
6. Maters, E.C., Delmelle, P., Bonneville, S.: Atmospheric processing of volcanic glass: effects on iron solubility and redox speciation. Environ. Sci. Technol. **50**(10), 5033–5040 (2016)
7. Olgun, N., Duggen, S., Andronico, D., Kutterolf, S., Croot, P.L., Giammanco, S., Censi, P., Randazzo, L.: Possible impacts of volcanic ash emissions of Mount Etna on the primary productivity in the oligotrophic Mediterranean Sea: results from nutrient-release experiments in seawater. Mar. Chem. **152**, 32–42 (2013)
8. Bains, S., Norris, R.D., Corfield, R.M., Faul, K.L.: Termination of global warmth at the Palaeocene/Eocene boundary through productivity feedback. Nature **407**(6801), 171–174 (2000)
9. Sigman, D.M., Boyle, E.A.: Glacial/interglacial variations in atmospheric carbon dioxide. Nature **407**, 859–869 (2000)
10. Cather, S.M., Dunbar, N.W., McDowell, F.W., McIntosh, W.C., Scholle, P.A.: Climate forcing by iron fertilization from repeated ignimbrite eruptions: the icehouse-silicic large igneous province (SLIP) hypothesis. Geosphere **5**(3), 315–324 (2009)
11. Houghton, J.: Global warming. Rep. Prog. Phys. **68**(6), 1343–1403 (2005)
12. Gottschalk, F., Nowack, B.: The release of engineered nanomaterials to the environment. J. Environ. Monit. **13**(5), 1145 (2011)
13. Kaur, J., Kaur, G., Sharma, S., Jeet, K.: Cereal starch nanoparticles—a prospective food additive: a review. Crit. Rev. Food Sci. Nutr. **58**(7), 1097–1107 (2018)
14. Caputo, F., De Nicola, M., Sienkiewicz, A., Giovanetti, A., Bejarano, I., Licoccia, S., Traversa, E., Ghibelli, L.: Cerium oxide nanoparticles, combining antioxidant and UV shielding properties, prevent UV-induced cell damage and mutagenesis. Nanoscale **7** (38), 15643–15656 (2015)

15. Yang, D., Ma, P., Hou, Z., Cheng, Z., Li, C., Lin, J.: Current advances in lanthanide ion (Ln^{3+})-based upconversion nanomaterials for drug delivery. Chem. Soc. Rev. **44**(6), 1416–1448 (2015)
16. Liu, Y., Deng, Y., Dong, H., Liu, K., He, N.: Progress on sensors based on nanomaterials for rapid detection of heavy metal ions. Sci. China Chem. **60**(3), 329–337 (2017)
17. You, M., Zhong, J., Hong, Y., Duan, Z., Lin, M., Xu, F.: Inkjet printing of upconversion nanoparticles for anti-counterfeit applications. Nanoscale **7**(10), 4423–4431 (2015)
18. Ray, P.C., Yu, H., Fu, P.P.: Toxicity and environmental risks of nanomaterials: challenges and future needs. J. Environ. Sci. Heal. Part C. **27**(1), 1–35 (2009)
19. Jeevanandam, J., Barhoum, A., Chan, Y.S., Dufresne, A., Danquah, M.K.: Review on nanoparticles and nanostructured materials: history, sources, toxicity and regulations. Beilstein J. Nanotechnol. **9**, 1050–1074 (2018)
20. Klaine, S.J., Alvarez, P.J., Batley, G.E., Fernandes, T.F., Handy, R.D., Lyon, D.Y., Mahendra, S., McLaughlin, M.J., Lead, J.R.: Nanomaterials in the environment: behavior, fate, bioavailability, and effects. Environ. Toxicol. Chem. **27**(9), 1825–1851 (2008)
21. Buzea, C., Pacheco, I.I., Robbie, K.: Nanomaterials and nanoparticles: Sources and toxicity. Biointerphases **2**(4), MR17–MR71 (2007)
22. Ernst, W.G.: Overview of naturally occurring Earth materials and human health concerns. J. Asian Earth Sci. **59**, 108–126 (2012)
23. Trovato, M.C., Andronico, D., Sciacchitano, S., Ruggeri, R.M., Picerno, I., Di Pietro, A., Visalli, G.: Nanostructures: between natural environment and medical practice. Rev. Environ. Health. **33**, 305–317 (2018)
24. Horwell, C.J.: Grain-size analysis of volcanic ash for the rapid assessment of respiratory health hazard. J. Environ. Monit. **9**(10), 1107 (2007)
25. Ermolin, M.S., Fedotov, P.S.: Separation and characterization of environmental nano- and submicron particles. Rev. Anal. Chem. **35**(4), 185–199 (2016)
26. Faucher, S., Le Coustumer, P., Lespes, G.: Nanoanalytics: history, concepts, and specificities. Environ. Sci. Pollut. Res. 1–15 (2018)
27. Wang, Y.: Nanogeochemistry: nanostructures, emergent properties and their control on geochemical reactions and mass transfers. Chem. Geol. **378–379**, 1–23 (2014)
28. Alekseyev, V.A.: Nanoparticles and nanofluids in "water–rock" interactions. Geochem. Int. **64**(4), 343–355 (2019)
29. Ermolin, M.S., Fedotov, P.S., Ivaneev, A.I., Karandashev, V.K., Fedyunina, N., Eskina, V.: Isolation and quantitative analysis of road dust nanoparticles. J. Anal. Chem. **72**(5), 520–532 (2017)
30. Ermolin, M.S., Fedotov, P.S., Karandashev, V.K., Shkinev, V.M.: Methodology for separation and elemental analysis of volcanic ash nanoparticles. J. Anal. Chem. **72**(5), 533–541 (2017)
31. Ivaneev, A.I., Faucher, S., Ermolin, M.S., Karandashev, V.K., Fedotov, P.S., Lespes, G.: Separation of nanoparticles from polydisperse environmental samples: comparative study of filtration, sedimentation, and coiled tube field-flow fractionation. Anal. Bioanal. Chem. **411**(30), 8011–8021 (2019)
32. Dzherayan, T.G., Ermolin, M.S., Vanifatova, N.G.: Effectiveness of the simultaneous application of capillary zone electrophoresis and static light scattering in the study of volcanic ash nano- and submicroparticles. J. Anal. Chem. **75**(1), 67–72 (2020)
33. Loosli, F., Wang, J., Sikder, M., Afshinnia, K., Baalousha, M.: Analysis of engineered nanomaterials (Ag, CeO_2 and Fe_2O_3) in spiked surface waters at environmentally relevant particle concentrations. Sci. Total Environ. **715**, 136927 (2020)
34. ISO/DIS 19749 Nanotechnologies—Measurements of particle size and shape distributions by scanning electron microscopy. International Organization of Standards (2018)
35. Bell, J.M.: BCR Draft Method for Particle Size Distributions by Scanning Electron Microscopy and Image Analysis. ICI Chemicals and Polymers Limited, Runcorn, England (1993)
36. Ivaneev, A.I., Ermolin, M.S., Fedotov, P.S.: Separation, characterization, and analysis of environmental nano- and microparticles: state-of-the-art methods and approaches. J. Anal. Chem. **76**(4), 413–429 (2021)
37. Shkinev, V.M., Ermolin, M.S., Fedotov, P.S., Borisov, A.P., Karandashev, V.K., Spivakov, B.Y.: A set of analytical methods for the estimation of elemental and grain-size composition of volcanic ash. Geochem. Int. **54**(13), 1252–1260 (2016)
38. Fedotov, P.S., Ermolin, M.S., Karandashev, V.K., Ladonin, D.V.: Characterization of size, morphology and elemental composition of nano-, submicron, and micron particles of street dust separated using field-flow fractionation in a rotating coiled column. Talanta **130**, 1–7 (2014)
39. Adachi, K., Tainosho, Y.: Characterization of heavy metal particles embedded in tire dust. Environ. Int. **30**(8), 1009–1017 (2004)
40. Mummullage, S., Egodawatta, P., Ayoko, G.A., Goonetilleke, A.: Use of physicochemical signatures to assess the sources of metals in urban road dust. Sci. Total Environ. **541**, 1303–1309 (2016)
41. Varrica, D., Bardelli, F., Dongarrà, G., Tamburo, E.: Speciation of Sb in airborne particulate matter, vehicle brake linings, and brake pad wear residues. Atmos. Environ. **64**, 18–24 (2013)
42. Thorpe, A., Harrison, R.M.: Sources and properties of non-exhaust particulate matter from road traffic: a review. Sci. Total Environ. **400**(1–3), 270–282 (2008)
43. McKenzie, E.R., Money, J.E., Green, P.G., Young, T.M.: Metals associated with stormwater-relevant brake and tire samples. Sci. Total Environ. **407**(22), 5855–5860 (2009)
44. Hjortenkrans, D.S.T., Bergbäck, B.G., Häggerud, A.V.: Metal emissions from brake linings and tires: case studies of Stockholm, Sweden 1995/1998 and 2005. Environ. Sci. Technol. **41**(15), 5224–5230 (2007)
45. Councell, T.B., Duckenfield, K.U., Landa, E.R., Callender, E.: Tire-wear particles as a source of zinc to the environment. Environ. Sci. Technol. **38**(15), 4206–4214 (2004)
46. Jang, H.N., Seo, Y.C., Lee, J.H., Hwang, K.W., Yoo, J.I., Sok, C. H., Kim, S.H.: Formation of fine particles enriched by V and Ni from heavy oil combustion: anthropogenic sources and drop-tube furnace experiments. Atmos. Environ. **41**(5), 1053–1063 (2007)
47. Barefoot, R.R.: Distribution and speciation of platinum group elements in environmental matrices. TrAC - Trends Anal. Chem. **18**(11), 702–707 (1999)
48. Zereini, F., Wiseman, C., Beyer, J.M., Artelt, S., Urban, H.: Platinum, lead and cerium concentrations of street particulate matter (frankfurt am main, Germany). J. Soils Sediments. **1**(3), 188–195 (2001)
49. Mohammadi, S.Z., Karimi, M.A., Hamidian, H., Baghelani, Y.M., Karimzadeh, L.: Determination of trace amounts of Pd(II) and Rh (III) ions in PtIr alloy and road dust samples by flame atomic absorption spectrometry after simultaneous separation and preconcentration on non-modified magnetic nanoparticles. Sci. Iran. **18**(6), 1636–1642 (2011)
50. Okorie, I.A., Enwistle, J., Dean, J.R.: Platinum group elements in urban road dust. Curr. Sci. **109**(5), 938–942 (2015)
51. Ermolin, M.S., Fedotov, P.S., Malik, N.A., Karandashev, V.K.: Nanoparticles of volcanic ash as a carrier for toxic elements on the global scale. Chemosphere **200**, 16–22 (2018)
52. Degueldre, C., Favarger, P.Y.: Thorium colloid analysis by single particle inductively coupled plasma-mass spectrometry. Talanta **62** (5), 1051–1054 (2004)

53. Degueldre, C., Favarger, P.-Y., Rossé, R., Wold, S.: Uranium colloid analysis by single particle inductively coupled plasma-mass spectrometry. Talanta **68**(3), 623–628 (2006)
54. Degueldre, C., Favarger, P.-Y.Y., Wold, S.: Gold colloid analysis by inductively coupled plasma-mass spectrometry in a single particle mode. Anal. Chim. Acta. **555**(2), 263–268 (2006)
55. Laborda, F., Bolea, E., Jiménez-Lamana, J.: Single particle inductively coupled plasma mass spectrometry: a powerful tool for nanoanalysis. Anal. Chem. **86**(5), 2270–2278 (2014)
56. Ermolin, M.S., Ivaneev, A.I., Fedyunina, N.N., Fedotov, P.S.: Nanospeciation of metals and metalloids in volcanic ash using single particle inductively coupled plasma mass spectrometry. Chemosphere **281** (2021)
57. Rietmeijer, F.J.M., Mackinnon, I.D.R.: Bismuth oxide nanoparticles in the stratosphere Bi from which we derive the particle number densities (p.m.-3) for average. J. Geophys. Res. **102**(96), 6621–6627 (1997)
58. Hochella, M.F., Lower, S.K., Maurice, P.A., Penn, R.L., Sahai, N., Sparks, D.L., Twining, B.S.: Nanominerals, mineral nanoparticles, and earth systems. Science **319**(5870), 1631–1635 (2008)
59. Raiswell, R., Benning, L.G., Davidson, L., Tranter, M.: Nanoparticulate bioavailable iron minerals in icebergs and glaciers. Mineral. Mag. **72**(1), 345–348 (2008)
60. Tepe, N., Bau, M.: Importance of nanoparticles and colloids from volcanic ash for riverine transport of trace elements to the ocean: evidence from glacial-fed rivers after the 2010 eruption of Eyjafjallajökull Volcano, Iceland. Sci. Total Environ. **488–489** (1), 243–251 (2014)
61. Hawkings, J.R., Benning, L.G., Raiswell, R., Kaulich, B., Araki, T., Abyaneh, M., Stockdale, A., Koch-Müller, M., Wadham, J.L., Tranter, M.: Biolabile ferrous iron bearing nanoparticles in glacial sediments. Earth Planet. Sci. Lett. **493**, 92–101 (2018)
62. Poulton, S.W., Raiswell, R.: Chemical and physical characteristics of iron oxides in riverine and glacial meltwater sediments. Chem. Geol. **218**(3–4), 203–221 (2005)
63. Raiswell, R., Tranter, M., Benning, L.G., Siegert, M., De'ath, R., Huybrechts, P., Payne, T.: Contributions from glacially derived sediment to the global iron (oxyhydr)oxide cycle: Implications for iron delivery to the oceans. Geochim. Cosmochim. Acta. **70**(11), 2765–2780 (2006)
64. Kadar, E., Dyson, O., Handy, R.D., Al-Subiai, S.N.: Are reproduction impairments of free spawning marine invertebrates exposed to zero-valent nano-iron associated with dissolution of nanoparticles? Nanotoxicology **7**(2), 135–143 (2013)
65. Kadar, E., Fisher, A., Stolpe, B., Calabrese, S., Lead, J., Valsami-Jones, E., Shi, Z.: Colloidal stability of nanoparticles derived from simulated cloud-processed mineral dusts. Sci. Total Environ. **466–467**, 864–870 (2014)
66. Buffle, J., Wilkinson, K.J., Stoll, S., Filella, M., Zhang, J.: A generalized description of aquatic colloidal interactions: the three-culloidal component approach. Environ. Sci. Technol. **32** (19), 2887–2899 (1998)
67. Wang, H., Burgess, R.M., Cantwell, M.G., Portis, L.M., Perron, M.M., Wu, F., Ho, K.T.: Stability and aggregation of silver and titanium dioxide nanoparticles in seawater: role of salinity and dissolved organic carbon. Environ. Toxicol. Chem. **33**(5), 1023–1029 (2014)
68. Ermolin, M.S., Dzherayan, T.G., Vanifatova, N.G.: Stability of volcanic nanoparticles using combined capillary zone electrophoresis and laser diffraction. Environ. Chem. Lett. **19**(1), 751–762 (2021)
69. Ermolin, M.S., Fedotov, P.S., Ivaneev, A.I., Karandashev, V.K., Fedyunina, N.N., Burmistrov, A.A.: A contribution of nanoscale particles of road-deposited sediments to the pollution of urban runoff by heavy metals. Chemosphere **210**, 65–75 (2018)

Layered Titanosilicates Melting: Experimental Study at 1 Atmosphere and Application for Agpaitic Rocks Petrology

V. A. Zaitsev

1 Introduction

Alkaline, especially agpaitic and hyperagpaitic magmatism forms important deposits of critical metals of different geochemical groups [e.g., 1–3]. The behavior of critical elements during the evolution of agpaitic magma is controlled by the mineralogy of titanium: high field strength elements (HFSEs), such as Nb and Zr) may isomopthically substitude Ti, while like large ion lithophile elements (LILE), such as Li, Rb, and Cs) and rare earth elements (REEs) substitute calcium, alkaline metals or occupy their own position in the minerals of titanium.

Geochemistry and mineralogy of titanium in alkaline massifs are very complicated: more then 200 titanosilicates have been described [4] and most of them occur only in alkaline magmatic rocks, agpaitic pegmatites and postmagmatic derivates. Some of these minerals are present in trifling amount, but others, first of all, the layered titanosilicates of lamprophyllite and lomonosovite groups may play role of rock-forming minerals.

Mineral diversity of titanosilicates in agpaitic rocks makes the mineral forms of titanium the sensitive indicators of mineral forming conditions, but experimental data, providing the connection between mineralogical observations and numerical estimations of chemical and physical conditions of mineral-forming environment are scarce.

Although the applicability of experimental results for understanding natural processes has always remained a subject of discussion, since artificial systems are always simpler than natural ones, the author believes that the value of experimental research lies in the fact that they make it possible to control the degree of approximation. The simpler the experimental system, the clearer it illustrates the fundamental mechanisms of natural processes, but the worse is the quantitative correspondence between the model and the natural process. Complication, i.e. the introduction of additional components and parameters makes it possible to achieve a better quantitative match, but makes the interpretation more vague, since there is an uncertainty: is it possible to achieve the same match using a different set of parameters.

Accordingly, when we interpret experimental results, on the one hand, we must take into account what are the differences between experimental and natural conditions, and what (in terms of size and direction) discrepancy we can expect when applying experimental results to petrological observations, and on the other hand, consider, that the experiment does not reproduce the conditions of a natural process, but allows us to evaluate the constraints on these conditions.

For example: it is obvious that a mineral cannot crystallize at a temperature higher than its melting point. Thus, the experimentally determined melting point is always the upper estimate of the possible formation temperature. Complication of the composition of the system—the transition to two-phase and polymineral paragenesis will reduce the melting point of each of the minerals, thus, the temperature of the two-phase eutectic is the upper estimate of the temperature of formation of two-phase paragenesis, etc.

The aim of our study is to provide experimental data on stability of widely spread of titanosilicates: lamprophyllite group minerals and lomonosovite for estimation of stability fields if these phases the formation conditions of titanosilicates in natural systems like the Lovosero massif, which provides the classical example of a layered peralkaline intrusion.

Before our works, only the simplest titanosilicates: lorentsenite ($Na_2Ti_2Si_2O_9$), narsarsukite (Na_2TiSiO_5) and paranatisite ($Na_2TiSi_2O_7$), were synthesized from melt in system Na_2O–TiO_2–SiO_2 [5]. Information about experimental study of Sr-lamprophyllite—nepheline phase

V. A. Zaitsev (✉)
Vernadsky Institute of Geochemistry and Analytical Chemistry, Russian Academy of Sciences, 19 Kosygin St., Moscow, 119991, Russia
e-mail: va_zaitsev@inbox.ru

V. P. Kolotov and N. S. Bezaeva (eds.), *Advances in Geochemistry, Analytical Chemistry, and Planetary Sciences*,
https://doi.org/10.1007/978-3-031-09883-3_6

diagram was previously published [6, 7], and will partially repeat here to provide a coherent picture of the story.

1.1 Studied Minerals in the Nomenclature of Titanosilicates

Our particular interest are widespread phyllosilicates of lamprophyllite $(Sr,Ba,Na,K)_2Na(Na,Fe,Mn)_2Ti[Ti_2(Si_2O_7)_2]O_2(OH,F,O)_2$—barytolamprophyllite $(Ba,Sr,K)_2Na(Na,Fe,Mn)_2Ti[Ti_2(Si_2O_7)_2]O_2(OH,F,O)_2$ isomoprhic series and lomonosovite $Na_{10}Ti_4(Si_2O_7)_2(PO_4)_2O_4$. These minerals belong to the seidozerite supergroup that currently contains 50 mineral species [8].

These minerals have structures based on a titanium-silicate (TS) blocks = "seidozerite blocks" = "HOH blocks" consists of octahedral (O) sheet, composed by combination of ochatedra, of different types (centered by Na, Ti, Mn, Fe, Ca etc.) sandwiched between two heteropolyhedral (H) sheets constituted by Ti (or Nb)—centred octahedra or 'semioctahedra' (tetragonal pyramids) and Si_2O_7 groups. Sokolova [9] based on the topology, chemical composition, and stereochemistry of the TS block divide the seidozerite supergroup into rinkite, bafertisite, lamprophyllite, and murmanite groups, containing 1, 2, 3, and 4 apfu (atoms per formula unit) of Ti + Nb + Zr (+ Fe + Mg + Mn). This nomenclature does not take into account the filling of the space between the layers.

However, this classification is far from controversial. In particular, other authors [e.t. 10–13] aggregate into lamprophyllite group the minerals, containing only the LIL cations in the interlayer positions (lamprophyllite, barytolamprophyllite, nabalamprofillire etc.) and five-coordinated titanium in the heteropolyhedral sheet, and aggregate into the epistolite group, previously named "murmanite group" or "lomonosovite group", [14, 15] the minerals, containing $(PO_4)^{3-}$ groups and H_2O in in the interlayer space. This viewpoint is much better correspond to the geochemical data on variations of chemical compositions of this minerals: it was shown that most of natural compositions fill the composition range between lamprophyllite, baritolamprothyllite and nabalamprophyllite and show wide variations in the octahedral positions [10, 11]. It was also shown good linear correspondence between average Shennon radius of cations occupying the interlayer position and a parameter of the unit sell [16].

For the lomonosovite the wide concentration range was shown on the Ti–Nb substitution, up to Nb domination in the one of octahedra [17], in the same it was found no significant presense of divalent LIL cations in the interlayer positions.

2 Experimental Methods and the Starting Materials

Starting materials were samples of natural lamprophyllite and barytolamprophyllite from pegmatites of Lovozersky, Khibina, and Malourunsy massifs (Russia), lomonosovite from Khibina massif and partly crystallized glass with nepheline $NaAlSiO_4$ composition. Their compositions are presented in Table 1.

The pulverized material was then welded in Pt ampoules, which were held in vertical electric furnaces with Ni–Cr and Pt heaters and then quenched in iced water. The experiments typically lasted from 5 to 360 h.

The temperature was measured by a Pt–Rh thermocouple, which was calibrated against the melting points of NaCl and KCl. The temperature was measured accurate to ±15 °C.

The experiments were conducted by approaching equilibrium either «from above» (the ampoule with the experimental charge was heated to 1000–1100 °C and then cooled to the experimental temperature or quenched and then heated to the required temperature) or «from below» (the ampoules were not preliminarily heated). Run products were indentified by optical method in immersion oils, supplemented by electron microprobe analysis in the Camebax SX-100 at an accelerating voltage of 15 kV and a beam current of 30 nA (analysist V. G. Senin).

Preliminary, one visual control experiment on lomonosovite melting was carried out in the miniature open platinum crucible, pleased in the vertical furnace, located on the microscope stage.

3 Experimental Results

3.1 Lamprophyllite Group Minerals Melting

The conditions and results of the high-temperature experiments are given in Table 2.

The products of experiments with lamprophyllite contained titanosilicate glass, lamprophyllite, $SrTiO_3$, TiO_2 and $Na_2(Fe,Mn)Ti_7O_{16}$. Representative microprobe analyses of oxides are shown in Table 3.

In the products of experiments «from below» with lamprophyllite with temperatures 850 and 870 °C was found only lamprophyllite and minor glass. Product of run at 890 °C consist of titanosilicate melt, titanium oxides and lamprophyllite relicts. No lamprophyllite was found in product of experiment at temperature 915 °C and above. Newly formed lamprophyllite was found in products of runs at 860 and 850 °C in association with glass and titanium oxides.

Table 1 Starting materials composition

Charge name	Lam	X-Lam	M-Lam	Lom
	Lamprophyllite	Barytolamprophyllite		Lomonosovite
	Lovozero massif	Khibina massif	Murun massif	Khibina massif
SiO_2	31.78	33.32	29.72	23.53–24.08
TiO_2	29.49	23.99	28.55	19.42–26.87
Al_2O_3	0.17	0.24	0.23	0
FeO	2.15	4.33	3.26	1.29–2.52
MnO	4.02	0.89	2.23	1.85–0.78
MgO	0.63	1.14	0.39	0.25–0.45
CaO	0.87	1.09	1.29	1.19–1.62
SrO	15.05	6.42	6.57	
BaO	1.05	13.88	16.15	
Na_2O	12.07	10.87	8.6	27.19–28.62
K_2O	0.49	1.4	2.48	
Nb_2O_5	0.21	0.12	0.07	3.52–10.55
F	2.05	2.5	1.04	
P_2O_5				13.48–14.06
Total	100.03	100.19	100.58	100.60–100.67

Table 2 Conditions and products of high-temperature experiments with lampropyllite and barytolamprophyllite

Charge	T °C	Duration (h)	Type of experiment	Run products*
Lam	850	8.3	From above	**Lam** + **Per** + **Ru** + **Gl**
Lam	850	8.3	From below	**Lam**
Lam	860	204	From above	Lam + Per + Freu
Lam	870	48.5	From below	**Lam**
Lam	880	304	From above	**Lam +** Per **+ Freu + Gl**
Lam	890	5.5	From above	Per + **Ru + Gl**
Lam	890	5.5	From below	**Lam** + **Per** + Ru + **Gl**
Lam	915	4.5	From below	**Per** + Ru + **Freu + Gl**
Lam	915	4.5	From above	**Per** + **Ru +** Freu + Gl
Lam	965	70	From below	Per + Freu + Ru + Gl
Lam	1020	8	From below	Per + Ru + Gl
Lam	1090	3.5	From below	Per + Gl
Lam	1100	7	From below	Per + **Gl**
Lam	1120	4.3	From below	**Gl**
X-Lam	800	193	From above	**Lam + BNTS + Per + Gl**
X-Lam	860	204	From below	**Lam + Per + Gl**
X-Lam	870	48.5	From below	**Lam + BFT + Gl**
X-Lam	880	304	From above	**BNTS + BFT + Per + Gl**
M-Lam	800	193	From above	Lam
M-Lam	870	204	From above	**BFT + Per + BNTS** + Gl
M-Lam	880	304	From above	Per + BNTS + Gl

Lam—lamprophyllite, Per—Sr-perovskite (tausonite), Ru—TiO2 , Freu - Na-Fe- titanate (freudenbergite), BNTS–Ba–Na titanosilicate, Gl—glass. Bolded the phases confirmed by EMPA

Table 3 Composition of newly formed lamprophyllite and glass

Charge	Lam		M-Lam		X-Lam		X-Lam	
T °C	851		868		868		798	
Type of run	From above		From below		From below		From above	
	Lampr	Gl	Lampr	Gl	Lampr	Gl	Lampr	Gl
Na_2O	12.50	4.05	10.30	4.29	9.57	5.76	10.07	6.63
MgO	1.01	0.67			0.94	0.84	0.81	0.89
Al_2O_3	0.02	0.51	0.12	1.32	0.15	1.49	0.10	0.76
SiO_2	31.43	49.89	37.20	50.70	28.90	40.46	27.47	46.91
K_2O	0.21	1.28	1.94	2.76	1.89	3.14	1.22	6.22
CaO					1.24	1.69	1.27	1.74
TiO_2	30.42	19.26	27.63	16.18	28.22	16.32	27.83	11.12
MnO	4.23	4.36	1.25	1.28	1.10	1.35	0.92	1.01
FeO	1.26	6.76	3.16	5.43	4.00	9.31	2.02	14.41
SrO	18.01	4.72	8.36	3.15	10.68	3.40	13.07	2.11
Nb_2O_5	0.00	2.56	0.26	0.13	0.27	0.08	0.17	0.20
BaO	1.16	0.56	12.36	7.69	11.30	7.57	13.21	2.48
	100.25	94.60	102.57	92.94	102.02	96.54	100.93	98.25
Sr/Ba, molar	22.93	12.46	1.00	0.61	1.40	0.67	1.46	1.26

The products of runs 915 and 965 °C both «from below» and «from above» contain glass, TiO_2, Sr-titanate and Na–Fe titanate.

Newly formed lamprophyllite forms prismatic crystals up to 1 mm with inclusions of glass and titanium oxides. Color of crystals is slightly greenish or yellowish, birefringence is strong. Newly formed lamprophyllite is significantly poorer in K (<0.2 mass % K_2O), Fe (<1.6 mass % FeO), Nb (<0.2% Nb_2O_5) and, richer in Sr (usually more than 17% SrO), in Ba (>1.1% BaO) and Mn (>4.2% MnO), and have similar Ba/Sr ratio 0.04–0.07 (molar) comparing the starting composition.

Sr-titanate—synthetic analog of tausonite (the mineral of perovskite group) forms cubic crystals or fluorite law twins. The crystals contain 0.77–0.87 Sr atoms, 0.10–0.15 Na atoms 0.91–1.00 Ti atoms, and up to 0.05 Nb, 0.02 Fe atoms and up to 0.25 atoms F per formula unit. The simplified formula of the titanate is $Sr_{1-x}Na_xTiO_{3-x}F_x$. By the other words, the composition of phase may be described as solid solution of $SrTiO_3$ and $NaTiO_2F$ endmembers.

TiO_2 crystallizes as long thin cryctals with quadratic sections. They have strong birefringence and contain up to 4% Nb_2O_5.

Na-Fe titanate forms reddish-brown prismatic crystals with strong birefringence. It contains 6.5–7.5 atoms per formula units of Ti, 1.7–2 Na, 0.4–0.9 Fe, 0.25–0.4 Mn and up to 0.2 atoms of Mg per formula unit (apfu). This composition is close to $Na_2(Fe,Mn)Ti_7O_{16}$. So in may be named the synthetic analog of high-titanium variety of freudenbergite.

Glass generated in the experiments is yellow–brown. Its refraction index is always >1.640. Glass composition is heterogenis and vary depending from the temperature and type of experiment, the silica content decrease from 46–53 mas% to 32 mass%, Na_2O—increase from 4 to 12 mass% TiO_2 from 19 to 30 mass%, SrO from 5 to 15 mass%, Ba/Sr ratio decrease from 0.1–0.2 to 0.02.

The products of experiments with barilamprophyllite contain titanosilicate glass, lamprophyllite, $SrTiO_3$ (tausonite), Ba-Fe titanate and Ba–Na titanosilicate $(Ba,Sr)(Na,K)_2(Ti,Fe)_2(Si_2O_7)_2$.

Lamprophyllite was found in the products of experiment with at 800, 860 and 870 °C, both from below and from above. Ba/Sr ratio in lamprophyllite is lower than in starting material. This lamprophyllite is significantly richer in Sr (6–14 mass%) and Ca (1.2–1.4 mass%), but poorer in Na (9.5–10.3 Na_2O), Mg (0.7–1 mass% MgO) and Al (<0.15 mass% Al_2O_3).

The newly formed lamprophyllite in experiment «from above» is poorer in potassium (1.2–1.3 mass% K_2O) and iron (~2 mass % FeO), than starting material while lamprophyllite in experiment from below has similar with starting material concentration of iron and even higher concentration of potassium 1.7–2.5% K_2O.

$SrTiO_3$, formed from the baritolamprophyllite is similar to one, formed in the runs with lamprophyllite: it contains admixture of Na 0.14–0.15, and F 0.12–0.16 athoms per formula, and minor admixtures of Nb 0.02–0.03. The main difference is admixes of Ca 0.1–0.12, and Ba 0.02–0.03 atoms per formula.

The prismatic crystals of Ba-Fe titanate was found in the products of the experiments at 870 and 880 °C. Their simplified empirical formula is about to $(Ba,K,Na)FeTi_4O_{10}$.

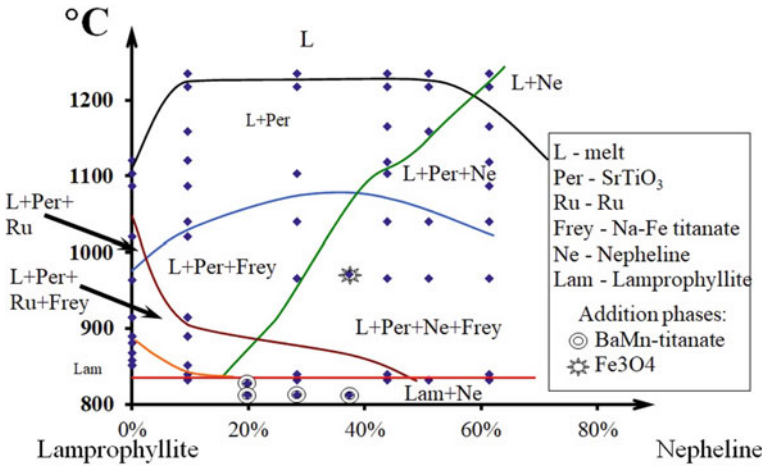

Fig. 1 Pseudobinare phase diagram lamprophyllite-nepheline. Modified after [7]

The run products contain also Ba–Na titanosilicate with is richer in silica and SrO and poorer in TiO_2 and BaO whan lamprophillite. The empirical formula, recalculated on the basis of 4 atoms of Si is $(Ba,Sr)(Na,K)_2(Ti,Fe)_2(Si_2O_7)_2$.

The composition glass, formed in the experiments with baritolamprophtyllite strongly vary inside one depending the run temperature, type of experiment and charge: 40–50% SiO_2, 4–6% Na_2O, 11–16% TiO_2, 2–4% SrO. The Sr/ Ba ratio of glass is lower than that of the lamprophyllite, formed in the same this run.

These results show that lamprophyllite melts incongruently, with the formation of melt, titanium oxide, Sr-perovskite, and freudenbergite. The temperature of five-phase equilibrium lies between 870 °C (temperature of newly lamprophyllite formation) and 915 °C (the temperature at which no lamprophyllite relics are preserved).

Baritolamprophyllite melts incongruently with formation of Ba-Fe titanate and Ba–Na titanosilicate $(Ba,Sr)(Na,K)_2$ $(Ti,Fe)_2(Si_2O_7)_2$ at the lower temperature than lamprophyllite (between 800 and 870 °C). The incomplete decomposition of barytolamprophyllite may result in formation of lamprophyllite.

Both lamprophyllite and barytolamprophyllite are characterised by higher Sr/Ba ratio than relative to the coexisting melt. It means that lamprophyllite minerals crystallisation must deplete the melt by Sr stronger then by Ba.

3.2 Lamprophyllite-Nepheline Phase Diagram

The products of experiments with lamprophyllite-nepheline charges contained glass, lamprophyllite, Sr-titanate, TiO_2, and Na–Fe titanate, nepheline and BaMn-titanate (in subsolidus).

Lamprophyllite, Sr-titanate, TiO_2, and Na–Fe titanate are similar with founded in the products of experiments with lamprophyllite.

Nepheline crystallizes as isometric colorless crystals with low refraction and low birefringence. Newly formed nepheline contain 0.4–0.7 wt% K_2O (0.01–0.02 apfu) and excess of silica by 0.02–0.06 apfu.

BaMn titanate $(Ba,Na)_2Mn_4(Ti,Fe)_8O_{21}$ was found as a brown prismatic crystals, very similar with freudenbergite. It was found only in experiments with lamprophyllite and nepheline at 810 and 830 °C.

The phase diagram is shown in Fig. 1.

The first compound to appear was tausonite in compositions up to 61 wt % nepheline. The temperature of tausonite appearing is 1110 °C for lamprophyllite composition and rise to the 1220–1235 in the intermediate part of the diagram. The second phase, crystallising in the lamprophyllite composition system was rutile and the third was freudenbergite. The liquidus temperature of rutile strongly decrease towards the nepheline side, while liquidus freudenbergite have maximum in the middle part of the diagram at 1050 °C. This is a consequence of the pseudobynary character of the diagram.

The temperature minimum on this diagram corresponds to the six-phase equilibrium melt + tausonite + rutile + freudenbergite + lamprophyllite + nepheline. The six-phase equilibrium point has composition 20 wt % nepheline + 80 wt % lamprophyllite at a temperature of 830 °C.

This temperature is a limit of nepheline-lamprophyllite paragenesis stability, but real temperature limit of lamprophyllite crystallization in alkaline agpaitic rocks must be appreciably lower because of presence of additional components.

Glass, tausonite, freudenbergite and/or Ba-Mn titanate were found together with lamprophyllite and nepheline in «up» experiments below 830 °C. The presence of additional phases is a consequence of the non-binary character of the system and lack of chemical equilibrium: during the incongruent melting of lamprophyllite, significant amounts of strontium and titanium are fixed in oxides, while melt is

enriched in sodium and silica compared with the starting composition. In the chemical space the figurative point of the melt lie outside the lamprophyllite-nepheline section, as temperature decreases, lamprophyllite encapsulates part of oxide phases, especially tausontite. This results in an excess of melt in the reaction melt + tausonite + rutile + freudenbergite = lamprophyllite (±nepheline). Nepheline and lamprophyllite crystallization led to the enrichment of residual melt in silica and incompatible components. An increase in silica concentration in the melt changes the proportion of crystallizing phases in accordance with the principle of acid-base interaction. As titanium is a more acid component then alumina, silica enrichment expands the crystallization field of lamprophyllite at the expense of that of nepheline. As a result, the residual melt is enriched in alumina.

3.3 Lomonosovite Melting

Preliminary experiment in open open platinum crucible showed that the first droplets of liquid appeared at 820 °C, and extensive melting started at 866 °C.

After equilibration during 7 ours at 890° C quenched experimental products consisted of glass, Na–Ca phosphate globules and two titanates.

One titanate forms long crystals and is chemically similar to freudenbergite.

The other titanate forms small isometric crystals and was chemically identified as the solid solution of 70% lueshite and 30% perovskite.

In an experiment at 964 °C titanates were not observed, and only silicate glass and phosphate globules were present. In experiments at 1045 °C or higher, only brown glass of the lomonosovite composition was found.

The phosphate globules that formed at 890 and 944 °C are rounded or oval. The compositions of phosphate material are given in Table 4.

Two analyses in the table with lowest titanium and silica contents are close to the formula $Na(Ca,Mg,Mn,Fe)PO_4$. Other globules have higher contents of titanium and silica, but some of them are richer in phosphorus. This implies that they can be mixture of this phosphate and quenched phosphate melt.

Figure 2 shows the projection of these analyses onto the $CaO–Na_2O–P_2O_5$ diagram. Pure $NaCaPO_4$ is solid at the experimental temperature but other points lie in the low-temperature part of the diagram. This means that the phosphate globules consisted at high temperatures of phosphate liquid or a mixture of phosphate liquid and phosphate crystals (it is impossible to be sure if phosphate crystals result of quenching crystallisation or not).

4 Petrologic Applications for Lovosero Massif

One of the classical localities for titanosilicate minerals is Lovosero alkaline massif, located in Kola peninsula. This massif is a world's-largest intrusion of agpaitic nepheline syenites.

Several intrusive phases and a pegmatite stage was recognized in the massif by earlier studies [20, 21 and others]. The oldest intrusive phase (or phases) occupy only about 5% of the massif area, includes essentially miaskitic nepheline syenites and nepheline-sodalite syenites. The most part of area of Lovosero massif is occupied by differentiated rhythmically layered complex of urtites, foyaites, juvites, and lujavrites. Complex of *Eudialyte lujavrites* unconformably overlying the differentiated complex. It forms a thick (up to 800 m) plate-like weakly-layered body, of eudialyte lujavrites, foyaites, and juvites with cutting veined and layered bodies of porphyroid lujavrites up to 200 m thick.

The Lovozero massif provide an outstanding example of a layered alkaline intrusion. One of the main petrological

Table 4 Electron-microprobe analyses of phosphate globules

Temperature (°C)	890	890	890	890	964	964	964
Na_2O	13.17	10.35	9.22	12.03	11.79	13.6	11.26
MgO	1.49	1.25	1.83	1.97	1.72	2.93	2.48
Al_2O3	0.14	0.5	0.17	0.32	0.13	0.22	0.31
SiO_2	9.71	7.25	8.64	5.17	6.44	2.72	3.15
P_2O_5	33.43	40.38	33.54	35.05	42.39	35.97	30.14
CaO	8.47	8.55	10.16	10.93	8.37	16.56	12.53
TiO_2	7.45	3.98	2.29	1.84	4.15	1.66	1.33
MnO	3.82	3.51	5.56	6.56	4.86	5.88	5.97
FeO	0.89	0.81	2.83	3.05	1.93	3.13	3.09
Nb_2O_5	2.57	1.22	0.73	0.31	1.1	0.27	0.2
Total	81.14	77.8	74.97	77.23	82.88	82.94	70.46

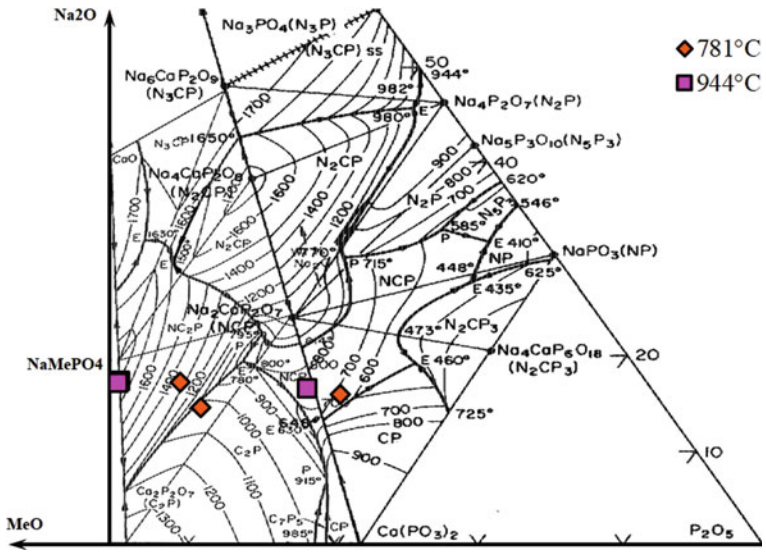

Fig. 2 Analyses of phosphate materials projected onto the CaO–Na_2O–P_2O_5 melting diagram (synthesis of [18, 19])

features of layered intrusions is hidden layering—graduate changing of composition of rock-forming and accessory minerals towards of layered sequence. Previously, L. N. Kogarko and co-authors found that the evolution of loparite and pyroxene upwards through the intrusion is consistent with idea of they crystallization from convecting magma and sedimentation to the bottom of magmatic chamber [22, 23].

Titanosilicates of lamprophylite group and lomonosovite-murmanite series are a spatially distributed in differentiated complex, mainly as a part of poly-mineral aggregates, replacing loparite crystals.

In the eudialyte lujavrites they became volumetrically important accessory minerals. In these rocks lamprophyllite usually form prismatic crystals, located between laths of microcline and crystals of eudialyte and nepheline, together with needle-shape aegirine sometimes with inclusions of aegirine.

4.1 Lamprophyllite Evolution

Three varieties of lamprophyllite-group minerals discovered in rocks of Lovozero massif: Sr-lamprophyllite, contain <0.2 apfu Ba and 0.08 apfu K, Ba–Sr lamprophyllite, contain 0.4–0.9 apfu Ba and 0.10–0.20 apfu K and baritolamprophyllite, contain 1.4 and more apfu Ba. Sr lamprophyllite is the most abounded. Sometimes it is corroded by the Ba-lamprophyllite [24].

The spatial variation of lamprophyllite composition was studied in vertical cryosections of eudialyte lujavrites at Kedykverpakh mountain and porphyritic lujavrites if Parguave mountain [24]. It was found that in 300 m crossection of eudialyte lujavrites lamprophyllitecomposition is stable, only the Fe content in lamprophyllite systematically increase upward. In crossection of 200 m thick body of porphyritic lujavrites in lamprophyllite upward increase Mn content whereas Mg, Ca and Fe content decrease. Ba/Sr ratio does not show any tendency in both cases.

Evolution of lamprophyllite composition inside one rock mainly from lamprophyllite to barytolamprophyllite is in agreement with experimentally founded dependence of the melting temperature on lamprophyllite composition, as well as Sr/Ba distribution between melt and lamprophyllite.

On other hand, independence of Ba/Sr ratio in lamprophyllite from the vertical position of sample show that during the crystallization of agpaitic magma of Lovozero massif lamprophyllite wasn't the cumulus mineral, but crystallise from interstitial melt.

4.2 Titanosilicate Melting as Model Reactions for Late-Magmatic Decomposition of Loparite

The incongruent melting of studied titanosilicates can be described by reactions:

$$\begin{aligned}
\text{Lamprophyllite} &= \mathrm{SrTiO_3} + \mathrm{TiO_2} + \mathbf{Na_2(Fe,Mn)Ti_7O_{16}} \\
&\quad + \text{titanosilicatemelt} \qquad \sim 890\,^{\circ}\mathrm{C} \\
\text{Barytolamprophyllite} &= \mathrm{SrTiO_3} + \mathrm{(Ba,K,Na)FeTi_4O_{10}} \\
&\quad + \mathrm{(Ba,Sr,)(Na,K)_2(Ti,Fe)_2(Si_2O_7)_2} \\
&\quad + \text{titanosilicatemelt} \qquad \sim 840\,^{\circ}\mathrm{C} \\
\text{Lomonosovite} &= \mathbf{Na_2(Fe,Mn)Ti_7O_{16}} + \mathrm{(Na,Ca)(Ti,Nb)O_3}. \\
&\quad + \text{phosphate melt}(+ \text{phosphate?}) \\
&\quad + \text{titanosilicate melt} \qquad \sim 860\,^{\circ}\mathrm{C}
\end{aligned}$$

Temperatures of these reactions are the maximal limits of stability temperatures for titanosilicates. But really crystallization temperatures of these minerals must be lower: for example, lamprophyllite-nepheline association must be stable lower 830 °C. Naturally, addition of any components must decrease possible temperature of crystallization of liquidus association, I believe that crystallization temperatures of these minerals in alkaline rocks must be at least 100 °C lower, then temperatures of they decomposition.

The interest feature of lomonosivite melting is immiscible salt and titanosilicate melts formation. Separation of lomonosovite components into salt and silicate parts allows us to assume that lomonosovite can be formed through interaction between immiscible silicate and salt melts. It is supposed, that silicate-salt liquid immiscibility can be important during late stages of alkaline magma evolution [1]. The spatial movement of these immiscible liquids (for example, in the interstitial space) can be responsible for the non-uniform distribution of lomonosovite (and formed after the lomonosovite betalomonosovite and murmanite) in the rocks.

There is extremely significant analogy: presence of titanosilicates in pseudomorphoses after the loparite and presence of perovsite-type solid solutions between melting products of titanosilicates: it shows that melting of titanosilicates may be a model of loparite decomposition.

The separation of lomonosovite components into salt and silicate parts allows us to assume that silicophosphates can be formed through interaction between loparite, immiscible silicate and salt (phosphate) melts.

Seven reactions between loparite with late magmatic melt were recognised by L. N. Kogarko and co-authors [22] as associations of secondary minerals after the loparite:

$$\text{Loparite} + L_1 = \text{Mosandrite} + \text{Lamprophyllite} + \text{Monazite} + L_2$$

$$\text{Loparite} + L_1 = \text{Barytolamprophyllite} + \text{Lomonosovite} + \text{Vitusite} + \text{Steenstrupine} + \text{REE, Sr Apatite} + L_2$$

$$\text{Loparite} + L_1 = \text{Monazite} + \text{Cerite} + \text{Barytolamprophyllite} + \text{unknown phase } (Na, K)_2(Ca, Mg, Fe, Mn)_{0.88}Ba_{0.93}Nb_{0.77}Ti_2Si_{4.09}O_{17}(F, OH, H_2O) + L_2$$

$$\text{Loparite} + L_1 = \text{Nenadkevichite} + \text{Monazite} + L_2$$

$$\text{Loparite} + L_1 = \text{Nordite} + \text{Lomonosovite} + L_2$$

$$\text{Loparite} + L_1 = \text{Vuonemite} + \text{Monazite} + L_2$$

$$\text{Loparite} + L_1 = \text{Barytolamprophyllite} + \text{Ba, Si rich belovite} + L_2$$

All of these associations contain phosphates and silicophosphates. The fact that phosphates and phosphosilicates are the common part of pseudomorphoses after the loparite shows that phosphate melt play an important rule in the processes of loparite decomposition.

All of these associations contain at least one mineral of Ti, Nb and REE. It indicate that Ti, Nb and REE never migrate away during loparite replacement, but only change mineral form. The inert (in the thermodynamic sense) behaviour of Ti, Nb and REE in the loparite decomposition processes allow as to calculate the simplified reactions between loparite and two melts (we believe that rocks contain NaF (villiamite) and $NaFeSi_2O_6$ (aegirine)):

1) $4(Na, REE)TiO_3 + 4Me_2 + {}_3(Si_2O_7) + 3NaF = Na_2Me_2 + {}_3REE_2Ti(Si_2O_7)_2F_2 + Me_2 + {}_2Na_3Ti_3(Si_2O_7)_2O_3F$
(mosandrite)(lamprophyllite)

2) $6(REE_{0,5x}Na_{1-0.5x})(Ti_xNb_{1-x})O_3 + 4SiO_2 + {}_2NaF + 4Na_3PO_4 + 6xNa_3PO_4 = (melt)_2Na_{11}Ti_4 + Nb_2[Si_2O_7]_2[PO_4]_2O_3F + 6xREEPO_4$
(vuonnemite)(monazite)

3) ${}_2(Na, REE)TiO_3 + Na_3PO_4 + {}_2Na_2MeSi_4O_{13} = Na_2Ti_2Si_2O_9 * Na_3PO_4 + Na_3REEMe_2Si_6O_{17}$
(silicate melt)(lomonosovite)(nordite)

4) $18(Na, REE)TiO_3 + Na_2Me_2 + {}_9Si_{31}O_{72} + 2H_2O + 6\ NaF + NaFeSi_2O6$
$(\text{silicate melt}) = 6\ Me_2 + {}_2Na_3Ti_3(Si_2O_7)_2O_3F + REE_9FeSi_7O_{27}(OH)_4$
(barytolamprophyllite)(cerite)

5) $6(Na, REE)TiO_3 + 2MeSi_4O_9 + 3NaF + 9NaMePO_4 = (\text{silicate melt})Me_2 + {}_2Na_3Ti_3(Si_2O_7)_2O_3F + NaMe_3REE(PO_4)_3(F)$
(barytolamprophyllite) + (belovite)

The composition of phosphate and silicate melts are plotted in Fig. 3. An accordance between silicate and salt melt composition consistent with idea that both melts can be the result of deep evolution of residual interstitial melt. It shows that the diversity of mineral associations, forming after the loparite can be explained by the variations in proportion and evolution degree of silicate and salt melts, effecting to the loparite.

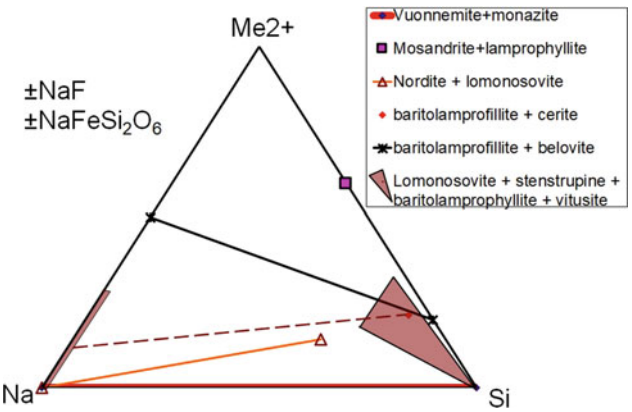

Fig. 3 Composition of phosphate and silicate melts which should react with loparite to produce observed mineral associations in pseudomorthoses after the loparite

5 Conclusions

Mineralogical diversity of titanosilicates and their chemical variations makes them the sensitive evident of agpaitic rocks forming conditions. But we need the experimental data, to connect the mineralogical observation and petrological processes understanding. To make a step on this way, melting of lamprophyllite, barytolamprophyllite and lomonosovite—widely spread titanosilicates of agpaitic rocks: was studied at 1 atm. The experiments show that lamprophyllite and barytolamprophyllite melt incongruently with formation of titanosilicate melt, $SrTiO_3$, TiO_2 and Na–Fe or Ba–Mn titanate respectively. Melting temperature decrease from lamprophyllite (~890 °C) to baritolamprophyllite (~840 °C). Lomonosovite melts incongruently at 820–866 °C with formation of immiscible titanosilicate and phosphate melts, $(Na,Ca)(Ti,Nb)O_3$, and Na–Fe titanate.

These temperatures should be considered as upper limits of their stability. The temperature of crystallization of these minerals are significantly lower, for example, coexisting of lamprophyllite and nepheline is limited by the reaction equilibrium lamprophyllite + nepheline = melt + tausonite + rutile + freudenbergite at ~ 830 °C.

The direction of evolution of lamprophyllite minerals: from Sr-rich to Ba-rich members, usually fixed in peralkaline rocks correspond to the relationship between temperatures of lamprophyllite and barytolamprophyllite decomposition.

The lamprophyllite crystallization from the melt was experimentally obtained for the frist time. Newly formed lamprophyllite always has higher Sr/Ba ratio than coexisting melt. It means that crystallization of lamprophyllite group minerals must result in decreasing Sr/Ba ratio of the melt. The independence of Ba/Sr ratio in lamprophyllite from the vertical position of sample shows that lamrophyllite wasn't cumulative mineral during crystallization of magma of Lovozero massif. Incongruent melting of titanosilicates serves as model reactions of late-magmatic loparite decomposition. The mineral associations formed by loparite replacement in Lovozero rocks was interpreted as the evidence of influence on loparite phosphate and silicate melts from this point of view.

The significant similarity between the experimental results on the titanosilicate melting and natural observations show that even so simplified systems may provide useful models, demonstrating the principles, reactions and directions of petrological processes.

Acknowledgements This article is dedicated to the memory of L. D. Krigman, who had real contribution to the article, as he designed the furnaces in which the experiments described in the article were performed. The author thanks I. V. Pekov and N. V. Vladykin for providing samples of lomonosovite from Khibina massif and barytolamprophylite from Murun massif. The author is grateful to V. G. Senin for help with microprobe analysis. The understanding of petrogenetical aspects has been enhanced by discussions with academician L. N. Kogarko.

References

1. Kogarko, L.N.: Problems of Agpaitic Magmas Genesis. Nauka, Moscow (1977) (in Russian)
2. Sørensen, H.: The agpaitic rocks: an overview. Mineral. Mag. **61**, 485–498 (1997)
3. Marks, A.W.M., Markl, G.: A global review on agpaitic rocks. Earth Sci. Rev. **173**, 229–258 (2017)
4. Athena Mineralogy, Search Mineral Formula: Ti Si. https://athena.unige.ch/cgi-bin/minfind.cgi. Last Accessed 10 November 2021
5. Glasser, F., Marr, J.: Phase relations in the system Na_2O–TiO_2–SiO_2. J. Am. Ceram. Soc. **62**, 42–47 (1979)
6. Zaitsev, V.A.: Krigman, L.D., Kogarko, L.N.: Pseudobinare phase diagram lamprophyllite-nepheline. In: 10th International Symposium on Experimental Mineralogy, Petrology and Geochemistry 2004 Lithos, Vol. 73, Issue no. 1–2, pp. S122–S122 (2004)
7. Zaitsev, V.A., Kogarko, L.N., Senin, V.G.: Phase equilibria in the system lamprophyllite-nepheline. Geochem. Int. **51**, 889–895 (2013)
8. MINDAT, Seidozerite Supergroup, https://www.mindat.org/min-50368.html. Last Accessed 10 November 2021
9. Sokolova, E.: From structure topology to chemical composition. I. Structural hierarchy and stereochemistry in titanium disilicate minerals. Can. Mineral. **44**, 1273–1330 (2006)
10. Zaitsev, V.A., Kogarko, L.N.: Compositions of minerals of the lamprophyllite group from alkaline massifs worldwide. Geochem. Int. **40**(4), 355–364 (2002)
11. Chukanov, N., Moiseev, M., Pekov, I., Lazebnik, K., Rastvetaeva, R., Zayakina, N., Ferraris, G., Ivaldi, G.: Nabalamprophyllite Ba(Na,Ba){$Na_3Ti[Ti_2O_2Si_4O_{14}](OH,F)_2$}, a new layer titanosilicate of the lamprophyllite group from Inagli and Kovdor alkaline-ultramafic massifs, Russia. Zapiski Vserossiiskogo Mineral Obshchestva. **133**, 59–73 (2004)
12. Back, M.E., Mandarino, J.A.: Fleischer's Glossary of Mineral Species. The Mineralogical Record Inc., Tucson (2008)
13. Rastsvetaeva, R., Chukanov, N., Aksenov, S.: The crystal chemistry of lamprophyllite-related minerals: a review. Eur. J. Mineral. **28**(5), 915–930 (2016)
14. Lykova, I.S., Pekov, I.V., Zubkova, N.V., Chukanov, N.V., Yapaskurt, V.O., Chervonnaya, N.A., Zolotarev, A.A.: Crystal chemistry of cation-exchanged forms of epistolite-group minerals, Part I. Ag- and Cu-exchanged lomonosovite and Ag-exchanged murmanite. Europ. J. Mineral. **27**(4), 535–549 (2015)
15. Lykova, I.S., Pekov, I.V., Chukanov, N.V., Belakovskiy, D.I., Yapaskurt, V.O., Zubkova, N.V., Giester, G.: Calciomurmanite, (Na,□)2Ca(Ti, Mg, Nb)4[Si2O7]2O2(OH, O)2(H2O)4, a new mineral from the Lovozero and Khibiny alkaline complexes, Kola Peninsula, Russia. Europ. J. Mineral. **28**(4), 835–845 (2016)
16. Zaitsev, V.A.: Numerical dependence of the unit-cell parameters of minerals of the lamprophyllite group on the cationic composition in the interlayer position. Crystallogr. Rep. **50**(3), 379–381 (2005)
17. Rastsvetaeva, R.K., Zaitsev, V.A., Pekov, I.V.: Crystal structure of niobium-rich lomonosovite with symmetry P1 from the Khibiny Massif (Kola Peninsula). Crystallogr. Rep. **65**(3), 422–427 (2020)
18. Berak, J., Znamierowska, T.: Phase equilibria in the system CaO–Na_2O–P_2O_5. Part II. The partial system $Ca(PO_3)_2$–Na_2O–P_2O_5. Roczniki chemii **46**(100), 1697–1708 (1972)

19. Berak, J., Znamierowska, T.: Phase equilibria in the system CaO–Na_2O–P_2O_5. Part III. The partical system $Ca_2P_2O_7$–$Ca(PO_3)_2$–Na_2O. Roczniki chemii **46**(11), 1921–1929 (1972)
20. Gerasimovsky, V.I., Volkov, V.P., Kogarko, L.N., Polyakov, A.I., Saprykina, T.V., Balashov, Y.A.: Geochemistry of the Lovozero Alkaline Massif. Nauka, Moscow (1966)
21. Bussen, I.V., Sakharov, A.S.: 1967 Petrology of the Lovozero Alkaline Massif. Leningrad, Nauka (1972)
22. Kogarko, L.N., Williams, C.T., Wooley, A.R.: Chemical evolution and petrogenetic implications of loparite in the layered, agpaitic Lovozero complex, Kola Peninsula, Russia. Mineral. Petrol. **74**, 1–24 (2002)
23. Kogarko, L.N., Williams, C.T., Wooley, A.R.: Compositional evolution and cryptic variation in pyroxenes of the peralkaline Lovozero intrusion, Kola Peninsula, Russia. Mineral. Magaz. **70** (4), 347–359 (2006)
24. Zaitsev, V.A.: Features of the Chemical Composition and Conditions for the Formation of Titanite and Minerals of the Lamprophyllite Group in the Lovozersky Massif, Kola Peninsula. PhD Dissertation Moscow (2005)

The Scale of Extraction of Ore Elements Zn and Pb by Aqueous Chloride Fluids in the Process of Degassing of Granite Magmas During Their Rise to the Surface and Crystallization

O. A. Lukanin

1 Introduction

The separation of magmatic fluids from granitic magmas during their rise to the surface and crystallization is one of the most important factors in the formation of ore-forming hydrothermal systems, genetically related to granitoid magmatism. The behavior of a number of ore and rare elements during the degassing of hydrous granitic magmas is closely related to the behavior of chlorine. The ability of chlorine to form stable complexes with such ore elements as Zn, Pb, Cu, Sn and others in the aqueous fluid phase determines its extremely important role in extraction of these "chlorophilic" elements from magmas and their transport by high-temperature fluids [1–10]. The experimental data available to date on the study of the equilibria of aqueous-chloride fluid-aluminosilicate melt at high temperatures and pressures indicate a significant influence on the distribution of volatile and ore components between the fluid and the melt of multiple physico-chemical factors. For Zn, Pb and other ore chlorophilic elements, in addition to temperature and pressure, the concentration of Cl in the fluid phase, the pH of the fluid, and the composition of the aluminosilicate melt itself are of great importance [1, 2, 11–16]. The evolution of natural fluid-magmatic systems, their degassing and crystallization are accompanied by simultaneous change in various physical and chemical parameters. Therefore, a quantitative description of the behavior of volatile and ore components in degassing processes of magmas is obviously possible only with the use of numerical modeling methods based on generalization of experimental and thermodynamic data for fluid-magmatic systems.

This report presents the results of numerical simulation of zinc and lead behavior during the degassing of H_2O-and Cl-bearing granitic magmas caused by pressure decrease as they rise to the surface, as well as during their crystallization at different depths. They make it possible to reveal some important regularities in the formation of the composition of magmatic fluids, concentration in them of such ore elements as Zn, Pb, depending on the initial concentration of volatile components in the magmatic melt, the depth at which degassing occurs, the ratio of crystallizing mineral phases, and the degree of system openness in relation to fluid phase. In addition, the data obtained make it possible to quantify the possible scale of ore elements removal from magmas in the process of their degassing at different depths.

O. A. Lukanin (✉)
Vernadsky Institute of Geochemistry and Analytical Chemistry, Russian Academy of Sciences, 19 Kosygin St., Moscow, 119991, Russia
e-mail: lukanin@geokhi.ru

2 Model

2.1 Experimental Basis

The empirical computer model developed by us for the joint behavior of volatile (H_2O, Cl) and ore components (Zn, Pb) in the process of degassing of granitic magmas caused by pressure decrease and/or crystallization of the melt consists of two main program blocks. The first one describes redistribution of water and chlorine between the melt and the fluid phase during magma degassing and is based on the generalization of experimental data on the solubility of H_2O in granitic melts [17–22], as well as data on the partition coefficients of chlorine between aqueous fluid and granitic melt ($D_{Cl}^{fl/m}$) of meta-and subaluminous composition [23–28]. The model takes into account the important feature of fluid-magmatic systems containing Cl and H_2O, namely, the existence of *PT*C region (P < 1.5–2 kbar, T = 800–1150 °C), where the fluid decomposes into two phases which are in equilibrium with aluminosilicate melt: essentially water-dominated chloride bearing fluid (aq) and Cl-rich aqueous chloride liquid (brine) (lq). The *PT*C boundaries of the existence of a heterogeneous fluid (aq + lq) are specified in the model based on experimental data for the NaCl–H_2O system [29]. The principles of building this model, its properties and limitations, as well as the results of modeling various cases of degassing of granitic magmas containing Cl and H_2O, were described by us earlier [30, 31].

V. P. Kolotov and N. S. Bezaeva (eds.), *Advances in Geochemistry, Analytical Chemistry, and Planetary Sciences*,
https://doi.org/10.1007/978-3-031-09883-3_7

The second program block describing distribution of zinc and lead between aqueous chloride fluid phase, melt and crystalline phase, is based on generalization of experimental data on partition coefficients of Zn and Pb fluid/melt ($D_{Me}^{fl/m}$) at high pressures [1, 11–16, 32], as well as data on partition coefficients of these elements crystal/melt ($D_{Me}^{cr/m}$) for the basic mineral phases of granitic magmas, obtained mainly by determining the contents of Zn and Pb in phenocryst minerals and in the bulk natural samples of volcanic rocks of acid composition [33].

All available experimental data indicate that with constant *PT* parameters, an increase in the concentration of Cl-ion in an aqueous fluid (C_{Cl}^{fl}), where Na and K chlorides predominate, causes a significant increase in the partition coefficients of ore elements fluid/melt ($D_{Me}^{fl/m}$). In the first approximation, the isobaric-isothermal dependence $D_{Me}^{fl/m}$ on C_{Cl}^{fl} can be described by an empirical equation like

$$\log D_{Me}^{fl/m} = A * \log C_{Cl}^{fl} + B, \quad (1)$$

where C_{Cl}^{fl} is the chlorine concentration in the fluid, expressed in *m* (mol/1 kg of fluid), *A* and *B* are the constants for the given *P* and *T*. The constant *B* is the limiting value of $D_{Me}^{fl/m}$ at infinite dilution of the fluid with water, when the Cl content in the fluid and, accordingly, in the melt tends to zero.

An increase in pressure at constant *T* and C_{Cl}^{fl} has the opposite effect—it leads to a decrease in $D_{Me}^{fl/m}$, which is especially pronounced in the area of low pressures up to 2–3 kbar, at higher pressures the effect is noticeably weaker. The influence of pressure on $D_{Me}^{fl/m}$ is reflected in a regular change in the values of the coefficients *A* and *B* in Eq. 1, which is approximately described by linear or polynomial equations $A = f(P)$ and $B = f(P)$. Substituting them into Eq. (1) we obtain an expression of the form

$$\log D_{Me}^{fl/m} = A(P) * \log C_{Cl}^{fl} + B(P), \quad (2)$$

which can be used to calculate the values of $D_{Me}^{fl/m}$ within the entire studied interval of *P* and C_{Cl}^{fl}.

In this version of the model, the experimental data of Urabe [13, 14] were used, which were obtained by the unified methodology for two natural compositions of granite melt in a relatively wide pressure range of 1.6–5 kbar at 800 °C. The dependence of $D_{Zn}^{fl/m}$ and $D_{Pb}^{fl/m}$ on the chlorine concentration in the fluid at 1.6 and 3.5 kbar (T = 800 °C) for the equilibria of high-silica and meta-alumina granite melts with an aqueous-chloride fluid is shown in Fig. 1a, b. On the whole, there is good agreement between experimental and model values of $D_{Zn}^{fl/m}$ and $D_{Pb}^{fl/m}$ values, taking into account the experimental errors, as well as the influence of variations in the composition of the granitoid melt. The change in model values of $D_{Zn}^{fl/m}$ and $D_{Pb}^{fl/m}$ at 800 °C in a wider pressure range is shown in Fig. 1c, d.

Model calculations assume degassing processes running under conditions close to isothermal (800 ± 25 °C). According to the limited data available so far, a change in

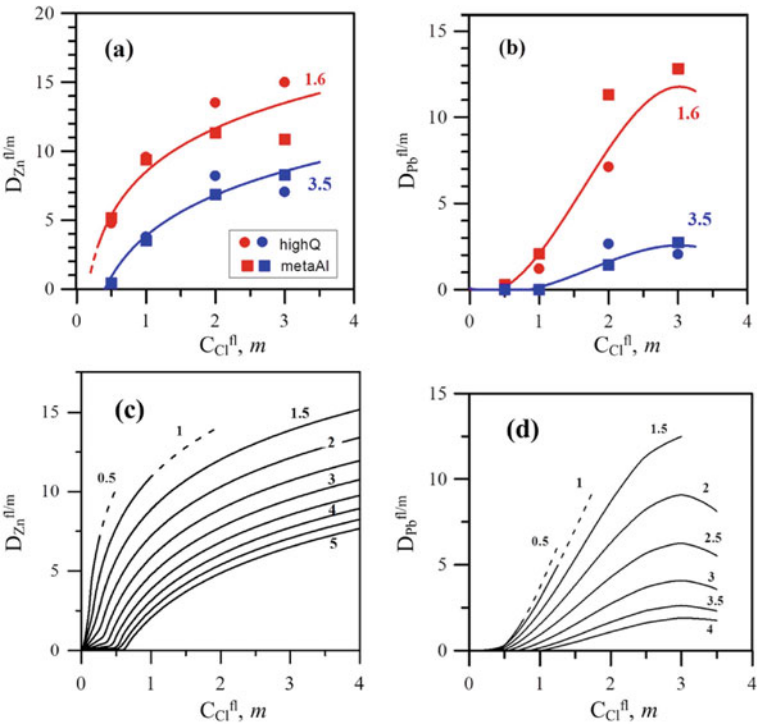

Fig. 1 Influence of the concentration of chlorine in the fluid (C_{Cl}^{fl}, mol/kg H_2O) on the partition coefficients of Zn and Pb fluid/melt ($D_{Zn}^{fl/m}$, $D_{Pb}^{fl/m}$). **a**, **b**—Comparison of the calculated model values of $D_{Zn}^{fl/m}$ and $D_{Pb}^{fl/m}$ with experimental data by Urabe, 1987 [14], obtained for the equilibria of high silica (highQ) and meta-alumina (metaAl) granite melts with a aqueous chloride fluid at 1.6 kbar, 800 °C **(a)** and 3.5 kbar, 800 °C **(b)**, **c**, **d**—Influence of C_{Cl}^{fl} and total pressure on the model partition coefficients $D_{Zn}^{fl/m}$ **(c)** and $D_{Pb}^{fl/m}$**(d)**. Numbers at the curves are the pressure in kbar

temperature within the range of 750–850 °C has no significant effect on fluid-melt partition coefficients both for water and chlorine, and for zinc and lead [11, 15, 32]. Therefore, in the first approximation, the calculated degassing paths obtained for the same initial composition within the given temperature range are likely to be close to each other.

2.2 Calculation Scheme

A simplified scheme for calculating the paths of changes in concentrations of volatile and ore components in fluid, melt and solid phases during degassing is shown in Fig. 2. The initial state of the system assumes a homogeneous melt with given concentrations of H_2O, Cl, as well as Zn and Pb. For a given composition of the melt, the pressure of its fluid saturation (P_{sat}) is first calculated. Further calculations of degassing paths are carried out by the method of successive approximations in two stages. At the first stage, the paths of change in concentrations of volatile components of H_2O and Cl in the fluid phase (C_{H2O}^{fl}, C_{Cl}^{fl}) and residual melt (C_{H2O}^{m}, C_{Cl}^{m}) are calculated at each successive step of decreasing pressure (in the case of decompression degassing) or increasing the degree of crystallization (in the case of the crystallization degassing). The step of increasing the degree of crystallization at a given total pressure (equal to P_{sat}) is determined by the amount of melt silicate matter that turns into a solid state. It is assumed that the resulting crystalline phases do not contain Cl and H_2O, i.e., the volatiles dissolved in the melt behave during crystallization as completely incompatible components. For more details on the procedure for calculating the concentrations and balance of volatiles, see [30, 31].

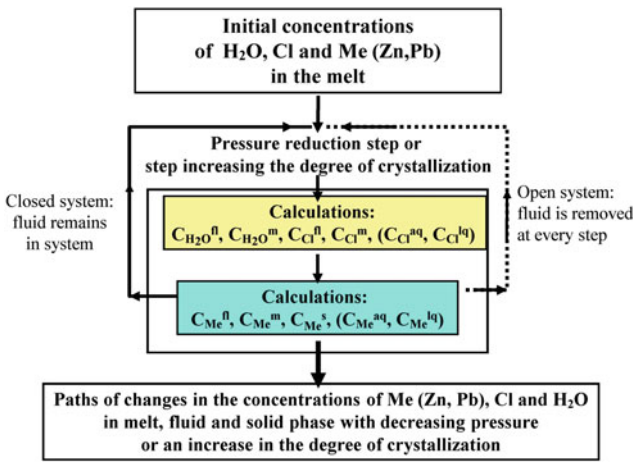

Fig. 2 Scheme for calculation of paths of the behavior of volatile (H_2O, Cl) and ore metals (Zn and Pb) during decompression and crystallization degassing of granite melts

At the second stage, for each case, for which H_2O and Cl concentrations in fluid and melt were calculated at the first stage, the distribution of ore elements Zn and Pb between fluid, melt, and in case of crystallization degassing and crystalline phases is calculated. In case of decompression degassing (crystalline phase is absent, or its content remains constant) on each subsequent step of pressure reduction, using the dependence of $D_{Me}^{fl/m}$on C_{Cl}^{fl} (Eq. 2), the equilibrium metal concentrations in the fluid and melt are calculated by carrying out repeated cycles of calculations C_{Me}^{fl} and C_{Me}^{m}, taking in each new cycle values $D_{Me}^{fl/m}$ which have been obtained in the previous cycle. In order to achieve the "equilibrium" condition, the calculations are repeated in this sequence until the absolute value of the difference between the $D_{Me}^{fl/m}$ values obtained in two subsequent calculation cycles ($|\Delta D_{Me}^{fl/m}|$) becomes $\leq$ 0.0001.

In the case of crystallization degassing (at P = constant), a part of ore elements is distributed into formed crystalline phases, being in equilibrium with the melt and fluid. Therefore, after the first stage of calculation at each step of crystallization C_{Me}^{fl} and C_{Me}^{m} for fluid-melt equilibrium in the above described way (without taking into account the presence of crystalline phases), the concentration of the ore element in "solid phase" (C_{Me}^{s}), which should be in equilibrium with the melt, is calculated at the second stage. The term "solid phase" here refers to the resulting ensemble of mineral crystalline phases typical for granitoid magmas (quartz, plagioclase, potassium feldspar, biotite and magnetite) in arbitrarily specified ratios. In the calculations it is assumed that the crystal-melt partition coefficients of Zn and Pb for each individual mineral ($D_{Me}^{cr/m}$) and, accordingly, the bulk partition coefficients for the entire crystallizing solid mineral association ($D_{Me}^{s/m}$) remain constant regardless of the pressure and composition of the melt. The calculation of C_{Me}^{s} at each crystallization step (decrease in the mass of the melt) is carried out by the approximation method using the values of $D_{Me}^{s/m}$, calculated for a given mineral association. The condition for the equilibrium of crystalline mass with the melt in relation to the distribution of ore elements is the achievement of the absolute difference between the values of $D_{Me}^{s/m}$, in the two subsequent cycles of calculations, the value $\leq$ 0.0001. As a result of the transition of a part of the metal from the melt to the solid phase, C_{Me}^{m} decreases, so the equilibrium distribution of metal between the melt and the fluid is disturbed. Therefore, the first stage of calculating of the new "equilibrium" values of C_{Me}^{fl} and C_{Me}^{m} is repeated again. Thus, by successive approximations, both stages of calculations are repeated until metal concentrations in the melt and in the solid phase are equalized and the absolute value of the difference between the C_{Me}^{m} values obtained in two subsequent calculation cycles remains less than 0.0001 ppm.

The calculations can be performed both for conditions corresponding to a closed system, when the fluid phase is preserved in the magma, and for conditions corresponding to an open system, when the resulting fluid phase is completely (or partially) removed from the magmatic system after each subsequent step of pressure decrease (or increase in the degree of crystallization). As a result, at the output we obtain the calculated paths of changes in concentrations of H_2O, Cl, as well as Zn and Pb in the melt and fluid during either pressure decrease or crystallization at certain constant pressure. In the latter case, the change of total Zn and Pb content in crystalline phases is additionally calculated. Calculation of the balance of metals between fluid, melt and crystalline phases allows to quantify the degree of their extraction by the fluid phase in the process of degassing of magmas during their ascent and/or crystallization.

In general, the used complex of computer programs makes it possible to simulate the joint behavior of volatile (H_2O, Cl) and ore components (Zn, Pb) during degassing of granite melts at depths corresponding to the Earth's crust, in the pressure range from 0.3–0.5 to 3.5–4 kbar. The main limitations of this model will be considered below when discussing the results of numerical simulations.

3 Numerical Simulation Results

Model calculations were carried out for the melts with initial chlorine content typical for natural granitic magmas of meta- and subaluminous composition that, according to determinations of Cl in melt inclusions in phenocryst minerals, as well as in volcanic glasses of acid igneous rocks, can vary in a wide range 0.05–0.25 wt % (on average about 0.15–0.20 wt %) [34]. For simplicity, the initial zinc and lead concentrations in the melt were taken equal to 100 ppm, which is much higher than the average concentrations of these elements in granites of 60 and 20 ppm, respectively [35]. The obtained calculated concentrations in fluid, melt and solid phase can be easily recalculated for other specific initial metal contents in the melt ($C_{Cl}^{m\#}$) by multiplying the calculated values by coefficient $K = [C_{Cl}^{m\#}]/100$.

3.1 Melt Degassing Caused by Pressure Decrease

The concentration of Zn and Pb in the aqueous chloride fluid phase formed in the magmatic system during pressure decrease and/or crystallization, and, correspondingly, the degree of extraction of these metals from the melt, is largely determined by the behavior of chlorine, its concentration in the fluid C_{Cl}^{fl}. In turn, the value of C_{Cl}^{fl} depends on the initial Cl content in the melt C_{Cl}^{m}, as well as the depth (pressure) of the beginning of degassing, which mainly depends on the initial H_2O content in the melt (C_{H2O}^{m}) [30]. Therefore, before proceeding to the results of ore element behavior modeling, let us briefly review the main features of chlorine behavior.

3.1.1 Chlorine Behaviour

To illustrate the behavior of chlorine during decompression degassing, Fig. 3 shows the change in C_{Cl}^{fl} and C_{Cl}^{m} during degassing of granite melt with different initial Cl content, fluid saturation of which is reached at 3 kbar. In the process of lifting and degassing, C_{Cl}^{fl} decreases rapidly. Under open conditions, when the fluid phase is completely removed from the system after each pressure reduction step, the C_{Cl}^{fl} drop is most dramatic. The higher the initial Cl concentration in the melt, the higher its concentration in the fluid throughout the entire pressure reduction range. Under open conditions, the Cl concentration in the melt decreases during degassing, as well as in the fluid. However, under closed conditions, C_{Cl}^{m} behaves in a more complex way. After reaching a minimum, the Cl concentration in the melt increases and at

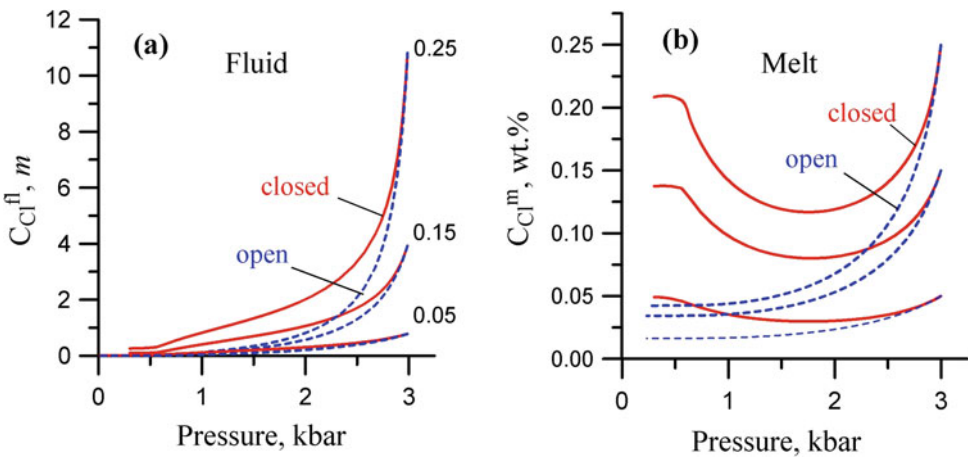

Fig. 3 Changes in the Cl concentration in the fluid **(a)** and melt **(b)** during decompression degassing of the melt, the fluid saturation of which is reached at 3 kbar (initial H_2O content in the melt is 7.6 wt %). The numbers at the curves in Fig. 3a are the Cl content in the initial melt in wt %

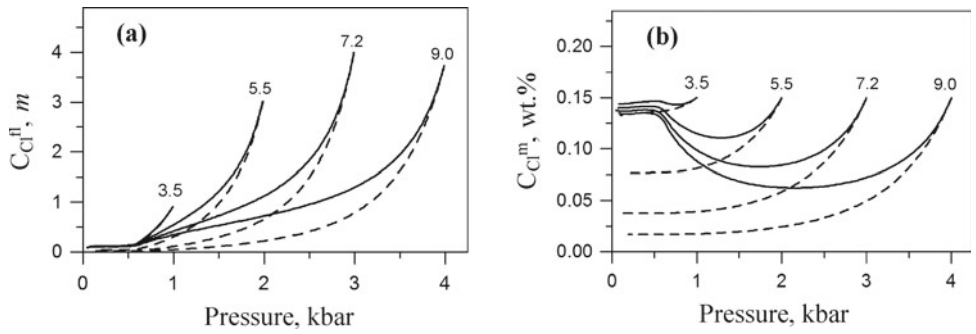

Fig. 4 Influence of the pressure of the beginning of degassing (P_{sat}) on the Cl concentration in the melt **(a)** and fluid **(b)** during decompression degassing. The initial melt contains 0.15 wt % Cl and various concentrations of H_2O, the degassing of which begins at 1, 2, 3 and 4 kbar. The solid lines are paths in the closed system. The dashed lines are paths in the open system, when the formed fluid phase is completely removed from the system after each step of pressure reduction. The numbers near the curves are initial concentrations of H_2O in the melt in wt %

low pressures ($\leq$ 0.5–0.6 kbar) approaches the initial value of C_{Cl}^{m} before its degassing, due to a decrease in $D_{Cl}^{fl/m}$.

Figure 4 demonstrates how the pressure of the beginning of degassing (P_{sat}) and, respectively, the initial H_2O content affects chlorine behavior during decompression degassing of the melt with a constant initial Cl content of 0.15 wt %. The general character of C_{Cl}^{fl} and C_{Cl}^{m} paths during degassing under closed and open conditions, when P_{sat} varies between 1 and 4 kbar, remains unchanged-the same as in Fig. 3. Let us note two features of the influence of P_{sat} on chlorine behavior: (1) C_{Cl}^{fl} in the very first portions of the fluid formed when P_{sat} decreases from 4 to ~3 kbar, first increases, reaches a maximum, and then at lower pressures (< 2 kbar) decreases sharply. (2) With a decrease in the degassing start pressure the C_{Cl}^{fl} and C_{Cl}^{m} paths converge for closed and open conditions. This is especially pronounced for the case shown for P_{sat} = 1 kbar.

3.1.2 Behaviour of Zn and Pb

The change in the concentrations of zinc and lead in the fluid during the ascent of the magmatic melt in the process of decompression degassing under conditions close to isothermal is largely similar to C_{Cl}^{fl}. The first deepest portions of the forming fluid phase, regardless of the pressure of the beginning of degassing and the degree of the openness of the system, have the highest concentrations of chlorine, as well as ore elements, which then decrease during degassing as the pressure decreases. During the ascent of melts enriched with volatile components with initial contents of 5.5–7.6 wt % H_2O, 0.15–0.25 wt % Cl and 100 ppm metal, degassing of which starts at relatively large depths corresponding to 2–3 kbar, the concentration of Cl, as well as Zn and Pb in the first portions of fluid can reach high values: C_{Cl}^{fl} 4–10 m, and C_{Zn}^{fl} and C_{Pb}^{fl} respectively 1100–1500 and 300–600 ppm.

As an example, Fig. 5 shows the case of melt degassing with initial contents of 7.5 wt % H_2O and 0.2 wt % Cl, when the concentrations of Zn and Pb in the fluid phase occurring at a pressure of 3 kbar are ~1300 and 375 ppm respectively. The C_{Cl}^{fl} values within range from 3 to 2.75 kbar at the first stages of degassing in a closed and open system are close to each other and decrease to ~950 ppm. On the other hand, the lead concentration in a fluid in the same pressure range first increases slightly (up to 500–550 ppm), that is a consequence of more significant increase of $D_{Pb}^{fl/m}$ with a decrease in P compared to $D_{Zn}^{fl/m}$ (see Fig. 1). With a further decrease in P during degassing, C_{Zn}^{fl} and C_{Pb}^{fl} as well as C_{Cl}^{fl} fall sharply, especially in the case of an open system, when the fluid is removed from the system. At low P, the difference in concentrations of metals in fluids formed in closed and open conditions increases and can be quite significant. For example, at P = 1 kbar, the C_{Zn}^{fl} value in closed conditions (~670 ppm) is more than five times higher than in open conditions (~120 ppm). Compared to zinc, the behavior of lead in the open and closed system is even more contrasting: already at 2 kbar the C_{Pb}^{fl} value in closed conditions is almost 7 times higher than in open conditions (~350 and 50 ppm, respectively). A decrease in pressure, as mentioned above, leads to an increase in $D_{Zn}^{fl/m}$ and $D_{Pb}^{fl/m}$ at C_{Cl}^{m} = const (Fig. 1). However, in this case, we observe a decrease in C_{Zn}^{fl} with a decrease in P in both open and closed system. This means that in the process of decompression degassing, the change in the Cl concentration in the fluid, rather than pressure, is of decisive importance on the behavior of metals: the effect of a decrease in $D_{Me}^{fl/m}$ with a decrease in C_{Cl}^{fl} is stronger than the effect of an increase in $D_{Me}^{fl/m}$ with a decrease in pressure.

Figure 5a, b also show changes in the concentrations of Zn and Pb in the melt in equilibrium with the fluid. In the process of decompression degassing, C_{Zn}^{m} gradually decreases. At 0.5 kbar, C_{Zn}^{m} is 80 and 83 ppm under closed and open conditions, respectively. The value of C_{Pb}^{m} remains practically constant or even slightly increases,

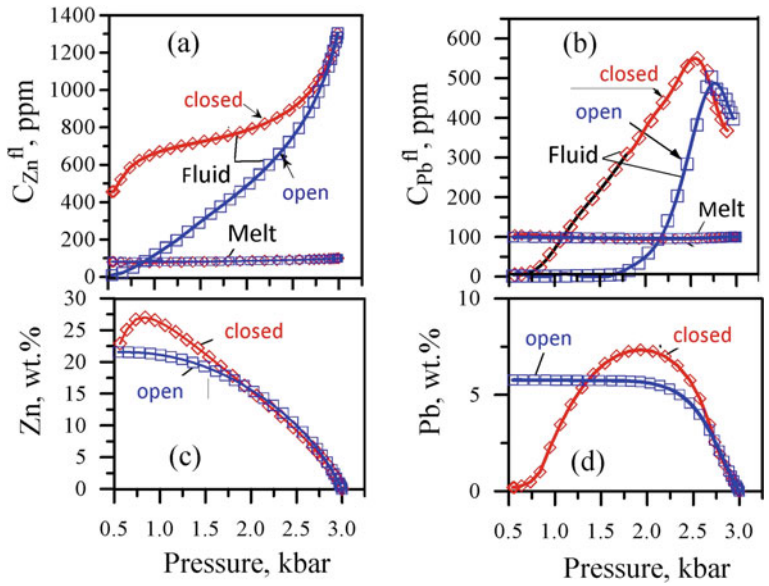

Fig. 5 Behavior of Zn and Pb during decompression degassing of Cl- and H_2O-containing granite melt. The initial melt contains 7.5 wt % H_2O, 0.2 wt % Cl and 100 ppm metal (Zn, Pb). **a, b**—Change in the concentration of Zn **(a)** and Pb **(b)** in fluid and melt during degassing under closed and open conditions. **c, d**—The degree of extraction of Zn **(c)** and Pb **(d)** from the initial melt during decompression degassing (in wt % of the initial metal content in the melt). The distance between the icons corresponds to the step of pressure decreasing in the calculations (hereinafter in other figures)

which is a consequence of lower values of $D_{Pb}^{fl/m}$ than $D_{Zn}^{fl/m}$ under given *PT*C conditions, as well as a decrease of H_2O concentration in the melt during degassing.

The degree of extraction of Zn and Pb by the fluid phase from the initial melt (in wt % of the initial C_{Me}^{m}) at different stages of decompression degassing is shown in Fig. 5c, d. It remains approximately the same both in closed and open conditions with a decrease in *P* down to ~1.5 kbar for Zn and down to 2.5 kbar for Pb. Only in the area of lower pressures (in the range of 1.5–0.7 kbar for Zn, and 2.5–1.5 kbar for Pb), when C_{Me}^{fl} in the closed conditions becomes significantly higher than C_{Me}^{fl} in the open conditions, the amount of extractable fluid metal in the closed system becomes slightly higher in comparison with an open system. It should be noted that the degree of Pb extraction under open conditions remains practically unchanged over the whole range of pressures below 1.5 kbar.

During degassing at low *P* (< 1 kbar for Zn and < 2 kbar for Pb) the recovery of metals in a closed system decreases. The metal from the fluid phase is partially transferred to the melt, as a result of decreasing chlorine concentration in the fluid and, correspondingly, a decrease in $D_{Me}^{fl/m}$. It is especially pronounced for lead, the degree of extraction of which at $P \leq 1$ kbar in the open system becomes significantly higher than in a closed one.

Effect of C_{Cl}^{m}. Let us consider the effect of the initial Cl content in the melt on the change in C_{Zn}^{fl} during decompression melt degassing as an example of zinc behavior. Figure 6, as Fig. 5 shows the case when fluid saturation of the melt containing 0.05–0.25 wt % Cl occurs at 3 kbar. An increase in C_{Cl}^{m} in the initial melt (at C_{H2O}^{m} = constant) leads to an increase in the concentration of both chlorine and Zn in the fluid phase formed during melt degassing at a given depth under both closed and open conditions. Accordingly, the higher C_{Cl}^{m} in the initial melt, the higher the degree of metal extraction by the fluid phase during degassing.

The effect of C_{H2O}^{m}. The calculations presented in Fig. 7, demonstrate the effect of C_{H2O}^{m} in the initial melt and on the pattern of change in C_{Zn}^{fl} and the degree of zinc extraction during decompression degassing. The case is shown when the Cl concentration in the initial melt is constant and equal to 0.2 wt %. A decrease in initial C_{H2O}^{m} leads to a decrease in fluid saturation pressure P_{sat}. The first portions of fluid phase formed during the degassing of melts with different H_2O/Cl ratios at P_{sat} = 1–3 kbar are highly enriched with zinc (Fig. 7a, c). With a decrease in the pressure of the beginning of degassing C_{Zn}^{fl} in the very first portions of the fluid initially even slightly increases, despite the fact that Cl concentration in these fluids decreases (see Fig. 4a). In this case, the opposite effect of pressure on $D_{Cl}^{fl/m}$ and $D_{Zn}^{fl/m}$ is manifested. The decrease in $D_{Cl}^{fl/m}$ with decreasing pressure is compensated by simultaneous increase in $D_{Zn}^{fl/m}$. As a result, metal concentrations in the fluid remain very high. Only at pressures below 1.5 kbar there is a sharp decrease in $D_{Cl}^{fl/m}$ in the first portions of the fluid, due to the growing

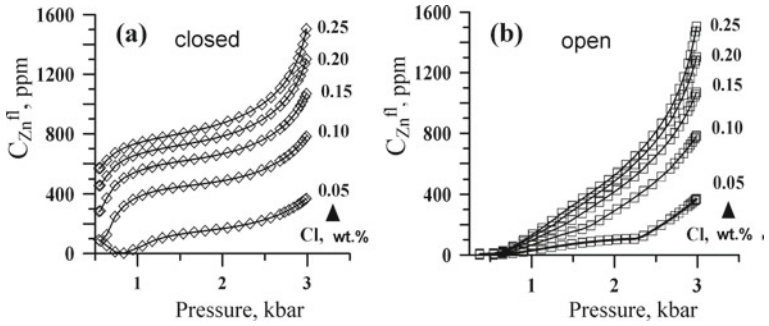

Fig. 6 Influence of the initial chlorine concentration on the Zn concentration in the fluid formed at decompression degassing of granite melt, fluid saturation of which is reached at 3 kbar, under closed **(a)** and open **(b)** conditions. The numbers at the curves are the initial Cl content in the melt in wt %

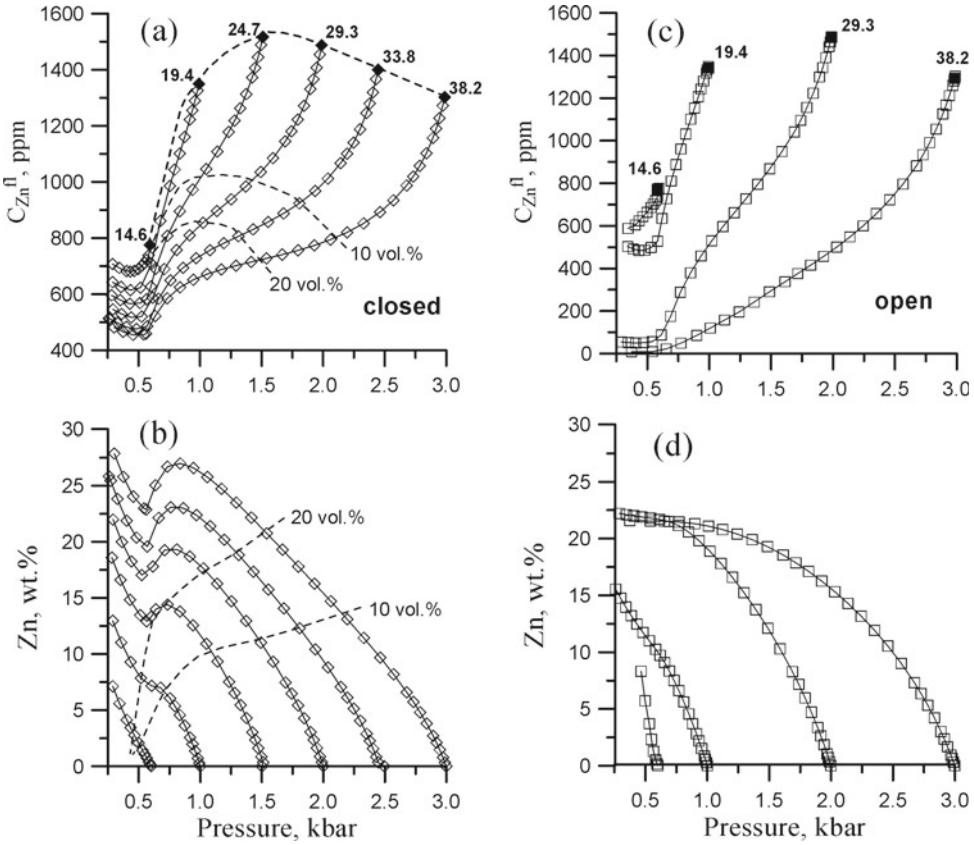

Fig. 7 Influence of water concentration in the initial melt on the behavior of zinc during decompression degassing of the melt containing 0.2 wt % Cl and 100 ppm Zn at 800 °C. **a**, **c**—Change in Zn concentration in the fluid under closed **(a)** and open **(c)** conditions. **b**, **d**—The amount of Zn, released together with the fluid phase (in wt % of its initial content in the melt) under closed **(b)** and open **(d)** conditions. Figures 7a,c show the H_2O/Cl (wt.) ratio in the initial melt by the numbers next to the filled symbols. In Fig. 7a, b the dashed lines show the volumes of fluid phase in the magmatic system (10 and 20 vol %) that are achieved during degassing in the closed system. In the calculations, we used data on the specific volumes of water at high *P* and *T* [36, 37]. The melt specific volume was assumed constant at 0.425 cm^3/g (density 2.35 g/cm^3). The influence of the presence of chlorides and other dissolved components in an aqueous solution was not considered

release of water from the melt (an increase in mass of the fluid) and, accordingly, a significant decrease in C_{Cl}^{fl}. In this case, the pressure decrease is no longer able to compensate for the associated sharp decrease in $D_{Zn}^{fl/m}$.

The degree of metal extraction from the melt during decompression degassing is determined by C_{Me}^{fl} and the mass of the fluid phase formed. A decrease in the water content in the initial melt (at C_{Cl}^{m} = constant) causes a

decrease in the mass of the fluid formed during decompression and thus leads to a significant reduction in the amount of metal extracted by the fluid in both closed and open conditions (Fig. 7b, d). For example, at degassing of melts with different initial water content of 7.5 and 5.3 wt % for which P_{sat} is achieved, accordingly, at 3 and 2 kbar, the degree of metal recovery at P = 1.5 kbar in the first case is about 21%, and in the second about 11%, although C_{Zn}^{fl} in the first case is much lower (~700 ppm) than in the second one (~1020 ppm).

Figure 7a, b additionally shows pressures, as well as zinc concentrations in fluid and degree of its extraction from the initial melt during degassing in closed conditions at the moment when due to fluid accumulation and increase of its volume up to 10 or 20 vol % (of total system volume), it becomes possible to remove fluid from the system.

Scale of extraction of Zn and Pb. The results of balance calculations, presented in Fig. 8, demonstrate quantities of ore elements, which can be removed together with fluids in conditions of open magmatic system during decompression degassing at different depths. The calculations were executed for the initial melt with mass of 2.3×10^9 tons (volume 10^6 m^3), containing 0.2 wt % Cl, 7.5 wt % H_2O, 100 ppm Zn or Pb, the degassing of which during decompression starts at 3 kbar (the paths of ore elements concentration changes in the fluid and melt for this case are shown above in Fig. 5). The filled part of the columns in Fig. 8 corresponds to the mass of metal extracted by the fluid from the melt at a certain range of P, equal to ~0.5 kbar. It was calculated by summing up the masses of metal released from the melt into the fluid within a given pressure (depth) interval at each pressure reduction step. The non-filled part of the columns corresponds to the mass of metal released into the fluid during the previous steps of melt ascent. Thus, the total height of the column shows the total amount of metal that is removed from the melt in this and all previous pressure intervals, after the beginning of its degassing at 3 kbar. The figure clearly shows that in conditions of an open system the largest amounts of ore metals are extracted from magma at the first stages of decompression degassing, despite the fact that the total mass of fluid removed from the system is very small. It is especially indicative for lead. Total amount of zinc extracted from the melt at depths corresponding to 0.5 kbar (about 5000 tons) exceeds more than 3.5 times the amount of lead extracted in the same depth interval (~1300 tons).

These model estimates are made for the melt with equal initial metal contents of 100 ppm for the case when all the fluid phase is completely removed from the system at each step of pressure reduction. For natural magmatic systems, these estimates will obviously be overestimated especially for lead, taking into account, firstly, that typical granitic magmas are characterized by lower Zn (40–70 ppm) and Pb (10–30 ppm) contents and, second, under natural conditions the dynamics of fluid removal from the magmatic system may be more complicated and depends on the rate of magma ascent, the volume of the fluid phase released from the melt and other factors. Thus, it can be assumed that the calculated estimates of amount of ore elements extracted from magmatic melts by fluid during their rise to the surface are the maximum possible.

3.2 Degassing During Crystallization of Melts

Numerical modeling of degassing processes during crystallization of granite magmas saturated with aqueous chloride fluid was carried out for isobaric-isothermal conditions, i.e. the case of eutectoid crystallization was considered, when

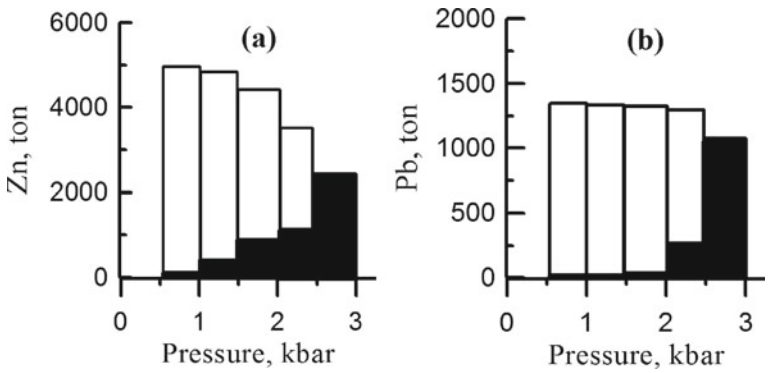

Fig. 8 Amounts of Zn **(a)** and Pb **(b)** extracted by the fluid phase during decompression degassing of the melt under open conditions in the range from 3 to 0.5 kbar. The melt mass is 2.3×10^9 tons (volume 10^6 m^3), initial concentrations: 0.2 wt % Cl, 7.5 wt % H_2O, 100 ppm Zn and Pb. The filled part of the columns is the amount of metal released in a given pressure range. The non-filled part of the columns is the amount of metal released during the entire previous stage of degassing. The height of the columns corresponds to the total amount of metal released at a given stage of rise of the melt

the ratios of crystallizing mineral phases and correspondingly bulk partition coefficients of ore elements between solid phase and melt remain constant. The concentrations of zinc, lead and other "chlorophilic" metals in fluids released from the melt during the crystallization of magmas depend on the initial concentrations in the melt of the metals themselves and volatile components, especially chlorine, as well as on the total pressure (depth) at which crystallization occurs, the type and ratio of crystallizing mineral phases, the crystal/melt metal partition coefficients, as well as the degree of system openness.

3.2.1 Chlorine Behavior

It is important to note that chlorine behavior during crystallization degassing of granitic melts essentially depends on pressure [31]. This should inevitably be reflected in peculiarities of zinc, lead and other "chlorophilic" elements behavior during magma crystallization at different depths. At relatively high pressures ($P \geq 1.6$ kbar), degassing of melts is accompanied by a decrease in chlorine concentration in the fluid and melt regardless of the degree of system openness. The higher the pressure at the start of degassing and the initial Cl content in the melt, the more clearly this trend manifests itself, especially in the conditions of an open system.

At moderate pressures in the interval 0.9–1.6 kbar this tendency is expressed much weaker and in the process of crystallization can change to the opposite one—a slight increase in C_{Cl}^{m} and C_{Cl}^{fl}. Degassing caused by crystallization at "low" pressures < 0.8–0.9 kbar from the very beginning of degassing leads to chlorine accumulation in the fluid phase and residual melts. As a result, at a certain stage of crystallization of initial melt, a heterogeneous fluid may be formed, consisting of an essentially aqueous-chloride phase (aq) and chloride liquid (brine, lq). With further crystallization, the chlorine concentrations in aq and lq, as in the silicate melt, C_{Cl}^{aq}, C_{Cl}^{lq} C_{Cl}^{m}, remain constant, while only the mass ratios of these phases change. The reasons for the inversion in chlorine behavior with decreasing pressure are mainly related to the decrease in $D_{Cl}^{fl/m}$ and incoherent behavior of Cl during crystallization (see in more detail in [31]).

As an illustration, Fig. 9 shows calculated paths of C_{Cl}^{fl} change during crystallization of a fluid-saturated granite melt at "high" (2 kbar) and "low" total pressure (0.6 kbar). Crystallization and, accordingly, a decrease in the proportion of melt in the system at 2 kbar causes a decrease in C_{Cl}^{fl} both under closed and open conditions. Moreover, the higher the initial Cl content in the melt, the higher C_{Cl}^{fl} at the initial crystallization stages and the more abruptly it decreases during further crystallization, especially under open conditions (Fig. 9a).

A fundamentally different situation takes place at 0.6 kbar. In this case the fluid phase formed at the initial stages of crystallization has much lower C_{Cl}^{fl} (at the same initial C_{Cl}^{m} in the melt) and during crystallization C_{Cl}^{fl} increases rather than decreases. Upon reaching a certain degree of crystallization, the fluid phase splits into aq and lq. Under closed conditions, during further crystallization, the total mass of the fluid (aq + lq) increases and becomes enriched in chlorine as a result of an increase in the lq/aq ratio. In open conditions, when the fluid at each step of crystallization is completely removed from the system at each crystallization step, the composition of the separating heterogeneous fluid changes abruptly and further remains constant (Fig. 9b).

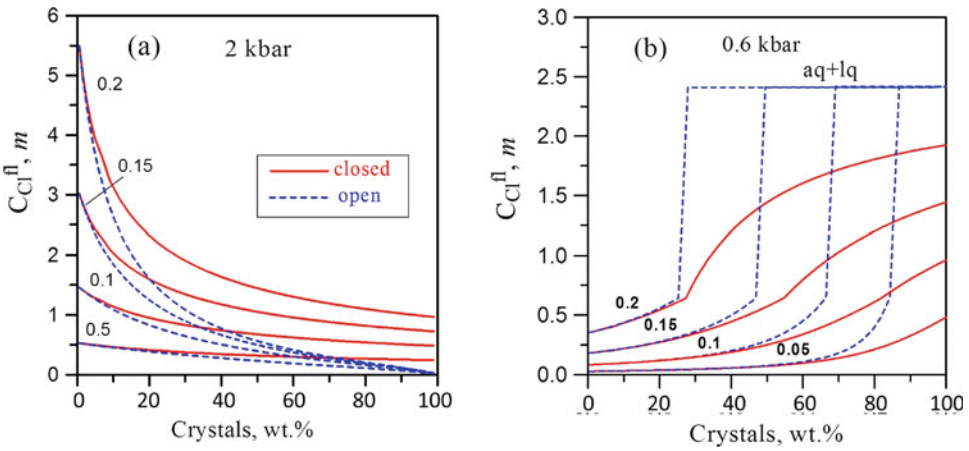

Fig. 9 Change in Cl concentration in the fluid during crystallization degassing at 2 kbar (**a**) and at 0.6 kbar (**b**). Solid lines-under closed conditions, dashed lines-under open conditions. The numbers near curves are the initial chlorine content in the melt in wt %. aq + lq is the region of existence of a heterogeneous fluid consisting of an aqueous chlorine-containing phase (aq) and chloride liquid (lq). The inflection points on the C_{Cl}^{fl} paths in a closed system (solid lines) correspond to the moment when fluid splits during crystallization with formation of aq and lq, the composition of which remains constant during further crystallization at given P and T

3.2.2 Partition Coefficients of Zn and Pb Crystal/Melt

Before proceeding to results of numerical modeling of Zn and Pb behavior during crystallization degassing of Cl-and H_2O-bearing granitic magmas at different depths, let us consider possible variations of partition coefficients of these metals between solid phase and melt. For this purpose we use the database on partition coefficients of Zn and Pb crystal/melt for the main mineral phases of granitic magmas from GERM Partition Coefficient Database [33], which are summarized in the Table 1. Most of these data were obtained by analyzing the phenocryst minerals and their host main mass (matrix) of natural samples of volcanic rocks of acid composition (rhyolites, dacites). An exception is the zinc sulfide/silicate melt partition coefficient, which was determined experimentally in the FeS–FeO–SiO_2 system. $D_{Me}^{cr/m}$ values for quartz, which obviously should be much lower than for other mineral phases, were taken arbitrarily.

For the model calculations presented below, it was assumed in the first approximation that the major rock-forming minerals plagioclase (Pl), potassium feldspar (Kfs), and quartz (Qz) crystallize from the melt in the mass ratio 1:1:1. In this case average bulk coefficients $D_{Zn}^{s/m}$ and $D_{Pb}^{s/m}$ are 0.16 and 0.62, respectively.

From the Table 1 we can see that the greatest influence on the value of the bulk zinc coefficient, $D_{Zn}^{s/m}$, is exerted by the fraction of crystallizing dark-colored minerals magnetite, biotite, ilmenite and amphibole. Compared to these minerals, the influence of possible changes in the ratio of quartz and feldspars crystallizing from melts of granite composition is relatively small. The calculated data on the change in $D_{Zn}^{s/m}$ depending on the amount of dark-colored minerals biotite (Bi) and magnetite (Mt) in the mineral association crystallizing from the melt (with the given ratio Pl:Kfs:Qz = 1:1:1) are presented in Fig. 10. For the most widespread meta-and subaluminous granitic magmas, in which the proportion of biotite and magnetite (+ilmenite) among crystallizing phases

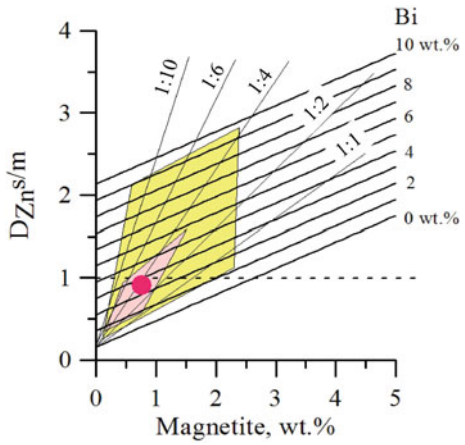

Fig. 10 Changes in bulk zinc partition coefficient $D_{Zn}^{s/m}$ (crystals/melt) depending on the amount of crystallizing dark-colored minerals biotite (Bi) and magnetite (Mt). It is supposed that the ratio of the main crystallizing phases is plagioclase (Pl): potassium feldspar (Kfs): quartz (Q) = 1:1:1. Areas of possible $D_{Zn}^{s/m}$ variations in granite magmas are shaded. Red circle-average values of $D_{Zn}^{s/m}$ for the most widespread meta-alumina granitic magmas. Thin straight lines correspond to the change in $D_{Zn}^{s/m}$ at a constant Bi:Mt ratio

is on average 2–3 and 0.5–1%, accordingly, the $D_{Zn}^{s/m}$ value varies in the range 0.8 ± 0.2. For the leucocratic alaskite and aplite granites, in which the fraction of dark-colored minerals is very small (Bi < 1%, Mt < 0.2%), the value of $D_{Zn}^{s/m}$ is significantly less than 1 (~0.3–0.4), whereas for the biotite granites with high Bi (> 8%) and Mt (> 1.5%) the $D_{Zn}^{s/m}$value becomes more than 1 and can reach 2–2.5. Thus, during crystallization of different types of granitic magmas, $D_{Zn}^{s/m}$ can vary within a fairly wide range from 0.3 to 2.5, and taking into account possible errors in determining $D_{Zn}^{cr/m}$, these limits can be even wider (Fig. 10). The crystallization of apatite due to its insignificant amount and the precipitation of sulfide phase at the final stage of magma crystallization, obviously, cannot appreciably affect the value of zinc bulk coefficient $D_{Zn}^{s/m}$.

Table 1 $D_{Zn}^{cr/m}$ and $D_{Pb}^{cr/m}$ values for natural acid magmas (*According to* GERM Partition Coefficient Database)

Mineral	Type of rock	$D_{Zn}^{cr/m}$			$D_{Pb}^{cr/m}$		
		n	Medium	± Δ	n	Medium	± Δ
Plagioclase	Rhyolites, Dacites	9	0.38	0.29	8	0.66	0.56
Kalispat	Rhyolites	6	0.09	0.06	7	0.92	0.48
Quartz[a]	Rhyolites		≤ 0.02	–		≤ 0.05	–
Biotite	Rhyolites, Dacites	5	19.9	8.56	3	0.40	0.1–0.9
Magnetite	Rhyolites, Dacites	8	31.87	14.48	4	0.79	0.41
Ilmenite	Rhyolite	5	11.20	6.25	3	0.68	0.29
Amphibole	Dacites, Rhyolites	4	6.97	3.87	6	0.35	0.18
Apatite	Trachyte Leucosome	1	1.8	–	1	0.77	–
Sulphide[b] Pyrrhotite	(Experiment) Rhyolite	1	0.50		1	2	

Note a-accepted values, b-experimental determinations in the system FeS–FeO–SiO_2

The average values of individual $D_{Pb}^{cr/m}$ for magnetite and other dark-colored minerals (0.4–0.8) are close to bulk partition coefficient of lead $D_{Pb}^{s/m}$ for association of basic rock-forming mineral phases (0.6). Therefore, crystallization of dark-colored phases has no significant influence on $D_{Pb}^{s/m}$, in contrast to $D_{Zn}^{s/m}$. The variations in the ratio of potassium feldspar and quartz, which have maximum and minimum $D_{Pb}^{cr/m}$ values (0.9 ± 0.5 and ~ 0.05, respectively), may have a more significant influence. The separation of the sulfide phase, which leads to some increase in $D_{Pb}^{s/m}$, can be expected only at the final stage of melt crystallization. Thus, $D_{Pb}^{s/m}$ will substantially depend on the melt content of K_2O and SiO_2. For meta—and subaluminous compositions $D_{Pb}^{s/m}$ may vary from 0.4–0.5 to 1–1.2.

3.2.3 Crystallization Degassing at Great Depths (P = 2 kbar)

Let us consider the behavior of zinc and lead during crystallization degassing of the melt at 2 kbar under closed and open system conditions. Figure 11 shows the case when the initial melt saturated with fluid phase contains 0.2 wt % Cl and 5.8 wt % H_2O, and the concentration of each of metals Zn and Pb is 100 ppm. The values of bulk partition coefficients of Zn and Pb between the melt and the crystalline phase are taken equal to 0.4 and 1.2, respectively. The first portions of the formed fluid phase enriched with chlorine, as in the case of decompression degassing, have the highest metal concentrations. With increasing degree of crystallization C_{Zn}^{fl} and C_{Pb}^{fl}, as well as C_{Cl}^{fl} decreases, especially sharply under conditions of open system. The concentrations of both metals in the residual melt during crystallization under closed conditions gradually increase slightly. However, under open conditions at the final stages of crystallization, there is a significant increase in C_{Zn}^{m}, whereas this is not observed for lead—C_{Pb}^{m} paths during crystallization in open and closed conditions practically coincide. The main reason for the different behavior of Zn and Pb is the significantly lower value of $D_{Zn}^{s/m}$ compared to $D_{Pb}^{s/m}$. In more detail, the effect of $D_{Zn}^{s/m}$ variation in the range from 0.1 to 4 on the behavior of zinc-on C_{Zn}^{fl} and C_{Zn}^{m} paths during crystallization degassing of the melt-is shown in Fig. 12.

Influence of $D_{Zn}^{s/m}$. At the first stages of crystallization and degassing of the melt, the Zn concentration in the fluid decreases at all $D_{Zn}^{s/m}$ values used in the calculations. This is especially noticeable in an open system, when the fluid phase is removed from the magmatic system as it is formed (Fig. 12). The effect of lowering C_{Zn}^{fl} at a given degree of crystallization of the initial melt is the more significant the higher $D_{Zn}^{s/m}$ is. In the closed system, with an increase of crystallization degree more than 40–50 wt % at values $D_{Zn}^{s/m} < 0.4$ wt %, after reaching a minimum, C_{Zn}^{fl} increases, that is associated with the accumulation of zinc in the residual melt during crystallization (Fig. 12b). As a result, despite of a decrease of Cl concentration in the fluid (see Fig. 9) and, consequently, a certain decrease in $D_{Zn}^{fl/m}$, the Zn concentration in the fluid increases. Under open

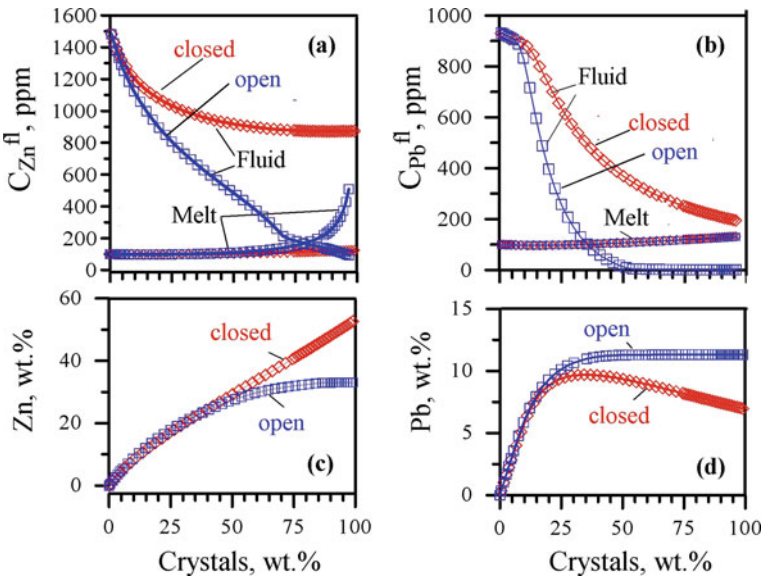

Fig. 11 Behavior of Zn and Pb in the process of crystallization degassing of the melt at 2 kbar under closed and open system conditions. The initial melt contains 0.2 wt % Cl, 5.8 wt % H_2O, 100 ppm Zn or Pb. The values of $D_{Zn}^{s/m}$ and $D_{Pb}^{s/m}$ are assumed to be 0.4 and 1.2, respectively. **a, b**—Change in the concentration of Zn **(a)** and Pb **(b)** in the fluid and melt during degassing in closed and open conditions. **c, d**—The degree of extraction of Zn **(c)** and Pb **(d)** from the initial melt during decompression degassing (in wt % of its initial content in the melt)

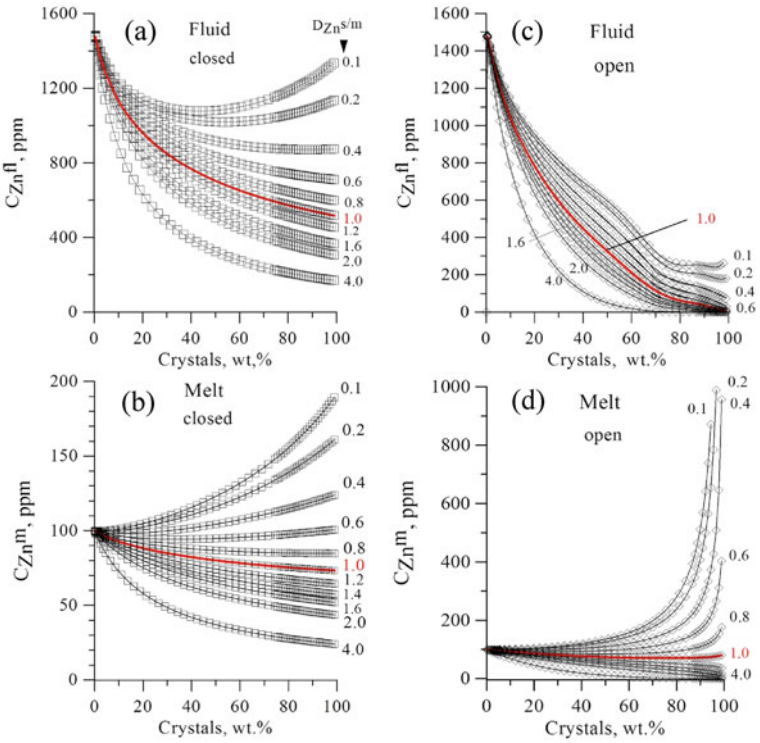

Fig. 12 Effect of $D_{Zn}^{s/m}$ on Zn concentrations in fluid and melt during crystallization degassing at 2 kbar under closed (**a**, **b**) and open (**c**, **d**) system conditions. The initial melt contains 5.8 wt % H_2O, 0.2 wt % Cl and 100 ppm Zn. The numbers at in the curves are the values of the bulk coefficient $D_{Zn}^{s/m}$

conditions such effect is not observed. Irrespective of $D_{Zn}^{s/m}$, Zn concentration in the fluid decreases throughout the degassing process. However, it should be noted that at the very final stages of degassing, when the crystal mass exceeds 60–80% for values $D_{Zn}^{s/m} < 0.8$, the Zn concentration in the residual melt can significantly increase, exceeding the initial one by several times (Fig. 12d).

How the degree of zinc extraction from magma by the fluid phase changes depending on $D_{Zn}^{s/m}$ is shown in Fig. 13. At the first stages of crystallization (up to ~15–20 wt % of solid phase), the $D_{Zn}^{s/m}$ value has almost no effect on the amount of extracted metal, regardless of whether the system is open or not. The influence of $D_{Zn}^{s/m}$ begins to manifest itself only during further crystallization. The higher $D_{Zn}^{s/m}$, the more zinc is redistributed into the crystalline phases and, accordingly, the less is released into the fluid. As the degree of crystallization increases, this tendency becomes more and more pronounced, especially in a closed system.

For $D_{Zn}^{s/m}$ values typical for typical widespread granite magmas of metaluminous composition (~0.8), when crystallization degree reaches 75–80%, about 1/3 of initial amount of zinc is extracted by the fluid. At the same time, a degree of Zn extraction is practically identical in the process of degassing both in a closed (30–32%) and open system (27–28%). For lower values of $D_{Zn}^{s/m}$, characteristic for leucocratic granites (~0.4), at the same degree of

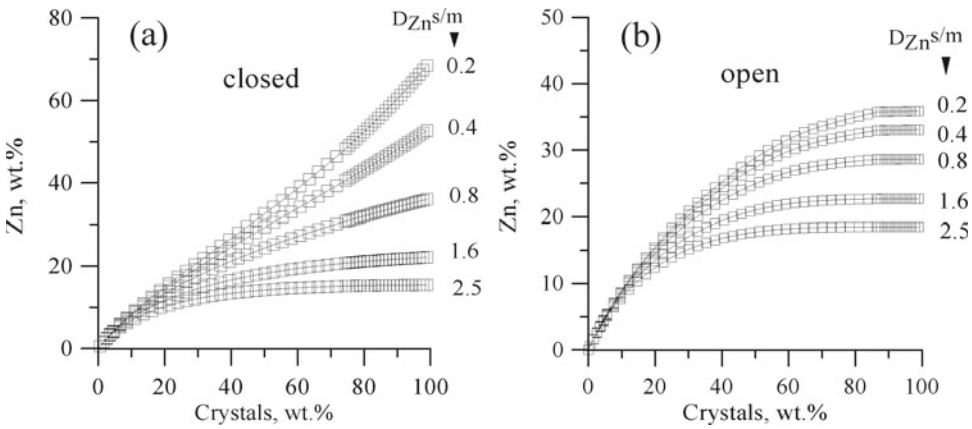

Fig. 13 Influence of the bulk zinc crystal/melt partition coefficient $D_{Zn}^{s/m}$ on the degree of zinc extraction by the fluid phase from granitic magma during its crystallization degassing at 2 kbar in closed **(a)** and open conditions **(b)** The numbers at the curves are $D_{Zn}^{s/m}$ values

crystallization, the amount of extracted Zn increases: 40–42% in a closed and 32–33% in an open system. For high values of $D_{Zn}^{s/m}$, typical for melanocratic granites (~2.5), upon crystallization of the initial melt by 75–80%, the degree of fluid extraction of Zn is 15–16% in closed and 18% in open conditions respectively, i.e. about 2 times lower than for leucocratic granites. With an increase in the crystalline mass in closed conditions up to 90–95%, this difference becomes more than 3 times (Fig. 13a). Thus, in the process of deep crystallization degassing at the same initial PTC conditions, the fluid extraction of Zn from leucocratic granite magmas should be more significant in comparison with more ferruos granites, the crystallization of which leads to the formation of mineral associations containing increased amount of dark-colored minerals.

Influence of $D_{Pb}^{s/m}$. Let us consider some peculiarities of the influence of variation of the bulk partition coefficient of lead, $D_{Pb}^{s/m}$, on the degree of its fluid extraction during crystallization degassing in the range of $D_{Pb}^{s/m}$, which is typical for natural metaluminous granite magmas (0.4–1.2). Figure 14 shows the case of crystallization of melts with the same initial concentrations of volatile components and ore element as in the case considered above for zinc. As the crystalline mass increases to 25–35%, the degree of Pb extraction in closed and open systems increases to 10–12%. In the process of further crystallization under closed conditions at $D_{Pb}^{s/m} > 0.6$ it (unlike zinc) gradually decreases, and in open conditions remains practically constant remaining within 11–13%. It should be noted that, in general, the degree of Pb extraction is significantly lower than that of Zn regardless of the degree of system openness due to lower values of fluid/melt partition coefficients for lead as compared to zinc under given PTC conditions.

Scale of Zn and Pb extraction. Balance calculations, presented in the form of graphs in Fig. 15, allow quantifying possible scales of the removal of Zn and Pb by fluid phase during crystallization degassing of a certain mass of initial magmatic melt, equal to 2.3×10^9 tons. The graphs show the masses of metals (in tons) removed from the magmatic system together with the fluid in stages with an increase in the crystalline mass at each stage by about 10 wt %. In addition, the masses of metals removed cumulatively at this and all previous crystallization stages are shown. As in the case of decompression degassing, most of the ore component is extracted by the fluid phase during the first crystallization stages. With the same concentrations of ore and volatile components in the initial melt, the total mass of Zn extracted by the fluid during the crystallization of the melt by 90% (~7000 tons) is more than twice that of lead (~2700 tons). Note that with simultaneous removal of Zn and Pb from the crystallizing magma during crystallization, the Zn/Pb ratio in the fluid should increase significantly.

3.2.4 Crystallization Degassing at Low Pressures (*P* = 0.6 kbar)

The behavior of ore components, like chlorine, in the process of crystallization degassing of granite magmas at shallow depths at pressures below 0.8–1 kbar changes radically in comparison with high pressures. One of the main features of degassing at these depths is the possibility of the appearance, at a certain stage of degassing, of a heterogeneous fluid consisting of an essentially aqueous phase (aq) and a high-chloride saline liquid-brine (lq) (see Fig. 9b). It is important to note that, according to the available experimental data, the partition coefficients of such ore

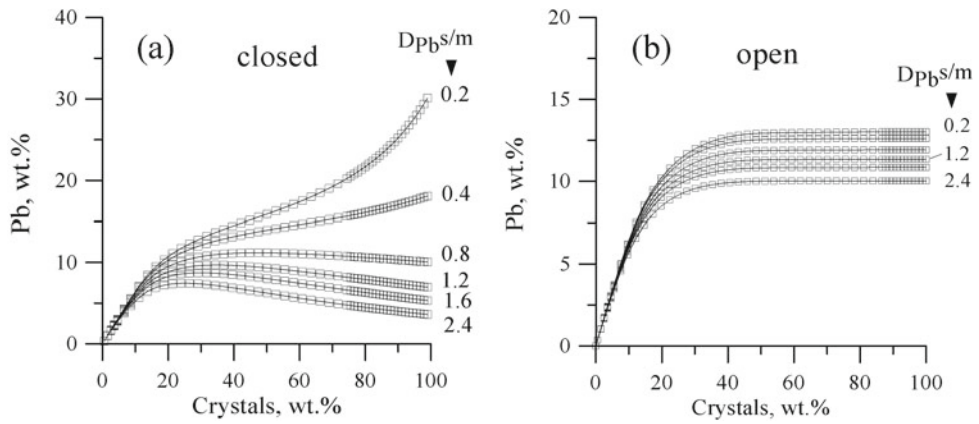

Fig. 14 Influence of the bulk lead partition coefficient crystal/melt $D_{Pb}^{s/m}$ on the degree of lead extraction by the fluid phase from granitic magma during its crystallization degassing at 2 kbar in closed **(a)** and open conditions **(b)** The initial melt contains 0.2 wt % Cl, 5.8 wt % H_2O, and 100 ppm Pb. The numbers at the curves are $D_{Pb}^{s/m}$ values

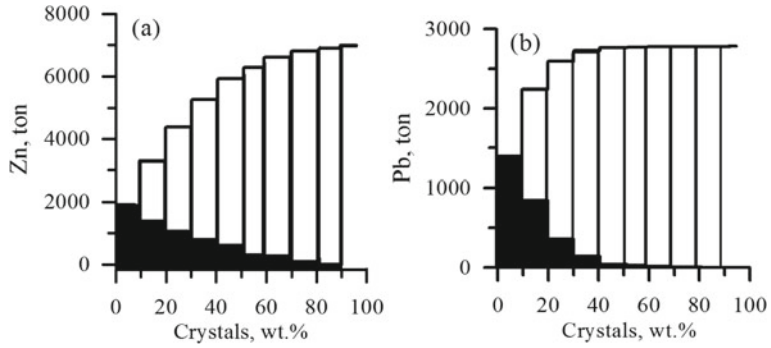

Fig. 15 Amounts of Zn **(a)** and Pb **(b)** extracted from the melt during its crystallization by degassing under open conditions at 2 kbar. The calculations were performed for a melt weighing 2.3×10^9 tons (10^6 m^3 by volume), initially containing 0.2 wt % Cl, 5.8 wt % H_2O and 100 ppm of each metal (Zn and Pb). It was assumed that $D_{Zn}^{s/m} = 0.6$ and $D_{Pb}^{s/m} = 0.7$. The filled part of the columns is the amount of metal released from the melt at ~10 wt % of crystallization. The non-filled part of the columns is the amount of metal released during the entire previous stage of degassing. The height of the columns corresponds to the total amount of metal released at this stage of crystallization degassing

metals as zinc and lead between lq and the granite melt $D_{Me}^{lq/m}$ can be more than 5–10 times higher than the partition coefficients of these metals between an aqueous fluid aq being in equilibrium with lq and a melt of the same composition, $D_{Me}^{aq/m}$ at the same PTC parameters [15]. Thus, the appearance of a heterogeneous fluid during degassing, which is a mixture of aq and lq, significantly affects the concentration of metal in the fluid and, accordingly, the degree of its extraction from the melt.

Let us consider the main features of the behavior of chlorophilic ore elements during crystallization degassing at low pressures (0.6 kbar) using the example of zinc, for which there are more reliable data in this pressure range than for lead. Figure 16 shows the calculated paths of changes in the concentration of zinc in the fluid, C_{Zn}^{fl}, during the crystallization degassing of the initial granite melt saturated with fluid at 0.6 kbar and containing 0.15 wt % Cl, 2.9 wt % H_2O, 100 ppm Zn, under closed and open conditions. At the same time, it was assumed that $D_{Zn}^{lq/m}$ is 10 times higher than $D_{Zn}^{aq/m}$, i.e. $D_{Zn}^{lq/aq} = 10$. At the first stage of crystallization, an essentially aqueous fluid phase aq is released from the melt. The paths C_{Zn}^{fl} for the closed and open systems practically coincide at this stage of degassing. With an increase in the degree of crystallization to ~50%, C_{Zn}^{fl} increases by about 2.5 times: from 500 (in the first portions of the fluid) to ~1200–1250 ppm. With further crystallization, the separating fluid phase becomes heterogeneous. In a closed system, the increase in the proportion of the aqueous-chloride liquid lq, with a higher content of Cl and Zn than aq, in the fluid occurs gradually. Therefore, the total concentration of Zn in the heterogeneous fluid also increases smoothly during degassing, reaching ~1500 ppm at the final stages of crystallization. In an open system, when the entire fluid phase leaves the system at each step of increasing the degree of crystallization, the total Zn concentration in the separated first portion of the heterogeneous fluid (aq + lq) increases abruptly more than twofold to ~2600 ppm. With further crystallization, despite the fact that the ratio lq/aq and C_{Cl}^{fl} in the fluid remain constant (see Fig. 9b), there is a slight decrease in C_{Zn}^{fl}, due to a decrease in the concentration of zinc in the melt during its degassing.

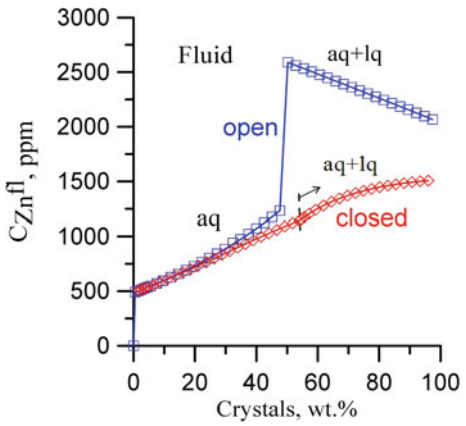

Fig. 16 Change in Zn concentration in the fluid phase during crystallization degassing of granite melt at 0.6 kbar under closed and open conditions. Initial contents in the melt H_2O = 2.9 wt %, Cl = 0.15 wt %, Zn = 100 ppm. It was assumed that $D_{Zn}^{s/m} = 0.6$; $D_{Zn}^{lq/aq} = 10$. The arrow shows the beginning of the release of a heterogeneous fluid from the melt (aq + lq) under closed conditions

The change in the amount of released Zn together with the fluid phase during magma crystallization at 0.6 kbar is shown in Fig. 17. In closed and open conditions, a very similar dynamics of Zn extraction by fluid from magma is observed. With the appearance of a heterogeneous fluid, the degree of zinc recovery increases significantly. The amount of zinc that can be removed in this case from the system at different stages of crystallization 2.3×10^9 tons of the initial melt is shown in Fig. 18. Thus, during crystallization at

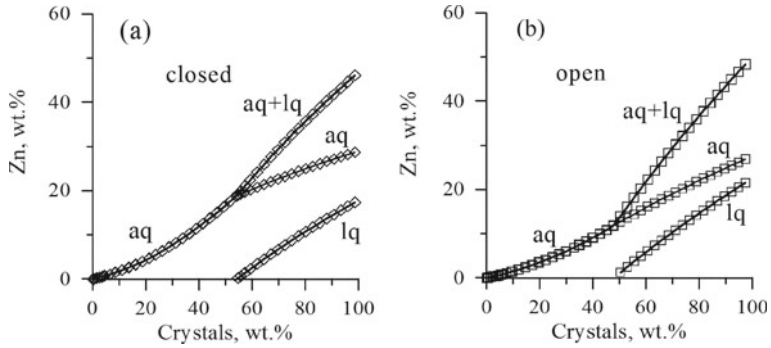

Fig. 17 The degree of zinc extraction in the process of crystallization degassing of granite melt at 0.6 kbar under closed **(a)** and open **(b)** conditions. Initial contents in the melt: H_2O = 2.9 wt %, Cl = 0.15 wt %, Zn = 100 ppm. It was assumed that $D_{Zn}^{s/m} = 0.6$; $D_{Zn}^{lq/aq} = 10$. The degree of Zn extraction since heterogeneous fluid is shown separately for aqueous chloride phase (aq), chloride liquid (lq), and heterogeneous fluid as a whole (aq + lq)

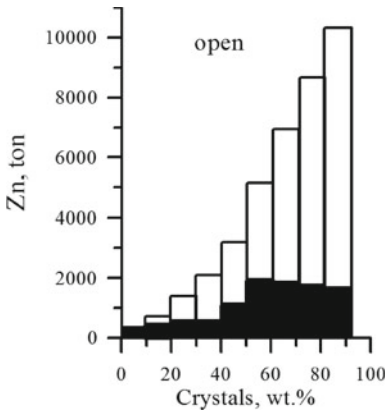

Fig. 18 The amount of Zn extracted by fluid phase during crystallization degassing of granite melt under open conditions at 0.6 kbar. Calculations for a melt with mass of 2.3×10^9 tons and with initial concentrations of 0.15 wt % Cl, 2.9 wt % H_2O, 100 ppm Zn. In the calculations, it was assumed that $D_{Zn}^{s/m} = 0.6$; $D_{Zn}^{lq/aq} = 10$. Other designations are the same as in Fig. 15

relatively shallow depths, the main part of fluid extraction of metal, in contrast to crystallization degassing at great depths, can occur at the middle and final stages of magma solidification.

4 Discussion

The available experimental data do not cover the entire possible range of variations of *PT*C conditions which can be realized during degassing of natural granitoid magmas. The used set of computer programs makes it possible to simulate a joint behavior of volatile (H_2O, Cl) and ore components (Zn, Pb) during degassing of granite melts at depths corresponding to the Earth's crust, in the pressure range from 0.3–5 to 3.5–4 kbar under isothermal conditions (800 ± 25 °C). It should be noted that the model takes into account the simultaneous influence on partition coefficients of Cl, Zn and Pb fluid/melt of two most important factors: Cl concentration in fluid (or melt) and pressure. It allows to reveal the main factors influencing the concentrations of ore "chlorophilic" elements Zn and Pb in the fluid and the degree of their extraction from the melt during degassing of granite magmas: (1) the pressure at which fluid saturation of melts is achieved during their rise, which is determined mainly by the initial water content in the melt; (2) the initial chloride content in the melt; (3) the degree of crystallization of fluid-saturated melt, (4) the openness of magmatic system in relation to fluid phase, (5) the change in value of bulk partition coefficient of Zn and Pb between crystals and melt, depending on the ratio of crystallizing mineral phases.

Limitations of the model. The most important limitations of this version of the model are as follows.

1. The consistency of the initial melt composition in relation to the main petrogenic components, which corresponds to the most widespread meta-and subaluminous granites with the agpaitic coefficient $(Na_2O + K_2O)/Al_2O_3$ (mol) close to 1. It is assumed that the composition of the melt in the process of degassing and crystallization remains constant or changes so insignificantly that it does not greatly affect the solubility of water in the melt, as well as the values of partition coefficients $D_{Cl}^{fl/m}$, $D_{Zn}^{fl/m}$, $D_{Pb}^{fl/m}$ and $D_{Zn}^{cr/m}$, $D_{Pb}^{cr/m}$ used in model calculations. According to experimental data, the Cl solubility in melts of alkaline and high-alumina granites, granodiorites, and more basic rocks in equilibrium with aqueous chloride fluids is noticeably higher under given *PT*C conditions than in the model granite melt [26, 38–42]. This leads to a decrease of both $D_{Cl}^{fl/m}$, and, apparently, $D_{Zn}^{fl/m}$, $D_{Pb}^{fl/m}$.

2. Simulation of decompression and crystallization degassing is carried out under isothermal conditions at ~800 °C, which is caused, mainly, by the fact that most experimental data on the distribution of Cl, Zn and Pb fluid/melt were obtained at 800 °C or close temperatures. This limitation implies that model crystallization of granite melt has eutectoid nature, i.e. proceeds at insignificant changes in temperature and melt composition, as well as with constant set and ratio of crystallizing mineral phases. Experimental data obtained in the range 700–900 °C 1–5 kbar indicate a relatively small increase in $D_{Zn}^{fl/m}$ and $D_{Pb}^{fl/m}$ with temperature decrease [11, 15, 32]. This is consistent with the results of thermodynamic modeling in ZnO_{cr}–NaCl–HCl–H_2O and PbO_{cr}–NaCl–HCl–H_2O systems, which show an insignificant increase in Zn and Pb concentration in fluid at constant *P* and C_{Cl}^{fl} in the same range of *PT* parameters [7]. At the same time, it is obvious that the effect of temperature on $D_{Me}^{fl/m}$ is not as significant as the effect of C_{Cl}^{fl}, pH and pressure.
3. Limited pressure range from 0.3–0.5 to 3.5–4 kbar, which is caused by the lack of available experimental and thermodynamic data. Outside this interval simulation results based on the extrapolation of the empirical dependences $D_{Cl}^{fl/m}$, $D_{Zn}^{fl/m}$ and $D_{Pb}^{fl/m}$ on $C_{Cl}^{fl/m}$ and *P* become much less reliable.
4. Equilibrium release of fluid from the melt is assumed when the melt is saturated with volatile components in the process of magma ascent and/or crystallization. The influence of melt oversaturation with volatile components, as well as the mechanisms of fluid release from the melt and its subsequent removal from the magmatic system, which are determined by many factors: the composition and physical properties of the silicate fluid, the rate of magma ascent and cooling and others [43, 44], is not considered in the model.
5. When modeling of processes of crystallization degassing, partition coefficients of ore elements between individual mineral phases and the melt and, accordingly, their bulk partition coefficients are assumed to be constant.
6. The model does not take into account the presence of other important volatile components (CO_2, S, F) in addition to water and chlorine in the initial melts.

Despite the above limitations, the model allows, in a first approximation, to analyze the influence of the main factors affecting the concentration of zinc and lead in magmatic fluids, as well as to estimate possible scale of their fluid extraction from the melt during degassing of granite magmas containing H_2O and Cl, both in closed and open conditions in relation to fluid phase. The model can be improved with the appearance of new empirical data.

Forms of Zn and Pb presence in fluid. The results of experimental and thermodynamic modeling indicate the leading role of chlorocomplexes in the distribution of Zn and Pb between aqueous chloride fluids and melts of granitoid composition in the considered range of *PT* parameters. Calculations performed in the systems ZnO_{cr}–Na(K)Cl–HCl–H_2O and PbO_{cr}–Na(K)Cl–HCl–H_2O show that for zinc such complexes are $ZnCl^+$, $ZnCl_2^0$, $ZnCl_3^-$, $ZnCl_2^{4-}$, and for lead $PbCl_2^0$, $PbCl_3^-$, $PbCl_2^{4-}$. An increase in C_{Cl}^{fl} (at *P*, *T*, pH = const) and/or pressure (at C_{Cl}^{fl}, *T*, pH = const) leads to an increase in the concentration of metal chlorocomplexes. At the same time the type of predominant Zn and Pb chlorocomplexes changes in the direction of increasing the number of chlorine atoms in them. An increase in fluid acidity with the addition of HCl to the system also leads to an increase in total solubility of metal oxides and concentration of chloride complexes Zn and Pb in the fluid, while suppressing the concentration of hydroxocomplexes. In general, under *PT*C conditions characteristic for magmatic fluid formation, $ZnCl_2^0$ and $ZnCl_2^{4-}$prevail among zinc-containing complexes in slightly alkaline, neutral and acidic environments, and $PbCl_2^0$ and $PbCl_3^-$prevail among lead-containing ones [7].

It should be noted that experimentally revealed general regularities of the influence of C_{Cl}^{fl}, *P* and pH on $D_{Zn}^{f/m}$ and $D_{Pb}^{f/m}$, namely: (1) an increase in $D_{Zn}^{f/m}$ and $D_{Pb}^{f/m}$ with an increase in C_{Cl}^{fl} and a decrease in pH upon HCl is added to the fluid phase (at C_{Cl}^{fl} = const), (2) higher $D_{Zn}^{f/m}$ values compared to $D_{Pb}^{f/m}$ at given *PT*C parameters, (3) decrease in $D_{Zn}^{f/m}$ and $D_{Pb}^{f/m}$ with increasing *P* (at C_{Cl}^{fl} = const)—are in general agreement with the results of thermodynamic modeling of simple $ZnO(PbO)_{cr}$–Na(K)Cl–HCl–H_2O systems. Indeed, the calculations demonstrate a significant increase in the solubility of ZnO_{cr} and PbO_{cr} and, respectively, C_{Zn}^{fl} and C_{Pb}^{fl} with an increase in C_{Cl}^{fl} and a decrease in pH by adding HCl to the system. It can be assumed that the solubility of ZnO_{cr} and PbO_{cr} being in the silicate melt as an impurity will also increase with increase in C_{Cl}^{fl} and acidity of the fluid in the case when the influence of other melt components is insignificant and Zn and Pb chlorocomplexes remain the predominant forms of their presence in the fluid. Thus, increase in C_{Cl}^{fl} and decrease in pH should lead to increase in the concentration of metals in the fluid and increase in $D_{Zn}^{f/m}$ and $D_{Pb}^{f/m}$. According to the calculated data, the solubility of ZnO_{cr} is significantly higher than PbO_{cr} at the given *PT*C parameters, which corresponds to higher values of $D_{Zn}^{f/m}$ in comparison with $D_{Pb}^{f/m}$.

According to thermodynamic modeling data in the systems $ZnO(PbO)_{cr}$-fluid (H_2O–Cl) the pressure (at C_{Cl}^{fl}, *T* = const) promotes solubility of oxides in aqueous chloride

solutions and increases C_{Zn}^{fl} and C_{Pb}^{fl} and, respectively, $D_{Zn}^{f/m}$ and $D_{Pb}^{f/m}$. Based on this it could be supposed that for the systems granite melt—aqueous chloride fluid the influence of pressure would be similar as well. However, it has been experimentally established that an increase in pressure causes not an increase, but a decrease in $D_{Zn}^{f/m}$ and $D_{Pb}^{f/m}$. This contradiction can be eliminated if we take into account the influence of P on pH of the fluid phase being in equilibrium with granite melt. In this case increase of P will be accompanied by relative increase of pH of aqueous chloride fluid and consequently a decrease in C_{Zn}^{fl} and C_{Pb}^{fl} and, respectively, in $D_{Zn}^{f/m}$ and $D_{Pb}^{f/m}$ (see in more detail [7]).

Influence of fluid removal dynamics. Model estimates of fluid extraction of ore components are made for two limiting cases of magmatic system evolution—for the case of a closed system, when the fluid phase formed during degassing remains completely in the system, and for the case when the fluid phase is completely removed from the system at each step of pressure reduction or crystallization. Let us note some possible consequences of different regime of fluid removal from magmatic systems.

Formation of fluid phase during decompression and crystallization degassing of melts in closed conditions is accompanied by an increase of its mass and volume. At a certain stage of degassing, it can lead to explosive or quieter removal of fluid from the system, depending on the kinetics of separation and segregation of the fluid phase, rate of rise and cooling of magmas, and other factors. Therefore, degassing in proper closed conditions, apparently, can be carried out only until the volume of fluid phase in the system reaches a certain critical value. Removal from the system of the first portions of fluid enriched with chlorine and ore components, the volume of which is very small, is obviously very difficult. In the case of crystallization degassing, a considerable part of such fluid, apparently, can be preserved in the form of fluid inclusions in crystallizing mineral phases.

Crystallization degassing of melts in long-lived magma chambers can be accompanied by periodic removal of the fluid phase from the system when a certain critical volume is reached. Concentrations and ratios of ore elements in fluids entering in portions at some time intervals into the host rocks will vary depending on the depth of the chamber and the degree of crystallization of the initial melt.

A special situation occurs during crystallization degassing of magmas at shallow depths ($P < 1$ kbar), which leads to formation of heterogeneous fluid consisting of essentially aqueous phase and chloride-aqueous liquid (brine), which is several times more enriched by ore elements than the aqueous phase. Thus, it becomes possible to separate them in a magma chamber into two independent fluid phases with different content of ore elements and different modes of removal from the chamber.

5 Conclusion

1. The complex of computer programs developed on the basis of generalization of the available experimental data allows to simulate the interphase distribution of volatile components (H_2O, Cl), as well as ore "chlorophilic" elements (on the example of Zn and Pb) in the process of decompression and crystallization degassing of granite melts in the pressure range from 0.3–0.5 to 3.5–4 kbar. Model calculations, despite a number of assumptions which are mainly associated with a lack of experimental and thermodynamic information, make it possible to reveal a number of important regularities in the formation of composition of magmatic fluids, depending on content of volatiles in the initial melt, the depth at which degassing occurs, the ratio of crystallizing mineral phases, the degree of system openness in relation to the fluid phase. They allow to quantify the possible scale of the removal of ore element from magmas during their degassing at different depths.
2. The results of numerical simulation show that the Cl concentration in the initial melt, H_2O/Cl ratio in it, pressure (depth) of degassing as well, as dynamics of the separation of the fluid phase from the magmatic system are important factors influencing the concentration of Zn, Pb and other "chlorophilic" metals in fluid and the degree of their extraction from magmas. There are two most favorable environments for the formation of magmatic fluids with high concentration of Cl as well as Zn and Pb, which are capable to extract considerable amounts of metals from granite magmas. First, these are the initial stages of degassing of melts during their rise or crystallization at relatively great depths ($P_{tot.} \geq 0.5$–2 kbar). The volume and mass of such fluids in magma should be small. Therefore, obviously, special conditions are required for their separation from magmas. During crystallization degassing, a considerable part of fluid with high contents of ore element can, apparently, be preserved in the form of fluid inclusions in minerals. Second, crystallization of fluid-saturated magmas in near-surface magmatic chambers ($P_{tot.} \leq 1$ kbar), which may be accompanied by formation of heterogeneous fluid consisting of essentially aqueous chloride-containing phase and high-chloride saline liquids (brines).
3. On the example of zinc and lead, it is shown that the amount of ore components extracted by fluid phase during crystallization degassing of granite magmas can essentially depend on the composition of the crystallizing mineral phases, especially at the final stages of

crystallization. In the process of deep degassing under the same initial PTC conditions the fluid extraction of Zn from leucocratic granite magmas should be more significant in comparison with more ferruginous granites, during the crystallization of which mineral associations are formed containing an increased amounts of dark-colored minerals biotite and Fe-Ti oxides.

4. Balance calculations of the interphase distribution of Zn and Pb in degassing processes demonstrate the maximum amounts of metal that can be extracted from magmas together with the fluid phase. They confirm the previously made general conclusion that the amount of metals extracted by the fluid phase from granitic magmas having average concentrations of Zn (20–40 ppm) and Pb (10–30 ppm) may be quite sufficient for the subsequent formation of large deposits [2, 45, and others]. The degree of Pb extraction is significantly lower than that of Zn, regardless of the degree of system openness due to lower values of fluid/melt partition coefficients for lead as compared to zinc under given PTC conditions. At the same time, it should be noted that the amount of removed ore elements essentially depends on two factors: first, on concentration of volatile components (for such elements as Zn and Pb primarily on concentration of Cl) and, second, on the specific mechanism of separation of the fluid phase from magma at different stages of its degassing. In general, we can conclude that the ability of separating magmatic fluids to be a source of ore components during the formation of large deposits is determined not so much by the initial concentration of ore elements in magmas, but by the initial content of volatile components in it, as well as by the dynamics of the separation of the fluid phase in the process of degassing of magmas during their rise to the surface and crystallization.

Acknowledgements The author is sincerely grateful to Prof. B.N. Ryzhenko and Dr. T.I. Shchekina for a discussion of the problems considered in the article. This work is conducted under the GEOKHI RAS state assignment.

References

1. Holland, H.D.: Granites, solutions and base metal deposits. Econ. Geol. **67**(3), 281–301 (1972)
2. Ryabchikov, I.D.: Thermodynamics of the fluid phase of granitoid magmas, p. 282. Nauka, Moscow (1975).[in Russian]
3. Burnham, C.W.: Magmas and hydrothermal fluids. In: Barnes, H. L. (ed.) Geochemistry of hydrothermal deposits, vol. 3, pp. 63–123. Wiley, New York (1997)
4. Candela, P.A.: A review of shallow, ore-related granites: textures, volatiles, and ore metals. J. Petrol. **38**(12), 1619–1633 (1997)
5. Halter, W.E., Webster, J.D.: The magmatic to hydrothermal transition and its bearing on ore-forming systems. Chem. Geol. **210**, 1–6 (2004)
6. Lukanin, O.A., Dernov-Pegarev, V.F.: Partitioning of rare earth elements between an aqueous chloride fuid phase and melt during the decompression driven degassing of granite magmas. Geochem. Int. **48**(10), 961–978 (2010)
7. Lukanin, O.A., Ryzhenko, B.N., Kurovskaya, N.A.: Zn and Pb solubility and speciation in aqueous chloride fluids at T-P parameters corresponding to granitoid magma degassing and crystallization. Geochem. Int. **51**(10), 802–830 (2013)
8. Dolejš D., Zajacz, Z.: Halogens in silicic magmas and their hydrothermal systems. In: Harlov, D.E., Aranovich, L. (eds.) The role of halogens in terrestrial and extraterrestrial geochemical processes surface, crust, and mantle, pp. 431–544. Springer International Publishing AG (2018)
9. Lecumberri-Sanchez, P., Bodnar, R.J.: Halogen geochemistry of ore deposits: Contributions towards understanding sources and processes. In: Harlov, D.E., Aranovich, L. (eds.) The role of halogens in terrestrial and extraterrestrial geochemical processes surface, crust, and mantle, pp. 261–306. Springer International Publishing AG (2018)
10. Pirajno, F.: Halogens in hydrothermal fluids and their role in the formation and evolution of hydrothermal mineral systems. In: Harlov, D.E., Aranovich, L. (eds.) The role of halogens in terrestrial and extraterrestrial geochemical processes surface, crust, and mantle, pp. 759–804. Springer International Publishing AG (2018)
11. Malinin, S.D., Khitarov, N.I.: Ore and petrogenic elements in the magmatic melt–fluid system. Geokhimiya **2**, 183–196 (1984).[in Russian]
12. Chevychelov, V.Yu., Epelbaum, M.B.: Distribution of Pb, Zn and rock-forming components in the granitic melt-fluid system. Essays Phys.Chem. Petrol. (XIII), pp. 120–136 (1985).[in Russian]
13. Urabe, T.: Aluminous granite as source magma of hydrothermal ore deposits: an experimental study. Econ. Geol. **80**(1), 148–157 (1985)
14. Urabe, T.: The effect of pressure on the partitioning ratios of lead and zinc between vapor and rhyolite melts. Econ. Geol. **82**(4), 1049–1052 (1987)
15. Chevychelov, V.Yu, Salova, T.P, Epelbaum, M.B.: differentiation of ore components (Pb, Zn and W, Mo) in a fluid-magmatic (granitoid) system. Exp. Probl. Geol., pp. 104–121. Nauka, Moscow (1994).[in Russian]
16. Chevychelov, V.Yu., Chevychelova, T.K.: Partitioning of Pb, Zn, W, Mo, Cl and major elements between aqueous fluid and melt in the systems granodiorite (granite, leucogranite)-H_2O–NaCl–HCl. Neues Jahrbuch für Mineralogie–Abhandlungen, **172**(1), 101–115 (1997)
17. Kadik, A.A., Lebedev, E.B., Khitarov, N.I.: Water in magmatic melts, 267 p. Nauka, Moscow (1971).[in Russian]
18. McMillan, P.F.: Water solubility and speciation models. Rev. Mineral. **30**, 131–156 (1994)
19. Dingwell, D.B., Harris, D.W., Scarf, C.M.: The solubility of H_2O in melts in the system system SiO_2-Al_2O_3-Na_2O-K_2O at 1 to 2 Kbars. J. Geol. **92**(4), 387–395 (1984)
20. Holtz, F., Behrens, H., Dingwell, D.B., Johannes, W.: H_2O solubility in haplogranitic melts: compositional, pressure, and temperature dependence. Am. Miner. **80**, 94–108 (1995)
21. Ihinger, P.D., Zhang, Y., Stolper, E.M.: The speciation of dissolved water in rhyolitic melt. Geochim. Cosmochim. Acta **63**, 3567–3578 (1999)
22. Liu, Y., Zhang, Y., Behrens, H.: Solubility of H_2O in rhyolitic melts at low pressures and a new empirical model for mixed H_2O-CO_2 solubility in rhyolitic melts. J Volcanol. Geoth. Res. **143**, 219–235 (2005)

23. Kilinc, I.A., Burnham, C.W.: Partitioning of chloride between a silicate melt and coexisting aqueous phase from 2 to 8 Kilobars. Econ. Geol. **67**(2), 231–235 (1972)
24. Shinohara, H., Iiyma, J.T., Matsuo, S.: Partition of chlorine compounds between silicate melt and hydrothermal solution: I. Partition of NaCl–KCl. Geochim. Cosmochim. Acta **53**, 2617–2630 (1989)
25. Malinin, S.D., Kravchuk, I.F.: Behavior of chlorine in equilibria between silicate melts and aqueous chloride fluids. Geokhimiya **8**, 1110–1130 (1995) [in Russian]
26. Mettrich, N., Rutherford, H.J.: Experimental study of chlorine in hydrous silisic melts. Geochim. Cosmochim. Acta **56**, 607–616 (1992)
27. Webster, J.D.: Fluid-melt interactions involving Cl-rich granites: experimental study from 2 to 8 kbar and 800°C. Geochim. Cosmochim. Acta **56**(2), 679–687 (1992)
28. Webster, J.D.: Chloride solubility in felsic melts and the role of chloride in magmatic degassing. J. Petrol. **38**, 1793–1807 (1997)
29. Bodnar, R.J., Burnham, C.W., Sterner, S.M.: Synthetic fluid inclusions in natural quartz III. Determination of phase equilibrium properties in the system H_2O–NaCl to 1000°C and 1500 bars. Geochim. Cosmochim. Acta **49**, 1861–1873 (1985)
30. Lukanin, O.A.: Chlorine partitioning between melt and aqueous chloride fluid during granite magma degassing I. Decompression induced melt degassing**.** Geochem. Int. **53**(9), 786–810 (2015)
31. Lukanin, O.A.: Chlorine partitioning between melt and aqueous chloride fluid phase during granite magma degassing. Part II. Crystallization-induced degassing of melts. Geochem. Int. **54**(8), 660–680 (2016)
32. Malinin, S.D., Kravchuk, I.F.: Distribution of elements in equilibria involving fluids. In: Kadik, A.A. (ed) Borisov, A.A., Zharkova, E.V., Kadik, A.A., Kravchuk, I.F., Lukanin, O.A., Malinin, S.D., Shilobreeva, S.N.: Fluids and redox equilibria in magmatic system, ch. 2, pp. 57–117. Nauka, Moscow (1991).[in Russian]
33. GERM Partition Coefficient Database (KdD). https://kdd.earthref.org/KdD/search. Accessed 20 Oct 2021
34. GEOROCK. http://georoc.mpch-mainz.gwdg.de/georoc/. Accessed 16 Aug 2021
35. Vinogradov, A.P.: Average contents of chemical elements in the major types of igneous rocks of the Earth's crust. Geokhimiya **7**, 555–571 (1962).[in Russian]
36. Burnham, C.W., Holloway, J.R., Davis, N.F.: The specific volume of water in the range 1000 to 8900 bars, 20° to 900°C. Am. J. Sci. **267-A**, 70–95 (1969)
37. Greenwood, H.J.: The compressibility of gaseous mixtures of carbon dioxide and water between 0 and 500 bars pressure and 450 and 800 °C. Am. J. Sci. **267-A**, 191–208 (1969)
38. Webster, J.D., Kinzler, R.J., Mathez, A.: Chloride and water solubility in basalt and andesite melts and implications for magmatic degassing. Geochim. Cosmochim. Acta **63**, 729–738 (1999)
39. Chevychelov, V.Yu.: Chlorine dissolution in fluid-rich granitic melts: the effect of calcium addition. Geochem. Int. **37**(5), 456–467 (1999)
40. Signorelli, S., Caroll, M.R.: Experimental study of Cl solubility in hydrous alkaline melts: constraints on the theoretical maximum amount of Cl in trachytic and phonolithic melts. Contrib. Mineral. Petrol. **143**, 209–218 (2002)
41. Botcharnikov, R.E., Behrens, H., Holtz, F., Koepke, J., Sato, H.: Sulfur and chlorine solubility in Mt Unzen rhyodacite melt at 850 ° C and 200 MPa. Chem. Geol. **213**, 207–225 (2004)
42. Zajacz, Z., Candela, P.A., Piccoli, P.M., Valle, C.S.: The partitioning of sulfur and chlorine between andesite melts and magmatic volatiles and the exchange coefficients of major cations. Geochim. Cosmochim. Acta **89**, 81–101 (2012)
43. Candela, P.A.: Combined chemical and physical model for plutonic devolatilization: a non-Rayleigh fractionation algorithm. Geochim. Cosmochim. Acta **58**(10), 2157–2167 (1994)
44. Gonnermann, H.M., Manga, M.: Nonequilibrium magma degassing: results from modeling of the ca. 1340 AD eruption of Mono Craters. California. Earth Planet. Sci. Lett. **238**(1–2), 1–16 (2005)
45. Hedenquist, J.W., Lowenstern, J.B.: Role magmatism in the formation hydrothermal ore deposits. Nature **370**(6490), 519–527 (1994)

Spontaneous Solution Distillation in a Closed Silica-Water System at the Water–Vapor Interface: Review of Experimental Studies

V. A. Alekseyev

1 Introduction

Silica (SiO_2) forms the basis of silicates and passes into solution during their dissolution. It also forms its own minerals, among which the most common are quartz (meaning low-temperature trigonal quartz) and opal [1]. Quartz is stable up to 573 °C and 20 kbar, i.e. in this region it has minimal solubility among all silica modifications [2]. Opal under these conditions is a metastable mineral (has higher solubility) and over time it turns into quartz [3, 4]. These firmly established facts once entered into apparent contradiction with the results of our experiments on deposition of silica from supersaturated solution at 300 °C (Fig. 1a). In the presence of quartz seeds silica behavior was normal, i.e. its concentration decreased to the solubility of quartz, and then stabilized at this level. However, in the absence of seeds silica concentration (m) fell well below the solubility of quartz, which cannot be explained only by known (traditional) knowledge about this system. Our subsequent research was initiated by this as well as other controversies and difficulties that arose in the process. As a result, a number of articles united by one theme have been published [5–11]. This paper is a summary of these articles in the order in which the research progressed, with all the difficulties and misconceptions revealed later. The logic of reasoning in choosing the scheme of subsequent experiments based on the results of previous experiments is also shown.

2 Methods

Experiments were usually performed in gold or platinum thin-walled (0.15 mm) ampoules, which provided chemically inert behavior of the walls in relation to the system under study. Natural quartz (powder or crystals), purified from impurities, and bidistilled water were loaded into the ampoules [5]. After filling the ampoules were hermetically welded with electric arc, placed in autoclaves, and then in vertical electric furnaces, equipped with good thermal insulation and aluminium blocks for temperature equalization. Sometimes a solution saturated with quartz or amorphous silica was used instead of water and quartz. In all cases, water or solution at the temperature of experiments (300 °C) filled only the lower part of the ampoule, and the upper part was occupied by saturated water vapor at a pressure of 86 bar. At first a constant for a series of experiments was given a fraction of the ampoule filling with solution, but then a constant mass of water was kept, which was more correct from the point of view of the reaction mechanism. Autoclaves with ampoules were inserted into aluminum block of electric furnace usually in pairs on each other.

The temperature in the electric furnace was measured and controlled by chromel–alumel thermocouples (corrected for the temperature of cold junctions) connected to the temperature controller and to the computer, where the measurement results were displayed. After the set time the autoclaves were removed from the electric furnace and quickly (20 s) cooled in cold water. Autoclaves and ampoules were opened, solutions were filtered under vacuum (filter pore size 0.05 μm), diluted with HCl (2%) for solution stabilization (preservation) and analyzed for Si by colorimetry and/or ICP-AES. The location of the solid phase in the ampoule was determined using an endoscope. The solid phase was then extracted, washed on a filter and examined using X-ray analysis, infrared spectroscopy, Raman spectroscopy, scanning electron microscopy, and X-ray energy dispersive analysis [5]. Large quartz crystals were subjected to

V. A. Alekseyev (✉)
Vernadsky Institute of Geochemistry and Analytical Chemistry, Russian Academy of Sciences, 19 Kosygin St., Moscow, 119991, Russia
e-mail: alekseyev-v@geokhi.ru

V. P. Kolotov and N. S. Bezaeva (eds.), *Advances in Geochemistry, Analytical Chemistry, and Planetary Sciences*,
https://doi.org/10.1007/978-3-031-09883-3_8

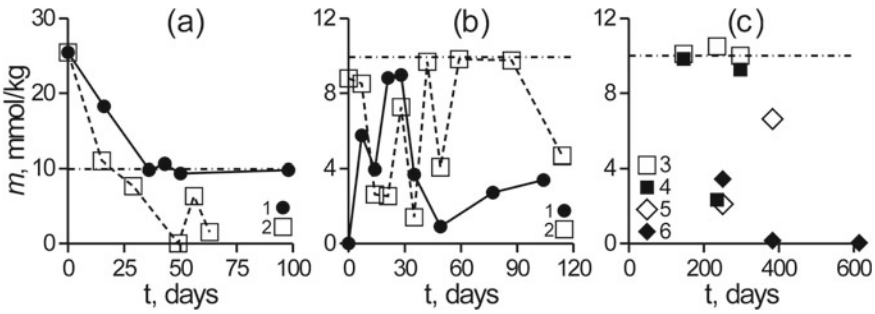

Fig. 1 Change of dissolved silica concentration (m) in time (t) at 300 °C [5]. **a, b** initial were quartz powder and water with mass ratio 0.001 (1) or only water containing dissolved silica (2), **c** initial were quartz and water in gold (3, 4) or platinum (5, 6) ampoules, quartz as crystals (3, 5) or powder (4, 6). Dashed dotted line shows solubility of quartz

3d-scanning before and after experiments [10]. Sometimes the ampoules were cut lengthwise after the experiments and studied by profilometer and atomic force microscopy [11].

The work started with ampoules, for which the term "used" is applicable. In the same series of experiments with different times, the ampoules could have different height, diameter, material (Au or Pt) and different "freshness", i.e. different duration and intensity of its previous use. Later on, the ampoules for the same series were chosen of approximately the same size and made of the same material. Still later, experiments were carried out in new ampoules of the same size. These changes in methodology were related to the need for greater standardization of experimental conditions in order to reduce the variation in the results of the experiments. However, complete identity of the conditions could not be achieved, because the ampoule in the subsequent run was shorter than in the previous one by 1–2 mm as a result of cutting the edge before welding and at opening. Between experiments the ampoule was cleaned of SiO_2 (boiling in H_3PO_4), straightened the walls (rolling with inserted steel rod) and annealed on a gas burner.

3 Results and Discussion

3.1 First Experiments and Diagnosis of Newly Formed Silica [5]

The very first results (Fig. 1a) have already been discussed in the introduction. It was assumed that there was an unknown silica modification with solubility lower than that of quartz. It was necessary to measure its solubility and to obtain its sufficient quantity for analyses. For this purpose experiments with SiO_2-containing solution only, as well as experiments with quartz and water were performed (Fig. 1b). In both series of experiments the dependences of dissolved silica concentration on time (m-t) had a sawtooth character, and solid phases were represented by kidney-shaped aggregates, which had a non-crystalline concentric-zone structure (Fig. 2a) or contained microcrystals (Fig. 2b). Numerous attempts to study these solid phases by electron diffraction were unsuccessful mainly due to the lack of a good specialist working on a modern transmission electron microscope. The following conclusions were drawn from these studies: (1) to reach constant SiO_2 concentrations, it is necessary to increase the duration of experiments and to use quartz powder with a large specific surface, (2) to obtain a large amount of newly formed SiO_2, sufficient for its diagnostics, it is necessary to use quartz crystals, from which it will be easier to separate new formations. Experiments with water and quartz powder did show a strong decrease in m with time from 10 mmol/kg at 100–300 days to 0.03 mmol/kg at 614 days (Fig. 1c), and experiments with water and quartz crystals were able to obtain large amounts of newly formed silica, which equaled the mass loss of the crystals. These losses were dozens of times greater than the amount of SiO_2 needed to achieve solubility of quartz. There was no problem to separate the new solid phase from the original crystals because they were located in different places: the crystals were in water at the bottom of ampoules and the new silica crusts were located above the water level on the inner walls of ampoules. The latter peculiarity of the location in the future proved to be characteristic of all experiments where anomalous silica behavior was observed. According to the X-ray diffraction, infrared and Raman spectroscopy, the new crusts consisted mainly of ordinary microcrystalline opal (cristobalite or cristobalite-tridimite) with an admixture of quartz. This quartz was secondary, which was confirmed by the longest experience with water and quartz powder (614 days), where a druse of secondary quartz (without an opal admixture) was formed on the ampoule wall above the water level. Mass of the druse was exactly equal to initial mass of quartz powder, i.e. quartz powder dissolved in water at the bottom of the ampoule, silica was transferred above water and the druse crystallized on the ampoule wall. The material for the druse was supplied by complete dissolution of the powder and complete depletion of the solution volume by silica, which means strongly non-equilibrium conditions.

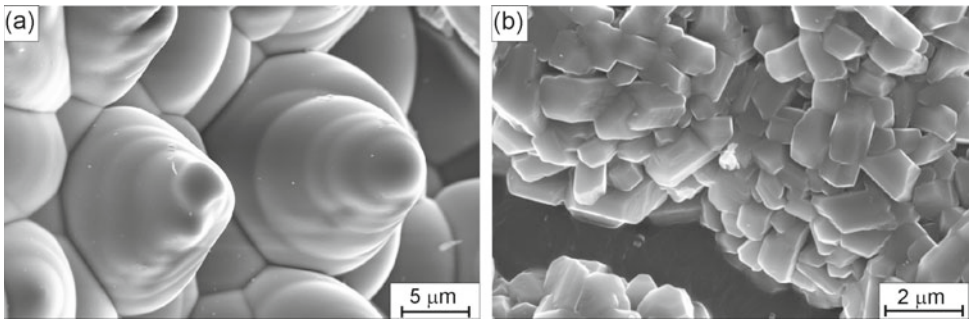

Fig. 2 SEM image of newly formed silica crusts [5] **a** from experiments with water and quartz (Fig. 1b, line 1, 105 days), **b** from experiments with water containing dissolved silica (Fig. 1b, line 2, 115 days)

In similar experiments, but performed at 400 °C and 700 bar, the SiO_2 concentration in the solution was quite consistent with the solubility of quartz, and the anomalous silica behavior did not appear, probably due to the lack of water–vapor interface.

Before explaining the unusual results of the work, it was necessary to make sure that there were no methodological errors, first of all, the possible effect of depressurization of the ampoules and the quenching effect. The tightness of the ampoules was controlled by weighing them before and after the experiments. The discrepancy of masses did not exceed 1 mg. In rare cases of depressurization the weight of ampoules after the run strongly increased (by 0.2–2 g), and such runs were discarded. Deposition of silica during quenching was excluded as a result of calculations using kinetic constants and equations [12] with real values *S/M* (*S*-surface area of mineral, *M*-water mass).

The hypothesis of the formation of a new mineral with low solubility fell away after it was found that the new minerals in the experiments were the well-known old minerals opal and quartz.

Another hypothesis related to the reduction of mineral solubility in pores of small size was considered. For example, in pores with a radius of 10 nm, the solubility of amorphous silica was 54% of its usual solubility [13]. Such a decrease in concentration is too small compared to some of our experiments, where the SiO_2 concentration was hundreds of times lower than the solubility of quartz.

The hypothesis based on preferential evaporation of water at the meniscus edge turned out to be the most probable one. This phenomenon is well known, but continues to be intensively studied [14]. It is related to an increase in the thermal conductivity of the liquid film due to a decrease in its thickness below 100 nm, which causes overheating and an increase in the evaporation flux. The increase in temperature from the bottom to the top of the aluminum block where autoclaves were inserted (0.25°/cm) should contribute to this overheating. In addition, fluids smaller than 100 nm acquire properties different from their properties in a large volume due to the increased contribution of surface energy [15]. Evaporation of water at the meniscus edge in a closed system is compensated by its condensation on the rest of the solution surface, i.e. actually the solution is distilled, although the word "distillation" in [5] has not been pronounced yet. The absence of clear *m-t* dependences in the experiments so far is explained by the fact that some silica crusts are weakly attached to the walls and can fall into the solution volume, dissolve and increase *m* randomly [16]. As a result of such "natural selection" in long-term experiments only strongly attached crusts are preserved, and the value of *m* stabilizes at a low level.

3.2 Influence of Temperature Gradient and Transformation Stages of Newly Formed Silica [7]

In this work two series of experiments with quartz powder (10–60 microns) and with water were carried out. Mass of quartz was 8 times more than that which is necessary for achievement of solubility of quartz at 300 °C (~10 mmol/kg). The Q + H_2O series had gold ampoules, the Q + H_2O# series had platinum ampoules. In the latter case there were still platinum grids inside the ampoules, which could probably enhance the rise and evaporation of the solution. A stricter control of conditions of experiments consisted in known position of autoclave in electric furnace (top or bottom). In the top autoclaves of both series the value of *m* did not change with time and corresponded to solubility of quartz (symbols 1 in Fig. 3), and the initial quartz powder was preserved at the bottom of ampoules, i.e. silica behavior was normal. In the longest experiment (860 days), rare larger crystals of secondary quartz were visible among the small pieces of primary quartz, indicating recrystallization (Ostwald ripening). In the lower autoclaves of both series *m* values were lower and they decreased with time (symbols 2 in Fig. 3), reaching in the two longest experiments of the series Q + H_2O# minimum values 0.03 mmol/kg, which coincides with the minimum values in previous experiments (Fig. 1c) and close to the solubility of quartz in water vapor at 300 °C

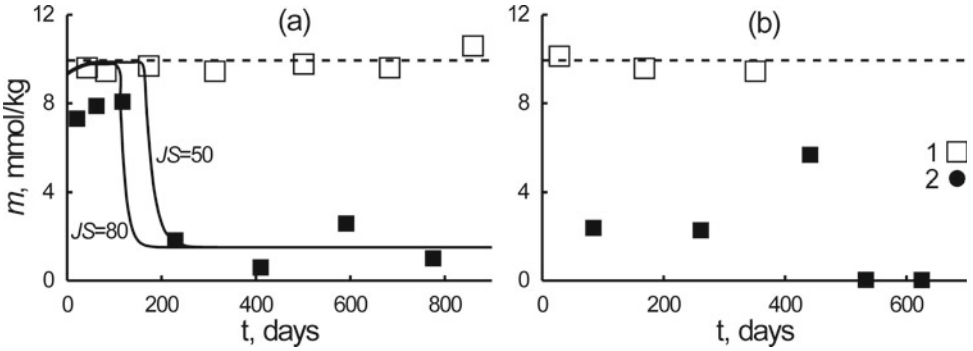

Fig. 3 Change of dissolved silica concentration (m) in time (t) at 300 °C [7] in series Q + H_2O (**a**) and Q + H_2O# (**b**) in upper (1) and lower (2) autoclaves. The dotted line shows the solubility of quartz. The solid curves correspond to distillation model at evaporation rates JS = 50 and 80 mg/day

0.05 mmol/kg [17]. New silica crusts were found on the walls of the ampoules and on the framework which supported the meshes (in both cases well above the solution level).

According to the X-ray diffraction analysis, the new silica crusts were represented, as in the previous experiments, by microcrystalline opal and secondary quartz. According to SEM data, opal is represented by kidney-like aggregates which consist of small lamellar or isometric crystals similar to those obtained earlier (Fig. 2b). Secondary quartz is represented by larger crystals which contain numerous pores (Fig. 4). Therefore the specific surface of this porous quartz, measured by the BET method, is very high ($\sim$100 m^2/g), and opal is even higher.

According to results of main experiments in lower autoclaves 3 stages of process are distinguished: (1) up to 200 days in Fig. 3a initial quartz was still present, and m value was only slightly below solubility of quartz; (2) after 200 days in Fig. 3a and up to 500 days in Fig. 3b the original quartz was absent, above solution opal was formed, and the value of m decreased; (3) after 500 days in Fig. 3b opal turned into secondary quartz, and the value of m became minimal.

The reason of divergence of experimental results in upper and lower autoclaves could be different temperature gradient (TG), but it seemed to contradict to TG measurements on Al block surface, where autoclaves were inserted in 2 floors. Previous measurements showed the same TG = 0.25°/cm across the entire height of the block. In reality, however, the TG on the autoclave surface (closer to the reaction zone) could be different than on the surface of the Al block. To check this assumption, careful measurements of vertical TG at the surface of the upper and lower autoclave were performed. The hot junctions of ten chromel–alumel flexible thermocouples were placed in 2 rows on opposite sides of the autoclave. The measuring technique included the use of aluminum pads with a concave surface for hot junctions, aging of thermocouples, thermal insulation of cold junctions, determining corrections to the thermocouple readings relative to the lead melting temperature (327.4 °C), the same depth of thermocouple immersion in the oven, and measurements at the same point by different thermocouples. The measurements showed that from bottom to top the surface temperature of the lower and upper autoclaves increases (0.15°/cm) and decreases (−0.08°/cm) respectively. These measurements seemed to unambiguously confirm the relationship of the results of the experiments with TG. Moreover, in the original discussion of these data [6] a new thermodiffusion hypothesis was put forward explaining the unusual behavior of SiO_2 in the lower autoclaves by different TGs. However, the subsequent analysis of literature data forced to reject this hypothesis because of insufficient efficiency of thermodiffusion in change of SiO_2

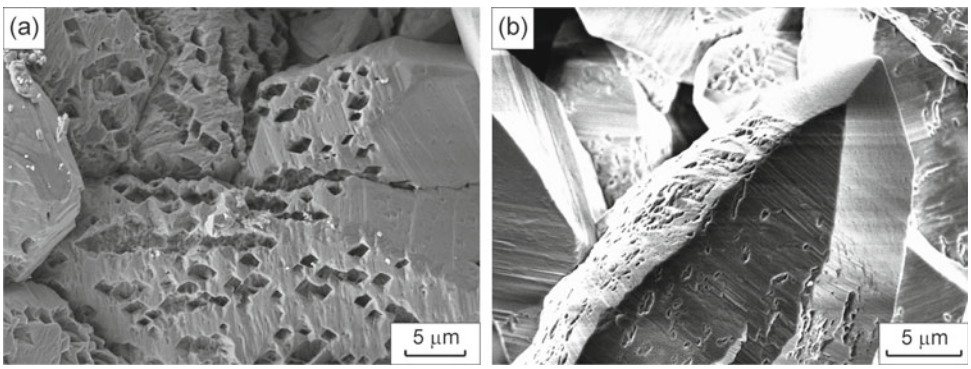

Fig. 4 SEM image of porous secondary quartz crystals at the end of Q + H_2O# series [7]

concentration, even if autoclaves represented an ideal thermogravitational column [7].

Methodical experiments were also set to check the influence of quenching effect on *m* value. In two experiments with quartz and water with high *S/M* ratio (1200 m^2/kg), typical for the main experiments, *m* values in the upper autoclaves after 15 h were equal to the solubility of quartz. These data experimentally confirmed the results of calculations [5] and convincingly showed that low SiO_2 concentrations measured in quenching solutions of the main experiments are not a consequence of the quenching effect but are characteristic of the temperature of the experiments.

The return to the hypothesis of preferential evaporation was accompanied by the realization that evaporation at the meniscus edge in a closed system must be compensated by vapor condensation on the rest of the solution surface. As a result, spontaneous distillation of solution must occur, i.e. water with high SiO_2 concentration is replaced by water with low SiO_2 concentration (condensate). A simple mathematical model of distillation was constructed which took into account this replacement as well as the dissolution rate of quartz. Solution of this model by finite difference method showed good agreement with experimental data at evaporation rates of 50–80 mg/d (solid curves in Fig. 3a), at which the sharp decrease of *m* occurs after ~200 days, when all initial quartz is consumed. Up to this point, the loss of dissolved silica due to distillation was compensated (and masked) by additional dissolution of quartz. This masking, as well as the short duration of experiments used to measure quartz solubility or dissolution rate, explains the fact why the unusual silica behavior has not been detected until now.

3.3 Reducing the Scatter of Data and Finding the Root Cause of Distillation [8]

At the next stage of researches it was planned to receive quantitative kinetic data describing rate of distillation process. For this purpose it was supposed to put experiments in lower parts of electric furnaces where this effect is shown, but only with water containing silica (without quartz). Such scheme of experiments should exclude masking of distillation by additional dissolution of quartz. If earlier in a series of experiments the coefficient of filling the ampoules with a solution was identical, now, according to the distillation model, the mass of a solution became identical. A large number of experiments were carried out according to this scheme, but they showed a very large (unacceptable) scatter of data in coordinates *m-t* (concentration–time), similar to the first experiments on this topic (Fig. 1b). To reduce scatter of data, we began to fix the ampoule in autoclave and autoclave in electric furnace in the same position, and experiments of the same series were carried out in the same

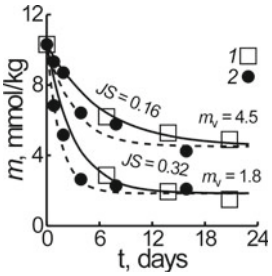

Fig. 5 Averaged (by 4–5 values) *m-t* dependences for ampoules with low and high values of *m* during the experiments [8]. Initial values of *m* for all experiments are the same (10.3 mmol/kg). Mass of a solution is 1 (1) or 0.5 g (2). Lines correspond to calculation according to Eq. (1) with given values *JS* (g/day) and m_v (mmol/kg)

ampoules, autoclaves and sockets of electric furnaces. Moreover, the same experiments were performed in nine ampoules, the results of these experiments (*m-t* values) were divided into 2 groups (with high and low values of *m*) and within each group, the *m* values for the same time were averaged. This allowed to obtain within groups smoother experimental data (symbols in Fig. 5), which were approximated by the distillation equation [8]:

$$m = (m_0 - m_v)\exp\left(-\frac{JSt}{M}\right) + m_v, \qquad (1)$$

where m_0 and *m* are initial and final (at time *t*) concentration of silica in solution, *JS* is evaporation (distillation) rate, *M* is mass of water in solution, m_v is concentration of silica in water vapor (and in condensate). For the group of ampoules with low values of *m* the *JS* value was greater and m_v less than for the group of ampoules with high values of *m*. The reason for these discrepancies was not clear. But a careful analysis of the results of these and other experiments revealed that, at the same duration of experiments, the value of *m* depends not on the position of ampoules in the autoclave and autoclave in the Al block seat, but on some property of the ampoule itself. And this property is capable to change at repeated experiments in the same ampoule. A suitable property turned out to be the roughness of the internal walls of the ampoules. This property is capable of increasing or weakening with repeated use of ampoules in experiments, because the ampoules are subjected to crumpling, leveling, exposure to strong acids and high temperatures.

3.4 Effect of Wall Roughness [11]

To check this assumption, experiments with water containing dissolved silica were carried out, first in nine new platinum ampoules, and then in the same ampoules, but with rough inner walls. The roughness was created by the friction of the steel rod inserted in the ampoule, against the wall

(between them there was quartz powder). Nine ampoules were divided into 3 groups of 3 ampoules each. The quartz grain size was different when treating different groups of ampoules, but the same within the same group: 63–100 μm for ampoules 1, 2, 3; 20–50 μm for ampoules 4, 5, 6; 10–20 μm for ampoules 7, 8, 9. For more accurate determination of *m* at the temperature of experiments, the measured values of *m* in quenching solutions began to be corrected to take into account the different dilution of solutions with condensate during quenching in ampoules with different proportion of filling of ampoules with solution [18].

After 4 days the value of *m* in the new ampoules practically did not change, while in the rough ampoules it decreased (Fig. 6). And both cases manifested themselves in both lower and upper autoclaves. These results initiated a revision of previous data (Fig. 3), where the discrepancy between the results in the upper and lower autoclaves was initially attributed to different *TGs*. Re-analysis of records of those experiments revealed that the experiments in the upper and lower autoclaves (symbols 1 and 2 in Fig. 3) were performed in new and old ampoules, respectively. Mainly this circumstance and not *TG* probably explains the discrepancy of results of experiments in Fig. 3.

Returning to Fig. 6, we should also note the stabilizing effect of roughness on *m*, i.e., the proximity of *m* values in the ampoules of the same group. This circumstance

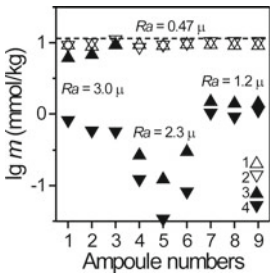

Fig. 6 Concentrations of dissolved silica (*m*) in ampoules 1–9 after 4 days at 300 °C and a temperature gradient of −0.08 (1, 3) or 0.15°/cm (2, 4) [11]. The experiments were performed first in new ampoules (1, 2), and then in the same ampoules, but with rough inner walls (*Ra* is the arithmetic mean deviation of surface points from the mean line in absolute value)

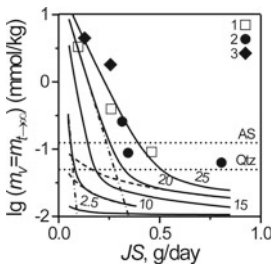

Fig. 8 Minimum silica concentrations in the solution volume ($m_{t\to\infty}$) during solution distillation at different rates (*JS*) [11]. Symbols show the results of experiments with temperature gradients of − 0.08 (1) and 0.15°/cm (2, 3). The solid lines show the simulation results at different water film base thickness δ_0 (μm) on the ampoule wall. For δ_0 = 10 and 20 μm, the contributions of SiO_2 diffusive transport in the film (dash-dotted line) and SiO_2 transport through the vapor (dashed line) to the overall dependence are shown. The horizontal lines show the solubility of quartz (Qtz) and amorphous silica (AS) in the vapor

stimulated setting of kinetic experiments in the same ampoules with the purpose to estimate influence of roughness on distillation rate. The results of these experiments (symbols in Fig. 7) showed good agreement with the equation of distillation (1) (lines in Fig. 7), and in the top ampoules (empty symbols) the distillation also went, though with lower rate *JS* (slope of lines), than in the bottom ampoules (filled symbols). According to Eq. (1), the value of *m* at long time *t* ($m_{t\to\infty}$) is equal to m_v. With increasing *JS* to 0.8 g/day the value of $m_{t\to\infty}$ in the experiments decreased to 0.06 mmol/kg, and this dependence was the same for the upper and lower ampoules (symbols in Fig. 8).

One of the ampoules after all series of experiments was cut lengthwise and its inner surface was examined in SEM. These studies made it possible to clearly show the place of silica deposition in the form of a rim ∼5 mm wide above the solution level by ∼10 mm (Fig. 9a). The rim consisted of non-crystalline silica spheres (Fig. 9b), which merged into a continuous crust in places. The presence of a clear space on the wall of the ampoule between the level of the solution and the silica rim suggests that the solution in the form of a film was rising along the wall. At the beginning of ascent the film solution was undersaturated, so the opal was not deposited. At the end of rise as a result of water

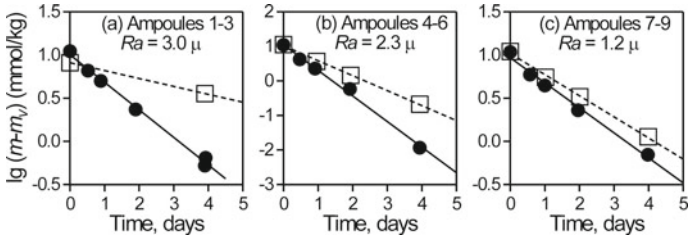

Fig. 7 Approximation of the averaged experimental data (symbols) by Eq. (1) (straight lines) for rough ampoules 1, 2, 3 (**a**), 4, 5, 6 (**b**), 7, 8, 9 (**c**) heated at 300 °C with a temperature gradient of − 0.08 or 0.15°/cm (empty and filled symbols) [11]

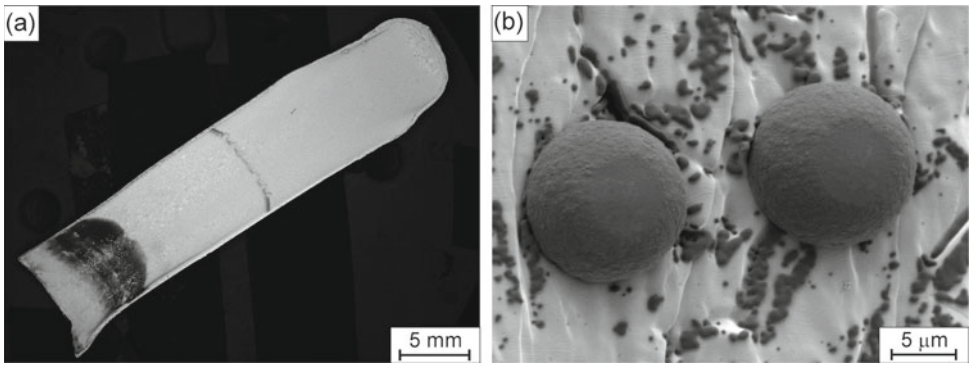

Fig. 9 SEM image of newly formed opal (dark) on the inner rough surface of platinum ampoule no. 1 (light) after heating the water containing 10.3 mmol/kg SiO_2 during 1.88 days at 300 °C with temperature gradient of 0.15°/cm [11]. **a** general view of the ampoule (the upper end of the ampoule at the bottom left), **b** spheres of opal in the upper part of the ampoule at higher magnification

evaporation film solution became supersaturated that led to precipitation of opal. Rise of liquid on rough wall is possible if equilibrium contact angle of liquid on smooth wall (θ) is less than critical angle θ_c which has expression [19]:

$$\cos\theta_c = (1 - \emptyset)/(r - \emptyset) \quad (2)$$

where ϕ is the fraction of dry protrusions in the total area of the rough surface, r is the ratio of the actual and projected (smooth) surface area. For water on smooth platinum at 300 °C $\theta = 0$ [20], i.e. the condition of water film rise in our experiments is fulfilled for any rough surface ($r > 1$) and at any value ϕ from 0 to 1. The feature of this process is that the solution penetrates into the structure of the rough surface along the depressions, leaving the protrusions dry. As a result, liquid micromenisci form around the protrusions [21], and the wall-liquid–vapor boundary line, where evaporation occurs, elongates, which accelerates evaporation and, consequently, distillation.

This process was modeled using AFM data obtained in a series of sections parallel to the average plane for which the total volumes of protrusions and depressions are equal. In order to simplify the model, it was assumed that the rough surface cross-section plane in the depression area is identical to the free surface of the solution, i.e., the formation of menisci was ignored. As the solution film moves up the rough wall, the film thickness monotonically decreases (*V/S* in Fig. 10b from right to left) due to evaporation, and the contact line length passes through the maximum (Fig. 10a from right to left). For ampoule #1, the value of L/a^2 averages close to 10 m/cm^2, which for an ampoule diameter of 8 mm and for a film height of 15 mm (Fig. 9a) gives $L = 36$ m. This value exceeds L for the smooth wall (circumference of the ampoule) by more than 3 orders of magnitude, which explains the accelerating effect of roughness on solution distillation. It was noted in [9] that the only standard roughness parameter that increases with increasing *JS* is the oil retention volume (the volume of the

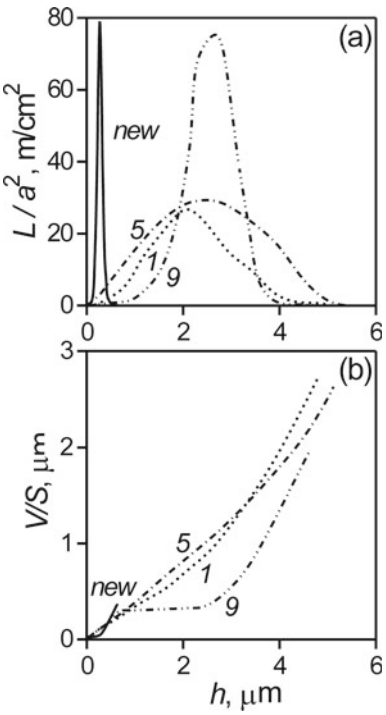

Fig. 10 Atomic force microscopy data obtained in cross-sections of the rough surface of the inner walls of ampoules 1, 5, 9 and the new ampoule (new) in square sites with side $a = 100$ μm [11]. **a** length of the contact line (L), which is formed by intersecting the protrusions with the secant plane, normalized to the surface area of the site (a^2). **b** the ratio of the volume of the depressions to their surface area (*V/S*). The sections are parallel to the median plane and are located at different distances from the deepest depression (h)

deepest depressions). The increase in L/a^2 in the region of $h = 0$–2 μm (Fig. 10a) for ampoules 9, 1, 5, i.e., in the sequence of *JS* increase in these ampoules at the bottom of the electric furnaces, would seem to be consistent with this fact. However, the height of film rise and locations of opal deposition in ampoules with different roughness remained unknown, which prevents accurate identification of the

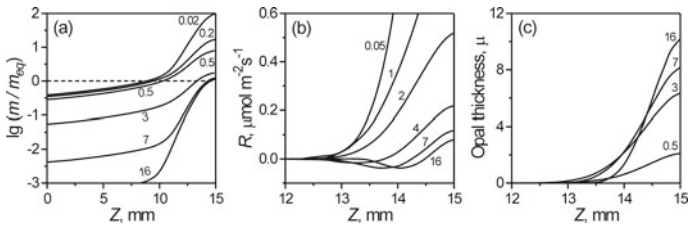

Fig. 11 Solution saturation **a** opal deposition/dissolution rate **b** and opal thickness **c** at different height (Z) of the solution film and at different times (days) based on numerical distillation simulations for JS = 0.34 g/d and δ_0= 2.5 μm [11]

causes of JS differences in these ampoules. In the new ampoule, where distillation did not occur at all, the maximum L/a^2 value was higher than in the roughness ampoules 1 and 5, where distillation occurred. This contradiction can be explained by the fact that Eq. (2) probably does not take into account the limit minimum value of r, below which the rough surface is perceived by the solution as smooth, which excludes the rise of the solution film on the wall.

In [11] numerical simulation of the distillation process taking into account the solution film rise along the rough wall, SiO_2 diffusion in the film, water evaporation and condensation, opal nucleation and growth under conditions of equilibrium ratio of molal concentrations of dissolved silica in vapor and in solution film (m_v/m = 0.0047) [17] was performed. The simulation showed an increase in the degree of saturation in the solution film and redeposition of opal from bottom to top (Fig. 11), which is consistent with the experimental data (Fig. 9a). At initial water film thickness δ_0 near the surface of the main solution volume equal to 2.5 μm (maximum V/S values in Fig. 10b), $m_{t\to\infty}$ values in the solution volume, according to the model, are close to 0.01 mmol/kg, which is noticeably lower than the minimum $m_{t\to\infty}$ value in the experiments (0.06 mmol/kg) (Fig. 8). Kinetic calculations showed that this difference can be explained by the reverse quenching effect when opal dissolves during quenching.

The experimental JS-$m_{t\to\infty}$ dependence (symbols in Fig. 8) has a kink at JS = 0.34 g/d, which, according to modeling, means a change in the sources of silica which enters the solution volume. For the gently sloping section of this dependence the main source is vapor condensation, and for the steep section-SiO_2 diffusion from the film downwards, against the film movement. The steep section of the experimental dependence coincided with the model only when increasing δ_0 to 20–25 μm (Fig. 8), which significantly exceeds the height difference between depressions and protrusions of the rough surface (~5 μm in Fig. 10). Such a film should cover all the protrusions of the rough surface in a thick layer, which eliminates the formation of a tortuous wall-water–vapor line around the protrusions and, consequently, eliminates the acceleration of distillation by the rough surface. Moreover, the very retention of such a thick film on the wall is questionable.

In the previous experiments [8], the lower edge of opal crusts was not above the solution, as in Fig. 9a, but directly at the level of the solution volume. Since the JS-$m_{t\to\infty}$ values obtained in these experiments are located on the steep section of the experimental curve (rhombuses in Fig. 8), it can be assumed that this feature is characteristic of the entire steep section of the curve. As opal is porous, film of solution gets an opportunity to rise through opal pores under capillary forces and evaporate at meniscus edges in places where pores exit to crust surface. Thickness of such film is determined not by height of protrusions of rough surface, but by thickness of opal crust, i.e. formation of thick and quickly evaporating films of solution becomes quite real.

In the mathematical model of distillation the equilibrium ratio of molal concentrations of SiO_2 in the vapor and in the solution film equal to 0.0047 [17] was accepted, but the fact that the same equilibrium ratio the system tends to create at the boundary of vapor and solution volume was not considered. Therefore, at large JS values in the model (Fig. 8) $m_{t\to\infty} = m_v$, which agrees with Eq. (1), but means an overestimated $m_v/m_{t\to\infty}$ ratio (1 instead of 0.0047). The following picture seems more realistic here. The equilibrium m_v/m ratio is established within 1 h [22], i.e., much faster than the distillation process proceeds. The equilibrium value m_v/m could easily be maintained throughout the entire distillation process if it were not for the existence of two solution surface areas with different values of m, large in the solution film on the ampoule wall and small at the surface of the main solution volume. Maintaining equilibrium m_v/m ratios at these sites means that the value of m_v at the film must be larger than at the surface of the main solution volume, i.e. there must be a m_v gradient in the vapor. The picture becomes more complicated if we consider that when m_v decreases below the solubility of amorphous silica, the opal deposited on the ampoule wall must dissolve in the vapor and increase m_v.

Reaching the minimum values of $m_{t\to\infty}$ means not the end of distillation, but reaching its steady state, at which the loss of SiO_2 from the solution volume as a result of rise and evaporation of the solution film is compensated by gain of SiO_2 as a result of vapor condensation and diffusion of SiO_2 from the film. The initial formation of metastable opal instead of stable quartz during distillation is explained by the

low energy of the opal-solution interface, which leads to the small size of the critical opal nucleus [23]. In more extended time interval the regular process of metastable opal recrystallization into stable quartz is added [5, 7], but even here *m* value remains at low level or becomes even less, i.e. non-equilibrium relations of quartz with water are preserved.

3.5 Deposition of Opal Directly on Quartz [10]

The aim of the experiments was to obtain the deposition of opal directly on quartz as a result of solution distillation. This would be a strong argument that distillation is associated not only with metal walls with high thermal conductivity, but also can proceed on mineral walls, typical for natural cavities. Experiments were carried out not in ampoules but directly in autoclaves since quite large columnar quartz crystals (0.8–1 cm in cross-section and 6–7 cm in length) and water which surface crossed crystals in their middle were used. As a result, at temperature of experiments (300 °C) the lower half of crystal was in liquid water and upper half was in water vapor. Clamps with tendrils (stainless steel), put on crystal, fixed it vertically along an axis of autoclave and prevented its contact with a wall.

In the bottom autoclave, which was heated at 300 °C for 42 days, on one of faces of quartz crystal above water level opal was found, which was formed as a result of solution lifting on natural groove, solution spreading on face and water evaporation from it (Fig. 12a). Trough-shaped etch pits, which were formed as a result of dissolution of quartz (Fig. 12b), are found below the level of solution on this facet. Opal is represented by spherical aggregates (Fig. 12c) and, according to the X-ray diffraction analysis, has cristobalite-tridimite structure.

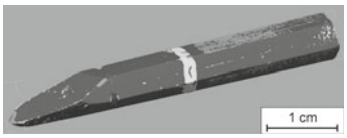

Fig. 13 Combined image of 3d-models of quartz crystal before and after its interaction with water [10]. The light transverse rim shows a local increase in crystal size up to 0.1 mm at the water–vapor interface level (the crystal was placed vertically in the experiment)

In a similar experiment, but with duration of 77 days, the faces of quartz crystal were made rough. Opal was formed as a transverse rim in the middle part of the crystal (Fig. 13). Traditional kinetic calculations using the data of [12] showed that equilibrium of quartz with water or vapor should be reached in ~2 days but the value of *m* in the experiments even after 42 and 77 days was only 60 and 70% of the equilibrium value since dissolved silica was spent for opal formation. According to traditional approach (kinetic calculations), in these conditions after quartz-water equilibrium is reached quickly, only slow quartz recrystallization caused by existence of small TG is possible. In reality, however, stable quartz transformed into metastable opal directly on quartz at a rate 3.5 orders of magnitude higher than the possible rate of quartz recrystallization at this TG.

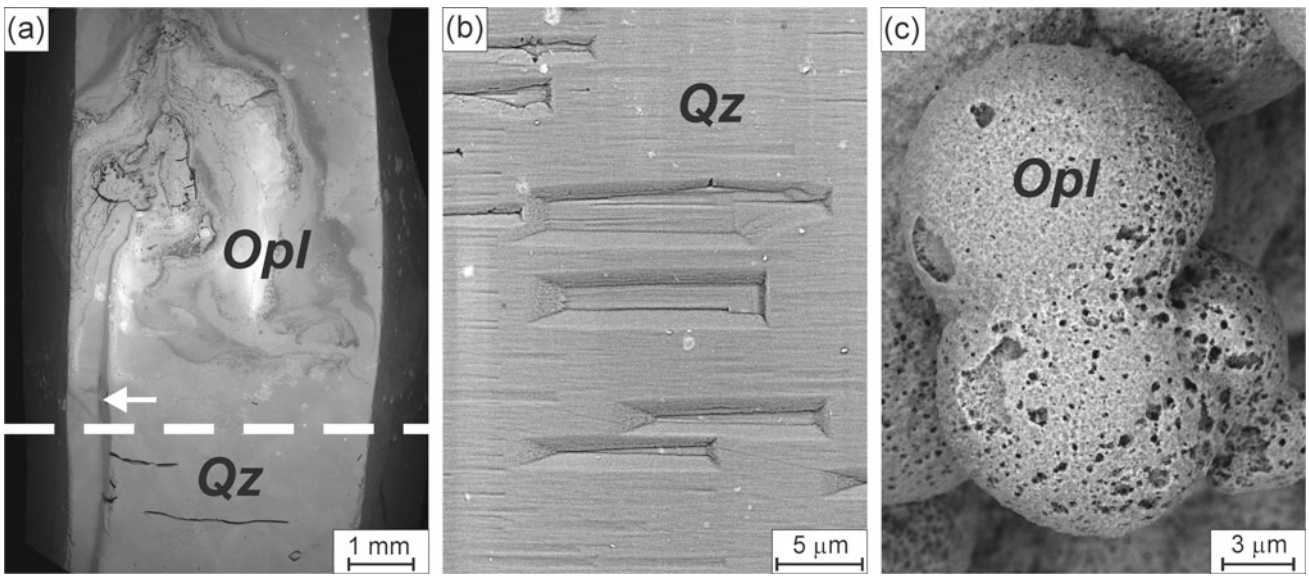

Fig. 12 SEM-image of opal (*Opl*) deposited on quartz (*Qz*) in water at 300 °C [10]. **a** general view of opal deposition on quartz crystal (dashed line shows water level in the experiment, arrow shows the groove along which the solution rose); **b**, **c** shows details of lower b and upper c parts of image a

4 Geochemical Applications

The spontaneous distillation, causing violation of chemical equilibria between minerals, aqueous solution and vapor, by virtue of its universal character is capable to show itself in systems of different composition. This should be taken into account in experimental investigations of solubility and dissolution rate of different minerals. To avoid this phenomenon, experiments should be carried out in reaction containers with smooth walls. In natural cavities, however, the walls are always rough, and there this phenomenon is quite probable at the stage of magmatic activity attenuation (decrease of T and P), when heterogenization of hydrothermal solution occurs, and in cavities the water–vapor boundary is formed. A favorable factor of distillation is the existing hydrophilicity of minerals and rocks [24, 25], which intensifies with temperature increase [26, 27].

In natural cavities, larger mineral crystals are usually located at the top and smaller crystals at the bottom. Such asymmetry may mean dissolution of minerals at the bottom and their deposition at the top of cavities [28]. The process that causes this redeposition of minerals may well be the distillation described in this paper. Prolonged distillation in the cavity can cause migration of the cavity downwards.

5 Summary

This review has shown the great difficulties in the study of a previously unknown phenomenon associated with the search for the main influencing parameters, obtaining reproducible experimental data and their correct interpretation. Overcoming these difficulties was made possible by careful evaluation of the significance of different experimental conditions, finding descriptions of similar phenomena or related processes in the published literature, and a critical analysis of possible hypotheses explaining experimental results.

Studies began after experiments where the concentration of dissolved silica (m) fell below the solubility of quartz with time (Fig. 1a). It was unusual result because quartz in these conditions is stable mineral and has minimal solubility among all silica modifications. Subsequent experiments with quartz and water as well as with water containing SiO_2 showed a sawtooth character of silica concentration dependence on time (m-t) (Fig. 1b), and the solid phase at low values of m was represented by kidney-like noncrystalline or microcrystalline aggregates (Fig. 2). Kinetic calculations and methodical experiments showed that low values of m in quenching solutions are not the result of ampoule depressurization or solid phase precipitation during quenching, but are characteristic of the temperature of the experiments (300 °C). Long experiments (up to 614 days) with water and quartz powder showed a decrease in m from 10 to 0.03 mmol/kg (Fig. 1c), and in some experiments with water and quartz crystals a large amount of newly formed silica was formed which was located on the ampoule walls above the water level. X-ray diffraction, infrared and Raman spectroscopy showed that this silica is represented by ordinary cristobalite opal. For this reason, the hypothesis of the formation of an unknown mineral with low solubility was rejected. Decrease m in hundreds times cannot be explained by other hypotheses associated with thermodiffusion or with reduction of solubility of the mineral in pores of small size. The most probable hypothesis is based on known effect of preferential evaporation of liquid in thin layer (< 100 nm) at meniscus edge. In a closed system this evaporation should be compensated by condensation on the rest surface of a solution, i.e. there should be distillation.

In the following long experiments (up to 860 days) with quartz and water different behavior of SiO_2 in upper and lower autoclaves was found: normal at the top and anomalous at the bottom (Fig. 3). In the latter case, m values were lower, and they decreased to 0.03 mmol/kg in the longest experiment, where the only solid phase was secondary quartz with high porosity (Fig. 4) and high specific surface ($\sim$100 m^2/g). Careful measurements of temperature on the autoclave surface showed its increase from bottom to top in the lower autoclaves (0.15°/cm) and decrease in the upper autoclaves (−0.08°/cm). These data seemed to unambiguously confirm the influence of the temperature gradient (TG). However, it later emerged that another, main parameter affecting distillation was inadvertently changed simultaneously with the TG. A simple distillation model showed good agreement with the experimental data (Fig. 3a) and clarified the masking role of quartz dissolution for the distillation process.

For studying of rate of distillation process the large number of experiments without quartz, but with water containing dissolved silica is executed, to exclude masking of distillation by additional dissolution of quartz. The initial large scatter of m-t points in the experiments was reduced by increasing the number of parallel series of experiments and performing each series in the same ampoules, autoclaves and electric furnace sockets. As a result, smoothed experimental dependences m-t were obtained, which were satisfactorily described by the distillation equation (Fig. 5). However, the minimum values of m in these experiments were rather high, which indicated a shallow depth of distillation. During these studies it turned out that the value of m depends not on the location of the ampoule, but on its property, which may be the roughness of the internal walls of the ampoules.

Similar experiments in new ampoules with smooth walls and in the same ampoules with artificial roughness of the

walls really showed respectively high and low values of *m*, and at different signs of *TG* (Fig. 6). These data confirmed the assumption made and stimulated revision of the previous results, since it was found that the upper and lower autoclaves (Fig. 3) contained, respectively, new and old ampoules i.e., the small influence of *TG* was overridden by the large influence of roughness. The experimental *m-t* data for the rough ampoules were well described by the distillation equation (Fig. 7), and the minimum SiO_2 concentration decreased with increasing distillation rate *JS* (Fig. 8). At the average *JS* value (0.34 g/d), the newly formed opal was located 1 cm above the solution level (Fig. 9a), which is consistent with this wetting mode, when the solution film rises along the deepening of the rough wall, leaving the protrusions dry. As a result, a long convoluted wall-liquid–vapor boundary forms around the protrusions, accelerating evaporation and hence distillation. This process was illustrated by processing AFM data and plotting parallel cross sections of the rough surface at different distances from the deepest depression (Fig. 10).

Numerical simulation of distillation predicted opal deposition in the upper part of the solution film (Fig. 11), i.e., as in the experiment (Fig. 9a). It also explained the kink in the experimental m_v-*JS* dependence (Fig. 8) by a change in the processes that make the main contribution of SiO_2 to *m*, from diffusion from the solution film (at low *JS*) to vapor condensation. The experimental points of the steep section of the curve in Fig. 8 coincided with the model only when the initial solution film thickness was increased to 20–25 μm, which is consistent with a different location of the opal (directly from the solution surface). In this case, the thickness of the solution film is determined not by the height of the protrusion of the rough surface, but by the thickness of the porous opal crust.

At distillation the value of m_v (in vapor) at the solution film is always higher than at the surface of the solution volume, and at low values of m_v the contribution of SiO_2 to m_v from dissolution of opal in vapor is added. As a result, the m_v/m ratio turns out to be higher than the equilibrium one.

In long experiments (42 and 77 days), where the lower and upper halves of quartz crystal were in water and in vapor respectively, the value of *m* was only 60–70% of the equilibrium value, which, according to traditional kinetic calculations, should be reached already in ~2 days. The newly formed opal was deposited directly on quartz (Figs. 12 and 13) at a rate which was 3.5 orders of magnitude higher than the recrystallization rate of quartz. These data have convincingly shown that distillation can occur not only on metallic, but also on mineral walls typical for natural cavities.

Spontaneous distillation can be shown in the form of violation of chemical equilibria in systems of different composition in experimental and natural conditions if there is a boundary water–vapor and walls are hydrophilic and rough. The sign of this process in natural conditions can be known asymmetry of crystallization cavities with larger crystals at the top.

References

1. Dana, J.D., Dana, E.S., Frondel, C.: The system of mineralogy, vol. 3. Silica Minerals, Wiley, New York (1962)
2. Dove, P.M.: Kinetic and thermodynamic controls on silica reactivity in weathering environments. Rev. Mineral. **31**, 235–290 (1995)
3. Bettermann, P., Liebau, F.: The transformation of amorphous silica to crystalline silica under hydrothermal conditions. Contrib. Mineral. Petrol. **53**, 25–36 (1975)
4. Lynne, B.Y., Campbell, K.A., Moore, J.N., Browne, P.R.L.: Diagenesis of 1900-year-old siliceous sinter (opal-A to quartz) at Opal Mound, Roosevelt Hot Springs, Utah, U.S.A. Sed. Geol.**179**, 249–278 (2005)
5. Alexeyev, V.A., Medvedeva, L.S., Starshinova, N.P.: Paradoxical transformation of the equilibrium quartz–water system into an unequilibrated one. Geochem. Int. **51**(5), 382–404 (2013)
6. Alekseyev, V.A., Medvedeva, L.S.: Disturbance of thermodynamic equilibrium of the quartz-water system and silica separation from the liquid phase at a small temperature gradient. Procedia Earth Planet. Sci. **7**, 6–9 (2013)
7. Alekseyev, V.A., Medvedeva, L.S.: Silica distribution in the system quartz–water–vapor depending on the temperature gradient. Geochem. Int. **56**(2), 136–147 (2018)
8. Alekseyev, V.A., Medvedeva, L.S., Balashov, V.N., Burmistrov, A.A., Gromyak, I.N.: Experimental study of unequilibrated silica transfer from liquid water to the vapor phase. Geochem. Int. **56**(7), 617–627 (2018)
9. Alekseyev, V., Balashov, V., Medvedeva, L., Opolchentsev, A.: Spontaneous distillation of silica-bearing solution in closed system with rough walls. E3S Web of Conferences **98**, 04001 (2019)
10. Alekseyev, V.A., Burmistrov, A.A., Gromiak, I.N.: Quartz transformation into opal at the water–vapor interface. Geochem. Int. **59**(4), 377–387 (2021)
11. Alekseyev, V.A., Balashov, V.N., Medvedeva, L.S., Opolchentsev, A.M.: Natural distillation of solutions and opal formation in closed vapor-liquid hydrothermal systems. Geochem. Int. (in press) (2022)
12. Rimstidt, J.D., Barnes, H.L.: The kinetics of silica-water reactions. Geochim. Cosmochim. Acta **44**(11), 1683–1699 (1980)
13. Mizele, J., Dandurand, J.L., Schott, J.: Determination of the surface energy of amorphous silica from solubility measurements in micropores. Surface Sci. **162**(1–3), 830–837 (1985)
14. Plawsky, J.L., Ojha, M., Chatterjee, A., Wayner, P.C., Jr.: Review of the effects of surface topography, surface chemistry, and fluid physics on evaporation at the contact line. Chem. Engin. Commun. **196**, 658–696 (2008)
15. Alekseyev, V.A.: Nanoparticles and nanofluids in water–rock interactions. Geochem. Int. **57**(4), 357–368 (2019)
16. Alekseev, V.A., Medvedeva, L.S.: Disturbance of equilibrium in quartz-water-vapor system. Vestnik Otdelenia Nauk o Zemle Ran № 1 (27) (2009). http://onznews.wdcb.ru/publications/asempg/hydroterm-3.pdf. [in Russian]
17. Plyasunov, A.V.: Thermodynamics of $Si(OH)_4$ in the vapor phase of water: henry's and vapor-liquid distribution constants, fugacity and cross virial coefficients. Geochim. Cosmochim. Acta **77**, 215–231 (2012)

18. Verma, M.P.: Chemical thermodynamics of silica: a critique on its geothermometer. Geothermics **29**, 323–346 (2000)
19. Bico, J., Thiele, U., Quéré, D.: Wetting of textured surfaces. Colloids Surf. A **206**, 41–46 (2002)
20. Shi, B., Sinha, S., Dhir, V.K.: Molecular simulation of the contact angle of water droplet on a platinum surface. In: American Society of Mechanical Engineers, Heat Transfer Division, (Publication) HTD, 376 HTD (1), pp. 93–97 (2005)
21. Xiao, R., Enright, R., Wang, E.N.: Prediction and optimization of liquid propagation in micropillar arrays. Langmuir **26**(19), 15070–15075 (2010)
22. Lukashov, Yu.M., Fursenko, V.F., Popov, A.S.: Procedure of experimental investigation of silicic acid distribution between boiling water and equilibrium vapor in a wide range of pressures and concentrations In: Shtokman, E.A. (ed.) Problems of heating and ventilation. Ministry of Higher and Secondary Special Education of the RSFSR, Rostov-on-Don, pp. 113–123 (1971) [in Russian]
23. Okamoto, A., Saishu, H., Hirano, N., Tsuchiya, N.: Mineralogical and textural variation of silica minerals in hydrothermal flow-through experiments: implications for quartz vein formation. Geochim. Cosmochim. Acta **74**(13), 3692–3706 (2010)
24. Mazurek, A., Pogorzelski, S.J., Boniewicz-Szmyt, K.: Adsorption of natural surfactants present in sea waters at surfaces of minerals: contact angle measurements. Oceanologia **51**(3), 377–403 (2009)
25. Kowalczuk, P.B., Akkaya, C., Ergun, M., Janicki, M.J., Sanbaz, O., Drzymala, J.: Water contact angle on corresponding surfaces of freshly fractured fluorite, calcite and mica. Physicochem. Physicochem. Miner. Process. **53**(1), 192–201 (2017)
26. Adamson, A.W., Gast, A.P.: Physical chemistry of surfaces, 6th edn. Wiley, New York (1997)
27. Friedman, S.R., Khalil, M., Taborek, P.: Wetting transition in water. Phys. Rev. Lett. **111**(22), 226101 (2013)
28. Askhabov, A.M.: Crystallogenesis and evolution of "crystal-environment" system. Nauka, St. Petersburg (1993) [in Russian]

Influence of Water Exchange on the Equilibrium Composition of Aqueous Phase and Mineral Association

O. A. Limantseva, B. N. Ryzhenko, and Yu. V. Shvarov

1 Introduction

Studying analyzes of the chemical composition of natural waters, Vernadsky expressed the opinion about the many possible types of water in the Earth's crust [1], which are formed in natural water–rock systems due to various combinations of water and rocks.

We consider this process from the position of phase equilibria. The water–rock–gas system can be represented schematically as a trihedral pyramid with a base in the form of an equilateral triangle, the top of which is H_2O, the left corner of the base of the triangle is the composition of well-soluble minerals *H* (salts, carbonates, secondary silicates), the right corner of the base is the composition of poorly soluble minerals *L* (oxides, diasporas, goethite), the composition of the gas phase (O_2, CO_2) vertically (Fig. 1). The compositions of the aqueous solution are points in the field between the top of the triangle and the phase equilibrium curve (thick line). Points *h* and *l* are the solubilities of phases *H* and *L*, respectively. The ratio of the mass of the rock and water *R*/*W* (water exchange parameter) is the ray from the top of the triangle to the base. The point at which the ray of the parameter *R*/*W* cuts the curve separating the field of the aqueous solution and the field of mineral phases is the composition of the aqueous solution and the equilibrium mineral association.

From a consideration of the phase diagram of the water–rock–gas system and model calculations performed in the HCh software environment [2, 3] (Tables 1 and 2), the reason for the variety (quite natural) of the observed compositions of natural waters and the reliability of the mechanisms of composition change in various climatic zones of mountain-folded are clear regions of Central Eurasia [4], which can be considered as an illustration of the position of Vernadsky [1] on the variety of chemical types of natural waters in the Earth crust.

2 Research Methods

The efforts of many experts were directed to elucidating the causes and mechanism of the formation of the chemical composition of natural waters [5, 6]. The chemical and mineral composition of rocks, water exchange, landscape, climatic and tectonic conditions were considered by them as basic, determining factors. But the establishment of the dependence of the chemical composition of waters on these factors was usually not quantitative (numerically expressed). Only with the development of methods of mineral and isotope equilibria [2, 7–11] and the development of computer modeling of water–rock–gas systems [2, 3, 6, 10, 12–15] it became possible to quantitatively consider the processes of formation of the chemical composition of Earth crust natural waters.

In [12] it was shown that the chemical composition of natural waters is determined by:

(a) the chemical potentials of inert and perfectly mobile components (PMC, according to Korzhinsky) of the water–rock–gas system, i.e. chemical and mineral composition of reacting rocks and water, and partial pressure (volatility) of gases;
(b) the mass ratio of reacting rocks and water (*R*/*W*), i.e. water exchange;
(c) temperature and pressure.

As can be seen, the necessary natural characteristics can be obtained by studying the object, and the thermodynamic

O. A. Limantseva (✉) · B. N. Ryzhenko
Vernadsky Institute of Geochemistry and Analytical Chemistry, Russian Academy of Sciences, 19 Kosygin St., Moscow, 119991, Russia
e-mail: wri-lab@geokhi.ru

Yu.V. Shvarov
Geological Department, M.V.Lomonosov Moscow State University, Leninskie gory, 1, Moscow, 119234, Russia

V. P. Kolotov and N. S. Bezaeva (eds.), *Advances in Geochemistry, Analytical Chemistry, and Planetary Sciences*,
https://doi.org/10.1007/978-3-031-09883-3_9

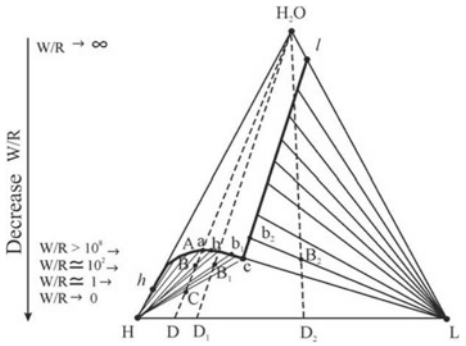

Fig. 1 Diagram (scheme) of the three-component system H_2O–well soluble component *H*-poorly soluble component *L*

characteristics of the components can be taken from the thermodynamic literature [13, 16].

3 Computer Simulation

In [1], the results of studying the chemical composition of natural waters and corresponding mineral associations in various landscape and climatic zones are presented and the mechanisms of their formation are proposed. It seems appropriate to simulate the water–rock–gas systems studied on natural material and compare the results of a traditional study of natural objects and their thermodynamic models.

A study of the regions of the Polar Urals and Lake Poyanhu (China) in [4] are established the dissolution of rocks and the transition in to an aqueous solution the hydrolyzed elements Fe, Al, Mn, as well as rare earth elements (REE) and silicon. The formation of the chemical composition of water is due to the combined action of dissolution of rock minerals and complex formation of dissolved forms of the elements.

Under permafrost conditions, the geochemical environment contributes to the accumulation of elements in an aqueous solution, and in a subtropical climate, the geochemical groundwater environment helps to remove these elements from the solution and their accumulation in the secondary mineral phase. In the studied areas, bicarbonate calcium, calcium-magnesium waters are common. A similar ionic composition and low water salinity is determined by the short time of interaction with rocks. Only in the conditions of permafrost this is due to the presence of water in the

Table 1 "Clay rock-water" system open in respect to the atmosheric gases, O_2 (0.2 bar) and CO_2 (0.0004 bar) at 5 °C

Step modeling *R/W* = 100 × 1.2 ^ (−75 + step number)									
R/W	0.00019	0.00071	0.0010	0.0012	0.011	0.057	0.14	0.29	3.76
Mineral assemblage, mole									
Apatite-F	0	0	0	0	0	1.01E−11	8.20E−11	1.73E−10	2.24E−09
Calcite	0	0	0	0	0	0	5.57E−05	8.91E−04	1.91E−02
Clinochlore	0	0	0	0	0	0	0	4.08E−06	4.08E−04
Diaspore	4.00E−07	1.11E−06	2.36E−07	0	0	0	0	0	0
Goethite	0	7.22E−12	1.13E−11	1.40E−11	1.32E−10	6.83E−10	1.70E−09	3.52E−09	4.52E−08
Kaolinite	0	1.64E−07	9.15E−07	1.24E−06	1.06E−05	2.78E−05	6.50E−05	1.30E−04	1.32E−03
Muscovite	0	0	0	0	0	0	0	0	2.83E−05
Pyrolusite	0	0	2.92E−13	7.82E−13	1.26E−11	6.52E−11	1.62E−10	3.37E−10	4.32E−09
Stilbite	0	0	0	0	4.31E−07	2.92E−05	7.69E−05	1.60E−04	2.00E−03
Dissolved element bulk concentrations, mg/dm^3									
Al	1.39E−05	9.87E−06	9.24E−06	8.17E−06	2.01E−06	1.79E−05	6.20E−05	6.41E−05	7.30E−05
Ca	4.61E−02	1.64E−01	2.37E−01	2.84E−01	2.52E+00	1.19E+01	2.72E+01	2.52E+01	1.95E+01
Fe	1.34E−07	7.65E−08	5.73E−08	4.94E−08	1.18E−08	7.86E−09	7.31E−09	7.29E−09	7.25E−09
K	7.00E−04	2.51E−03	3.61E−03	4.34E−03	3.86E−02	1.99E−01	4.97E−01	1.03E+00	1.16E+01
Mg	2.77E−03	9.97E−03	1.43E−02	1.72E−02	1.53E−01	7.91E−01	1.97E+00	3.57E+00	2.76E+00
Mn	1.26E−08	4.51E−08	4.89E−08	3.49E−08	5.07E−10	2.56E−11	5.98E−12	5.60E−12	4.48E−12
Na	4.28E−04	1.53E−03	2.20E−03	2.64E−03	2.35E−02	1.21E−01	3.01E−01	6.26E−01	7.73E+00
Si	2.68E−02	8.68E−02	8.68E−02	9.61E−02	7.97E−01	3.25E−01	2.06E−01	2.06E−01	2.07E−01
P	1.37E−01	3.09E−01	4.27E−01	5.05E−01	4.34E+00	2.06E+01	4.67E+01	4.86E+01	5.58E+01
$HCO_3 + CO_3$	2.69E−01	6.09E−01	8.42E−01	9.94E−01	8.55E+00	4.07E+01	9.30E+01	9.68E+01	1.11E+02
pH	5.733	6.087	6.227	6.301	7.229	7.897	8.245	8.262	8.32

Table 2 "Basic rock-water" system open in respect to the atmospheric gases, O_2 (0.2 bar) and PCO_2 variable at 5 °C

Step modeling $R/W = 100 \times 1.2$ ^ (−75 + step number)													
R/W	0.0002	0.00034	0.00041	0.00071	0.0012	0.0021	0.0026	0.0044	0.0092	0.12	7.79	57.87	83.33
CO_2,g,bar	0.0004	0.00039	0.00039	0.00039	0.00039	0.00038	0.00038	0.00038	0.00038	0.00036	0.00034	0.00033	0.00033
Mineral assemblage, mole													
Apatite-F	0	0	0	0	0	0	0	0	2.4E−13	6.8E−11	4.6E−09	3.5E−08	5E−08
Calcite	0	0	0	0	0	0	0	3.2E−05	0.00051	0.0115	0.787	5.87	8.45
Clinochlore	0	0	0	0	3.5E−07	2.6E−05	3.2E−05	5.2E−05	9.3E−05	0.00105	0.0688	0.511	0.736
Goethite	5.4E−06	9.4E−06	1.1E−05	2E−05	3.4E−05	5.8E−05	7E−05	0.00012	0.00025	0.00321	0.213	1.58	2.27
Kaolinite	2.5E−06	2.6E−06	0	0	0	0	0	0	0	0	0	0	0
Pyrolusite	3E−11	5.2E−11	6.2E−11	1.1E −10	1.9E−10	3.2E−10	3.9E−10	6.7E−10	1.4E−09	1.8E−08	1.2E-06	8.7E-06	1.3E-05
Quartz	0	0	0	1.5E-05	0.0001	0.00035	0.00044	0.00078	0.00146	0.0172	1.13	8.4	12.1
Rutile	0	0	0	0	0	0	0	0	0	1.7E−08	7.7E-06	5.8E-05	8.3E-05
Saponit-Na	0	0	0	0	0	0	0	0	0	0	0.00049	0.0227	0.034
Saponit-K	0	0	0	0	0	0	0	0	0	0	0	6E-06	1.5E-04
Saponit-Ca	0	0	0	0	0	0	0	3E−06	0.00002	0.00041	0.0272	0.183	0.262
Stilbite	0	1.6E−06	5.1E−06	8.8E−06	1.5E−05	1.6E−07	0	0	0	0	0	0	0
Bassanite	0	0	0	0	0	0	0	0	0	0	0	0	0.00012
Dissolved element bulk concentrations, mg/dm^3													
Al	2.7E−05	2.7E−05	2.8E−05	4.9E−06	3.7E−06	2.6E−06	8.8E−07	8.1E−08	8.1E−08	8.6E−08	4.2E-07	4.2E-07	4.1E-07
Ca	0.83366	1.37875	1.52705	2.63726	4.56912	8.93784	10.7014	17.0741	16.9939	16.032	1.17034	1.29058	1.3547
K	8.3E−05	0.00014	0.00017	0.0003	0.00052	0.00089	0.00107	0.00185	0.00384	0.04927	3.29613	25.6496	26.3143
Mg	0.52267	0.90433	1.08423	1.8743	3.20892	2.40669	2.86858	4.01115	3.93822	3.57357	0.21198	0.22973	0.24213
Mn	1.2E−09	4.3E−10	3.2E−10	1.1E−10	4.3E−11	2.8E−11	2.2E−11	1.6E−11	1.6E−11	1.5E−11	4.1E-11	4.1E-11	4E-11
Na	0.00405	0.00699	0.00839	0.01451	0.02506	0.04322	0.05196	0.08966	0.18645	2.39096	137.25	143.688	147.826
Si	1.25843	1.94664	1.89046	2.83709	2.86518	2.89327	2.89327	2.94945	2.94945	2.94945	3.53934	3.53934	3.53934
P	1.1E−08	1.9E−08	2.3E−08	3.9E−08	6.6E−08	1.1E−07	1.3E−07	2.2E−07	4.5E−07	2E−07	1.9E-06	8.8E-07	7.3E-07
$HCO_3 + CO_3$	5.14756	8.66058	10.0024	17.2602	29.4582	38.4237	45.8035	68.9187	68.9187	69.5286	321.417	308	300.071
Ti	9.5E−06	1.6E−05	2E−05	3.4E−05	5.9E−05	0.0001	0.00012	0.00021	0.00044	0.00479	0.00479	0.00479	0.00479
SO_4	0.00019	0.00033	0.00039	0.00067	0.00115	0.00198	0.00236	0.00402	0.00833	0.10759	7.28135	57.636	73.3898
pH	7.129	7.357	7.428	7.656	7.889	8.006	8.082	8.261	8.264	8.286	8.962	8.954	8.944

solid state for most of the year, and in the conditions of the subtropical climate-with active water exchange.

It is interesting to compare the results of the field study with the model of formation of the composition of natural waters proposed by Kraynov [12]. For this purpose, equilibrium model concentrations of chemical elements and mineral phases were calculated in the system "water-clay-rock-atmospheric gases", thermodynamically open by O_2 (0.2 bar) and CO_2 (0.0004 bar) of the atmosphere at 5 °C (Table 1) and graphs were constructed "Model concentrations as a function of the *R*/*W* parameter (water exchange characteristic)" (Fig. 2). Analytically established minimum and maximum concentrations of dissolved elements are plotted on the same graphs (Table 3, Fig. 2).

It should be noted that the accumulation of macrocomponents in the aqueous phase of the thermodynamic model, corresponding to the observed concentrations in natural objects of the active water exchange zone, occurs in the range of *R*/*W* values from 0.01 to 0.9 (Table 3). As can be seen, the model concentrations are consistent with the analytical concentrations of the dissolved elements; on the other hand, the range of model *R*/*W* values indicated in Table 3 corresponds to the real groundwater flow velocities of the active water exchange zone, 10^{-2}–10^{-3} cm/s [6]. Thermodynamic calculations show decrease the number of minerals for which the model solution is saturated with the growth of runoff (decrease of *R*/*W* value), which increases the potential diversity of hydrochemical type of natural water [17].

At the initial stages of the evolution of the water–rock–gas system (Table 1), the accumulation of Fe, Al, Mn hydrolyzates, as well as REE and Si, occurs in the natural waters of the humid regions. Under the conditions of a subtropical climate, the formation of colloidal compounds Fe and Al, as a result of the deposition of which these elements are removed from the solution and accumulate in the secondary mineral phase. A type of water is formed in equilibrium with the hydroxides of aluminum and iron at *R*/*W* = 0.00014–0.00071. With an increase in the *R*/*W* parameter, the iron–aluminum type of water reaches equilibrium with kaolinite and turns into the aluminum–silicon type [4] (*R*/*W* > 0.000713).

In a system open to atmospheric oxygen, the manganese content is negligible due to the formation of pyrolusite (*R*/*W* > 0.001). With a further increase (*R*/*W* > 0.011) in an aqueous solution, saturation with fluoroapatite (*R*/*W* > 0.057) is achieved and stilbite precipitates (at *R*/*W* > 0.01), and further accumulation of K, Ca, Mg, Mn, Si, precipitation of calcite (at *R*/*W* > 0.14), clinochlor (at *R*/*W* > 0.29) and muscovite (at *R*/*W* > 3.76). Curves of changes in the analytical concentrations of dissolved elements (Fig. 2) indicate a change in water types: siliceous

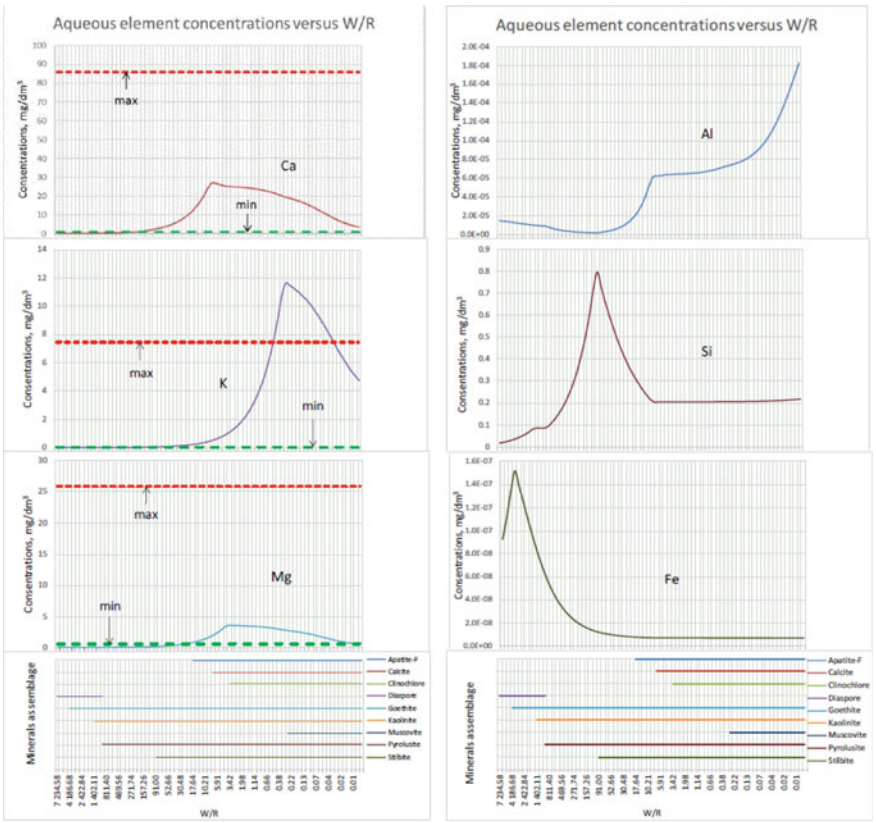

Fig. 2 Comparison of analytically determined and model concentrations of elements in the system "water-clayey rock-atmospheric gases" at 5 °C at equilibrium with the association of mineral phases

Table 3 Determination of the value of the *R*/*W* parameter by comparing analytically determined and model concentrations of elements in the system "water-clayey rock-atmospheric gases" at 5 °C

Components of the aqueous phase	Analytical concentrations, mg/dm^3		*R*/*W* corresponding to the average analytical concentration value	Remark
	min. ÷ max	Mean		
Ca	0.93 ÷ 85.87	8.6	0.039	
K	0.024 ÷ 7.47	0.39	0.10	
Mg	0.61 ÷ 25.9	4.51	0.29	Max model concentration 3.5 mg/dm^3
Na	0.05 ÷ 42.49	1.89	0.873	
HCO_3	4.7 ÷ 324.5	57.9	0.082	
Fe_{total}	0.05 ÷ 278.9	1.6	–	The model concentration values are 10^{-8}–10^{-7} mg/dm^3
Al	0.01 ÷ 42.1	0.19	–	The model concentration values are 10^{-6}–10^{-5} mg/dm^3
Si	0.1 ÷ 74.4	3.7	0.011	Max model concentration 0.79 mg/dm^3
Mn	0.003 ÷ 37.1	0.3	–	The model concentration values are 10^{-12} – 10^{-8} mg/dm^3

Ca-Mg-Na type of water is replaced by aluminum-siliceous, then a siliceous carbonate-calcium type of water is formed in equilibrium with calcite, kaolinite, stilbite (at $R/W = 0.141$).

In water–rock systems of the main composition-gases (Table 2) goethite, pyrolusite and kaolinite precipitate at $R/W > 0.00014$, a further increase in $R/W > 0.00034$ leads to the dissolution of kaolinite. Stilbite is stable in the mineral association at $R/W > 0.00034$, quartz–at $R/W > 0.00071$, clinochlore–at $R/W > 0.00123$, F-apatite–at $R/W > 0.00916$, rutile–at $R/W > 0.118$.

As Ca, Mg, Na, K accumulates in the aqueous phase at $R/W > 0.00442$, Ca-saponite and calcite are formed, siliceous Ca, Mg, Na type water forms in equilibrium with Ca-saponite. As sodium and potassium accumulate in the aqueous phase, Na-saponite ($R/W > 7.789$) and K-saponite ($R/W > 57.87$) are formed. The formation of minerals of the saponite group is favored by an increase in the pH of the aqueous phase.

In orogenic regions with carbon dioxide releases [4], the considered water–rock–gas systems are retained as thermodynamically open in CO_2, but at a partial pressure of CO_2 substantially higher than atmospheric value, the type of aqueous solution changes to carbon dioxide-siliceous-carbonate-calcium in equilibrium with calcite, at an increased partial pressure of CO_2, saponites are not formed.

Oxidation of sulfides adds sulfates to the composition of water, and leaching of sodium chloride-chloride ion, converting water to siliceous-sulfate-sodium in equilibrium with calcite and clays and siliceous sodium chloride in equilibrium with calcite and clays. Aqueous solutions of the above compositions do not produce significant changes in the composition of the equilibrium mineral association, except for the appearance of sulfate minerals.

4 Conclusion

Based on physicochemical factors [12] and using modern computer programs for calculating the equilibrium state of water–rock–gas systems [3, 9, 14, 18], as well as the rate of reaching the equilibrium state [16, 19], it is possible to predict the equilibrium compositions of water phase and mineral associations, and evaluate the time to reach equilibrium. Materials on the study of natural waters and mineral associations of Central Asia published in [4] confirm the conclusion of Vernadsky that many mineral associations and types of water are formed in the Earth crust. Also water and time are responsible for countenance of the rock planets.

References

1. Shvartsev, S.L., Yanshina, F.T. (eds.): Vernadsky, V.I: History of natural waters. Nauka, Moscow (2003)
2. Shvarov, Yu.V.: Algorithmization of the numeric equilibrium modeling of dynamic geochemical processes. Geochem. Int. **37**(6), 571–576 (1999)
3. Shvarov, Yu.V.: HCh: New potentialities for the thermodynamic simulation of geochemical systems offered by windows. Geochem. Int. **46**(8), 834–839 (2008)
4. Guseva, N.V.: Features of the formation of geochemical types of natural waters in certain regions of central Eurasia. Geochem. Int. **58**(13), 1443–1576 (2020)
5. Zaitsev, I.K. (ed.): Hydrogeochemical studies (hypergenesis zone). Nedra, Moscow (1985)
6. Zverev, V.P.: The role of underground waters in the migration of chemical elements. Nedra, Moscow (1982)
7. Naumov, G.B., Ryzhenko, B.N., Khodakovsky, I.L.: Handbook of thermodynamic data US department of commerce. Natl Tech. Inf. Serv., Washington (1974)

8. Garrels, R.M., Christ, C.L.: Solutions, minerals, and equilibria. Harper & Row, New York (1965)
9. Borisov, M.V., Shvarov, Yu.V.: Thermodynamics of geochemical processes. Moscow State University Publishing House, Moscow (1992)
10. Shvartsev, S.L.: Hydrogeochemistry of the hypergenesis zone. Nedra, Moscow (1998)
11. Karpov, I.K., Kiselev, A.I., Letnikov, F.A.: Chemical thermodynamics in geochemistry and petrology. Publishing house of the USSR Academy of Sciences, Irkutsk (1971)
12. Kraynov, S.R., Ryzhenko, B.N., Shvets, V.M.: Geochemistry of underground waters: theoretical, applied and ecological aspects. CentrLitNefteGas, Moscow (2012)
13. Ovchinnikov, A.M.: Hydrogeochemistry. Nedra, Moscow (1970)
14. Charykova, M.V., Charykov, N.A.: Thermodynamic modeling of evaporite sedimentation processes. Nauka, Saint-Petersburg (2003)
15. Chudnenko, K.V.: Thermodynamic modeling in geochemistry: theory, algorithms, software, applications. GEO, Novosibirsk (2010)
16. Kraynov, S.R., Shvarov, Yu.V., Grichuk, D.V., et al.: Methods of geochemical modeling and forecasting in hydrogeology. Nedra, Moscow (1988)
17. Limantseva, O.A.: The role of groundwater saturation in formation of hydrochemical water type with reference to the minerals of water-bearing rocks. In: Proceedings of higher educational establishments. Geol. Explor. **2**, 46–53 (2007)
18. Nordstrom, D.K., Plummer, L.N., Parkhurst D.L. et al.: Chemical modeling in aqueous systems: a comparison of computerized chemical models for equilirium calculations in aqueous systems. Symp. Ser. **93**, 857–892. American Chemical Society (1979)
19. Mironenko, M.V., Zolotov, M.Yu.: Equilibrium–kinetic model of water–rock interaction. Geochem. Int. **50**(1), 1–7 (2012)

Thermodynamic Modeling of Stage Formation of Oil from Type II Kerogen

E. S. Sidkina and M. V. Mironenko

1 Introduction

Kerogen is an organic substance of sedimentary rocks, insoluble in aqueous alkaline solutions and organic solvents. According to the theory of the organic origin of oil, kerogen contained in the rocks is the source of the hydrocarbons. When kerogen is exposed to elevated temperatures and pressures its degradation occurs, i.e. decrease of molecular weight and oxidation accompanied by formation of oil and gas. In natural conditions the process of oil formation takes a relatively long time and occurs mainly at a temperature of 80–150 °C [1–3]. Numerous attempts have been made to obtain oil from kerogen in the laboratory. In these works samples of kerogen-bearing rocks or kerogen separated from them (without a mineral matrix) were exposed to temperature influence. In all experiments, oil was produced at higher temperatures than under natural conditions. In experiments with samples of the Bazhenov formation [4, 5] oil was formed in the temperature interval of 250–350 °C with maximum yield at 300 °C. At rise in temperature up to 450 °C only gaseous products are formed. From Lower Thoar clays of Paris basin the oil was obtained at temperature higher than 350 °C [1]. In works [6, 7] on the basis of experiments the two-stage model of formation of oil from kerogen has been proved: at the first stage from kerogen large high-molecular organic compounds (bitumens) are formed, and then from them hydrocarbons are formed. Apart from theoretical significance these works have practical application. On their basis technologies of shale oil production were developed.

Process of oil formation from kerogen can be described by method of thermodynamic modeling. Earlier attempts of modeling of systems with participation of hydrocarbons have demonstrated applicability of method for study of oil formation [8–11]. Calculations [11] reproduced the observed in nature chemical orientation of kerogen transformation and change of rock mineral paragenesis against the background of temperature and pressure increase. At the same time the liquid hydrocarbon phase was obtained at temperatures corresponding to its formation in experiments (300–350 °C). It should be noted, that previously we considered a very simplified component composition of the oil solution, composed mainly of low-molecular alkanes, cyclic and aromatic hydrocarbons. In the course of this work, information from [12] on the thermodynamic properties of decalin, cyclic hydrocarbons with side chains of alkyl groups, and aromatic hydrocarbons consisting of several rings was added to the database. This allowed us to significantly expand the list of oil components and, thus, bring the composition closer to real.

The aim of the work is to create a model of stage formation of oil using extended thermodynamic database. The goal is achieved by consecutive solution of two tasks: (1) thermodynamic simulation of the impact of high temperatures and pressures on the kerogen-bearing rock, and (2) simulation of further transformation of the newly formed bitumen in the reservoir rock at high T and P.

2 Thermodynamic Data and Calculation of Equilibria

The software package GEOCHEQ [13] was used to solve these tasks. It consists of a thermodynamic database and code for calculation of equilibria in multicomponent multiphase systems. The basis of thermodynamic database is well-known SUPCRT92 [14]. The GEOCHEQ thermodynamic database was designed in such a way that it can be supplemented with new information. For calculating the thermodynamic properties of minerals and gases for a given temperature, the three-dimensional Maier-Kelley heat

E. S. Sidkina (✉) · M. V. Mironenko
Vernadsky Institute of Geochemistry and Analytical Chemistry, Russian Academy of Sciences, 19 Kosygina St., Moscow, 119991, Russia
e-mail: sidkinaes@yandex.ru

V. P. Kolotov and N. S. Bezaeva (eds.), *Advances in Geochemistry, Analytical Chemistry, and Planetary Sciences*,
https://doi.org/10.1007/978-3-031-09883-3_10

capacity equation is used. Using the Helgeson-Kirkham-Flowers model [15] allows to calculate the thermodynamic properties of ions and neutral molecules of the water phase in a wide range of temperatures (0–1000 °C) and pressures (1–6000 bar). The thermodynamic properties of water were calculated using the equation [16] and the Hill equation [17]. Activity coefficients for aqueous solution components were calculated according to the Debye–Huckel model, fugacity coefficients of gas solution components were calculated according to the Peng-Robinson equation [18]. The equilibrium composition of the system was calculated by minimizing the free energy of the system using the convex simplex algorithm.

Oil in the model was considered as an ideal hydrocarbon solution. To create it, the GEOCHEQ database was updated with thermodynamic information about hydrocarbons (free energy of formation, enthalpy, entropy, molar volume for standard temperature and pressure, heat capacity equation coefficients, critical temperature, temperature and enthalpy of phase transitions). The hydrocarbon solution had 128 components. Data for alkanes, aromatic hydrocarbons consisting of one ring and side chains, and cyclic hydrocarbons (cyclopentane, cyclohexane, cycloheptane, and cyclooctane) were taken from [19]. For higher molecular weight substances, the information was taken from [12]. These included polyaromatic hydrocarbon (for example, pyrene, biphenyl, etc.), cyclic hydrocarbons with chains (for example, decylcyclopentane), decalin. A complete list of oil solution components is given in the Table 1.

In addition to hydrocarbons, information on thermodynamic properties of kerogens of different types and degrees of maturity ($C_{515}H_{596}O_{72}$, $C_{415}H_{698}O_{22}$, $C_{406}H_{528}O_{19}$, $C_{292}H_{288}O_{12}$, $C_{128}H_{68}O_7$) was entered into the database. They were considered as phases of constant composition. Thermodynamic information on kerogens was taken from [8]. Kerogen $C_{292}H_{288}O_{12}$ belongs to type II of medium maturity. Kerogen of composition $C_{128}H_{68}O_7$ also corresponded to type II, but in terms of maturity corresponded to the end of catagenesis stage. Type II kerogen was formed in a reducing environment in marine sediments containing autochthonous organic matter (a mixture of phytoplankton, zooplankton, and bacteria residues). It is widespread and is the source of hydrocarbons in numerous oil and gas fields. For example, kerogen of Bazhenov Formation (Western Siberia, Russia) belongs to type II. Rather well-studied kerogen of Lower Torey clays of Paris basin also belongs to type II. In addition to the above, fields originating from oil-bearing sediments with type II kerogen exist in Western Canada (Devonian and Cretaceous sediments), North Africa (Paleozoic sediments), West Africa (Cenozoic sediments) and in other areas [1].

In addition to kerogens, 85 minerals from GEOCHEQ database were included in the model as solid phases. The aqueous phase with 58 possible solution components and the gaseous phase (CH_4,g, CO_2,g, H_2,g, H_2O,g, H_2S,g, O_2,g) were considered. Full list of considered phases and components is given in the Table 1.

3 Input Data

Transformation of Kerogen-Bearing Rock at High T and P

The mineral composition of the Bazhenov Formation sample was taken as the initial composition of the parent rock. To obtain the presented mineral composition, the results of X-ray fluorescence and X-ray phase analyses of a sample of the Bazhenov Formation of the Malobalykskoye field (Western Siberia) were used. The amount of organic matter was calculated from pyrolysis data. The obtained analytical data were summarized and corrected according to previously published data [3, 20, 21]. Thus, we obtained a typical mineral composition of the Bazhenov shale: quartz 62.9%, Mg-montmorillonite 7.6%, illite 6.9%, albite 3.4%, pyrite 3.3%, calcite 1.3%, and kerogen $C_{292}H_{288}O_{12}$ 14.6%. The mass of water in the calculated system was 100 g per 1 kg of rock.

Bitumoid Transformation in the Reservoir Rock at High T and P

The mineral composition of the reservoir was obtained by summary of the data on the compositions of the Western Siberia terrigenous reservoirs [22, 23]: quartz (40%), albite (15%), anorthite (15%), microcline (15%), muscovite (4.5%), illite (3%), clinochlorite (3%), kaolinite (2%), pyrite (0.2%), calcite (2.1%), dolomite (0.1%), siderite (0.1%.) The reservoir rocks are more watered than the oil matrix rocks. Based on the reservoir porosity value of 20%, we assumed in calculations the amount of water equal to 250 g per 1 kg of rock.

4 Scheme of Calculations

Transformation of Kerogen-Bearing Rock at High T and P

Modelling of kerogen-bearing rock transformation was carried out in an 11-component (C, H, O, K, Mg, Ca, Na, Al, Si, Fe, S) closed system of the above described composition. A series of chemical equilibria in the temperature range 50–400 °C at gradually increasing pressure from 300 to 2200 bar was calculated.

Bitumoid Transformation in the Reservoir Rock at High T and P

Bitumoid produced in the previous task from kerogen-bearing rock at 50 °C and 300 bar was moved to a reservoir where further oil maturation took place. A series of

Table 1 List of phases and components considered in modeling

Solid phases			
Akermanite	Cordierite	Huntite	Pargasite
Albite	Corundum	Hydromagnesite	Periclase
Analcime	Cristobalite	Iron,native	Phlogopite
Andalusite	Daphnite	Jadeite	Portlandite
Andradite	Diopside	Kalsilite	Potassium-oxide
Anhydrite	Dolomite	Kaolinite	Prehnite
Annite	Enstatite	K-feldspar	Pyrite
Anorthite	Epidote	Laumontite	Pyrophyllite
Anthophyllite	Fayalite	Lawsonite	Pyrrhotite
Antigorite	Ferroactinolite	Lime	Quartz
Artinite	Ferrosilite	Magnesite	Sanidine
Brucite	Ferrotremolite	Magnetite	Sepiolite
Ca-Al-pyroxene	Ferrous-oxide	Margarite	Siderite
Calcite	Fe-talc	Merwinite	Sillimanite
Chalcedony	Forsterite	Microcline	Sodium-oxide
Chrysotile	Gehlenite	Monticellite	Spinel
Clinochlore	Goethite	Muscovite	Talc
Clinoenstatite	Greenalite	Nepheline	Tremolite
Clinoferrosilite	Grossular	Orthodiopside	Wairakite
Clinozoisite	Hedenbergite	Orthohedenbergite	Wollastonite
Coesite	Hematite	Paragonite	Zoisite
Cohenite	$C_{515}H_{596}O_{72}$	$C_{415}H_{698}O_{22}$	$C_{406}H_{528}O_{19}$
$C_{292}H_{288}O_{12}$	$C_{128}H_{68}O_7$		
Hydrocarbon phases			
Methane(l)	2-Methylhexane	Cyclooctane	trans-decaline
Ethane(l)	2-Methylheptane	methylcyclopentane	Benzene
Propane(l)	2-Methyloctane	1,1-dimethylcyclopentane	Toluene
Butane(l)	2-Methylnonane	cis-1,2-dimethylcyclopentane	Ethylbenzene
n-Pentane	2-Methyldecane	trans-1,2-dimethylcyclopentane	Propylbenzene
n-Hexane	2-Methylundecane	ethycyclopentane	Butylbenzene
n-Heptane	2-Methyldodecane	n-propylcyclopentane	Pentylbenzene
n-Octane	2-Methyltridecane	n-butylcyclopentane	Hexylbenzene
n-Nonane	2-Methyltetradecane	n-pentylcyclopentane	Heptylbenzene
n-Decane	2-Methylpentadecane	n-hexylcyclopentane	Octylbenzene
n-Undecane	2-Methylhexadecane	n-heptylcyclopentane	Nonylbenzene
n-Dodecane	2-Methylheptadecane	n-octylcyclopentane	Decylbenzene
n-Tridecane	2-Methyloctadecane	n-nonylcyclopentane	Undecylbenzene
n-Tetradecane	2-Methylnonadecane	n-decylcyclopentane	Dodecylbenzene
n-Pentadecane	3-Methylpentane	n-undecylcyclopentane	Tridecylbenzene
n-Hexadecane	3-Methylhexane	n-dodecylcyclopentane	Tetradecylbenzen
n-Heptadecane	3-Methylheptane	methylcyclohexane	1,2-Dimethylbenzene
n-Octadecane	3-Methyloctane	1,1-dimethylcyclohaxane	1,3-Dimethylbenzene
n-Nonadecane	3-Metylnonane	cis-1,2-dimethylcyclohexane	1,4-Dimethylbenzene
n-Eicosane	3-Methyldecane	trans-1,2- dimethylcyclohexane	1,2,3-Trimethylbenzene

(continued)

Table 1 (continued)

n-Heneicosane	3-Methylundecane	ethylcyclohexane	1,2,4-Trimethylbenzene
n-Docosane	3-Methyldodecane	n-propylcyclohexane	1,3,5-Trimethylbenzene
n-Tricosane	3-Methyltridedecane	n-butylcyclohexane	1,2,3,4-Tetramethylbenzene
n-Tetracosane	3-Methyltetradecane	n-pentylcyclohexane	Naphthalene
n-Pentacosane	3-Methylpentadecane	n-hexylcyclohexane	1-methylnaphtalene
n-Hexacosane	3-Methylhexadecane	n-heptylcyclohexane	biphenyl
n-Heptacosane	3-Methylheptadecane	n-octylcyclohexane	1,8-dimethylnaphtalene
n-Octacosane	3-Methyloctadecane	n-nonylcyclohexane	2,7-dimethylnaphtalene
n-Nonacosane	3-Methylnonadecane	n-decylcyclohexane	Anthracene
n-Triacontane	Cyclopentane	n-dodecylcyclohexane	pyrene
2-Methylbutane	Cyclohexane	cis-hexahydroindane	triphenylene
2-Methylpentane	Cycloheptane	trans-hexahydroindane	trans-decalin
Gas phase			
CH_4,g	CO_2,g	H_2,g	H_2O,g
H_2S,g	O_2,g		
Aqueous solution			
H_2O,aq	$MgCO_3$,aq	$HFeO_2$,aq	$MgHSiO_3^+$
HCO_3^-	FeO,aq	HS^-	$MgOH^+$
AlO_2^-	FeO^+	$HSiO_3^-$	$MgSO_4$,aq
$AlOH^{+2}$	FeO_2^-	HSO_3^-	Na^+
Ca^{+2}	$FeOH^+$	HSO_4^-	$NaHSiO_3$,aq
$CaCO_3$,aq	$FeOH^{+2}$	K^+	NaOH,aq
$CaHCO_3^+$	Formate, aq	$KHSO_4$,aq	$NaSO_4^-$
$CaHSiO_3^+$	Formic acid,aq	KOH,aq	O_2,aq
$CaOH^+$	H^+	KSO_4^-	OH^-
$CaSO_4$,aq	H_2,aq	Metanol,aq	Propane,aq
CH_3COO^-	H_2S,aq	Methane,aq	SiO_2,aq
CO,aq	Al^{+3}	Mg^{+2}	SO_2,aq
CO_2,aq	CO_3^{-2}	AlO^+	SO_3^{-2}
Fe^{+3}	$HFeO_2^-$	$MgHCO_3^+$	SO_4^{-2}
Fe^{+2}	$HAlO_2$,aq		

chemical equilibria in this system in the temperature range 50–400 °C at gradually increasing pressure from 300 to 2200 bar was calculated.

5 Simulation Results

Transformation of Kerogen-Bearing Rock at High T and P

The summarized results of kerogen-bearing rock transformation calculations are shown in Fig. 1. Quartz and albite were stable throughout the investigated temperature range. The pyrophyllite-illite association was present in calculations at 50 and 100 °C. This association is characteristic of rocks of an extremely low stage of metamorphism [24]. In our calculations andalusite was formed in the system starting from 150 °C. At temperatures above 250 °C, the andalusite-illite association was replaced by andalusite-microcline, and at 325 °C by andalusite-muscovite. It is noteworthy that the formation of muscovite is associated with a sharp increase in the fraction of liquid hydrocarbons in the system (Fig. 1).

Dolomite was stable in the considered range of temperatures and pressures. Calcite existed up to 200 °C, and magnesite appeared above 250 °C. Siderite existed in insignificant amounts.

Pyrite was present throughout the temperature range. Some pyrite converted to pyrrhotite at 300 °C. The amount of pyrrhotite increased with increasing temperature.

With increasing temperature the kerogen $C_{292}H_{288}O_{12}$ transformed into oil and methane-carbon dioxide gas phase

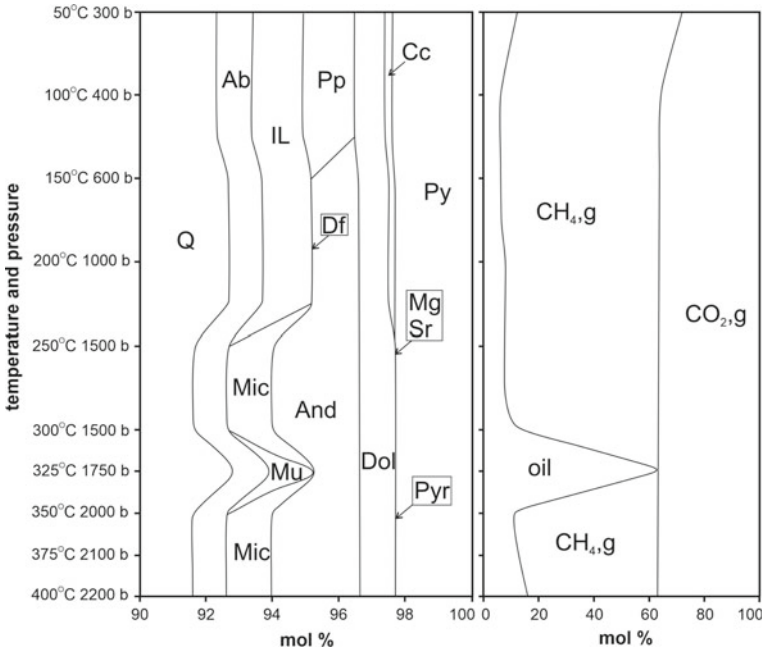

Fig. 1 Transformation of mineral composition of oil source rock and distribution of organic carbon by phases. Mineral symbols: Q-quartz, Ab-albite, IL-illite, Mic-microcline, Mu-muscovite, Pp-pyrophyllite, And-andalusite, Df-daphnite, Dol-dolomite, Cc-calcite, Mg-magnesite, Sr-siderite, Py-pyrite, Pyr-pyrrhotite

(Fig. 1). It should be noted that in a previously published paper [11], oil described by a solution of low molecular weight hydrocarbons was obtained by heating the kerogen-bearing rock to 325 °C at 1750 bar. In this model, which considered polyaromatic hydrocarbons, oil was formed in the system as early as 50 °C. This phase was an immature oil (bitumoid) whose group composition was dominated by aromatic hydrocarbons (Fig. 2), with polyaromatic substances playing the major role. At low temperatures (50–150 °C) pyrene sharply dominated. At higher temperatures, methylnaphthalene and naphthalene dominated. At 325 °C there was a sharp increase in the amount of oil formed and a change in its group composition. Alkanes became dominating type (Fig. 2).

Bitumoid Transformation in the Reservoir Rock at High T and P

A simulation of the transformation of bitumoid produced in the previous task at 50 °C and moved into the reservoir rock with more water-encroached conditions, with a further increase in temperature and pressure was carried out. The general scheme of the calculated transformations is shown in Fig. 3. In the considered temperature and pressure interval

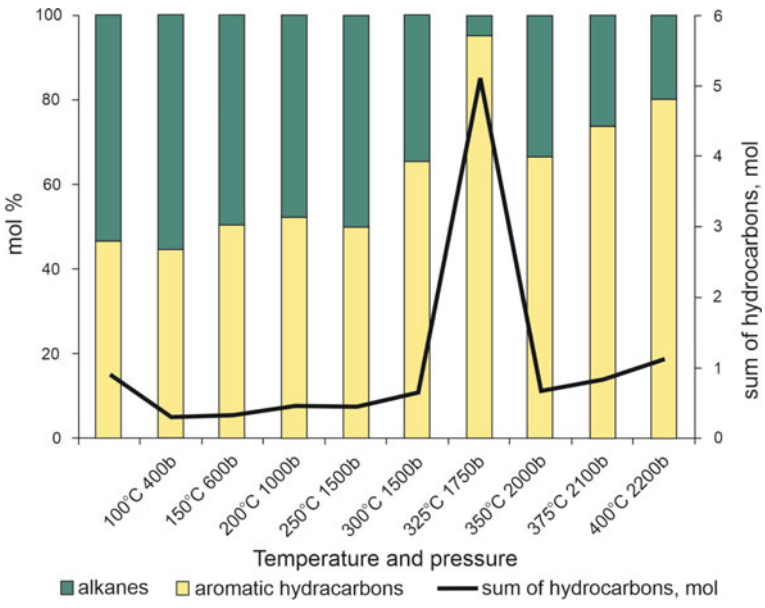

Fig. 2 Group composition of oil obtained by thermodynamic modeling of transformation on kerogen-bearing rock at high *T* and *P*

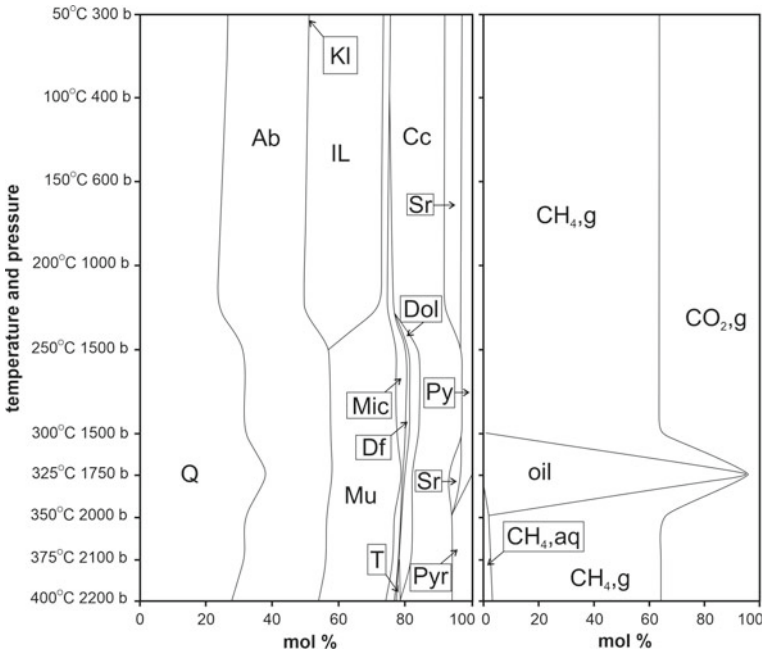

Fig. 3 Transformations of mineral composition of reservoir rock and distribution of organic carbon by phases. Mineral symbols: Q-quartz, Ab-albite, IL-illite, Kl-kaolinite, Mu-muscovite, Mic-microcline, Df-daphnite, T-talcum, Cc-calcite, Dol-dolomite, Sr-siderite Py-pyrite, Pyr-pyrrhotite

quartz, albite, calcite and muscovite were present. The content of the latter considerably increases from temperature 250 °C with disappearance of illite. Kaolinite was stable at temperatures up to 100 °C in small amounts. From 100 °C microcline appears, and from 250 °C daphnite. Among the carbonate minerals, in addition to calcite, dolomite and siderite were present in the rock. Pyrite converted to pyrrhotite at 350 °C.

The main product of bitumoid transformation under the influence of temperature and pressure in the presence of water and reservoir rocks was the methane-carbonate gas phase. A small amount of organic carbon mainly in the form of methane is dissolved in the aqueous solution.

According to our calculations, oil is formed in a narrow temperature range around 325 °C. It was a light alkane oil. In addition to these calculations, we considered the system with a smaller initial amount of water (100 g per 1 kg of rock). As a result, as in the first task, in the absence of free water in the system, the crude oil was not converted to lighter hydrocarbons, but remains heavy. Thus, it can be argued that the presence of water in the system plays a decisive role in the conversion of crude oil.

6 Comparison of the Results Obtained with Natural Observations and Experiments

For comparison of the obtained results with natural observations the calculated data on group composition of the oil received in calculations are plotted (Fig. 4) on the triangular diagram of oil compositions [1].

As seen in the diagram (Fig. 4), cyclic hydrocarbons are unstable in our model and a series of dots representing model oil compositions line up along the alkane-aromatic hydrocarbon axis. From the kerogen-bearing rocks in the interval from 50 °C 300 bar to 300 °C 1500 bar a heavy oil is formed which is mainly composed of aromatic compounds. According to the classification [1] it is classified as aromatic-asphaltene. At 325 °C and 1750 bar there is a sharp increase of liquid hydrocarbons formation and their composition radically changes. The oil obtained at these *T-P* conditions belongs to the alkane class. At the further rise in temperature and pressure the basic product again becomes gaseous methane and the formed oil becomes heavy, but there is a tendency to lightening with increase in temperature. This oil belongs to the aromatic-asphaltene class (calculated at 350 °C 2000 bar) or aromatic (calculated at 375 °C 2100 bar and 400 °C 2200 bar). The same trend was observed in earlier calculations [11].

The composition of the oil obtained by simulating *T-P* impact on the bitumoid released into the reservoir is shown in green in the graph. This oil is an alkane oil with a strong predominance of light hydrocarbons. We assume that the main process of formation of this oil is hydrocracking of heavy oil.

According to fundamental understanding, natural oil starts to form at temperatures above 60 °C, and the main phase of oil formation occurs in a window between 80 and 150 °C. Light oils and condensate form at 150–180 °C. In our calculations, heavy oil was formed at these temperatures, while light oil requires a temperature of 325 °C to form.

The calculated results we obtained can be compared with experimental works carried out mainly in connection with

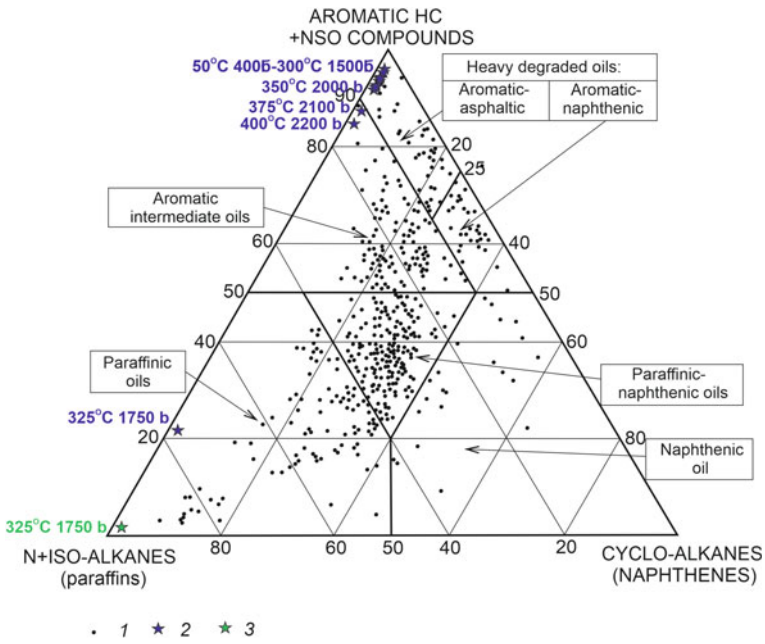

Fig. 4 Triangular diagram of oil compositions [1] with application of compositions obtained by thermodynamic modeling. The compositions of oils are shown: *1* natural; *2* calculated when exposed to high *T* and *P* on kerogen-bearing rock; *3* calculated when exposed to high *T* and *P* on bitumoid in the reservoir rock

issues of shale oil production. Experiments on heating rocks with high organic matter content from different regions of the world were conducted mainly at temperatures ranging from 250 to 470 °C [1–2, 4–7, 25–27 and others]. In these experiments, oil was obtained mainly at temperatures of 300 and 350 °C. According to [20], the lightest alkane oil was obtained when heating a sample of Bazhenov Formation rock at 300 °C. As the temperature increases to 350 °C, the fraction of aromatic compounds increases, which probably indicates the beginning of the graphitization process. At 250 °C the yield of liquid hydrocarbons was insignificant. The foregoing allows us to conclude that the results of thermodynamic modeling and experimental work on hydrothermal treatment of the Bazhenov Formation rocks are comparable.

The carried out modeling of stage formation of oil as a whole agrees with results of experimental works. According to [6, 7] at the first stage transformation of kerogen occurs: separation of non-hydrocarbon components (CO_2, H_2S, H_2O), asphaltenes and resins containing heteroatoms, a small amount of lighter hydrocarbons. Then in the second stage lighter hydrocarbons are formed from high-molecular compounds by aqueous cracking. We were able to describe schematically the stages of oil formation process with formation of high-molecular hydrocarbons at the first stage when simulating the impact of high *T* and *P* on kerogen-bearing rock and formation of alkane oil from bituminous released into the reservoir.

7 Conclusions

Calculated transformations of minerals of rocks of the oil-maternal formation by the example of the Bazhenov and terrigenous reservoir (Western Siberia) are consistent with natural observations and generally accepted ideas about the mineral associations of rocks of low degree of metamorphism.

Modeling of stage formation of oil is consistent with the published results of experimental works on stage formation of oil. It is shown that high-molecular weight hydrocarbons can be an intermediate element in crude oil formation.

The most favorable temperature for generation of light hydrocarbons proved to be 325 °C. At this temperature, light alkane oil was produced in the oil source rock. At the same temperature, even lighter oil was produced from the primary bitumoid (immature oil) under reservoir conditions. This suggests that movement of the primary bitumoid into the reservoir and its secondary transformation results in lighter oil. The results obtained may be useful in developing the technology for producing shale oil from Bazhenov Formation rocks.

Acknowledgements This work is conducted under the GEOKHI RAS state assignment.

References

1. Tissot, B.P., Welte, D.H.: Petroleum formation and occurrence, 2nd edn. Springer-Verlag, Berlin (1984)
2. Hunt, J.M.: Petroleum geochemistry and geology. W.H. Freeman and Company, San Francisco (1979)
3. Bazhenova, O.K., Burlin, Yu.K., Sokolov, B.A., Khain, V.E.: Geology and geochemistry of oil and gas, 3rd edn. Moscow University Press, Moscow (2012)
4. Bychkov, A.Yu, Kalmykov, G.A., Bugaev, I.A., Kalmykov, A.G., Kozlova, E.V.: Experimental investigations of hydrocarbon fluid recovery from hydrothermally treated rocks of the Bazhenov formation. Mosc. Univ. Geol. Bull. **70**(4), 299–304 (2015)
5. Kalmykov, A.G., Bychkov, A.Yu, Kalmykov, G.A., Bugaev, I.A., Kozlova, E.V.: Generation potential of kerogen of the Bazhenov formation and possibility of its implementation. Georesources. Special issue (2), 165–172 (2017)
6. Behar, F., Lorant, F., Lewan, M.: Role of NSO compounds during primary cracking of a Type II kerogen and a Type III lignite. Org. Geochem. **39**, 1–22 (2008)
7. Behar, F., Roy, S., Jarvie, D.: Artificial maturation of a Type I kerogen in a closed system: mass balance and kinetic modeling. Org. Geochem. **41**, 1235–1247 (2010)
8. Helgeson, H.C., Richard, L., McKenzie, W.F., Norton, D.L., Schmitt, A.: A chemical and thermodynamic model of oil generation in hydrocarbon source rocks. Geochim. Cosmochim. Acta **73**, 594–695 (2009)
9. Ryzhenko, B.N., Sidkina, E.S., Cherkasova, E.V.: Thermodynamic modeling of water-rock systems to evaluate their generative potential for hydrocarbons. Geochem. Int. **53**(9), 825–837 (2015)
10. Ryzhenko, B.N., Sidkina, E.S., Cherkasova, E.V.: Computer simulation of the transformation of natural living matter into kerogen. Geochem. Int. **54**(8), 706–711 (2016)
11. Sidkina, E.S., Mironenko, M.V.: Thermodynamic modeling of catagenetic transformation of rock with a high organic matter content. Geochem. Int. **58**(13), 1505–1510 (2020)
12. Richard, L., Helgeson, H.C.: Calculation of the thermodynamic properties at elevated temperatures and pressures of saturated and aromatic high molecular weight solid and liquid hydrocarbons in kerogen, bitumen, petroleum, and other organic matter of biogeochemical interest. Geochim. Cosmochim. Acta **62**, 3591–3636 (1998)
13. Mironenko, M.V., Akinfiev, N.N., Melikhova, T.Yu.: GEOCHEQ complex for thermodynamic modeling of geochemical processes. Vestn. OGGN RAS **5**(15) (2000)
14. Johnson, W., Oelkers, E.H., Helgeson, H.C.: SUPCRT92: a software package for calculating the standard molal thermodynamic properties of minerals, gases, aqueous species, and reactions from 1 to 5000 bars and 0° to 1000 °C. Comp. Geosci. **18**, 899–947 (1992)
15. Helgeson, H.C., Kirkham, D.H., Flowers, G.C.: Theoretical prediction of the thermodynamic behavior of aqueous electrolytes by high pressures and temperatures; IV Calculation of activity coefficients, osmotic coefficients, and apparent molal and standard and relative partial molal properties to 600 degrees C and 5 kb. Am. J. Sci. **281**(10), 1249–1516 (1981)
16. Archer, D.G.: Wang the dielectric constant of water and Debye-Hückel limiting law slopes. J. Phys. Chem. Ref. Data **19**, 371–411 (1990)
17. Hill, P.G.: A unified fundamental equation for the thermodynamic properties of H_2O. J. Phys. Chem. Ref. Data. **19**, 1233–1274 (1990)
18. Peng, D., Robinson, D.B.: A new two-constant equation of state. Ind. Eng. Chem. Res. **15**(1), 59–64 (1976)
19. Helgeson, H.C., Owens, C.E., Knox, A.M., Richard, L.: Calculation of the standard molar thermodynamic properties of crystalline, liquid, and gas organic molecules at high temperatures and pressures. Geochim. Cosmochim. Acta. **62**, 985–1081 (1998)
20. Bychkov, A.Yu, Kalmykov, G.A., Bugaev, I.A., Balushkina, N.A., Kalmykov, A.G.: Geochemical features of Bazhenov and Abalak formations (Western Siberia). Mosc. Univ. Geol. Bull. **6**, 86–93 (2016)
21. Sidkina, E.S., Bugaev, I.A., Bychkov, A.Y., Kalmykov, A.G.: A thermodynamic model of the water-rock interaction under hydrothermal exposure of the Bazhenov formation. Mosc. Univ. Geol. Bull. **73**(4), 375–379 (2018)
22. Borodkin, V.N., Kurchikov, A.R., Nedosekin, A.S., Lukashov, A. V., Shimansky, V.V.: Geological model characteristic and oil and gas potential prospects of Urevsky seismo-facies complex in the north of the Western Siberia. Geol. Geophys. Dev.Oil Gas Fields **5**, 4–17 (2015)
23. Borodkin, V.N., Kurchikov, A.R., Samitova, V.I., Nedosekin, A. S., Lukashov, A.V.: Paleo-geo-morphological and lithologic-facies characteristics of the Neokomian basic seismic-facies complexes located in the north of the Western Siberia as the basis of their geological modeling. Geol. Geophys. Dev.Oil Gas Fields **5**, 4–17 (2017)
24. Marakushev, A.A.: Petrology of metamorphic rocks. Moscow University Press, Moscow (1973)
25. Behar, F., Vandenbroucke, M., Tang, Y., Marquis, F., Espitalie, J.: Thermal cracking of kerogen in open and closed systems: determination of kinetic parameters and stoichiometric coefficients for oil and gas generation. Org. Geochem. **26**, 321–339 (1997)
26. Burdelnaya, N.S., Bushnev, D.A., Mokeev, M.V.: Changes in the composition of bitumen extracts and chemical structure of kerogen during hydrous pyrolysis. Geochem. Int. **51**(9), 738–750 (2013)
27. Leushina, E., Mikhaylova, P., Kozlova, E., Polyakov, V., Morozov, N., Spasennykh, M.: The effect of organic matter maturity on kinetics and product distribution during kerogen thermal decomposition: the bazhenov formation case study. J. Petrol. Sci. Eng. **204**, 108751 (2021)

Quantitative Parameters of Pleistocene Sediments in the World Ocean

M. A. Levitan

1 Introduction

In the Earth sciences, as is well known, the quantitative parameters of the natural phenomena and mechanisms under study are as important as the results of their qualitative analysis. This conclusion also fully applies to sedimentology and sedimentary geochemistry. The basic research methods in this area in the Vernadsky Institute RAS are the volumetric method of Ronov [1] and the worldwide applied [2–7] mass accumulation rate (MAR) method.

The volumetric method was used by Ronov, Khain and their collaborators in studying the quantitative lithological-geochemical evolution of the Earth's stratisphere [8, 9]. For this purpose, overview lithological-paleogeographic maps were created for large stratigraphic subdivisions of individual regions, or continents, or oceans, which were then processed with obtaining of such quantitative sedimentation parameters as areas and volumes of mapped lithological gradations, masses of dry sediment, mass of matter per unit time (i.e., accumulation rate). Consistent analysis of the data obtained in a historical-geological perspective allowed reconstructing the sedimentation history at a quantitative level. This method was used only at the Vernadsky Institute, but has been recognized worldwide; for example, suffice it to point to the confirmation of Ronov's data on 1st order ocean level fluctuations in [10].

Unfortunately, work by the volumetric method was stopped at the Pliocene level and research of the Quaternary period was not carried out due to the death of Ronov. They resumed only in the XXI century, with the Pleistocene deposits of the World Ocean being the main object of study. The first paper by the Vernadsky Institute RAS team on this topic was not published until 2013 [11].

M. A. Levitan (✉)
Vernadsky Institute of Geochemistry and Analytical Chemistry, Russian Academy of Sciences, 19, Kosygin St., Moscow, 119991, Russia
e-mail: m-levitan@mail.ru

The main factual material (data on lithology and stratigraphy of Pleistocene sediments, their water content and density) was obtained from the processing of deep-sea drilling cruise reports. Data on the recorded trips and their supervisors are given in the book [12]. We adopted the lithological classifications used by the participants of the cruises, controlling the given descriptions with the materials of smear-slide studies and laboratory analyses of $CaCO_3$ contents. In the following, only the most widespread sediments are shown on the maps compiled. Sediments such as metalliferous sediments, edaphogenic sediments, manganese nodules, phosphorites, etc. are not shown in the maps. For the southern deep-water Pacific Ocean floor and for the Scotia Sea, due to lack of deep-sea drilling data, we had to use data from long cores obtained during the cruises of the "Eltanin" (USA) [13].

In terms of stratigraphy, it was decided to follow the "old" Pleistocene scale [14]. According to one of the Russian versions of the Quaternary stratigraphic scale [15], the Middle and Upper Pleistocene (summarily corresponding to the Brunhes Magnetic Chron) were termed the Neopleistocene (rounded from 0.8 to 0.01 Ma). The part of the Lower Pleistocene (from the top of the Olduvai Subchron to the Brunhess/Matuyama boundary) was named the Eopleistocene [15] (between 1.8 and 0.8 Ma).

We have constructed lithological-facies overview maps in transverse azimuthal equal-area projection at 1:35,000,000 scale for pelagic areas of the Pacific, Indian and Atlantic Oceans, and a number of maps in the same projection at 1:10,000,000 scale (less frequently-1:20,000,000) for key areas of submarine continental margins. The method of actualism as understood by N.M. Strakhov [16] and facies-genetic analysis of oceanic sediments [17] were used. Data from the International Bathymetric Chart of the Ocean [18] and the Geomorphological Chart of the World Ocean [19] were actively used. All maps were created for two time slices-Neopleistocene and Eopleistocene-and were processed using the Ronov volumetric method. As a result, 54 maps

V. P. Kolotov and N. S. Bezaeva (eds.), *Advances in Geochemistry, Analytical Chemistry, and Planetary Sciences*,
https://doi.org/10.1007/978-3-031-09883-3_11

were compiled. The maps themselves, their descriptions, tables of quantitative parameters-all this material is placed in the book [12]. In total, more than 80% of the ocean floor area was mapped for the above-mentioned oceans.

Article contains the analysis of the quantitative parameters received by a volumetric method, and also results of application of a method of mass accumulation rates received at division of rates of accumulation of those or other lithological gradations on areas of their distribution. It is necessary to note priority character of the received data and conclusions, as the volumetric method of Ronov is applied only in Vernadsky Institute RAS.

2 Factual Material and Research Methods

The factual material for this article is the tables of quantitative sedimentation parameters of Pleistocene deposits [12]. We note some of their specific features. For a number of key areas of submarine continental margins (Indo-Ocean margins of Australia, Gulf of Mexico, Arctic Ocean), maps were made taking into account the average coastline position for the Neopleistocene and Eopleistocene. Thus, based on the data [20], the position of the Neopleistocene coastline coinciding with the modern 50 m isobath, and for the Eopleistocene coastline-with the 25 m isobath was chosen for the Arctic Ocean. It is impossible to make the same lithological-facies maps for this ocean as for other ocean basins due to too few deep-sea drilling holes. Therefore, the data for the Arctic below are purely hypothetical and based on information on its modern topography [21], lithology of Upper Quaternary sediments [22], seismostratigraphy [23], deep-sea drilling materials [24], review of average sedimentation rates for the last five marine isotope stages [25].

In the Research results section below, quantitative parameters are provided not only for the mapped lithological gradations but also for the main lithological groups: lithogenic, carbonate and siliceous. In addition, the calculations also include data on the main sediment-forming components: lithogenic matter, $CaCO_3$, and biogenic opal. The calculation methods are given in the respective paragraphs.

3 Research Results

3.1 Weighted Average Lithological Composition of Pleistocene Sediments of the World Ocean

Academician Ronov has repeatedly pointed out, particularly in his monograph [26], that a correct understanding of the geochemical features of a synchronous layer requires data not on its arithmetic average chemical composition but on the weighted average chemical composition. The latter, in turn, can be calculated only on the basis of the weighted average lithological composition obtained by applying Ronov's volumetric method to the lithological-paleogeographical or lithological-facies maps compiled for this layer. The calculation of the weighted average lithological composition then requires data on the masses of dry sediment of those material-genetic types or lithological complexes, which are reflected in the above maps.

The total area of the Pacific Ocean floor is 156836 thous. km^2, corresponding to 87.8% of its total area with seas [27]. For the Indian Ocean the same figures are 62,116 thous. km^2, which corresponds to 82.7% of the total area of the Indian Ocean without the back island-arc seas [27]. In the Atlantic the corresponding figures are 79,332 thous. km^2, equal to 86.6% of the entire Atlantic Ocean area [27]. In the Arctic Ocean, the pelagic area is 2873 thous. km^2 and the submarine continental margins are 6661 thousand km^2 [21]. The drained shelf area in the Neopleistocene was 1,159,000 km^2 and in the Eopleistocene was 299,000 km^2. Consequently, the cumulative area of continental margins in the Neopleistocene was 5502 thous. km^2, and in the Eopleistocene 6362 thous. km^2. Thus, the ratio of the total floor area of continental margins to the pelagic floor area is 1.9 for the Neopleistocene and 2.2 for the Eopleistocene. The total area of the mapped areas of the World Ocean floor and of the entire Arctic Ocean equals 307,818 thous. km^2, which constitutes 85.3% (rounded off) of the World Ocean floor area [27].

Table 1 presents the results of calculations of the total weighted average lithological composition for Pleistocene sediments of all major ocean basins from mapped areas of the ocean floor both in the pelagic facies megabasin and on continental margins. To compile the table, the author has combined a number of similar lithological units into common subdivisions. Thus, eu- and miopelagic clays; weakly carbonate (up to 30% $CaCO_3$) and hemipelagic clays are considered together. All biogenic oozes are considered together with appropriate biogenic clays (both carbonate and siliceous); carbonate-clastic sediments include benthogenic formations of reef limestone type and shelly accumulations. Volcanogenic deposits include volcanic ash, volcanogenic clastic sediments and volcanogenic clays.

Pacific Ocean

Taken together (without data on continental diamictites), the mass of Neopleistocene sediments in the Pacific is 2243×10^{18} g, of the Eopleistocene 1628×10^{18} g, and of all Pleistocene sediments 3871×10^{18} g. Thus, the mass of dry sediment in marine (oceanic) sediments in the Pacific Ocean was 1.38 times greater than in the Eopleistocene.

Based on the data in Table 1 for the Pacific Ocean, we calculate the ratio of dry sediment masses of various sediments

Table 1 Weighted average lithological composition of Pleistocene sediments of the World Ocean (in 10^{18} g)

Pacific Ocean												
Age	Eu- and mio-pelagic clay	Hemipelagic clay	Terrigenous turbidites	Sands	Diamictites	Nano oozes and nano clays	Nano-foraminifer oozes and clays	Benthic and carbonate-detrital deposits	Carbonate turbidites	Diatom oozes and clays	Diatom-radiolarian oozes and clays	Volcanic ash and volcano-detrital deposits
Neopleistocene	209.1	757.1	453.1	172	37	249.4	162	87.7	7.9	78.1	50.6	15.5
Eopleistocene	332.2	706.5	168.5	46	4.3	117.4	148.1	22.4	14.6	35.7	33.4	3.1
Pleistocene	541.3	1463.6	621.6	218	41.3	366.8	310.1	110.1	22.5	113.8	84	18.6
Indian Ocean												
Age	Pelagic clay	Hemipelagic clay	Terrigenous turbidites	Sands	Diamictites	Nano oozes and nano clays	Nano-foraminifer oozes and clays	Benthic and carbonate-detrital deposits	Diatom oozes and clays	Diatom-radiolarian oozes and clays		
Neopleistocene	54.7	157.8	657.2	4.9	1.4	167.1	157.2	32.7	23	86.1		
Eopleistocene	137.9	109.6	372.3	15.4	1.5	198.3	55.9	39.6	70.4	15.1		
Pleistocene	192.6	267.4	1029.5	20.3	2.9	365.4	213.1	72.3	93.4	101.2		
Atlantic Ocean												
Age	Pelagic clay	Hemipelagic clay	Terrigenous turbidites	Sands	Nano oozes and nano clays	Nano-foraminifer oozes and clays	Benthic and carbonate-detrital deposits	Carbonate turbidites	Diatom oozes and clays	Volcano-genous deposits		
Neopleistocene	60.7	440.7	558.4	35.5	168.4	238.3	22.7	27.8	72.2	34.5		
Eopleistocene	135.3	216.3	91.2	29.9	502.9	477.7	35.9	25.6	84.1	7.4		
Pleistocene	196	657	649.6	65.4	671.3	716	58.6	53.4	156.3	41.9		
World Ocean												
Age	Eu- and mio-pelagic clay	Hemipelagic clay	Terrigenous turbidites	Sands	Diamictites	Nano oozes and nano clays	Nano-foraminifer oozes and clays	Benthic and carbonate-detrital deposits	Carbonate turbidites	Diatom oozes and clays	Diatom-radiolarian oozes and clays	Volcano-genous deposits
Neopleistocene	324.5	1624.6	1668.7	212.4	1.4	584.9	557.5	143.1	35.7	173.3	136.7	50
Eopleistocene	605.4	1277.4	632	91.3	1.5	818.6	681.7	97.9	40.2	190.2	48.5	10.5
Pleistocene	929.9	2902	2300.7	303.7	2.9	1403.5	1239.2	241	75.9	363.5	185.2	60.5

in the Neopleistocene to the Eopleistocene. The obtained values are: hemipelagic clays 1.07, terrigenous turbidites 2.69, nano (coccolite) sediments 2.12, pelagic clays 0.63, sands 3.74, nano-foraminiferal sediments 1.09, carbonate-clastic deposits-3.92, diatom sediments-1.97, diatom-radiolarian sediments-1.51, volcanogenic sediments-5.00 and carbonate turbidites-0.54. Consequently, in the Neopleistocene compared to the Eopleistocene, dry sediment masses increased for all sediments except for pelagic clays and carbonate turbidites. In the first case, this is explained by a greater dilution of pelagic clay with sediment of a different composition, and in the second, by the specific behaviour of carbonate slopes on carbonate platforms in the Coral Sea.

Let us present the data in Table 1 as a percentage of the corresponding total masses and arrange them in rows as they decrease. Then the series for the Neopleistocene will look as follows: hemipelagic clays 33.6, terrigenous turbidites 20.2, nano (coccolith) sediments 11.1, pelagic clays 9.3, sands 7.7, nano-foraminiferal sediments-7.2, carbonate-clastic deposits-3.9, diatom sediments-3.5, diatom-radiolarian sediments-2.2, volcanogenic sediments-0.7 and carbonate turbidites-0.3.

For the Eopleistocene the following series are arranged: hemipelagic clays-43.3, pelagic clays-20.4, terrigenous turbidites-10.3, nano-foraminiferal sediments-9.1, nano (coccolith) sediments-7.2, sands-2.8, diatom sediments-2.4, diatom-radiolarian sediments-2.1, carbonate-clastic deposits-1.4, carbonate turbidites-0.9, volcanogenic deposits-0.2.

Thus, the relative role of different sediments (structure of the weighted average lithological composition) changed during the Pleistocene. There was a decrease in this role for hemipelagic clays, pelagic clays, coccolith sediments, nano-foraminiferal sediments, carbonate turbidites; an increase in the contribution for all other sediments. Consequently, the role of terrigenous clastic, volcanogenic and siliceous sediments increased and that of carbonate sediments and clayey sediments of various genesis (both terrigenous and pelagic) decreased.

The decreasing contribution of various sediments for the entire Pleistocene (in %) is as follows: hemipelagic clays-37.4, terrigenous turbidites-15.9, pelagic clays-13.8, nano (coccolith) sediments-9.4, nano-foraminiferal sediments-7.9, sands-5.6, diatom sediments-3.7, carbonate-clastic deposits-2.8, diatom-radiolarian sediments-2.6, carbonate turbidites-0.6, volcanogenic deposits-0.6.

From the point of view of the genetic composition of sediments and approaching to the knowledge of their chemical composition it is more correct to operate not with the masses of the main groups of sediments, but with the masses of the main sediment-forming components: lithogenic matter, $CaCO_3$ and biogenic opal. For the calculations we took an average content of $CaCO_3$ in carbonate sediments of 85% (respectively, lithogenic matter content of 15%), opal in siliceous oozes-60% (i.e., lithogenic matter content is 40%). In low carbonate sediments there is on average 50% of $CaCO_3$ and 50% of lithogenic matter, and in low siliceous sediments there is 40% of opal and 60% of lithogenic matter.

Now let us consider the results of calculations of the sum masses of dry sediment for the main components of the bottom sediments. In the Neopleistocene, the total masses (in 10^{18} g) are as follows: lithogenic material 1853, $CaCO_3$ 411, and biogenic opal 49. For the Eopleistocene, the same range is represented by values of 1513, 268 and 54. In total for the Pleistocene we obtain: 3366, 679 и 103.

In terms of the contribution structure (in %) we have the following three series: for the Neopleistocene 81.2% of lithogenic matter, 16.6% of $CaCO_3$, and 2.2% of biogenic opal; for the Eopleistocene 82.5, 14.2, and 3.3%, respectively; for the entire Pleistocene 81.0, 16.4, and 2.6%, respectively. Thus, in terms of the structure of the average weighted lithological composition by major sediment-forming components, one may speak of a stable sedimentation structure in the Pleistocene of the Pacific Ocean with the dominance of lithogenic material fluxes, a subordinate role of carbonate and almost minimal of siliceous material. During the Pleistocene, the relative contribution of terrigenous and siliceous material decreased and that of carbonate material increased.

Indian Ocean

The total mass of Neopleistocene sediments is 1342.1×10^{18} g, of the Eopleistocene 1016.0×10^{18} g and of all Pleistocene sediments 2358.1×10^{18} g. Thus, the Indian Ocean accumulated 1.3 times more dry sediment mass in the Neopleistocene than in the Eopleistocene.

Based on the data in Table 1, we calculate the ratio of dry sediment masses of different sediments in the Neopleistocene to the Eopleistocene. The obtained values are: hemipelagic clays 1.4, terrigenous turbidites 1.8, nano (coccolith) sediments 0.8, pelagic clays 0.4, sands 0.3, nano-foraminiferal sediments 2.8, carbonate-clastic deposits 0.8, diatom sediments 0.5, diatom-radiolarian sediments 6.8, and diamictites 0.9. Consequently, the masses of dry sediment increased in the Neopleistocene compared to the Eopleistocene for basic terrigenous sediments and nano-foraminiferal sediments, and for diatom-radiolarian sediments. The decrease in masses during the Pleistocene affected sands, pelagic clays, coccolith sediments, carbonate-clastic and diatom sediments.

Let us present the data in Table 1 as a percentage of the corresponding total masses and arrange them in rows as they decrease. Then the series for the Neopleistocene would look as follows: terrigenous turbidites-49.2, nano (coccolith) sediments-12.5, hemipelagic clays-11.8, nano-foraminiferal sediments-11.8, diatom-radiolarian sediments-4.9, pelagic

clays-4.1, carbonate-clastic deposits-2.5, diatom sediments-2.7, sands-0.4, diamictites-0.1.

For the Eopleistocene there are the following series: terrigenous turbidites-36.7, nano (coccolith) sediments-19.5, pelagic clays-13.6, hemipelagic clays-11.8, diatom sediments-7.4, nano-foraminiferal sediments-5.5, carbonate-clastic deposits-3.9, sands-1.5, diatom-radiolarian sediments-1.0, diamictites-0.2.

Thus, the relative role of different sediments (structure of the weighted average lithological composition) changed during the Pleistocene. There was a decrease in this role for pelagic clays, coccolith sediments, carbonate-clastic formations, diatom sediments, sands and diamictites; an increase in the contribution for terrigenous turbidites, hemipelagic clays, nannofossil sediments and diatom-radiolarian sediments.

The decreasing contribution of different sediments for the whole Pleistocene (in %) is as follows: terrigenous turbidites-43.8, nano (coccolith) sediments-15.6, hemipelagic clays-11.4, nano-foraminiferal sediments-9.1, pelagic clays-8.2, diatom-radiolarian sediments-3.2, diatom sediments-4.7, carbonate-clastic deposits-3.1, sands-0.9, diamictites-0.1.

Let us consider the results of calculations of the sum masses of dry sediment for the main components of bottom sediments. In the Neopleistocene, the total masses (in 10^{18} g) are as follows: lithogenic matter 1009, $CaCO_3$ 293, and biogenic opal 65. For the Eopleistocene, the same range is represented by values 791, 248 and 51. In total for the Pleistocene we obtain: 1800, 541 и 116.

In terms of the contribution structure (in %), we have the following three series: for the Neopleistocene, 73.8% of lithogenic material, 21.4% of $CaCO_3$, and 4.8% of biogenic opal; for the Eopleistocene, 72.6, 22.7, and 4.7%, respectively; and for the entire Pleistocene, 73.3, 22.0, and 4.7%, respectively. Thus, in terms of the structure of the average weighted lithological composition in terms of the main sediment-forming components, one can speak of a stable sedimentation structure in the Pleistocene of the Indian Ocean with the dominance of lithogenic material fluxes, a subordinate role of carbonate and almost minimal of siliceous material. During the Pleistocene, the relative contribution of lithogenic (in this case, terrigenous) material slightly increased and that of biogenic material decreased.

Atlantic Ocean

In sum, the mass of Neopleistocene sediments amounts to 1659.2×10^{18} g, the Eopleistocene to 1606.3×10^{18} g and the entire Pleistocene to 3265.5×10^{18} g. Thus, in the Neopleistocene, the Atlantic Ocean accumulated almost as much dry sediment mass as the Eopleistocene (ratio equal to 1.02).

Based on the data in Table 1, we calculate the ratio of dry masses of different sediments in the Neopleistocene to the Eopleistocene. The values obtained are equal for: hemipelagic clays-2.0, terrigenous turbidites-6.1, nano (coccolith) sediments-0.3, pelagic clays-0.5, sands-1.2, nano-foraminiferal sediments-0.5, carbonate-clastic deposits-0.6, diatom sediments-0.3, carbonate turbidites-1.1, volcanogenic sediments-4.7. Consequently, in the Neopleistocene compared to the Eopleistocene, the masses of dry sediments increased for the main terrigenous and volcanogenic sediments and (slightly) for the carbonate turbidites. Almost all biogenic sediments in the Eopleistocene had greater masses than in the Neopleistocene.

Let us present the data in Table 1 as a percentage of the corresponding total masses and arrange them in descending order. The series for the Neopleistocene would then look as follows: terrigenous turbidites 33.7, hemipelagic clays 26.6, nano-foraminiferal sediments 14.3, nano (coccolith) sediments 10.1, diatom sediments-4.3, pelagic clays-3.7, sands-2.1, volcanogenic sediments-2.1, carbonate turbidites-1.7, carbonate-clastic deposits-1.4.

For the Eopleistocene the following series are constructed: nano (coccolith) sediments-31.3, nano-foraminiferal sediments-29.8, hemipelagic clays-13.4, pelagic clays-8.4, terrigenous turbidites-5.7, diatom sediments-5.2, carbonate-clastic deposits-2.2, sands-1.9, carbonate turbidites-1.6, volcanogenic deposits-0.5.

Thus, the relative role of different sediments (structure of the weighted average lithological composition) changed during the Pleistocene. There was a decrease in this role for pelagic clays, carbonate sediments (except turbidites), diatom sediments; an increase in the contribution-for terrigenous turbidites, hemipelagic clays, sands, volcanogenic deposits. The role of carbonate turbidites did not change in Pleistocene.

The decreasing contribution of different sediments for the whole Pleistocene (in %) is as follows: nano-foraminiferal sediments-21.9, nano (coccolith) sediments-20.6, hemipelagic clays-20.1, terrigenous turbidites-19.9, pelagic clays-6.0, diatom sediments-4.8, sands-2.0, carbonate-clastic deposits-1.8, carbonate turbidites-1.6, volcanogenic deposits-1.3.

Let us now consider the results of calculations of the sum masses of dry sediment for the main components of the bottom sediments. In the Neopleistocene, the total masses (in 10^{18} g) are as follows: lithogenic matter 1339, $CaCO_3$ 361, and biogenic opal 99. For the Eopleistocene, the same range is represented by values 985, 1077 and 116. In total for the Pleistocene we obtain: 2324, 1438 и 215.

Thus, the relative role of different sediments (structure of the weighted average lithological composition) changed

during the Pleistocene. There was a decrease in this role for pelagic clays, carbonate sediments (except turbidites), diatoms sediments; an increase in the contribution-for terrigenous turbidites, hemipelagic clays, sands, volcanogenic sediments. The role of carbonate turbidites did not change in Pleistocene.

In terms of the contribution (in %) we have the following three series: for the Neopleistocene 74.4% of lithogenic matter, 20.1% of $CaCO_3$, 5.5% of biogenic opal; for the Eopleistocene 45.3, 49.4 and 5.3%, respectively; for the entire Pleistocene 58.5, 36.1 and 5.4%, respectively. Thus, it can be concluded that probably during the Middle Pleistocene transition the weighted average lithological composition in the Atlantic had changed its structure: during the Pleistocene the contribution of lithogenic matter clearly increased and the contribution of $CaCO_3$ decreased. The proportion of biogenic opal remained virtually unchanged.

Arctic Ocean

Earlier [28] it was suggested that the mass of dry lithogenic (in this case, terrigenous) matter of pelagic sediments makes 34×10^{18} g for the Neopleistocene and 31×10^{18} g for the Eopleistocene (after recalculations). Biogenic sediments are practically absent.

Based on the scheme of distribution of average sedimentation rates in the Arctic Ocean over the last five marine isotopic stages (130 thousand years) [25], it can be assumed that during this period of time, the average sedimentation rates at the continental margins exceeded the same parameter in the pelagic zone by a factor of 3. Let us assume that this ratio was maintained throughout the Pleistocene.

By multiplying the area ratio (1.9 and 2.2 for Neopleistocene and Eopleistocene, respectively) by the ratio of sedimentation rates, we obtain coefficients equal to 5.7 for the Neopleistocene and 6.6 for the Eopleistocene. If we multiply the above hypothetical dry masses of terrigenous matter for the Neo- and Eopleistocene in the pelagic by these ratios, we obtain the corresponding dry masses for the continental margins, correspondingly 194 and 205×10^{18} g. The sums of dry terrigenous matter for the Neo-, Eo- and Pleistocene of the entire Arctic Ocean will then be 228, 236 and 464×10^{18} g, respectively.

World Ocean

Here, the data for the main ocean basins described in the previous paragraphs will be summarised. The total area of the mapped areas of the World Ocean floor and the entire Arctic Ocean equals 307,818 thousand km^2, which constitutes 85.3% (rounded) of the World Ocean floor area [27].

In sum, the mass of Neopleistocene sediments is 5505.2×10^{18} g, of the Eopleistocene 4498.3×10^{18} g and of all Pleistocene sediments $10{,}003.5 \times 10^{18}$ g. Thus, in the Neopleistocene the mass of dry sediment accumulated in the World Ocean was 1.22 times greater than in the Eopleistocene.

Expressing the contributions from the individual oceans as a percentage, we have the following series for the Neopleistocene: Pacific Ocean 40.8, Indian Ocean 24.3, Atlantic Ocean 30.2, and Arctic Ocean 4.7. For the Eopleistocene the corresponding series are as follows: Pacific Ocean: 36.3, Indian Ocean: 22.6, Atlantic Ocean: 35.7, and Arctic Ocean: 5.4. Finally, for the Pleistocene as a whole, the percentage contributions from the individual oceans are: Pacific Ocean 38.6, Indian Ocean 23.6, Atlantic Ocean 33.0, Arctic Ocean 4.8. Attention should be paid to some features of the series: (1) the Atlantic Ocean's increased contribution in the Eopleistocene (caused mainly by the mass of carbonate matter in the pelagic zone); (2) the Arctic Ocean's contribution is insignificant in comparison with other oceans due to its small area.

Based on the data in Table 1, we calculate the ratio of dry sediment masses of various sediments in the Neopleistocene to the Eopleistocene. The obtained values are: hemipelagic clays 1.3, terrigenous turbidites 2.6, nano (coccolith) sediments 0.7, pelagic clays 0.5, sands 2.3, nano-foraminiferal sediments 0.8, carbonate-clastic deposits-1.5, diatom sediments-0.9, diatom-radiolarian sediments-2.7, carbonate turbidites-0.9, diamictites-0.9, volcanogenic sediments-4.9. Consequently, the masses of dry sediment increased in the Neopleistocene compared to the Eopleistocene for basic terrigenous and volcanogenic sediments, as well as for diatom-radiolarian sediments and carbonate-clastic deposits. A decrease in masses was noted for basic carbonate sediments, pelagic clays and diatom sediments.

Let us present the data in Table 1 as a percentage of the corresponding total masses and arrange them in descending order. The series for the Neopleistocene would then be as follows: terrigenous turbidites-30.3, hemipelagic clays-29.5, nano (coccolith) sediments-10.6, nano- foraminiferal sediments-10.1, pelagic clays-5.9, sands-3.9, diatom sediments-3.4, carbonate-clastic deposits-2.6, diatom-radiolarian sediments-2.1, volcanogenic deposits-0.9, carbonate turbidites-0.6, diamictites-0.03.

For the Eopleistocene the following series are constructed: hemipelagic clays-28.4, nano (coccolith) sediments-18.2, nano-foraminiferal sediments-15.2, terrigenous turbidites-14.0, pelagic clays-13.5, diatom sediments-4.4, carbonate-clastic deposits-2.2, sands-2.0, diatom-radiolarians-1.0, carbonate turbidites-0.9, volcanogenic deposits-0.2, diamictites-0.03.

Thus, the relative role of various sediments (the structure of the weighted average lithological composition) had been changed during the Pleistocene. There was a decrease in this role for pelagic clays, carbonate sediments (except for carbonate-clastic deposits) and diatom sediments; an

increase in the contribution for terrigenous turbidites, sands, hemipelagic clays, volcanogenic deposits, diatom-radiolarian sediments.

The series of decreasing contributions of various sediments for the Pleistocene (in %) is as follows: hemipelagic clays-29.0, terrigenous turbidites-23.0, nano (coccolith) sediments-14.0, nano-foraminiferal sediments-12.4, pelagic clays-9.3, diatom sediments-3.8, sands-3.0, carbonate-clastic deposits-2.4, diatom-radiolarian sediments-1.6, carbonate turbidites-0.8, volcanogenic deposits-0.6, diamictites-0.03.

To calculate the masses of major components in the main sediment groups, we used the data given in this section (Pacific Ocean part). Now consider the results of calculations of dry masses of sediment for the main sediment components. In the Neopleistocene, the total masses (in 10^{18} g) were: for lithogenic matter 4246, for $CaCO_3$ 1065, and for biogenic opal 213. For the Eopleistocene, the same range is represented by the values 3358, 1593 and 220. The total for the Pleistocene is: 7604, 2658 and 433.

In terms of the contribution structure (in %) we have the following three series: for the Neopleistocene 76.8% of lithogenic material, 19.3% of $CaCO_3$, 3.9% of biogenic opal; for the Eopleistocene 64.9, 30.8, and 4.3%, respectively; for the entire Pleistocene 71.1, 24.9 and 4.0%, respectively. Thus, we can conclude that, probably, during the Middle Pleistocene transition, the weighted average lithological composition in the World Ocean has changed its structure: during the Pleistocene the contribution of lithogenic matter clearly increased and that of $CaCO_3$ decreased. The proportion of biogenic opal remained almost unchanged (slightly decreased).

If we express the percentage contribution of the separate oceans, we obtain the following series for the Neopleistocene by component (lithogenic matter, $CaCO_3$, opal): Pacific Ocean-42.0, 38.6, 23.0; Indian Ocean-22.7, 27.5, 30.5; Atlantic Ocean-30.2, 33.9, 46.5; Arctic Ocean-5.1, 0. For the Eopleistocene the corresponding series are as follows: Pacific Ocean: 42.9, 16.8, 24.4; Indian Ocean: 22.4, 15.6, 23.1; Atlantic Ocean: 27.9, 67.6, 52.5; Arctic Ocean: 6.7, 0. Finally, for the Pleistocene as a whole, the percentage contributions from the separate oceans are: Pacific Ocean-42.3, 25.3, 23.7; Indian Ocean-22.6, 20.4, 26.7; Atlantic Ocean-29.2, 54.3, 49.6; Arctic Ocean-5.9, 0, 0.

Consequently, in Pleistocene the first place by contribution of lithogenic substance is occupied by the Pacific Ocean, the second-by the Atlantic Ocean, then by the Indian Ocean and the Arctic Ocean. By $CaCO_3$ masses (in %) the Atlantic Ocean is on the first place, followed by the Pacific Ocean and then the Indian Ocean. In terms of biogenic opal contribution, the Atlantic Ocean ranks first, followed by the Indian Ocean and then the Pacific Ocean. In the Arctic Ocean, there are practically no carbonates or biogenic silica. Overall, in the Neopleistocene, the percentage contribution of the Pacific Ocean to the total dry ocean mass was 40.6, of the Indian Ocean-23.9, of the Atlantic Ocean-31.5, of the Arctic Ocean-4.0. For the Eopleistocene a similar series is as follows: 34.4, 20.4, 40.8, 4.4. In the Pleistocene, the sequence is similar: 37.6, 22.2, 36.0, 4.2. Consequently, during the Pleistocene the contribution of the Pacific and Indian Oceans increased and that of the Atlantic Ocean decreased. The role of the Arctic probably has not changed much.

3.2 Accumulation Rates

As noted above, accumulation rates are the quotient of dry sediment masses (see Table 1) divided by the duration of the time interval in question (i.e. for the Neopleistocene 0.79 Ma, the Eopleistocene 1.0 Ma, the Pleistocene 1.79 Ma).

Pacific Ocean

Here are the results of dividing the accumulation rates in the Neopleistocene by the same parameter in the Eopleistocene ($IQ_{2\text{-}3}/IQ_1$). Thus, for pelagic clays-0.80, hemipelagic clays (also including glacio-marine deposits, etc.)-1.36, terrigenous turbidites-3.40, sands-4.73, nannofossil oozes and clays-2.69, nanno-foraminiferal oozes and clays-1.38, carbonate-clastic deposits-4.96, carbonate turbidites-0.68, diatom oozes and clays-2.50, diatom-radiolarian oozes and clays-1.92, volcanogenic deposits-6.32.

Consequently, during the Pleistocene an increase in accumulation rates for hemipelagic clays, terrigenous turbidites, sands, all carbonate sediments (except for carbonate turbidites), siliceous and volcanogenic sediments can be ascertained. Accumulation rates for pelagic clays have clearly decreased. Thus, all major types of terrigenous, carbonate, siliceous sediments and volcanogenic sediments increased their accumulation rates during the Pleistocene. The data on carbonate turbidites in this case are rather characteristic of the development of carbonate platform slopes in the northern Coral Sea than specifics of carbonate accumulation. The decrease in the rate of accumulation of pelagic clays is caused by a strong increase in the rate of accumulation of other (diluting) sediment types and, above all, terrigenous and carbonate sediments.

Values of accumulation rates (in 10^{18} g/mln years) in general for Pleistocene sediments of the Pacific Ocean in the same sediment series are as follows: 302.4, 817.7, 621.6, 121.8, 366.8, 310.1, 61.5, 22.5, 65.8, 50.0, 10.4.

Indian Ocean

Here are the results of dividing the accumulation rates in the Neopleistocene by the same parameter in the Eopleistocene ($IQ_{2\text{-}3}/IQ_1$). So, for pelagic clays-0.50, hemipelagic clays

(also including glacio-marine deposits, etc.)-1.82, terrigenous turbidites-2.23, sands-0.40, diamictites-1.18, nannofossil oozes and clays-1.07, nanno-foraminiferal oozes and clays-3.56, carbonate-clastic deposits-1.05, diatom oozes and clays-0.61, diatom-radiolarian oozes and clays-8.55.

Consequently, an increase in accumulation rates for hemipelagic clays, terrigenous turbidites, diamictites, all carbonate sediments, diatom-radiolarian oozes and clays can be ascertained during the Pleistocene. Rates of accumulation of pelagic clays, sands and diatom sediments have clearly decreased. Thus, all major types of terrigenous and carbonate sediments, as well as diatom-radiolarian sediments, increased their accumulation rates during the Pleistocene. The decrease in the rate of accumulation of pelagic clays is primarily due to a strong increase in the rate of accumulation of other (diluting) sediment types and above all, terrigenous and carbonate sediments.

Values of accumulation rates (in 10^{18} g/mln years) for the Pleistocene sediments of the Indian Ocean as a whole in the same sediment series are as follows: 107.60, 149.39, 575.10, 11.34, 1.62, 204.3, 119.05, 40.39, 62.00, 42.05.

Atlantic Ocean

Below are the results of dividing the accumulation rates in the Neopleistocene by the same parameter in the Eopleistocene ($IQ_{2\text{-}3}/IQ_1$). So, for pelagic clays-0.57, hemipelagic clays (also including glacio-marine deposits, etc.)-2.58, terrigenous turbidites-7.75, sands-1.50, nannofossil oozes and clays-0.42, nano-foraminiferal oozes and clays-0.63, carbonate-clastic deposits-0.80, carbonate turbidites-1.40, diatom oozes and clays-1.09, volcanogenic sediments-5.90.

Thus, an increase in accumulation rates for hemipelagic clays, terrigenous turbidites, sands, carbonate turbidites, volcanogenic sediments can be ascertained during Pleistocene. Accumulation rates of pelagic clays and all carbonate sediments (except for carbonate turbidites) clearly decreased. Accumulation rates of diatom oozes and clays were practically unchanged. Decrease of pelagic clays accumulation rate is caused by strong increase of accumulation rates of other (diluting) sediment types and first of all-terrigenous and carbonate. The reasons for the fall in the rate of accumulation of basic carbonate sediments are related to their outstripping dissolution in the pelagic area since the Middle Pleistocene transition on the background of the general growth of carbonate production. The origin of carbonate turbidites is not related to carbonate accumulation, but rather to the history of the slopes of various ridges and rises in the pelagic region, as well as to the history of some continental margins.

The values of accumulation rates (in 10^{18} g/mln years) for the Pleistocene sediments of the Atlantic Ocean as a whole in the same sediment series are as follows: 109.50, 367.04, 362.91, 35.54, 375.03, 400.00, 32.74, 29.83, 87.32, 23.41.

Arctic Ocean

The rate of accumulation of terrigenous deposits (hemipelagic clays) of the Neopleistocene is 288.6, of the Eopleistoceneis 236.0 and of the entire Pleistocene is 259.2×10^{18} g/mln years. The $IQ_{2\text{-}3}/IQ_1$ratio is 1.22.

World Ocean

Below are the results of dividing the accumulation rates in the Neopleistocene by the same parameter in the Eopleistocene ($IQ_{2\text{-}3}/IQ_1$). Thus, for pelagic clays-0.68, hemipelagic clays (also including glacio-marine deposits, etc.)-1.58, terrigenous turbidites-2.64, sands-2.94, diamictites-1.18, nannofossil oozes and clays-0.90, nanno- foraminiferal oozes and clays-1.04, carbonate-clastic deposits-1.85, carbonate turbidites-1.12, diatom oozes and clays-1.15, diatom-radiolarian oozes and clays-3.57, volcanogenic deposits-6.03.

Thus, we can state that during the Pleistocene the rates of accumulation of hemipelagic clays, terrigenous turbidites, sands, diamictites, carbonate-clastic deposits, carbonate turbidites, siliceous and volcanogenic sediments increased. The rate of accumulation of terrigenous, siliceous and volcanogenic groups of sediments increased. Accumulation rates of pelagic clays, nannofossil oozes and nannofossil clays have evidently decreased. Accumulation rates of nano-foraminiferal oozes and clays were virtually unchanged. The decrease in accumulation rate of pelagic clays is due to a strong increase in accumulation rates of other (diluting) sediment types and primarily-terrigenous and carbonate.

The values of accumulation rates (in 10^{18} g/mln years) of Pleistocene sediments of the World Ocean as a whole in the same sediment series are as follows: 519.50, 1593.30, 1285.31, 169.64, 1.62, 784.08, 692.29, 134.64, 42.40, 209.07, 95.10, 33.80.

3.3 Mass Accumulation Rates

It was already mentioned in the introduction that the method of mass accumulation rates is very widely used in marine geology by specialists around the world. Mass accumulation rates (MAR) or simply absolute masses are as versatile a parameter for comparing sediments of different composition and age as the accumulation rates discussed above. Moreover, they have a definite advantage, as the masses are normalized not only by age but also by area. Thus the intensity of sedimentation processes, i.e. the fluxes of particular sediments or their components, can be discussed.

Bottom Sediment Fluxes

Table 2 presents the results of calculations of the fluxes of the most common types of Pleistocene sediments in the World Ocean.

From the analysis of Table 2 for *terrigenous turbidites* at least two unambiguous conclusions follow: (1) for all studied age slices, there is an increase in the mass accumulation rates of terrigenous turbidites in the series: Pacific Ocean-Indian Ocean-Atlantic Ocean; (2) in all main ocean basins (and, naturally, in the World Ocean as a whole) the fluxes of terrigenous turbidites increased during the Pleistocene.

Increased values of terrigenous turbidite fluxes in the Pleistocene were more typical for the oceans with dominating passive margins, in which the character of the bottom relief and the size of its main forms provide an opportunity for nucleation, development of turbid currents and accumulation of matter from them within the abyssal plains. In contrast, in the Pacific Ocean, the development of turbid currents was generally confined to steep continental slopes and continental rises truncated by depressions of deep-water trenches. Only in some areas could the turbid currents break out beyond the submarine parts of the active margins and unload as turbidites on the abyssal plains.

Table 2 Mass accumulation rates (g/cm^2/thousand years) of oceanic sediments in the Pleistocene of the World Ocean

Age	Pacific Ocean	Indian Ocean	Atlantic Ocean	World Ocean
Terrigenous turbidites				
Neopleistocene	10.01	11.80	27.51	13.76
Eopleistocene	3.60	5.92	7.00	5.15
Pleistocene	6.67	8.62	18.75	9.31
Hemipelagic clays				
Neopleistocene	16.29	1.91	16.17	8.46
Eopleistocene	10.68	0.77	5.69	3.88
Pleistocene	13.10	1.21	8.76	5.76
Glacio-marine sediments				
Neopleistocene	5.92	1.12	1.59	2.47
Eopleistocene	4.63	0.94	0.93	1.88
Pleistocene	5.21	1.04	1.26	2.15
Nano-foraminifer and foraminifer oozes and clays				
Neopleistocene	0.82	0.76	1.83	1.14
Eopleistocene	0.58	0.25	1.82	0.88
Pleistocene	0.68	0.48	1.82	0.96
Nano oozes and clays				
Neopleistocene	0.49	1.36	2.55	1.47
Eopleistocene	0.51	0.99	4.89	1.96
Pleistocene	0.50	1.15	3.72	1.72
Pelagic clays				
Neopleistocene	0.39	0.51	1.01	0.46
Eopleistocene	0.52	0.57	1.94	0.63
Pleistocene	0.46	0.55	1.40	0.56
Diatom oozes and clays				
Neopleistocene	1.02	0.20	1.12	0.78
Eopleistocene	0.25	0.51	1.64	0.80
Pleistocene	0.51	0.37	1.31	0.79
Diatom-radiolarian oozes and clays				
Neopleistocene	0.66	1.67	0	0.78
Eopleistocene	0.07	0.24	0	0.10
Pleistocene	0.18	0.93	0	0.37

The second conclusion should be interpreted in terms of the growth of terrigenous sedimentary matter fluxes in the Pleistocene, primarily caused by the final phase of neotectonic orogenic movements on the Earth's continental blocks. It is likely that this phenomenon was accompanied by intensification of seismic events, which served as triggers for nucleation of turbid currents. Development of glaciation in both hemispheres, in particular, glacioeustatic changes in the sea level at the background of its declining trend have also played a role. For example, recent data suggest that in the Eopleistocene, the average level was at − 25 m, and in the Neopleistocene, at − 50 m [20]. In turn, lowering of the erosion base inevitably led to an increase in fluviogenic fluxes of matter into the oceans.

The study of Table 2 showed that, at all age slices, there was an increase in *hemipelagic clay* fluxes in the series: Indian Ocean-Atlantic Ocean-Pacific Ocean. In the oceans with prevailing passive margins (Indian and Atlantic), the fluxes of hemipelagic clays are significantly less than in the ocean with prevailing active margins (Pacific Ocean), where (according to our data) the overwhelming part of the hemipelagic clay matter accumulated in the natural traps of sedimentation systems of the underwater parts of continental margins.

Similarly to the flows of terrigenous turbidites, the increase in the fluxes of hemipelagic clays from the Eopleistocene to Neopleistocene is pronounced. It is obvious that in this case, too, the same set of natural causes, mentioned in the previous section, was at work. Only the mechanisms of sediment transport and accumulation differed.

The study of Table 2 showed that at all age slices there was an increase in the fluxes of *glacio-marine sediments* in the series: Indian Ocean-Atlantic Ocean-Pacific Ocean. This phenomenon seems to be explained by a larger and more dynamically active glaciation of the Northern Hemisphere compared to the Southern Hemisphere glaciation. In addition, the strong influence of the warm Gulf Stream on the ice regime of the North Atlantic and the Nordic seas played a role.

The unequivocal increase in glacio-marine sediment fluxes during the Pleistocene in all major ocean basins is due to a worsening marine climate associated with the global development of the Earth's glaciation.

The study of Table 2 showed that there was a clear pattern at all levels of the Pleistocene: increasing fluxes of *coccolith-foraminiferal deposits* in the series: Indian Ocean-Pacific Ocean-Atlantic Ocean. The second pattern is reduced to an increase in mass accumulation rates during the Pleistocene: strongest in the Indian Ocean, moderate in the Pacific and quite insignificant in the Atlantic.

Interpretation of the data obtained from the first pattern is a difficult task, because data on present values of primary production, the B/L ratio (ratio of catchment area to sedimentation basin area), the bottom topography character (ratio of total area of submarine rises and ridges to total area of deep-sea basins) and dissolution fluxes must be taken into account.

Data on contemporary primary production show roughly similar averages for the Pacific and Indian Oceans, and 1.24 times higher average primary production in the Atlantic Ocean [29]. B/L ratios clearly increase in the Pacific-Indian-Atlantic series [3]; same is true for ratio of areas of rises and ridges to areas of deep-sea basins in pelagic realm [30]. According to our data, which are not strictly quantitative, dissolution fluxes have increased in the series: Pacific Ocean-Indian Ocean-Atlantic Ocean.

Thus, the data in Table 2 show that despite the dissolution of carbonates, the mass accumulation rates of residual coccolith-foraminiferal and foraminiferal oozes and clays are rather clearly affected by nutrient inputs from land, transformed into primary production (and production of carbonates), and the predominant accumulation of plankton carbonates on the rises and ridges.

The second pattern coincides in principle with the patterns noted in this section for different types of terrigenous sediments. This probably proves a certain synchronous arrival of both terrigenous matter and nutrients from the land during the Pleistocene. Intensification of vertical circulation in the Neopleistocene due to increasing thermal gradients between surface and bottom waters may have played an additional role.

For *coccolith oozes and clays*, one pattern is evident: mass accumulation rates increase at all stratigraphic levels in the series: Pacific Ocean-Indian Ocean-Atlantic Ocean (Table 2). As mentioned in the previous paragraph, it is in this series that the B/L ratios and the ratio of the areas of rises and ridges to the areas of deep-sea basins in the pelagic zones of the oceans clearly increase. In spite of the fact that dissolution fluxes grow in exactly the same direction, nevertheless, the features of carbonate production in the euphotic layer due to increased nutrient supply in the Pleistocene and the features of their accumulation in comparatively shallower environments proved to be more important in terms of residual carbonate matter fluxes.

The changes in the fluxes studied during the Pleistocene were different, with an increase in the Indian Ocean and a decrease in the other oceans, particularly in the Atlantic. This indicates different relationships between the fluxes of matter and dissolution fluxes in the individual ocean basins.

It is interesting to compare the calculated mass accumulation rates for coccolith- foraminiferal and coccolith sediments. Only in the Pacific Ocean the fluxes of significantly foraminiferal sediments were higher than those of coccolith sediments. In the other oceans the opposite trend was observed. Probably, such a phenomenon can be explained by

a substantially higher ratio of dissolution fluxes to carbonate matter fluxes in the Indian Ocean and-in particular-in the Atlantic Ocean. Naturally, the upper boundary of effective dissolution was higher in the Indian and Atlantic Oceans.

From the analysis of Table 2 for *pelagic clays* at least two unambiguous conclusions follow: (1) for all studied age slices there is an increase in the mass accumulation rates of pelagic clays in the series: Pacific-Indian-Atlantic; (2) in all main ocean basins (as well, naturally, in the World Ocean in general) there was a decrease in the flux of pelagic clays during the Pleistocene.

The first conclusion can logically be explained, first of all, by an increase in the B/L ratio in this series, i.e. the ratio of the catchment area to the area of the sedimentation basin [3].

The second conclusion is more complicated. The method of mass accumulation rates is known to allow for the abstraction of diluting components. From this point of view, it is obvious that the Eopleistocene accumulated more dry sediment masses of pelagic clays and had higher accumulation rates than in the Neopleistocene, which is also proved by the direct calculations above.

There seems to be only one explanation for the observed excess of mass accumulation rates of pelagic clays in the Eopleistocene over the Neopleistocene for all the oceans. According to the results of the first cruises of deep-sea drilling as early as the 1970s, it was established that during the Cenozoic (including Pleistocene), the CCD (carbonate compensation depth) in the World Ocean was deepening [31]. Consequently, based on the notion that the pelagic clays are essentially the "insoluble residue" of the carbonate matter fluxes to the bottom, it is clear that with a lower CCD, the mass accumulation rates of pelagic clays in the Eopleistocene will be higher and the accumulation of these clays in the Eopleistocene will occur over a larger area than later in the Neopleistocene.

Table 2 shows a rather complex pattern in the Pleistocene accumulation history of *diatom sediments*. It can be confidently stated that diatom matter in the Atlantic Ocean at all stratigraphic levels accumulated markedly more intensely than in other major ocean basins, with the accumulation of diatom oozes and clays on the deep-sea bottom rather than in the upwelling areas. This fact is probably due primarily to the marked superiority of the Atlantic in the flux of incoming nutrients and hence in the magnitude of primary production [29] with respect to area.

Equally important is the evolution of the vertical circulation in the Southern Ocean, which was most active in the late Pliocene and early Eopleistocene [32]. It cannot be overlooked that in the Pacific the mass accumulation rates of diatom sediments mainly accumulated in the northern hemisphere and in the Indian and Atlantic Oceans—in the southern hemisphere. The difference between the Pleistocene history of diatom sedimentation in the Pacific on the one hand, and in the Indian Ocean and Atlantic on the other, can most likely be explained from the «two oceans» concept [33]. This implies that the Pacific Ocean was dominated by the «ice-free» ocean type, while the other two basins were dominated by the «ice» ocean type.

As for the oceans, the Pleistocene diatom sedimentation is rather stable, i.e. both types of diatom accumulation seem to counterbalance each other in terms of the global silica cycle.

The analysis of the data in Table 2, first of all, shows the absence of any significant *radiolarian sediment* fluxes in the Atlantic. Competitive (diluting) fluxes of carbonate matter in the equatorial zone of this ocean are so great that they do not allow for accumulation of significant masses of radiolarian oozes. In the south of the same ocean, diatom fluxes play a similar role.

There is a clear predominance of radiolarian fluxes at all Pleistocene stratigraphic levels in the Indian Ocean compared to the Pacific. Since, as noted above, B/L ratios are also much higher in the Indian Ocean than in the Pacific, we can conclude that nutrient fluxes into the Indian Ocean are also significantly higher. According to our calculations based on data [29], primary production in the Indian Ocean in the modern era is about 1.5 times higher than in the Pacific Ocean. Thus, increased fluxes of nutrients result in higher primary production, which is realized by markedly higher fluxes of radiolarians to the bottom, mainly in the tropical ocean.

The sharp increase in the mass accumulation rates of radiolarian sediments in the Neopleistocene compared to the Eopleistocene is due to increased nutrient fluxes to the equatorial-tropical zone of both oceans, both due to increased supply from the continents and to increased intensity of vertical circulation in the equatorial divergence zone.

Fluxes of the Main Sediment-Forming Components

According to our data, we can calculate the ratios of mass accumulation rates of lithogenic matter and $CaCO_3$ on the submarine continental margins of all major oceans in the Neopleistocene and Eopleistocene. For the Pacific Ocean, these ratios are, respectively, 7.12 and 6.28; for the Indian Ocean, 5.04 and 2.29; and for the Atlantic Ocean, 4.75 and 2.76. Thus, on all continental margins of the main oceans, the ratio of lithogenic matter fluxes to $CaCO_3$ fluxes was higher in the Neopleistocene than in the Eopleistocene. Without attempting (in this case) to explain the obtained values, let us try to understand: why did the ratio of MAR of lithogenic matter to MAR of $CaCO_3$ in the Pleistocene change in exactly the same direction in all main ocean basins?

Let us assume that the fluxes of lithogenic matter from continents to continental margins mainly represent the solid

river discharge [34], whereas the fluxes of biogenic carbonates mainly represent the dissolved matter runoff from continents to oceans. It turns out, then, that the ratio of solid river discharge to dissolved substance runoff was higher in the Neopleistocene than in the Eopleistocene. Consequently, one may assume that the ratio of mechanical weathering to chemical weathering was also greater. There is every reason to link the established phenomenon with global climate deterioration, a decrease in the mean annual temperature and atmospheric humidity during the Pleistocene.

It should be noted that the MAR of components used in the calculations are residual and characterise the amount of components retained in the sediments only. The fact is that lithogenic matter is generally not susceptible to dissolution in the water column and on the surface of the sediment. Biogenic opal dissolves to a certain extent (up to 30%, mainly at the bottom surface [35]), and $CaCO_3$ dissolves at various levels (from aragonite lysocline and below) up to complete dissolution below the CCD [34].

Calculations based on dry sediment masses have shown that in the Neopleistocene the mass accumulation rates of lithogenic matter for the Pacific Ocean, Indian Ocean, Atlantic Ocean, Arctic Ocean and World Ocean were 1.50, 2.06, 2.14, 2.54 and 1.68 g/cm^2/thousand years, respectively. For $CaCO_3$ the same range is as follows: 0.33, 0.60, 0.58, 0, and 0.44 g/cm^2/thousand years. Mass accumulation rates of biogenic opal in Neopleistocene for the same ocean sequence were 0.04, 0.13, 0.16, 0 and 0.09 g/cm^2/thousand years.

In the Eopleistocene, the situation with mass accumulation rates looked different. The MAR of lithogenic matter for the Pacific, Indian Ocean, Atlantic Ocean, Arctic Ocean, and World Ocean were 0.96, 1.27, 1.24, 2.54, and 1.68 g/cm^2/thousand years, respectively. For $CaCO_3$ the same range is as follows: 0.17, 0.40, 1.36, 0, and 0.52 g/cm^2/thousand years. MAR of biogenic opal in Eopleistocene for the same ocean sequence were 0.03, 0.08, 0.15, 0 and 0.07 g/cm^2/thousand years.

In general in Pleistocene the MAR of lithogenic matter for Pacific, Indian, Atlantic, Arctic and World Ocean were 1.20, 1.62, 1.64, 2.94 and 1.94 g/cm^2/thousand years, respectively. For $CaCO_3$ the same range is as follows: 0.24, 0.49, 1.01, 0, and 0.48 g/cm^2/thousand years. MAR of biogenic opal in Pleistocene for the same sequence of oceans were 0.04, 0.10, 0.15, 0 and 0.08 g/cm^2/thousand years.

A brief conclusion can be drawn from the above data. During the Pleistocene, fluxes of lithogenic matter in all the oceans increased. The greatest values probably characterized the Arctic and Indian Oceans. We recall that only lithogenic matter accumulated in the Arctic Ocean, so the following conclusions about the biogenic components do not apply to this ocean.

The discussion of the mass accumulation rates of $CaCO_3$ refers to the carbonate matter in the sediments, rather than its fluxes from the water column to the seafloor. In the Pacific and Indian Oceans, there was an increase in the MAR of $CaCO_3$ in sediments during the Pleistocene. In contrast, in the Atlantic Ocean, the MAR of $CaCO_3$ was higher in the Eopleistocene than in the Neopleistocene. However, the excess was so large that it mirrored the results for the World Ocean. In all the oceans except the Eopleistocene Atlantic, the MAR of lithogenic matter exceeded the MAR of $CaCO_3$ by a factor of 3–5. In the Eopleistocene, the MAR of $CaCO_3$ in the Atlantic Ocean even slightly exceeded the MAR of lithogenic matter. The reason for this phenomenon is still unknown. We can only assume (due to the author's lack of data on the Pleistocene history of terrigenous matter in La Plata, Niger Fan and the Eopleistocene supply by Amazon River) that in the Eopleistocene of the Atlantic, the ratio of MAR of lithogenic matter to MAR of $CaCO_3$ was in fact higher than obtained by our calculations.

In all the oceans, there was a slight increase in MAR of biogenic opal during the Pleistocene. The ratio was maintained, with the Atlantic Ocean in first place, the Indian Ocean in second place and the Pacific Ocean in third place. Average MAR of biogenic opal in Pleistocene sediments of the oceans is 3–10 times less than MAR of $CaCO_3$.

Curious results were obtained in the study of MAR of biogenic sediments in the Neopleistocene to MAR in the Eopleistocene. This value is 2.29 for carbonate sediments of the pelagic Pacific Ocean and 1.37 for continental margins; for siliceous sediments it is 1.80 and 1.28, respectively. The ratios for the Indian Ocean are 1.69, 1.51, 1.64 and 1.70. In the Atlantic these ratios are 0.66, 1.45; 1.12 and 0.37. Thus, if we keep in mind a production of carbonates and biogenic silica in the euphotic layer, a global regularity of the growth of these values in the Pleistocene in the World Ocean caused by the primary production growth appears. Exceptions related to MAR of residual pelagic carbonates in the Atlantic have already been explained above by the reasons unrelated to the primary production. Exceptions in the MAR of siliceous sediments at the continental margins of the Atlantic Ocean are due to upwelling associated with the high-latitude circulation (see the concept of "two oceans"). The general increase in primary production in the oceans is primarily due to the increased flux of nutrients from the land (especially in an "ice-free" ocean).

The decrease in the MAR of lithogenic matter in the series Arctic, Atlantic (Indian), Pacific (Fig. 1) is most likely due to a decrease in the B/L ratio in the same series.

It has already been noted that MAR $CaCO_3$ in the Neopleistocene reflects the result of the dynamic interaction of carbonate flux from the euphotic layer and its dissolution potential at great depths (this is especially true for the

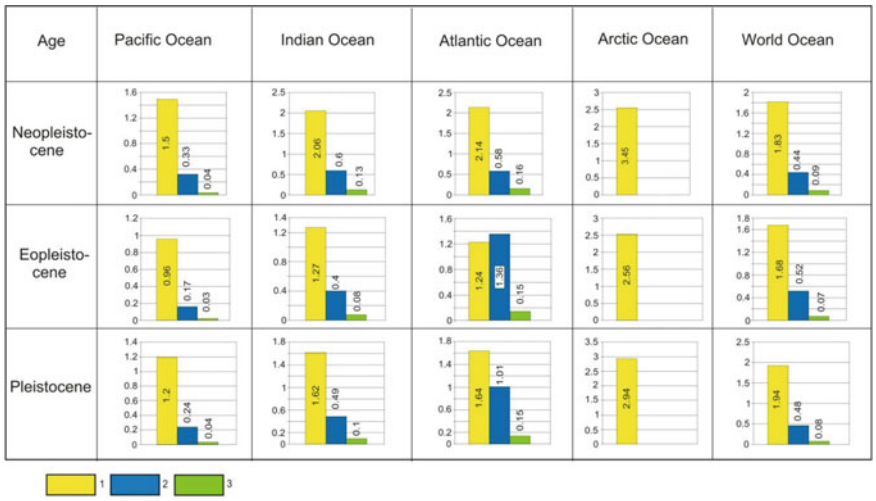

Fig. 1 Distribution of mass accumulation rates (g/cm^2/thousand years) of the main sediment-forming components of the Pleistocene sediments of the World Ocean Legend: 1—lithogenic matter; 2—$CaCO_3$; 3—biogenic opal

Atlantic). In the Eopleistocene, however, the dissolution potential was much smaller, so it is interesting to compare the MAR of $CaCO_3$ of the different oceans for this part of the Pleistocene. It appears that this parameter in the Atlantic Ocean was greater than in the Indian Ocean by almost 2.5 times, and in the latter exceeded the value in the Pacific Ocean by more than 2.0 times. According to the author, this phenomenon is primarily explained by the decreasing share of the ocean floor area occupied by submarine ridges, elevations and rises of various genesis in this series [19]. Another reason could be the decreasing supply of nutrients from the land in this series. Furthermore, if the MAR of $CaCO_3$ ratio in the Neopleistocene of the Pacific Ocean to the same parameter in the Eopleistocene (equal to about 2.0) is conventionally considered as almost unaffected by dissolution, then potential MAR of $CaCO_3$ in the Neopleistocene of the Indian and Atlantic Oceans could be calculated on this basis if there were no dissolution. This approach makes it possible to calculate the mass of dissolved $CaCO_3$ in the Neopleistocene.

The same decreasing series as for MAR of $CaCO_3$, i.e. Atlantic-Indian Ocean-Pacific, is also revealed for MAR of biogenic opal (Fig. 1). In this case, however, we should most likely speak of a reduction in nutrient supply from land.

4 Discussion of Results

It should be noted that data on both dry sediment masses, rates of its accumulation and mass accumulation rates characterize the same pattern of the Pleistocene sedimentation structure (if we abstract from dissolution of carbonates and from the Arctic Ocean): domination of terrigenous matter with a clearly inferior role of $CaCO_3$ and negligible participation of biogenic opal. Such a pattern may be called the basic law of Pleistocene sedimentation in the "ice-free" World Ocean (with the only exception-in the Eopleistocene of the Atlantic).

It appears that this phenomenon is primarily related to the fluvial discharge structure. It should be noted that in terms of the composition of modern and Pleistocene sediments, the submarine parts of continental margins are represented by terrigenous, carbonate, terrigenous-carbonate and siliceous-terrigenous varieties, which depends on the combination of tectonic and climatic features. Carbonate margins are located in arid climates and are adjacent to landlocked areas. They will not be considered. Other types of margins involve more or less terrigenous matter, especially fluvial.

The modern river runoff in the World is characterized by an excess in mass of suspended runoff over the runoff of dissolved substances of about 5.4 times [36]. The ratio of carbonates to silica in the composition of dissolved runoff is about 5. On continental margins the ratio of terrigenous matter to the sum of carbonates and opal may increase due to the preferential accumulation of solid suspended material in natural sedimentation traps. In addition, one should keep in mind the geochemical processes, according to which the water column above the areas of continental margins is a "realm" of suspended forms of elements, and in the pelagic areas-a "realm" of dissolved forms [36].

From all the material presented, it can be concluded that there are a number of global patterns in the distribution of major sediment groups during the Pleistocene. These include: (1) an obvious increase in the flux of lithogenic (terrigenous and volcanogenic) matter into the World Ocean; (2) a slight increase in the flux of biogenic siliceous matter to the ocean floor from the euphotic zone; (3) a decrease in the rates of pelagic clay accumulation in all oceans. A sharply expressed regional peculiarity is the decrease of residual rates of carbonate oozes accumulation on the deep floor of the Atlantic Ocean in the Neopleistocene against the background of their

increase on the continental margins of this ocean, and in the Pacific and Indian Oceans as a whole.

These patterns are due to the evolution of the Earth's natural system since the mid-Cenozoic. In general, it is quite obvious that there is a connection between the overall decrease in atmospheric and global ocean temperatures during the Pleistocene, the increase in land and ocean ice volumes, the trend in sea-level fall, and the increase in the ratio of mechanical weathering intensity to the intensity of chemical weathering on land. Naturally, all the above trends are modulated by changes during glacial-interglacial cycles and natural processes of shorter duration.

5 Conclusion

Based on the sum of the data presented in the paper, it can be stated that such global trends in the Pleistocene sedimentation history as the increase in terrigenous matter fluxes and the overall increase in primary production, expressed by the increased production of biogenic carbonate and silica, are due to a combination of increased neotectonic activity [37], climate deterioration [38], glaciation in the Northern and Southern Hemispheres [39], the trend of sea-level fall [20], and an increase in the ratio of mechanical weathering intensity to chemical weathering intensity on land [40].

The global pattern of increasing volcanogenic sediment flux is caused by increasing volcanic-tectonic activity at the continental margins and, above all, within the active margins.

The global pattern of decreasing rates of pelagic clay accumulation in the Neopleistocene compared to the Eopleistocene is due to a greater increase in diluting terrigenous and carbonate sediment fluxes than in pelagic clay matter fluxes, as well as a deepening CCD.

These patterns for the Pleistocene, as seen in the Indian Ocean [41], inherit trends for Oligocene-Pliocene time.

The strong dissolution of relatively deep-water planktonic Neopleistocene carbonates in the Atlantic caused a regional pattern of carbonate sedimentation and changes in the sedimentation patterns of this and the World Ocean.

In general, the "ice-free" Pleistocene World Ocean was governed by the basic law of sedimentation, with lithogenic sedimentation dominating over carbonate biogenic sedimentation, which in turn dominates over biogenic siliceous sedimentation, all inherited from the river flow patterns on the continents. An exception to the general rule (for reasons unknown yet) is the Eopleistocene of the Atlantic Ocean.

Thus, the sedimentary system of the World Ocean in the Pleistocene should be considered as part of the global system of sediment formation, transit and accumulation. The history of Pleistocene ocean sedimentation inherits trends formed during the geological and climatic evolution of the Earth since at least the mid-Cenozoic [42].

Acknowledgements The author expresses his sincere thanks to his colleagues in the International Project of Deep-Sea Drilling. Without their results on Pleistocene sediments in the World Ocean, the creation of this article would not have been possible. This work is conducted under the GEOKHI RAS state assignment.

References

1. Ronov, A.B.: History of sedimentation and oscillatory movements of the European part of the USSR (according to volumetric method), p. 136. Tr. Geophys. Inst. of AS USSR 3, Leningrad (1949)
2. Strakhov, N.M.: Types of sedimentary process and sedimentary rock formations. Izv. USSR Acad. Sci. Ser. Geol. **5**, 3–21 (1956)
3. Lisitsin, A.P.: Sedimentation in the oceans. Quantitative distribution of sedimentary matter, p. 438. Nauka, Moscow (1974)
4. van Andel, T.H., Heath, C.R., Moore, T.C.: Cenozoic tectonics, sedimentation and paleoceanography of the central equatorial Pacific. Geol. Soc. Amer. Mem. **143**, 1–65 (1975)
5. Levitan, M.A., Bogdanov, Yu.A., Lisitsin, A.P.: Organic carbon in upper Cretaceous-Pliocene sediments of the oceans. Dokl. USSR Acad. Sci. **254**(4), 962–965 (1980)
6. Thiede, J., Ehrmann, W.U.: Late Mesozoic and Cenozoic sediment flux to the Central North Atlantic. In: Summerhayes, C.P., Shackleton, N.J. (eds.) North Atlantic Paleoceanography. Geol. Soc. Amer. Spec. Publ. **21**, 3–15 (1986)
7. Farrell, J.W., Raffi, I., Janecek, T.R., Murray, D.W., Levitan, M. A., Dadley, K.A., Emeis, K.-C., Lyle, M., Flores, J.-A., Hovan, S. Late Neogene sedimentation patterns in the eastern equatorial Pacific. In: Pisias, N.G., Mayer, L.A., Janecek, T.R., Palmer-Julson, A., van Andel, T.H. (eds.) Proc. ODP, Sci. Results, vol. 138, pp. 717–756. College Station, Texas (1995)
8. Ronov, A.B.: The Earth's sedimentary cover (quantitative regularities of structure, composition and evolution), p. 78. Nauka, Moscow (1980)
9. Ronov, A.B.: Stratisphere or the Earth's sedimentary cover, p. 144. Nauka, Moscow (1993)
10. Miller, K.G., Kominz, M.A., Browning, J.V., Wright, J.D., Mountain, G.S., Katz, M.E., Sugarman, P.J., Cramer, B.S., Christie-Blick, N., Pekar, S.F.: Phanerozoic record of global sea-level change. Science **310**, 1293–1298 (2005)
11. Levitan, M.A., Balukhovsky, A.N., Antonova, T.A., Gelvi, T.N.: Quantitative parameters of Pleistocene pelagic sedimentation in the Pacific Ocean. Geochem. Intern. **51**(5), 345–352 (2013)
12. Levitan, M.A.: Pleistocene sediments of the World Ocean, p. 408. RAS Publication House, Moscow (2021)
13. Goodell, H.G., Watkins, N.D.: The paleomagnetic stratigraphy of the Sourthern Ocean: 20° West to 160° East. Deep Sea Res. Oceanogr. Abstracts **15**(1), 89–112 (1968)
14. Gradstein, F.M., Ogg, J.G., Smith, A.G.: A geologic time scale 2004, p. 599. Cambridge University Press, Cambridge (2004)
15. Alekseev, M.N., Borisov, B.A., Velichko, A.A., et al.: On the general stratigraphic scale of the Quaternary system. Stratigr. Geol. Correl. **5**(5), 105–108 (1997)
16. Strakhov, N.M.: On the comparative-lithological direction and its immediate objectives. Bull. MOIP. Geol. **20**(3/4), 34–48 (1945)
17. Murdmaa, I.O.: Facies of the oceans, p. 304. Nauka, Moscow (1987)
18. www.gebco.org (2004)

19. Harris, P.T., Macmillan-Lawler, M., Rupp, J., Baker, E.K.: Geomorphology of the oceans. Mar. Geol. **352**, 4–24 (2014)
20. Miller, K.G., Browing, J.V., Schmelz, W.J., Kopp, R.E., Mountain, G.S., Wright, J.D.: Cenozoic sea-level and cryospheric evolution from deep-sea geochemical and continental margin records. Sci. Adv. **6**(20) (2020). https://doi.org/10.1126/sciadv.aaz1346
21. Jakobsson, M., Grantz, A., Kristoffersen, Y., Macnab, R.: Physiography and bathymetry of the Arctic Ocean. In: Stein, R., Macdonald, R. (eds.) The Arctic Ocean organic carbon cycle: present and past, pp. 1–5. Springer, Berlin (2004)
22. Levitan, M.A., Lavrushin, Yu.A.: Sedimentation history in the Arctic Ocean and Subarctic Seas for the last 130 kyr, p. 387. Springer, Berlin (2009)
23. Jokat, W., Ickrath, M., O'Connor, J.: Seismic transect across the Lomonosov and Mendeleev ridges: constraints on the geological evolution of the Amerasian Basin. Arctic Ocean. Geophys. Res. Lett. **40**, 5047–5051 (2013)
24. Backman, J., Moran, K., McInroy, D.B., Mayer, L.A., Expedition 302 Scientists.: Arctic coring expedition (ACEX). In: Proceedings of the integrated ocean drilling program, vol. 302 (2006). https://doi.org/10.2204/iodp.proc.302.2006
25. Levitan, M.A.: Sedimentation rates in the Arctic Ocean during the last five marine isotope stages. Oceanology **55**(3), 425–433 (2015)
26. Ronov, A.B., Yaroshevsky, A.A., Migdisov, A.A.: Chemical structure of the Earth's crust and geochemical balance of major elements, p. 183. Nauka, Moscow (1990)
27. Atlas of the oceans terms, concepts, reference tables. M: GUONK USSR (1980)
28. Levitan, M.A.: Quantitative parameters of Pleistocene pelagic sedimentation in the World Ocean: global trends and regional features. Geochem. Intern. **55**(5), 428–441 (2017)
29. Vinogradov, M.E., Shushkina, E.A., Kopelevich, O.V., Sheberstov, S.V.: Photosynthetic production of the World Ocean from satellite and expeditionary data. Oceanology **36**(4), 566–575 (1996)
30. Stepanov, V.N.: Main dimensions of the World Ocean and its main parts. Oceanology **1**(1), 3–18 (1961)
31. Hay, W.W.: Calcium carbonate compensation. In: Initial Reports of DSDP, vol. 4, pp. 672–673. U.S. Government Printing Office, Washington, DC (1970)
32. Cortese, G., Gersonde, R., Hillenbrand, C.-D., Kuhn, G.: Opal sedimentation shifts in the World Ocean over the last 15 Myr. Earth Planet. Sci. Lett. **224**, 509–527 (2004)
33. Levitan, M.A.: Comparative analysis of pelagic Pleistocene silica accumulation in the Pacific and Indian oceans. Geochem. Intern. **54**(3), 257–265 (2016)
34. Lisitsin, A.P.: Ocean sedimentation processes. Lithology and geochemistry, p. 392. Nauka, Moscow (1978)
35. Tréguer, P., De La Rocha, C.L.: The World Ocean silica cycle. Ann. Rev. Mar. Sci. **5**(1), 477–501 (2013)
36. Gordeev, V.V.: Geochemistry of the river-sea system, p. 452. IP Matushkina I.I, Moscow (2012)
37. Trifonov, V.G., Sokolov, S.Yu: Towards post plate tectonics. Bull. Russ. Acad. Sci. **85**(7), 605–615 (2015)
38. Zachos, J., Pagani, M., Sloan, L., Thomas, E., Billups, K.: Trends, rhythms, and aberrations in global climate 65 Ma to present. Science **292**(5517), 686–693 (2001)
39. Chumakov, N.M.: Glaciations of the earth. History, stratigraphic significance and role in the biosphere, p. 160. GEOS, Moscow (2015)
40. Lipp, A.G., Shorttle, O., Brocks, J.J., et al.: The composition and weathering of the continents over geologic time. Geochem. Persp. Lett. **17**, 21–26 (2021)
41. Levitan, M.A.: Paleoceanography of the Indian Ocean in the Cretaceous-Neogene, p. 248. Nauka, Moscow (1992)
42. Ronov, A., Khain, V., Balukhovsky, A.: Atlas of lithological-paleogeographical maps of the World (Mesozoic and Cenozoic of continents and oceans), p. 79. VSEGEI, Leningrad (1989)

Geochemical Provinces of Surface Sediments in the Laptev Sea

R. A. Lukmanov, V. Yu. Rusakov, T. G. Kuz'mina, T. V. Romashova, and A. V. Kol'tsova

1 Introduction

The bottom sediments of shelf seas can be divided into 5 facies-genetic types: inner estuarine or deltaic sediments, outer estuarine sediments (mud-bank sediments), inner and middle shelf sediments, outer shelf sediments, and edaphogenic sediments [e.g., 1–7]. The facies-genetic type, lithological and geochemical composition, and sedimentation rates of shelf sediments have been closely correlated [8, 9].

Shelf seas are not only zones of sediment transit, but also zones of accumulation of clastic particles and at least partial accumulation of clay minerals [10, 11]. The results of lithological and geochemical studies of Eurasian shelf surface sediments have shown that, genetically, they are a mechanical mixture of clastic (bulk non-clay) minerals of wide composition with clay minerals in different proportions [12–14]. The ratio between these components will determine their grain-size and chemical composition as well as their facies-genetic affiliation. For example, as the degree of energetic influence of waves and sea currents on the bottom sediments decreases, the proportion of fine fraction, consisting predominantly of fine clay minerals, will naturally increase, whereas the proportion of coarse fraction, consisting predominantly of clastic minerals, decreases. In other words, the inner and middle shelf terrigenous sediments, which are most heavily hydrodynamically influenced, will include a relatively higher proportion of clastic minerals in the sand and silt-sand fractions and be characterized by higher silica content. Deeper outer shelf sediments tend to contain a relatively higher proportion of clay minerals in the silt and clay-silt fractions. The latter are also characterized by higher aluminium content. An independent facies-genetic group is formed by estuarine sediments that include a significant proportion of clay minerals due to the relative isolation of the estuary from the hydrodynamic action of waves and near-bottom currents. In addition, due to sea transgression, the accumulation zones of Holocene sediments of Arctic seas are only locally developed, the rest of the shelf being occupied by relict sediments accumulated during previous regression-transgression cycles or bedrock outcrops [15]. The products of their destruction as a result of bottom erosion are distinguished in a separate group of edaphogenic sediments of wide grain-size composition, the genetic relationship between which is established only on the basis of more complex geochemical criteria [6–8].

This paper is a continuation of the series of our studies on the lithological and geochemical composition of the shelf sediments of the Russian Arctic [6–9]. It contains facies-genetic typification of the surface (0–2 cm) layer of the Laptev Sea sediments based on the study of their lithological and geochemical composition.

1.1 Study Area

The Laptev Sea is part of the continental margin of the Eurasian continent with one of the largest river deltas in the world, the Lena River delta. Relatively large rivers such as the Khatanga, Yana and Olenek also enter the sea (Fig. 1). The total river input into the sea is 738 km^3/year and the total solid river runoff is 28.6×10^6 t/year [17–19], which is about a third of the total input into the seas of the Arctic.

Geomorphologically, the one of the main features of the Laptev Sea is the combination of the Khatanga River estuary and the Lena River delta. This is presumably determined by the complex tectonic regime of the divergent boundary between the Eurasian and North American plates [20]. The shelf structure in the sea area is represented by a horst and graben system that forms a series of deep rifts and high-standing basement blocks overlain by a Late

R. A. Lukmanov (✉) · V. Yu. Rusakov · T. G. Kuz'mina · T. V. Romashova · A. V. Kol'tsova
Vernadsky Institute of Geochemistry and Analytical Chemistry, Russian Academy of Sciences, 19, Kosygin St., Moscow, 119991, Russia
e-mail: rusakov@geokhi.ru

V. P. Kolotov and N. S. Bezaeva (eds.), *Advances in Geochemistry, Analytical Chemistry, and Planetary Sciences*,
https://doi.org/10.1007/978-3-031-09883-3_12

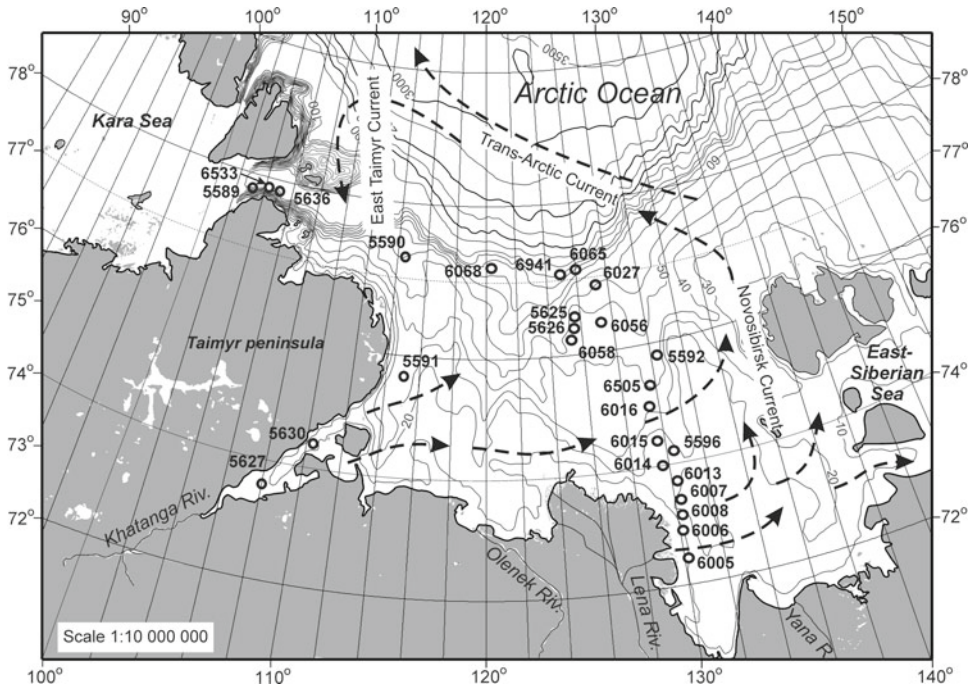

Fig. 1 Overview map of the Laptev Sea with the location of sediment sampling stations (Table 1). Circulation pattern of surface water currents is indicated by dotted arrows [16]

Cretaceous-Quaternary sedimentary cover [21]. According to multichannel seismic profiling [21–24], a seismically transparent stratigraphic complex, covering the sea floor as a continuous layer up to 2.2–2.7 km of Late Miocene-Holocene age, is identified in the upper part of the sedimentary section. More detailed studies of the upper part of the sedimentary section with the shipboard Parasound at 4 kHz made it possible to identify 4 thinner seismic stratigraphic complexes that form a chronological sequence of sedimentation changing in the Late Pleistocene and Holocene [25]. Of these, the upper and youngest complex has a blanket form and is almost ubiquitous. Its thickness varies greatly, increasing in the central deep parts of the troughs and local depressions and decreasing towards the higher reliefs. On average, its thickness is 1.0–2.5 m, but it may reach 18 m in local depressions or be absent on banks and shallows. It should be noted that the use of seismic data generally does not allow the detection of fine structures of the sedimentary section that are less than 1 m thick. This is particularly true in the case of surface sediments. To fill this gap, direct sampling of sediments is indispensable, allowing not only the detection of fine sediment structures, but also the study of their composition.

Recent sedimentation in the Laptev Sea, as in other Arctic shelf seas, are controlled by such factors as the coastal abrasion, sea-ice regime, wave activity, bottom topography, and sea current pattern. The sea currents control the lateral transport of the finest particles (suspended matter).

Due to the fact that surface water temperatures are close to freezing point for most of the year, the Laptev Sea is covered in sea ice from October to May, making it one of the harshest Arctic seas. The sea is dominated by a cyclonic circulation of surface waters, the southern branch of which is a longshore current moving from west to east [16, 26] (Fig. 1). In the area of the Lena River delta, it is reinforced by river discharge. On further eastward movement, most of it deviates to the north and northwest and, in the form of the Novosibirsk Current, goes beyond the sea, joining the Trans-Arctic Current. At the northern tip of the Severnaya Zemlya archipelago, the East Taimyr Current branches off from the latter and moves southward along the eastern shores of the Severnaya Zemlya and the Taimyr Peninsula, thereby closing the cyclonic ring.

2 Materials and Methods

The data presented in the article (Table 1) were collected during 4 expeditions on the R/V "Akademik Mstislav Keldysh" from 2017 to 2020 (69, 73, 78 and 82 cruises, respectively). Sediments in the study area (Fig. 1) were sampled using a box corer. We sampled upper 2 cm of sediment which represent the top of the oxidized layer. It should be noted that no reduced sediments were observed anywhere in the surface horizon, indicating good ventilation of the water column.

The wet samples were dispersed using ultrasound in an ultrasonic bath for 5 min at a vibration frequency of 21–22 kHz and then by water-mechanical separation into individual fractions by sieve and decantation method [27–29].

Table 1 Station numbers (samples), coordinates, and water depth

St. no.	Coordinates		Water depth, m
	N	W	
5589	77°50.33′	103°45.5′	240
5590	77°10.9′	114°39.815′	63
5591	75°24.73′	115°27.33′	44.5
5592	75°48.9′	130°29.79′	47
5596	74°15.01′	130°29.6′	29.6
5625	76°46.4′	125°49.3′	71
5626	76°43.7′	125°32.6′	61
5627	73°29.69′	108°10.59′	14.3
5630	74°16′	110°21.07′	26.7
5636	77°54.4′	104°54′	222
6005	72°29.76′	130°29.76′	14
6006	72°42.36′	130°30.12′	18
6007	73°7.38′	130°30′	25
6008	72°54.66′	130°30′	22
6013	73°35.58′	130°16.8′	24
6014	73°51.66′	129°19.08′	14
6015	74°23.22′	129°14.64′	21
6016	74°54.42′	129°11.52′	40
6027	76°53.58′	127°47.82′	64
6056	76°40.74′	127°19.02′	62
6058	76°23.76′	125°25.14′	52
6065	77°6.18′	126°25.44′	251
6068	77°14.76′	120°36.84′	185
6505	75°11.986′	129°8.542′	40
6533	77°56.976′	104°19.036′	230
6941	77°06.075′	125°05.741′	360

To calculate the content of fine silt and clay fractions (<0.01 mm), the specific gravity of the average sample was taken as 2.55 g/cm^3. The sedimentation rate of the fine particles in water column and the time for pouring the suspension out of the cans were calculated using the Stokes law and the Arkhangelsky formulas (coefficients 2/9 and 0.16, respectively). The results of the grain-size analysis are presented in Table 2.

The chemical composition was studied using X-ray fluorescence analysis (XRF) on an AXIOS Advanced scanning channel stationary spectrometer from PANalytical B.V. (Holland), which has an X-ray tube with a rhodium anode as the excitation source for the characteristic radiation. The content of the following elements was determined: Si, Al, Ti, Fe, Mn, K, Ca, Mg, Na, P, Cr, S, V, Co, Ni, Cu, Zn, Rb, Sr, Y, Zr, Nb, Ba, Pb + loss on ignition (LOI). The results of the chemical analyses are summarized in Table 3.

Data processing of grain-size and chemical composition of the samples was carried out by methods of mathematical statistics. To assess the degree of heterogeneity of the studied samples, such methods of statistical analysis as factor and cluster analysis were applied. Factor analysis in the R-modification reveals the relationship between objects. The *R*-modification is based on the concept of similarity between objects. As such, the proximity of the relative contents of macronutrients was used. The degree of similarity between between two objects (X_i and X_j) is defined through the cosine of the angle between the corresponding vector rows of the original data matrix:

$$\cos\,\Theta_{ij} = \sum x_{in}x_{jn} \Big/ \left(\sum x_{in}^2 \sum x_{jn}^2\right)^{1/2} \qquad (1)$$

One of the purposes of factor analysis is to identify the minimum number of extreme members.

The purpose of cluster analysis is to divide the set of objects under study into homogeneous groups or clusters, using sets of some parameters. We used Ward's method for cluster analysis. In this method, the intra-group sum of

Table 2 Grain-size composition of surface (0–2 cm) sediments in wt%, lithotype and Grain-Size Cluster (GSC), fractions in mm

St. no.	Gravel	Sand					Silt		Clay	Lithotype	GSC
	> 2	2–1	1–0.5	0.5–0.25	0.25–0.125	0.125–0.063	0.063–0.01	0.01–0.002	< 0.002		
5596	0.00	0.00	1.66	22.24	60.23	4.93	6.13	3.43	1.38	Sand	I
5630	1.67	0.00	2.26	8.48	33.18	41.70	2.74	4.41	5.56	Sand	I
6013	0.00	0.00	4.23	38.10	30.65	6.52	2.94	2.66	14.90	Sand	II
6014	0.17	0.00	0.68	54.14	42.32	1.18	0.50	0.50	0.51	Sand	II
6015	0.00	0.00	0.08	53.46	40.16	1.83	2.60	1.12	0.75	Sand	II
6065	0.00	0.05	0.64	11.26	62.04	11.16	8.06	1.35	5.44	Sand	I
6027	0.00	0.00	0.76	7.88	52.33	7.12	12.60	12.21	7.10	Silty sand	I
6941	0.06	0.19	0.59	1.92	29.00	37.70	12.52	8.79	9.23	Silty sand	I
5589	0.00	8.51	1.06	29.45	22.93	5.45	21.64	2.97	7.99	Silty sand	IIa
6056	0.00	0.00	1.02	7.42	31.68	6.83	20.95	16.73	15.37	Clayey silty sand	I
6058	0.19	0.00	0.53	2.72	47.95	10.98	12.94	13.03	11.66	Clayey silty sand	I
6068	0.25	0.00	1.80	3.34	22.79	21.12	18.33	19.38	12.99	Clayey silty sand	I
6505	0.14	0.00	0.68	1.63	29.01	8.00	30.09	6.06	24.39	Clayey silty sand	I
5591	2.05	0.00	1.85	9.53	22.86	10.25	18.20	15.27	19.99	Clayey silty sand	I
5625	0.40	0.00	0.66	3.10	45.80	9.30	17.05	10.11	13.58	Clayey silty sand	I
5626	0.49	0.00	0.85	2.13	50.60	8.72	16.24	9.08	11.89	Clayey silty sand	I
5627	2.68	0.31	6.65	45.35	16.67	3.29	12.45	2.28	10.32	Clayey silty sand	II
6005	0.00	0.03	1.23	22.68	8.03	14.29	29.94	17.36	6.44	Sandy silt	I
6006	0.35	0.00	0.35	2.12	2.70	5.29	33.05	42.03	14.11	Clayey silt	III
6016	0.00	0.00	0.12	0.12	1.05	5.35	37.82	34.63	20.91	Clayey silt	III
6533	0.16	0.00	0.00	0.16	0.16	1.64	40.13	28.16	29.59	Clayey silt	III
5590	0.00	0.00	0.41	0.50	2.73	4.97	31.89	27.17	32.33	Clayey silt	III
5592	0.00	0.00	0.05	0.20	2.42	8.58	31.37	22.56	34.82	Clayey silt	III
5636	0.00	0.00	0.09	0.18	1.06	6.63	39.23	30.28	22.53	Clayey silt	III
6007	1.04	0.00	0.30	0.89	1.41	2.74	39.43	30.87	23.32	Clayey silt	III
6008	0.89	0.00	0.30	0.50	0.99	2.58	38.25	28.15	28.34	Clayey silt	III

squares of deviation, which is nothing but the sum of squares of distances between each point (object) and the average of the cluster containing this object, is used as the target function. The square of the Euclidean distance (distance measured in conventional units) over the raw data is used as a measure of similarity (affinity):

$$d_e(X_i, X_j) = \sum_n (x_{in} - x_{jn})^2,\ n = 1.\ldots.p, \quad (2)$$

where p is the number of parameters used.

3 Results

3.1 Grain-Size Composition

Based on the results of grain-size analysis, 5 lithotypes of the surface sediments were identified (Table 2 and Fig. 2). It is interesting to note that there are no clayey sediments among them. The latter indicates that the Laptev Sea shelf is largely a transit zone for clay fraction. The portion of clay fraction in the finest clayey silt sediments does not exceed 34 wt%,

Table 3 Chemical composition of surface sediments in wt% (XRF data) and Chemical Cluster (CC)

St. no.	LOI	SiO_2	Al_2O_3	TiO_2	Fe_2O_3	MnO	K_2O	CaO	MgO	Na_2O	P_2O_5	Cr	S	V	Co	Ni	Cu	Zn	Rb	Sr	Y	Zr	Nb	Ba	Pb	CC
6056	7.6	60.02	14.86	0.73	6.01	0.048	2.92	1.12	3.27	2.94	0.162	0.0053	0.253	0.0194	0.0017	0.0049	0.002	0.0089	0.011	0.0225	0.0027	0.0186	0.0012	0.063	0.0016	I
6505	8.49	58.22	15.21	0.65	6.56	0.19	2.82	1.14	2.88	3.35	0.19	0.0064	0.15	0.017	0.0016	0.0039	0.0014	0.009	0.0103	0.023	0.0031	0.021	0.0015	0.07	0.0025	I
6005	9.99	57.63	14.38	0.71	6.31	0.105	2.97	1.09	2.94	3.41	0.22	0.0072	0.11	0.012	0.0018	0.0043	0.0025	0.011	0.013	0.023	0.0031	0.017	0.0013	0.072	0.0024	I
6006	10.26	57.35	14.3	0.76	6.53	0.143	2.87	1.3	2.78	3.2	0.25	0.0074	0.09	0.011	0.0012	0.0049	0.0027	0.011	0.012	0.024	0.0031	0.021	0.001	0.063	0.0023	I
5592	8.03	59.74	15.3	0.68	6.31	0.08	2.81	1.07	2.56	3.02	0.2	0.0061	0.11	0.016	0.001	0.0037	0.0015	0.0086	0.0112	0.022	0.0024	0.021	0.0014	0.074	< 0.001	I
6007	11.35	55.33	14.25	0.76	6.98	0.159	2.89	1.27	2.97	3.38	0.26	0.0069	0.1	0.014	0.0017	0.0046	0.0027	0.011	0.013	0.023	0.0032	0.021	0.0012	0.07	0.0019	I
6008	10.8	56.23	14.7	0.74	6.51	0.065	2.8	1.58	2.83	3.15	0.34	0.0063	0.1	0.008	0.0016	0.0044	0.0026	0.011	0.012	0.021	0.003	0.02	0.0012	0.066	0.0022	I
5589	6.59	63.72	13.83	0.73	6.09	0.61	2.17	0.88	2.14	2.74	0.22	0.0069	0.13	0.015	0.0026	0.0055	0.002	0.0075	0.0078	0.02	0.0021	0.033	0.0015	0.061	0.0009	II
6068	6.13	62.62	14.52	0.77	5.84	0.06	2.61	1.74	2.59	2.89	0.23	0.0085	0.08	0.015	0.0017	0.0042	0.0021	0.008	0.0094	0.027	0.0024	0.022	0.0012	0.063	< 0.001	II
5591	6.42	64.15	13.4	0.69	5.65	0.11	2.36	1.49	2.4	3.02	0.22	0.0078	0.11	0.015	0.0021	0.0037	0.002	0.0066	0.008	0.025	0.0021	0.025	0.0014	0.067	0.0005	II
5627	6.59	64.06	11.61	0.77	6.39	0.16	2.03	2.76	3.1	2.47	0.17	0.0072	0.06	0.013	0.0022	0.0043	0.0032	0.0077	0.006	0.027	0.0024	0.021	0.0013	0.067	0.0014	II
5590	8.29	59.07	15.11	0.81	6.42	0.14	2.29	1.66	2.77	3.16	0.19	0.0078	0.12	0.017	0.002	0.004	0.0021	0.0078	0.0085	0.023	0.0022	0.021	0.0013	0.056	0.0013	II
6533	9.59	52.19	16.79	0.86	8.26	1.25	2.44	1.08	3.39	3.39	0.28	0.0091	0.17	0.023	0.0031	0.0083	0.0025	0.0102	0.0096	0.024	0.0028	0.016	0.0016	0.074	0.0026	IIa
5636	9.27	56.16	14.85	0.79	7.78	0.66	2.39	1.16	2.65	3.31	0.32	0.0091	0.13	0.019	0.0024	0.006	0.0025	0.0085	0.011	0.023	0.0026	0.017	0.0014	0.079	0.0015	IIa
5596	2.42	72.48	12.33	0.63	3.63	0.11	2.82	1.33	1.18	2.97	0.16	0.0053	0.07	0.006	0.0012	0.0014	0.0005	0.0042	0.0079	0.033	0.002	0.055	0.0016	0.085	0.0013	III
5630	nd	74,63	9,93	0,47	3,43	0,08	2,57	1,50	1,48	н.д	0,13	0,0037	0,07	0,008	0,0011	0.0018	0.0008	0.0043	< 0.001	nd	nd	nd	nd	nd	nd	III
6014	0.95	79.93	7.48	0.54	3.11	0.109	2.49	1.56	0.48	2.99	0.1	0.0056	0.04	0.005	0.0007	0.001	0.0007	0.0034	0.0091	0.037	0.0028	0.069	0.0014	0.104	0.0021	III
6015	1.22	78.42	8.31	0.44	2.52	0.104	2.99	1.49	0.59	3.52	0.13	0.0074	0.05	0.004	0.0009	0.0013	0.0003	0.0032	0.0102	0.04	0.0026	0.042	0.0015	0.115	0.0014	III
6065	3.71	69.68	11.79	0.48	4.11	0.17	2.93	1.41	1.65	3.67	0.3	0.0054	0.1	0.008	0.0013	0.0018	0.0005	0.005	0.0093	0.038	0.0019	0.028	0.0013	0.1	< 0.001	III
6058	4.44	68.19	12.15	0.71	4.27	0.278	2.91	1.42	2.19	3.24	0.197	0.004	0.096	0.0105	0.0012	0.0023	0.0007	0.0058	0.0102	0.0321	0.0026	0.0409	0.0015	0.112	0.0008	III
5626	4.24	68.15	12.58	0.59	4.57	0.23	2.8	1.3	1.89	3.39	0.17	0.0061	0.12	0.013	0.0013	0.0022	0.0012	0.0058	0.009	0.031	0.0022	0.032	0.0014	0.085	0.0011	III

LOI–loss on ignition, nd–no data

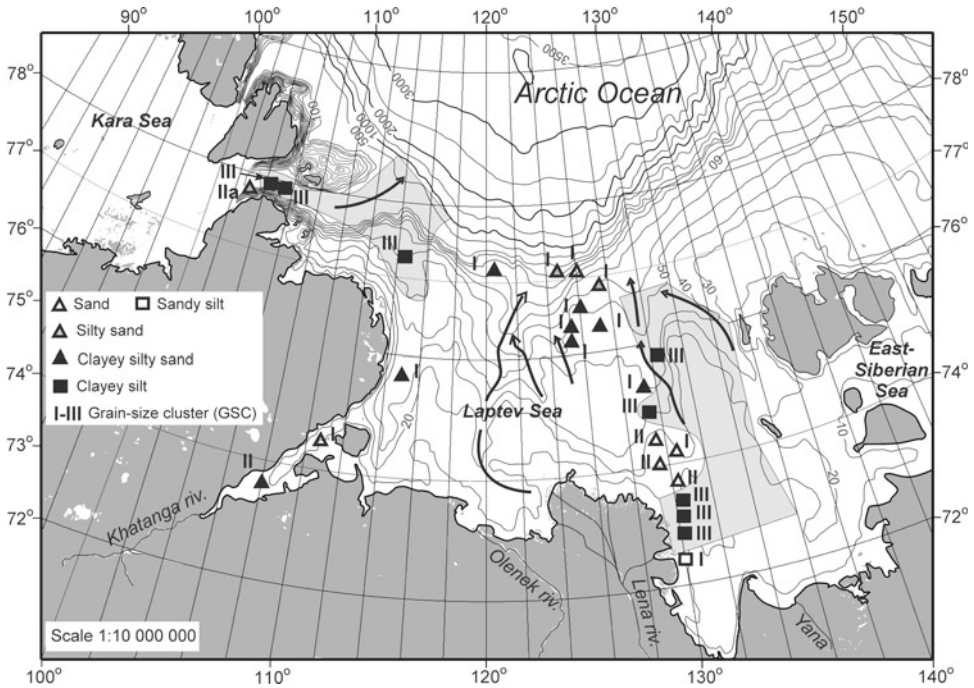

Fig. 2 Overview map of the Laptev Sea with the location of lithotypes and Grain-Size Clusters (GSC; Table 2). Main channels for the transportation of sedimentary material along depressions of the bottom topography is marked by black arrows. Light gray areas show sediments with a high content of fine fractions (not significantly affected by waves and bottom currents; GSC-III)

being on average 26 wt%. In coarser sediments the clay fraction is even lower.

The results of the factor analysis (Fig. 3) revealed the 4 most significant factors, which together explain 88% of the variation in the grain-size composition of the samples studied. The first of these (factor 1), which explains 45% of the variation in grain-size composition, is a competition between the sum of the fine fractions (clay + silt) and the sum of the coarse fractions (sand + gravel). On this basis, it can be considered that factor 1 reflects the degree of hydrodynamic differentiation of sediments in terms of their grain-size composition. According to the lithotypes identified (Table 2), sediments that have not been exposed to significant hydrodynamic effects of waves and currents are represented by clayey silt. Accordingly, the remaining four lithotypes (sandy silt, clayey silty sand, silty sand, and sand) were affected to varying degrees by hydrodynamic differentiation (reworking). The remaining three factors (Fig. 3) reflect varying degrees of influence of gravel and sand sub-fractions, which would seem to indicate a more complex interaction between the composition of the sediment entering the sedimentation basin and the degree of reworking in the basin.

The results of cluster analysis allowed us to distinguish three grain-size clusters (GSC), grouping the studied samples according to the influence of individual fractions and sub-fractions (Fig. 4). GSC-I comprises samples of a wide grain-size composition including 4 different lithotypes (Table 2). This cluster is characterized by higher content of sand (0.25–0.125 and 0.125–0.063 mm) fractions and coarse silt (0.063–0.01 mm fraction) (Fig. 5). GSC-II combines samples characterized by increased content of two sand fractions (0.5–0.25 and 0.25–0.125 mm). An independent sub-cluster GSC-IIa is formed by sample 5589, which has a high proportion of coarse silt and, on this basis, occupies an intermediate position between GSC-I and GSC-II. GSC-III combines samples containing the maximum amount of the fine fractions, clayey silt. As we have shown above, this lithotype characterizes the sediments least susceptible to reworking by waves and bottom currents. The latter mark the areas of accumulation of sedimentary material of a composition similar to that which enters the sedimentation basin with river discharge and as a result of the coastal abrasion.

3.2 Chemical Composition

A factor analysis of the chemical composition of 21 sediment samples/stations (Table 3 and Fig. 6) identified 3 most significant factors, which together explain 77% of the variation in their chemical composition (Fig. 7). The most significant factor 1 (53%) is the competition between elements which are mainly incorporated in the sand grains of quartz, zircon, feldspars (SiO_2, Zr, Ba, Sr) and other elements which are incorporated in or adsorbed on aluminosilicates (on clastic + clay minerals). Factor 2 (14%) shows a positive correlation between heavy metals (Cr, Ni, Cu, Zn, and Pb) and elements related to aluminosilicates (Al, Ti, Fe, K, Mg, and P). The least significant factor 3, explaining 10% of the variations in the chemical composition of the studied

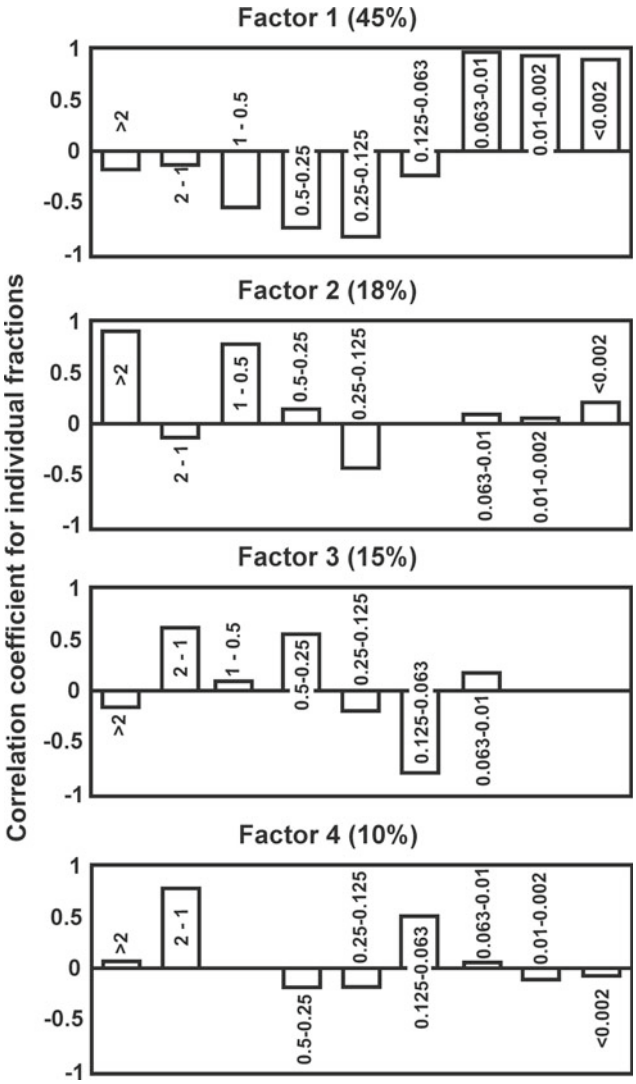

Fig. 3 Factor analysis results of grain-size composition of surface sediments in the Laptev Sea with indication of the factor loading in %. Individual fractions are in mm

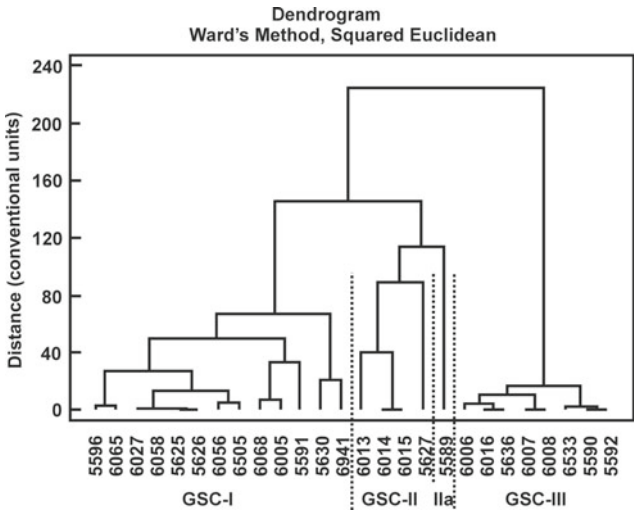

Fig. 4 Cluster analysis results of grain-size composition of surface sediments in the Laptev Sea with indication of Grain-Size Clusters (GSC). See also Table 2

samples, is the positive correlation of Mn with such heavy metals as Cr, V, Co, Ni, as well as with Nb. It seems that factor 3 is determined by diagenetic processes, for example, by sorption of these elements on the surface of Mn oxyhydroxide which enriches the surface sediments as the result of diagenesis.

The results of the cluster analysis (Table 3 and Fig. 8) identified 3 groups of samples with the highest Euclidean distance > 200 conventional units between them (hereafter referred to as the chemical cluster-CC). CC-I included samples collected in the eastern part of the Laptev Sea. CC-II includes samples collected in the western part of the sea. Correspondingly, CC-III included samples collected in the central part of the sea. This geographical division of the CC indicates that there are geochemical provinces of the Laptev Sea surface sediments, which are defined by different potential sources of sedimentary matter input. Thus, according to the above results of the study of the chemical composition of the Laptev Sea surface sediments, at least three geochemical provinces of the sea can be identified, reflecting different sources of sediment supply: western (CC-II), central (CC-III), and eastern (CC-I; Fig. 6). The presence of the geochemical provinces is also confirmed by the fact that the identified CC belong to different lithotypes, i.e. do not depend only on the grain-size composition of the studied samples (Tables 2 and 3, Fig. 6). This result should be taken as empirical evidence indicating that the dominant criterion determining the chemical composition of surface sediments in the Laptev Sea is not the sediment lithotype, but the feeding province. Also it is important that same grain-size fractions can have different chemical composition.

4 Discussion

The geochemical provinces of the Laptev Sea that we have identified differ in the composition of sediment-forming chemical elements and heavy metals, indicating different sources of sedimentary matter supply, i.e., feeding provinces, as we noted above. It is convenient to illustrate these differences by means of a diagram of the relationship between the average composition of the CC and the average composition of the upper continental crust (UCC; Fig. 9). From the diagram one can see that CC-III sediments are characterized by slightly higher content of SiO_2 (as quartz) and lower content of Al_2O_3 (as clay and clastic minerals), Fe_2O_3 (iron oxides), and MgO, as well as lower heavy metal content, both relative to CC-I and CC-II, and relative to

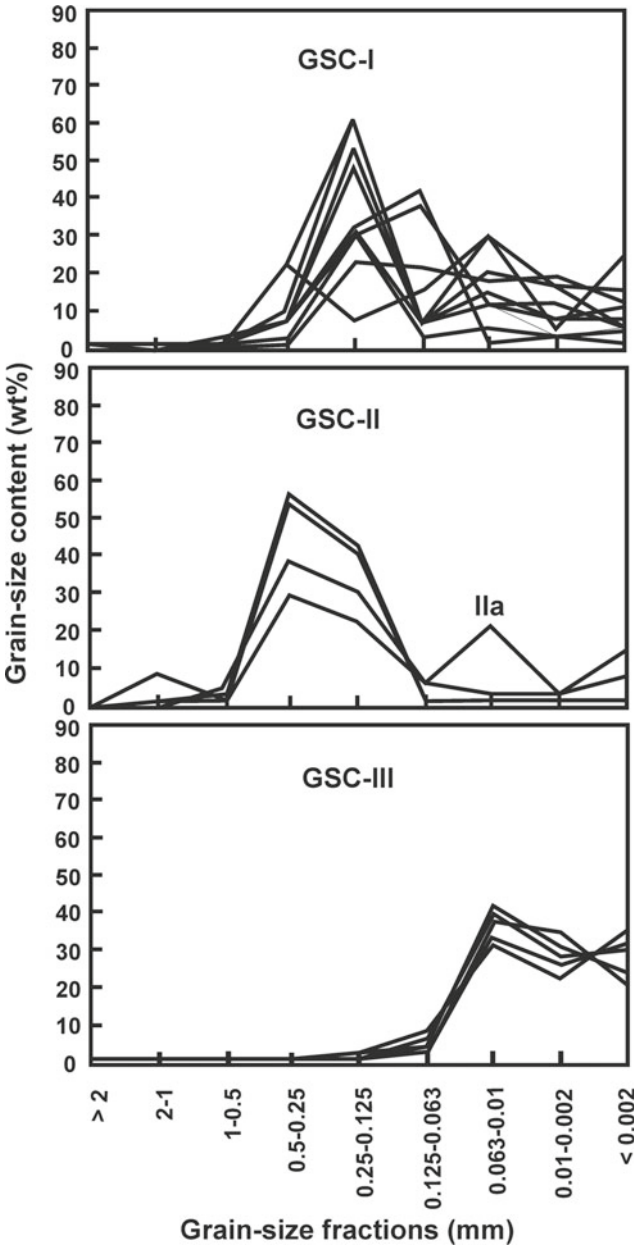

Fig. 5 Percentage (wt%) of individual fractions of surface sediments in the Laptev Sea for individual Grain-Size Clusters (GSC). See also Table 2

UCC. On this basis, we may assume that the sediments of the central geochemical province of the sea are more mature (quartz-rich) sediments, relative to both the eastern and western provinces. At the same time, the sediments of the western and eastern provinces contain more weathering products (more finer grain-size fractions) carried into the sedimentation basin by meltwater and fluvial discharge, as well as by the coastal abrasion.

4.1 Western Geochemical Province

Geographically, the western geochemical province of the sea is adjacent to the Severnaya Zemlya archipelago and the Taimyr Peninsula (Fig. 6). This part of the sea is the deepest and is characterized by a strong water depth gradient, as there is a deep-water trough originating from the Vilkitsky Strait with maximum water depth of 240 m, and extending to the northeast, cutting the continental slope. In this part of the sea, clayey silt sediments predominate at water depths greater than 100 m (Fig. 2). An exception is the sediments of station 5589 located in the deep-water part of the strait at a depth of 240 m (Table 2). Their anomalously coarse composition can be explained highly likely by the winnowing of fine fractions by bottom currents. The latter may presumably develop seasonally as a result of the formation of supercooled and more saline waters during winter ice formation [31, 32].

Sedimentary matter entering the western part of the sea can be divided into material from glacial runoff from the Severnaya Zemlya (glacial component), solid river runoff from the Taimyr Peninsula (fluvial component), and material from coastal abrasion, including insoluble products of permafrost degradation [33–35]. Suspended matter is transported here from the north by the East Taimyr Current [16] and through Vilkitsky Strait from the west [36] (Fig. 1).

Geochemically, it is common to divide the surface sediments of the Laptev Sea into western and eastern parts [14, 37]. According to Schoster et al. [14], the sediments of the western part of the sea are characterized by relatively high Ti/Al, Cr/Al and Ca/Al ratios and increased contents of smectite and clinopyroxene. Data from Viscosi-Shirley et al. [37] indicate that the sediments of the western part of the sea are also characterized by a low Mg/K ratio. Our data show that the western geochemical province is characterized only by a higher Ti/Al ratio (mean for CC-II is 0.054), whereas the central province has the highest Ca/Al ratio (mean for CC-III is 0.13) and the lowest MgO/K_2O ratio (mean for CC-III is 0.48; Fig. 10). Such differences are related to the fact that previous authors did not identify the central part of the sea as a separate geochemical province. At the same time, we have shown above that the western province of the sea differs from the central province not only in grain-size composition of sediments (Table 2), but, more importantly, in chemical composition of sediments (Table 3), reflecting a different sources of sedimentary matter. The main difference in the western province is a lower SiO_2 content and SiO_2/Al_2O_3 ratio and higher Fe_2O_3 content, indicating a high role of clay minerals and Fe oxyhydroxides in sediments. The higher MgO/K_2O ratio also reflects the high proportion of magnesian aluminosilicates, represented mainly by chlorites [14, 37] (Fig. 10).

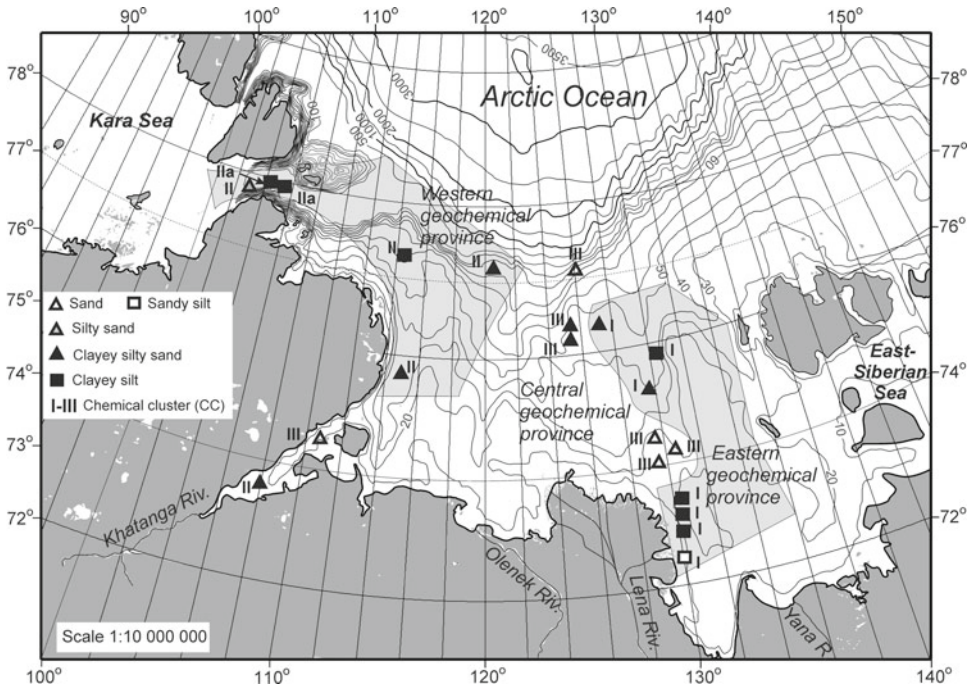

Fig. 6 Overview map of the Laptev Sea with the location of lithotypes and Chemical Clusters (CC; Table 3). Light gray areas show geochemical provinces

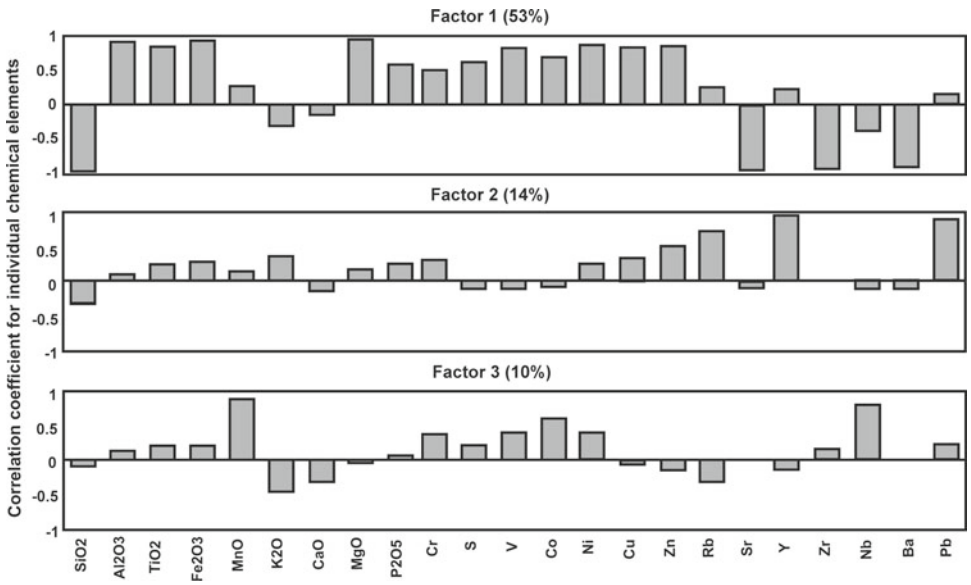

Fig. 7 Factor analysis results of chemical composition of surface sediments in the Laptev Sea with indication of the factor load in %

4.2 Central Geochemical Province

The central geochemical province is characterized by its relatively shallow depths (Fig. 6). To the south, the inner shelf of the province adjoins the Lena River delta. The sediments of this province are predominantly clayey silty sand. The exceptions are stations located on the outer shelf at water depths greater than 50 m (stations 6941, 6065, and 6027). Despite the relative large water depth of these stations their sediments are sand and silty sand. The coarser grain-size distribution of the deep-sea sediments may indicate both gravitational transport of sediment down the slope and the influence of bottom currents, possibly seasonal as we discussed above.

It is convenient to divide sedimentary rocks by their degree of weathering or mature, at each stage of which a transformation takes place, expressed in a regular change in their mineral and chemical composition. The chemical index of alteration (CIA) proposed by Nesbitt and Young [38] is commonly used to assess the degree of this change. The CC we have identified also differ in this index. The most weathered sediments are those of the central geochemical

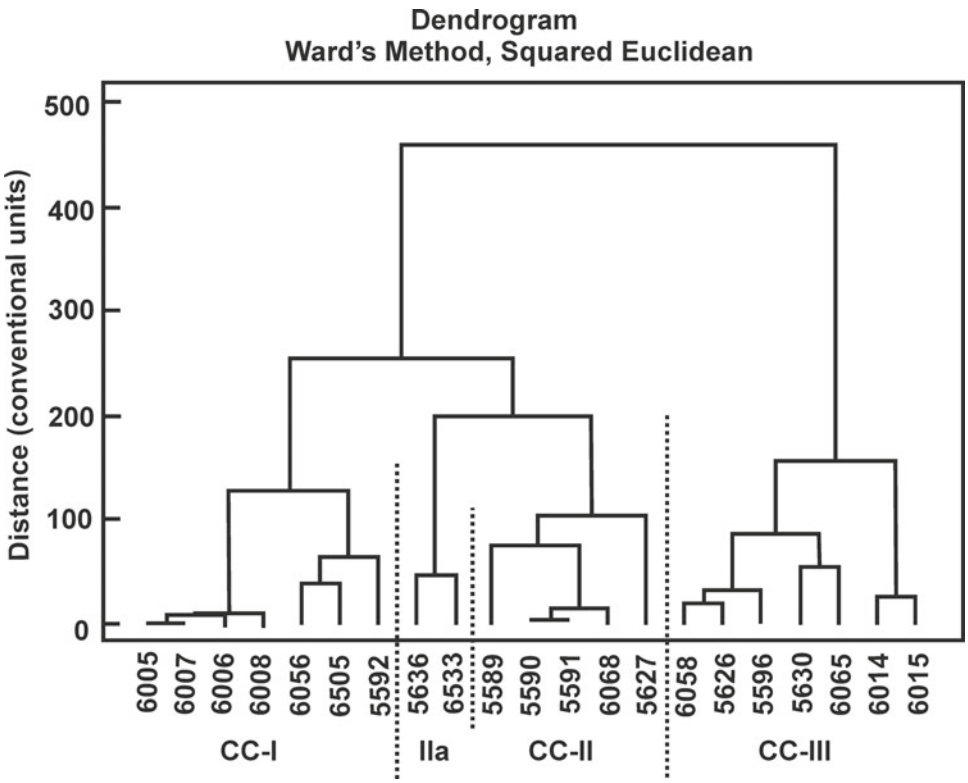

Fig. 8 Cluster analysis results of chemical composition of surface sediments in the Laptev Sea with indication of Chemical Clusters (CC). See also Table 3

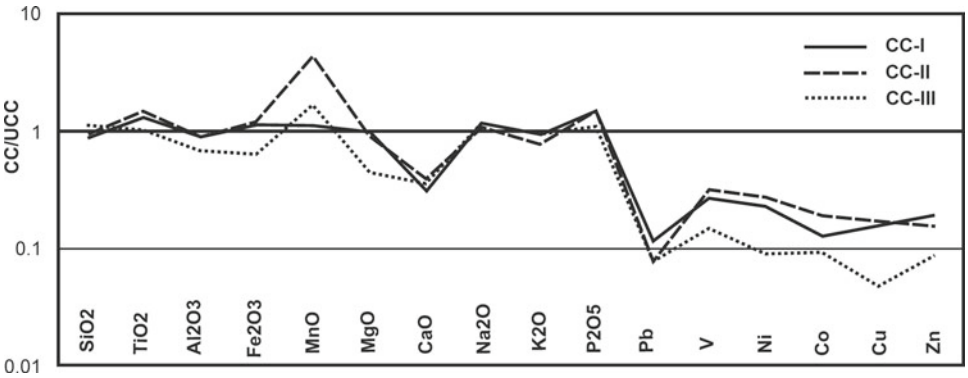

Fig. 9 Average chemical composition of the geochemical provinces in the Laptev Sea, according to Chemical Clusters (CC), normalized to average composition of the Upper Continental Crust (UCC) [30]

province of the sea (CC-III), with an index value of 58.8. At the same time, sediments of the eastern and western provinces (CC-I and CC-II, respectively) have higher index values (66.8 and 67.6, respectively), indicating a higher proportion of secondary minerals formed during weathering (clay minerals and iron oxyhydroxides).

The sediments of the central province are chemically very different from the rest of the sea (Fig. 10). First of all, they have higher silica content, reflecting a high proportion of quartz resistant to weathering processes, and a low iron content, much of which comes with solid river discharge as suspended matter (Fe oxyhydroxides). The low MgO/K_2O ratio in central province sediments also indicates a low proportion of magnesian aluminosilicates (primarily chlorites, as we noted above) and a high proportion of potassium-bearing minerals such as illite and potassium feldspar. On this basis, it can be assumed that the sediments of the central geochemical province represent outcrops of more weathered sediments accumulated within paleo-delta of the Lena River.

Similar to the Kara Sea upland, formed during periods of low sea level (Quaternary glaciations) as the Ob' and Yenisei delta, the central part of the Laptev Sea appears also to be a submerged Lena River delta [39, 40]. During periods of sea-level rise, the area of avalanche accumulation of river-borne sediment is localized in the area of the present-day delta. When the sea level is low, the delta expands and the area of entrained sediment accumulation shifts towards the receding sea. Thus, the sum of the data presented indicates that sediments in the central geochemical

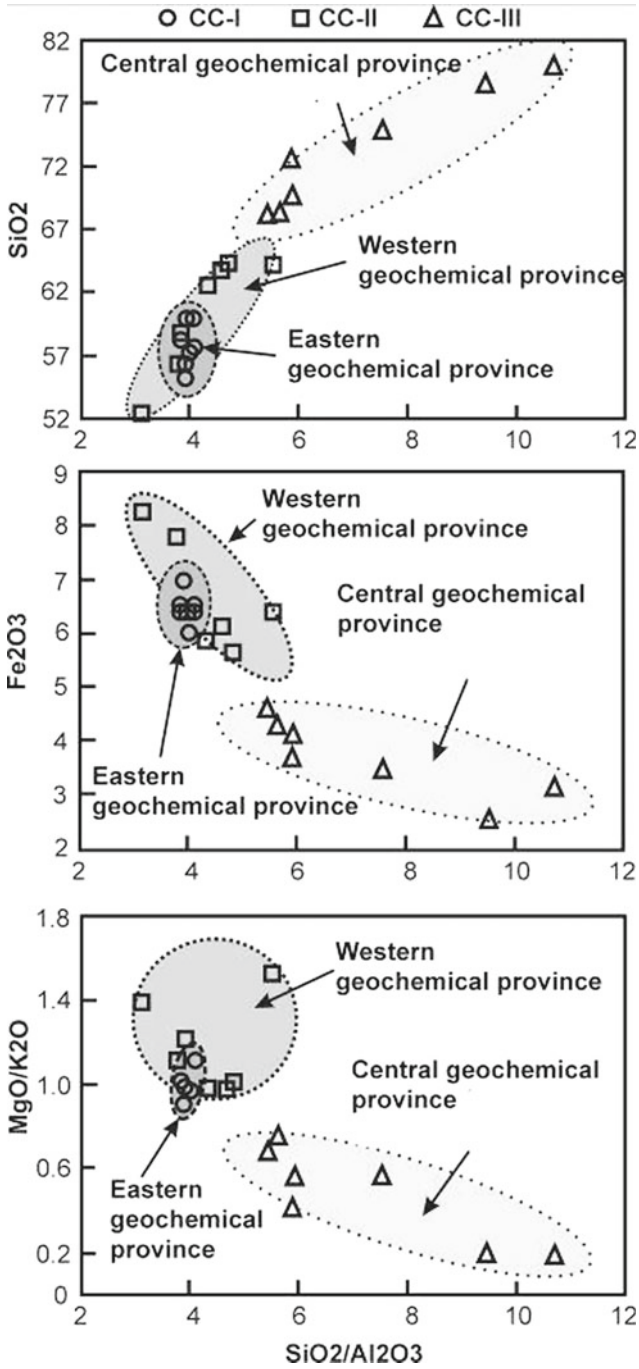

Fig. 10 Position of genetic types of surface sediments in the Laptev Sea in coordinates: MgO/K_2O (Fe_2O_3, SiO_2)–SiO_2/Al_2O_3. CC–Chemical Cluster

province of the sea may represent deposits of the submerged Lena River delta (variant A–avandelta, variant B–relict delta) and characterized by an increased content of coarse fraction consisting mainly of well-sorted clastic minerals.

4.3 Eastern Geochemical Province

The eastern part of the sea is the shallowest. The average water depth of the inner part of the shelf adjacent to the Lena River delta is less than 20 m (Figs. 1 and 6). A strong eastward longshore current and river discharge force a suspended matter to move eastward and northeastward, as if pressing it against the western tip of the Novosibirsk Islands (Novosibirsk Current). As a result, the bulk of the solid suspended matter accumulates here, forming the fine sediment of a clayey silt composition, abnormally fine for such shallow conditions of the inner shelf. In contrast to the sediments in the central part of the sea, transported by the current along the bottom, suspended material transported by the Novosibirsk Current in the water column dominates in the eastern area. Such a relatively fine sediment composition of the eastern geochemical province, combined with the shallowness of the sea, can be explained by the highest rates of sediment accumulation and a calm hydrodynamic sea regime. Clayey silt sediments do not be able to be reworked by the hydrodynamic action of waves and sea currents. Their accumulation is also facilitated by prolonged sea-ice cover that protects the surface sediments from sea waves. The situation is similar to the accumulation of fine sediments in the outer part of the estuary (mud-bank sediments) [9]. Exceptions are stations 6005 and 6505. The first station is located opposite the main Denisovsky channel of the Lena River at a water depth of 14 m. Such shallow sediments are under strong hydrodynamic influence and are more reminiscent of river delta sediments in their composition. The second station is located on the middle shelf at the boundary with the central geochemical province at a water depth of 40 m. Here, sedimentation rates are probably not as high and sediments are recycled by waves and currents.

5 Conclusion

A study of the lithological and geochemical composition of the surface sediments of the Laptev Sea allowed the identification of at least three different geochemical provinces: western, central, and eastern. The lithological and geochemical composition of sediments, in turn, is controlled not only by different feeding provinces, but also by different sedimentation mechanisms. In the western deepest part of the sea, in addition to the bathymetric control of sedimentation, gravitational transport of sediment is added, due to sediment transport into this part of the sea from areas of Severnaya Zemlya. The East Taimyr Current contributes to

the transport of the sediments from continental glacial sedimentary geochemical province in the sea.

We reveal the central geochemical province of the sea for the first time. Its surface sediments, compared to the rest of the sea bottom, are distinguished by a coarser particle size distribution (sand, silty sand, and clayey silty sand) and a high degree of reworking of the primary sediment. In terms of their lithological and geochemical composition, the sediments of this province are similar to Late Pleistocene delta deposits which retained their local position following the sea-level rise and flooding of the Lena River delta.

The sediments of the eastern geochemical province of the sea are similar in grain-size and chemical composition to the sediments of the western province, but differ by their poor sorting.

Acknowledgements The authors express their deep gratitude to the crew of the R/V Akademik Mstislav Keldysh and personally to the head of the expedition, Corresponding Member of the Russian Academy of Sciences Dr. I.P. Semiletov for help in the work and the opportunity to obtain scientific material, as well as O.V. Tumskaya for her help in carrying out grain-size analysis. The work is conducted under the GEOKHI RAS state assignment.

References

1. Swift, D.J.P.: Continental shelf sedimentation. In: Burk, C.A., Drake, C.L (eds.) The geology of continental margins, pp. 117–135. Springer, Berlin, Heidelberg (1974)
2. McCave, I.N.: Erosion, transport and deposition of fine grained marine sediments. In: Stow, D.A.V., Piper, D.J.W. (eds.) Fine-grained sediments, pp. 35–69. Blackwells Scientific Publications, Oxford (1984)
3. Tillman, R.W., Siemers, Ch.T.: Siliciclastic shelf sediments. SEPM Special Publication 34, Tulsa (1984)
4. Frolov, V.T.: Lithology. Book 1 (Litologiya. Kniga 1). Moscow University, Moscow (1992).[in Russian]
5. Li, M.Z., Sherwood, Ch.R., Hill, Ph.R. (eds.): Sediments, morphology and sedimentary processes on continental shelves: advances in technologies, research and applications. Wiley-Blackwell, Hoboken (2012)
6. Rusakov, V.Yu, Kuz'mina, T.G., Levitan, M.A., Toropchenova, E. S., Zhilkina, A.V.: Lithology and geochemistry typification of surface bottom sediment at the Kara Sea. Oceanol. **57**(1), 214–226 (2017a)
7. Rusakov, V.Yu, Kuz'mina, T.G., Levitan, M.A., Toropchenova, E. S., Zhilkina, A.V.: Heavy metal distribution in the surface layer of bottom sediments of the Kara Sea. Geochem. Int. **55**(12), 1079–1089 (2017b)
8. Rusakov, V.Yu, Kuz'mina, T.G., Toropchenova, E.S., Zhilkina, A. V.: Modern sedimentation in the Kara Sea: evidence from the lithological–geochemical investigation of surface bottom sediments. Geochem. Int. **56**(12), 1076–1096 (2018)
9. Rusakov, V.Yu., Borisov, A.P., Solovieva, G.Yu.: Sedimentation rates in different facies genetic types of bottom sediments in the Kara Sea: evidence from the ^{210}Pb and ^{137}Cs radionuclides. Geochem. Int. **57**(11), 1185–1200 (2019)
10. Frolov, V.T.: Lithology. Book 2 (Litologiya. Kniga 2). Moscow University, Moscow (1993).[in Russian]
11. Viscosi-Shirley, C., Pisias, N., Mammone, K.: Sediment source strength, transport pathways and accumulation patterns on the Siberian-Arctic's Chukchi and Laptev shelves. Cont. Shelf Res. **23**, 1201–1225 (2003)
12. Silverberg, N.: Sedimentology of the surface sediments of the east Siberian and Laptev Sea. Ph. D. thesis, University of Washington (1972)
13. Wahsner, M.: Mineralogical and sedimentological characterization of surface sediments from the Laptev Sea. In: Kassens, H., Piepenburg, D., Thiede, J., Timokhov, L., Hubberten, H., Priamikov, S.M. (eds.) Russian-German cooperation: the Laptev Sea system. Rep. Polar Res. **176**, 303–313 (1995)
14. Schoster, F., Behrends, M., Müller, C., Stein, R., Wahsner, M.: Modern river discharge and pathways of supplied material in the Eurasian Arctic Ocean: evidence from mineral assemlages and major and minor element distribution. Int. J. Earth Sci. **89**, 486–495 (2000)
15. Gurevich, V.I.: Modern sedimentogenesis and geoecology of the West Arctic shelf of Eurasia (Sovremenniy sedimentogenes I geoekologiya Zapadno-Arcticheskogo shelfa Eurasii). Nauchniy Mir, Moscow (2002).[in Rusian]
16. Dobrovolskiy, A.D., Zalogin, B.S.: USSR seas (Morya SSSR). Moscow University, Moscow (1982)
17. Aagaard, K., Carmack, E.C.: The role of sea ice and other fresh water in the Arctic circulation. J. Geophys. Res. **94**, 14485–14498 (1989)
18. Gordeev, V.V., Martin, J.M., Sidorov, I.S., Sidorova, M.V.: A reassessment of the Eurasian river input of water, sediment, major elements and nutrients to the Arctic Ocean. Am. J. Sci. **296**, 664–691 (1996)
19. Gordeev, V.V.: Geochemistry of the river-sea system (Geokhimiya sistemi reka-more). Moscow, I.P Matushkin (2012).[in Russian]
20. Avetisov, G.P.: Some questions of the dynamics of the Laptev Sea lithosphere. Izvestiya Phys. Solid Earth **5**, 28–38 (1993)
21. Drachev, S.S.: Tectonics of the Laptev Sea bottom rift system. Geotectonics **6**, 43–58 (2000)
22. Ivanova, N.M., Sekretov, S.B., Shkarubo, S.I.: Data on the geological structure of the Laptev Sea shelf based on seismic data. Oceanol. **24**(5), 789–795 (1989)
23. Roeser, H.A., Block, M., Hinz, K., Reichert, C.: Marine geophysical investigations in the Laptev Sea and the western part of the Eastern Siberian Sea. Rep. Polar Res. **176**, 367–377 (1995)
24. Drachev, S.S., Savostin, L.A., Groshev, V.G., Bruni, I.E.: Structure and geology of the continental shelf of the Laptev Sea. East. Russ. Arctic. Tectonophysics **298**, 357–393 (1998)
25. Kleiber, H.P., Niessen, F., Weiel, D.: The Late quaternary evolution of the western laptev sea continental margin, arctic Siberia–implication from sub-bottom profiling. Global Planet. Change **31**, 105–124 (2001)
26. Gorshkov, S.G. (ed.): Atlas of the oceans. Arctic Ocean. USSR Ministry of Defense. Voenno-Morskoy Flot Press, Moscow (1980).[in Russian]
27. Petelin, V.P.: Grain-size analysis of the marine bottom sediments (Granulometricheskiy analiz morskikh donnikh osadkov). Nauka, Moscow (1967).[in Russian]
28. Andreeva, I.A., Lapina, N.N.: Method of grain-size analysis of bottom sediments of the World Ocean and geological interpretation of the results of laboratory study (Methodica granulometricheskogo analiza donnikh osadkov Mirovogo okeana i geologicheskaya interpretatsiya resultatov laboratornogo izucheniya veschestvennogo sostava). VNIIOkeangeologia, St. Petersburg (1998) [in Russian]
29. Wentworth, C.K.: A scale of grade and class terms for clastic sediments. Journ. Geology. **30**, 3–35 (1922)

30. Taylor, S.R., McLennan, S.M.: The continental crust; its composition and evolution; an examination of the geochemical record preserved in sedimentary rocks. Blackwell, Oxford (1985)
31. Bauch, D., Cherniavskaia, E., Timokhov, L.: Shelf basin exchange along the Siberian continental margin: modification of Atlantic water and lower halocline water. Deep Sea Res. Part I **115**, 188–198 (2016)
32. Khare, N., Khare, R.: Chapter 9-Arctic ocean circulation. In: The Arctic: a barometer of global climate variability, pp. 127–137. Elsevier Inc. (2021)
33. Günther, F., Overduin, P.P., Sandakov, A.V., Grosse, G., Grigoriev, M.N.: Short-and long-term thermo-erosion of ice-rich permafrost coasts in the Laptev Sea region. Biogeosci. **10**, 4297–4318 (2013)
34. Tesi, T., Muschitiello, F., Smittenberg, R.H., Jakobsson, M., Vonk, J.E., Hill, P., Andersson, A., Kirchner, N., Noormets, R., Dudarev, O., Semiletov, I., Gustafsson, Ö.: Massive remobilization of permafrost carbon during post-glacial warming. Nat. Commun. **7**, 13653 (2016)
35. Tesi, T., Semiletov, I., Hugelius, G., Dudarev, O., Kuhry, P., Gustafsson, Ö.: Composition and fate of terrigenous organic matter along the Arctic land-ocean continuum in East Siberia: insights from biomarkers and carbon isotopes. Geochim. Cosmochim. Acta **133**, 235–256 (2014)
36. Osadchiev, A.A., Pisareva, M.N., Spivak, E.A., Shchuka, S.A., Semiletov, I.P.: Freshwater transport between the Kara, Laptev, and East-Siberian seas. Sci. Rep. **10**, 13041 (2020)
37. Viscosi-Shirley, C., Mammone, K., Pisias, N., Dymond, J.: Clay mineralogy and multi-element chemistry of surface sediments on the Siberian-Arctic shelf: implications for sediment provenance and grain size sorting. Cont. Shelf Res. **23**, 1175–1200 (2003)
38. Nesbitt, H.W., Young, G.M.: Early Proterozoic climates and plate motions inferred from major element chemistry of lutites. Nature **299**, 715 (1982)
39. Syvitski, J.P.: Sediment discharge variability in Arctic rivers: implications for a warmer future. Reports on Polar Research **21**, 323–330 (2002)
40. Bauch, H.A., Mueller-Lupp, T., Taldenkova, E., Spielhagen, R.F., Kassens, H., Grootes, P.M., Thiede, J., Heinemeier, J., Petryashov, V.V.: Chronology of the Holocene transgression at the North Siberian margin. Glob. Planet. Change **31**, 125–139 (2001)

Study of Hydrodynamic Processes in the Ocean by Remote Laser-Optical Methods

V. N. Nosov, S. G. Ivanov, S. B. Kaledin, A. S. Savin, V. I. Timonin, V. I. Pogonin, T. V. Glebova, and E. A. Zevakin

1 Introduction

Various hydrodynamic processes (HDPs) occurring in the sea strata influence the changes in the physical-chemical properties and characteristics of the sea surface and the near-surface layers of the marine environment and the atmosphere. This is manifested in the form of anomalies—areas with changed, compared to the background, characteristics of sea wave, stratification of phytoplankton, inorganic suspended matter and air bubbles in the near-surface sea layers, as well as in the form of changes in concentration and dispersion of the drive aerosol compared to the background values. Such manifestations of the HDPs can be investigated by remote laser-optical methods both from the shipboard and from airborne and spaceborne carriers. In the first case, due to the low ship speed, it is possible to study relatively slowly changing HDPs of a limited scale. However, such observations can be made continuously for a long time in different areas of the World Ocean with high spatial resolution. A significant advantage of using remote laser-optical methods from an airborne vehicle is the operational efficiency of research and the large spatial scale of the phenomena under study. The use of laser-optical methods from a space carrier makes it possible to conduct research of global in spatial scale phenomena in the ocean. However, in this case, the area of observation is limited in choice due to the rigid trajectory of the spacecraft motion and with a long break for repeated observations due to the spacecraft orbit precession. Among optical methods, the use of color scanners and video spectrometers when placed on satellites is widespread in the study of large-scale HDPs in the form of currents, synoptic eddies, etc. [1, 2].

At present the most interesting for research are such HDPs as internal waves, currents, upwelling zones, gas emissions from faults and gas-condensate fields, flowing around the bottom relief and artificial obstacles in the form of supports of structures and pipelines, etc.

We use as remote laser optical methods: (1) for measuring the sea surface characteristics—the method of scanning the sea surface with a narrow laser beam [3, 4], (2) for measuring the optical properties of the near-surface layers of the sea medium—the method of sea brightness photometry [5–7], (3) for recording the properties of the near-surface layers of the atmosphere—the method of aerosol laser scattering [8, 9]. Based on these methods, we developed setups of laser-optical equipment (LOE), which were used in our studies.

In order to reveal the impact of the HDPs on the sea surface and the near-surface layers of the marine environment and the atmosphere, we obtained the estimated relations for the measured characteristics and developed the statistical methods for signal processing. To understand the hydrodynamic processes occurring in the sea medium thickness, the use of machine learning and artificial intelligence methods in a number of cases also seems promising. Such an approach makes it possible to perform effective detection and study of manifestations of HDPs on the sea surface and near-surface layers of the marine environment and the atmosphere.

2 Method of Sea Surface Scanning with a Narrow Laser Beam

The method used is based on the method of scanning the sea surface with a narrow laser beam and registration of specular laser glare reflections [3, 4]. Mirror laser reflections appear at the moment when the combined axes of the laser beam and

V. N. Nosov (✉) · S. G. Ivanov · V. I. Pogonin · T. V. Glebova · E. A. Zevakin
Vernadsky Institute of Geochemistry and Analytical Chemistry, Russian Academy of Sciences, 19 Kosygin St., Moscow, 119991, Russia
e-mail: ivanovsg5167@yandex.ru

S. B. Kaledin · A. S. Savin · V. I. Timonin
Bauman Moscow State Technical University, 2-d Bauman Str., 5, Moscow, Russia

V. P. Kolotov and N. S. Bezaeva (eds.), *Advances in Geochemistry, Analytical Chemistry, and Planetary Sciences*,
https://doi.org/10.1007/978-3-031-09883-3_13

the receiving optical system coincide with the normal to the sea surface at the place of reflection. Since the sea surface, taking into account wind ripples, has a random profile, laser glare reflections also occur randomly, but in accordance with the wave profile. The power of the laser glare depends on the curvature of the wave. And the time interval between them is determined by the spatial period of the wave.

Earlier, different variants of shipborne setups of Scanning Laser Locators (SLLs) allowing one to measure the sea surface characteristics were developed and used in full-scale studies at the Vernadsky Geochemical Institute of the Russian Academy of Sciences [10–12]. These setups were placed onboard the research vessel and recorded the changes in the laser-light pattern in the process of vessel motion.

The analytical relation of the laser beam reflection intensity from the sea surface in the flare area with the main wave parameters is known [13, 14]. In the general case the received signal depends on such parameters as: energy density of laser radiation on the sea surface, curvature of the sea surface profile in the reflection zone, sensitivity of the receiving equipment, aperture of the receiving lens, etc. It is more convenient to consider the random profile of the sea surface in the form of the equivalent surface of a spherical shape. This model is simplified because we neglect wave anisotropy [15, 16]. This allows us to conduct the analysis using the parameter of the equivalent radius of curvature. In addition, an important informative parameter is the value of the angle relative to the vertical at which the laser-glare signal is received. This angle depends on the gradient of the wave in the glare reflection. The method is based on accumulation and processing of statistical data on the reflected laser-glare signals.

The radius of the equivalent sea surface can be calculated by the formula [13]:

$$R = \frac{2H}{D}\sqrt{\frac{4\mu\Phi_0 A_0}{\pi\rho\tau\tau_A^2 P}} \qquad (1)$$

where μ—coefficient of signal/noise ratio, Φ_0—threshold flux of the photodetector (PD), A_0—the area of surface illuminated by a laser beam, H—height of placement of the setup, ρ—sea surface reflectance coefficient, τ, τ_A—optical and atmospheric transmission coefficients, respectively, P—laser emission power, D—diameter of the entrance pupil of the receiving lens.

When designing the setup, the magnitude of the background signal coming from the sea should be taken into account. The background from the sea when observed near the nadir in the visible part of the spectrum is mainly determined by the radiation rising from the sea from the Sun and the sky (the brightness of the sea). The Fresnel reflection power of the solar and sky radiation from the sea surface in this case is several times less than the radiation rising from the sea.

Background power from sea brightness can be calculated by the formula [17]:

$$\mathrm{P_B} = L_S(\lambda)\frac{\pi * D^2}{4} * \Omega_m * \Delta\lambda_{if} * \tau * \tau_A, \qquad (2)$$

where $L_S(\lambda)$—is the brightness of the sea at wavelength λ. On a bright sunny day in the green region of the spectrum $L_\mathrm{M}(\lambda) \approx 6 * 10^{-3}$ W/(sr*nm) [18];

$\Omega_m = \frac{\pi * r_d^2}{F^2}$—is the receiving solid angle of the lens with focal length F (r_d is the radius of the field aperture placed in the lens focus);

$\Delta\lambda_{if}$—spectral bandwidth of the interference filter;

τ и τ_A—transmittance of the layout optics and atmosphere, respectively.

Taking into account the values of the parameters of the airborne SLL (ASLL) layout developed by us: D = 9 cm, $\Omega_m = 6,3 * 10^{-7}$ sr, $r_d = 0.36$ mm, F = 0.8 m, $\Delta\lambda_{if} =$ 5 nm, τ = 0.5 and τ_A = 0.9 we can obtain an estimate for the background radiation power from the sea during the daytime:

$$\mathrm{P_B} = 5,4 * 10^{-11}\,\mathrm{B_T}$$

This value is approximately 2700 times higher than the dark current noise power of the photodetector based on the PM-114 photomultiplier calculated from the light equivalent of dark current noise $\Phi_\nu = 7.3 * 10^{-14}$ lm/Hz$^{1/2}$ in the 30 kHz frequency band.

Using the value of power of background radiation from the sea $\mathrm{P_B}$ as a threshold flux of photodetector Φ_0 from formula (1) we can obtain an estimate for the smallest radius of curvature of the wave R_min, from which the reflected laser glare radiation can be measured with a threefold exceeding of the signal. When placing the model on the airborne vehicle at its flight height H = 300 m and the parameter values: μ = 3; ρ = 0.02; A = $6.4 * 10^{-3}$ m^2; D = $9 * 10^{-2}$ m; P = 1.5 W, it can be obtained that R_min = 7 cm.

Statistical processing of the measured data on wave radii and slopes allows one to analyze the sea surface condition. In the undisturbed state, the sea surface has some initial, "background" statistical characteristics. Under influence of hydrodynamic disturbances (HDD) or films of surface-active substances these statistical characteristics change. The most informative is the gravitational-capillary region of the sea-wave spectrum, which has smaller equivalent radii of curvature [19, 20].

Figure 1 shows a typical structural and functional diagram of SLL setup. It was used to create both shipboard and Aircraft SLL (ASLL).

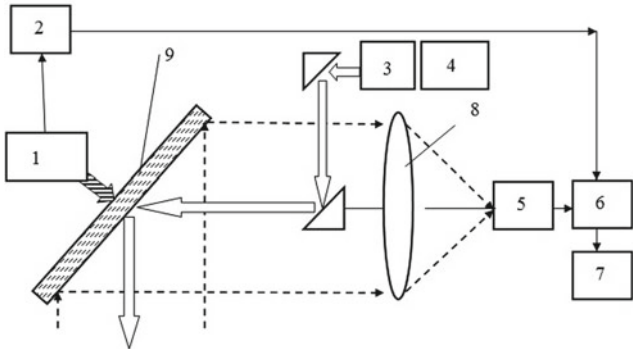

Fig. 1 Structure-functional diagram of SLL setup. 1—electric drive, 2—synchronization system, 3—shaping optical system, 4—laser, 5—photodetector, 6—analog–digital converter (ADC), 7—personal computer, 8—lens, 9—scanning mirror [21]

Two channels can be distinguished in the structural scheme of the SLL and ASLL setups: a laser illumination channel, consisting of a laser and a forming optical system (FOS), and a receiving channel, including a lens and a photo-receiving device (PRD). In order to combine the area of laser illumination on the sea surface with the instantaneous angular field of the receiving channel, a schematic solution of the setup optical scheme with the combined optical axis of the named channels has been chosen.

For scanning the sea surface by the laser beam the drive with the oscillating scanning mirror is used. The drive is performed from an electric motor through a crank mechanism. The angular position of the scanning mirror is tracked using a synchronization system based on an optocoupler and a gating disk. Such a device makes it possible, when processing the information, to determine the angular position of the laser flare relative to the vertical at the moment of its registration by the PRD, and, hence, to obtain data on the sea surface wave slope. The general view of the sea surface (SS) scanning trajectory is shown in Fig. 2.

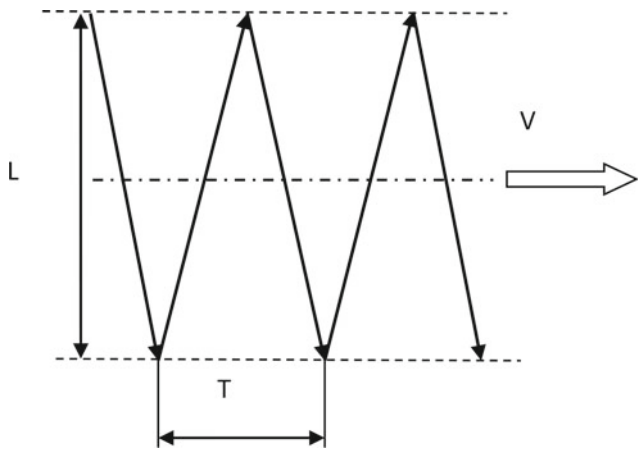

Fig. 2 Laser beam scanning trajectory across the sea surface [13]

The scanning is performed transverse to the direction of the media motion. The basic parameters of the scanning trajectory are determined by: the velocity of the carrier movement V, the deflection angle of the scanning mirror and the distance from the device to the SS, and the step T depends on the frequency of the mirror swinging.

In our in-situ studies from a research vessel (RV), the SLL setup was placed in the bow of the vessel at a height of 8 m. As a rule, the ship speed was not higher than 9 knots, and the scanning frequency was 7 Hz, which provided a linear spread of L = 1.8 m, with a step of about 0.5 m per SS. This mode of operation allowed obtaining sufficient signal statistics with high spatial resolution. Taking into account the small distance to SS, we didn't need a big laser power, that's why in the scheme there was used a semiconductor laser module with output power not more than 80 mW at a wavelength of 660 nm. The aperture of the receiving channel was 50 mm.

Figure 3 shows a photograph of the placement of the SLL setup on board the RV.

The results of application of the SLL dummy for investigation of HDD in the form of a trailing vessel trace are described in detail in papers [10–12]. Figures 4 and 5 present histograms of time intervals between SLL pulses and their amplitudes for 6–3 s before and at the moment of crossing the trace of the 120-ton displacement boat BGK-889.

On the abscissa axis in Fig. 4 is the time interval between pulses in fractions of 0.1 ms, determined by the signal digitization frequency of 10 kHz used in the ADC. From the presented histograms it can be seen that the greatest changes in the histograms when crossing the trace of BGK-889 occur in the area of small time intervals between SLL pulses in the range of 0–5 ms. The number of pulses in this range in the interval of 6–3 s before the intersection is 90–97, and the number of pulses in the intersection area is almost 2 times less—54 (Fig. 4a, b).

Histograms of amplitudes are constructed for pulses with small amplitude (less than 200 mV). Significant differences are observed in the histograms of SLL signal amplitudes outside the trace and into the trace of BGK-889. Outside the trace of BGK-889 (6–3 s before the crossing) the number of SLL pulses with the lowest amplitudes is 2 times higher than the number of pulses from the same range in the trace area (Fig. 5a, b). The observed pattern can be explained by "smoothing" of the sea surface under the action of the ship's hull—wave ripples with small wave curvature are reduced. This leads to reduction of the number of reflected laser-glare pulse signals with small amplitudes.

We also carried out studies of HDD in the form of the RV own trace with a displacement of 2000 ton. The "age" of the trace was about 40 min. The results of measurements using the SLL dummy and dummies of the Sea Brightness

Fig. 3 Arrangement of the SLL setup in the windshield the casing on board the RV in its forward section

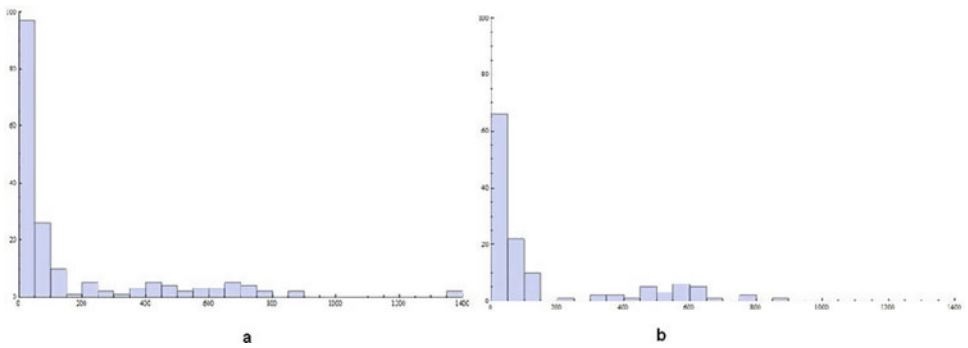

Fig. 4 Histograms of time intervals between SLL pulses: **a** in the interval of 6–3 s before trace crossing and **b** at the moment when BGK-889 boat crossed the trace [12]

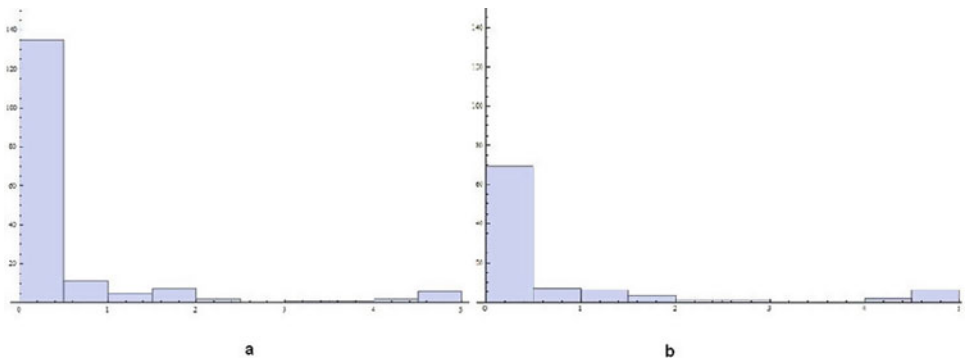

Fig. 5 Histograms of SLL pulse amplitudes: **a** in the interval of 6–3 s before trace crossing and **b** at the moment of BGK-889 boat trace crossing. Pulse amplitudes in relative units are plotted along the OX axis [12]

Photometer (SBP) and Aerosol Lidar (AL) are presented in Fig. 6. Details of the SBP and AL setups are described below.

The data in Fig. 6 are given: for SLL as average values of the number of laser flashes for a given time (pulse frequency), for SBP as relative frequency of oscillations of the high-frequency component of the L_S(440 nm)/L_S(540 nm) sea brightness ratio, for aerosol lidar as accumulated values of the signal. It can be seen that in the region of the ship's trace, indicated by vertical lines, there are significant

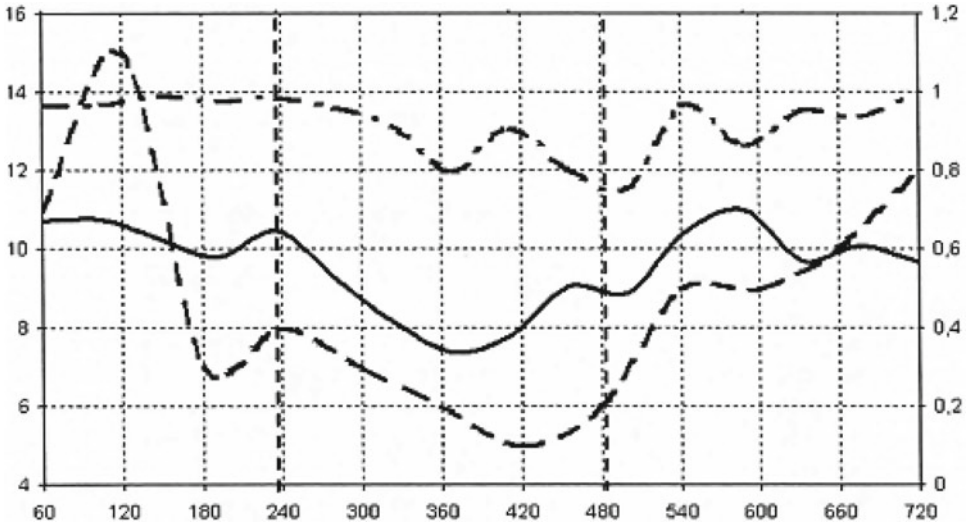

Fig. 6 Plots of time dependences of parameters of registered signals of three setups at crossing of own lagging trace of RV. SLL data—solid curve (right scale); SBP data—dashed curve (left scale); AL data—dashed curve (right scale). F is the relative frequency of oscillation of the L_S(440 nm)/L_S(540 nm) sea brightness ratio, N is the accumulated value of the aerosol lidar signal and the average number of specular flares registered by SLL. Data for SLL and AL are given in relative units [11]

changes in the parameters of all three setups. Such changes can be explained by "smoothing" of the sea surface under the influence of HDD for SLL, removal of more transparent deep water to the upper layers of the marine medium—for SBP and "depletion" of the number of air bubbles in the nearrsurface layers of the marine medium and dissipation of the HDD energy—for AL.

Earlier attempts were made to study the characteristics of the wave from the airborne vehicle [22–24]. However, in these studies, laser beam scanning over the water surface was not used.

In order to perform research onboard an aircraft, we have developed a setup of the ASLL (aircraft scanning laser locators). Figure 7 shows a photo of the ASLL setup with the shroud removed. When developing the setup, we took into account the following operating conditions: the carrier flight speed is about 400 km/h, and the flight altitude is 300–350 m. To increase the SS coverage and the viewing density, the scanning frequency was increased to 28 Hz, which provided a scanning step along the flight direction T = 3.8 m.

A continuous DPSS laser with an emission power of 2500 mW at a wavelength of 532 nm was used in the illumination channel. Divergence of the laser beam is 1.5 mrad, diameter is 4 mm. FOS is a telescopic Galileo system with apparent magnification of 3×. When it is used in a backward beam path, the divergence of the laser beam is reduced to 0.5 mrad with an increase in diameter to 12 mm.

SAMYANG mirror-lens lens with a focal length of 800 mm and an entrance pupil diameter of 100 mm was used in the receiving channel of the ASLL setup. Availability of the central shielding allows injecting the laser beam coaxially with the lens optical axis without additional losses of the received radiation. A field point aperture with a diameter of 0.7 mm is set in the image plane. In this case the instantaneous angular field of the receiving channel is 0.9 mrad that exceeds the angular divergence of the laser beam. This ratio allows a confident overlap of the irradiation and acquisition light fields on the sea surface and simplifies setup alignment.

For spectral filtering of the received radiation an interference filter with a bandwidth of 5 nm installed in front of the input window of the photomultiplier tube is used. The filtering allows to single out a narrow spectral band at the working wavelength of laser radiation and to suppress significantly the interfering background solar radiation coming from the sea.

The SLL and ASLL setups were successfully used in experimental studies in the Black Sea, the Barents Sea, and the Pacific Ocean. It should be noted that the shipboard SLL setup was used as part of a complex of laser-optical equipment for a joint marine and space experiment [25].

Based on the calibration of the ASLL signal from the topographic reflector, a method of recalculating the amplitudes of the ASLL signals into the values of equivalent SS curvature radii [26] was developed.

A setup of an ASLL was used for test measurements over Onega Lake in the summer of 2020. The flights took place at heights of 300–350 m above the water surface at a flight speed of about 400 km/h. To process the results obtained, programs were developed to build histograms of various signal parameters: mean values of signal amplitudes (determined by wave curvature radii), time intervals between individual pulses (determined by spatial periods of the wave), pulse durations, dependence of pulse amplitudes on the angle of mirror rotation (determined by wave gradients),

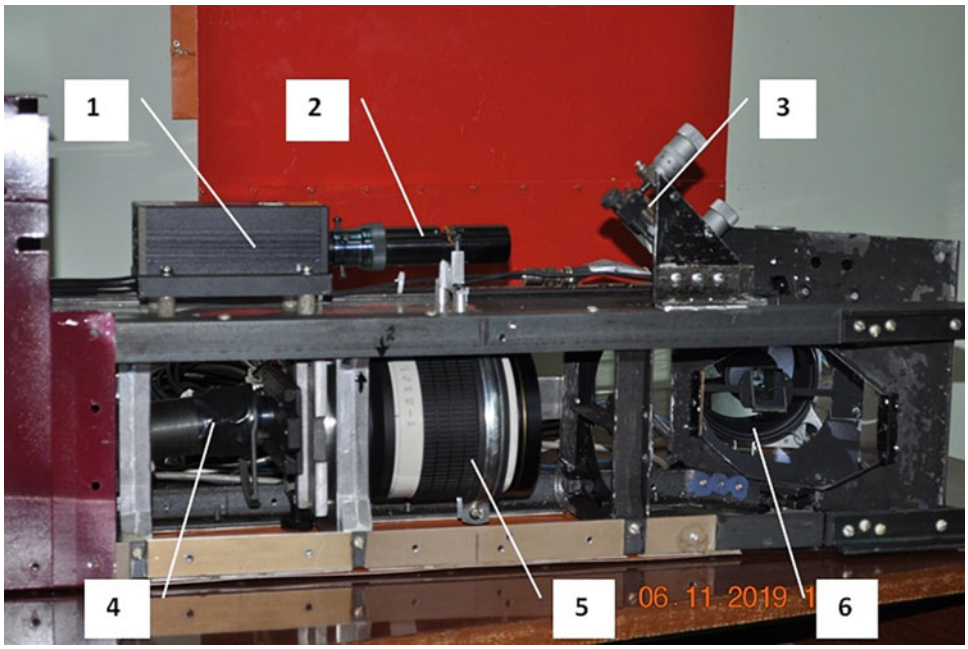

Fig. 7 Setup of ASLL with the cover removed: 1—laser, 2—collimator laser beam expander, 3—rotating alignment mirror, 4—photodetector, 5—receiving lens, 6—scanner with a mirror

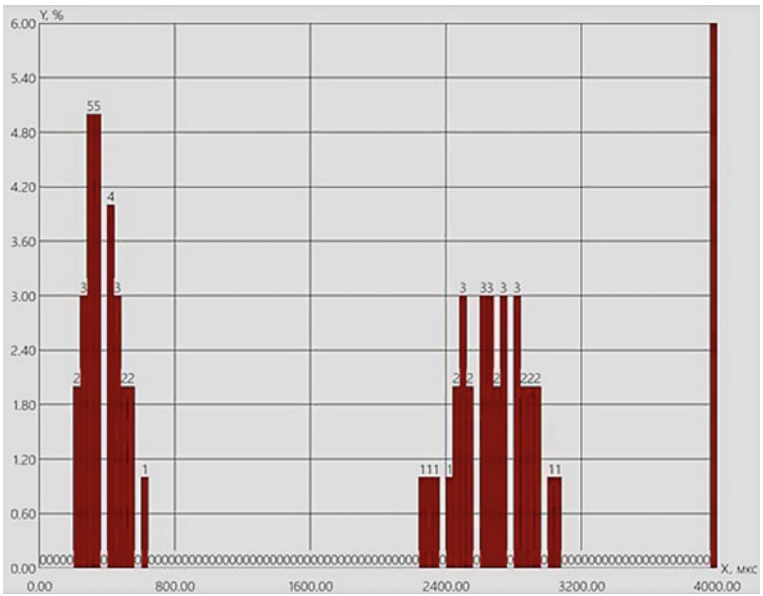

Fig. 8 Histogram of pulse intervals recorded during one of the aircraft's tack [21]

pulse repetition frequencies. Figure 8 shows a histogram of the pulse intervals, measured during one of the aircraft's tack of about 7 min.

The histogram was processed using noise clipping and signal averaging. By the position of the peaks in this histogram, the spatial period of the wave was estimated.

The scanning speed of the laser beam over the sea surface can be calculated by the formula: $V_{sc} = 4\alpha f_M * H$, where the scanning angle of the laser beam is: $\alpha = \pm 10^0$. At scanning frequency f_M = 28 Hz and a flight height H = 330 m the scanning speed of the laser beam over the sea surface is $V_{sc} = 6450$ M/C. The spatial period of the wave is defined by the relation: L = $V_{sc} * \Delta t$, where Δt—is the time interval between the peaks in the histogram of the ASLL pulse intervals. Taking into account the calculated value of the laser beam scanning speed on the sea surface and the average values of pulse intervals of 312.5 μs and 2650 μs, the estimates of the spatial period of the wave are obtained, about 2 m and 17 m, respectively.

The data obtained indicate that two wave systems with different spatial periods are present on the water surface. The water surface photographs taken from the aircraft during measurements also show the water surface wave structure with a minimum period of about 3 m.

The presence of two surface wave systems with significantly different lengths can be explained by the fact that the shorter wave system is in the initial stage of its formation under the wind impact, and the long wave system is in the relaxation stage after the earlier wind impact ends. This situation is typical of large lakes and seas [27, 28].

Using the setup calibration technique by topographic reflector [26] performed before the setup flight tests and taking into account the average amplitude of the laser glare signal pulse of 60 mV obtained from the amplitude histogram, the effective, most probable radius of wave curvature over Onega Lake on the day of measurements is estimated to be 10 cm. Estimations show that with the help of the ASLL setup it is possible to measure sea surface curvature radii within the range of 5–80 cm and spatial scales of waves from 0.2 m and more. The spatial resolution of the ASSL setup is about 10 cm at a flight altitude of 300 m. At a flight speed of 400 km/h, the length of the investigated area of the sea surface can be tens to hundreds of kilometers, which determines the scale of the HDPs under study.

However, researches with application of manned aviation require big financial expenses and considerable organizational efforts. In this sense, it is expedient to change to unmanned aerial vehicle (UAV) deployment. If more modern components are used and flight altitude and speed are reduced, the mass-dimensional and energy parameters of the UAV setup we have developed can be significantly reduced, which will allow the UAV to be used. This will significantly expand the possibilities of solving the problems of operational oceanology, due to the cost-effectiveness of UAVs that can be launched both from the shore and from the ship [13].

3 Method of Photometry of Sea Brightness

3.1 General Principles

We used the Sea Brightness Photometry method for remote studies of the near-surface layers of the marine environment [5–7]. This method is passive. It makes it possible to register the brightness of the light flux ascending from the sea, which depends on the optical properties of the nearsurface layers of the marine environment—on the depth distribution of absorption and scattering coefficients. The latter in turn depend on the presence and concentration of phytoplankton, inorganic suspended matter and dissolved organic matter in seawater.

There is extensive information in the literature on the use of a sea brightness photometer placed on board a ship and on the sea surface (floating photometer), e.g. [29, 30].

Figure 9 shows a schematic diagram of the setup Sea Brightness Photometer (SBP) developed at the Vernadsky Institute RAS. A detailed schematic is given in [31].

The measured quantities in the SBP setup are the luminance of radiation $Ls(440)$ coming from the sea surface at wavelength 440 nm corresponding to the absorption maximum of chlorophyll "a" contained in phytoplankton, and the sea luminance $Ls(540)$ at wavelength 540 nm where the absorption from chlorophyll "a" is negligible. In addition, the three-channel version of the SBP additionally measures sea surface illumination from above (from the sun and sky) at a wavelength of 440 nm. When the sun's glare from the sea surface is not caught by the receiving objective of the SBP the brightness value $Ls(\lambda)$ detected by the instrument depends on two components, namely $L_T(\lambda)$, the brightness of radiation coming from the sea layer of the near-surface layer 12–35 m thick (depending on water transparency) and $L_n(\lambda)$, the brightness of the sky radiation reflected by the sea surface:

$$L_s(\lambda) = L(\lambda) + r \cdot \tau \cdot L_n(\lambda), \tag{3}$$

where r is the Fresnel reflectance of the sea surface;

τ is the transmission coefficient of the polarizer installed at the SBP setup input.

The sighting axis of the SBP when placed on a ship is set at a Brewster angle of 53° to the sea surface (37° from the horizon). In this case, radiation from the sea surface is reflected from the sky mainly with horizontal polarization. The polarizer is oriented so as to suppress the horizontal polarization of the sky radiation reflected from the sea surface. The polarizer transmittance for crossed polarization is estimated to be of the order of 2% ($\tau \approx 0.02$). At this

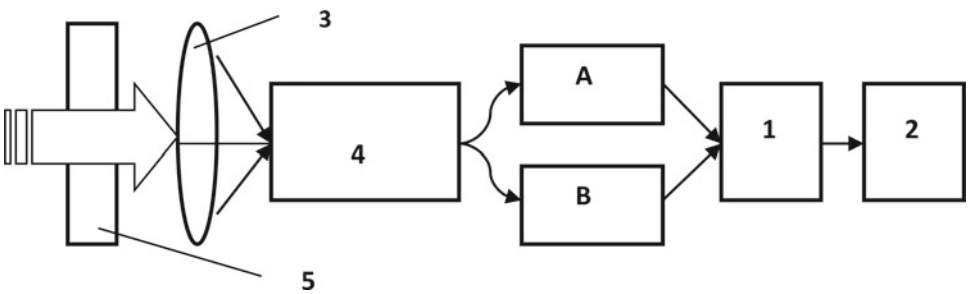

Fig. 9 Schematic diagram of the model of Sea Brightness Photometer: A and B—photodetectors for registration of radiation at 440 and 540 nm wavelengths, 1—analog–digital converter, 2—PC, 3—lens, 4—polarizer, 5—monochromator [12]

polarizer orientation, the brightness of the radiation coming from the sea will be mainly determined by the brightness of the radiation coming directly from the thickness.

When the SBP is placed on a moving medium, the changes in time of the sea brightness value $Ls(\lambda)$ are related in a different degree to the changes in each of the three quantities included in formula (3): $L_T(\lambda)$, $L_n(\lambda)$, r.

The changes manifested in the brightness of radiation coming from the sea column $L_T(\lambda)$ are informative in nature and form a useful signal related to changes in the optical characteristics (scattering and attenuation coefficients) of the near-surface sea layer under the effect of HDD. These characteristics depend on the phytoplankton and inorganic suspended matter content and their stratification in the near-surface layers of the marine environment.

Sea disturbance affects the intensity of the sky radiation reflected by the sea surface because the reflection coefficient r, according to the Fresnel formulas, depends on the angle of incidence of the radiation on the reflecting surface. The presence of a wave causes the field of view of the SBP to include portions of the sea surface from which radiation from the sky that falls on the surface at angles other than the Brewster angle is reflected. Such radiation will be polarized on the incidence plane and hence will be missed by the polarizer tuned to suppress the horizontal polarization, thereby increasing the background signal from the sky. The high-frequency component of this signal is determined by wave characteristics and can, generally speaking, be used to measure these characteristics with a spatial resolution determined by the field of view of the SBP setup (in the presented layout this value is 1.1°) and its elevation above sea level (12 m, as a rule). For these parameters, the spatial resolution is 0.7 m.

To reduce the influence of external factors (sea state and sky cloudiness) on the sea brightness signal $Ls(\lambda)$, the instrument measures the brightness ratio at the indicated wavelengths of 440 and 540 nm:

$$I = L_S(440)/L_S(540) \tag{4}$$

Measurements carried out on the breakwater of the Feodosiya port at stationary placement of SBP showed that such a technique allows reducing the influence of the wave by about 3 times [32].

A number of in-situ marine experiments were performed with the SBP setup to investigate various HDD: when stationary on the breakwater and from the shipboard [22, 23, 30, 31].

3.2 Experiments on the Breakwater

During full-scale marine experiments on a breakwater at a stationary placement of the SBP setup, measurements of the sea brightness ratio I were made [31, 32]. The SBP was located at a height of 8 m above sea level at a distance of about 500 m from the shore. A jet from a submersible pump with a flow rate of 18 m^3/h was used as a HDD source. When the jet was horizontal at a depth of 0.2 m, the signal ratio had a value of $I = 0.98 \pm 0.02$, whereas when there was no jet, this value was $I = 1.33 \pm 0.06$. Thus, the presence of a submerged jet resulted in a 30% change in the I ratio, which indicates a change in the stratification of phytoplankton and suspended sediment, when more transparent water that weakly dissipates the radiation falling on them from the Sun and sky enters the near-surface water layers under the influence of the jet.

In addition, it follows from the measurements that the registered fluctuations of sea brightnesses at wavelengths 440 nm and 540 nm (channels A and B, respectively) were about 10%. The fluctuations in the brightness ratio I were about 3%. Thus, this approach makes it possible to reduce the influence of waves on the useful (informative) signal coming from the near-surface layers of the sea and allows one to investigate the HDPs by changes in the optical properties of the near-surface layers of the sea.

The fluctuations of the SBP signals are also related to the "lensing effect" caused by waves: due to refraction of radiation from the Sun and the sky on the excited sea surface, nonstationary light fields arise in the nearrsurface sea layer [33]. This radiation, scattered on optical inhomogeneities (phytoplankton and inorganic suspended matter), is secondary refracted on the excited sea surface and enters the SBP as a fluctuating signal.

3.3 Experiments on Detecting HDD in the Form of a ship's Trace

In addition, full-scale studies were carried out in which the SBP setup was mounted on board the RV (Fig. 10). At the same time, it was located at a height of 12 m. In addition to the SBP setup, the setup of the Aerosol Lidar (AL) was also used in these experiments, whose description is given below. All instruments were mounted on a stabilizing device to reduce the influence of ship's rocking (Fig. 10). The RV was moving at a speed of about 6 knots during the measurements. In some episodes, the sea area under study was photographed from the International Space Station (ISS) [25].

The launcher of the HDD was a large hydrographic boat BGK-889 of 120 ton displacement. It created a surface trace moving at a speed of about 6 knots. In the course of the experiments, RV with setups crossed the track of BGK-889. Signals were recorded before and after crossing the trace (background section), as well as in the trace area. Experimental field studies were conducted in the Black Sea with sea state up to 3 points.

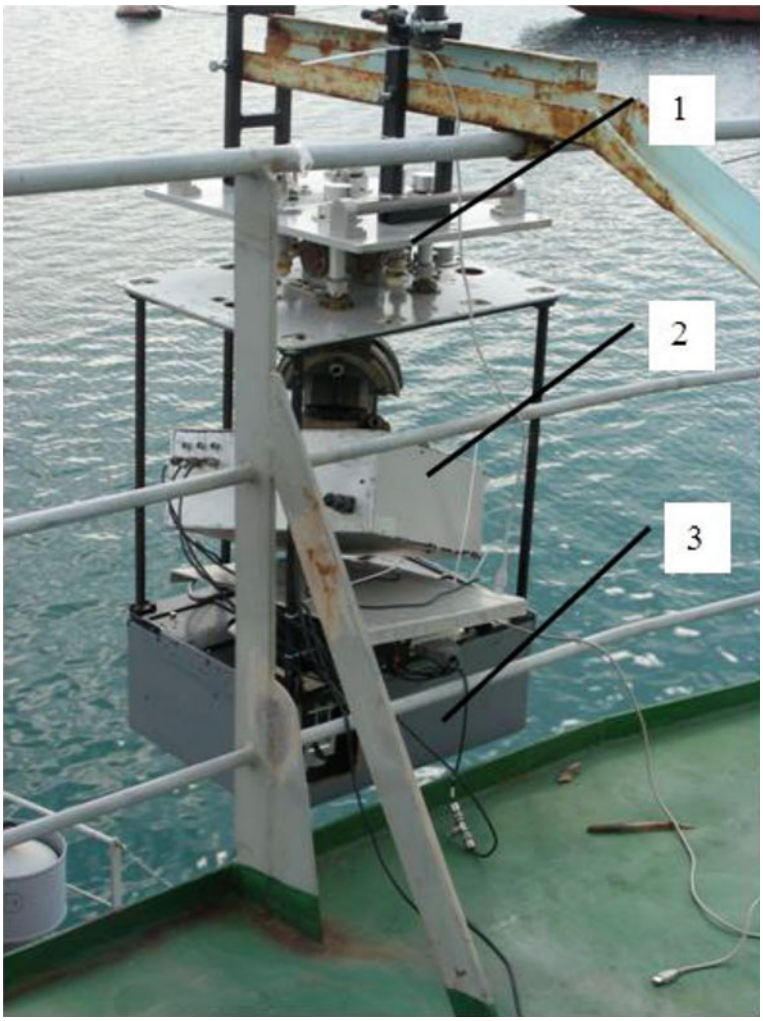

Fig. 10 Placement of SBP (2) and AL (3) setups onboard the RV in a rack with a stabilizing device (1)

When processing SBP signals, average values were calculated for each two hundred signals of the analog-to-digital converter (ADC) operating at a digitization frequency of 10 kHz. Figure 11a and b shows histograms of signal amplitudes of channel A(440 nm), which are proportional to the sea brightness at wavelength of 440 nm, at time intervals outside and in the area of crossing the boat track of BGK-889.

The histogram data indicate a shift of SBP signal amplitudes towards lower values in the boat trace area. Such behavior of signals can be explained by displacement of upper more turbid water layers from the sea surface to greater depths under the action of the boat hull and their replacement by more transparent lower water layers, which create upward radiation from the sea with less brightness due to weaker scattering of the incident radiation from the Sun and the sky. A similar phenomenon, as described above, was also observed in experiments on the breakwater with a submerged jet.

3.4 Experiments with RV Own Trace Crossing

As mentioned above, the SBP setup was used in the study of the HDD in the form of the ship's own trace. In the course of the experiments, two crossings of the RV own trace with a displacement of 2000 ton were performed. The age of the trace was 40 min in both cases. The SBP signals were processed by calculating the number of zeros of the high-frequency component of the signal ratio $Ls(440)/Ls(540)$ for a given time. The obtained dependences are presented in Fig. 12 for two crossings of the RV own turbulence trace.

For two moments of the RV own trace crossing time, a decrease in the number of zeros of the high-frequency component of the SBP signal ratio is observed. This indicates changes in distribution of near-surface phytoplankton or suspended solids under the influence of the HDD from the ship, when strong mixing of near-surface water layers takes place. In this case the natural “patchiness” of phytoplankton and suspended sediment distribution is disturbed, and their

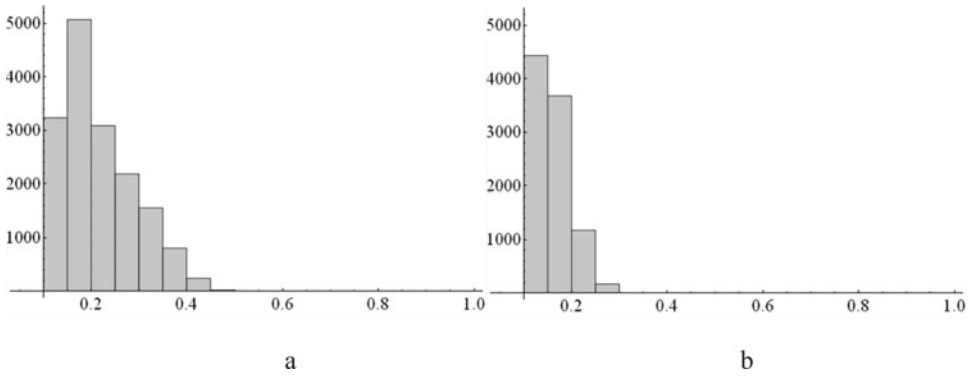

Fig. 11 SBP amplitude histograms in channel A (440 nm) over a time interval of 6 s: **a** outside the boat track and **b** when crossing the boat track [12]

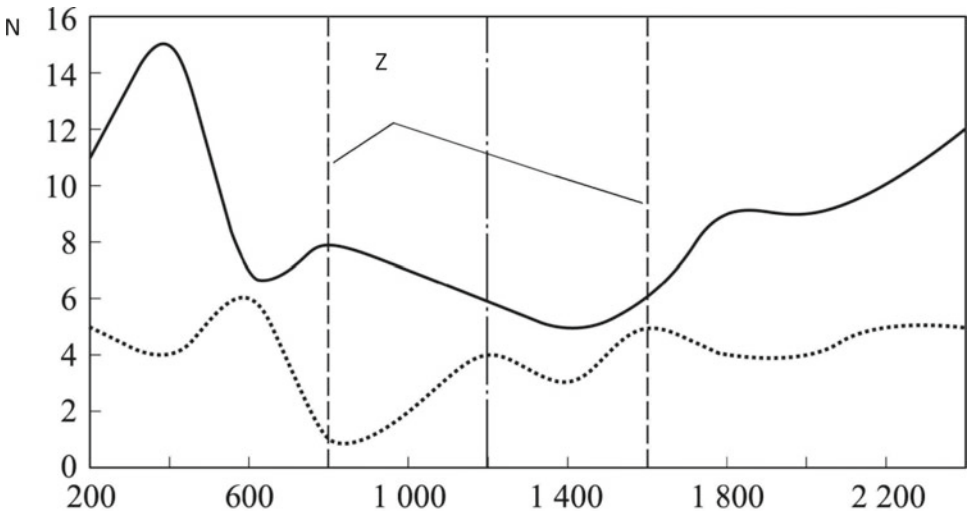

Fig. 12 Dependence of number of zeros no. of high-frequency component of signal ratio *Ls* (440)/*Ls*(540) on RV movement time for two crossings of RV own trace. X—spatial scale in meters, Z—trace area [32]

distribution becomes more homogeneous. Besides, it is also possible that relatively long-lasting "smoothing" of the sea surface itself also influences, resulting in reduction of the number of bright highlights in the radiation of the Sun and the sky reflected from the sea surface. This radiation is not completely suppressed by the polarizer and partially enters the SBP measurement channel, which can also reduce the fluctuations of the SBP signals.

The spatial scale of changes in the parameters of the fluctuations of the SBP signals (about 600–800 m) agrees quite well with the estimate of the transverse size of the turbulent part of the RV trace, made on the basis of photographs obtained from the International Space Station (ISS).

4 Aerosol Scattering Method

4.1 Experiments on the Breakwater

The dependence of the aerosol concentration in the driven atmospheric layer on the processes occurring in the marine strata was recorded in some in-situ experiments. In [34], a change in the scattering properties of the atmosphere above the bottom ledge streamlined by the sea current was observed. In [35, 36], the height distribution of aerosol concentration in the shelf zone was measured using lidar. Based on the data obtained in these works, it was concluded that the aerosol concentration can be influenced by the bottom topography, wave breaking, and wind speed.

Gas bubbles are always present in the near-surface layer of the marine environment. The impact of HDDs, as a rule, leads to the release of these bubbles into the atmosphere, which changes the existing "background" concentration and disperse composition of aerosols above the water surface [37, 38]. This changes the optical properties of the driven aerosol. Aerosol lidars placed onboard the RV can be used to detect areas with changed optical properties.

Using the developed setup of a laser unit based on a continuous laser with a wavelength of 808 nm and a power of 4 W, the altitude distribution of the aerosol scattering intensity near the sea surface was investigated in the presence and absence of HDDs in the near-surface layer [37]. The HDDs was generated by the jets from three pumps with a total capacity of 45 m^3/h. The outlet nozzles of the pumps were located horizontally at a depth of 0.5 m from the water surface and could be adjusted in height.

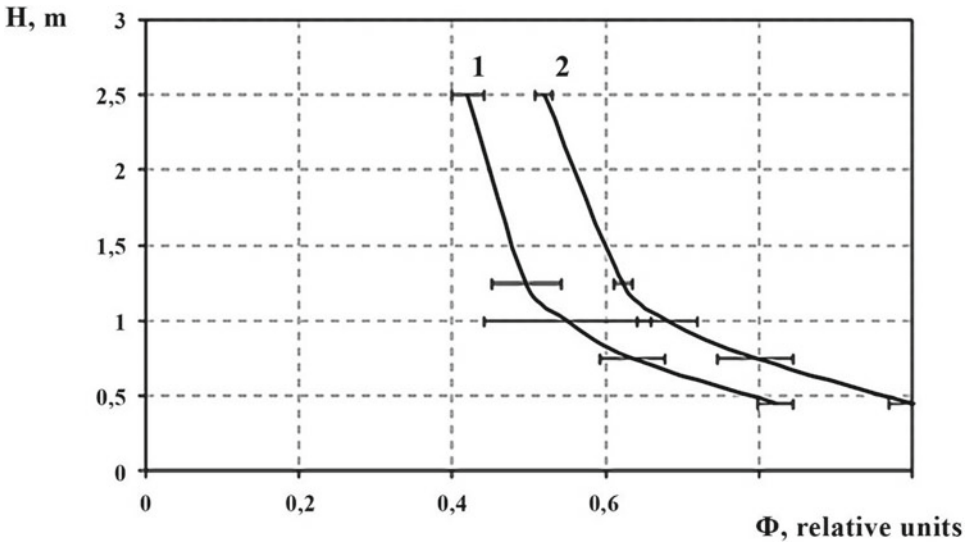

Fig. 13 Averaged altitude profiles of scattered radiation flux Φ [37]. 1—in absence of hydrodynamic disturbance, 2—under hydrodynamic disturbance. H—altitude above sea level, F—mean scattered flux in arbitrary units

Relative changes in the aerosol scattering signal above the pump jets at heights up to 2.5 m were recorded.

During the experiments, the wind had a stable direction and speed of about 1 m/s. Figure 13 shows the obtained dependences of the normalized to maximum mean scattered radiation flux Φ on the height H above the water surface.

The horizontal bars mark the boundaries of variation of the measured value Φ along the ensemble of obtained altitude scattering profiles.

We see that the dependence of the scattered radiation flux on height in both cases is monotonically decreasing. In this case, curves (1) and (2) are located strictly one below the other for the same height in the whole range of heights realized in this experiment. Such a character of their mutual location indicates the effect of increasing the flux scattered from the driving aerosol of laser radiation in the presence of hydrodynamic perturbation of the marine environment. It can be assumed that this is associated with an increase in the intensity of the release of gas contained in the liquid under the action of the sea medium perturbation jets. The formed bubbles rise upward toward the sea surface and, when released into the atmosphere, burst [39, 40]. Together with the gas, small water particles also enter the atmosphere, on which additional scattering of laser radiation occurs. The relation between the microphysical parameters of aerosol particles and the scattering intensity for coastal smokes is discussed in detail in [41].

4.2 Experiments on Board the RV

An Aerosol Lidar based on a bistatic optical scheme was developed at the Vernadsky Institute RAS for performing marine research. The setup uses a continuous laser with an emission wavelength of 532 nm and a power of 100 mW. Subsequently, the laser has been replaced by a more powerful one with power up to 1 W. The laser emission is interrupted with a frequency of 1.5 kHz. A long-focus receiving mirror lens (focal length 0.8 m, aperture 100 mm) is used in the setup. The scattered radiation is fed through a narrowband interference filter to a photomultiplier tube. Synchronous signal detection is used to suppress solar illumination.

The results of studies of the influence of hydrodynamic perturbations of the marine environment on the optical characteristics of the drive aerosol were obtained during the expedition from board the RV under open sea conditions. The conditions of instrumentation placement are given above in the section devoted to the operation of the SBP setup. In these experiments, as indicated above, the ship itself was used as a source of the HDD of the marine environment. Its backward trace was crossed twice in the process of experimental measurements. To reduce the influence of possible aerosol emissions from the research ship itself on the received signal, the area of aerosol scattering registration was moved forward along the ship's course.

Figure 14 shows the time dependence of the laser scattering intensity when the RV moves at a speed of 6 knots in the area of two intersections of its trace with an age of about 40 min.

It can be seen that over the lagging ship's trace there is some decrease in the scattering of laser radiation on the aerosol with respect to its background values. This effect is observed both at the first and at the second crossing of the ship's trace. The results obtained show that, above the region of intense hydrodynamic disturbances of the marine environment, the scattering of laser radiation on the driving aerosol can not only increase, as established in [37], but also decrease.

The scattering reduction effect can be explained by the fact that the trailing ship trace, which represents a longglived

hydrodynamic disturbance of the marine medium, was crossed after a very considerable time (about 40 min) from its formation. During this time, the possibility of generating a sufficiently large number of new gas bubbles due to the energy of hydrodynamic disturbances was exhausted, which led to a decrease in further particle emission. On the contrary, in the experiments at the breakwater [37], where an increase in scattering was observed, measurements were carried out during the operation of pumps generating jets coming to the surface. Since the aerosol scattering over the outgoing jets was recorded for a very short time interval, the gas dissolved in the liquid was sufficient to maintain the process of intense bubble formation and emission of aerosol particles into the drive layer of the atmosphere during the entire experiment.

4.3 Statistical Processing of Aerosol Scattering Data

Some statistical methods of analysis can also be used to increase the probability of detecting a HDDs. Figures 15 and 16 show empirical correlation matrix calculated from accumulated data of aerosol lidar signal for consecutive segments of trace crossing of lagging RV own trace. The presented section corresponds to the motion of the RV during two crossings of the lagging self-track. Bright areas (high values $\eta(\Delta_i, \Delta_j)$) correspond to "similarity" of trace sections, dark areas (low values $\eta(\Delta_i, \Delta_j)$) correspond to the difference of these sections. Two areas are clearly identified on the matrix, corresponding to the time of vessel crossing of its own trace (marked by boxes).

The age of the trace at its first crossing was 18 min, and 41 min at the second crossing. For both crossings a symmetric structure of correlation dependences of signals for different segments is traced.

The analysis of the structure of empirical correlation matrices is given below in Sect. 6.

4.4 Statistical Processing Based on Integrated Application of Laser-Optical Equipment Signals

The best way to detect the presence of HDDs can be performed by performing measurements simultaneously using the three laser-optical methods used, followed by processing using the selected statistical method.

The complex application of optical methods of sea surface sounding makes it possible to take into account possible correlation dependences between the signals of different layouts of laser-optical equipment (LOE). In this case the subject of the analysis are samples from three-dimensional vectors of $\vec{X} = (\mathrm{S}, \mathrm{L}, \mathrm{F})$ LOE signals (let us denote by S—any Scanner Laser Locator characteristic, by L—Aerosol Lidar, by F—Sea Brightness Photometer). The differences between trace segments without and with anomalies are determined by methods of multivariate statistical comparison of samples of complex signals $\vec{X}_{1\phi}, \ldots, \vec{X}_{n\phi}$, and $\vec{X}_{1a}, \ldots, \vec{X}_{ma}$, extracted from these segments. In particular, a convenient tool of such analysis is the statistical criterion of rank sums of homogeneity check of two multivariate samples. It is described in detail in [42].

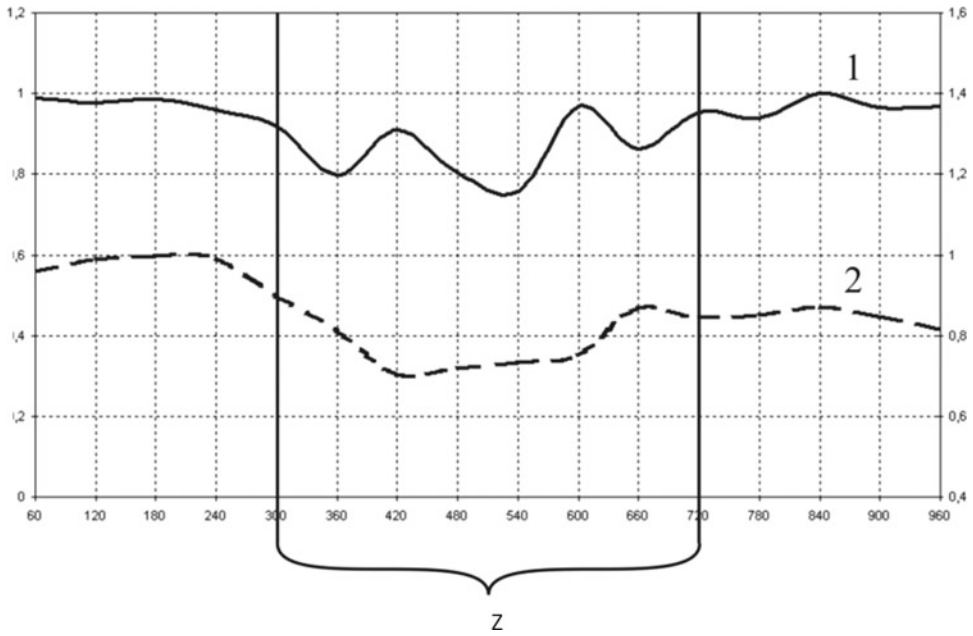

Fig. 14 Time dependence of the intensity (I) of the aerosol scattering signal in arbitrary units during two crossings of the RV own track. Curve 1—transect 1 (left scale), curve 2—transect 2 (right scale). t—time in seconds, Z—trace area [38]

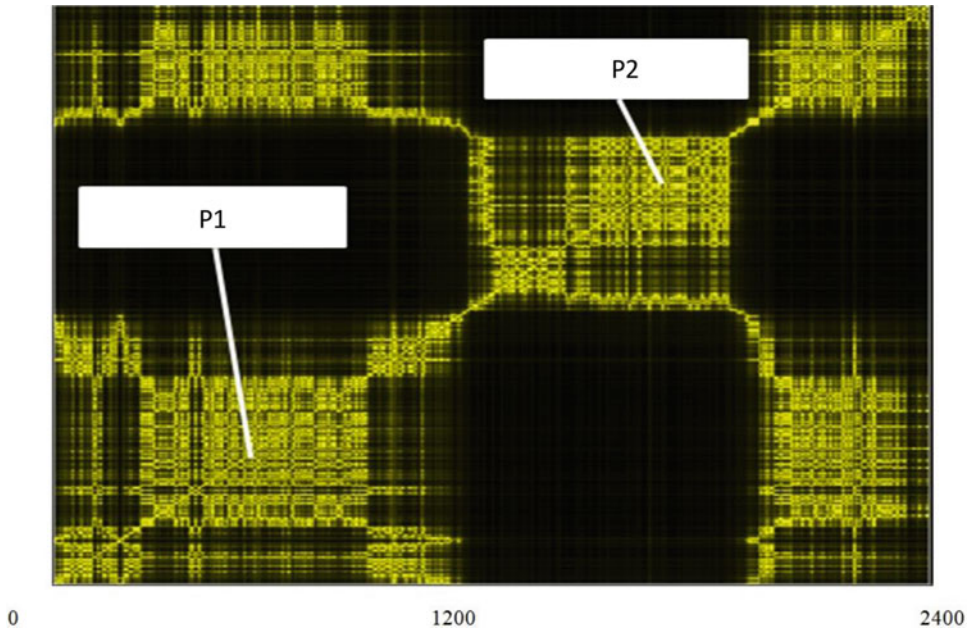

Fig. 15 Empirical correlation relation matrix calculated from the accumulated aerosol lidar signal data during the RV movement in the P1 and P2 intersection area. Time in seconds is plotted along the axes [11]

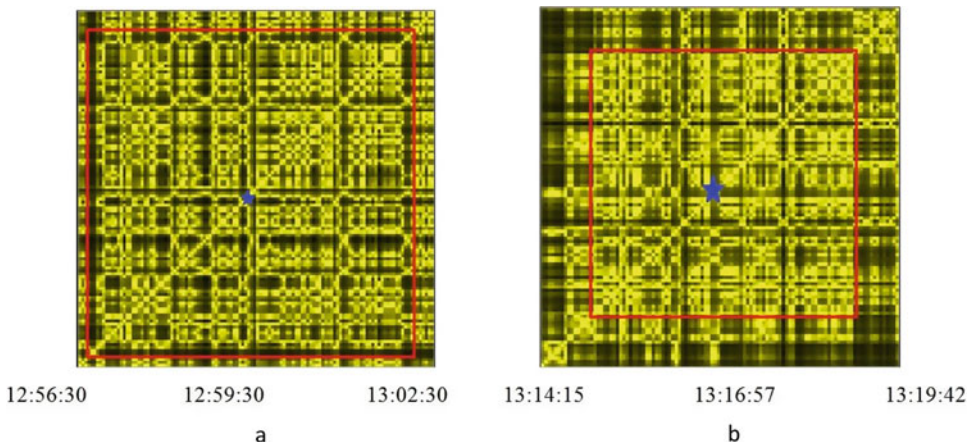

Fig. 16 Empirical correlation relation matrices calculated in the vicinity of the first (**a**) and second (**b**) intersections of the lagged RV eigen foot print. The current time is plotted along the axes [11]

The statistic of the criterion is

$$U^* = N^{-1}U'(V)^{-1}U = U'(NV)^{-1}U \qquad (5)$$

Here $U_i = \sum_{t=1}^{n}\left[\frac{R_{it}}{N+1} - \frac{1}{2}\right]$, $U' = (U_1, U_2, U_3)$.

R_{it}—is the rank of the ith component $\vec{X}_{t\phi}$ in the combined sample of ith components of all vectors $\vec{X}_{1\phi}, \ldots, \vec{X}_{n\phi}$, and $\vec{X}_{1a}, \ldots, \vec{X}_{ma}$.

The elements of the sample covariance matrix V are

$$\widehat{v}_{ii} = \frac{mn}{12N(N+1)}$$

$$\widehat{v}_{ij} = \frac{mn}{N^2(N-1)(N+1)^2}\left[\sum_{t=1}^{N} R_{it}R_{jt} - \frac{N(N+1)^2}{4}\right].$$

If the statistic (5) takes large values, it indicates a difference in the structures of the two samples, i.e. the presence of anomalies in one of the segments.

Figure 17 shows a plot of the values of the rank sum statistics for samples from successive segments of the trace trace intersection of the lagged RV trace (the plot was constructed using data different from those used to construct the correlation matrices). These samples were compared with a single sample extracted from the background trace segment. The figure clearly shows the peak of the plot, coinciding with the moment when the RV crosses its lagged own trace.

An important, in our opinion, additional gain in increasing the efficiency of solving the problem of detecting the influence of HDDs on the marine environment is that the integrated application of optical methods of sensing the sea

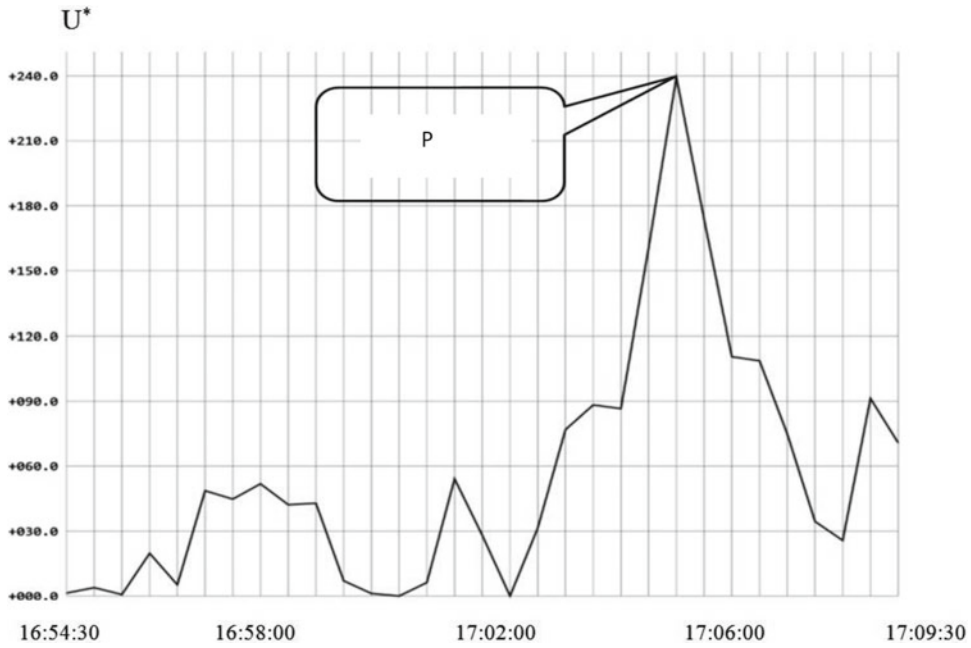

Fig. 17 Plot of the time dependences of the values of the rank sum statistics calculated at the intersection of the lagged RV own trace (P). t—current time [11]

surface and the near-surface layers of the marine environment and the atmosphere can provide remote detection of hydrodynamic disturbances with significantly less dependence on hydrometeorological conditions. Each of the system channels has a certain range of hydrometeorological conditions, in which its data are reliable. In this case, knowing limits of possibilities of each method, it is possible to increase efficiency of the whole system due to combination of channels. In-situ experimental studies with the use of LOE complex of three setups confirmed the correctness of the proposed concept [11].

5 Model Laboratory Experiments on Aerosol Scattering

Under marine conditions, aerosol particles above the sea surface are produced by the collapse of air bubbles produced by wave collapse, gas release or HDP effects. This produces a small number of large particles that quickly settle and many small "film-like" particles that are long-lived and can be carried long distances by the wind [39, 40].

We have carried out model laboratory experimental studies of the influence of HDP of various types on the intensity of laser radiation scattering in the driving layer of the atmosphere. The experiments were carried out in trays with flowing and non-flowing aerated water. Hydrodynamic disturbances were created by an obstacle at the bottom of the tray, the current and rotating propellers [43–45].

5.1 Experiments in a Non-flowing Tray Under Water Disturbance by Propellers

As shown by numerical calculations performed by other authors, for small particles the intensity of elastic scattering of optical radiation is proportional to the particle size [8, 41]. This is true for a certain ratio of aerosol particle size and incident radiation wavelength, when the value ρ of the "relative size" of the aerosol particle is less than 4:

$$\rho = 2\pi a/\lambda < 4$$

Here a-radius of the particle, λ-wavelength of the incident laser radiation. For the wavelength of radiation of the laser we used (660 nm) the value of the maximum particle diameter, when the above relationship is fulfilled, is estimated to be 0.8 μm.

In our experiments, when aqueous flow is aerated, mainly bubbles 1–2 mm in size are formed. In [46], it was experimentally established that aerosol particles having characteristic sizes of 0.1–0.3 μm are formed when air bubbles with a diameter of 1–2 mm are bubbled through water. On this basis, we believe that aerosol particles of the same diameters are formed in the experiments conducted. On this basis, it can be assumed that the observed laser scattering signals are proportional to the sizes of aerosol particles. For this reason, histograms of scattering signal amplitudes appear to be equivalent to the aerosol particle size distribution.

It should be noted that above the sea surface aerosol particles in the absence of strong wind have basically the

same dimensions of 0.1–0.3 μm [39, 40, 46], which makes the performed model experiments correct from the point of view of transferring their results to marine conditions.

Two water trays were used for the experiments, a non-flow and a flow-through with flow.

The unit with a non-flow tray used the rotation of two propellers from a ship model (Fig. 18) to generate HDD.

Experiments on investigating the influence of HDD on the intensity of laser radiation scattering on the driven aerosol were carried out at aeration of water in the tray, carried out by pumping air through the ceramic rods lying at the bottom of the tray. The experimental setup is described in detail in [43]. The laser beam was propagated along the water surface at a height of 50 mm. Measurements were performed by recording the intensity of scattering of laser radiation on individual aerosol particles when they fell into the focal region of the lens. The signal recording time was 300 s. Measurements were performed 3 times and then the obtained data were averaged. The processing was carried out within the Excel program. During signal processing, averaging was carried out according to 5 discrete measurements of the analog-to-digital converter (ADC), which performed digitization of the signal with a frequency of 12.5 kHz. In order to reduce the file volume, large pulse amplitudes (up to 2.5 V) were cut off, since there were very few such pulses. After that, histograms of amplitude distribution of aerosol scattering signals normalized to the total number of ADC digitizing pulses were constructed with a step of 2.5 mV. This number of pulses, in turn, is proportional to the total number of aerosol particles that entered the focal zone of the lens during the measurement time. Further, the difference histograms were plotted for measurements without and in the presence of HDDs. For the convenience in comparing the results, all histograms were multiplied by the multiplier 10^6.

It turned out that the rotation speed of the propellers significantly affects the dispersion composition of aerosols above the disturbance zone in water. Figure 19 shows typical normalized histograms of the amplitudes of aerosol scattering signals for the HDDs in the form of propellers at their different rotation speed, which differed by a factor of 1.3.

One can see from the presented data that the HDD in the form of propellers leads to a noticeable change in the shape of histograms of aerosol scattering signal amplitudes. This indicates a change in the dispersed composition of aerosols under the influence of such HDD on the aquatic environment. The obtained distributions of amplitudes of the registered scattering signals also noticeably change with a change in the rotation speed of propellers. In the case of higher rotation speed, a larger number of larger particles is formed, since the maximum of the difference histogram is observed at larger signal amplitudes compared to the minimum. For lower rotation speed of the propellers, the location of the maximum and minimum of the difference histogram is reversed, i.e., in this case, more fine particles are formed under the influence of HDD from the propellers than in the absence of HDD.

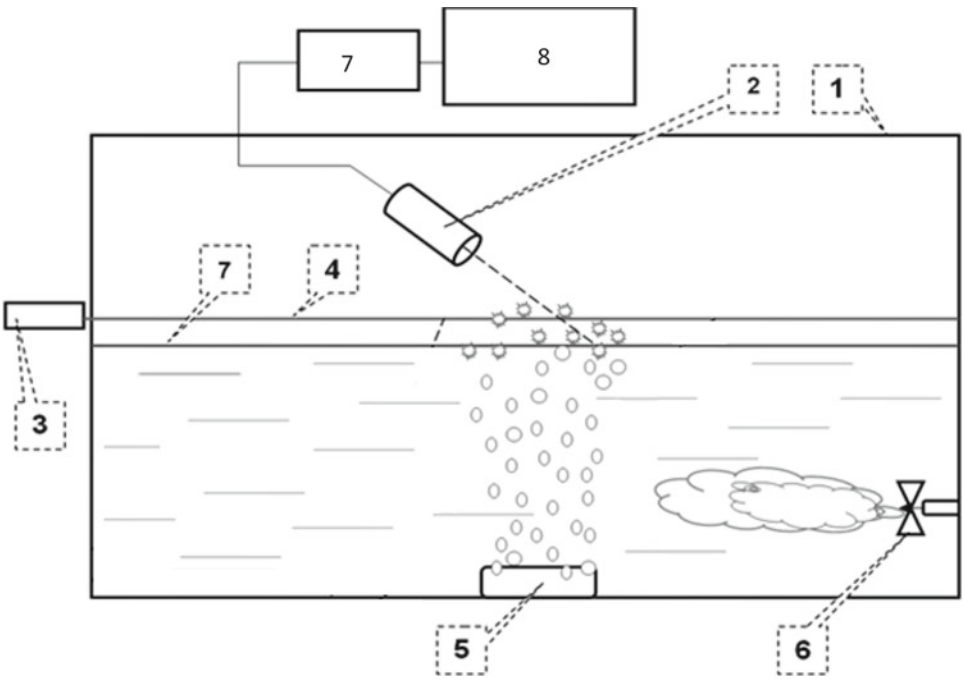

Fig. 18 Schematic of laboratory setup with a nonflowing tray. 1—tray; 2—objective lens with photomultiplier tube; 3—laser emitter (λ = 660 nm); 4—laser beam; 5—aerator; 6—turbulent flow generator (propellers); 7—water surface; 8—ADC; 9—laptop [43]

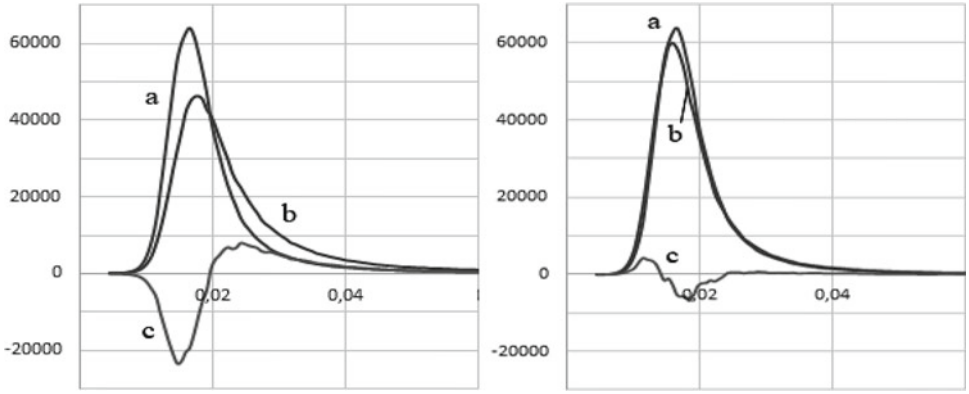

Fig. 19 Normalized histograms of aerosol scattering signal amplitudes without the influence of HDD—(**a**), when water is disturbed by propellers—(**b**) and their difference—(**c**). The left figure refers to higher propeller rotation speed than the right figure. The amplitudes of signals in volts are plotted along the OX axis [43]

5.2 Experiments in the Flow Tray

5.2.1 Underwater Obstacle Experiments

The experiments were also carried out in a flow tray [43]. A smooth profile hump at the bottom of the tray was used as a source of disturbance.

Water from the water supply system was supplied to the flowing tray through a comb with holes. Aeration of water in this case was carried out by feeding air from a compressor into the comb. The water flowed out from the opposite end of the tray, which ensured constant flow with a certain speed in the tray. In order to perturb the water flow, an underwater barrier was installed at the bottom of the tray. The distance from the top of the obstacle to the water surface was 40–50 mm. Measurements of aerosol scattering were performed at several positions of the barrier, which was shifted horizontally in 5 cm steps in the direction of the flow. The position of the registration zone determined by the focal area of the objective lens did not change.

Figure 20 shows normalized histograms of signals in the absence of an obstacle and in its presence, as well as the difference of these histograms at the position of an underwater obstacle, which had the maximum influence on the histogram of amplitudes of aerosol scattering pulses.

It can be seen that the presence of an obstacle under water leads to the formation of aerosol particles with larger sizes above the obstacle. For different positions of the obstacle, the dependence of the spread of the normalized histogram differences (the difference between the maximum and minimum values) was obtained [43]. It turned out that there is a significant dependence of the aerosol particle size distribution on the location above the underwater obstacle: the spread value changes by a factor of 5.

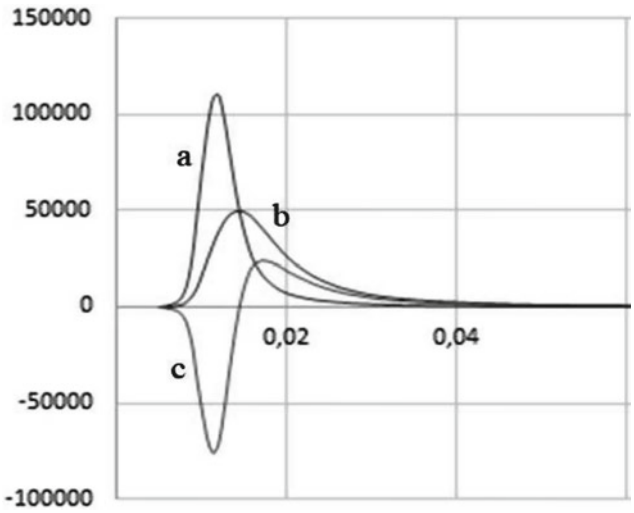

Fig. 20 Normalized histograms of amplitudes of aerosol scattering signals without disturbance of water flow by a barrier (**a**), when water flow is disturbed by a barrier (**b**), and their difference (**c**). Signal amplitudes in volts are plotted along the OX axis [43]

5.2.2 Experiments with Counter Flow

An experiment on recording aerosol scattering near the water surface in the presence of a counter flow and stream generated by a propeller was performed in a flow tray. A 35 mm diameter propeller was submerged to a depth of 60 mm and offset 300 mm downstream from the focal area of the lens from which the scattering was collected. The experimental setup is described in detail in [44, 45].

Figures 18 and 19 show the main results obtained on changes in aerosol size distribution under the action of HDD from the propeller and oncoming stream. Here, as indicated above, we take into account that for aerosol particles with a diameter of 0.1–0.3 μm the scattering intensity is

proportional to the particle size. The amplitude of pulses from the photodetector, in turn, is proportional to the intensity of the radiation scattered on aerosols falling on it.

Figure 21 shows a comparison of experiments in the presence of flow, when the joint effect of HDD from the propeller and aeration on the particle size distribution is manifested.

In this case, the HDD from the propeller and the presence of flow aeration leads to an increase in the number of particles with large sizes.

Figure 22 shows experiments where the effect of HDD from a propeller directing the flow against on particle distribution in the presence of flow with aeration is investigated.

The data shown in Fig. 22 show that for the flow with aeration, the presence of HDD from the propeller, as in the previous case, leads to an increase in the number of "film" particles with larger sizes.

5.2.3 Discussion of Results and Conclusions

The difference in histograms reflects the redistribution of aerosol particles by size in the presence of HDD and its absence. The obtained data indicate that the addition to the aerated flow HDD in the form of a propeller operating against the flow leads to a change in the distribution of aerosol particles towards larger sizes. The observed redistribution may be related to the appearance of turbulence in the water motion caused by the propeller impact on the laminar flow, which possibly affects the process of bubble collapse. This phenomenon has not been investigated theoretically before.

The presented experimental data testify to the possibility of studying under laboratory conditions the effect of various HDDs on the process of aerosol formation over the water surface using the method of laser scattering on aerosol particles. To estimate absolute values of aerosol particle sizes, it

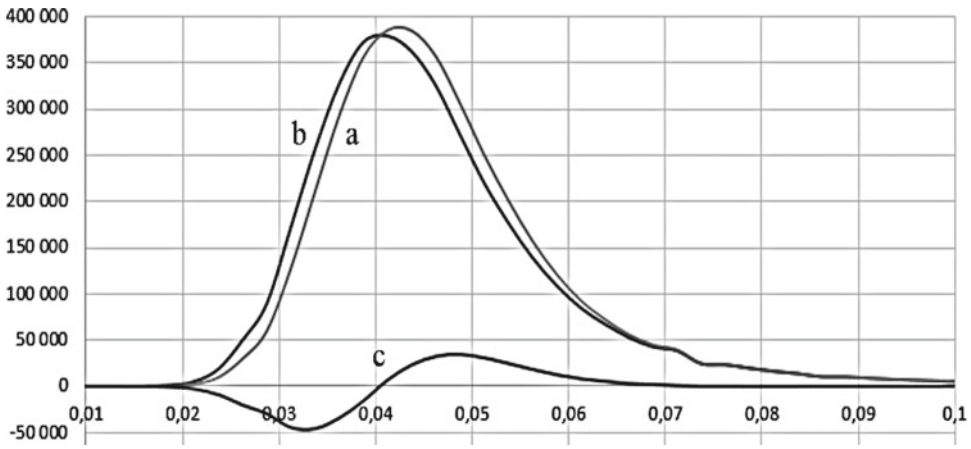

Fig. 21 "Signal" histogram of signal amplitudes in the presence of flow, screw and aeration—(**a**); "background" histogram of signal amplitudes in the presence of stream only—(**b**); difference of "signal-background" histograms—(**c**). The signal amplitudes in volts are plotted along the OX axis [45]

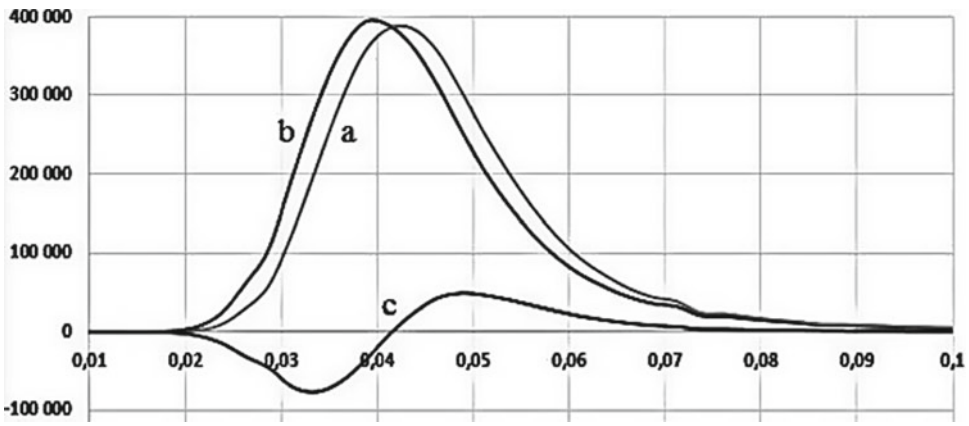

Fig. 22 "Signal" histogram of signal amplitudes in the presence of flow, screw and aeration—(**a**); "background" histogram of signal amplitudes in the presence of stream and aeration—(**b**); difference of "signal-phone" histograms—(**c**). The signal amplitudes in volts are plotted along the OX axis [45]

is necessary to use numerical calculations based on Mie scattering theory [8].

The obtained data can be used in full-scale experimental studies on registration of manifestations of different HDPs in the atmospheric drive layer.

6 Algorithms of Anomalies Detection in Laser-Optical Equipment Signals, Caused by HDD Influence

Different algorithms of information processing (both known and original) designed for identification of anomalous manifestations on the sea surface as well as in its near-surface layers were used in processing the results of laser-optical equipment (LOE) signal measurements. They can be conventionally divided into two groups:

- the first group—is intended for transformation of the initial signal of LOE devices to the form necessary for their statistical processing;
- the second group is designed for statistical analysis of the obtained data and making a decision on the presence or absence of anomalies (algorithms of multivariate statistical analysis, correlation analysis, cluster analysis, spectral analysis and time series analysis);

For all algorithms, software was developed to implement them.

6.1 Scanning Laser Locator (SLL)

As an example of the first group algorithm, Fig. 23 shows the pulse generation scheme from the SLL signal. The figure shows the SLL signal (broken line), the upper and lower envelopes of the signal, the middle line of the two envelopes, the threshold line (dotted line), above which the SLL signal forms a pulse. Comparison of pulse flux characteristics (amplitude, interval between them, pulse duration, angle of laser beam reflection from the surface and others) in different sections of the LOE carrier trace allows finding HDD in the near-surface layers of the marine environment.

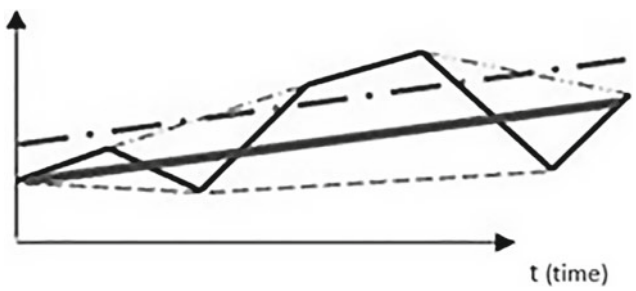

Fig. 23 Pulse generation from SLL signal

Figure 24 shows a typical realization of the averaged SLL characteristic—the angle of reflection from the sea surface (averaging interval is 1 s) in one of the above-described experiments on the vessel crossing its own trace. The moments of crossings of the lateral and turbulent components of the vessel's trace are clearly distinguished on the registergram.

The average value of the signal $x(t)$ in Fig. 24 is shown by a yellow line, the green line is the value of the value $x(t) + 2\sigma$, where σ is the standard deviation of the signal calculated from the averaging segment.

Anomaly detection—signal binarization method

For automated anomaly identification, an algorithm for SLL signal binarization was developed that compares the signs of SLL signal increments in the vicinity of SLL carrier trace points. The algorithm provides binarization of the signal by the formula

$$\Delta X_i = \left\{ \begin{array}{ll} sign\,(X_i - X_{i-1}), & |X_i - X_{i-1}| > \delta \\ 0, & |X_i - X_{i-1}| < \delta \end{array} \right\},$$

where δ—binarization threshold (sensitivity threshold).

Functional statistics is determined by the formula

$$S(t_j) = \sum_{i=h}^{H} \left(\Delta X_{j+i} + \Delta X_{j-i}\right),$$

where $H + h + 1 < j < n - H - h$.

Here h is the width of the indent area, H—the width of the working area.

The application of this method in many cases makes it possible to level the influence of SLL performance outliers caused by hardware interference, as well as changes in meteorological conditions during the experiments.

Figure 25 shows the results of SLL signal processing performed according to the algorithm described above. The visualization matrix of statistic values $S(t)$ is given, in which large statistic values correspond to light tones of rectangles, with the bases on the time axis. The section of the SLL signal corresponding to the lateral components of the ship's track is clearly distinguished.

Detecting anomalies—applying a correlation relationship

The time interval under study is $[t_0\,,\,t_n]$ divided into intervals $\Delta_1 = [t_0\,,\,t_1]$, $\Delta_2 = [t_1\,,\,t_2]$, ..., $\Delta_n = [t_{n-1}\,,\,t_n]$. For each pair of intervals, we calculate statistics $(\Delta_i\,,\,\Delta_j)S_{ij} = \sqrt{1 - \eta^2(\Delta_i\,,\,\Delta_j)}$ for the values of the selected characteristic of impulses from the SLL signals on these intervals. Here $\eta(\Delta_i\,,\,\Delta_j)$ is correlation ratio of samples from values of

Fig. 24 Registrogram of the averaged angle of SLL signal reflection. t—current time

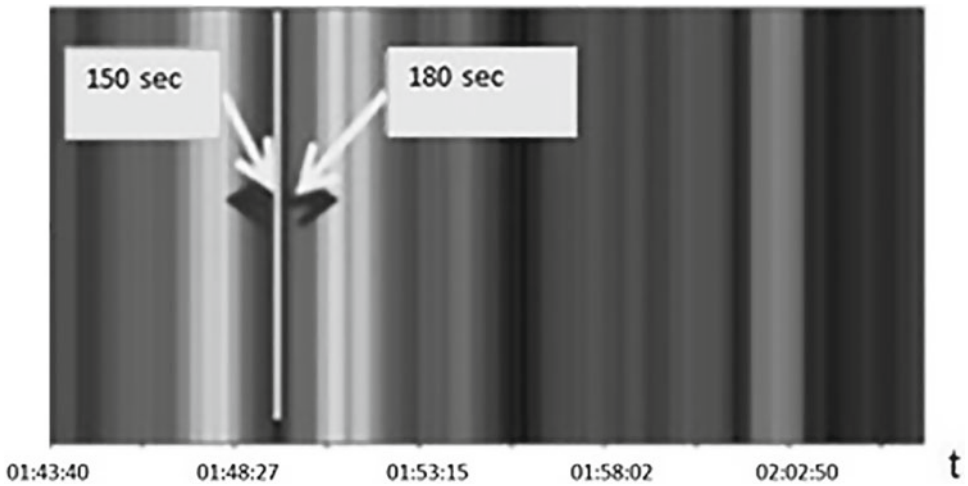

Fig. 25 Identification of lateral components of the ship's track by S(t) values. t—current time

selected characteristic. The closer the values are S_{ij} to 1, the less the difference between the samples. Then we construct a symmetric matrix $S = (s_{ij})$, in which the hue of each element is determined in accordance with the selected scale. The matrix S will be called correlation relation matrix.

Figure 26 shows the matrix S calculated from the data whose registergram is shown in Fig. 24. The arrows indicate the vertical white-tone lines, which correspond to anomalously small values of s_{ij}. The times of occurrence of these anomalies fully correspond to the times of ship crossings of the lateral and turbulent components of the ship track.

In addition to the described methods, other methods were also used in the analysis of SLL signals—comparison of pulse flux intensities at different sea surface areas, spectral analysis of pulse characteristics and others.

6.2 Sea Brightness Photometer (SBP) and Aerosol Lidar (AL)

The difference in the nature of the analyzed information in the signals of SBP and AL from the information in the SLL signals is that for these signals the procedure of pulse streams extraction is not carried out, but the realizations of readings of these devices (subjected to insignificant preliminary processing) are investigated directly. For detection of

Fig. 26 Matrix of correlation relations S. The current time is plotted along the axes

anomalous manifestations in signals standard statistical methods of comparison of readings of devices on various sites of a ship route were applied.

Figure 27 shows the matrices for comparing the ratio of PNM signals at wavelengths of 540 and 440 nm for two sections of the ship's track corresponding to two successive intersections of the lagging own wake of the ship (with lower and higher ages). Each of them consists of three parts —two background (before and after crossing the side components of the ship's wake) and one intermediate (between these components). The passage time for each section was divided into time intervals of 20 s each. Comparison of signal ratios for each pair of intervals $(\Delta_i\,,\,\Delta_j)$ was carried out using statistics χ^2. A symmetric matrix $\chi = (\chi_{ij})$ was built based on the values of the statistics $\chi^2(\Delta_i\,,\,\Delta_j) = \chi^2_{ij}$, in which large values of statistics (indicating a difference in the samples) are highlighted in yellow, otherwise—in blue. The intervals Δ_i are measured from the upper left corner of the matrix. In Fig. 27a, which corresponds to the intersection with a younger age, three time zones of approximately the same size are clearly distinguished. The first and third zones have the same statistical characteristics of signals on the segments Δ_i both inside themselves and among themselves —blue rectangles in the corners of the matrix. These zones correspond to the background portions of the track. The statistical characteristics of the signals on the segments within the second zone are equal to each other (blue rectangle in the center of the matrix), but have significant differences with the same characteristics of the first and third zones (all yellow rectangles). This area corresponds to the portion of the track between the lateral trail intersections. A roughly similar picture is observed in Fig. 27b, which corresponds to the intersection with a greater age.

Figure 27 shows matrices comparing the ratio of SBP signals at wavelengths of 540 and 440 nm for different sections of the ship's path in the experiment with the ship crossing its own trace (for two consecutive crossings). Comparison of signals for each pair of 20-s intervals $(\Delta_i\,,\,\Delta_j)$ was performed using statistics χ^2. A symmetric matrix is constructed $\chi^2(\Delta_i\,,\,\Delta_j) = \chi^2_{ij}\chi = (\chi_{ij})$ using the values of the statistics, in which large values of the statistics (indicating the difference in the samples) are highlighted in white, otherwise—in dark color. The figure clearly shows the area between the lateral components of the vessel track for the first crossing of small age and a similar area (with fuzzy boundaries) for the second crossing of larger age.

Spectral analysis of the signals of the SBP and AL was applied using a similar method—comparing the periodograms of the signals in different sections of the carrier path. Figure 28 shows a graph of AL signal with a linear trend during the time interval of 20 s, 160 s before the intersection of the ship's own track axis. The periodogram of its detrended part has a distinct maximum at relative frequency $\omega = 0,21$, which corresponds to the intersection of the wave (lateral) component of the ship's wake. Periodograms of signals on other time intervals of similar length have a structure with considerably more uniform distribution by signal power frequencies.

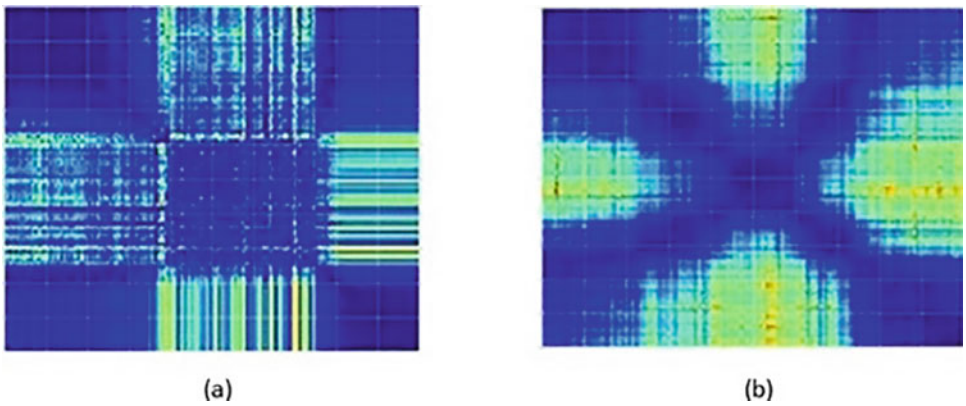

Fig. 27 Visualization matrices of statistical values χ^2 when analysis of the SBP signal ratio for the first (**a**) and second (**c**) crossings of the ship's own track

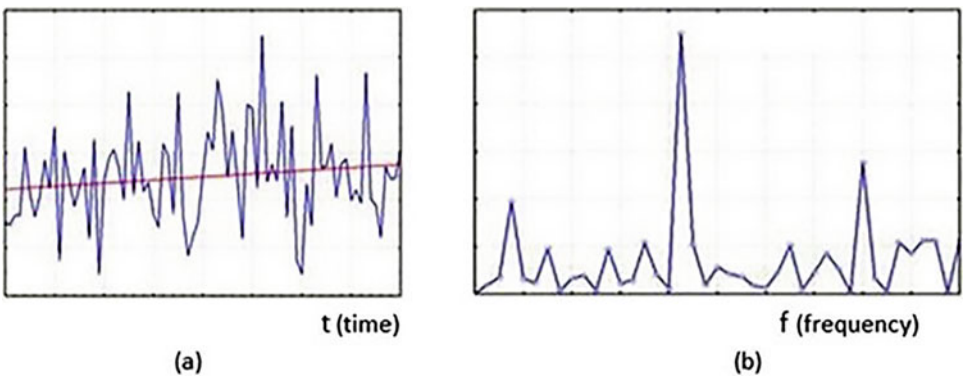

Fig. 28 Plot of the AL signal and its linear trend (**a**); periodogram of its detrended part (**b**)

6.3 Statistical Analysis of Space Images of Sea Surface

The Vernadsky Geochemical Institute of the Russian Academy of Sciences is also working on the analysis of sea surface changes (caused by hydrodynamic processes in the sea strata) identified on sea surface satellite images.

Earth remote sensing (ERS) and the analysis of Earth surface imagery is a high-tech IT activity of great importance in a number of applications [47, 48].

The advantages of the ERS method are as follows [51–53]:

- high speed of obtaining data on a large area of the Earth's surface;
- high accuracy of data processing due to the application of GPS-technologies;
- high informativeness;
- content of more information on images than on maps (except for semantic data);
- economic viability.

At the same time, as noted earlier, when analyzing satellite images of the sea surface (SS), along with the problem of processing huge data sets, many factors affecting the reliability of the conclusions need to be taken into account:

- change in light,
- -Unclear/unambiguous attributes,
- perspective distortion caused by the camera angle;
- the effects of weather and time conditions.

The Vernadsky Institute RAS works consider a slightly different approach to anomaly detection on space images of the sea surface, which differs from the ones presented, for example, in [54, 55] and is intended to minimize the influence of the above factors. It is based on the identification of anomalous regions, having a similar structure, which significantly differs from the structure of the rest of the surface. It does not matter what exactly these structures look like—only their difference is important. In the method, for each sliding fragment in the image, certain statistical characteristics are computed, and then the geometrical configuration of the set of fragments with extreme similarities is checked against the geometrical configuration corresponding to the supposed phenomenon (e.g., ship track). The described procedure is a modification of the method proposed in [56], the difference from which is a significantly smaller amount of necessary calculations.

Description of procedure

In [57, 58], a method of ship trace detection on sea surface images was proposed based on comparison of statistical

characteristics of color intensities (R, G, B) in individual image sections Δ_{ij} , $i = \overline{1,n}$, $j = \overline{1,m}$ (pixel $N = k\,s$ size each) with their values in the whole image ($\Delta = \bigcup_{ij} \Delta_{ij}$ or in the image of the background section). It was proposed to use correlation coefficients of indicator gradients $Xr\,(grad\,X(\,\alpha),\ grad\,X(\beta)) = r(\alpha, \beta)$ (rates of change X) in directions making angles α, β with fixed axis (e.g. horizontal axis of the image) as statistical characteristics. For the sake of brevity, the gradient is the derivative in the corresponding direction (i.e., a scalar). A characteristic X may be an intensity of some colour, the main component of these intensities, or another parameter. The velocity $grad\,X(\omega,\ \alpha)$ for a particular pixel ω in a direction α is calculated using standard differential operators [50], the estimates of correlation coefficients over the section Δ_{ij} , $i = \overline{1,n}$, $j = \overline{1,m}$ are computed using a set of vectors $(grad\,X(\omega_{rt}, \alpha),\ grad\,X(\omega_{rt}, \beta))$, $\omega_{rt} \in \Delta_{ij}, r = \overline{1,k},\ t = \overline{1,s}$.. The statistics [47] was used α, β as a function to compare the correlation coefficients and $r_{ij}(\alpha, \beta)$ $\overline{r}(\alpha, \beta)$ respectively on the plot Δ_{ij} and the whole image Δ in the directions:

$$Z_{ij}\,(\alpha,\ \beta) = \frac{Arth\ (\overline{r}(\alpha, \beta)) - Arth\,(\,r_{ij}(\alpha, \beta))}{1/\sqrt{N-3}}, \qquad (6)$$

where $Arth(x) = \frac{1}{2}\ \ln \frac{1+x}{1-x}$ is the arctangent hyperbolic x.

It was shown empirically in [58] that, depending on the choice of α and β, one can obtain either significant differences in the coefficients $r_{ij}(\alpha, \beta)$ and $\overline{r}(\alpha, \beta)$ on the areas of Δ_{ij}, located on one or two lateral components of the trace, or no significant differences on all Δ_{ij}.

Figure 29a shows the averaged structure of the ship's track with parameters that are weakly dependent on its speed (the angle between the lateral lines of the track, pitch angles of longitudinal waves to the track axis, longitudinal and transverse wave lengths). Based on this model, the method of identifying track lateral lines was based on the extraction of image fragments with the highest modulo values of statistic (6) for all possible pairs of directions shown in Fig. 29b. As an example of the adequacy of the method, Fig. 29c and d show, respectively, a test image of the sea surface (with the horizontal axis of the footprint) and the infogram of values (6) for a fixed pair of directions ($\alpha = 26°,\ \beta = 180°$ here and below the angles are counted from the positive direction of the abscissa axis). In Fig. 29d, the left lateral line of the ship track is clearly identified.

Let us clarify that an infogram is a digital representation of an image, each pixel of which is colored in accordance with a certain scale corresponding to the values of statistics

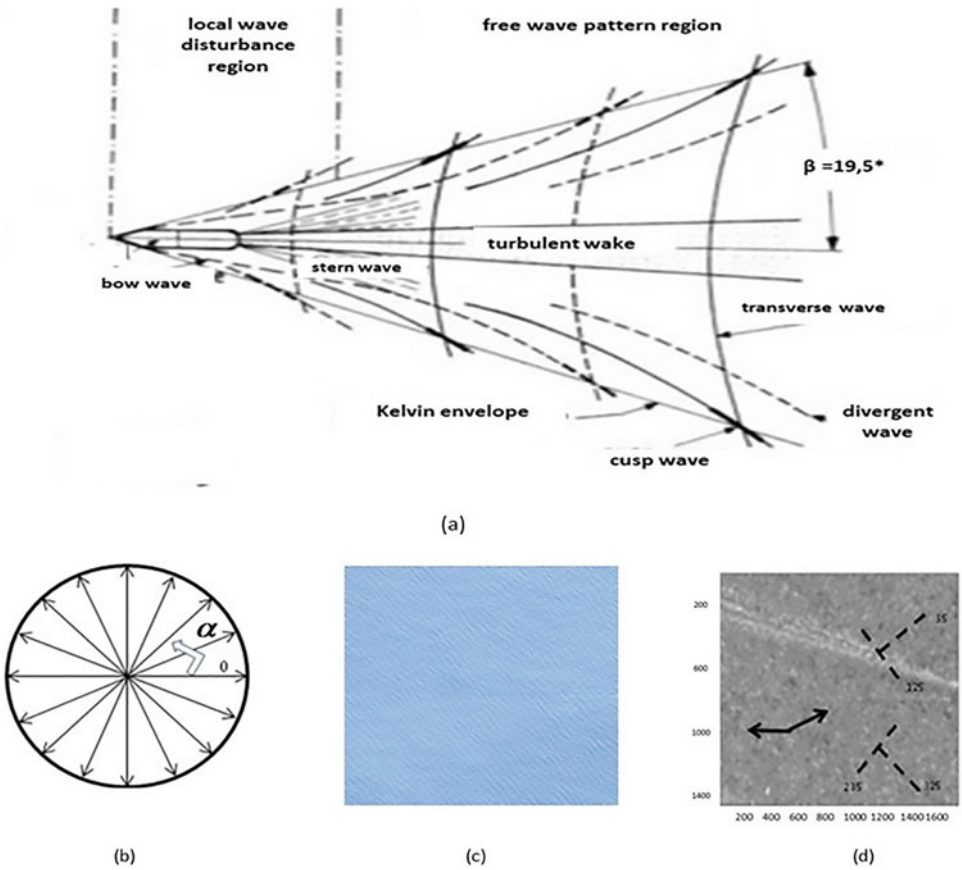

Fig. 29 Vessel trace structure (**a**); field of gradient directions (**b**); tested SS image (**c**); infogram for SS image at ($\alpha = 26^0,\ \beta = 180^0$d)

(6). In the black-and-white version, the pixels of the infogram have different shades of gray, with light areas corresponding to extreme positive values of statistics (6), dark areas—to its extreme negative values.

However, the procedure of identification of anomalous fragments of MF image consistent with the ship track configuration (Fig. 29a) has 2 significant drawbacks.

First, it provides the enumeration of all possible pairs of angles in the (α, β) calculation of the statistic values (6). The consequence of this is that in the automatic extraction of areas consisting of anomalous fragments (by cluster analysis methods), it is necessary to analyze huge amounts of data, which increases the analysis time to a very large extent.

Second, statistic (3) gives the scaled value of the difference of fragment correlation coefficients from the average value of correlation coefficient for the whole image. However, due to the fact that the mean values may differ significantly for different directions, it is impossible to compare the correlation coefficients themselves for different fragments in different directions.

Below a statistical analysis of ship track structure based on comparison of gradient correlation coefficients for different image fragments is carried out, allowing to reduce the number of direction pairs (α, β) required for anomaly identification (Fig. 30).

In addition, the features of the correlation pattern that allow identifying the anomaly exactly as a manifestation of the trace on the lateral lines of the ship's trace were revealed.

Note 1. For the convenience of presentation in the following we will often refer to correlation coefficients as correlations.

Note 2. The following correlation infograms of the test image (Figs. 31, 32, 33, 34 and 35 and Fig. 37) are shown either in color or in black and white versions. For color variants, the color scale of correlation values is indicated in the column to the right of the infographics; for black and white variants, light areas correspond to extreme positive values of correlations, and dark areas—to their extreme negative values.

Note 3. Hereafter, the unit vectors in the direction of angles (α, β) will be denoted by $\vec{v}(\alpha)$, $\vec{v}(\beta)$.

Figure 30 shows the left side line element of the trace at gradient directions $\alpha = 0°$, $\beta = 116°$. The axis of the track is directed horizontally. In accordance with the parameters of the ship's trace (Fig. 29a) the dotted line shows the longitudinal waves, which visually represent light and dark bands alternating with a certain period. The normal to the longitudinal waves is indicated by $\vec{n}$.

For various combinations of directions (α, β), the features of the correlation patterns were analyzed depending on the relative position of the vectors $\vec{n}$, $\vec{v}(\alpha)$, $\vec{v}(\beta)$.

When analyzing the test image, it was found that the most significant anomalous manifestations were observed in the case where the directions $\vec{v}(\alpha)$, $\vec{v}(\beta)$ were close to the direction of the normals to the longitudinal trace waves. In addition, in this case there is an effect of "splitting" of the lateral wave into 2 components—one with anomalously negative velocity correlations and the other with anomalously positive correlations. As an example, Fig. 31 shows an infogram of the correlation pattern of the image at $(\alpha, \beta) = (26, 206)$. The vector $\vec{v}(26)$ makes a small angle of the order of 6° with the normal $\vec{n}$ to the longitudinal waves of

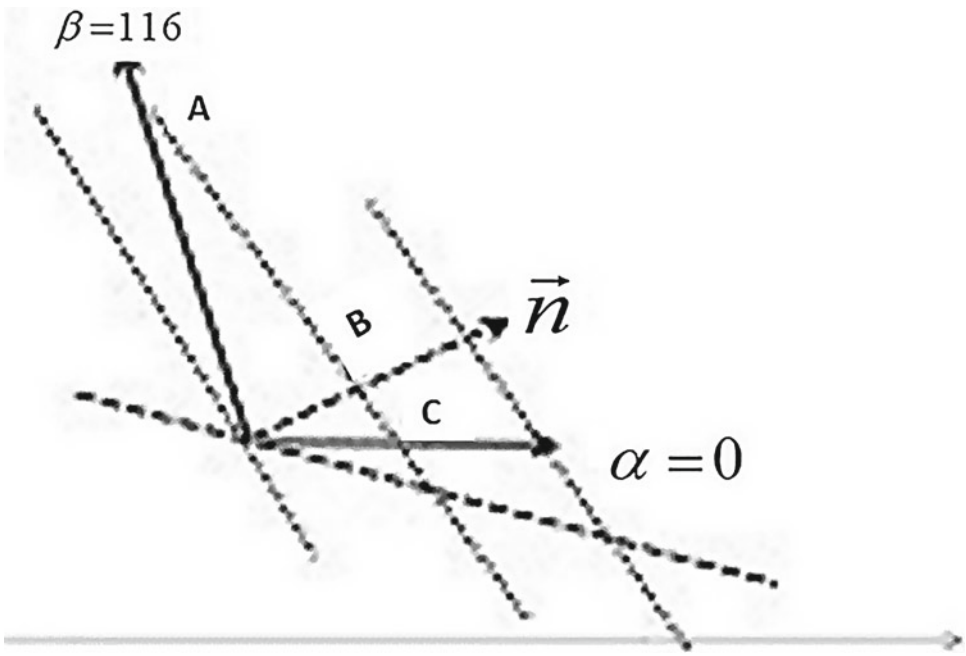

Fig. 30 Schematic of the left lateral trace line element for the $\alpha = 0^0$, $\beta = 116^0$ horizontal position of the trace axis

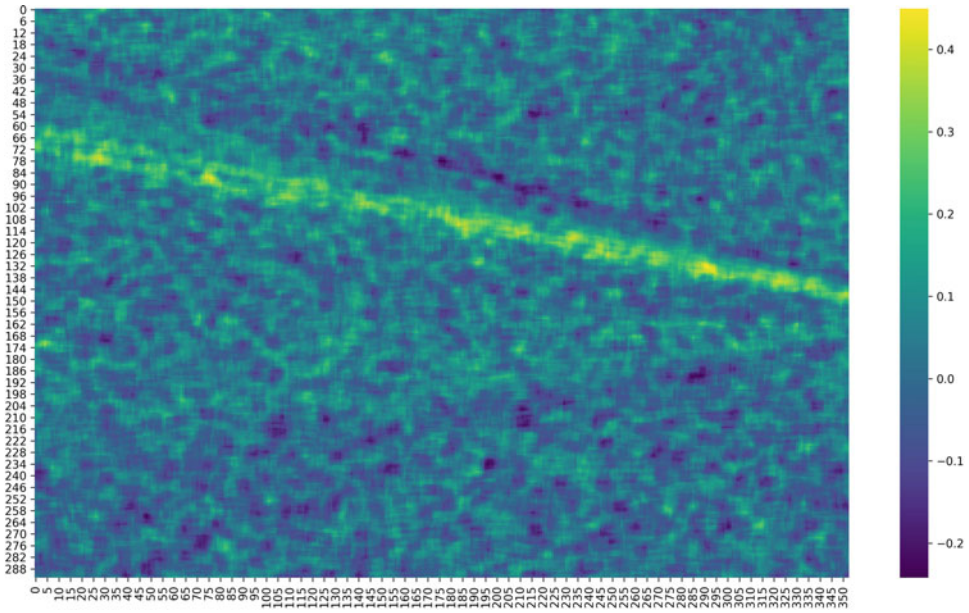

Fig. 31 Value infogram $r_{ij}(26, 206)$

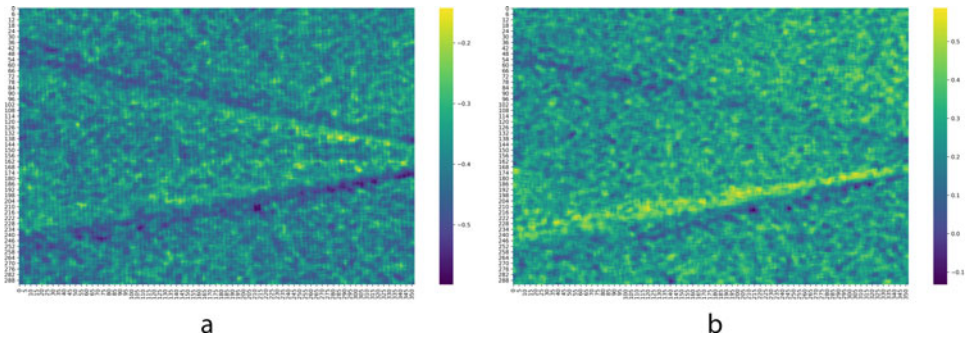

Fig. 32 Value infogram $r_{ij}(90, -90)$—(**a**), $r_{ij}(116, -64)$—(**b**)

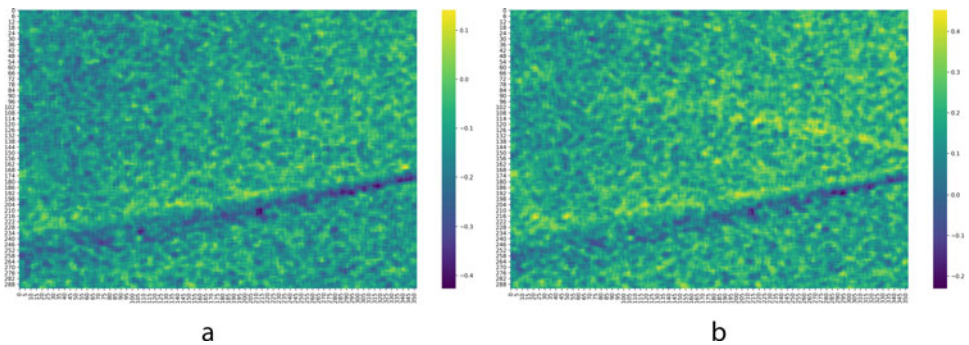

Fig. 33 Value infogram $r_{ij}(135, -45)$—(**a**), $r_{ij}(154, -26)$—(**b**)

the left side line of the trace. This line clearly shows splitting of the left "sidewall" into two components. At the same time for this pair (α, β) noticeable manifestation of anomalies in place of the right sidewall is not fixed, because the angle between $\vec{v}(\alpha)$, $\vec{v}(\beta)$ and the normal to its longitudinal waves is significantly different from the zero angle. If we carry out calculations for the pair $(\alpha, \beta) = (-26, 154)$, the picture is reversed: the right side trace is distinguished with a similar splitting into positive and negative correlation regions, while the left side trace is not identified (see Fig. 33 below).

To optimize the number of pairs to be analyzed, (α, β) calculations were performed for 8 pairs of directions forming the unfolded angles of 180°. Table 1 shows the values of (α, β).

The aggregate of these angles is formed by successive counterclockwise rotation of the vertical unfolded angle.

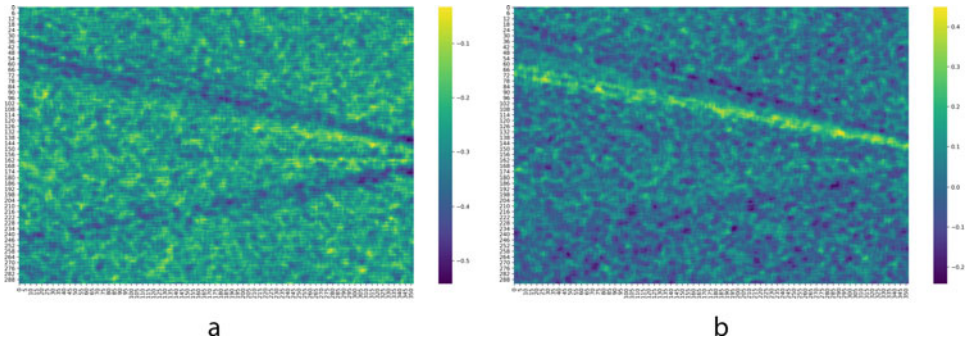

Fig. 34 Value infogram $r_{ij}(180, 0)$—(**a**), $r_{ij}(206, 26)$—(**b**)

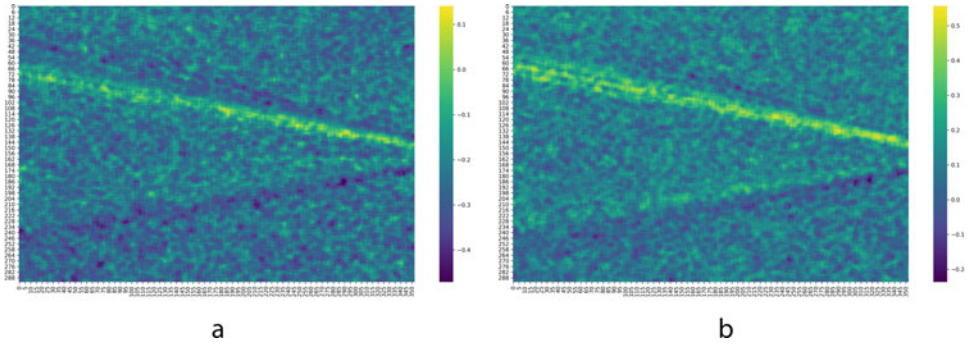

Fig. 35 Value infogram $r_{ij}(225, 45)$—(**a**), $r_{ij}(244, 64)$—(**b**)

Table 1 Values of directions of unfolded angles (in degrees)

α	90	116	135	154	180	206	225	244
β	−90	−64	−45	−26	0	26	45	64

Figures 32, 33, 34 and 35 demonstrate infograms of image correlation patterns for selected directions.

The analysis of the infograms confirms the assumption that lateral trace splitting is most pronounced in the case when the vectors $\vec{v}(\alpha)$, $\vec{v}(\beta)$ are collinear to the normal vector $\vec{n}$ to the longitudinal waves of the corresponding lateral trace. The presence of the "splitting" property also makes it possible to verify the correspondence of the detected anomalies to the ship's track—the angle between the assumed "sidewalls" should be about 40–50°, according to Fig. 29a.

When processing real imagery, when the location of the ship's track is unknown, a larger number of unfolded angles with a fixed difference between them may be needed. However, it is reasonable to assume that no more than 16–18 of them will be needed. In the absence of a clear picture of structural anomaly presence in the infograms, the configuration of angles should be rotated by several degrees and the algorithm should be repeated. The final result is a decision on the presence of a trace or its absence.

Another important feature of a ship's track is the symmetry of the lateral lines of the track relative to its axis.

The symmetry check should be based on the symmetry of some numerical (or vector) index of detected anomalies. The paper proposes a two-dimensional indicator based on the symmetry of intervals of correlation changes for the set of unfolded angles. Its qualitative description is given below.

Table 2 shows the characteristics of the correlation patterns for all the extended angles. One of them is the interval of correlation values for these patterns.

Figure 36 shows 2 graphs, the minimum and maximum correlation values for each expanded angle. The directions of α are postponed along the abscissa axis. The dotted vertical line marks the correlation interval corresponding to the horizontal expanded angle. Symmetry in changes of both minimum and maximum values of correlation coefficients relative to the center is observed. It should be specified that the symmetry is broken with respect to any other angle.

Note 4. The information value of the method is greatly influenced by the size of fragments, into which the sea surface image is divided. The optimal size (30 × 30) pixels was found for the calculations. Figure 37 shows infograms of image correlation patterns for the angle (0, −45) and several image fragment sizes.

Table 2 Correlation characteristics of luminance gradients for unfolded angles

Angles of direction of brightness gradients (α, β)	Correlation anomalies of different sign of the right lateral trace	Correlation anomalies of different sign of the left lateral trace	Presence of "splitting" of the anomaly structure	Correlation interval on the whole image	Background value of correlations
[−90, 90]	Expressed minimal $\rho = -0.6$ Weak maximum $\rho = -0.05$	Expressed minimal $\rho = -0.5$ Weak maximum $\rho = -0.1$	Very faintly pronounced on the left lateral trace	[−0.6; −0.1]	$\rho = -0.3$
[−64, 116]	Weak minimum $\rho = -0.1$ Expressed maximum $\rho = 0.6$	Weak minimum $\rho = -0.1$ No maximum	Strongly pronounced on the right lateral trace	[−0.18; 0.6]	$\rho = -0.3$
[−45, 135]	Expressed minimal $\rho = -0.45$ Weak maximum $\rho = -0.05$	No maximum There is no minimum	Medium pronounced on the right lateral trace	[−0.45; 0.15]	$\rho = -0.1$
[−26, 154]	Expressed minimal $\rho = -0.25$ Average maximum $\rho = 0.4$	There is no minimum Average maximum	Medium pronounced on the right lateral trace	[−0.25; 0.45]	$\rho = 0.2$
[0, 180]	Expressed minimal $\rho = -0.5$ Very weak maximum	Expressed minimal $\rho = -0.5$ Very weak maximum	Not available	[−0.5; 0]	$\rho = -0.2$
[26, 206]	Average minimum $\rho = -0.15$ No maximum	Average minimum $\rho = -0.15$ Expressed maximum $\rho = 0.5$	Strongly pronounced on the left lateral trace	[−0.2; 0.5]	$\rho = -0.1$
[45, 225]	Average minimum $\rho = -0.5$ No maximum	Average minimum $\rho = -0.45$ Expressed maximum $\rho = 0.15$	Medium pronounced on the left lateral trace	[−0.5; 0.15]	$\rho = -0.25$
[64, 244]	Expressed minimal $\rho = -0.5$ No maximum	Average minimum $\rho = -0.3$ Expressed maximum $\rho = 0.15$	Medium pronounced on the left lateral trace	[−0.25; 0.6]	$\rho = -0.15$

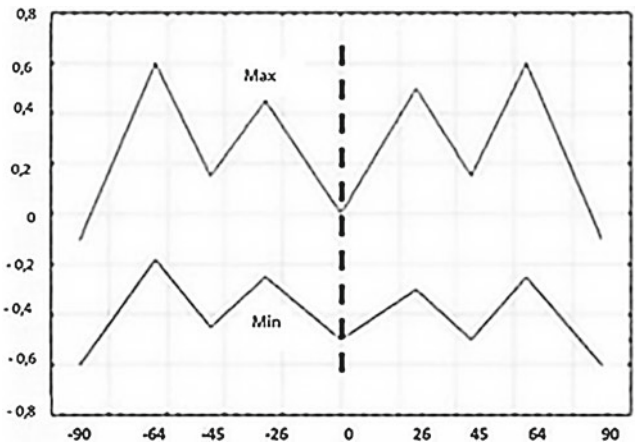

Fig. 36 Symmetry of brightness correlation boundaries relative to axial correlation

Discussion of results and conclusions

The described statistical methods for detecting anomalies on the sea surface make it possible to detect HDPs occurring in the marine medium thickness by changing the statistical characteristics of the sea surface parameters and the nearrsurface layers of the marine medium and the atmosphere. It is shown that the sensitivity of the laser-optical equipment used is sufficient to register "echoes" of phenomena that occurred not only at a given time, but also occurred before the time of the experiments.

In addition, a method of ship track detection in sea surface space images based on the analysis of color gradient correlations in different directions is proposed. It is shown that the structure of correlations has a specific appearance when the unfolded angle is perpendicular to the longitudinal waves of the ship's lateral traces. The method allows, at detection of one of possible lateral traces, to carry out purposeful search of the second lateral trace which should have similar structure of correlations.

7 Machine Learning Approach to Underwater Processes in the Marine Environment

The deep processes occurring in the marine environment are inaccessible for direct observation, but they affect the entire marine environment and are manifested at the sea surface, so

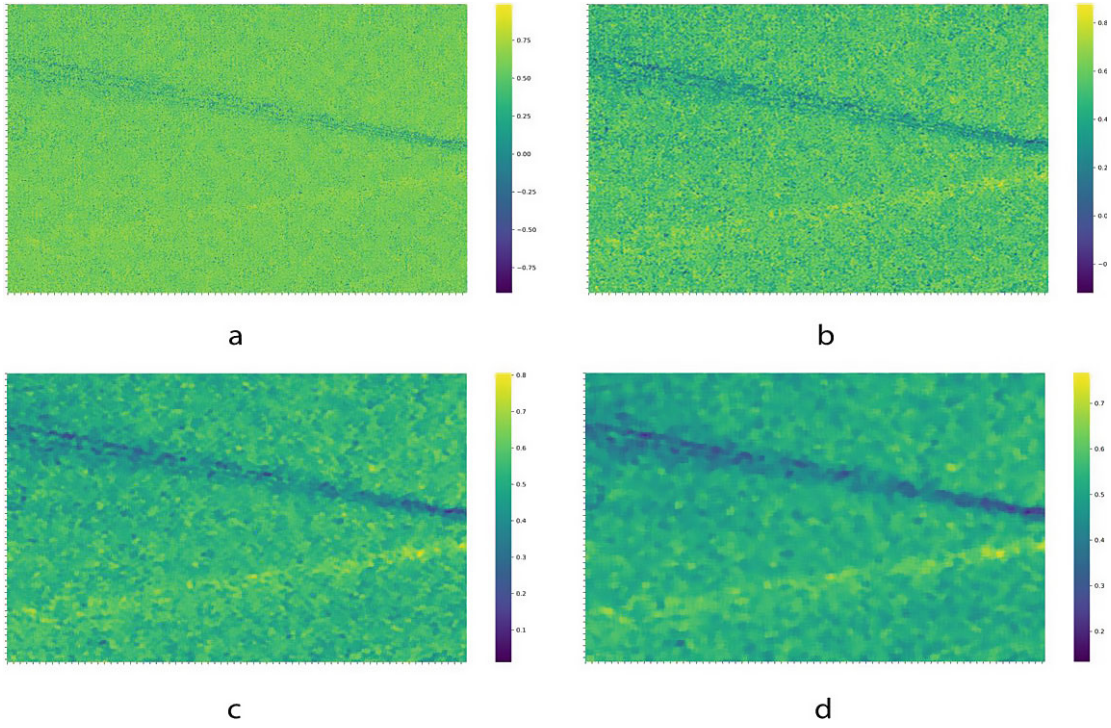

Fig. 37 Sensitivity of the method to the size (pix. × pix.) of the analyzed sea surface fragments. **a**—5 × 5, **b**—10 × 10, **c**—20 × 20, **d**—30 × 30

it is possible to study them using the sea surface monitoring data. Such an approach has led to the development of the concept of computer radio-tomography of the marine environment [59], which is based on various realizations of the solutions of the problems of the continuation of the hydrophysical fields in the marine environment thickness by the data on the sea surface disturbances. These problems, as a rule, belong to the class of incorrectly formulated problems, their solution is sensitive to small variations in the initial data [60]. Therefore, the solution of the problem of recovery of parameters of a point hydrodynamic feature, streamlined by a plane flow, by perturbations of a free surface [61] did not give satisfactory results using data of laboratory experiments [62], in which measurements of angles of inclination of the water surface perturbed by a moving cylinder and a wing profile were performed.

A fundamentally different approach to solving this problem, based on machine learning methods, was proposed in [63, 64]. Machine learning methods are now widely used in data processing and analysis problems [65–72]. In [63], data on the free surface of water perturbed by a transversely moving cylinder and wing profile obtained in experiments [62] were processed. Sets of measured values of the tangent angle of the free surface of the fluid at different points of the axis of motion of the model were used as a training sample. Spectral and statistical analysis was applied to these sequences, which revealed three main frequencies and a strong correlation between them and the perturbation source parameters. In this regard, the calculated parameters of the training vector with three coordinates having the values of the main amplitudes of the spectrum were used to train the neural network. The method of stochastic gradient descent [72] made it possible to significantly reduce the calculation time and obtain results that coincide with the experimental data within an error of 5%.

In [64] the data of experiments were processed, which were carried out on an experimental setup representing a channel 300 cm × 50 cm × 50 cm filled with water [73]. In the experiments, surface waves arising from the horizontal motion in the water column of a ball of 35 mm diameter and an ellipsoid with large and small axis lengths of 120 and 35 mm, respectively, were observed. The tangent of the angle of inclination of the perturbed free surface of water to the horizon was measured in the vertical plane passing through the longitudinal axis of model symmetry in different points of this axis. The ball moved at depths of 66 and 96 mm with velocities ranging from 235 to 950 mm/s, and the ellipsoid moved at depths of 66, 96 and 126 mm with velocities ranging from 265 to 838 mm/s. Data for 8 modes of ball motion and 14 modes of ellipsoid motion were processed.

For each mode of model motion, a sequence of values of the tangent angle of the liquid surface at different points of its axis of motion was obtained. These sequences were used as training samples to determine the depth and velocity of moving models. Learning with a teacher was applied; for this

purpose, a forward propagation network of the multilayer perseptron type, trained by algorithms based on the method of backward error propagation, was used [65, 66]. The training set was the sequence of values of tangents of the angles of inclination of free surface of liquid, measured in different points. Recently, for the selection of the main features of such a set, which characterize the properties and the behavior of the process or object under study, deep learning networks are used [70], but for this, apart from the large volume of initial information, considerable computational resources or a long time of the learning process are required. Therefore, to identify the characteristic features of the observed process and to reduce the training sample, spectral analysis was applied to the data obtained during the experiment, which allowed us to move from the entire sequence of observed coordinates of the training vector to a few lines of the spectrum. This significantly reduced the size of the neural network and the duration of its learning process.

The use of classical method of gradient descent, based on the choice of weights of connections between neurons to achieve the minimum error of approximation of the target function for the minimum number of training steps, led to the fact that in some cases the minimization process did not converge to the global value. This difficulty was overcome by the stochastic gradient descent method [71, 72], which helped to avoid "getting stuck" in the model at the point of local minimum.

After conducting a sufficient number of numerical experiments, a three-layer neural network architecture was chosen. From the original data a larger sample was generated by 5% noise sampling with a uniform distribution density. The choice of the noise interval was revealed by computational experiment. For training on the variability of the factors, data normalization, that is, reduction to relative units in the interval (0, 1) by dividing each parameter by its maximum value, was carried out. Training of the neural network is reduced to minimization of the error function by adjusting the weight coefficients of synaptic connections between neurons. The expression for the root-mean-square error is presented in the following form

$$E = \frac{1}{2p}\sum_{j=1}^{p}\left(d_j - y_j\right)^2,$$

where: y_j—the actual result, d_j—the desired network response.

Numerical experiments with the neural network allowed us to reconstruct the values of depth and velocity of the sphere and ellipsoid moving in the water column in each experimental mode with an error within 7%.

Machine learning methods have shown their effectiveness in solving the inverse problem of determining the parameters of models moving in a fluid by the perturbations of the free surface of the fluid created by them. The application of the described approaches to other incorrectly posed problems of fluid mechanics and geophysics is a practically significant task and requires further study.

References

1. Ginzburg, A.I., Kostyanoy, A.G., Krivosheya, V.G., Nezlin, N.P., Solovyev, D.M., Stanichny, S.V., Yakubenko, V.G.: Features of water dynamics and chlorophyll a distribution in the north-east part of the Black Sea in autumn 1997. Oceanology **40**(3), 344–356 (2000) (in Russian)
2. Rogachev, K.A., Shlyk, N.V.: Mechanism of formation of an anticyclonic vortex in Sakhalin Bay based on satellite observations. Earth Explor. Space **5**, 12–20 (2013). (in Russian)
3. Wu, J., Heimbach, S.P., Hsu, Y.L.: Scanning device for the study of wind ripples on the sea surface. Instr. Sci. Res. **8**, 120–126 (1981)
4. Buften, J.L., Hoge, F.E., Swift, R.N.: Airborn measurements of laser backscatter from the ocean surface. Appl. Opt. **22**, 2603–2618 (1983)
5. Shifrin, K.S.: Optics of the ocean and atmosphere. Nauka, Moscow (1981)
6. Lee M.E., Martynov O.V.: Some results of sea color index studies. Marine Hydrophys. Res. **1**(72), 133–138 (1976) (in Russian)
7. Degtyarev, V.I., Konstantinov, O.G., Nelepa, A.A., Kostenko, I.P.: Differential sea surface spectral brightness coefficient meter. Marine Hydrophys. Res. **1**(72), 124–132 (1976)
8. Hinckley, E.D.: Laser control of the atmosphere. Mir, Moscow (1979)
9. Mejeris, R.: Laser remote sensing. Mir, Moscow (1987)
10. Gorelov, A.M., Zevakin, E.A., Ivanov, S.G., Kaledin, S.B., Leonov, S.O., Nosov, V.N., Savin, A.S.: On a complex approach to remote registration of hydrodynamic disturbances of the marine environment by optical methods. Phys. Basis Instr. **1**(4), 58–64 (2012) (in Russian)
11. Nosov, V.N., Kaledin, S.B., Ivanov, S.G., Glebova, T.V., Timonin, V.I.: On increase of efficiency of detection of anomalies excited by a sea underwater source at complex use of laser-optical methods of registration. Process. GeoMedia **1**(5), 85–94 (2016) (in Russian)
12. Nosov, V.N., Kaledin, S.B., Ivanov, S.G., Timonin, V.I.: Remote tracking to monitor ship tracks at or near the water surface. Optics Spectros. **127**, 669–674 (2019). https://doi.org/10.21883/OS.2019.10.48366.165-19
13. Nosov, V.N., Ivanov, S.G., Kaledin, S.B., Petukhov, A.V., Savin, A.S.: Prospects of application of drones for laser sensing of sea surface. Phys. Basis Instr. **10**(1), 70–81 (2021). https://doi.org/10.25210/jfop-2101-070081
14. Belov, M.L., Gorodnichev, V.A., Kozintsev, V.I., Strelkov, B.V.: Laser signal power received by the locator from a random area of an uneven sea surface. Bulletin of the Bauman Moscow State Technical University. Ser. Instr. Eng. **3**, 3–15 (2008) (in Russian)
15. Nosov, V.N., Ivanov, S.G., Timonin, V.I., Kaledin, S.B.: Anisotropy study of statistical characteristics of wind waves under the influence of hydrodynamic perturbations in laser-reflective method. In: Olegovna, C. (eds.) Processes in GeoMedia, vol. I, pp. 93–100. Springer Geology. Springer, Cham (2020). https://doi.org/10.1007/978-3-030-38177-6_11
16. Dubovik, A.N.: On the role of curvature anisotropy in light reflection from specular points of sea surface. Izv. FAO. **32**(1), 147–151 (1996) (in Russian)

17. Onemetto, N.: Analytical laser spectroscopy. Mir, Moscow (1982)
18. Artemyev, V.A., Burenkov, V.I., Voznyak, S.B., Grigoryev, A.V., Daretski, M., Demidov, A., Kopelevich, O.V., Frantsov, O.N., Khrapko, A.N.: Sub-satellite measurements of ocean color: a field experiment in the Black and Aegean Seas. Oceanology. **40**(2), 192–198 (2000) (in Russian)
19. Esipov, I.B., Naugolnykh, K.A., Nosov, V.N., Pashin, S.Yu.: Measurement of probability distribution of sea surface curvature radiuses. Izv. FAO. **22**(10), 1115–1117 (1986) (in Russian)
20. Nosov, V.N., Pashin, S.Yu.: Statistical characteristics of wind waves in the gravitational-capillary spectral region. Izv. FAO. **26** (11), 1161–1169 (1990) (in Russian)
21. Nosov, V.N., Kaledin, S.B., Ivanov, S.G., Zevakin, E.A., Serebrinikov, L.V., Savin, A.S., Timonin, V.I. (2022) On possibility of applying aircraft scanning laser locator for solving problems of operational oceanology. In: Chaplina, T. (eds) Processes in GeoMedia, vol. V. pp 179–188. Springer Geology. Springer, Cham. https://doi.org/10.1007/978-3-030-85851-3_20
22. Goldin, Yu.A., Kagain, V.E., Kelbalikhanov, B.F., Locke, Y.F., Pelevin, V.N.: Location of an undulating sea surface by means of OKG from the helicopter board. In: Galaziy, G.I. (ed.) Optical methods of research of the oceans and inland waters, pp. 135–140. Nauka, Novosibirsk (1979) (in Russian)
23. Byalko, A.V., Locke, Y.F., Pelevin, V.I.: Study of heterogeneities of wind waves from a helicopter board. In: Ozmidov, R.V. (eds.) Study of variability of optical properties of the Baltic Sea, pp. 34–44. Tallinn (1983) (in Russian)
24. Bunkin, F.V., Voliak, K.N., Malyarovsky, A.I., et al.: Airborne measurements of sea waves by reflection of continuous laser beam. Dokl. Acad. Sci. USSR **281**(6), 1441–1445 (1985) (in Russian)
25. Nosov, V.N., Ivanov, S.G., Timonin, V.I., Podgrebenkov, A.L., Plishkin, A.N., Kaledin, S.B., Glebova, T.V., Yadrentsev, A.N., Zakharov, V.K.: Joint space and sea experiment on integrated vessel trace registration using subsatellite measurements. Fund. Appl. Hydrophys. **8**(4), 34–35 (2015) (in Russian)
26. Glebova, T.V., Ivanov, S.G., Kaledin, S.B., Nosov, V.N., Savin, A.S., Timonin, V.I.: Estimation of surface wave curvature radii from measured amplitudes of laser-glare signals in full-scale experiments. Phys. Bases Instr. **10**(2), 76–82 (2021). https://doi.org/10.25210/jfop-2102-074080
27. Shuleikin, V.V.: Sea physics. Nauka, Moscow (1968)
28. Davidan, I.N., Lopatukhin, L.I., Rozhkov, V.A.: Wind waves in the World Ocean. Gidrometeoizdat, Leningrad (1985)
29. Kelbalikhanov, B.F.: Hydrooptical studies in waters of the World Ocean. Komi Scientific Center of the Ural Branch of Academy of Sciences of USSR, Syktyvkar (1992)
30. Artemyev, V.A., Burenkov, V.I., Vortman, M.I., Grigoryev, A.V., Kopelevich, O.V., Khrapko, A.N.: Sub-satellite ocean color measurements: a new floating spectroradiometer and its metrology. Oceanology **40**(1), 148–155 (2000) (in Russian)
31. Ivanov, S.G., Nosov, V.N., Pogonin, V.I., Zevakin, E.A., Savin, A.S., Gorelov, A.M., Leonov, S.O.: Application of brightness photometer to obtain information of hydrodynamic disturbances in marine environment. In: Actual directions of applied mathematics in energy. energy efficiency and information and communication technologies: Proceedings of international scientific conference, pp. 277–280. Bauman Moscow State Technical University, Moscow (2010)
32. Ivanov, S.G., Nosov, V.N., Kaledin, S.B., Plishkin, A.N., Pogonin, V.I., Leonov, S.O., Molchanova, T.V., Zevakin, E.A.: Study of small-scale variability of near-surface layers of the marine environment under the hydrodynamic disturbances using the sea brightness photometer. Bulletin of Bauman State Technical University. Ser. Natural Sci. **5**(56), 53–65 (2014) (in Russian)
33. Matyushenko, V.A., Pelevin, V.N., Rostovtseva, V.V.: Measurement of the sea brightness coefficient by a three-channel spectrophotometer from board the RV. Optics Atmos. Ocean. **9** (5), 664–669 (1996) (in Russian)
34. Bakhanov, V.V., Goryachkin, Yu.N., Korchagin, N.N., Repina, I. A.: Local manifestations of deep processes at the sea surface and in the atmospheric drive layer. Doklady RAN **414**(1), 111−115 (2007) (in Russian)
35. Piskozub, J.: Study of spatial distribution of marine aerosol over sea coast with a multifrequency lidar system. Proc SPIE **2471**, 387–389 (1995)
36. Zielinski, A., Piskozub, J., Irczuk, M.: Lidar studies of marine aerosol in the coastal zone. Proc. SPIE **2471**, 428–438 (1995)
37. Nosov, V.N., Gorelov, A.M., Kaledin, S.B., Kuznetsov, V.A., Leonov, S.O., Savin, A.S.: Laser emission scattering over the sea surface in the presence of hydrodynamic disturbances in the water column. DAN USSR **433**(1), 111–112 (2010) (in Russian)
38. Nosov, V.N., Kaledin, S.B., Gorelov, A.M., Leonov, S.O., Kuznetsov, V.A., Pogonin, V.I., Savin, A.S.: Features of light scattering in the driven atmospheric layer over regions of long-lived hydrodynamic disturbances of the marine environment. DAN USSR **442**(4), 559–550 (2012) (in Russian)
39. Resch, F.J., Darrozes, J.S., Afeti, G.M.: Marin liquid production from bursting of air bubbles. J. Geophys. Res. **91**(C1), 1019–1029 (1986)
40. Leifer, I.: Secondary bubble production from breaking waves: the bubble burst mechanism. Geophys. Res. Letter. **27**(24), 4077–4080 (2000)
41. Krekov, G.M.: Optical properties of coastal smoke. Nauka, Novosibirsk (1988)
42. Hettmansperger, D.: Statistical inference based on ranks. Finance and Statistics, Moscow (1989)
43. Nosov, V.N., Ivanov, S.G., Pogonin, V.I., Timonin, V.I., Zavyalov, N.A., Zevakin, E.A., Savin, A.S.: Influence of hydrodynamic perturbations on dispersion characteristics of a near-water aerosol. In: Karev, V., Klimov, D., Pokazeev, K. (eds.) Physical and mathematical modelling of earth and environment processes. PMMEEP 2017. Springer Geology. Springer, Cham, pp. 282–288 (2018). https://doi.org/10.1007/978-3-319-77788-7_29
44. Nosov, V.N., Ivanov, S.G., Zavyalov, N.A., Kaledin, S.B., Pogonin, V.I., Zevakin, E.A.: Study of the influence of the oncoming interaction of the flow and stream from a propeller on the parameters of the driven aerosol. Process. Geomedia. **1**(23), 611–616 (2020) (in Russian)
45. Nosov, V.N., Ivanov, S.G., Pogonin, V.I., Kaledin, S.B., Zevakin, E.A., Zavyalov, N.A.: Investigation of influece of the screw propeller working towards the flow on parameters of near water aerosol. In: Chaplina, T. (ed.) Processes in GeoMedia, vol. V. Springer Geology. Springer, Cham. https://doi.org/10.1007/978-3-030-85851-3_23
46. Zhulanov, Yu.V., Petryanov, I.V.: Investigation of the mechanism of generation of marine aerosols. Reports of the Academy of Science of the USSR. Ser. Geophys. **253**(4), 845–848 (1980) (in Russian)
47. Kashkin, V.B., Sukhinin, A.I.: Remote sensing of the Earth from space. Logos Publisher, Moscow, Digital image processing (2008)
48. Schowengerdt, R.: Remote sensing. Models and methods of image processing—technosphere, Moscow (2010)
49. Aivazyan, S.A., Buchshtaber, V.M., Enyukov, I.S., et al.: Applied statistics. Classification and Dimensionality Decreasing. Finance and Statistics, Moscow (1989)
50. Gonzalez, R.: Digital image processing: monograph, translated from English. Technosphere, Moscow (2006)
51. Ahmed, N.: Recent review on image clustering. Image Processing, IET **9**(11), 1020–1032 (2015)

52. Aggarwal, C.C., Reddy C.K.: Data clustering: algorithms and applications. CRC Press (2014)
53. Osowski S.: Neural networks for information processing: transl. from Polish. I.D. Rudinsky Finance and Statistics, Moscow (2017)
54. Graves, A., Schmidhuber, J.: Offline Handwriting Recognition with Multidimensional Recurrent Neural Networks. NIPS 2008, pp. 545–552, Vancouver, Canada (2008)
55. Bondur, V.G.: Modern approaches to processing large flows of hyperspectral and multispectral aerospace information. Earth Explor. Space **1**, 3–17 (2014). (in Russian)
56. Nosov, V.N., Timonin, V.I., Klementiev, M.K., Budovskaya, L. M.: Method for detection of the vessel trace anomalies in the sea surface images based on analysis of color gradient correlations. In: Chaplina, T. (ed.) Processes in GeoMedia, vol. II, pp. 219–224. Springer Geology. Springer, Cham (2021). https://doi.org/10.1007/978-3-030-53521-6_25
57. Timonin, V.I., Kurbatov, R.A., Nosov, V.N.: On one statistical method of anomaly detection on sea surface images. Process. GeoMedia **4**, 363–370 (2016). (in Russian)
58. Timonin, V.I., Tyannikova, N.D., Nosov, V.N., Ivanov, S.G., Klimentiev, M.K.: Application of multidimensional correlation procedures for identification of trace structures on sea surface space images. Process. GeoMedia **4**, 1221–1225 (2018). (in Russian)
59. Nesterov, S.S., Shamaev, A.S., Shamaev, S.I.: Methods, procedures and tools of aerospace computerized radiotomography of near-surface regions of the Earth. Scientific World, Moscow (1996)
60. Tikhonov, A.N., Arsenin, V.Ya.: Methods of solving incorrect problems. Nauka, Moscow (1979)
61. Savin, A.S.: Determination of parameters of hydrodynamic features in the flat flow by data on its free surface. Izvestiya RAN MZHG **2**, 139–146 (2001). (in Russian)
62. Boyarintsev, V.I., Lednev, A.K., Prudnikov, A.S., Savin, A.S., Savina, E.O.: Modelling and experimental study of disturbances of free boundary of plane flow by submerged sources. Preprint IPM RAS 720, Moscow (2002) (in Russian)
63. Voronin, E.A., Nosov, V.N., Savin, A.S.: Neural network approach to solving the inverse problem of surface-waves generation. J. Phys. Phys. Conf. Ser. Conf. **1**, 1392. 012022. IOP Publishing (2019). https://doi.org/10.1088/1742-6596/1392/1/012022
64. Voronin, E.A., Nosov, V.N., Savin, A.S.: Determination of submerged source parameters by liquid surface disturbances based on machine learning methods. Dokl. RAS. Earth Sci. **493**(1), 103–106 (2020) (in Russian)
65. Osowski, S.: Neural networks for information processing. Finance and Statistics, Moscow (2002)
66. Haikin, S.: Neural networks: full course, 2nd edn. Williams Publishing House, Moscow (2006)
67. Manning, C.: Introduction to Information Retrieval. Cambridge University Press (2008)
68. Max, K., Kjell, J.: Applied Predictive Modeling. Springer (2013)
69. Nathan, M., James, W.: Big Data: Principles and Best Practices of Scalable Real-Time Data Systems: Manning Publications (2015)
70. Goodfellow, J., Bengio, I., Courville, A.: Deep Learning. DMK Press, Moscow (2017)
71. Flach, P.: Machine Learning. The science and art of building algorithms that extract knowledge from data. DMK Press, Moscow (2015)
72. Shalev-Schwartz, S., Ben-David, S.: Ideas of machine learning: from theory to algorithms. DMK Press, Moscow (2019)
73. Barmin, A.A., Boyarintsev, V.I., Lednev, A.K., Savin, A.S., Savina, E.O.: Modelling and experimental study of disturbances of free liquid surface by ball and ellipsoid. Preprint 763 Institute of Problems of Mechanics of RAS, Moscow (2004) (in Russian)

Meteoritics, Cosmochemistry, Lunar and Planetary Sciences

Studies of the Problems of Planetary Cosmogony, Geochemistry and Cosmochemistry by Methods of Mathematical Modeling

V. A. Dorofeeva, A. N. Dunaeva, S. I. Ipatov, V. A. Kronrod, E. V. Kronrod, O. L. Kuskov, M. Ya. Marov, and A. V. Rusol

1 Introduction

This paper is based on the studies made by leading researchers of the Laboratory of thermodynamics and mathematical modeling of natural processes at the Vernadsky Institute of Geochemistry and Analytical Chemistry of the Russian Academy of Sciences in the field of cosmogony, geochemistry and cosmochemistry. The main research method is mathematical modeling using the restrictions obtained from experimental studies of bodies of the Solar System and exoplanetary systems. Verification of models is also carried out by comparing the obtained results and available experimental data. The article consists of four sections reflecting the main directions of the laboratory's work. The section "Studies in the field of stellar-planetary cosmogony is written by scientists under the leadership of Academician M. Ya. Marov. The section includes studies of the formation and evolution of dust clusters, primary bodies, the terrestrial planets, and some exoplanets, the delivery of water to the terrestrial planets, and the problem of the asteroid-comet hazard. The sections containing the results of the study of the internal structure of the satellites—the Moon and Titan, were carried out under the guidance of the Corresponding Member of RAS O. L. Kuskov. The section "Estimation of the composition and mass of the ice component in primary ice-rock bodies of the protoplanetary disk" contains some results obtained by D.Sc. V. A. Dorofeeva in the study of the behavior and conditions of accumulation of volatile components in the early Solar System.

V. A. Dorofeeva (✉) · A. N. Dunaeva · S. I. Ipatov · V. A. Kronrod · E. V. Kronrod · O. L. Kuskov · M. Ya.Marov · A. V. Rusol
Vernadsky Institute of Geochemistry and Analytical Chemistry, Russian Academy of Sciences, 19 Kosygin St., Moscow, 119991, Russia
e-mail: dorofeeva@geokhi.ru

2 Studies in the Field of Stellar-Planetary Cosmogony

2.1 Introduction

Research on the problems of stellar-planetary cosmogony is a topical section of the laboratory's work. According to present concepts, the formation of planetary systems is due to physico-chemical and dynamic processes in gas-dust disks formed from fragments of interstellar molecular clouds together with stars in the process of their birth and evolution [1]. The tremendous progress in stellar-planetary cosmogony over the past two decades has been provided by data on the structure and composition of circumstellar gas-dust disks and the discovery of exoplanets [2]. The most significant results on the structure and properties of protoplanetary disks were obtained by observations with a high angular resolution of disks in main sequence stars, while planets are predominantly formed near stars of late spectral types of high metallicity. The reconstruction of the processes occurring in protoplanetary disks leading to the formation of planetary systems is based on the methods and tools of mathematical modeling. They are based on original theoretical research in the field of continuum mechanics, heterogeneous mechanics, physical kinetics, and magnetohydrodynamics. Extensive studies in these scientific areas as applied to solving the problems of cosmogony are contained in monographs [3, 4].

The processes of evolution of protoplanetary disks and the formation of planets include three main stages:

- the formation of dust clusters and primary solids as a result of hydrodynamic (streaming) and gravitational (Jeans) instabilities [5–8];
- the growth of primary solids from dust aggregates (clusters) to the size of planetesimals and the formation of planetary embryos in mutual collisions [9, 10];

V. P. Kolotov and N. S. Bezaeva (eds.), *Advances in Geochemistry, Analytical Chemistry, and Planetary Sciences*,
https://doi.org/10.1007/978-3-031-09883-3_14

- oligarchic growth of planetary embryos due to scooping out planetesimals and due to dynamic processes (tides, migration, resonances) [11].

Migration processes are associated with the transport of matter in the planetary system, including the transfer of volatiles from the outer to the inner zones, including the possibility of the mechanism of water abundance to the Earth in the Solar System due to exogenous processes and heterogeneous accretion.

All these areas of research are represented by the work of the laboratory. Some of the research objectives and some of the results obtained to date are discussed below.

2.2 Formation and Evolution of Dust Clusters and Primary Bodies

The problem of the formation and evolution of the primary solid-state component in protoplanetary gas-dust disks, as the basis for the formation of planetary embryos, underlies the genesis of planetary systems.

Protoplanetary disks contain, along with gas, a solid component consisting of dust and condensates. The solid-state component is dominated by icy chemical compounds with low condensation temperatures (<200 K), from which planetesimals are formed at large radial distances and, together with gas and ice, form giant planets. High-temperature condensates are responsible for the formation of the terrestrial planets. It can be assumed that the preferred birthplaces of planets are regions near the condensation fronts of the main volatiles in the disks, which is indicated, in particular, by the detection of particles containing carbon and oxygen in the atmospheres of exoplanets [12, 13]. The radial distribution of volatiles makes it possible to evaluate high spatial resolution millimeter wave images from the ALMA radio telescope system [14]. Existing observations and models support the idea that water vapor can concentrate in areas near its condensation front at certain stages of the evolution of protoplanetary disks, and that dust aggregates grow rapidly near condensation fronts of various volatiles.

Simulation of the evolution of gas-dust disks is mainly carried out by two different methods. In the first method, the disk is represented as consisting of a homogeneous medium, the properties of which are obtained by averaging or homogenizing the properties of the gas and solid components. With this approach, it is possible to study, however, only the earliest stages of the formation of protoplanetary disks in the process of stellar evolution. In the second method, the gas-dust disk is considered as a heterogeneous medium, and the joint evolution of the gas and solid-state components is investigated, which is much closer to reality. For the gas component, the most important sources of physical processes are viscosity forces arising from interaction with solid particles or proto-planetesimals before gas is swept out of the disk. At the stage of particle growth, along with viscous friction, growth by coagulation and radial drift relative to the gas make a significant contribution.

The growth of dust particles during collisions can be limited by a number of factors. The most important restrictions are:

- *Rebound barrier*. As it was shown in a series of computational experiments, there is a range of velocities at which the bounce of particles in collisions occurs. Such a barrier exists only for a limited combination of collision velocities and properties of the particles themselves, and this mechanism significantly affects the growth of particles under certain conditions (Figs. 1, 2, 3 and 4) [15].
- *Collisional fragmentation barrier*. This barrier, which depends on the relative collision velocity, increases with increasing particle size. This is due to the increased influence of turbulence and radial drift. Obviously, if the collision energy exceeds the forces of internal bonds, then it becomes destructive, which leads to the enrichment of the disk with secondary small particles [16].
- *Thermal fragmentation barrier.* It occurs at the intersection of condensation fronts of volatiles due to the sublimation of some substances, which leads to fragmentation of clusters due to the destruction of internal bonds between agglomerates and also enriches the disk with secondary small particles [17].
- *Drift barrier*. This barrier is due to an increase in the drift velocity of particles as they grow (and, accordingly, in the cross section) until the Stokes number becomes approximately equal to unity. Calculations have shown that under certain conditions the drift time scale becomes shorter than the growth time scale.

At low relative velocities of cluster collisions, the values of the recovery coefficient k are in the range from 0 to 1, while, at k close to 1, a rebound occurs without noticeable structural changes. As the ratio of collision energies grows, the process of cluster unification predominates. When the ratio of kinetic and internal energies exceeds unity, the phenomena of destruction of clusters during collisions prevail, which imposes quite definite restrictions on the dynamics and chronology of evolutionary processes during the formation of primary solid bodies and the formation of planetesimals.

The listed mechanisms strongly prevent to the enlargement of objects by simple aggregation. The range of decimeter-meter sizes is especially problematic, when the role of electrostatic charges in the interaction of particles is

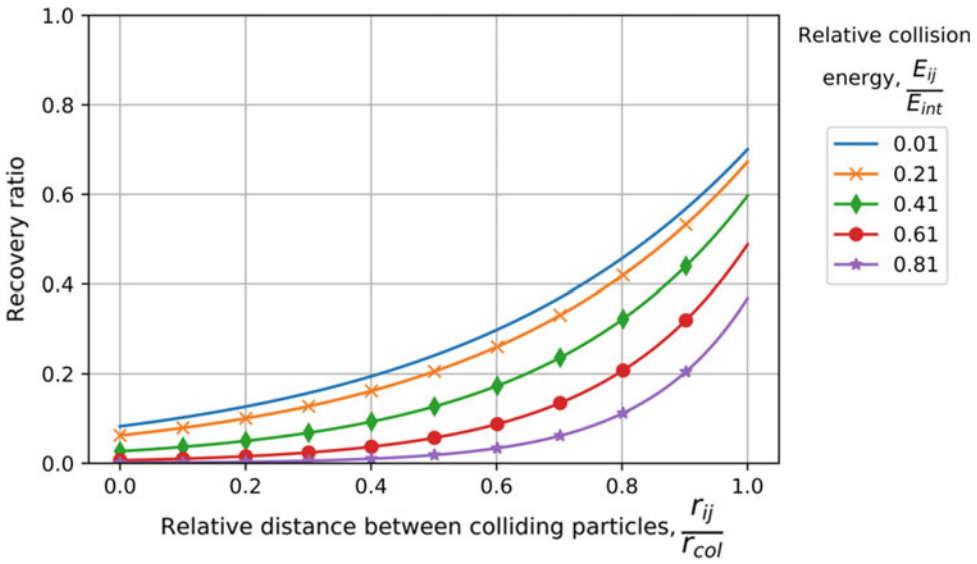

Fig. 1 Dependences of the recovery factor based on the results of a numerical parametric study based on numerical simulation of the interaction of dusty fractal clusters with $D_\beta = 2.11$

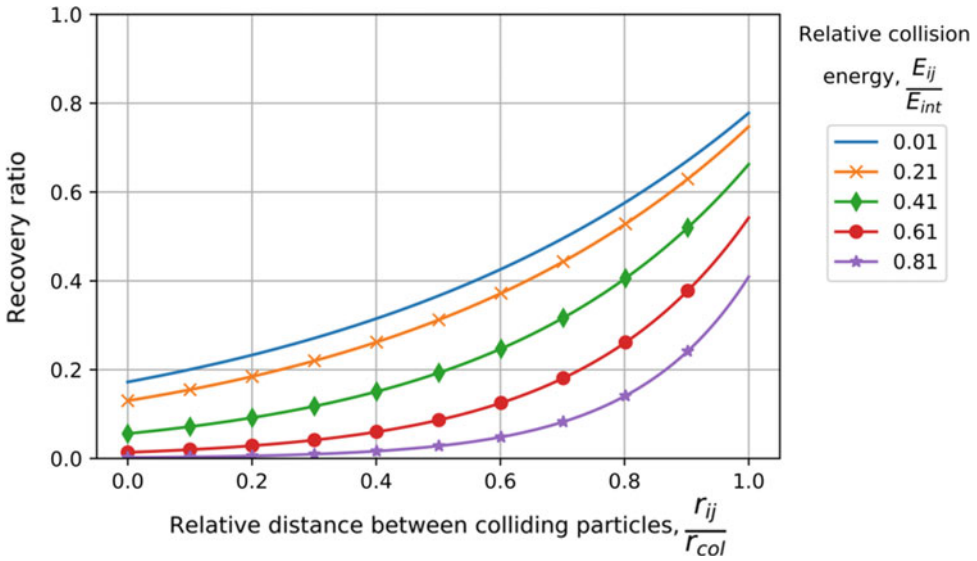

Fig. 2 Dependences of the recovery factor based on the results of a numerical parametric study based on numerical simulation of the interaction of dusty fractal clusters with $D_\beta = 2.33$

significantly weakened, and the forces of gravity are still negligible. The ineffectiveness of the direct collision of individual particles has been confirmed by laboratory experiments [18]. The authors proposed a modified scheme of collisions of dust fractal clusters forming in a dust subdisk (formed in the equatorial plane of a gas-dust disk during compression and an increase in the dust/gas ratio) due to gravitational and hydrodynamic instabilities. In this scenario, the efficiency of combining and growing particles within the cluster increases significantly.

Currently, there are a number of modifications of the disk evolution process, which provide the possibility of the growth of primary dust particles:

- *Gravitational instability and formation of dusty fractal clusters.* According to this model, gravitational instability in the subdisk leads to the formation of dust clusters of a fractal structure with a developed pore space, which never condenses to the state of consolidated matter. In this case, the probability of coarsening of dust particles in collisions inside the cluster, exceeding the radial drift, increases. This is the first stage in the formation of a solid primary substance and its enlargement to the size of pebbles-cobblestones, which serve as the basis for further growth up to the formation of protoplanethesimals. At the subsequent stages of the enlargement of these objects to the size of planetesimals, self-gravity and continuing collisions play the main role [19].
- *Hydrodynamic (streaming) instability and particle enlargement.* At the initial stages of the evolution of a gas-dust disk, an important contribution to the growth of

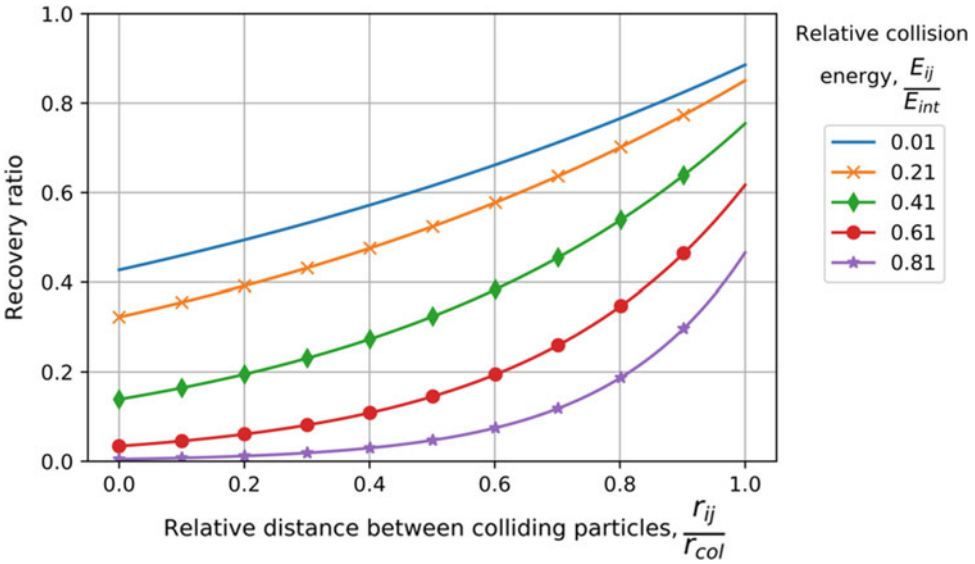

Fig. 3 Dependences of the recovery factor based on the results of a numerical parametric study based on numerical simulation of the interaction of dusty fractal clusters with $D_\beta = 2.66$

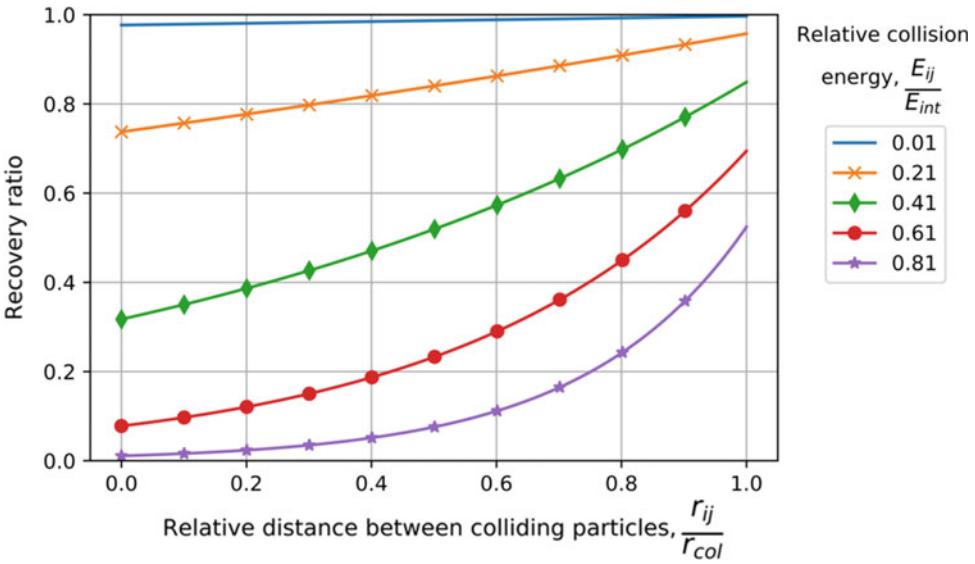

Fig. 4 Dependences of the recovery factor based on the results of a numerical parametric study based on numerical simulation of the interaction of dusty fractal clusters with $D_\beta = 2.99$

dust particles is made by hydrodynamic (streaming) instability. In a dispersed medium with particles whose Stokes numbers are close to unity, it can lead to a local concentration of particles and thereby contribute to an increase in the surface density and the emergence of gravitational instability, with the formation of individual large protoplanetesimals.

- *Turbulent and "vortex assembly*". In a turbulent gas-dust environment, conditions can be created under which particles are concentrated in separate local areas—turbulent eddies. They promote the growth of dust clusters up to the size of protoplanethesimals.

All these mechanisms are discussed in more detail in the cited list of references and other papers and monographs by the authors containing the statement of problems, description of mathematical models and developed algorithms for their numerical implementation. Here, we restrict ourselves to considering the process of formation of primary dust fractal clusters. The proposed and developed approach to modeling the evolution of the solid-state components contained in them is based on the method of permeable particles [20]. The method allows simulation of collisional processes involving dust agglomerates and clusters.

2.3 Formation of Primary Dust Aggregates

The problem of modeling the processes occurring in a protoplanetary gas-dust disk at the stage of formation of "loose" dust structures and fractal dust clusters can be divided into several separate stages:

- the formation of initial fractal clusters with a characteristic size from 5 to 500 nm, corresponding to the size of the initial dust particles;
- the study of the influence of the internal fractal structure and relative collision rates of primary clusters on the processes of their evolution with the formation of fractal clusters with a characteristic size of more than 500 nm;
- the study of the thermal evolution of large fractal clusters.

The spatial scales in which the processes under consideration take place differ from 100 to 10,000 times or more. This requires the construction of slightly different models to describe the nature of the interactions of model particles, within the framework of the method of permeable particles.

Despite our limited computational capabilities, we managed to move on to considering the internal structure of dusty fractal clusters containing only a few particles (supramolecules). This makes it possible to study not only the mechanical properties and the internal structure of clusters, but also opens up the opportunity to proceed to the consideration of heterogeneous processes occurring at the junction of physics and chemistry, which, in turn, provides an approach to studying the physico-chemical evolution of matter in the solid-state component of protoplanetary disks.

When constructing models for the formation and growth of fractal clusters with a complex internal structure, one of the fundamental issues is to determine the interaction forces between dust particles (clusters), their constituent molecular aggregates, and particle surfaces. We have adopted the following types of particle interaction: electrostatic force; force described by modified potentials; gravity.

At the initial stage of the formation of fractal clusters, dust particles with a characteristic size of $\sim$1–2 nm were considered. Only a few particles can be accommodated in such spatial volumes. Due to the large relative distance, the particles are electrically neutral, and at the collision distance, it is necessary to take into account the spatial inhomogeneity of their electric field. Such field inhomogeneity is associated with the spatial distribution of charges in the molecular structure of objects that make up dust particles. In numerical simulation for particles with a diameter of 1 nm and a density of 1.5×10^{-21} g/nm^3, taking into account the quasineutrality of the medium, it was assumed that the particles have a unit elementary charge (a half of the particles are negatively charged, a half are positively charged). The gravitational interaction for the particles themselves is negligible and should be taken into account only when a significant total mass of particles in the enlarging clusters is reached.

At the qualitative level, the growth process of a dusty fractal cluster can be represented as a result of sticking together of dust particles. The properties and composition of such a fractal cluster depends on the conditions under which the growth process takes place. These processes make it possible to analyze numerical models based on various algorithms for describing the motion and conditions of particle and cluster adhesion during the formation of multifractals.

2.4 Computational Experiments with Dust Clusters

2.4.1 Formation of Initial Structures

Numerical simulation of the growth of particles for a cubic region with a volume of 10^6 nm^3 (a side of a cube is 100 nm) containing 10,000 particles with the characteristics described above has been carried out. Fluctuations of dust of such density can be formed both as a result of various vortex motions of the gas carrying the dust, and under the influence of inhomogeneous electromagnetic fields of the protoplanetary disk. The total duration of the calculated simulation time was $2 \cdot 10^{-5}$ s, after which the process of formation of the structure of the dust cluster slowed down significantly. The rate of change in the structure of the forming dust clusters exponentially decreases as free particles are "scooped up" and further growth occurs when individual clusters approach each other. Numerical modeling, starting with denser configurations, leads to the formation of enlarged fractal dust clusters. Particles' characteristics are assumed to be the same as in previous models. The resulting cluster has a characteristic size of about 20 nm.

2.4.2 Collisional Evolution of Initial Clusters

The study of collisions of dusty fractal clusters is impossible without studying their internal structure. Numerical modeling show that, in spite of the substance density significantly increasing with an increase in the number of particles, its complex spatial organization remains. The mechanical properties of such objects can be satisfactorily described within the framework of the developed method of permeable particles; however, to construct sets of control parameters, a more detailed study of the dynamic behavior of clusters in collisions with different relative velocities is required. Collisions of dusty fractal clusters in the contact region lead to a rearrangement of the structure and, as a consequence, to a change in the fractal dimension. So the rheological characteristics of dusty fractal clusters are unsteady. Since the structural integrity of a cluster depends on the bonds of particles with each other, it can be assumed that there is a dependence of the rate at which colliding clusters are destroyed on the energy of the internal bond of particles in the cluster.

2.4.3 Structure and Properties of Heterogeneous Fractal Dust-Ice Clusters on the Snow Line

Modeling of the fragmentation process of dust fractal clusters at the intersection of the water ice line in the near–solar and near-stellar protoplanetary disks is necessary to clarify the conditions for the formation of fragments of significantly different sizes: from small, containing several dust particles, to large dust agglomerates comparable in linear size and mass with the original cluster. The data on the chemical composition and particle size ranges required for modeling the structure of dusty fractal clusters are presented in [21–24].

Numerical modeling has shown that if the sizes of the refractory aggregates composing the cluster are close to or larger than the sizes of ice aggregates, mainly small fragments with masses less than 1–2% of the total mass of the refractory component of the cluster are formed on the ice line. This trend continues up to the maximum possible, according to cometary data, mass fraction of refractory matter, which is 90%. If the boundaries of the size range of the refractory component are significantly smaller than the corresponding radii of the ice components (by 5 or more times), then with a mass fraction of the refractory component from 60 to 90%, large fragments with a developed internal structure are formed as a result of ice sublimation, and the masses of the largest fragments can reach up to 35–40% of the total mass of the refractory substance in the cluster, their sizes can be comparable to the diameter of the initial cluster. At the same time, a small number of the largest fragments concentrate more than half of the total mass of the refractory component of the cluster substance. Such large fragments drift from the ice line into the inner zone of planet formation, which is associated with the loss of angular momentum due to friction with the gas.

The distribution of the mass and size of the fragments formed on the ice line depends on the ratio of the densities of refractory and ice aggregates and the ratio of their mass fractions in the cluster (δ). The larger the specific volume of the refractory component, the more massive are the largest fragments, which concentrate a large fraction of the mass of the refractory component, and their sizes are commensurate with the initial cluster. If the density of the refractory component is only three times higher than the density of the ice component, then even with a relatively small (close to protosolar δ = 1.5–2) ratio of the mass fractions of the refractory and ice components, after the sublimation of ice, large massive fragments are formed, in which most of the masses of the refractory material of the cluster is concentrated. At the same time, if the density of refractory aggregates is an order of magnitude higher than the density of ice aggregates, then for the formation of massive fragments containing the bulk of the refractory material of the cluster, the ratio of the masses of the refractory component and ice, which is consistent with cometary data, is necessary (δ = 9).

The developed model provides an approach to understanding the fragmentation process of dust-ice fractal clusters on the ice line in protoplanetary disks around young stars. This indicates the importance of studying the ratio of sizes, densities, and mass fractions of predominantly refractory and ice components of dust fractal clusters. The latter is especially important when simulating mutual collisions of loose, “fluffy” fractal dust aggregates considered earlier.

Numerical modeling of fragmentation of dusty fractal clusters with a diameter of 0.1 m, for which the fractal dimension varied in the range from 2.01 to 2.99. For this modelling, the ratio of the mass fraction of the refractory component to the mass fraction of ice equals to 9. The form of the considered fractal clusters before ice sublimation is shown in Figs. 5, 6, 7 and 8.

As can be seen from Figs. 9, 10, 11 and 12, fractal dust clusters with dimensions less than 2.8 after ice sublimation break up into extended fragments with some spatial structure. As the fractal dimension increases, the size, mass and number of constituent particles of the largest fragments increase. For fractal dimensions from 2.01 to 2.5, fragments contain from several tens to thousands of particles. For fractal dimensions from 2.5 to 2.8, the largest fragments can contain up to several tens of thousands of particles. However, with a further increase in the fractal dimension, the density of clusters increases, which leads to a sharp decrease in the size, mass and number of constituent particles of fragments. For a fractal dimension from 2.99 up, the largest fragments contain about ten particles.

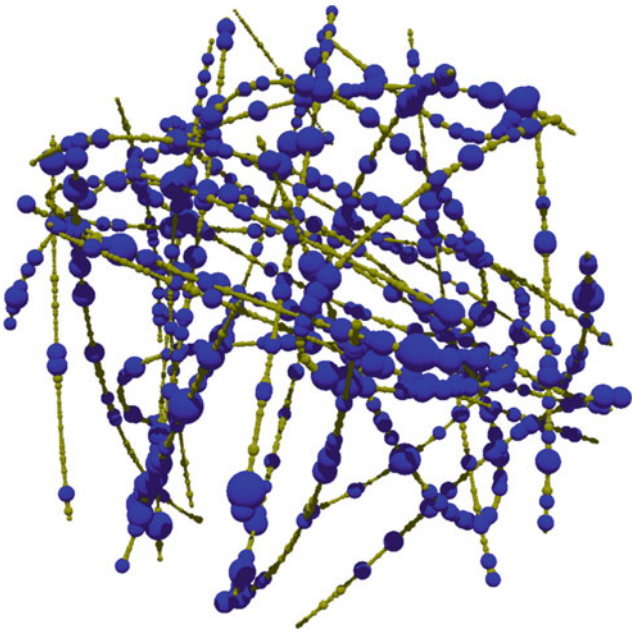

Fig. 5 Structure of fractal dust clusters for different fractal dimensions $D_\beta = 2.11$

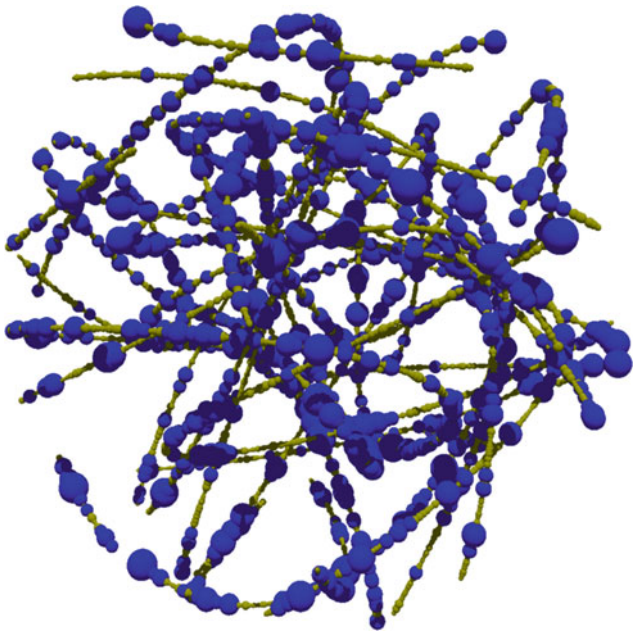

Fig. 6 Structure of fractal dust clusters for different fractal dimensions $D_\beta = 2.33$

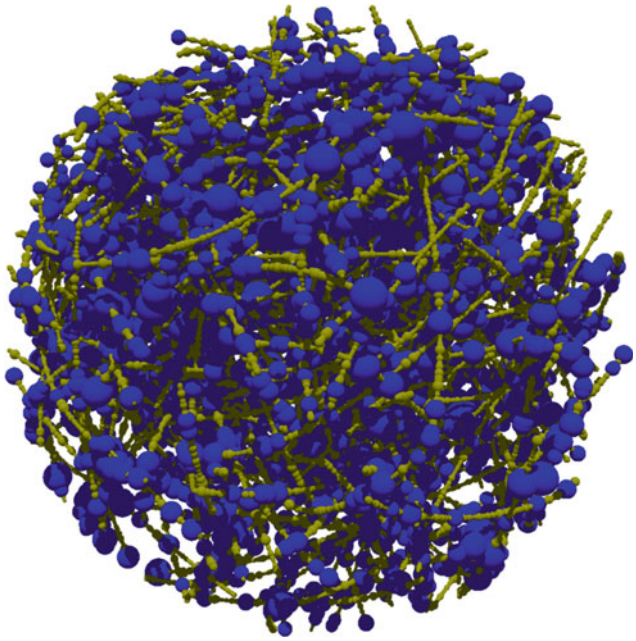

Fig. 7 Structure of fractal dust clusters for different fractal dimensions $D_\beta = 2.66$

The obtained results make a significant contribution to the study of the processes of the early stage of evolution of the circumstellar protoplanetary disks, first of all, the protosolar disk.

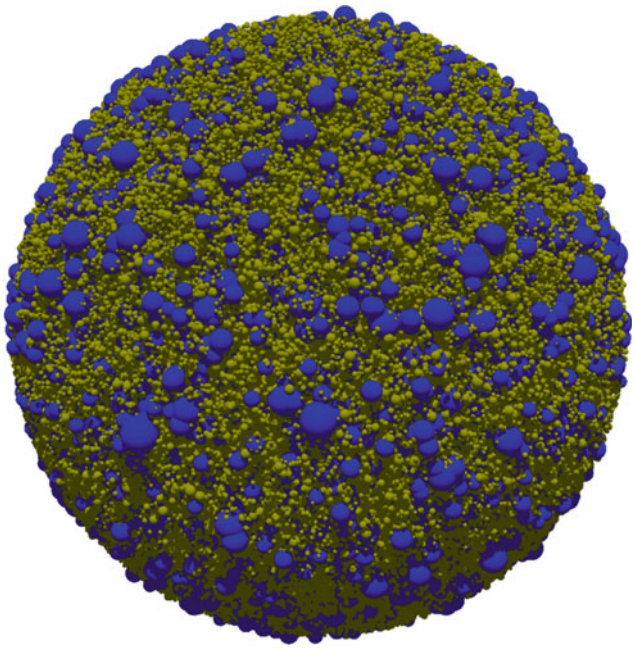

Fig. 8 Structure of fractal dust clusters for different fractal dimensions $D_\beta = 2.99$

2.5 Accumulation of the Terrestrial Planets and the Moon

The study of the accumulation of terrestrial planets is based on computer simulation of the evolution of disks of gravitating bodies that unite in collisions. The basic concepts of this approach are contained e.g. in [25–31]. In our later paper [32], we simulated the migration of planetesimals from the feeding zone of the terrestrial planets, divided, depending on the distance from the Sun, into seven regions. The gravitational influence of planets or their embryos was taken into account. In some variants of calculations, the masses of the embryos of the planets were 10 times, and in others were 3 times less than the present masses of the planets. Based on the arrays of the obtained orbital elements of migrated planetesimals, the probabilities of their collisions with planetary embryos at several stages of embryo growth were calculated. Later, for the initial data from [32], additional calculations were carried out, in which, when integrating the equations of motion of planetesimals, the moments of their collisions with planets were determined, and such planetesimals were not taken into account in further integration. In the new series of calculations, the conclusions on the mixing of planetesimals in the disk remained mainly the same, but in some cases, the times before the fallout of planetesimals onto planets increased, since in the model of planets-material points, the planetesimal continued to be in the disk after the expected collision.

Fig. 9 Fragments of fractal dust clusters after ice sublimation for cluster with $D_\beta = 2.11$

Fig. 10 Fragments of fractal dust clusters after ice sublimation for cluster with $D_\beta = 2.33$

Fig. 11 Fragments of fractal dust clusters after ice sublimation for cluster with $D_\beta = 2.66$

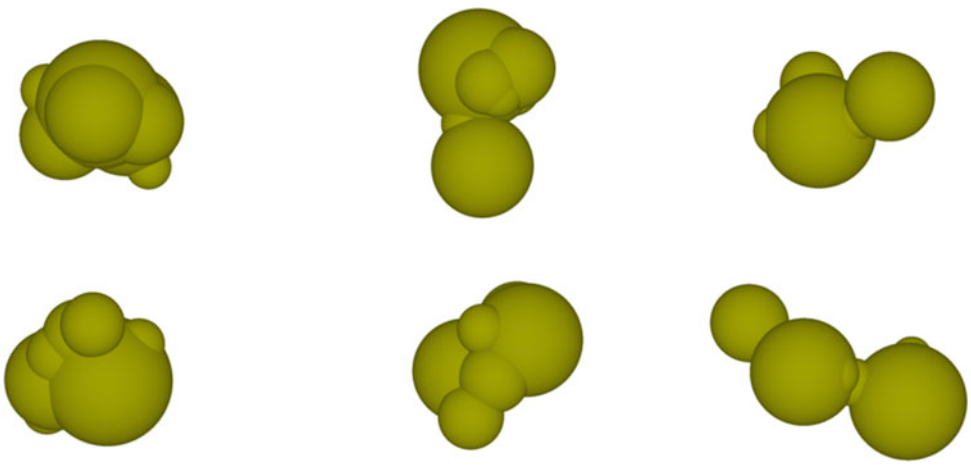

Fig. 12 Fragments of fractal dust clusters after ice sublimation for cluster with $D_\beta = 2.99$

Based on the results obtained, an important conclusion was made that each relatively small embryo of the terrestrial planet accumulated mainly material from the neighbourhood of its orbit. The embryos of the terrestrial planets had not yet reached the masses of the present planets when they accumulated also the planetesimals that migrated from the feeding zone of Jupiter and Saturn. So inner layers of the terrestrial planets can include material (e.g., water and volatiles) delivered from the zone of these giant planets. For planetesimals initially located at different distances from the Sun in the range from 0.7 to 2 AU, the ratio of the number of planetesimals collided with almost formed the Earth and Venus mainly differed for these planets by no more than a factor of two. For most calculation variants (not for all), for planetesimals with initial semi-major axes in the ranges between 1.1 and 1.3 AU, between 1.3 and 1.5 AU, and between 1.5 and 2 AU from the Sun, the fraction of planetesimals collided with almost formed the Earth and Mars differed for these planets from the ratio of the masses of the planets by no more than a factor of two.

According to [33], the mass of Mars reached roughly its present value in less than 5 million years. Results of our calculations showed that Mars could not acquire most of its mass in 5 million years. Some planetesimals from its feeding zone could still move in elliptical orbits after a few hundreds of million years. Therefore, it can be assumed that a sufficiently large embryo of Mars (for example, with a mass not less than $0.02m_E$, where m_E is the Earth' s mass) could have formed by compression of a rarefied condensation. Some planetesimals from the vicinity of the orbit of Mars could be removed by the planetesimals that came from the feeding zone of Jupiter and Saturn. The latter planetesimals could also increase eccentricities of the orbits of Mercury and Mars. In [32] it was also supposed that the embryo of Mercury with a mass of about $0.02m_E$ could also form by compression of the initial condensation. Some planetesimals that formed Mercury could lost part of silicate composition during their motion near the Sun. Together with the loss of some silicate shell during high-velocity impacts, it could be one of explanations of the high iron content in the core of Mercury.

Not more that 10% of planetesimals were ejected from the feeding zone of the terrestrial planets into hyperbolic orbits, and less than 1% of planetesimals collided with Jupiter. For the initial distances of planetesimals from the Sun in the ranges from 0.3 to 2.0 AU the fraction of planetesimals falling onto the Sun usually exceeded 20%. With the ratio of the masses of the embryos of the Earth and the Moon equal to 81 (as in the present era), the ratio of the probabilities of planetesimals falling onto the embryos of the Earth and the Moon in the considered variants did not exceed 54. These estimates do not indicate that the growth of the Moon relative to the Earth was faster, since as in high-speed collisions, the fraction of material ejected from the less massive Moon is greater than that from the Earth.

One of the important sections in the study of the role of planetesimals in the accumulation of planets is the formation of the Moon. For a long time, the mega-impact model of the formation of the Moon dominated [34–36]. Criticism of this model based on geochemical (isotope) restrictions is given in [37–39], which considered the formation of the Earth-Moon system from a rarefied condensation with a mass equal to the sum of the present masses of the Earth and the Moon. The model [40] also considered the formation of the embryos of the Earth and the Moon from a rarefied condensation, but with a mass 10–100 times less than the present mass of the Earth. It was assumed that the angular momentum of the condensation required for the formation of the satellite system was obtained as a result of the collision of two initial condensations. The later accumulation of the Earth and the Moon occurred due to the fallout of planetesimals from the vicinity of the orbit of the Earth. However, in contrast to other papers on the multi-impact model (for example, [41]), in this scenario, the initial embryo of the Moon was formed from a rarefied condensation, and not from bodies ejected from the Earth. In order for the formed Moon to have a present composition of iron (about 8%), the mass of matter ejected from the Earth's mantle (containing 5% iron) and included in the composition of the Moon would have to be about an order of magnitude greater than the mass of matter in planetesimals and in the initial embryo of the Moon (in which the fraction of iron could be about 33%). Note that the model of the formation of the embryos of the Earth and the Moon from the common rarefied condensation is similar to the model of the formation of satellite systems of trans-Neptunian objects, considered earlier in [42, 43].

2.6 Time Scale of Migration Processes and Velocities of Collisions of Bodies with the Earth and the Moon

Of interest is the question of what time scale these migration processes take place on. Estimates of the characteristic time for which planetesimals reach the Earth depend on the initial distances of planetesimals from the Sun. Times elapsed until collisions with the Earth were generally within one million years for planetesimals which initial orbits crossed the orbit of Jupiter and were during the first 10 million years for planetesimals originally located at a distance of 4–5 AU from the Sun. The times elapsed before the bodies that migrated from the zone of Uranus and Neptune fell onto the Earth could exceed 20 million years and depended on the appearance of large embryos of these planets in this zone. Large embryos of Uranus and Neptune could initially have formed near the orbit of Saturn, where they acquired

hydrogen envelopes [44, 45]. Due to the mutual gravitational influence of planetesimals, these embryos could migrate to the present orbits of these planets [25, 26]. The dynamic lifetimes of bodies that were originally in the feeding zone of Uranus and Neptune could reach hundreds of millions of years. Finally, according to the model, which takes into account only the gravitational influence of the planets, some bodies initially located at a distance from 3 to 3.7 AU from the Sun, could fall onto the Earth and the Moon in a few billion years. Therefore, bodies from the zone of the outer asteroid belt could participate in the "late heavy bombardment" (LHB) of the Earth and the Moon.

During the accumulation of terrestrial planets, the ratio of the number of planetesimals from the feeding zone of these planets collided with the Earth and the Moon varied mainly from 20 to 40. For bodies arriving from distances from the Sun greater than 3 AU, this ratio was mainly in the range from 16.4 to 17.4. The characteristic velocities of collisions of planetesimals from the feeding zone of the terrestrial planets with the Moon varied from 8 to 16 km/s depending on the initial distances of planetesimals from the Sun and their initial eccentricities. The velocities of collisions with the Moon of bodies that came from the feeding zones of Jupiter and Saturn were mainly in the range from 20 to 23 km/s [46]. The characteristic velocities of collisions of planetesimals, originally located at radial distances from 0.7 to 1.1 AU, with the embryos of the Earth and the Moon with masses 10 times less than their modern masses, were in the range from 7 to 8 km/s for the embryo of the Earth and from 5 to 6 km/s for the embryo of the moon. For planetesimals that came to the feeding zones of the terrestrial planets from regions more distant from the Earth's orbit, the characteristic velocities were from 9 to 11 km/s for collisions with the embryo of the Earth, and from 7 to 10 km/s for collisions with the embryo of the Moon.

2.7 Water on the Earth and Other Terrestrial Planets

From the point of view of studying the sources of water and other volatiles on the Earth and the terrestrial planets, not retained by these planets during the formation of a gas-dust disk in the vicinity of the Sun in the high-temperature zone, the problem of migration of planetesimals enriched in volatiles from the outer regions of the Solar system is of primary interest. The problem of delivery of water and volatiles to the Earth is directly related to the key issues of the origin and evolution of life in the Solar System and its possible existence in exoplanetary systems [1, 47, 48]. An exogenous source of water on the Earth does not exclude a certain contribution from an endogenous source of juvenile water, which makes it possible to explain the observed differences in the D/H ratio in ocean water and water contained in comet nuclei and asteroids such as carbonaceous chondrites.

In calculating the migration of bodies to the Earth from beyond the orbit of Mars, we took into account the gravitational influence of 7 planets (from Venus to Neptune). In each variant of the calculations, the initial values of the semi-major axes of the planetesimals' orbits varied from $a_{\min}$ to $a_{\max} = a_{\min} + d_a$, their initial eccentricities were equal to e_o, and the initial inclinations were equal to $e_o/2$ rad. In one series of calculations, $d_a = 0.1$ AU, and $a_{\min}$ took values from 3.0 to 4.9 AU with a step of 0.1 AU. The initial eccentricities e_o in this series were 0.02 or 0.15. In another series of calculations, $d_a = 2.5$ AU, and $a_{\min}$ took values from 5 to 40 AU with a step of 2.5 AU. Initial eccentricities were 0.05 or 0.3. In each variant of calculations, 250 planetesimals were considered, but for the same values of $a_{\min}$, d_a, and e_o, several (up to 8) variants of calculations were carried out. On the basis of the obtained arrays of elements of the orbits of migrated planetesimals, similarly to [49], the probabilities of collisions of planetesimals with the Earth were calculated.

Figure 13 shows the values of the probability p_E of a collision of a planetesimal with the Earth, multiplied by a million, depending on the value of $a_{\min}$ of the minimum initial semi-major axis of the planetesimal's orbit (in AU). Axis values are in logarithmic scale. Different lines correspond to different initial orbital eccentricities. The values of p_E are the mean values averaged over the planetesimals (from 250 to 2000) considered for the given $a_{\min}$ and e_o values.

At $a_{\min} \leq 7.5$ AU, the value of the probability p_E of a collision of a planetesimal with the Earth, averaged over 250 bodies in one variant, could vary hundreds of times for different variants of calculations with the same values of $a_{\min}$, d_a, and e_o. The value of p_E for various calculation options could vary from a value less than 10^{-6} to a value of the order of 10^{-3}. At $a_{\min} \geq 15$ AU, the value of p_E for various calculation variants varied from values of the order of 10^{-7} to 5×10^{-6}.

Assuming the total mass of planetesimals in the feeding zone of Jupiter and Saturn to be equal to about $100m_E$ (which is less than a quarter of the total present mass of these planets), at $p_E = 2 \times 10^{-6}$, we find that the total mass of planetesimals that fell onto the Earth was $2 \times 10^{-4} m_E$, which corresponds to the mass of the Earth's oceans. Approximately the same number of bodies could have been delivered to the Earth from the zone of the outer asteroid belt (from distances of $3 \leq R \leq 4$ AU). The value of p_E for the feeding zone of Jupiter and Saturn could exceed 2×10^{-6} by a factor of several. It increases the estimates of the total mass of ice bodies delivered to the Earth from beyond the snow line. The ices, however, constituted only a part of the

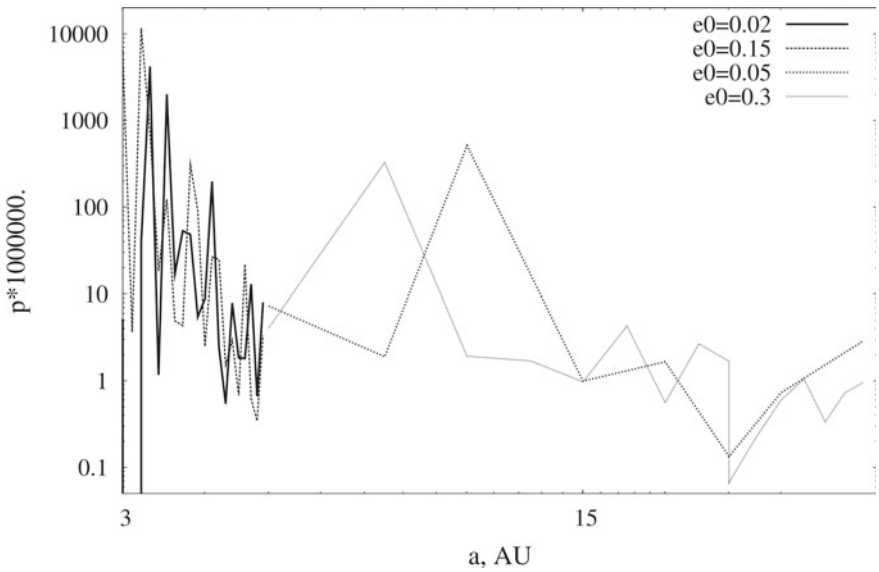

Fig. 13 The probability p of a collision of a planetesimal with the Earth depending on the initial value a_{min} of the semi-major axis of the planetesimal's orbit (in AU). Axis values are in logarithmic scale. Different lines correspond to different initial orbital eccentricities

planetesimals' matter. Thus, the fraction of water ice in the nuclei of comets does not exceed 33%, although it could have been more in the initial planetesimals. The conclusion about the possible delivery of such an amount of water to the Earth from the feeding zones of the giant planets was made by us earlier on the basis of calculations of planetesimal migration by the method of spheres of action [26, 50, 51]. The ratio of the total mass of planetesimals that came from the feeding zones of Jupiter and Saturn and collided with the planet turned out to be slightly higher for Mercury and Venus, and for Mars were 2 or 3 times more than for the Earth [52].

2.8 Migration of Bodies from Beyond the Orbit of Mars and the Problem of Asteroid-Comet Hazard

The main asteroid belt, the trans-Neptunian belt (the Kuiper belt), and the Oort cloud are considered to be the main sources of near-Earth objects (NEOs), for which the perihelion distance $q < 1.33$ AU. The fraction of close encounters of active comets with the Earth among the approaches of all bodies is of the order of 0.01. However, the number of comets that have lost their activity (are "extinct"), whose nuclei, like asteroids, do not show activity, can be much greater than that of active ones.

The migration of small bodies (asteroids, comets, and meteoroids) to the Earth is associated with the problem of the asteroid-comet hazard, which is attracting growing attention as a potential source that threatens to the Earth's civilization. The level of the hazard depends on the size of the body and the expected frequency of events. Among NEOs, the groups of Amor, Apollo and Aten are the most dangerous. Some NEOs reach kilometers in size, and their collisions with the Earth can cause a global catastrophe, as has happened several times in the geological history of our planet (see, for example, [48]). A detailed discussion of studies on the migration of celestial bodies in the forming and present Solar System, closely related to the problem of asteroid-comet hazard, is presented in [53].

Bodies continue to migrate to the Earth's orbit at the present time, and much attention is paid to this problem (see [51, 54]). The fall of the Chelyabinsk meteorite that occurred in 2013 shows [55, 56] the serious consequences of the fallout of even a relatively small ($\sim$20 m) body onto the Earth in a densely populated area.

Asteroids are usually considered to be the main source of NEOs [54, 57]. Comets are very dangerous because of the suddenness of their appearance. Most NEOs probably came from the interior of the Main Asteroid Belt (31% from the 3:1 resonance with Jupiter, 40% from the secular υ_6 resonance, 13% from an intermediate source of orbits crossing the orbit of Mars, and 16% are former Jupiter-family comets) [54].

Eneev [58] believed that almost all NEOs came from the trans-Neptunian belt. According to [26, 59], about 20% of near-Earth objects with a diameter $d \geq 1$ km could have come from the zone of the trans-Neptunian belt. These estimates used the results of the evolution of the orbits of one hundred Kuiper belt objects under the gravitational influence of the planets. It was found that during the evolution, the perihelion distances of the orbits of two such objects decreased to 1 AU, respectively, in 25 and 64 million years. The average time of motion of a body in an orbit of a Jupiter-crossing object (JCO) is 200 thousand years. In this case, the fraction of the former JCOs that reach the Earth's orbit during their lifetime is 0.2, and the average time

during which the JCO crosses the Earth's orbit is about 5000 years. It was concluded that at the number of 1-km objects in the Kuiper belt equal to 10^{10}, and the number of 1-km Earth crossing objects (ECOs) equaled to 750, the number of present JCOs arriving from the trans-Neptunian belt is N_J = 30,000. At the same time, about 170 1-km former trans-Neptunian objects (TNOs) cross the Earth's orbit, accounting for approximately 20% of ECOs.

Some comets can move for quite a long time (up to tens of millions of years) in orbits crossing the Earth's orbit. During this time, they can lose cometary activity and look like asteroids. The time of cometary activity was estimated by many scientists, on average it is about 10^3–10^4 years (according to [60]—from $3{\cdot}10^3$ to $3{\cdot}10^4$ years). Therefore, the number of extinct comets can exceed the number of active comets by several orders of magnitude. Objects that cross the Earth's orbit and have lost their cometary activity move relatively far from the Earth for a significant part of the time and are more difficult to observe than ordinary ECOs.

An example of the time variations of the semi-major axis, aphelion and perihelion distances, eccentricity and sine of the inclination of the orbit of a body, the initial orbit of which was close to the orbit of the Comet 10P, is given in Figs. 14 and 15, which are based on results from [49]. The semi-major axis, eccentricity, and inclination of the initial orbit of the body were taken equal to 3.1 AU, 0.53, and 12.0°, respectively. The calculations took into account the gravitational influence of the planets and the Sun. For about 30 million years, the semi-major axis of the body's orbit varied in the range from 2 to 3 AU, and its orbit often crossed the Earth's orbit. The transition of comets to asteroid orbits is rare, but is possible.

Asteroids and comet nuclei are responsible for the formation of craters on the surfaces of planets, their satellites and small bodies themselves. Data on their size and time of formation serve as an important statistical source of information in the problem of asteroid-comet hazard. It is believed that during the last 3 billion years the flow of crater-forming bodies was approximately constant, and about 4 billion years ago, during the Late Heavy Bombardment (LHB), it was 100–500 times more intense [61, 62]. According to [63], collisions with asteroids probably prevailed in the formation of terrestrial craters with a diameter of $D < 30$ km, while collisions of comets were responsible for the formation of craters with $D > 50$ km. This feature can be explained by the fact that trans-Neptunian objects can leave the trans-Neptunian belt practically without collisions, in contrast to asteroid bodies of the main belt that have experienced multiple collisions.

The paper [64] represents the comparison of the number of lunar craters with a diameter greater than 15 km and an age of less than 1.1 billion years with the estimates of the number of craters of this size that could form in 1.1 billion years if the number of objects approaching the Earth and their orbital elements during this time would be close to their present values. These estimates do not contradict the increase in the number of objects approaching the Earth, after the possible catastrophic destruction of large asteroids in the main belt, which could have occurred during the last 300 million years, but they do not prove this increase either. For Copernican (with an age of no more than 1.1 billion years) craters on the lunar seas and continents, the number of craters per unit area and the dependence of the ratio of a crater depth to its diameter on the crater diameter are different [65].

2.9 Migration of Bodies in Exoplanetary Systems

Obviously, similar to the migration of ice bodies from behind the snow line to the inner planets of the Solar System, the migration of ice bodies could also occur in exoplanetary systems. As an example, a comparison was made of the delivery of water and volatile comet-like bodies to potentially habitable planets in in the Proxima Centauri system and in our Solar System [66]. Migration of planetesimals that were originally located in the feeding zone of the exoplanet c with a semi-major axis a_c = 1.489 AU was studied. The exoplanet b is located in the habitable zone in

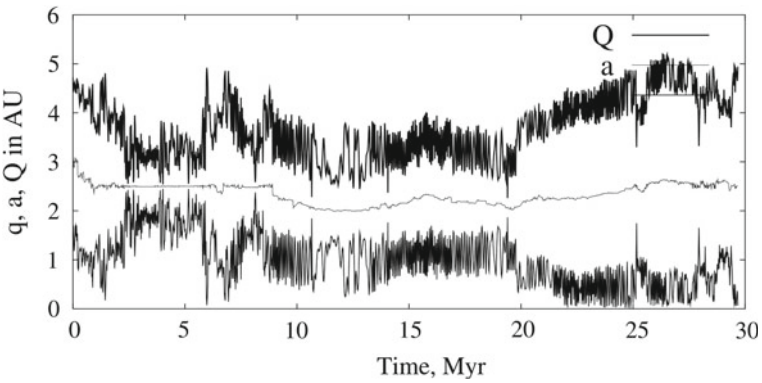

Fig. 14 Variations with time (in millions of years) of the semi-major axis, aphelion and perihelion distances (in astronomical units) of the orbit of a body whose initial orbit was close to the orbit of the Comet 10P

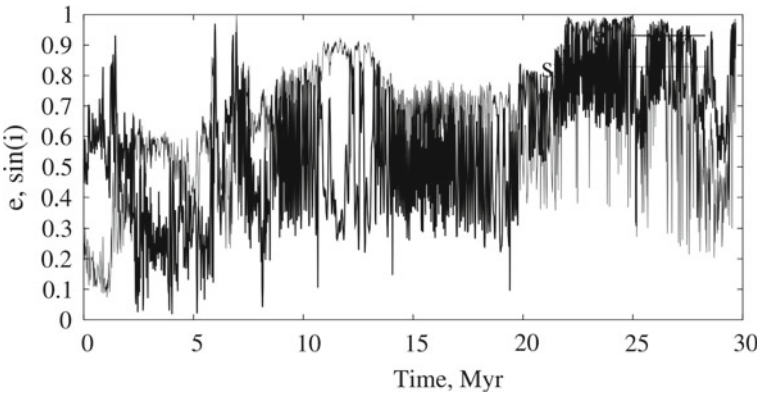

Fig. 15 Variations with time (in millions of years) of eccentricity and sine of the inclination of the orbit of a body whose initial orbit was close to the orbit of the Comet 10P

the Proxima Centauri system. In the first series of calculations, the following initial semi-major axes of the orbits and the masses of two exoplanets were considered: a_b = 0.0485 AU, a_c = 1.489 AU, $m_b = 1.27m_E$ and $m_c = 12m_E$. The initial eccentricity e_b and the initial inclination i_b of the exoplanet *b* were considered to be equal to 0, and the initial eccentricity e_c of the exoplanet *c* was equal to 0 or 0.1. The initial inclination of the orbit of the exoplanet *c* was $i_c = e_c/2 = 0.05$ rad or $i_c = e_c = 0$. In the second series of calculations, based on later observational data, it was assumed that $a_b = 0.04857$ AU, $e_b = 0.11$, $m_b = 1.17m_E$, $a_c = 1.489$ AU, $e_c = 0.04$, $m_c = 7m_E$ и $i_b = i_c = 0$. In each variant of the calculations, the initial values of the semi-major axes of 250 planetesimals were in the range from a_{min} to $a_{min} + 0.1$ AU, where a_{min} varied from 1.2 to 1.7 AU with a step of 0.1 AU. The initial eccentricities e_o of orbits of planetesimals were 0 or 0.15 for the first series of calculations, and $e_o = 0.02$ or $e_o = 0.15$ for the second series of calculations. The initial inclinations of the planetesimals' orbits were $e_o/2$ rad. The calculations were carried out for two models (*MP* and *C*). In the model *MP*, for simulation of the motion of planetesimals, the planets were considered as material points. On the basis of the orbital elements of migrated planetesimals (similar to [49], but for other masses of the star and planets), the probabilities of collisions of migrated planetesimals with exoplanets were calculated. These probabilities were adjusted taking into account that the integration did not simulate collisions of planetesimals with exoplanets, and the number of planetesimals in the disk decreased only due to ejection into hyperbolic orbits and due to collisions with the parent star. At calculations of the motion of planetesimals, two planets (*b* and *c*) were considered, but the probabilities of collisions were also calculated for the unconfirmed exoplanet *d* ($a_d = 0.029$ AU, $e_d = 0$, $m_d = 0.29$ *mE*). For the model *C*, we carried out calculations in which, at integration of motion equations of planetesimals, the moments of collisions of planetesimals with planets were determined, and such collided planetesimals were removed from the calculations. For the *C* model, the probabilities of collisions of planetesimals with the planet *c* were generally slightly higher, and the probabilities of collisions with the planet *b* were less than for the *MP* model. However, the main conclusions were approximately the same for the both models.

It was obtained that over 10 million years most of the planetesimals were thrown into hyperbolic orbits or collided with the exoplanet *c*. Some planetesimals may have continued to move in elliptical orbits after 50 million years. The number of planetesimals ejected into hyperbolic orbits at $e_o = 0.15$ was greater than the number of planetesimals that collided with exoplanets. Therefore, a cometary cloud similar to the Oort cloud can exist in the Proxima Centauri system. The ratio of the number of planetesimals ejected into hyperbolic orbits to the number of planetesimals that collided with exoplanets is greater for the larger mass of the Proxima Centauri *c* and for large initial eccentricities of planetesimals. This ratio mainly increased with an increase of the considered time interval. Only one of several hundreds or thousands of planetesimals that migrated from the vicinity of the orbit of the Proxima Centauri *c* reached the orbit of the exoplanet Proxima Centauri *b* (with a semi-major axis $a_b = 0.0485$ AU) and often simultaneously also the orbit of the unconfirmed exoplanet Proxima Centauri *d* (with a semi-major axis $a_d = 0.029$ AU). However, the probability of a collision of such a planetesimal (having reached these orbits) with the exoplanets Proxima Centauri *b* or Proxima Centauri *d* could reach 1. This probability of collision, averaged over all planetesimals considered, was $\sim 10^{-4}$–10^{-3}. When averaged over all planetesimals under consideration that migrated from the vicinity of the orbit of the Proxima Centauri *c*, the probability of a collision of a planetesimal with the exoplanets *b* or *d* is greater than the probability of a collision with the Earth of a planetesimal migrating from the feeding zone of giant planets of the Solar System. The latter probability per one planetesimal is usually less than 10^{-5}. A lot of icy matter and volatiles could be delivered to the exoplanets Proxima Centauri *b* and Proxima Centauri *d*.

As the Earth and Venus, some neighbouring planets in the TRAPPIST-1 exoplanetary system accumulated planetesimals initially located at the same distance. This system includes the star with a mass equal to 0.0898 of the mass of the Sun and 7 planets (from *b* to *h*). Semi-major axes of orbits of the planets are from 0.012 to 0.062 AU, and their masses are from $0.33m_E$ to $1.37m_E$. We studied separately the migration of planetesimals from the vicinity of an orbit of each 'host' planet under the gravitational influence of all planets and the probabilities of their collisions with planets. In some calculations initial eccentricities were equal to 0.02, and in other calculations equaled 0.15. Mixing of planetesimals was smaller for the calculations *C* than for calculations *MP* (such calculations were similar to those for the Proxima Centauri system presented above). Below the estimates based on the *C* calculations (at which collided planetesimals excluded from integrations) are discussed. More than a half of planetesimals from disks near orbits of planets *b*–*g* collided with planets in less than 1000 year, and for disks *b*–*d* even in 250 year. A small fraction of planetesimals from an initial disk in the vicinity of the planet *h* could still move in elliptic orbits after 1 million year. There were no collisions of planetesimals with the host star. Less than 2% of planetesimals were ejected into hyperbolic orbits. There was no ejection for disks near orbits of the planets *b* and *c*. The fraction of planetesimals collided with the 'host' planet (compared to collisions with all planets) decreased with the considered time interval. In each calculation variant there was at least one planet for which the number of collided planetesimals was greater than 0.25 of the number of collisions of planetesimals with the 'host' planet. The fraction of collisions of planetesimals with the 'host' planet was usually smaller for disks located farther from the star. For the initial disk near the orbit of the planet *h*, the number of collisions of planetesimals with the planet *g* was about that with the planet *h*. For disks near orbits of planets from *d* to *h*, planetesimals collided with all planets. Therefore, outer layers of neighbouring planets in the TRAPPIST-1 system can have similar composition, if there were a lot of planetesimals near their orbits at the late stages of the accumulation of the planets. We discuss the late bombardment of the planets, which could be formed at greater distances. Our considered model of mixing of bodies in the zone of the TRAPPIST-1 planets can also characterize the migration of bodies ejected from some planets after collisions of these planets with some planetesimals or other bodies.

2.10 Conclusions

The study of the processes of the origin and evolution of the Solar System and the formation of planetary systems around other stars is one of the fundamental problems of present natural science. In terms of its content, this problem is interdisciplinary and requires the development of a generalizing theory underlying the development of mathematical models of the physical structure and evolution of a gas-dust accretion disk around solar-type stars. The validity of such models is supported by observational data on protoplanetary disks and extrasolar planetary systems.

The creation of cosmogonic models is associated with the study of a turbulized multicomponent gas and dust medium with the participation of kinetic processes in the protoplanetary disk and taking into account its dynamic and thermal evolution, including a change in the state of aggregation of the main components of preplanetary matter and the location of condensation-sublimation fronts. Of primary interest is the development of numerical models of the formation and structure of an accretion disk around single and binary stars, taking into account the energy transfer in the disk by radiation and turbulence, and the formation of primary gas-dust clumps (dust clusters), from which primary solids are subsequently formed, growing to the size of pebbles-cobblestones, from which planetesimals are formed, forming, taking into account gravitational interactions, the embryos of planets and, in the process of their oligarchic growth, planetary systems. An important place is given to the numerical modeling of the mechanism of development of gravitational and streaming instabilities in a dusty subdisk and its compaction with simultaneous radial and vertical compression, taking into account shear stresses in the boundary layers and the polydispersity of suspended dust particles, as well as the growth of solid particles at the boundary of the snow line.

The progress in improving the mathematical models of gas-dust accretion disks is due to the development of effective methods for invariant modeling of turbulent flows in heterogeneous and multicomponent chemically active media, based on phenomenological models, and the development of methods for modeling dust fractal clusters. Much attention is paid to the problems of accumulation of planets and the Moon in the Solar System and planetary systems around other stars on the basis of the study and numerical modeling of migration processes. It is shown that the outer layers of the Earth and Venus could accumulate approximately the same material for these planets from different parts of the feeding zone of the terrestrial planets. The zone of the outer asteroid belt could be one of the sources of the late heavy bombardment. The total mass of water delivered to the Earth from beyond Jupiter's orbit could roughly be equal to the mass of Earth's oceans. The velocities of collisions with the Moon of bodies that came from the zones of Jupiter and Saturn were generally 20–23 km/s.

In the Proxima Centauri system, the total mass of planetesimals, initially located near the orbit of the outer exoplanet *c*, located behind the ice line, and thrown into

hyperbolic orbits at initial planetesimal eccentricities equal to 0.15, exceeded the mass of planetesimals that collided with exoplanets. An analogue of the Oort cloud may exist in the Proxima Centauri system. The probability of a collision of a planetesimal with exoplanets *b* or *d* is greater than the probability of a collision with the Earth of a planetesimal that migrated from the feeding zone of the giant planets of the Solar System. A lot of icy material and volatiles could be delivered to exoplanets Proxima Centauri *b* and *d*.

3 Estimation of the Composition and Mass of the Ice Component in Primary Ice-Rock Bodies of the Protoplanetary Disk

3.1 Introduction

Already at the earliest stages of the formation and evolution of the Solar System, the accumulation of planetesimals took place in the near-solar gas-dust protoplanetary disk (nebula), which then became part of protoplanetary and protosatellite bodies, largely determining their current composition. Therefore, the estimation of the composition of these primary planetesimals is important when developing models of the formation and internal structure of bodies in the Solar System. In this paper, the composition of ice-rock planetesimals, in particular their ice component, as well as its possible mass fraction of the total mass of bodies, depending on the region of formation, is considered. This estimation was carried out based on methods of equilibrium thermodynamics, the radial distribution of temperature and pressure in the near-solar gas-dust accretion protoplanetary disk (nebula) at various times of its evolution, the elemental and chemical composition of the nebula, as well as the component composition of the substance of the gas-dust cloud from which our Solar System has formed 4.567 billion years ago.

3.2 Statement of Problem

To estimate the radial distribution of temperature and pressure in the near-solar nebula, we used models of the internal structure of the near-solar gas-dust accretion protoplanetary disk [67–69]. Those models examined in detail the evolution of the main thermodynamic parameters in the protoplanetary near-solar disk both at the stage of its formation around a forming star inside a collapsing protostellar envelope and at the stage of evolution and dissipation of the accretion disk around an already formed young star at the T Tauri stage. Although new data on young protostars and solar-type stars have appeared in recent years, calculations of models of the protoplanetary disk carried out in these works still mostly correctly reflect the nature of the distribution inside the disk and changes in time of the main thermodynamic parameters: temperature, pressure, surface and bulk density. This is largely due to the fact that for the calculations of models of the structure of the accretion gas-dust near-solar protoplanetary disk, parameter values were chosen that mainly satisfy current astronomical data.

The most important result obtained using the above models was the calculation of the distribution of the main thermodynamic parameters on the height and radius of the gas-dust disk for various time points of its formation and evolution, some of which are shown in Figs. 16 and 17. Thus, Fig. 16 shows the evolution of temperature in the middle plane of the protoplanetary disk at various points of its formation lasting $\sim 10^5$ years: 1—0.25; 2—0.5; 3—0.75; 4—0.95 from the total time of the collapse stage, the duration of which, according to modern data, is estimated to be ~0.1 million years. Figure 17 shows the evolution of the temperature distribution in the equatorial plane of the near-solar disk at the stage of its viscous evolution and dissipation also for four time points:1—0.02; 2—0.05; 3—0.13; 4—1 from the total time of the stage which is estimated to be ~5–10 million years. It follows from the results obtained that the maximum temperatures in the disk are reached near the end of the formation stage, but before the onset of accretion attenuation, since in the last period of collapse the shell gradually becomes transparent and the heating of the disk by external radiation decreases. The formation stage lasting 0.1 million years is the most active stage of the evolution of the near-solar disk. As interstellar matter fell onto the disk and fed the Sun, a large amount of mechanical energy was converted into thermal energy. After the cessation of the precipitation of matter, a quieter and longer-lasting second stage of the evolution of the pre-planetary disk begins—the stage of its evolution around the young Sun at the T Tauri stage. As we move to this stage, the accretion shell that surrounded the Sun and absorbed its optical radiation disappears, and the Sun appears as a young star visible in the optical range and illuminating the pre-planetary disk with its direct, rather than scattered radiation in the shell. Since, according to calculations, the distribution of the density of matter over the thickness of the disk is uneven—up to 75% of the matter is concentrated near the equatorial plane, which is characterized by maximum temperatures at a given heliocentric distance (r), in the future, we will consider them. The radial distribution of the maximum temperatures in the nebula at both stages is shown in Figs. 16 and 17. They also show the formation temperatures of the main phases accumulating sodium, potassium, and sulfur, as well as the condensation temperatures of water ice. They are obtained by calculating the conditions of equilibrium condensation of gas of solar composition according to [70] at pressures corresponding to the specified temperatures.

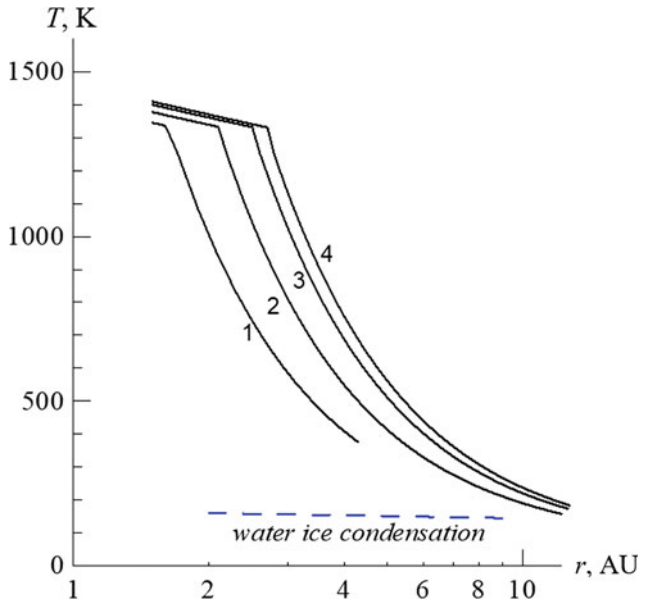

Fig. 16 Radial temperature distribution in the equatorial plane of the near-solar gas-dust accretion protoplanetary disk for various time points for the formation stage of the near-solar disk: 1—0.25; 2—0.5; 3—0.75; 4—0.95 from the full time of the collapse stage ($\sim 10^5$ years)

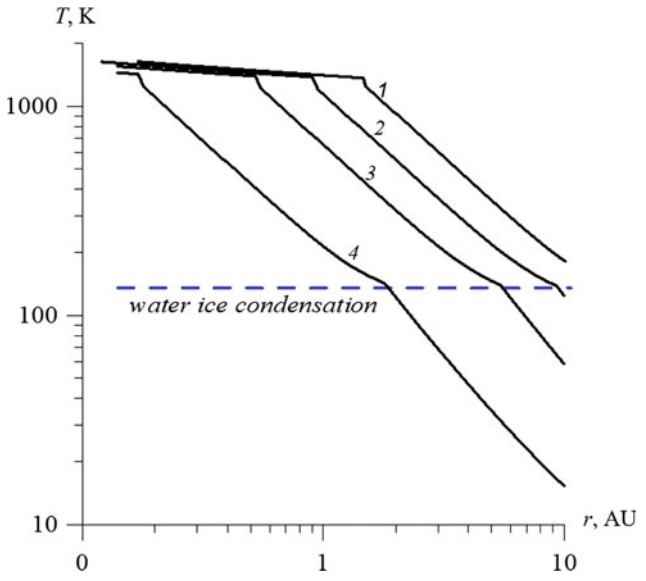

Fig. 17 Radial temperature distribution in the equatorial plane of the near-solar gas-dust accretion protoplanetary disk for various time points for the formation stage of the near-solar disk: 1—0.02; 2—0.05; 3—0.13; 4—1 from the total time of the stage ($\sim$(5–10) $\times$ 10^6 years)

Results presented in Figs. 16 and 17 show that within 10 AU, the condensation of water ice from the gas phase of the near-solar nebula, and, consequently, the accumulation of ice-rock planetesimals, became possible only at the final stage of its evolution. During this period, the H_2O_{ice} condensation boundary, called the "snow line", moved from $r \sim 8$ AU into the interior of the disk up to the outer boundary of the Main Asteroid Belt. This created conditions for the accumulation of water ice in ice-rock bodies in the entire specified range of heliocentric distances.

Note that for the first time the conditions of H_2O_{ice} condensation were considered in the so-called minimum-mass solar nebula (MMSN) models, in which it was assumed that $M_{disk} < \sim 0.1 M_{Solar}$. These models appeared as if in contrast to the large-mass models [71, 72], in which it was assumed that $M_{disk} \sim M_{Solar}$ when it turned out that it was difficult to propose a mechanism for the dissipation of such a large mass of nebula matter in a relatively short period of time.

One of the first MMSNs was a model by [73] in which the mass of the near-solar nebula was assumed to be ~ 0.01 M_{Solar}. However, since in this model the mass of the disk was too small—it was defined as the sum of the masses of all the planets of the Solar system, supplemented by the mass of gases in accordance with the solar proportion, there was a certain difficulty in ensuring the formation of the nuclei of giant planets, in particular Jupiter, whose core mass was assumed to be equal to 15 Earth masses. Therefore, in the model [73], it was assumed that the entire dust component of the disk from the region from $r = 1.55$ AU entered the core of Jupiter up to $r \sim 7$ AU, and the missing mass was supplemented by water ice, which, as assumed in the model, condensed starting from $r = 2.7$ AU; this radial distance corresponded to $T = 170$ K, calculated as the blackbody temperature. Thus, in the model [73], the question of the existence of a conditional boundary in the near-solar gas-dust protoplanetary disk dividing it into two zones was considered for the first time—the inner one, where water existed in a gaseous state and the outer one, where it was in the ice phase. At this boundary there was an abrupt change in the surface density of the solid-state component of the disk, which ensured the early formation of the nuclei of Jupiter and Saturn and the subsequent accretion of the nebula gas phase on them; later this boundary was called the "snow line". The estimate of $T_{cond}(H_2O_{ice})$ obtained in the model [73] is still quite often used, for example [74, etc.], but more often, especially in the cosmochemical literature, the estimate of $T_{cond}(H_2O_{ice}) = 145$ K obtained in the work [75] is used. In the authors' data disk model, this value corresponds to the position of the snowline in the outer part of the Main Asteroid Belt at $r = 3.7$ AU. Values of 145 K, or close to it, are used, for example, in [76–78, etc.]. This assessment also seems more reasonable to us, since it allows us to explain the existence of bodies in the Main Asteroid Belt that include water, the accumulation of which was possible only in the form of ice, for example Ceres, and bodies without water, as Vesta.

3.3 Results and Discussion

The objective of this work is to estimate the composition of the ice component and the proportion of water ice in it relative to the refractory component in the ice-rock proto-bodies formed in the nebula conditions at various heliocentric distances.

For the inner region of the nebula, which includes the asteroid belt, the M_{H_2O}/M_{Solid} estimate was previously given in [79]. In it, the composition of the solid phase was adopted similar to the composition of enstatite chondrites of the EH type: in addition to Mg-silicates and iron in the form of metal and sulfide, it included oxides of titanium and calcium, as well as iron phosphide schreibersite (Fe_3P), the formation of which requires significantly more reduced conditions than in the solar composition system: C/O $\sim 0.85 - 1$ [80]. In [79], $M_{H_2O}/M_{solid} = 1.17$ was obtained, which, from our point of view, is significantly overestimated, since its calculation did not take into account that in the nebula gas phase, along with H_2O, there were other compounds containing oxygen, the main of which was CO and CO_2. The relationship between these three gases can be estimated based on the results of calculations of thermodynamic equilibria in the gas phase of the disk, the results of which are presented in Fig. 18.

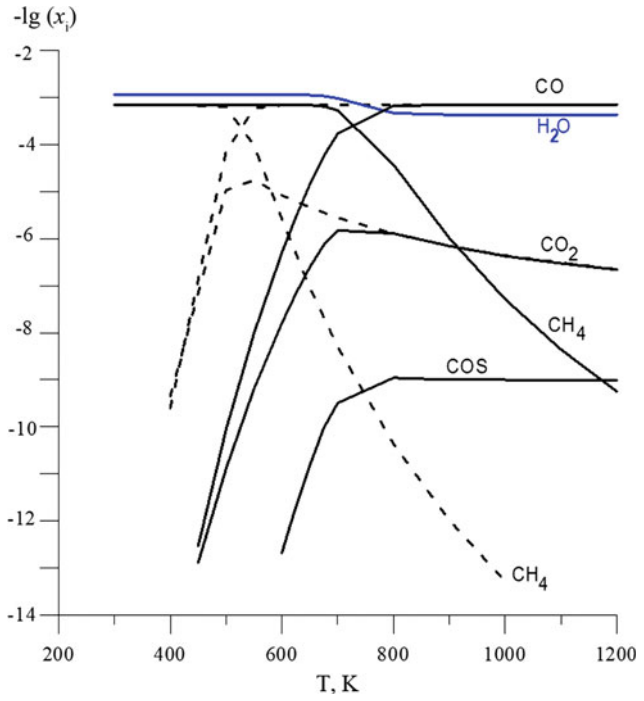

Fig. 18 Change in the equilibrium composition of C- and O-containing phases in the gas phase of the pre-planetary disk during its cooling, taking into account the formation of condensed phases. Solid lines correspond to the $P_{tot} = 10^{-3}$ bar dotted line $P_{tot} = 10^{-7}$ bar. Only components for which the molar fraction $x_i > 10^{-17}$ are specified. Solar system abundances 4.56 Ga ago by [70]

As follows from the results presented in Fig. 17, at radial distances of $r < 4$ AU, the minimum temperatures was ~ 400 K on $r = 4$ AU, and by the end of the stage of viscous evolution and temperature dissipation they dropped to T_{cond} of water ice at $r = 2$ AU. The total pressure (P_{tot}) varied in the range of 10^{-3}–10^{-7} bar. The calculated equilibrium distribution of the components of the gas phase of the protoplanetary disk corresponding to the specified temperature range is shown in Fig. 18 for the $P_{tot} = 10^{-3}$ bar with solid lines and a dotted line for the $P_{tot} = 10^{-7}$ bar. It can be seen that at $T > 650$ K, the main carbon-containing compound is carbon monoxide, the molar fraction of which is 10^{-3}; the value close to it is the molar fraction of water—$10^{-3.5}$. At $T < 650$ K, methane becomes the main carbon-containing phase, and all oxygen is bound into water. The content of CO, as well as CO_2, drops sharply. Similar calculations carried out at $P_{tot} = 10^{-7}$ bar (dotted line in Fig. 18), show that the pressure change within these limits does not significantly affect the ratios of the main components of the nebula gas phase, but only reduces the temperature at which CH_4 begins to prevail over CO to $T < 520$ K.

However, the study of the kinetics of the reaction of carbon monoxide reduction by hydrogen

$$CO + 3H_2 = CH_4 + H_2O \quad (1)$$

Showed [81, 82] that at pressures characteristic of the inner region of the protoplanetary disk (10^{-3}–10^{-5} bar), the reaction (1) is inhibited and the time to achieve chemical equilibrium at $T \approx 700$ K is $\sim 10^{13}$ s, i.e. $\sim 10^7$ years, which is commensurate with the lifetime of the pre-planetary disk itself.

In the work [83], the time of establishing thermodynamic equilibrium for the reaction (1) was compared with the characteristic times of physical processes in a gas-dust disk, i.e. with the time of transfer of matter within one turbulent vortex, the largest in the spectrum, and the time of radial transfer of matter in the disk at a distance of several turbulent vortices. The comparison showed that the deviation of the CO/CH_4 ratio from the equilibrium value occurs already at $T \sim 1350$ K, and the freezing temperature of the reaction is ~ 750 K. At this T, $\sim 10\%$ of carbon is in the form of methane, and thus the relative CO content in the solar composition system will be $0.9 \times 7.19 = 7.11$ mol per 1 mol Si. As for CO_2, its content, as follows from Fig. 18, is 2 orders of magnitude lower. Note, however, that the obtained CO values are "estimates from above", so we estimated the possible ratio of the mass of water to the mass of the refractory component, which in the inner part of the solar nebula included exclusively mineral phases, in a certain narrow range of the CO/CO_2 molar ratio: from 10 to 8 (Fig. 19). The refractory component in the inner part of the

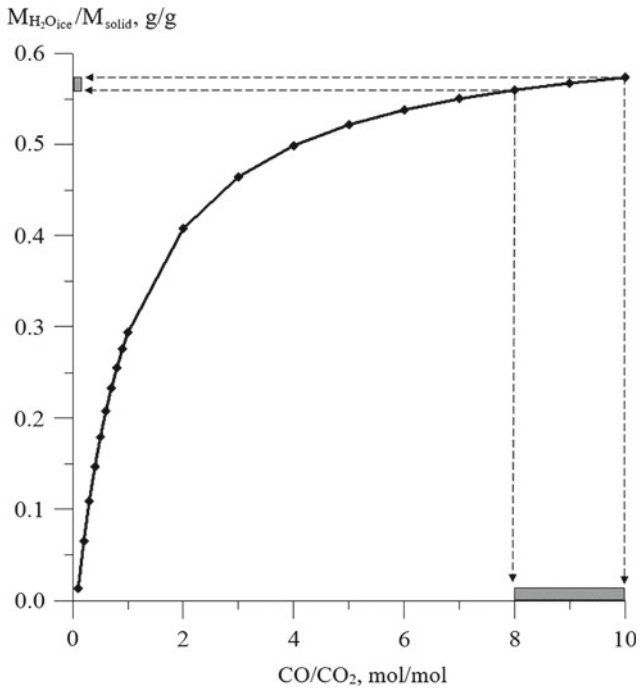

Fig. 19 The maximum possible values of the ratio of the ice mass of water and mineral components in planetesimals formed in the inner zone of the near-solar nebula, depending on the value of the molar ratio of CO/CO_2 in the gas phase. Solar system abundances 4.56 Ga ago by [70]

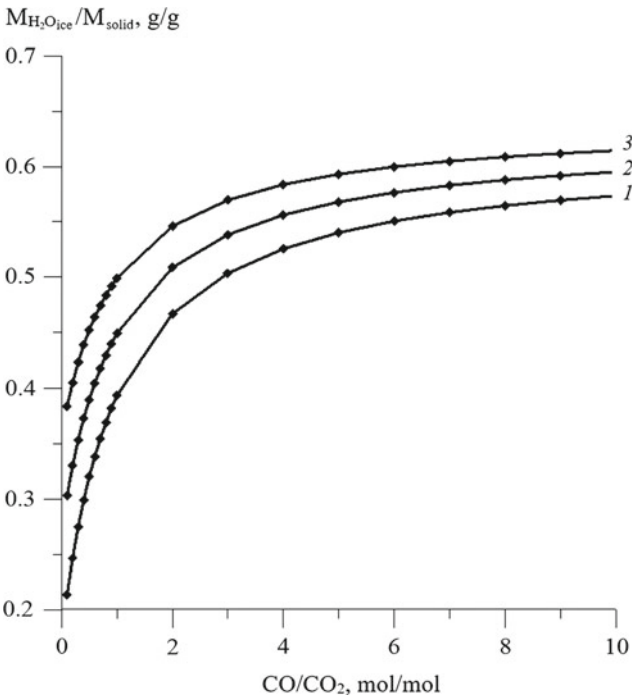

Fig. 20 The maximum possible values of the ratio of the mass of water ice and the mass of the mineral component in planetesimals formed in the Jupiter and Saturn region, depending on the value of the molar ratio of CO/CO_2 in the nebula gas phase and the content of refractory organic compounds (CHON) in it. Solar system abundances 4.56 Ga ago by [70]

near-solar nebula included exclusively mineral phases, since the refractory organic fraction was thermally destroyed: according to [84], it is stable at $T < 600$ K.

As can be seen from Fig. 19, the ratio of M_{H2Oice}/M_{solid} = 0.56–0.57 g/g. Thus, it follows from the simulation results that the proportion of water in the ice-rock proto-bodies formed in the inner zone of the near-solar nebula did not exceed ≈ 0.36, which is close to the value of water content on the Ceres obtained in the models based on the results of the Dawn experiment [85, 86].

Let's consider the composition of primary planetesimals in the region of formation of Jupiter and Saturn. As the simulation results show (Fig. 17) at r = 4–10 AU, the maximum temperatures in the protoplanetary disk did not exceed 500 K. It follows from this that the refractory organic substance, designated by the abbreviation of the main chemical elements that make up them—CHON, contained in the dust component of the protosolar nebula, once in the disk, was not thermally destroyed [84]. According to existing estimates, in particular, according to the composition of comet dust [21], it contained from 30 to 50% of the total carbon content in the system (C_{tot}) [87, 88]. It is impossible to accurately describe the elemental composition of CHON, so we, following [84], provisionally accepted its formula as $C_{100}H_{70}O_{20}N_4$. Thus, the composition of the solid phase indicated in Fig. 20 as "solid" is calculated as the sum of the masses of the mineral component, the composition of which was adopted similar to its composition in the inner region, and refractory organic compounds with a variable proportion of carbon in CHON. The ice component in the region under consideration could contain only H_2O_{ice}, since the condensation temperatures of all other components of nebula gas, as follows from Table 1, are significantly lower than those that could be in this region of the disk.

The results of the evaluation of the ratio of water ice masses to the solid component in planetesimals formed in the region of the Jupiter and Saturn systems, depending on the ratio of CO and CO_2 in the gas phase, as well as the proportion of the total carbon content in the refractory organic component are shown in Fig. 20. Since it is almost impossible to estimate the real value of the CO/CO_2 ratio both in the near-solar nebula in the region of formation of gas giant planets and in their protosatellite disks, we can only indicate the maximum possible value of the H_2O_{ice}/-solid ratio in the primary ice-rock protosatellite bodies of the Jupiter and Saturn systems: $M_{H_2Oice}/M_{solid} \sim 0.6$ g/g. It follows that the maximum proportion of water in the composition of the regular satellites of Jupiter and Saturn, most likely could not exceed ∼40 wt%.

This assessment does not contradict the results of model calculations of the composition and internal structure of the

Table 1 Estimates of sublimation temperatures of the main components of cometary ice in models of a low-mass near-solar gas-dust disk ($P_{tot} \sim 10^{-7}$–10^{-9} bar) according to [75, 76, 89] and the minimum heliocentric distances at which these temperatures could be reached in MMSN models

Ice	$T_{subl.}$ (K)	r_{min} (AU)	Ice	$T_{subl.}$ (K)	r_{min} (AU)
H_2O	145	3.7	CH_4	30	85.9
CH_3OH	100	7.7	CO	25	123.7
HCN	100	7.7	N_2	22	159.7
CO_2	80	12.1	Ar	22	159.7
NH_3	70	15.8	O_2	22	159.7

regular satellites of Jupiter and Saturn, set out in particular in the works of O. L. Kuskov and his colleagues (see Sect. 5), the results obtained by us [90] and the results of other authors.

However, in the Saturn region, the ice had a more complex composition than in the Jupiter region. Guided by the results presented in Fig. 17 and the data in Table 1, it can be assumed that in addition to water ice, they could also contain ices of CO_2, CH_3OH, NH_3, and HCN in their composition. According to the data on the composition of interstellar molecular clouds [91], we assume that the molar fraction of ammonia was ~10% N, and CH_3OH and HCN did not exceed 1%. The composition of the refractory component is assumed to be the same as for the Jupiter region. By varying the values of the molar ratios of CO/CO_2 in the system, as well as the content of refractory organic compounds (CHON) in it, we obtained the values of the ratios of the masses of the water ice and the refractory component M_{H_2Oice}/M_{solid}, shown in Fig. 21, from which it can be seen that they could vary widely: from 1.2 to 0.7.

Comparing the composition of icy planetesimals formed in the Jupiter and Saturn zones, it should be noted that in the Saturn zone, with a decrease in the CHON content in the refractory component and low CO/CO_2 values, the value of the M_{ice}/M_{solid} ratio approaches 1 and even exceeds it. For the Jupiter zone, the mass of ice, due to the absence of components other than H_2O ice in it, never exceeds the mass of the refractory component (Fig. 22).

Considering the conditions for the formation of ice-rock bodies in the trans-Neptunian region, which primarily include comet nuclei, as well as Kuiper Belt Objects (KBOs), the following should be noted. In this region, in addition to Mg-silicates, the mineral component of refractory components should include Fe–Mg-silicates of extrasolar origin, and the more the region is remoted from the Sun, the higher their fraction will be [92]. In this calculation, we assumed that the shares of Fe^0 and FeO are equal. This explains that the values of the mass ratios of water ice and refractory components at the same parameters in the trans-Neptunian zone are less than in the Saturn and Jupiter zones: M_{H_2Oice}/M_{solid} does not exceed 0.6 g/g, and the mass

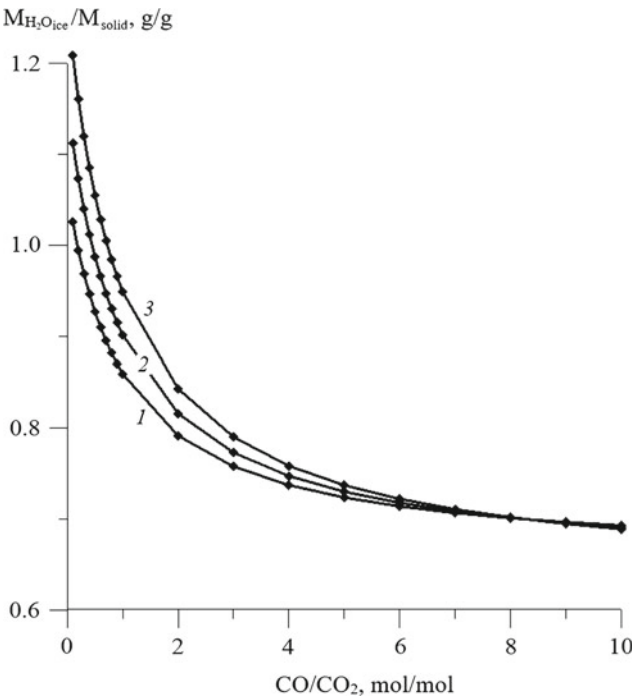

Fig. 21 The maximum possible values of the ratio of the mass of ice and mineral components in planetesimals formed in the Saturn region, depending on the value of the molar ratio of CO/CO_2 in the nebula gas phase and the content of refractory organic compounds (CHON) in it. Solar system abundances 4.56 Ga ago by [70]

fraction of H_2O_{ice} does not exceed ~0.35. This result does not contradict the opinion that the proportion of water ice in cometary nuclei is ~0.25. But to accept the point of view that it can be 1/6, i.e. 0.17, expressed in several papers [93, 94], it should be assumed that there is no CO_2 in the solar nebula at all, and the proportion of carbon that is part of refractory organic compounds is no more than 0.2. Both of these assumptions contradict known data on the composition of cometary nuclei [21].

Another feature of the composition of the icy component of planetesimals formed in the trans-Neptunian region is that in addition to NH_3 ice, it also includes N_2 ice, the proportion of which increases as it moves away from the Sun. The ratio

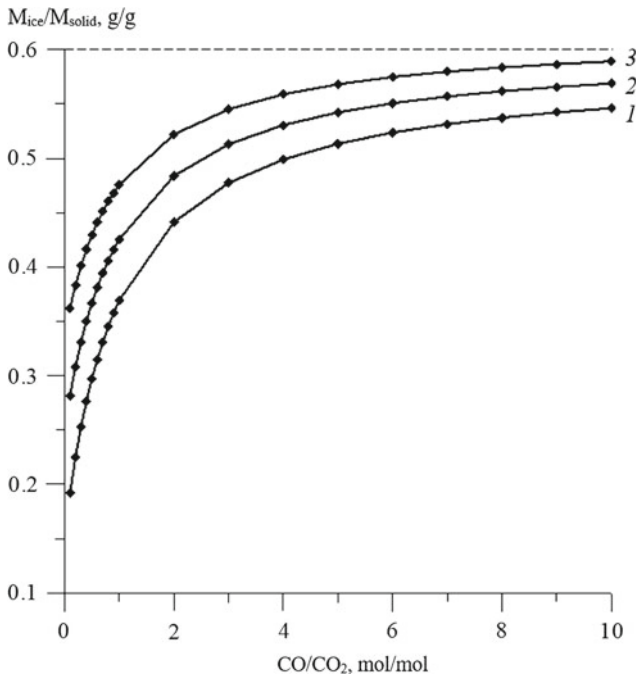

Fig. 22 The ratio of the mass of ice and mineral components in planetesimals formed in the trans-Neptunian region, depending on the value of the molar ratio of CO/CO_2 in the nebula gas phase and the content of refractory organic compounds (CHON) in it. Solar system abundances 4.56 Ga ago by [70]

of the mass of ice and the refractory component in the planetesimals of the trans-Neptunian region is shown in Fig. 23. Calculations are made on the assumption that the composition of ice includes not only the components specified for the Saturn region but also ice N_2, H_2CO, C_2H_2, C_2H_6, following the data in [95].

From the obtained mass ratio of the ice and refractory components for the ice-rock bodies formed in the trans-Neptunian region, it follows (Fig. 23) that the ratio very weakly depends on the change in the CO/CO_2 ratio in the nebula gas phase, and is mainly determined by the proportion of carbon contained in the refractory component—the smaller this proportion, the greater the mass of ice in the system.

3.4 Conclusions

Estimates of the composition and relative content of the ice component in the primary ice-rock planetesimals formed in different regions of the near-solar gas-dust accretion protoplanetary disk were obtained in the work.

1. For the inner region, only water ice was part of the ice, and its fraction in the ice-rock proto-bodies did not exceed 0.36, which is close to the value obtained for Ceres, the largest asteroid of the Main Asteroid Belt, in the recent Dawn experiment.
2. In the region of the formation of the Jupiter and Saturn systems, the refractory component of the ice-rock planetesimals included, in addition to the mineral component, also refractory organic compounds of the provisional composition $C_{100}H_{70}O_{20}N_4$ (CHON). It was found that the maximum possible value of the H_2O_{ice}/solid ratio in the primary ice-rock protosatellite bodies of the Jupiter and Saturn systems is $\sim$0.6 g/g. It follows that the maximum proportion of water in the composition of the regular satellites of Jupiter and Saturn most likely could not exceed $\sim$40 wt%.
3. In the region of the formation of the Saturn system, the composition of the ice, in addition to the ice of water, also included the ice of CO_2, CH_3H, NH_3, and HCN. With variations in the values of the molar CO/CO_2 ratios in the system, as well as the content of CHON in it, the values of the mass ratios of ice and the refractory

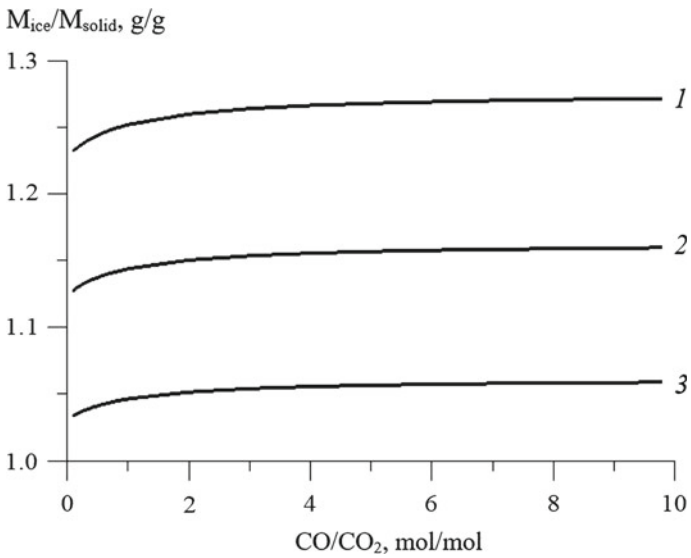

Fig. 23 The maximum possible values of the ratio of the mass of ice and mineral components in planetesimals formed in the Saturn region, depending on the value of the molar ratio of CO/CO_2 in the nebula gas phase and the proportion of carbon in refractory organic compounds (CHON) from its total content. Solar system abundances 4.56 Ga ago by [70]

component M_{ice}/M_{solid} could vary widely: from 1.2 to 0.7. They approach 1 and even exceed it with a decrease in the content of CHON in the refractory component and low values of CO/CO_2. For the Jupiter zone, the mass of ice, due to the absence of components other than H_2O ice in it, never exceeds the mass of the refractory component.

4. For the trans-Neptunian region, the value of the ratio of the masses of water ice and the refractory component in the ice-rock planetesimals with the same parameters is less than in the Saturn and Jupiter zone: it does not exceed 0.6 g /g, and the mass fraction of H_2O_{ice} is not higher than $\sim$0.35. The value of M_{ice}/M_{solid} very weakly depends on the change in the ratio of CO and CO_2 and is mainly determined by the proportion of carbon included in the refractory component – the smaller this proportion, the greater the mass of ice in the system.

4 Thermo-Chemical Constraints on the Bulk Composition and Core Sizes of the Moon

4.1 Introduction

The study of the Moon began more than 50 years ago in the XX century with the spacecrafts Luna, Apollo, Clementine, Lunar Prospector and continues in the XXI century with LRO (Lunar Reconnaissance Orbiter), GRAIL (Gravity Recovery and Interior Laboratory), Kaguya/SELENE, Chang 'E, Chandrayaan. The information obtained led to extremely important conclusions for the geology, geochemistry and geophysics of the Moon and created a fairly solid basis for constructing modern models of its internal structure, based on a set of geophysical and geochemical constraints, including the mass and moment of inertia of the Moon, the velocity of seismic waves, Love numbers, rock composition and laboratory experiments [96–99]. However, questions regarding the problem of the origin and bulk composition of the Moon (BSM), the chemical composition of the mantle, physical properties and sizes of the core are still the subject of numerous discussions [38, 100, 102].

The solution to these questions is usually based on solving inverse problems [96, 97, 103]. The same approach is implemented in this work. The main geophysical constraints were taken from the Apollo seismic experiments [104] and the GRAIL mission [98], in which detailed information on the gravitational field of the Moon was obtained: mass (7.3463×10^{22} kg), average radius (1737.151 km), mean moment of inertia (MOI = I_S = (I/MR^2) = 0.393112 ± 0.000012). The composition and structure of the mantle and the size of the core are a priori unknown and are determined as a result of solving the inverse problem based on the existing constraints.

Determination of the geochemical and geophysical parameters of the five-layer model (anorthosite crust, three-layer mantle, subdivided into upper, middle and lower shells, and the core) of a spherically symmetric Moon, differentiated as a result of partial melting of an initially homogeneous body, is based on the joint inversion of seismic and selenodetic data by the Monte Carlo method, taking into account the lunar magma ocean concept and mass balance ratios [105–109].

Modeling of the phase composition and physical properties of the mantle in the system Na_2O-TiO_2-CaO-FeO-MgO-Al_2O_3-SiO_2 was carried out by Gibbs free energy minimization and the equations of state of minerals in the Mie-Grüneisen-Debye approximation. Concentrations of oxides in the mantle (wt%) varied over a wide range $25 \leq MgO \leq 45\%$, $40 \leq SiO_2 \leq 55\%$, $5 \leq FeO$ 15%, $0.1 \leq CaO, Al_2O_3 \leq 7\%$, with $CaO \sim 0.8\ Al_2O_3$, and the concentrations of Na_2O and TiO_2 were 0.05 wt% and 0.2 wt%, respectively. Two scenarios of the thermal state of the lunar interior were considered at fixed temperatures at average depths (km) of the upper, middle and lower mantle: cold model—T_{150} = 600 °C, T_{500} = 900 °C, T_{1000} = 1100 °C and hot model—T_{150} = 700 °C, T_{500} = 1100 °C, T_{1000} = 1300 °C. A shift of 100–200 °C makes it possible to estimate the effect of temperature variations on the chemical composition of the three-layer mantle and the size of the lunar core.

4.2 Geochemical Characteristics of the Moon

In the geochemical and geophysical literature, various options for the chemical composition of the mantle and the bulk composition of the silicate Moon have been considered. Bulk composition models are largely contradictory, depend on methodological (geochemical or geophysical) approaches, and vary from a composition similar to the ultramafic matter of the Earth's upper mantle to a composition sharply enriched in Ca and Al (Fig. 24).

Geochemical estimates of the BSM are model-dependent, since they are based on the use of elemental correlations Mg/Si, Al/Si, Mg/Al and the correlation between the contents of Th, U and refractory oxides in lunar rocks and chondrites [113, 116, 117]. The best known are two limiting models of the BSM: the TWM model (Taylor Whole Moon model), which is enriched (relative to the Earth's mantle) in refractory oxides by about 50% [112], and the LPUM model (Lunar Primitive Upper Mantle model), which has a concentration of refractory oxides close to terrestrial, at a level of $\sim$4% Al_2O_3 [115]. Both models differ in FeO content by almost two times (Fig. 24). BSM geophysical estimates depend on the seismic model—their reliability is largely determined by the degree of reliability of seismological

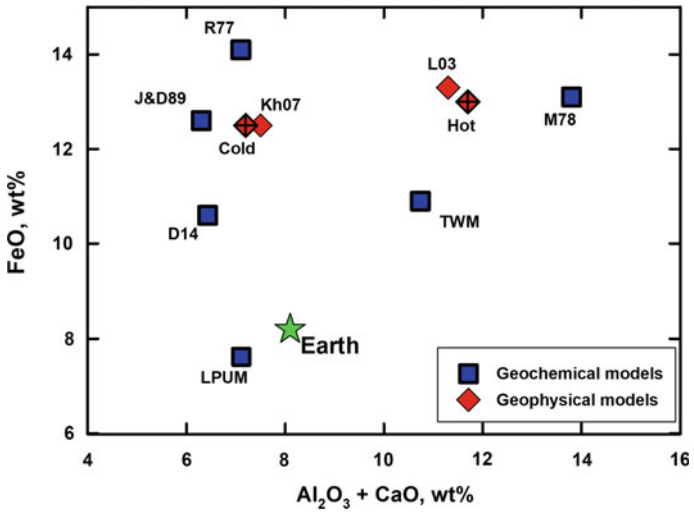

Fig. 24 Geochemical and geophysical models of the bulk composition of the Moon (crust + mantle) according to literature data in comparison with the bulk composition of silicate Earth, BSE (star). M78 = Morgan et al. [110]; R77 = Ringwood [111]; TWM = Taylor [112]; J&D89 = Jones and Delano [113]; L03 = Lognonné et al. [114]; LPUM = Longhi [115]; Kh07 = Khan et al. [103]; D14 = Dauphas et al. [116]; Cold, Hot = compositional models with different contents of refractory oxides for cold and hot selenotherms [106]

information associated with the problem of first arrivals and the interpretation of seismic boundaries in the mantle [104, 114].

From the solution of the inverse problem for cold and hot temperature profiles, it follows that the lunar mantle is chemically stratified with different concentrations of oxides in different zones of the mantle [105, 107–109]. The calculation results (Fig. 24) show that for cold and hot selenotherms the bulk 11–14 wt% FeO and magnesian number Mg# 80–83 [106] are within rather narrow limits, which sharply differ from those for BSE (FeO ~ 8% and Mg# 89), which indicate a fundamental difference in the chemical composition of the silicate shells of the Moon and the Earth and rejects the possibility of the formation of the Moon from the material of the Earth's primitive mantle, despite the coincidence of the isotopic composition of oxygen and a number of other elements [38, 116]. In contrast, bulk Al_2O_3 concentrations are temperature dependent. The alumina concentration is 4–5 wt% for cold and 5–7% for hot BSM models. SiO_2 concentrations are 50–55% in the upper and 45–50 wt% in the lower mantle; low-Ca orthopyroxene, not olivine, is the predominant mineral in the upper mantle. The high pyroxene content of the upper mantle is a geochemical consequence of the inversion of geophysical constraints for chemical composition. Note, that pyroxene with a low Ca content dominates the spectral characteristics in the shock melt formed from the mantle of the South Pole-Aitken Basin (e.g., [118]).

For both compositional models with different contents of Al_2O_3 and concentrations of other oxides equilibrium phase assemblages and their physical properties (density, velocities of seismic waves) were calculated, which, along with the physical characteristics of the system Fe-S have been used to determine the size of the lunar core [106, 108, 109, 119, 120].

4.3 Physical Properties and Sizes of the Lunar Core

A special place in the geophysics of the Moon is occupied by the problem of the structure of the central region, which in its thermodynamic parameters is close to the terrestrial asthenosphere (T ~ 1700–2000 K, P ~ 5 GPa). This area includes a partially molten transition layer, a liquid outer and a solid inner core. Determination of the physical and chemical properties of the central zone is necessary for understanding the thermal regime, the history of the lunar dynamo, the origin and evolution of the Moon.

High-precision trajectory measurements by Lunar Prospector and Kaguya, lunar laser ranging and GRAIL data on the gravitational field suggest the presence of a metal core [98, 121–123]. The results of Apollo's experiments led to the construction of a number of seismic models of the Moon, but did not provide direct information on the presence of a core [96]. Although the resolution of seismic sources is insufficient to reliably reveal the structure of the core, Garcia et al. [99] and Weber et al. [124] for the first time obtained constraints on the radius of the lunar core. The estimates were obtained from the results of the Apollo seismic network using array and stack processing methods based on the analysis of lunar seismograms, taking into account the waves reflected from the core.

It is generally accepted that the cores of the terrestrial planets and the Moon represent a solid and/or liquid Fe–Ni

solution with an admixture of a number of light elements. Gravity and seismic data provide rather strict constraints on core sizes [97–99, 123–126], but for their verification they must be supplemented by laboratory measurements of elastic properties. Models built on this general basis should satisfy geodetic (mass, polar moment of inertia, Love numbers) and seismological (travel times of body waves) data, as well as results on modeling the physical properties of liquid Fe–Ni alloys with an admixture of one or more light elements, such as Si, O, S, C.

Recently, experimental measurements of the physical properties of Fe–Ni-S-C-Si liquids (density, viscosity, speed of sound, etc.) under *P–T* conditions of the lunar core have been published. The most important of them are the experimental determination of the velocities of longitudinal waves of liquid alloys by ultrasonic methods [127–129], as well as calculations of the speed of sound and the density of solid and liquid Fe-S solutions by the molecular dynamics [119, 120], which allow comparing with the speed of sound in the central part of the Moon according to Apollo data. The composition of the core remains unknown, so a number of candidate elements need to be considered. Geophysical constraints on the mass and moment of inertia make it possible to find the density distribution in the interior of the Moon and estimate the size of the core, and measurements of the speed of sound of liquid Fe–Ni-S-C-Si alloys make it possible to check the reliability of seismic determinations.

In Figs. 25 and 26, we present the results of experiments to determine the speed of sound of Fe(Ni)-S-C-Si melts (Fig. 25) in comparison with Apollo seismic data [124], as well as histograms of the radii of the outer liquid Fe-S core (Fig. 26), obtained on the basis of joint inversion of seismic, gravity and geochemical data [109]. The sizes of the core are in the range of 50–360 km with the most probable value of 250–350 km (Fig. 26 and Table 2) and rather weakly depend on the compositional models of the mantle with different contents of refractory elements, FeO and concentrations of other oxides, as well as on the thermal regime of the Moon. This is due to the fact that, firstly, changes in the FeO and Al_2O_3 concentrations lead to a trade-off in the variations in velocities and densities for both geochemical models [107, 108], and, secondly, the temperature difference by 200 °C for cold and hot selenotherms leads to a change in the density of the Fe-S liquid only within 1% [109, 119, 120].

It follows from Fig. 25 that the V_P values of Fe(Ni)-S-C-Si liquids depend on which of the alloying elements S, C, Si is included in the Fe-alloy and its concentration, as well as on the redox conditions in the interior of the Moon. Since the oxygen fugacity in the lunar mantle is estimated at a level of $\Delta IW \sim -2$ [100], the incorporation of silicon into the Fe core during its formation becomes problematic. The speed of sound for the liquid outer core was estimated at 4100 ± 200 m/s (±5%) according to [124]. At 5 GPa, the speed of sound of liquids Fe and Fe-10% Ni, Fe (Ni)-3–5 wt % C and Fe (Ni)-10–17 wt% Si is characterized by values exceeding 4500 m/s (Fig. 25), which is about 10% higher than the V_P for the outer core according to [124]. If the seismic velocity estimate is reliable enough, then the

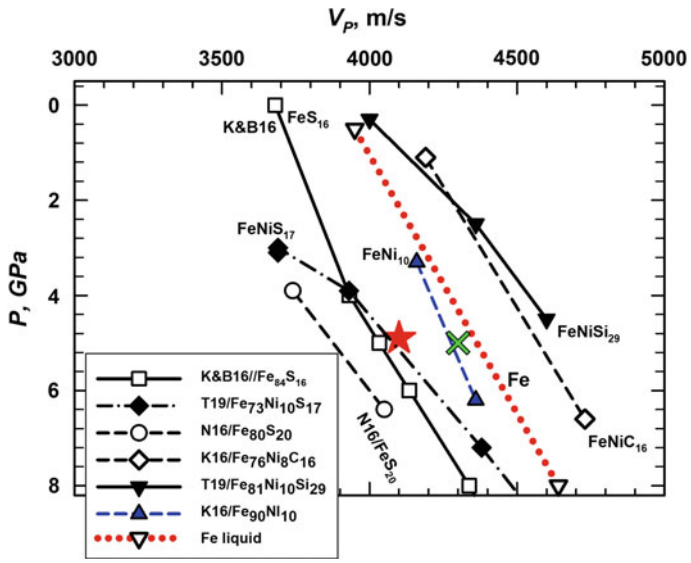

Fig. 25 Comparison of the speed of sound (V_P) of Fe(Ni)-S-C-Si liquids (all concentrations in at%) with Apollo seismic data according to Weber et al. [124] for the outer (V_P = 4100 m/s, filled star) and inner (V_P = 4300 m/s, cross) core. V_P values of ultrasonic experiments at 1800–2000 K: N16 = Nishida et al. [128], $Fe_{80}S_{20}$ (13 wt% S); T19 = Terasaki et al. (2019) [129], $Fe_{73}Ni_{10}S_{17}$ (10.5 wt%S); T19 = Terasaki et al. [129], $Fe_{61}Ni_{10}Si_{29}$ (17 wt% Si); K16 = Kuwabara et al. [127], $Fe_{75.4}Ni_{8.3}C_{16.3}$ (Ni = 10 wt%, C = 4 wt%) and $Fe_{90.4}Ni_{9.6}$ (Ni ~ 10 wt%); V_P for liquid Fe (dotted line) according to Nishida et al. [128]. K&B16 = Kuskov and Belashchenko [119], molecular dynamics calculation for a Fe-S melt at 2000 K and sulfur concentration of 16 at% (10 wt%)

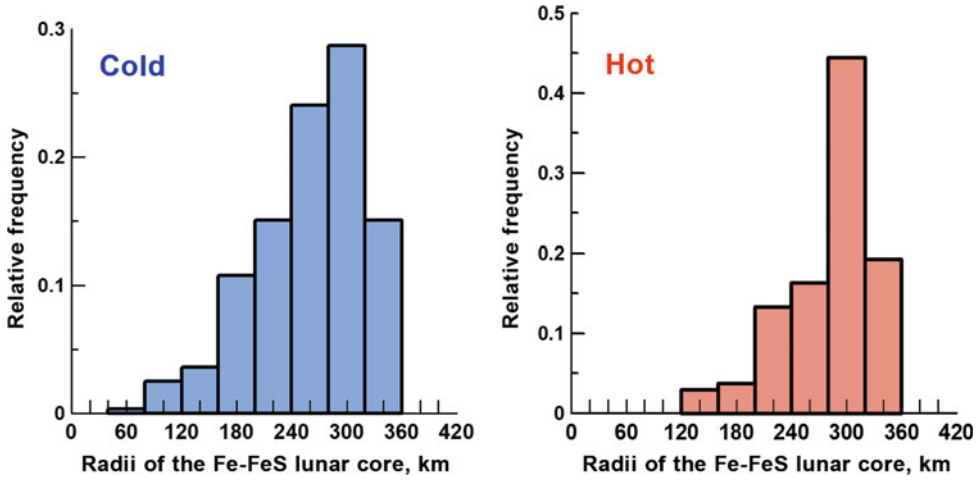

Fig. 26 Histograms of the Fe-S radii of the lunar core with an average density of 7.1 g/cm^3 and a sulfur content of up to 10 wt%. Calculations are based on the joint inversion under given conditions for the thickness and density of the crust, the mass and moment of inertia of the Moon, and the seismic models [98, 104, 130], as well as taking into account the constraints on the chemical composition (Fig. 25), mineralogy, and density of the three-layer mantle for cold and hot temperature profiles

Table 2 Summary of lunar core size estimates, methods and data

Liquid outer core			Method
Core radius (km)	Density (g/cm^3)	Speed of sound, V_P (m/s)	
250–430			Lunar Prospector and Kaguya, $\rho_d(\omega)$ [121, 122]
200–380			LLR, GRAIL [98, 123]
330–380	4.5–5		M, I/MR^2, k_2, $\rho_a(\omega)$ [97]
310–350	5.1	4100	Apollo lunar seismograms, Fe-6 wt% S [124]
340–420	4.2–6.2		Apollo T_P, T_S and seismograms, M, I/MR^2, k_2 [99]
220–395	4.5–5.5	4000–6000	M, I/MR^2, T_P, T_S, k_2, Q from Apollo, GRAIL, LLR [126]
200–410	4.7–7.6		M, I/MR^2, k_2, h_2 from GRAIL, LLR, LOLA [131]
310–370	5.7		Seismic models and M, I/MR^2, Fe-3.5–10 wt% S [132]
250–350	7.1	4000	Seismic models and M, I/MR^2, BSM models, and MD for a Fe-3.5–10 wt% S melt at 5 GPa and 2000 K [107, 108, 119, 120]

Note M, I/MR^2—the mean mass and normalized mean solid moment of inertia, k_2, h_2—2nd degree tidal Love numbers, Q—quality factor, T_P, T_S—lunar seismic travel times, $\rho_a(\omega)$—frequency-dependent electromagnetic sounding data, GRAIL—the Gravity Recovery and Interior Laboratory, LLR—Lunar Laser Ranging, LOLA—Lunar Orbiter Laser Altimeter, BSM—bulk silicate Moon compositional models, MD—molecular dynamics

incorporation of carbon and silicon into the liquid core seems unlikely. If sulfur is the only light element in the liquid outer core, then $V_P \sim$ 3900–4100 m/s of liquid Fe (Ni)-S alloys with an amount of sulfur up to ~16 at% S/~10 wt% S [119, 120, 128, 129] is in good agreement with the Apollo seismic data [124].

Table 2 presents a summary of lunar core size estimates obtained as a result of processing gravity, electromagnetic, and seismic observations, as well as by inverting lunar geophysical and geochemical data (mean mass and moment of inertia, tidal Love numbers, seismic and electromagnetic sounding data, and bulk silicate Moon compositional models). It can be seen that, in most models, the core radius does not exceed 400 km. Thus, the results of selenophysical determinations and numerical simulations indicate that the Moon has a relatively small dense, electrically conductive and, apparently, partially molten core.

4.4 Conclusion

On the basis of the joint inversion of geophysical and geochemical constraints, the models of the chemical composition and internal structure of the initially homogeneous

Moon, differentiated as a result of partial melting, are investigated. The results show that for cold and hot temperature profiles the bulk FeO concentrations are 11–14 wt %, which sharply differ from those for BSE (FeO ~ 8%). On the contrary, bulk concentrations of Al_2O_3 depend on temperature and amount to 4–5% for cold and 5–7% for hot thermal models. SiO_2 contents are 45–55 wt%, with low-Ca orthopyroxene, rather than olivine, being the predominant mineral in the upper mantle of the Moon. The analysis of experiments on determining the speed of sound of Fe(Ni)-S-C-Si melts in comparison with seismic data is carried out. If sulfur is the only light element in the liquid outer core, then the speed of sound of liquid Fe(Ni)-S with an amount of sulfur up to ~10 wt% S is in good agreement with the Apollo seismic data. The sizes of the core are in the range of 50–360 km with the most probable value of 250–350 km and rather weakly depend on the chemical composition of the mantle with different contents of major oxides and the thermal regime of the Moon.

5 Estimates of H_2O Content in Titan with Different Degrees of Differentiation of Iron-Rock and Rock-Ice Substance

5.1 Introduction

Water controls many physical and chemical processes occurring at all stages of formation and further evolution of many cosmic objects. When interacting with the primordial substance of the Solar System, water changes its mineral composition in hydration reactions, leading to the production of secondary hydrous minerals. Accounting the influence of water on the chemical and physical properties of natural environments is essential in the modeling of any water-containing systems, which include the ice bodies in the Kuiper belt, comets and ice satellites of giant planets, to which Titan belongs. The H_2O content in Titan (H_2O (water, ice)/rock ratio) is one of the reference parameters when modeling temperature conditions in the protosatellite Saturnian disk, and is also used to study the formation and thermal evolution of the satellite [133–136].

The main task of our study was to estimate the total H_2O content in Titan for various models of the internal structure and different composition of the rock-iron substance of the satellite.

5.2 Models of Titan's Internal Structure and Rocky Composition

In this paper, the most debated models of Titan's internal structure are examined. The first type of models—the models of partially differentiated Titan [137–139]—assume incomplete separation of the ice and rock components in the satellite interiors and the formation of an extended rock-ice mantle in Titan (Fig. 27a). The second type of models—the models of fully differentiated Titan [140–142]—represent the complete separation of ice and rock and the formation in the satellite either of a hydrous silicate mantle with the release of a central silicate core (Fig. 27b), or the formation of a uniform hydrated core (Fig. 27c). The sizes of the structural layers in the considered models (core radius, mantle and water–ice shell thicknesses), were calculated using software algorithms [138], and are given in Table 3.

The structure of the water-ice shell of Titan (the thicknesses of the outer I_h-crust and the internal ocean) is determined by the heat flux value. According to the calculations [143], the heat flux of Titan weakly depends on the differentiation degree of the satellite's substance (on the model of the internal structure) and equals 5.8 mW/m^2. This value corresponds to the thickness of the outer icy crust of 100 km and the thickness of the internal ocean of 290 km, adopted in further calculations.

The composition of the rock-iron component in the partially differentiated Titan is modeled by the substance of L/LL or CI chondrites as the most suitable for the constructing of satellite's models [144–146]. Based on the chondritic mineral assemblage, the following averaged compositions of the rocky component were used in the work:

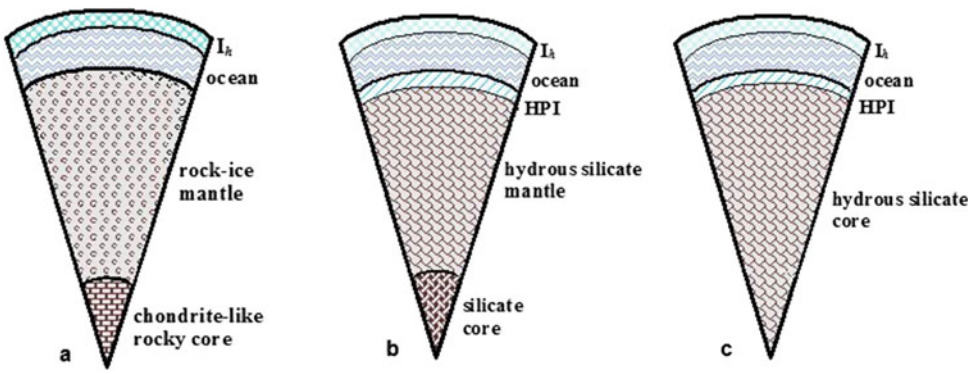

Fig. 27 Models of internal structure of partially differentiated (**a**) and fully differentiated Titan with hydrous silicate mantle (**b**) and hydrous silicate core (**c**)

Table 3 Structural and physical characteristics of Titan interior

Physical characteristic	Titan models			
	Partially differentiated with chondrite-like rocky component		Fully differentiated	
	LL	Hydrated LL	Silicate core	Hydrous silicate core
Water-ice shell (ice Ih + internal ocean + HPI)				
H_{Ih}, km	100			
ρ_{Ih}, g/cm^3	0.94			
H_w, km	290			
ρ_w, g/cm^3	1.12			
H_{HPI}, km	–	10	110	90
ρ_{HPI}, g/cm^3	–	1.28	1.28	1.33
Ice-rock mantle			*Hydrous silicate mantle*	
H_m, km	1580	1400	1510	–
ρ_m, g/cm^3	2.46	2.40	2.63	–
Rocky core				
R_c, km	600	765	565	2095
ρ_c, g/cm^3	3.99	3.96	3.69	2.56
Water content				
H_2O, wt. %	53	45	38	36
H_2O/rock mass ratio	1.12	0.82	0.61	0.56

Note Symbols H, ρ denote the thickness and density of the structural layers of Titan. R_c and ρ_c are the radius and density of the core. Subscripts Ih, w, HPI and m refer to outer Ih-ice crust, internal ocean, high pressure ices V–VI and the mantle in Titan, respectively. H_2O—the total water content in Titan

- L/LL chondrite-like substance: 70% silicates (olivine + pyroxene) + 30% minor minerals;
- CI chondrite-like substance: 85% hydrous silicates (serpentines) + 15% minor minerals.

The minor minerals include mainly various forms of iron (Fe^o, sulfides, oxides), as well as feldspars, spinels, phosphates, sulfates, carbonates, small amounts of 3–5 wt.% organic compounds (in the case of CI-chondrite substance). The density of the minor mineral fraction used in the calculations was estimated at 4.00 g/cm^3.

Hydrated forms of silicates in Titan are modeled by minerals of serpentine group (antigorite, chrysotile, and lizardite). The density of hydrous silicates and dry (anhydrous) silicates was calculated according to the equations of state [141 144].

A specific set of calculations was performed for the L/LL chondritic composition of the rocky Titan substance, taking into account the possible hydration of the constituent dry silicates. Hydration of L/LL chondrite-like substance could occur in the chondrite parent bodies at ~3–5 million years after CAIs formation [147]. The hydrated substance could then become part of the rocky-ice planetesimals accreted by Titan in the protosatellite Saturnian gas-dust disk. Hydration processes can also occur in Titan at post-accretionary history. The sources of the necessary thermal energy, initiating an ice melting and hydrothermal reactions, can be: the energy of gravitational differentiation released due to redistribution of substance inside Titan, long-lived radiogenic isotopes, heat release from hydration reactions, tidal heating of the satellite, impact energy. During these processes, the temperature rises in various regions of Titan, leading to local melting of ice and, as a consequence, to hydration of the silicates in contact with liquid water. To assess the effect of silicate hydration on the bulk water in Titan, the hydrated L/LL chondrite-like substance was additionally considered as a Titan's rocky component, which is represented by 65% hydrous silicates +5% silicates +30% minor minerals.

The total water content in Titan was estimated as the H_2O quantity in the water-ice shell (I*h*-crust, internal ocean ± high pressure ices) + H_2O ices of rock-ice mantle (if available, Fig. 27a) + bound water in the hydrous silicates or water bound/adsorbed in chondrite material, depending on the model. For models of partially differentiated Titan (Fig. 27a), water trapped in the primordial chondritic material was taken into account. For CI chondrite-like substance, the amount of bound/adsorbed water is 18–22% [148], for L/LL chondrites— ~0.4–0.8% [149]. The fraction of water bound in hydrated minerals was taken to be 13 wt.%—typical value for serpentine group minerals. Thus, for the

chondritic composition of the rock-iron component of Titan (Fig. 27a, with dry LL/L or CI-like chondritic substance), the amount of water in the rock was taken to be 1% or 22%, which was valid for the rock as in mantle and in the core. For model with solely hydrous silicates (Fig. 27a with hydrated L/LL chondrites, Figs. 27b–c), the amount of water in the rock was taken as 13%.

5.3 Results and Discussion

For each model of the Titan internal structure (Figs. 27a–c), as well as for various compositions of the satellite's rock-iron material (L/LL, CI, hydrated L/LL, anhydrous and/or hydrous silicates), parameters of the Titan structural layers were obtained, and the total water content with the H_2O (water, ice)/rock ratio in the satellite were calculated (Table 3).

In the course of computer simulations of partially differentiated Titan, it was found that the volume fraction of CI-chondritic rock in the rock-ice mantle exceeds 0.62, which is inconsistent with the model of a convective rock-ice mixture in large rock-ice planetary bodies including Titan [150]. It is shown in this work that for a hydrated silicate substance of the satellite, the critical volume fraction of hydrous silicates in rock-ice mixture, above which at least partial melting of ice must occur, is 0.43–0.62, depending on the parameters of convective model. Above these values, the properties of the rock-ice mixture are close to those of a firm silicate framework, where ice cannot reduce the viscosity of the mixture to values that provide convection. This leads to radiogenic temperature rise, ice melting and differentiation. Consequently, the mantle of the satellite is thermally unstable under the CI-chondrite composition of the rocky component, and probably the model of partially differentiated Titan is unlikely. Therefore, the results obtained for this model are not considered. The final results for the other models are shown in Table 3 and Fig. 28.

The research results show that the water content in fully differentiated/partially differentiated Titan varies in the range of 36–53% (Table 3). The minimum value corresponds to the model of fully differentiated Titan with complete hydration of the silicate substance (Fig. 27c). The low water content in Titan obtained for this model mainly follows from limitations on the 13% bound water in the hydrous silicates. However, the calculations allow for large variations in the water amount contained in the water-ice shell, so that the resulting H_2O total value could be significantly higher due to the HPI-water. However, solutions with a massive water-ice shell did not work out because of the Titan balance relations on the mass and moment of inertia, which are also limitations of the model.

The maximum H_2O total value is achieved in models of partially differentiated Titan (Fig. 27a) in the absence of hydrated mineral phases in the satellite (the rocky component is composed of L/LL chondritic matter). Thus, an increase in the amount of hydrous silicates in Titan leads to a decrease in its total water content.

The water-ice/rock mass ratio is an important cosmochemical indicator of the origin and formation conditions of cosmic icy bodies. Within the framework of the theory of equilibrium condensation of chemical compounds in the Solar System [79], this ratio is estimated at 1.17, which indicates a greater abundance of H_2O (H_2O-ice) in comparison with rock-iron substance. For the Titan models under consideration, the water-ice/rock ratio is in the range of 0.6–1.12, i.e. Titan is depleted in H_2O compared to the solar composition. As follows from Fig. 28b, the models of partially differentiated Titan with the L/LL chondritic composition of the rocky component are the closest to the solar

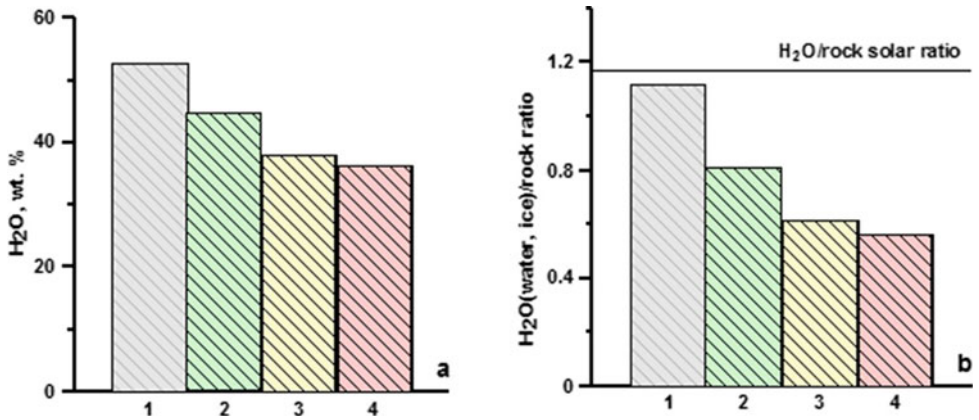

Fig. 28 Total H_2O content (**a**) and H_2O (water, ice)/rock mass ratio (**b**) in Titan depending on the internal structure and rock composition of the satellite. Water content for the model of Titan with rock-ice mantle (Fig. 27a): 1—LL chondrite-like composition of rocky component, 2—LL chondrite-like composition with full hydration of silicates; 3, 4—water content for Titan with hydrous silicate mantle and hydrated core (Fig. 27b-c). The line in panel (**b**) indicates the H_2O/rock solar ratio of 1.17 [79]

proportion. The largest deviation of the obtained H_2O/rock value from the solar proportion occurs in the models of fully differentiated Titan. Nevertheless, the H_2O/rock value obtained in the fully differentiated models (0.6) falls perfectly into the 0.5–0.7 interval obtained for rock-ice planetesimals, which were the building material for Titan [133].

The observed water depletion of Titan relative to rock may indicate the ice loss during accretion processes (as a result of collision and ablation of planetesimals in the gaseous medium of the accretion disk). Significant amounts of water can also be lost due to impact vaporization. It has been shown [136] that icy space objects with radii exceeding 1000 km can lose water during accretion if the surface temperature of the growing body is high enough to melt and evaporate the ice, but the gravity is not high enough to prevent the primary atmosphere from dissipating.

Figure 28b also shows meaningful differences in water-ice/rock ratio between fully and partially differentiated Titan: 0.56 vs 1.12. This difference may reflect the thermal features of accretion processes. The formation of partially differentiated Titan proceeded according to the "cold" accretion model [137]: the satellite grew slowly (for at least 0.8–0.9 m.y.) from small (50–100 m) rock-ice particles/bodies with sufficient low temperatures (≤ 253 K), not exceeding the melting temperature of ice. Under such a model, no significant losses of volatile components occurred in Titan, and its water-ice/rock ratio remains close to the solar ratio.

The formation of fully differentiated Titan is consistent with the "hot" accretion model [151], which assumes rapid (such as 10^4 years) growth of Titan from large (>1 km) rocky-ice planetesimals. The released accretion and radiogenic energy leads to the melting and vaporization of planetesimal ice and the formation of a massive satellite early atmosphere. The later escape of proto-atmosphere into space is a plausible mechanism to cause the depletion in icy materials of Titan [152].

5.4 Conclusions

1. The total H_2O content in Titan was estimated for the range of models of the satellite's internal structure, taking into account the type of rock-iron silicate substance and the amount of constituent hydrated minerals. It is shown that water content in Titan varies between 36 and 53 wt. %. The largest amount of water (53 wt.%) is found in partially differentiated Titan with a composition of the rocky component close to that of anhydrous L/LL chondrites. The smallest amount of water (36 wt.%) occurs in the model of fully differentiated Titan with a hydrous silicate core.
2. Regardless of the internal structure model, there is a decrease of Titan's H_2O (water-ice)/rock ratio from the cosmic value. The model of partially differentiated Titan with a rocky component similar to L/LL chondrites is the most compliant with the cosmic proportion. The water-ice/rock ratio for such a model is 1.12. The models of fully differentiated Titan result in water-ice/rock ratio equal to 0.6.

6 Conclusions

The main results obtained in this paper can be formulated as follows.

The paper discusses the main problems of the processes of the origin and evolution of the Solar System and the formation of planetary systems around other stars. The problems include the formation and evolution of dust clusters and primary bodies and formation of primary dust aggregates in circumsolar gas-dust disk. Computer experiments with dust clusters were carried out. Models of dusty fractal clusters formed in protoplanetary disks are constructed, taking into account the existing cosmochemical and physical limitations. When constructing the models, the effective method of permeable particles proposed by the authors was used. We studied the formation of initial structures, collisional evolution of initial clusters, structure and properties of heterogeneous fractal dust-ice clusters on the snow line.

The accumulation of the terrestrial planets and the Moon was studied. The obtained results showed that the outer layers of the Earth and Venus could accumulate approximately the same for these planets material from different parts of the feeding zone of the terrestrial planets. It was obtained that the total mass of water delivered to the Earth from beyond the orbit of Jupiter could be approximately equal to the mass of Earth's oceans. The zone of the outer asteroid belt could be one of the sources of the late heavy bombardment. The problem of asteroid-comet hazard is discussed based on our studies of migration of bodies to the Earth from different regions of the Solar System. Calculations of the migration of planetesimals from beyond the ice line to the inner planets were carried out both for the Solar System and for the Proxima Centauri exoplanetary system. The calculation results indicate that a lot of icy material and volatiles could have been delivered to exoplanets Proxima Centauri *b* and *d*.

The composition and relative content of the ice component in the primary ice-rock planetesimals formed in different regions of the gas-dust protoplanetary disk were obtained. For the inner region, water ice fraction in the ice-rock proto-bodies did not exceed 0.36, which is close to the value obtained for Ceres. In the region of the formation

of the Jupiter and Saturn systems the maximum proportion of water in the composition of the regular satellites of Jupiter and Saturn most likely could not exceed ~40 wt%. For the Jupiter zone, the mass of ice never exceeds the mass of the refractory component. In the region of the formation of the Saturn system, the values of the mass ratios of ice and the refractory component could vary from 1.2 to 0.7. For the trans-Neptunian region, the value of the ratio of the masses of water ice and the refractory component in the ice-rock planetesimals with the same parameters is less than that in the zone of Saturn and Jupiter: it does not exceed 0.6 g/g, and the mass fraction of H_2O_{ice} is not higher than ~0.35.

The models of the chemical composition and internal structure of the initially homogeneous Moon were investigated on the basis of the joint inversion of geophysical and geochemical constraints. The results show that the bulk FeO concentrations independent of temperature and consists of 11–14 wt%, which sharply differ from those for BSE (FeO ~ 8%). On the contrary, bulk concentrations of Al_2O_3 depend on temperature and amount up to 4–5% for cold and 5–7% for hot thermal models. The analysis of experiments on determining the speed of sound of Fe(Ni)-S-C-Si melts in comparison with seismic data is carried out. If sulfur is the only light element in the liquid outer core, then the speed of sound of liquid Fe(Ni)-S with an amount of sulfur up to ~10 wt% S is in good agreement with the Apollo seismic data.

The total H_2O content in Titan was estimated for the range of models of the satellite's internal structure. It is shown that water content in Titan varies between 36 and 53 wt. %. The largest amount of water (53 wt.%) is found in partially differentiated Titan with a composition of the rocky component close to that of anhydrous L/LL chondrites. The smallest amount of water (36 wt.%) occurs in the model of fully differentiated Titan with a hydrous silicate core. The water-ice/rock ratio for the models of fully differentiated Titan result in water-ice/rock ratio equal to 0.6.

The obtained results make a significant contribution to the study of the processes of the early stage of evolution of the circumstellar protoplanetary disks and the present internal structure and composition of bodies of the Solar system.

Acknowledgements This article was written by leading scientists of the Laboratory of Thermodynamics and Mathematical Modeling of Natural Processes of the Vernadsky Institute of Geochemistry and Analytical Chemistry of the Russian Academy of Sciences. The authors of section 2 «Studies in the field of stellar-planetary cosmogony» are: M. Ya. Marov, S. I. Ipatov, and A. V. Rusol, the author of section 3 «Estimation of the composition and mass of the ice component in primary ice-rock bodies of the protoplanetary disk» is V. A. Dorofeeva, the authors of section 4 «Thermo-chemical constraints on the bulk composition and core sizes of the Moon» are O. L. Kuskov, E. V. Kronrod, and V. A. Kronrod, and the authors of section 5 «Estimates of H_2O content in Titan with different degrees of differentiation of iron-rock and rock-ice substance» are A. N. Dunaeva, V. A. Kronrod, and O. L. Kuskov.

References

1. Marov, M.Ya.: Kosmos. Ot Solnechnoy sistemy v glub' Vselennoy (Space. From the Solar system deep into the universe), 3rd edn. Corrected and supplemented. Fizmatlit, Moscow (in Russian) (2021)
2. Marov, M.Ya, Shevchenko, I.I.: Exoplanets: nature and models. Phys. Usp. **63**(9), 837–871 (2020)
3. Kolesnichenko, A.V., Marov, M.Ya.: Turbulentnost' i samoorganizatsiya. Problemy modelirovaniya kosmicheskikh i prirodnykhsred (Turbulence and self-organization. Problems of modeling space and natural environments), 2nd edn. BINOM, Moscow (in Russian) (2012)
4. Marov, M.Ya., Kolesnichenko, A.V.: Turbulence and self-organization: modelling astrophysical objects. Springer, New York. Heidelberg. Dordrecht. London (2013)
5. Kolesnichenko, A.V., Marov, M.Ya.: Streaming instability in the gas–dust medium of the protoplanetary disc and the formation of fractal dust clusters. Sol. Syst. Res. **53**(3), 181–198 (2020)
6. Youdin, A.N.: On the formation of planetesimals via secular gravitational instabilities with turbulent stirring. Astrophys. J. **731** (99) (2011)
7. Youdin, A.N., Goodman, J.: Streaming instabilities in protoplanetary disks. Astrophys. J. **620**, 459–469 (2005)
8. Carrera, D., Gorti, U., Johansen, A., Davies, M.B.: Planetesimal formation by the streaming instability in a photoevaporating disk. Astrophys. J. **839**(16) (2017)
9. Marov, M.Ya., Rusol, A.V.: Gas-dust protoplanetary disc: modeling primordial dusty clusters evolution. J. Pure Appl. Phys. **3**, 16–23 (2015)
10. Blum, J., Gundlach, B., Krause, M., Fulle, M., Johansen, A., Agarwal, J., Borstel, I.V., Shi, X., Hu, X., Bentley, M., Capaccioni, F., Colangeli, L., Corte, V., Fougere, N., Green, S., Ivanovski, S., Mannel, T., Merouane, S., Migliorini, A., Rotundi, A., Schmied, R., Snodgrass, C.: Evidence for the formation of comet 67P/Churyumov-Gerasimenko through gravitational collapse of a bound clump of pebbles. Mon. Notic. Roy. Astron. Soc. **469**, S755–S773 (2017)
11. Marov, M.Ya., Rusol, A.V.: A model for the impact interaction of bodies in a gas-dust protoplanetary disk. Doklady Phys. **56** (12), 597–601 (2011)
12. Drążkowska, J., Alibert, Y.: Planetesimal formation starts at the snow line. Astron. Astrophys. **608**(A92) (2017)
13. Schoonenberg, D., Ormel, C.W.: Planetesimal formation near the snowline. Astron. Astrophys. **602**(A21) (2017)
14. Carrasco-González, C., Sierra, A., Flock, M., Zhu, Z., Henning, T., Chandle, C., Galván-Madrid, R., Macías, E., Anglada, G., Linz, H., Osorio, M., Rodríguez, L., Testi, L., Torrelles, J., Pérez, L., Liu, Ya.: The radial distribution of dust particles in the HL Tau disk from ALMA and VLA observations. Astrophys. J. **883** (71) (2019)
15. Marov, M.Ya., Rusol, A.V.: Estimating the parameters of collisions between fractal dust clusters in a gas–dust protoplanetary disk. Astron. Lett. **44**(7), 474–481 (2018)
16. Fulle, M., Blum, J.: Fractal dust constrains the collisional history of comets. Mon. Notic. Roy. Astron. Soc. **469**, S39–S44 (2017)
17. Marov, M.Y., Rusol, A.V., Makalkin, A.B.: Modeling the fragmentation of dust-ice clusters on the snowline in protoplanetary disks. Sol. Syst. Res. **55**(3), 244–264 (2021)
18. Blum, J.: Dust evolution in protoplanetary discs and the formation of planetesimals. What have we learned from laboratory experiments? Space Sci. Rev. **214**(2, 52), 19 (2018)
19. Makalkin, A.B., Artyushkova, M.E.: On the formation of planetesimals: radial contraction of the dust layer interacting

with the protoplanetary disk gas. Sol. Syst. Res. **51**(6), 491–526 (2017)
20. Rusol, A.V.: Simulation of the structure of dust fractal clusters in protoplanetary gasdust disks. Sol. Syst. Res. **55**(3), 232–243 (2021)
21. Dorofeeva, V.A.: Chemical and isotope composition of comet 67P/Churyumov−Gerasimenko: the Rosetta−Philae mission results reviewed in the context of cosmogony and cosmochemistry. Sol. Syst. Res **54**(2), 96–120 (2020)
22. Davidsson, B.J.R., Sierks, H., Güttler, C., Marzari, F., Pajola, M., Rickman, H., A'Hearn, M.F., Auger, A.-T., El-Maarry M.R., Fornasier, S., Gutiérrez, P.J., Keller, H.U., Massironi, M., Snodgrass, C., Vincent, J.-B., Barbieri, C., Lamy, P.L., Rodrigo, R., Koschny, D., Barucci, M.A., Bertaux, J.-L., Bertini, I., Cremonese, G., Da Deppo, V., Debei, S., De Cecco, M., Feller, C., Fulle, M., Groussin, O., Hviid, S.F., Höfner, S., Ip, W.-H., Jorda, L., Knollenberg, J., Kovacs, G., Kramm, J.-R., Kührt, E., Küppers, M., La Forgia, F., Lara, L.M., Lazzarin, M., Lopez Moreno, J.J., Moissl-Fraund, R., Mottola, S., Naletto, G., Oklay, N., Thomas, N., Tubiana, C.: The primordial nucleus of comet 67P/Churyumov–Gerasimenko. Astron. Astrophys. **592**(A63) (2016)
23. Fulle, M., Blum, J., Green, S.F., Gundlach, B., Herique, A., Moreno, F., Mottola, S., Rotundi, A., Snodgrass, C.: The refractory-to-ice mass ratio in comets. Mon. Notic. Roy. Astron. Soc. **482**, 3326–3340 (2019)
24. Lorek, S., Gundlach, B., Lacerda, P., Blum, J.: Comet formation in collapsing pebble clouds. What cometary bulk density implies for the cloud mass and dust-to-ice ratio. Astron. Astrophys. **587** (A128) (2016)
25. Ipatov, S.I.: Migration of bodies in the accretion of planets. Sol. Syst. Res. **27**(1), 65–79 (1993)
26. Ipatov, S.I.: Migratsiya nebesnykh tel v Solnechnoi sisteme (Migration of Celestial bodies in the Solar System), URSS, Moscow (in Russian) (2000)
27. Chambers, J.E., Wetherill, G.W.: Making the terrestrial planets: N-body integrations of planetary embryos in three dimensions. Icarus **136**, 304–327 (1998)
28. Raymond, S.N., Quinn, T., Lunine, J.I.: Making other earths: dynamical simulations of terrestrial planet formation and water delivery. Icarus **168**, 1–17 (2004)
29. Raymond, S.N., Quinn, T., Lunine, J.I.: High-resolution simulations of the final assembly of Earth-like planets I. Terrestrial accretion and dynamics. Icarus **183**, 265–282 (2006)
30. Raymond, S.N., O'Brien, D.P., Morbidelli, A., Kaib, N.A.: Building the terrestrial planets: constrained accretion in the inner Solar System. Icarus **203**, 644–662 (2009)
31. Chambers, J.: Late-stage planetary accretion including hit-and-run collisions and fragmentation. Icarus **224**, 43–56 (2013)
32. Ipatov, S.I.: Probabilities of collisions of planetesimals from different regions of the feeding zone of the terrestrial planets with the forming planets and the Moon. Sol. Syst. Res. **53**(5), 332–361 (2019)
33. Elkins-Tanton, L.T.: Rapid formation of Mars. Nature **558**(7711), 522–523 (2018)
34. Canup, R.M.: Forming a Moon with an Earth-like composition via a giant impact. Science **338**, 1052–1055 (2012)
35. Cuk, M., Hamilton, D.P., Lock, S.J., Stewart, S.T.: Tidal evolution of the Moon from a high-obliquity, high-angular-momentum Earth. Nature **539**, 402–406 (2016)
36. Barr, A.C.: On the origin of Earth's Moon. J. Geophys. Res.: Planets **121**, 573–1601 (2016)
37. Galimov, E.M., Krivtsov, A.M., Zabrodin, A.V., Legkostupov, M.S., Eneev, T.M., Sidorov, Yu.I.: Dynamic model for the formation of the Earth-Moon system. Geochem. Int. **43**(11), 1045–1055 (2005)
38. Galimov, E.M.: Formation of the Moon and the Earth from a common supraplanetary gas-dust cloud (lecture presented at the XIX all-Russia symposium on isotope geochemistry on November 16, 2010). Geochem. Int. **49**(6), 537–554 (2011)
39. Galimov, E.M., Krivtsov, A.M.: Origin of the Moon. New concept. De Gruyter, Berlin (2012)
40. Ipatov, S.I.: Formation of embryos of the Earth and the Moon from the common rarefied condensation and their subsequent growth. Sol. Syst. Res. **52**(5), 401–416 (2018)
41. Rufu, R., Aharonson, O.: A multiple-impact origin for the Moon. Nat. Geosci. **10**, 89–94 (2017)
42. Ipatov, S.I.: Formation of trans-Neptunian satellite systems at the stage of condensations. Sol. Syst. Res. **51**(4), 294–314 (2017)
43. Ipatov, S.I.: Origin of orbits of secondaries in the discovered trans-Neptunian binaries. Sol. Syst. Res. **51**(5), 409–416 (2017)
44. Zharkov, V.N.: The role of Jupiter in the formation of planets. Evolution of the Earth and Planets. Geophys. Monogr. Ser. 74 IUGG **14**, 7–17 (1993)
45. Zharkov, V.N., Kozenko, A.V.: On the role of Jupiter in the formation of the giant planets. Soviet Astron. Lett. **16**(1), 73–74 (1990)
46. Marov, M.Ya., Ipatov, S.I.: Formation of the Earth and Moon: influence of small bodies. Geochem. Int. **59**(11), 1010–1017 (2021)
47. Marov, M.Ya., Kolesnichenko, A.V., Makalkin, A.B., Dorofeeva, V.A., Ziglina, I.N., Chernov, A.V.: From a protosolar cloud to a planetary system: a model of the evolution of a gas-dust disk. In: Galimov, E.M. (ed.) Problems of the Origin and Evolution of the Biosphere, pp. 223–274. LIBROKOM, Moscow (in Russian) (2008)
48. Marov, M.Ya.: The formation and evolution of the solar system. In: Read, P. et al. (eds.) Oxford Research Encyclopedia of Planetary Science, id.2. Oxford University Press, Oxford (2018)
49. Ipatov, S.I., Mather, J.C.: Migration of Jupiter-family comets and resonant asteroids to near-Earth space. Ann. N Y Acad. Sci. **1017**, 46–65 (2004)
50. Ipatov, S.I.: Migration of small bodies to the Earth. Sol. Syst. Res. **29**(4), 261–286 (1995)
51. Marov, M.Ya., Ipatov, S.I.: Volatile inventory and early evolution of planetary atmospheres. In: Marov, M.Ya., Rickman, H. (eds.) Collisional Processes in the Solar System. Astrophysics and Space Science Library, vol. 261, pp. 223–247. Kluwer Academic Publishers, Dordrecht (2001)
52. Marov, M.Ya., Ipatov, S.I.: Delivery of water and volatiles to the terrestrial planets and the Moon. Sol. Syst. Res. **52**(5), 392–400 (2018)
53. Marov, M.Ya, Ipatov, S.I.: Migration processes in the solar system and their role in the evolution of the Earth and planets. Phys. Usp. **64** (2022)
54. Bottke, W.F., Morbidelli, A., Jedicke, R., Petit, J.-M., Levison, H.F., Michel, P., Metcalfe, T.S.: Debiased orbital and absolute magnitude distribution of the near-Earth objects. Icarus **156**, 399–433 (2002)
55. Marov, M.Ya.: Meteorite Chelyabinsk: an overview. In: Lloyd, C. (ed.) Astrophysics: New Research, pp. 27–64. Nova Science Publishers (2016)
56. Popova, O.P., Jenniskens, P., Emel'yanenko, V., Kartashova, A., Biryukov, E., Khaibrakhmanov, S., Shuvalov, V., Rybnov, Y., Dudorov, A., Grokhovsky, V.I., et al.: Chelyabinsk airburst, damage assessment, meteorite recovery, and characterization. Science **342**, 1069–1073 (2013)
57. Farinella, P, Gonczi, R., Froeschle, Ch., Froeschle, C.: The ejection of asteroid fragments into resonances. Icarus **101**, 174–187 (1993)

58. Eneev, T.M.: Evolution of the outer solar system—possible structure beyond Neptune. Soviet Astron. Lett. **6**(3), 163–166 (1980)
59. Ipatov, S.I.: Migration of trans-Neptunian objects to the Earth. Celest. Mech. Dyn. Astron. **73**(1), 107–116 (1999)
60. Nakamura, T., Kurahashi, H.: Collisional probability of periodic comets with the terrestrial planets: an individual case of analytic formulation. Astron. J. **115**, 848–854 (1998)
61. Shustov, B.M., Rykhlova, L.V. (eds.): Asteroidno-kometnayaopasnost': vchera, segodnya, zavtra (Asteroid-comet hazard: yesterday, today, tomorrow). Fizmatlit, Moscow (in Russian) (2010)
62. Werner, S.C., Ivanov, B.A.: Exogenic dynamics, cratering, and surface ages. In: Treatise on Geophysics, vol. 10, pp. 327–365, 2nd edn. Elsevier (2015)
63. Shoemaker, E.M., Wolfe, R.F., Shoemaker, C.S.: Asteroid and comet flux in the neighborhood of Earth. In: Sharpton, V.L., Ward, P.D. (eds.) Global Catastrophes in Earth History, pp. 155–170. Geological Society of America (1990)
64. Ipatov, S.I., Feoktistova, E.A., Svetsov, V.V.: Number of near-Earth objects and formation of lunar craters over the last billion years. Sol. Syst. Res. **54**(5), 384–404 (2020)
65. Feoktistova, E.A., Ipatov, S.I.: Depths of Copernican craters on lunar maria and highlands. Earth Moon Planets **125**(1) (2021)
66. Ipatov, S.I.: Delivery of water and volatiles to planets in the habitable zone in the Proxima Centauri system. Bull. Am. Astron. Soc. **53**(3), e-id 2021n3i1126 (2021)
67. Makalkin, A.B., Dorofeeva, V.A.: Stroeniye protoplanetnogo akkretsionnogo diska vokrug Solntsa na stadia T Tel'tsa. I. Iskhodnyye dannyye, uravneniya I metody postroyeniya modelei (The structure of the protoplanetary accretion disk around the Sun at the Taurus stage. I. Initial data, equations and methods of constructing models). Sol. Syst. Res. **29**(2), 99–122 (1995)
68. Makalkin, A.B., Dorofeeva, V.A.: The structure of the protoplanetary accretion disk around the Sun at the Taurus stage. II. Model calculation results). Sol. Syst. Res. **30**(6), 496–513 (1996) (in Russian)
69. Dorofeeva, V.A., Makalkin, A.B.: Evolution of the early solar system. Cosmochemical and physical aspects. URSS, Moscow (2004)
70. Lodders, K.: Solar system abundances of the elements. In: Goswami, A., Reddy, B.E. (eds.) Principles and Perspectives in Cosmochemistry, pp. 379–417. Springer-Verlag, Berlin Heidelberg (2010)
71. Cameron, A.G.W., Pine, M.R.: Numerical models of the primitive solar nebula. Icarus **18**(3), 377–406 (1973)
72. Cameron, A.G.W.: Physics of the primitive solar accretion disk. The moon and the planets **18**(1), 5–40 (1978)
73. Hayashi, C.: Structure of the solar nebula, growth and decay of magnetic fields and effects of magnetic and turbulent viscosities on the nebula. Prog. Theor. Phys. Suppl. **70**, 35–53 (1981)
74. Martin, R.G., Livio, M.: On the evolution of the snow line in protoplanetary discs. Mon. Not. R. Astron. Soc. **425**, L6–L9 (2012)
75. Podolak, M., Zucker, S.: A note on the snow line in protostellar accretion disks. Meteorit. Planet. Sci. **39**(11), 1859–1868 (2004)
76. Marboeuf, U., Thiabaud, A., Alibert, Y., Cabral, N., Benz, W.: From stellar nebula to planetesimals. Astron. Astrophys. **570**, A35 (2014)
77. Mandt, K.E., Mousis, O., Marty, B., Cavalié, T., Harris, W., Hartogh, P., Willacy, K.: Constraints from comets on the formation and volatile acquisition of the planets and satellites. Space Sci. Rev. **197**, 297–342 (2015)
78. Mousis, O., Lunine, J.I., Luspay-Kuti, A., Guillot, T., Marty, B., Ali-Dib, M., Wurz, P., Altwegg, K., Bieler, A., Hässig, M., Rubin, M., Vernazza, P., Waite, J.H.: Protosolar nebula origin for the ices agglomerated by comet 67P/Churyumov-Gerasimenko. Astrophys. J. Letters **819**(2), L33 (2016)
79. Lodders, K.: Solar system abundances and condensation temperatures of the elements. Astrophys. J. **591**(2), 1220–1247 (2003)
80. Dorofeeva, V.A., Petaev, M.I., Khodakovsky, I.L.: On the influence of nebula gas chemistry on condensate composition. In: Lunar Planet Science XIII. Abstracts, pp. 181–182. Lunar and Planetary Institute, Houston (1982)
81. Lewis, J.S., Prinn, R.G.: Kinetic ingibition of CO and N reduction in the solar nebula. Astrophys. J. **238**, 357–364 (1980)
82. Mendybaev, R.A., Dorofeeva, V.A., Makalkin, A.B., Khodakovsky, I.L., Lavrukhina, A.K.: On the forms of carbon and nitrogen in the gas phase of the preplanetary nebula. In: Lunar Planet Science XV. Abstracts, pp. 540–541. Lunar and Planetary Institute, Houston, USA (1984)
83. Mendybaev, R.A., Makalkin, A.B., Dorofeeva, V.A., Khodakovsky, I.L., Lavrukhina, A.K.: Rol' kinetiki reaktsii vosstanovleniya CO i N_2 v khimichekoi evolutsii protoplanetnogo oblaka (the role of kinetics of CO and N_2 reduction reactions in the chemical evolution of a protoplanetary cloud). Geochemiya. **8**, 1206–1217 (1985). (in Russian)
84. Pollack, J.B., Hollenbach, D., Beckwith, S.B., Simonelly, D.P.: Composition and radiative properties of grains in molecular clouds and accretion disks. Astrophys. J. **421**, 615–639 (1994)
85. Fu, R.R., Ermakov, A.I., Marchi, S., Castillo-Rogez, J.C., Raymond, C.A., Hager, B.H., Zuber, M.T., King, S.D., Bland, M.T., De Sanctis, M.C., Preusker, F., Park, R.S., Russell, C.T. The interior structure of Ceres as revealed by surface topography. Earth Planet. Sci. Lett. **476**, 153–164 (2017)
86. Zolotov, M. Yu.: The composition and structure of Ceres' interior. Icarus **335**, 113404 (2019)
87. Kissel, J., Krueger, F.R.: The organic component in dust from comet Halley as measured by the PUMA mass spectrometer on board Vega 1. Nature **326**(6115), 755–760 (1987)
88. Bardyn, A., Baklouti, D., Cottin, H., Fray, N., Briois, C., Paquette, J., Stenzel, O., Engrand, C., Fischer, H., Hornung, K., and 16 coauthors.: Carbon-rich dust in comet 67P/Churyumov-Gerasimenko measured by COSIMA/Rosetta. Mon. Notic. Roy. Astron. Soc. **469**(Suppl. 2), S712–S722 (2017)
89. Fray, N., Schmitt, B.: Sublimation of ices of astrophysical interest: a bibliographic review. Planet. Space Sci. **57**(14–15), 2053–2080 (2009)
90. Dorofeeva, V.A.: Genesis of volatile components at Saturn's regular satellites. Origin of Titan's atmosphere. Geochem. Int. **54** (1), 7–26 (2016)
91. Müller, B., Giuliano, B.M., Goto, M., Caselli, P.: Spectroscopic measurements of CH_3OH in layered and mixed interstellar ice analogues. Astron. Astrophys. **652**, A126 (2021)
92. Dorofeeva, V.A.: The role of radial transport in the formation of small bodies of the outer Solar system. Sol. Syst. Res. **56**(2) (2022a)
93. Rotundi. A., Sierks, H., Della Corte, V., Fulle, M., Gutierrez, P. J., Lara, L., Barbieri, C., Lamy, P.L., Rodrigo, R., et al.: Dust measurements in the coma of comet 67P/Churyumov-Gerasimenko in bound to the Sun. Science **347**(6220), aaa3905 (2015)
94. Moreno, F., Snodgrass, C., Hainaut, O., Tubiana, C., Sierks, H., Barbieri, C., Lamy, P.L., Rodrigo, R., Koschny, D., Rickman, H., et al.: The dust environment of comet 67P/Churyumov-Gerasimenko from Rosetta OSIRIS and VLT observations in the 4.5 to 2.9 AU heliocentric distance range inbound. Astron. Astrophys. **587**, A155 (2016)
95. Russo, N.D., Kawakita, H., Vervack, R.J., Jr., Weaver, H.A.: Emerging trends and a comet taxonomy based on the volatile

chemistry measured in thirty comets with high-resolution infrared spectroscopy between 1997 and 2013. Icarus **278**, 301–332 (2016)
96. Lognonné, P.: Planetary seismology. Annu. Rev. Earth Planet. **33**, 571–604 (2005)
97. Khan, A., Connolly, J.A.D., Pommier, A., Noir, J.: Geophysical evidence for melt in the deep lunar interior and implications for lunar evolution. J. Geophys. Res. Planets **119**, 2197–2221 (2014)
98. Williams, J.G., Konopliv, A.S., Boggs, D.H., Park, R.S., Yuan, D-N., Lemoine, F.G., Goossen, S., Mazarico, E., Nimmo, F., Weber, R.C., Asmar, S.W., Melosh, H.J., Neumann, G.A., Phillips, R.J., Smith, D.E., Solomon, S.C., Watkins, M.M., Wieczorek, M.A., Andrews-Hanna, J.C., Head, J.W., Kiefer, W. S, Matsuyama, I., McGovern, P.J., Taylor, G.J., Zuber, M.T.: Lunar interior properties from the GRAIL mission. J. Geophys. Res.: Planets. **119** (7), 1546–1578 (2014). LNCS Home page. https://doi.org/10.1002/2013JE004559
99. Garcia, R.F., Gagnepain-Beyneix, J., Chevrot, S., Lognonné, P.: Very preliminary reference Moon model. Phys. Earth Planet. Inter. **188**, 96–113 (2011)
100. Wieczorek, M.A., Jolliff, B.J., Khan, A., Pritchard, M.E., Weiss, B.J., Williams, J.G., Hood, L.L., Righter, K., Neal, C.R., Shearer, C.K., McCallum, I.S., Tompkins, S., Hawke, B.R., Peterson, C., Gillis, J.J., Bussey, B.: The constitution and structure of the lunar interior. New views of the Moon. Rev. Mineral. Geochem. **60**, 221–364 (2006)
101. Meier, M.M.M., Reufer, A., Wieler, R.: On the origin and composition of Theia: constraints from new models of the giant impact. Icarus **242**, 316–328 (2014)
102. Jolliff, B.L.: Science and Exploration of the Moon: Overview. Oxford Research Encyclopedias, Planetary Science (2021). LNCS Home page. https://doi.org/10.1093/acrefore/9780190647926.013.19
103. Khan, A., Connolly, J.A.D., Maclennan, J., Mosegaard, K.: Joint inversion of seismic and gravity data for lunar composition and thermal state. Geophys. J. Int. **168**, 243–258 (2007)
104. Gagnepain-Beyneix, J., Lognonné, P., Chenet, H., Lombardi, D., Spohn, T.: A seismic model of the lunar mantle and constraints on temperature and mineralogy. Phys. Earth Planet. Inter. **159**(3–4), 140–166 (2006)
105. Kronrod, E.V., Kronrod, V.A., Kuskov, O.L., Nefedyev, Yu.A.: Geochemical constraints for the bulk composition of the Moon. Doklady Earth Sci. **483**(1), 1475–1479 (2018)
106. Kuskov, O.L., Kronrod, E.V., Kronrod, V.A.: Geochemical constraints on the cold and hot models of the Moon's interior: 1–Bulk composition. Sol. Syst. Res. **52**(6), 467–479 (2018)
107. Kuskov, O.L., Kronrod, E.V., Kronrod, V.A.: Geochemical constraints on the cold and hot models of the Moon's interior: 2–Three-layer mantle. Sol. Syst. Res. **53**(2), 75–90 (2019)
108. Kuskov, O.L., Kronrod, E.V., Kronrod, V.A.: Thermo-chemical constraints on the lunar bulk composition and the structure of a three-layer mantle. Phys. Earth Planet. Inter. **286**, 1–12 (2019)
109. Kuskov, O.L., Kronrod, E.V., Kronrod, V.A.: Effect of thermal state on the mantle composition and core sizes of the Moon. Geochem. Int. **57**, 605–620 (2019)
110. Morgan, J.W., Hertogen, J., Anders, E.: The Moon: composition determined by nebula processes. Moon Planets **18**, 465–478 (1978)
111. Ringwood, A.E.: Basaltic magmatism and the bulk composition of the Moon. I. Major and heat-producing elements. Moon **16**, 389–423 (1977)
112. Taylor, S.R.: Planetary Science: A Lunar Perspective. LPI, Houston. TX (1982)
113. Jones, J.H., Delano, J.W.: A three component model for the bulk composition of the Moon. Geochim. Cosmochim. Acta **53**, 513–527 (1989)
114. Lognonné, P., Gagnepain-Beyneix, J., Chenet, H.: A new seismic model of the Moon: implications for structure, thermal evolution and formation of the Moon. Earth Planet. Sci. Lett. **211**, 27–44 (2003)
115. Longhi, J.: Petrogenesis of picritic mare magmas: constraints on the extent of early lunar differentiation. Geochim. Cosmochim. Acta **70**, 5919–5934 (2006)
116. Dauphas, N., Burkhardt, C., Warren, P.H., Fang-Zhen, T.: Geochemical arguments for an Earth-like Moon-forming impactor. Phil. Trans. R. Soc. A. **372**, 20130244 (2014)
117. Taylor, S.R., Taylor, G.J., Taylor, L.A.: The Moon: a Taylor perspective. Geochim. Cosmochim. Acta **70**, 594–5918 (2006)
118. Moriarty, D.P., Dygert, N., Valencia, S.N., Watkins, R.N., Petro, N.E.: The search for lunar mantle rocks exposed on the surface of the Moon. Nat. Comm. **12**(1) (2021)
119. Kuskov, O.L., Belashchenko, D.K.: Thermodynamic properties of Fe-S alloys from molecular dynamics modeling: implications for the lunar fluid core. Phys. Earth Planet. Inter. **258**, 43–50 (2016)
120. Kuskov, O.L., Belashchenko, D.K.: Molecular dynamics estimates for the thermodynamic properties of the Fe–S liquid cores of the Moon, Io, Europa, and Ganymede. Sol. Syst. Res. **50**(3), 165–183 (2016)
121. Hood, L.L., Mitchell, D.L., Lin, R.P., Acuña, M.H., Binder, A. B.: Initial measurements of the lunar induced magnetic dipole moment using lunar prospector magnetometer data. Geophys. Res. Lett. **26**, 2327–2330 (1999)
122. Shimizu, H., Matsushima, M., Takahashi, F., Shibuya, H., Tsunakawa, H.: Constraint on the lunar core size from electromagnetic sounding based on magnetic field observations by an orbiting satellite. Icarus **222**, 32–43 (2013)
123. Williams, J.G., Boggs, D.H., Yoder, C.F., Ratcliff, J.T., Dickey, J.O.: Lunar rotational dissipation in solid body and molten core. J. Geophys. Res. **106**, 27933–27968 (2001)
124. Weber, R.C., Lin, P., Garnero, E.J., Williams, Q., Lognonné, P.: Seismic detection of the lunar core. Science **331**, 309–312 (2011)
125. Garcia, R.F., Khan, A., Drilleau, M., Margerin, L., Kawamura, T., Sun, D., Wieczorek, M.A., Rivoldini, A., Nunn, C., Weber, R. C., Marusiak, A.G., Lognonné, P., Nakamura, Y., Zhu, P.: Lunar seismology: an update on interior structure models. Space Sci. Rev. **215**(50) (2019)
126. Matsumoto, K., Yamada, R., Kikuchi, F., Kamata, S., Ishihara, Y., Iwata, T., Hanada, H., Sasaki, S.: Internal structure of the Moon inferred from Apollo seismic data and selenodetic data from GRAIL and LLR. Geophys. Res. Lett. **42**(18) (2015)
127. Kuwabara, S., Terasaki, H., Nishida, K., Shimoyama, Y., Takubo, Y., Higo, Y., Shibazaki, Y., Urakawa, S., Uesugi, K., Takeuchi, A., Kondo, T.: Sound velocity and elastic properties of Fe–Ni and Fe–Ni–C liquids at high pressure. Phys. Chem. Min. **43**, 229–236 (2016)
128. Nishida, K., Suzuki, A., Terasaki, H., Shibazaki, Y., Higo, Y., Kuwabara, S., Shimoyama, Y., Sakurai, M., Ushioda, M., Takahashi, E., Kikegawa, T., Wakabayashi, D., Funamori, N.: Towards a consensus on the pressure and composition dependence of sound velocity in the liquid Fe–S system. Phys. Earth Planet. Inter. **257**, 230–239 (2016). LNCS Home page. https://doi.org/10.1016/j.pepi.2016.06.009.
129. Terasaki H., Rivoldini A., Shimoyama Y., Nishida K., Urakawa S., Maki M., Kurokawa F., Takubo Y., Shibazaki Y., Sakamaki T., Machida A., Higo Y., Uesugi K., Takeuchi A., Watanuki T., Kondo T.: Pressure and composition effects on sound velocity and density of core-forming liquids: Implication to core compositions of terrestrial planets. J. Geophys. Res. Planets. **124**(8), 2272–2293 (2019). LNCS Home page https://doi.org/10.1029/2019JE005936

130. Wieczorek, M.A., Neumann, G.A., Nimmo, F., Kiefer, W.S., Taylor, G.J., Melosh, H.J., Phillips, R.J., Solomon, S.C., Andrews-Hanna, J. C., Asmar, S.W., Konopliv, A.S., Lemoine, F.G., Smith, D.E., Watkins, M.M., Williams, J.G., Zuber, M.T.: The crust of the Moon as seen by GRAIL. Science **339**(6120), 671–675 (2013)
131. Matsuyama, I., Nimmo, F., Keane, J.T., Chan, N.H., Taylor, G.J., Wieczorek, M.A., Kiefer, W.S., Williams, J.G.: GRAIL, LLR, and LOLA constraints on the interior structure of the Moon. Geophys. Res. Lett. **43**, 8365–8375 (2016)
132. Kronrod, V.A., Kuskov, O.L.: Inversion of seismic and gravity data for the composition and core sizes of the Moon. Izv. Phys. Solid Earth **47**, 711–730 (2011)
133. Dorofeeva, V.A., Devina, O.A.: Evaluation of the mass fraction of water ice in the rock-ice planetesimals for cosmochemical data. Experim. GeoSci. **24**(S1), 22–24 (2018)
134. Makalkin, A.B., Dorofeeva, V.A.: Accretion disks around Jupiter and Saturn at the stage of regular satellite formation. Sol. Syst. Res. **48**(1), 62–78 (2014)
135. Makalkin, A.B., Dorofeeva, V.A.: Conditions of formation of regular satellites in the accretion disks of Jupiter and Saturn. Mech. Contr. Inform. **7**(3(56)), 425–455 (2015)
136. Stevenson, D.J.: Cosmochemistry and structure of the giant planets and their satellites. Icarus **62**(1), 4–15 (1985)
137. Barr, A.C., Citron, R.I., Canup, R.M.: Origin of a partially differentiated Titan. Icarus. **209**(2), 858–862 (2010)
138. Dunaeva, A.N., Kronrod, V.A., Kuskov, O.L.: Physico-chemical models of the internal structure of partially differentiated Titan. Geochem. Intern. **54**(1), 27–47 (2016)
139. Tobie, G., Lunine, J.I., Monteux, J., Mousis, O., Nimmo, F.: The origin and evolution of Titan. In: Müller-Wodard, I., Griffith, C. A., Lellouch, E., Cravens, Th.E. (eds.) Titan: Interior, Surface, Atmosphere, and Space Environment, pp. 29–62. Cambridge University Press, Cambridge Planetary Science. Cambridge, UK (2014)
140. Baland, R.-M., Tobie, G., Lefèvre, A., Van Hoolst, T.: Titan's internal structure inferred from its gravity field, shape, and rotation state. Icarus **237**, 29–41 (2014)
141. Castillo-Rogez, J.C., Lunine, J.I.: Evolution of Titan's rocky core constrained by Cassini observations. Geophys. Res. Lett. **37**, L20205 (2010)
142. Sohl, F., Solomonidou, A., Wagner, F.W., Coustenis, A., Hussmann, H., Schulze-Makuch, D.: Structural and tidal models of Titan and inferences on cryovolcanism. J. Geophys. Res. Planets **119**(5), 1013–1036 (2014)
143. Kronrod, V.A., Dunaeva, A.N., Gudkova, T.V., Kuskov, O.L.: Matching of models of the internal structure and thermal regime of partially differentiated Titan with gravity field. Sol. Syst. Res. **54**(5), 405–419 (2020)
144. Fortes, A.D.: Titan's internal structure and the evolutionary consequences. Planet. Space Sci. **60**(1), 10–17 (2012)
145. Kuskov, O.L., Kronrod, V.A.: Internal structure of Europa and Callisto. Icarus **177**, 550–569 (2005)
146. Néri, A., Guyot, F., Reynard, B., Sotin, C.: A carbonaceous chondrite and cometary origin for icy moons of Jupiter and Saturn. Earth Planet. Sci. Lett. **530**, 115920 (2020)
147. Krot, A.N., Nagashima, K., Alexander, C.M.O'd., Ciesla, F.J., Fujiya, W., Bonal, L.: Sources of water and aqueous activity on the chondrite parent asteroids. In: Michel, P., DeMeo, F.E., Bottke, W. F., Dotson, R. (eds.) Asteroids IV, pp. 635–660. University of Arizona Press (2015)
148. Weisberg, M.K., McCoy, T.J., Krot, A.N.: Systematics and evaluation of meteorite classification. In: Lauretta, D.S., Sween, H.Y., Jr. (eds.) Meteorites and the Early Solar System II, pp. 19–52. University of Arizona Press (2006)
149. Schaefer, L., Fegley, B.: Outgassing of ordinary chondritic material and some of its implications for the chemistry of asteroids, planets, and satellites. Icarus **186**(2), 462–483 (2007)
150. Friedson, A.J., Stevenson, D.J.: Viscosity of rock-ice mixtures and applications to the evolution of icy satellites. Icarus **56**(1), 1–14 (1983)
151. Lunine, J.I., Stevenson, D.J.: Clathrate and ammonia hydrates at high pressure: application to the origin of methane on Titan. Icarus **70**(1), 61–77 (1987)
152. Kuramoto, K., Matsui, T.: Formation of a hot protoatmosphere on the accreting giant icy satellite: Implications for the origin and evolution of Titan, Ganymede, and Callisto. J. Geophys. Res. Planets **99**(E10), 21183–21200 (1994)

Global Stratigraphy and Resurfacing History of Venus

M. A. Ivanov and J. W. Head

1 Introduction

The idea of the global stratigraphy on Venus is based on two observational facts discovered during a photogeological analysis of 36 randomly selected regions [1, 2]. First, in all cases, sets of morphologically distinct units that make up the surface were relatively small and repetitive. Second, all these units show similar relationships of relative ages and, thus, form similar stratigraphic sequence in each study area. Because the 36 regions of investigation were large ($\sim$1,000,000 km^2 each) and selected at random (each was centered at impact craters with prominent dark parabola), they collectively form a representative, global and unbiased stratigraphic sample of the surface of Venus.

An independent support of the idea of the global stratigraphy came from the results of implementation of the USGS program of geological mapping of Venus. Under this program, different groups of researches mapped independently some of the 62 quadrangles that represent various geologic situations on Venus. So far, geological maps of 35 quadrangles have been compiled and published. These mapping efforts have resulted in a large array of names proposed for the units mapped in different regions [3 and references therein]. An analysis of published maps shows, however, that an apparent chaos of names is related to the preferences and philosophy of different mappers and, despite these different local nomenclatural variations, describes the same unit types of geomorphologies and units [3, 4]. For example, the independent groups of geologists have mapped a ubiquitous unit of regional plains under different names, although this unit shows about the same morphology in all quadrangles (Fig. 1). The same is true for the most strongly tectonized terrain on Venus, such as tessera, and for plains characterized by prominent internal flow-like features.

2 The Model of Global Stratigraphy of Venus

In all published geological maps of Venus, the sets of units that make up the surface are usually smaller than those that characterize morphological variations on Mars [e.g., 5, 6]. This is a consequence of harsh conditions on Venus. Due to strong greenhouse effect on Venus the surface temperature is $\sim$500 °C and the temperature/pressure gradients in the lower atmosphere are apparently low. These conditions cause the hyper-dry, almost stagnant near-surface environments to preclude water-driven erosional processes and to significantly lower the level of aeolian activity. Thus, the common Earth-like sedimentary cover and geological record of sedimentary materials intricately sculptured by water and wind does not add to the complexity of current Venus.

Only three geological processes are important on the planet: volcanism, tectonism, and impact cratering. There are only about a thousand impact craters on Venus [7, 8]. This means that: (1) the surface of the planet is relatively young (the mean age estimates vary from $\sim$750 to $\sim$300 Ma [7, 9, 10]), (2) the contribution of impact craters to resurfacing is minor [11], and (3) volcanism and tectonism were the principal geological processes during the accessible geologic history of Venus. The lack of free water and the reduced wind activity lead to a high level of preservation of the original tectonic and volcanic features, which has resulted in a limited variety of observable morphologies.

Another important conclusion that can be made from the analysis of the 35 published maps is that the key units always show stable relationships of relative ages. For example, regional plains, which are mildly deformed by networks of wrinkle ridges, are always shown as being younger than tectonized units, such as tessera, and usually older than plains

M. A. Ivanov (✉)
V. I. Vernadsky Institute of Geochemistry and Analytical Chemistry, 19, Kosygina Str., Moscow, 119991, Russia
e-mail: mikhail_ivanov@brown.edu

J. W. Head
Brown University, Providence, RI, USA

V. P. Kolotov and N. S. Bezaeva (eds.), *Advances in Geochemistry, Analytical Chemistry, and Planetary Sciences*,
https://doi.org/10.1007/978-3-031-09883-3_15

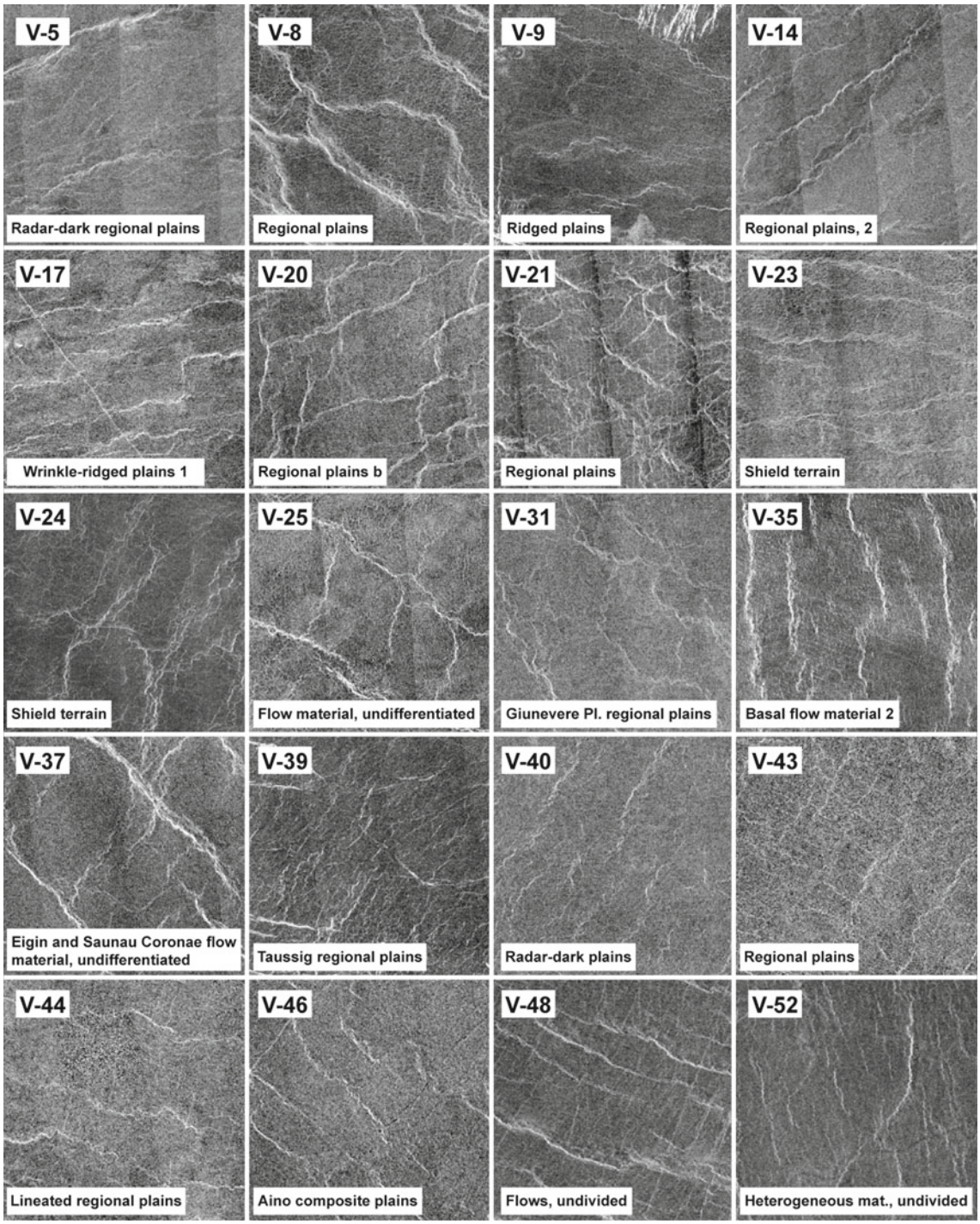

Fig. 1 Examples of regional plains occurring in different USGS maps compiled by different investigators (the map number is in upper left corner) and mapped by different names (bottom of each image). Modified from [3]

with prominent internal flow-like features (lobate plains) that are mostly undeformed by tectonic structures.

Thus, all 35 published maps portray the most areally important types of morphologies that appear to show a generally consistent pattern of relative ages (Fig. 2). The major differences among the 35 maps are usually related to more detailed mapping of features characterizing plains with flow-like features. These flows often show clear relationships of superposition among themselves and these local relationships allow a detail definition of the stratigraphy of the host flow complexes [e.g., 12–14].

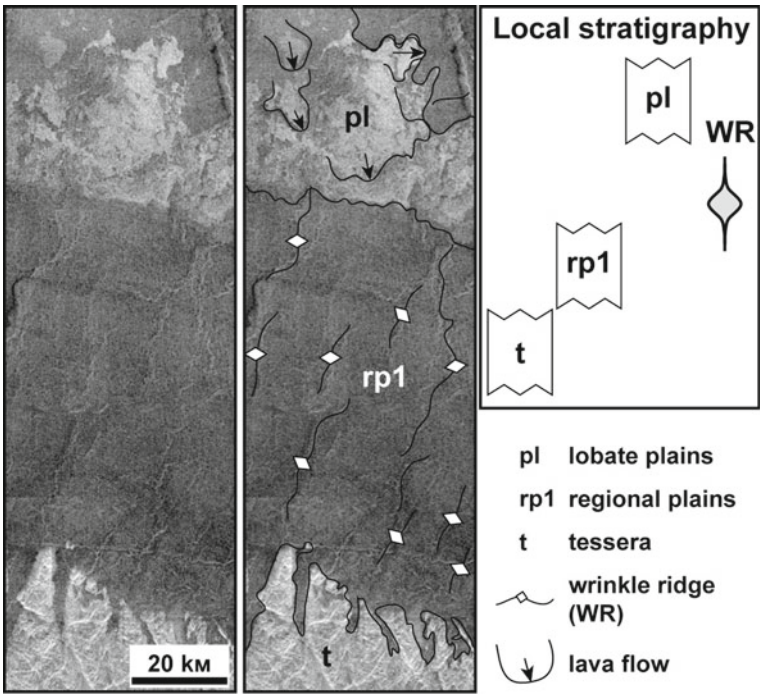

Fig. 2 Typical age relationships among tessera (t), the lower unit of regional plains (rp1) and lobate plains (pl). These relationships are repeated in each region of Venus where these units are observed

As a rule, these flows make up flanks of large but isolated volcanic centers that likely formed at different times in regions portrayed by specific quadrangles. Being considered at the global, planet-wide, scale the flow-like features always embay structures of wrinkle ridges typical of the surrounding regional plains and, thus, represent younger volcanic events, but clearly, their activity was dominated by local environments and settings are thus are not likely to be globally correlative in their detailed activity.

The photogeological analysis of the 36 random regions [1, 2] was summarized in the form of a hypothesis that the observed planet-wide geological record of Venus is made up of globally correlative units and that the accessible geologic history of the planet consists of a series of specific episodes which different volcanic and/or tectonic processes characterized Venus' geological evolution [15, 16]. This observation-based conclusion was drawn from a thorough documentation of different morphologies and assessment of their relative ages in different regions of Venus spread randomly across the globe. This hypothesis is broadly consistent with the lack of evidence of plate tectonics during the observable part of the Venus' history and suggests a possible alternative mechanism of internal heat loss (primarily conduction) in the latter stages of evolution of the planet in the context of the geological, geodynamic and thermal evolution of the terrestrial planets [e.g., 17].

In their work, Guest and Stofan [18] have called this hypothesis a "directional" stratigraphic model, suggested that it is implausible, and proposed a "nondirectional" model, "in which most geologic processes have operated in a nondirectional fashion to a greater or lesser extent throughout the planet's history" [18].

Both "directional" and "nondirectional" models have testable predictions. In the framework of the nondirectional model, the repetitive sets of units and their sequences require the presence of a series of domains that are characterized by similar sequences of morphologically similar units. A time shift between and among the domains precludes any global-wide synchroneity of the units and by definition, gives them a diachronous character. The possible analogues of this situation are similar sequences of units/events at convergent lithospheric plate boundaries on Earth, formed in different regions at different times (e.g., [18]).

The necessary existence of domains (to explain the documented sequences) and their multi-aged nature (to prevent the global synchroneity) in the framework of the nondirectional model inevitable would cause situations shown in Fig. 3. At the boundaries between the domains, the common stratigraphic progression from tessera to regional plains to lobate plains should be violated and as a result, reverse stratigraphic relationships are predicted to emerge. In region A, the regional plains can be younger and overlay the lobate plains (Fig. 4a). In region B, tessera represent the youngest unit and then examples of "tesserization" of regional or/and lobate plains may occur (Fig. 4b). The directional model is consistent with the existence of the domains that, however, have no time shift and the global-wide synchroneity of the units appears.

A potential weak point of the directional model is that it was based on observations made in isolated, discontinuous

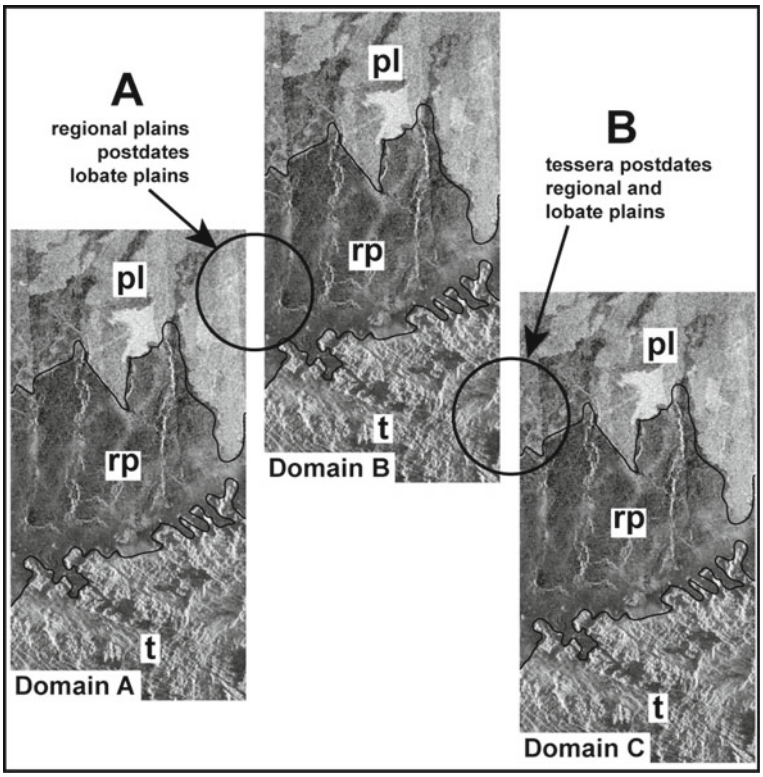

Fig. 3 Possible domain structure of the surface of Venus. Modified from [3]

regions, which could correspond to the interior portions of the domains and may reflect geologic histories of individual areas, and thus the units might be diachronous at a global scale.

3 Results of Global Geological Mapping of Venus

To test the applicability of the observations made in isolated areas and, thus, the existence of the global correlations among units with similar morphology in different regions of the planet, geological mapping in sizable and, most important, contiguous areas was required. Ivanov and Head [19] thus attempted such a test by compiling a geologic map consisting of a geotraverse centered at 30° N ± 7.5° that extended completely around the Venus globe. The geotraverse comprises ~11% of the surface of Venus, was selected at random (based on available Magellan C1-MIDRs with resolution of 225 m/px), and connects several isolated regions from the stratigraphic sample of Basilevsky and Head [1, 2] and quadrangles of the USGS program (Fig. 5).

The major questions addressed by mapping in the geotraverse were: Are units that characterize isolated areas [1, 2, 16] laterally continuous? If similar sequences of units characterize different regions, do they correlate in time or do they represent sequences formed independently in different areas at different times? The mapping results in the geotraverse revealed: (1) the absence of examples of a reverse stratigraphic order (Fig. 4) and (2) that regional plains with uniform morphology can be traced continuously for thousands of kilometers and link remote regions [19]. This extensive and pervasive unit everywhere in the geotraverse embays most of heavily tectonized units (e.g., tessera, ridge belts, and groove belts) and is superposed by flows of lobate plains (Fig. 2).

Although the geotraverse has connected isolated regions of mapping (Fig. 5) and showed no reverse stratigraphic relationships, it is still a narrow strip around the Venus globe that potentially could not be representative for the entire Venus.

The observations made during mapping of the geotraverse and in several USGS quadrangles, V-3, 4, 7, 13, 55, and 61 [20–25], have suggested, however, that only a small number of units (14 units) with clearly different morphology make up the majority of the surface of Venus (Fig. 6). These findings allowed a compilation of a global morphological map of Venus at 1:10,000,000 scale that portrays the spatial distribution of the defined units/terrains.

The global map has shown that the defined units (Fig. 6) (1) clearly describe the variety of morphologies at the global scale, and that (2) they form a generalized sequence that consist of three major (composite) units: (1) the older tessera, t (and the other heavily tectonized terrains), (2) mildly deformed regional plains, rp (and the other units of the plains volcanism), in the middle of the generalized sequence, and

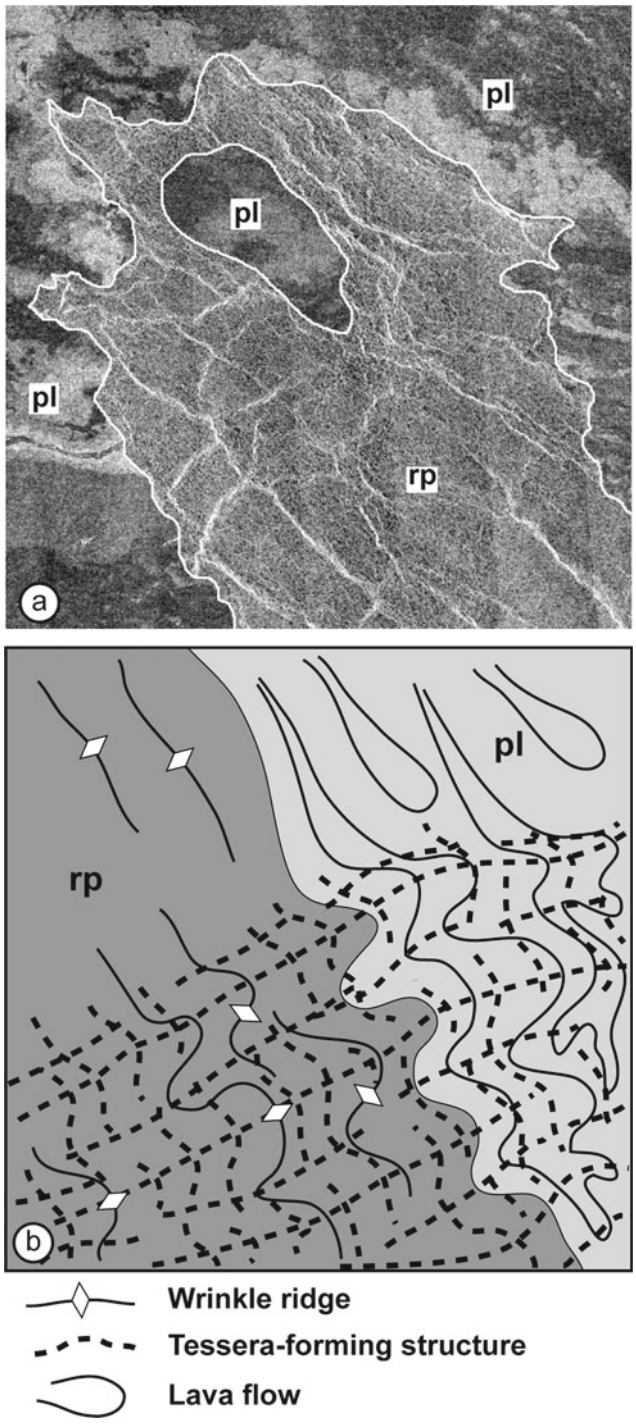

Fig. 4 Expected consequences of the domain structure of the surface of Venus with the time shift between the domains. **a** A "flow" of regional plains overlies lobate plains (an artificially made image). **b** Involvement of the plains units (regional plains and lobate plains) in the formation of tessera, "tesserization" of plains. Modified from [3]

(3) mostly non-tectonized lobate plains, pl, at the top of the sequence (Fig. 2, 6).

A key element of the global map is the unit of regional plains that occupies ~30% of the surface of Venus and that always has a uniform morphology suggesting a uniform mode of emplacement and post-emplacement modification. Occurrences of the plains extend for hundreds to thousands of kilometers, link different regions, always show regular age relationships with the neighboring units and, thus, may represent a reference unit.

The reference unit, however, can have a time-transgressive nature and thus in different locations the morphologically same unit could form at different times (Fig. 7a). If the regional plains (unit rp1) are time-transgressive, units that postdate them (e.g., lobate plains) must also be time-transgressive (Fig. 7b) and, thus, regional plains in one region (C in Fig. 7b) should be younger than lobate plains in the other region (A in Fig. 7b). This implies realization of one of the predictions of the nondirectional model (Fig. 4a). If the older units (e.g., tessera) are also time-transgressive then the other prediction of the nondirectional model (e.g., tesserization of the plains units) is also satisfied (Fig. 4b).

None of these situations (Fig. 4) have been documented during compilation of the global geologic map [3]. We can conclude from this that the prediction of the nondirectional model lack observational support. This suggests that the preserved geologic record of Venus (the last < ~1 Ga), an Earth-like planet in many ways, may be characterized by a mechanism of the internal heat loss, global conduction [26], that is radically different from the global plate tectonics mode of heat loss that has characterized Earth through much of its history, and that may even have had an episodic character [27, 28].

The currently observed global surface of Venus is characterized by a common and consistent stratigraphic sequence which is divided by the lower unit of regional plains (rp1) into the older (t, pdl, pr, gb, psh) and younger (rp2, sc/ps/pl/rz) parts. This general stratigraphic division and characteristic age relationships among units that pre- and postdate the regional plains allow construction of a global-scale correlations chart and representation of the morphological map of terrains in a geological map that illustrates the distribution of units in space and time (Fig. 8) [3].

In places where unit rp1 (the lower unit of regional plains) contacts units with abundant tectonic structures (e.g., tessera, densely lineated plains, or ridge belts), clear evidence of embayment of the teconized terrains is present (Fig. 9a–c). In the cases where unit rp1 is in contact with groove belts t [12, 13, 19, 29, 30], the plains mostly embay the belts but some belt structures appear to cut the plains. This type of relationships suggests that the main phase of the belts development predated the emplacement of regional plains but the belts evolution did not stop by the time of the regional plains formation and continued longer but at diminished rate.

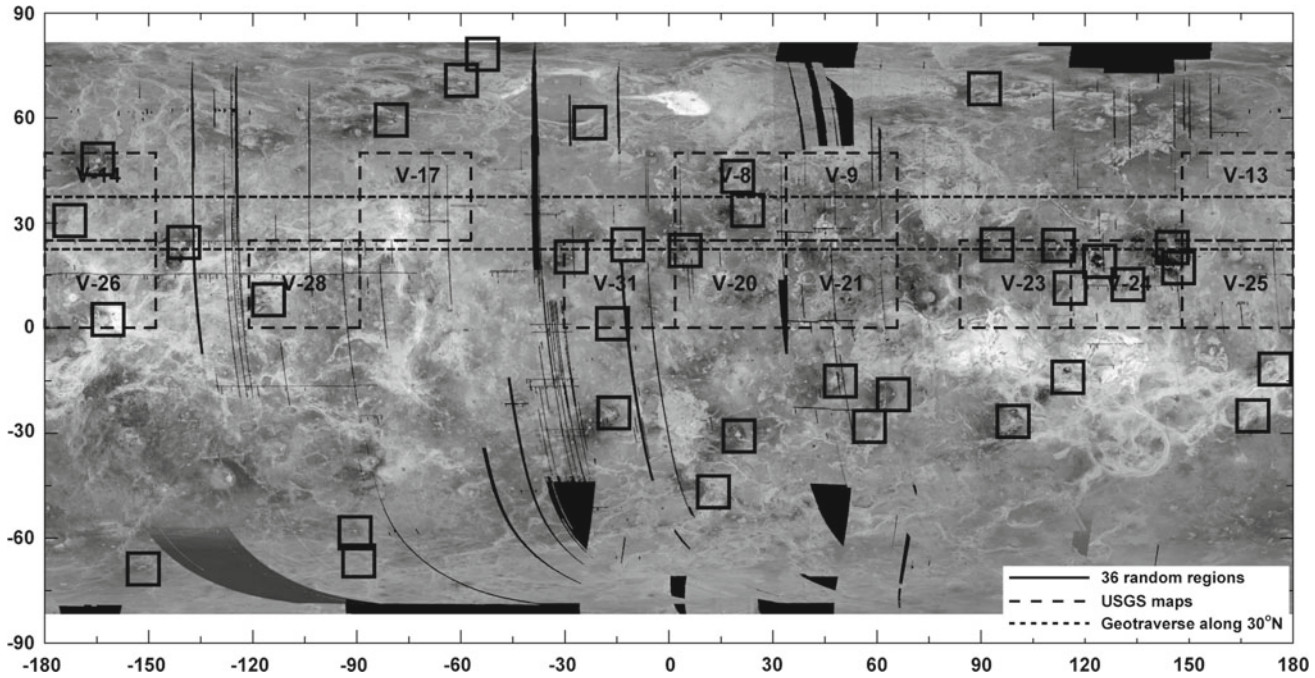

Fig. 5 Location of the 36 random regions analyzed by Basilevsky and Head [1, 2], the geotraverse at 30° N, and published USGS maps that are crossed by the geotraverse

Rift zones are among the younger structural zones on Venus and their structures deform all older tectonized terrains such as tessera, densely lineated plains, ridged plains and groove belts. The rift zone graben and fractures also deform extensive volcanic units of shield plains and both units of regional plains (rp1 and rp2, Fig. 10a). In contrast, at the contacts of rift zones with lobate plains, the rift zone structures can deform the plains and be embayed by the plains materials as well (Fig. 10b). These relationships suggest that both rift zones and lobate plains formed broadly synchronously and both units manifest the results of younger endogenous activity.

4 Major Regimes of Resurfacing on Venus

These characteristic age relationships of units reveal important features of the planet's later evolution and suggest that the accessible part of the geologic history of Venus consists of three major episodes, each with a specific style of resurfacing (Fig. 11) [31]: (1) A global tectonic regime, when tectonic resurfacing dominated. Exposed occurrences of units of this regime comprise ~20% of the surface of Venus. (2) A global volcanic regime, when volcanism was the most important process and resurfaced ~60% of the surface of Venus. (3) A network rifting-volcanism regime, when both tectonic and volcanic activity were about equally important. During this regime, ~16% of the surface of Venus was modified.

The global tectonic regime, is defined by such units as t, pdl, pr/RB and gb. Ridges of tesserae and ridge belts suggest that during the earlier phases of the global tectonic regime compressional forces dominated. They were responsible for the formation of bulk of tesserae over the sites of mantle downwelling and ridge belts due to limited horizontal displacement and warping/buckling of crustal materials at the periphery of the major downwelling cells [32, 33].

Groove belts characterize the later phase of the global tectonic regime and are spatially associated with coronae [31]. The contractional structures that are complementary to groove belts both stratigraphically and by scale are not observed. This may suggest that during the later phase of the global tectonic regime vertical displacement and rupture of lithosphere prevailed and was caused by a plume-dominated tectonic style.

During the global volcanic regime, vast volcanic plains (shield and regional plains, the lower and upper units) were emplaced. The main volcanic plains have different morphologies that indicate different volcanic styles. Small and abundant volcanic constructs of the older shield plains imply that their sources were pervasive and nearly globally distributed, but that the supply of magma at individual sources was limited. The small size of the constructs of shield plains and their association with the steep-sided domes are most consistent with shallow crustal melting and differentiation of magma in reservoirs and/or partial melting of the crustal materials. The lower unit of regional plains that postdate shield plains is very abundant (~1/3 of the surface of

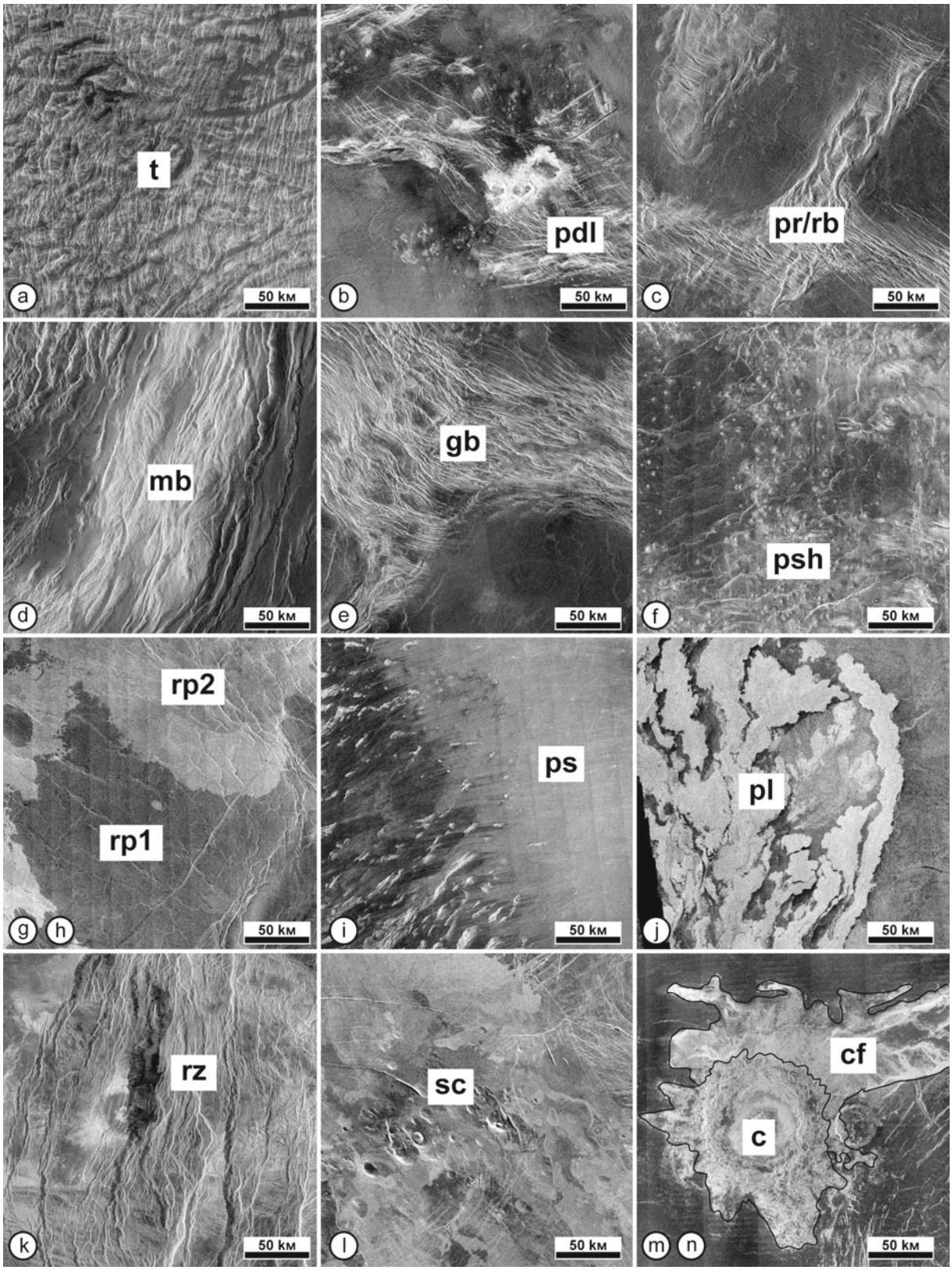

Fig. 6 Morphologically distinct units that have been defined and mapped during compilation of the global geological map of Venus

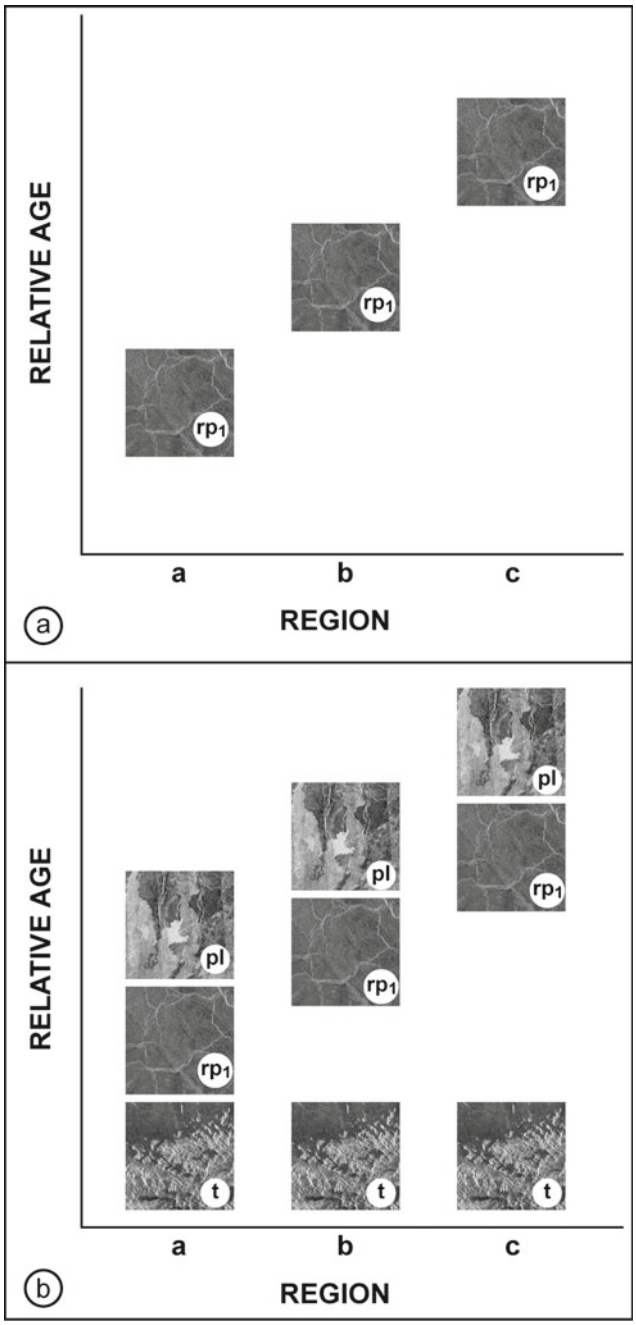

Fig. 7 A time-transgressive model for the emplacement of the lower unit of regional plains (rp1). **a** Diachronous formation of this unit leads to its emplacement in different regions at different times. **b** In the case of time-transgressive emplacement of unit rp1, the units that superpose it are also form in a diachronous manner, which may cause situation shown in Fig. 4a. Modified from [3]

Venus) and ubiquitous but its sources are not visible at the available resolution. These features strongly suggest that unit rp1 formed by voluminous volcanic eruptions from near globally distributed sources. This style of volcanic activity resembles that of terrestrial flood volcanism, but its scale is more easily reconciled with the decompression melting of a fertile mantle layer that underplated the crust. The style of volcanism of the younger lobate plains (rp2) was distinctly different from those of shield plains and regional plains and this unit show evidence of concentration within specific regions and around some large volcanic centers.

Tectonic structures mildly deform the surface of units of the volcanic regime and volcanism was the principal contributor to the resurfacing during this time [34]. The major tectonic structures of the global volcanic regime are wrinkle ridges and graben swarms radiating from distinct volcano-tectonic centers [35–39]. Both types of structures deform the surfaces of the vast plains but do not conceal the original morphologies of the plains and are not related directly to specific patterns of mantle circulation.

Each of units, the rift zones and lobate plains, make up about 5% of the surface of Venus and occur at the top of the global stratigraphic column. The formation of these units established the third major episode of the geologic history of Venus, the network rifting-volcanism regime. Although rift zones are very prominent morphologically, they occur as concentrated structural zones and significantly less abundant than units of the global tectonic regime. This suggests both diminishing of tectonic resurfacing at the later stages of the geologic history of Venus and a change of the tectonic resurfacing from broadly distributed deformation to the highly concentrated deformation during the later network rifting-volcanism regime.

Rift zones are closely associated with the large dome-shaped rises such as Beta and Atla Regiones. This type of the spatial association of rift zones suggests that they likely formed as the dome-shaped swells raised over the sites of large mantle upwellings and in this way rift zones on Venus may resemble continental rifts on Earth [40, 41]. Characteristic feature of lobate plains is their numerous overlapping lava flows that manifest multiple episodes of volcanic activity. In contrast to the earlier vast volcanic plains (e.g., shield and regional plains) lobate plains are strongly concentrated at distinct source regions suggesting that during the network rifting-volcanism regime volcanism was linked to large and discrete sources that probably were active at different times. This character of volcanic activity during the network rifting-volcanism regime is one of the major features of the non-directional model [18] that adequately describes the geological events on Venus during the later episodes of its geologic history. In contrast, the alternative model [3, 16] embraces the entire visible portion of the geologic history of Venus.

The density of impact craters on units representing different resurfacing regimes and their stratigraphic relationships provide additional evidence for the structured nature of the visible portion of the geologic history of Venus. The earliest tectonic and the following volcanic regimes are practically identical by their crater density (Fig. 12).

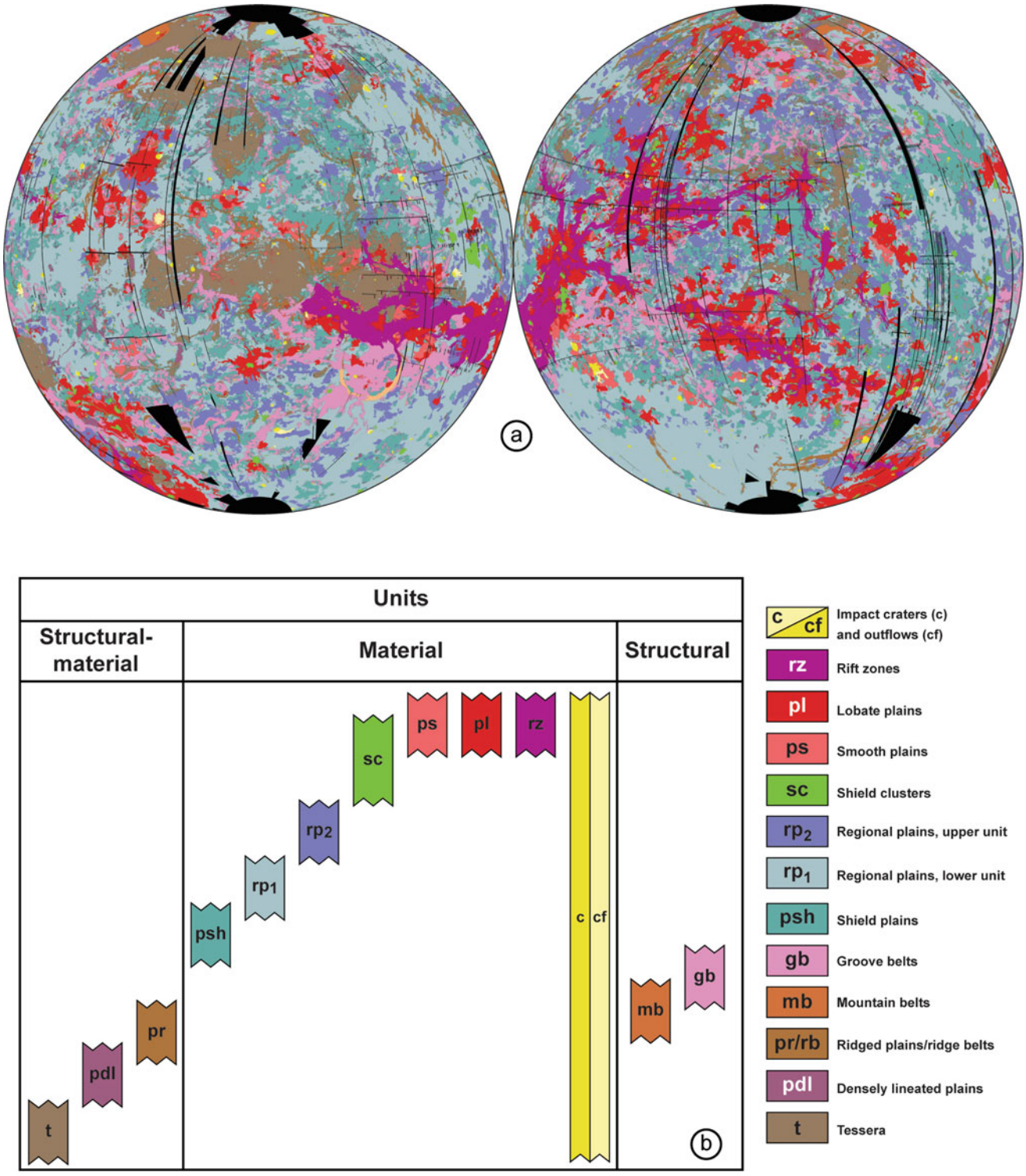

Fig. 8 **a** Global geological map, **b** global-wide correlation chart. Modified from [3]

However, units of the volcanic regime (shield plains and both units of regional plains) always embay the strongly tectonized units of the tectonic regime (t, pdl, pr/RB, and gb, Fig. 9). Such a discrepancy between the crater density and stratigraphic relationships suggests that although the tectonic and the volcanic regimes were close in time, the transition between them was abrupt and had a global character. This may be indicative of the major changes of the pattern of mantle convection.

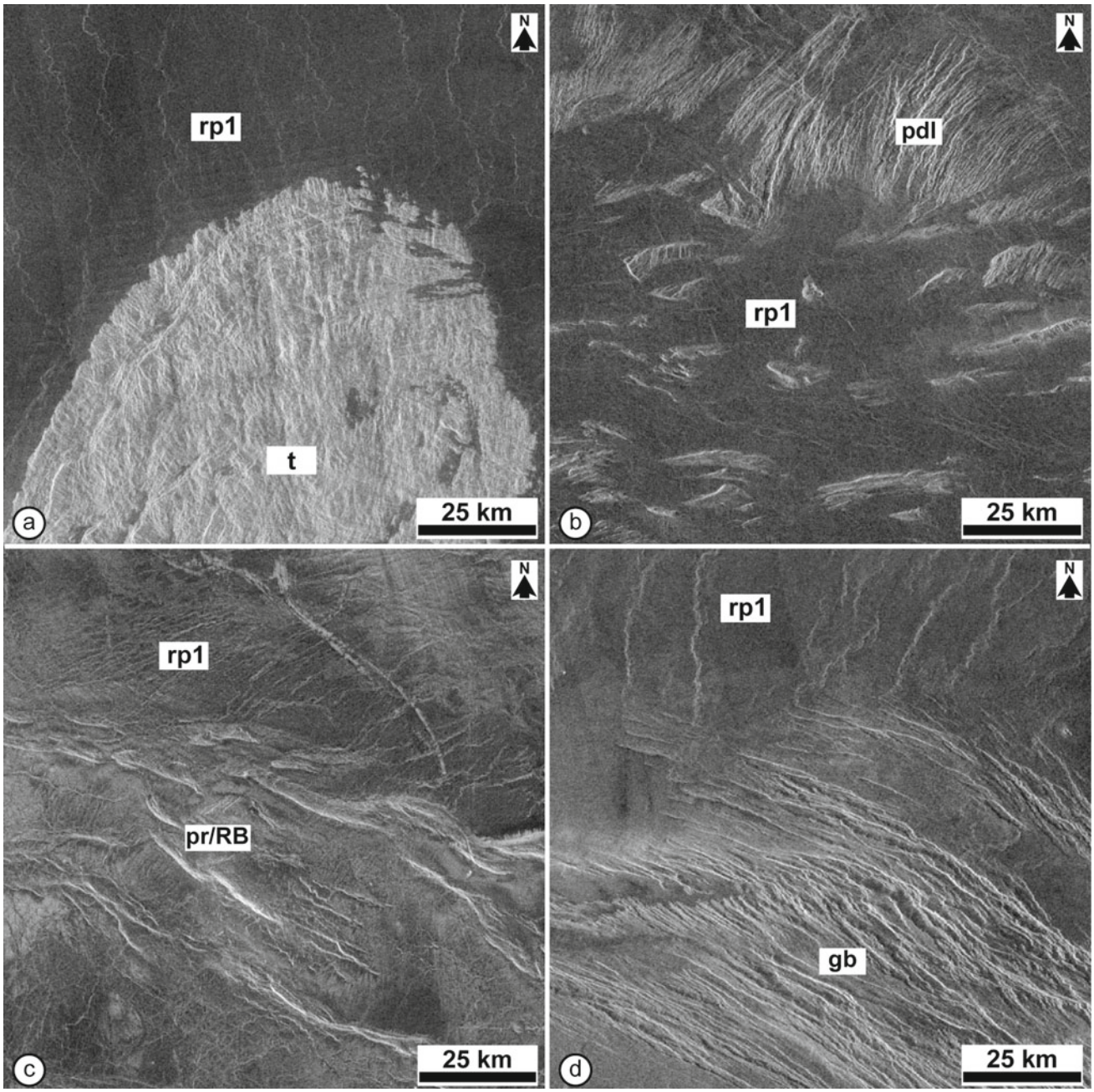

Fig. 9 Examples of embayment of heavily tectonized units (t, pdl, pr, gb) by the lover unit of regional plains (rp1). Modified from [3]

In contrast, both the crater density (Fig. 12) and stratigraphic relationships (Fig. 10a) indicate the younger age of units of the network rifting-volcanism regime [42, 43]. The coincidence of the crater density and stratigraphy suggest that the transition from the volcanic to the fully developed network rifting-volcanism regime was rather gradual and prolonged and may reflect a gradual increase of the lithosphere thickness.

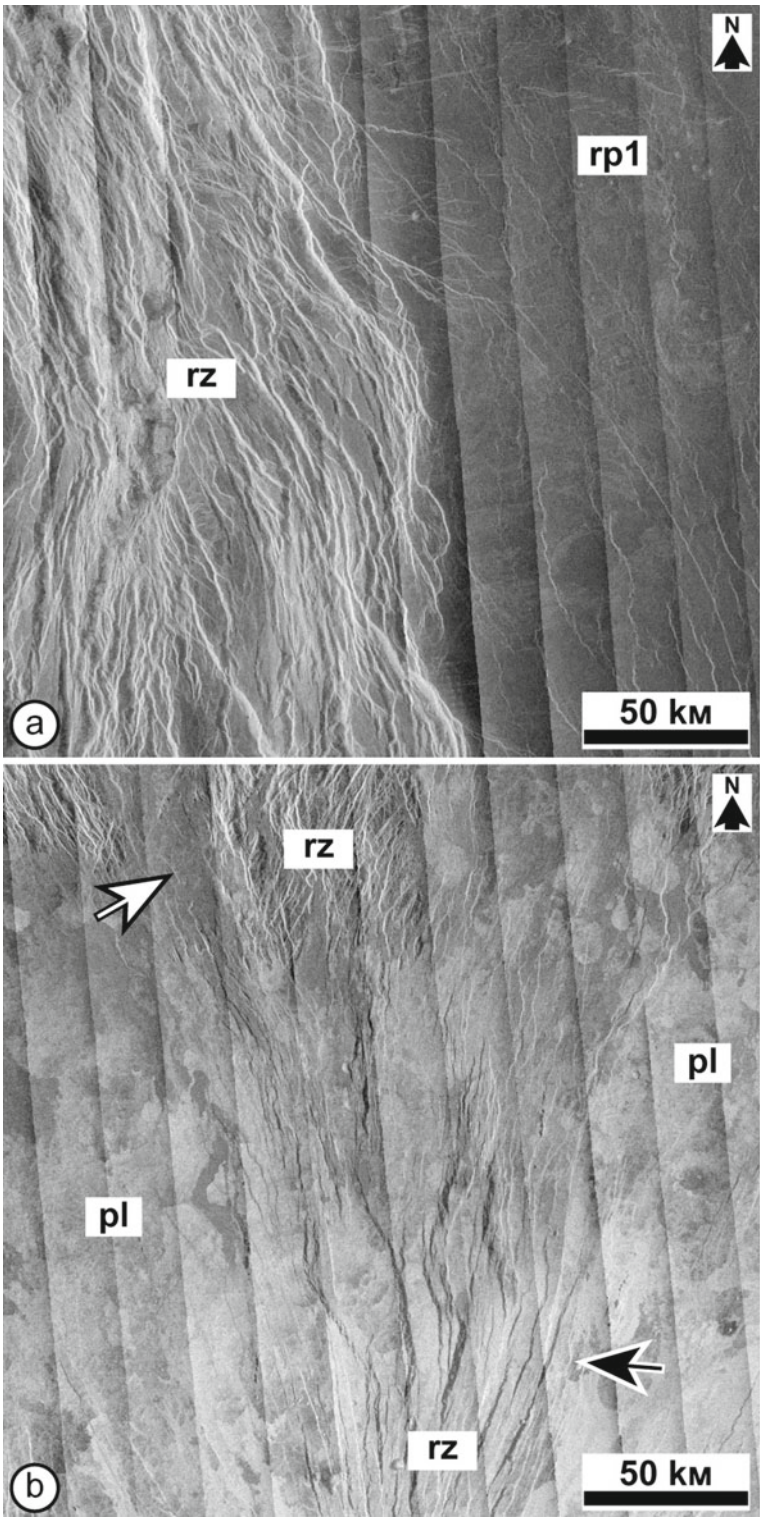

Fig. 10 **a** Structures of a rift zone (rz) cut regional plains. **b** Rift zones and lobate plains (pl) show relationships that suggest their contemporaneous formation: black arrow indicates an area where structures of a rift zone cut the plains; white arrow indicate an area where same plains embay the same rift zone. Modified from [3]

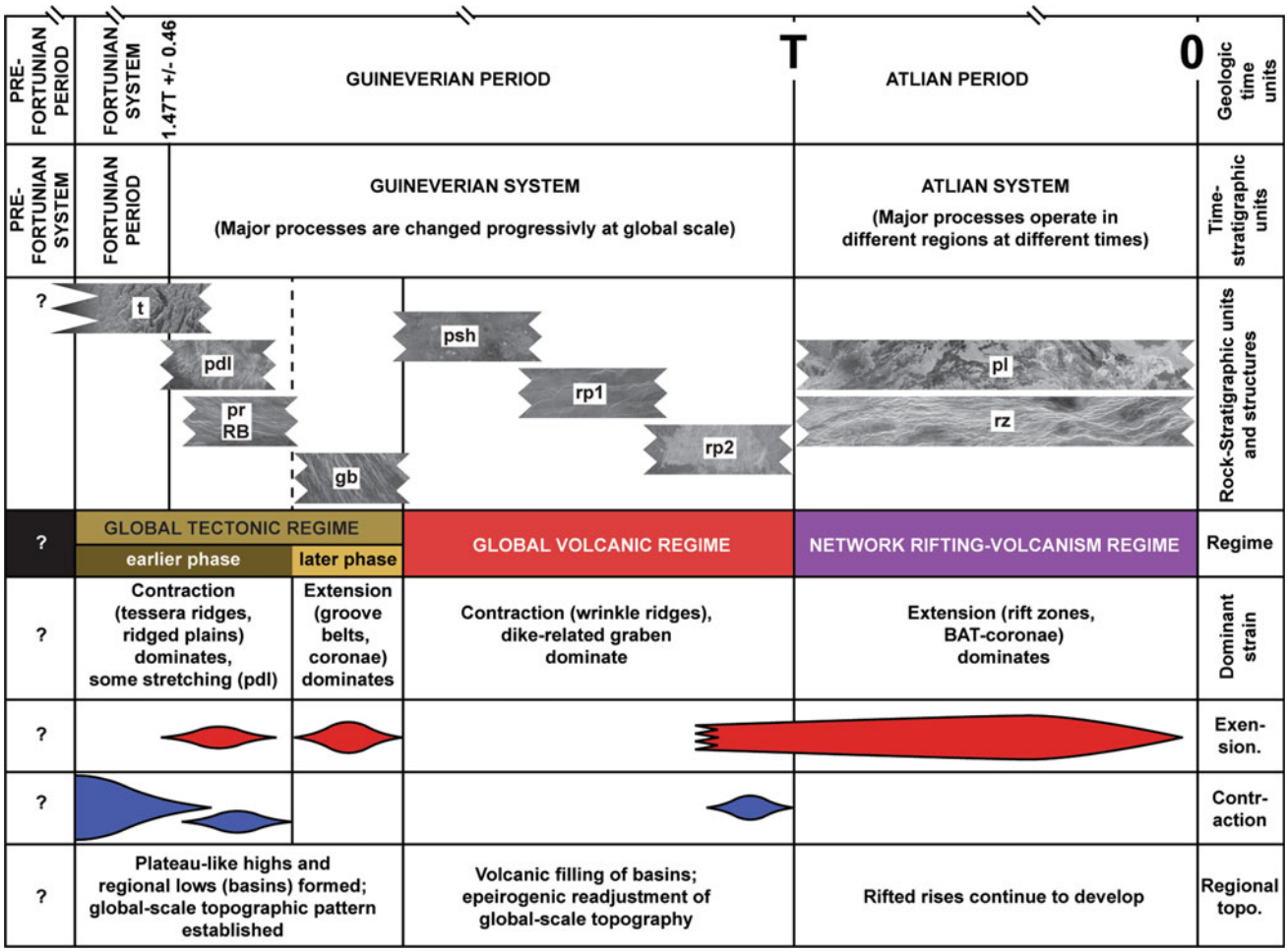

Fig. 11 Three major regimes of resurfacing (see text for discussion). Modified from [3]

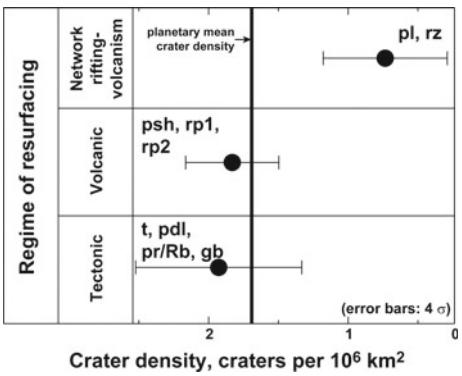

Fig. 12 Mean crater density on units that formed during different regimes of resurfacing on Venus. Modified from [3]

Acknowledgements This work is conducted under the GEOKHI RAS state assignment.

References

1. Basilevsky, A.T., Head, J.W.: Global stratigraphy of Venus: analysis of a random sample of thirty-six test areas. Earth Moon Planet. **66**, 285–336 (1995)
2. Basilevsky, A.T., Head, J.W.: Regional and global stratigraphy of Venus: a preliminary assessment and implications for the geological history of Venus. Planet. Space Sci. **43**, 1523–1553 (1995)
3. Ivanov, M.A., Head, J.W.: Global geological map of Venus. Planet. Space Sci. **59**, 1559–1600 (2011)
4. Basilevsky, A.T., Head, J.W.: Geologic units on Venus: evidence for their global correlation. Planet. Space Sci. **48**, 75–111 (2000)
5. Greeley, R., Guest, J.E.: Geologic Map of the Eastern Equatorial Region of Mars, 1:15,000,000 Scale. USGS Scientific Investigations Map I-1802-B (1987)
6. Tanaka, K.L., Skinner, J.A., Hare, T.M.: Geologic Map of the Northern Plains of Mars, 1:5,000,000 Scale. USGS Scientific Investigations Map 2888 (2005)

7. Schaber, G.G., Strom, R.G., Moore, H.J., Soderblom, L.A., Kirk, R.L., Chadwick, D.L., Dawson, D.D., Gaddis, L.R., Boyce, J.M., Russel, J.: Geology and distribution of impact craters on Venus: what are they telling us? J. Geophys. Res. **97**, 13257–13301 (1992)
8. Herrick, R.R., Phillips, R.J.: Implications of a global survey of Venusian impact craters. Icarus **111**, 387–416 (1994)
9. Phillips, R.J., Raubertas, R.F., Arvidson, R.E., Sarkar, I.C., Herrick, R.R., Izenberg, N., Grimm, R.E.: Impact craters and Venus resurfacing history. J. Geophys. Res. **97**, 15923–15948 (1992)
10. McKinnon, W.B., Zahnle, K.J., Ivanov, B.A., Melosh, H.J.: Cratering on Venus: models and observations. In: Bougher, S.W., Hunten, D.M., Phillips, R.J. (eds.) Venus II Geology, Geophysics, Atmosphere, and Solar wind environment, University Arizona Press Tucson, pp. 969–1014 (1997)
11. Garvin, J.B.: The global budget of impact-derived sediments on Venus. Earth Moon Planet. **50**(51), 175–190 (1990)
12. Bridges, N.T., McGill, G.E.: Geologic map of the Kaiwan Fluctus Quadrangle (V-44), Venus. USGS Scientific Investigations Map I-2747 (2002)
13. McGill, G.E.: Geologic map of the Bereghinya Planitia Quadrangle (V-8), Venus. USGS Scientific Investigations Map I-2794 (2004)
14. Stofan, E.R., Guest, J.E., Brian, A.W.: Geologic Map of the Hecate Chasma Quadrangle (V-28), Venus. USGS Scientific Investigations Map I-3163 (2012)
15. Herrick, R.R.: Resurfacing history of Venus. Geology **22**, 703–706 (1994)
16. Basilevsky, A.T., Head, J.W.: The geologic history of Venus: a stratigraphic view. J. Geophys. Res. **103**, 8531–8544 (1998)
17. Solomon, S.C., Head, J.W.: Mechanisms for lithospheric heat transport on Venus: implications for tectonic style and volcanism. J. Geophys. Res. **87**, 9236–9246 (1982)
18. Guest, J.E., Stofan, E.R.: A new view of the stratigraphic history of Venus. Icarus **139**, 56–66 (1999)
19. Ivanov, M.A., Head, J.W.: Geology of Venus: mapping of a global geotraverse at 30 N latitude. J. Geophys. Res. **106**, 17515–17566 (2001)
20. Ivanov, M.A., Head, J.W.: Geologic map of the Lavinia Planitia Quadrangle (V-55), Venus. USGS Scientific Investigations Map I-2684 (2001)
21. Ivanov, M.A., Head, J.W.: Geologic Map of the Atalanta Planitia (V4) Quadrangle. USGS Scientific Investigations Map I-2792 (2004)
22. Ivanov, M.A., Head, J.W.: Geologic Map of the Nemesis Tesserae quadrangle (V-13), Venus. USGS Scientific Investigations Map 2870 (2005)
23. Ivanov, M.A., Head, J.W.: Geologic Map of the Mylitta Fluctus (V61) quadrangle. USGS Scientific Investigations Map 2920 (2006)
24. Ivanov, M.A., Head, J.W.: Geologic Map of the Meskhent Tessera Quadrangle (V-3), Venus. USGS Scientific Investigations Map 3018 (2008)
25. Ivanov, M.A., Head, J.W.: Geologic Map of the Lakshmi Planum Quadrangle (V-7), Venus. USGS Scientific Investigations Map 3116 (2010)
26. Solomon, S.C., Head, J.W., Kaula, W.M., McKenzie, D., Parsons, B.E., Phillips, R.J., Schubert, G., Talwani, M.: Venus tectonics: initial analysis from Magellan. Science **252**, 297–312 (1991)
27. Parmentier, E.M., Hess, P.C.: Chemical differentiation of a convecting planetary interior: consequences for a one plate planet such as Venus. Geophys. Res. Lett. **19**, 2015–2018 (1992)
28. Turcotte, D.L.: An episodic hypothesis for Venusian tectonics. J. Geophys. Res. **98**, 17061–17068 (1993)
29. Stofan, E. R., Guest, J.: Geologic Map of the Aino Planitia Quadrangle (V-46), Venus. USGS Scientific Investigations Map I-2779 (2003)
30. Campbell, B.A., Clark, D.A.: Geologic Map of the Mead Quadrangle (V-21), Venus. USGS Scientific Investigations Map 2897 (2006)
31. Ivanov, M.A., Head, J.W.: The history of tectonism on Venus: a stratigraphic analysis. Planet. Space Sci. **113–114**, 10–32 (2015)
32. Gilmore, M.S., Head, J.W.: Sequential deformation of plains at the margins of Alpha Regio, Venus: implications for tessera formation. Meteorit. Planet. Sci. **35**, 667–687 (2000)
33. Gilmore, M.S., Head, J.W.: Morphology and deformational history of Tellus Regio, Venus: evidence for assembly and collision. Planet. Space Sci. **154**, 5–20 (2018)
34. Ivanov, M.A., Head, J.W.: The history of volcanism on Venus. Planet. Space Sci. **84**, 66–92 (2013)
35. Ernst, R.E., Head, J.W., Parfitt, E., Grosfils, E., Wilson, L.: Giant radiating dyke swarms on Earth and Venus. Earth Sci. Rev. **39**, 1–58 (1995)
36. Ernst, R.E., Grosfils, E.B., Mege, D.: Giant dike swarms: Earth, Venus, and Mars. Annu. Rev. Earth Planet. Sci. **29**, 489–534 (2001)
37. Ernst, R.E., Desnoyers, D.W., Head, J.W., Grosfils, E.B.: Graben-fissure systems in Guinevere Planitia and Beta Regio (264–312 E, 24–60 N), Venus, and implications for regional stratigraphy and mantle plumes. Icarus **164**, 282–316 (2003)
38. Sandwell, D.T., Johnson, C.L., Bilotti, F., Suppe, J.: Driving forces for limited tectonics on Venus. Icarus **129**, 232–244 (1997)
39. Bilotti, F., Suppe, J.: The global distribution of wrinkle ridges on Venus. Icarus **139**, 137–157 (1999)
40. McGill, G.E., Steenstrup, S.J., Berton, C., Ford, P.G.: Continental rifting and the origin of Beta Regio, Venus. Geophys. Res. Lett. **8**, 737–740 (1981)
41. Stofan, E.R., Head, J.W., Campbell, D.B., Zisk, S.H., Bogomolov, A.F., Rzhiga, O.N., Basilevsky, A.T., Armand, N.: Geology of a rift zone on Venus: Beta Regio and Devana Chasma. Geol. Soc. Am. Bull. **101**, 143–156 (1989)
42. Ivanov, M.A., Head, J.W.: Volcanically embayed craters on Venus: testing the catastrophic and equilibrium resurfacing models. Planet. Space Sci. **106**, 116–121 (2015)
43. Kreslavsky, M.A., Ivanov, M.A., Head, J.W.: The resurfacing history of Venus: constraints from buffered crater densities. Icarus **250**, 438–450 (2015)

The Snow Line in Red Dwarf Systems

D. D. Mironov and E. A. Grishakina

1 Introduction

To date, more than 4.5 thousand exoplanets have been confirmed, about 3/4 of which were discovered by transit photometry [1, 2]. In 1987 A. V. Tutukov calculated that every third star has a planetary system. The formation of the planetary system is caused by the momentum of the protoplanetary cloud, and the masses of the planets are determined by the amount of matter of the protoplanetary disk in the zones of their accumulation [3, 4]. One of the main factors that play an important role in the formation of the planets is temperature. Due to the decrease of temperature at the distance from the star, we can distinguish several parts in the planetary system according to the nature of the dust particles, as well as relatively larger bodies, which are the building material for the planets. Thus, due to high temperatures, the inner part of the planetary system is devoid of dust, due to which the formation of planets in such region is impossible, because the condensation of CAI occurs in the range of 1650–1300 K, and in the range 1300–1200 K condenses almost all the gas of the solar composition. Closer to the equilibrium temperatures at which Mercury exists and up to the temperatures at which water, ammonia and methane begin to crystallize (273 K and ~180 K respectively), the formation of rocky planets with silicate rocks dominating in their composition is possible. Beyond the snow line in the planetary systems begin to form gas and ice giants, respectively. This model of the formation of different types of planets depending on the temperature is acceptable to apply not only for the solar system, but also for other planetary systems (Fig. 1) [4].

Particular attention is given to the study of exoplanets within the zone of possible water in the liquid state. However, in addition to the star-planet distance and the temperature on the planet's surface, there are a number of other conditions necessary for the occurrence and maintenance of liquid water on the planet. Among other main-sequence star classes, according to the Hertzsprung-Russell diagram, red dwarfs are the most suitable sites for the development of earth-like life in their planetary systems. Typically, red dwarfs have a late K spectral class, such as the star K2-43 [5], which has a K7 V spectral class, or M. Red dwarf temperatures range from 3889.7 to 2250 K [6], while their mass does not exceed a third of solar mass, with the lower limit of red dwarf mass, the so-called Kumar limit, being 0.0767 solar mass [7]. Although they are colder than the Sun, the lives of red dwarfs are known to be much longer than those of stars in other spectral classes, including G. This is explained by the fact that the rate of thermonuclear reactions of hydrogen combustion occurring in the bowels of red dwarfs is much lower. For example, with an average solar-type lifetime of $5 * 10^9$ years for yellow dwarfs, for stars with a mass of 0.1 $M^{\odot}$ will burn for 10^{13} years [8]. This value can be determined using the formula:

$$\tau^* = 10^{10}\,\mathrm{yr}[M^*/M^{\odot}]^{-\alpha},$$

where M^* is the mass of the star, α is the solar index. For a red dwarf with a mass of 0.1 $M^{\odot}$ a value of α index of 3 can be used, while for a red dwarf with a mass equal to the Kumar limit, a value of 4 is used, and such a red dwarf will burn for $2.9 \cdot 10^{14}$ years.

The study of red dwarfs is complicated by the fact that, due to the low brightness of modern methods, it is impossible to obtain more accurate data. At present, it is reliably known that red dwarfs are the most common types of stars [9], and their metallicity is greater than the metallicity of the Sun [10]. Evidence of high metallicity may be the giant planets in red dwarf systems [11]. So far there is no model that most accurately describes the formation of exoplanets at relatively low temperatures and high metallicity. Theoretical ideas about the formation of exoplanets in extrasolar systems

D. D. Mironov (✉) · E. A. Grishakina
Vernadsky Institute of Geochemistry and Analytical Chemistry, Russian Academy of Sciences, 19 Kosygin St., Moscow, 119991, Russia
e-mail: d.mironov@geokhi.ru

V. P. Kolotov and N. S. Bezaeva (eds.), *Advances in Geochemistry, Analytical Chemistry, and Planetary Sciences*,
https://doi.org/10.1007/978-3-031-09883-3_16

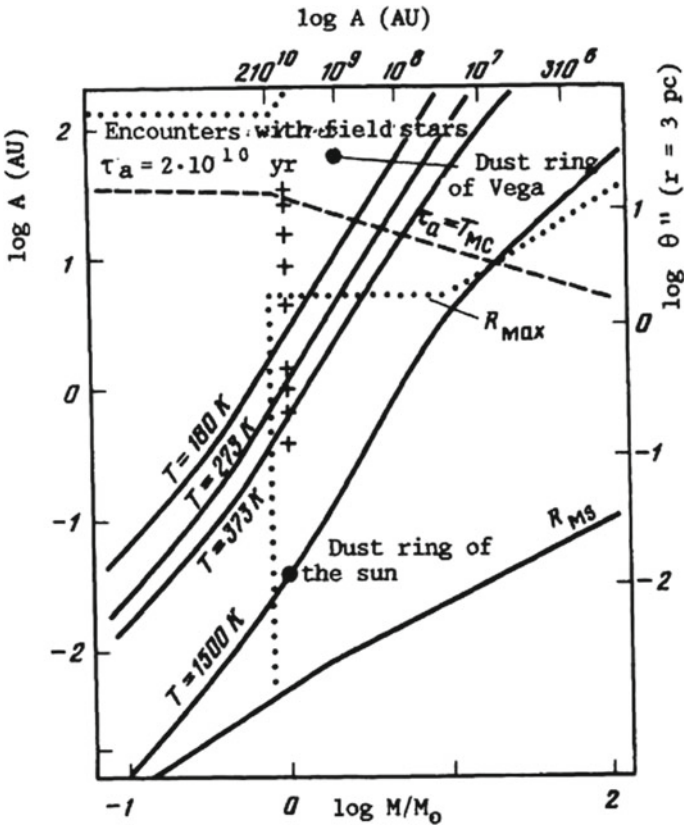

Fig. 1 The dependence of the mass of space bodies on the distance from the Sun. The boundaries of zones of those or other aggregate states of water and impurities, the evolution of the Sun and the boundaries of zones, planets of the solar system (indicated by crosses) are given [4]

in red dwarfs are available only for gas giants with masses exceeding the mass of Jupiter, as about 30% of exoplanets in red dwarfs belong to this type of planets. According to hydrodynamic modeling [12], disk instability is the most likely way for gas giant planets to form around M dwarfs, provided that the disks have at least 30% of their parent star masses in the initial stages of their formation. Such a model shows [12] that the formation of such planets proceeds relatively quickly and at a distance of about 50 a.u. from the parent star, and the formation temperatures are extremely high and characteristic of temperatures at accretion jumps around planets formed as a result of core accretion (up to 1200 K). It is noted that the physical parameters of the planets are formed depending on the long-term interactions in the disk-planet or planet-planet systems. Nevertheless, the process of formation of solid rocky planets in exoplanetary systems in red dwarfs remains not fully understood. Also, rather little attention has been paid to the exoplanet systems themselves in red dwarfs. Due to the fact that red dwarfs are longer-lived stars, by studying their systems it is possible to understand whether the existing hypotheses about the formation of planets and planetary systems are unique, or whether the conditions of formation differ sharply from those under which the solar system and exoplanet systems formed in G-class stars. Of particular importance is the study of the model of the zone of possible existence of liquid water in exoplanetary systems in red dwarfs. In addition to those parameters usually considered in the study of the zone of possible liquid water existence, it will be necessary to consider red dwarf activity, tidal capture, and slow nucleosynthesis in red dwarf nuclei. Potential life on exoplanets in red dwarfs is thought to be more highly structured due to the longevity of the star. It is also believed that the light emanating from red dwarfs is more suitable for photosynthetic organisms, since the emission spectrum of red dwarf light corresponds to the most suitable spectrum for photosynthetic organisms [13].

In our study, we conduct a comprehensive analysis of exoplanet systems in red dwarfs to identify the conditions for the formation of planets of different types. To achieve this goal we carried out the following works: (1) analysis of the available databases containing information on the known characteristics of exoplanets in extrasolar systems in red dwarfs, to determine some parameters determining the formation of planets of different types, such as the average distance from the parent star; (2) determination of the average distance at which in exoplanetary systems in red dwarfs the astronomical snow line is formed; (3) calculation of the circum-stellar zone of possible existence of liquid water for exoplanetary systems.

2 Source Data

A merged catalog of known parameters of exoplanets in red dwarf systems (table in the Appendix) was created as input data based on the following materials.

First, we used the NASA Exoplanet archive (https://exoplanetarchive.ipac.caltech.edu/index.html). This is the most comprehensive online catalog of astronomical exoplanets and stars and a data service that collates and correlates astronomical data and information about exoplanets and their parent stars, and provides tools for working with this data. The archive is designed to collect and maintain important publicly available data sets related to the search and characterization of extrasolar planets and their parent stars. These data include stellar parameters (positions, magnitudes and temperatures), exoplanet parameters (mass, orbital parameters) and discovery data, as well as their characteristics such as radial velocity curves, photometric light curves, images and spectra. The NASA Exoplanet Archive also has mechanisms available to provide the publications from which the data are published.

Second, we checked the type of planets against the NASA Exoplanet catalog (https://exoplanets.nasa.gov/), NASA's catalog of exoplanets, which is a continuously updated encyclopedia of exoplanets. In addition to providing data about the physical parameters of the planets (mass, radius, eccentricity, type of planet, astronomical radius), the NASA Exoplanet Catalog also gives users a visual presentation based on the parameters available. This database combines interactive visualizations with detailed data on all known exoplanets.

A third important source of data for the analysis was the SIMBAD database (http://simbad.u-strasbg.fr/simbad/), a database providing basic data, existing identifications, bibliographies and measurements for astronomical objects outside the solar system. Data on surveyed objects can be retrieved by object name, coordinates, and various other criteria.

The study of exoplanet systems predominantly used three types of planets.

1. Planets of the Earth group (T)—stone planets, identical to the Earth, as a rule have similar parameters to the Earth and consist mainly of rocks [14].
2. Super-Earths (sE)—planets similar to Earth, but usually twice the size of the Earth. It is assumed that they are rocky, which may be evidenced by Earth-like density, such as planets like GJ 357 b, Kepler-138 c or L 98–59 c, but since the nature of these planets is unknown, it is assumed that they may be similar to planets like Neptune or gas giants, as evidenced not only by the similar density to Neptune (like Kepler-138 d), but also by our data on the snow line in exoplanet systems in red dwarfs, as their formation took place in approximately the same conditions as the characteristic planets like Neptune.
3. Ice giants, or planets like Neptune (N)—planets, commensurate with Neptune and Uranus, having hydrogen, helium, ammonia, water atmosphere. It has been suggested that such planets may have a solid core and even be rocky, but from the available data they are more similar to Neptune. When studying the snow line in the exoplanetary systems, it is the planets of this type that are a reliable indicator for its determination, because the presence of such planets may indicate the presence of the freezing limits of some substances, such as water, in the system.

3 Snow Line

In the study of exoplanetary systems, the determination of the snow line is an important task, the performance of which allows us to obtain an insight into the formation of planets in extrasolar systems. Also, the snow line makes it possible to estimate the amount of volatile compounds in the systems. Generally, with the help of the snow line it is possible to determine the conditions in which volatile and even compounds such as CO, CO_2, CH_4 can be detected. For example, in the study of the snow line in the solar system, it was determined that at the present solar luminosity level, the snow line is at a distance of 2.7 astronomical units from the Sun and can reach a distance of 3.1 astronomical units [15]. In the solar system this corresponds to the asteroid belt between the orbits of Mars and Jupiter (Fig. 2).

The snow line can also be defined as a boundary of stable existence of solid water under the influence of solar or stellar irradiation. In such a case, it is commonly referred to as the frost line and is located at a distance of approximately 5 astronomical units for the solar system. The frost line will be noticeable when studying exoplanetary systems by optical methods, for example, a sharp change in the optical thickness of protoplanetary disks, which indicates that the disk temperature is approaching such a state that the ice begins to condense [16].

Due to the weak luminosity of red dwarfs, the observation of such lines in exoplanet systems is a difficult task. Models that would predict the occurrence of the snow line in such systems are most actively developed. In the authors' analysis of databases to determine the exoplanet systems in red dwarfs, it was obtained that most systems have an equilibrium temperature of the planets does not fall below 200 K, which makes it difficult to find the snow line in such systems, but it is likely that the temperature in such systems

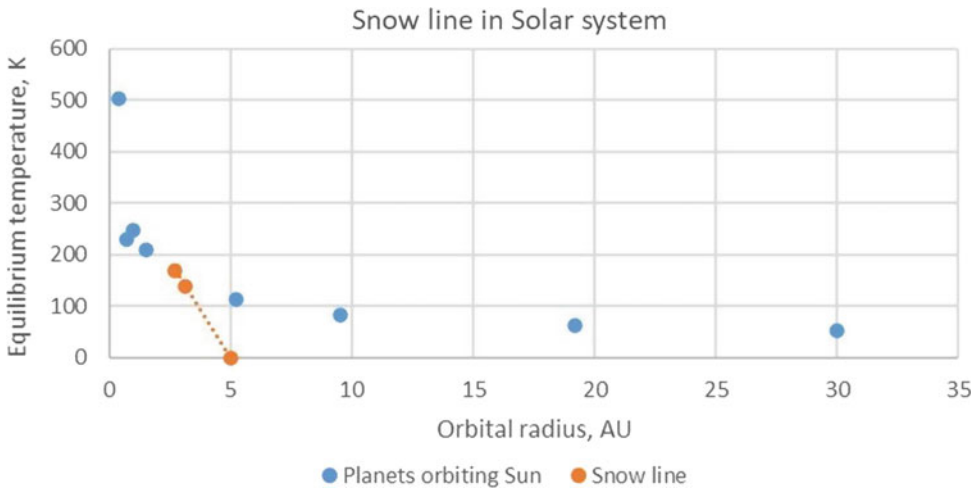

Fig. 2 Snow line in the solar system

may be lower. We proposed the determination of the snow line by analyzing the type of planets and the distance from the parent star. We plotted the planets according to their type depending on the equilibrium temperature and the distance to the parent star (Fig. 3). Further, the squares most convenient for quantitative calculation were selected, after which the density of each type of planets in the squares was determined.

Squares 1 with coordinates (0.00; 200), (0.00; 600), (0.05; 600), (0.05; 200) and square 2 with coordinates (0.05; 200), (0.05; 600), (0.1; 600), (0.1; 200) were selected. It has been determined, that the concentration of the terrestrial type

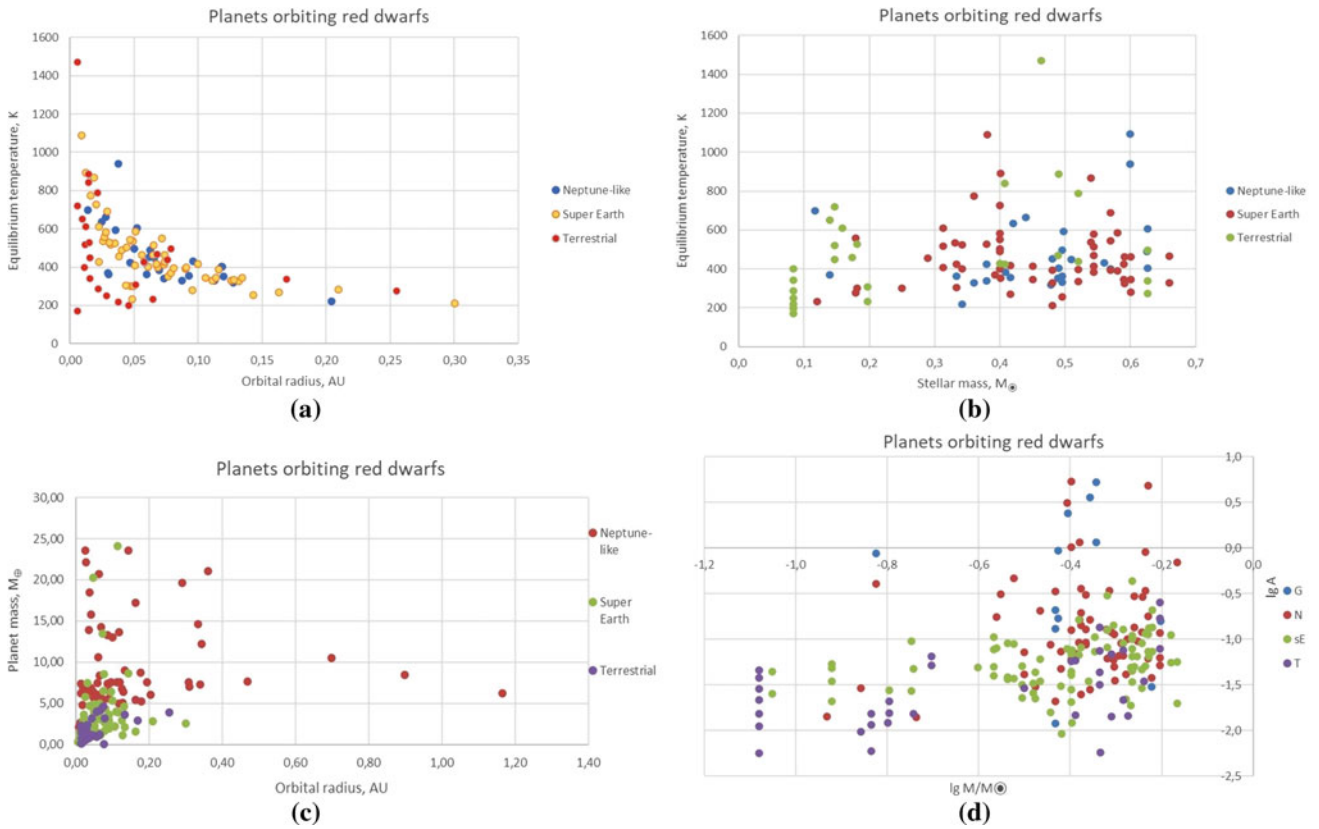

Fig. 3 **a** Dependence of equilibrium temperature of a planet on the distance to the parent star in red dwarf exoplanet systems. **b** Dependence of equilibrium temperature of a planet on the mass of the parent star in red dwarf exoplanet systems. **c** Dependence of planetary mass on the orbital radius in red dwarf exoplanetary systems. **d** Dependence of planetary mass on the orbital radius in exoplanetary systems near red dwarfs

planets in square 1 is 0.45, while in square 2 it is 0.35. However the comparison of the concentration of the ice giant planets is more remarkable: in the first square this value is 0.25, while in square 2 it is 0.50. One can also observe the growth of concentration of Super-Earths, where in the first square the density was 0.8, while in the second one it was 0.9.

When analyzing the relationship between the mass of the parent star and the distance at which planets of different types are formed from it, we find that predominantly the formation of ice dwarfs and super-Earths occurs at red dwarf masses of 0.3–0.6 star masses from the solar masses. It is also found that predominantly the formation of ice giants and super-Earths in such exoplanet systems proceeds at equilibrium temperatures from 600 to 400 K, which confirms the previous data, where in the square 2 at the same temperature conditions there is an increase in the concentration of ice giants and super-Earths. The temperature conditions of formation in exoplanetary systems similar to ice giants in red dwarfs, as well as the size of the planets suggest that the presented super-Earths have a more similar structure and properties to ice and gas giants, than the planets would consist of rocks.

Thus, in Fig. 3d, we can see that this graph has a similar trend to the graph presented in Fig. 3b. We can detect a tendency to the formation of more massive planets at a significant distance from the parent star. Based on these graphs, we can determine that the formation of different types of planets in exoplanet systems in red dwarfs will be differently dependent on these or other factors. Thus, the formation of ice giants will be in direct dependence on the size of the star, which is determined by the amount of incoming material, but also in inverse dependence on the equilibrium temperature.

The increasing concentration of ice giants and super-Earths indicates that the formation of planets of this type occurs at an average distance of 0.05–0.1 astronomical units, from which we can conclude that the snow line will form in different systems at the same distance from the parent star.

4 Probable Liquid Water Existence Area

Exoplanets near red dwarfs are considered the most likely candidates for the search for extraterrestrial life. Several factors contribute to this. One of them is that the long lifetime of red dwarfs is an important condition for the emergence, development, and formation of higher life forms. The simplest climatic simulations of surface temperature in red dwarfs show [17] that planets in the habitable zone near M-dwarf stars can have a surface temperature distribution that supports liquid water and complex organic molecules, at least on part of their surface, for a wide range of atmospheric properties and heat transport. Since the maintenance and emergence of life depends on many factors, and the little accumulated data on exoplanetary systems in red dwarfs does not allow an accurate model of the emergence and evolution of life in such systems, for the time being the zone of habitability in such systems will be defined as the zone of liquid water existence on the planet surfaces.

A special phenomenon that may limit life on the surface of exoplanets in red dwarfs is flares, which are an abrupt and non-periodic increase in the luminosity of a star [18]. It is assumed that the analogue of such a phenomenon is solar flares, which are a process of energy release, and, as is often the case, coronal mass, in the atmosphere of the Sun. The consequence of such flares in the solar system is harsh ultraviolet and X-ray radiation, which negatively affects the Earth's biosphere. Taking into account that the frequency and power of such phenomena in exoplanetary systems in red dwarfs is higher, it would be logical to assume that such phenomena will have a stronger influence in such systems.

For the solar system the zone of habitability also can be defined by aggregate states of water. Thus, temperature boundaries of zones at which in the solar system dust particles lose (at T = 373 K, evaporation takes place) or on the contrary, condense water in solid state, as well as other various impurities such as CH_4 or NH_3 (at T = 180 K) quite correspond to the boundaries at which the existence of liquid water is possible. Thus, such planets as Venus and Earth fall into these boundaries, but the existence of liquid water on Venus is impossible because of the enhanced greenhouse effect. Mars is beyond the boundary at which water passes from solid to liquid state. However, taking into account development and evolution of the Sun, it is expected that the existing boundaries of the lines of freezing and evaporation of water will also shift, which, accordingly, will lead to a shift of habitability zone in the solar system towards Mars.

A feature of exoplanet systems in red dwarfs is also closer to the parent star than, for example, in planetary systems such as the solar one. Because of this, the potential liquid water zone is located much closer to the parent star, as are the planets. The liquid water zone can be determined by the formula:

$$d = \sqrt{\frac{\frac{L}{L_{sun}}}{S_{eff}}},$$

where d is the radius of the habitability zone, which is measured in AU, L is the luminosity of the red dwarf, L_{sun} is the luminosity of the Sun, S_{eff} is the effective solar flux, and for red dwarfs it is suggested to use S_{eff} values 1.05 for inner radius and 0.27 for outer [19]. Stellar L can be calculated by the formula:

$$L = 4\pi R^2 \sigma T^4,$$

where R is the radius of the star, σ—Stefan-Boltzmann constant, T is the effective temperature of the star.

In this study, the analysis of the liquid water zone highlighted a sequence determined by the fact that the distance at which liquid water can exist on planets in exoplanetary systems near red dwarfs increases as the temperature of the star increases (Fig. 4).

It is defined [20] that because of this, the planet may be in the corotation zone, i.e. planets synchronize their orbits with the rotation around the star, due to which the planet becomes turned one side to its star. To determine the radius of corotation, measured in a.u., we can use the formula [21]:

$$r_T = 0.027 M^{\frac{1}{3}} \left(\frac{Pt}{Q}\right)^{\frac{1}{6}},$$

where M is the mass of the parent star, in solar masses, P is the period of the planet's orbit around its star, in days, t is the age of the star, Q is the parameter defining the solid body and the specific dissipation function in the ocean. In calculations for exoplanet systems it is proposed to use Q = 100 and t = 4.5 Gyr [22]. To calculate the tidal capture radius, the remaining parameters are taken from the analyzed databases. However, combining the obtained radii with the main sequence of the liquid water zone for exoplanetary systems in red dwarfs reveals that hypothetical planets caught in the corotation zone cannot get into a certain liquid water zone; accordingly, the emergence of potential life on the surface under tidal capture conditions is unlikely.

5 Summary

As a result of this work, it is shown that the snow line in exoplanet systems in red dwarfs can be formed at a distance of 0.05–0.1 astronomical units from the parent star, but it should be noted that these estimates are obtained taking into account the current assumptions about exoplanets in red dwarfs. Thus, it is assumed that the super-Earths are rocky, which can be proved by the Earth-like density, for example, of such planets as GJ 357 b, Kepler-138 c or L 98–59 c. However, since the nature of super-Earths is unknown, it is suggested that they may be similar to Neptune-type planets or gas giants, as indicated not only by Neptune-like density (as in Kepler-138 d), but also by our data on the snowline in exoplanet systems in red dwarfs. The current calculations have been made based on currently known properties about planets of this type, such as super-Earths. If future studies show that the properties of such planets differ from the current understanding, the definition of the snow line for exoplanet systems in red dwarfs will require clarification and additional calculations. It is also worth considering the factor that planets like Neptune, as well as gas giants could have been formed beyond their existing orbits, but later moved closer to the parent star, which leads to the idea of the existence of a single mechanism for moving such planets, but the presence of such a mechanism will complicate the search for the snow line in the future.

It is determined that potential planets caught in the tidal capture do not fall into the liquid water zone in exoplanet systems near red dwarfs. From this we can conclude that life on such planets is unlikely, and the search for potential life

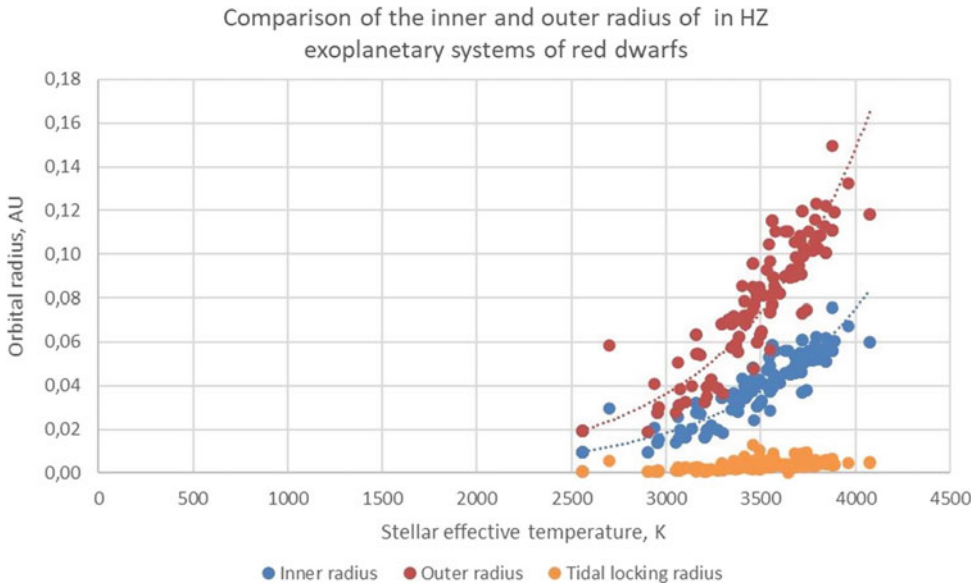

Fig. 4 Liquid water zone in exoplanetary systems near red dwarfs

should be focused on planets that fall into the sequence defined by the authors, but do not fall into the corotation zone.

Acknowledgements The authors would like to express their gratitude to an A. V. Tutukov and also M. Ya. Marov, D. D. Badyukov, S. I. Ipatov for very helpful comments that have considerably improved the manuscript. Studies of liquid water existence area was carried out as a part of the state assignments of the V. I. Vernadsky Institute of Geochemistry and Analytical Chemistry of RAS. Studies of astronomical databases were supported by Ministry of Science and Higher Education of the Russian Federation under the Grant 075-15-2020-780 (N13.1902.21.0039).

Appendix

See Table 1.

Table 1 Parameters of studied exoplanets and their parent red dwarf stars

No.	Planet	Type	a (au)	Mp ($M^{\oplus}$)	Teq (K)	Stellar	Sp. T	$M^{*}(M^{\odot})$	Teff (K)	L
1	G 9-40 b	sE	0.04	4.76000	456.00	G 9-40	M2.5 V	0.2900000	3348	0.0009006
2	GJ 1061 b	sE	0.02	1.37000		GJ 1061	M5.5 V	0.1200000	2953	0.0002047
3	GJ 1061 c	sE	0.04	1.74000		GJ 1061	M5.5 V	0.1200000	2953	0.0002047
4	GJ 1061 d	sE	0.05	1.64000		GJ 1061	M5.5 V	0.1200000	2953	0.0002047
5	GJ 1132 b	T	0.02	1.66000	529.00	GJ 1132	M4.5 V	0.1810000	3270	0.0004127
6	GJ 1132 c	sE	0.05	2.64000	300.00	GJ 1132	M4.5 V	0.1810000	3270	0.0004127
7	GJ 1214 b	N	0.01	6.26125		GJ 1214	M4.5 V	0.1836070	3074	0.0004032
8	GJ 1252 b	sE	0.01	2.09000	1089.00	GJ 1252	M3	0.3810000	3458	0.0015060
9	GJ 15 A b	sE	0.07	3.03000	550.00	GJ 15 A	M1 V	0.3996483	3743	0.0015025
10	GJ 15 A c	N	5.40	36.00000		GJ 15 A	M1 V	0.3996483	3743	0.0015025
11	GJ 163 b	N	0.06	10.60000		GJ 163	M3.5 V	0.4000000	3500	0.0018435
12	GJ 163 c	N	0.13	6.80000		GJ 163	M3.5 V	0.4000000	3500	0.0018435
13	GJ 163 d	N	1.03	29.40000		GJ 163	M3.5 V	0.4000000	3500	0.0018435
14	GJ 180 b	N	0.09	6.49000		GJ 180	M2 V	0.4300000	3562	0.0017899
15	GJ 180 c	N	0.13	6.40000		GJ 180	M2 V	0.4300000	3562	0.0017899
16	GJ 180 d	N	0.31	7.56000		GJ 180	M2 V	0.4300000	3562	0.0017899
17	GJ 229 A c	N	0.34	7.26800		GJ 229	M1.5 V	0.5800000	3564	0.0021483
18	GJ 229 b	N	0.90	8.47800		GJ 229	M1.5 V	0.5800000	3564	0.0021483
19	GJ 27.1 b	N	0.10	13.00000		GJ 27.1	M0.5 V	0.5300000	3542	0.0029422
20	GJ 273 b	sE	0.09	2.89000		GJ 273	M3.5 V	0.2900000	3382	0.0008271
21	GJ 273 c	sE	0.04	1.18000		GJ 273	M3.5 V	0.2900000	3382	0.0008271
22	GJ 3138 b	sE	0.02	1.78000		GJ 3138	M0 V	0.6810000	3717	0.0026471
23	GJ 3138 c	sE	0.06	4.18000		GJ 3138	M0 V	0.6810000	3717	0.0026471
24	GJ 3138 d	N	0.70	10.50000		GJ 3138	M0 V	0.6810000	3717	0.0026471
25	GJ 317 b	G	1.15	794.50000		GJ 317	M2.5 V	0.4533000	3493	0.0018568
26	GJ 317 c	G	5.23	522.45000		GJ 317	M2.5 V	0.4533000	3493	0.0018568
27	GJ 3293 b	N	0.14	23.54000		GJ 3293	M2.5 V	0.4200000	3466	0.0016115
28	GJ 3293 c	N	0.36	21.09000		GJ 3293	M2.5 V	0.4200000	3466	0.0016115
29	GJ 3293 d	N	0.19	7.60000		GJ 3293	M2.5 V	0.4200000	3466	0.0016115
30	GJ 3293 e	sE	0.08	3.28000		GJ 3293	M2.5 V	0.4200000	3466	0.0016115
31	GJ 3470 b	N	0.04	13.90000	593.50	GJ 3470	M1.5 V	0.4977570	3552	0.0025265
32	GJ 3473 b	sE	0.02	1.86000	773.00	GJ 3473	M4 V	0.3600000	3347	0.0012633
33	GJ 3473 c	N	0.09	7.41000	329.10	GJ 3473	M4 V	0.3600000	3347	0.0012633
34	GJ 357 b	sE	0.04	1.84000	525.00	GJ 357	M2.5 V	0.3420000	3505	0.0011339
35	GJ 357 c	sE	0.06	6.10000	401.20	GJ 357	M2.5 V	0.3420000	3505	0.0011339

(continued)

Table 1 (continued)

No.	Planet	Type	a (au)	Mp ($M^{\oplus}$)	Teq (K)	Stellar	Sp. T	$M^{*}(M^{\odot})$	Teff (K)	L
36	GJ 357 d	N	0.20	3.40000	219.60	GJ 357	M2.5 V	0.3420000	3505	0.0011339
37	GJ 411 b	sE	0.08	2.69000	370.10	GJ 411	M1.5 V	0.3920000	3720	0.0014429
38	GJ 433 b	N	0.06	6.04300		GJ 433	M1.5 V	0.5900000	3461	0.0024648
39	GJ 433 c	N	4.82	32.42200		GJ 433	M1.5 V	0.5900000	3461	0.0024648
40	GJ 433 d	N	0.18	5.22300		GJ 433	M1.5 V	0.5900000	3461	0.0024648
41	GJ 436 b	N	0.03	22.10000	663.50	GJ 436	M2.5 V	0.4400000	3400	0.0019613
42	GJ 536 b	N	0.07	5.36000		GJ 536	M1 V	0.5200000	3685	0.0026243
43	GJ 581 b	N	0.04	15.80000		GJ 581	M3 V	0.3160000	3480	0.0009712
44	GJ 581 c	N	0.07	5.50000		GJ 581	M3 V	0.3160000	3480	0.0009712
45	GJ 581 e	T	0.03	1.70000		GJ 581	M3 V	0.3160000	3480	0.0009712
46	GJ 682 b	sE	0.08	4.40000		GJ 682	M4 V	0.2750000	3172	0.0008024
47	GJ 682 c	N	0.18	8.70000		GJ 682	M4 V	0.2750000	3172	0.0008024
48	GJ 685 b	N	0.13	9.00000		GJ 685	M0.5 V	0.5500000	3816	0.0031698
49	GJ 687 b	N	0.16	17.20000		GJ 687	M3 V	0.4180000	3561	0.0016021
50	GJ 687 c	N	1.17	6.26000		GJ 687	M3 V	0.4180000	3561	0.0016021
51	GJ 720 A b	N	0.12	13.64000	401.00	GJ 720 A b	M0.5 V	0.5700000	3837	0.0034277
52	GJ 832 b	G	3.56	216.10400		GJ 832	M1.5 V	0.4400000	3681	0.0021899
53	GJ 832 c	N	0.16	5.40000		GJ 832	M1.5 V	0.4400000	3681	0.0021899
54	GJ 876 b	G	0.21	723.22350		GJ 876	M4 V	0.3696072	3294	0.0012637
55	GJ 876 c	G	0.13	226.98460		GJ 876	M4 V	0.3696072	3294	0.0012637
56	GJ 876 d	N	0.02	6.83000		GJ 876	M4 V	0.3696072	3294	0.0012637
57	GJ 876 e	N	0.33	14.60000		GJ 876	M4 V	0.3696072	3294	0.0012637
58	GJ 887 b	T	0.07	7.60000	468.00	GJ 887	M1 V	0.4890000	3688	0.0023326
59	GJ 887 c	N	0.12	4.20000	352.00	GJ 887	M1 V	0.4890000	3688	0.0023326
60	GJ 9066 b	N	0.40	30.90000		GJ 9066	M4.5 V	0.1500000	3102	0.0002875
61	GJ 9066 c	G	0.87	71.60000		GJ 9066	M4.5 V	0.1500000	3102	0.0002875
62	GJ 96 b	N	0.29	19.66000		GJ 96	M2 V	0.5719740	3785	0.0036347
63	Gl 49 b	N	0.09	5.63000		Gl 49	M1.5 V	0.5150000	3805	0.0028303
64	HD 180,617 b	N	0.34	12.21400		HD 180,617	M2.5 V	0.4840000	3534	0.0023291
65	HD 285,968 b	N	0.07	8.40000	450.00	HD 285,968	M2 V	0.5092889	3703	0.0024126
66	HD 95,735 c	N	3.10	18.05265		GJ 411	M1.5 V	0.3920000	3720	0.0014429
67	K2-117 b	sE	0.02	4.78000	868.00	K2-117	M1 V	0.5400000	3778	0.0027992
68	K2-117 c	sE	0.05	4.90000	537.00	K2-117	M1 V	0.5400000	3778	0.0027992
69	K2-133 b	T	0.03	2.36000		K2-133	M1.5 V	0.4610000	3655	0.0021555
70	K2-133 c	T	0.04	3.20000		K2-133	M1.5 V	0.4610000	3655	0.0021555
71	K2-133 d	T	0.07	4.67000		K2-133	M1.5 V	0.4610000	3655	0.0021555
72	K2-133 e	T	0.13	3.64000		K2-133	M1.5 V	0.4610000	3655	0.0021555
73	K2-137 b	T	0.01	158.90000	1471.00	K2-137	M3 V	0.4630000	3492	0.0019434
74	K2-14 b	N	0.06	20.70000	488.00	K2-14	M0 V	0.6256100	3960	0.0047364
75	K2-146 b	sE	0.03	5.77000	534.00	K2-146	M3 V	0.3310000	3385	0.0010501
76	K2-146 c	sE	0.03	7.49000		K2-146	M3 V	0.3310000	3385	0.0010501
77	K2-18 c	N	0.06	7.51000	363.00	K2-18	M2.5 V	0.4951000	3457	0.0019457
78	K2-18 d	sE	0.14	8.63000	254.90	K2-18	M2.5 V	0.4951000	3457	0.0019457
79	K2-239 b	sE	0.04	1.37000	502.00	K2-239	M3 V	0.4000000	3420	0.0012626

(continued)

Table 1 (continued)

No.	Planet	Type	a (au)	Mp ($M^{\oplus}$)	Teq (K)	Stellar	Sp. T	$M^{*}(M^{\odot})$	Teff (K)	L
80	K2-239 c	T	0.06	0.97200	427.00	K2-239	M3 V	0.4000000	3420	0.0012626
81	K2-239 d	sE	0.07	1.37000	399.00	K2-239	M3 V	0.4000000	3420	0.0012626
82	K2-240 b	sE	0.05	4.66000	586.00	K2-240	M0.5 V	0.5800000	3810	0.0031648
83	K2-240 c	sE	0.12	3.89000	389.00	K2-240	M0.5 V	0.5800000	3810	0.0031648
84	K2-257 b	T	0.02	0.49800	789.00	K2-257		0.5200000	3725	0.0026528
85	K2-26 b	N	0.10	7.61000	430.00	K2-26	M1 V	0.5600000	3785	0.0029154
86	K2-264 b	N	0.05	5.61000	496.00	K2-264	M2.5 V	0.4960000	3660	0.0023326
87	K2-264 c	N	0.11	7.60000	331.00	K2-264	M2.5 V	0.4960000	3660	0.0023326
88	K2-316 b	T	0.01	2.33000	841.00	K2-316		0.4080000	3436	0.0014059
89	K2-316 c	T	0.06	4.01000	423.00	K2-316		0.4080000	3436	0.0014059
90	K2-320 b	N	0.01	7.37000	698.00	K2-320		0.1170000	3157	0.0008094
91	K2-323 b	N	0.13	5.06000	318.00	K2-323		0.4780000	3710	0.0031853
92	K2-43 b	N	0.04	18.50000	939.30	K2-43	K7 V	0.6000000	3890	0.0038309
93	K2-72 b	sE	0.04	1.28000		K2-72	M2 V	0.2713650	3497	0.0010914
94	K2-72 c	sE	0.08	1.65000		K2-72	M2 V	0.2713650	3497	0.0010914
95	K2-72 d	sE	0.05	1.01000		K2-72	M2 V	0.2713650	3497	0.0010914
96	K2-72 e	sE	0.11	2.21000		K2-72	M2 V	0.2713650	3497	0.0010914
97	K2-88 b	sE	0.03	2.04000		K2-88		0.4368730	3572	0.0019789
98	K2-89 b	T	0.01	0.17000		K2-89		0.5316160	3677	0.0029987
99	K2-95 b	N	0.07	14.30000	383.00	K2-95	M3 V	0.4082830	3411	0.0016733
100	Kapteyn c	N	0.31	7.00000		Kapteyn	M2 V	0.2810000	3550	0.0008563
101	Kepler-1049 b	T	0.03	0.80900		Kepler-1049		0.5777210	3875	0.0060446
102	Kepler-1089 b	sE	0.05	4.01000		Kepler-1089		0.5496440	3753	0.0032919
103	Kepler-1229 b	sE	0.30	2.54000	212.00	Kepler-1229		0.4800000	3577	0.0032990
104	Kepler-1350 b	N	0.04	6.90000		Kepler-1350		0.5272670	3786	0.0030338
105	Kepler-1350 c	sE	0.02	3.64000		Kepler-1350		0.5272670	3786	0.0030338
106	Kepler-138 b	T	0.08	0.06600	439.00	Kepler-138	M1 V	0.5200000	3841	0.0027354
107	Kepler-138 c	sE	0.09	1.97000	398.00	Kepler-138	M1 V	0.5200000	3841	0.0027354
108	Kepler-138 d	sE	0.13	1.17000	335.00	Kepler-138	M1 V	0.5200000	3841	0.0027354
109	Kepler-1628 b	N	0.30	33.80000		Kepler-1628		0.5500000	3724	0.0028685
110	Kepler-1649 b	T	0.05	1.20000	307.00	Kepler-1649	M5 V	0.1977000	3240	0.0004955
111	Kepler-1649 c	T	0.06	1.03000	234.00	Kepler-1649	M5 V	0.1977000	3240	0.0004955
112	Kepler-186 b	sE	0.03	1.24000	579.00	Kepler-186	M1 V	0.5432760	3876	0.0033134
113	Kepler-186 c	sE	0.05	2.10000	470.00	Kepler-186	M1 V	0.5432760	3876	0.0033134
114	Kepler-186 d	sE	0.08	2.54000	384.00	Kepler-186	M1 V	0.5432760	3876	0.0033134
115	Kepler-186 e	sE	0.11	2.15000		Kepler-186	M1 V	0.5432760	3876	0.0033134
116	Kepler-186 f	sE	0.43	1.71000		Kepler-186	M1 V	0.5432760	3876	0.0033134
117	Kepler-231 b	sE	0.07	35.40000	426.00	Kepler-231	M1 V	0.5900000	4078	0.0037742
118	Kepler-231 c	sE	0.11	24.10000	345.00	Kepler-231	M1 V	0.5900000	4078	0.0037742
119	Kepler-236 b	sE	0.07	3.09000	462.00	Kepler-236	M1 V	0.5910000	3750	0.0027785
120	Kepler-236 c	sE	0.13	4.66000	325.00	Kepler-236	M1 V	0.5910000	3750	0.0027785
121	Kepler-296 b	T	0.08	3.22000	495.00	Kepler-296	M2 V	0.6260000	3558	0.0035882
122	Kepler-296 c	N	0.05	4.66000	606.00	Kepler-296	M2 V	0.6260000	3558	0.0035882
123	Kepler-296 d	N	0.12	5.02000	403.00	Kepler-296	M2 V	0.6260000	3558	0.0035882

(continued)

Table 1 (continued)

No.	Planet	Type	a (au)	Mp ($M^{\oplus}$)	Teq (K)	Stellar	Sp. T	$M^{*}(M^{\odot})$	Teff (K)	L
124	Kepler-296 e	T	0.17	2.96000	337.00	Kepler-296	M2 V	0.6260000	3558	0.0035882
125	Kepler-296 f	T	0.26	3.89000	274.00	Kepler-296	M2 V	0.6260000	3558	0.0035882
126	Kepler-327 b	sE	0.03	1.41000	690.00	Kepler-327	M1 V	0.5700000	3717	0.0038756
127	Kepler-327 c	sE	0.05	20.30000	544.00	Kepler-327	M1 V	0.5700000	3717	0.0038756
128	Kepler-327 d	sE	0.09	3.64000	392.00	Kepler-327	M1 V	0.5700000	3717	0.0038756
129	Kepler-42 b	T	0.01	0.39900	519.00	Kepler-42	M4 V	0.1464630	3204	0.0002845
130	Kepler-42 c	T	0.01	0.31500	720.00	Kepler-42	M4 V	0.1464630	3204	0.0002845
131	Kepler-42 d	T	0.02	0.13000	450.00	Kepler-42	M4 V	0.1464630	3204	0.0002845
132	Kepler-445 b	sE	0.02	3.12000	426.00	Kepler-445	M4 V	0.3340000	3157	0.0010828
133	Kepler-445 c	N	0.03	6.85000	362.00	Kepler-445	M4 V	0.3340000	3157	0.0010828
134	Kepler-445 d	sE	0.04	2.10000	305.00	Kepler-445	M4 V	0.3340000	3157	0.0010828
135	Kepler-446 b	sE	0.02	2.86000	727.00	Kepler-446	M4 V	0.4000000	3359	0.0013817
136	Kepler-446 c	sE	0.03	1.41000	583.00	Kepler-446	M4 V	0.4000000	3359	0.0013817
137	Kepler-446 d	sE	0.04	1.35000	489.00	Kepler-446	M4 V	0.4000000	3359	0.0013817
138	Kepler-54 b	N	0.06	292.37600	453.00	Kepler-54	M1 V	0.4800000	3712	0.0022375
139	Kepler-54 c	sE	0.08	117.59000	395.00	Kepler-54	M1 V	0.4800000	3712	0.0022375
140	Kepler-54 d	sE	0.13	2.96000	329.00	Kepler-54	M1 V	0.4800000	3712	0.0022375
141	Kepler-691 b	sE	0.06	5.02000		Kepler-691		0.5578980	3626	0.0032886
142	Kepler-732 b	N	0.07	5.39000	403.00	Kepler-732	M2 V	0.4900000	3631	0.0021886
143	Kepler-732 c	T	0.01	2.15000	886.00	Kepler-732	M2 V	0.4900000	3631	0.0021886
144	L 98-59 b	sE	0.02	1.01000	610.00	L 98-59	M3 V	0.3130000	3367	0.0009337
145	L 98-59 c	sE	0.03	2.42000	517.00	L 98-59	M3 V	0.3130000	3367	0.0009337
146	L 98-59 d	sE	0.05	2.31000	409.00	L 98-59	M3 V	0.3130000	3367	0.0009337
147	LHS 1140 b	sE	0.03	1.79000	559.00	LHS 1140	M4.5 V	0.1790000	3216	0.0004192
148	LHS 1140 c	sE	0.10	6.38000	278.00	LHS 1140	M4.5 V	0.1790000	3216	0.0004192
149	LP 791-18 b	T	0.01	5.95000	650.00	LP 791-18	M6.1 V	0.1390000	2960	0.0002466
150	LP 791-18 c	N	0.03	1.46000	370.00	LP 791-18	M6.1 V	0.1390000	2960	0.0002466
151	LSPM J2116 + 0234 b	N	0.09	13.30000		LSPM J2116 + 0234	M3 V	0.4300000	3475	0.0018388
152	LTT 3780 b	sE	0.01	8.60000	892.00	LTT 3780	M4 V	0.4010000	3331	0.0013272
153	LTT 3780 c	sE	0.08	2.62000	353.00	LTT 3780	M4 V	0.4010000	3331	0.0013272
154	Proxima centauri b	sE	0.05	1.27000	234.00	Proxima centauri	M5.5 V	0.1200000	3050	0.0002061
155	Ross 128 b	sE	0.05	1.40000	301.00	Ross 128	M4 V	0.2500000	3135	0.0004322
156	Teegarden's star b	sE	0.03	1.05000		Teegarden's star	M7 V	0.0890000	2904	0.0000947
157	Teegarden's star c	sE	0.04	1.11000		Teegarden's star	M7 V	0.0890000	2904	0.0000947
158	TOI-1266 b	sE	0.07	13.50000	413.00	TOI-1266	M3 V	0.4500000	3600	0.0018090
159	TOI-1266 c	sE	0.11	2.20000	344.00	TOI-1266	M3 V	0.4500000	3600	0.0018090
160	TOI-270 b	sE	0.03	2.09000	528.00	TOI-270	M3.0 V	0.3800000	3551	0.0014607
161	TOI-270 c	N	0.05	6.44000	424.00	TOI-270	M3.0 V	0.3800000	3551	0.0014607
162	TOI-270 d	N	0.07	5.18000	340.00	TOI-270	M3.0 V	0.3800000	3551	0.0014607
163	TOI-540 b	T	0.01		611.00	2MASS J05051443-4756154			3216	0.0003290
164	TOI-674 b	N	0.03	23.60000	635.00	TOI-674	M2 V	0.4200000	3514	0.0017658
165	TOI-700 b	sE	0.07	1.11000	417.00	TOI-700	M2 V	0.4160000	3480	0.0017487

(continued)

Table 1 (continued)

No.	Planet	Type	a (au)	Mp ($M^{\oplus}$)	Teq (K)	Stellar	Sp. T	$M^{*}(M^{\odot})$	Teff (K)	L
166	TOI-700 c	N	0.09	7.51000	356.00	TOI-700	M2 V	0.4160000	3480	0.0017487
167	TOI-700 d	sE	0.16	1.57000	268.80	TOI-700	M2 V	0.4160000	3480	0.0017487
168	TOI-776 b	sE	0.07	4.00000	514.00	TOI-776	M1 V	0.5440000	3709	0.0030581
169	TOI-776 c	sE	0.10	5.30000	415.00	TOI-776	M1 V	0.5440000	3709	0.0030581
170	TRAPPIST-1 b	T	0.01	0.85000	400.00	TRAPPIST-1	M8 V	0.0830700	2559	0.0000998
171	TRAPPIST-1 d	T	0.02	0.41000	288.00	TRAPPIST-1	M8 V	0.0830700	2559	0.0000998
172	TRAPPIST-1 e	T	0.03	0.62000	251.00	TRAPPIST-1	M8 V	0.0830700	2559	0.0000998
173	TRAPPIST-1 f	T	0.04	0.93400	219.00	TRAPPIST-1	M8 V	0.0830700	2559	0.0000998
174	TRAPPIST-1 g	T	0.05	1.14800	199.00	TRAPPIST-1	M8 V	0.0830700	2559	0.0000998
175	TRAPPIST-1 h	T	0.01	0.33100	170.00	TRAPPIST-1	M8 V	0.0830700	2559	0.0000998
176	TRAPPIST-1 c	T	0.02	1.38000	342.00	TRAPPIST-1	M8 V	0.0830700	2559	0.0000998
177	YZ cet b	T	0.02	0.75000		YZ cet	M4.5	0.1600000	3069	0.0002586
178	YZ cet c	T	0.02	0.98000		YZ cet	M4.5	0.1600000	3069	0.0002586
179	YZ cet d	sE	0.03	1.14000		YZ cet	M4.5	0.1600000	3069	0.0002586

sE—super-Earths, T—rocky planets, N—neptun-like planets, G—gas giants

References

1. NASA Exoplanet Catalog. https://exoplanets.nasa.gov/. Accessed on 1 September 2021
2. Marov, M.Y., Shevchenko, I.I.: Exoplanets. Exoplanetology. M. Izhevsk: Institute of Computer Research, p. 138 (2017)
3. Safronov, V.S.: Evolyutsiya doplanetnogo oblaka i obrazovanie Zemlya i planetov (Evolution of the Protoplanetary Cloud and Formation of the Earth and Planets). Nauka, Moscow (1969)
4. Tutukov, A.V.: Stars and Planetary Systems, Astron. Zh., vol. 64, p. 1264 [Sov. Astron. (Eng. Transl.), 1987, vol. 31, p. 663] (1987)
5. Dressing, C.D., Newton, E.R., Schlieder, J.E., Charbonneau, D., Knutson, H.A., Vanderburg, A., Sinukoff, E.: Characterizing K2 candidate planetary systems orbiting low-mass stars. I. Classifying low-mass host stars observed during campaigns 1–7. Astrophys. J. **836**(2) (2017)
6. Caballero, J.A.: The widest ultracool binary. Astron. Astrophys. **462**(3), L61–L64 (2007)
7. Burrows, A., Hubbard, W.B., Saumon, D., Lunine, J.I.: An expanded set of brown dwarf and very low mass star models. Astrophys. J. **406**(1), 158–171 (1993)
8. Adams, F.C., Laughlin, G.: A dying universe: the long term fate and evolution of astrophysical objects. Rev. Mod. Phys. **69**, 337–372 (1997)
9. Chabrier, G.: Galactic stellar and substellar initial mass function. Publ. Astronom. Soc. Pacific **115**(809), 763–795 (2003)
10. Fischer, D.A., Valenti, J.: The planet-metallicity correlation. Astrophys. J. **622**, 1102–1117 (2005)
11. Neves, V., Bonfils, X., Santos, N.C., Delfosse, X., Forveille, T., Allard, F., Udry, S.: Metallicity of M dwarfs. III. Planet-metallicity and planet-stellar mass correlations of the HARPS GTO M dwarf sample. Astron. Astrophys. **551**(A36), 1–17 (2013)
12. Mercer, A., Stamatellos, D.: Planet formation around M dwarfs via disc instability. Fragmentation conditions and protoplanet properties. Astron. Astrophys. **633**(A116), 1–24 (2020)
13. Claudi, R., Alei, E., Battistuzzi, M., Cocola, L., Erculiani, M.S., Pozzer, A.C., Salasnich, B., Simionato, D., Squicciarini, V., Poletto, L., Rocca, N.L.: Super-earths, M dwarfs and photosynthetic organisms: habitability in the lab. Life **11**(1), 10 (2021)
14. Marov, M.Y.K.: Ot solnechnoi sistemy vglub' Vselennoi (Space. From the Solar System deep into the Universe), Fizmatlit, Moscow, p. 536 (2016) (in Russian)
15. Martin, R.G., Livio, M.: On the evolution of the snow line in protoplanetary discs. Monthly Notices of the Royal Astronomical Society. Letters **425**(1), L6–L9 (2012)
16. Cieza, L.A., Casassus, S., Tobin, J., Bos, S., Williams, J.P., Perez, S., Zhu, Z., Caceres, C., Canovas, H., Dunham, M.M., Hales, A., Prieto, J.L., Principe, D.A., Schreiber, M.R., Ruiz-Rodriguez, D., Zurlo, A.: Imaging the water snowline during a protostellar outburst. Nature **535**, 258–261 (2016)
17. Wandel, A.: On the biohabitability of M-dwarf planets. Astrophys. J. **856**(165) (2018)
18. Kulkarni, S.R., Rau, A.: The nature of the DLS fast transients. Astrophys. J. Lett. **644**(2006), L63–L66 (2006). https://doi.org/10.1086/505423
19. Kaltenegger, L., Eiroa, C., Fridlund, C.V.M.: Target star catalogue for Darwin Nearby Stellar sample for a search for terrestrial planets. Astrophys. Space Sci. **326**(2), 233–247 (2010)
20. Dole, S.H.: Habitable Planets for Man. American Elsevier, New York (1970)
21. Peale, S.J.: Rotation histories of the natural satellites. Planetary satellites. In: Burns, J.A. (ed.) Proceedings of IAU Colloq. 28, held in Ithaca, NY. University of Arizona Press, p. 87 (1977)
22. Kasting, J.F., Whitmire, D.P., Reynolds, R.T.: Habitable zones around main sequence stars. Icarus **101**(1), 108–128 (1993)

Micrometeorites from the Novaya Zemlya Ice Sheet

D. D. Badyukov

1 Introduction

Solid particles of extraterrestrial origin that have fallen onto the Earth are called micrometeorites (MMs). They sizes vary from 30 μm to about 1 mm. The micrometeorite flux is hundred times higher than that of meteorites. According to various estimates, the accretion rate of cosmic dust before atmospheric entry ranges from 10,000 to 40,000 ton/year on the whole Earth [1–4] with the average accretion rate of 22,000 ton/year [5 and references therein]. MM chemical compositions are close to chondritic mostly. Among MM varieties having an affinity to carbonaceous chondrites of CI, CM, CR, and CO groups predominate [6] but differ from them in details. This distinguishes them from components of the meteorite stream, where ordinary chondrites constitute the majority. At once studies of large cosmic spherules have shown a predominance of OC parentage [7, 8]. Thus, the lithological composition of the MM stream differs from that of the meteorite stream. This is due to the fact that the source of MMs may be the whole variety of different space bodies—asteroids, comets, and non-atmospheric rocky planets and their satellites. In this regard, among the MMs can be found specific varieties of extraterrestrial matter that is absent in the meteorite collections, which makes the study of their diversity very relevant. On the other hand the particle sizes (on average 200–300 μm) significantly limit their representativeness on centimeter—meter scales in comparison with meteorites possessing macroscopic sizes and giving sufficiently complete idea about their petrography, mineralogy and chemistry that allow to characterize their parent bodies. Despite this problem, the study of MMs can provide important information about new types of extraterrestrial matter and processes occurring in the solar system.

In relatively recent times there has been great progress in both the study and collection of MMs. In the past century MMs were collected from oceanic sediments characterized by accumulation rates of a few mm per 10,000 years [e.g. 9]. Another source of MMs is Arctic and Antarctic glaciers. These glacier ices in addition to registering atmospheric temperatures and compositions contain solid components brought in by wind. These components include ash particles from powerful volcanic eruptions, traces of nuclear weapons testing, traces of the Chernobyl disaster, which serve as benchmarks for these events. In addition to terrestrial matter, they contain buried MMs. Thus, in the last 30 years, MMs have been collected from ice from Antarctic glaciers [2, 10], snow [4], from the bottom sediments in a cavity produced by melting ice to supply water at South Pole Station [11]. A large MM collection were recovered from the Transantarctic Mountain micrometeorite traps [12], MMs were also collected from the bottoms of temporary lakes on the surface of the Greenland Glacier [13]. In this paper, I characterize the MM isolated from organo-mineral particles (cryoconite) collected at the surface of the Novaya Zemlya glacier. The main objective of this study was to establish the diversity of their mineralogical and petrographic types.

2 Material and Methods

Ice sheet of the Northern Island of Novaya Zemlya. The northern island of the Novaya Zemlya archipelago has the largest ice sheet both in area and thickness among other islands of the Russian Arctic sector. The length of the glacier is about 410 km with a width of 90 km. Inostrantsev ice valley divides the glacier into two parts—the main glacial shield and the approximately 80-km northern cap. A characteristic feature of the northern part of the cap is the presence of numerous outlet glaciers on the Barents Sea side and their absence in the northern part facing the Kara Sea. The thickness of the glacier cover is not precisely known and may vary from 0.3 to 0.7 km. The glacier has existed since at least the Late Pleistocene [14] and has been calculated to

D. D. Badyukov (✉)
V. I. Vernadsky Institute of Geochemistry and Analytical Chemistry RAS, 19, Kosygin str, 119991 Moscow, Russia
e-mail: badyukov@geokhi.ru

V. P. Kolotov and N. S. Bezaeva (eds.), *Advances in Geochemistry, Analytical Chemistry, and Planetary Sciences*,
https://doi.org/10.1007/978-3-031-09883-3_17

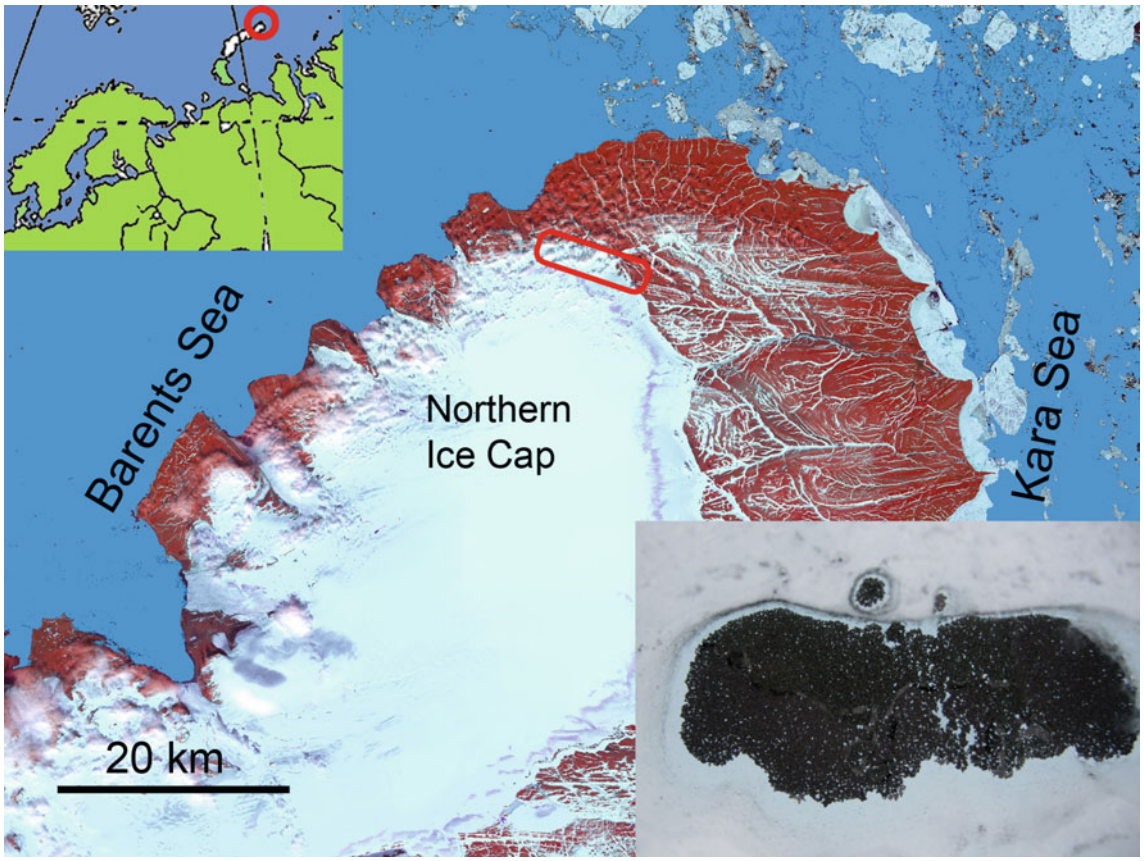

Fig. 1 The composite Landsat 7 image shows the northern part of North Island of the Novaya Zemlya archipelago. The area of the fieldwork is marked by a rectangle. The inset in the low right corner demonstrate a typical cryoconite hole that is approximately 20 cm in length

be as old as 1000 years at the base of the ice [15]. Observations and records of the position of the glacier edge show that its area has been decreasing over the last century [14, 15], and the average annual ice loss is estimated to be between 2.6 and 2.9 km^3 [14]. In the abnormally warm year of 1965, ablation increased to 11.8 km^3 with a total negative ice balance of 7.5 km^3 [16]. Such a situation favors to the release of solid ice components, which accumulate in specific areas—e.g. without outlet glaciers. Such areas can be passive margins of the northern and eastern sectors of the Northern ice cap (Fig. 1). It has been suggested [19] that at these margins there is an accumulation of solid ice components on the glacier surface due to ice flow to this margin. In this case, the greatest enrichment should occur at the very edge area of the glacier. The area has a very low level of industrial contamination. Sampling of micrometeorites in this area is also facilitated by rather easily accessibility.

2.1 Material

The field work was carried out on the marginal parts of the ice sheet in the area of Ivanov Bay (2006 expedition) and near the sources of the Snezhnaya River (2012 expedition). The local basement is present by Lower Silurian terrigenous rocks—different shales with sandstone interlayers. The study area was limited by a zone of clear ice, extending from the marginal moraine towards the glacier for 500–700 m with a 1°–3° slope towards the edge and dissected by numerous temporary watercourses. In this zone there are holes from 1 to the first tens of centimeters in diameter and 10–30 cm in depth. These wells form clusters near watercourses. The prevalence of holes and their sizes decrease with distance from the glacier edge, and their disappearance occurs at a distance of 500–700 m, where the glacier flattens out. Clusters of millimeter spherical particles of cryoconite are located at the bottoms of the water-filled holes (Fig. 1). The cryoconite particle consists of mineral grains on the surface of which bacteria develop that hold these grains together due to intensely developed filaments, often a larger central mineral grain is present, apparently serving as the germ of the cryoconite particle [20]. It seems that clusters of cryoconite holes are formed in the areas of former watercourses, where deposition of the solid ice component took place.

In the laboratory the collected samples of cryoconite were washed for separation of mineral and rock particles from

clay and other constituents of cryoconite. The resulting sand and silt particles were sieved on fractions of 1–0.5 mm, 0.5–0.25 mm, 0.25–0.15 mm, 0.15–0.08 mm and 0.08–0.03 mm. The fractions were separated double in a water column in a strong magnetic field on non-magnetic and magnetic portions. From the lasts the particles of interest were further selected under the microscope. The counting of cosmic spherules showed that a >0.08 mm sandy bulk fraction of a cryoconite sample weighing 156 g contained about 3100 cosmic spherules so that their concentration was about 20 pcs. per 1 g of this fraction. Due to extremely low content of ore and iron-bearing minerals in local rocks—the main component of the fractions—and their non-magnetic behavior, the selection of their magnetic part allows us to enrich the fractions with MM a 100-fold approximately (Fig. 2). No MMs were found in non-magnetic fractions.

2.2 Methods

While the recognition under a stereomicroscope of cosmic spheres and partially melted particles is not difficult, a confident optical criteria for the recognition of unmelted MMs encountered certain difficulties. The criteria for the selection of unmelted MMs were their isometric shape, more matt luster, black or dark color and structural differences from particles of local rocks—shale and sandstone. Further study using SEM showed that the content of MMs in polished particle mounts is ~50%. The contamination by a terrestrial matter is due to the fact that all "suspicious" particles were selected.

Some particles were previewed on SEM. Further from the selected material polished mounts were made, which were studied by the methods of SEM and EMPA. SEM (Zeiss

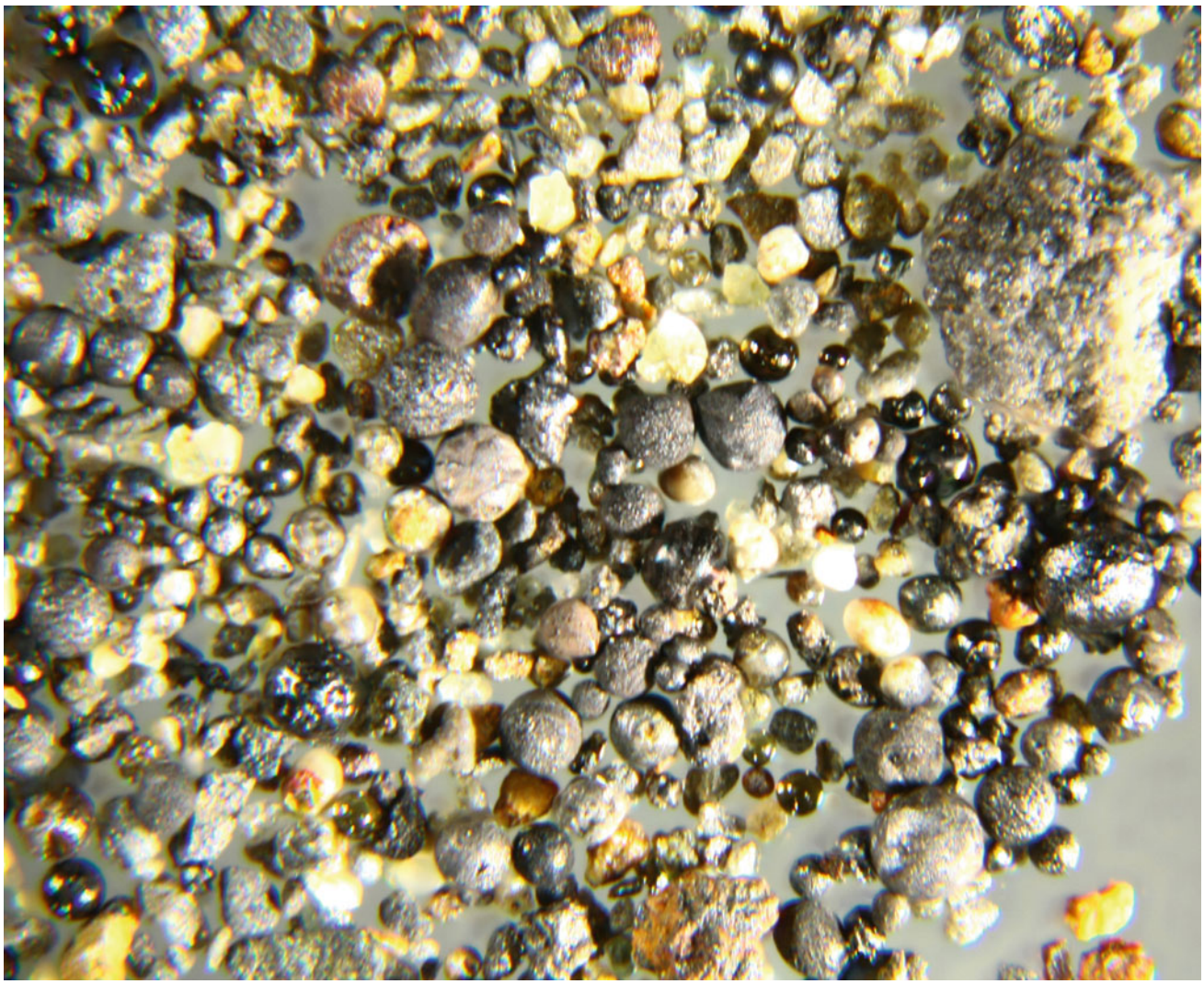

Fig. 2 The micrograph of a magnetic fraction containing both numerous cosmic spherules and scoriaceous and unmelted MMs. The field of view is 2.7 mm

ULTRA plus FESEM, the Centre for Material Analysis, University of Oulu, Finland, and Jeol JSM-6610LV, Museum of Natural History, Vienna, Austria) equipped with energy dispersive spectrometers and microprobe JEOL SUPERPROBE 8200 (University of Oulu, Finland) were used.

2.3 Identification of MMs

Reliable determination of the extraterrestrial origin of matter is given by the determination of the content of isotopes formed by cosmic rays, such as ^{53}Mn, ^{59}Ni, ^{10}Be and ^{26}Al [19], and the isotopic composition of noble gases [10, 21, 22]. However, this technique is destructive, time-consuming, and cannot be applied to routine work. Therefore, we used the criteria previously applied to micrometeorites from Antarctic collections [23], as well as some additional considerations, for the identification of NMM:

(1) Overall chondritic composition of the particle. (2) The presence of a magnetite thin shell, entirely or partially covering the MM. It is assumed that this envelope arises as a result of iron deposition in the E atmospheric layer [24] or heating of the particle by its entering in the atmosphere, melting of the troilite with formation of a melt film on the surface, and its oxidation [25]. Despite the debatability of the mechanism of the presence of a magnetite shell is a sufficient, but not necessary sign of the cosmic origin of particles. (3) Traces of melting on the outer part of the particle caused by its heating in the atmosphere. Usually they are easily recognized by formation of glass sometimes with magnetite, often increased porosity, recrystallization, and changes in original compositions of mineral grains at their mantles. (4) The presence of Ni-Co-containing iron—kamacite and/or taenite. (5) The presence of minerals occurring in chondrites and extremely rare in terrestrial rocks—for example, olivine $Fa_{1\text{-}5}$ and/or low-Ca pyroxene $Fs_{1\text{-}5}$. All features 1–4 alone or together are sufficient to identify a particle as MM.

3 Observations and Results

3.1 Varieties of Micrometeorites

We used the scheme proposed by [25] for classifying the micrometeorites of the Novaya Zemlya collection. According to the degree of high-temperature heating during the particle's passage through the atmosphere, three groups are distinguished: melted MMs or cosmic spherules (CSs), partially melted MMs, and unmelted CMs. CSs are divided into classes, types and subtypes, differing both in structures, generally determined by heating temperature, cooling rate, melt viscosity, and their composition. Partially melted MMs include fine-grained scoriaceous particles (SgMM) and coarse-grained relict grain bearing MMs (RGB), which have experienced though significant but insufficient for complete melting heating. Under a stereomicroscope they are easily recognized by the smoothed outlines and black color. SgMMs are characterized by porosity, usually high (up to 50–60%), although relatively dense SgMMs are also observed, and mainly consist of the smallest (<1 μm) olivine crystals, and sometimes pyroxene in amorphous mesostasis; in addition, larger magnetite and sulfide grains as well as fragments of pyroxene, olivine, and other minerals may be present. The matrix structure is usually not resolved by SEM observation. RGB MMs are not porous, contain a significant fraction of unmelted source material—40–70%—and are composed of glass (sometimes partially crystallized) with partially dissolved grains of relic material—usually olivine or/and pyroxene. Unmelted MMs are divided into two large classes [21]—fine-grained (i.e. with a matrix in which mineral individuals are usually insoluble in SEM) and coarse-grained. Fine-grained unmelted MMs (FgMMs) have a matrix consisting of water-bearing phases (minerals of saponite and serpentine groups), or, much more often, products of their dehydration. The composition of the matrix may be both homogeneous and heterogeneous, differing mainly in Fe content, and often contains magnetite, sulfides (pyrrhotite, pentlandite), and fragments of minerals and rocks. Coarse-grained MMs (CgMMs) are characterized by igneous textures and are mostly close in composition to chondrites in a broad sense although achondritic compositions are present.

3.2 Cosmic Spherules

Melted MMs (CSs) are characterized in general by a rounded shapes, which vary from purely spherical to ellipsoidal and ovoid. It should be noted that we apply the term CSs to all melted MMs of various shapes. 97% of CSs are composed mainly of silicate matter (type S). Iron MMs (I) consist of Ni-containing magnetite and sometimes wustite (Fig. 3a) and metal core enriched in Ni (up to 70 wt %). The rare glassy type (G) is characterized by an abundance of magnetite, whose grains form a continuous network in glass (Fig. 3b), in contrast to magnetite in other types of CSs. S-type CSs have different textures. There are CSs consisting of transparent glass of different colors (Fig. 3c) and cryptocrystalline CSs (Fig. 3d and e) consisting of olivine tiny grains in a heterogeneous glassy mesostasis. The cryptocrystalline CSs show "brickwork" microtextures formed by minute parallel olivine crystals [26]. The glass has pyroxene–plagioclase composition sometimes with nanometer-sized SiO_2 globules, also silica forms rims around olivine crystals. CSs with

porphyritic structure characterized by euhedral crystals of olivine in magnetite—bearing glass (Fig. 3f and g). Barred olivine CSs have systems of olivine bars in glass (Fig. 3h–k). The bars of each system have the same crystallographic orientation. Skeleton or dendritic magnetite is very often present in the glass as well as tiny pyroxene crystals. Ovoid CSs (Fig. 3h and i) at one end have either a spherical metal inclusion or a spherical depression, probably as a result of metal loss. We believe that such CSs were formed earlier either as a result of rotation of metal-silicate immiscible liquid droplets during the flight in the atmosphere or owing to the deceleration expelled in a front face a denser droplet, without rotation [27]. Compositions of the S-type CSs correspond to chondrites or are close to them, although a few HED-like CSs have been reported [28]. However, evaporation processes in the Earth's atmosphere leads to a strong loss of S, P, Na, K and other volatile elements, and metal loss leads to their depletion by Fe and Ni. Also in some cases, partial evaporation of Mg and Si leads to the enrichment of CSs by Ca, Al and Ti and the formation of so-called CAT spherules. A spherule consisting of spinel—magnetite—olivine porous aggregate was found among CSs from Novaya Zemlya (Fig. 3l). The spinel $Mg_{0.99}Fe_{0.01}Al_{1.99}V_{0.01}O4$ is present by irregular aggregates bordered by Ni—containing (3.0–8.2 wt.% of NiO) magnetite with MgO (8.0–13.5 wt.%); olivine is $Fa_{15\text{-}30}$. Thus, among CS from the Novaya Zemlya MM collection both usual types and in rare cases exotic are present. Alteration of CSs in terrestrial environment is expressed in dissolution on their surface olivine crystals with preservation of glass matrix, the thickness of the dissolution zone does not exceed 10 μm as a rule, although there are CSs with greater thickness of this zone. In addition, in type I spherules the core is often transformed into iron hydroxides.

3.3 Fine-Grained and Scoriaceous Micrometeorites of the Novaya Zemlya Collection

A portion of MMs is present by particles that matrices are composed of sub-micron mineral grains. Very often these particles contain “large” (>3 μm) isolated mineral and rock grains embedded in the fine-grained matrix. In accord to thermal alteration in the atmosphere there are two types of the fine-grained MMs. MMs belonging to the first type do not demonstrate clear traces of the thermal decomposition and have the original textures and the unmodified or slightly modified compositions and are called fine grained unmelted micrometeorites or FgMMs (Fig. 4a–f). Stronger heating leads to formation of porous particles of the second type—scoriaceous fine-grained micrometeorites (SgMM) that lost their original textures (Fig. 4g–h) but more or less preserved the chemical compositions.

It can be distinguished 2 sub-types of fine grained unmelted MMs. The first sub-type is characterized by homogeneous composition (Fig. 4a and b). These particles are either compact or highly porous (Fig. 4d). Frequently they contain mineral and rock inclusions. Among them there are anhedral or suhedral grains of pyroxene and/or olivine, magnetite, including its framboidal aggregates, sulfides, and others (Fig. 4e and f). The particles of second type with heterogeneous composition (Fig. 4e) are characterized by areas of different Fe/Mg ratios. The composition of mineral inclusions is the same as in the first type.

Saponite and/or serpentine are main precursors of FgMMs matrices and they were found in rare particles [25–27]. However, the matrices of the vast majority of particles are composed of amorphous matter [26]. Higher temperature causes the appearance of olivine micrograins in glass [23].

Stronger heating lead to intense dehydration of phyllosilicates and matrix melting, which is reflected in the appearance of numerous spherical pores (Fig. 4g and h) and the formation of ScMMs, whose matrix is composed of olivine grains of less than micron size in glass. At the same time there are non-porous varieties. The most high-temperature varieties are characterized by presence of olivine crystals in glass, with the sizes about micron and more. In this case the contours of pyroxene and olivine inclusions are smoothed as a result of their partial melting.

The Fs content in the low-Ca pyroxene inclusions and fragments in FgMMs and ScMMs ranges from 0 to 24% with a strong predominance of pyroxenes with $Fs_{0–3}$. The high-Ca pyroxene inclusions are mainly endiopside, though more ferrous varieties with Fs 17% are observed. Olivines also low in iron with $Fa_{0–4}$ mostly, though olivine with higher content of Fa up to 20–35% is observed. Among the inclusions of refractory minerals like spinel and others were noted. The matrices FgMM and CgMM show the bimodal distribution of atomic Fe/Si ratios that allows to distinguish among them two chemical types—low-iron and high-iron with conditional boundary Fe/Si ~ 0.4 [32]. These groups correspond to (a) FeO content of 5–20 wt.% and SiO_2 content of 45–60 wt.% and (b) with FeO content of 20–45 wt.% and SiO_2 content of 30–45 wt. %, respectively (for matrix analyses with totals reduced to 100%). The two types also differ in the prevalence of abundances of olivine and pyroxene inclusions in FgMMs and SgMMs. So, the ratio of pyroxene grains to olivine grains Px/Ol ~ 5 in the low-iron group, whereas in the high-iron group this ratio is ~ 0.6. No

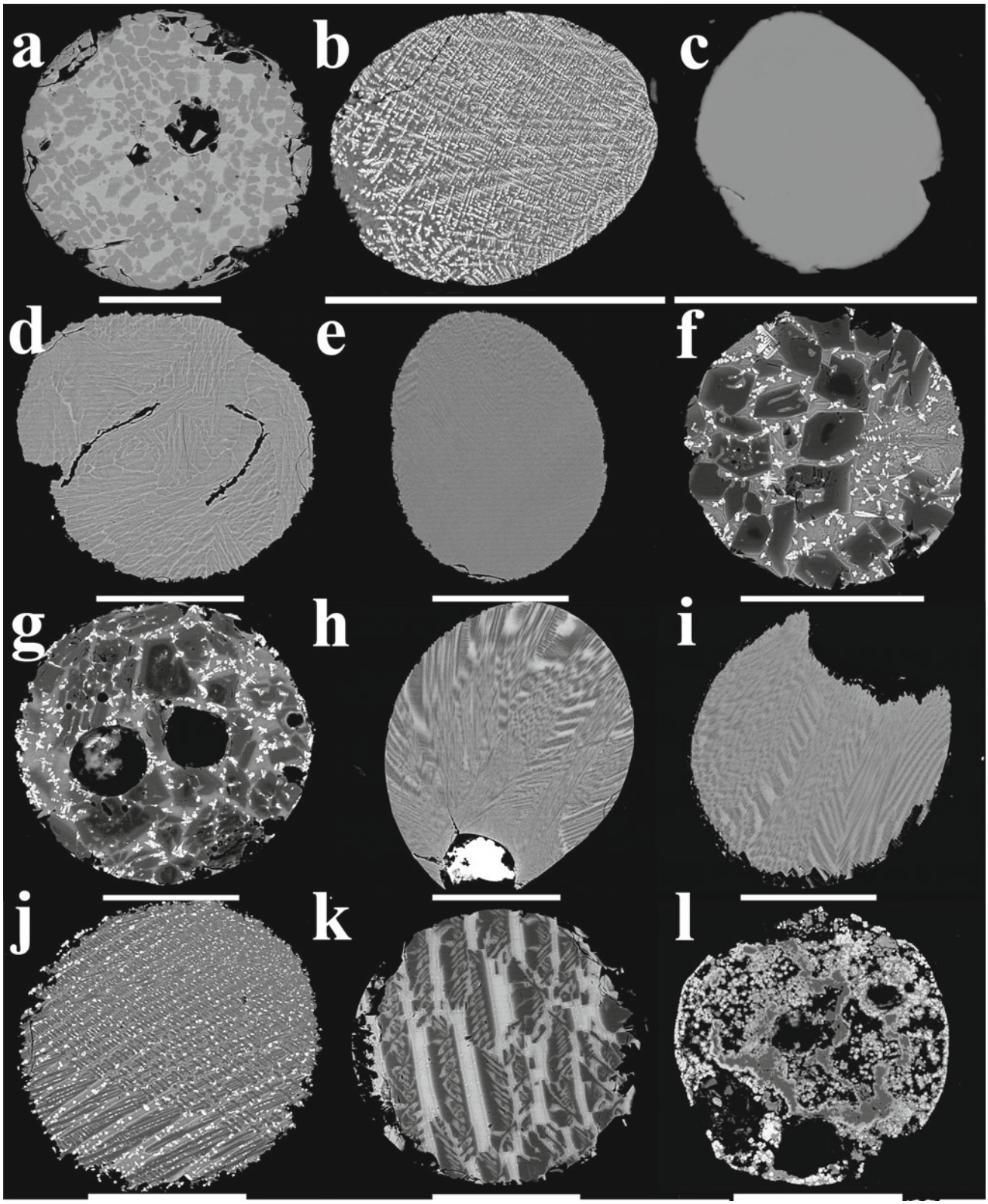

Fig. 3 Backscattered electron images of Novaya Zemlya cosmic spherules. **a** An I-type spherule consisting of magnetite and wüstite. **b** A G-type spherule with magnetite net in a glass. **c** A glass spherule. **d** and **e** Cryptocrystalline silicate spherules. **f** and **g** Porphyritic spherules consisting of olivine crystals in a glassy matrix. Some crystals contain relict forsterite cores. **h**–**k** Barred olivine spherules. **h** and **i** have ovoid shapes and **h** contains taenite inclusion (white). **h** and **i** are intermediate between cryptocrystalline and barred olivine spherules. **l** A spherule consisting of spinel $MgAl_2O_4$ forming worm-like structure (dark grey), magnetite (white) and anhedral olivine inclusions (grey). The scale bar is 100 μm

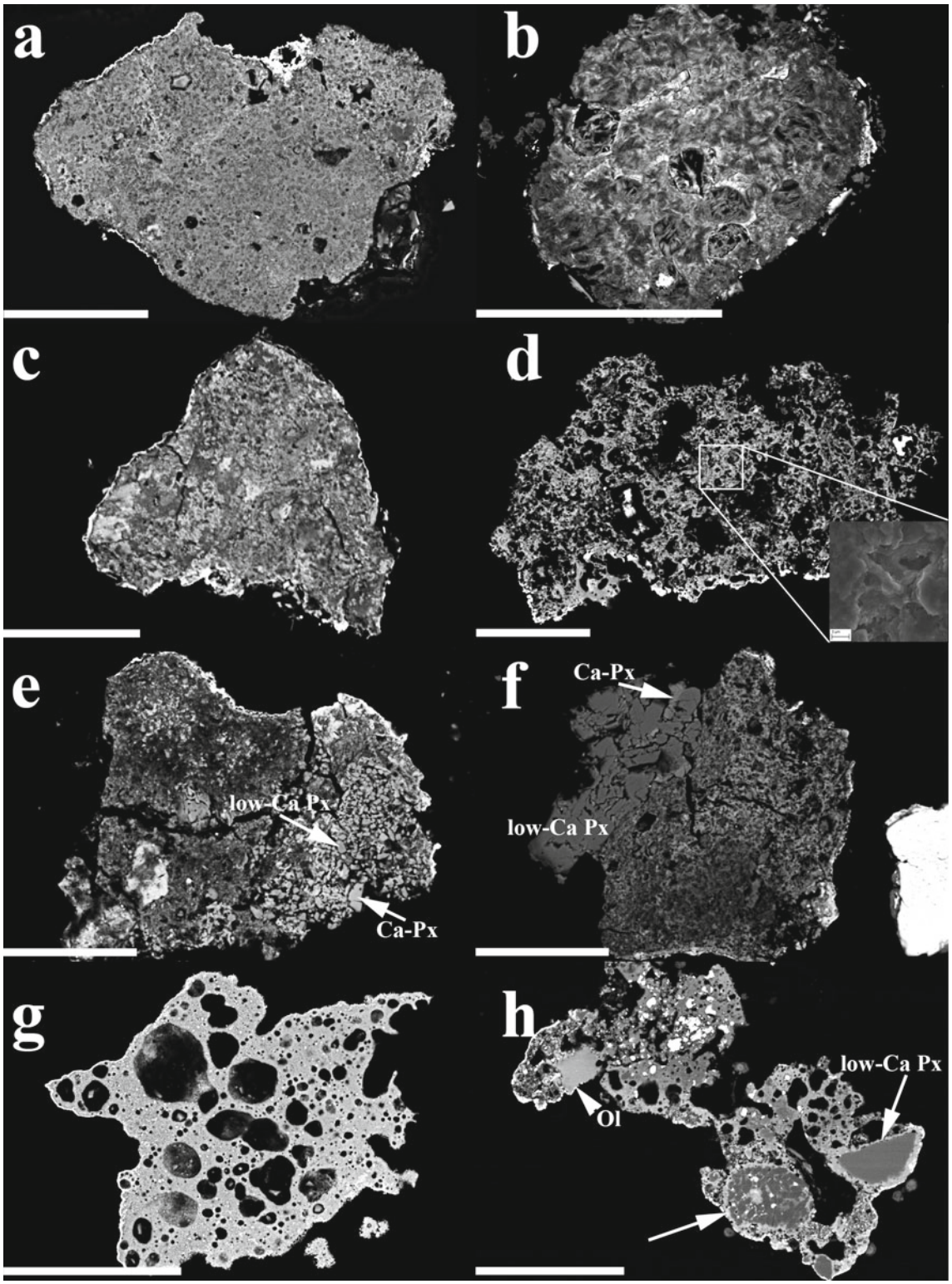

Fig. 4 Backscattered electron images of Novaya Zemlya fine-grained micrometeorites. **a** A homogeneous fine-grained micrometeorite without inclusions. **b** A micrometeorite having a chondritic composition and composed of an acicular matter. **c** A heterogeneous micrometeorite having areas rich and poor in Fe. **d** A highly porous groundmass of a micrometeorite (see the inset in the low right corner, an SE image). Magnetite is white. **e** An example of a micrometeorite including the aggregate of low-Ca pyroxene Fs_2Wo_4 and Ca-pyroxene Fs_1Wo_{44}. **f** A micrometeorite including low-Fe pyroxene (Fs_1Wo_{1-4} and Fs_1Wo_{40-44}) grains. **g** A porous scoriaceous micrometeorite. **h** A scoriaceous micrometeorite, there are inclusions of olivine Fa_{40}, pyroxene Fs_5Wo_2, and the porphyritic olivine chondrule marked by the arrow. The scale bar is 50 μm

evident traces of terrestrial changes in FgMMs and SgMMs are observed, except, maybe, dissolution of carbonates, which are completely absent in FgMMs, metal (if it was present), and sulfides.

3.4 Coarse-Grained Unmelted MMs and Relict Grain Bearing MMs

Coarse-grained unmelted MMs (SgMMs) are dominated by phases (or phases) with the sizes more than several microns (Fig. 5). Frequently these MMs have structures typical for crystallization from the melt. Partially melted coarse-grained MMs consist of products of atmospheric heating and some relic minerals (Fig. 6). They are attributed to relict grain bearing (RGB). It can be distinguished four main types of CgMM: (i) single grains of olivine or pyroxene (Fig. 5a and d); (ii) aggregates of monomineralic grains of olivine or pyroxene (Fig. 5b and c); (iii) chondritic (Fig. 5e–g); (iv) achondritic (Fig. 5h). Low-Ca pyroxenes ($Wo_{0.5–3.0}$) from monomineralic CgMMs are present by two groups—rather rich in Fe ($Fs_{10–25}$) and poor in Fe ($Fs_{0–4.5}$) although there are some intermediate compositions. The Fe-poor pyroxene grains very often contain rounded pores (Fig. 5c and d). Some of the grains also include globules of taenite (~10–15 wt.% Ni) or kamacite. I suggest that these rounded pores were formed under terrestrial conditions as a result of metal oxidation and subsequent removing of iron oxides. Olivine MMs are divided into 2 groups—Fe-poor with Fa_{1-10} (at the average Fa_3) and Fe-rich with $Fa_{10–50}$ (at the average Fa_{25}). Chondritic MMs are divided by structure into porphyritic and granular. The porphyritic MM with a glassy matrix can be olivine, pyroxene, and olivine-pyroxene. Olivine-pyroxene MMs with glass have textures of crystallization from melt, often the pyroxene grains contain rounded inclusions of the first crystallized olivine, interstitial glass is homogeneous, composition is close to plagioclase $An_{10–40}$ with some Mg and Fe. In the olivine grains Fa content varies from 10 to 45%, low-Ca pyroxene grains have composition $Fs_{10–30}Wo_{1–3.5}$, sometimes at margins they are overgrown by high-Ca pyroxene ($Fs_{8.5–15}Wo_{30–40.5}$). Ferrous olivine-pyroxene MMs with feldspar or glass show textures of crystallization from melt and have euhedral and subhedral olivine ($Fa_{20–45}$), subhedral pyroxene ($Fs_{15–24}$), and interstitial plagioclase $An_{20–40}$. rarely the An content reaches 90%. High-Ca pyroxene and magnetite and silica are also present. The low-iron CgMMs include particles consisting of euhedral low-Ca pyroxene ($Fs_{0.5–5}Wo_{1–3.5}$), endiopside, and interstitial aggregate with micrographic structure consisting of plagioclase ($An_{85–90}$) with inclusions of silica. Several achondritic particles related to eucites were also found among the CgMM [33].

RGB MMs are present by spherical, sub-spherical, and rounded irregular shaping particles (Fig. 6). They consist of relict olivine and pyroxene grains embedded glassy matrices sometimes with magnetite. In RGB MMs, whose precursors were ferrous olivine Fa_{20-40} rocks, the products of atmosphere melting are glass with inclusions of magnetite and relic olivine grains are rimmed by more magnesian olivine (Fig. 6a–e). For particles a and b the new-formed phases are olivine $Fa_{20–25}$ bordering original olivine Fa_{30-35}, magnetite and glass. Obviously, the less ferruginous olivine began first to crystallize from the resulting melt of Fa_{30} composition, simultaneously or slightly later Fe^{2+} in melt was oxidized to Fe^{3+} by atmospheric oxygen, leading to a more silicic melt from that glass and magnetite were formed. On the contrary, forsteritic relict olivine grains are rimmed by more ferrous olivine (Fig. 6f).

4 Discussion

4.1 Terrestrial Alteration

The studied MMs were isolated from cryoconite—pellets comprising rock and mineral particles and various bacteria living on the surface of cryoconite pellets. Thus, micrometeorites were inevitably exposed to both weakly acidic glacier water and biologically active environment. For CSs this exposure is expressed in the dissolution of grains of newly formed olivine at the periphery, forming rims of the first microns to the first tens of microns thick, while the glass matrix remains unaffected. However, no traces of dissolution of forsterite, the most unstable silicate during weathering [34], are observed in FgMM and ScMM. It can be attributed to the presence of a protective shell consisting either of magnetite and/or products of thermal transformation of the matrix. Also no traces of olivine alteration are observed in CgMM. It is possible that the rounded pores in the enstatite MM are associated with dissolution of metallic droplets in the enstatite matrix. The average Ni, Na, S, and P contents in FgMM are lower compared to the matrix of carbonaceous chondrites that can be attributed to their leaching and/or loss during atmospheric heating, whereas the Mg and Ca contents are close to those in the matrix of carbonaceous chondrites. This suggests that the observed terrestrial changes do not significantly affect the mineral and the chemical composition excluding metal and some unstable minerals.

4.2 Links Among MM

Since the sources of MM are asteroids, comets, and possibly planetary satellites and planets, this diversity makes it

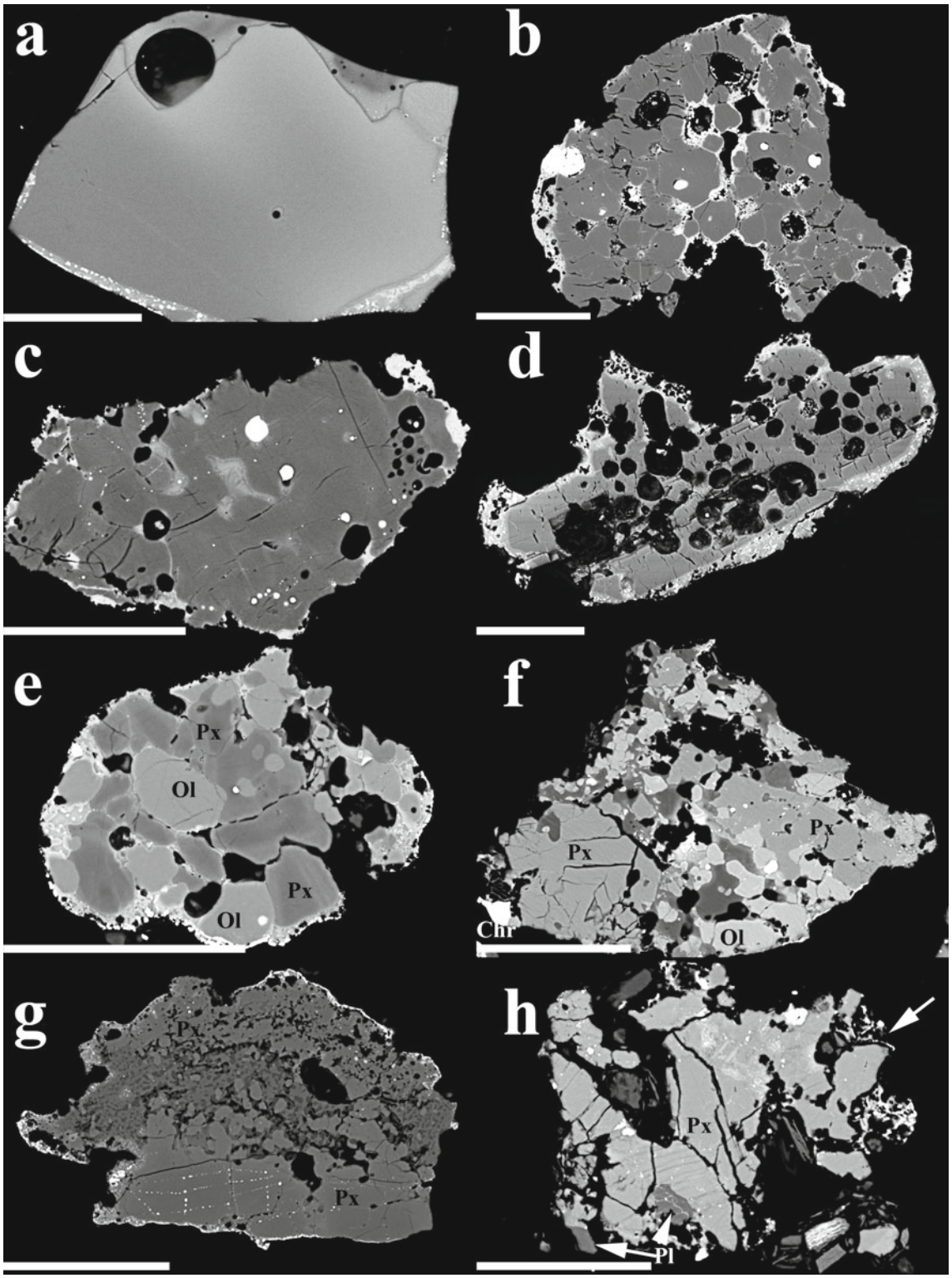

Fig. 5 Backscattered electron images of Novaya Zemlya coarse-grained unmelted micrometeorites. **a** Single olivine $Fa_{13–21}$ grain micrometeorite with traces of atmosphere melting (the fringe at the bottom) and the probably original glass at the top of the particle. **b** An aggregate of olivine $Fa_{2.5}$ grains with round inclusions of taenite (9 wt.% of Ni). Other white phase are magnetite. **c** A pyroxene ($Fs_5Wo_{0.5}$) grain with inclusions of kamacite (white). **d** A pyroxene $Fs_2Wo_{1.5}$ grain with spherical cavities. The grain has the fringe composed of a matter similar to groundmass of scoriaceous micrometeorites. **e–g** Chondritic micrometeorites. Olivine and pyroxenes in e are Fa_{24}, $Fs_{12}Wo_2$, and Fs_2Wo_7, respectively. **f** is composed of olivine Fa29, pyroxene $Fs_{24}Wo_{1.5}$, and an albite $An_{8–9}$ glass. **g** consists of pyroxene that compositions vary from $Fs_{12}Wo_7$ to $Fs_{17}Wo_8$ and an interstitial mass of plagioclase An ~70 with silica. **h** A possible basaltoid micrometeorite consisting of pyroxene $Fs_{36}Wo_{1.5}$, augite, plagioclase An_{80}, and chromite. The scale bar is 50 μm

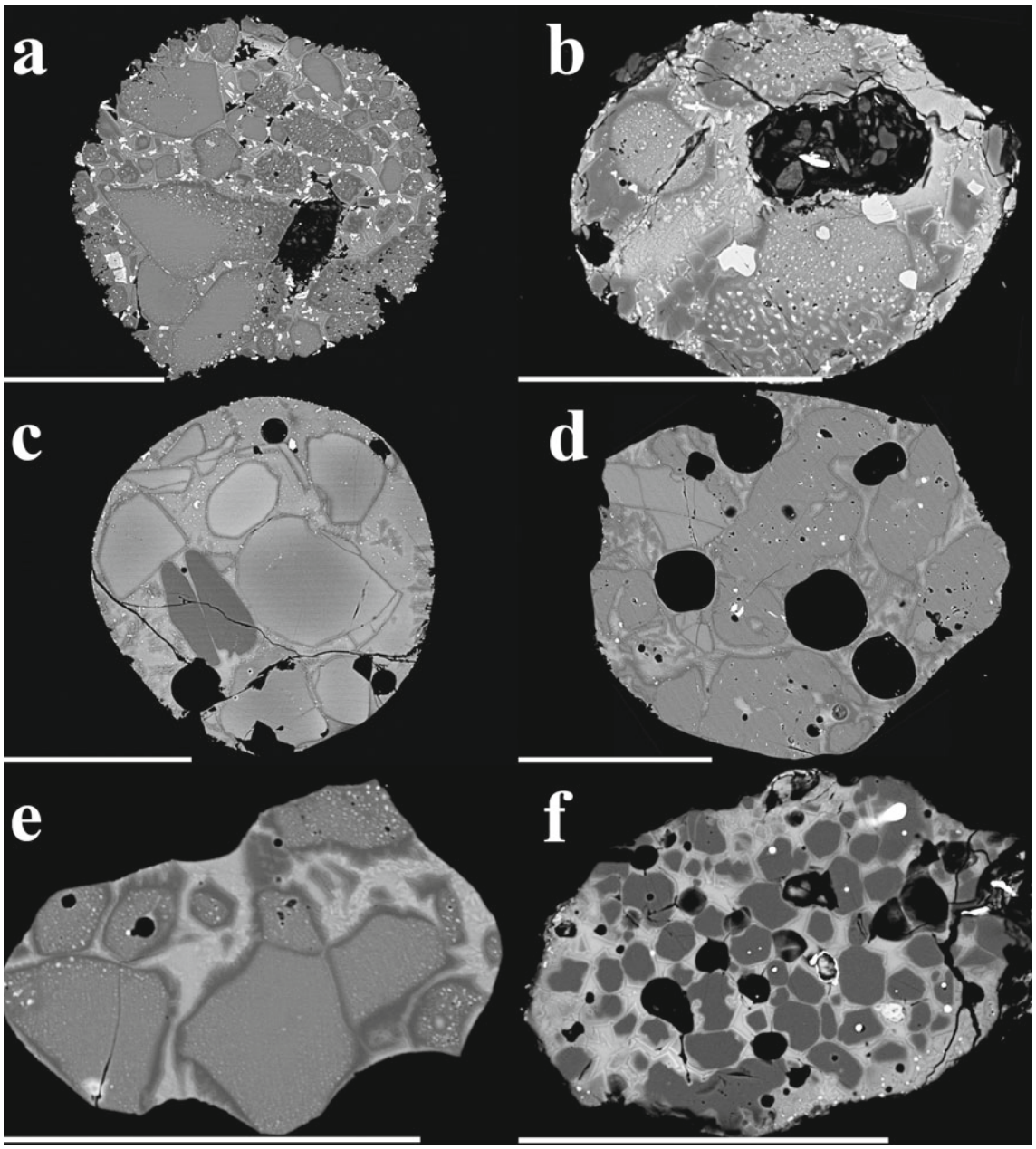

Fig. 6 Backscattered electron images of Novaya Zemlya relict grain bearing micrometeorites. **a** and **b**) Fe-rich ($Fa_{>30}$) relict olivine grains bordered by more magnesian olivine and glass-magnetite mesostasis. **c** and **d** Olivine-pyroxene relicts in glassy matrices. **e** An Fe-rich olivine bearing particle of an irregular shape. **f** A relict forsterite grains with rims of new-formed Fe-rich olivine in a glassy matrix. The scale bar is 100 μm

difficult to establish relationships between different types of MM. At the same time, it has been suggested that micrometeoroids having an affinity to low-iron FgMMs may be a source material for the formation of glassy and cryptocrystalline CS, whereas barred olivine and porphyritic CS may be formed from high-iron micrometeoroids [32]. On the other hand, enstatite and forsterite CgMM varieties, which sometimes have rims of ScMM matter (Fig. 5d), are most likely associated with FgMMs. Obviously, these CgMMs varieties were inclusions in a matrix of fine-grained micrometeoroids, some of which in turn served as a source material for ScMM. On the other hand, the establishment of the common origin both for different types and for one type of MM faces certain difficulties using only mineralogical and chemical data.

4.3 Bias of the Novaya Zemlya MM Collection

The Antarctic MM collections are considered as unbiased, i.e., the quantitative ratios of the MM types in the samples correspond to the ones in the MM flux [6]. This is related to the fact that MMs into the Antarctic glaciers occur without their significant relocation and sorting. The situation is somewhat different on the Novaya Zemlya ice sheet, where the deposited particles are rewashed in temporary water streams and subjected to aeolian blowing. This may lead to bias of this collection by some types of MM and, accordingly, enrichment by others. I compared the relative abundance of the major MM types in the Novaya Zemlya collection and the SPWW collection as well as other Antarctic collections [6, 8, 9, 35, 36]. The SPWW collection is considered unbiased because it was sampled from the bottom of a 6 m diameter cavity formed by ice melting to provide the South Pole station with water. The comparison was made for the relative numbers of CSs, FgMMs, ScMMs, and CgMMs. The content of CSs in the Novaya Zemlya collection is 77%, whereas in the collections from SPWW, Cap Prudhomme and CONCORDIA stations its content is 77%, 42% and 30% respectively. The contents of FgMMs, ScMMs, and CgMMs for the Novaya Zemlya collection are 2.5, 7.2, and 13.2%, respectively, whereas for the SPWW collection they are 9.5, 6.3, and 3.7%, respectively [6]. Obviously, the Novaya Zemlya collection is biased in comparison with the SPWW collection due to the lower amount of FgMM. It can be assumed that the depletion of FgMMs is due to their lower stability in strong currents in temporary watercourses and/or their redeposition elsewhere due to their lower specific gravity.

5 Conclusions

Cryoconite sediments on the margins of the Novay Zemlya ice sheet provide an opportunity to collect massive samples of cryoconite containing MMs quite easily. Calculations show that 25 kg of cryoconite can contain from 1,00,000 to 1,50,000 MM particles. Although their extraction is rather complicate compared to the extraction of MMs from Antarctic ice, it is nonetheless compensated by the large number of obtained MMs. The disadvantages of this collection should include the possibility of weathering, signs of which are present in a number of MMs. These include dissolution of olivine grains at the periphery of CS, partial oxidation and disappearance of metal and possible removal of a number of easily mobile elements. The collection also shows the depletion of FgMMs. On the other hand, it leads to enrichment of the CgMMs, among that there are rare and exotic varieties not represented in the meteorite collections.

Acknowledgements This work is conducted under the GEOKHI RAS state assignment. The author is grateful to Dr. F. Brandstätter, Dr. J. Raitala, and the staff of the Centre for Material Analysis, University of Oulu, Finland for their help. The author acknowledges the collective of the North hydrometeorological survey and the former chief of the survey L. Yu. Vasilyev, the former capitan of the ship "Mikhail Somov" Yu. A. Nasteko, and the crew of the "Russian Arctic" National park at the "Cap of Desire" polar station.

References

1. Love, S.G., Brownlee, D.E.: A direct measurement of the terrestrial mass accretion rate of cosmic dust. Science **262**, 550–553 (1993)
2. Yada, T., Nakamura, T., Takaoka, N., Noguchi, T., Terada, K., Yano, H., Nakazawa, T., Kojima, H.: The global accretion rate of extraterrestrial materials in the last glacial period estimated from the abundance of micrometeorites in Antarctic glacier ice. Earth Planets Space **56**, 67–79 (2004)
3. Cremonese, G., Borin, P., Martellato, E., Marzari, F., Bruno, M.: New calibration of the micrometeoroid flux on Earth. Astrophys. J. Lett. **749**(2), L40 (2012)
4. Rojas, J., Duprat, J., Engrand, C., Dartois, E., Delauche, L., Godard, M., Gounelle, M., Carrillo-Sánchez, J.D., Pokorný, P., Plane, J.M.C.: The micrometeorite flux at Dome C (Antarctica), monitoring the accretion of extraterrestrial dust on Earth. Earth Planet. Sci. Lett. **560**, 116794 (2021)
5. Badyukov, D.D.: Micrometeoroids: the flux on the Moon and a source of volatiles. Sol. Syst. Res. **54**(4), 263–274 (2020)
6. Taylor, S., Matrajt, G., Guan, Y.: Fine-grained precursors dominate the micrometeorite flux. Meteorit. Planet. Sci. **47**(4), 550–564 (2012)
7. Suavet, C., Cordier, C., Rochette, P., Folco, L., Gattacceca, J., Sonzogni, C., Damphoffer, D.: Ordinary chondrite-related giant (>800μm) cosmic spherules from the Transantarctic Mountains Antarctica. Geochim. Cosmochim. Acta **75**(20), 6200–6210, https://doi.org/10.1016/j.gca.2011.07.034 (2011)
8. Van Ginneken, M., Gattacceca, J., Rochette, P., Sonzogni, C., Alexandre, A., Vidal, V., Genge M.J. The parent body controls on cosmic spherule texture: Evidence from the oxygen isotopic compositions of large micrometeorites. Geochim. Cosmochim. Acta **212**(1), 196–210, https://doi.org/10.1016/j.gca.2017.05.008 (2017)
9. Blanchard, M.B., Brownlee, D.E., Bunch, T.E., Hodge, P.E., Kyte, F.T.: Meteoroid ablation spheres from deep sea sediments. Earth Planet. Sci. Lett. **46**, 178–190 (1980)
10. Maurette, M., Olinger, C., Michel-Levy, M.C., Kurat, G., Pourchet, M., Brandstaetter, F., Bourot-Denise, M.: A collection of diverse micrometeorites recovered from 100 tonnes of Antarctic blue ice. Nature **351**, 44–47 (1991)
11. Taylor, S., Lever, J.H., Harvey, R.P.: Numbers, types, and compositions of an unbiased collection of cosmic spherules. Meteorit. Planet. Sci. **35**, 651–666 (2000)
12. Rochette, P., Folco, L., Suavet, C., Van Ginneken, M., Gattacceca, J., Perchiazzi, N., Braucher, R., Harvey, R.P.: Micrometeorites from the transantarctic mountains. Proc. Natl. Acad. Sci. **105**, 18206–18211 (2008)
13. Maurette, M., Hammer, C., Brownlee, D.E., Reeh, N., Thomsen, H.H.: Placers of cosmic dust in the blue ice lakes of Greenland. Science **233**, 869–872 (1986)
14. Forman, S.L., Lubinski, D.J., Zeeberg, J.J., Polyak, L., Gifford, H., Miller, G.H., Matishov, G., Tarasov, G.: Postglacial emergence

and Late Quaternary glaciation on northern Novaya Zemlya, Arctic Russia. Boreas **28**, 133–145 (1999)
15. Koryakin, V.S.: Arctic glaciers. M., "Nauka press", p. 158 (1988) (in Russian)
16. Koryakin, V.S.: Novaya Zemlya glaciers and climate. Priroda **8**, 23–29 (1990). (in Russian)
17. Zeeberg, J., Forman, S.L.: Changes in glacier extent on north Novaya Zemlya in the twentieth century. Holocene **11**, 161–175 (2001)
18. Govorukha L.S.: Modern glaciation of Arctic Ocean islands. In: Budyko, M.I. (ed.) "Soviet Arctic". Nauka press, pp. 215–233 (1970) (in Russian)
19. Badjukov, D.D., Raitala, J.: Micrometeorites from the northern ice cap of the Novaya Zemlya archipelago, Russia: the first occurrence. Meteorit. Planet. Sci. **38**, 329–340 (2003)
20. Hodson, A., Cameron, K., Bøggild, C., Irvine-Fynn, T., Langford, H., Pearce, D., Banwart, S.: The structure, biological activity and biogeochemistry of cryoconite aggregates upon an Arctic valley glacier: Longyearbreen, Svalbard. J. Glaciol. **56**, 349–361 (2010)
21. Nishiizumi, K., Arnold, J.R., Brownlee, D.E., Caffee, M.W., Finkel, R.C., Harvey, R.P.: Beryllium-10 and aluminum-26 in individual cosmic spherules from Antarctica. Meteoritics **30**, 728–732 (1995)
22. Osawa, T., Nakamura, T., Nagao, K.: Noble gas isotopes and mineral assemblages of Antarctic micrometeorites collected at the meteorite ice field around the Yamato mountains. Meteorit. Planet. Sci. **38**, 1627–1640 (2003)
23. Genge, M.J., Engrand, C., Gounelle, M., Taylor, S.: The classification of micrometeorites. Meteorit. Planet. Sci. **43**, 497–515 (2008)
24. Kurat, G., Koeberl, C., Presper, T., Brandstätter, F., Maurette, M.: Petrology and geochemistry of Antarctic micrometeorites. Geochim. Cosmochim. Acta **58**, 3879–3904 (1994)
25. Genge, M.J.: Igneous rims on micrometeorites. Geochim. Cosmochim. Acta **70**, 2603–2621 (2006)
26. Khisina, N.R., Badyukov, D.D., Wirth, R.: Microtexture, nanomineralogy, and local chemistry of cryptocrystalline cosmic spherules. Geochem. Int. **54**(1), 68–77 (2016)
27. Suavet, C., Gattacceca, J., Rochette, P., Folco, L.: Constraining the terrestrial age of micrometeorites using their record of the Earth's magnetic field polarity. Geology **39**(2), 123–126, https://doi.org/10.1130/G31655.1 (2011)
28. Cordier, C., Suavet, C., Folco, L., Rochette, P., Sonzogni, C.: HED-like cosmic spherules from the Transantarctic Mountains Antarctica: Major and trace element abundances and oxygen isotopic compositions. Geochim. Cosmochim. Acta **77**, 515–529, https://doi.org/10.1016/j.gca.2011.10.021 (2012)
29. Nakamura, T., Noguchi, T., Yada, T., Nakamuta, Y., Takaoka, N.: Bulk mineralogy of individual micrometeorites determined by X-ray diffraction analysis and transmission electron microscopy. Geochim. Cosmochim. Acta **65**, 4385–4397 (2001)
30. Noguchi, T., Nakamura, T., Nozaki, W.: Mineralogy of phyllosilicate-rich micrometeorites and comparison with Tagish Lake and Sayama meteorites. Earth Planet. Sci. Lett. **202**, 229–246 (2002)
31. Sakamoto, K., Nakamura, T., Noguchi, T., Tsuchiyama, A.: A new variant of saponite-rich micrometeorites recovered from recent Antarctic snowfall. Meteorit. Planet. Sci. **45**, 220–237 (2010)
32. Badyukov, D.D., Brandstaetter, F., Topa, D.: Fine-grained scoriaceous and unmelted micrometeorites: sources and relationships with cosmic spherules. Geochem. Int. **56**(11), 1071–1083 (2018)
33. Badjukov, D.D., Brandstätter, F., Raitala, J., Kurat, G.: Basaltic micrometeorites from the Novaya Zemlya glacier. Meteorit. Planet. Sci. **45**, 1502–1512 (2010)
34. Kowalewski, M., Rimstidt, J.D.: Average lifetime and age spectra of detrital grains: toward a unifying theory of sedimentary grains. J. Geol. **111**(4), 427–439 (2003)
35. Duprat, J., Engrand, C., Maurette, M., Kurat, G., Gounelle, M., Hammer, C.: Micrometeorites from central Antarctic snow: The CONCORDIA collection. Adv. Space Res. **39**, 605–611 (2007)
36. Genge, M.J., Van Ginneken, M., Suttle, M.D.: Micrometeorites: Insights into the flux sources and atmospheric entry of extraterrestrial dust at Earth. Planet. Space Sci. **187**(104900), https://doi.org/10.1016/j.pss.2020.104900 (2020)

The Effect of 30 to >100 GPa Shock on the Magnetic Properties of Chinga Iron Meteorite

N. S. Bezaeva, D. D. Badyukov, J. M. Feinberg, M. Kars, and A. Kosterov

1 Introduction

Hypervelocity impacts represent an important mechanism for the evolution of the solid matter in our solar system through impact cratering processes and changes in the physical properties of colliding bodies. Indeed, impact craters are widespread on Earth [1] and in the Solar System, e.g. on the Moon, Mars, Mercury, etc. [2, 3]. Shock waves generated during impact events are associated with elevated pressures and temperatures, which can profoundly modify all physical properties of solid matter, including the bulk magnetic properties and the remanent magnetization of extraterrestrial matter, thus erasing or overprinting its paleomagnetic record.

Understanding the physical mechanisms associated with shock-induced changes in the magnetic properties is important for the correct interpretation of paleomagnetic records in lunar rocks, meteorites, and cratered planetary surfaces. Laboratory shock experiments using extraterrestrial material represent a step towards such understanding. Several shock experiments were conducted on rock samples such as stony meteorites [4, 5], lunar samples [6–8], and their terrestrial analogues [9–12].

Fe–Ni metal is a major magnetic mineral in most groups of meteorites. Metallic asteroids are also known in the Solar System (some M-type asteroids, e.g. 16 Psyche). So, it is very important to understand how shock metamorphism processes affect the physical properties of Fe–Ni meteorite metal. Previous works considered shock-induced transformations in iron and different steels. However, very few shock experiments directly used meteorite metal [13]. Shock experiments, described in [13] used Odessa meteorite (Iron, IAB-MG; octahendrite); shock-induced pressures in these experiments did not exceed 100 GPa.

Two types of shock-recovery experiments can be distinguished according to their geometry: (1) planar shock experiments using the techniques such as laser [8, 14, 15], gas gun [9, 12, 16–21], explosive products [22–24] and (2) spherical shock experiments [4, 5, 11, 25]. Spherical shock experiments have several advantages over planar shock experiments: (1) higher attainable pressures; (2) shock durations (within a millisecond range) closer to natural impacts; (3) no contamination of target rocks by impactor's matter nor by explosive products; (4) a wide range of pressures and temperatures may be investigated in a single shock experiment (see below).

We conducted the spherical shock-recovery experiment on the Chinga iron meteorite [13, 26]. Chinga was chosen due to its homogeneous structure, lack of large mineral inclusions, and a relatively large number of samples at the Vernadsky Institute meteorite collection, which made it available for the shock experiment. First results, including a detailed petrographic description of shock effects, were previously reported in [27]. This paper focuses on the magnetic properties of a set of Chinga specimens coming from a spherically shocked sample.

N. S. Bezaeva (✉) · D. D. Badyukov
Vernadsky Institute of Geochemistry and Analytical Chemistry, Russian Academy of Sciences, 19, Kosygin St., Moscow, 119991, Russia
e-mail: bezaeva@geokhi.ru

J. M. Feinberg
Institute for Rock Magnetism, University of Minnesota, 150 John T. Tate Hall, 116 Church St. SE, Minneapolis, MN 55455, USA

M. Kars
Center for Advanced Marine Core Research, Kochi University, B200 Monobe, Nankoku, 783-8502, Japan

A. Kosterov
St. Petersburg State University, 7/9 Universitetskaya Emb., St. Petersburg, 199034, Russia

V. P. Kolotov and N. S. Bezaeva (eds.), *Advances in Geochemistry, Analytical Chemistry, and Planetary Sciences*,
https://doi.org/10.1007/978-3-031-09883-3_18

2 Samples and Measuring Techniques

2.1 Description of Samples

We chose for our shock experiment an unoxidized piece of the Chinga iron meteorite shower (sample ID: #108-15435) from the meteorite collection of the Russian Academy of Sciences (Vernadsky Institute RAS). The selected sample had a roughly isometric shape and was not subject to plastic deformations. So all the below-described effects result from shock metamorphism (see the Results section). It was further shaped into a sphere of ~56-mm diameter (see below) with an initial (pre-shock) density of 7.92 g/cm^3.

Chinga is an ataxite. It is classified as Iron, ungrouped (MetBase v.7.1 [28]). Ni content is 16.58% [13]. It was found in 1912 scattered along the Chinge steam (51°3′30″ N, 94°24′0″ E, Imperial Russia, later Tuva Republic, RSFSR). According to previous investigations [13, 27], Chinga is characterized by a fine-grained structure and consists of taenite (Ni ~20–50 wt.%, face-centered cubic structure, fcc, ferromagnetic at room temperature for Ni >30 wt.%) and kamacite (Ni ≤7 wt.%, body-centered cubic structure, bcc). We also used a single small piece of intact Chinga sample (further subdivided into individual cubic specimens) from the RAS meteorite collection, further referred to as unshocked, for comparison with the shocked specimens. After the shock experiment (see Sect. 2.2 for details), the sample was cut along the equatorial plane using the electrospark method, and thus a few mm-thick spherical slice was extracted. A set of cubic specimens was extracted along the radius (*chs-2*… *chs-12*). All specimens apart for *chs-2* (which was then subdivided into *chs-2a* and *chs-2b*) had roughly cubic shapes. Specimen *chs-2* had an irregular but nearly isometric (equidimensional) shape.

2.2 Instruments and Methods

Shock experiment

Following [4, 11], we conducted a spherical implosion shock experiment on Chinga iron meteorite. The spherical sample was put into a 3.845 mm thick stainless-steel container covered by an 8-mm thick explosive layer of RDX-based composition (RDX is an abbreviation of Research Department eXplosive, also known as hexogen), which was triggered simultaneously on its outer surface. Explosively generated converging shock wave traveled first from the sample's periphery to its center. After having focused on the sample's center, a second diverging compression wave traveled outwards from the sample's center towards its periphery, forming a roughly spherical cavity with a radius of ~7.5 mm. Further details on spherical shock wave propagation patterns can be found in [29, 30].

Instruments

Magnetic measurements were carried out in three research centers: the Institute for Rock Magnetism (Minneapolis, USA), CEREGE (Aix-en-Provence, France), and the Center for Advanced Marine Core Research, Kochi University (Nankoku, Japan).

Low-field magnetic susceptibility χ_0 at room temperature was measured using a KLY-2 AGICO susceptibility bridge operating at 300 A/m, 920 Hz driving field, and having a nominal sensitivity of 4×10^{-8} SI assuming a nominal sample volume of 10 cm^3. Natural remanent magnetization (NRM) and saturation isothermal remanent magnetization (SIRM), as well as the corresponding demagnetization by alternating field (AF) curves, were measured using a 2G Enterprises Model 760 SQUID (Superconducting Quantum Interference Device) cryogenic magnetometer equipped with an inline AF demagnetizer at the Institute for Rock Magnetism. This magnetometer allows for the measurement of the magnetic moment up to 10^{-4} Am^2, with a practical background noise level of 10^{-11} Am^2, and AF demagnetization up to fields of 170 mT. A 1 T SIRM was imparted using a 2G Enterprises 670 pulse magnetizer. For pressure demagnetization experiments, a 3 T SIRM was imparted using pulse magnetizer MMPM9 from Magnetic Measurements Ltd. (see below). In this study, the median destructive field (MDF_i) is defined as the alternating magnetic field needed to reduce SIRM by 50%.

Low-temperature (10–300 K) magnetic measurements included FC-ZFC (field-cooled—zero-field-cooled) remanence and RT-SIRM (room-temperature SIRM) cooling-warming cycles and were collected using a Quantum Design MPMS2 (Magnetic Property Measurement System 2). This instrument allows the measurement of magnetic moment in the 10^{-10} to 10^{-3} Am^2 range under applied magnetic fields ranging from 0 to 5 T. The MPMS was also used to measure the temperature and frequency dependence of χ_0 in the 10–300 K range at three frequencies: $F_1 = 1$, $F_2 = 10$, and $F_3 = 100$ Hz.

We used Princeton Micromag Vibrating Sample Magnetometers (VSM) at the Institute for Rock Magnetism and at CEREGE with magnetic moment sensitivity of $\sim 10^{-8}$ Am^2 to measure major hysteresis loops yielding saturation magnetization M_s, saturation remanent magnetization M_{rs}, coercivity B_c, and backfield remanence demagnetization curves yielding M_{rs} and coercivity of remanence B_{cr} at room temperature, as well as in low- (from 10 to 300 K) and high-temperature range (from room temperature to 750 °C). VSM at CEREGE has a maximum applicable field of 1 T and VSM at the Institute for Rock Magnetism has a

maximum applicable field of 1.7 T, so all hysteresis loops acquired beyond 1 T were measured at the Institute for Rock Magnetism. The same instrument was also used to collect thermomagnetic curves, which monitor the saturation magnetization (M_s) in a 1 T field as a function of temperature up to 750 °C in a constantly flowing stream of hot helium gas serving both to heat the sample and to inhibit oxidation.

Pressure demagnetization experiments were carried out using a nonmagnetic high-pressure cell of piston-cylinder type [31], allowing direct measurements in a 2G Enterprises SQUID magnetometer (model 755R) at CEREGE. The pressure cell has several modifications compared to the cell described in [32]. It is made entirely of the so-called Russian alloy ($Ni_{57}Cr_{40}Al_3$), its inner diameter is 8 mm, and the maximum applicable calibrated pressure is 1.8 GPa. Furthermore, the Teflon plug, described in [32], was replaced by a special inner piston-plug made of Russian alloy with a CuBe anti-extrusion gasket. The reported (actual) pressure values are 10% less regarding the external load (for details, see [31–34]). The pressure cell was intercalibrated with the previous one used in [33].

We used the following protocol for all pressure demagnetization experiments. After acquiring 3 T SIRM, the sample was placed into a Teflon capsule filled with inert polyethylsiloxane (PES-1) liquid and locked with a special piston plug. PES-1 allows converting the uniaxial pressure on the pistons into a purely hydrostatic pressure on the sample [35]. After loading the cell with a Graseby Specac 15011 hydraulic press, the pressure inside the cell was locked by clamping. In order to isolate pressure demagnetization effect on remanent magnetization and exclude the creation of piezoremanent magnetization (PRM) after pressure application [36–39], in this work, the pressure was always applied in an ambient magnetic field low enough (<5 μT) to be considered having a negligible effect on the initial sample's SIRM acquired in a strong field (3 T). This was ensured by placing the press with the cell inside at the center of three pairs of perpendicular Helmholtz coils connected to stabilized DC supplies. Due to the presence of mobile metallic parts in the press, it was not possible to obtain a stable lower ambient field. The magnetic field in the area of the investigated sample was monitored using a 3-axis fluxgate magnetometer and was always <5 μT. Thus, in these experiments, any possible PRM acquisition was negligible compared to the pressure demagnetization. We used a 16-step pressure demagnetization protocol: 0 → 0.09 → 0.18 → 0.27 → 0.36 → 0.46 → 0.55 → 0.64 → 0.73 → 0.91 → 1.09 → 1.28 → 1.46 → 1.64 → 1.82 → 0 GPa. The magnetic moment of the sample under pressure at every pressure up to 1.8 GPa and upon decompression was measured using the SQUID magnetometer described above (model 755R at CEREGE). The remanence of the empty pressure cell at ambient pressure and room temperature is $\sim 3 \times 10^{-8}$ Am^2; at each subsequent pressure step up to 1.8 GPa, it was always two orders of magnitude lower than the remanence of the investigated sample. Sample remanence, therefore, was not corrected for cell remanence. After decompression, the sample was extracted from the cell and demagnetized by AF, then resaturated in a 3 T magnetic field and demagnetized by AF again.

For petrographic observations, a polished sector of a slab cut out along an equatorial plane of the sphere (see Sect. 2.1 above) was studied using the Leica optical microscope and Tescan Mira3 scanning electron microscope (SEM) equipped with an energy dispersive X-ray spectrometer (EDS) at the Vernadsky Institute RAS.

3 Results and Discussion

3.1 Pressure–Temperature Profiles

Pressure–temperature profiles along the radius of the spherically shocked Chinga iron meteorite are presented in Fig. 1. Note that we present P–T profiles for the recovered sample, i.e. the sample with central cavity formed as a result of shock wave propagation (Fig. 2).

It was recalculated after [29] under the assumption of a minor difference between shock compressibility of iron [29] and Chinga metal and was then corrected for the displacement of shocked matter within a newly formed shock-generated central cavity (see below). 0, I, II, III labels

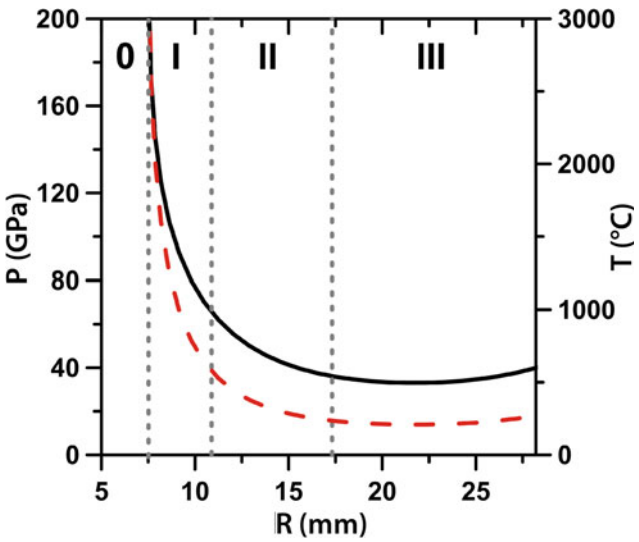

Fig. 1 Pressure (P) and temperature (T) profiles along the radius R of the recovered Chinga sample with the central cavity ~7.5 mm in radius (see Fig. 2). The solid line corresponds to pressure, and the dashed line corresponds to temperature. Central cavity and zones of shock metamorphism are indicated by '0' and 'I–III' labels, respectively (recalculated after [29], see Sect. 3.2 for details)

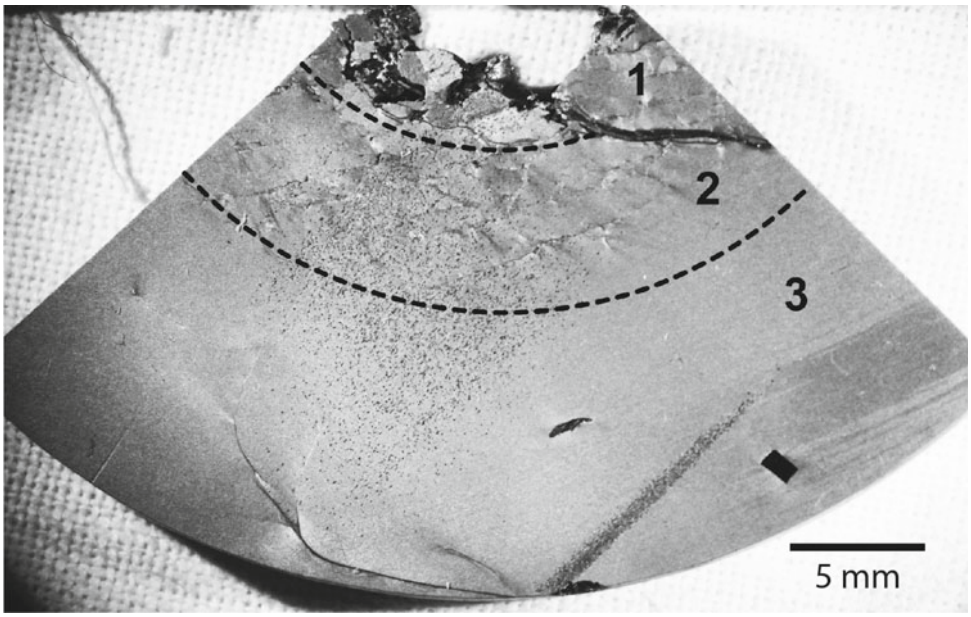

Fig. 2 Polished and etched section of the shocked Chinga meteorite sphere. Three zones of different stages of shock deformations are marked according to the intensities of the deformations (see text). Zone III contains one taenite vein, which is a thin curved line at the bottom of the image. The black rectangle at the bottom on the right side is a schreibersite crystal. Streak and diffuse bands at the right side of zone III and dots at the image center are defects of sectioning and polishing. Figure reworked after Fig. 3 in [27]

in Fig. 1 correspond to the central cavity (0) and three different concentric zones of shock metamorphism (I-III). As seen from Fig. 1, peak shock pressure and temperature values along the radius vary in the 33 GPa to >200 GPa range and in the 200 °C to several thousand °C ranges, respectively.

For investigated cubic specimens cut along the radius of the shocked Chinga sphere, average shock-induced pressure and temperature values vary in the 33 GPa to 85 GPa and the 208 °C to 875 °C ranges, respectively.

3.2 Shock Effects and Zonation

The polished and etched in the nital (3% solution of HNO_3 in ethanol) section of the Chinga iron meteorite is presented in Fig. 2. Details on geochemistry and petrographic description of unshocked Chinga sample as well as shock effects illustrated by SEM images were previously reported in [27]. Here, we will briefly summarize the main points for the consistency of the presentation.

Post-shock diameter of the spherical Chinga sample was ~57 mm. Three concentric zones of varying intensity shock metamorphism were developed in the shocked sample. A central spherical cavity (see Sect. 2.2, shock experiment) with a ragged surface of irregular shape is adjacent to zone I. Zone I is 3–4 mm wide and is characterized by cracks, intense plastic deformation as well as textureless taenite veins (Fig. 3), and shear bands (Fig. 4a). Specimens *chs-2a*, *chs-2b*, are extracted from zone I.

Zone II is a zone of intense development of shear bands which often accommodate the taenite veins at their central axes. An illustration of a shear band from zone II is presented in Fig. 4b. Taenite is homogeneous, and its composition (15–17 wt.% of Ni) is very close to a bulk composition of the unshocked sample. Specimens *chs-3*, *chs-4*, *chs-5*, and partly *chs-6* are extracted from zone II. Zone III is a zone of separate thin shear bands and veins (Fig. 2). Specimens *chs-7* through *chs-12* are extracted from Zone III.

Considering estimated shock temperatures at the sphere center and corresponding lower post-shock temperatures (Fig. 1), if melting occurred, it could have occurred only as incipient equilibrium bulk melting with limited melt volume. We did not observe traces of the bulk melting. It is supposed that the taenite veins (Figs. 3 and 4a) located inside the shear bands were formed by melting of metal due to very high local temperatures induced by flow and slipping of matter during shear bands formation. If this happened in a shock wave by high pressure, the temperature of the melt could have exceeded 2500 ºC [27].

In our experiments, shock pressures exceeded 30 GPa (Fig. 1). However, using optical and scanning electron microscopy, we did not observe any traces of α-iron → ε-iron → α-iron transition in kamacite, which is known to occur at 13 GPa [40]. We suppose that the lack of visible traces is due to the small size of kamacite grains and that other methods, such as transmission electron microscopy, could reveal the presence of such distortions.

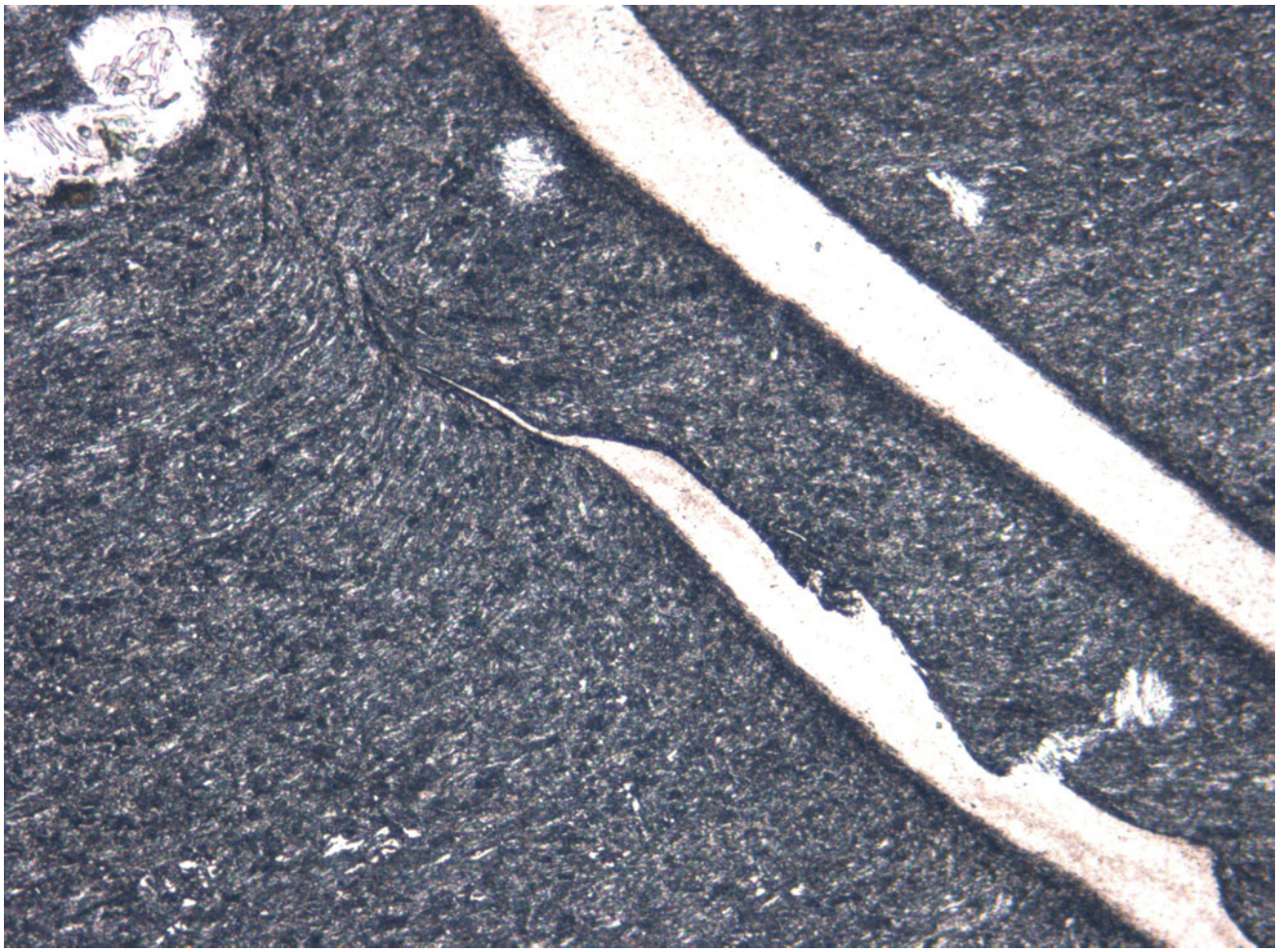

Fig. 3 Optical image of a shock-induced taenite vein inside a shear band (zone I). Etched in nital. The field of view is 0.23 mm

3.3 Magnetic Measurements

Magnetic carriers and bulk magnetic properties of unshocked Chinga ataxite

In this section, we discuss the magnetic properties of unshocked Chinga specimens. According to previous investigations, Chinga is made of kamacite and taenite. In order to confirm major magnetic carriers in Chinga ataxite, we conducted in-field thermomagnetic analyses (Fig. 5) on an unshocked Chinga specimen (*ch-3*, Table 1). To further characterize major magnetic minerals, we conducted hysteresis measurements and acquired backfield remanence demagnetization curves in low (10–300 K) and high-temperature (20–750 °C, measurements under helium atmosphere) ranges, respectively, on another unshocked Chinga specimen (*ch-1*, Table 1, Fig. 6, 7).

In Fig. 5, inflections are observed near ~550 °C and ~730 °C on the heating curve, which most likely corresponds to apparent Curie temperature of tetrataenite and Curie temperature of kamacite, respectively. Tetrataenite is a magnetic mineral with $T_c \sim 550$ °C, tetragonal structure, and chemical formulae $Fe_{0.5}Ni_{0.5}$ [41, 42]. Taenite is not visible on the thermomagnetic curve (Fig. 5) since it is paramagnetic at room temperature. Indeed, as stated above, taenite is paramagnetic at room temperature for Ni content <30 wt.% [42], and in Chinga meteorite average Ni content is ~16 wt.%, as indicated in Sect. 3.2. The paramagnetic nature of taenite present is also confirmed by several attempts to measure first-order-reversal-curve (FORC) diagrams, which disappeared every time paramagnetic correction was applied.

Figure 6 displays hysteresis loops and back-field remanence demagnetization curves for the unshocked specimen *ch-1*, acquired in the high (from room T to 750 °C) and low-T (10–300 K) ranges. Low-temperature data (Fig. 6c–d) where the corresponding back-field remanence demagnetization curves (Fig. 6d) were acquired in the same temperature range as MPMS data (MPMS data for both unshocked and shocked specimens are discussed in the next section) did not reveal any specific features of Chinga ataxite nor the

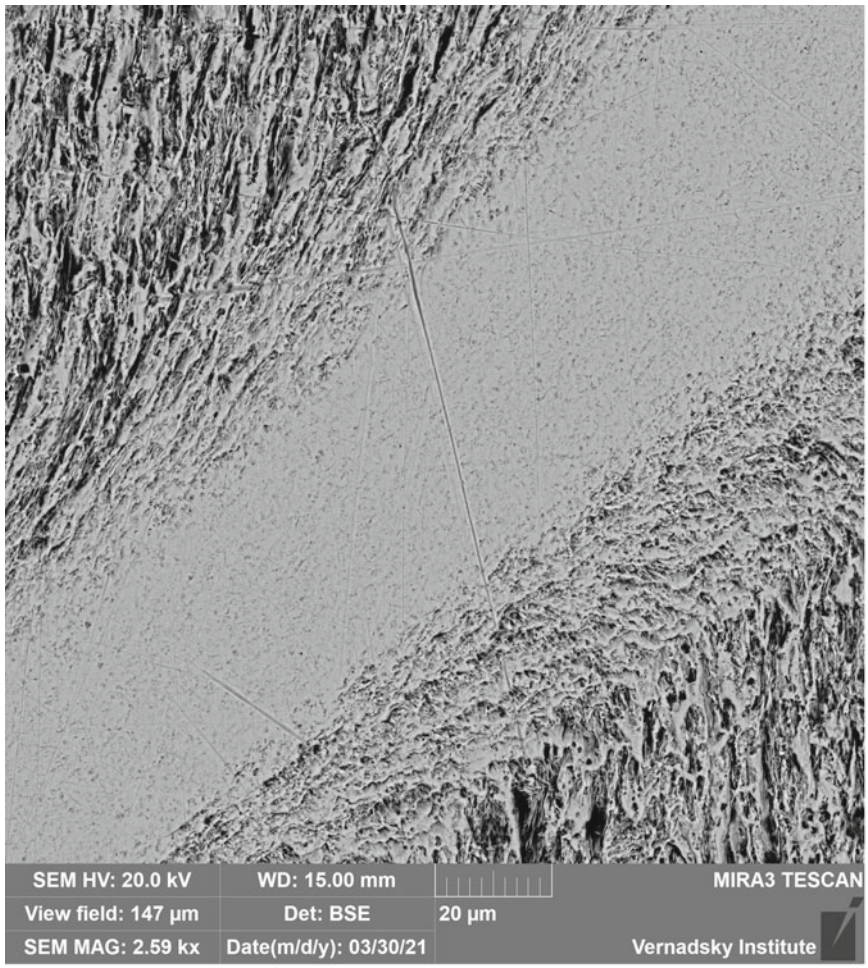

Fig. 4 **a** BSE image of a shear band with a central taenite melt zone (zone I). Etched in nital. **b** SE image of the shear band (zone II). Slide surface etched in nital. Image (**b**) reprinted after [27]

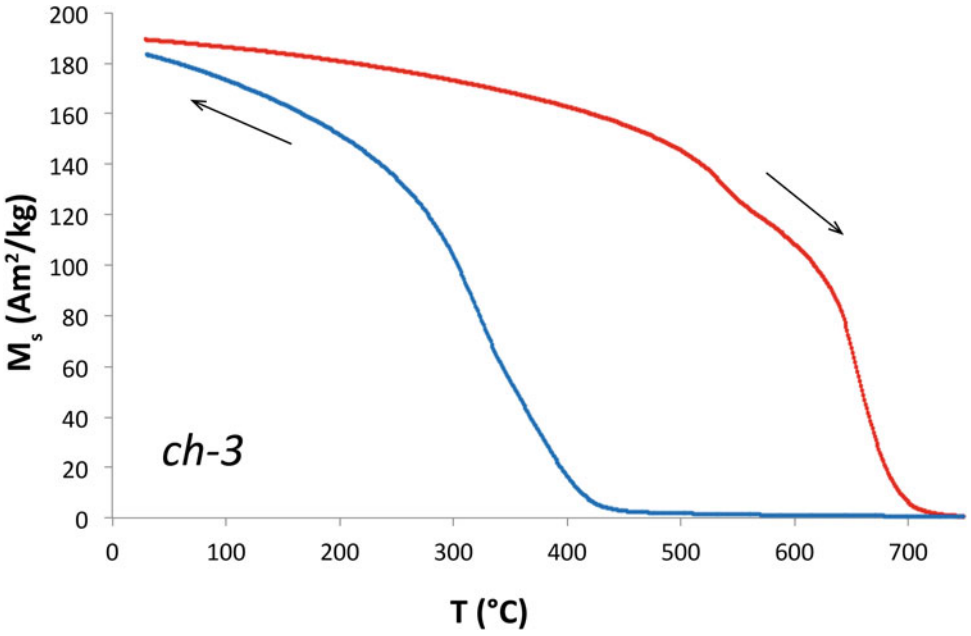

Fig. 5 Strong-field thermomagnetic curves for an unshocked cubic sample of Chinga ataxite (*ch-3*) acquired under a helium atmosphere. The red line corresponds to heating and the blue line corresponds to cooling. M_s is saturation magnetization

Table 1 Bulk magnetic properties of unshocked Chinga specimens

Sample ID	*m*	χ_0	M_{rs}	M_s	M_{rs}/M_s	B_c	B_{cr}	B_{cr}/B_c
ch-1	6.30	422.5	0.871 ± 0.080	192 ± 2	0.005	2.3 ± 0.03	72 ± 5	31 ± 3
ch-2*	5.10	–	0.414 ± 0.062	200 ± 2	0.002	0.9 ± 0.14	26 ± 7	27 ± 4
ch-3	6.00	525.7	–	–	–	–	–	–
ch-1 m	46.43	–	0.673 ± 0.074	185 ± 4	0.004	1.8 ± 0.04	51 ± 5	29 ± 3
ch-2 m	64.26	–	0.621 ± 0.076	182 ± 2	0.003	1.7 ± 0.11	51 ± 2	30 ± 1
ch-4 m	56.99	–	0.573 ± 0.054	184 ± 3	0.003	1.6 ± 0.12	52 ± 4	31
ch-5 m	42.35	–	0.618 ± 0.083	182 ± 2	0.003	1.7 ± 0.11	48 ± 1	28 ± 1
ch-6 m	52.05	–	0.584 ± 0.024	182 ± 2	0.003	1.6 ± 0.15	40 ± 9	24 ± 3

m is mass in mg; χ_0 is low-field magnetic susceptibility (in 10^{-6} m^3/kg); M_{rs} is saturation remanent magnetization (in Am^2/kg); M_s is saturation magnetization in (Am^2/kg); B_c is coercivity, and B_{cr} is remanent coercivity (in mT). Sample *ch-2** was heated to 500 °C under argon atmosphere before measurements. For all samples hysteresis loops and back-field remanence demagnetization curves were measured in 3 perpendicular directions. This table displays averaged values of M_{rs}, M_s, M_{rs}/M_s, B_c, B_{cr}, B_{cr}/B_c with corresponding standard deviation values

presence of other minerals paramagnetic at room temperature but ferrimagnetic in the low-temperature range. Room-temperature hysteresis and backfield parameters point out to magnetically soft multidomain behavior (Table 1) of magnetic minerals.

One of the parameters sensitive to the presence of tetrataenite is remanent coercivity B_{cr} obtained from back-field remanence demagnetization curves. B_{cr} values of unshocked samples (Table 1) indicate the presence of a small amount of tetrataenite. Indeed, when a tetrataenite-to-taenite disordering transition occurs, it dramatically lowers B_{cr} values. For instance, B_{cr} values of unshocked tetrataenite-bearing Saratov ordinary chondrite range from 124 to 162 mT but drop to 15–39 mT for shock-heated samples over tetrataenite-to-taenite disordering temperature [4]. The same happened to the unshocked but heated sample. High-temperature data (Fig. 6a and b) illustrate this tetrataenite-to-taenite transformation and stepwise decay of B_{cr} with increasing temperature.

Figure 7 displays B_{cr} versus temperature up to 750 °C. A curvature at ~530–550 °C most likely indicates the presence of tetrataenite. A curvature at 670 and 750 °C can be interpreted to be due to two generations of kamacite differing in composition. Considering the theoretical value of saturation magnetization of multidomain kamacite $M_s(\alpha)$ = 224 Am^2/kg [43] and following Dos Santos et al. [44] we calculated the ratio $M_s/M_s(\alpha)$, which indicates the contribution of kamacite to the induced properties of unshocked Chinga samples. Mean $M_s/M_s(\alpha)$ = 0.8, which also points out the presence of tetrataenite [44]. In all, the main

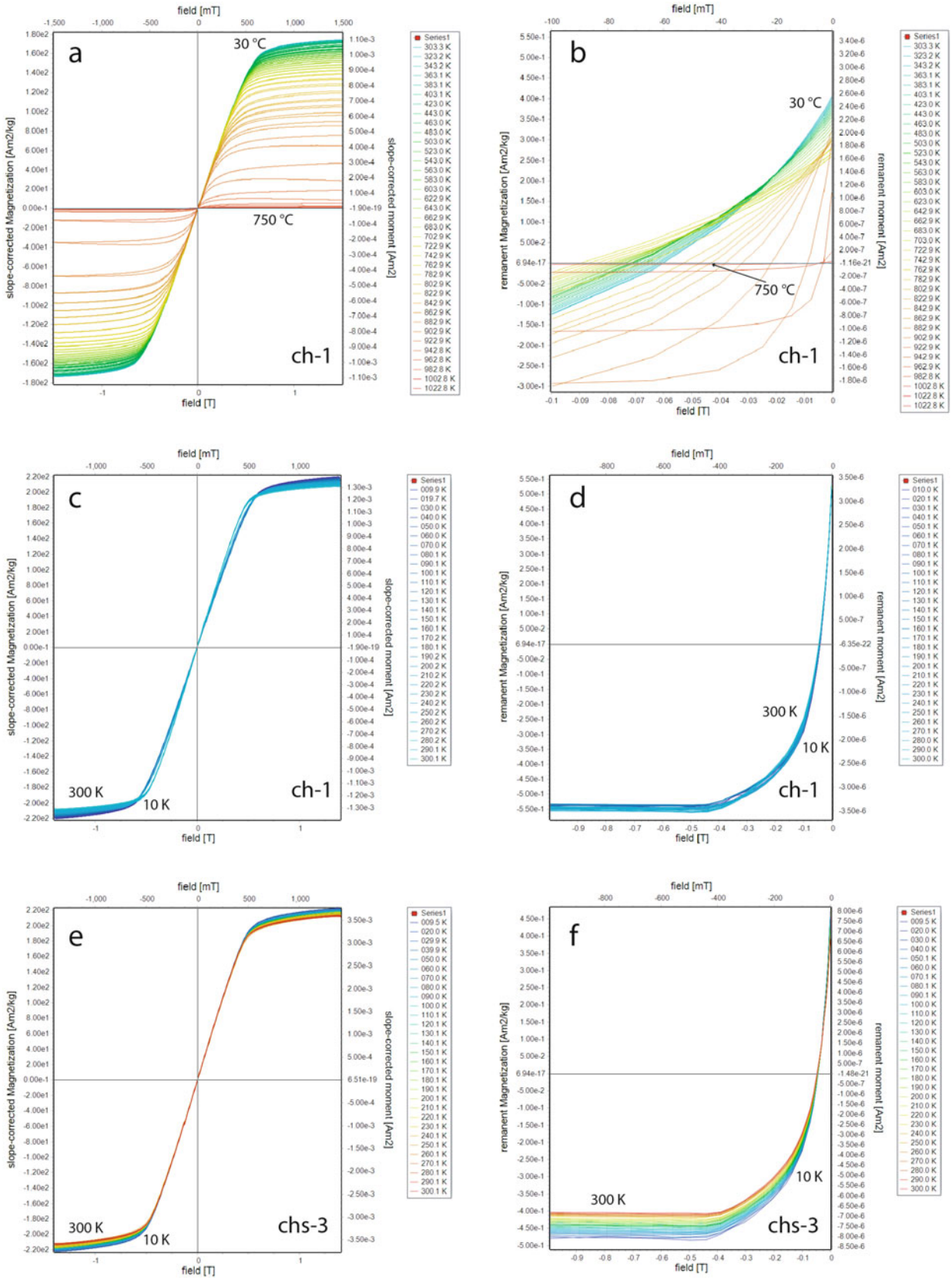

Fig. 6 Low and high-T hysteresis loops (**a**, **c**, **e**) and back-field remanence demagnetization curves (**b**, **d**, **f**) acquired on unshocked (*ch-1*) and shocked (*chs-3*) Chinga specimens. **a** and **b** *ch-1*, temperature range: 30–750 °C; **c** and **d** *ch-1*, temperature range: 10–300 K; **e** and **f** *chs-3*, temperature range: 10–300 K. High temperature data was acquired under helium atmosphere

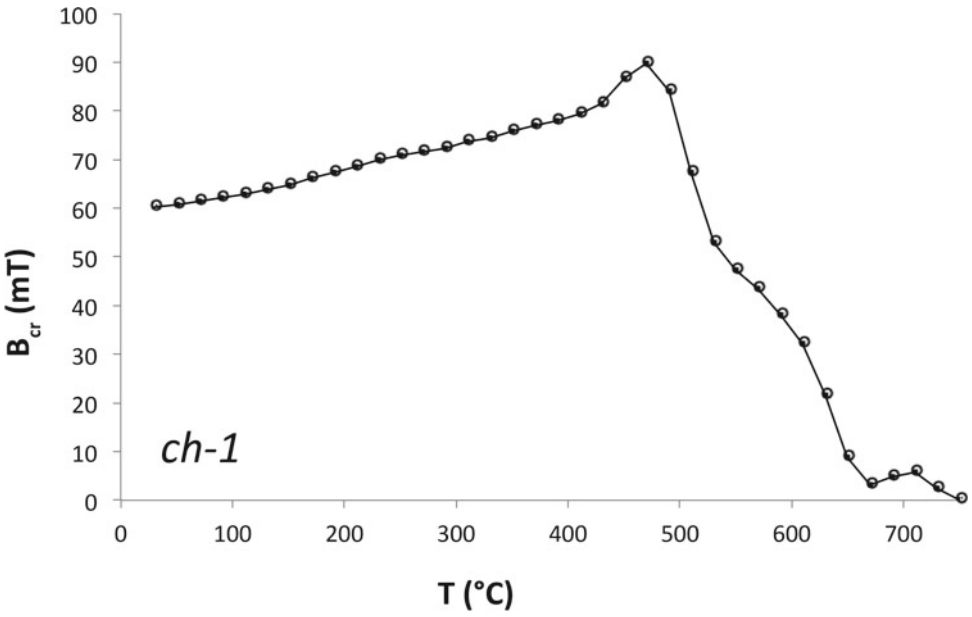

Fig. 7 Remanent coercivity B_{cr} versus temperature, extracted from back-field remanence demagnetization curves (Fig. 6b), which were measured under helium atmosphere on the unshocked specimen of Chinga iron meteorite *ch-1* in the temperature range from room temperature up to 750 °C

magnetic carriers in natural Chinga ataxite are kamacite and tetrataenite. Tetrataenite is most likely present in form of fine grains as we could not photograph it using SEM. The occurrence of tetrataenite in Chinga ataxite was also previously reported in [45] using high-resolution Mössbauer spectroscopy.

The degree of anisotropy of unshocked Chinga samples is relatively low. Table 1 summarizes measurements in three perpendicular directions: mean values with standard deviation are presented. The standard deviation for B_{cr} is 2–9%, whereas the standard deviation for M_s does not exceed 1–3%.

Using the predictive model of Bezaeva et al. [46], we estimated the possible sensitivity of Chinga remanence to hydrostatic load up to 1.8 GPa and then measured it experimentally. Estimations yielded 8%, while experimentally, 6% of SIRM pressure demagnetization was observed. Pressure demagnetization data acquired on an unshocked specimen (*ch-1*) are discussed below in comparison pressure demagnetization data acquired on shocked Chinga specimens.

In terms of Ni content and magnetic properties, Chinga is similar to another Ni-rich iron meteorite—Gebel Kamil (Fig. 8) [44, 47]. However, Gebel Kamil shows shear bands, and its shock stage is estimated as 60 GPa [47]. Contrary to Gebel Kamil, Chinga does not have any shear bands, and according to the authors' current knowledge, its natural shock stage remains unknown.

Magnetic properties of Chinga specimens after spherical shock loading

Bulk magnetic properties of shocked Chinga specimens are summarized in Table 2, which also includes average shock-induced pressure and temperature estimates for each specimen (Fig. 1).

One parameter sensitive to shock loading is remanent coercivity B_{cr}. Figure 9 displays the B_{cr} values of shocked samples versus sample position on the radius of the spherical sample. Data for unshocked specimens and a heated (unshocked) specimen are also presented for comparison. All measurements were conducted in three perpendicular directions and then averaged, so they are presented with their standard deviations. It is noteworthy that the standard deviation of B_{cr} considerably increases for shocked specimens, up to 33% (Table 2), against several percent for unshocked specimens (Table 1). It is most likely due to the increase in the degree of anisotropy resulting from shock wave propagation.

A drop in B_{cr} in zone I is observed (Fig. 9). Shock-induced temperatures in this zone exceed the temperature of tetrataenite-to-taenite disorder transition (~550 °C). To verify whether this is a temperature effect related to mineral transformation, we conducted a heating experiment on a piece of unshocked Chinga meteorite. As seen from Fig. 9, the B_{cr} of a heated sample dropped to the B_{cr} level characteristic of zone I. A similar temperature effect was observed in the spherical shock experiment of Saratov meteorite [4]. Thus, decreased B_{cr} values in the specimens of zone I (*chs-2a*, *chs-2b*) are most likely due to the mineralogical transformation of tetrataenite to taenite.

In zones II and III, variations of B_{cr} of shocked specimens fall within the range of natural dispersion of B_{cr} of unshocked specimens. There is no clear trend of shock-induced magnetic hardening as observed in [11] nor shock-induced magnetic softening as observed in [4]. However, as stated in Sect. 3.2, melt pockets and shear

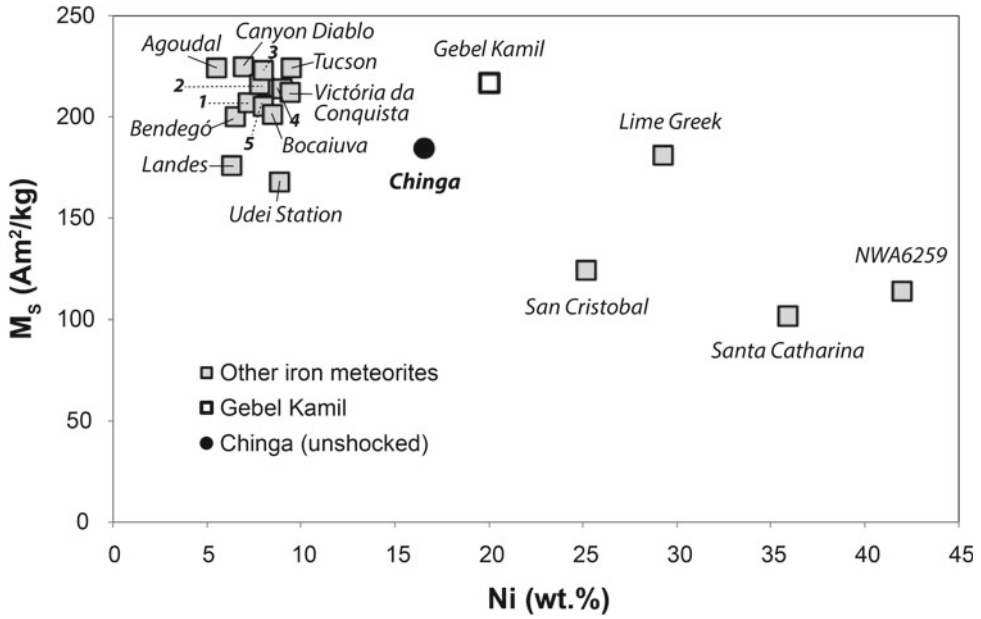

Fig. 8 The saturation magnetization (M_s) versus metal Ni content for Chinga ataxite and other iron meteorites. Data for Chinga comes from this paper (Table 1), data for the other iron meteorites are from Table 4 of [44]. All iron meteorites are labeled accordingly and include the following species: 1—*Itutinga* (IIIAB), 2—*Toluca* (IAB–sLL), 3—*Pará de Minas* (IVA), 4—*Crathéus* (IIC), 5—*São João Nepomuceno (SJN)* (IVA-an); *Landes* (IAB-MG), *Canyon Diablo* (IAB-MG), *Udei Station* (IAB-ung), *San Cristobal* (IAB-ung), *Lime Greek* (IAB-ung), *Santa Catharina* (IAB-ung), *Bendegó* (IC), *Agoudal* (IIAB), *Victória da Conquista* (IVA), *Bocaiuva* (Ungrouped), *Tuscon* (Ungrouped), *Gebel Kamil* (Ungrouped), *NWA 6259* (Ungrouped)

Table 2 Bulk magnetic properties of shocked Chinga specimens

Sample ID	*m*	*D*	Shock zone	*P*	*T*	χ_0	M_{rs}	M_s	M_{rs}/M_s	B_c	B_{cr}	B_{cr}/B_c
chs-2a	40.2	9.8	I	85	875	507.0[+]	0.554 ± 0.088	190 ± 6	0.003	1.1 ± 0.1	18 ± 3	17 ± 2
chs-2b	30.2	9.8	I	85	875	507.0[+]	0.578 ± 0.059	188 ± 4	0.003	1.0 ± 0.02	18 ± 2	17 ± 1
chs-3[*]	16.9	11.9	II	58	475	479.3	0.411	225	0.002	0.9	47	52
chs-4	24.4	13.7	II	47	345	470.4	0.360 ± 0.017	201 ± 2	0.002	0.9 ± 0.01	50 ± 1	54 ± 1
chs-5	30.7	15.5	II	40	273	451.3	0.383 ± 0.012	201 ± 2	0.002	0.9 ± 0.02	44 ± 6	48 ± 5
chs-6	9.3	17.3	II/III	37	235	437.4	–	–		1.0 ± 0.01	43 ± 7	45 ± 7
chs-7	34.4	19.2	III	34	218	440.6	0.344 ± 0.018	196 ± 4	0.002	0.9 ± 0.04	49 ± 9	52 ± 8
chs-8	35.0	21,1	III	33	208	429.5	0.379 ± 0.009	193 ± 1	0.002	1.0	41 ± 1	40 ± 1
chs-9	34.1	23.0	III	34	210	407.5	0.390 ± 0.001	201 ± 1	0.002	1.0 ± 0.01	38 ± 4	38 ± 4
chs-10	25.2	24.9	III	35	223	408.4	0.384 ± 0.022	191 ± 1	0.002	1.0 ± 0.09	53 ± 16	50 ± 11
chs-11	20.4	26,4	III	37	238	450.6	0.490 ± 0.078	186 ± 14	0.003	1.1 ± 0.08	44 ± 15	38 ± 10
chs-12	18.1	27.9	III	40	265	425.1	0.397 ± 0.047	197 ± 5	0.002	1.1	61 ± 4	54 ± 3

m is mass in mg; *D* is a distance from the specimen's center to the sphere center (in mm); shock zone corresponds to one of three concentric zones of shock metamorphism (see Fig. 1 and Sect. 3.1 for details); *P* is average shock-induced pressure (in GPa), experienced by the specimen (see Fig. 1 and Sect. 3.1 for details); *T* is the average shock-induced temperature (in °C), experienced by the specimen (see Fig. 1 and Sect. 3.1 for details); χ_0 is low-field magnetic susceptibility (in 10^{-6} m^3/kg); M_{rs} is saturation remanent magnetization (in Am^2/kg); M_s is saturation magnetization in (Am^2/kg); B_c is coercivity, and B_{cr} is remanent coercivity (in mT)

[*] For all samples apart from *chs-3* hysteresis loops and backfield remanence demagnetization curves were measured in 3 perpendicular directions. This table displays average values of M_{rs}, M_s, M_{rs}/M_s, B_c, B_{cr}, B_{cr}/B_c with corresponding standard deviation values

[+] Measured on *chs-2* specimen, which was further subdivided into *chs-2a* and *chs-2b*

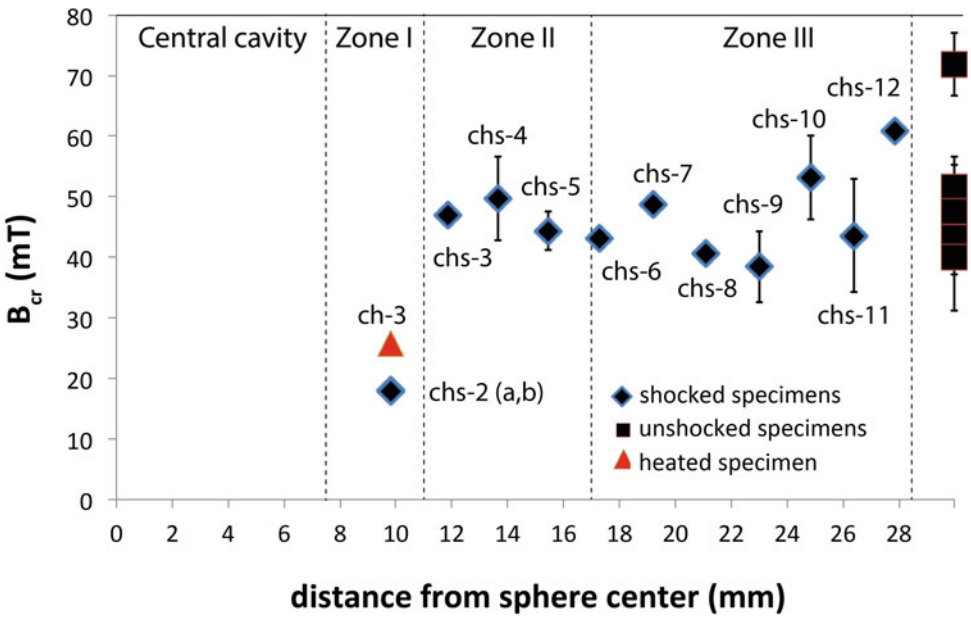

Fig. 9 The remanent coercivity of unshocked (black squares), shocked (black diamonds) and heated (red triangle) specimens versus distance of sphere center. B_{cr} data are presented with standard deviations as all samples apart from *ch-3* (unshocked, heated to 550 °C) and *chs-3* (shocked) were measured in three perpendicular directions, and the corresponding measurements were averaged

bands are abundant in zone I but are also observed in all three concentric zones of continuous shock metamorphism. No shear bands are observed in unshocked Chinga as observed in other iron meteorites (e.g. Gebel Kamil), so shear bands must have appeared in Chinga ataxite as a result of the shock experiment. Artificially developed shear bands as a result of experimental shock are documented for the first time.

This led to the conclusion that, in nature, Chinga ataxite never experienced shock pressures over ~30 GPa. In addition, the presence of tetrataenite in natural Chinga samples indicates that shock-induced temperatures in the natural environment (both pre-terrestrial and terrestrial) never exceeded temperatures of the order of ~500 °C. Another important conclusion is that shear bands in iron meteorites develop starting from 30 to 40 GPa peak shock pressures.

Figure 6e and f displays a set of hysteresis loops and back-field remanence demagnetization curves acquired in the 10–300 K temperature range on a shocked specimen from zone II (*chs-3*). As seen from Fig. 6e and f, the shocked specimen is magnetically soft (very low values of coercivity B_c) and demonstrates multidomain behavior (see Table 2).

The same specimen (*chs-3*) was subjected to MPMS measurements which included demagnetization on warming in zero field of SIRM given at 10 K after FC and ZFC, respectively, cooling-warming cycles to 10 K of SIRM given at 300 K, and temperature-and-frequency dependence of magnetic susceptibility. The results compared against the same measurements for an unshocked specimen (*ch-1*) are shown in Fig. 10. Magnetic susceptibility values in the 10–300 K range changes only by a small amount, ~1% for unshocked and ~5% for shocked specimens, respectively (Fig. 10a and b). Near-zero frequency dependence of magnetic susceptibility in both shocked and unshocked specimens indicates that there are no superparamagnetic (SP) metallic grains of nanometric size in natural Chinga ataxite, and SP grains did not form as a result of a shock either. Variation of remanence in the 10–300 K range (Fig. 10c and d), however, shows some difference between shocked and unshocked specimens. Both LT- and RT-SIRM (LT stands for low temperature and RT stands for room temperature) are some 20% lower in the shocked specimen. Also, somewhat surprisingly, LT- and RT-SIRM of the shocked specimen show opposite stability trends compared to the unshocked specimen, LT-SIRM (ZFC curves in Fig. 10e) and RT-SIRM being less and more stable, respectively. Low-temperature data further indicate that there are no phases that become ferrimagnetic in the low-temperature range.

There are no clearly pronounced shock-induced changes in low-field magnetic susceptibility (measured at RT) along the radius. χ_0 values for the unshocked (Table 1) and shocked (Table 2) specimens are very close. The same applies to saturation magnetization M_s and M_{rs}/M_s ratio. M_{rs}/M_s ratio for shocked samples is slightly lower than that of unshocked samples, but both point out to multidomain behavior [48].

Figure 11 compares alternating field (AF) demagnetization spectra of SIRM for unshocked and shocked Chinga specimens. A shocked sample appears slightly less resistant to AF demagnetization and is characterized by a lower MDF_i value. Thus, there is a slight trend of shock-induced magnetic softening, which could be related to the annealing of defects in the crystalline lattice as a result of shock-induced temperatures.

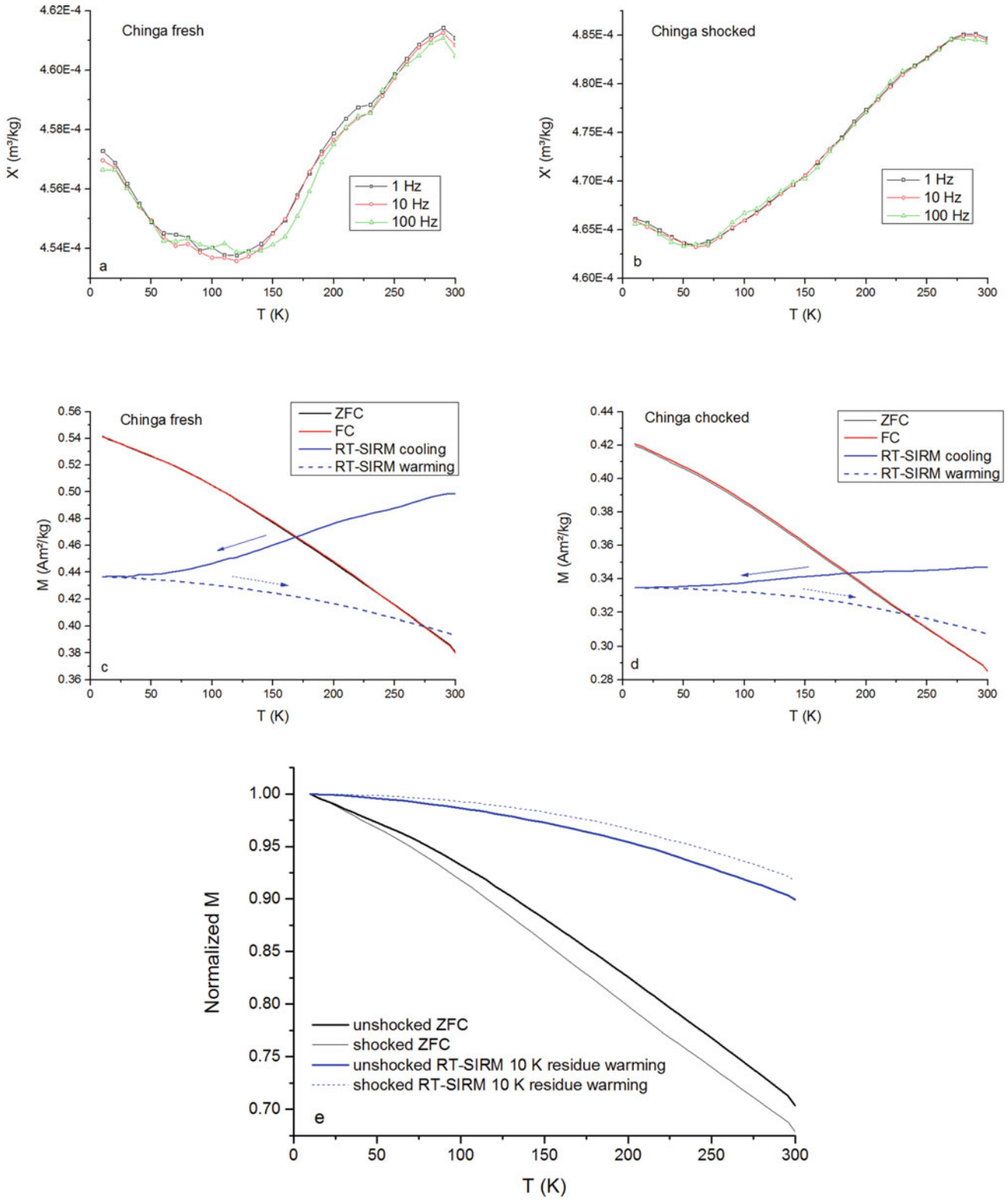

Fig. 10 Behavior of frequency-dependent in-phase component χ' of magnetic susceptibility χ_0 (**a**, **b**) and SIRM (**c**, **d**) of unshocked (*ch-1*) and shocked (*chs-3*) Chinga specimens in the 10–300 K range. **e** Compares stability of remanence for unshocked and shocked specimen

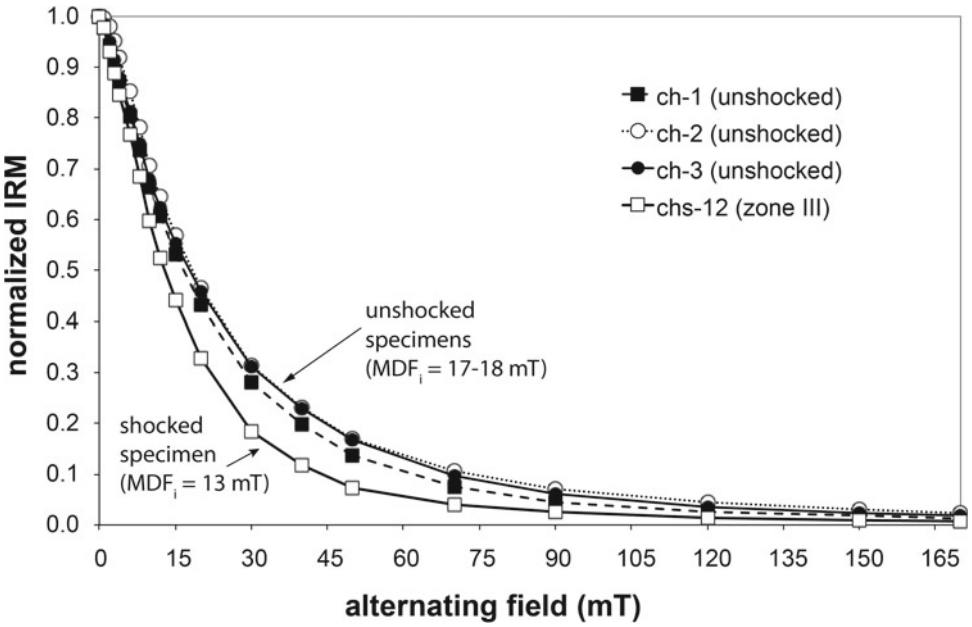

Fig. 11 Spectra of alternating field demagnetization of IRM, normalized to its initial value of SIRM, for unshocked and shocked Chinga specimens

We do not discuss NRM of shocked samples in detail since they were most likely remagnetized after shock experiment due to post-shock magnetic contamination. The magnetic hardness of both unshocked and shocked Chinga specimens is too low to consider them as reliable paleomagnetic recorders.

Behaviour under hydrostatic pressure up to 1.8 GPa

The above magnetic analyses showed only minor changes in bulk magnetic properties as a result of shock wave propagation. In addition to conventional rock magnetic analyses, we subjected our specimens to hydrostatic pressure loads up to 1.8 GPa. Figure 12 displays the results of pressure demagnetization experiments on unshocked and shocked specimens from zone I (*chs-2a*), zone II (*chs-4*), and zone III (*chs-12*). The unshocked specimen and the shocked specimen from the periphery (the outer edge of zone III) appear rather pressure-resistant, pressure demagnetization degree of SIRM not exceeding 5–6%. Simultaneously, the pressure demagnetization degree for the shocked specimens from zones I and II varies between 57 and 75%, indicating the profound intrinsic changes in the samples due to shock wave propagation. It is interesting to note that shock-induced pressures and temperatures for the sample *chs-4* (47 GPa,

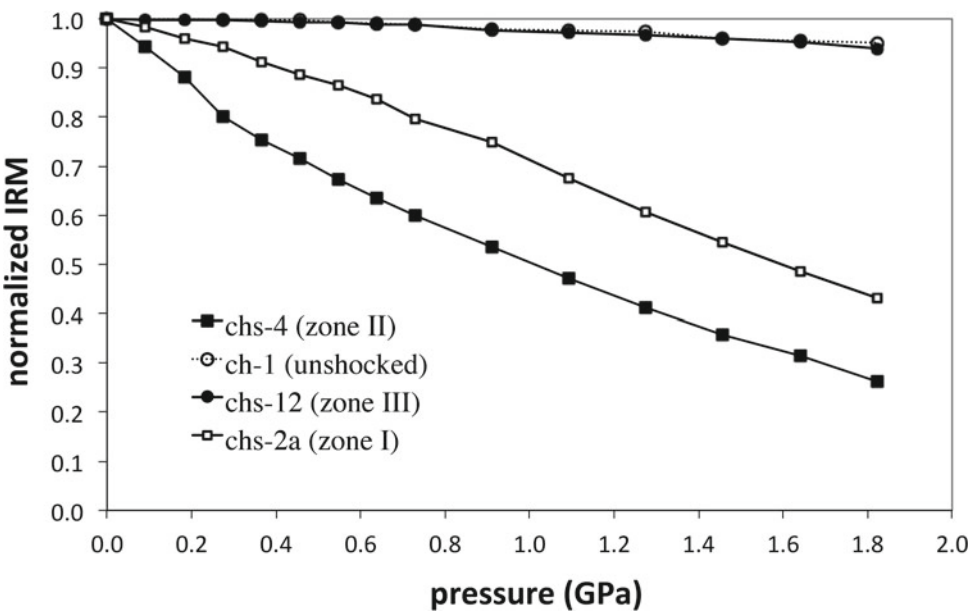

Fig. 12 Isothermal remanent magnetization (IRM), normalized to SIRM versus hydrostatic pressure up to 1.8 GPa for unshocked (*ch-1*) and shocked Chinga specimens from zone I (*chs-2a*), zone II (*chs-4*), and zone III (*chs-12*)

345 °C, Table 2) are not much different from those for the sample *chs-12* (40 GPa, 265 °C, Table 2), whereas their pressure demagnetization degrees are dramatically different (74% of pressure demagnetization for the shocked specimen *chs-4* from zone II against 6% of pressure demagnetization for the shocked specimen *chs-12* from zone III, Fig. 12). This may be related to a difference between 40 and 50 GPa shock effects, and possibly also that shock affected Chinga matter heterogeneously on a millimeter-scale (the size of our cubic samples is on average about 1.5 mm). Indeed, shock-induced shear bands and melt pockets are unevenly distributed in the shocked matter, and cubic samples extracted along the radius of the shocked Chinga sphere and used for magnetic measurements may or may not include one of these. The difference between pressure sensitivity of unshocked and shocked specimens could also be related to a pressure-resistant population of magnetic grains, which was somehow affected by shock (see the difference between shocked and unshocked specimens, Fig. 10e).

In all, though there is no clear shock-induced trend in bulk magnetic properties along the radius for most parameters, shock dramatically affected the intrinsic structure of the shocked specimens, as evidenced by the sensitivity of shocked specimens from different zones of shock metamorphism to hydrostatic pressure load.

4 Conclusions

1. We conducted a spherical shock experiment on Chinga iron meteorite, allowing to reach pressures between 33 GPa and >100 GPa, which formed a central cavity (without any visible traces of melting) and three concentric zones of shock metamorphism. Corresponding shock-induced temperatures ranged between 200 °C and >1000 °C. Recovered cubic specimens used for magnetic measurements were extracted along the radius of the meridional plane and did not contain any visible traces of melting.
2. Major magnetic carriers in Chinga ataxite are kamacite and tetrataenite. Chinga is dominated by multidomain behavior. It is magnetically soft and is not suitable for paleomagnetic investigations. In terms of texture and magnetic properties, Chinga ataxite is similar to another Ni-rich iron meteorite—Gebel Kamil.
3. Petrographic and microscopic investigations revealed the formation of shear bands in all three concentric zones of shock metamorphism. This is the first report of shear bands formation in iron meteorites in a laboratory shock experiment.
4. Shear bands in iron meteorites can form starting from a shock stage of 30–40 GPa. No shear bands are observed in unshocked Chinga iron meteorite, and therefore natural shock stage of Chinga did not exceed 30 GPa. This is the first published estimate of the natural shock stage of Chinga ataxite. At the same time, shock-induced heating of Chinga in natural environment never exceeded 550 °C, as evidenced by the presence of a small amount of tetrataenite.
5. No systematic changes are observed in the magnetic hardness of the samples as expressed by remanent coercivity B_{cr}, which experienced peak shock pressures of 30–60 GPa and shock-induced temperatures up to 475 °C. However, in zone I, there is an abrupt decrease in B_{cr}, which we explain by the temperature-induced tetrataenite-to-taenite disorder, in line with shock-induced temperatures in this zone over 550 °C.
6. Shock to > 45 GPa dramatically affected the sensitivity of remanent magnetization to hydrostatic load up to 1.8 GPa. Pressure demagnetization degree is only 4% for the original (unshocked) Chinga sample, 6% for the shocked sample from the periphery (the edge of zone III), and 57–74% for the samples from zones I and II. Such difference evidences the profound changes due to shock and may be related to the effect of shock-induced annealing of defects, which promotes displacement of domain walls as a result of hydrostatic pressure application.

Acknowledgements This work is conducted under the GEOKHI RAS state assignment. NSB benefited from a U.S. National Science Foundation IRM Visiting Fellowship, which helped to fund her stay at the IRM. NSB is grateful to Pierre Rochette and Jerome Gattacceca for helpful discussions. We thank Edivaldo Dos Santos (Filho Instituto de Ciência e Tecnologia—ICT/UFVJM, Rio de Janeiro, Brazil) and anonymous reviewer for their reviews, which helped to improve the manuscript.

References

1. Gottwald, M., Kenkmann, T., Reimold, W.U.: Terrestrial impact structures. In: The TanDEM-X Atlas, 1st edn, p. 608. Pfeil Verlag, Munchen (2020)
2. Ivanov, B.A., Neukum, G., Wagner, R.: Size-frequency distributions of planetary impact craters and asteroids. In: Marov, M.Y., Rickman, H. (eds.) Collisional Processes in the Solar System. Astrophysics and Space Science Library, vol. 261, pp. 1–34. Springer, Dordrecht (2001)
3. Osinski, G.R., Pierazzo, E.: Impact cratering: processes and products. Hoboken, NJ, Wiley-Blackwell, Chicago, p. 336 (2012)
4. Bezaeva, N.S., Badjukov, D.D., Rochette, P., Gattacceca, J., Trukhin, V.I., Kozlov, E.A., Uehara, M.: Experimental shock metamorphism of the L4 ordinary chondrite Saratov induced by spherical shock waves up to 400 GPa. Meteorit. Planet. Sci. **45**(6), 1007–1020 (2010)
5. Kohout, T., Petrova, E.V., Yakovlev, G.A., Grokhovsky, V.I., Penttila, A., Maturilli, A., Moreau, J.-G., Berzin, S.V., Wasiljeff, J., Danilenko, I.A., Zamyatin, D.A., Muftakhetdinova, R.F., Heikkila, M.: Experimental constraints on the ordinary chondrite shock darkening caused by asteroid collisions. Astr. Astrophys. **639**, A146 (2020)

6. Cisowski, C.S., Dunn, J.R., Fuller, M., Rose, M.F., Wasilewski, P. J.: Impact processes and lunar magnetism. In: Proceedings of the Fifth Lunar Conference Suppl. 5, Geochim. Cosmochim. Acta 3, pp. 2841–2858 (1974)
7. Cisowski, S.M., Fuller, M.D., Wu, Y.M., Rose, M.F., Wasilewski, P.J.: Magnetic effects of shock and their implications for magnetism of lunar samples. In: Proceedings of the 6th Lunar Science Conference 3, New York, Pergamon Press, Inc., pp. 3123–3141 (1975)
8. Gattacceca, J., Boustie, M., Hood, L., Cuq-Lelandais, J.-P., Fuller, M., Bezaeva, N.S., De Resseguier, T., Berthe, L.: Can the lunar crust be magnetized by shock: experimental groundtruth. Earth Planet. Sci. Lett. **299**, 42–53 (2010)
9. Cisowski, S.M., Fuller, M.: The effect of shock on the magnetism of terrestrial rocks. J. Geophys. Res. **83**, 3441–3458 (1978)
10. Louzada, K.L., Stewart, S.T., Weiss, B.P., Gattacceca, J., Bezaeva, N.S.: Shock and static pressure demagnetization of pyrrhotite and implications for the Martian crust. Earth Planet. Sci. Lett. **290**(1–2), 90–101 (2010)
11. Bezaeva, N.S., Swanson-Hysell, N.L., Tikoo, S.M., Badyukov, D. D., Kars, M., Egli, R., Chareev, D.A., Fairchild, L.M., Khakhalova, E., Strauss, B.E., Lindquist, A.K.: The effects of 10 to >160 GPa shock on the magnetic properties of basalt and diabase. Geochem. Geophys. Geosyst. **17**, 4753–4771 (2016)
12. Badyukov, D.D., Bezaeva, N.S., Rochette, P., Gattacceca, J., Feinberg, J.M., Kars, M., Egli, R., Raitala, J., Kuzina, D.M.: Experimental shock metamorphism of terrestrial basalts: agglutinate-like particle formation, petrology and magnetism. Meteorit. Planet. Sci. **53**(1), 131–150 (2018)
13. Buchwald, V.F.: Handbook of Iron Meteorites, vols. 1; 2, pp. 125–136; 461–464. University of California Press, Berkeley (1975)
14. Sorokin, E.M.: Reduced Iron in the Regolith of the Moon: Review, Advances in Geochemistry, Analytical Chemistry, and Planetary Sciences: Special Publication Commemorating the 75th Anniversary of the Vernadsky Institute of Geochemistry and Analytical Chemistry of the Russian Academy of Sciences, Chapter 23 (in press)
15. Sorokin, E.M., Yakovleva, O.I., Slyuta, E.N., Gerasomiv, M.V., Zaitsev, M.A., Shcherbakov, V.D., Ryazantsev, K.M., Krasheninnikov, S.P.: Experimental modeling of a micrometeorite impact on the moon. Geochem. Int. **58**(2), 113–127 (2020)
16. Hornemann, U., Pohl, J., Bleil, U.: A compressed air gun accelerator for shock magnetization and demagnetization experiments up to 20 kbar. J. Geophys. **41**, 13–22 (1975)
17. Pohl, J., Bleil, U., Hornemann, U.: Shock magnetization and demagnetization of basalt by transient stress up to 10 kbar. J. Geophys. **41**, 23–41 (1975)
18. Martelli, G., Newton, G.: Hypervelocity cratering and impact magnetisation of basalt. Nature **269**, 478–480 (1977)
19. Srnka, L.J., Martelli, G., Newton, G., Cisowski, S.M., Fuller, M. D., Schaal, R.B.: Magnetic field and shock effects and remanent magnetization in a hypervelocity impact experiments. Earth Planet. Sci. Lett. **42**, 127–137 (1979)
20. Dickinson, T.L., Wasilewski, P.: Shock magnetism in fine particle iron. Meteorit. Planet. Sci. **35**, 65–74 (2000)
21. Louzada, K.L., Stewart, S.T., Weiss, B.P.: Effect of shock on the magnetic properties of pyrrhotite, the Martian crust, and meteorites. Geophys. Res. Lett. **34**, L05204 (2007)
22. Hargraves, R.B., Perkins, W.E.: Investigations of the effect of shock on natural remanent magnetism. J. Geophys. Res. **74**, 2576–2589 (1969)
23. Pesonen, L.J., Deutsch, A., Hornemann, U., Langenhorst, F.: Magnetic properties of diabase samples shocked experimentally in the 4.5–35 GPa range. In: Proc. 28th Lunar Planet. Sci. Conf., p. 1370, LPI, Houston (1997)
24. Gattacceca, J., Lamali, A., Rochette, P., Boustie, M., Berthe, L.: The effects of explosive-driven shocks on the natural remanent magnetization and the magnetic properties of rocks. Phys. Earth Planet. Inter. **162**, 85–98 (2007)
25. Kozlov, E.A., Sazonova, L.V.: Phase transformations of enstatite in spherical shock waves. Petrology **20**(4), 301–316 (2012)
26. Grady, M.M.: Catalogue of Meteorites, 5th edn. Cambridge University Press, Cambridge (2000)
27. Badyukov, D.D., Bezaeva, N.S.: Experimental shock metamorphism of the Chinga iron meteorite. Experim. Geosci. **24**(1), 9–12 (2018)
28. https://www.lpi.usra.edu/meteor/metbull.php?code=5353
29. Kozlov, E.A., Zhukov, A.V.: Phase transitions in spherical shock waves. In: Schmidt, S.C., Shaner, J.W., Samara, G.A., Ross, M. (eds.) High Pressure Science and Technology, pp. 977–980. New York, American Institute of Physics (1994)
30. Kozlov, E.A., Petrovtsev, A.V.: Cumulation of a spherically converging shock wave in metals and its dependence on elastic-plastic properties, phase transitions, spall and shear fractures. Int. J Model. Simul. Sci. Comp. **6**(1), 1550001 (2015)
31. Sadykov, R.A., Bezaeva, N.S., Rochette, P., Gattacceca, J., Axenov, S.N., Trukhin, V.I.: Nonmagnetic high-pressure cell for measurements weakly magnetic rock samples up to 2 GPa in a superconducting quantum interference device magnetometer. In: Proceedings of the 10th Conference on "Physical-Chemical and Petrophysical Researches in Earth's Sciences, (Geophysics Center RAS, 2009), pp. 305–306 (2009)
32. Sadykov, R.A., Bezaeva, N.S., Kharkovskiy, A.I., Rochette, P., Gattacceca, J., Trukhin, V.I.: Nonmagnetic high pressure cell for magnetic remanence measurements up to 1.5 GPa in a SQUID magnetometer. Rev. Sci. Instr. **79**, 115102 (2008)
33. Bezaeva, N.S., Gattacceca, J., Rochette, P., Sadykov, R.A., Trukhin, V.I.: Demagnetization of terrestrial and extraterrestrial rocks under hydrostatic pressure up to 1.2 GPa. Phys. Earth Planet. Int. **179**(1–2), 7–20 (2010)
34. Bezaeva, N.S., Chareev, D.A., Rochette, P., Kars, M., Gattacceca, J., Feinberg, J.M., Sadykov, R.A., Kuzina, D.M., Axenov, S.N.: Magnetic charecterization of non-ideal single-domain monoclinic pyrrhotite and its demagnetization under hydrostatic pressure up to 2 GPa with implications for impact demagnetization. Phys. Earth Planet. Int. **257**, 79–90 (2016)
35. Kirichenko, A.S., Kornilov, A.V., Pudalov, V.M.: Properties of polyethilsiloxane as a pressure-transmitting medium. Instrum. Exp. Tech. **48**(6), 813–816 (2005)
36. Nagata, T., Kinoshita, H.: Studies on piezo-magnetization (I). Magnetization of titaniferous magnetite under uniaxial compression. J. Geomagn. Geoelectr. **17**(2), 121–135 (1965)
37. Nagata, T.: Main characteristics of piezo-magnetization and their qualitative interpretation. J. Geomagn. Geoelectr. **18**, 81–97 (1966)
38. Kinoshita, H.: Studies on piezo-magnetization (III) PRM and relating phenomena. J. Geomagn. Geoelectr. **20**, 155–167 (1968)
39. Nagata, T., Funaki, M., Dunn, J.R.: Piezomagnetization of meteorites. Mem. Natl Inst. Polar Res. **25**, 251–259 (1982)
40. Bancroft, D., Peterson, E.L., Minshall, S.: Polymorphism of iron at high pressure. J. Appl. Phys. **27**, 291 (1956)
41. Sugiura, N., Strangway, D.W.: Magnetic studies of meteorites. In: Kerridge, J.F., Mathews, M.S. (eds.) Meteorites and the Early Solar System, pp. 595–615. The University of Arizona Press, Tucson (1988)
42. Gattacceca, J., Suavet, C., Rochette, P., Weiss, B.P., Winklhofer, M., Uehara, M., Friedrich, J.: Metal phases in ordinary chondrites:

magnetic hysteresis properties and implications for thermal history. Meteorit. Planet. Sci. **49**, 652–676 (2014)
43. Crangle, J., Hallam, G.C.: The magnetization of face-centered cubic and bodycentered cubic iron + nickel alloys reviewed. Proc. R Soc. Lond. A Math. Phys. Sci. **272**, 119–132 (1963)
44. Dos Santos, E., Gattacceca, J., Rochette, P., Scorzelli, R.B., Fillion, G.: Magnetic hysteresis properties and ^{57}Fe Mössbauer spectroscopy of iron and stony-iron meteorites: implications for mineralogy and thermal history. Phys. Earth Planet. Int. **242**, 50–64 (2015)
45. Oshtrakh, M.I., Grokhovsky, V.I., Abramova, N.V., Semionkin, V.A., Milder, O.B.: Iron–nickel alloy from iron meteorite Chinga studied by Mössbauer spectroscopy with high velocity resolution. Hyperfine Interact **190**, 135–142 (2009)
46. Bezaeva, N.S., Gattacceca, J., Rochette, P., Sadykov, R.A.: Demagnetization of ordinary chondrites under hydrostatic pressure up to 1.8 GPa. Geochem. Int. **60**(5), 421–429 (2022). https://doi.org/10.1134/S0016702922050032
47. D'Orazio, M., Folco, L., Zeoli, A., Cordier, C.: Gebel Kamil: The iron meteorite that formed the Kamil crater (Egypt). Meteorit. Planet. Sci. **46**(8), 1179–1196 (2011)
48. Dunlop, D., Özdemir, Ö.: Rock Magnetism: Fundamentals and Frontiers, pp. 573. Cambridge University Press, Cambridge (1997)

Thermodynamic Study of Fractional Evaporation of Refractory Meteorite Matter Melts Under Various Redox Conditions

S. I. Shornikov

1 Introduction

The refractory meteorite matter found in carbonaceous chondrites includes Ca–Al–inclusions (CAIs), amoeboid olivine aggregates (AOAs) and chondrules. CAIs consist mainly of refractory silicates, perovskite, and calcium and magnesium aluminates. AOAs consist mainly of olivine-forsterite with accessories, Al-diopside and spinel. Chondrules consist of iron-magnesian silicates (olivines and pyroxenes) in a fine-grained matrix. Neglecting the content of various minor components, the substance of CAIs, AOAs and chondrules can be described by chemical and mineral compositions within the framework of the CaO–MgO–FeO–Al_2O_3–TiO_2–SiO_2 oxide system. The detailed information describing various types of inclusions can be found in the reviews [1, 2]. Two main processes of formation of the refractory material and their components, can be distinguished in the evolution of meteoritic material—primary condensation and fractional evaporation.

The evaporation process is characterized by a change in the aggregate state of a matter—the transition from the condensed phase to the gas phase, including transition from the crystalline to gas phase (sublimation). As a rule [3, 4], the open evaporation of simple oxides (including simple oxides forming refractory inclusions in the crystalline and liquid phase (melt), occurs without changing of composition of the condensed phase (congruent evaporation). Evaporation of solutions of complex oxide compounds (melts and solid solutions) occurs with change in the condensed phase composition (incongruent evaporation), due to the different individual volatility of the components forming the solution. Typical temperature dependences of the volatility of simple oxides forming the refractory substance of meteorites are shown in Fig. 1. According to Konowalow [6], a compound in the crystalline phase can also be considered as a solution, sublimation of which occurs without significant change in the condensed phase composition and can probably be explained by the narrow range of the compound concentration compared to the concentration ranges of solid and liquid solutions.

Early experimental studies of phase equilibria in isolated systems of aqueous solutions of alcohols and organic acids and their gas phases, performed by the static method by Konowalow [7] and Wrewsky [8], allowed to formulate the basic laws of dependencies of the total pressure (tension) of vapor over a solution on the composition and temperature of the solution used for the thermodynamic characteristics of the evaporation process. The regularities established by Konowalow characterize changes of the total vapor pressure over a solution of double systems under isobaric and isothermal conditions, but the regularities formulated by Wrewsky characterize such changes for an established (constant) composition of the solution under varying pressure and temperature. Later, using the thermodynamic regulations obtained by Gibbs [9], these regularities were theoretically justified by Van der Waals [10] and Storonkin [11] and were extended for the case of multicomponent systems.

However, the mentioned experimental and theoretical studies of binary and multicomponent systems did not provide the presence of various molecular species in the gas phase that is typically for an oxide melt. The presence of oxygen in the gas phase over the oxide melt (mainly in atomic and molecular form) causes its possible interaction with the components of the external environment resulting to a change in the redox conditions of the evaporation process that was not previously considered.

The aim of the present study is the thermodynamic calculations of the fractional evaporation of the refractory meteorite matter melts, including Ca–Al–inclusions and their most important minerals—perovskite and forsterite. The

S. I. Shornikov (✉)
Vernadsky Institute of Geochemistry and Analytical Chemistry, Russian Academy of Sciences, 19 Kosygin St., Moscow, 119991, Russia
e-mail: sergey.shornikov@gmail.com

V. P. Kolotov and N. S. Bezaeva (eds.), *Advances in Geochemistry, Analytical Chemistry, and Planetary Sciences*,
https://doi.org/10.1007/978-3-031-09883-3_19

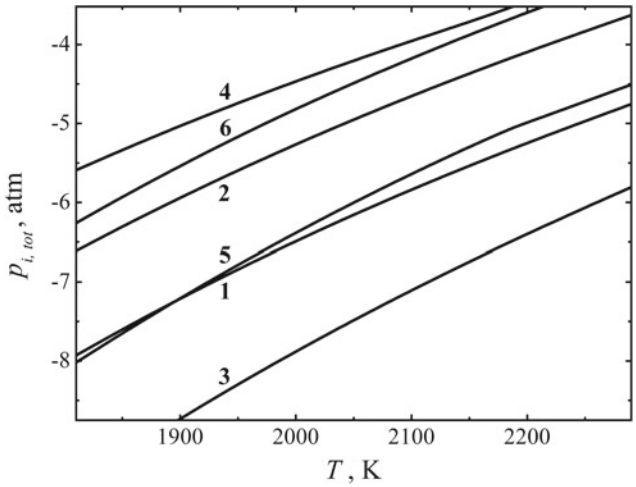

Fig. 1 The calculated temperature dependence of the volatility of simple oxides [5]: 1—CaO, 2—MgO, 3—Al_2O_3, 4—FeO, 5–TiO_2, 6—SiO_2

results of calculations taking into account the diversity of vapor species over the melt were compared with those performed within the framework of classical concepts (without taking into account the diversity of molecular forms above the melt). Special attention was paid to the influence of redox conditions on the fractional evaporation of the oxide melt.

Theoretical calculations were performed within the framework of the thermodynamic model described in detail earlier [12]. The model was based on the theory of ideal associated solutions providing the formation of stable compounds (associates) in the melt and the presence of pure components (monomers) which do not interact with each other. That made possible to describe a melt with significant mixing energy. The activity of the pure component in the melt is equal to the mole fraction of molecules not including in the compound. These values were calculated from finding the equilibrium conditions in the melt at a given composition and temperature by the Gibbs total energy minimization method. The initial data were the standard Gibbs energies for condensed phases and vapor species over the melt that approximately took into account the chemical interaction in the melt [13].

The few experimental thermodynamic data characterizing the fractional evaporation of refractory meteorite matter melts were considered in detail in the reviews [14, 15], as well as in our studies [16–20]. Limited information led to the choice of objects for theoretical study: perovskite [21–24], synthetic oxide samples of Solar composition [25, 26], Ap-16 68415,40 lunar basalt [27], the Krymka and Murchison chondrites and pyroxene chondrules of the Saratov chondrite [28–30], as well as synthetic analogues of CAIs [31–35].

A significant number of publications have been devoted to the study of the forsterite evaporation. However, only Hashimoto [36] and Davis et al. [37] studied the evaporation of its melt. Note, that the experiments of Davis et al. [37] performed in the temperature range 2023–2323 K were focused on isotopic fractionation of the forsterite melt, and the experiments performed by Hashimoto [36] in the same temperature range were limited by determining of the melt evaporation rate and did not consider its chemical fractionation. Nevertheless, Hashimoto [36] and other researchers [38, 39] claimed that the Mg_2SiO_4 melt evaporates congruently. At the same time, the increase in the silicon oxide content in the condensation products of evaporated forsterite observed in shock [40] and pulsed (using a laser) [41] experiments showed the predominant evaporation of silicon oxide from the forsterite melt corresponding to incongruent evaporation that was confirmed by the results of thermodynamic calculations [18].

The experimental results were obtained under vacuum conditions (no more than 10^{-9} atm) by two different approaches were considered to investigate redox conditions: (1) the study of the melt evaporation in vacuum furnaces (according to Langmuir) and (2) the study of melt evaporation from an effusion cell by the mass spectrometric method (according to Knudsen). In both experimental approaches the presence of a metal material (a vacuum furnace or an effusion cell) led to reducing evaporation conditions but different from each other. The experimental and theoretical results obtained in various reducing evaporation conditions were compared with those calculated for the neutral evaporation conditions. The initial compositions of oxide melts are given in Table 1.

2 Calculation of Fractional Evaporation of Oxide Melt

Based on the Van't-Hoff isobar equation [44] for vapor species of the gas phase over an oxide melt, it was found [45] that the evaporation process of both complex oxide compounds and their melts can be represented as the transition of a condensed phase substance into a gas phase of the similar molecular composition:

$$[\mathrm{A}_i\mathrm{B}_j\mathrm{O}_k] = (\mathrm{A}_i\mathrm{B}_j\mathrm{O}_k), \quad (1)$$

dissociating subsequently in the simpler vapor species (up to atomic):

$$(\mathrm{A}_i\mathrm{B}_j\mathrm{O}_k) = (\mathrm{A}_i\mathrm{O}_{k-l}) + (\mathrm{B}_j\mathrm{O}_l) = i(\mathrm{A}) + j(\mathrm{B}) + k(\mathrm{O}), \quad (2)$$

and, at the same time, capable of polymerization:

$$n(\mathrm{A}_i\mathrm{O}_k) = (\mathrm{A}_{ni}\mathrm{O}_{nk}) \quad (3)$$

Table 1 Conditions and experimental results on the evaporation of perovskite, forsterite and CAIs melts

Melt composition, mol. %						T, K	Experimental approach	Material of cell, heater	Research results	References
CaO	MgO	FeO	Al_2O_3	TiO_2	SiO_2					
31.6–49.2	–	–	–	50.8–68.4	–	2278	I[a]	W	$x_i(t,T)$	Zhang et al. [21]
50.00	–	–	–	50.00	–	1791–2398	II[b]	Mo	p_i, a_i	Shornikov [22, 23]
6.8–62.1	–	–	–	37.9–93.2	–	2241–2441	II	Mo	p_i, a_i	Shornikov [24]
–	22.0–79.5	–	–	–	21.5–78.0	1973	II	Pt–Ir, Pt–Rh	a_i	Kambayashi and Kato [42, 43]
–	66.67	–	–	33.33	–	1873–2323	I	W	p_{tot}	Hashimoto [36], Davis et al. [37]
2.58	33.90	1.78	27.95	–	33.79	1973–2173	I	W	$x_i(t,T)$	Hashimoto [25]
19.44	7.26	18.72	3.98	0.25	50.35	1574–2502	II	Re	p_i, $x_i(t,T)$	Markova et al. [27]
1.95	36.50	1.47	20.71	0.07	39.31	1438–2378	II	Re	p_i, $x_i(t,T)$	Yakovlev et al. [28, 30]
6.51	47.47	2.35	5.15	–	38.52	1580–2156	II	Re	$x_i(t,T)$	Yakovlev et al. [29]
15.00	10.03	12.22	6.08	–	56.67	1749–2063	II	Re	$x_i(t,T)$	Yakovlev et al. [29]
2.20	34.82	1.76	10.31	0.07	50.83	1406–2147	II	Re	p_i, $x_i(t,T)$	Yakovlev et al. [30]
3.11	33.16	1.77	29.60	0.07	32.30	1500–2237	II	Re	p_i, $x_i(t,T)$	Yakovlev et al. [30]
2.08	35.15	29.18	1.38	0.08	32.13	1673–2273	I	W	$x_i(t,T)$	Wang et al. [26]
26.76	17.05	–	11.41	–	44.78	2173	I	W	$x_i(t,T)$	Richter et al. [31]
2.03	63.49	–	1.40	–	33.08	2173	I	W	$x_i(t,T)$	Mendybaev et al. [32]
12.94	44.39	–	8.06	–	34.61	2173	I	W	$x_i(t,T)$	Mendybaev et al. [32]
8.68	45.52	–	7.35	–	38.45	2173	I	W	$x_i(t,T)$	Mendybaev et al. [33]
23.41	23.88	–	16.44	–	36.27	2173	I	W	$x_i(t,T)$	Mendybaev et al. [34]
14.43	25.60	–	23.83	–	36.14	2173	I	W	$x_i(t,T)$	Ivanova et al. [35]

Note
[a]I—studies using vacuum furnaces (according to Langmuir)
[b]II—effusion mass spectrometric method (according to Knudsen)

(here and further, the gas phase is indicated by parentheses brackets, square—condensed).

In the case of high-temperature evaporation of compounds and melts in the CaO–MgO–FeO–Al_2O_3–TiO_2–SiO_2 system, dissociation processes are significant: the content of $(A_iB_jO_k)$ complex vapor species in the gas phase is very small (no more than 0.1 mol. %) and the content of simple molecules is small too. Their content in the gas phase over simple oxides at 2300 K are following: CaO (0.63 mol. %), MgO (5.10 mol. %), FeO (9.05 mol. %), Al_2O_3 (10^{-5} mol. %), SiO_2 (5.93 mol. %), except for gaseous TiO_2 (83.38 mol. %).

From the equilibria (2) and (3) it follows that the possible presence of excess oxygen in the environment or substance X, capable to forming oxide in the gas (or condensed) phase according to a typical reaction:

$$i[\mathrm{X}] + j(\mathrm{O}) = (\mathrm{X}_i\mathrm{O}_j), \tag{4}$$

will immediately result to increase or, conversely, to decrease in the oxygen content in the gas phase that will cause a change in the oxygen partial pressure over the melt and subsequent changes in the partial pressures of all vapor species (p_i) in equilibria (2) and (3). A change of the gas phase composition over the melt will lead to a change of the relative volatility of the oxide from the melt, and, accordingly, will cause a change of the fractionation process of the melt composition.

Based on classical concepts (not taking into account the complex gas phase composition over the melt), the melt fractionation can be calculated using the Hertz-Knudsen equation for the oxide evaporation rate (J) from the melt taking into account the Raoul-Henry law [46]:

$$J = \varphi a p^{\circ} / \sqrt{2\pi RTM}, \tag{5}$$

where φ, a, p°, M are the evaporation coefficient, activity, vapor pressure and molecular weight of the oxide, respectively. In the case of CaO–MgO–FeO–Al_2O_3–TiO_2–SiO_2 melt evaporation, the oxide evaporation coefficients are close to unity and they can be neglected in the relation (5) [47]. Note, it follows from the relation (5) that it is intended only

for calculating of the fractional melt evaporation under neutral conditions and does not allow to take into account the influence of redox conditions determined by the equilibria (2)–(4).

To account for the complex gas phase composition over the melt, the data on the equilibrium constants of reactions (1)–(4) and the oxide activities corresponding to a given melt composition should use to calculate the partial pressure of all vapor species and the total vapor pressure over the melt

$$p_{tot} = \sum_i p_i \tag{6}$$

(from the condition of the minimum value of p_{tot}, corresponding to the equilibrium), and also to determine the gas phase composition over it:

$$x_i = p_i / p_{tot}. \tag{7}$$

Since the content of complex and simple vapor species over the melt is insignificant, the vapor pressure of the oxide in the melt can be approximately calculated from the partial pressure of the dominant vapor specie corresponding to this oxide by the relation:

$$p \approx p_d / x_d^\circ, \tag{8}$$

where x_d° is the dominant vapor specie content over a pure oxide. Their values are: Ca (54.81 mol. %), Mg (58.73 mol. %), Fe (57.41 mol. %), Al (29.72 mol. %), SiO (59.80 mol. %) and TiO_2 (83.38 mol. %) at 2300 K.

Then the melt fractionation can be calculated by an equation similar to the relation (5):

$$J = \varphi p / \sqrt{2\pi RTM}. \tag{9}$$

Formally, the Eqs. (5) and (9) are identical if we do not take into account the differences of redox conditions of the evaporation of a pure oxide and the same oxide from the melt, that is due to the difference in the oxygen vapor partial pressures.

3 Fractional Evaporation of Perovskite

Perovskite $CaTiO_3$ is the only congruently melting compound at 2241 ± 10 K in the CaO–TiO_2 system [23]. The CaO–TiO_2 phase diagram in the perovskite region [48] and the oxide activities in melts at 2278 K determined experimentally by the Knudsen mass spectrometric effusion method [24] and calculated in [17] are shown in Fig. 2.

It was shown [22, 23] that the perovskite melt evaporated as a gaseous ($CaTiO_3$) by reaction (10), dissociating by reaction (11) to gaseous (CaO) and (TiO_2) which subsequently dissociate by reactions (12)–(17) presented in Table 2.

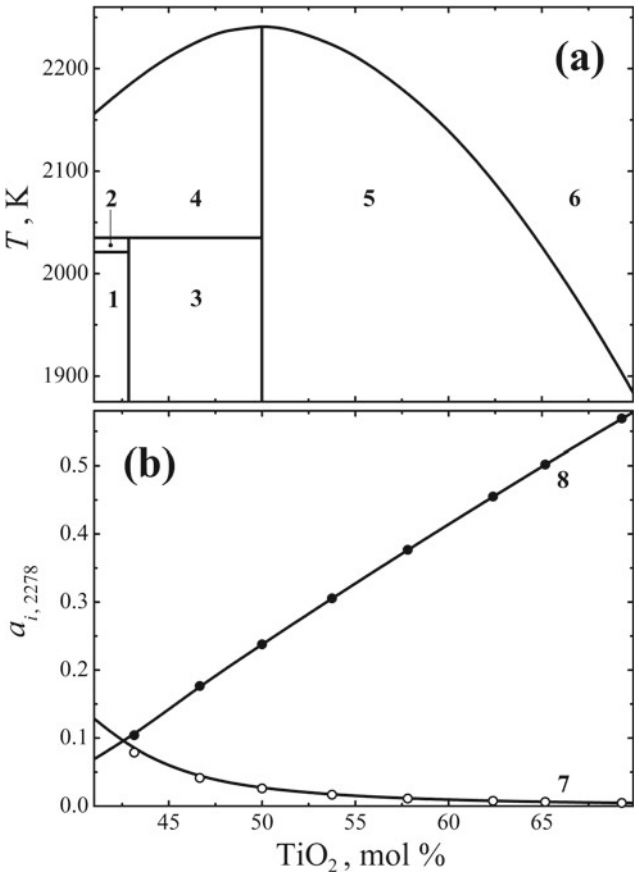

Fig. 2 The phase diagram of the CaO–TiO_2 system [48] in the perovskite field (1—$Ca_3Ti_2O_7$ + $Ca_4Ti_3O_{10}$; 2—$Ca_4Ti_3O_{10}$ + liquid; 3—$Ca_4Ti_3O_{10}$ + $CaTiO_3$; 4, 5—$CaTiO_3$ + 6—liquid) and the activities of CaO (7) and TiO_2 (8) in the CaO–TiO_2 melts determined by mass spectrometric method [24] (symbols) and calculated in [17] (lines) at 2278 K

The vapor pressures of the perovskite melt components (calcium and titanium oxides) are 1.514×10^{-5} and 2.702×10^{-5} atm, respectively, at 2278 K [5, 49]. Based on these data, the perovskite melt fractional evaporation under neutral conditions (without taking into account the complex composition of the gas phase over the melt) was calculated by the Eq. (5): the melt loses titanium oxide to a concentration of 41.25 mol. % TiO_2 (Fig. 3, line 1) and then congruently evaporates. The results of calculations based on relations (8) and (9) taking into account the gas phase complex composition over the melt were close: a decrease of titanium oxide to a concentration of 44.83 mol. % TiO_2 followed by congruent evaporation (Fig. 3, line 2).

However, in the case of melt evaporation under reducing conditions—from a molybdenum effusion cell (Fig. 3, line 3) and in a vacuum furnace with a tungsten heater (Fig. 3, line 4), the results of calculations and experiments are fundamentally different from the case of evaporation under neutral conditions (Fig. 3, lines 1 and 2): the melt

evaporation occurs with increase of titanium oxide to concentrations of 55.18 and 68.30 mol. % TiO_2 (Fig. 3, lines 3 and 4), respectively, with the residual melt weight loss exceeding 80 wt. %.

The observed differences in the perovskite melt fractional evaporation are due to the typical reactions (4) with the molybdenum effusion cell resulting to the formation of (Mo_iO_j) gaseous oxides according to reactions (18)–(20) (Table 2). In another case—by the reactions with the tungsten heater of vacuum furnace with the possible formation of (W_iO_j) gaseous oxides. The presence of [WO_3] condensate from 0.06 to 0.6 wt. % in the residues of non-evaporated CaO–MgO–FeO–Al_2O_3–TiO_2–SiO_2 melt was found in similar experiments of Wang et al. [26] using the same equipment as Zhang et al. [21]. It indicates the reaction (21) characterizing similar interactions with the heater material.

The observed fundamental change in the fractional evaporation trend is explained by the dependences of the gas phase composition over the perovskite melt (Fig. 4) and over the CaO–TiO_2 melts (Fig. 5) from the oxygen content characterizing the reduction conditions. In the case of neutral conditions of melt evaporation, the predominant component of the gas phase is (TiO_2), as can be seen in Fig. 4 and 5a (line 3). It leads to increase in calcium oxide in the melt. Under reducing conditions, the predominant component is (Ca), evaporation of which leads to increase of titanium oxide in the melt (Fig. 4 and 5b, line 1). The behavior of (TiO) in the composition of the gas phase over perovskite (Fig. 4, line 2) is interesting—it is antibate with respect to (TiO_2) (Fig. 4, line 3) and, accordingly, symbate with respect to the atomic (Ca) (Fig. 4, line 1) that is due to the equilibrium constant of the dissociation reaction (13).

Note, that the results of the theoretical calculations of the oxide activities in the CaO–TiO_2 melts, perovskite evaporation trends, partial pressures and the composition of the gas phase over the melts, presented by the lines in Figs. 2b, 3, 4 and 5b, satisfactorily correspond to the experimental values [21, 22, 24] that indicates their correctness.

4 Fractional Evaporation of Forsterite

Forsterite Mg_2SiO_4 is the only congruently melting compound at a temperature of 2171 ± 11 K in the MgO–SiO_2 system [51]. The MgO–SiO_2 phase diagram in the forsterite region [52] and the oxide activities in melts at 2173 K calculated by Shornikov [16] based on the experimental data obtained by the Knudsen effusion mass spectrometric method [42, 43], are shown in Fig. 6.

In the case of forsterite evaporation, we assume, as before, the typical reactions (1)–(3) forming gaseous forsterite (Mg_2SiO_4) dissociating into oxides (MgO) and (SiO_2). Their dissociation forms the gas phase over the melt, which is in equilibrium (17), (22)–(25), listed in Table 2.

Table 2 The reaction equilibrium constant values used in calculations [5, 22, 23, 49, 50]

Reaction		Reaction equilibrium constant	$K_{r_i,2173}$	$K_{r_i,2278}$
[$CaTiO_3$] = ($CaTiO_3$)	(10)	$K_{10} = p_{CaTiO_3}/a_{CaTiO_3}$	–	7.267×10^{-9}
($CaTiO_3$) = (CaO) + (TiO_2)	(11)	$K_{11} = p_{CaO}p_{TiO_2}/p_{CaTiO_3}$	–	2.372×10^{-6}
(CaO) = (Ca) + (O)	(12)	$K_{12} = p_{Ca}p_O/p_{CaO}$	–	3.573×10^{-4}
(TiO_2) = (TiO) + (O)	(13)	$K_{13} = p_{TiO}p_O/p_{TiO_2}$	–	1.917×10^{-7}
(TiO) = (Ti) + (O)	(14)	$K_{14} = p_{Ti}p_O/p_{TiO}$	–	5.351×10^{-10}
2(TiO_2) = (Ti_2O_4)	(15)	$K_{15} = p_{Ti_2O_4}/p^2_{TiO_2}$	–	3.197×10^{-3}
(Ti_2O_4) = (Ti_2O_3) + (O)	(16)	$K_{16} = p_{Ti_2O_3}p_O/p_{Ti_2O_4}$	–	2.092×10^{-8}
(O_2) = 2(O)	(17)	$K_{17} = p^2_O/p_{O_2}$	5.102×10^{-6}	1.872×10^{-5}
[Mo] + (O) = (MoO)	(18)	$K_{18} = p_{MoO}/a_{Mo}p_O$	3.955×10^{-1}	4.920×10^{-1}
[Mo] + 2(O) = (MoO_2)	(19)	$K_{19} = p_{MoO_2}/a_{Mo}p^2_O$	1.848×10^{7}	4.637×10^{6}
[Mo] + 3(O) = (MoO_3)	(20)	$K_{20} = p_{MoO_3}/a_{Mo}p^3_O$	2.605×10^{13}	1.436×10^{12}
[W] + 3(O) = [WO_3]	(21)	$K_{21} = a_{WO_3}/a_W p^3_O$	1.234×10^{16}	2.895×10^{14}
(MgO) = (Mg) + (O)	(22)	$K_{22} = p_{Mg}p_O/p_{MgO}$	1.657×10^{-4}	–
(SiO_2) = (SiO) + (O)	(23)	$K_{23} = p_{SiO}p_O/p_{SiO_2}$	1.705×10^{-4}	–
(SiO) = (Si) + (O)	(24)	$K_{24} = p_{Si}p_O/p_{SiO}$	3.038×10^{-13}	–
2(SiO) = (Si_2O_2)	(25)	$K_{25} = p_{Si_2O_2}/p^2_{SiO}$	5.345×10^{-1}	–

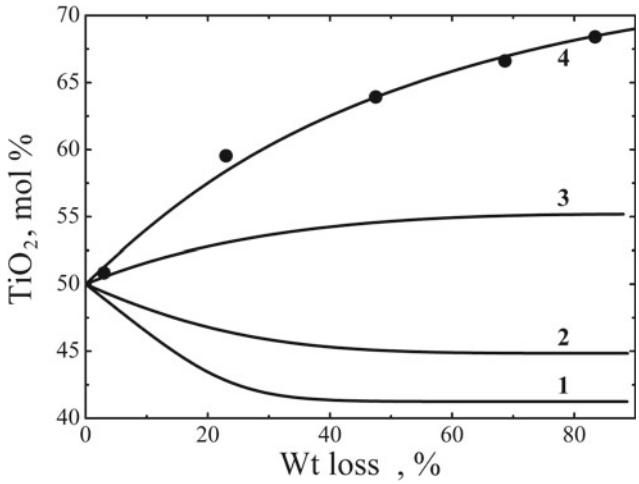

Fig. 3 The perovskite melt fractionation during evaporation at 2278 K, determined experimentally [21] (symbols) and calculated (lines) for neutral conditions without taking into account (1) and taking into account (2) the complex gas phase composition over the melt, and for the melt evaporation under reducing conditions from a molybdenum effusion cell (3) and in a vacuum furnace with a tungsten heater (4)

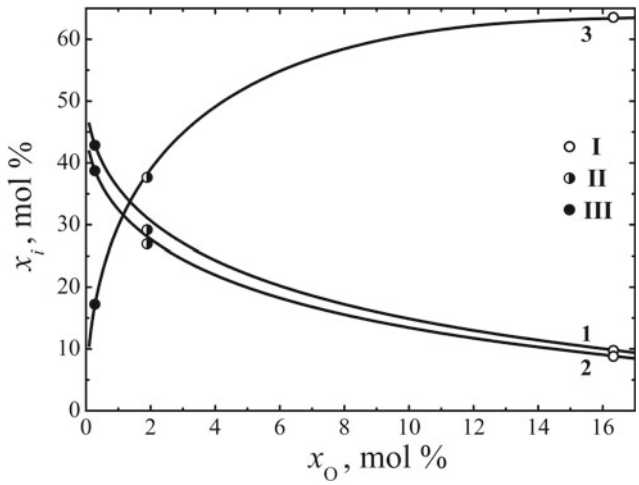

Fig. 4 The gas phase composition over the perovskite melt *vs*. the atomic oxygen content at 2278 K under neutral (I) and reducing conditions during evaporation of $CaTiO_3$ from a molybdenum effusion container (II) and in a vacuum furnace with a tungsten heater (III): 1—Ca; 2—TiO; 3—TiO_2

Based on the vapor pressures of the forsterite melt components—MgO and SiO_2, equal to 5.831×10^{-5} and 2.771×10^{-4} atm at 2173 K [5, 50], respectively, the forsterite melt fractional evaporation under neutral conditions (excluding the gas phase complex composition over the melt) was calculated by the Eq. (5). As can be seen from Fig. 7 (line 1), the melt loses an insignificant amount of magnesium oxide (up to a concentration of 65.56 mol. % MgO) and then congruently evaporates. The results of calculations based on relations (8) and (9), taking into account the gas phase

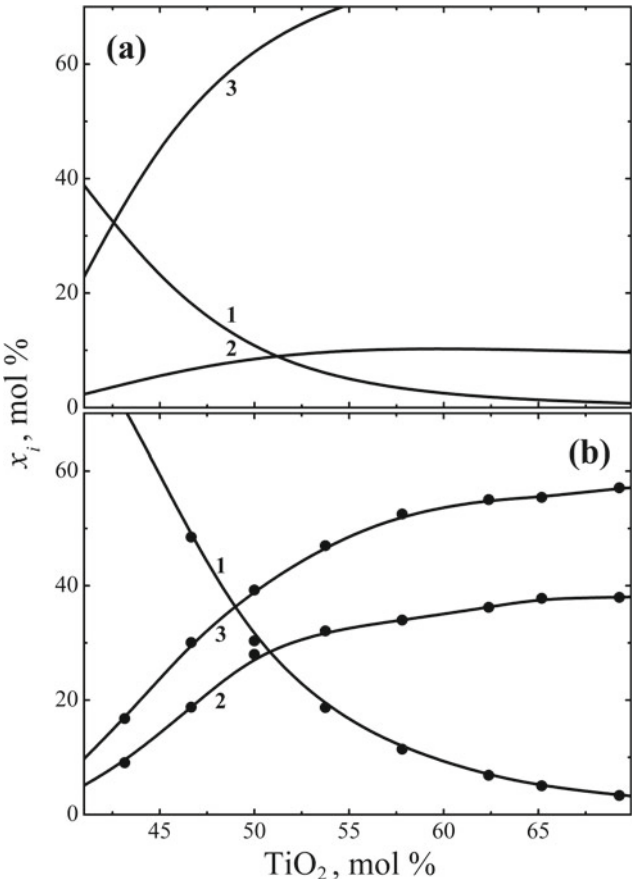

Fig. 5 The gas phase composition over the CaO–TiO_2 melts at 2278 K in neutral (**a**) and reducing (**b**) evaporation conditions (from a molybdenum effusion cell), determined experimentally [24] (symbols) and calculated in [17] (lines): 1—Ca; 2—TiO; 3—TiO_2

complex composition over the melt were differed slightly, although they indicated the predominant evaporation of silicon oxide from the melt to a concentration of 67.20 mol. % of MgO evaporating congruently (Fig. 7, line 2).

The coincidence of the calculation results of forsterite melt fractional evaporation under neutral and reducing conditions corresponding to the melt evaporation from the molybdenum effusion cell (Fig. 7, line 3) was interesting. The detected coincidence, as well as in the case of perovskite melt evaporation, could be due to changes in the gas phase composition over the forsterite melt (Fig. 8) and over the MgO–SiO_2 melts (Fig. 9) depending on the oxygen content in the gas phase.

It is easy to notice the coincidence of these tendencies for the forsterite melt: (Mg) and (SiO) (Fig. 8, lines 1 and 3), as well as (MgO) and (SiO_2) (Fig. 8, lines 2 and 4) with a slight advantage (SiO), that determines the fractionation trend during forsterite melt evaporation to the periclase field (Fig. 7, line 3). It should be noted the symbate behavior of (Mg) and (SiO) contents in neutral (Fig. 9, lines 1 and 3) and reducing (Fig. 9, lines 2 and 4) conditions of the MgO–SiO_2

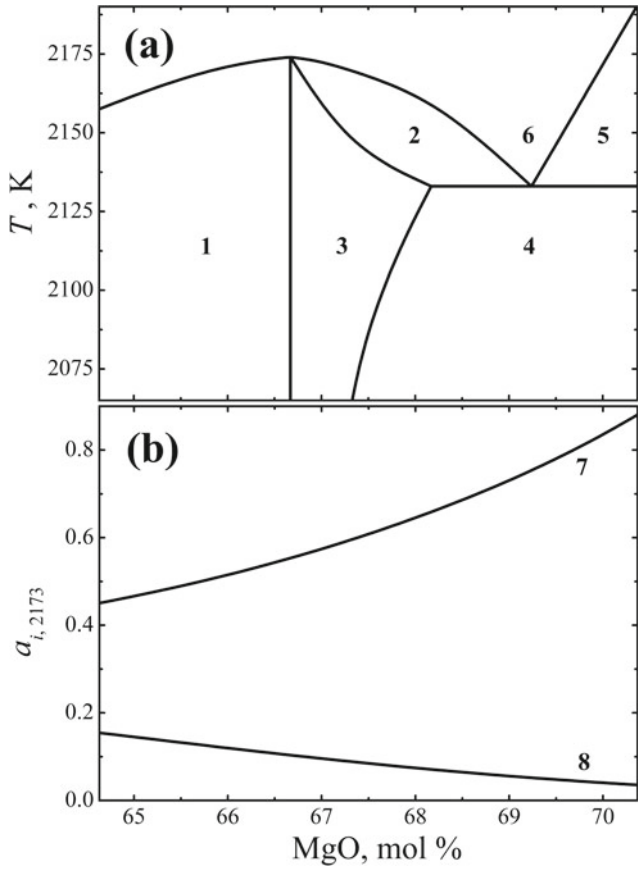

Fig. 6 The phase diagram of the MgO–SiO_2 system [52] in the forsterite region (1, 2—Mg_2SiO_4 + liquid; 3—Mg_2SiO_4 (solid solution); 4—Mg_2SiO_4 + MgO; 5—MgO + liquid; 6—liquid) and the activities of MgO (7) and SiO_2 (8) in the MgO–SiO_2 melts calculated at 2173 K [16]

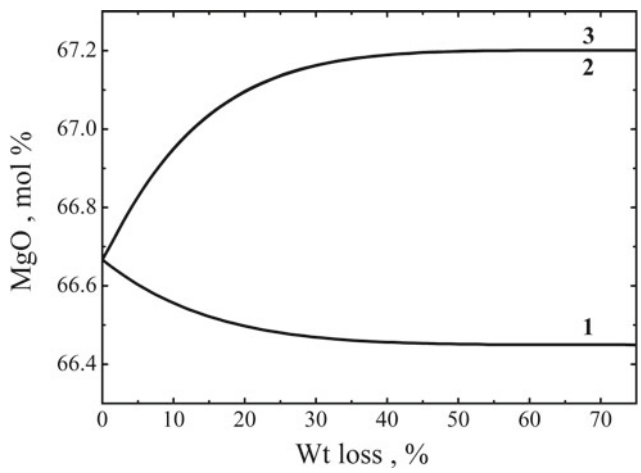

Fig. 7 The fractional evaporation of the forsterite melt at 2173 K, calculated for neutral conditions without taking into account (1) and taking into account (2) the complex gas phase composition over the melt, including for the melt evaporation under reducing conditions (from a molybdenum effusion cell) (3)

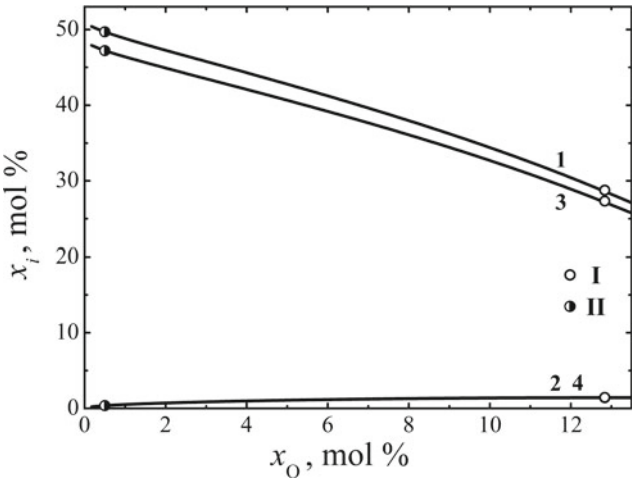

Fig. 8 The gas phase composition over the forsterite melt *vs*. the atomic oxygen content at 2173 K (1—Mg; 2—MgO; 3—SiO; 4—SiO_2). The symbols correspond to the calculated values for neutral (I) and reducing (from molybdenum effusion cell) (II) evaporation conditions

melt evaporation (Fig. 9), that is fundamentally different from those for the CaO–TiO_2 melts (Fig. 5).

Thus, Hashimoto's statement [36] about the Mg_2SiO_4 melt congruent evaporation is almost true in the case of a temperature of 2173 K (slightly exceeding the forsterite melting point), since the difference in the initial and final compositions does not exceed 0.6 mol. %. However, this difference will increase with increasing temperature as follows from the studies [16, 40, 41].

5 Fractional Evaporation of Refractory Inclusions

The developed theoretical approach to the calculation of the fractional evaporation of the oxide melt, taking into account the diversity of the gas phase composition over the melt and various redox conditions during evaporation, was also applied to the refractory meteorite matter melts, including Ca–Al–inclusions.

The influence of reducing conditions on the oxide melts evaporation on the example of the CaO–MgO–FeO–Al_2O_3–SiO_2 melts has already been considered earlier [53]. It was shown that the evaporation of these multicomponent oxide melts occurs mainly by the simple oxide evaporation reactions, since the content of complex gaseous oxide compounds is insignificant. Therefore, the evaporation of these melts in the first approximation can be explained on the basis of the studied regularities of evaporation of simple oxides.

As follows from the experimental results presented in Figs. 10 and 11, changes of the condensed phase composition at high-temperature evaporation of lunar basalt [27],

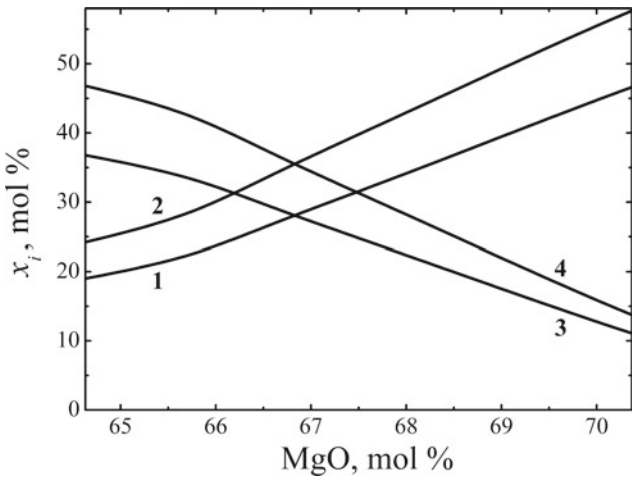

Fig. 9 The gas phase composition over the MgO–SiO_2 melt under neutral (1, 3) and reducing (2, 4) conditions of evaporation (from molybdenum effusion cell) at 2173 K (1, 2—Mg; 3, 4—SiO)

substance of Solar composition [26], the Krymka chondrite [28], chondrules of the Saratov chondrite [30], as well as various synthetic compositions corresponding to the compositions of refractory inclusions CAI B [31], CAI CMS–1 [33], CAI 4 [34] and CAI 5aN-3 [35] occur in the same way regardless of the initial composition of the oxide melt despite their apparent heterogeneity.

It was shown [54] that the evaporation of these melts the initial compositions of which are presented in Table 1, is characterized by a sequential loss of compounds formed by iron, magnesium, silicon and titanium oxides up to the compositions of the most refractory calcium aluminates, and up to the corundum region.

This observation can be illustrated in Fig. 12 showing the calculated contents of atomic and molecular oxygen in the gas phase over the residual melts of the chondrule of the Saratov chondrite depending on the Al_2O_3 content in the melt at 2000 K. The initial ratio of O/O_2 contents shows the predominance of molecular oxygen which is formed as a result of evaporation of the most volatile compounds mentioned above from the melt of silicates, spinel and perovskite. A sharp change in this ratio is associated with the end of their evaporation and the beginning of the predominant evaporation of the refractory component of the residual melt—calcium aluminates, for which the predominance of atomic oxygen in the gas phase over the melt is typical.

Thus, it seems appropriate to consider the ratio of O/O_2 contents in the gas phase over the oxide melt at evaporation depending on the evaporation parameters (temperature,

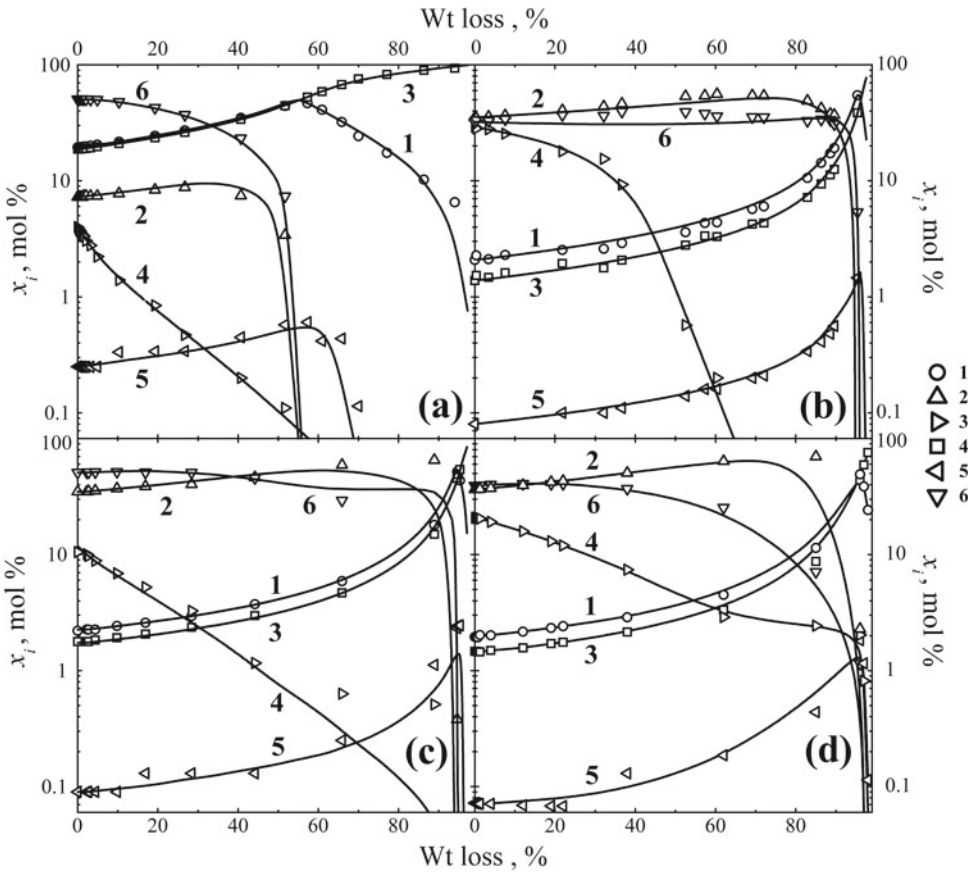

Fig. 10 Fractionation of melts of lunar basalt (**a**), substance of Solar composition (**b**), chondrule of the Saratov chondrite (**c**) and the Krymka chondrite (**d**) during evaporation at 2278 K, determined experimentally (symbols) by Markova et al. [27], Wang et al. [26], Yakovlev et al. [30] and Yakovlev et al. [28], respectively, and the calculated at present study (lines): 1—CaO; 2—MgO; 3—Al_2O_3; 4—FeO; 5—TiO_2; 6—SiO_2

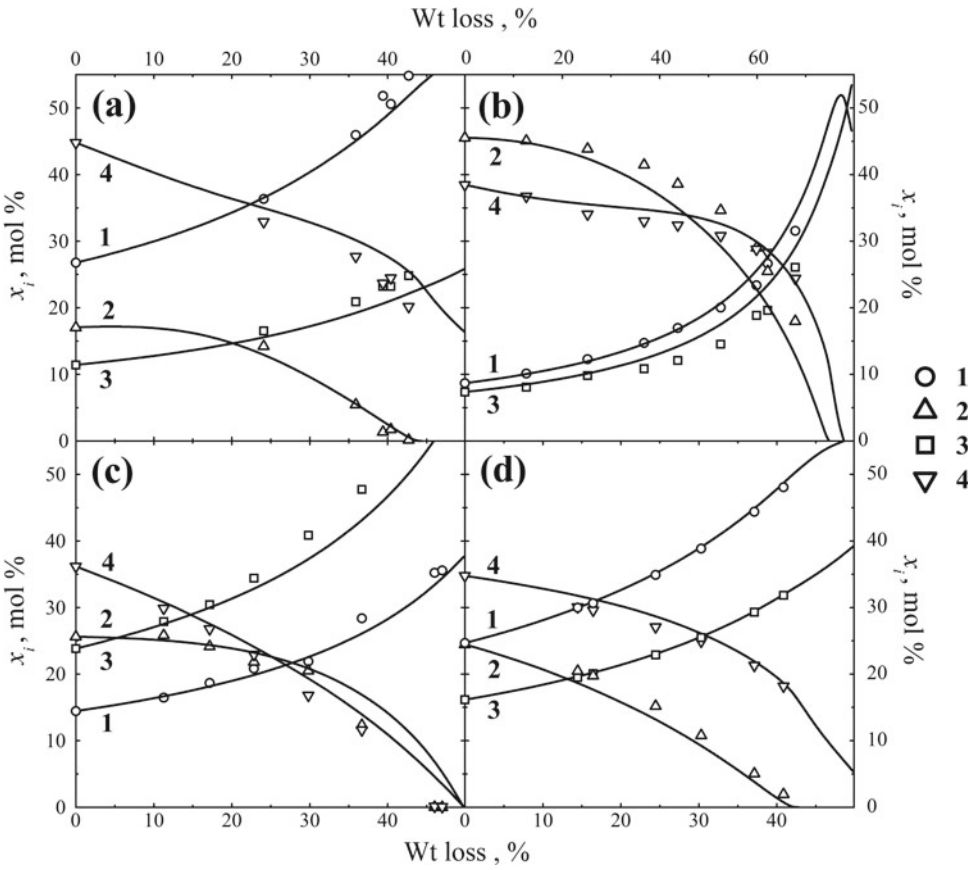

Fig. 11 Fractionation of melts of synthetic samples corresponding to CAI B (**a**), CAI CMS-1 (**b**) CAI 5aN–3 (**c**) and CAI 4 (**d**) during evaporation at 2173 K, determined experimentally (symbols) by Richter et al. [31], Mendybaev et al. [33], Ivanova et al. [35] and Mendybaev et al. [34], respectively, and calculated at present study (lines): 1—CaO; 2—MgO; 3—Al_2O_3; 4—SiO_2

weight loss of residual melt, content of the most refractory component in the residual melt). The O/O_2 ratio can characterize the fractionation of the oxide melt composition during evaporation. Figure 13 shows dependences of the partial pressures of atomic and molecular oxygen ratio over the oxide melts of various refractory meteorite matter including CAIs from the weight loss of the residual melt during evaporation at 2173 K. The initial stage of melt evaporation can be distinguished characterizing by a constant O/O_2 ratio in the gas phase over the melt (up to 40% weight loss of residual melts). Then this ration is sharply

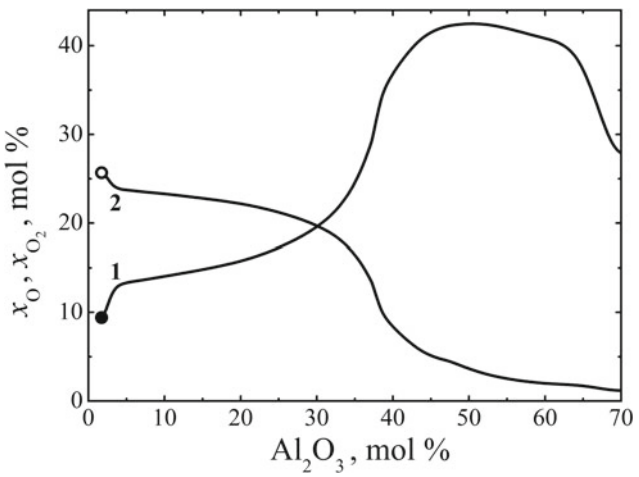

Fig. 12 The calculated atomic (1) and molecular (2) content of oxygen in the gas phase over the residual melt chondrules of Saratov chondrite vs. the Al_2O_3 content in the melt at 2000 K

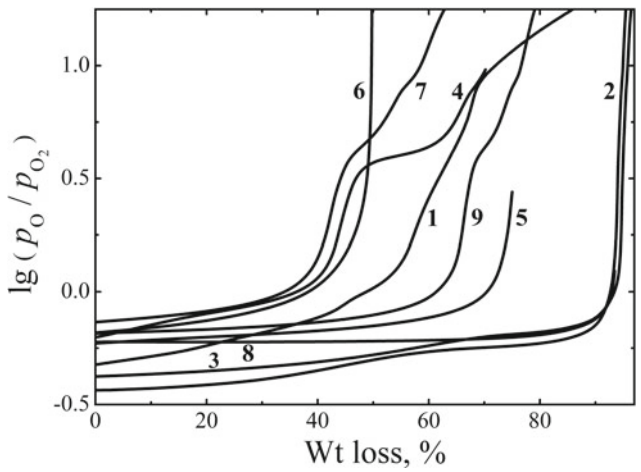

Fig. 13 The calculated ratio of partial pressures of atomic and molecular oxygen over the melts of lunar basalt (1), chondrules of the Saratov chondrite (2), the Krymka chondrite (3), CAI B (4) CAI CMS–1 (5), CAI 5aN–3 (6), CAI 4 (7), CAI FUN1 (8) and CAI FUN2 (9) during evaporation at 2173 K

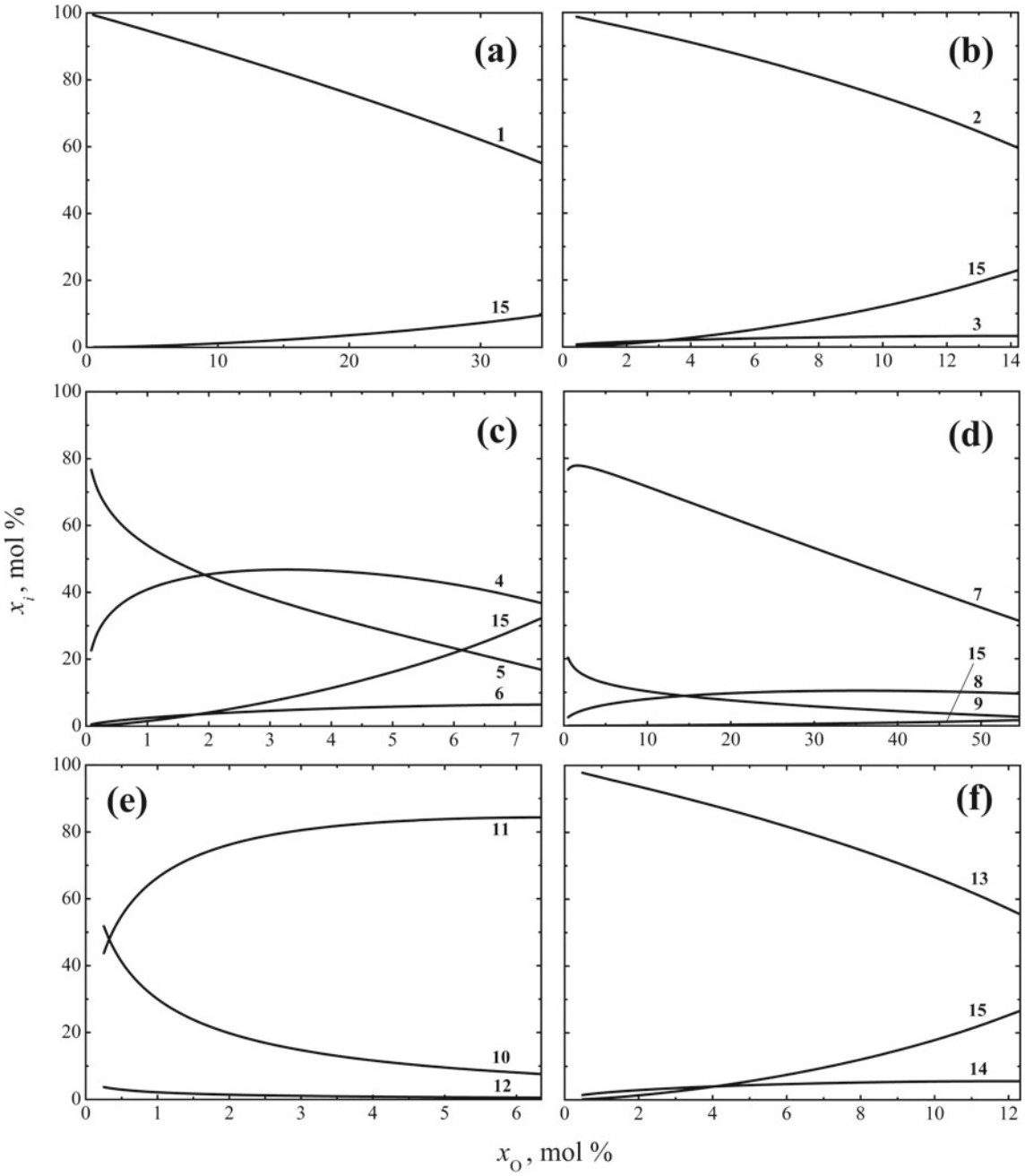

Fig. 14 The gas phase composition over the oxides of calcium (**a**), magnesium (**b**), iron (**c**), aluminum (**d**), titanium (**e**) and silicon (**f**) versus the atomic oxygen content in the gas phase over the oxides at 2200 K (1—Ca; 2—Mg; 3—MgO; 4—Fe; 5—Fe_2; 6—FeO; 7—Al; 8—AlO; 9—Al_2O; 10—TiO; 11—TiO_2; 12—Ti_2O_3; 13—SiO; 14—SiO_2; 15—O_2)

increased indicating the beginning of evaporation of refractory calcium aluminates.

It should be noted that the calculated changes in the condensed phase composition of all these multicomponent melts of lunar and meteoritic matter as well as CAIs analogues during evaporation satisfactorily coincide with the experimental values (Figs. 10 and 11), despite the fact that the calculations did not take into account the presence of reducing conditions at high-temperature experiments. In particular, the experiments performed by the Knudsen mass spectrometric effusion method by Yakovlev et al. [28–30] and Markova et al. [27] were carried out under conditions similar to neutral: the melt evaporation was carried out from a rhenium cell (Table 1), and studies by Wang et al. [26],

Richter et al. [31], Mendybaev et al. [32–34] and Ivanova et al. [20, 35] were conducted under extremely reducing conditions in a vacuum furnace with a tungsten heater.

The reason for such fractionation of the oxide melt composition is the symbate behavior of the vapor species belonging to different melt components (oxides), depending on the atomic (or molecular) oxygen content in the gas phase over the melt during evaporation. It was observed in the case of forsterite melt evaporation (Fig. 7, lines 2 and 3) and it is a characteristic of calcium, magnesium, iron, aluminum and silicon oxides (Fig. 14). The perovskite content in the multicomponent oxide melts is low (Table 1), therefore, the observed antibate of the titanium oxide behavior in perovskite (Fig. 4, line 3), which is also a characteristic of individual titanium oxide (Fig. 14e), cannot have a noticeable effect on the melt fractional evaporation.

6 Conclusions

Thus, based on the results of thermodynamic calculations of fractional evaporation of refractory meteorite matter performed without taking into account the complex gas phase composition over the oxide melt and taking into account the variety of vapor species of the gas phase and redox conditions of melt evaporation, we concluded:

1. Perovskite melt fractional evaporation largely depends on the presence of reducing conditions during evaporation. The melt fractional evaporation occurs to the calcium oxide field under neutral conditions and, on the contrary, to the titanium oxide field under reducing conditions. Neglect in thermodynamic calculations of fractional evaporation of the diversity of the gas phase composition over perovskite melt under reducing conditions leads to a discrepancy with experimental data.
2. The forsterite melt fractionation during evaporation is insignificant and practically does not depend on the redox conditions of evaporation when temperature is slightly exceeding its melting point. The absence of significant melt fractional evaporation can be explained by the observed symbatic dependence of the content of vapor species belonging to various oxides *vs*. the oxygen content.
3. Discovered symbateness in the behavior of the vapor species of different origin over the forsterite melt appears to be typical for other CaO–MgO–FeO–Al_2O_3–SiO_2 compounds and melts that explains the absence of differences in the results of calculations of fractional evaporation of melts under neutral conditions and experimental data obtained under neutral and reducing evaporation conditions. The presence of titanium oxide in the melt, which is characterized by an antibate dependence, does not have a noticeable effect on the melt fractional evaporation due to its low content.
4. The ratio of atomic and molecular oxygen contents in the gas phase over the oxide melt is a parameter characterizing the residual melt composition in evaporation process.
5. The results obtained within the framework of the developed thermodynamic approach which makes it possible to calculate the fractional evaporation of refractory meteorite matter melts including CAIs, satisfactorily correspond to the available experimental data that indicates their correctness.

Acknowledgements The author is grateful to O. I. Yakovlev (Vernadsky Institute of Geochemistry & Analytical Chemistry, Russian Academy of Sciences) for his constant attention and useful comments, and to M. A. Ivanova (Vernadsky Institute of Geochemistry & Analytical Chemistry, Russian Academy of Sciences) for her continued help.

References

1. MacPherson, G.J.: Calcium-aluminum-rich inclusions in chondritic meteorites. Met. Cosmochem. Process **2**, 139–179 (2014)
2. Ivanova, M.A.: Ca–Al–rich inclusions in carbonaceous chondrites: the oldest solar system objects. Geochem. Int. **54**(5), 387–402 (2016)
3. Kulikov, I.S.: Thermodynamics of Oxides. Metallurgiya, Moscow (1986).[in Russian]
4. Kazenas, E.K., Tsvetkov, Y.V.: Evaporation of Oxides. Nauka, Moscow (1997).[in Russian]
5. Glushko, V.P., Gurvich, L.V., Bergman, G.A., Veits, I.V., Medvedev, V.A., Khachkuruzov, G.A., Youngman, V.S.: Thermodynamic Properties of Individual Substances. Nauka, Moscow (1978–1982) [in Russian].
6. Konowalow, D.P.: On the vapor tensions of solutions. J. Russ. Phys.-Chem. Soc. **16**(1), 11–84 (1884) [in Russian]
7. Konowalow, D.P.: Ueber die dampfspannunqen der flussigkeitsgemische. Ann. Phys. **250**(9), 34–52; (10), 219–226 (1881)
8. Wrewsky, M.S.: On the composition and vapor tensions of solutions. J. Russ. Phys.-Chem. Soc. **43**(8), 1446–1457 (1911) [in Russian]
9. Gibbs, J.W.: On the equilibrium of heterogeneous substances. Trans. Connecticut Arts & Sci. **3**, 108–248, 343–524 (1874)
10. Van der Waals, J.D., Kohnstamm, P.: Lehrbuch der thermostatik: das heisst des thermischen gleichgewichts materieller systeme. 1. Allgemeine thermostatik. Barth, Leipzig (1927)
11. Storonkin, A.V.: On the conclusions and limits of applicability of the laws of M. S. Wrewsky. In: Works on the Theory of Solutions, pp. 311–334. AN USSR, Leningrad (1953) [in Russian]
12. Shornikov, S.I.: Thermodynamic modelling of evaporation processes of lunar and meteoritic substance. Geochem. Int. **57**(8), 865–872 (2019)

13. Prigogine, I., Defay, R.: Chemical Thermodynamics. Longmans, London (1954)
14. Davis, A.M., Richter, F.M.: Condensation and evaporation of Solar System materials. In: Treatise on Geochemistry, vol. 1, pp. 407–430. Elsevier Ltd, Oxford (2005)
15. Davis, A.M., Richter, F.M.: Condensation and evaporation of solar system materials. In: Treatise on Geochemistry, 2nd edn, vol. 1, pp. 335–360. Elsevier Ltd, Oxford (2014)
16. Shornikov, S.I.: Thermodynamic properties of $MgO–SiO_2$ melts. Exp. Geosci. **13**(1), 56–57 (2006)
17. Shornikov, S.I.: Thermodynamic properties of the $CaO–TiO_2$ melts. In: Proceedings of All-Russian Annual Seminar on Experimental Mineralogy, Petrology & Geochemistry, pp. 191–194. GEOKHI RAS, Moscow (2015) [in Russian]
18. Shornikov, S.I.: Thermodynamics of forsterite evaporation. Exp. Geosci. **22**(1), 12–14 (2016)
19. Shornikov, S.I.: Thermodynamics of perovskite: solid, liquid and gas phases. In: Perovskite & Piezoelectric Materials, pp. 115–138. IntechOpen, London (2021)
20. Ivanova, M.A., Mendybaev, R.A., Shornikov, S.I., Lorenz, C.A., MacPherson, G.J.: Modeling the evaporation of CAI–like melts, and constraining the origin of CH–CB CAIs. Geochim. Cosmochim. Acta **296**, 97–116 (2021)
21. Zhang, J., Huang, S., Davis, A.M., Dauphas, N., Hashimoto, A., Jacobsen, S.B.: Calcium and titanium isotopic fractionations during evaporation. Geochim. Cosmochim. Acta. **140**, 365–380 (2014)
22. Shornikov, S.I.: Mass spectrometric investigation of evaporation processes of perovskite. Russ. J. Phys. Chem. A **93**(6), 1024–1031 (2019)
23. Shornikov, S.I.: High temperature mass spectrometric study of thermodynamic properties of $CaTiO_3$ perovskite. Russ. J. Phys. Chem. A **93**(8), 1428–1434 (2019)
24. Shornikov, S.I.: Study of $CaO–TiO_2$ melts by Knudsen effusion mass spectrometry. Russ. J. Phys. Chem. A **94**(7), 1289–1299 (2020)
25. Hashimoto, A.: Evaporation metamorphism in the early solar nebula—evaporation experiments on the melt $FeO–MgO–SiO_2–CaO–Al_2O_3$ and chemical fractionations of primitive materials. Geochem. J. **17**(3), 111–145 (1983)
26. Wang, J., Davis, A.M., Clayton, R.N., Mayeda, T.K., Hashimoto, A.: Chemical and isotopic fractionation during the evaporation of the $FeO–MgO–SiO_2–CaO–Al_2O_3–TiO_2$ rare earth element melt system. Geochim. Cosmochim. Acta **65**(3), 479–494 (2001)
27. Markova, O.M., Yakovlev, O.I., Semenov, G.A., Belov, A.N.: Some general results of experiments on the evaporation of natural melts in the Knudsen cell. Geochem. Int. **23**(11), 1559–1569 (1986)
28. Yakovlev, O.I., Markova, O.M., Semenov, G.A., Belov, A.N.: Results of the experiment on the evaporation of Krymka chondrite. Meteoritika **43**, 125–133 (1984). [in Russian]
29. Yakovlev, O.I., Markova, O.M., Belov, A.N., Semenov, G.A.: On the formation of a metallic form of iron when heating chondrites. Meteoritika **46**, 104–118 (1987). [in Russian]
30. Yakovlev, O.I., Markova, O.M., Manzon, B.M.: The role of evaporation and dissipation processes in the formation of the Moon. Geochem. Int. **24**(4), 467–482 (1987)
31. Richter, F.M., Janney, P.E., Mendybaev, R.A., Davis, A.M., Wadhwa, M.: Elemental and isotopic fractionation of type B CAI-like liquids by evaporation. Geochim. Cosmochim. Acta **71** (22), 5544–5564 (2007)
32. Mendybaev, R.A., Richter, F.M., Bastian Georg, R., Janney, P.E., Spicuzza, M.J., Davis, A.M., Valley, J.W.: Experimental evaporation of Mg- and Si-rich melts: implications for the origin and evolution of FUN CAIs. Geochim. Cosmochim. Acta **123**, 368–384 (2013)
33. Mendybaev, R.A., Williams, C.D., Spicuzza, M.J., Richter, F.M., Valley, J.W., Fedkin, A.V., Wadhwa, M.: Thermal and chemical evolution in the early solar system as recorded by FUN CAIs: part II—laboratory evaporation of potential CMS–1 precursor material. Geochim. Cosmochim. Acta **201**, 49–64 (2017)
34. Mendybaev, R.A., Kamibayashi, M., Teng, F.-Z., Savage, P.S., Bastian Georg, R., Richter, F.M., Tachibana, S.: Experiments quantifying elemental and isotopic fractionations during evaporation of CAI-like melts in low-pressure hydrogen and in vacuum: constraints on thermal processing of CAIs in the protoplanetary disk. Geochim. Cosmochim. Acta **292**, 557–576 (2021)
35. Ivanova, M.A., Mendybaev, R.A., Shornikov, S.I., Ryazantsev, K. M., MacPherson, G.J.: Evaporation of spinel-rich CAIs melts: a possible link to CH–CB CAIs. In: 49th Lunar Planetary Science Conference Abs. #1965 (2018)
36. Hashimoto, A.: Evaporation kinetics of forsterite and implications for the early Solar nebula. Nature **347**(6288), 53–55 (1990)
37. Davis, A.M., Hashimoto, A., Clayton, R.N., Mayeda, T.K.: Isotope mass fractionation during evaporation of Mg_2SiO_4. Nature **347**(6294), 655–658 (1990)
38. Mysen, B.O., Kushiro, I.: Condensation, evaporation, melting, and crystallization in the primitive solar nebula: experimental data in the system $Mg_2SiO_4–SiO_2–H_2$ to 1.0×10^{-9} bar and 1870 °C with variable oxygen fugacity. Amer. Miner. **73**(1), 1–19 (1988)
39. Nagahara, H., Ozawa, K.: Mechanism of forsterite evaporation as inferred from surface microstructures. Proc. Japan Acad. B **75**(2), 29–34 (1999)
40. Yakovlev, O.I., Dikov, Y.P., Gerasimov, M.V.: Experimental study of shock and pulse evaporation of the ultrabasic substance. Geochem. Int. **33**(8), 1235–1247 (1995)
41. Dearnley, P.A., Anderson, K.: A preliminary evaluation of the potential of laser-beam heating for the production of high melting-point oxide coatings. J. Mater. Sci. **22**(2), 679–682 (1987)
42. Kambayashi, S., Kato, E.: A thermodynamic study of (magnesium oxide + silicon dioxide) by mass spectrometry. J. Chem. Thermodyn. **15**(6), 701–707 (1983)
43. Kambayashi, S., Kato, E.: A thermodynamic study of (magnesium oxide – silicon dioxide) by mass spectrometry at 1973 K. J. Chem. Thermodyn. **16**(2), 241–248 (1984)
44. Van't Hoff, J.H.: Etudes de dynamique chimique. Frederik Muller & Co., Amsterdam (1884)
45. Shornikov, S.I., Yakovlev, O.I.: Study of complex molecular species in the gas phase over the $CaO–MgO–Al_2O_3–TiO_2–SiO_2$ system. Geochem. Int. **53**(8), 690–699 (2015)
46. Yakovlev, O.I., Shornikov, S.I.: Chemical and isotopic fractionation of magnesium and silicon at evaporation of Ca–Al–inclusions of chondrites. Geochem. Int. **57**(8), 851–864 (2019)
47. Shornikov, S.I.: Vaporization coefficients of oxides contained in the melts of Ca–Al–inclusions. Geochem. Int. **53**(12), 1080–1089 (2015)
48. Gong, W., Wu, L., Navrotsky, A.: Combined experimental and computational investigation of thermodynamics and phase equilibria in the $CaO–TiO_2$ system. J. Amer. Ceram. Soc. **101**(3), 1361–1370 (2018)
49. Balducci, G., Gigli, G., Guido, M.: Identification and stability determinations for the gaseous titanium oxide molecules Ti_2O_3 and Ti_2O_4. J. Chem. Phys. **83**(4), 1913–1916 (1985)
50. Shornikov, S.I., Archakov, I.Yu., Shultz, M.M.: Mass spectrometric study of evaporation and thermodynamic properties of silica: III. Equilibrium reactions of molecules occurring in the gas phase over silica. Russ. J. Gener. Chem. **70**(3), 360–370 (2000)

51. Chase, M.W.: NIST-JANAF thermochemical tables. J. Phys. Chem. Ref. Data **9**, 1–1951 (1998)
52. Wu, P., Eriksson, G., Pelton, A.D., Blander, M.: Prediction of the thermodynamic properties and phase diagrams of silicate systems evaluation of the FeO–MgO–SiO_2 system. ISIJ Intern. **33**(1), 26–35 (1993)
53. Shornikov, S.I.: Effect of redox conditions on the evaporation of oxide melts in the CaO–MgO–FeO–Al_2O_3–SiO_2 system. Geochem. Int. **46**(7), 724–729 (2008)
54. Shornikov, S.I.: High temperature thermodynamic study of Ca–Al–inclusion's compound volatility. Exp. Geosci. **20**(1), 75–77 (2014)

Moon's Formation from Gas-Dust Cloud: New Geochemical and Astronomical Data

S. A. Voropaev

1 Introduction

The binary planetary system, the Earth and the Moon, is an unique formation in the Solar System. The gas giants Jupiter, Saturn and Neptune also have a system of satellites, but with an incomparably smaller mass. The features of the Moon's orbit, inclination and precession of its axis of rotation are also quite unusual. Since Laplace, the mystery of the Moon's origin has worried astronomers. The last, most popular hypothesis of megaimpact [1, 2], explained the origin of the Moon by the ejection of matter from the Earth's mantle during a catastrophic collision with a giant protosimal, about the size of Mars. Recently, arguments against this hypothesis have begun to accumulate, related both to the mechanics of the collision and to the isotopic geochemistry of lunar rocks. Taking this into account, academician Galimov E. M. during 2001–2020 at Vernadsky Institute RAS developed an alternative original model of the birth of the Moon and the Earth at the final stage of the collapse of a common protoplanetary cloud of gas and dust [3]. This model was confirmed by a number of numerical calculations by A. M. Krivtsov, Saint-Petersburg Technical University, using the method of particles interacting by the forces of attraction and repulsion with a potential of a certain type [4]. At a certain initial state of the cloud, the model predicted different times of planet formation (the Moon in 50 million years, the Earth in 120 million years), which was subsequently confirmed by isotope geochronology methods.

Detailed isotopy analysis of the Moon's rocks regarding the ratio of oxygen isotopes ($^{16}O/^{17}O/^{18}O$) demonstrated a close match with the Earth' one. However, the above ratios of oxygen isotopes are highly individual for different regions of the Solar system and are a recognized marker of the origin of matter. Meanwhile, detailed numerical studies of the dynamics of the process showed that the molten matter ejected into near-Earth orbit as a result of a megaimpact does not originate from the Earth's mantle but consists of 80% of the impactor matter [5, 6]. Since the origin and chemical composition of the impactor are unknown, this deprived the mega impact hypothesis of its main geochemical argument. In order to save the shock hypothesis, various assumptions were put forward, for example, that the substance which formed the Moon stayed in the atmosphere of the Earth's silicate vapor caused by the megaimpact. At the same time, the oxygen isotopic composition of the Moon and the Earth has supposedly rebalanced [7], which is unlikely. Another assumption was that the Earth and the impactor were formed in the same region of the Solar System, practically on the same orbit, and therefore had the same oxygen isotope composition inherent to this zone. One of the variants of this hypothesis is the accumulation of the material of the future impactor in the Lagrangian points [8]. However, numerical calculations of the three-body system Sun-Earth-Moon showed that the possibility of stable accumulation and residence in one of the Lagrange points of a body with a mass commensurate with the mass of the Earth is practically ruled out [9].

Another difficulty of the megaimpact hypothesis is related to the absence of traces of isotopic fractionation of elements lost in the form of volatiles. It is known that the Moon is depleted in volatiles compared to the Earth. From numerical calculations of the dynamics of the megaimpact, it follows that the material ejected into Earth orbit should have consisted of 10–20% melt and 80–90% steam [10]. It was shown experimentally that the isotopic compositions of K, Mg, and Si can change markedly during melt evaporation—within a few ppm [11, 12]. Under the process scenario adopted for the megaimpact, the process of evaporation and loss of volatiles should have been accompanied by a kinetic isotope effect [13]. Meanwhile, no shift in the isotopic composition, between the lunar and terrestrial matter, has

S. A. Voropaev (✉)
Vernadsky Institute of Geochemistry and Analytical Chemistry, Russian Academy of Sciences, 19 Kosygin St., Moscow, 119991, Russia
e-mail: voropaev@geokhi.ru

V. P. Kolotov and N. S. Bezaeva (eds.), *Advances in Geochemistry, Analytical Chemistry, and Planetary Sciences*,
https://doi.org/10.1007/978-3-031-09883-3_20

been detected. The explanation that the vapor loss occurred in the hydrodynamic regime [14] is not adequate, since the kinetic isotope effect occurs not only during gas dissipation, but also at the liquid-vapor interphase transition.

As a result of the analysis of all the above difficulties of the shock model, E. M. Galimov put forward the idea of formation of the Moon as a fragment of a double system, simultaneously with the Earth. At the same time it was emphasized that the early emergence and growth of solid bodies in the Solar system is beyond doubt. About it speaks all set of the meteorites studied and presented in a meteorite collection of Vernadsky Institute RAS. The assumption, on which Galimov E. M. relied was that probably different ways of evolution of the protoplanetary nebula were possible. Namely, in addition to solid-state accretion, local large-scale gas-dust clumps could nucleate and grow. This possibility has been considered in many works, starting from the work of Gurevich and Lebedinsky [14]. Back in the 70s, Eneev and Kozlov [15–17] made a numerical simulation of the formation of planets and satellite systems from the gas-dust state. Ruskol E. L. considered a model of the formation and growth of the Moon from a near-Earth satellite swarm during the accumulation of the Earth [18]. Zharkov V. N. paid great attention to the composition, internal structure and origin of the Moon in relation with other planets [19].

The emergence and evolution of clumps may have been related to the development of turbulence in the gas-dust disk [20]. Studies in this direction were continued in Vernadsky Institute RAS for a long time [21–23]. It was shown that the presence of gas in the thickening prevents its gravitational contraction. However, as the gas is blown out by the solar wind, there come conditions when the gravitational interaction is sufficient to compress the dust cloud. Compression of the particle cloud is accompanied by an adiabatic temperature rise. The solid particles are heated and partially vaporized. In the presence of sufficient angular momentum, the contracting dust cloud disintegrates into two, sometimes more, fragments. As a result, the bodies that became the proto-Earth and proto-Moon could be formed from the proto-planetary clump. Earth and the Moon, or rather their embryos, were formed in this case from a single source [24].

2 New Geochemical Data

2.1 Siderophile Elements at the Earth Mantle

To support the developed model Galimov E. M. considered some new geochemical mechanisms arising in collapsing gas-dust thickening. The main ones were the role of hydrogen, release and deposition of iron at heterogeneous accretion of the early Earth. It was assumed that the initial gas and dust for the Earth and the Moon had a composition close to the original proto planetary cloud. Chemically, the matter should be similar with the carbonaceous chondrites (CI). For instance, iron was contained in the reduced form as FeO, and the gas was represented by hydrogen, mainly. Hydrogen served both as a carrier gas, providing during compression of gas-dust thickening hydrodynamic removal of compounds and elements, released into gas phase, and as an effective reducing agent.

During the dust and gas cloud compression temperature in the centre was increased and evaporation of FeO became possible. It was pointed out that if the evaporation of FeO occurs incongruently, i.e., Fe + O_2 are present in the gas, hydrogen is bound with oxygen and iron as metal's nanoparticles is released. Early small Earth and Moon had low iron content, losing it in the form of FeO. But, after ongoing Earth's growth at an environment rich with hydrogen, the finely iron combined as metal's microparticles. When sticking together, large metal particles could be deposited in spite of gas flow towards the central part. So, initial Earth's core material began to form by the deposition of iron as metal's particles passing through the gas. The Moon retained residual iron mainly in the form of FeO, while the Earth, during further accretion, increased the metallic iron content and formed a massive core.

Starting the cloud compression, temperature inside was increased and this was followed by decomposition of FeO to Fe and O_2. Abundant hydrogen was bound with oxygen and iron as metal's nanoparticles was released. After ongoing Earth's growth at an reducing environment, the finely iron combined as metal's microparticles. When sticking together, large metal particles moved in spite of gas flow towards the central part because of the gravity. Ni behaves similarly to iron, whose oxide has volatility comparable to that of FeO. When NiO was reduced, it transforms into metallic Ni, which was removed together with iron into the core. At the same time, high sidrophilic metals, which were more refractory as Ni due to its non-volatility remain in silicate particles. They don't moved as metalls' particles out because of particles retention. Therefore silicates have acquired more metals than would be expected by the usual geochemical redistribution of elements between melt and minerals.

As pointed out by Galimov E. M., the realization of such a scenario entails several important consequences. So, it was hard to explain why the planets of the Earth's group have huge reduced iron core, while the primary matter contains iron in oxidized form. Namely, the primary matter of the composition of carbonaceous chondrites contains iron only in an oxidized state—in the form of FeO. Ordinary chondrites contain metallic iron, but only in a subordinate amount. The metals core formation assumes that the all oxygen was removed, but an acceptable process for this was not found. Iron oxides reduction by cloud's hydrogen provided a natural solution to this problem. Water released in

this process is squeezed out together with hydrogen in the vapor-gas phase from the compressing cloud and leaves the future proto-Earth.

An important addition to the above gas-phase reactions should be made here. Evaporation rates should be small at time scales of the fragmentation process. The experimentally studied FeO evaporation rate is 1.14×10^{-5} g/cm^2 s at 1900 °K [25]. At this temperature, half of the FeO content will evaporate from particles with a radius of 1 mm for 0.2×10^4 s. Obviously, the temperatures in the cloud should have been significantly lower and not exceed 1100–1200 °K or 800–900 °C. But, at temperatures below 830 °C, carbon monoxide (CO) is a stronger reducing agent than hydrogen (H_2), and, starting from 570 °C, the following exothermic reaction of FeO reduction becomes possible

$$\mathrm{FeO} + \mathrm{CO} \rightarrow \mathrm{Fe} + \mathrm{CO_2} + 224\ \mathrm{kJ/kg} \quad (1)$$

At the same time, the FeO reduction is effective only at high concentration of CO in the gas phase and with increasing temperature the value of the required excess of the reducing agent increases. As we know, CI carbonaceous chondrites contain a large amount of carbon-containing compounds and their thermal decomposition is quite capable of providing a large amount of water in the form of steam, carbon monoxide (CO) and carbon dioxide (CO_2). In this case, the equilibrium of the gas reaction

$$\mathrm{H_2O} + \mathrm{CO} \leftrightarrow \mathrm{CO_2} + \mathrm{H_2} \quad (2)$$

up to 830 °C is shifted to the right, and above 830 °C—to the left. Thus, at high temperatures in the collapsing gas-dust thickening there should be intensive production of carbon monoxide, which at subsequent cooling actively regenerates FeO (see Fig. 1).

Geochemical analysis of the megaimpact consequences predicts a redistribution of incompatible elements close to the ideal due to the significant melting of the milicate mantle of the early Earth. But, it was observed that the distribution of elements by phases does not correspond to the equilibrium one [26]. To explain this fact, a number of authors investigated the dependence of the siderophilicity of the element on pressure, temperature and chemical composition of the medium. With a certain combination of these conditions, it is possible to achieve for some elements compliance with the observed distribution, for example, for molybdenum and phosphorus [27]. Also, taking into account the different partial pressures of oxygen in the mantle at different depths, it is possible to bring the distribution of vanadium, niobium and chromium to the observed [28]. But, for each selected group of elements, it will be need some individual set of conditions each time. In the Galimov E. M. model, there is a separate movement of silicate particles and iron

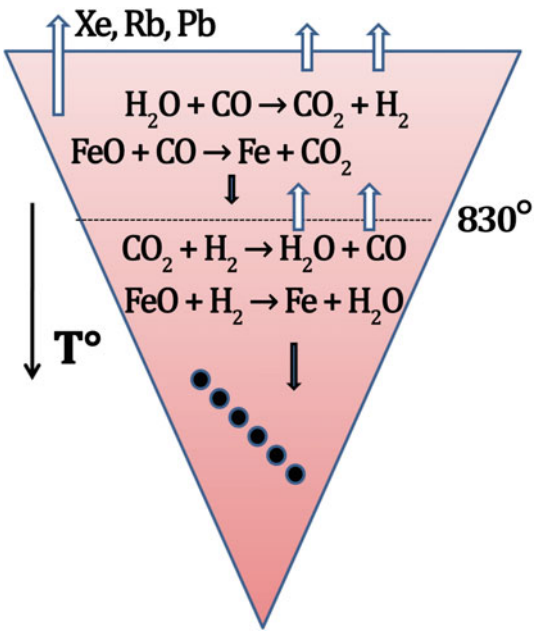

Fig. 1 Segregation of metallic iron and volatile export during Earth formation, according to Galimov E. M. model [1]

particles, and the distribution of elements should not initially meet the equilibrium between silicate melt and iron.

Here we should also add that the explanation of nonequilibrium contents of siderophile elements in the Earth's mantle proposed by Galimov E. M. within the framework of his model is not exhaustive. Recent studies of molybdenum isotope ratios (^{92}Mo, ^{94}Mo, ^{95}Mo etc.) using Thermo Scientific Neptune Plus multicollector inductively coupled plasma mass spectrometer (MC-ICP-MS), Institute for Planetology at the University of Munster, showed a significant addition of carbonaceous and ordinary chondrites material at the late stage of Earth accretion, already after formation and separation of its metal core from silicate mantle [29]. The refined Mo isotopic ratios are presented as $^{\varepsilon i}$Mo in 10,000 fractions of deviations from the standard

$$\varepsilon_i Mo = [(^{\varepsilon_i}\mathrm{Mo}/^{\varepsilon 96}\mathrm{Mo})_{\mathrm{sample}}/(^{\varepsilon_i}\mathrm{Mo}/^{\varepsilon 96}\mathrm{Mo})_{\mathrm{standard}} - 1] \times 10^4, \quad i = 92, 94, 95, 97, 100 \quad (3)$$

for carbonaceous chondrites (CC) and non-carbonaceous meteorites (NC), such as ordinary and enstatite chondrites, achondrites, and iron and iron-stone meteorites (see Fig. 2). It was shown that there is a dichotomy of isotopic ratios between these two groups, with the bulk silicate Earth (BSE) mantle bulk composition being intermediate.

The estimates showed that in the case of predominantly CC impacts, at least 0.1 of the total mass was added during the late stage of the accretion of the early Earth.

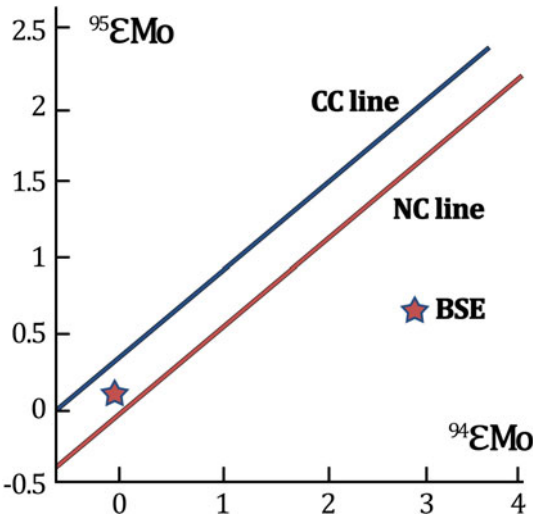

Fig. 2 Mo isotopic ratios for CC, NC and BSE, according to [29]

2.2 Siderophile Elements at the Moon

Since Larimer [30] and Grossman [31] published the classical scheme of sequential condensation, iron has been perceived as one of the hard-volatile substances. Indeed, the first condensates are Ca, Al, Ti oxides, then Fe and Ni, and later silicates and Mg and Si oxides. Of the rock-forming ones, K and Na are relatively volatile. Even more volatile are Rb, Pb. However, if we consider not the condensation of solids (CAI, chondra) from high-temperature solar gas, but the evaporation of carbonaceous-chondritic matter, enriched with iron oxide, it appears that iron may be lost in the form of FeO. Oxide iron is not volatile per se, but can decompose into elemental iron and oxygen. In this case, volatilization of iron from the silicate or oxide mineral phase is more efficient than from the purely metallic phase. As experiments conducted at Vernadsky Institute RAS have shown, iron in FeO form follows after potassium and sodium oxides in degree of volatility [32]. The Moon is FeO depleted relative to CI in approximately the same degree as similar in volatility Mn and Cr. Calculations conducted by Galimov [2] based on experimental data by Hashimoto [33] have shown that when evaporating ca. 40% of mass of primary chondritic composition matter, iron content in it is reduced to the value of iron content characteristic of the Moon. This can be seen from Table 1, which presents comparative data on the composition of carbonaceous chondrites, the Moon and the composition of the matter remaining during evaporation of 40% of the mineral composition of carbonaceous chondrites.

It should only be noted that this is true if we take as a reference for the composition of the Moon data by Taylor [34]. He proceeded from the fact that the Moon is enriched in refractory elements Al, Ca, Ti. But not all geochemists share this point of view. For instance if S. Taylor's Al_2O_3 content in the Moon is 6% then A. Ringwood's estimate is 3.7% [35], i.e. according to Ringwood the Moon is not enriched by Al relative to the Earth. The same estimates have O'Neil [36]. The upper shell of the Moon is really enriched in minerals Al, Ca and Ti, which makes S. Taylor's estimates plausible. But we do not know the internal chemical structure of the Moon. Perhaps the deep interior of the Moon is depleted in refractory elements. Then the total content of Al and other refractory elements is generally not higher than on Earth. Since there is a relationship between the elastic properties of rocks and their mineral and chemical composition, it is possible to make estimates of the chemical composition of the mantle from seismic data. Such estimates have been made in Vernadsky Institute RAS by corresponding member O. L. Kuskov and colleagues [37]. They indicate an increased Al content in the mantle of the Moon, and therefore the overall increased content of refractory elements in the Moon.

In the megaimpact hypothesis there is no reason to expect significant differences in the content of siderophile elements in the silicate mantles of the Earth and the Moon, since the latter was created from the former. It is known that the Moon's core is ca. 5% of the total size and is much smaller than the Earth's core ($\sim$ 30%). At the same time, the degree of depletion of the Moon siderophile elements is higher than that of the Earth's mantle [38]. According to Galimov E. M. model it follows that the hydrodynamic export process prevails in the accretion period after fragmentation, i.e. applies mainly to the Earth. As for the Moon, after its formation as a consolidated body, the segregation of the core of the Moon took place predominantly in the system of silicate and metallic melts with the corresponding distribution coefficients of elements (see Table 2).

Due to the significant discrepancy between the observed and calculated values (at full melt silicate shell), the distribution of siderophile elements in the lunar mantle is better studied using the model of gradual formation of magmatic ocean and separation of crystalline silicate minerals with partial volatilization taken into account [39].

Isotopes of hafnium (Hf) and tungsten (W) are very convenient for this purpose. As we know, ^{182}Hf is a short-lived isotope, which with a half-life of 8.9 million years passes into ^{182} W. Hafnium and tungsten are separated during the separation of iron from silicates, as Hf is a lithophile retained in silicates and W is predominantly a sidorophile, escaping to the metallic phase. As the source ^{182}W, the radioisotope ^{182}Hf, remains in the silicates, the $^{182}W/^{184}W$ ratio increases there compared to the undifferentiated chondritic matter. The earlier the differentiation occurred, the greater will be the magnitude of the shift

Table 1 Comparison of the composition of the Moon (according to Taylor [34]) and the composition of restite obtained at 40% CI evaporation—composition calculated from experimental data (according to [33])

Component	CI weight %	Remainder (40% mass evaporation)	Moon
SiO_2	35.0	42.9	43.4
MgO	23.4	31.9	32.0
FeO	36.9	15.8	13 + Fe nuclei
$CaO + Al_2O_3$	4.6	9.4	10.8

Table 2 Lunar depletion by siderophile elements in comparison with CI chondrites

Element	$D_{metal/sil.melt}$ (from [35])	$D_{cr.silicate/sil.melt}$	Depletion (according to [35])	
			Observed	Calculated (melt 100%)
V	1.7	0.004	1.9	1.03
W	36	0.01	22	2.9
P	160	0.05	115	9.4
Co	350	1.8	12	19.5
Mo	2500	0.05	1200	133.4
Ni	5000	5	50	266
Re	1.6×10^5	1	3×10^4	8.5×10^3
Ir	1.7×10^6	1	0.9×10^5	0.9×10^5

$$\varepsilon^{182}\mathrm{W} = \left[\left(^{182}\mathrm{W}/^{184}\mathrm{W}\right)_{\mathrm{sample}}/\left(^{182}\mathrm{W}/^{184}\mathrm{W}\right)_{\mathrm{standard}} - 1\right] \times 10^4 \quad (4)$$

For a meaningful shift, the metal-silicate separation must occur in the first tens of millions of years before the short-lived ^{182Hf} completely decays. Modern isotopic studies of the Hf-W system [40] have shown that:

(1) The Hf/W ratios are different for the modern Earth and Moon: 17 ± 5 and 26 ± 2, respectively.
(2) W isotopic composition is practically identical for the Earth and the Moon within $\Delta\varepsilon^{182}\mathrm{W} = 0.09 \pm 0.01$.
(3) W isotopic compositions of the Earth and the Moon insignificantly differ from chondrite $\varepsilon^{182}\mathrm{W} = +1.9$

Since the isotopic composition of tungsten of the Moon and Earth are the same, but Hf/W ratio is different, the observed difference arose after the source ^{182}Hf radiogenic ^{182}W, completely decomposed. Kleine and collaborators [40] obtained the following estimate: for the value of $\Delta\varepsilon^{182}\mathrm{W}$ to be within 0.09 the age of the event must be $\sim$ 60 million years after the origin of the solar system. This value represents an important time constraint for events in both the Galimov E. M. model and in the megaimpact model. In the first one it is the fragmentation time, when the geochemical history of the Moon and the Earth separated. Up to that moment they accumulated common matter, and the isotopic composition of tungsten was the same for both bodies. After $\sim$ 60 million years, the Hf/W ratio became different, but it could no longer noticeably change the W isotopic composition of either the Moon or the Earth. In the impact model, this should mean the time of the collision of the proto-Earth and the impactor. But, at that, the bodies having different geochemical history have met, and they either by chance must have coinciding isotopic compositions of tungsten, or after the collision there was a complete homogenization of the isotopic composition of the whole arisen common mass. This problem is similar to the problem of the coincidence of the oxygen isotope composition for the Moon and the Earth.

2.3 Water on the Moon

The opinion that the Moon was "dry", i.e., that its mantle contained no water, has recently begun to change under the pressure of geochemical data obtained for both volcanic rocks [41] and lunar regolith [41]. The impact hypothesis predicts that much of the water and other volatiles were lost to the proto-Luna after the impact, but the primary crust of the Moon appears to have contained a significant amount of water [42]. In recent work, Hui and collaborators analyzed plagioclase grains in lunar anorthosite delivered by the Apollo mission that are samples of the primary crust [43].

The absorption lines of –OH hydroxyl groups were determined by infrared Fourier spectroscopy, followed by recalculation to the weight content of water. As a result, approximately 6 ppm water was detected in anorthosite and up to 2.7 ppm water was detected in plagioclase grains from lunar continental troctolites. Based on these measurements, the gross initial water content of the magmatic ocean was estimated to be approximately 320 ppm. Water accumulating in the residual magmatic melt could be as high as 1.4 wt %, which is sufficient to explain the water content measured in the lunar volcanic rocks. The presence of water in the primary crust implies a longer crystallization of the lunar magmatic ocean than in the "dry" Moon scenario, and changes our view on the possible composition and volatile content in the lunar regolith.

It is interesting to note that the first measurement of water content in the lunar regolith delivered by the Luna-24 station was made at Vernadsky Institute RAS in 1978. M. V. Akhmanova and co-workers used the diffuse reflectance infrared spectra method to study the layers from different depths of the soil column (total length 200 cm) [44]. Regolith samples were taken from depths of 92, 118, 143, and 184 cm and separated into fine (< 100 μm) and coarse fractions (> 100 μm). The reflectance spectra were broadly similar, with the coarse fraction yielding less reflectance. For soil from a depth of 143 cm, reflection minima were found at about 3 and 6 μm, corresponding to water absorption bands (see Fig. 3).

The value of water concentration estimated from the characteristics of the absorption bands for similar intensities was 0.1 wt%. Since the landing site of the Luna-24 station was in the southeast of the Mare Crisium on the edge of the impact crater, it can be assumed that such water content is typical of the lunar pre-Imbrian marine basalts, approximately 3.98 billion years old.

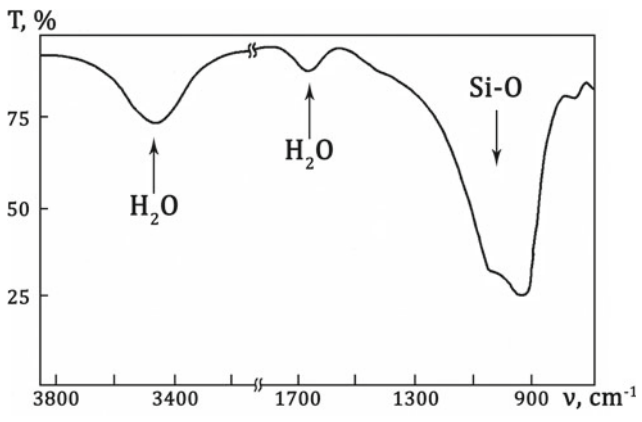

Fig. 3 IR transmission spectrum of lunar regolith Luna-24 samples from the depth of 143 cm, according to [44]

3 Accretion Model

3.1 Numerical Framework

Galimov E. M. and Krivtsov A. M. used the particle dynamics method [45] for numerical simulation of the dust densification compression process. The ensemble of particles was described by the classical Newtonian equation of dynamics. The compression dynamics of the dust clump was considered both in the version of a two-dimensional disk characterized by an angular momentum corresponding to the angular momentum of the Earth-Moon system and in the three-dimensional version of a finite-thickness disk. In the standard formulation, the interaction force between particles was determined by three components: the gravitational interaction, the elastic interaction when the particles collided, and a component describing dissipative losses, i.e., the transfer of mechanical energy into heat. As initial conditions, besides the rotational momentum of the dust body as a whole, a random velocity vector of particles modeling their chaotic motion and a certain distribution of particle density along the radius were introduced.

Computer simulations showed that, in the standard version, fragmentation does not occur during compression of the disk. The rotational moment of the Earth-Moon system turned out to be insufficient for fragmentation, as in other models linking the formation of the Moon to its separation from the Earth. However, in all cases it was found that the angular momentum of the Earth, under any reasonable assumptions, could not ensure the separation of a fragment of lunar dimensions from it. E. M. Galimov has shown that the problem is solved if the repulsive force due to gas flowing out from the surface of evaporating particles is included into the balance of forces determining the dynamics of dust cloud compression. This force is subtracted from the gravitational attraction force and weakens its effect. In this case, the fragmentation is achieved at those values of the angular momentum that characterize the Earth-Moon system.

Figure 4 shows the phases of fragmentation development obtained by numerical computer simulation of cloud compression, taking into account the process of evaporation of particles [46]. Thus, the evaporation factor, which allowed Galimov E. M. to explain the iron depletion of the Moon in a new way, turned out to be crucial for the dynamics of the compressing gas-dust clump. Initially, both fragments, the one that was to become the Moon and the one that was to become the Earth, were depleted in volatiles and iron practically to the same degree.

Additional computer simulations have shown that if one of the fragments happens to be (accidentally) slightly more massive than the other, the larger embryo grows much faster

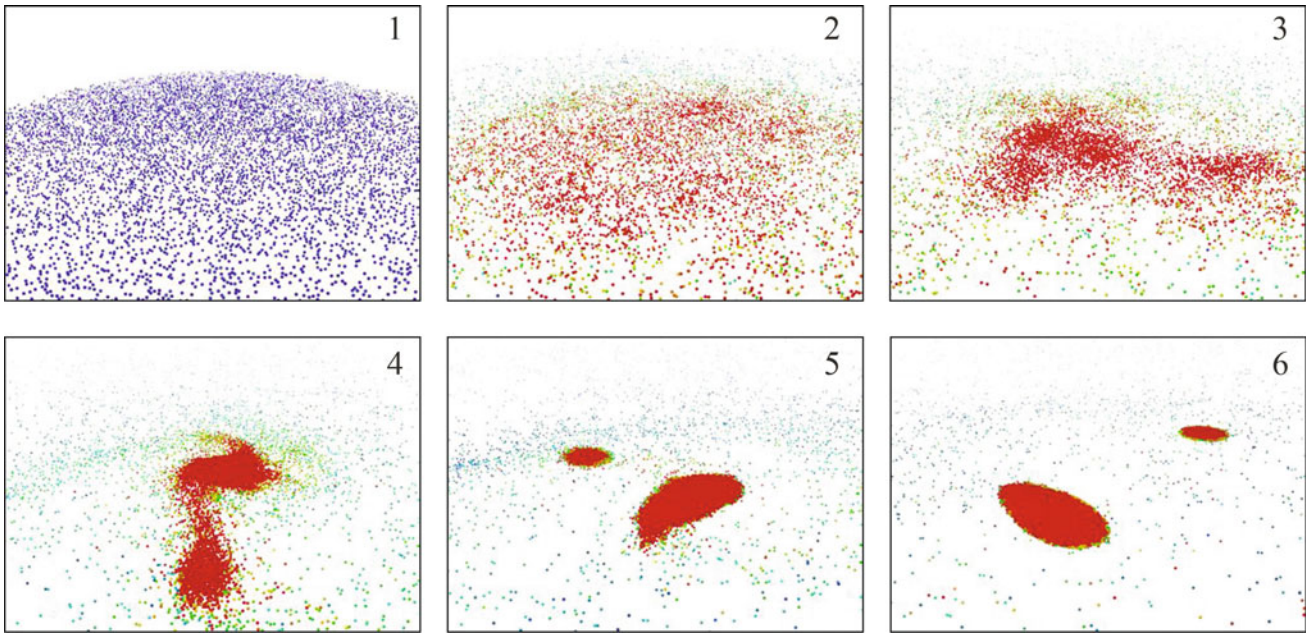

Fig. 4 Stages of dust disk fragmentation according to the results of numerical simulation [4]

[47]. As a result, the smaller embryo only slightly changes its initial composition, keeping its appearance depleted in volatiles and enriched in refractory elements (future Moon), while the larger embryo (future Earth) accumulates almost all primary matter of the cloud and, eventually, acquires a composition very close to that of the primary chondritic matter, except for the most volatile components.

3.2 Analytical Extension

At the final stage of the thickening evolution, two massive embryos (masses M_2 and M_1) are distinguished, rotating around a common center of masses in the dust and gas cloud (see Fig. 4, stages 5 and 6). Each of them has its own "feeding zone" where its gravitational force exceeds its neighbor's gravity. To estimate the size of these zones, one can use the model of Egleton, who considered Roche cavities for a system of binary stars [48]. His result can be expressed by the following formula for the radius of the ball whose volume is equal to the volume of the corresponding Roche cavity

$$r_2 = 0.49 \cdot q^{2/3} / \left[0.6 \cdot q^{2/3} + \ln\left(1 + q^{1/3}\right)\right], \qquad (5)$$

where r_2 is the effective radius of the Roche cavity, related to the distance d between the embryos; $q = M_2/M_1$ is the ratio of embryo masses, where M_2 is the mass of the embryo for which the Roche cavity radius is sought.

Assuming that the matter from the two contiguous Roche cavities accretes completely to the embryos over time, forming the shells of the future Moon (m_2) and Earth (m1), we obtain the following ratio of their masses:

$$r_1 + r_2 = 1, \quad S = m_2/m_1 = r_2{}^3/(1 - r_2)^3 \qquad (6)$$

As the result, for two zones the mass conservation condition should be fulfilled

$$m_2 + M_2 = M_{\text{Moon}}, \quad m_1 + M_1 = M_{\text{Earth}}, \qquad (7)$$

expressing the final distribution of the thickening substance. Substituting the expression for r_2 from (5) into the relation (6), we obtain the following formula for S

$$S(q) = 0.118 \cdot q^2 / [0.11 \cdot q^{2/3} + \ln\left(1 + q^{1/3}\right]^3 \qquad (8)$$

Figure 5 shows the graphical dependence of the masses of the falling out shells m_1/m_2 per embryos M_1 (larger) and M_2 (smaller), at $q < 1$.

It is noticeable how much the masses of the shells diverge at the initial, relatively small, difference in the masses of the embryos. For example, at $q = 0.2$, i.e. the mass difference of a large embryo M_1 in 5 times from the mass of small M_2, the mass ratio of the dropped out shells will make already $m_1/m_2 = 26$ (see Fig. 5).

Using the restriction on the masses of embryos and shells (7) we can estimate the upper limits of the Earth and Moon embryonic masses. Since $m_2 = S \cdot m_1$, $M_2 = q \cdot M_1$, then

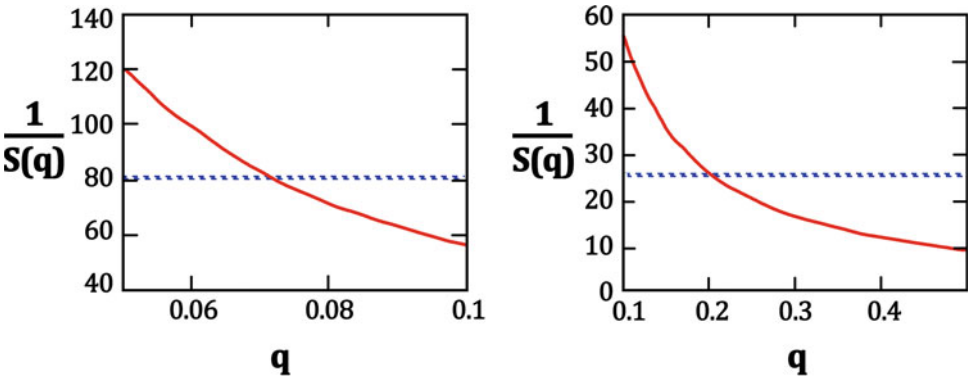

Fig. 5 Dependence of the masses of the precipitating shells m_1/m_2 on the embryos masses $q = M_2/M_1$: (left) $0.01 < q < 0.1$; (right) $0.1 < q < 0.5$

$$M_{Moon} = S \cdot m_1 + q \cdot M_1 = S \cdot (M_{Earth} - M_1) + q \cdot M_1,$$

from where, after transformation, follows

$$M_1/M_{Earth} = (1/81 - S(q))/(q - S(q)) = E(q) \qquad (9)$$

The applicability limits of this model are defined by the interval of values q at which $0 < E(q) < 1$, i.e., $0 < M_1 < M_{Earth}$ (see Fig. 5):

$$0.0123 < q < 0.0718 \qquad (10)$$

Considering the nucleus density of the Earth and the Moon close to the density of ordinary chondrites ($\approx$ 3.3 g/cm3), we can estimate the minimal possible nucleus radii at $q = 0.0717$ as

$$R_1 \approx 480 \text{ km}, \quad R_2 \approx 200 \text{ km}$$

These sizes are close to large relict planetosimals in the asteroid belt. For example, the average equatorial radius of the asteroid Vesta is $\approx$ 280 km and, judging by the composition of HED meteorites, it was formed rather quickly—the first 5–10 million years of the Solar System development.

4 Conclusions

The model of the formation of the Earth and the Moon from a large gas-dust clump proposed by E. M. Galimov allows us to solve a number of problems arising in the megaimpact model. The common source of matter of the Moon and the Earth explains the coincidence of isotopic fractionation lines $^{16}O/^{17}O/^{18}O$, as well as the coincidence of isotopic composition of tungsten $^{182}W/^{184}W$. The observed deficiency of iron on the Moon and its enrichment with refractory and weakly volatile elements: Al, Ca, Ti, etc. is explained elegantly. Isotopic exchange in the particle vapor-cloud system helps to explain why the loss of lunar volatiles was not accompanied by isotopic fractionation. In the metaimpact model, the kinetic isotopic effect due to the departure of volatiles seems inevitable.

The dynamic model of the formation of a binary planetary system in a gas-dust cloud gives reasonable estimates of the initial size of the embryos. The question arises: why is the Earth-Moon system unique in the Solar System? The satellites Phobos and Deimos at Mars are most likely captured asteroids, as are the Jupiter and Saturn systems. Perhaps, the matter is in the peculiarities of the behavior and different gas-dynamic regimes of the inner and outer parts of the proto-planetary cloud of the early Solar System. The question about the mechanism of nebula evolution that leads to the formation and long-term (up to 10 million years) development and preservation of large gas-dust clouds remains open. A more detailed model of the processes occurring in the shrinking and fragmenting proto-planetary disk, including estimates of temperature and pressure changes in time and space, must be constructed. More precise observations of exoplanetary systems could provide clues in the case of large gas-dust clouds detected near the outer stars.

Acknowledgements The author expresses his gratitude to ac. Marov M. Y. and corresponding member of RAS Kolotov V. P. for pointing out the original measurements of water content in Vernadsky Institute RAS using samples of lunar regolith delivered by Luna-24 station. Graphic processing of the drawings was done by Fedulova Valeria. This work is conducted under the GEOKHI RAS state assignment.

References

1. Hartmann, W.K., Davis, D.R.: Satellite sized planetesimals and lunar origin. Icarus **24**, 504–515 (1975)
2. Cameron, A.G.W., Ward, W.: The origin of the Moon. In: Proceedings of the Lunar Conference 7th Houston, pp. 120–122 (1976)
3. Galimov, E.M.: Formation of the Moon and the Earth from a common supraplanetary gas-dust cloud. Geochem. Int. **49**(6), 537–554 (2011)

4. Galimov, E.M., Sidorov, Yu.I., Krivtsov, A.M., Zabrodin, A.V., Legkostupov, M.S., Eneev, T.M.: Dynamic model for the formation of the Earth-Moon system. Geochem. Int. **43**(11), 1045–1055 (2005)
5. Melosh, H.J.: A new and improved equation of state for impact computations. In: Lunar Planet Conference 31st, 1903 (2000)
6. Canap, R.M.: Simulations of a late lunar forming impact. Icarus **168**, 433–456 (2004)
7. Stivenson, D.: Earth formation: combining physical models with isotopic and elemental constraints. Geochim. Cosmochim. Acta, 15th Goldshmidt Conference Abstract, A382 (2005)
8. Belbruno, E., Gott, J.R.: Where did the Moon come from? Astronom. J. **129**, 1724–1745 (2005)
9. Byalko, A.V.: Zodiac light: an old problem and new hypotheses. Priroda **6**, 22–31 (2020)
10. Canap, R.M., Esposito, L.W.: Accretion of the Moon from an impact generated disk. Icarus **119**, 427–446 (1996)
11. Wang, J., Davis, A.M., Clayton, R.N., Hashimoto, A.: Evaporation of single crystal forsterite: evaporation kinetics, magnesium isotopic fractionation and implication of mass dependent isotopic fractionation of mass controlled reservoir. Geochim. Cosmochim. Acta **63**, 953–966 (1999)
12. Humayun, M., Clayton, R.N.: Precise determination of the isotopic composition of potassium: application to terrestrial rocks and lunar soils. Geochim. Cosmochim. Acta **59**, 2115–2130 (1995)
13. Humayun, M., Cassen, P.: Processes determining the volatile abundances of the meteorites and terrestrial planets. In: Canap, R. M., Righter, K. (eds.) Origin of the Earth and Moon. Univ. Arizona Press (2000)
14. Pahlevan, K., Stevenson, D.J.: Volatile loss following the Moon forming giant impact. Goldschmidt Conference Abstracts, A716 (2008)
15. Gurevich, L.E., Lebedinsky, A.I.: Planetary formation. Proc. Acad. Sci. USSR, ser. Phys. **14**(6), 765–775 (1950)
16. Kozlov, N.N., Eneev, T.M.: Numerical modeling of the process of planet formation from a protoplanetary cloud. Preprint No. 134 of the Institute of Applied Mathematics, USSR Academy of Sciences, Moscow (1977)
17. Eneev, T.M.: A new accumulation model of planet formation and structure of outer regions of the solar system. Preprint No. 166. Institute of Applied Mathematics, USSR Academy of Sciences, Moscow (1979)
18. Ruskol, E.L.: Moon Genesis. Moscow, Ed. «Nauka» (1975)
19. Jarkov, V.N.: Interiors of the Earth and Planets. Moscow, Ed. «Nauka» (1983)
20. Kolesnichenko, A.V., Marov, M.Ya. : Fundamentals of mechanics of heterogeneous media in the circumsolar dopplanetary cloud: effect of solid particles on turbulence in the disk. Astron. Vestn. **40** (1), 2–62 (2006)
21. Marov, M.Y., Kolesnichenko, A.V., Makalkin, A.B., Dorofeeva, V.A., Ziglina, I.N., Chernov, A.V.: From a protosolar cloud to a planetary system: a model of gas-dust disk evolution. In: Galimov, E.M. (ed.) Problems of the Origin and Evolution of the Biosphere, pp. 223–273. URSS Publishing House, Moscow (2008)
22. Adushkin, V.V., Vityazev, A.V., Pechernikova, G.V.: In development of the theory of origin and evolution of the earth. In: Galimov, E.M. (ed.) Problems of the Origin and Evolution of the Biosphere, pp. 275–296. URSS Publishing House, Moscow (2008)
23. Zabrodin, A.V., Zabrodina, E.A., Legkostupov, M.S., Manukovsky, K.V., Pliner, L.A.: Some models for the description of the protoplanetary disk of the Sun at the initial stage of its evolution. In: Galimov, E.M. (ed.) Problems of the Origin and Evolution of the Biosphere, pp. 297–315. URSS Publisher, Moscow (2008)
24. Galimov, E.M.: Current state of the problem of the origin of the Earth-Moon system. In: Galimov, E.M. (ed.) Problems of the Origin and Evolution of the Biosphere, pp. 213–222. Publishing house URSS, Moscow (2008)
25. Kazenas, E.K., Tsvetkov, Yu.V.: Thermodynamics of Oxide Evaporation. LKI Publishing House, Moscow (2008)
26. Jones, J.H., Drake, M.J.: Geochemical constraints on core formation in the Earth. Nature **322**, 221–228 (1986)
27. Righter, K., Pando, K.M., Danielson, L., Lee, Cin-Ty.: Partitioning of Mo, P and other siderophile elements (Cu, Ga, Sn, Ni, Co, Cr, Mn, V, and W) between metal and silicate melt as a function of temperature and silicate melt composition. Earth Planet. Sci. Lett. **291**, 1–9 (2010)
28. Wood, B.J., Wade, J., Kilburn, M.R.: Core formation and the oxidation state of the Earth: addition constraints from Nb, V and Cr partitioning. Geochim. Cosmochim. Acta **72**, 1415–1426 (2008)
29. Budde, G., Burkhardt, C., Kleine, T.: Molybdenum isotopic evidence for the late accretion of outer solar system material to Earth. Nat. Astronomy **3**, 736–741 (2019)
30. Larimer, J.W.: The condensation and fractionation of refractory lithophile elements. Icarus **40**, 446–454 (1979)
31. Grossman, L., Larimer, J.W.: Early chemical history of the solar system. Rev. Geophys. Space Phys. **12**, 71–101 (1974)
32. Markova, O.M., Yakovlev, O.I., Semenov, G.L., Belov, A.N.: Some general results of experiments on evaporation of natural melts in the Knudsen chamber. Geochemistry **11**, 1559–1569 (1986)
33. Hashimoto, A.: Evaporation metamorphism in the early solar nebula—evaporation experiments on the melt FeO–MgO–SiO_2–CaO–Al_2O_3 and chemical fractionations of primitive materials. Geochem. J. **17**, 111–145 (1983)
34. Taylor, S.R.: The origin of the Moon: a geochemical consideration. In: Hartmann, W.K., Phillips, R.J., Taylor, G.J. (eds.) Origin of the Moon, pp. 125–144. Lunar Planet. Inst. Houston (1986)
35. Ringwood, A.E.: Composition and origin of the Moon. In: Hartmann, W.K. et al. (eds.) Origin of the Moon, pp. 673–698. Lunar Planet. Inst., Houston (1986)
36. O'Neill, H.St.: The origin of the Moon and the early history of the Earth: a chemical model. Part 1: The Moon. Geochim. Cossmochim. Acta **55**, 1135–1157 (1991)
37. Kuskov, O.L., Kronrod, V.A.: Gross composition and size of the Moon's core. In: Galimov, E.M. (eds.) Problems of the Origin and Evolution of the Biosphere, pp. 317–327. URSS Publisher, Moscow (2008)
38. Newsom, H.E.: Constraints on the origin of the Moon from the abundance of molybdenum and other siderophile elements. In: Hartman, W.K., Phillips, R.J., Taylor, G.J. (eds.) Origin of the Moon, pp. 203–230. Lunar Planet. Inst. of the Moon, Huston (1986)
39. Elkins-Tanton, L.T., Burgess, S., Yin, Q.Z.: The lunar magma ocean: reconciling the solidification process with lunar petrology and geochronology. Earth Planet. Sci. Lett. **304**, 326–336 (2011)
40. Kleine, T., Touboul, M., Bourdon, B., Nimmo, F., Mezger, K., Palme, N., Jacobsen, S., Yin, Q., Halliday, A.: Hf-W chronology of the accretion and early evolution of asteroids and terrestrial planets. Geochim. Cosmochim. Acta **73**, 5150–5188 (2009)
41. Saal, A.E., et al.: Volatile content of lunar volcanic glasses and the presence of water in the Moon's interior. Nature **454**, 192–195 (2008)
42. Liu, Y., et al.: Direct measurement of hydroxyl in the lunar regolith and the origin of lunar surface water. Nature Geosci. **5**, 779–782 (2012)
43. Hui, H., Peslier, A., Zhang, Y., Neal, C.R.: Water in lunar anorthosites and evidence for a wet early Moon. Nature Geosci. **6**, 177–180 (2013)

44. Akhmanova, M.V., Dementiev, B.V., Markov, M.N.: Water in the regolith of the Mare Crisium (Luna-24)? Geochemistry **2**, 285–287 (1978). (in Russian)
45. Krivtsov, A.M., Krivtsova, N.V.: Method of particles and its use in mechanics of deformable solids. Far Eastern Math. J. **3**(2), 254–276 (2002)
46. Le Zakharov, A.A., Krivtsov, A.M.: Development of algorithms for calculating the collision dynamics of gravitating particles to model the Earth-Moon system formation as a result of dust cloud gravitational collapse. In: Galimov, E.M. (ed.) Problems of the Origin and Evolution of the Biosphere, pp. 329–344 (2008)
47. Vasiliev, S.V., Krivtsov, A.M., Galimov, E.M.: Study of the planet-satellite system growth process as a result of the accumulation of dust cloud material. Sol. Syst. Res. **45**(5), 410–419 (2011)
48. Eggleton, P.P.: Approximations to the Radii of Roche Lobes. Astrophys. J. **268**, 368–369 (1983)

Helium-3 in the Lunar Soil

E. N. Slyuta and O. I. Turchinskaya

1 Introduction

Ionizing irradiation by the solar wind and galactic cosmic radiation is one of the main factors of cosmic weathering and accumulation of cosmogenic isotopes in the lunar soil. The study of the gross isotope composition of the solar wind has a long history and practically began with the launching of the first interplanetary automatic stations at the dawn of the space age. For the first time, the ion component of solar wind streams outside the Earth's magnetosphere was detected and measured during the Luna-2 mission in September 1959. These measurements finally confirmed the hydrodynamic theory of the solar wind proposed in 1958 by the American physicist Eugene Parker [1], which was immediately criticized by physicists.

The solar wind is formed during solar corona gasdynamic expansion into space and is a plasma flow of approximately the same density, consisting mainly (about 95%) of electrons and hydrogen ions (protons) [1, 2]. In addition to protons, helium ions are present in the solar wind, whose ratio to hydrogen ions ranges from 0.037 to 0.056 [3, 4]. Atoms of Ne, Ar, Kr, and Xe and oxygen, silicon, sulfur, iron ions, etc. are also present in small amounts. With the distance from the Sun the solar wind velocity increases and its flux density decreases. At the Earth's orbit, its speed is about 500 km s^{-1}. The temperature of protons (or electrons) is about 100,000 K and concentration 10–20 particles per cubic centimeter. The solar wind characteristics on the Earth's orbit vary depending on the solar activity level. The velocity of any ions is the same, and the ion energy depends on the nucleus mass in accordance with the hydrodynamic theory of the solar wind propagation [1, 5]. Accordingly, at the same ion velocity, the kinetic energy of helium nuclei is 4 times greater than proton energy. The normal proton energy on the Earth's orbit varies from 0.3 to 3 keV, reaching 100 keV and more during solar flares.

Solar Wind Composition (SWC) experiments to study the gross isotopic composition of the solar wind directly on the lunar surface have been conducted since 1969 in almost all manned Apollo missions except Apollo 17. A thin aluminum foil measuring 30 × 140 cm (4000 cm^2 area), 15 μm thick, and weighing 127 g for direct measurement of captured solar wind elements was unfolded on a L-shaped support at some angle to the lunar surface and perpendicular to the solar wind flow. The exposure time of each subsequent experiment increased from 77 min at Apollo 11 to 45 h 05 min at Apollo 16 [6–10]. After completing the experiment, the foil was rolled up, placed in a container, and transported to Earth for further study under laboratory conditions. According to SWC experiments, the average ratio of helium isotopes $^4He/^3He$ in the solar wind near the lunar surface was 2350 ± 120 [11].

The study of the bulk composition of helium isotopes in the solar wind continued in 1978–1982 in the International Sun Earth Explorer 3 (ISEE-3) mission (the Ion Composition Instrument (ICI)) [12, 13] and in 1991–1996 in the Ulysses mission using the Solar Wind Ion Composition Spectrometer (SWICS) [14–16], and in the Solar and Heliospheric Observatory (SOHO) and Advanced Composition Explorer (ACE) missions [17, 18]. Analysis of the data obtained showed that the ratio of helium isotope ions $^4He/^3He$ in the slow and fast solar wind fluxes is different and varies from 2450 to 3030 [15], while the average ratio of helium isotopes in the outer convective zone of the Sun (in the corona and chromosphere) is 2632 [19]. From 2001 to 2004, the Genesis spacecraft exposed solar wind traps made of various ultrapure materials at the Lagrangian point L1 at a distance of 1.5 million km from Earth for 852.83 Earth days, which were then delivered to Earth [20, 21]. According to these measurements, the average ratio of helium isotopes in the bulk composition of the solar wind is 2155 [22].

E. N. Slyuta (✉) · O. I. Turchinskaya
Vernadsky Institute of Geochemistry and Analytical Chemistry, Russian Academy of Sciences, 19 Kosygina St., Moscow, 119991, Russia
e-mail: slyuta@geokhi.ru

V. P. Kolotov and N. S. Bezaeva (eds.), *Advances in Geochemistry, Analytical Chemistry, and Planetary Sciences*,
https://doi.org/10.1007/978-3-031-09883-3_21

The purpose of studying the gross isotope composition of solar wind isotopes was to estimate the average solar element composition of matter, because due to its mass the Sun represents 99.8% of the Solar system composition, and to check the theory of proton-proton cycle of thermonuclear fusion reaction in the bowels of our star on the basis of helium isotope ratio. The study of isotopic composition of implanted noble gases in the lunar soil besides the above mentioned tasks allows to estimate the change of solar wind composition since the formation of lunar rocks and regolith and on the basis of Ar and Xe isotopic composition to estimate the age of lunar regolith exposure on the surface and trace the geochemical history of its formation [23]. Since the 1986 publication of [24], helium-3 isotope has also been considered as a possible promising source for thermonuclear energy based on the "pure" thermonuclear reaction $D + {}^3He = p\ (14.68\ meV) + {}^4He\ (3.67\ meV)$, where p is a proton [25–27]. On Earth, helium-3 is observed in trace amounts, i.e., on the verge of its practical absence. Rare in nature, the gas is mainly formed because of the radioactive decay of tritium produced in nuclear reactors and during the storage of nuclear and thermonuclear weapons. This gas is collected in quantities of several tens of kilograms per year and is commercially available for use in low temperature physics and in neutron detectors used for both scientific and security purposes [28, 29].

In contrast to the Earth, helium isotopes and other noble gases and cosmogenic isotopes have accumulated in particles and minerals of the lunar regolith throughout the geological history of the Moon because of constant irradiation by the solar wind. Direct measurements of concentrations of helium isotopes and other noble gases from the solar wind trapped by regolith particles have been performed for all regolith samples taken from different regions of the Moon by Soviet lunar stations Luna-16, Luna-20, Luna-24, and manned Apollo missions. The study of regolith samples from the Apollo 11 expedition has revealed almost all basic features of helium isotope concentration and distribution in particles and minerals of lunar regolith, which were confirmed by the study of samples from other stations and expeditions. It was found that the content and isotope ratio of implanted helium in the lunar soil depend on the size of the regolith particles: the smaller the size, the greater the concentration and the smaller the $^4He/^3He$ isotope ratio [30, 31]. The concentration also increases with increasing age of exposure and the maturity regolith, i.e., it depends on the ionizing irradiation dose. However, the greatest change in the concentration of implanted helium is observed depending on the chemical and mineral composition of the regolith particles and can vary in a very wide range, up to 3 orders of magnitude and more [32]. The maximum content of helium-3 is observed in ilmenite ($FeTiO_3$), which is the main ore mineral of titanium in mare lunar basalts. Selective enrichment by solar wind ions of regolith depending on the mineral composition leads to heterogeneous regional distribution of helium isotope concentration and other noble gases in lunar soil [33–35].

To estimate the concentration, distribution and predicted helium-3 stocks in the lunar soil on the Near and Far sides of the Moon, different models based on remote optical sensing of distribution of chloroform elements TiO_2 and FeO with correlation of helium-3 content in regolith, as well as the degree of soil maturity and solar wind flux density at different latitudes [35, 36], and model regolith thickness [34, 37] were used. The purpose of this work is studying the concentration and distribution of helium isotopes in the lunar soil based on direct measurements of helium content in different minerals, in the bulk composition of regolith in areas of distribution of mare low-titanium and high-titanium basalts and Highlands's anorthosites, as well as estimating predicted helium reserves in different geological complexes with different bulk composition of regolith and underlying rocks, different helium content and different regolith thickness.

2 Helium Implantation and Trapping in Minerals of the Lunar Regolith

Lunar soil consists of bedrock fragments and such particles as glass, breccias, agglutinates, which were formed during meteoritic bombardment. The main rock-forming minerals are anorthite, bitovnite (basic plagioclase), olivine and pyroxenes. The main ore mineral in mare basalt is ilmenite. The regolith contains a significant amount of glass, mainly of impact origin. The regolith composition is mainly defined by underlying rocks composition, with the addition of impact craters ejects from other areas, and meteoritic component ($\sim$1 to 2 wt%). The regolith depletion in volatile components due to impact melting and evaporative differentiation is observed [38]. Constant influence of solar wind and cosmic radiation enriches particles and minerals of regolith with hydrogen, helium isotopes, rare gases, cosmogenic isotopes, and probably, promotes formation of reduced forms Fe, Ti, Si and other elements in surface layers of mineral particles. According to experimental data, metallic iron Fe^0 may form without participation of reducing agent (implanted hydrogen ions of solar wind), as well as bypassing process of iron condensation from impact-formed steam. Formation of chains of nanophase iron spherules in glasses and on surfaces of particles and minerals can occur thermo-reductive way during shock wave passage in shock melt because of meteorite and micrometeorite bombardment [39].

The general structure of the noble gas content in the lunar soil quite corresponds to the predicted cosmic prevalence of

these gases. The observed saturated ^{4}He concentration on the surface of ilmenite grains equal to 10^{-3} cm^3 ^{4}He cm^{-2} (3×10^{16} atoms ^{4}He cm^{-2}) corresponds to the integral solar wind flux of 7×10^{17} atoms cm^{-2} [30]. Such a dose of irradiation corresponds to an exposure time of about 300 years at the present intensity of the solar wind flux. At such radiation levels, heavy saturation effects are expected, which are likely to affect the relative content of captured solar wind ions. For example, the maximum experimental dose of saturation with protons on the quartz surface is observed at 5×10^{16} atom cm^{-2} [40].

Lunar soil has a complex layered structure and its own stratigraphic and geochemical history, which can be traced back to the formation of underlying rocks (Fig. 1). An average lunar soil formation rate is approximately 1.5 mm per 1 Ma [41]. Layers are a stratified sequence of unstable along strike deposits of ejections from the surrounding impact craters, spaced from the first meters to several hundred kilometers, depending on size of these craters. Therefore, a layer of more mature (older) regolith can partially overlap a layer of immature young regolith. Hyperbolic distribution of lunar soil density with depth and excessive compaction and over compaction of regolith not deep from the surface is explained by micrometeorite and fine meteorite bombardment, which loosens the surface layer and, on the contrary, compacts underlying regolith layers [42]. Complete mixing occurs only in the uppermost layer with a thickness of about 1 mm, until a new ejection covers this layer and removes it from the exposure zone by solar wind and exogenous recycling. During this time, the 0.1 mm thick layer will turn over more than 2000 times, the 1 mm thick layer will turn over 250 times, and the 1 cm thick layer will turn over once in 10^7 years [43].

Each layer can differ in bulk chemical and mineral composition, particle size, regolith maturity, and exposure age. At the same time in the layer itself there may be particles and minerals of lunar rocks not only of different composition, but also age of formation. The solar wind exposure age on the lunar soil determined by maturity index is about 200 Ma [44]. Sometimes the lunar soil exposure age exceeds this value twice and more. The soil exposure age buried in 62 cm depth in the Taurus-Litre Valley (Apollo 17) is estimated to be 550 ± 60 Ma [45]. Thus, the irradiation dose of minerals and regolith particles by protons and helium significantly exceeds the saturation dose.

Depending on the mechanism of retention in lunar soil of trapped noble gases from solar wind two main types of helium are distinguished: weakly bound, saturating pore space of lunar regolith, and implanted in particles and minerals of lunar soil. Due to the high diffusion and evaporation rate of weakly bound helium, which reaches 10^2 s [34], most of the helium escapes from the lunar regolith. Nevertheless, the content of the remaining helium exceeds the solubility of helium in the lunar regolith by 15–20 orders of magnitude under the conditions of rarefied lunar atmosphere [46], which indicates a certain ability of the lunar soil to retain implanted volatile components.

The content of weakly bound helium in the lunar soil is determined by diffusion, the rate of which is determined by the temperature and different densities of the solar wind flux at different latitudes [34]. The accumulation of weakly bound helium in the lunar regolith largely depends on the surface temperature and does not depend on regolith composition. The content of this helium type substantially increases at high lunar latitudes characterized by low diurnal temperatures and the minimum amplitude of the diurnal temperature variations. It is assumed that the content of weakly bound isotope ^{3}He in the Polar Regions of the Moon can reach 40–50 ppb [34, 36]. This type of helium, as compared to the implanted component, is characterized by a more uniform distribution, the highest availability, and, apparently, the highest concentration in the Polar Regions. Weakly bound helium is easily released under thermal and mechanical effect on the lunar soil and requires the development of special methods for in situ research. The weakly bound type of gases is one of the least studied in the lunar regolith [47].

In contrast to weakly bound gases, implanted gases are stable under mechanical and temperature effects on regolith within several hundred degrees and can be sampled and delivered to the Earth together with lunar soil without special losses and studied in laboratory conditions. This property makes this type of gas the most studied type. Direct measurements of concentrations of noble gases trapped by regolith particles from the solar wind composition were performed for all regolith samples delivered by Soviet automatic lunar stations and operated Apollo expeditions. The study of ^{3}He concentration in size fractions of regolith showed a clear dependence of concentration on the size of fraction—the smaller the size of regolith particles, the greater the concentration of helium-3. The observed distinct inverse proportional correlation of gas content depending on regolith grain size (Table 1) is approximated by the expression

$$c \infty d^{-n},$$

where c is a gas concentration, d is a particle size, and an exponent n is estimated in the range from 0.58 to 0.65 for all noble gases [30]. Lunar regolith consists of 50% of particles < 50 μm in size [48], which contain up to 80% of all trapped helium [49]. Thus 90% of the trapped helium in lunar regolith is contained in fraction of size < 100 μ [31].

For ilmenite grains also observed a clear dependence of the content of trapped gases on the grain size. The exponent

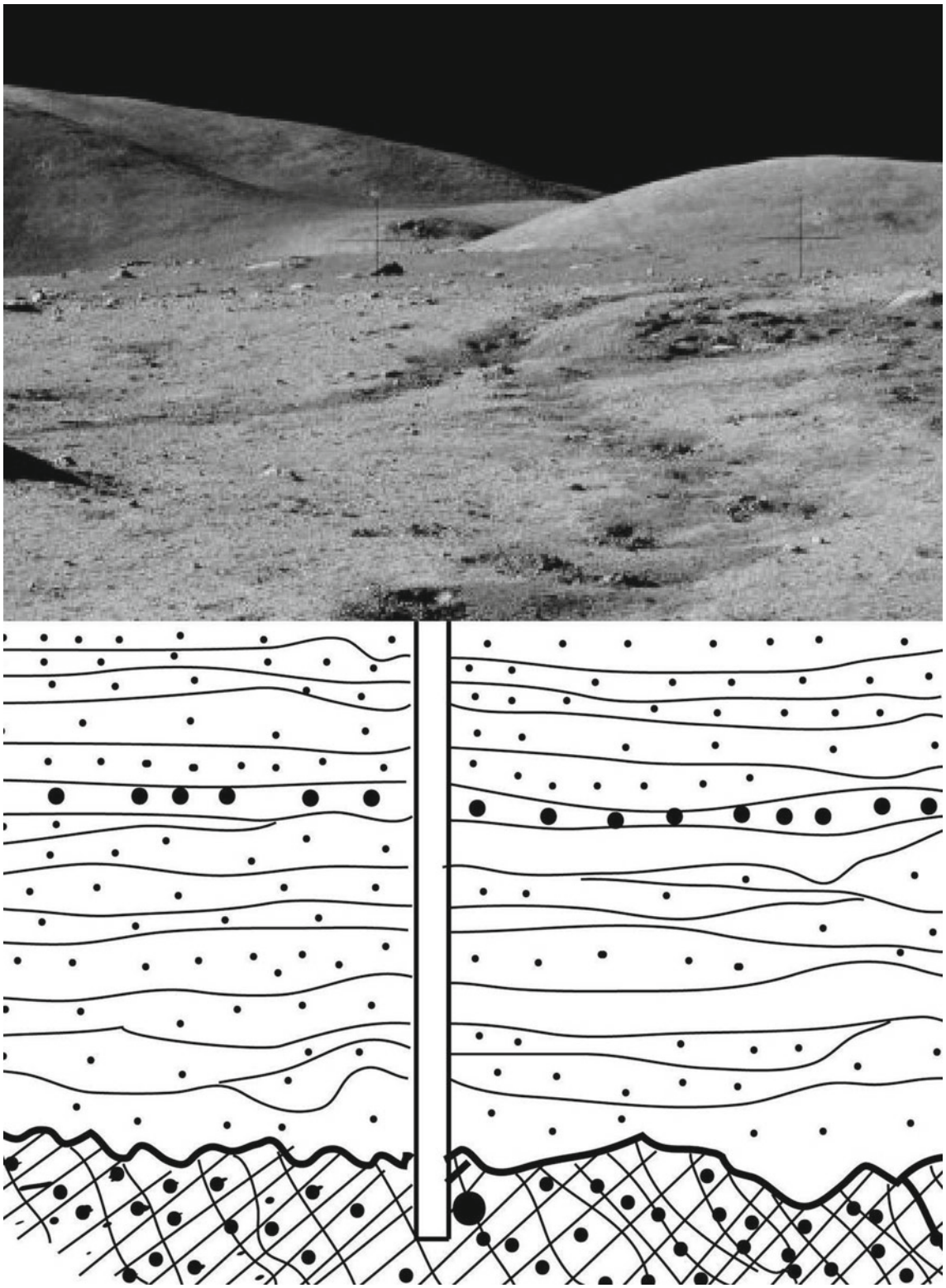

Fig. 1 Schematic section of the structure of the loose layer of lunar regolith with a borehole in the center. Parallel shading shows the layered structure of the regolith. The underlying rocks are shown by cross-hatching. Above is a photo panorama from the Apollo 17 landing site (*Credit* NASA)

Table 1 Distribution of helium isotopes by size fractions of regolith from the Apollo 11 landing site [30]

#	Fraction, μm	Content ^{3}He, ppb	Content ^{4}He, ppm
1	130	4.6	11.5
2	90	5.6	14.5
3	42	6.8	17.8
4	15	15.8	40.6
5	3.7	37.2	89.3
6	2.0	64.2	153.4
7	1.4	95.0	221.4

(n) for grains of ilmenite mineral ($FeTiO_3$) ranges from 1.15 to 0.82. This dependence of a gas content on the grain size can be explained by concentration of gases in the surface layer of individual grains, i.e., the smaller the particle size, the greater the particle surface relative to the soil density. The dependence degree of gas content on grain size for ilmenite is higher (Table 2) than for bulk regolith composition and is approximately constant per unit particle surface. This means that saturation time of regolith with noble gases does not depend on size of regolith particles and is determined only by the exposure time. Helium content in fractions of approximately the same size of ilmenite in comparison with a similar fraction of regolith, where ilmenite in its natural percentage is also present, is almost 4 times higher (Tables 1 and 2). Separate particles of regolith, for example, glass spherules, which possess an amorphous structure, in relation to bulk composition of regolith are characterized by even greater intensity of diffusion losses of helium and contain the smallest amount of trapped helium in comparison with other rock-forming minerals [30].

Using the method of successive etching of the surface of ilmenite particles, it was found that practically all trapped helium and other noble gases are concentrated in the surface layer 200 nm thick (Table 3). The content of the isotope ^{3}He formed as a result of fission of radioactive element nuclei in mineral particles of regolith was determined in heavily etched samples of ilmenite grains, in which the surface layer containing the implanted isotope ^{3}He was removed. The amount of helium-3 formed by nuclear reactions was estimated to be 0.7 ± 0.2 ppb, which is generally in good agreement with the regolith age estimated from xenon decay [30]. Taking into account this value, the corrected ratio of implanted ^{4}He/^{3}He isotopes in ilmenite is within 2590–2840 and averages 2720 ± 90. For regolith bulk composition for different size fractions the isotopes ratio is not homogeneous. For coarse fractions the measured isotope ratio ^{4}He/^{3}He exceeds 2500, and with correction this value increases about 10% and agrees with the value characteristic of ilmenite [30]. The isotope ratio for thin regolith fraction is less than 2400. The isotope ratio correction for this fraction is less than 2%. The difference can be explained either by the effect of grain size or by a systematic difference in mineral composition of different fractions. The addition of the ^{4}He isotope because of decay of U and Th over 4.5 billion years is negligibly small compared to the implanted helium.

The implanted helium content is determined by composition and structure of minerals in lunar regolith and varies in a very wide range up to three orders of magnitude or more. Crystal lattice radiation-induced defects trap and retain helium ions much efficiently than ones in the amorphous structure retain [50]. The binding energy of a trapped helium atom in vacancy traps of the crystal lattice is determined by the occupied defect type and reaches more of 1 eV [51, 52].

The theoretical calculations using the SRIM2010 program [53] showed that the maximum ionization energy losses of hydrogen ions (dE/dx) during interaction with quartz should occur at 80–90 keV energy (Fig. 2) [54]. When hydrogen ions with energies less than 80 keV and more than 90 keV are irradiated, the ionization losses in the interaction of hydrogen ions with quartz decrease. This is explained by the fact that at low velocities of ionizing radiation particles, when $v \leq u$, where u is the mean velocity of electron in atom, the overcharge effect becomes significant, which consists in the fact that the passing particle captures (and sometimes, on the contrary, loses) electrons and becomes neutral [55]. Overcharging leads to a reduction of ionization losses. At high energies, the effect of electric polarization of the medium under the action of the particle

Table 2 Content of helium isotopes in different fractions of ilmenite from the Apollo 11 landing site [30]

#	Fraction, μm	Content ^{3}He, ppb	Content ^{4}He, ppm
1	105	7.5	19.4
2	65	15.3	37.9
3	41	22.2	59.3
4	22	45.6	120.4

Table 3 Distribution of implanted helium in the surface layers of ilmenite grain [30]

#	Fraction, μm	Layer thickness, μm	Content ^{3}He, ppb	Content ^{4}He, ppm
1	41	–	27.0	69.4
2	41	0.16	19.9	52.7
3	41	0.19	10.8	26.4
4	41	0.35	3.3	6.7

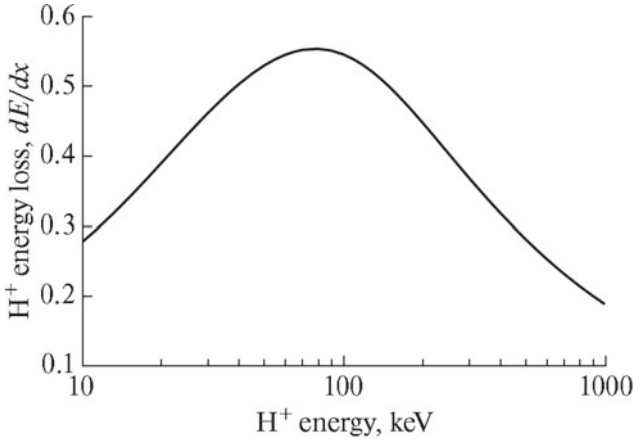

Fig. 2 Ionization energy loss of hydrogen ions (*dE/dx*) related to interaction with quartz as a function of irradiation energy calculated using the SRIM2010 program [53]

field is effective. Polarization leads to sharp reduction or, as they say, to screening of the particle's field and, consequently, to reduction of losses.

At low irradiation energies and doses at which hydrogen ions saturation of quartz samples surface occurs, rapid destruction of quartz crystal lattice and formation of amorphous film on the crystal surface [54]. At energies close to the maximum ionization loss energy of hydrogen ions in quartz about 90 keV, as X-ray diffraction analysis shows, inter-nodal defects develop to a depth of 1 μm, which lead to the increase of the quartz lattice parameter Δd/d [54]. In this case, the amorphous layer is not formed, but the microcrystalline structure of the disturbed layer is preserved.

Unlike quartz, in ilmenite at low irradiation energies, the microcrystalline structure of the disturbed layer is preserved, in which radiation defects of the crystal lattice continue to develop [56], which increases the adsorption capacity and reduces the degree of diffusion losses of trapped ions. Amorphization of the crystal structure of ilmenite begins at energies of about 120 keV [57], which is approximately an order of magnitude higher than that of quartz and aluminosilicates [58]. Unlike rock-forming minerals of dielectrics, the main ore mineral of lunar basalts ilmenite is a semiconductor with a hole conductivity [59]. It is supposed, that presence of conductivity at interaction with charged particles of solar wind allows keeping crystal structure to a mineral.

As in radiation-induced amorphous films of silicates and aluminosilicates [60], the chemical composition of the disturbed microcrystalline layer of ilmenite also changes. At the boundary with the unchanged phase of the host mineral, compared with its composition, iron depletion is observed, while in the upper part of the disturbed layer, on the contrary, enrichment with reduced metallic iron [57]. Titanium in the disturbed layer also changes its valence from Ti^{+4} to Ti^{+3} and Ti^{+2}. When the ions destroy the bonds of the ilmenite crystal lattice, a 2–threefold decrease in the O/Fe and O/Ti ratios is also observed, indicating a significant loss of oxygen.

Under influence of ionizing irradiation in amorphized layer of silicates, aluminosilicates and oxides, apparently, radiation-induced fractionation of isotopes Fe and, probably, isotopes Ti and other elements can occur. During irradiation of quartz samples with energy of 20 and 110 keV by protons with implanted $^{54}Fe^{+}$ and $^{56}Fe^{+}$ isotopes it has been founded, that not only general shift of Fe isotope concentration in depth on the quantity about 20 nm occurs, but at enough high energy of hydrogen ions (65–200 keV) radiation-induced fractionation of Fe isotopes is observed [61]. The value of the radiation-induced fractionation of Fe isotopes (5 nm) is approximately equal to the observed value of the kinetic mass fractionation (5.8 nm), but with the opposite sign.

The metallic Fe^{0} content in the amorphous mineral layer is determined by the signal intensity of ferromagnetic resonance (I_s) [62]. The ratio of the signal intensity I_s to the total FeO content in regolith by weight % characterizes the regolith maturity degree. The parameter ($TiO_2 \times I_s$/FeO) is used to describe the total dependence of the ^{3}He content on the ilmenite content and the regolith maturity (Fig. 3)

$$^{3}\mathrm{He(ppb)} = 0.2043(\mathrm{TiO_2} \times I_s/\mathrm{FeO})^{0.645},$$

The formation of an amorphous layer on the mineral surface as a result of ionizing irradiation, apparently, leads to decrease in the efficiency of traps and, accordingly, to a decrease in the helium content. Implantation depth of solar wind ions is determined by the ion mass, their energy and the target composition (Fig. 4). If hydrogen ions implantation with energy of 20 keV into quartz does not exceed 250 nm, the implantation depth of hydrogen ions with

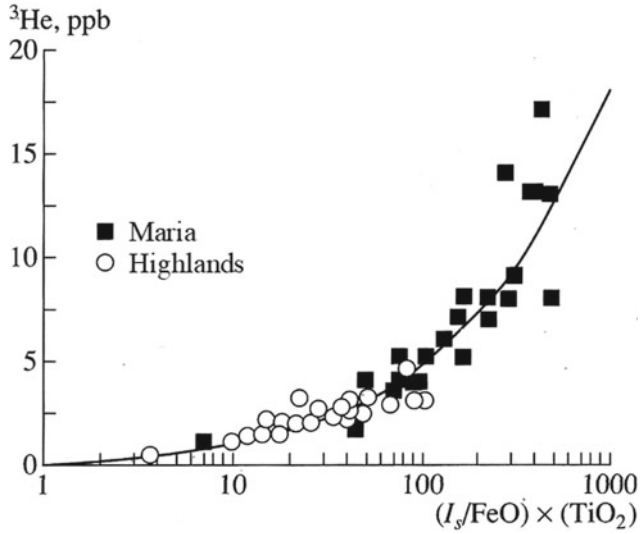

Fig. 3 Content of He depending on the parameter ($TiO_2 \times I_s$/FeO) [28]

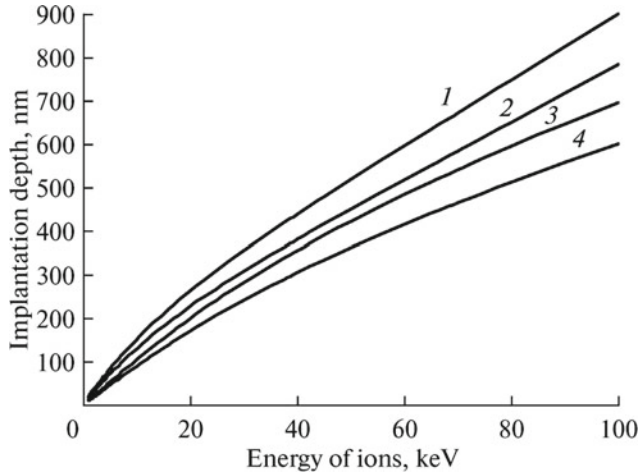

Fig. 4 Dependence of the implantation depth of protons and He^+ ions in quartz and anorthite on the ions' energy [32]: 1—implantation of protons in quartz; 2—implantation of protons in anorthite; 3—implantation of He nuclei in quartz; 4—implantation of He nuclei in anorthite

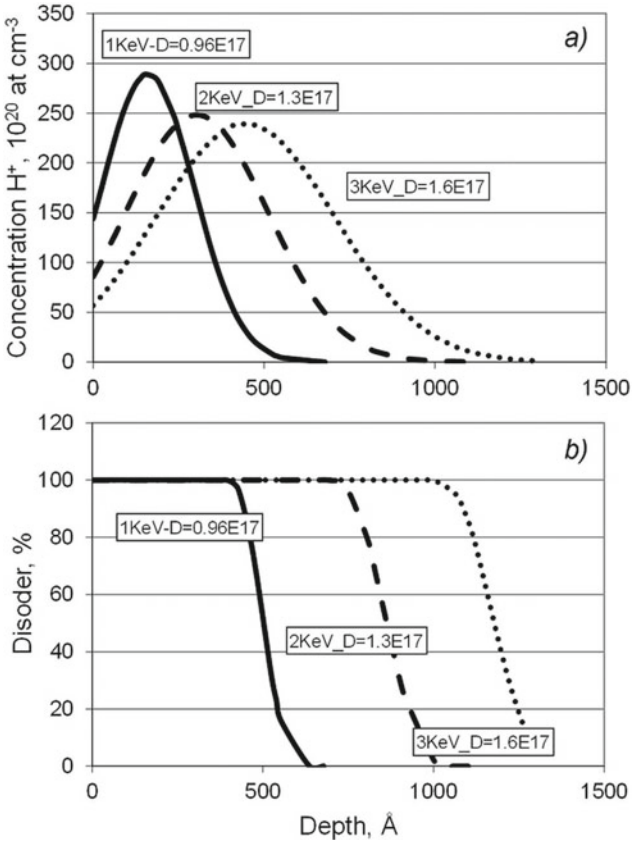

Fig. 5 Protons' implantation depth and amorphization degree (disorder) in anorthite depending on protons' energy and a dose for 1 keV D = 0.96 × 10^{17} atom cm^{-2}, for 2 keV D = 1.3 × 10^{17} atom cm^{-2}, for 3 keV D = 1.6 × 10^{17} atom cm^{-2}: **a** distribution of the implanted protons' concentration; **b** amorphization degree (disorder) of an anorthite lattice

energy of 90 keV increases three times and reaches 850 nm [32]. The similar distribution of hydrogen on depth depending on irradiation energy is observed in crystals of silicon, and the value of average run of hydrogen ions with energy about 100 keV also makes about 1 μ [40].

Calculations with the program SUSPRE [63] show that with the increase of energy from 1 to 3 keV the depth of proton implantation in anorthite ($Ca(Al_2Si_2O_8)$) increases three times regardless of the flux density, whereas the degree and depth of amorphization much more depends on the flux density [58]. If at a flux density of 1 × 10^{15} atom cm^{-2}, the implantation depth outpaces the development and depth of amorphization, then at a flux density of about 1.6 × 10^{17} atom cm^{-2} the implantation is actually localized inside an already well-developed amorphous layer (Fig. 5). The same tendencies are observed in the case of irradiation by He^+ ions with the only difference that the thickness of the amorphous layer at high flux density coincides with the maximum depth of He^+ implantation. At the same time the implantation depth and thickness of the amorphous layer at helium irradiation is approximately two times greater than at proton irradiation (Fig. 6).

At increase of energy from 1 to 3 keV the depth of proton implantation in quartz (SiO_2) as well as in anorthite increases almost three times regardless of flux density. The extent and depth of amorphization of quartz surface under the action of ionizing irradiation depends mainly not on energy, but on flux density. At flux densities of 1 × 10^{16} atom cm^{-2} and less, the implantation depth greatly exceeds the development and depth of amorphization, regardless of the proton energy. At doses, exceeding 1 × 10^{16} atom cm^{-2} the implantation is actually localized inside the forming amorphous layer

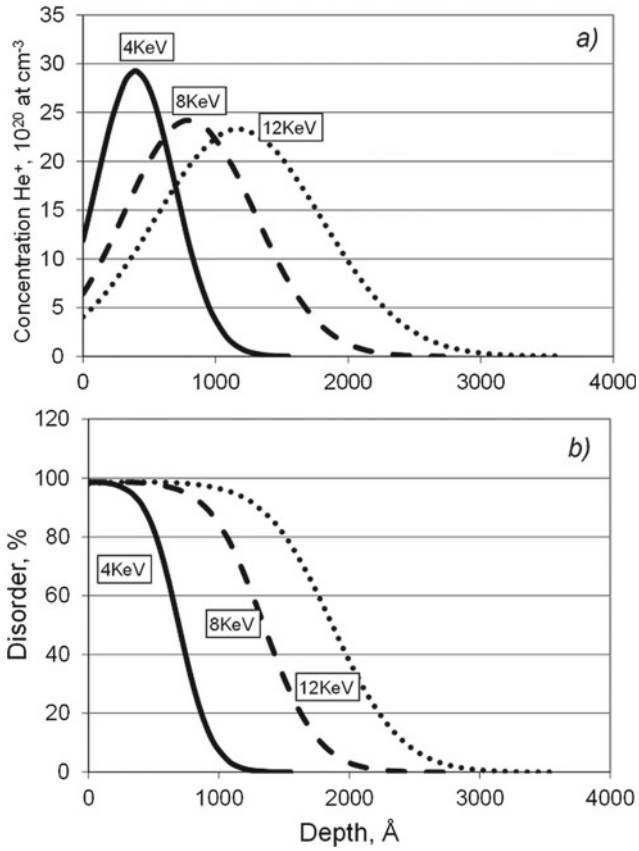

Fig. 6 Implantation depth of He^+ and amorphization degree (disorder) in anorthite depending on ions energy and a dose for 4 keV D = 2 × 10^{16} atom cm^{-2}, for 8 keV D = 2.8 × 10^{16} atom cm^{-2}, for 12 keV D = 3.5 × 10^{16} atom cm^{-2}: **a** distribution of the implanted helium concentration; **b** an amorphization degree (disorder) of an anorthite lattice

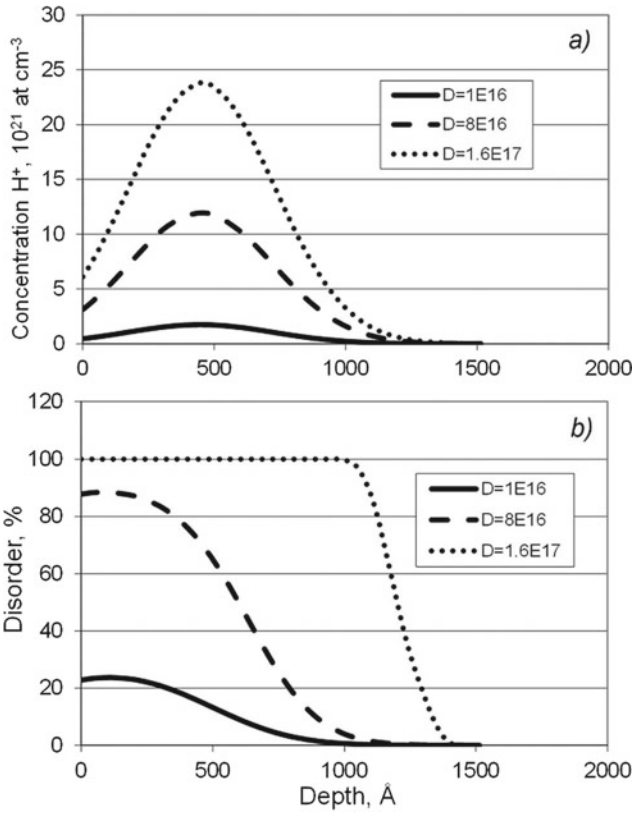

Fig. 7 Protons' implantation depth and amorphization degree (disorder) in quartz at constant energy of 3 keV and a doses D = 1 × 10^{16} atom cm^{-2}, D = 8 × 10^{16} atom cm^{-2}, and D = 1.6 × 10^{17} atom cm^{-2}: **a** distribution of the implanted protons' concentration; **b** an amorphization degree (disorder) of a quartz lattice

regardless of the proton energy (Fig. 7). The complete (100%) amorphization of quartz surface is developed at the doses exceeding 8 × 10^{16} atom cm^{-2}, and at flux density of 1.6 × 10^{17} atom cm^{-2}, the thickness of amorphous layer on the quartz surface achieves 100 nm (Fig. 7). When irradiated with He^+ ions, the depth of quartz structure destruction and amorphization, regardless of energy and dose, always coincides with the maximum ion implantation depth (Fig. 8). Intensity of amorphization is also mainly defined by a dose of irradiation (Fig. 8).

Thus, at dose increase up to integral value of flux (7 × 10^{17} atom cm^{-2}) observed in lunar regolith, all chemical and physical processes of space (geochemical) weathering of anorthite and quartz particles in lunar regolith, apparently, will occur inside the formed radiation-induced amorphous film on crystal surface, not reaching the crystal structure of mineral. In contrast to protons, the maximum concentration of He^+ ions regardless of dose in both anorthite and quartz will accumulate in the transition zone between the amorphous and crystalline phases of the mineral.

The lowest content of noble gases in impact and volcanic glasses is observed. Helium-3 in green glass spheres in lunar soil samples of Apollo-15 is in the range of 0.02–0.3 ppb (average for all size fractions about 0.2 ppb), and Helium-4 in the range 7–605 ppb (average for all size fractions 100–200 ppb) [64–66]. It is about 100 times less, than in the bulk regolith composition.

Similar small helium content in basic plagioclase are observed, where ^3He content varies in the range 0.02 to 0.2 ppb, and ^4He from 33 to 500 ppb [66, 67]. As noted above, for all crystalline minerals of lunar regolith, including plagioclase, there is an inverse proportional dependence of helium concentration on particle size—the smaller the size, the higher the concentration [30, 66, 68]. In contrast, a direct proportional dependence, although not as pronounced, is observed for green glasses: the smaller the particle size, the smaller the helium concentration [64, 66]. Probably, this dependence is explained by the inclusions of mafic minerals in larger glasses. Helium content in magnetic glasses with

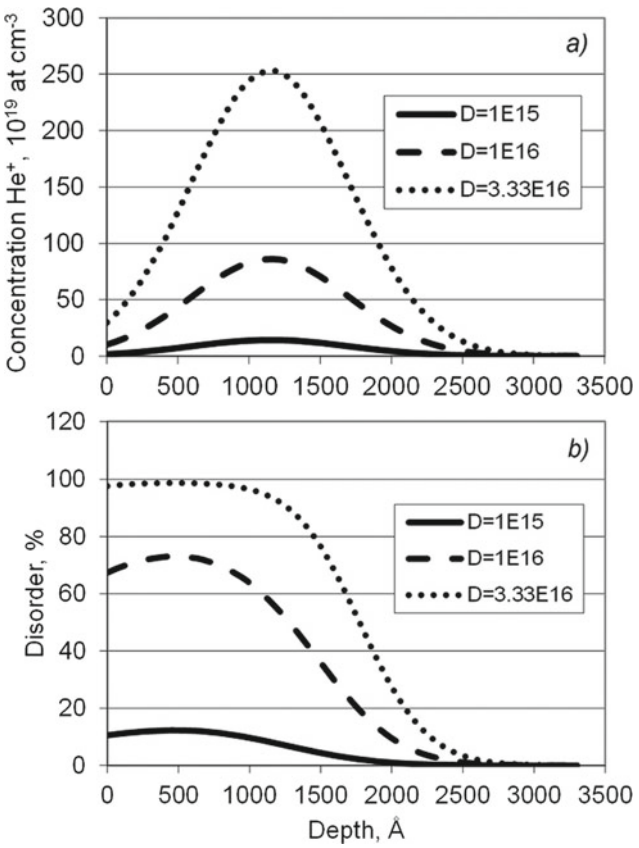

Fig. 8 Implantation depth of He^+ and amorphization degree (disorder) in quartz depending on dose of $D = 1 \times 10^{15}$ atom cm^{-2}, $D = 1 \times 10^{16}$ atom cm^{-2} and $D = 3.33 \times 10^{16}$ atom cm^{-2} at constant energy of 12 keV: **a** distribution of concentration of the implanted helium; **b** an amorphization degree (disorder) of a quartz lattice

large number of such inclusions significantly increases compared to green glasses [67].

The helium highest content in ilmenite are observed. In grains of ilmenite sized 10–14 μm, the ^{3}He content can reach 130 ppb, and ^{4}He—360 ppm [68]. Helium isotopes content in bulk regolith composition of the same fraction in lunar soil samples of Apollo 12 is 12 ppb of ^{3}He and 30 ppm of ^{4}He. ^{3}He content in bulk regolith composition without separation into size fractions is almost two times less and is 7.1 ppb and ^{4}He is 16.5 ppm.

The ^{3}He content in olivine with a grain size of 25–42 μm is 2.9 ppb and ^{4}He is 6.24 ppm [65]. In the mixed fraction of olivine and pyroxene grains with a grain size of 25–42 μm, the helium isotope content is similar: 2.9 ppb and 6.2 ppm, respectively [66]. However, the pure pyroxene fraction with approximately similar grain size of 30–48 μm contains implanted helium two times more (5.7 ppb ^{3}He and 13.4 ppm ^{4}He) than olivine [67].

Thus, helium content in glasses and plagioclases of the lunar soil is approximately 100 times less than in bulk regolith composition, but helium content in ilmenite, on the contrary, is approximately 10–12 times more than in bulk regolith composition of similar fraction and about 20 times more in comparison with bulk regolith composition without separation into fractions. Olivine and pyroxene are characterized by the medium helium content compared to glass and ilmenite. Obviously, under equal irradiation conditions, in which the ilmenite grains were together with other minerals of the regolith, the different helium content is due to the different mineral composition and structure of the target, i.e. due to the variety and number of defects-traps.

3 Helium Content in Regolith of Lunar Maria and Highlands

Mare rocks are represented mainly by lava rocks of the basalt type, which fill the depressions of lunar mares. Pyroclastic material is also found. In general, mare rocks compose about 1% of the lunar crust. The predominant mare rocks of the Moon are mare basalts. In bulk chemical composition marine basalts correspond to rocks of gabbro-basalts group and are usually defined as ilmenite, olivine, cristobalite basalts (gabbro), etc. [69, 70]. The petrographic specificity of mare basalts is in the smaller grain size (hundreds of microns) and in the practical absence of volcanic glass. The major rock-forming minerals are clinopyroxenes and plagioclase (An50-95), sometimes olivine (Fo50-75); the major ore mineral is ilmenite ($FeTiO_3$). The ilmenite content varies from 0.1–1 wt% in low-titanium basalts [71, 72] to 10–20 wt% in high-titanium basalts [73]. Formation of mare basalts which cover about 20% of the Moon's surface [74] is connected with the processes of partial mantle melting, and the difference in mineral composition of basalts, apparently, with different depth of melt formation, and/or lateral changes in composition of lower crustal layers and upper mantle [41, 75].

Lunar pyroclastic material is a rare type of lunar marine formations [76, 77]. Pyroclastic material is represented by green and orange glasses—mainly in the form of glass globules and their fragments, which have no direct equivalents in chemical composition among crystalline rocks. Green glasses have a primitive mafic composition and are considered to be the least differentiated lunar matter. The particle surface of green and orange glasses is strongly enriched with Zn, Pb, F and other volatile components, which is associated with the processes of condensation of volcanic (fumarolic) products. The glasses have an amorphous structure and are characterized by the lowest content of noble gases trapped from the solar wind.

Ultrabasic rocks, which, as well as pyroclastic material, are extremely rare, occur as xenoliths in mare basalts. The rocks are represented by cataclased and recrystallized dunites, and less frequently by peridotites. They consist mainly of olivine (Fo9-12) with an admixture of pyroxenes,

plagioclase, metallic iron, and troilite. Formation of these rocks is associated both with the early stage of global differentiation of the Moon (age of mantle dunites is close to the age of the Moon), and with later stages of formation of the lunar crust [69, 70].

Highlands's rocks are represented by feldspathic rocks, which are subdivided according to their chemical and mineralogical composition into two main groups: lunar anorthosite rocks and lunar non-maria basalts [69, 70]. Structurally, these rocks are predominantly breccias with blast and cataclase matrix, granulites, and cataclasites. They are the oldest lunar rocks whose age—up to 4.5 billion years—is close to the time of planetary body formation. Minimum age of brecciation (metamorphism) is ~ 3.9 billion years. Formation and brecciation of Highland rocks occurred during intense meteorite bombardment. Highlands's rocks are the main type of lunar crust rocks.

Among Highlands's rocks the most widespread are rocks of anorthosite-norite-troctolite (ANT) series, gabbro-norites and gabbro-anorthosite. The latter are the main type of rocks of the lunar Highlands. The rocks are characterized by high content of Al ($Al_2O_3 > 24$ wt%), Ca, Mg and some rare elements. The main minerals are basic plagioclase (mainly anorthite), olivine (Fo70-95), orthopyroxenes (enstatite and bronzite), and clinopyroxenes (diopside, augite, pigeonite). The content of ilmenite in the anorthosite rocks is usually less than 0.1–0.2 wt% [78]. It is assumed that the rocks of the ANT series are the product of gravitational differentiation, i.e., plagioclase surfacing or precipitation of ferromagnesian minerals in the primary mafic melt [75].

Lunar non-mare basalts are a sparsely distributed group of Highland rocks of the Moon with Al_2O_3 content of 15–24 wt%. An important feature of non-mare basalts is the increased content in some of them of the so-called KREEP-component characterized by enrichment of K, REE (rare-earth elements) and P (English abbreviation K-REE-P), as well as Zr, Ba, U, Th and some other lithophile elements. According to this parameter, basalts with low content of KREEP elements and KREEP-basalts are distinguished. In the American special literature, the "non-marine basalt" is a medium-potassium Fra Mauro basalt. The petrographic specificity of all non-mare basalts is that most of them are breccias, which consist of clasts with a pronounced magmatic structure with grain sizes up to hundreds of microns. The formation of non-mare basalts is associated with the processes of partial melting of lunar crust rocks at relatively low pressures.

Acidic rocks of the Moon are the most exotic type of lunar matter. Lunar acidic rocks occur as individual small fragments in regoliths and breccias, and as cementing masses of breccias. The main minerals are pyroxene, tridymite, cristobalite, and K-Ba-feldspar; secondary minerals are medium plagioclase, apatite, vitlockite, and zircon. The biggest and the most famous granite specimen is breccia 12013, delivered from the Apollo-12 landing site [79]. Formation of acidic rocks of the Moon is associated with the process of residual melt liquation during fractional crystallization of basaltic magma.

Regolith samples delivered from 9 different regions of the Moon by Soviet lunar automated stations and American Apollo manned expeditions have made it possible to measure the content in the bulk composition of regolith of different rocks—from low-titanium to high-titanium mare basalts and in Highland anorthosite.

The observed dependence of the helium isotope content on the size and composition of the regolith particles imposes significant restrictions on the use of measured values to estimate predicted reserves of this isotope in the lunar soil. First of all, it concerns representativeness of these estimates to reflection of total particle size in regolith and total (bulk) composition of regolith. The content estimates obtained for discrete size fractions of the regolith as well as for separate components of the regolith distinguished by mineral, chemical, or other characteristics are unsuitable for use. In contrast, the most objective and optimal estimates are those obtained for representative samples of regolith with a full range of particle sizes (< 1 mm) without partitioning into fractions and components, i.e., for bulk samples. If data are available for several bulk samples of regolith, the weighted average value of ^{3}He content is found for the mass of the investigated sample, which is taken as the basic value for the specified landing area.

The average weighted contents of helium in bulk samples of regolith with particle size fraction < 1 mm from the Apollo 11 landing site can be obtained only for two values (16.5 and 14.6 ppb) out of four, for which the mass of the studied sample is indicated (Table 4). The weighted average content of the isotope ^{3}He, equal to 15.1 ppb, and the isotope ^{4}He, equal to 41.1 ppm, is taken as a value characterizing the average isotope content in the regolith in the Apollo 11 station area and in the Mare Tranquillitatis. The weighted average value for the data in Table 1 is 20.4 ppb, but also cannot be used for reserves assessment because it characterizes only a few discrete size fractions of the regolith.

The ^{3}He content for a representative sample of regolith from the Apollo 12 landing area in the Oceanus Procellarum is 7.1 ppb and ^{4}He is 16.4 ppm [68]. The absence of data on the mass of the investigated regolith samples from the Apollo-14, and -15 landing sites does not allow us to obtain an average weighted helium content for each of the landing sites (Table 5), but the small scatter of values allows us to use the average value [82]. An average value of ^{3}He equal to 5.7 ppb is taken for Apollo-14 station and 4.4 ppb for Apollo-15 station. The average ^{4}He isotope content is taken to be 15.1 ppm and 11.1 ppm, respectively.

Table 4 Content of helium isotopes in regolith samples from the Mare Tranquillitatis at the Apollo 11 landing site

#	Sample	Mass, mg	Content ^{3}He, ppb	Content ^{4}He, ppm	^{4}He/^{3}He	References
1	10,084.40	3.507	16.5	44.0	2665	[80]
2	10,084.40	10.827	14.6	40.2	2750	[80]
3	10,084.18	–	14.1	36.0	2550	[31]
4	10,084.59	–	24.3	51.8	2130	[81]

Table 5 The content of helium isotopes in the regolith at the Apollo 14 and Apollo 15 landing sites [82]

#	Spacecraft	Sample	Content ^{3}He, ppb	Content ^{4}He, ppm
1	Apollo 14	14,003	5.3	15.4
		14,163	5.7	14.3
		14,259	6.2	15.5
2	Apollo 15	15,601	4.6	11.0
		15,091	4.2	11.2

Table 6 Content of helium isotopes in the regolith in the Highland region at the Apollo 16 landing site [83]

#	Sample	Content ^{3}He, ppb	Content ^{4}He, ppm
1	63,321.7	1.6	4.5
2	63,341.4	1.5	4.2
3	63,501.22	1.4	3.9
4	67,941.15	1.0	3.0

Average concentration of ^{3}He and ^{4}He in regolith in the landing area of manned expedition Apollo 16 (Table 6) is 1.4 ppb and 3.9 ppm accordingly.

The content of helium isotopes in bulk samples of regolith at depth to 3 m according to the data of core drilling in the area of Apollo 17 expedition landing in the southwest part of the Mare Serenitatis (Table 7) is characterized by relatively uniform distribution with small variations on depth. This is also quite consistent with the relatively uniform distribution of the absolute age of the regolith exposure, which averages over 62 cm depth to 550 ± 60 Ma [45]. The average content of ^{3}He and ^{4}He isotopes in this area is 8.0 ppb and 20.8 ppm, respectively.

At the Soviet Luna-16 station in the eastern part of the Mare Fecunditatis, sampling was carried out by means of core drilling to a depth of 35 cm. Data on helium content are known from several sources with different degrees of representativeness of the samples depending on the fraction size of the samples studied (Table 8). The most representative sample of regolith studied is sample L16-19 [84], which is the least enriched and most fully reflects the size range of lunar regolith particles among the values presented in Table 8. Thus, the content of ^{3}He equal to 7.9 ppb and ^{4}He equal to 20.1 ppm is taken as the most representative.

Core drilling to a depth of 30 cm was carried out at the landing site of the Luna-20 station in the Highland area. The data obtained [88] were evaluated for the thin regolith fraction with particle size less than 83 μm, the larger regolith fraction was withdrawn (Table 9). The 2002-1 regolith sample was taken from a depth of 5–10 cm from the lunar

Table 7 Content of helium isotopes in regolith in the Apollo 17 landing site [45]

#	Depth, cm	Content ^{3}He, ppb	Content ^{4}He, ppm	Exposure soil age, Ma
1	0–5	11.2	27.7	360
2	26	3.4	8.9	330
3	62	7.0	19.1	560
4	93	6.6	16.8	610
5	133	7.1	18.2	490
6	173	8.2	21.6	530
7	213	9.6	26.1	610
8	253	8.5	22.6	550
9	290	9.8	26.0	490

Table 8 Content of helium isotopes in the regolith at the Luna-16 landing site

#	Sample	Fraction, μm	Content ^{3}He, ppb	Content ^{4}He, ppm	References
1	L16-19	1–400	7.9 ± 0.35	20.1	[84]
2	7-1a	≤ 83	12.4	33.1	[85]
3	G-7	≤ 125	14.3	33.6	[86]
4	G-49	40–150	4.2	14.1	[87]

Table 9 The content of helium in the regolith at the Luna-20 landing site

#	Sample	Content ^{3}He, ppb	Content ^{4}He, ppm	References
1	L2010	3.1	8.2	[89]
2	2002–1	4.0 ± 0.36	10.0	[88]
3	2004–1	5.89 ± 0.45	15.0	[88]

surface and the 2004-1 sample from a depth of 15–20 cm from the surface. The data obtained [89] were evaluated for the size fraction of regolith < 400 μm. Taking into account the dependence of the helium concentration on the size fraction of regolith particles, this sample is less enriched and, accordingly, more representative. Therefore, the ^{3}He content equal to 3.1 ppb and ^{4}He content equal to 8.2 ppm are taken as characteristic for the Highland area between the Mare Fecunditatis and the Mare Crisium at the landing site of the Luna-20 station.

The helium content for the offshore area in the southern part of the Mare Crisium was obtained by studying the regolith samples delivered by the Luna-24 station. Sampling at the station-landing site was carried out using core drilling to a depth of 225 cm. Helium content data were obtained for regolith fractions of size ≤ 375 μm [89] and ≤ 250 μm [90]. Table 10 shows the weighted average values for each regolith sample for a particular depth interval, since the regolith samples were divided into three or four size groups during the study. The interval-weighted average ^{3}He content at the landing site of Luna-24 station at a depth of 218 cm is 3.4 ppb and ^{4}He content is 7.2 ppm. It should be noted that the data for station Luna-24 are the most optimal from the point of view of estimation of ^{3}He reserves as they not only reflect almost all basic size range of regolith particles without exclusion, but also allow to estimate average weighted content at a depth up to 218 cm. It should be noted that the content of implanted helium isotopes in the regolith of low-titanium basalts in the Mare Crisium gradually decreases with depth [92].

In general, the average ratio of ^{4}He/^{3}He isotopes in the regolith of different bulk composition is about 2500. Based on the analysis of the available data on the content of helium in the lunar regolith in the landing areas of Soviet automatic stations and American manned expeditions, the most representative values have been determined, which are recommended for use at estimation the predicted reserves of helium in the lunar regolith of the corresponding composition (Table 11).

Thus, the loose regolith layer in the area of distribution of high-titanium basalts is characterized by the highest concentration of implanted helium isotopes and, accordingly, other noble gases. The concentration of implanted helium isotopes in the bulk composition of regolith decreases with

Table 10 The content of helium in the regolith at the Luna-24 landing site

#	Sample	Depth, cm	Content ^{3}He, ppb	Content ^{4}He, ppm	References
1	24,077.9	77–85	4.9	12.1	[91]
2	24,092.4	92–95	4.4	10.9	[90]
3	24,109.13	109–121	3.3	7.4	[91]
4	24,118.4	118–121	4.3	10.4	[90]
5	24,143.4	143–146	4.1	10.5	[90]
6	24,149.15	149–163	3.1	5.9	[91]
7	24,174.10	174–183	3.1	7.3	[91]
8	24,182.15	182–196	2.2	4.3	[91]
9	24,184.4	184–187	2.3	5.7	[90]
10	24,210.9	210–218	2.6	6.0	[91]

Table 11 The average content of helium isotopes in the regolith at the landing sites of the Soviet automatic stations and the American Apollo expeditions

#	Spacecraft	Landing site	Regolith composition	Content ^{3}He, ppb	Content ^{4}He, ppm
1	Apollo 11	Mare Tranquillitatis	High-titanium basalts	15.1	41.1
2	Apollo 12	Oceanus Procellarum	Basalts with medium ilmenite content	7.1	16.4
3	Apollo 14	Fra Mauro	Low-titanium basalts	5.7	15.1
4	Apollo 15	Mare Imbrium	Low-titanium basalts	4.4	11.1
5	Apollo 16	Highland	Highland anorthosites	1.4	3.9
6	Apollo 17	Mare Serenitatis	Basalts with medium ilmenite content	8.0	20.8
7	Luna 16	Mare Fecunditatis	Basalts with medium ilmenite content	7.9	20.1
8	Luna 20	Highland	Highland anorthosites	3.1	8.2
9	Luna 24	Mare Crisium	Low-titanium basalts	3.2	7.2

decrease of ilmenite content in basalts from high-titanium to low-titanium. The minimum concentration of helium is observed in Highlands's anorthosite rocks characterized by the minimum content of ilmenite and a lower content of mafic rock-forming minerals olivine and pyroxenes.

4 Lunar Soil Thickness

One of the first estimates of the thickness of the loose regolith layer according to data from automatic stations was made at the landing site of Luna-9 station in the Southeastern part of the Oceanus Procellarum. Based on the analysis of the depths of the largest craters (about 1 m) observed on the panoramic images, it was concluded that the thickness of the regolith at the landing site exceeded 0.2 m [93]. Attempts to directly measure the thickness of the regolith were made in the process of sampling the regolith by means of core drilling and core tubing at the landing sites of the Luna-16, Luna-20, Luna-24, and Apollo manned expeditions. The maximum drilling depth (225 cm) by the automatic drill rig LB-9 was achieved at the landing site of Luna-24 in the Mare Crisium [94], and the maximum drilling depth (305 cm) by the hand-held perforator was achieved at the Apollo-17 landing site in the Mare Serenitatis [95]. At the Apollo-15, and -16 stations, core drilling was performed to a depth of 236 cm and 224.3 cm, respectively [95]. Regolith sampling with core pipes was carried out to a depth of 70 cm at all Apollo stations [96]. In none of the 9 sites of direct sampling of the regolith at the landing sites, the base of the loose regolith layer was reached.

The thickness of the regolith was also evaluated by the size of the craters, which had uncovered the underlying rocks at the base of the regolith. The evidence of opening of the underlying rocks was the presence of a placer of rocks on the rim and in the area of the ejection of such a crater. This method of estimation was used in the analysis of the regolith thickness according to Lunokhod-1 and Lunokhod-2 data. In the western part of the Mare Imbrium, in the Lunokhod-1 study area, the regolith thickness was estimated to be within 1–5 m [97]. Regolith thickness in the eastern part of the Mare Serenitatis in the Lemonier Crater (Lunokhod-2) was estimated within of 2–3 m [98].

Studies of the granulometric composition of lunar regolith have shown a close relationship between the parameters of particle size distributions, regolith thickness and regolith maturity indices, which characterize the degree of processing of lunar regolith [99]. The standard deviation of particle sizes has the highest correlation dependence among the parameters of particle size distributions with regolith thickness. The found dependence is defined by expression

$$\sigma_{cm} = 1.53 + 0.102h,$$

where h is the regional regolith thickness. The regolith thickness estimates thus obtained at the landing sites of Luna-16 (Eastern part of the Mare Fecunditatis) and Luna-20 (Highland area to North of the Mare Fecunditatis) were 5.3 and 11.6 m, respectively [99].

The statistical analysis of impact crater morphology and crater population characteristics has also been successfully applied to estimate the regolith thickness [100]. The former is based on the dependence of crater shape on the regolith thickness, the latter on the determination of the characteristic crater size from which the deviation of the equilibrium crater distribution is observed. The size of these craters at the boundary of the equilibrium and non-equilibrium crater populations is directly proportional to the age of the surface and, correspondingly, the regolith thickness. Regolith

thickness data were obtained for 12 sites ranging from 336 to 3179 km^2 [100]. According to these estimates, the lowest thickness (3.3 m) is observed in the Southern part of the Oceanus Procellarum in the area of the Flamsteed crater (landing area of the Servier 1 spacecraft). Moderate regolith thickness (4.6 m) is observed in western and southern parts of the Mare Tranquillitatis (Landing Region of Apollo 11), in the southern part of the Sinus Medii (Landing Region of SC Servier 6), in the northern part of the Mare Cognitum (Landing Region of SC Servier 3 and manned expedition Apollo 12), and in the central part of the Oceanus Procellarum (Landing Region of SC Luna-13). The increased for mare areas regolith thickness (7.5 m) is observed in the northern part of the Sinus Medii and in the central part of the Mare Imbrium. The regolith thickness at the Hipparchus crater bottom in the Highland area reaches 16 m [100].

The regolith thickness at the landing sites of the Apollo manned expeditions was also determined by instrumental methods using electrical and seismic surveys. As a result of seismic experiments it was found that the lunar regolith layer is characterized by very low velocities of elastic longitudinal waves (80–120 m s^{-1}). The landing areas of the Apollo 11, -12 and -15 expeditions are distinguished by relatively young surface age and moderate thickness of the regolith. The regolith thickness in the south-western part of the Mare Tranquillitatis in the area of the spacecraft Apollo 11 landing according to the data of seismic experiment is estimated at 4.4 m, in the northern part of the Mare Cognitum in the landing area of the spacecrafts Servier 3 and Apollo 12 it is estimated at 3.7 m, and in the foothills of the Montes Apenninus in the Hadley Rille area in the Apollo 15 landing area it is estimated at 4.4 m [101]. The thickness of the low-velocity layer of lunar regolith (104 m s^{-1}) in the Fra Mauro area in the area of the Apollo 14 landing, according to instrumental data, was 8.5 m, and in the Highland area in the area of the Apollo 16 landing, 12.2 m [102]. The regolith thickness within the mare area in the area of the Apollo 17 station landing (intermountain plain Taurus-Littrow to the east of the Mare Serenitatis) according to less detailed regional seismic model is estimated in the range of 7–12 m [102]. The regolith thickness in the area of Apollo 17 station according to the assessment [103], also made on the basis of seismic experiment, does not exceed 8.5 m. A step change of the dielectric constant typical of the transition from loose regolith to denser underlying rocks according to electrical prospecting data in the same area was observed at a depth of 7 ± 1.0 m [104].

A model map of the regolith thickness distribution for the Moon Near Side based on the correlation of the depolarized and polarized components of the radio response at a wavelength of 70 cm with the optical albedo (0.65 μm) and the color index (0.65/0.42 μm) with a resolution of about 3 km in the center of the hemisphere was obtained [105], which is in satisfactory agreement with data obtained by other methods (Table 12). The highest thicknesses of regolith (more than 13 m) in Highland areas are observed in the southeastern part of the Moon Near Side in the Highland region. In the southwest part of the Near Side in Highland region are observed moderate thicknesses of regolith—7 to 11 m. This area represents the framing of the Mare Orientale and corresponds to the age of formation of the Mare Orientale basin. The northeastern part of the Moon Near Side is represented by the Highland region with regolith thickness from 9 to 13 m.

The model distribution of regolith thickness has a bimodal character with maximums of about 5 and 10 m, which corresponds to the average values of regolith thickness for mare and Highlands [105]. The regolith thickness in mare areas varies from 3 to 11 m. A small regolith thickness (about 3 m) in some small areas of the Mare Serenitatis and the Mare Nubium is observed. The maximum regolith thickness in mare areas (9–10 m) in the areas adjacent to some large craters (e.g., Aristillus Crater) is observed. Among the mares, the Mare Humorum is characterized by an average minimum regolith thickness of about 4.0 m, and the Mare Nectaris is characterized by the deepest, about 9.6 m (Table 13).

The dispersion of regolith thickness at Highland areas is much wider—from 1 m in the highlands to 18 m and more in the plateau areas with the age of underlying rocks of the Donectarian system (>3.92 billion years). The minimum values at the bottoms of impact craters (craters Tycho, Theophilus, Langren, Copernicus, etc.) and near Schickard Crater are observed. The highest thickness of regolith (more than 13 m) in the southeastern part of the Moon Near Side at Highland areas formed at the Donectarian period (>3.92 billion years) [108] is observed. The Donectarian age Highland rocks are distributed at the southern, southeastern, and central part of the Moon Far Side and occupy about half of the hemisphere. Moderate regolith thicknesses of 7–11 m at the southwestern part of the Near Side in the Highland region [107] are observed. This area represents the framing of the Mare Orientale and corresponds to the age of the formation of the Mare Orientale basin in the early Imbrian epoch. Approximately equal in area part of this framing is traced on the Far Side of the Moon. The northeastern part of the Near hemisphere of the Moon is represented by Highland of the Nectarian period with a regolith thickness from 9 to 13 m. Highlands of the Nectarian age at the Far Side occupies about one third of the area in the northeastern and western parts of the hemisphere.

There is a direct dependence of the regolith thickness on the surface age, which is explained by the time of exposure of the rocks' surface from the moment of their formation - the greater the surface age, the greater the regolith thickness. This dependence agrees rather well with the

Table 12 The regolith thickness at the landing sites of unmanned spacecrafts and Apollo expeditions

Spacecraft	Regolith thickness [105], m	Regolith thickness, m	References
Luna-9	4.8	> 0.2	[93]
Luna-13	3.6	4.6	[100]
Luna-16	4.0	4.0	[106]
		5.3	[99]
Luna-17	5.1	1.0–5.0	[97]
		4.0	[106]
Luna-20	9.2	0.4	[106]
		11.6	[99]
Luna-21	3.9	2.0	[106]
		2.0–3.0	[98]
Luna-24	3.0	> 2.0	[94]
Surveyor 1	3.5	3.3	[100]
Surveyor 3	5,3	4.6	[100]
Surveyor 5	4.6	–	
Surveyor 6	–	4.6	[100]
Apollo 11	4.7	4.6	[100]
		4.4	[101]
Apollo 12	5.3	4.6	[100]
		3.7	[101]
Apollo 14	8.1	8.5	[102]
Apollo 15	6.0	4.4	[101]
Apollo 16	10.1	12.2	[102]
Apollo 17	7.0	7–12	[102]
		8.5	[103]
		7.0 ± 1.0	[104]

Table 13 Average regolith thickness in lunar Maria [107]

Mare	Regolith thickness, m	Standard deviation (σ_h), m
Mare Serenitatis	4.1	0.8
Mare Tranquillitatis	4.1	1.1
Mare Crisium	4.6	1.6
Mare Fecunditatis	5.9	1.4
Mare Frigoris	7.4	2.1
Mare Imbrium	6.2	2.0
Mare Humorum	4.0	0.9
Mare Nectaris	9.6	2.3
Mare Vaporum	5.4	1.1
Mare Nubium	5.7	1.7
Mare Cognitum	4.9	0.7
Sinus Roris	7.5	1.9
Sinus Iridium	4.6	0.6
Sinus Aestuum	6.3	1.4
Oceanus Procellarum	4.8	1.6

chronostratigraphic subdivisions of lunar formations [101, 109], i.e. with the age of rocks of mare and Highland regions. Thus, based on the geological map [108] it is possible to extrapolate these data for the Far Side of the Moon, which can also be used to estimate the predicted helium reserves on the Moon.

5 Predicted Reserves of Helium in the Lunar Soil

Selective enrichment by cosmogenic isotopes of regolith depending on its mineral composition, which is determined mainly by underlying rocks, leads to non-uniform regional distribution of concentration of helium isotopes and other implanted gases in lunar soil. The highest concentration of helium isotopes, as shown above, is observed in high-titanium mare basalts, in which the content of the main ore mineral ilmenite reaches 20 wt%. The areas of spreading of high contents of TiO_2 oxides (5–10%) according to the spectral remote sensing data actually reflect the content of ilmenite in regolith and, correspondingly, the distribution of high-titanium mare basalts. The spectral survey method is based on correlation of the content of the main chromophore elements Fe and Ti for albedo with albedo and color indices in the visible and near-IR spectral ranges [110–112]. The percentage content of TiO_2 according to spectral survey data varies in the range from 0.01 in Highland areas to 10% and more in mare areas (Fig. 9).

High-titanium mare basalts are distributed in the equatorial region in the Mare Tranquillitatis, the Oceanus Procellarum, the Mare Humorium, the Mare Nubium, the Mare Vaporum, and the Sinus Aestuum, and in subordinate amounts in the Mare Imbrium, the Mare Serenitatis, and the Mare Fecunditatis (Fig. 9). Five main zones of TiO_2 concentration distribution in regolith based on the titanium oxide distribution map were identified and delineated: V—0.01 to 1 wt%, IV—1.0 to 3.0 wt%, III—3.0 to 5.0 wt%, II—5.0 to 8.0 wt% and I—8.0 to 10.0 wt% (Fig. 10). Each zone corresponds to a particular composition of lunar regolith with different ilmenite content, including Highland anorthosites and a series of mare rocks from low-titanium to high-titanium basalts.

The selected zones depending on regolith mineral composition, as it was considered above, are characterized by different concentration of implanted helium isotopes and different thickness of regolith (Table 14). Thus, depending on the concentration we can distinguish five different categories of implanted helium deposits on the Moon and estimate the area of their distribution. For the estimation of

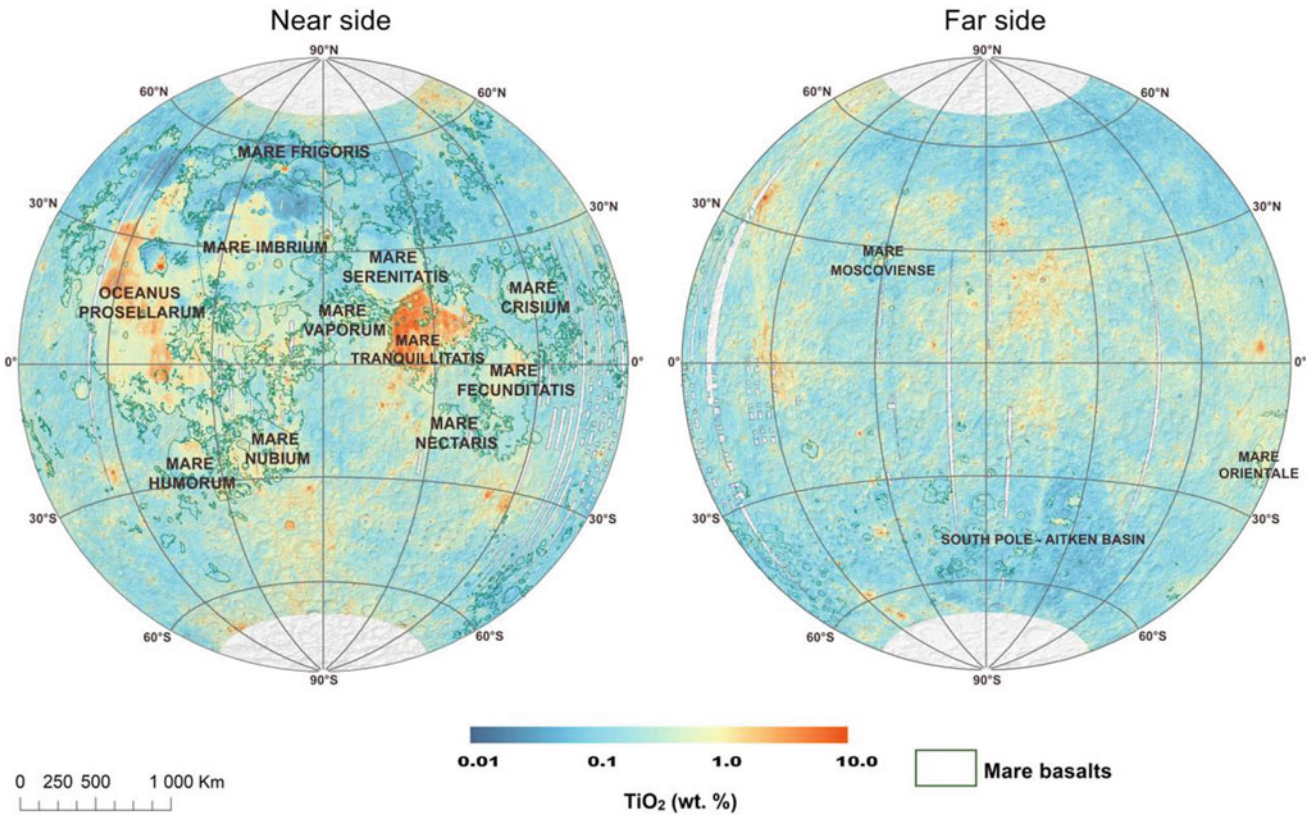

Fig. 9 Map of the TiO_2 (wt%) distribution in the lunar soil on the Moon according to the spectral survey data of the Clementine spacecraft [111]

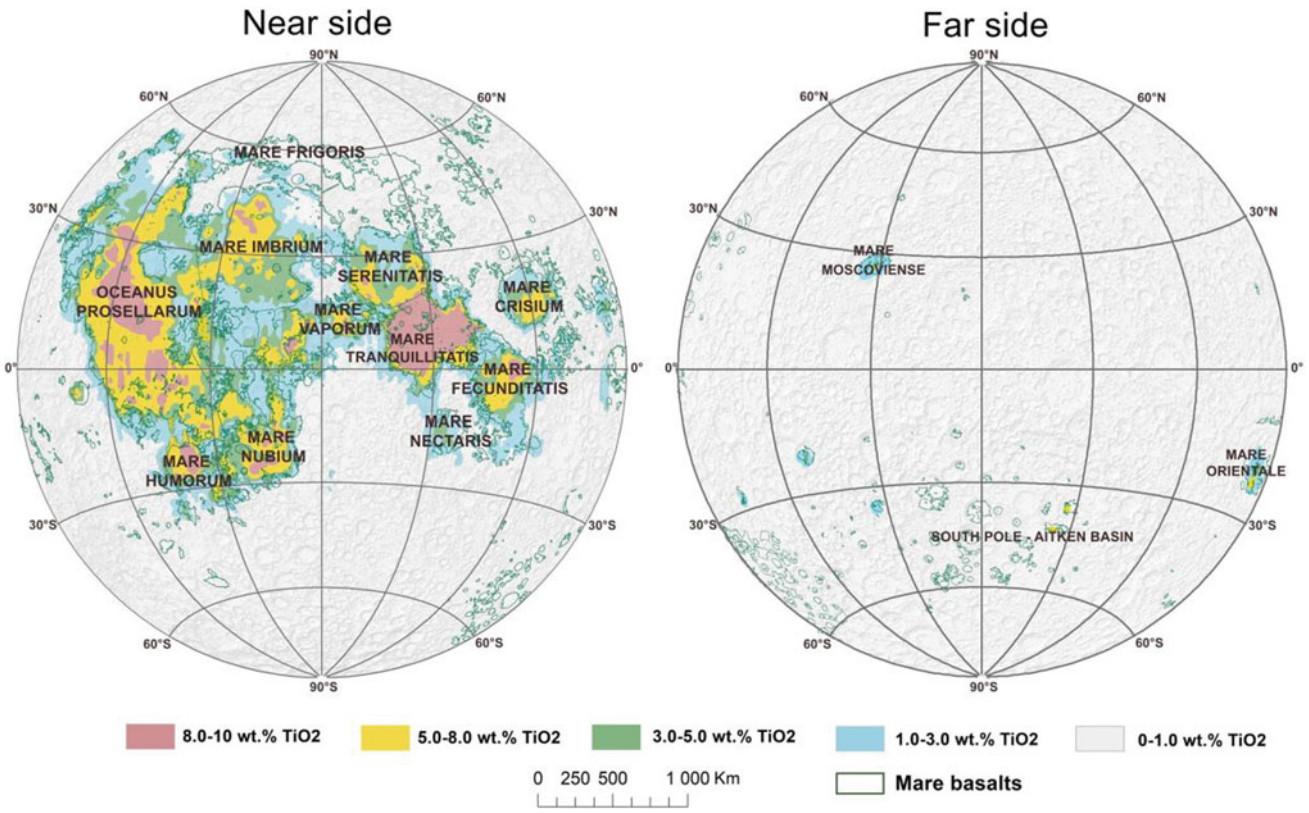

Fig. 10 Zonal map of TiO_2 concentration in lunar soil

Table 14 Characteristics of the identified Categories of deposits of implanted helium in the lunar soil

Category	TiO_2, wt %	Near Side, km^2	Far Side, km^2	^3He, ppb	^4He, ppm	Soil thickness m
I	8.0–10.0	732,477	0	15.1	41.1	4.1
II	5.0–8.0	1,571,842	9264	8.0	20.80	4.8
III	3.0–5.0	1,648,869	10,283	4.4	11.1	4.1
IV	1.0–3.0	2,432,985	92,484	3.1	8.2	9.2
V	0.01–1.0	12,613,827	18,887,969	1.4	3.9	10.1

predicted reserves of implanted helium, the average density of the lunar soil at a depth down to 10 m is taken to be 2.0 g cm^2 [48].

The measured content of ^3He and ^4He isotopes in high-titanium basalts of category I deposits is 15.1 ppb and 41.1 ppm, respectively (Table 14). Deposits with the maximum concentration of helium are distributed extremely heterogeneously and are located mainly in the Mare Tranquillitatis and the Oceanus Procellarum, and in subordinate quantities in the Mare Fecunditatis, in the Mare Humorum, in the Mare Nubium and in the northern part of the Mare Imbrium (Fig. 10). These are mare flat areas with a minimum average thickness of the loose regolith layer of about 4.1 m, typical of the Mare Tranquillitatis (Table 13). Deposits of this category on the Moon Far Side are practically absent. The total area of the richest helium deposits is about 733,000 km^2, the probable reserves of ^3He are about 9.1×10^4 tons and ^4He are about 2.5×10^8 tons (Table 15).

The measured helium-3 contents in basalts with an average ilmenite content in category II deposits at the Apollo-12, Apollo 17, and Luna-16 landing sites are close and vary from 7.1 to 8.0 ppb (Table 11). To estimate the probable reserves in mare basalts of this type, the content of ^3He and ^4He is taken to be 8.0 ppb and 20.8 ppm respectively, since measurements at the landing site of the Apollo 17 expedition reflect the average content of helium isotopes in the regolith to a depth of 3 m and are the most representative (Table 14). Reserves of this category are widespread in mare plains in the Oceanus Procellarum, in the

Table 15 Predicted reserves of implanted helium isotopes in the lunar soil

Category deposits	Near side		Far side		Total, t	
	^{3}He, t	^{4}He, t	^{3}He, t	^{4}He, т	^{3}He, t	^{4}He, т
I	90,695	246,859,399	–	–	90,695	246,859,399
II	120,717	313,865,411	711	1,849,836	121,428	315,715,247
III	59,491	150,080,056	371	935,959	59,862	151,016,015
IV	138,777	367,088,777	5275	13,953,986	144,052	381,042,763
V	356,719	993,717,291	534,152	1,487,994,198	890,871	2,481,711,489
Total, t	766,399	2,071,610,934	540,509	1,504,733,979	1,306,908	3,576,344,913

Mare Imbrium, in the Mare Fecunditatis, in the Mare Vaporum, in the Sinus Aestuum and in the Mare Nubium (Fig. 10). The minimum average regolith thickness in this category, which is characteristic of the Oceanus Procellarum, is about 4.8 m (Table 13). Compared to category I, helium reserves are distributed much more evenly and occupy an area twice as large (Table 14), but this type of deposits is twice as poor in helium content. Therefore, the total probable reserves in the second category are only a quarter higher than the reserves of the first category of deposits (Table 15).

Category III deposits cover the areas of low- titanium mare basalt distribution, in which the minimum measured content of ^{3}He and ^{4}He isotopes at the landing sites of the Apollo 14 and 15 expeditions is 4.4 ppb and 11.1 ppm, respectively (Tables 5, 11 and 14). The minimum thickness of the regolith in this category is observed in the Mare Serenitatis and is 4.1 m (Table 13). Relatively small and poor category III reserves, as a rule, outline the richer category II deposits and are quite widespread in the Mare Serenitatis and in the eastern part of the Mare Imbrium (Fig. 10). In terms of area, this category exceeds category II (Table 14), but in terms of helium reserves, it is significantly inferior to deposits of a higher category (Table 15).

The fourth category includes low-titanium mare basalts adjacent to the mareshore and mainly coastal complexes of Highland rocks, characterized by an increased content of TiO_2 (1.0–3.0 wt%) and, accordingly, ilmenite as compared to anorthosites of the Highlands (0.01–1 wt%). Typical for this category of deposits is the content of helium-3 at the landing site of the Luna-20 spacecraft in the region of coastal Highland rocks, which is 3.1 ppb (Tables 9, 11 and 14), and at the landing site of the Luna-24 spacecraft in the region coastal low- titanium basalts, which is 3.2 ppb (Tables 10 and 11). The horizontal transfer of the high-velocity component of ejections explains the enrichment of coastal Highland rocks with a component of mare basalts from impact craters with the formation of extensive coastal mixing zones [113, 114]. This process is reciprocal, in the same way, coastal Highland rocks dilute mare rocks with anorthosite component and reduce the concentration of ilmenite in mare basalts, which, together with coastal low-titanium basalts, form IV category of deposits and outline almost all mare areas on the Moon Near and Far Side. The minimum average regolith thickness is twice the regolith thickness in the mare areas and in the area of the Luna-20 landing, according to [104], is 9.2 m (Table 12). The distribution area of the IV category is one third larger than the III category area on the Moon Near side and almost ten times more on the Far Side (Table 14). The total probable reserves of helium in the regolith of this category are similar to those of category II, which is characterized by a much smaller area and regolith thickness (Tables 14 and 15).

The last V category with the lowest ilmenite content and the lowest background concentration of helium isotopes (1.4 ppb ^{3}He and 3.9 ppm ^{4}He) (Tables 11 and 14) covers Highland anorthosite rocks, which occupy more than 80% of the lunar surface and are characterized by an average regolith thickness of about 10.1 m (Table 12) [105]. This category is actually characterized by background minimum possible content of the implanted helium-3 in the lunar soil, and has no promising industrial significance. The content of implanted helium isotopes in the regolith of Highland anorthosites is the poorest, but given that the Highlands occupy almost the entire surface of the Moon and are characterized by the largest thickness of the loose regolith layer, the total predicted reserves of helium isotopes in the regolith of Highland anorthosites significantly exceed the total reserves of higher categories of deposits (Tables 14 and 15). However, on the Moon Near Side in the equatorial region, where the richest deposits are found, the total reserves of helium in the regolith of Highland anorthosites are even less than the total reserves of higher categories of deposits.

Thus, in a loose regolith layer on the Moon, about 1.3×10^6 tons of helium-3 and about 3.5×10^9 tons of helium-4 can be accumulated, which are extremely unevenly distributed on the lunar surface. Of greatest practical interest are the reserves of implanted helium isotopes in the richest deposits of I and II categories, in which, over a relatively small area, the total reserves of ^{3}He are about 2.1×10^5 tons, and ^{4}He—about 5.6×10^8 tons.

6 Summary

Depending on the mechanism of trapping and accumulation of trapped noble gases in lunar regolith, weakly bound helium, which saturates the pore space of lunar regolith, and helium implanted into particles and minerals of lunar regolith are released from solar wind. The accumulation of weakly bound helium in the lunar regolith largely depends on surface temperature and solar wind flux density depending on geographic longitude and latitude, and practically does not depend on regolith composition. The content of this type of helium increases essentially at high lunar latitudes characterized by low diurnal temperature and minimal amplitude of diurnal temperature variations; it is extremely unstable and is easily released during temperature and mechanical influences on the lunar soil, and requires development of special methods of in situ investigation [115]. It is assumed that the reserves of weakly bound helium in the polar regions of the Moon may significantly exceed the reserves of implanted helium.

Capture and accumulation of implanted helium in the lunar soil depends on chemical and mineral composition of regolith particles, on age of exposure and regolith maturity degree, on particle sizes, and can vary in a very wide range up to few orders of magnitude. The helium and noble gases lowest content are characteristic of glasses of impact and volcanic origin and the main rock-forming mineral of lunar Highland rocks—anorthite. The highest concentration of implanted helium is characteristic for the main ore mineral of mare basalts—ilmenite. Amorphization of the crystalline structure of ilmenite under solar wind irradiation begins at energies of ions an order of magnitude higher than those of silicates and aluminosilicates, and crystal lattice radiation-induced defects trap and retain helium ions much stronger than amorphous structure retain. As the content of ilmenite in basalts decreases from high-titanium to low-titanium, the concentration of implanted helium isotopes in the bulk composition of regolith decreases correspondingly. Minimal concentration of helium is observed in Highland anorthosite rocks characterized by minimal content of ilmenite and lower content of mafic rock-forming minerals olivine and pyroxenes with average helium content as compared to basalts. Selective enrichment of regolith with solar helium depending on its mineral composition, which is determined mainly by underlying rocks, leads to non-uniform regional distribution of helium isotope concentration and other implanted gases in lunar regolith. The highest concentration of helium isotopes is observed in high-titanium mare basalts, in which the content of the main ore mineral ilmenite reaches 20 wt%.

Depending on mineral composition of regolith and concentration of implanted isotopes five categories of deposits are distinguished. The first three categories cover areas of distribution of high-titanium and low-titanium basalts and are located in the territory of lunar mares in the Moon equatorial region. Deposits with maximum content belong to the richest and highest I category. Most reserves of implanted helium in this category are concentrated in the two largest fields located in the Mare Tranquillitatis and in the Oceanus Procellarum. The predicted reserves of helium in Category II deposits occupy an area twice as large, are distributed much more evenly and are located in almost all mare regions of the Moon. Approximately the same distribution is typical for the deposits of the third category. The fourth category of deposits unites low-titanium mare basalts and adjacent complexes of Highland rocks in the coastal zone where the mutual enrichment of Highland and mare components occurs due to horizontal transfer of emissions from impact craters with formation of extensive coastal mixing zones. The fifth category, the poorest by helium content in lunar soil but the largest by reserves unites all lunar Highlands that occupy more than 80% of lunar surface.

In general, in the loose regolith layer on the Moon, the total predicted reserves of helium-3 are estimated as 1.3×10^6 tons, and helium-4 as 3.5×10^9 tons, that are characterized by an extremely inhomogeneous distribution. The reserves of implanted helium isotopes in the richest deposits of categories I and II, which are of the greatest practical interest, are concentrated on a relatively small area and are estimated at about 2.1×10^5 tons of ^{3}He and about 5.6×10^8 tons of ^{4}He.

Acknowledgements The article is dedicated to the memory of Academician E. M. Galimov, a scientist and teacher, who initiated these studies at the Vernadsky Institute. Chapter 5. "Predicted reserves of helium in the lunar soil" was supported by a grant from the Russian Science Foundation No. 21-17-00120, https://rscf.ru/project/21-17-00120/.

References

1. Parker, E.N.: Dynamics of the interplanetary gas and magnetic fields. Astrophys. J. **128**, 664–676 (1958)
2. Parker, E.N.: The Solar Wind. McGraw-Hill, New York (1961)
3. Hundhausen, A.J.: Coronal Expansion and Solar Wind. Springer, New York (1972)
4. Bame, S.J., Feldman, W.C., Gosling, J.T., Young, D.T., Zwickl, R.D.: What magnetospheric workers should know about solar wind composition. In: Johnson, R.G. (ed.) Energetic Ion Composition in the Earth's Magnetosphere, pp. 73–98. Terra Scientific, Tokyo/Dordrecht (1983)
5. Kovalenko, V.A.: Solar Wind. Nauka, Moscow (1983)
6. Geiss, J., Eberhardt, P., Signer, P., Buehler, F., Meister, J.: The solar wind composition experiment. In: Apollo 11. Preliminary Science Report, pp. 183–187. NASA. Washington, D.C. (1969)
7. Geiss, J., Eberhardt, P., Signer, P., Buehler, F., Meister, J.: The solar wind composition experiment. In: Apollo 12. Preliminary Science Report, pp. 99–102. NASA. Washington, D.C. (1970)

8. Geiss, J., Buehler F., Cerutti, H., Eberhardt, P., Meister, J.: Solar-wind composition experiment. In: Apollo 14. Preliminary Science Report, pp. 221–226. NASA. Washington, D.C. (1971)
9. Geiss, J., Buehler, F., Cerutti, H., Eberhardt, P.: Solar-wind composition experiment. In: Apollo 15. Preliminary Science Report, pp. 15-1–15-7. NASA. Washington, D.C. (1972)
10. Geiss, J., Buehler, F., Cerutti, H., Eberhardt, P., Filleux, Ch.: Solar wind composition experiment. In: Apollo 16. Preliminary Science Report, pp. 14-1–14-10. NASA. Washington, D.C. (1972)
11. Geiss, J., Buehler, F., Cerutti, H., Eberhardt, P., Filleux, C.H., Meister, J., Signer, P.: The Apollo SWC experiment: results, conclusions, consequences. Space Sci. Rev. **110**, 307–335 (2004)
12. Ogilvie, K.W., Coplan, M.A., Bochsler, P., Geiss, J.: Abundance ratios of ^{4}He++/^{3}He++ in the solar wind. J. Geophys. Res. **85**, 6021–6024 (1980)
13. Coplan, M.A., Ogilvie, K.W., Bochsler, P., Geiss, J.: Interpretation of ^{3}He abundance variations in the solar wind. Solar Phys. **93**, 415–434 (1984)
14. Bodmer, R., Bochsler, P., Geiss, J., von Steiger, R., Gloeckler, G.: Solar windhelium isotopic composition from SWICS/ULYSSES. Space Sci. Rev. **72**, 61–64 (1995)
15. Gloeckler, G., Geiss, J.: Measurement of the abundance of Helium-3 in the Sun and in the local interstellar cloud with SWICS on ULYSSES. Space Sci. Rev. **84**(1/2), 275–284 (1998)
16. von Steiger, R., Schwadron, N.A., Fisk, L.A., Geiss, J., Gloeckler, G., Hefti, S., Wilken, B., Wimmer-Schweingruber, R.F., Zurbuchen, T.H.: Composition of quasi-stationary solar wind flows from Ulysses/solar wind ion composition spectrometer. J. Geophys. Res. **105**, 27217–27238 (2000)
17. Giammanco, C., Wurz, P., Karrer, R.: Minor ion abundances in the slow solar wind. Astrophys. J. **681**, 1703–1707 (2008)
18. Wimmer-Schweingruber, R.F., Bochsler, P., Wurz, P.: Isotopes in the solar wind: new results from ACE, SOHO and WIND. In: Solar Wind Nine, AIP Conference Proceedings, vol. 471, pp. 147–152. Nantucket, MA, USA (1999)
19. Geiss, J., Gloeckler, G.: Abundances of deuterium and HELIUM-3 in the protosolar cloud. Space Sci. Rev. **84**(1/2), 239–250 (1998)
20. Burnett, D.S., Barraclough, B.L., Bennett, R., Neugebauer, M., Oldham, L.P., Sasaki, C.N., Sevilla, D., Smith, N., Stansbery, E., Sweetnam, D., Wiens, R.C.: The genesis discovery mission: return of solar matter to earth. Space Sci. Rev. **105**, 509–534 (2003)
21. Reisenfeld, D.B., Burnett, D.S., Becker, R.H., Grimberg, A., Heber, V.S., Hohenberg, C.M., Jurewicz, A.J.G., Meshik, A.P., Pepin, R.O., Raines, J.M., Wieler, R., Wiens, R.C., Zurbuchen, T.H.: Elemental abundances of the bulk solar wind: analyses from genesis and ACE. Space Sci. Rev. **130**, 79–86 (2007)
22. Heber, V.S., Wieler, R., Baur, H., Olinger, C., Friedmann, T.A., Burnett, D.S.: Noble gas composition of the solar wind as collected by the genesis mission. Geochim. Cosmochim. Acta **73** (24), 7414–7432 (2009)
23. Eberhardt, P., Eugster, O., Geiss, J., Graf, H., Grogler, N., Guggisberg, S., Jungck, M., Maurer, P., Morgeli, M., Stettler, A.: Solar wind and cosmic radiation history of Taurus-Littrow Regolith. In: Proceedings Lunar Science Conference 5th, pp. 197–199. Houston, USA (1974)
24. Wittenberg, L.J., Santarius, J.F., Kulcinski, G.L.: Lunar source of He-3 for commercial fusion power. Fusion Technol. **10**(2), 167–178 (1986)
25. Kulcinski, G.L., Cameron, E.N., Santarius, J.F., Sviatoslavsky, I. N., Wittenberg, L.J., Schmitt, H.H.: Fusion energy from the Moon for the twenty-first century. In: Proceedings of the 2nd Conference on Lunar Bases and Space Activities of the 21st Century in Houston, pp 459–474. NASA Conference. Publication 3166 (1992)
26. Murali, A.V., Jordan, J.L.: Helium-3 inventory of lunar samples: a potential future energy resources for mankind? In: The 24th Lunar and Planetary Science Conference, pp. 1023–1024. Houston, USA (1993)
27. Galimov, E.M.: Project Moon–Helium-3. Nauka v Rossii **6**, 15–23 (2006)
28. Taylor, L.A., Kulcinski, G.L.: Helium-3 on the Moon for fusion energy: the Persian Gulf of the 21st century. Solar Syst. Res. **33** (5), 338–345 (1999)
29. Cho, A.: Helium-3 shortage could put freeze on low-temperature research. Science **326**, 778–779 (2009)
30. Eberhardt, P., Geiss, J., Graf, H., Grogler, N., Krahenbuhl, U., Schwaller, H., Schwarzmuller, J., Stettler, A.: Trapped solar wind noble gases, exposure age and K/Ar-age in Apollo 11 lunar fine material. In: Proceedings Apollo 11 Lunar Science Conference, pp. 1037–1070. Houston, USA (1970)
31. Hintenberger, H., Weber, H.W., Voshage, H., Wanke, H., Begemann, F., Vilscek, E., Wlotzka, F.: Rare gases, hydrogen, and nitrogen: concentrations and isotopic composition in lunar material. Science **167**(3918), 543–545 (1970)
32. Slyuta, E.N., Yakovlev, O.I., Voropaev, S.A., Dubrovskii, A.V.: He implantation and concentrations in minerals and lunar regolith particles. Geochem. Int. **51**(12), 959–967 (2013)
33. Cameron, E.N.: Helium mining on the moon: site selection and evaluation. In: Proceedings of the 2nd Conference on Lunar Bases and Space Activities of the 21st Century in Houston, pp. 189–197. NASA Conference Publication 3166 (1992)
34. Shkuratov, Yu.G., Starukhina, L.V., Kaidash, V.G., Bondarenko, N.V.: ^{3}He distribution over the lunar visible hemisphere. Solar Syst. Res. **33**(5), 409–420 (1999)
35. Johnson, J.R., Swindle, T.D., Lucey, P.G.: Estimated solar wind-implanted helium-3 distribution on the Moon. Geophys. Res. Let. **26**(3), 385–388 (1999)
36. Cocks, F.H.: ^{3}He in permanently shadowed lunar polar surfaces. Icarus **206**, 778–779 (2010)
37. Fa, W., Jin, Y.: Quantitative estimation of helium-3 spatial distribution in the lunar regolith layer. Icarus **190**, 15–23 (2007)
38. Sorokin, E.G., Yakovlev, O.I., Slyuta, E.N., Gerasimov, M.V., Zaitsev, M.A., Shcherbakov, V.D., Ryazantsev, K.M., Krasheninnikov, S.P.: Experimental modeling of a micrometeorite impact on the Moon. Geochem. Int. **58**(2), 113–127 (2020)
39. Sorokin, E.G., Yakovlev, O.I., Slyuta, E.N., Gerasimov, M.V., Zaitsev, M.A., Shcherbakov, V.D., Ryazantsev, K.M., Krasheninnikov, S.P.: Experimental model of the formation of nanophase metallic iron in the lunar regolith. Dokl. Earth Sci. **492** (2), 431–433 (2020)
40. Mokrushin, A.D., Agafonov, Yu.A., Zinenko, V.I., Pustovit, A. N.: Distribution of implanted hydrogen in α-SiO_2 amorphous silica dioxide. Poverkhnost. Rentgen., Sinkhrotron. Neitron. Issled. **12**, 5–8 (2004)
41. French, B.M.: The Moon Book. Penguin Books, London (1977)
42. Carrier, W.D. III, Mitchell, J.K., Mahmood, A.: The relative density of lunar soil. In: Proceedings 4th Lunar Science Conference, pp. 2403–2411. Houston, USA (1973)
43. Herz, F., Morrison, D.A., Gault, D.E., Oberbeck, V.R., Quaid, V. L., Vedder, J.F., Brownlee, D.E., Hartung, J.B.: The micrometeoroide complex and evolution of the lunar regolith. In: Pomeroy, J.H., Hubbard, N.J. (eds.) The Soviet-American conference on cosmochemistry of the Moon and planets, pp. 605–636. NASA, Washington D.C. (1977)
44. Morris, R.V.: Surface and near surface exposure ages of lunar soils: exposure ages based on the fine grained metal and

cosmogenic ^{21}Ne. In: Proceedings 8th Lunar Planet Science Conference, pp. 685–687. Houston, USA (1977)
45. Eberhardt, P., Eugster, O., Geiss, J., Graf, H., Grogler, N., Guggisberg, S., Jungck, M., Maurer, P., Morgeli, M., Stettler, A.: Solar wind and cosmic radiation history of Taurus-Littrow Regolith. In: Proceedings 5th Lunar Science Conference, pp. 197–199. Houston, USA (1974)
46. Haskin, L., Warren, P.: Lunar chemistry. In: Heiken, G.H., Vaniman, D., French, B.M. (eds.) Lunar Sourcebook, pp. 357–474. Cambridge University Press, New York (1991)
47. Slyuta, E.N.: Basic types of Moon's resources and their mining and processing. Gornyi zhurnal **4**, 13–18 (2017)
48. Slyuta, E.N.: Physical and mechanical properties of the lunar soil (A review). Sol. Sys. Res. **48**(5), 330–353 (2014)
49. Taylor, L.: Helium-3 on the Moon: model assumptions and abundances. In: 2nd Wisconsin Symposium on Helium-3 and Fusion Power, pp. 49–56. University of Wisconsin-Madison (1993)
50. Scherzer, B.: Development of surface topography due to gas implantation. In: Behrisch, R. (ed.) Sputtering by Particle Bombardment, vol. 2, pp. 271–355. Springer, Berlin-Heidelberg (1983)
51. Harris-Kuhlman, K.R.: Trapping and duffusion of Helium in lunar materials. Ph.D. thesis. Fusion Technol. Inst., Wisconsin (1998)
52. Futagami, T., Ozima, M., Nagai, S., Aoki, Y.: Experiments on thermal release of implanted noble gases from minerals and their implications for noble gases in lunar soil grains. Geochim. Cosmochim. Acta **57**(13), 3177–3194 (1993)
53. Ziegler, J.F., Biersack, J.P., Littmark, U.: The Stopping and Range of Ions in Solids. Pergamon Press, New York (2009)
54. Slyuta, E.N., Petrov, V.S., Yakovlev, O.I., Voropaev, S.A., Monakhov, I.S., Prokof'eva, T.V.: Application of thermodesorption mass spectrometry for studying proton water formation in the lunar regolith. Geochem. Int. **55**(1), 27–37 (2017)
55. Shirokov, Yu.M., Yudin, I.P.: Nuclear Physics. Nauka, Moscow (1980)
56. Bernatowicz, T.J., Nichols, R.H. Jr., Hohenberg, C.M.: Origin of amorphous rims on lunar soil grains. In: 25th Lunar Planet Science Conference, pp. 105–106. Houston, USA (1994)
57. Christoffersen, R., Keller, L.P., Dukes, C., Rahman, Z., Baragiola, R.: Experimental investigation of space radiation processing in lunar soil ilmenite: combining perspectives from surface science and transmission electron microscopy. In: 41th Lunar Planet Science Conference, ID 1532. Houston, USA (2010)
58. Slyuta, E.N., Shilobreeva, S.N., Kashkarov, L.L., Kalinina, G.V., Voropaev, S.A.: Amorphization depth of anorthite and quartz in dependence on H^+ and He^+ ion energy and irradiation dose. In: 42nd Lunar and Planet Science Conference ID 1127. Houston, USA (2011)
59. Sominskiy, M.S.: Semiconductors. Nauka, Leningrad (1967)
60. Keller, L.P., McKay, D.S.: The nature and origin of rims on lunar soil grains. Geochim. Cosmochim. Acta **61**(11), 2331–2341 (1997)
61. Slyuta, E.N., Shilobreeva, S.N., Voropaev, S.A,. Kashkarov, L. L., Zinenko, V.I., Saraykin, V.V.: Preliminary experimental data on irradiation-induced fractionation of isotopes ^{54}Fe and ^{56}Fe. In: 42th Lunar Planet Science Conference, ID 1195. Houston, USA (2011)
62. Morris, R.V.: The surface exposure (maturity) of lunar soils: some concepts and Is/FeO compilation. In: Proceedings Lunar 9th Planet Science Conference, pp. 2287–2297. Houston, USA (1978)
63. Webb, R.P.: SUSPRE, V 1.4. Guilford, UK (1987)
64. Lakatos, S., Heymann, D.: Green spherules from Apollo 15: inferences about their origin from inert gas measurements. In: The Moon 7, pp. 132–148. Lunar Planet. Inst., Houston, USA (1973)
65. Frick, U., Baur, H., Funk, H., Phinney, D., Schäfer, C., Schultz, L., Signer, P.: Diffusion properties of light noble gases in lunar fines. In: Proceedings Lunar Science Conference 4th, vol. 2, pp. 1987–2002. Houston, USA (1973)
66. Frick, U., Baur, H., Ducati, H., Funk, H., Phinney, D., Signer, P.: On the origin of helium, neon, and argon isotopes in sieved mineral separates from an Apollo 15 soil. In: Proceedings Lunar Science Conference 6th, pp. 2097–2129. Houston, USA (1975)
67. Baur, H., Frick, U., Funk, H., Schultz, L., Signer, P.: Thermal release of helium, neon, and argon from lunar fines and minerals. In: Proceedings Lunar Science Conference 3rd, vol. 2, pp. 1947–1966. Houston, USA (1972)
68. Eberhardt, P., Geiss, J., Graft, H., Groegler, N., Mendia, M.D., Moergeli, M., Schwaller, H., Guggisberg, S., Stettler, A., Krähenbühl, U., von Gunten, H.R.: Trapped solar wind noble gases in Apollo 12 lunar fines 12001 and Apollo 11 breccia 10046. In: Proceedings Lunar Planet Science Conference 3rd, vol. 2, pp. 1821–1856. Houston, USA (1972)
69. BVSP (Basaltic Volcanism on the Terrestrial Planets). Pergamon Press, New York (1981)
70. Bogatikov, O.A. (ed.): Igneous Rocks. Part 3. Basic rocks. Nauka, Moscow (1985)
71. Tarasov, L.S., Nazarov, M.A., Shevaleevsky, I.D., Kudryashova, A.F., Gaverdovskaya, A.S., Korina, M.I.: Mineralogy and petrography of lunar Rockw from Mare Crisium (preliminary data). In: Proceedings 8th Lunar Science Conference, vol. 3, pp. 3333–3356. Houston, USA (1977)
72. Barsukov, V.L., Dmitriev, L.V., Tarasov, L.S., Kolesov, G.M., Shevaleevsky, I.D., Ramendik, G.I., Garanin, A.V.: Geochemical and petrochemical features of regolith and rocks from the Mare Crisium. In: Barsukov, V.L. (ed.) Lunar Soil from the Mare Crisium, pp. 158–165. Nauka, Moscow (1980)
73. Cast, P.W., Phinney, W.C., Hubbard, N.J., et al.: Preliminary examination of lunar samples. Apollo 17 preliminary science report, pp. 7-1–7-45. NASA, Washington D.C. (1973)
74. Head, J.W., Wilson, L.: Lunar mare volcanism: stratigraphy, emption conditions, and the evolution of secondary crusts. Geochem. Cosmochim. Acta. **56**, 2155–2175 (1992)
75. Moriarty, III D.P., Watkins, R.N., Valencia, S.N., Kendall, J.D., Evans, A.J., Dygert, N., Petro, N.E.: Evidence for a stratified upper mantle preserved within the South Pole—Aitken Basin. J. G.R. Planets **121**(e2020JE006589), 1–27 (2020)
76. Gaddis, L.R., Pieters, C.M., Hawke, B.R.: Remote sensing of lunar pyroclastic mantling deposits. Icarus **61**, 461–489 (1985)
77. Gaddis, L.R., Staid, M.I., Tyburczy, J.A., Hawke, B.R., Petro, N. E.: Compositional analyses of lunar pyroclastic deposits. Icarus **161**(2), 262–280 (2003)
78. Vinogradov, A.P.: Preliminary data on the lunar soil delivered by the automatic station "Luna-20". In: Barsukov, V.L., Surkov, Yu. A. (eds.) Soil from the Highland Region of the Moon, pp. 7–17. Nauka, Moscow (1979) (in Russian)
79. The Lunar Sample Preliminary Examination Team. Preliminary examination of lunar samples. In: Apollo 12. Preliminary Science Report, pp. 189–216. NASA. Washington, D.C. (1970)
80. Heymann, D., Yaniv, A., Adams, J.A.S., Fryer, G.E.: Inert gases in lunar samples. Science **167**(3918), 555–558 (1970)
81. Reynolds, J.H., Hohenberg, C.M., Lewis, R.S., Davis, P.K., Kaiser, W.A.: Isotopic analysis of rare gases from stepwise heating of lunar fines and rocks. Science **167**(3918), 545–548 (1970)

82. Heymann, D., Yaniv, A.: Inert gases from Apollo 12, 14, and 15 fines. Geochim. Cosmochim. Acta. Suppl. **4**(2), 1857–1863 (1972)
83. Eberhardt, P., Eugster, O., Geiss, J., Groegler, N., Guggisberg, S., Moergeli, M.: Noble gases in the Apollo 16 special soils from the East-West split and the permanently shadowed area. In: Proceedings Lunar Science Conference 7th, pp. 563–585. Houston, USA (1976)
84. Eugster, O., Grögler, N., Mendia, M.D., Eberhardt, P., Geiss, J.: Trapped solar wind noble gases and exposure age of Luna 16 lunar fines. Geochim. Cosmochim. Acta **37**(9), 1991–2003 (1973)
85. Vinogradov, A.P., Zadorozhny, I.K.: Noble gases in the regolith from the Mare Fecunditatis. In: Vinogradov, A.P. (ed.) Lunar Soil from the Sea of Abundance, pp. 379–386. Nauka, Moscow (1974)
86. Kaiser, W.A.: Rare gas studies in Luna-16-G-7 fines by stepwise heating technique. A low fission solar wind Xe. Earth Planet. Sci. Lett. **13**, 387–399 (1972)
87. Heymann, D., Yaniv, A., Ladatos, S.: Inert gases in twelve particles and one "dust" sample from Luna 16. Earth Planet. Sci. Lett. **13**, 400–406 (1972)
88. Vinogradov, A.P., Zadorozhny, I.K.: Inert gases in regolith and rock fragments delivered by the automatic station "Luna-20." In: Barsukov, V.L., Surkov, Yu.A. (eds.) Soil from the Highland Region of the Moon, pp. 547–556. Nauka, Moscow (1979)
89. Eugster, O., Eberhardt, P., Geiss, J., Grogler, N., Jungck, M., Morgeli, M.: Solar wind trapped and cosmic-ray produced noble gases in Luna 20 soil. In: Proceedings Lunar Science Conference 6th, pp. 1989–2007. Houston, USA (1975)
90. Zadorozhny, I.K., Ivanov, A.V.: Content and isotopic composition of inert gases in the base samples of the Luna-24 regolith. In: Barsukov, V.L., (ed.) Lunar Soil from the Mare Crisium, pp. 289–299. Nauka, Moscow (1980)
91. Bogard, D.D., Hirsch, W.C.: Noble gases in Luna 24 core soils. In: Mare Crisium: The View from Luna 24, pp. 105–116. Pergamon Press, Inc., New York (1978)
92. Slyuta, E.N., Abdrahimov, A.M., Galimov, E.M.: Does Helium-3 abundance decrease in dependence on depth at Mare Crisium? In: 39th Lunar Planet Science Conference ID 1054. Houston, USA (2008)
93. Gault, D.E., Quaide, W.L., Oberbeck, V.R., Moore, H.J.: Lunar 9 photographs: evidence for a frag-mental surface layer. Science **153**, 985–988 (1966)
94. Florensky, K.P., Pronin, A.A., Bazilevsky, A.T.: Geology of the Luna-24 landing site. In: Vinogradov, A.P. (ed.) Lunar Soil from the Mare Fecunditatis, pp. 7–18. Nauka, Moscow (1980)
95. Carrier, W.D. III.: Apollo drill core depth relationships. The Moon 10, pp. 183–194. Lunar Planet. Inst., Houston, USA (1974)
96. Heiken, G.H., Vaniman, D.T., French, B.M. (eds.): Lunar Sourcebook. Cambridge University Press, New York (1991)
97. Florensky, K.P., Bazilevsky, A.T., Pronin, A.A., Popova, Z.V.: Preliminary results of a geomorphological study of panoramas. In: Mobile Laboratory on the moon. Lunokhod-1, pp. 96–115. Nauka, Moscow (1971)
98. Florensky, K.P., Bazilevsky, A.T.: The processes of transformation of the lunar surface in the Lemonnier region based on the results of a detailed study on the "Lunokhod-2". In: Tectonics and structural geology, pp. 205–235. Nauka, Moscow (1976)
99. Stakheev, Yu.I., Lavrukhina, A.K.: Granulometric characteristics of the lunar regolith and the thickness of the regolith layer at the landing sites of the Luna-16 and -20 spacecrafts. In: Barsukov, V. L., Surkov, Yu.A. (eds.) Soil from the Highland Region of the Moon, pp. 74–76. Nauka, Moscow (1979)
100. Oberbeck, V.R., Quaide, W.L.: Genetic implication of lunar regolith thickness variations. Icarus **9**(3), 446–465 (1968)
101. Nakamura, Y., Dorman, J., Duennebier, F., et al.: Shallow lunar structure determined from the passive seismic experiment. Moon **13**(1), 3 (1975)
102. Cooper, M.R., Kovach, R.L., Watkins, J.S.: Lunar near-surface structure. Rev. Geophys. Space Phys. **12**, 291–308 (1974)
103. Duennebier, F.K., Watkins, J., Kovach, R.: Results from the lunar surface profiling experiment. In: Lunar and Planetary Science Conference, vol. 5, p. 183. Houston, USA (1974)
104. Strangway, D.W., Pearce, G.W., Olhoeft, G.R.: Magnetic and dielectric properties of lunar samples. In: Pomeroy, J.H., Hubbard (eds.) The Soviet-American Conference on Cosmochemistry of the Moon and Planets, pp. 417–432. N.J. NASA, Washington D. C. (1977)
105. Bondarenko, N.V., Shkuratov, Yu.G.: A map regolith layer thickness for the visible lunar hemisphere from radar and optical data. Solar Sys. Res. **32**, 264–271 (1998)
106. Bazilevsky, A.T.: Estimation of the thickness and degree of reworking of the lunar regolith by the prevalence of craters. Cosmich. Issled. **12**(4), 606–609 (1974)
107. Shkuratov, Yu.G., Bondarenko, N.V.: Regolith layer thickness mapping of the Moon by radar and optical data. Icarus **149**, 329–338 (2001)
108. Wilhelms, D.E.: The geologic history of the Moon. USGS Professional Paper 1342, Washington (1987)
109. Boyce, J.M., Johnson, D.A.: Ages of flow units in the far eastern Maria and implications of basin-filling history. In: Proceedings Lunar Planet Science Conference 9th, pp. 3275–3284. Houston, USA. (1978)
110. Blewett, D.T., Lucey, P G., Hawke, B.R., Jolliff, B.L.: Clementine images of the lunar sample-return stations: refinement of FeO and TiO_2 mapping techniques. J. Geophys. Res. **102**(E7), 16319–16326 (1997)
111. Lucey, P.G., Blewett, D.T., Hawke, B.R.: Mapping the FeO and TiO_2 content of the lunar surface with multispectral imagery. J. Geophys. Res. **103**(E2), 3679–3699 (1998)
112. Lucey, P.G., Blewett, D.T., Taylor, G.J., Hawke, B.R.: Imaging of lunar surface maturity. J. Geophys. Res. **105**(E8), 20377–20387 (2000)
113. Wood, J.A., Dickey, J.S., Marvin, U.B., Powell, B.N.: Lunar anorthosites and a geophysical model of the Moon. In: Proceedings of the Apollo 11 Lunar Science Conference, vol. 1, pp. 965–988. Houston, USA (1970)
114. Florensky, C.P., Ivanov, A.V., Basilevsky, A.T.: The role of exogenous factors in the formation of the lunar surface. In: Pomeroy, J.H., Hubbard, N.J. (eds.) The Soviet-American Conference on Cosmochemistry of the Moon and Planets, pp. 571–584. NASA, Washington D.C. (1977)
115. Marov, M.Ya., Slyuta, E.N.: Early steps toward the Lunar base deployment: some prospects. Acta Astronautica **181**, 28–39 (2021)

Stones on the Lunar Surface

E. N. Slyuta and O. S. Tretyukhina

1 Introduction

The absence of a dense atmosphere makes the surface of the moon unprotected from the impacts of meteorites of various sizes, down to the smallest micrometeorites. Because of the meteorite bombardment, which lasted throughout the geological history of the Moon, a layer of regolith formed on its surface, which consists of fragments of bedrock and secondary particles formed during impact-explosive processing of rocks—breccia, agglutinates and glass particles. The average regolith thickness on the Moon ranges from 4–5 m on Maria plains to 9–10 m on Highlands [1]. The regolith thickness is greater on the more ancient geological structures. The average rate of formation of regolith is very small and is about 1.5 mm per 1 million years [2]. About half of the lunar soil by mass consists of particles smaller than 50 microns, i.e. less than the resolution of the human eye [3].

Particles of the lunar soil on the surface, small and large fragments of rocks and stones are gradually covered with microcraters ranging in size from a submicron to some centimeters. Estimates and observations show that the stones on the lunar surface are destroyed not due to gradual erosion by microcraters—they are only "smoothed out" by ones, but because of cracking by larger meteorites. The average time of existence on the lunar surface of a stone weighing 1–2.5 kg before it is destroyed is about 11 million years [4].

Cracking lunar rocks as a result of thermoelastic stresses due to compression and expansion as a result of daily temperature variations is also one of the agents for smoothing the lunar surface and the gradual destruction of stones, although in intensity and incomparable with meteorite bombardment. On the Moon, weak seismic signals due to thermal cracking of rocks were clearly recorded by seismometers and were allocated to a separate category of thermal moonquakes, which are very weak, but occur everywhere, and their total energy is comparable to the energy of tidal moonquakes [5]. In areas with a more contrasting relief, such as in the lunar Montes Apenninus (the landing site of Apollo 15), the number of thermal moonquakes increases by about an order of magnitude [6].

The study of stones distribution in different regions of the Moon and in various types of terrain is necessary not only for geomorphological studies, but also for creating reliable engineering models of the lunar surface for designing landing missions and testing landing vehicles, for creating lunar landscape for testing self-propelled or other vehicles for movement on the lunar surface, for creating soil intakes and technical means for excavating and transporting lunar soil, for designing and testing elements of the lunar infrastructure, etc.

2 Stones Shape and Distribution in Impact Craters

The bulk of stones on the surface are characterized by sizes from 1–2 to 40–50 cm (Fig. 1), and only close to relatively large craters with a diameter of several hundred meters or more can be observed placers of larger boulders, the size of which reaches several meters. Stones have a higher reflectivity than the fine-grained material of the regolith and therefore are easily recognized even with a high altitude of the Sun above the horizon (Fig. 2). The stones of irregular shape, having both round and acute-angled shapes, prevail. Occasionally there are stones of unusual regular shape. The lower part of most boulders is buried in regolith. Angular irregular-shaped stones are characterized by the brokenness of their outlines, apparently connected with a network of cracks, along which splits occurred at the time of crushing.

The shape and degree of preservation of the stones can be divided into a number of morphological varieties [7].

E. N. Slyuta (✉) · O. S. Tretyukhina
Vernadsky Institute of Geochemistry and Analytical Chemistry, Russian Academy of Sciences, 19 Kosygin St., Moscow, 119991, Russia
e-mail: slyuta@geokhi.ru

V. P. Kolotov and N. S. Bezaeva (eds.), *Advances in Geochemistry, Analytical Chemistry, and Planetary Sciences*,
https://doi.org/10.1007/978-3-031-09883-3_22

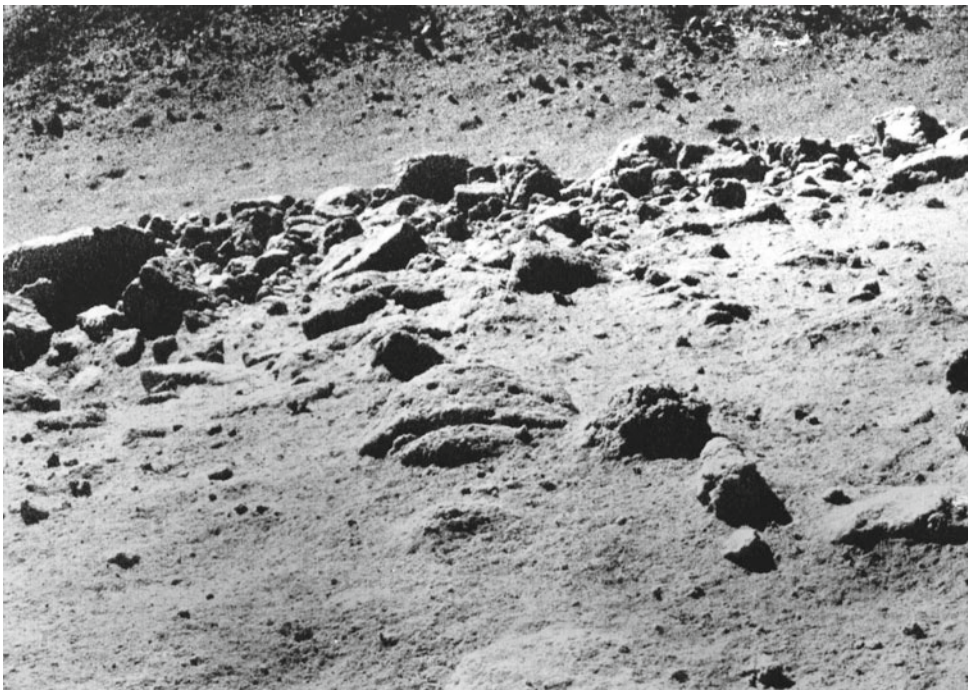

Fig. 1 The accumulation of stones on the edge of Fossa Recta. Fragment of the TV panorama Lunokhod-2. The diameter of the largest stone is ~ 1 m. In the background is the inner slope of the opposite side of the Fossa Recta

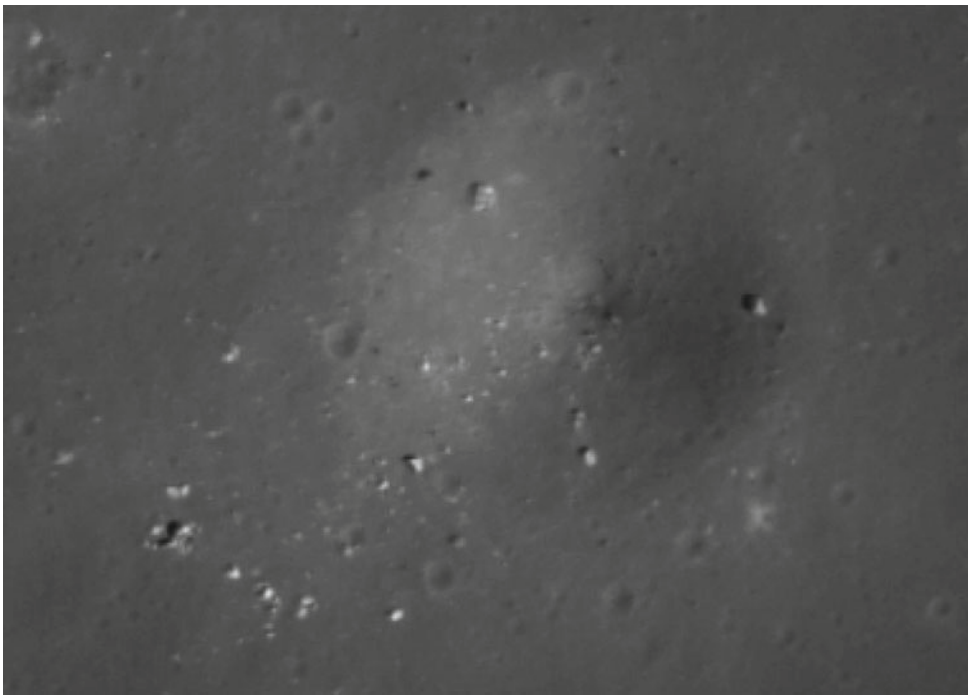

Fig. 2 Asymmetrical distribution of stones in a crater with a diameter of 90 m, located on a slope. The coordinates of the crater are 48.600° W, 24.724° E. Fragment of a mosaic LROC NAC (NASA)

Irregular stones with rounded or acute-angled shapes prevail. According to the degree of preservation, angular, angularly rounded and rounded forms of stones are distinguished (Fig. 3).

Stone sizes and their number per unit surface area around fresh craters increase dramatically due to crushing and ejection of underlying rocks. Depending on the regolith thickness, the sizes of such craters usually range from the first tens of meters to hundreds of meters and more. The largest stones, as a rule, are concentrated within the rim of an impact crater. Stony rims are observed in approximately 10% of craters with a diameter of 10–500 m [8]. The width of the zone of increased stoniness is on average close to half the diameter of the crater from its edge, but sometimes it

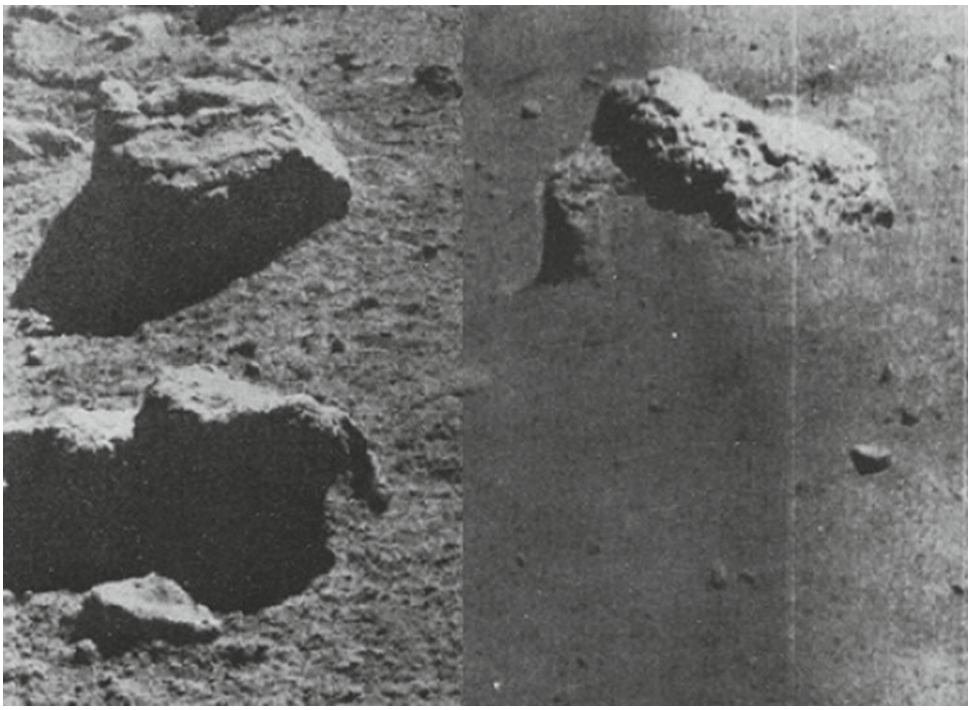

Fig. 3 Stones angular (in the picture on the left) and rounded (in the picture on the right) shape. Fragments of Lunokhod-2 TV panoramas

reaches 2–3 or more crater diameters. The concentration of stones within these zones is usually 3–6 times and in rare cases up to 2 orders of magnitude higher than the average value. The concentration of stones inside the craters is also several times their number outside the crater (Fig. 4). The size of the stones decreases with distance from the crater. Round-shaped stones are found mainly near mature craters, which indicate the smoothing of the outlines of these stones over time. The size and density of stones decreases near the crater with increasing age.

The stones in the craters and in the ejection of them are located approximately symmetrically relative to the center of the crater. In fresh craters located on slopes with a steepness of more than 10-15º, this symmetry is often broken [9] and the part of the crater located up the slope is characterized by a smaller number of stones than the opposite side of the

Fig. 4 The distribution of stones in the crater with a diameter of 240 m with coordinates of 158.569° W, 5.252° N. Fragment of a mosaic LROC NAC (NASA)

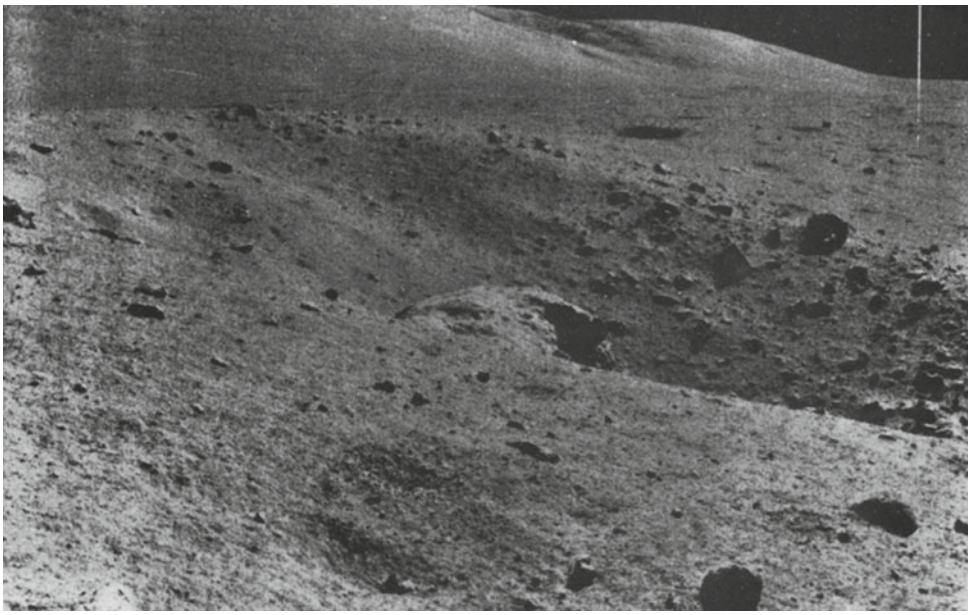

Fig. 5 Asymmetrical distribution of stones in the crater, located on a slope. Fragment of the TV panorama Lunokhod-2

crater down the slope (Figs. 2 and 5). This is probably because the stones were rolling down from the steeper part of the crater slope. With the distance from the crater, the size of the stones decreases.

3 Stones Distribution on Maria Plains

The distribution of boulders was investigated in the landing area of the Soviet spacecraft Luna-17 with Lunokhod-1 in the western coastal part of the Mare Imbrium, approximately 40 km from the Heraclides Promontory on the southern shore of the Sinus Iridium [7]. The Mare Imbrium is the largest ring-type structure on the Moon (impact basin), filled with vast basaltic lava effusions and surrounded by mountain structures. The Mare Imbrium in the southwest, where the mountain framing is absent, merges with the Oceanus Procellarum. Geologically and geomorphologically, the studied area represents a typical example of lunar maria regions free from the influence of large craters, crater rays and other large formations superimposed on the maria surface.

To stones recognize, the images of the LRO NAC with a resolution of about 0.72 m and an angular height of the Sun of 12.26° were used.

The area of the surveyed area was 8.68 km^2 (Fig. 6). Considering that the overwhelming amount of stones is associated with craters with a diameter of the first hundreds of meters, such an area of research is sufficient to estimate the density distribution of stones, characteristic of this type of terrain and representative of the region. The diameter of the largest crater, located on the study area and having coordinates of 35.006° W and 38.284° N, is 456 m. In total, 285 stones from 1.5 to 7 m in size were recognized on this area. Only about 7% (20 stones) fall on the area between craters, which corresponds to the density of less than 2.3×10^{-4} stones per 100 m^2. All other stones are concentrated mainly on the rims of impact craters of various sizes and, above all, on the rim and bottom of the largest crater, and practically do not occur outside this rim (Fig. 7). The density of stones of 1.5 m and more in size in the area of half the radius of the crater from its edge (including the area of the crater itself) reaches 4.2×10^{-2} stones per 100 m^2.

The average cumulative number of stones more than a certain diameter $N_{>D}$ per 100 m^2 on the maria plain is described by the equation (Fig. 8).

$$N_{>D} = 0.185D^{-3.8}, \quad (1)$$

where D is the diameter of the stones.

The calculated (1) and empirical (recognized) values of the cumulative density of stones per 100 m^2 on the lunar Maria plain (Table 1) correspond well to each other, which indicates sufficient reliability of the found mathematical model (1) of distribution of stones in this type of terrain.

4 Stones Distribution on the Aristarchus Plateau

The Aristarchus Plateau is located in the western part of the Oceanus Procellarum, is a gentle and low protrusion of smoothed Highland areas surrounded by a maria plain, and belongs to a transitional type of terrain. To stones recognize, the images of the LRO NAC with a resolution of about

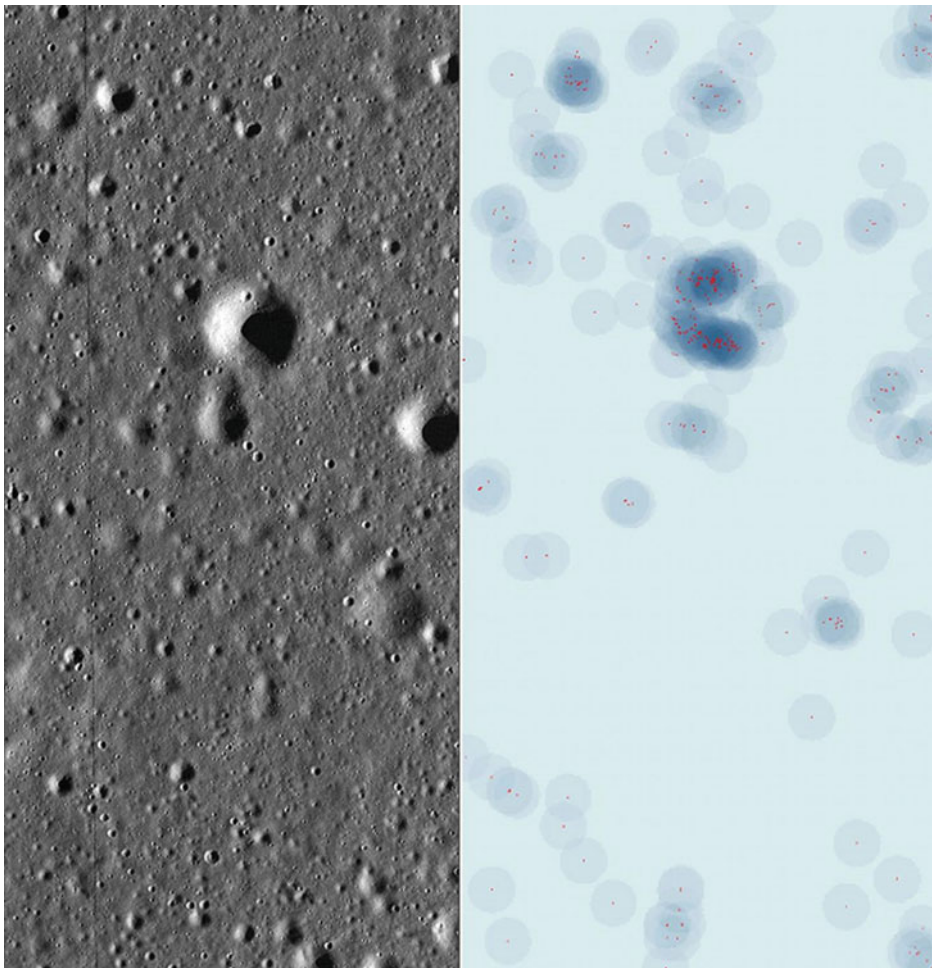

Fig. 6 Typical maria plain (left) located in the southwestern part of the Mare Imbrium in the study area of Lunokhod-1. The size of the region is 2000 × 4330 m. The diameter of the largest crater is 456 m. On the right is the relative density of stones in the area studied, shown by the nearest neighbor method in a circle with a radius of 100 m. The depth of the grey scale is divided into 32 classes. Red dots are stones. The coordinates of the crater are 35.006° W and 38.284° N. LROC NAC (NASA) mosaic fragment

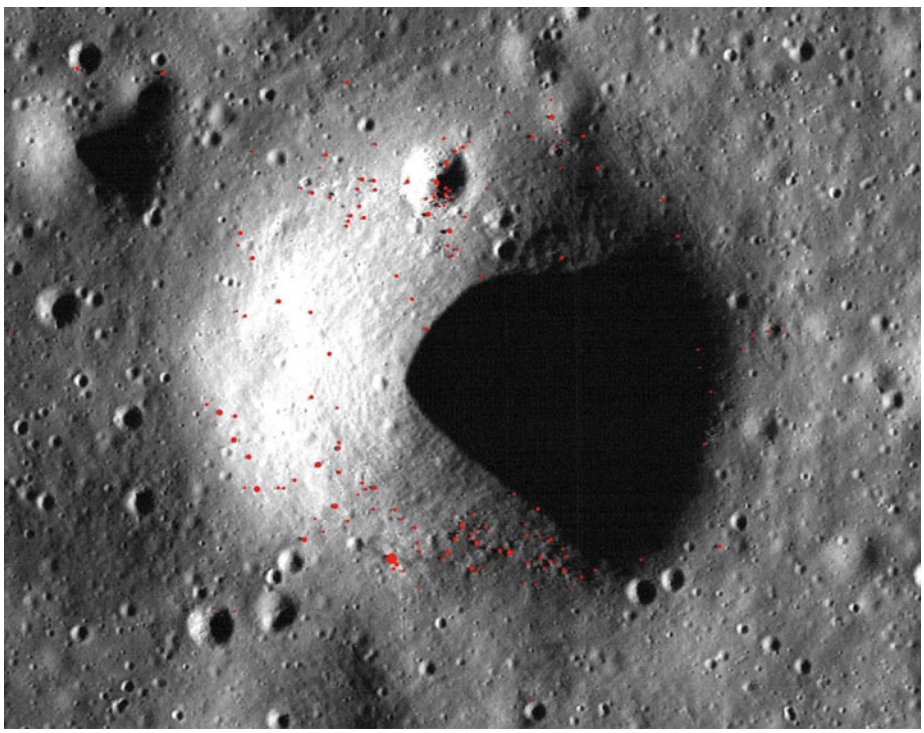

Fig. 7 Distribution of stones on the wall and bottom of the crater with a diameter of 456 m. The stones are shown in red circles depending on their size. Fragment of the LROC NAC mosaic (NASA)

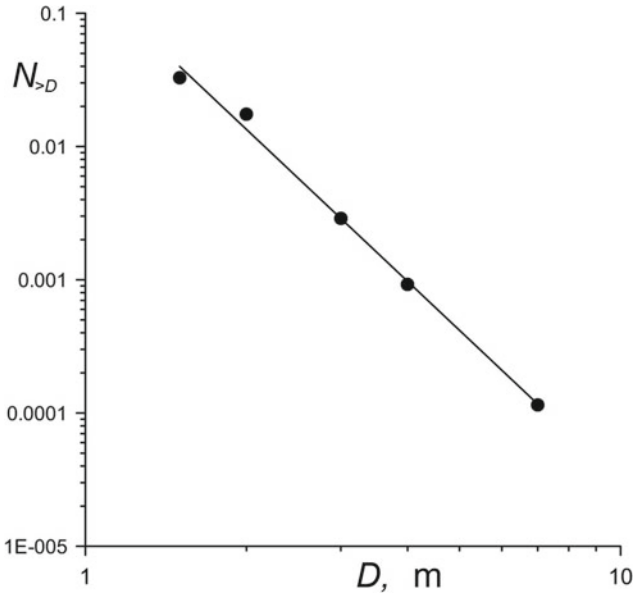

Fig. 8 Cumulative density of stones ≥ 1.5 m in size at lunar maria plain. The solid line shows the approximating curve. The ordinate axes are given in the logarithmic decimal scale

Table 1 The calculated (1) and observed cumulative density of stones more than a certain diameter $N_{>D}$ per 100 m^2 at lunar maria plains

Stone size, m	Calculated (1), $N_{>D}$	Observed, $N_{>D}$
0.20	83.80000	–
0.50	2.58000	–
1.00	0.18500	–
1.50	0.03900	0.03300
2.00	0.01300	0.01800
3.00	0.00280	0.00290
4.00	0.00095	0.00092
5.00	0.00041	–
6.00	0.00020	–
7.00	0.00011	0.00012

0.5 m and an angular height of the Sun of 52.05° were used. The total size of the site is approximately 4 × 5 km, the total area is 19.38 km^2 (Fig. 9). The study area extends to the North. The diameter of the largest crater with coordinates of 48.627° W and 24.718° N, located in the lower right part of the image (Fig. 9), is 400 m.

Stones compared to craters of similar size are characterized by an inverse arrangement of light and shadow and are recognized quite distinctly with the exception of spots that have no shadow (Fig. 10). It is assumed that such spots or hillocks with smooth transitions of light and shade represent either one of the stages of the surface destruction of stones [8], or the upper part of almost completely buried stones. The distribution of stones in general is much more uniform than on maria plains (Figs. 6 and 9). The absence of relatively large (tens and hundreds of meters) fresh class A craters and the low density of stones in the largest craters (Fig. 9) draws attention. The crater with a diameter of 90 m (Fig. 10) is characterized by the greatest density of stones, which in a zone of one radius from the edge of the crater (including the area of the crater itself) for stones of 1.5 m and more reaches 0.58 stones per 100 m^2 (Fig. 10). Stones average density on the inter-crater plains is characterized by the value of 7.9×10^{-3} st. per 100 m^2, which is more than ten times higher than on maria plains (2.3×10^{-4} stones per 100 m^2). A higher inter-crater density also indicates a more uniform distribution of stones on the Aristarchus Plateau compared to the maria plains.

In total, 1711 stones with a diameter of more than 1.5 m were recognized on the study area. The found average stones number greater than the diameter $N_{>D}$ per 100 m^2 on the Aristarchus plateau can be represented as (Fig. 11)

$$N_{>D} = 0.596 D^{-3.9}, \quad (2)$$

where D is the stone diameter.

There is good agreement between the calculated and observed distribution density of stones on the Aristarchus plateau (Table 2).

5 Stones Distribution on Lunar Highlands

To study stones distribution in a Highland region, a site of 4825 × 4160 m was taken on the Moon Far Side (Fig. 12). Plot coordinates 158.624° W, 5.280° N. To recognize, the images of the LRO NAC with a resolution of about 0.7 m and an angular height of the Sun of 42.73° were used. The difference in elevation on the site, the area of which is 20.073 km^2, reaches 1000 m. The site geomorphology is relatively smooth with a slight bumpy area. Within the study area are two large craters with a diameter of 2 km (Fig. 12) (upper left) and a diameter of 1.7 km (upper right). The distribution of stones within the area under study is sharply heterogeneous in contrast to the Maria plain and even more so from Aristarchus Plateau (Fig. 12). The highest stones density is observed in the vicinity of the two above-mentioned large craters and two small craters with dimensions of 320 m (158.682° W, 15.251° N) and 240 m (158.569° W, 5.252° N) (Fig. 12).

1471 stones with a diameter of 1.5 m and more were recognized within the site. The intercrater stones density is low and amounts to 2.6×10^{-4} per 100 m^2, i.e. about the same as on the Maria plains, where it is 2.3×10^{-4} stones per 100 m^2. The greatest stones density in the 220 m in size crater with coordinates 158.672° W, 5.282° N. (Fig. 13),

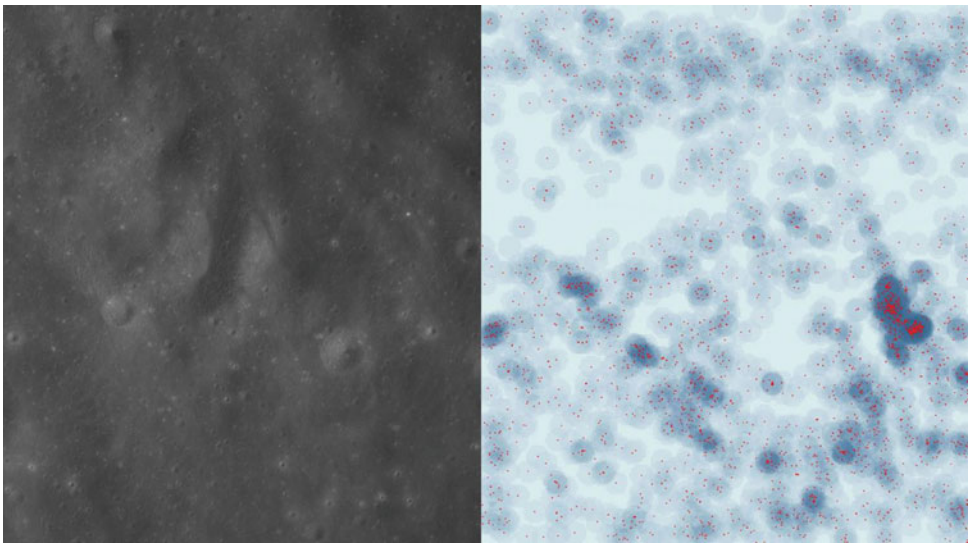

Fig. 9 Aristarchus Plateau region with a transitional type of terrain. The size of the area is 4136 × 4685 m. On the right is the relative density of the distribution of stones in the investigated area, shown by the method of the nearest neighbor in a circle with a radius of 100 m. The depth of the gray scale is divided into 32 classes. Black dots indicate stones. The coordinates of the center of the image are 48.655° W and 24.747° N. Fragment of a mosaic LROC NAC (NASA)

which is superimposed on the rim of 2 km in size crater, is observed. The stones density within area in two radius from the crater center reaches 0.20 stones per 100 m^2. It should be noted that if in both large craters stones concentrate mainly on crater rims, but in craters of hundreds meters in size stones concentrate mainly on the walls and bottom of craters (Figs. 14 and 15). The found average cumulative number of stones more than a certain diameter $N_{>D}$ per 100 m^2 at the Highland terrain is described by the equation (Fig. 16)

$$N_{>D} = 0.693D^{-4.4}, \quad (3)$$

where D is the diameter of the stones.

Table 3 shows the calculated (3) and the observed empirical values of the cumulative density of stones larger than 0.2 m per 100 m^2 in the Highland terrain. The marked decrease in the observed cumulative density of stones less than 2 m in size compared to the model one is due to the insufficient resolution of the images. A similar discrepancy between the model and observed data in these boundary sizes of stones is also observed in both previous cases (Figs. 8, 11; Tables 1 and 2).

6 Stones Distribution in the Oceanus Procellarum and in the Sinus Medii

The distribution of stones in the Oceanue Procellarum and the Sinus Medii was studied using the data of the Orbiter 2 spacecraft [8]. To determine the distribution density of stones in the study area, 10 sheets of large-scale images obtained by Orbiter 2 spacecraft were selected. Stones, taking into account their sizes, were counted on each sheet on a certain strip of the image, the area of which was 0.8 km^2. The total size of the each investigated area was approximately 8 km^2. About 1000 stones at the Oceanus Procellarum were counted. These two areas differ from each other in distribution density and size of stones (Fig. 17).

The average cumulative number of stones more than a certain diameter $N_{>D}$ per 100 m^2 in the Oceanus Procellarum is described by the equation (Fig. 17)

$$N_{>D} = 0.567D^{-5.1}, \quad (4)$$

and in the Sinus Medii-

$$N_{>D} = 0.059D^{-2.8}, \quad (5)$$

where D is a diameter of the stones.

The calculated (4, 5) and observed values of the cumulative density of stones per 100 m^2 at the Oceanus Procellarum and at the Sinus Medii shown in Tables 4 and 5, respectively. Especially good agreement between the calculated and empirical data is observed for the Sinus Medii (Table 5).

7 Discussion

Thus, the lowest cumulative density of stones compared with the transition terrain (Aristarchus Plateau) and Highland terrain (Fig. 18) characterizes lunar maria plains.

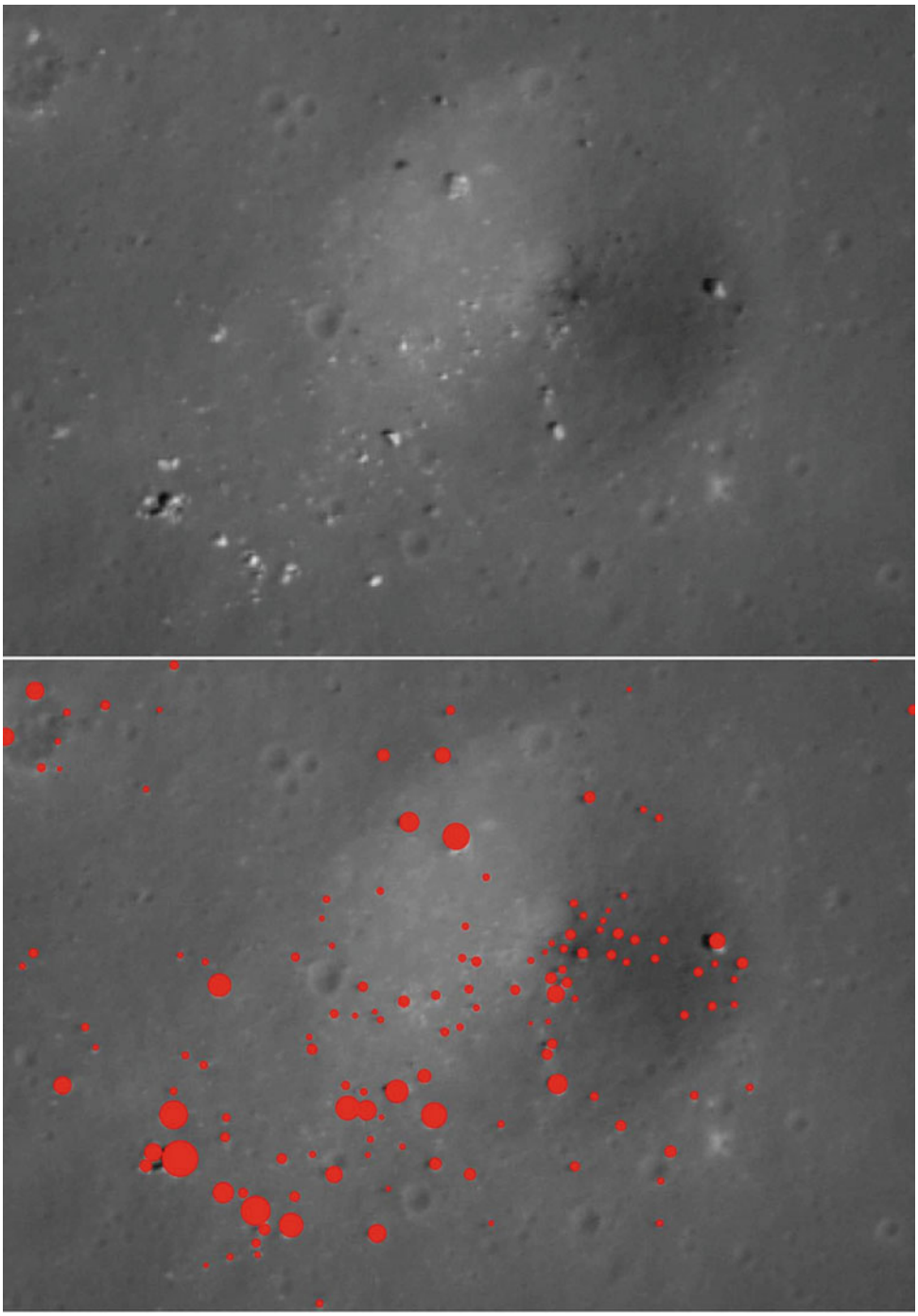

Fig. 10 Distribution of stones, shown by size as red circles in a crater with a diameter of 90 m. Crater coordinates—48.600° W, 24.724° E. Fragment of the LROC NAC mosaic (NASA)

Lunar maria plains are also characterized by the lowest inter-crater density of stones of 1.5 m in size and more (2.3×10^{-4} stones per 100 m^2), and the relatively high heterogeneity of their distribution, caused by the predominant concentration of stones in the craters tens and hundreds meters in size. The Highland terrain with a similar inter-crater stone density (2.6×10^{-4} per 100 m^2) is characterized by twice the average density (Fig. 18) (Tables 1 and 3) as compared with the lunar maria plains, which indicates also a much greater degree of heterogeneity in the distribution of stones.

Transitional terrain (Aristarchus Plateau) is distinguished not only by a higher density of stones, which is almost three times higher than the density on lunar maria terrain (Fig. 18) (Table 1 and 2), but also by their more uniform distribution with inter-crater density of 7.9×10^{-3} stones per 100 m^2, which is more than an order of magnitude higher than the values at the lunar maria and Highland terrains.

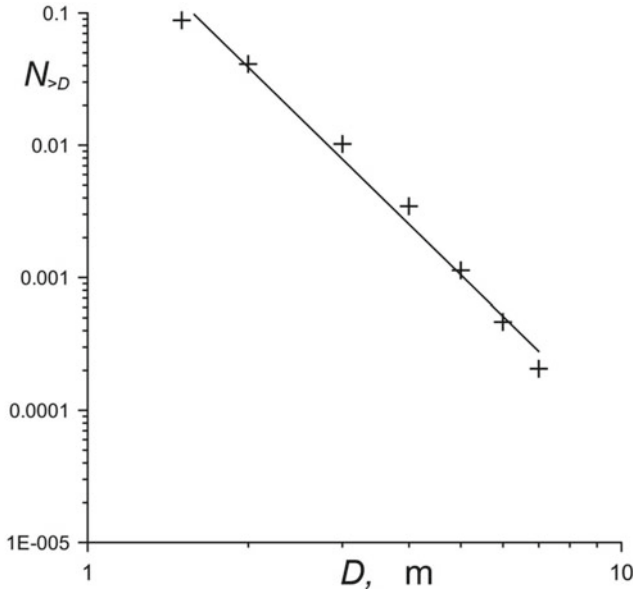

Fig. 11 The cumulative distribution density of stones is $\geq$ 1.5 m in size per 100 m^2 at the Aristarchus Plateau. The solid line shows the approximating curve. The ordinate axes are given in the logarithmic decimal scale

Table 2 The calculated (2) and observed cumulative density of stones more than a certain diameter $N_{>D}$ per 100 m^2 at the Aristarchus Plateau

Stone size, m	Calculated (2), $N_{>D}$	Observed, $N_{>D}$
0.20	317.10000	–
0.50	8.90000	–
1.00	0.60000	–
1.50	0.12000	0.08800
2.00	0.04000	0.04100
3.00	0.00820	0.01000
4.00	0.00270	0.00350
5.00	0.00110	0.00110
6.00	0.00055	0.00046
7.00	0.00030	0.00021

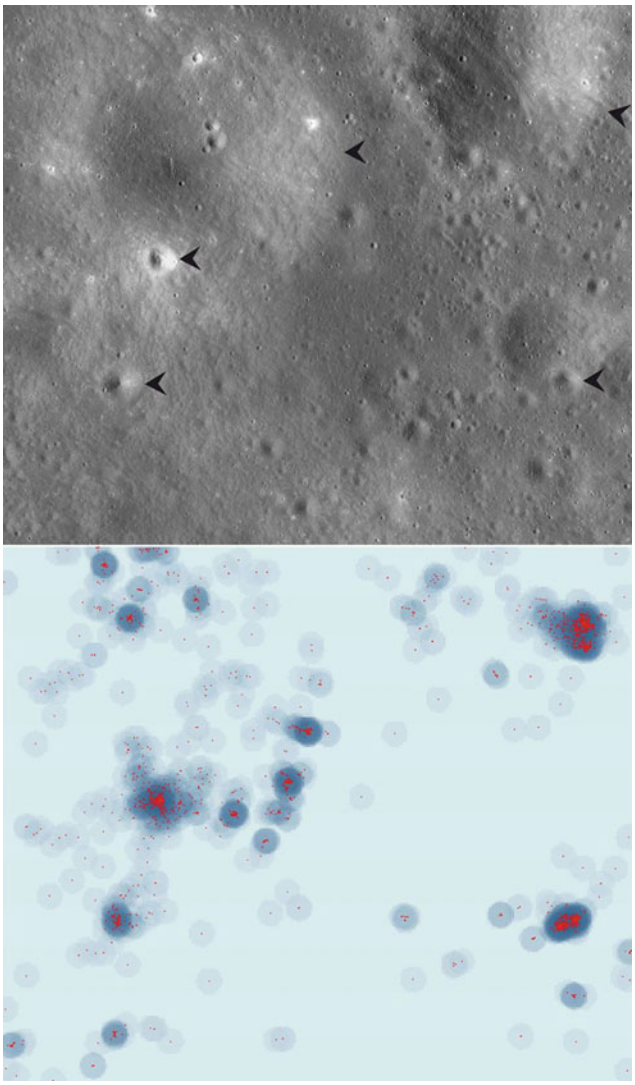

Fig. 12 Highland area on the Far Side of the Moon. The size of the region is 4825 × 4160 m. The diameter of the largest crater in the upper left corner is 2 km. Arrows indicate craters in which more than 90% of all stones are concentrated. On the right is the relative distribution density of stones, shown by the method of the nearest neighbor in a circle with a radius of 100 m. The depth of the gray scale is divided into 32 classes. Red dots indicate the stones. The coordinates of the center of the image are 158.624° W, 5.280° N. Fragment of a mosaic LROC NAC (NASA)

The distribution density of small stones less than 1 m in size in the Oceanus Procellarum is much higher in comparison with all other areas, and distribution density of stones larger than 3 m in size is much lower (Fig. 19). The distribution density of boulders less than 1 m in size in the Oceanus Procellarum is much higher in comparison with all other areas, and distribution density of boulders larger than 3 m in size is much lower. The opposite trend in comparison with other studied areas is characterized by Sinus Medii, where there is a significantly smaller number of stones less than 3 m in size [for stones less than 1 m in size, this difference can reach several orders of magnitude (Table 5)] and an excess of larger stones (Fig. 19). Given the opposite trend in the density of distribution of stones depending on the size, Oceanus Procellarum and Sinus Medii differ especially from each other in the dimensional composition of boulders (Fig. 17).

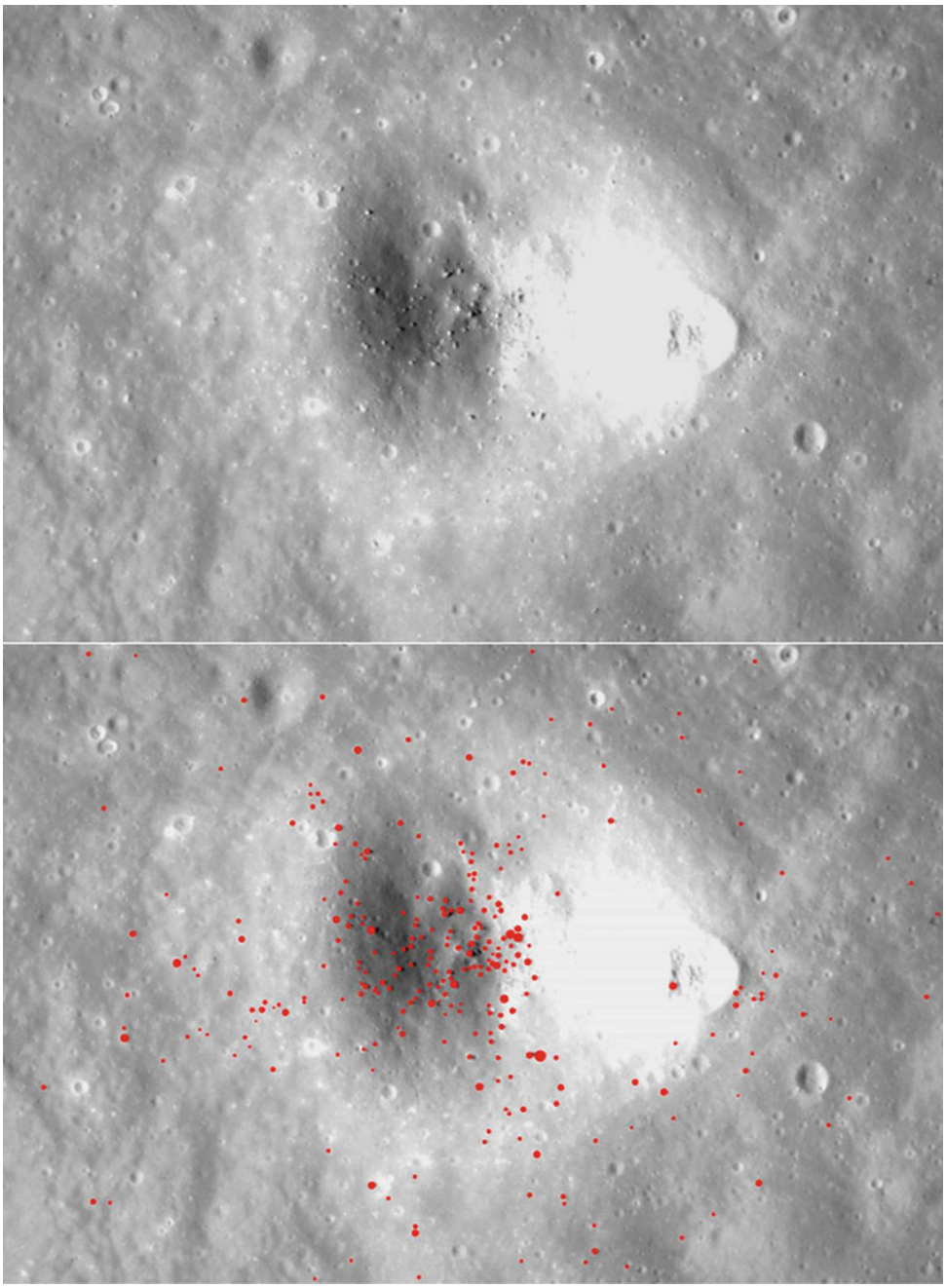

Fig. 13 The distribution of stones in the crater with a diameter of 220 m with coordinates of 158.672° W, 5.282° N, superimposed on the rim of the largest crater. Red circles show recognized stones. The size of the circle corresponds to the size of the stone. LROC NAC (NASA) mosaic fragment

8 Summary

The investigated three different types of terrain on the Moon are characterized by different density of boulders distribution. The maria plains are characterized by the lowest cumulative density of boulders in comparison with the transitional (Aristarchus Plateau) and Highland areas, as well as the lowest inter-crater stone density. The Highland area, in comparison with the maria plains, with a similar inter-crater density of stones, is characterized by twice the average density of boulders. The transitional area (Aristarchus Plateau) is distinguished not only by a higher density of boulders, which is almost three times higher than the density on the maria plains, but also by their more uniform distribution. At the same time, the intercrater density of boulders is more than an order of magnitude higher than the values in the maria and Highland areas.

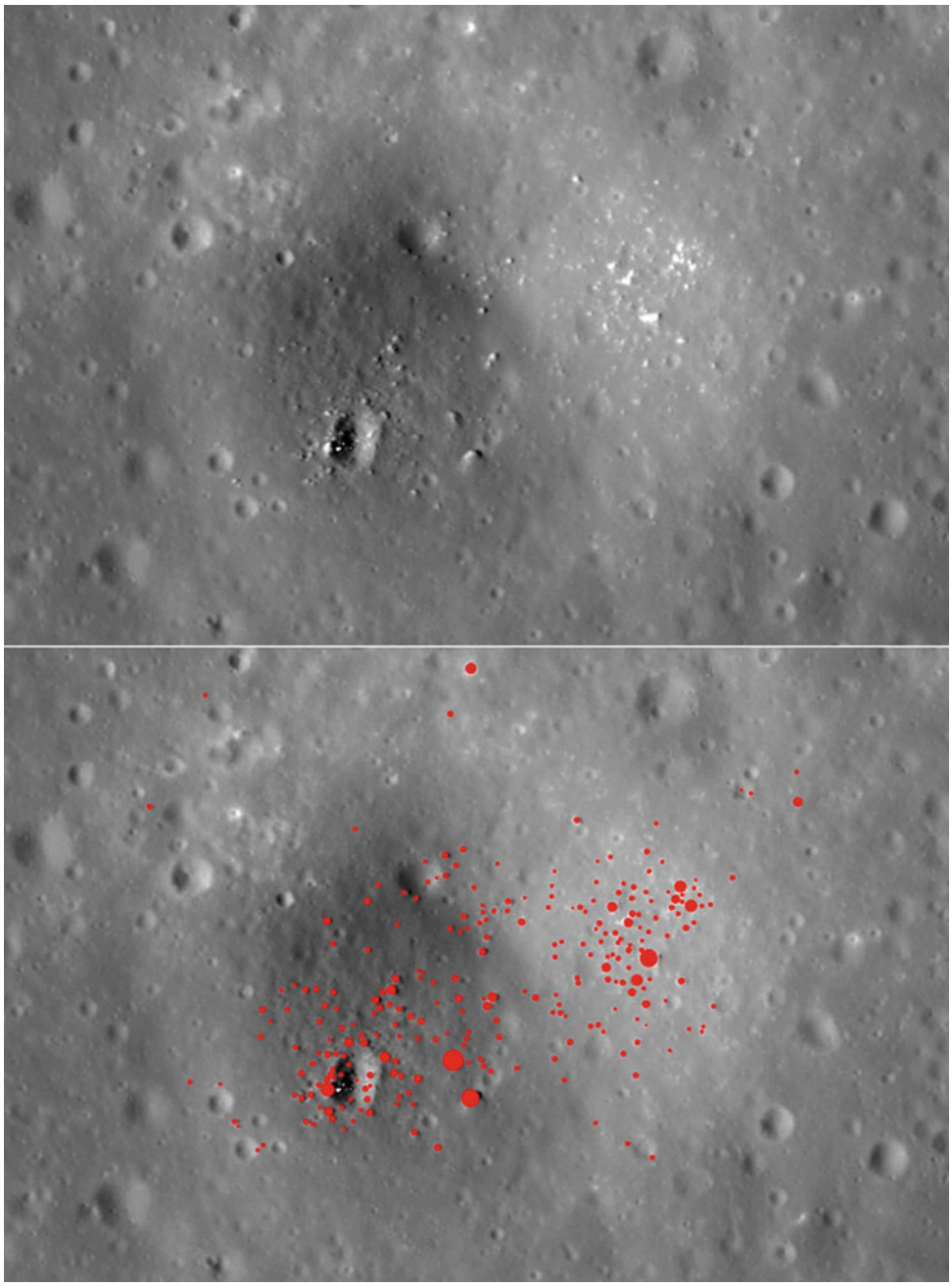

Fig. 14 The distribution of stones in the crater with a diameter of 240 m with coordinates of 158.569° W, 5.252° N. Red circles show recognized stones. The circle size corresponds to the stone size. LROC NAC (NASA) mosaic fragment

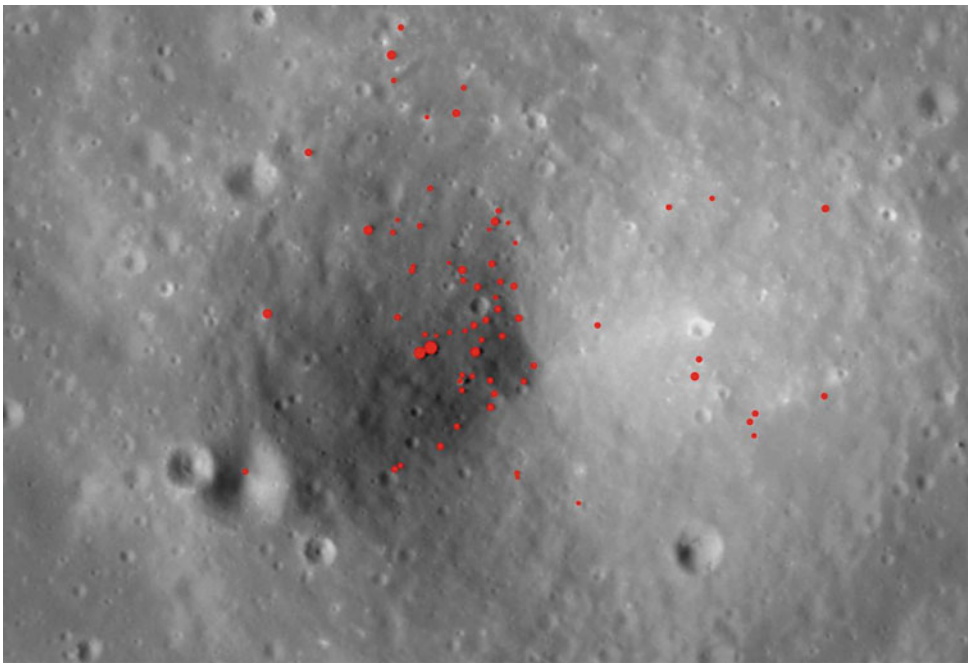

Fig. 15 The distribution of stones in the crater with a diameter of 320 m with coordinates of 158.682° W, 5.251° N. Red circles show recognized stones. The circle size corresponds to the stone size. LROC NAC (NASA) mosaic fragment

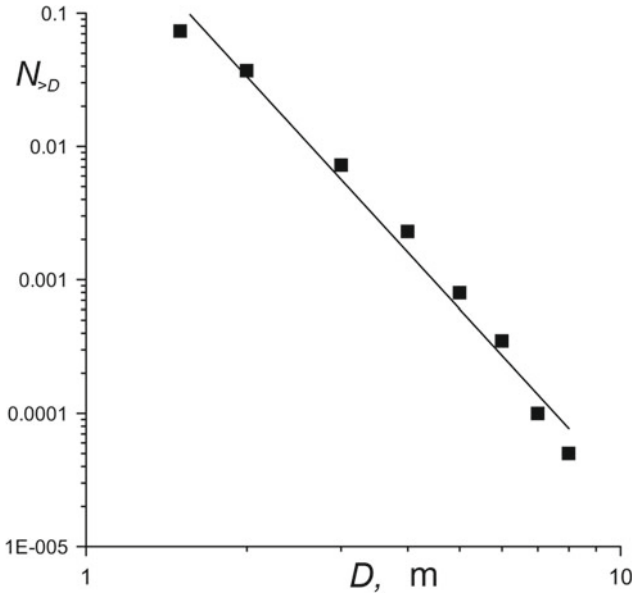

Fig. 16 The cumulative density of stones is $\geq$ 1.5 m per 100 m^2 in the Highland terrain. The solid line shows the approximating curve. The ordinate axes are given in the logarithmic decimal scale

Mathematical models of the density distribution of stones obtained from the observed empirical data allow estimating the density of stones ranging in size from 5–10 cm to 1.5 m to create reliable engineering models of the lunar surface for various types of terrain, as well as the density of stones ranging in size from 20 to 50 cm, which are the most dangerous for landing spacecraft.

Table 3 The calculated (3) and observed cumulative density of stones more than a certain diameter $N_{>D}$ per 100 m^2 at the Highland terrain

Stone size, m	Calculated (3), $N_{>D}$	Observed, $N_{>D}$
0.20	824.500000	–
0.50	14.630000	–
1.00	0.693000	–
1.50	0.116000	0.073000
2.00	0.033000	0.037000
3.00	0.005500	0.007200
4.00	0.001550	0.002300
5.00	0.000580	0.000800
6.00	0.000260	0.000350
7.00	0.000130	0.000100
8.00	0.000074	0.000050

Table 4 The calculated (4) and observed cumulative density of stones more than a certain diameter $N_{>D}$ per 100 m^2 at Oceanus Procellarum

Stone size, m	Calculated (4), $N_{>D}$	Observed, $N_{>D}$
0.20	2081.300000	–
0.50	19.450000	–
1.00	0.567000	–
1.50	0.072000	–
2.00	0.017000	0.015000
3.00	0.002100	0.003000
4.00	0.000480	0.000280
5.00	0.000150	0.000220
6.00	0.000061	0.000058
7.00	0.000028	0.000028

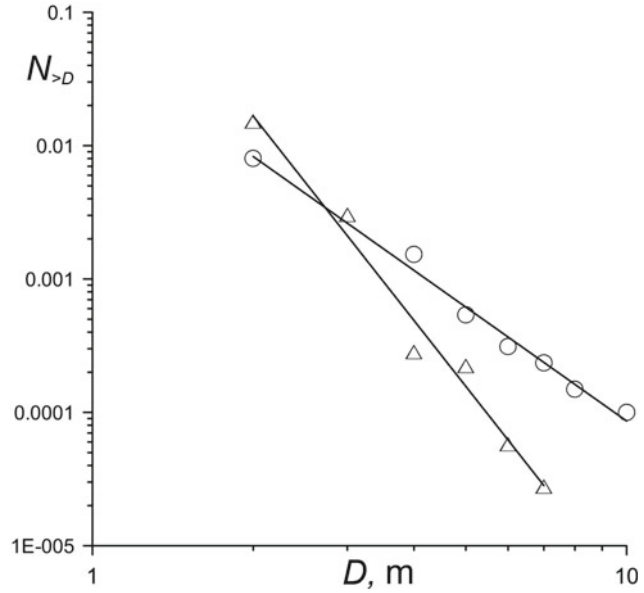

Fig. 17 The cumulative density of stones $\geq$ 2 m per 100 m^2 in the Oceanus Procellarum (Δ) and Sinus Medii (○) by data [8]. The approximating curves are shown as a solid line. The ordinate axes are given in the logarithmic decimal scale

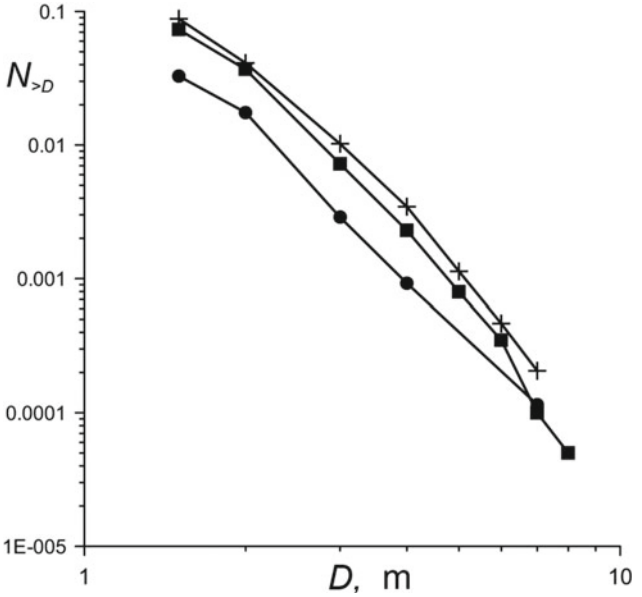

Fig. 18 The cumulative density of stones $\geq$ 1.5 m in size at different types of terrain: ●—stones distribution at the lunar maria plain; +—stones distribution at the Aristarchus Plateau; ■—stones distribution at the lunar Highland terrain

Table 5 The calculated (5) and observed cumulative density of stones more than a certain diameter $N_{>D}$ per 100 m^2 at Sinus Medii

Stone size, м	Calculated (5), $N_{>D}$	Observed, $N_{>D}$
0.20	5.350000	–
0.50	0.410000	–
1.00	0.059000	–
1.50	0.019000	–
2.00	0.008500	0.00800
3.00	0.002700	–
4.00	0.001200	0.00150
5.00	0.000650	0.00054
6.00	0.000390	0.00031
7.00	0.000250	0.00024
8.00	0.000170	0.00015
9.00	0.000130	–
10.00	0.000094	0.00010

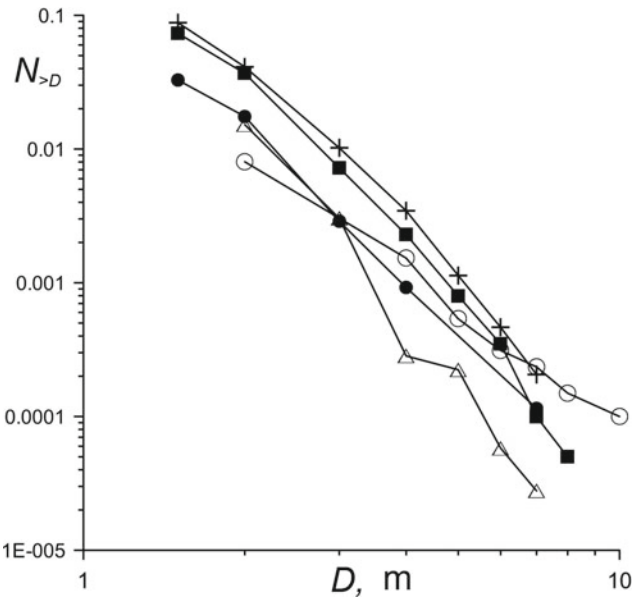

Fig. 19 The cumulative density of stones $\geq$ 1.5 m in size at different types of terrain: ●—stones distribution at the lunar maria plain; +—stones distribution at the Aristarchus Plateau; ■—stones distribution at the lunar Highland terrain; Δ—stones distribution at the Oceanus Procellarum; ○—stones distribution at the Sinus Medii

References

1. Shkuratov, Yu.G., Bondarenko, N.V.: Regolith layer thickness mapping of the Moon by radar and optical data. Icarus **149**, 329–338 (2001)
2. French, B.M.: The Moon Book. Penguin Books, Harmondsworth, Middlesex (1977)
3. Slyuta, E.N.: Physical and mechanical properties of the lunar Soil (A review). Sol. Sys. Res. **48**(5), 330–353 (2014)
4. Gault, D.E., Horz, F., Hartung, J.B.: Abrasion and catastrophic rupture of lunar rocks: some implications to the micrometeoroid flux at 1 AU. COSPAR Space Res. In: 13th Proceedings Open Meeting Working groups, Phys. Sci. 15th Planetary Meeting COSPAR, Madrid, 1972, vol. 2, Berlin, pp. 1085–1093 (1973)
5. Duennebier, F., Sutton, G.: Thermal moonquakes. J. Geophys. Res. **79**, 4351–4363 (1974)
6. Galkin, I.N.: Geophysics of the Moon. Nauka, Moscow (1978)
7. Florensky, K.P., Bazilevsky, A.T., Pronin, A.A., Popova, Z.V.: Preliminary results of geomorphological study of panoramas. In: Mobile Laboratory on the Moon Lunokhod-1, pp. 96–115. Nauka, Moscow (1971)
8. Florensky, K.P., Bazilevsky, A.T., Grushtiein, A.A., Zezin, R.B., Pronin, A.A., Polosukhin, V.P., Popova, Z.V., Taborko, I.M.: To the problem of the structure of the surface of the lunar maria. In: Florensky, K.P., Gurshtein, A.A. (eds.) Modern Ideas About the Moon, pp. 21–45. Nauka, Moscow (1972)
9. Florensky, L.P., Bazilevsky, A.T., Bobina, N.N., Burba, G.A., Grebennik, N.N., Kuzmin, R.O., Polosukhin, V.P., Popovich, V.D., Pronin, A.A.: Processes of transformation of the lunar surface in the Lemonnier region based on the results of a detailed study on Lunokhod-2. In: Tectonics and Structural Geology. Planetology, pp. 205–234. Nauka, Moscow (1976)

Estimation of the Influence of Contamination by Rocket Fuel Combustion Products on the Chemical and Isotopic Composition of the Lunar Regolith in the Polar Regions

C. A. Lorenz, A. T. Basilevsky, V. P. Dolgopolov, and T. O. Kozlova

1 Introduction

In recent years, the possible contamination of the lunar regolith by the exhaust gases from the engines of spacecraft operating in lunar orbits and, especially, landing on the surface of the Moon and taking off from it, has been discussed in the literature, e.g. [1–3]. This problem has previously been addressed in connection with Apollo lunar missions [4]. Combustion products of rocket fuel reaching the lunar surface can be sorbed by lunar regolith in areas where the temperature is low enough, so called cold traps, as it is in lunar night time and/or in shaded Polar Regions. The most favorable conditions for capturing exhaust gases are the permanently shaded bottoms of depressions, mostly craters, of polar regions (T = 20 – 100 °K [5–8]).

At the same time, in the planned missions to the Moon a priority is given to the study of its southern polar region, where the following factors are combined: (a) the presence of volatile compounds frozen in the regolith, mainly water, considered as a resource for future lunar bases and fuel for space flights, and (b) a unique geological situation—the rim of the largest and oldest lunar impact basin South Pole—Aitken, the study of which could provide information about the early stages of lunar evolution. Among the already planned expeditions to the Moon are the Russian Luna 25 spacecraft aimed to test landing in the polar region and beginning the study of the South Pole of the Moon, as well as the Luna 26 orbiter, the Luna 27 lander with the task of studying the regolith and exosphere in more detail, and Luna 28, which should deliver to Earth samples of material from the South Pole region according to the Roscosmos lunar exploration program [9]. China Republic is also planning to study the South Pole of the Moon by the missions "Chang'e 6, 7, 8" [10]. The American program Artemis [11] is aimed at the same goal. In addition, NASA announced a competition to develop an exploration of water ice resources at the South Pole of the Moon—NASA's Break the Ice Challenge [12].

In the craters of the Polar Regions and in their immediate vicinity, observations with neutron spectrometers from orbiters revealed elevated hydrogen content, probably present in the form of water ice (e.g., [13–15]). It is pertinent to note here that traces of water, about 0.1%, were detected in the Luna 24 regolith sample by IR spectroscopy [16]. However, at that time, there was a dominant idea of the Moon as an absolutely waterless body, extremely depleted in volatile components, and this result was not paid attention to at that time. Water and other volatile components concentrated in the permanently shadowed regions due to their sequential de-sorption on the daytime and sorption on the nighttime lunar surface [17]. Rocket gases could enter the polar cold traps by the same mechanism.

The composition of volatile compounds in the regolith of permanently-shadowed craters was established in the LCROSS experiment, during which the upper stage of the Centaur rocket crashed at high speed into the lunar surface in the polar crater Cabeus. The effects of the impact were monitored by an orbital tracking unit, the LCROSS spacecraft, which made spectroscopic observations of the impact cloud in the infrared (IR) spectral diapason [18, 19]. As follows from these publications, the regolith of Cabeus Crater contained 5.6 ± 2.9 wt% water and a number of other volatile compounds, including mercury. Taking the H_2O content as 100 parts, the concentrations of other volatiles in these units were estimated as follows: H_2S 16.75; NH_3 6.03;

C. A. Lorenz (✉) · A. T. Basilevsky
Vernadsky Institute of Geochemistry and Analytical Chemistry, Russian Academy of Sciences, 19 Kosygin St., Moscow, 119991, Russia
e-mail: c-lorenz@yandex.ru

V. P. Dolgopolov
S.A. Lavochkin Research and Production Association, Khimki, Moscow Region 141400, Russia

T. O. Kozlova
Space Research Institute, Russian Academy of Sciences, Moscow, 117997, Russia

V. P. Kolotov and N. S. Bezaeva (eds.), *Advances in Geochemistry, Analytical Chemistry, and Planetary Sciences*,
https://doi.org/10.1007/978-3-031-09883-3_23

SO_2 3.19; C_2H_4 3.12; CO_2 2.17; CH_3OH 1.55; CH_4 0.65; OH^- 0.03. The LAMP UV spectrometer showed the presence of H_2, CO and Hg atoms in the ejected products [19]. Since the Centaur unit performed the procedures of fuel and water residues remove prior to the experiment [18], the compounds detected by LCROSS should be mostly of natural origin and represent frozen sediment matter. Mandt et al. [20] noted that the relative amounts of volatiles in the LCROSS emission, particularly CO, may not be directly related to their content in the frozen regolith because the composition of the emission depends on the volatility of the substances and their forms in the regolith (condensed matter or clathrates). It is noteworthy that Dolgov and Shugurova [21] studied the composition of gases in inclusions in particles of impact glass and agglutinates extracted from regolith delivered by the Luna 16 spacecraft and showed the presence of a number of gases mentioned above—H_2, N_2, CO_2, H_2S, SO_2, NH_3 and also noble gases in various combinations and quantitative ratios. Also, a number of compounds of hydrogen, nitrogen, carbon, including organic ones, were released from the regolith delivered by the Luna 16 and Luna 20 spacecrafts [22]. Water, as already mentioned, was detected by Akhmanova et al. in the regolith sampled by Luna 24 [16].

For the Apollo lunar landing modules, a mixture of equal parts of asymmetrical dimethylhydrazine ($C_2H_8N_2$) and hydrazine (N_2H_4) was used as fuel, with nitrogen tetroxide (N_2O_4) as the oxidant [4]. For the Russian Luna 25, 27, and 28 spacecrafts, which are planned to be launched in the near future [9], it is assumed that dimethylhydrazine and nitrogen tetroxide are used and their reaction products are (mol.%) H_2 (0.281); N_2 (0.2813); H_2O (0.1957); CO (0.0292); CO_2 (0.2116). In [4] it is noted that due to the fast pressure and temperature drop at the engine nozzle outlet, the reactions between the fuel components are essentially stopped. However, it can be assumed that the components of the exhaust gases could react chemically with each other, e.g., during their gradual migration along the lunar surface toward the Polar Regions. These reactions could probably produce some of the compounds found in the ejecta from the Cabeus crater.

Thus, the obvious difference between the rocket exhaust products and the volatiles found in the LCROSS experiment is the absence of sulfur and mercury and the high content of molecular nitrogen and hydrogen in the exhaust gases. In addition, there may be differences in the isotopic composition of H, C, N, O, and S between the compounds contained in the polar regolith and in the rocket fuel combustion products.

It can be shown that noticeable contamination of the lunar regolith in the coldest parts of the Lunar Poles by the products of rocket fuel combustion has probably not yet occurred: The largest amount of exhaust gas was brought to the Moon by the six Apollo 11, 12, 14, 15, 16, 17 spacecraft modules—about 67,000 kg [23, 24]. It is interesting to note that this value is more than twice the estimate of the total mass of the Moon's atmosphere. Against this background, the mass of volatiles brought to the Moon by eight descent vehicles of the Soviet Luna 15, 16, 17, 18, 20, 21, 23, and 24 automatic stations (about 500 kg), and by descent vehicles of the American Surveyor 1, 2, 3, 4, 5, 6, 7 and Chinese Chang'e 3, 4 and 5 (in total, several hundred kg) adds little to what was brought by the Apollo missions. The area occupied by the permanently shadowed regions near the North Pole of the Moon is 12866 km^2 and near the South Pole is 16055 km^2, for a total of 28,921 km^2 [25]. Even assuming that all the exhaust gases from the mentioned landers were eventually captured by the polar permanently shadowed regions, their concentration will be $\sim$ 2.5 kg/km^2 (2.5 mg/m^2). In real conditions, a significant fraction of the rocket gases is generated during the transition from near-lunar orbit to the landing trajectory at high altitudes and leaves the Moon [1]. The simulations of the exhaust trace of Apollo 17 landing performed by [1] show that the concentration of exhaust gas trapped by the cold surface on the final stage of the landing trajectory can reach 4.6 g/km^2 over an area of about 2.5 km^2, which is equivalent to 0.2 ng/m^2. However, the local contamination of the regolith by exhaust gases at the spacecraft landing sites may be more significant due to the direct interaction of the jet with the regolith surface. The main task of this article is to estimate qualitative and quantitative physical and chemical effects of interaction between the lunar regolith and the products of rocket fuel combustion, which may arise during landing of the Luna 25, 27 and 28, and possible influence of these effects on experimental results during implementation of the scientific program of these spacecrafts.

2 Interaction of Engine Exhaust Gases with the Surface of Frozen Regolith

The astronauts of Apollo 11 on the final part of the landing saw that the jets of exhaust gas were blowing up the lunar soil, which prevented them from seeing the surface [26]. The same effect was observed by astronauts on subsequent Apollo landings. High-resolution LROC NAC images of the landing sites of Apollo 11, 12, 14, 15, 16, and 17, Luna 16, 17, 20, 23, 24, and Surveyor 1, 5, 6, and 7 show signs of ground blowing by rocket exhaust [27]. The signs of regolith blowing are visible in the images obtained at different time and phase angles (Fig. 1), which is demonstrated in the mentioned paper and by other researchers, e.g. [28, 29].

The authors of [27] describe the observed regolith blowing zone around the Apollo landing modules as area consisting of a visually dark inner part, departing from the

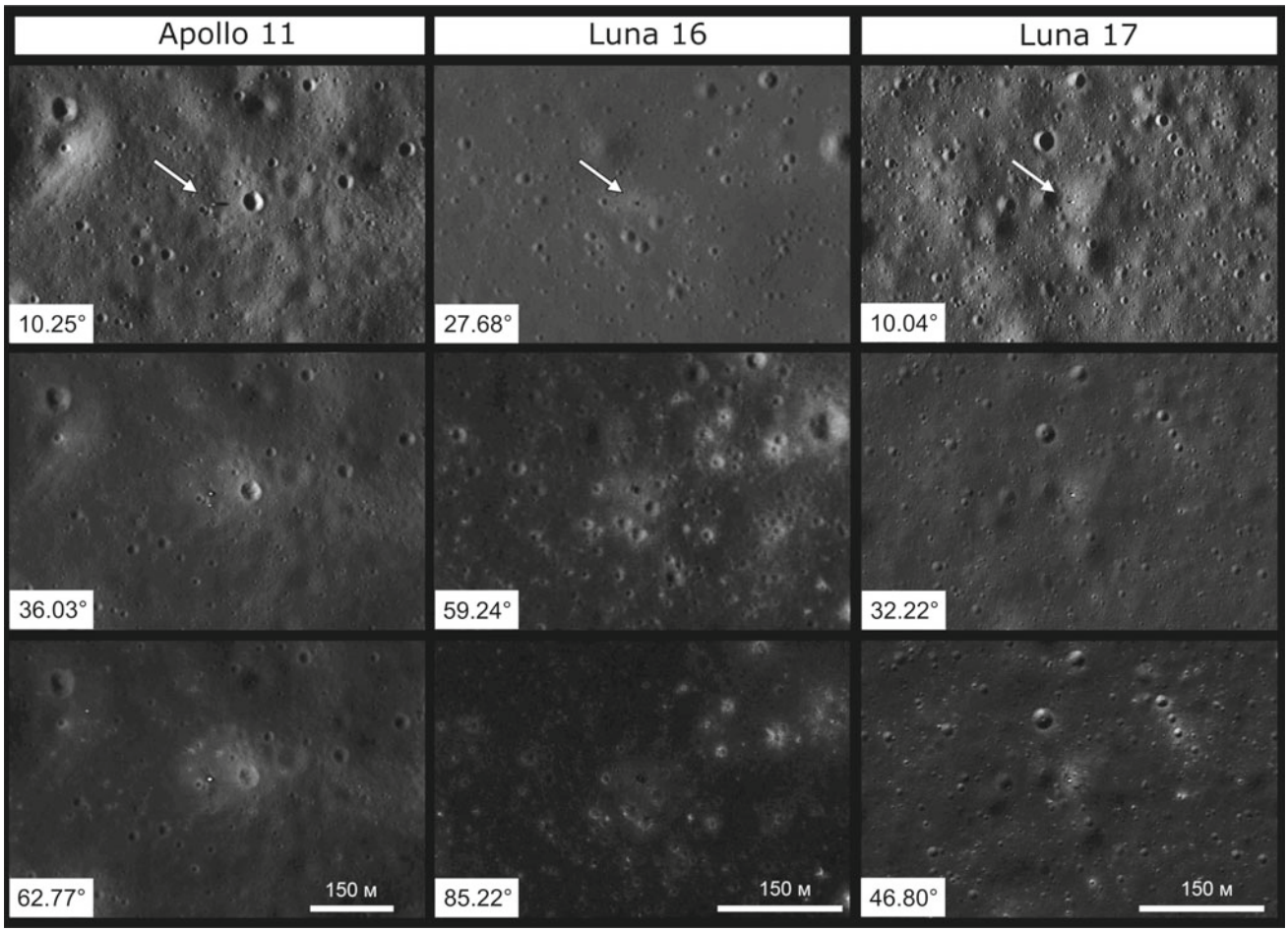

Fig. 1 Bright areas of blowing regolith around the Apollo 11, Luna 16 and Luna 17 landing modules. The arrow points to the landing module. The numbers in the lower left corner of the images are the height of the Sun above the horizon at the time of capture. Fragments of LROC NAC images

landing module by only a few meters, and an outer light part, whose average size they define as 175 ± 60 m by 200 ± 27 m. The average blowing zone area is $\sim$ 30,000 m^2. The Luna landers have about 10 times less blowing zone area, while the Surveyors have 100 times less, and no dark inner parts of the zones are visible.

On the basis of analysis of video and photos obtained during landing and takeoff of the Apollo lunar module and photos taken by astronauts on the lunar surface, as well as model experiments with dry granular soil on Mauna Kea, Hawaii, it was established that during landing the rocket gas jet causes erosion of the least durable surface layer of regolith of several centimeters thick. The layer particles of < 2 mm in size are picked up by the gas jet and transported in radial direction away from the spacecraft [30]. The mass of this material transported during the landing of the Apollo spacecraft is estimated to be from one to several tons. The radius of the zone where the loose regolith is blown out from the surface of the underlying layer can be tens of meters. The underlying stronger regolith is more resistant to the impact of the gas jet, which expands rapidly in a vacuum, so the erosion craters at the Apollo spacecraft landings are absent. It is likely that a similar pattern of interaction between the regolith and rocket gases took place during the landings of the Luna spacecrafts.

In the Polar Regions, this situation may be somewhat different. In the case of landing on the regolith containing frozen volatile species, the exhaust jet will probably first of all blow away the upper layer of loose regolith and expose a regolith, which may be more durable due to the presence of ice cementing the regolith particles. An evidence for occurrence of such a layer is shown by measurements of the depth of traces of slope-rolling rocks in areas of permanent shadow on LROC NAC images in very weak light reflected by the surface of nearby illuminated topographic highs. This depth was found to be slightly lower in several of the studied polar permanently shadowed zones than in areas with normal illumination [31]. A similar situation occurred when the

Phoenix spacecraft landed on Mars, where a layer of ice was exposed beneath the spacecraft engine [32, 33]. The horizontally propagating exhaust gases could probably partially condense on this uncovered ice-bearing surface. The exhaust would also penetrate into the pore space between the regolith grains and, cooling at some depth, could condense on the particles, creating contamination.

3 Landing of the Spacecrafts Luna 25, 27, 28

After the entering the orbit around the Moon, the spacecrafts Luna 25, 27 and 28 during the landing session will be transferred to the transition orbit with altitude over the landing site of 18 km (Fig. 2a). At the stage of main deceleration, the velocity of the spacecraft relative to the lunar surface, which should be extinguished, is ~ 1.6 km/s. The velocity of the exhaust gases relative to the spacecraft is ~ 1.8 km/s. Consequently, the exhaust velocity relative to the lunar surface in the direction tangential to the trajectory of movement at the beginning of braking is 3.4 km/s, which excludes the penetration of the exhaust on the lunar surface for most of the main deceleration trajectory.

As a result of the main deceleration, the spacecraft begins to fall to the lunar surface, oriented by the velocity vector. That is, the spacecraft turns by the engine in the direction of the lunar surface. From a height of 1–2 km, the stage of precision deceleration begins. The engine is directed along the normal to the lunar surface, and all spent fuel at this stage hits the surface at the landing site and its nearest vicinity. For Luna 25, 27, 28 spacecrafts, this is about 30–40 kg. At the stage of precision deceleration of the Luna spacecrafts about 80 kg of fuel was consumed. At the beginning of precision deceleration an area to which a jet of exhaust gas is directed is 3–10 km^2, at the end—some tens of m^2. The takeoff module of the Luna 28 spacecraft, when launched from the surface, of course, will introduce an additional amount of

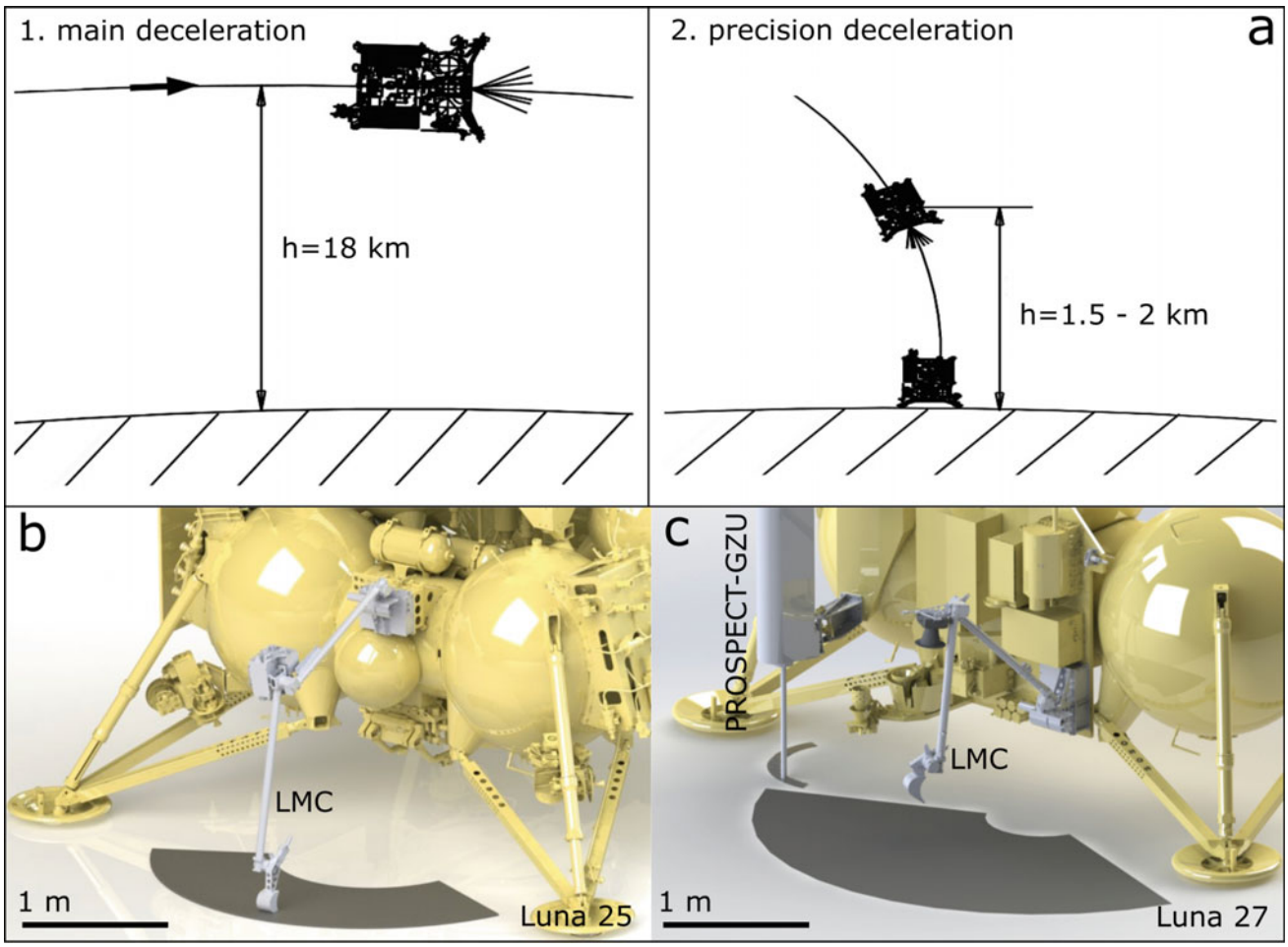

Fig. 2 **a** Scheme of the landing of the Luna 25, 27 and 28 spacecraft; (1) the stage of basic deceleration; (2) the stage of precision deceleration; **b** Lunar manipulator complex (light gray) and working area, from which it is possible to take soil samples (dark gray); **c** Landing module of "Luna 27" with LMC and PROSPECT-GZU units

exhaust into the regolith of the landing site. But this will not affect the composition of the samples delivered by this spacecraft to the Earth.

4 Sampling Procedures of the Luna 25, 27, 28 Spacecrafts

For studies of lunar regolith properties during the Luna 25 mission, the Lunar Manipulator Complex (LMC) was developed at Institute of Space Research of Russian Academy of Sciences (IKI RAS). This unit is intended for collecting soil samples from the surface and subsurface layer of regolith to a depth of 230 mm and transferring the soil samples to the LASMA-LR instrument for mass spectrometric analysis. The working area of LMC is limited by a segment of a circle with radius from 383 to 835 mm horizontally and from − 65° to + 65° by azimuth from the center of LMC mount (Fig. 2b).

The Luna 27 spacecraft is expected to carry out a much larger number of scientific studies than the Luna 25. For investigations of the lunar soil properties and composition, a complex of scientific equipment is being developed by IKI RAS. This payload includes the PROSPECT-GZU soil sampling device (being developed within the framework of the ROSCOSMOS-ECA collaboration) and the LMC manipulator complex (IKI RAS) to transfer soil samples to several analytical instruments (mass spectrometers, chromatographic complex) for analysis of these samples [34, 35] (Fig. 2c). The main purpose of the GZU is a sampling of the subsurface regolith layer, where volatile compounds, including water may persist, by the procedure providing minimal temperature influence on the sample to avoid sublimation of frozen volatile materials from the sample during its collection and transfer for analysis. LMC in the Luna 27 project has the same working area as in the Luna-25 lander, limited by a circle segment with a radius from 200 to 1000 mm horizontally and from − 65° to + 65° by azimuth from the center of the LMC mount and with a sampling depth up to 200 mm. PROSPEKT-GZU has the ability to drill the regolith and take samples of 20 mm in diameter from a depth of up to 1 m, at a radius of 245 mm from the point of attachment to the spacecraft in a segment of about 120°.

The Luna 28 project is still at the initial stage of defining the mission concept and main scientific tasks and working out proposals on the composition of the complex of scientific instruments. At the moment it is assumed that the main task of the Luna-28 mission will be cryogenic drilling of the lunar regolith at polar latitudes and delivery of the obtained samples to Earth. Drilling will be performed at a distance of up to 0.5 m from the position where the drilling unit is mounted to the spacecraft.

5 The Chemical and Isotopic Composition of Volatile Components in the Lunar Regolith

Theoretically, contamination of frozen regolith by rocket engine exhaust products can be detected as deviations of chemical or isotopic composition of volatile compounds from the values already established for lunar regolith. Since the main components of rocket gases and fuels are hydrogen, nitrogen, oxygen and carbon, it is necessary first of all to consider the content and isotopic composition of these elements in the lunar regolith.

The composition of volatile elements in silicate particles of polar regolith is probably close to that at low latitudes, but the forms of occurrence, chemical and isotopic composition of volatiles in polar ice are unknown. It has been suggested that volatiles may occur in polar regolith as ice or clathrates [20, 36]. In the simplest case, the composition of volatiles in frozen polar regolith may correspond to that in the low-latitude regolith, as these elements entering the lunar surface from different sources gradually move into cold traps of the poles [8, 17]. Therefore, the isotopic composition of volatiles in the low-latitude regolith is probably a mixture of components derived from different sources—endogenous (magmatic), and exogenous - solar wind and the so-called planetary component. The latter includes meteoritic and cometary matter and interplanetary dust particles, e.g. [37–43]. The composition of volatile elements in the planetary component arriving at the Moon should largely correspond to the composition of volatiles in the matter prevailing in the interplanetary particle flux. Morbidelli et al. [44] concluded that during the last 500 million years the flow of matter to the Moon was dominated by chondrites. Investigations of micrometeorite particles indicate that the solar system may be dominated by carbonaceous chondrite matter [45], which contains up to 14.5 wt% H_2O, up to 0.3 wt% N and up to 4 wt% C, e.g. [46, 47].

Theoretical modeling also shows that the modern flux of impactors to the Moon is dominated by chondrites rather than comets [48]. Moreover, small cometary bodies in the inner part of the solar system should be quickly destroyed due to sublimation erosion, and the falls of relatively large bodies are rare events. Analysis of the amount and isotopic composition of water delivered to the Moon during the early evolutionary period indicates that carbonaceous chondrites are the most suitable source of lunar water and nitrogen, but some amount, less than 20% of water, may have been delivered by comets [46]. The nitrogen isotopic composition of the lunar soil also suggests little admixture of a cometary component [49]. Nevertheless, at least some of the volatile elements in the lunar polar regolith must have a cometary source. Modeling of the lunar axis inclination also suggests

that the lunar regolith could contain ice formed during the collision with large comets in the period of 2–4 billion years ago [50].

5.1 Hydrogen

Hereinafter, the isotopic compositions of elements are expressed using the delta (δ) notation $\delta E(‰) = [(R_{sample} - R_{standart})/R_{standart}] \times 1000$, where E is the heavy isotope of the element; R is the corresponding isotope ratio D/H (hydrogen), $^{13}C/^{12}C$ (carbon), $^{15}N/^{14}N$ (nitrogen), $^{17}O/^{16}O$ or $^{18}O/^{16}O$ (oxygen), $^{34}S/^{32}S$ or $^{36}S/^{32}S$ (sulfur). The standard samples are hydrogen and oxygen—SMOW (Standard Average Ocean Water), carbon—PDB (Pee Dee Belemnite), nitrogen—atmospheric nitrogen, sulphur—V-CDT (Canyon Dyablo troilite), IAEA-S1 or IAEA-S2.

The average hydrogen content in fine-grained regolith is 31.2 ± 24.8 ppm [51]. Stephant et al. [52] determined the hydrogen isotopic composition interval in lunar rocks to be δD from − 200 to + 200‰ (Fig. 3a). Liu et al. [40] showed that agglutinate glasses in lunar soil contain OH^- groups, with solar wind being the main source of hydrogen (∼ 50%). Deuterium-poor compositions (δD < − 550‰) were determined for many of them. Based on these data, these authors suggested that ice in polar cold traps may contain significant amounts of hydrogen atoms produced by solar wind proton implantation. Stephant and Robert [53] also determined the isotopic-light hydrogen composition in agglutinate glasses (δD from − 680 ± 3‰ to + 7 ± 8‰ at the grain margins) and also concluded that the hydrogen contained in regolith particles is mostly (∼ 85%) of solar origin. The deuterium enrichment observed in the lunar matter of low latitudes compared to solar wind hydrogen is explained by isotopic fractionation during thermal diffusion and nuclear reactions of the matter with high-energy solar and galactic particles [40, 53].

The mechanism of reduction of metallic iron from Fe^{2+} as a result of proton implantation in regolith particles considered, for example, by Kerridge et al. [51] should lead to the formation of hydroxyl ions and water molecules. During redistribution of water formed by this mechanism [54], some water escapes from the regolith into the exosphere of the Moon due to thermal desorption, diffusion, and micrometeorite impacts, and may be gradually transported to the shaded polar regions through alternating processes of evaporation from the day surface and condensation on the night surface [17]. Some hydrogen in the exosphere is also present in molecular form [55]. Thus, since predominantly isotope-light hydrogen is implanted and desorbed, it is logical to assume that the isotopic composition of hydrogen in polar ice may be at least not heavier than in the low latitude regolith. However, if there is ancient cometary ice stored in the Polar Regions [50], the bulk isotopic composition of hydrogen in polar volatiles could be more deuterium-rich relative to the low latitude regolith.

5.2 Nitrogen

Measured N contents in immature regolith are from 18 to 96 ppm; in mature regolith,—from 85 to 150 ppm [49, 56, 57]; in basalts—from 43 to 44 ppm [56]. In the low-latitude regolith, the distribution of N components from different sources is opposite to that observed in the case of hydrogen. The contribution of solar ($\delta^{15}N = -407‰$ [58]), endogenous ($\delta^{15}N = +13.0 \pm 1.2‰$ [59]), and nitrogen arising from nuclear reactions in the lunar soil is insignificant, and the main source of nitrogen (∼ 80%) is the "planetary" component [49]. The composition of the planetary component $\delta^{15}N = +87 - +140‰$, which is consistent with data previously obtained for Luna 24 samples (+90 − + 130‰ [41]). Given the variations between N component contents at each heating step, planetary N may be even more enriched in ^{15}N than the bulk fraction compositions at least to + 300‰, which is higher than in carbonaceous chondrites [60], and may be in the field of interplanetary dust particles [61] and CB chondrites [62, 63]. Mortimer et al. [49] concluded that no more than 5–18% of all lunar nitrogen can originate from a cometary source, and that the main source of nitrogen in the low latitude regolith is chondrites or interplanetary dust (Fig. 3b). Kerridge et al. [51] found that the nitrogen and carbon contents in the lunar soil are strictly correlated, while their isotopic compositions are not.

5.3 Carbon

Average carbon contents in fine-grained regolith range from 67 to 225 ppm, in basalts from 16 to 70 ppm [51, 56, 57]. CO and CO_2 are dominant components of lunar volcanic gases [65–67]. The carbon isotopic composition of the Apollo 16 fine-grained regolith ($\delta^{13}C = +2.5$ to + 18‰ [51]), is heavier than that of the rocks (−15 to − 35‰ [51]) (Fig. 3b), except for soil samples 67,461 and 61,221 ($\delta^{13}C = -17‰$ [51, 68]). The regolith in Apollo 12 samples is also mostly enriched in heavy isotope ($\delta^{13}C = 1.2 - 17.8‰$) but samples 12,030.123 and 12,037.150 have $\delta^{13}C = -19.7$ and − 12.06‰ respectively [69]. Kaplan et al. [70] concluded that splitting by solar wind protons leads to an increase in $d^{13}C$ in the regolith due to preferential removal of the ^{12}C isotope.

The isotopic compositions of carbon released at the same temperature steps from five soil samples from Apollo 12, 14, 15, 16 collected are different [49]. At temperatures between 0

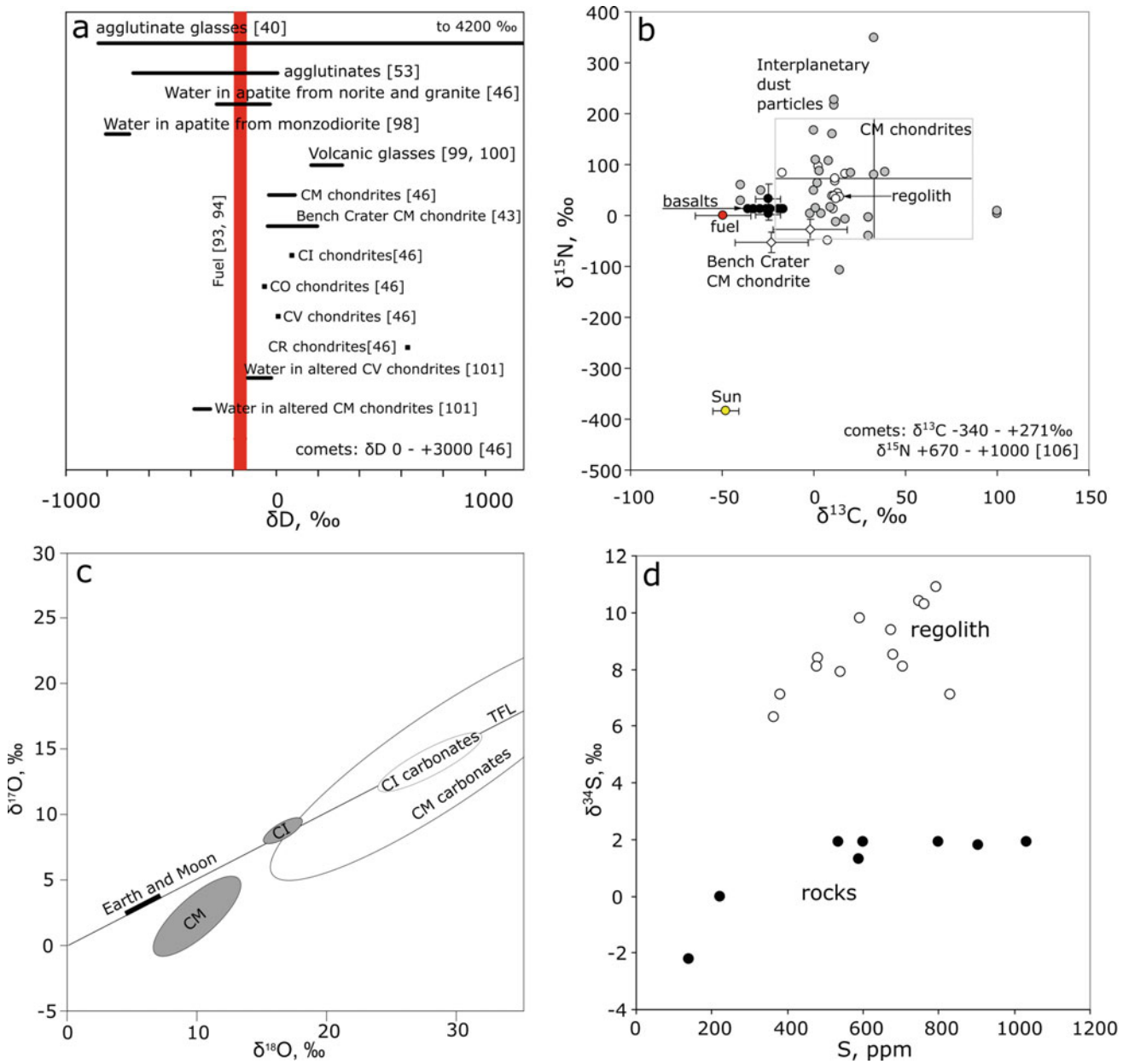

Fig. 3 **a** Hydrogen isotopic composition in the lunar matter [40, 46, 53, 98–100], carbonaceous chondrites [43, 46, 101], comets [46] and fuel [93, 94]; **b** Isotopic compositions of nitrogen and carbon in fuel (red), [93–95], lunar rocks (black) [51]; regolith (white) [59, 64]; carbonaceous chondrite Bench Crater found in a lunar soil sample (rhombes) [43], in interplanetary dust particles of a 'normal' nitrogen population (gray) [61], and intervals of carbon and nitrogen compositions in carbonaceous meteorites of the CM group (N—[46]; C—[47, 102–104]) and in the Sun (yellow) [58, 106]; **c** oxygen isotopic composition in lunar and Earth matter [76, 77] and in CI and CM carbonaceous chondrites [43, 78]. TFL—Earth mass-fractionation line; **d** Sulfur isotopic composition in rocks and regolith of the Moon [51]

and 600 °C the samples release n•10^2 ng of carbon, whose isotopic composition is in the $\delta^{13}C$ range of − 20 to − 40‰, and which the authors believe to be terrestrial contamination. At temperatures above 600 °C, carbon enriched in ^{13}C isotope (with positive values of $\delta\ ^{13}C$) is released from all samples.

Generally, the carbon isotopic composition in lunar regolith is in a range of carbonaceous chondrites of CM group and interplanetary dust particles (Fig. 3b).

5.4 Oxygen

The oxygen isotopic composition of the volatile compounds should represent a mixture of oxygen of lunar rocks, solar wind, planetary oxygen and, possibly, oxygen of the Earth's atmosphere. Solar wind oxygen is enriched in the isotope ^{16}O ($\delta^{18}O = -102.3 \pm 3.3$‰, $\delta^{17}O = -80.8 \pm 5.0$‰ [71]). Terada et al. [72] noted that the ^{16}O-depletion of the upper

layers of some regolith particles, as observed by Hashizume and Chaussidon [73], may be the result of implantation of stratospheric terrestrial oxygen. The presence of hematite in the polar regions of the Moon, detected by the Moon Mineralogy Mapper (Chandrayaan-1 satellite), is also attributed to oxidation of regolith particles by terrestrial oxygen from the magnetospheric tail of the atmosphere [74]. However, the flux of oxygen ions in the solar wind is three orders of magnitude smaller than hydrogen one (10^5 and $10^{8.2}$ ions /cm^2 s, respectively [75]). Thus, the proportion of solar wind oxygen in regolith is negligible, as is the oxygen entering the Moon with the terrestrial magnetospheric wind (whose flux is 2.6×10^{-4} ions/cm s^2 [72]), and the contribution of these two components to the oxygen isotopic composition of lunar water can probably be neglected. The average isotopic composition of lunar rock oxygen lies near the Earth mass-fractionation line [76, 77]. Water molecules that were formed by the reduction of iron from FeO by implanted solar wind protons should have an oxygen isotopic composition close to that in lunar rocks. If we assume that the main source of lunar hydrogen is solar wind [40, 53], then oxygen mobilized by protons from lunar rocks should dominate in water ice. However, the fraction of planetary hydrogen in the lunar regolith is estimated to be 15–50% [40, 53]. If a proportional amount of planetary oxygen is included in the water formed on the Moon from the planetary component, then a significant fraction of oxygen in polar ice may have a source of carbonaceous chondrites and comets. It is not clear how the oxygen composition of the lunar polar ices can be shifted relatively the terrestrial fractionation line on the triple-isotopic diagram due to addition of the planetary component since the oxygen isotopic composition of bulk carbonaceous chondrites and comets, e.g. [43, 78, 79] and their volatile components vary widely and these regions covers the terrestrial mass-fractionation line (Fig. 3c).

5.5 Sulfur

Sulfur concentrations in the fine- and medium-grained fractions of the regolith and in rock fragments vary within the same limits: Apollo 12 basalts 350–1520 ppm, average 874 ppm; 675 ± 180 ppm in rocks and 574 ± 225 ppm in regolith [51], average in soils 750 ppm [69]. The average S content in Luna-16 samples is 0.2 ± 0.03 wt% [80] and in Luna 24 samples is 0.13 ± 0.08 wt% [81]. Gibson and Andrawes [82] showed that sulfur content in lunar basalts correlates with titanium content.

Probably, the main source of sulfur in regolith of equatorial regions is iron sulfide (troilite) present as inclusions in magmatic rocks [83] and postmagmatic metasomatic formations [84–86]. Troilite is a stable phase under lunar day conditions. However, troilite can decompose and sulfur can evaporate during meteorite impacts. Endogenous gaseous sulfur compounds may also be released from rocks during the impacts or degassing of the magma. Lunar volcanic gases may also contain C–O–S compounds [87]. Dolgov and Shugurova [21] showed the presence of hydrogen sulfide in gas inclusions of fragments and beads of glass and fine-grained porous rocks (according to the description—impact glasses and agglutinates) sampled from the Luna 16 regolith.

Kerridge et al. [51, 60] showed an enrichment of the regolith in ^{34}S isotope (Fig. 3d), which correlates with the regolith maturity and is probably the result of fractionation due to partial escape of sulfur from the regolith into the open space. Kerridge et al. [60] showed that the sulfur content and distribution of sulfur isotopes are more consistent with a model in which sulfur loss and isotope fractionation compete with the introduction of sulfur from an exogenous (meteoritic) source and mixing with an endogenous component. Sulphur isotopic composition in the solar system materials varies widely [79]. Thus, the gaseous sulfur compounds found in the southern polar region [18] probably have both exogenous (cometary and meteoritic) and endogenous (magmatic) sources.

5.6 Mercury

The content of mercury in regolith and rock fragments from samples Luna 24 (0.005 ± 0.001 ppm [81] and Apollo 12 (0.003 ± 0.002 ppm [88, 89]) is lower than in regolith samples Luna 16 (0.14 ppm [80]). According to [90–92], the surface regolith layer with mercury content varies from 0.0016 (Apollo 12 [9]) to 0.06 ppm (Luna 16 [90]), is depleted in this element compared to deeper regolith layers where Hg content varies from 0.0082 (Apollo 14 [89]) to 0.22 ppm [80, 90]. Belyaev and Koveshnikova [90] concluded that the mercury content increases with decreasing particle size in the sample, and that some of the mercury in regolith is adsorbed by the particle surface. According to these authors, the lower content of mercury in the surface layers of regolith may be a result of desorption and evaporation of mercury during the lunar day and diffusion of the element to the underlying cooler layers. It is also shown that during the lunar day, 1 cm^2 of the surface can release about 10^{-6} g of mercury which condenses on the shaded night lunar surface, and possibly on the day side in the local shaded areas of the surface and thus mercury migrates to the shaded Polar Regions where accumulation of this element can occur.

6 Chemical and Isotopic Composition of Fuel

Hydrazine, methylhydrazine and nitrogen tetraoxide are synthesized from components (ammonia and its derivatives, urea) derived in turn from natural gas (hydrogen and carbon

source) and atmospheric air (nitrogen and oxygen source). This determines the isotopic characteristics of fuels and their combustion products (Fig. 3a–c). For example, the average isotopic composition of hydrogen in natural gas from Czech deposits is δD = − 166 (− 194‰ to − 151‰ VSMOW [93]), gas-bearing provinces of China δD = − 173‰ (−191‰ to − 148‰ VSMOW [94]). Nitrogen in ammonia, which is synthesized by the Haber–Bosch process from atmospheric nitrogen, has an isotopic composition of $\delta^{15}N = -0.2 \pm 2.1$ VSMOW [95]). The isotopic composition of carbon in natural gas varies with the composition of gaseous hydrocarbons and the geological situation of the deposit, e.g. [96]. In methane-dominated natural gas of the petroleum type, carbon should have $\delta^{13}C < -29‰$. For natural gas, Milicka et al. [93] report $\delta^{13}C$ values of − 39, − 43, − 67‰ (methane).

7 Estimation of the Influence of Fuel Impurity on the Isotopic Composition of the Sample

The diagrams shown in Fig. 3 illustrate the fact that the isotopic compositions of volatile elements on the Moon vary widely and the compositions of light elements in the fuel of spacecraft overlap with lunar ones. Thus, detection of relatively small (as shown above) admixture of engine-exhausted volatile elements in the sample of regolith containing frozen natural volatiles can be a difficult due to high background abundances of volatiles in the Polar regolith.

For example, the diagram in Fig. 4 shows that with a hydrogen content of 1 wt% (∼ 10 wt% H_2O in the regolith, which is twice as high as at the Cabeus crater impact site), fuel hydrogen contamination of the sample can be visible at fuel contents of 0.1 wt% or higher.

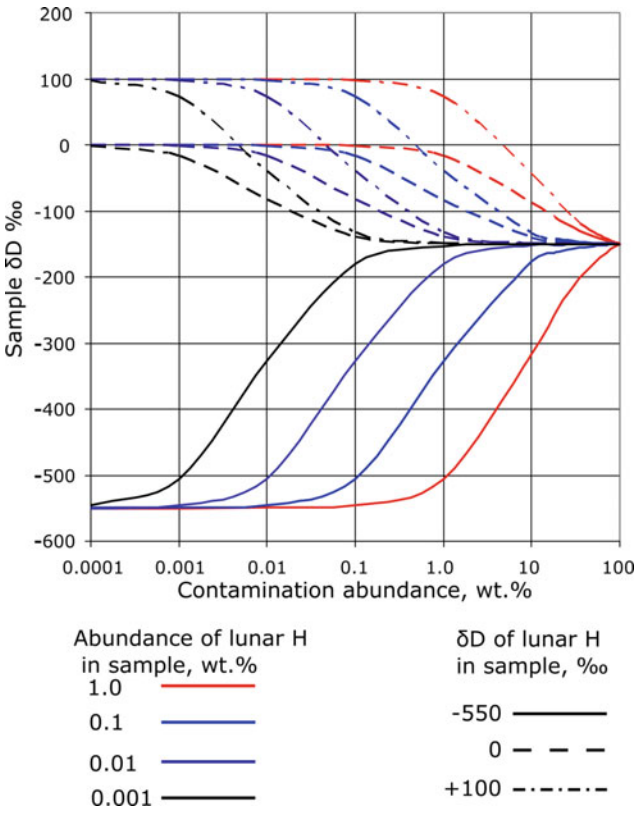

Fig. 4 Two-component mixing model for the hydrogen isotopic compositions of lunar and rocket exhaust hydrogen in a Polar regolith sample calculated for a hydrogen content of 12.5 wt% (hydrazine) and a hydrogen isotopic composition of the fuel δD = − 150‰ (see text). Curve sets for different hydrogen contents are shown (max. 1 wt% (10 000 g/t [107]) and several variants of hydrogen isotopic compositions in the polar soil: δD = − 550‰ (agglutinate glasses, [40]), 0 and + 100‰.

8 Conclusions

As described above, according to the LCROSS experiment, the ice in the shaded craters of the polar regions of the Moon contains an extensive set of volatile components [18, 19]. Some of them are also components of rocket engine exhaust. The composition and concentrations of these compounds in polar sediments other than the Cabeus crater impact site are, strictly speaking, unknown. At this stage of polar regolith studies, it is logical to assume that the composition of volatiles in the regolith of permanently shaded regions of the lunar poles should generally correspond to that established in the LCROSS experiment. Based on this assumption, the noticeable depletion of the products of low-temperature heating of the sample in volatile sulfur (and, possibly, mercury) compounds in comparison with the level of their contents established by LCROSS, may be an indirect indicator of the thermal effect of rocket gases on regolith. In this case, the sample should also be depleted in other natural volatile compounds, so that the distribution of volatile components in such a sample would differ from the natural one.

The above consideration of the isotopic compositions of H, C, N, O in lunar matter suggests that the isotopic composition of hydrogen in polar ice is likely to overlap with the isotopic composition of hydrogen in fuel. Nitrogen and carbon of polar volatiles may be isotopically heavier than in fuels, and oxygen may be depleted in ^{16}O isotope compared to fuels. However, since the isotopic compositions of light elements in polar ice are unknown, and, as the data on the sources of light elements and their fractionation processes on the Moon show, can vary within wide limits, it is not yet possible to establish the presence of contamination by rocket exhaust and perform its quantitative estimation from the isotopic composition of these four elements.

Significant progress in solving this problem can be expected with the results of mission of the American lunar rover VIPER (Volatiles Investigating Polar Exploration Rover), which is planned to land in the southern Polar Region of the Moon in 2023 [97]. VIPER is planned to travel 20 km across the lunar surface and thus move away from the potentially exhaust-contaminated landing site. It is planned that this rover will be equipped with three spectrometers and a drilling unit capable of taking samples from a depth of up to 1 m. In general, as shown above, global contamination of the Moon by exhaust gases of landing vehicles has not yet occurred. Local contamination at the landing sites is possible and even inevitable, but its scale is still unclear.

Acknowledgements The work is conducted under the GEOKHI RAS state assignment. The authors are grateful to colleagues N. A. Artemyeva, V. A. Dorofeeva and A. I. Buikin for helpful comments on the text of the manuscript, and Mark Robinson for the help with preparation of this work.

References

1. Shipley, S., Metzger, P., Lane, J.: Lunar cold trap contamination by landing vehicles. American Society of Civil Engineers Earth and Space. Conference paper (2014)
2. Prem, P., Hurley, D., Goldstein, D., Varghese, P.: The evolution of a spacecraft-generated lunar exosphere. J. Geophys. Res. Planets **125**, e2020JE006464 (2020)
3. Witze, A.: Will increasing traffic to the Moon contaminate its precious ice? Nature **589**, 180–181 (2021)
4. Aronowitz, L., Koch, F., Scanlon, J., Sidran, M.: Contamination of lunar surface samples by the lunar module exhaust. J. Geophys. Res. **73**, 3231–3238 (1968)
5. Paige, D., Siegler, M., Zhang, J., Hayne, P., Foote, E., Bennett, K., Vasavada, A., Greenhagen, B., Schofield, J., McCleese, D., Foote, M., DeJong, E., Bills, B., Hartford, W., Murray, B., Allen, C., Snook, K., Soderblom, L., Calcutt, S., Taylor, F., Bowles, N., Bandfield, J., Elphic, R., Ghent, R., Glotch, T., Wyatt, M., Lucey, P.: Diviner observations of cold traps in the lunar south polar region: spatial distribution and temperature. Science **330**(6003), 479–482 (2010)
6. Aye, K., Paige, D., Foote, M., Greenhagen, B., Siegler, M.: The coldest place on the Moon. LPI Contrib. **1719**, 3016 (2013)
7. Sefton-Nash, E., Williams, J., Greenhagen, B., Warren, T., Bandfield, J., Aye, K., Leader, F., Siegler, M., Hayne, P., Bowles, N., Paige, D.: Evidence for ultra-cold traps and surface water ice in the lunar south polar crater Amundsen. Icarus **332**, 1–13 (2019)
8. Davidsson, B., Hosseini, S.: Implications of surface roughness in models of water desorption on the Moon. Mon. Not. R. Astron. Soc. **506**, 3421–3429 (2020)
9. Efanov, V., Dolgopolov, V.: The Moon. From exploration to development (to the 50th anniversary of spacecraft "Luna-9" and "Luna-10"). Vestnik NPO S.A. Lavochkin **4**(34), 3−8 (2016)
10. NASA, Future Chinese Lunar Missions. https://nssdc.gsfc.nasa.gov/planetary/lunar/cnsa_moon_future.html. Last accessed 9 Nov 2021
11. Artemis program. https://www.nasa.gov/specials/artemis/. Last accessed 9 Nov 2021
12. NASA's Break the Ice Lunar Challenge. https://breaktheicechallenge.com. Last accessed 9 Nov 2021
13. Feldman, W., Maurice, S., Lawrence, D., Little, R., Lawson, S., Gasnault, O., Wiens, R., Barraclough, B., Elphic, R., Prettyman, T., Steinberg, J., Binder, A.: Evidence for water ice near the lunar poles. J. Geophys. Res. Planets **106**(E10), 23231–23251 (2001)
14. Mitrofanov, I., Sanin, A., Boynton, W., Chin, G., Garvin, J., Golovin, D., Evans, L., Harshman, K., Kozyrev, A., Litvak, M., Malakhov, A., Mazarico, E., McClanahan, T., Milikh, G., Mokrousov, M., Nandikotkur, G., Neumann, G., Nuzhdin, I., Sagdeev, R., Shevchenko, V., Shvetsov, V., Smith, D., Starr, R., Tretyakov, V., Trombka, J., Usikov, D., Varenikov, A., Vostrukhin, A., Zuber, M.: Hydrogen mapping of the Lunar south pole using the LRO Neutron detector experiment LEND. Science **330**, 483–486 (2010)
15. Sanin, A., Mitrofanov, I., Litvak, M., Bakhtin, B., Bodnarik, J., Boynton, W., Chin, G., Evans, L., Harshman, K., Fedosov, F., Golovin, D., Kozyrev, A., Livengood, T., Malakhov, A., McClanahan, T., Mokrousov, M., Starr, R., Sagdeev, R., Tret'yakov, V., Vostrukhin, A.: Hydrogen distribution in the lunar polar regions. Icarus **283**, 20–30 (2017)
16. Akhmanova, M., Dementyev, B., Markov, M.: Possible water in Luna 24 regolith from the sea of crises. Geochem. Int. **15**, 166–168 (1979)
17. Livengood, T., Chin, G., Sagdeev, R., Mitrofanov, I., Boynton, W., Evans, L., Litvak, M., McClanahan, T., Sanin, A., Starr, R., Su, J.: Moonshine: diurnally varying hydration through natural distillation on the Moon, detected by the Lunar Exploration Neutron Detector (LEND). Icarus **255**, 100–115 (2015)
18. Colaprete, A., Schultz, P., Heldmann, J., Wooden, D., Shirley, M., Ennico, K., Hermalyn, B., Marshall, W., Ricco, A., Elphic, R., Goldstein, D., Summy, D., Bart, G., Asphaug, E., Korycansky, D., Landis, D., Sollitt, L.: Detection of water in the LCROSS ejecta plume. Science **330**, 463–468 (2010)
19. Gladstone, G., Hurley, D., Retherford, K., Feldman, P., Pryor, W., Chaufray, J., Versteeg, M., Greathouse, T., Steffl, A., Throop, H., Parker, J., Kaufmann, D., Egan, A., Davis, M., Slater, D., Mukherjee, J., Miles, P., Hendrix, A., Colaprete, A., Stern, S.: LRO-LAMP observations of the LCROSS impact plume. Science **330**, 472–476 (2010)
20. Mandt, K., Mousis, O., Bouquet A., Hurley D., Luspay-Kuti, A.: The origin of volatiles sampled by the LCROSS mission in Cabeus crater. In: 52nd Lunar and Planetary Science Conference 2021. Abs. 2167 (2021)
21. Dolgov, Yu., Shugurova, N.: Results of study of gases from inclusions in lunar glasses. In: Vinogradov, A. (ed.) Lunar Soil from the Sea of Fertility, pp. 356−362. Nauka, Moscow (1974)
22. Simoneit, B., Vjolek, P., Christiansen, P., Dixon, R., Burlingame, A.: Carbon chemistry in samples delivered by Luna 16 and Luna 20. In: Barsukov, V., Surkov, Yu. (eds.) Grunt from the Highland Region of the Moon, pp. 566−572. Nauka, Moscow (1979)
23. Apollo Operations Handbook. https://history.nasa.gov/afj/aohindex.html. Last accessed 09 Nov 2021
24. The Apollo Spacecraft News Reference. https://www.hq.nasa.gov/alsj/LMNewsRef-Boothman.html. Last accessed 09 Nov 2021
25. Mazarico, E., Neumann, G., Smith, D., Zuber, M., Torrence, M.: Illumination conditions of the lunar polar regions using LOLA topography. Icarus **211**, 1066–1081 (2011)
26. Aldrin, E., Armstrong, N., Collins, M.: Crew observations. Apollo 11 Preliminary Science Report. NASA SP-214, pp. 35−40 (1969)

27. Clegg, R., Jolliff, B., Robinson, M., Hapke, B., Plescia, J.: Effects of rocket exhaust on lunar soil reflectance properties. Icarus **227**, 176–194 (2014)
28. Kaydash, V., Shkuratov, Yu., Korokhin, V., Videen, G.: Photometric anomalies in the Apollo landing sites as seen from the Lunar Reconnaissance Orbiter. Icarus **211**, 89–96 (2011)
29. Kaydash, V., Shkuratov, Yu.: Structural disturbances of the lunar surface near the Lunokhod-1 spacecraft landing site. Solar Syst. Res. **48**(3), 167–175 (2014)
30. Metzger, P., Smith, J., Lane, J.: Phenomenology of soil erosion due to rocket exhaust on the Moon and the Mauna Kea lunar test site. J. Geophys. Res. **116**(E6), E06005 (2011)
31. Sargeant, H., Bickel, V., Honniball, C., Martinez, S., Rogaski, A., Bell, S., Czaplinski, E., Farrant, B., Harrington, E., Tolometti, G., Kring D.: Determining the bearing capacity of permanently shadowed regions of the Moon using boulder tracks. In: 50th Lunar and Planetary Science Conference, abs. 1792 (2019)
32. Plemmons, D., Mehta, M., Clark, B., Kounaves, S., Peach, L., Renno, N., Tamppari, L., Young, S.: Effects of the Phoenix Lander descent thruster plume on the Martian surface. J. Geophys. Res. Planets **113**(E3), E00A11 (2008)
33. Manish, M., Renno, N., Marshall, J., Grover, M., Sengupta, A., Rusche, N., Kok, J., Arvidson, R., Markiewicz, W., Lemmon, M., Smith, P.: Explosive erosion during the Phoenix landing exposes subsurface water on Mars. Icarus **211**, 172–194 (2011)
34. Tretyakov, V., Zelenyi, L., Mitrofanov I.: 2021. Science program of Luna-25 and Luna-27 missions. In: The 12th Moscow Solar System Symposium, abs. 12MS3-MN-09 (2021)
35. Carpenter, J., Fisackerly, R.: PROSPECT: ESA's package for resource observation and in-situ prospecting for exploration, commercial exploitation, and transportation. In: The 48th Lunar and Planetary Science Conference, abs. 2514 (2017)
36. Duxbury, N., Nealson, K., Romanovsky, V.: On the possibility of clathrate hydrates on the Moon. J. Geophys. Res. Atmospheres **106**(E11), 27811–27813 (2001)
37. Nozette, S., Lichtenberg, C., Spudis, P., Bonner, R., Ort, W., Malaret, E., Robinson, M., Shoemaker, E.: The Clementine bistatic radar experiment. Science **274**, 1495–1498 (1996)
38. Feldman, W., Maurice, S., Binder, A., Barraclough, B., Elphic, R., Lawrence, D.: Fluxes of fast and epithermal neutrons from the Lunar prospector: evidence for water ice at the lunar poles. Science **281**, 1496–1500 (1998)
39. Hashizume, K., Marty, B., Wieler, R.: Analyses of nitrogen and argon in single lunar grains: towards a quantification of the asteroidal contribution to planetary surface. Earth Planet. Sci. Lett. **202**, 201–216 (2002)
40. Liu, Y., Guan, Y., Zhang, Y., Rossman, G., Eiler, J., Taylor, L.: Direct measurement of hydroxyl in the lunar regolith and the origin of lunar surface water. Nat. Geosci. **5**, 779–782 (2012)
41. Füri, E., Marty, B., Assonov, S.: Constraints on the flux of meteoritic and cometary water on the Moon from volatile element (N-Ar) analyses of single lunar soil grains, Luna 24 core. Icarus **218**(1), 220–229 (2012)
42. McCubbin, F., Vander Kaaden, K., Tartèse, R., Klima, R., Liu, Y., Mortimer, J., Barnes, J., Shearer, C., Treiman, A., Lawrence, D., Elardo, S., Hurley, D., Boyce, J., Anand, M.: Magmatic volatiles (H, C, N, F, S, Cl) in the lunar mantle, crust, and regolith: abundances, distributions, processes, and reservoirs. Am. Miner. **100**, 1668–1707 (2015)
43. Joy, K., Tartèse, R., Messenger, S., Zolensky, M., Marrocchi, Y., Frank, D., Kring, D.: The isotopic composition of volatiles in the unique Bench Crater carbonaceous chondrite impactor found in the Apollo 12 regolith. Earth Planet. Sci. Lett. **540**, 116265 (2020)
44. Morbidelli, A., Chambers, J., Lunine, J., Petit, J., Robert, F., Valsecchi, G., Cyr, K.: Source regions and timescales for the delivery of water to the Earth. Meteorit. Planet. Sci. **35**, 1309–1320 (2000)
45. Gounelle, M., Engrand, C., Maurette, M., Kurat, G., McKeegan, K., Brandstätter, F.: Small Antarctic micrometeorites: a mineralogical and in situ oxygen study. Meteorit. Planet. Sci. **40**, 917–932 (2005)
46. Barnes, J., Kring, D., Tartese, R., Franchi, I., Anand, M., Russell, S.: An asteroidal origin for water in the Moon. Nat. Commun. **7**, 11684 (2016)
47. Vacher, L., Piani, L., Rigaudier, T., Thomassin, D., Florin, G., Piralla, M., Marrocchi, Y.: Hydrogen in chondrites: influence of parent body alteration and atmospheric contamination on primordial components. Geochim. Cosmochim. Acta **281**, 53–66 (2020)
48. Svetsov, V., Shuvalov, V.: Water delivery to the Moon by asteroidal and cometary impacts. Planet. Space Sci. **117**, 444–452 (2015)
49. Mortimer, J., Verchovsky, A., Anand, M.: Predominantly non-solar origin of nitrogen in lunar soils. Geochim. Cosmochim. Acta **193**, 36–53 (2016)
50. Siegler, M., Paige, D., Williams, J., Bills, B.: Evolution of lunar polar ice stability. Icarus **255**, 78–87 (2015)
51. Kerridge, G., Kaplan, I., Petrowski, C., Chang, S.: Light element geochemistry of the Apollo 16 site. Geochim. Cosmochim. Acta **39**, 137–162 (1975)
52. Stephant, A., Anand, M., Tartèse, R., Zhao, X., Degli-Alessandrini, G., Franchi, I.: The hydrogen isotopic composition of lunar melt inclusions: an interplay of complex magmatic and secondary processes. Geochim. Cosmochim. Acta **284**, 196–221 (2020)
53. Stephant, A., Robert, F.: The negligible chondritic contribution in the lunar soils water. Proc. Natl. Acad. Sci. **111**(42), 15007–15012 (2014)
54. Benna, M., Hurley, D., Stubbs, T., Mahaffy, P., Elphic, R.: Lunar soil hydration constrained by exospheric water liberated by meteoroid impacts. Nat. Geosci. **12**, 333–338 (2019)
55. Crandall, P., Gillis-Davis, J., Kaiser, R.: Untangling the origin of molecular hydrogen in the lunar exosphere. Astrophys J **887**, 1–7 (2019)
56. Moore, C., Gibson, E., Larimer, J., Lewis, C., Nichiporuk, W.: Total carbon and nitrogen abundances in Apollo 11 lunar samples and selected achondrites and basalts. In: Proceedings of the Apollo 11 Lunar Science Conference. Geochimica et Cosmochimica Acta Supplement, pp. 1375−1382 (1970)
57. Moore, C., Lewis, C., Larimer, J., Delles, F., Gooley, R., Nichiporuk, W., Gibson, E., Jr.: Total carbon and nitrogen abundances in Apollo 12 lunar samples. In: Proceedings of the 2nd Lunar Science Conference, pp. 1343–1350 (1971)
58. Marty, B., Chaussidon, M., Wiens, R., Jurewicz, A., Burnett, D.: A ^{15}N-poor isotopic composition for the solar system as shown by Genesis solar wind samples. Science **332**, 1533–1536 (2011)
59. Mathew, K., Marti, K.: Lunar nitrogen: indigenous signature and cosmic ray production rate. Earth Planet. Sci. Lett. **184**, 659–669 (2001)
60. Pearson, V., Sephton, M., Franchi, I., Gibson, J., Gilmour, I.: Carbon and nitrogen in carbonaceous chondrites: elemental abundances and stable isotopic compositions. Meteorit. Planet. Sci. **41**(12), 1899–1918 (2006)
61. Floss, C., Stadermann, F., Bradley, J., Dai, Z., Bajt, S., Graham, G., Lea, A.: Identification of isotopically primitive interplanetary dust particles: a NanoSIMS isotopic imaging study. Geochim. Cosmochim. Acta **70**, 2371–2399 (2006)
62. Franchi, I., Wright, I., Pillinger, C.: 1986. Heavy nitrogen in Bencubbin, a light-element isotopic anomaly in a stony-iron meteorite. Nature **323**, 138–140 (1986)
63. Briani, G., Gounelle, M., Marrocchi, Y., Mostefaoui, S., Leroux, H., Quirico, E., Meibom, A.: Pristine extraterrestrial material with

unprecedented nitrogen isotopic variation. Proc. Natl. Acad. Sci. **106**(26), 10522–10527 (2009)
64. Mortimer, J., Verchovsky, A., Anand, M., Gilmour, I., Pillinger, C.: Simultaneous analysis of abundance and isotopic composition of nitrogen, carbon, and noble gases in lunar basalts: insights into interior and surface processes on the Moon. Icarus **255**, 3–17 (2015)
65. Housley, R.: Modeling lunar volcanic eruptions. In: Proceeding of 9th Lunar and Planetary Science Conference, pp. 1473–1484 (1978)
66. Sato, M.: The driving mechanism of lunar pyroclastic eruptions inferred from the oxygen fugacity behavior of Apollo 17 orange glass. In: Proceedings of 10th Lunar and Planetary Science Conference, pp. 311–325 (1979)
67. Wilson, L., Head, J.: Ascent of magma with volatiles on the Earth and Moon. In: 10th Lunar and Planetary Science Conference, pp. 1350–1352 (1979)
68. Epstein, S., Taylor, H.: D/H and $^{18}O/^{16}O$ ratios of H_2O in the 'rusty' breccia 66095 and the origin of 'lunar water'. In: Proceedings of the 5th Lunar Conference, Supplement 5, Geochimica et Cosmochimica Acta, pp. 1834–1854 (1974)
69. Kerridge, G., Kaplan, I., Kung, C., Winter, D., Friedman, D.: Light element geochemistry of the Apollo 12 site. Geochim. Cosmochim. Acta **42**, 391–402 (1978)
70. Kaplan, I., Smith, J., Ruth, E.: Carbon and sulfur concentration and isotopic composition in Apollo 11 lunar samples. Geochimica et Cosmochimica Acta Supplement. In: Proceedings of the Apollo 11 Lunar Science Conference, pp. 1317–1329 (1970)
71. McKeegan, K., Kallio, A., Heber, V., Jarzebinski, G., Mao, P., Coath, C., Kunihiro, T., Wiens, R., Nordholt, J., Moses, R., Jr., Reisenfeld, D., Jurewicz, A., Burnett, D.: The oxygen isotopic composition of the Sun inferred from captured solar winds. Science **332**, 1528–1532 (2011)
72. Terada, K., Yokota, S., Saito, Y., Kitamura, N., Asamura, K., Nishino, M.: Biogenic oxygen from Earth transported to the Moon by a wind of magnetospheric ions. Nat. Astronomy **1**(2), 0026 (2017)
73. Hashizume, K., Chaussidon, M.: Two oxygen isotopic components with extra-selenial origins observed among lunar metallic grains—in search for the solar wind component. Geochim. Cosmochim. Acta **73**, 3038–3054 (2009)
74. Li, S., Lucey, P., Fraeman, A., Poppe, A., Sun, V., Hurley, D., Schultz, P.: Widespread hematite at high latitudes of the Moon. Science Advances **6**(36), eaba1940 (2020)
75. Von Steiger, R., Zurbuchen, T., McComas, D.: Oxygen flux in the solar wind: Ulysses observations. Geophys. Res. Lett. **37**, L22101 (2010)
76. Greenwood, R., Barrat, J., Miller, M., Anand, M., Dauphas, N., Franchi, I., Sillard, P., Starkey, N.: Oxygen isotopic evidence for accretion of Earth's water before a high-energy Moon-forming giant impact. Sci. Adv. **4**(3), eaao5928
77. Cano, E., Sharp, D., Shearer, C.: Distinct oxygen isotope compositions of the Earth and Moon. Nat. Geosci. **13**, 270–274 (2020)
78. Maximilien, J., Verdier-Paoletti, J., Marrocchi, Y., Avice, G., Roskosz, M., Gurenko, A., Gounelle, M.: Oxygen isotope constraints on the alteration temperatures of CM chondrites. Earth Planet. Sci. Lett. **458**, 273–281 (2017)
79. Hoppe, P., Rubin, M., Altwegg, K.: Presolar isotopic signatures in meteorites and comets: new insights from the Rosetta Mission to Comet 67P/Churyumov–Gerasimenko. Space Sci. Rev. **214**, 106 (2018)
80. Vinogradov, A., Chupakhin, M., Shevaleevsky, I., Belyaev, Yu.: Chemical composition of the lunar regolith of Luna-16. In: Vinogradov, A. (ed.) Lunar soil from the sea of fertility, pp. 264–277. Nauka, Moscow (1974)
81. Barsukov, V., Dmitriev, L., Tarasov, L., Kolesov, G., Shevaleevsky, I., Ramendik, G., Garanin, A.: Geochemical and petrochemical features of regolith and rocks from the Crisis Sea (preliminary data). In: Barsukov, V. (ed.) Lunar soil from the Crisis Sea, pp. 158–165. Nauka, Moscow (1980)
82. Gibson, E., Andrawes, F.: The role of sulfur in the Apollo 12 basalts. In: 8th Lunar and Planetary Science Conference, pp. 351–353 (1977)
83. Frondel, J.: Lunar Mineralogy. Wiley (1975)
84. Lindstrom, M., Salpas, P.: Geochemical studies of feldspatic fragmental breccias and the nature of North Ray crater ejecta. J. Geophys. Res. **88**, A671–A683 (1983) (Proceedings of 13th Lunar Science Conference)
85. Norman, M., Taylor, G., Keil, K.: Additional complexity in the lunar crust—petrology of sodic anorthosites and sulfur-rich, ferroan noritic anorthosites. Geophys. Res. Lett. **18**, 2081–2084 (1991)
86. Colson, R.: Mineralisation on the Moon? Theoretical Considerations of Apollo 16 "Rusty Rocks", sulfide replacement in 67016, and surface-correlated volatiles on lunar volcanic glass. In: Proceedings of the 22nd Lunar and Planetary Science Conference, pp. 427−436 (1992)
87. Grove, T.: Compositional variations among Apollo 15 green glass spheres. In: 12th Lunar and Planetary Science Conference, pp. 935–948 (1981)
88. Morrison, G., Gerard, J., Kashuba, A., Gangadharam, E., Rothenberg, A., Potter, N., Miller, G.: Elemental abundance of lunar soil and rocks. In: Proceedings of the Apollo 11 Lunar Science Conference, pp. 1383–1392. Geochimica et Cosmochimica Acta Supplement (1970)
89. Morrison, G., Gerard, J., Potter, N., Gangadharam, E., Rottenberg, A., Burdo, R.: Elemental abundances of lunar soil and rocks from Apollo 12. In: Proceedings of the 2nd Lunar Science Conference, pp. 1169–1185 (1971)
90. Belyaev, Yu., Koveshnikova, T.: On the content of mercury in the regolith of the sea of tranquility, the sea of fertility and the ocean of storms. In: Vinogradov, A. (ed.) Lunar Soil from the Sea of Fertility, pp. 264–277. Nauka, Moscow (1974)
91. Reed, G., Goleb, J., Jovanovic, S.: Surface-related mercury in lunar samples. Science **172**, 258–261 (1971)
92. Jovanovic, S., Reed, G.: Trace-elements profiles, notably Hg, from a preliminary study of the Apollo 15 deep drill core. Earth Planet. Sci. Lett. **16**, 257–262 (1972)
93. Milicka, J., Massault, M., Francu, J.: Carbon and hydrogen isotopes in four natural gases from the Slovak and Czech part of the Vienna Basin. Geol. Carpath. **45**(4), 379–382 (1994)
94. Ni, Y., Liao, F., Yao, L., Gao, J., Zhang, D.: Hydrogen isotope of natural gas from the Xujiahe formation and its implications for water salinization in central Sichuan Basin, China. J. Nat. Gas Geosci. **4**(4), 215–230 (2019)
95. Michalski, G., Kolanowski, M., Riha, K.: Oxygen and nitrogen isotopic composition of nitrate in commercial fertilizers, nitric acid, and reagent salts. Isotopes Environ. Health Stud. pp. 1−10 (2015)
96. Dai, J., Qin, S., Tao, S., Zhu, G., Mi, J.: Development trends of natural gas industry and the significant progress on natural gas geological theories in China. Nat. Gas Geosci. **16**(2), 127–142 (2005)
97. VIPER Mission Overview. https://www.nasa.gov/viper/overview . Last accessed 9 Nov 2021
98. Robinson, K., Barnes, J., Nagashima, K., Thomen, A., Franchi, I., Huss, G., Anand, M., Taylor, G.: Water in evolved lunar rocks: evidence for multiple reservoirs. Geochim. Cosmochim. Acta **188**, 244−260 (2016)

99. Saal, A., Hauri, E., Van Orman, J., Rutherford, M.: Hydrogen isotopes in lunar volcanic glasses and melt inclusions reveal a carbonaceous chondrite heritage. Science **340**, 1317–1320 (2013)
100. Füri, E., Deloule, E., Trappitsch, R.: The production rate of cosmogenic deuterium at the Moon's surface. Earth Planet. Sci. Lett. **474**, 76–82 (2017)
101. Piani, L., Marrocchi, Y.: Hydrogen isotopic composition of water in CV-type carbonaceous chondrites. Earth Planet. Sci. Lett. **504**, 64–71 (2018)
102. Fujiya, W., Sugiura, N., Marrocchi, Y., Takahata, N., Hoppe, P., Shirai, K., Sano, Y., Hiyagon, H.: Comprehensive study of carbon and oxygen isotopic compositions, trace element abundances, and cathodoluminescence intensities of calcite in the Murchison CM chondrite. Geochim. Cosmochim. Acta **161**, 101−117 (2015)
103. Fujiya, W., Fukuda, K., Koike, M., Ishida, A., Sano, Y.: Oxygen and carbon isotopic ratios of carbonates in the Nogoya CM chondrite. In: 47th Lunar and Planetary Science Conference. LPI Contribution No. 1903:1712 (2016)
104. Fujiya, W., Hoppe, P., Fukuda, K., Lindgren, P., Lee, M., Koike, M., Shirai, K., Sano, Y.: Carbon isotopic ratios of carbonate in CM chondrites and the Tagish Lake meteorite. In: 49th Lunar and Planetary Science Conference. LPI Contribution No. 2083, abstract #1377 (2018)
105. Lyons, J., Gharib-Nezhad, E., Ayres, T.: A light carbon isotope composition for the Sun. Nat. Commun. **9**, 908 (2018)
106. Marty, B.: The origins and concentrations of water, carbon, nitrogen and noble gases on Earth. Earth Planet. Sci. Lett. **313–314**, 56–66 (2012)
107. Pieters, C., Goswami, J., Clark, R., Annadurai, M., Boardman, J., Buratti, B., Combe, J., Dyar, M., Green, R., Head, J., Hibbitts, C., Hicks, M., Isaacson, P., Klima, R., Kramer, G., Kumar, S., Livo, E., Lundeen, S., Malaret, E., McCord, T., Mustard, J., Nettles, J., Petro, N., Runyon, C., Staid, M., Sunshine, J., Taylor, L., Tompkins, S., Varanasi, P.: Character and spatial distribution of OH/H_2O on the surface of the Moon seen by M3 on Chandrayaan-1. Science **326**, 568–572 (2009)

Reduced Iron in the Regolith of the Moon: Review

E. M. Sorokin

1 Introduction

The problem of space weathering of airless bodies of the solar system, and this is action of the solar wind, cosmic rays and micrometeoroid bombardment, is an actual problem of remote sensing, surface layer formation, its history, and in the future for the Moon—using the surface to build a lunar base and extract resources.

Under the influence of the above-described factors there are changes in the surface layer of the airless body both physically (changes in grain size, optical characteristics, etc.) and in chemical and mineral composition. In order to characterize these changes, the notions of maturity and exposure age were introduced. Soil maturity is a term used to estimate the degree of accumulation of space weathering products in a given area of the lunar regolith [e.g., 1, 2]. Exposure age is a quantitative measure of how long a rock or soil grain has been exposed to the space environment. This method is based on accurate laboratory measurements of accumulated weathering products, such as noble gases from the solar wind or tracks from cosmic rays, and npFe0 content [e.g., 3, 4].

Space weathering processes can be roughly divided into two categories—(1) sporadic bombardment by micrometeoroids and (2) irradiation by electromagnetic radiation, atomic particles of solar wind and galactic cosmic rays (Fig. 1). It should be noted that the effect of different space weathering processes may depend on the position of the body in the Solar System (velocity and flux of meteoroids, radiation environment, temperature), the type of planetary surface (composition, dimensions, surface texture) and the duration of the influence on the surface. One of the main manifestations of space weathering in regolith grains is the appearance of metallic (reduced) iron spherules, further $npFe^0$.

One of the questions, raised an urgency of studying of space weathering and $npFe^0$, became a question about correlation of remote sensing data of S-type asteroids (reflection spectra), which make huge class of these celestial bodies, and spectrums of reflection from ordinary chondrites, which make the most part of meteorites falling on the Earth [6–8]. In general, the composition determined by remote sensing (low calcium pyroxene and olivine) and the measured composition of chondrites coincide, but in details the reflection spectra of these objects differ significantly. Reflection spectra obtained from the asteroids show reduced albedo, shift of the general continuum to the near-IR region in comparison with chondrites. The question arises what caused such difference—different genesis and/or formation history of S-type asteroids and chondrites or transformation of the surface of these asteroids by space weathering. In recent years such a question has become solvable, not least due to the samples delivered from the Itokawa asteroid by the Hayabusa mission, in favour of space weathering, i.e. that it is the factors of space weathering and $npFe^0$ formation that lead to changes in the surface layer of these bodies, which in turn lead to changes in the reflected spectra.

In order to study the type, nature, intensity, duration of the impact of space factors on the surface of airless bodies, various methods and techniques of experimental modeling of these processes are used, while taking into account the hypothesis adopted by researchers of the main mechanism of surface transformation. Such methods and techniques include: irradiation by solar wind high-energy ions of the solar wind (H+, He+, Ar, etc.), irradiation by pulsed lasers with different power and pulse duration, artificial growing of reduced iron nanospheres, as well as thermodynamic, spectroscopic, molecular dynamic calculations and others.

E. M. Sorokin (✉)
Vernadsky Institute of Geochemistry and Analytical Chemistry, Russian Academy of Sciences, 19 Kosygin St., Moscow, 119991, Russia
e-mail: egorgeohim@ya.ru

V. P. Kolotov and N. S. Bezaeva (eds.), *Advances in Geochemistry, Analytical Chemistry, and Planetary Sciences*,
https://doi.org/10.1007/978-3-031-09883-3_24

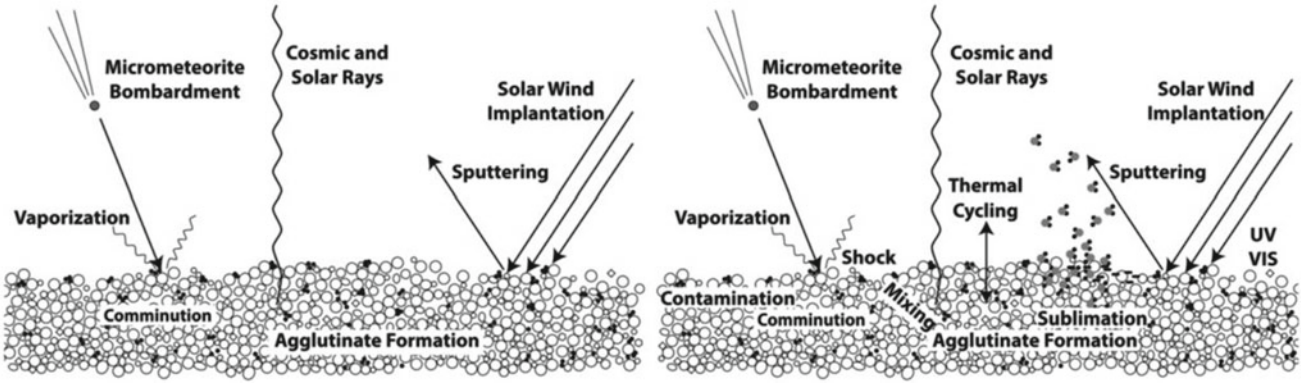

Fig. 1 Complex of space weathering processes on airless bodies. On the left—a general view of the processes for airless bodies, on the right—the dominant processes that play a role on the lunar surface, at a distance of 1 a.u. [5]

2 Problems of Detection, Research and Versions of the Mechanism of npFe^0 Formation

Almost immediately after the delivery of the first soil samples as part of the Apollo 11 mission, it was noted that the regolith and the grinded rocks from the same sampling site differed significantly from each other in their reflectance spectra. The lunar soil had a lower albedo (especially in the visible region), and the characteristic absorption bands (which are responsible for certain minerals, or more precisely the bonds in them) were weakly manifested [9, 10] (Fig. 2).

The results of studying the delivered samples of lunar soil by magnetic methods and Mössbauer spectroscopy showed the presence of metallic iron with content of about 0.5–1 wt %, which significantly exceeds the content of such iron in igneous rocks of the Moon (in 5–10 times). It was suggested that the source of the ferrimagnetic signal and, correspondingly, metallic iron are located in the glassy part of the regolith grains; the sizes of such particles were estimated to be about 40–170 angstroms, that is, they were superparamagnetic in nature [12–16]. This was confirmed using the electron spin resonance (ESR) method, which, also found ferromagnetic centers consisting of metallic iron [17]. The ferromagnetic resonance centers were found to have a roughly spherical shape, cubic syngony, and a diameter of approximately less than 1 μm. The authors estimated the content of such iron to be about 0.5 wt% [17].

In the study of glass agglutinates, which are the fused particles of the lunar soil as a result of micrometeorite

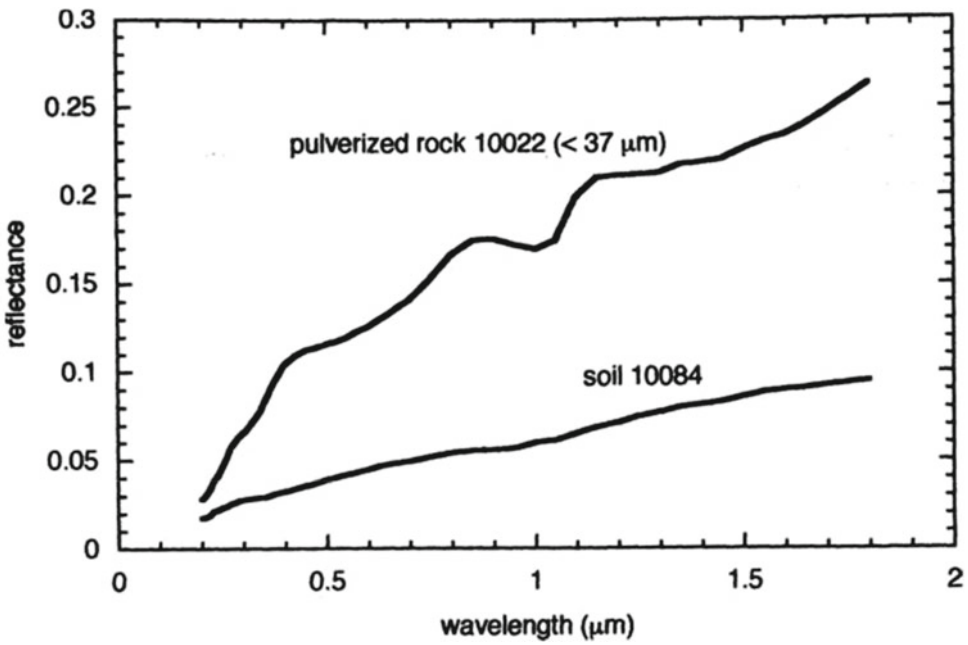

Fig. 2 Bidirectional reflectance spectra (i = e = 30°, g = 60°, where i is incident angle, e is viewing angle, g is phase angle) versus MgO standard, lunar soil sample 10,084 and crushed lunar rock 10,022 crushed to < 37 μm [11]

bombardment, was first used transmission electron microscope. Using this method, spherical particles of metallic alpha-iron, which were relatively uniformly distributed in the thickness of the glass, were identified [18]. These authors estimated the size distribution of the detected spherules, consisting in the interval from the first nanometers to a couple of tens of nanometers (Fig. 3).

To explain the origin of such nanospherules, it was hypothesized that the formation of $npFe^0$ occurs as a result of micrometeoroid bombardment of the upper regolith layer saturated with solar wind gases [18].

Schematically the process of agglutinates formation is shown in Fig. 4. It is noted that due to the high energy associated with the metal-silicate interface, the distribution of fine-grained metallic Fe in the glass, as shown in Fig. 4, is very unstable thermodynamically, and its preservation in the samples indicates that the metal production process was accompanied by extremely rapid quenching [18].

Thus, the main source of $npFe^0$ accumulation is agglutinate glass and/or regolith grains saturated by solar wind gases [18]. Minerals and/or mineral aggregates are intensely bombarded by high-energy solar wind ions, which accumulate in the surface layer of regolith grains. During the subsequent shock event and heating (about 1200 °C), the implanted components can segregate into nano-sized bubbles, which form voids in the agglutinate glass as it cools. Such nanoscale voids are widespread in agglutinates [18] and references therein]. Then there are two pathways for the formation of metallic iron from the ferrous state and the formation of spherules. Hydrogen, possessing small dimensions, can easily migrate from voids to the daytime surface of the Moon during diurnal temperature fluctuations, at such migration there is a probability of reaction of reduction of iron oxide to metallic state: $FeO + 2H \rightarrow Fe^0 + H_2O$. The reduced iron may remain in the form of isolated atoms or in the form of small atomic clusters. These clusters can behave superparamagnetically and give a characteristic pattern when studied by ESR. The second process involves exposure to a micrometeorite, which heats the target material and results in the same type of reduction, but with greater intensity, where the protons and/or carbon ions released by this exposure react with divalent iron oxide. Quite large (up to 20 nm) metallic iron spherules can be formed during this type of process [18].

However, there are objections against such mechanism. For example, solar wind ions implant into regolith grains only by hundreds of angstroms, besides, as hydrogen ions are rather small, they easily diffuse from these grains even at small temperature fluctuations, thus, not having time to reduce the observed amount of iron [19]. In addition, the study of agglutinate grains by Fourier spectroscopy showed that they did not contain H_2O, which would be sufficient to explain this mechanism of iron reduction [20]. The subsequent experimental data have shown that reduction process can proceed without participation of implanted gases of solar wind.

Other versions of the origin of $npFe^0$ have been proposed, which included subsolidus reduction in hot ejecta blankets [21] and as a result of disproportionation of Fe^{2+} to Fe^0 and Fe^{3+} [22]. In the first case, giant collision, a large amount of

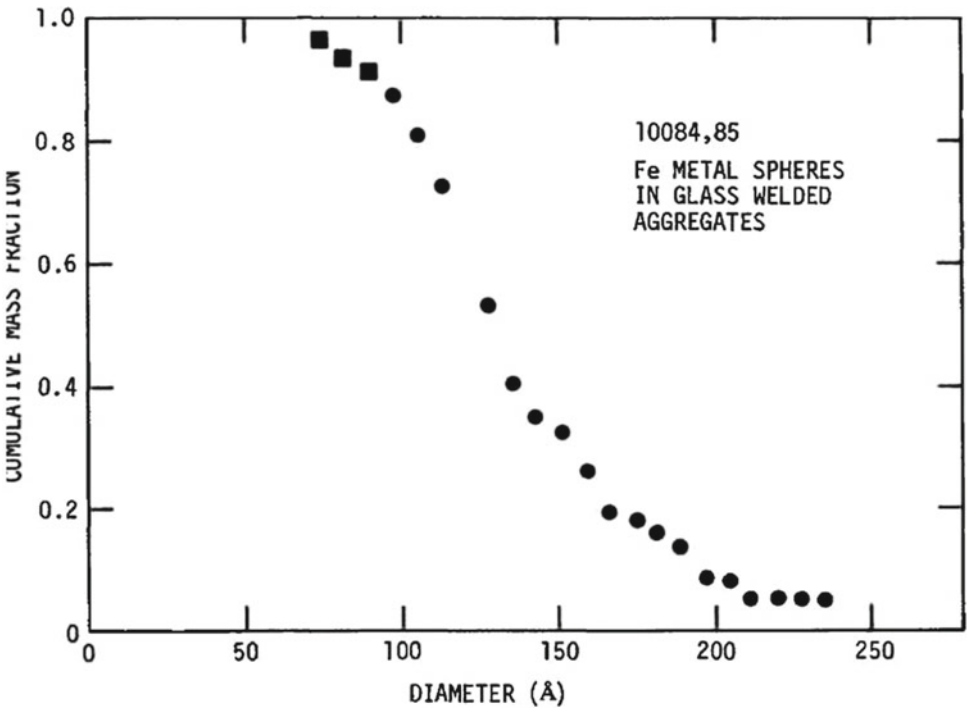

Fig. 3 Size distribution of metallic Fe spheres in quenched glass agglutinate grains (size 45–75 μm) from the fine fraction of samples 10,084, 85. The square points have sizes less than 40 Å, that is small enough to estimate them with a sufficient degree of confidence [18]

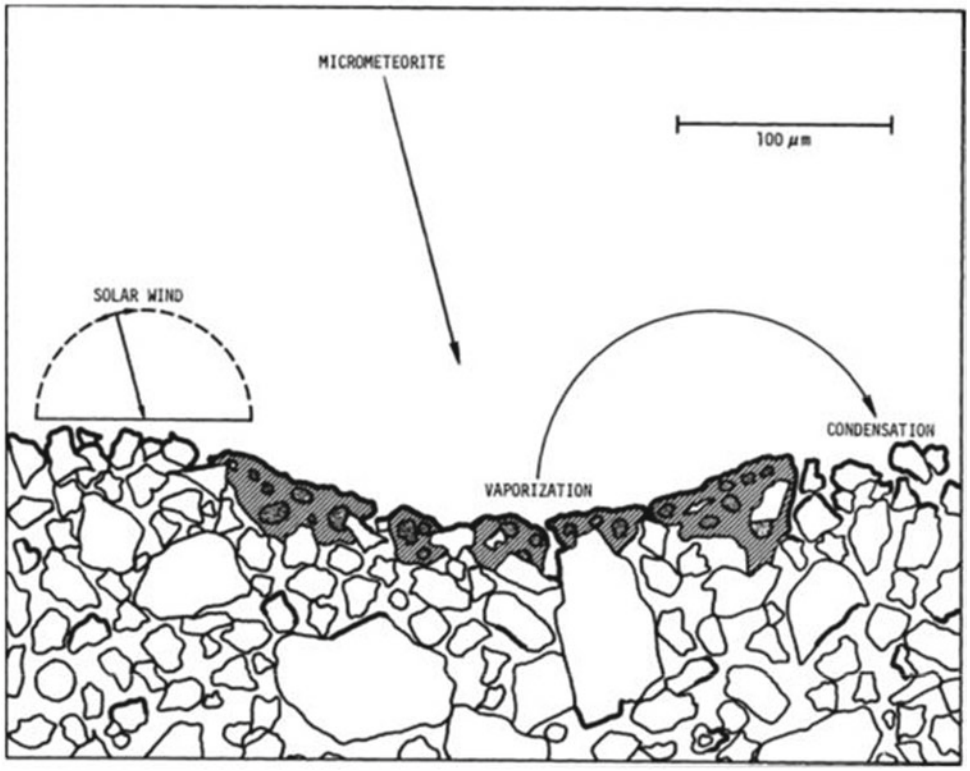

Fig. 4 Schematic section of lunar regolith illustrating the formation of sintered glass aggregates (shaded area) under the influence of micrometeorites [18]

matter is heated, with all this matter in a reducing environment, e.g., saturated with H^+ ions. This version meets with two contradictions—in such large volume, there could be simply not enough reducing agents for occurrence of observable metallic iron. The second—is that it is necessary not only to reduce iron ions to atomic state, but also to collect them in a spherule, which the proposed hypothesis does not explain. The second variant also is rejected because, disproportionation on Fe^0 and Fe^{3+} requires slow cooling and separation of ions with different valence states, while the agglutinate glass hardens very quickly. Besides the Fe^{3+} content in regolith of the Moon is very small and cannot correspond to this mechanism [18].

During the study of $npFe^0$ and analysis of ESR spectra, it was noticed that the content of metallic iron nanospherules increased with increasing exposure age estimated from particle tracks and the degree of accumulation of other space weathering products. A simple, nondestructive method for determining the exposure age by measuring the ratio of the paramagnetic resonance (ESR) intensity to the total iron content, i.e., the Is/FeO index, was proposed [23–25].

The study of the lunar soil in the impact experiment showed that the remanent magnetization and other magnetic characteristics increase with an increase in the impact load, which was associated with an increase in the amount of reduced iron ($npFe^0$), especially at severe shock loads (250 kbar) [26]. The authors assumed that impact reduction of divalent iron, which is a part of lunar regolith minerals, plays the main role in formation of such iron. Later on, this hypothesis was disproved by subsequent experiments; the acquired magnetization was not necessarily explained by iron reduction in shock [11, 27].

In [19] it was noted that the products of evaporation and condensation as a consequence of micrometeoroid bombardment or sputtering process (atomic sputtering by high-energy solar wind particles) play a significant role in changing the optical, physical and chemical characteristics of the lunar regolith. Rims and coatings formed by deposition of impact-generated vapor have a large, non-selective optical absorption capacity and contain a large number of submicroscopic superparamagnetic grains of metallic Fe, which give the ESR resonance characteristic of the lunar soil noted above [19].

It is necessary to emphasize that in the sputtering process the oxides included in the grains of lunar regolith decompose into elements and are transferred in the form of separate neutral atoms to the neighboring grains. Newly arrived atoms do not bind immediately directly to the growing film on the substrate, but depending on their chemical and volatile properties, have a certain probability of deposition and re-evaporation. Therefore, a lack of readily volatile oxygen is found, which allows some atoms, such as iron, to remain in a non-oxidized, metallic state. During thermal evaporation caused by micrometeoroid bombardment, the mechanism is different, but the result is the same, i.e., the precipitation of reduced iron atoms from impact-generated

vapor. In this case, coalescence of atoms or atomic clusters of reduced iron into nanospherules occurs [19]. In the case of micrometeoroid bombardment, different oxides dissociate differently upon heating, (the most common vapor types over evaporating lunar rocks according to [28] are Fe, SiO, TiO_2, TiO, Ca, K, Al, Mg, Na, O_2 and O) [see also 29–31] oxygen, as the most volatile, does not give any oxidizing effect, leaving iron in metallic state [19]. Thus, this paper provides the first suggestion on the formation of $npFe^0$ not as a result of interaction of solar wind ions but as a result of dissociation of iron oxides in the impact-generated vapor, deposition of such vapor, coalescence of iron nanospherules in films on regolith particles. Such mechanism assumes their formation in regolith of the Moon as result of micrometeoroid bombardment and/or spattering process [19]. In addition, estimates of the influence on the reflection spectrum of the described effects in the experiments coincide with the observed effects when comparing the spectra of the lunar soil and grinded rock of the same composition (see Fig. 2).

The same conclusions follow from series of experiments on irradiation by solar wind ions of other authors [32, 33]. Here the terrestrial samples of basaltic glass, olivine, pyroxene and plagioclase were exposed to irradiation. Irradiation resulted in general darkening of the reflection spectrum, subdued of characteristic absorption bands, and shift of the spectrum to the near-IR region (Fig. 5). In addition, a direct correlation between these spectral effects and the number and size of iron nanoparticles was detected. Such particles were detected when studied with a scanning electron microscope (Fig. 6).

Thus, this series of experiments puts forward sputtering as an important process in the formation of $npFe^0$, and, as a consequence, in the changes in the optical characteristics of the lunar soil.

The size and number of iron nanospherules play a role in the degree of manifestation of these effects and their nature. For example, it is noted that large spherules larger than 40 nm affect the overall darkening of the spectrum, not significantly affecting the shape of the spectrum, while spherules smaller than 10 nm affect only the reddening (i.e., a shift of intensity to the long-wave region of the spectrum). Intermediate sizes of nanospheres affect the spectrum differently, depending on their concentration. Results of the experimental growing nanoparticles indicate that the lunar soil continuum is best modeled by $npFe^0$ particles with bulk properties in the $\sim$ 15 to 25 nm size range [34–37].

With the accumulation of observational data on space bodies, the problem of space weathering has expanded from Mercury to the asteroid belt. At the same time, the expression of space weathering effects may depend on the location of the body in the Solar System, its size and surface composition, in particular, as a function of the size and amount of $npFe^0$ [5, 8, 11, 37–39]

Continuing to study the role of amorphous rims in the change of lunar soil optical characteristics, researchers applied scanning and transmission electron microscopy [35, 36, 40, 41]. Initially, it was supposed that such amorphous rims on regolith particles were formed by solar wind ions irradiation due to which they lost their crystalline structure (amorphized), i.e., in-situ formation (Fig. 7). However, studies of the composition of such rims showed that they differ from the parent mineral in chemical composition, and are composed of the deposition of impact-generated vapor after micrometeoroid bombardment, and the effect of amorphization from the solar wind during their formation was insignificant [40].

Here the depletion by refractory elements (Al, Ca, Ti) and enrichment by Si, Fe, S and alkalis is clearly traced, as well as the zoning, which can correspond to several episodes of vapor deposition on the regolith grains [40, 41]. Such enrichment and depletion series, correspond, for example, to the fugacity series of Al_2O_3, CaO, TiO_2, MgO, SiO_2, FeO, Na_2O, K_2O observed in experiments on micrometeorite bombardment simulation with laser [43]. Here the oxygen content was also measured directly. This made it possible to detect the depletion of Ca and Al in absolute values [41, 42].

Researchers, in an attempt to assess the role of impact-generated vapor (and the sputtering process) in the formation of such rims, have divided them into four groups: (1) amorphous, (2) inclusion-rich, (3) multiple rims, and (4) vesicular rims. The first type is characterized by the radiation component of weathering, whereas in the second type the deposition of impact-formed vapor plays a significant role. The third, multilayered type was probably formed due to the layering of impact vapor deposits on the radiation-amorphoused layer. The last type, apparently, was formed under the influence of small heating (not reaching melting) of grains saturated with solar wind gases, which were collected in vesicles [41, 42].

High content of iron nanospherules was observed in such rims; it should be emphasized that iron-containing rims were also found on the grains of minerals almost not containing iron in their structure, for example, on anorthite (Fig. 8) [35].

These studies have shown with certainty that most of the reduced iron ($npFe^0$) may be contained not so much in the agglutinate glass as in the amorphous rims produced by the deposition of impact-formed vapor and the spattering process [11, 20, 35]. The content of iron nanospherules in the agglutinates glass is explained by remelting of the rims and their inclusion in the glass as a result of micrometeorite impact, i.e., as a secondary process. Experiments and calculations on irradiation by high-energy particles also put first place the hypothesis on deposition of impact-generated vapor during sputtering process [33, 44] (see paragraph about experimental studies). As will be described below,

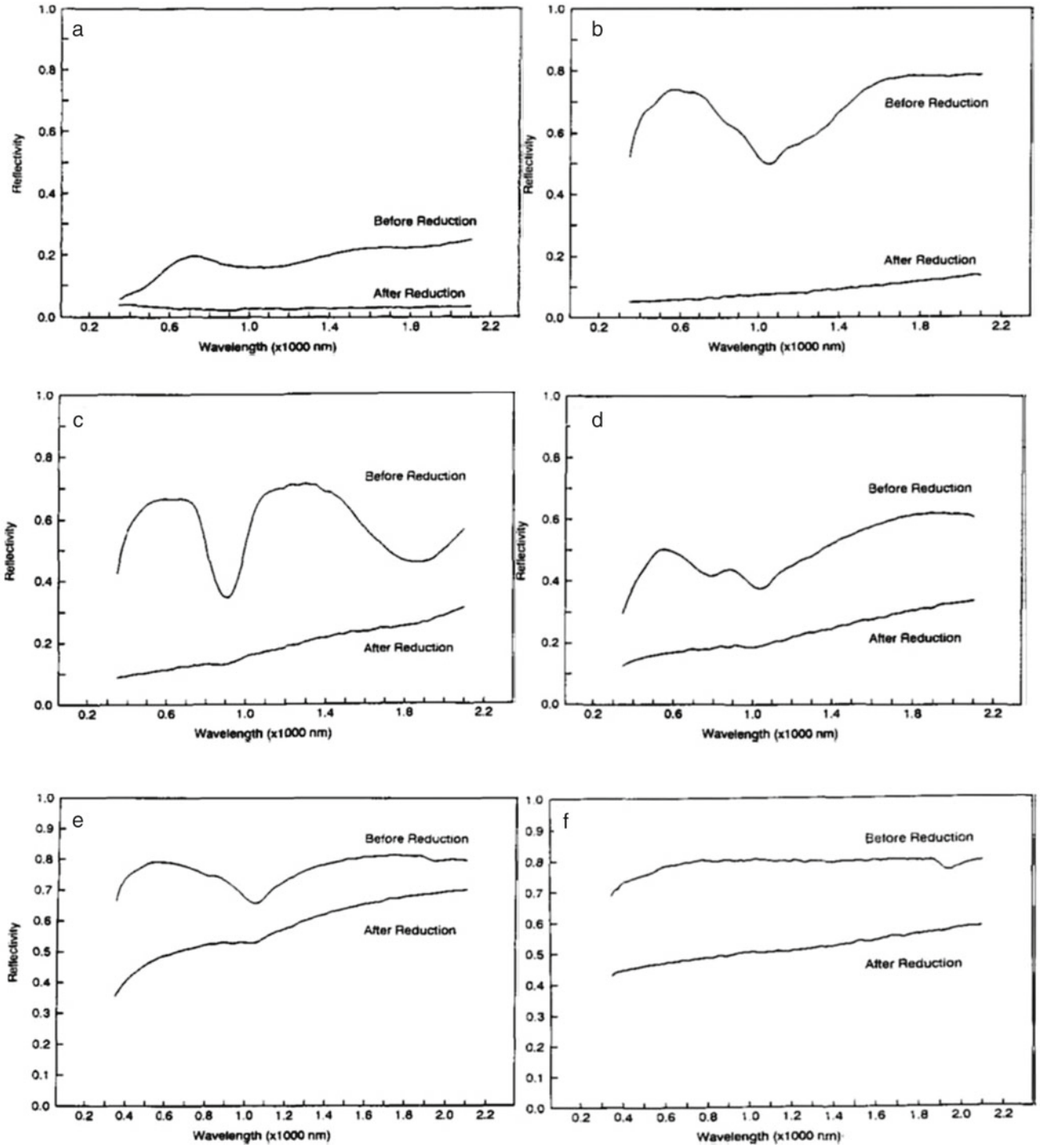

Fig. 5 VIS/NIR spectra before and after irradiation: **a** Synthetic basalt glass, **b** olivine, **c** enstatite, **d** augite, **e** diopside, **f** plagioclase [32]

according to the experimental studies of the authors of this paper, a third mechanism is also possible: the formation of nanospherules by in-situ reduction in the melt without the participation of a reducing agent, the sputtering process, and the deposition of impact-formed vapor.

The question arises, which of the two processes—irradiation by solar wind ions and Fe^{2+} reduction by in-situ or deposition of impact-generated vapor after micrometeoroidal bombardment and/or sputtering (i.e., allochthonous origin)—is the main in formation of metallic iron spherules on

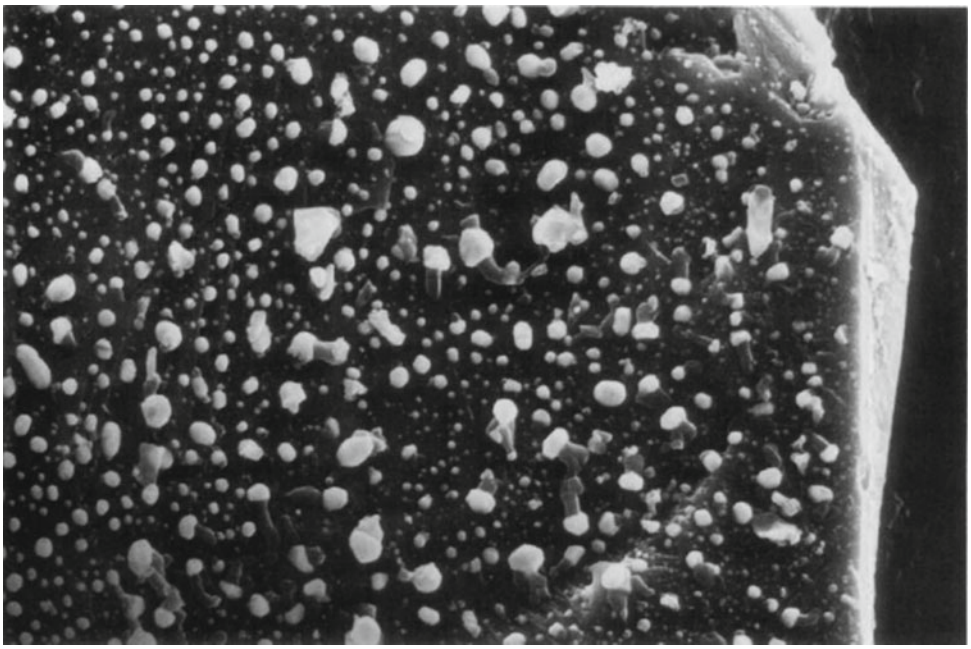

Fig. 6 Scanning electron microscope photograph of metallic droplets on the surface of an irradiated olivine sample. Field of view is 50 μm [32]

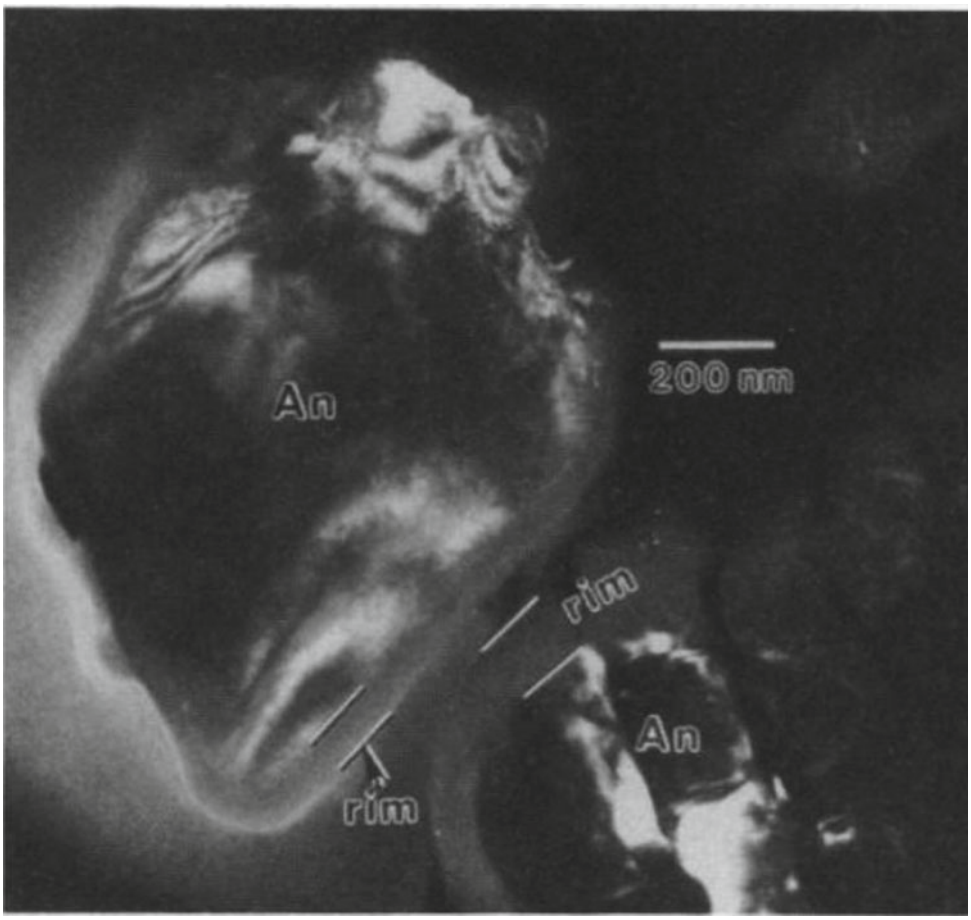

Fig. 7 The image obtained by transmission electron microscopy of grains of anorthite (An) with amorphous rims from the lunar soil sample 61,181 [40]

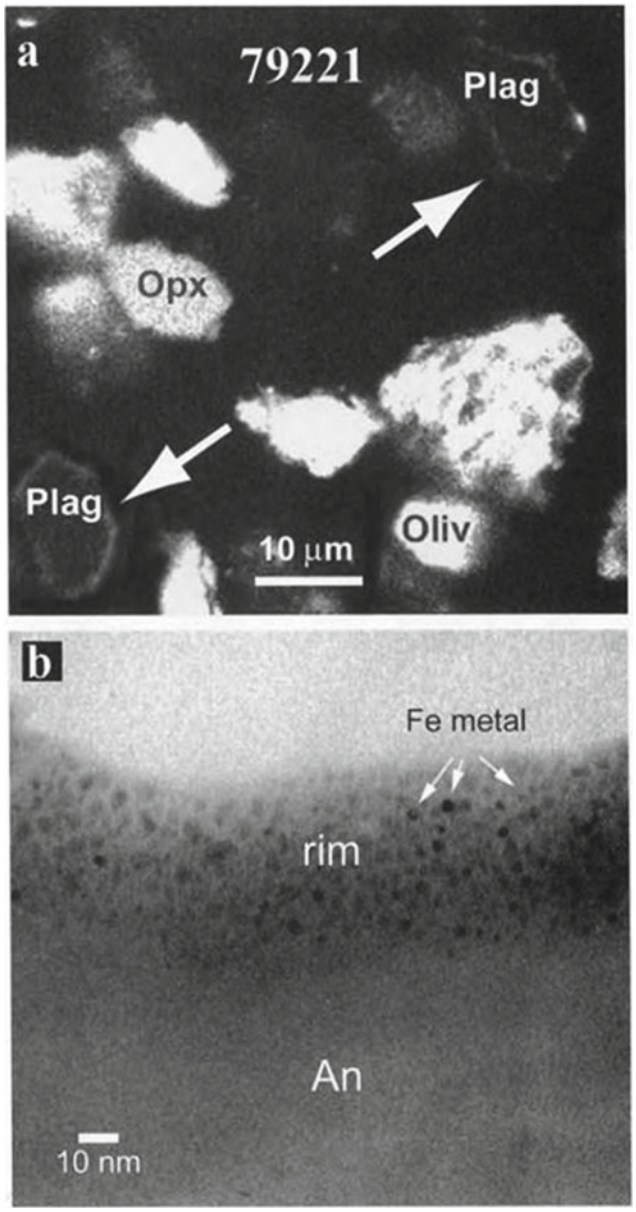

Fig. 8 **a** Digital X-ray FeKα image of diverse grains from the 10–20 μm soil fraction of sample 79,221. Here the iron-bearing minerals are bright. The arrows show the rims with high iron content. **b** Transmission electron microscope images of grains of anorthosite (An) from the soil sample 79,221. Dark points are spherules of metallic Fe ($npFe^0$), marked by white arrows [35]

airless bodies? Great importance in the choice between the two hypotheses of the origin of $npFe^0$, could be the study of the isotopic composition of nanophase iron. In the first scenario, i.e., the irradiation of the surface of regolith grains by solar wind ions should not result in the fractionation of iron isotopes, since the reduction of in-situ occurs. The second scenario, i.e., deposition of impact-generated vapor, implies a kinetic isotope effect during dispersion after impact (or sputtering), the lighter isotope flies away and the deposited part is enriched in heavy isotope, in comparison with the parent rocks and regolith.

Initially, researchers [45] measured $^{56}Fe/^{54}Fe$ isotopic ratios (as $\delta^{56}Fe$) in the thin fraction of the lunar soil sample and found a fractionation effect of up to 0.3 per mille in the mature soil relative to parent rocks (0.03 ± 0.05‰). At the same time, it was suggested that this may be related to $npFe^0$, since the increase in $\delta^{56}Fe$, is directly proportional to the increase in Is\FeO, the maturity index. Thus, confirming the hypothesis of impact-generated vapor deposition (allochthonous $npFe^0$ formation) [45]. In another study [46], an isotopic fractionation effect was also found in the thin fraction of different lunar soil samples—$0.11‰ < \delta^{56}Fe < 0.51‰$, $2.6‰ < \delta^{65}Cu < 4.5‰$, and $2.2‰ < \delta^{66}Zn < 6.4‰$. On the other hand, here the isotopic ratios directly in amorphous rims and iron nanospherules were not investigated, which significantly complicated the interpretation, in particular, the disperse from sample to sample appeared due to inclusion of non-fractionated iron of total sample mass into the calculation (i.e., giving underestimated values) [46].

More detailed studies were carried out in [47]. These authors measured the isotope ratio directly in the iron-bearing rims. In this study plagioclase grains of a very mature sample from the regolith of Apollo 16 collections were analyzed. Lunar grains were specially cleaned from all impurities and then were etched layer by layer with weak acid. The etching step was known (0.1 μm) and each time the isotope ratio in the resulting solution was measured. The isotope ratio was measured using a multicollector mass spectrometer and a standard solution for iron (IRMM-014). The outer layers of the grain showed a high δ56Fe ratio (0.39–0.71‰), the inner layers (after 20 h of etching) showed reduced fractionation ($\delta^{56}Fe = 0.22–0.36‰$) to typical values in plagioclase. Thus, this index was higher in the condensed band. Iron isotope ratio $\delta^{56}Fe$ for regolith is on average much less than obtained in experiment (0.3‰), and for parental magmatic rocks this index is even lower (0.1–0.2‰) (Fig. 9).

Here, it is also noted that this iron is not meteoritic or solar-wind iron. Thus, in this case the rims with nanophase iron were formed as a result of micrometeorite bombardment and deposition of impact vapor and/or deposition after the spattering effect, i.e. in this case the second hypothesis is most likely to explain the formation of iron nanospheres [47].

In addition, the authors cited temperatures at which evaporation and fractionation could occur (Fig. 10)—from 2750 to 3000 K, which confirm the previously obtained in the experiment and calculated values [e.g., 49].

On the other hand, the question which particular mechanism from the second hypothesis (allochthonous origin) dominates on the lunar surface—sputtering or micrometeoroid bombardment, remains open.

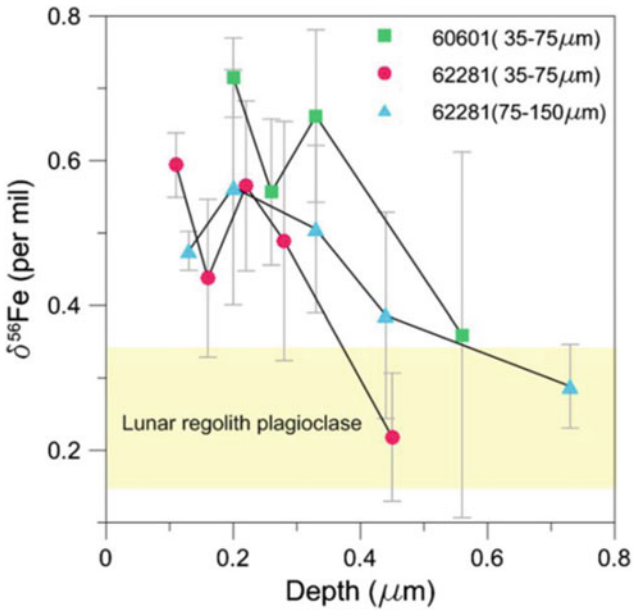

Fig. 9 Iron isotope ratios expressed as delta value (δ^{56}Fe) when compared to IRMM-014 (standard) versus etch depth. The etch depth values are taken from [48] derived from Ca concentrations. The yellow shaded area represents the plagioclase isotopic composition taken from lunar eruptive rocks [47]

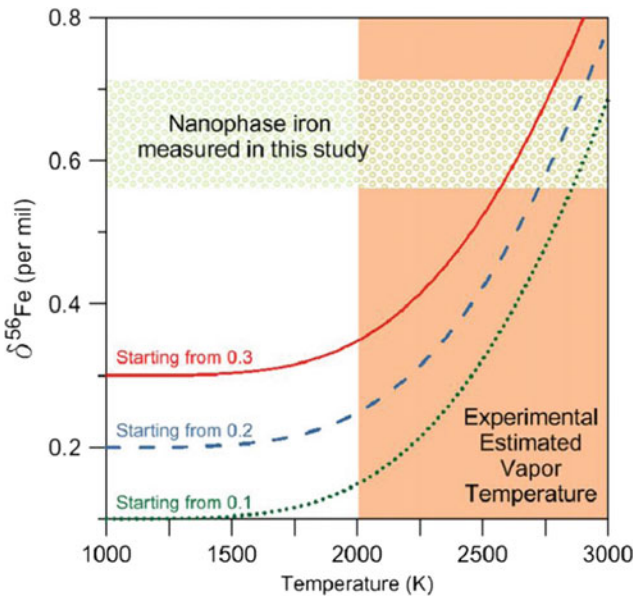

Fig. 10 Isotopic ratios (δ^{56}Fe) of nanophase Fe measured in this study can be explained by fractionation during the preferred thermal yield, starting from a typical lunar regolith value (red solid line, δ^{56}Fe = 0.3‰), a typical high-Ti value of lunar basalt (blue dashed line, δ^{56}Fe = 0.2‰), or a typical low-Ti value of lunar basalt/terrestrial rocks (green dashed line δ^{56}Fe = 0.2‰ = 0.1‰). The experimentally estimated vapor temperature range is between 2000 and 3000 K [see also 47, 50]

The complexity of the question was added by study of grains delivered from asteroid Itokawa by Hayabusa mission [50]. At studying of some of these grains under a layer of the deposited impact-generated vapor, the layer showing signs of partial amorphization, formed, obviously, by irradiation by high-energy ions has been revealed. In both layers, metallic iron spherules were found [50]. Thus, it was shown that both processes play an important role in the formation of $npFe^0$.

When studying the effect of $npFe^0$ on the reflection spectra, as well as the physical processes involved in the mechanisms of $npFe^0$ formation, the valence state of iron in the nanoparticle plays an important role. Such studies have been carried out recently due to the improvement of microscopic techniques of matter investigation. In [51] the aberration-corrected transmission electron microscope method and electron energy-loss spectroscopy (EELS) were used and the oxidation state of iron within nanosphere was determined. Samples from the Apollo collection, classified according to different maturity levels (immature, submature and mature), were taken for the study. It turned out that immature grains were saturated with $npFe^0$ spherules in which iron is exclusively represented in the zero-valent state. Both Fe^0 and Fe^{2+}, in different ratios, were found in submature grains. At the same time, in some grains the core consisting of Fe^0 is surrounded by Fe^{2+} border. Mature samples contain variable amounts of Fe^{2+} and Fe^{3+}. This suggests that as the particles mature (increasing degree of maturity), the state of iron in nanospherules turns into more oxidized, and that the particles undergo microchemical and microstructural changes after their formation (Fig. 11).

This microchemical transformation occurs due to the entry, over time, of oxygen from the glass matrix into the nanosphere and the gradual oxidation of iron starting from the surface [51].

3 Laboratory Simulation of Space Weathering.

As noted above, one common method for simulating space weathering and producing metallic iron nanospheres is to irradiate targets with high-energy ions [e.g., 11, 19, 32, 33, 52–56].

Thus, the irradiation of olivine by He^+ ions with energy of 4 keV resulted in significant changes in the reflection spectrum in the near-IR region and the chemical composition of the target surface [53]. The reflection shifted to the near-IR region ("reddening") and the characteristic Fe-3d absorption band decreased significantly. A direct correlation

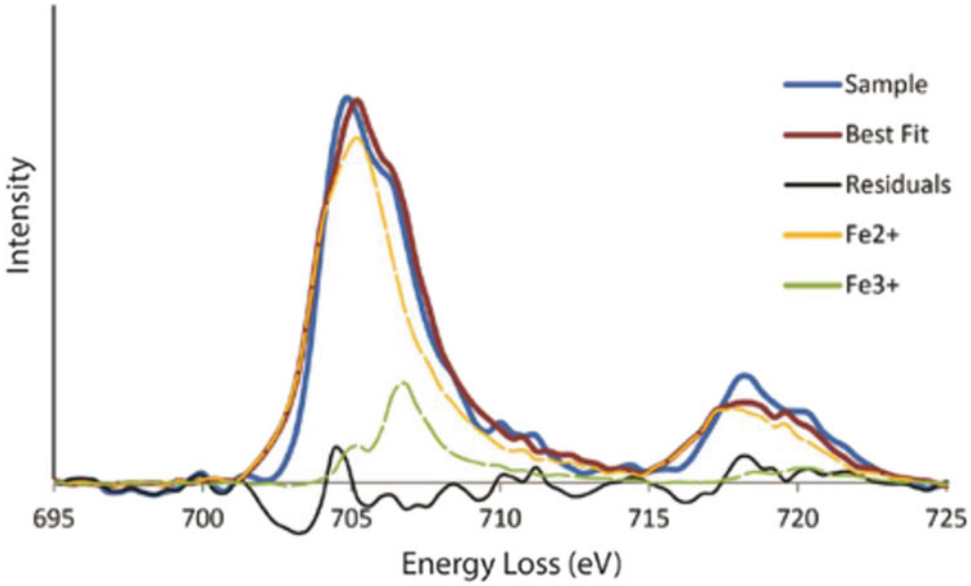

Fig. 11 EELS spectrum of nanoparticles from mature soil sample 79,221 showing Fe L2, 3. Shown are the measured sample (blue), simulated best fit (red), residuals from subtraction (black) and components corresponding to the spectrum, in this case Fe^{2+} (gold) and Fe^{3+} (green). This particle consists of 77% Fe^{2+} and 23% Fe^{3+} [51]

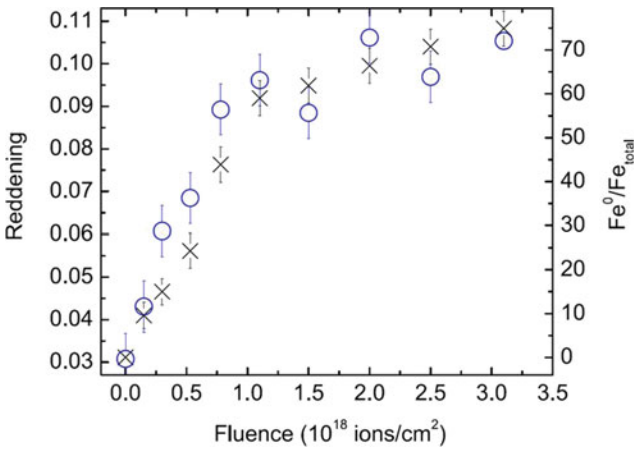

Fig. 12 Comparison of reddening (circles) in the NIR region and metallic iron formation (crosses) measured with XPS on olivine powder as a function of the flux of 4 keV He^+ ions [53]

between the number of metallic iron spherules and the degree of absorption was found (Fig. 12). In the calculations, the authors noted that at a distance of 1 a.u. spectral reddening caused by solar wind ion bombardment occurs twice as fast as comparable reddening caused by micrometeoroid bombardment. On the other hand, if the grain remains on the lunar surface for more than a million years, micrometeoroid bombardment appears to be a more important factor in the reddening of the grain spectrum [53].

In other series of experiments on irradiation by solar wind ions of model samples it has been revealed that during irradiation of olivine, reduction of Fe^{2+} to metallic state is more effective at irradiation by He^+ ions in comparison with H^+ ions [54]. Besides, in the same experiments it has been shown that reduction and formation of spherulas does not require redeposition of iron atoms on neighboring grains, i.e. occurs in-situ.

An important place is occupied by calculations of the effects of space weathering and the factors that caused it [44, 57–59]. For example, during computer simulation of the sputtering process by solar wind protons it was noted that concentration of reduced iron observed in mature regolith can be reached for the time of influence on regolith particles at the present flux in 10^5 years, i.e., the sputtering process may be responsible for the observed Fe^0 concentration in regolith [57]. Here, again, a large role in space weathering, in particular amorphization and reduction of $npFe^0$, is attributed to the process of irradiation by solar wind ions.

For elucidation of detailed mechanisms of space weathering of minerals the method of molecular dynamics was involved [58]. It has allowed describing process of change of crystal structure of olivine and pyroxene at atomic level at irradiation by high-energy particles.

Taking into account the structure of these minerals the difference in mechanisms of diffusion of defects in them has been noted (Kirkendall defects). Diffusion of cations in olivine is easier than in orthopyroxene, such fast diffusion leads to rapid formation of defect clusters (by merging of point defects). On the other hand, diffusion of anions and interstitial defects is faster in orthopyroxene, but here, there is a strong anisotropy of migration of these objects. In particular, entire chains of anion vacancies and interstitial are formed in the direction of the crystallographic axis c. As it was mentioned earlier, when olivine and pyroxene were irradiated by solar wind ions, olivine appeared to be more resistant to amorphization and formation of reducing environment on the surface than pyroxene [60, 61]. On the other hand, the experiments with pulsed lasers showed that the

optical effects are faster and more complete on olivine in comparison with pyroxene [62–64]. Authors of article [58] have made assumption on the basis of the data received in calculations, that speed and depth of space weathering is more in a case with olivine, than with pyroxene, and the above mentioned effect of less reduced environment on orthopyroxene surface is connected that oxygen easier migrates on structure of this mineral to surface, thereby suppressing formation of reducing environment. In olivine cations have easier migration, which form clusters of metallic iron on the surface [58].

To elucidate the role of micrometeoroid bombardment in space weathering, simulation of such impact with a pulsed laser is widely used [63, 65–68]. In the study [65], meteorite powders and terrestrial minerals—olivine and pyroxene—were taken as a target. It was shown that irradiation by laser with wavelength 1.06 μm, duration 0.5–1 μm s and power about 1.2 kW results in reduction of total albedo, subdued of characteristic absorption bands and overall shift of spectrum intensity to NIR region (Fig. 13).

In this study, the presence of $npFe^0$ was not directly determined; therefore, the authors of this paper [65] and other researchers have suggested that these changes in the spectrum are caused by the formation of glass in a long (0.5–1 ms) laser pulse [63]. As will be shown below, when describing the results of the laser experiment of the authors

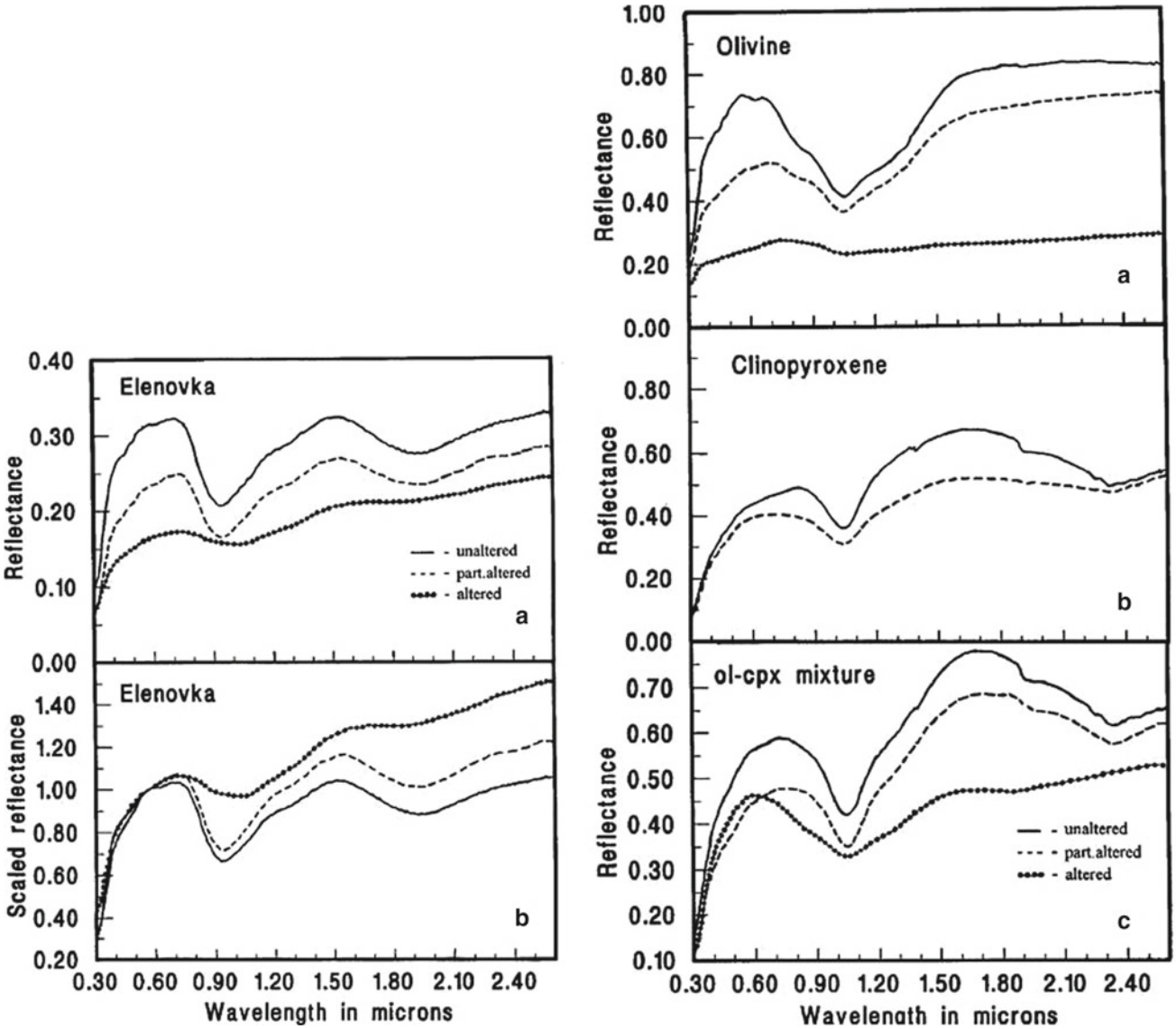

Fig. 13 Left: Absolute reflectance spectra in the visible and near-infrared regions (**a**) and normalized reflectance spectra in the Vis\NIR region (**b**) of powdered samples of the Yelenovka meteorite. The spectra in (**a**) were scaled to 1.0 at 0.56 μm. The line types are the same between (**a**) and (**b**). On the right: absolute reflectance spectra in VI/NIR area of powdered olivine (**a**), pyroxene (**b**) and olivine/clinopyroxene mixture (**c**) [65]

of this article, metallic iron nanospheres are formed at such pulse durations, and, accordingly, they can affect the change in the reflection spectrum.

In another series of experiments on laser irradiation of samples, similar results were obtained when olivine and pyroxene powders were irradiated with nanosecond laser [62–64, 69, 70]. That is, the albedo drop and other above described spectral changes. In addition, here by transmission electron microscopy were investigated thin rims formed by deposition of impact-generated steam on olivine grains (Fig. 14).

These amorphous rims (up to 200 nm wide) contain densely scattered metallic iron spherules, some up to 30 nm in diameter. The authors attribute the above optical effects to the presence of these $npFe^0$ (Fig. 15). Also, the degree of change in the reflection spectrum and increase in the number of $npFe^0$ directly correlated with the number of times the samples were irradiated with a nanosecond laser pulse [70]. On the other hand, after a certain number of irradiation pulses (between 5 and 10 times for olivine) there is a non-proportional change in the reflection spectrum and ESR spectrum, the effect becomes less pronounced (Figs. 15 and 16). The reason of such disproportionality is connected with increase of the size of $npFe^0$ spherules which cease to have superparamagnetic nature [70].

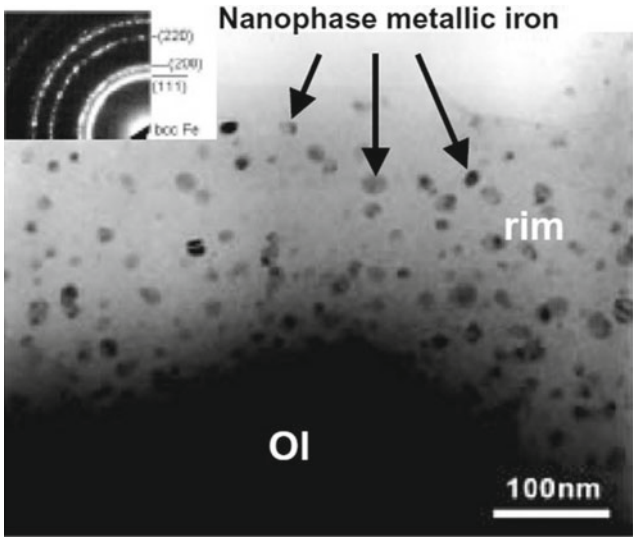

Fig. 14 TEM image of iron nanophase particles with electron diffraction patterns. Metal iron nanophase particles are shown in amorphous rims of fivefold laser-irradiated olivine grains [69]

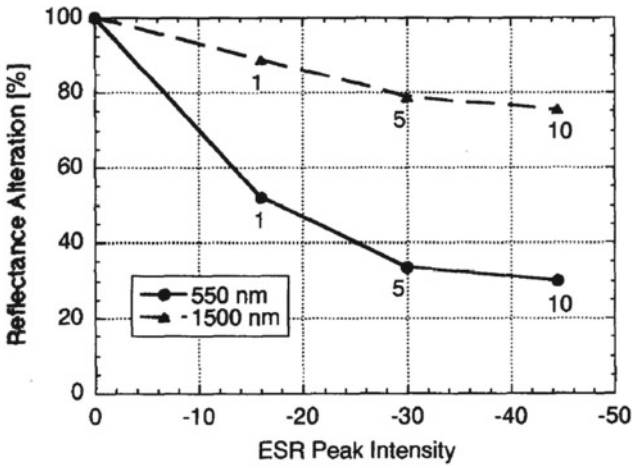

Fig. 16 Relationship between changes in reflection coefficient and ESR peak intensities of each sample. The vertical axis shows the change in reflection coefficient scaled compared to that of the unexposed sample. Data for two wavelengths (550 and 1500 nm) are shown. The numbers next to the dots in the graphs are the number of exposures to a laser pulse of 30 mJ [70]

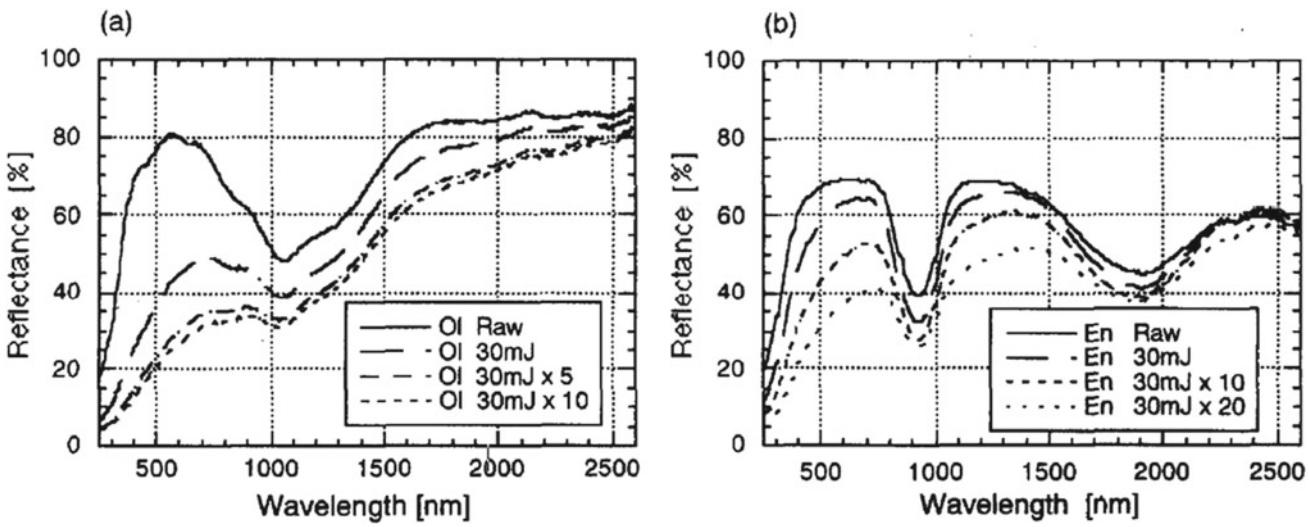

Fig. 15 Reflection spectra (250–2600 nm) from olivine (**a**) and enstatite (**b**) samples before and after pulsed laser irradiation [70]

Authors note [70] that pyroxene in contrast to olivine is less subject to changes at such influence, and as consequence should be less subject to processes of space weathering. This shows the essence the difference of number of times of irradiation of two minerals in experiment, i.e. for achievement of distinct effect on pyroxene, unlike olivine, the greater quantity of laser pulses was required. The data obtained from the transmission electron microscope show that the number and size of $npFe^0$ on the pyroxene grain surface is much lower than on olivine grains [70]. This fact once again draws attention that the effect of space weathering depends on the mineral composition of the surface.

The authors of this paper proposed a third mechanism of reduced iron formation—thermal reduction in the melt. As a result of a series of experiments with a millisecond laser of 10^6–10^7 W/cm^2 (wavelength 1.06 μm), different types of targets—crystalline basalt, basalt glass, olivine and peridotite—were irradiated. Rich placers of metallic iron spherules whose size reached hundreds of nanometers were obtained in all of them, except for crystalline basalt. It should be noted that experimental conditions and textures of the studied samples on a scanning electron microscope showed that the chains and placers of metallic iron nanospheres were formed in the melt thickness, bypassing the evaporation mechanism, besides there were no reducing agents (Fig. 17).

4 Conclusion

The problem of metallic iron nanospheres covers broad fields of research—spectroscopic, diffusive, kinetic and thermodynamic processes. The relevance of the research stems from the interpretation of remote sensing data of airless bodies of the Solar System, as well as, the possibility of using the lunar regolith as a construction material or dedusting the site of future lunar base [71].

The important question of correlation of the reflectance spectra from S-type asteroids and ordinary chondrites is resolved in favor of the processes of space weathering, in particular, the formation of metallic iron nanospherules. Such spherules decrease the total albedo, subdued the characteristic absorption bands, and shift the spectrum intensity to the NIR region. With correction for this effect, the spectra of S-type asteroids and ordinary chondrites coincide.

The same problem arises with comparison of reflected spectra from the lunar soil and grinded rock of the same composition from the same sampling site (see Fig. 2). Here, we also see a diminution in the total albedo and other above described changes in the reflectance spectrum obtained from the lunar soil. Rims containing $npFe^0$ are found on lunar soil particles, and in addition, such formations are found in the glasses of agglutinate particles. The content of such reduced iron in lunar regolith reaches 0.5 wt%, which is rather uncharacteristic for lunar rocks.

Since the first detection by magnetic and ESR methods in the 70s of the twentieth century, two hypotheses of the formation of such iron have appeared until now. The first one is thermal impact (e.g., micrometeorite bombardment) on regolith grains containing implanted solar wind gases, in which the interaction of divalent iron oxide with hydrogen ions and reduction of iron to metallic state, with subsequent coalescence of atoms into nano-spherules occurs. The second hypothesis shows that the presence of reducing agent ions is not necessary. Dissociation occurs in a cloud of impact-generated vapor, followed by precipitation of iron atoms and subsequent coalescence of these atoms to spherules. At the same time, the latter hypothesis breaks down into two competing processes—irradiation by high-energy solar wind particles and reduction in situ, and the second is the deposition of impact vapor and/or sputtering process with iron atoms already reduced on neighboring grains (i.e., the allochthonous hypothesis). Presence of metallic iron nanospherules in agglutinates glass is assigned a secondary role, i.e., rims of the deposited impact vapor on regolith grains were remelted during the subsequent micrometeoroid impact and combined into agglutinates, adding their metallic spherules to glass. At the same time, such nanospherules are often increasing in size. The first hypothesis has recently been considered as a less probable mechanism of formation of such iron, though still remains in demand.

The authors of this paper propose the third mechanism of formation of such iron—thermal reduction of iron and formation of spherules in the melt in-situ, without reducing agents and evaporation-deposition mechanism.

So far, extensive experimental studies have been performed to elucidate the formation mechanisms and properties of $npFe^0$. These include irradiation with different ions, with different energies, and pulsed laser irradiation with different powers, controlled in vitro growth [37, 72], shock experiments, different types of simulations and calculations, and other experiments.

It is shown that the size and amount of $npFe^0$ differently affects the reflection spectrum, so large, more than 40 nm, spherulas darken the albedo, leaving almost intact overall spectrum profile, and spherulas less than 10 nm, shift the intensity of the spectrum in the near-infrared region. In addition, different minerals are exposed to space weathering factors to different degrees. In particular, the formation and growth of $npFe^0$ in different minerals occurs with varying degrees of intensity. Thus, space weathering is differently manifested depending on the surface composition, location in the Solar System (different velocity and density of radiation flux, high-energy particles and micrometeoroids) and duration of exposure to the surface.

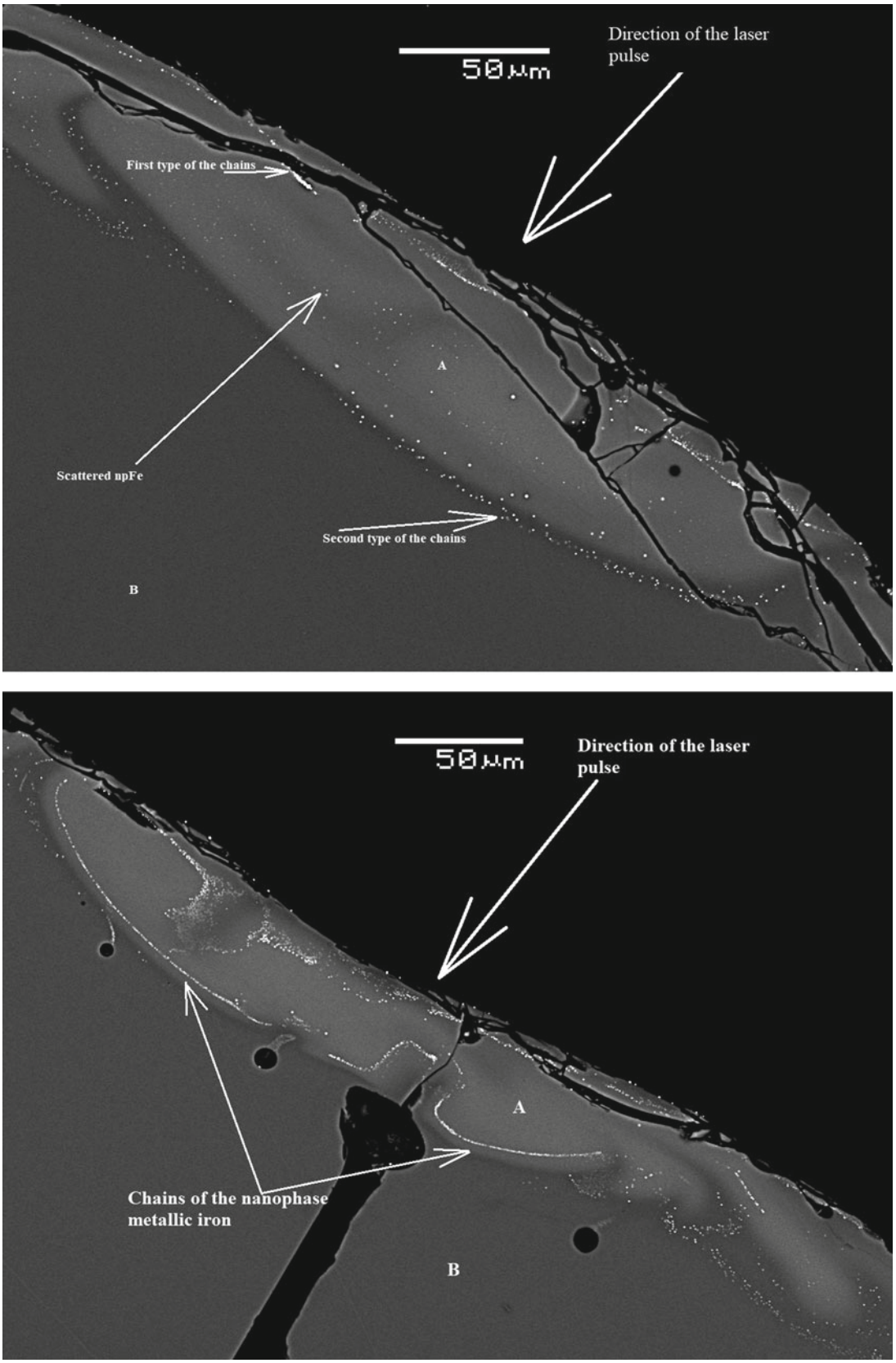

Fig. 17 SEM images of two cross section of basalt glass crater where zones with nanophase iron ($npFe^0$) were found. The diameter of the crater is about 6 mm and the depth is about 0.6 mm. **A**—a light zone depleted in moderate- and light-volatile components, **B**—a zone is of glass of untouched by laser "impact"

References

1. Morris, R.V.: The surface exposure (maturity) of lunar soils: some concepts and Is/FeO compilation. In: Proceedings of the 9th Lunar and Planetary Science Conference, pp. 2287–2297. Pergamon, New York (1978)
2. Lucey, P.G., Blewett, D.T., Taylor, G.J., Hawke, B.R.: Imaging of lunar surface maturity. J. Geophys. Res. **105**, 20377–20386 (2000)
3. Zinner, E.: On the constancy of solar particle fluxes from track, thermoluminescence and solar wind measurements in lunar rocks. In: Pepin, R.O., Eddy, J.A., Merrill, R.B. (eds.) The Ancient Sun: Fossil Record in the Earth, Moon and Meteorites, pp. 201–226. Pergamon, New York (1980)
4. Berger, E.L., Keller, L.P.: Solar flare track exposure ages in regolith particles: a calibration for transmission electron microscope measurements. In: Proceedings of the 46th Lunar and Planetary Science Conference, vol. 1543. The Woodlands, Texas (2015)
5. Pieters, C.M., Noble, S.K.: Space weathering on airless bodies. J. Geophys. Res. Planets **121**, 1865–1884 (2016)
6. Bell, P.M., Mao, H.K., Weeks, R.A.: Optical spectra and electron paramagnetic resonance of lunar and synthetic glasses—a study of the effects of controlled atmosphere, composition, and temperature. In: Proceedings of the 7th Lunar Science Conference, pp. 2543–2559. Pergamon, New York (1976)
7. Chapman, C.R.: S-type asteroids, ordinary chondrites, and space weathering: the evidence from Galileo's fly-bys of Gaspra and Ida. Meteorit. Planet. Sci. **31**(6), 699–725 (1996)
8. Chapman, C.R.: Space weathering of asteroid surfaces. Annu. Rev. Earth Planet. Sci. **32**(1), 539–567 (2004)
9. Adams, J., Jones, R.: Spectral reflectivity of lunar samples. Science **167**, 737–739 (1970)
10. Hapke, B., Cohen, A., Cassidy, W., Wells, E.: Solar radiation effects on the optical properties of Apollo 11 lunar samples. Geochim. Cosmochim. Acta, Suppl, **1**, 2199–2212 (1970)
11. Hapke, B.: Space weathering from Mercury to the asteroid belt. J. Geophys. Res. **106**, 10039–10073 (2001)
12. Nagata, T., Ishikawa, Y., Kinoshita, H., Kono, M., Syono, Y., Fisher, R.M.: Magnetic properties and natural remanent magnetization of lunar materials. Cosmochim. Acta, Suppl. **1**(3), 2325–2340 (In: Proceedings Apollo 11 Lunar Science Conference, Pergamon, New York (1970))
13. Runcorn, S.K., Collinson, D.W., O'Reilly, W., Battey, M.H., Stephenson, A., Jones, J.M., Manson, A.J., Readman, P.W.: Magnetic properties of Apollo 11 lunar samples. Geochim. Cosmochim. Acta, Suppl. **1**(3), 2369–2387 (In: Proceedings Apollo 11 Lunar Science Conference. Pergamon, New York (1970))
14. Housley, R.M., Blander, M., Abdel-Gawad, M., Grant, R.W., Muir, A.H. Jr.: Mossbauer spectroscopy of Apollo 11 samples. Geochim. Cosmochim. Acta, Suppl. **1**(3), 2251–2268 (In: Proceedings Apollo 11 Set Conference. Pergamon, New York (1970)
15. Housley, R.M., Grant, R.W., Muir, A.H. Jr., Blander, M., Abdel-Gawad, M.: Mossbauer studies of Apollo 12 Samples. Geochim. Cosmochim Acta, Suppl. **1**(3), 2125–2136 (In: Proceedings Apollo 11 Lunar Set Conference. Pergamon, New York (1971)
16. Housley, R.M., Grant, R.W., Abdel-Gawad, M.: Study of excess Fe metal in the lunar fines by magnetic separation, Mossbauer spectroscopy, and microscopic examination. Cosmochim. Acta, Suppl. **3**(1), 1065–1076 (In: Proceedings Third Lunar Science Conference. MIT Press (1972))
17. Tsay, F.D., Chan, S.I., Manatt, S.L.: Ferromagnetic resonance of lunar samples. Geochim. Cosmochim. Acta **35**, 865–875 (1971)
18. Housley, R., Grant, R., Paton, N.: Origin and characteristics of excess Fe metal in lunar glass welded aggregates. Geochim. Cosmochim. Acta Suppl., **4**, 2737–2749 (1973)
19. Hapke, B., Cassidy, W., Wells, E.: Effects of vapor-phase deposition processes on the optical, chemical and magnetic properties of the lunar regolith. Moon **13**, 339–354 (1975)
20. Taylor, L.A.: Origin of nanophase Fe^0 in agglutinates: a radical new concept. In: Proceedings The Moon Beyond 2002, vol. #3022. Taos, NM (2002)
21. Pearce, G., Williams, R., McKay, D.: The magnetic properties and morphology of metallic iron produced by subsolidus reduction of synthetic Apollo 11 composition glasses. Earth Planet Sci. Lett. **17**, 95–104 (1972)
22. Rao, K.J., Cooper, A.R.: Optical properties of lunar glass spherules from Apollo 14 fines. Geochim. Cosmochim. Acta, Suppl. **3**(3), 3143–3155 (In: Proceedings Third Lunar Science Conference. MIT Press (1972))
23. Housley, R.M., Cirlin, E.H., Paton, N.E., Goldberg, I.B.: Solar wind and micrometeorite alteration of the lunar regolith. Geochim. Cosmochim. Acta **3**, 2623–2642 (1974) (In: Proceedings of the Fifth Lunar Conference. Suppl. 5)
24. Housley, R.M., Cirlin, E.H., Goldberg, I.B., Crowe, H.: Ferromagnetic resonance as a method of studying the micrometeorite bombardment history of the lunar surface. In: Proceedings 6th Lunar Science Conference, pp. 3173–3186 (1975)
25. Morris, R.V.: Surface exposure indices of lunar soils: a comparative FMR study. Geochim. Cosmochim. Acta Suppl. **7**, 315–335 (1976)
26. Cisowski, C.S., Dunn, J.R., Fuller, M., Rose, M.F., Wasilewski, P. J.: Impact processes and lunar magnetism. Geochim. Cosmochim. Acta. **3**, 2841–2858 (1974) (In: Proceedings of the Fifth Lunar Conference Suppl. 5)
27. Cisowski, C.S., Fuller, M.: The effect of shock on the magnetism of terrestrial rocks. J. Geophys. Res. **83**(B7), 3441–3458 (1978)
28. DeMaria, G., Balducci, G., Guido, M., Piacente, V.: Mass spectrometric investigation of the vaporization process of Apollo 12 lunar samples. Geochim. Cosmochim. Acta Suppl. **2**, 1367–1380 (1971)
29. Yakovlev, O.I., Fainberg, V.S., Kaznacheev, E.A., Pilyugin, N.N., Baulin, N.N., Tikhomirov, S.G.: Experimental study of evaporation at high-speed impact. Geokhimiya **12**, 1698–1707 (1988). [in Russian]
30. Yakovlev, O.I., Lyul, A.Yu., Kolesov, G.M., Kiesl, V., Krazik, S.: Fractionation of elements in shock evaporation: experimental data. Geokhimiya **11**, 1426–1436 (1992) [in Russian]
31. Gerasimov, M.V., Dikov, Yu.P., Yakovlev, O.I.: Cluster type of silicate vaporization: newly obtained experimental data **20**(5), 399–407 (2012)
32. Allen, C.C., Morris, R.V., Lauer, H.V., Jr., McKay, D.S.: Microscopic iron metal on glass and minerals—a tool for studying regolith maturity. Icarus **104**, 291–300 (1993)
33. Allen, C.C., Morris, R.V., McKay, D.S.: Experimental space weathering of lunar soils. Meteoritics **30**, 479–607 (1995)
34. Pieters, S.M., Fischer, E., Rode, O., Basu, A.: Optical effects of space weathering: the role of the finest fraction. J. Geophys. Res. **98**, 20817–20824 (1993)
35. Pieters, C.M., Taylor, L.A., Noble, S.K., Keller, L.P., Hapke, B., Morris, R.V., Allen, C.C., McKay, D.S., Wentworth, S.: Space weathering on airless bodies: resolving a mystery with lunar samples. Meteorit. Planet. Sci. **35**(5), 1101–1107 (2000)
36. Keller, L., Wentworth, S., McKay, D.S.: Space weathering: reflectance spectroscopy and TEM analysis of individual lunar soil grains. In: Proceedings 29th Lunar Planetary Science Conference, Abstract 1762, Houston (1998)

37. Noble, S.K., Pieters, C.M., Keller, L.P.: An experimental approach to understanding the optical effects of space weathering. Icarus **192** (2), 629–642 (2007)
38. Starukhina, L.V., Shkuratov, Y.G.: Reduced iron grains from nano- to micron sizes in lunar and Mercurian regoliths: calculation of spectral effects. In: Proceedings 42 Lunar and Pl. Conference, vol. 1144 (2011)
39. Murl, J.N.: Sulfur compositional effects on space weathering. In: Undergraduate Fellowship Reports, Hawai'i Space Grant Consortium, Honolulu, pp. 42–49 (2014)
40. Keller, L., McKay, D.: Discovery of vapor deposits in the lunar regolith. Science **261**, 1305–1307 (1993)
41. Keller, L.P., McKay, D.S.: The nature and origin of rims on lunar soil grains. Geochim. Cosmochim. Acta **61**(11), 2331–2341 (1997)
42. Keller, L.P., Clemett, S.J.: Formation of nanophase iron in the lunar regolith. In: Proceedings 32nd Lunar and Planetary Science Conference, Abstract 2097, Houston (2001)
43. Sorokin, E.M., Yakovleva, O.I., Slyuta, E.N., Gerasomiv, M.V., Zaitsev, M.A., Shcherbakov, V.D., Ryazantsev, K.M., Krasheninnikov, S.P.: Experimental modeling of a micrometeorite impact on the Moon. Geochem. Int. **58**(2), 113–127 (2020)
44. Shkuratov, S.L.V., Yu, G.: A theoretical model of lunar optical maturation: effects of submicroscopic reduced iron and particle size variations. Icarus **152**, 275–281 (2001)
45. Wiesli, R.A., Beard, B.L., Taylor, L.A., Johnson, C.M.: Space weathering processes on airless bodies: Fe isotope fractionation in the lunar regolith. Earth Planet. Sci. Lett. **216**, 457–465 (2003)
46. Moynier, F., Albarede, F., Herzog, G.F.: Isotopic composition of zinc, copper, and iron in lunar samples. Geochim. Cosmochim. Acta **70**, 6103–6117 (2006)
47. Wang, K., Moynier, F., Podosek, F.A., Foriel, J.: An iron isotope perspective on the origin of the nanophase metallic iron in lunar regolith. Earth Planet. Sci. Lett. **17–24**, 337–338 (2012)
48. Kitts, B.K., Podosek, F.A., Nichols, R.H., Brannon, J.C., Ramezani, J., Korotev, R.L., Jolliff, B.L.: Isotopic composition of surface-correlated chromium in Apollo 16 lunar soils. Geochim. Cosmochim. Acta **67**, 4881–4893 (2003)
49. Yakovlev, O.I., Gerasimov, M.V., Dikov, Yu.P.: Conditions of condensate rim formation on the surface of lunar regolith particles. Geochem. Int. **49**(10), 967–973 (2011)
50. Noguchi, T., Kimura, M., Hashimoto, T., Konno, M., Nakamura, T., Zolensky, M.E., Okazaki, R., Tanaka, M., Tsuchiyama, A., Nakato, A., Ogami, T., Ishida, H., Sagae, R., Tsujimoto, S., Matsumoto, T., Matsuno, J., Fujimura, A., Abe, M., Yada, T., Mukai, T., Ueno, M., Okada, T., Shirai, K., Ishibashi, Y.: Space weathered rims found on the surfaces of the Itokawa dust particles. Meteorit. Planet. Sci. **49**(2), 188–214 (2014)
51. Thompson, M.S., Zega, T.J.: The oxidation state of nanophase Fe particles produced by space weathering as revealed through aberration-corrected transmission electron microscopy. Microsc. Microanal. **21** (Suppl. 3) (2015)
52. Hapke, B.: Darkening of silicate rock powders by solar wind sputtering. Moon **7**, 342 (1973)
53. Loeffler, M.J., Dukes, C.A., Baragiola, R.A.: Irradiation of olivine by 4 keV He^+: simulation of space weathering by the solar wind. J. Geophys. Res. **114**, E03003 (2009)
54. Dukes, C.A., Baragiola, R.A.: Surface modification of olivine by H^+ and He^+ bombardment. J. Geophys. Res. **104**, 1865–1872 (1999)
55. Lantz, C., Brunetto, R., Barucci, M., Fornasier, S., Baklouti, D., Bourcüois, J., Godard, M.: Ion irradiation of carbonaceous chondrites: a new view of space weathering on primitive asteroids. Icarus **285**, 43–57 (2017)
56. Kuhlman, K.R., Sridharan, K., Kvit, A.: Simulation of solar wind space weathering in orthopyroxene. Planet. Space Sci. **115**, 110–114 (2015)
57. Starukhina, L.V.: Computer simulation of sputtering of lunar regolith by solar wind protons: contribution to change of surface composition and to hydrogen flux at the lunar poles. Sol. Syst. Res. **37**(1), 36–50 (2003)
58. Quadery, A.H., Pacheco, S., Alan, A., Rizzacasa, N., Nichols, J., Le, T., Glasscock, C., Schelling, P.K.: Atomic-scale simulation of space weathering in olivine and orthopyroxene. J. Geophys. Res. Planets **120**, 643–661 (2015)
59. Escobar-Cerezo, J., Penttilä, A., Kohout, T., Muñoz, O., Moreno, F., Muinonen, K.: Simulations of effects of nanophase iron space weather products on lunar regolith reflectance spectra. Astrophys. J. **853**(1), 71 (2018)
60. Wang, S.X., Wang, L.M., Ewing, R.C., Doremus, R.H.: Ion beam-induced amorphization in $MgO–Al_2O_3–SiO_2$. I. Experimental and theoretical basis. J. Non-Cryst. Solids **238**, 198–213 (1998)
61. Christoffersen, R., Keller, L.P.: Space radiation processing of sulfides and silicates in primitive solar system materials: comparative insights from in situ TEM ion irradiation experiments. Meteorit. Planet. Sci. **46**(7), 950–969 (2011)
62. Yamada, M., Sasaki, S., Nagahara, H., Fujiwara, A., Hasegawa, S., Yano, H., Hiroi, T., Ohashi, H., Otake, H.: Simulation of space weathering of planet-forming materials: nanosecond pulse laser irradiation and proton implantation on olivine and pyroxene samples. Earth Planets Space **51**(11), 1255–1265 (1999)
63. Sasaki, S., Nakamura, K., Hamabe, Y., Kurahashi, E., Hiroi, T.: Production of iron nanoparticles by laser irradiation in a simulation of lunar-like space weathering. Nature **410**, 555–557 (2001)
64. Sasaki, S., Kurahashi, E.: Space weathering on Mercury. Adv. Space Res. **33**, 2152–2155 (2004)
65. Moroz, L.V., Fisenko, A.V., Semjonova, L.F., Pieters, C.M., Korotaeva, N.N.: Optical effects of regolith processes on S-asteroids as simulated by laser shots on ordinary chondrite and other mafic materials. Icarus **122**, 366–382 (1996)
66. Brunetto, R., Romano, F., Blanco, A., Fonti, S., Martino, M., Orofino, V., Verrienti, C.: Space weathering of silicates simulated by nanosecond pulse UV excimer laser. Icarus **180**, 546–554 (2006)
67. Loeffler, M.J., Baragiola, A., Murayama, M.: Laboratory simulations of redeposition of impact ejecta on mineral surfaces. Icarus **196**, 285–292 (2008)
68. Loeffler, M.J., Dukes, C.A., Chang, W.Y., McFadden, L.A., Baragiola, R.A.: Laboratory simulations of sulfur depletion at Eros. Icarus **195**, 622–629 (2008)
69. Kurahashi, E., Yamanaka, C., Nakamura, K., Sasaki, S.: Laboratory simulation of space weathering: ESR measurements of nanophase metallic iron in laser-irradiated materials. Earth Planets Space **54**, e5–e7 (2002)
70. Sasaki, S., Kurahashi, E., Yamanaka, C., Nakamura, K.: Laboratory simulation of space weathering: changes of optical properties and TEM/ESR confirmation of nanophase metallic iron. Adv. Space Res. **31**(12), 2537–2542 (2003)
71. Taylor, L.A., Meek, T.T.: Microwave sintering of lunar soil: properties, theory, and practice. J. Aerosp. Eng. **18**(3), 188–196 (2005)
72. Kohout, T., Čuda, J., Filip, J., Britt, D., Bradley, T., Tuček, J., Skála, R., Kletetschka, G., Kašlík, J., Malina, O., Šišková, K., Zbořil, R.: Space weathering simulations through controlled growth of iron nanoparticles on Olivine. Icarus **237**, 75–83 (2014)

Biogeochemistry and Ecology

Biogeochemistry of Hg, Cd and Pb in Surface Water: Bioaccumulation and Ecotoxicity

T. I. Moiseenko, N. A. Gashkina, Yu. G. Tatsiy, M. I. Dinu, M. M. Bazova, D. Y. Baranov, and E. O. Sharapova

1 Introduction

The most attention of the world science is paid to water pollution by such hazardous metals as Cd, Pb, Hg because of their high toxicity both for aquatic inhabitants and human consuming fish [1–5]. Numerous literature sources demonstrate the hazardous properties of these elements. Bioaccumulation and ecotoxic properties of metals largely depend on both the properties of metals and the environmental conditions determine elements bioavailability [6–8]. Many studies have been performed in the natural environment and in experiments that have provided insight into the local pollution effects on the metals accumulation in fish. However, greatest interest is how low metal concentration in water associated with global fluxes, diffuse contamination of water or acidic leaching are coonect witg metals bioaccumulation by fish. Metal bioaccumulation and toxicity depend on other factors such as pH, calcium and humic acid content and temperature conditions at low their concentrations in water [6, 9–12]. A review of the scientific literature shows that increasing temperature lead to metals bioaccumulation through increasing the growing season and fish metabolic levels, especially in northern regions [13–16].

The aim of the studies was to reveal general regularities and specifics of toxic metals bioaccumulation in fish of different water depending on environment and temperature factor (from northern Arctic lakes to southern mouth parts of the Volga River).

2 Materials and Methods

The studies were carried out in large rivers and small lakes of the European territory of Russia: from northern tundra and taiga to steppe regions (Volga River delta is located). In our studies, it was necessary to avoid local sources of pollution and assess the impact of diffuse and airborne pollution. Along with large rivers Pechora, Northern Dvina and Volga, fish from small lakes (tundra, mountain, taiga) that are located in Murmansk and Arkhangelsk oblasts, as well as in the Republic of Karelia were examined. The small lakes had no direct impact of any kind pollution and were only exposed to airborne deposition of metals due to regional production and transboundary transport [17].

Water samples were simultaneously taken in polyethylene Nalgen bottles, the surface of which has no sorption properties, at the places where fish were caught. The bottles were thoroughly cleaned in the laboratory and rinsed twice with lake water before sampling. Once prepared, the samples were placed in dark containers and transported on short notice (approximately + 4 °C) to the laboratories for further analysis when refrigerated (approximately + 4 °C). Bioaccumulation of Cd, Hg and Pb in fish was studied using different fish species inhabiting large river basins as well as a number of lakes in northern catchments (water samples in this habitat were taken simultaneously with fish samples). Special attention was paid to studying bioaccumulation of Hg, Cd and Pb in water near copper smelting and copper-nickel smelting production. Samples of organs and tissues (muscle, liver, kidneys, gills and skeleton) were taken in autumn period only from immature fish of close age (5+ and 6+). Sample preparation was performed by wet decomposition in concentrated nitric acid with the addition of hydrogen peroxide. Cd and Pb in water samples and biological samples were determined by atomic absorption spectrophotometry with graphite atomization using Perkin-Elmer equipment ("Perkin-Elmer-5000", "Aanalyst-800" with Zeeman's background correction). The

T. I. Moiseenko (✉) · N. A. Gashkina · Yu. G. Tatsiy · M. I. Dinu · M. M. Bazova · D. Y. Baranov · E. O. Sharapova
Vernadsky Institute of Geochemistry and Analytical Chemistry, Russian Academy of Sciences, 19 Kosygin St., Moscow, 119991, Russia
e-mail: moiseenko@geokhi.ru

V. P. Kolotov and N. S. Bezaeva (eds.), *Advances in Geochemistry, Analytical Chemistry, and Planetary Sciences*,
https://doi.org/10.1007/978-3-031-09883-3_25

maintenance of mercury was defined on the analyzer of mercury "FIMS-100" firms "Perkin-Elmer". For preparation of scales standard solutions of firm "Merck" were used. Quality control of measurements was carried out at rigid in-laboratory control. Accuracy of results of measurements was repeatedly checked during in-laboratory and international intercalibrations.

3 Results and Discussion

3.1 Water Chemistry

Data on the waters chemical composition are presented in Table 1. Water chemistry has a high variability. The indicators of water chemistry of the Pechora River are characterized by rather high conductivity and calcium content, as a consequence of the peculiarities of the watershed sedimentary rocks. Color and organic carbon contents were rather high in the study area due to development of bogs and forest massifs in the watershed. The Northern Dvina is characterized by lower water salinity and low organic matter content.

The largest river Volga has the highest conductivity, which increase from upstream to downstream sites almost twofold (from north to south). It also has the highest concentrations of calcium. In the upper reaches of the river, flowing among forested areas, the highest values of Color and TOC concentrations are observed.

The water chemistry of small lakes is also highly variable. The waters of lakes in the tundra zone of the Barents Sea coast are characterized by low salinityA mountain lake in the Chuna tundra also has extremely low calcium and organic matter content, and the water is close to atmospheric precipitation in terms of its characteristics. From northern taiga to the forest massifs, the humus acid content in water increases. The variability of salt composition is high. Ca concentrations in lakes differ by 2–4 times depending on a particular lake, the lowest Ca concentrations and pH values were typical for lakes of tundra zone (Chuna, Khariusnoe and Yenozero).

Hg concentrations in water were very low in all water where fish samples were taken. No abnormally high level of water pollution by this element was detected at the surveyed sites (less than 0.01 μg/l).

Cd concentrations in the studied water are very low, in the northern waters the concentrations of this element are more variable (Table 1). Probably, this phenomenon is related to acid leaching of the element in the zone of flue emissions spreading from Kola copper-nickel smelters. Small lakes of the Kola region are subjected to regional airborne technogenic pollution by acidic substances, mainly sulfates [17]. Cd content here is < 0.05–0.62 μg/l. It should be noted that the Ca content in the water of the surveyed lakes and rivers was less than 60 mg/l, which is generally typical for most of Russia. In the middle and lower reaches of the Volga River higher Cd concentrations in water were

Table 1 The main indicators of the aquatic environment of lakes and rivers in the areas of fish catching

Water body	Metal concentration in the water, g L^{-1}			pH	Conductivity, μCm cm^{-1}	Ca, mg L^{-1}	TOC, mgC L^{-1}	T > 10 °C*
	Hg	Cd	Pb					
Large rivers								
Pechora lower stream	< 0.01	0.08 ± 0.07	0.5 ± 0.2	7.4 ± 0.1	80 ± 17	9.7 ± 2.2	9.6 ± 2.6	350
Severnaya Dvina lower stream	< 0.01	0.07 ± 0.05	0.8 ± 0.1	7.4 ± 0.1	176 ± 19	24.1 ± 0.5	16.4 ± 1.8	1250
Volga upper stream Middle stream Lower stream	< 0.01 < 0.01 < 0.01	0.13 ± 0.04 0.12 ± 0.09 0.13 ± 0.07	0.5 ± 0.02 < 0.1 1.72 ± 0.9	7.7 ± 0.1 6.8 ± 0.3 7.4 ± 0.3	195 ± 35 255 ± 21 364 ± 8	29.2 ± 4.6 35.5 ± 2.1 34.6 ± 1.5	15.4 ± 3.4 9.4 ± 2.4 12.9 ± 2.2	1800 2100 3200
Lakes								
Kola Mountain	< 0.01	< 0.05	< 0.1	6.3 ± 0.1	9 ± 0.5	0. 8 ± 0.05	1.9 ± 1.7	350
Kola Tundra Enozero	< 0.01	< 0.05	< 0.1	6.3 ± 0.3	27 ± 4	0.5 ± 0.2	3.9 ± 2.3	350
Kola Taiga B. Hariysnoe Pirenga, Okhtozero	< 0.01 < 0.01	< 0.05 0.08 ± 0.05	< 0.1 < 0.1	6.3 ± 0.2 7.0 ± 0.2	9 ± 0.7 33 ± 7	0. 8 ± 0.1 2.8 ± 0.5	2.0 ± 1.7 4.5 ± 1.7	350 800
Arhangelsk Taiga Chernoe, Volch'e	< 0.01	0.06 ± 0.05	< 0.1	7.3 ± 0.2	56 ± 23	6.4 ± 2.6	13.7 ± 2.5	1150
Karelia Taiga Padmozero	< 0.01	0.10 ± 0.01	1.97 ± 1.29	7.9 ± 0.1	157 ± 1	17.9 ± 0.1	9.5 ± 2.6	1400

Note *the sum of air temperatures above10 °C for the region
The data presented in Tables 1 and 2 is obtained from [18–20]

observed, as in the Northern Dvina. Since this element is rather labile, its migration to water may be related to acid leaching.

The concentration of Pb in the water of the Volga and the Northern Dvina rivers varies greatly from 0.02 to 3.2 µg/L. The reasons for the global increase in its content in water systems are manifold—transport, fuel combustion, industrial pollution, transboundary transport, urbanization, etc.

3.2 Bioaccumulation of Mercury

Hg is characterised a variety of physical and chemical speciation with a great variety of properties and its complex mechanisms of distribution and accumulation in living organisms, as well as its toxic properties. The most significant chemical Hg speciation in aquatic ecosystems: elemental mercury (Hg0), inorganic mercury (Hg^{2+}), monomethylmercury (CH_3Hg^+), dimethylmercury Hg $(CH_3)_2$. Accumulators of Hg, especially in pollution conditions, are suspended and bottom sediments of water bodies. Bacterial transformation of inorganic mercury into monomethylmercury is an important feature of the Hg cycle in any aquatic ecosystem, the first stage in the whole process of migration through the trophic chain and bioaccumulation [21–23]. Methylation processes are particularly intense in the upper layer of organic-rich bottom sediments of water bodies, in suspended solids, and in mucus covering fish [24]. As the trophic structure of ecosystems progresses, Hg content increases in living organisms and reaches maximum values in fish predatory [25, 26]. Bioconcentration factor in predatory can reach 1000–10,000 in relation to the content in water [22].

Hg content in fish organs and tissues from different water bodies in the European Russia varied within a wide range depending on the water body and fish species (Table 2). Analysis of the data shows that the highest amounts of Hg accumulate in the liver of predatory fish. A striking example is lake trout from Lake Khariusnoe (0.196 µg/g dry weight), as well as pike and perch from forest lakes of the Kola and Karelian regions. It should be noted that Lake Khariusnoe is far from any source of contamination and Hg can be brought in by atmospheric transboundary transports. In lake trout, high concentrations of Hg are characterised not only in the liver, but also in the kidneys and gills, i.e., in the organs where metabolic processes are active. As is well known, lake troutis an active predator and has a high metabolic rate. In pike and perch the Hg content in liver is comparable to muscle. Among fish from river systems, Hg is present in fairly high concentrations in the pike liver from the Pechora and Northern Dvina rivers, as well as in the lower reaches of the Volga River. Mercury content in Volga River bream ranged from less than 0.001–0.127 µg/g dry weight. High bioaccumulation of Hg in bream is typical for Middle Volga. This part of river is located in urbanized and industrially developed regions, and catchment area experiences the highest complex anthropogenic load, which may result in Hg migration into these river parts.

Analysis of our data shows that different fish species accumulate Hg differently, i.e. Hg accumulation has species specificity. Predatory fish (lake trout pike and perch) have higher Hg content from all studied water than benthophagous fish (whitefish and bream). In generaly, species according to Hg content can be arranged in the following order:

$$\text{lake trout} > \text{pike} > \text{perch} > \text{whitefish} > \text{bream}.$$

In fish, the Hg content in the body increases with age, which is consistent with the data [27, 28]; the bioaccumulation of Hg is particularly characterized in large pike from Scandinavianlakes, which poses a risk to the local population [29]. Accumulation of Hg in water and fish has been reported in the High Arctic [1, 30].

In our studies, Hg accumulated in liver, muscle, and kidney of fish. In works [22, 24, 31, 32] it was shown that the largest amounts of Hg accumulate in liver and muscles of fish, therefore, these organs are recommended for Hg biomonitoring. However, our studies revealed high content of Hg also in kidneys, which reflects the accumulation of this element in fish. The large role of Hg intake with food has been noted [24]. Perhaps, this explains the relatively low content of this element in the gills and predominant accumulation in the fish liver. Meanwhile, Hg penetrates into the body of wild fish species and with food, since, as noted, it accumulates in the food chains in conditions of water pollution [33].

Predatory fish (pike and perch) taken in the lower of the Volga River had 4–5 times higher Hg content in organism in comparison with benthophages that is connected with their habitats specificity to thickets and silt sediments where mercury methylation processes actively take place. In work [8] high affinity of this element to the humus organic substance was marked. In colored waters, with high content of humic acids, Hg methylated prevail, which are more actively accumulated in fish [27, 34]. In our studies, this is reliably confirmed by the obtained dependences of Hg content in predators muscles and liver (pike and perch) with the concentration of organic carbon (TOC) in water:

$$\text{Hg muscles} = 0.137\,\text{Ln(TOC)} - 0.059,\ r = 0.880,\ p < 0.001;$$
$$\text{Hg liver} = 0.135\,\text{Ln(TOC)} - 0.093,\ r = 0.765,\ p < 0.001.$$

The second factor intensifying the processes of methylation of mercury is low pH. Hg methylation and

Table 2 Average values and standard errors of Hg, Cd and Pb concentrations in the organs and tissues of fish species from different water bodies

		Hg				Cd				Pb			
Water body	Species	Gills	Muscles	Liver	Kidney	Gills	Muscles	Liver	Kidney	Gills	Muscles	Liver	Kidney
		g g $^{-1}$dry weight											
Large rivers													
Pechora lower stream	Whitefish pike	0.02 ± 0.01 0.09 ± 0.01	0.02 ± 0.01 0.19 ± 0.05	0.12 ± 0.04 0.14 ± 0.03	0.01 ± 0.01 0.10 ± 0.02	0.10 ± 0.02 0.02 ± 0.01	< 0.01 < 0.01	0.19 ± 0.05 0.06 ± 0.02	0.75 ± 0.23 0.48 ± 0.13	– –	– –	– –	– –
Severnaya Dvina lower stream	Whitefish bream pike	0.02 ± 0.00 0.01 ± 0.00 0.15 ± 0.05	0.08 ± 0.04 0.07 ± 0.02 0.34 ± 0.09	0.09 ± 0.01 0.04 ± 0.03 0.25 ± 0.10	0.01 ± 0.00 0.01 ± 0.00 –	0.14 ± 0.04 0.26 ± 0.11 0.01 ± 0.00	0.03 ± 0.02 0.11 ± 0.06 0.01 ± 0.00	0.07 ± 0.02 0.82 ± 0.54 0.02 ± 0.01	0.72 ± 0.14 0.61 ± 0.33 0.12 ± 0.12	0.31 ± 0.21 0.19 ± 0.15 –	0.12 ± 0.01 0.19 ± 0.01 –	0.20 ± 0.12 0.75 ± 0.31 –	0.31 ± 0.24 0.23 ± 0.02 –
Volga upper stream Middle stream Lower stream	Bream pike Bream perch Bream perch pike	0.01 ± 0.00 0.01 ± 0.00 0.02 ± 0.00 0.01 ± 0.00 0.04 ± 0.01 0.05 ± 0.02	0.02 ± 0.00 0.05 ± 0.01 0.21 ± 0.03 0.03 ± 0.00 0.26 ± 0.06 0.31 ± 0.02	0.05 ± 0.01 0.05 ± 0.01 0.17 ± 0.03 0.05 ± 0.01 0.34 ± 0.07 0.24 ± 0.05	0.02 ± 0.00 0.03 ± 0.00 0.10 ± 0.05 0.01 ± 0.00 0.02 0.24 ± 0.06	0.05 ± 0.01 0.19 ± 0.02 0.01 ± 0.00 0.03 ± 0.01 0.05 ± 0.01 0.26 ± 0.05 0.51 ± 0.05	0.03 ± 0.01 < 0.01 < 0.01 0.01 ± 0.00 0.03 ± 0.01 0.06 ± 0.01 < 0.01	0.25 ± 0.04 0.05 ± 0.01 0.26 ± 0.04 0.48 ± 0.05 0.25 ± 0.04 0.89 ± 0.21 0.02 ± 0.00	1.09 ± 0.19 0.07 ± 0.04 1.94 ± 0.28 0.88 ± 0.11 1.09 ± 0.19 0.59 0.47 ± 0.04	0.33 ± 0.07 0.04 ± 0.03 0.04 ± 0.01 0.05 ± 0.04 0.07 ± 0.01 0.12 ± 0.06 0.08 ± 0.05	0.07 ± 0.02 < 0.01 0.06 ± 0.01 0.08 ± 0.01 0.02 ± 0.00 0.01 ± 0.00 < 0.01	0.25 ± 0.07 0.15 ± 0.08 0.19 ± 0.04 0.06 ± 0.01 0.06 ± 0.01 0.05 ± 0.02 0.01 ± 0.00	0.37 ± 0.12 0.07 ± 0.04 0.48 ± 0.10 1.49 ± 0.63 0.13 ± 0.02 0.18 0.18 ± 0.06
Lakes													
Kola Mountain	Salmon trout	–	–	–	–	2.94 ± 0.27	0.05 ± 0.02	10.4 ± 0.79	22.6 ± 1.9	–	–	–	–
Kola Tundra Enozero	Salmon trout	–	–	–	–	0.86 ± 0.04	0.16 ± 0.01	1.23 ± 0.16	6.26 ± 0.90	–	–	–	–
Kola Taiga B. Hariysnoe Pirenga, Okhtozero	Salmon trout whitefish perch pike	0.09 ± 0.02 – 0.04 ± 0.01 0.04 ± 0.02	0.05 ± 0.01 0.08 ± 0.02 0.20 ± 0.05 0.09 ± 0.03	0.20 ± 0.03 0.12 ± 0.03 0.11 ± 0.06 0.12 ± 0.01	0. 20 ± 0.03 0.13 ± 0.07 0.09 0.13 ± 0.02	0.98 ± 0.13 0.37 ± 0.07 0.32 ± 0.12 0.37 ± 0.07	0.03 ± 0.01 0.22 ± 0.02 0.21 ± 0.04 0.26 ± 0.04	5.48 ± 0.77 1.34 ± 0.29 1.22 ± 0.21 0.11 ± 0.02	5.51 ± 0.28 5.31 ± 0.71 1.08 ± 0.41 0.81 ± 0.23	0.06 ± 0.02 0.08 ± 0.04 –	0.02 ± 0.01 0.05 ± 0.02 0.01 ± 0.00 –	0.21 ± 0.08 0.25 ± 0.15 0.05 ± 0.01 –	0.89 ± 0.12 0.18 ± 0.03 0.80 ± 0.18 –
Arhangelsk Taiga Chernoe, Volch'e	Perch pike	0.01 ± 0.00 0.01 ± 0.00	0.09 ± 0.02 0.09 ± 0.02	0.03 ± 0.01 0.04 ± 0.01	– –	0.08 ± 0.01 0.04 ± 0.01	0.01 ± 0.01 0.01 ± 0.00	0.58 ± 0.14 0.07 ± 0.02	0.60 ± 0.25 –	0.26 ± 0.07 0.16 ± 0.08	0.10 ± 0.03 0.19 ± 0.15	0.19 ± 0.04 0.18 ± 0.06	– –
Karelia Taiga Padmozero	Perch pike	0.03 ± 0.01 0.02 ± 0.01	0.13 ± 0.03 0.26 ± 0.05	0.04 ± 0.01 0.28 ± 0.07	- 0.21 ± 0.06	0.19 ± 0.04 0.34 ± 0.02	0.01 ± 0.00 < 0.01	1.12 ± 0.25 0.16 ± 0.01	0.84 ± 0.28 0.67 ± 0.08	0.19 ± 0.05 –	0.08 ± 0.02 –	0.38 ± 0.11 –	– –

bioavailability in acidified water bodies have been proved [33]. In [35] are given the Hg content in the liver and kidneys was many times higher in acidified tundra lake in the Kola North than in a neutral lake in the same region. A high level of Hg bioaccumulation was noted in perch from acidified lakes in Karelia, as well as in lakes with a high content of humic acids [36]. In Norway, a high Hg content in trout lake and arctic char in 2000–2001 data was observed in acidified lakes; in Finland, an association of Hg accumulation in perch with low pH values was noted [37].

Despite the large variability of Hg in the studied fish, the Hg content in muscle does not exceed the limiting values for human fish consumption [38].

3.3 Bioaccumulation of Cadmium

Cadmium, as a labile metal, is easily leached from mineral under the acidic precipitation and is characterized by increased concentrations in water. Connect of Cd increased concentrations in water with pH decrease during flooding has been proven by Swedish streams as an example [39]. Cadmium in natural waters is mainly in ions and in the low molecular weight inorganic complexes [8]. In eutrophic waters may partially have complexes with organic matter or be adsorbed on suspended matter. In oligotrophic waters at pH $\leq$ 7.3 it is mainly contained as ions, the [Cd2+]/[Cdобщ] ratio is 0.8 and more [40]. In [8] similar data are given that in low salinity oligotrophic water the content of Cd ions is more than 90% of the total concentration and bioavailability of this element is high. Studies of Arctic ice have shown that Cd in aerosols and fine particles is able to be transported over long distances, falling out at considerable distances from pollution sources and creating increased concentrations in regions remote from industrial centers [1, 30].

Our researches demonstrate that this element is accumulated to the greatest extent in fish kidneys (Table 2). For the majority of species, no reliable relations between Cd content in water and accumulation in fish were established, which can be explained by strong influence of other exogenic factors on Cd bioaccumulation (pH values and Ca content in water). It should be noted, that organ and tissue of whitefish were taken from water with pH from 6.5 to 8; in lake trout—from 6.2 to 7.

More active Cd accumulation was observed in fish at lower pH values, which is confirmed by the dependence of cadmium accumulation in kidneys and liver on water pH. Along with the effect of low pH, Ca content in water affects the bioavailability of the element and its accumulation in fish. We calculated two-parameter equations that demonstrated the relationship between more active Cd penetration into the kidneys of benthophages at low pH and calcium content: for benthophages, this relationship is approximated by Eq:

$$\begin{aligned} \mathrm{Cd}_{\mathrm{kidney}} &= 160.71 - 81 * \mathrm{pH}\ 0.050 * \mathrm{Ca}^{-}_{\mathrm{water}}, r \\ &= 0.761, p < 0.005. \end{aligned}$$

For predatory fish species more reliable dependence only with pH is shown and influence of Ca has no big influence on Cd penetration into fish organism:

$$\begin{aligned} \mathrm{Cd}_{\mathrm{kidney}} &= 390.85 - 31 * \mathrm{pH} + 0.007 * \mathrm{Ca}_{\mathrm{water}}, r \\ &= 0.638, p < 0.01. \end{aligned}$$

Thus, Cd accumulation in the kidney of bentophagous predatory fish is more dependent on the concentration of Ca in the water, while in predators it depends more on the water pH.

In muscle, the accumulation of Cd is not high, below the permissible standards for human consumption [38]. However, due to the high accumulating capacity of this element in the kidneys, pathologies may occur in humans as demonstrated in [41]. Table 2 presents the Cd content in the body systems of different fish species in European Russia. In our studies, the maximum Cd content was detected in the organs and tissues of lake trout (22.56 µg/g dry weight) from the northern lakes Chuna and Khariusnoe, which may be associated with their residence in northern low-salinity waters.

Bioaccumulation of Cd is observed in kidneys and liver of the majority of species. Correlation coefficients between Cd content in kidney and liver were: for lake trout r = 0.94, n = 40; whitefish—r = 0.83, n = 15. Accumulation in the kidney and liver of lake trout is very closely related to accumulation in the gills as well: correlation coefficients of element content in the gills and liver are 0.96 and 0.99, n = 40, in the gills and kidney. Similar patterns are typical for whitefish and perch.

The results demonstrate that in low mineralized waters of northern regions of Cd accumulation in fish occurs in large quantities. For example, the element level in water of the Northern Dvina River is two times lower than in the Volga River, but Cd content in the organs and tissues in the Northern Dvina is higher by more than two times. Cd accumulation is more significant in whitefish and lake trout of small lakes of the Kola region.

3.4 Lead Bioaccumulation

Table 2 is shown Pb content in fish of different regionsThe highest Pb content in bream body was observed in Northern Dvina and in Upper and Middle Volga areas. Maximum

accumulation is in kidney and liver. With higher level of Pb content in waters of Lower Volga, maximum accumulation of this element is in fish of Upper and Middle Volga. Variability of Pb content in organs and tissues of different fish species is high. Species specificity in lead bioaccumulation is not clearly expressed. However, the frequency of high concentrations of the element in liver and kidney of perch is higher compared to other species, especially in forest lakes.

In fish from all surveyed water, the highest concentrations of Pb accumulate in functionally important organs: kidneys and liver; in muscles and gills lead content is low.

Higher (exceeding all other values) Pb content in perch kidney was found in the middle reaches of the Volga. In this river section higher Pb concentrations are also found in bream kidney. Middle Volga is characterized by developed industry and high urbanization and although in our studies we avoided pollution zones, generalized pollution from industrial activities and transport has an impact here. The fact of increasing Pb content in the environment, along with Hg and Cd, in terrestrial waters, especially in northern regions, has been proved [1, 3, 30, 42]. In low saline waters this element is mainly as ions, but with increasing salt content bioavailability of this element decreases [8]. Therefore, the accumulation of Pb depends on both: the total concentration in water and indicators such as pH and Ca content. Under conditions of Ca deficiency, Pb is more actively included in metabolic processes, which inevitably leads to their disruption and the development of pathologies in the body [43]. Concentrations of this element in water in our studies varied significantly, increasing in the waters of urbanized regions.

Pb content in gills, muscles and kidney of pike and perch as well as in kidney of lake trout has close inverse correlation with pH and Ca content in water. It indicates that Pb penetration into fish organism occurs more actively in conditions of low water Ca saturation and at low water pH, i.e., depends largely on concentration in water, but increases in waters with lower pH. For benthophages the dependence is obtained:

$$\text{Pb kidneys} = 0 - .5\text{pH}05 * +4.10, r = 0.533, p < 0.01$$

for predators: Pb kidneys = 0 − 0.480 * pH + 3.68, $r = 0.666$, $p < 0.01$.

In our researches it is proved that accumulation of Pb is more active in kidney, similarly to Cd and depends mainly on concentration in water. For benthophages dependence was obtained, which is approximated by the following equation:

$$\text{Pb kidneys} = 4.19 + 0.676 * \text{Pb}_{\text{water}} + 0.013\text{pH}*, r = 0.645, p < 0.01.$$

In this case, the positive relationship between lead accumulation in bream and pH is explained by the fact that Pb concentration increases in waters of southern regions characterized by higher salinity and pH, i.e. Pb content in kidney of benthophages depends to a greater extent on Pb concentration in water.

Saying of predatory fish living in a wide range of environmental conditions, the relationship demonstrates a positive correlation with concentration in water and a negative relationship with pH values:

$$\text{Pb kidneys} = 0.358 + 0.225 * \text{Pb } 0_{\text{water}} - 0.568 * \text{pH}, r = 0.725, p < 0.02.$$

Compared to European lakes, the level of Pb in water of northern lakes is < 0.5 µg/l, while in some mountain lakes affected by airborne pollution its concentration increases up to 3 µg/l. Accordingly, the Pb content in fish from the lakes of the Kola North and Karelia is also lower. Thus, its concentration in liver does not exceed 0.5 ppm, whereas in fish from the lakes of central Europe this value is more than 1 ppm [44]. Thus, water pollution by Pb leads to its accumulation in fish organisms. Pb penetrates most actively into fish organism in conditions of low-salinity water.

3.5 Ecotoxic Properties and Temperature Effects

Publications show that fish informatively reflect water pollution by metals, accumulating in their bodies even in cases when the content in water is not high [27, 32, 45–47]. Our studies were comprehensive, covering different fish species and a large variability of their habitat conditions from tundra to semi-desert zone, large rivers and small lakes. We emphasize that the works were aimed studying metals bioaccumulation in lakes and rivers fish with only diffuse or airborne pollution (outside local pollution zones). Therefore, no critical levels of contamination were observed (with few exceptions). Whereas the variability of habitat conditions and indicators such as the content of salts, calcium and organic matter was significant as found. The mechanism of toxic action of these metals on living organisms is widely known.

At very low levels of Hg in water, Hg contamination can be detected by examining the Hg content of fish [48]. A greater influence on metal accumulation in fish is caused by their habitat characteristics. Two key factors influence the activation of Hg methylation processes and consequently the accumulation in fish: (1) acid-alkaline balance and low pH and (2) organic matter content [49]. Mercury is dangerous due to its direct toxic properties, but the most serious problem is its ability to accumulate highly in living

organisms, increasing along the trophic chain and remote gonadotoxic, neurotoxic and carcinogenic properties [21, 22, 25, 31, 33, 38, 50]. The ecological hazard of mercury in the hydrosphere consists in its direct toxic influence on aquatic inhabitants, ability to be included in biogeochemical cycles with a tendency to bioaccumulation in the trophic structure of aquatic ecosystems, long-term cycling and accumulation in fish and dangerous for humans. Methylmercury has been found to inhibit the activity of enzymes in the cerebellum that are responsible for neuronal development in the early stages of life. The allowable daily intake of mercury is 0.005 mg per kg of body weight. It should be noted that people eating fish from polluted lakes are often exposed to much higher doses.

Cadmium can penetrate through the gill epithelium, similar to calcium transport in chloride cells, accumulates in the liver and kidneys of fish due to its strong interaction with cysteine and binding to metalltioneins [51]. Since Cd metabolism is closely related to essential elements and especially zinc, it is able to replace the latter in many vital enzymatic reactions, leading to their disruption and inhibition [51–55]. Cadmium can be considered as zinc antimetabolite. [43] suggested that the primary mechanism of cadmium toxic action may be related to inhibition of calcium transport by proteins. Hypocalcemia is the most common hypothesis to explain the acute toxic effects of Cd [56, 57]. Our studies confirm the effect of Cd penetration on the body's supply of essential elements, particularly with zinc. Having similar mechanisms of penetration and metabolism with Zn, Cd can replace it in a number of biochemical functions, causing their destruction [51, 58].

The migration of lead is similar to that of calcium in the processes of penetration and accumulation in fish. Ca2 + uptake occurs through the apical membrane of the gill Ca2+-channel, Ca2+ transport through the basolateral membrane is performed by Ca2+-ATPase [59]. Due to its high affinity with Ca, lead penetrates the body and is incorporated into metabolic processes. There is evidence that lead exposure shifts the nitrogen metabolism of carps towards the activation of catabolic processes, and also exhibits neurotoxic and gonadotoxic effects [3, 42, 55].

Research of climate impact on bioaccumulation and ecotoxicity of metals has been given great attention in world science [13, 60–65]. Reviews of studies show that the main negative impact of climate change on ecosystems and bioaccumulation of elements will occur through the risks of new stress conditions, under which the vulnerability of the organism to the action of chronic intoxication will be increased. Under these conditions, toxic elements and substances accumulated by organisms will lead to more pronounced negative effects. In work [14] show (in model calculations) that during climate warming, cycling of toxic elements in aquatic ecosystems is accelerated and their toxic properties are intensified.

In relation to the Hg biogeochemistry in the Arctic seas and lakes under warming conditions, on the one hand, the processes of methylation, hence the processes of element absorption, will intensify, on the other hand, the elimination of gaseous Hg will increase. An increase in the size of organisms in warmer conditions will affect the intensity of the absorption of this element [62]. In Canadian northern lakes, the phenomenon of more active Hg accumulation in large individuals living in more southern lakes was established by the example of the arctic char population. In [27] it is estimated that climate warming due to prolongation of vegetation period and increase of forage base will accelerate Hg bioaccumulation. Work [13] is devoted to the results of modeling the impact of climate warming on toxic elements bioaccumulation. Direct effects consist in increase of metabolism level and food consumption by fish.

Our studies have demonstrated that the primary effects of climate warming connect with biogeochemical cycles and aquatic environments are superimposed on secondary effects of metal bioaccumulation. This does not allow making directly conclusions about the influence of climatic factor on metal accumulation. However, for Hg, its bioaccumulation has been shown to increase with warmer conditions. For Cd and Pb effects of climate warming can be manifested under the condition of similar salt composition and low Ca concentrations in water.

4 Conclusion

Different fish species at relatively low concentrations of metals (Hg, Cd and Pb) in water have been shown to accumulate them in different ways. In most cases, predatory fish (Lake trout pike and perch) accumulate more toxic metals compared to benthophages - whitefish and bream. Under conditions of low pollution there is elements synchronous bioaccumulation in organs and tissues, with higher values in functionally important organs is bioaccumulation in kidneys and liver. The exception is Hg, which accumulates in the liver and muscles in almost equal amounts.

The research results show that conditions of aquatic environment and fish habitats have a significant impact on bioavailability of elements. At low Hg concentrations in water, reliable dependences of Hg accumulation in pike and perch and organic matter content in water were revealed. Habitats of predators (pike and perch) with developed aquatic vegetation, where Hg methylation is actively taking place, which is reflected in a higher accumulation of this element in fish. Cadmium accumulates in higher concentrations in fish kidney at low pH and Ca content in water.

In the greatest quantities it is accumulated in kidneys of fishes of northern regions where, probably, leaching of element by acid precipitations affects. The reliable inverse dependence of accumulation of this element in kidney of fish with the maintenance of zinc is proved, i.e. the maintenance of an organism of zinc, as an essential element, can decrease at pollution of waters with Cd.

Lead accumulates in fish from water in regions (middle and lower Volga) where industry and urbanization are developed. The second factor influencing Pb accumulation is the content of Ca in water; high content of the latter in water reduces Pb accumulation.

Using an extensive geographical coverage of fish studies in water of Russia it is shown that the climatic factor influences the intensity of toxic elements accumulation. Clear dependences of Hg accumulation in fish with water temperature have been obtained, which show that with increasing temperature fish accumulate Hg in large quantities. For other elements, a greater influence have calcium content, at low values of which the penetration of elements in fish increases. With a warming climate, salt content will increase, which will reduce the penetration of elements such as Cd and Pb.

Research of the bioaccumulation of metals and their toxic effects need to take into account the effects of habitat conditions and temperature factors that affect the metals bioavailability. This should be taken into account in the regulation of water quality standards and assessments of public health risks under a warming climate.

Detected Hg, Cd and Pb levels in the muscle of fish used as food were well below the established critical levels for public health. However, the possible effects of long-term human consumption of fish and the public health hazards of long-term fish consumption should be considered.

References

1. AMAP. Heavy Metals in the Arctic. https://amap.no/documents/doc/amap-assessment-2002-heavy-metalsin-TheArctic. Tromsø, Norway (2002)
2. AMAP/UNEP. Technical Background Report for the Global Mercury Assessment 263. AMAP Oslo, Norway. UNEP Geneva, Switzerland (2013)
3. Wood, C.M., Farrell, A.P., Brauner, C.J.: Homeostasis and Toxicology of Non-Essential Metals. In: Farrell, A.P., Brauner, C.J. (Eds.), pp. 67–123. Academic Press, San Diego (2012)
4. Renieri, E.A., Alegakis, A.K., Kiriakakis, M., Vinceti, M., Ozcagli, E., Wilks, M.F., Tsatsakis, A.M.: Cd, Pb and Hg biomonitoring in fish of the mediterranean region and risk estimations on fish consumption. Toxics **2**, 417–442 (2014)
5. Atobatele, O.E., Olutona, G.O.: Distribution of three non-essential trace metals (Cadmium, Mercury and Lead) in the organs offish from Aiba Reservoir, Iwo. Nigeria. Toxicology Reports **2**, 896–903 (2015)
6. Magalhaes, D., Marques, M., Baptista, D., Forsin, D., Buss, D.: Metal bioavailability and toxicity in freshwaters. Environ. Chem. Lett. **13**, 69–87 (2015)
7. Väänänena, K., Leppänen, M.T., Chen, X., Akkanenaa, J.: Metal bioavailability in ecological risk assessment of freshwater ecosystems: from science to environmental management. Ecotoxicol. Environ. Saf. **147**, 430–446 (2018)
8. Moiseenko, T.I., Gashkina, N.A., Dinu, M.I.: Metal bioavailability in northern low-salinity water: case study of lakes in the Kola region, Russia. Case study of lakes in the Kola region. Environ. Res. Lett. (2020).
9. Gandhi, N., Diamond, M.L., Huijbregts, M.A.J., Guinée, J.B., Peijnenburg, W.J.G.M., Van De Meent, D.: Implications of considering metal bioavailability in estimates of freshwater ecotoxicity: examination of two case studies. Int. J. Life Cycle Assess. **16**(8), 774–787 (2011)
10. Amde, M., Liu, J., Tan, Z., Bekana, D.: Transformation and bioavailability of metal oxide nanoparticles in aquatic and terrestrial environments. Environ. Pollut. **230**, 250–257 (2017)
11. Liu, Y., Du, Q., Wang, Q., Yu, H., Liu, J., Tian, Y., Chang, C., Lei, J.: Causal inference between bioavailability of heavy metals and environmental factors in a large-scale region. Environ. Pollut. **226**, 370–378 (2017)
12. Wijdevelda, A.J., Schipper, C.A., Heimovaara, T.J.: Variation in the availability of metals in surface water, an evaluation based on the dissolved, the freely dissolved and Biotic Ligand Model bioavailable concentration. CATENA **166**, 260–270 (2018)
13. Gouin, T., Armitage, J.M., Cousins, I.T., Muir, D.C.G., Ng, C.A., Reid, L., Tao, S.: Influence of global climate change on chemical fate and bioaccumulation: the role of multimedia models. Environ. Toxicol. Chem. **32**, 20–31 (2013)
14. Moe, S.J., Schamphelaere, K.D., Clements, W.H., Sorensen, M.T., Van den Brink, P.J., Liess, M.: Combined and interactive effects of global climate change and toxicants on populations and communities. Environ. Toxicol. Chem. **32**, 49–61 (2013)
15. Gashkina, N.A., Moiseenko, T.I.: Influence of thermal pollution on the physiological conditions and bioaccumulation of metals, metalloids, and trace metals in whitefish (*Coregonus lavaretus* L.). Int. J. Mole. Sci. **21**(12), 4343 (2020)
16. Gashkina, N.A., Moiseenko, T.I., Kudryavtseva, L.P.: Fish response of metal bioaccumulation to reduced toxic load on long-term contaminated Lake Imandra. Ecotoxicol. Environ. Saf. **191**, 110205 (2020)
17. Moiseenko, T.I., Dinu, M.I., Gashkina, N.A., Kremleva, T.A.: Aquatic environment and anthropogenic factor effects on distribution of trace elements in surface waters of European Russia and Western Siberia. Environ. Res. Lett. **14**, 065010 (2019)
18. Moiseenko, T.I., Gashkina, N.A.: Bioaccumulation of Mercury in fish as indicator of water pollution. Geochem. Int. **54**(6), 485–493 (2016)
19. Moiseenko, T.I., Gashkina, N.A.: Biogeochemistry of Cadmium: anthropogenic dispersion, bioaccumulation, and ecotoxicity. Geochem. Int. **56**(8), 798–811 (2018)
20. Moiseenko T.I., Gashkina N.A.: Distribution and bioaccumulation of heavy metals (Hg, Cd, and Pb) in fish: influence of the aquatic environment and climate. Environ. Res. Lett. (2020)
21. Gochfeld, M.: Case of mercury exposure, bioavailability and absorption. Ecotoxicol. Environ. Saf. **56**, 174–179 (2003)
22. William, F., Fitzgerald, Carl, H.: Marine biogeochemical cycling of mercury. Chem. Rev. **107**, 641–662 (2007)
23. Lavoie, R.A., Jardine, T.D., Chumchal, M.M., Kidd, K.A., Campbell, L.M.: Biomagnification of mercury in aquatic food webs: a worldwide meta-analysis. Environ. Sci. Technol. **47**, 13385–13394 (2013)

24. Heath, A.G.: Water pollution and fish physiology, 2nd edn., p. 384. CRC Press, Boca Raton (2018)
25. Watras, C.J., Back, R.C., Halvorsen, S.: Bioaccumulation of mercury in pelagic freshwater food webs. Sci. Total Environ. **219**, 183–208 (1998)
26. Rask, M., Jones, R.I., Jarvinen, M., Paloheimo, A., Salonen, M., Syvaranta, J.: Changes in fish mercury concentrations over 20 years in an acidified lake subject to experimental liming. Appl. Geochem. **22**, 1229–1240 (2007)
27. Chételat, J., Amyot, M., Arp, P., Blais, J.M., Depew, D., Emmerton, C.A., Evans, M., Gamberg, M., Gantner, N., Girard, C., Graydon, J., Kirk, J., Lean, D., Lehnherr, I., Muir, D., Nasr, M., Poulain, A.J., Power, M., Roach, P., Stern, G., Swanson, H., Van der Velden, S.: Mercury in freshwater ecosystems of the Canadian Arctic: recent advances on its cycling and fate. Sci. Total Environ. **509–510**, 41–66 (2015)
28. Backstrom, C.H., Buckman, K., Molden, E., Chen, C.Y.: Mercury levels in freshwater fish: estimating concentration with fish length to determine exposures through fish consumption. Arch. Environ. Contam. Toxicol. **78**(4), 604–621 (2020)
29. Sharma, C.M., Borgstrom, R., Huitfeldt, J.S., Rosseland, B.O.: Selective exploitation of large pike Esox lucius—effects on mercury concentrations in fish populations. Sci. Total Environ. **399**, 33–40 (2008)
30. Norton, S.A., Dillon, P.J., Evans, R.D.: The history of atmospheric deposition of Cd, Hg and Pb in North America: evidence from lake and peat bog sediments. In: Lindberg, A.L., Page, A.L., Norton, S. A. (Eds.) Acidic Precipitation. Sources, Deposition and Capony Interactions, pp. 73–101. Springer, New York (1990)
31. Rice, K.M., Walker, E.M., Wu, M., Jr., Gillette, C., Blough, E.R.: Environmental mercury and its toxic effects. J. Prev. Med. Public Health **7**(2), 74–83 (2014)
32. Kuczyńska, J., Paszczyk, B., Kuczyński, M.J.: Fish as a bioindicator of heavy metals pollution in aquatic ecosystem of Pluszne Lake, Poland, and risk assessment for consumer's health. Ecotoxicol. Environ. Saf. **153**, 60–67 (2018)
33. Jardine, T.D., Kidd, K.A., O'Driscoll, N.: Food web analysis reveals effects of pH on mercury bioaccumulation at multiple trophic levels in streams. Aquat. Toxicol. **132–133**, 46–52 (2013)
34. Rahmanikhah, Z., Esmaili-Sari, A., Bahramifar, N.: Total mercury and methylmercury concentrations in native and invasive fish species in Shadegan International Wetland, Iran, and health risk assessment. Environ. Sci. Pollut. Res. Int. **27**(7), 6765–6773 (2020)
35. Moiseenko, T.I., Gashkina, N.A.: Bioaccumulation of mercury in fish as an indicator of water pollution. Geochem. Int. **54**, 485–493 (2016)
36. Haines, T.A., Komov, V.T., Matey, V.E., Jagoe, C.H.: Perch mercury content is related to acidity and color of 26 Russian lakes. Water Air Soil Pollution **85**, 823–828 (1995)
37. Manio, J.: Responses of Headwater Lakes to Air Pollution Changes in Finland. Monographs of the Boreal Environment Research, Helsinki, p. 63(2001)
38. World Health Organization: Mercury and Health (2013). http://www.who.int/news-room/fact-sheets/detail/mercury-andhealth
39. Johansson, K., Bringmark, E., Lindevall, L., Wilanders, A.: Effects of acidification on the concentration of metals in running water in Sweden. Water Air Soil Pollution **85**, 779–784 (1995)
40. Cullen, J.T., Maldonado, M.T.: Biogeochemistry of cadmium and its release to the environment. In: Sigel, A., Sigel, H., Sigel, R. (eds.) Cadmium: From Toxicity to Essentiality, pp. 31–62. Springer, Dordrecht (2013)
41. Moiseenko, T.I., Morgunov, B.A., Gashkina, N.A., Megorskiy, V. V., Pesiakova, A.A.: Ecosystem and human health assessment in relation to aquatic environment pollution by heavy metals: case study of the Murmansk region, northwest of the Kola Peninsula, Russia. Environ. Res. Lett. **13**, 065005 (2018)
42. Garcia-Leston, J., Mendez, J., Pasaro, E., Laffon, B.: Genotoxic effects of lead: an updated review. Environ. Int. **36**(6), 623–636 (2010)
43. Wood, C.M.: Toxic responses of the gill target organ toxicity in marine and freshwater Teleosts. In: Schlenk, D., Benson, W.H. (Eds.), pp. 1–89. CRC Press/Elsevier, London (2001)
44. Acidification of mountain lakes. Acidification of mountain lakes and ecology of remote mountain lakes as indicators of air pollution and climate change (1995)
45. Monroy, M., Maceda-Veiga, A., Sostoa, A.: Metal concentration in water, sediment and four fish species from Lake Titicaca reveals a large-scale environmental concern. Sci. Total Environ. **487**, 233–244 (2014)
46. Wei, Y., Zhang, J., Zhang, D., Tu, T., Luo, L.: Metal concentrations in various fish organs of different fish species from Poyang Lake, China. Ecotoxicol. Environ. Safety **104**, 182–188 (2014)
47. Moiseenko, T.I., Dinu, M.I., Gashkina, N.A., Jones, V., Khoroshavin, V.Y., Kremleva, T.A.: Present status of water chemistry and acidification under nonpoint sources of pollution across European Russia and West Siberia. Environ. Res. Lett. **13**, 105007 (2018)
48. Cyr, A.P., López, J.A., Wooller, M.J., Whiting, A., Gerlach, R., O'Hara, T.: Ecological drivers of mercury concentrations in fish species in subsistence harvests from Kotzebue Sound, Alaska. Environ. Res. **177**, 108622 (2019)
49. Braaten, H.F.V., de Wit, H.A., Fjeld, E., Rognerud, S., Lydersen, E., Larssen, T.: Environmental factors influencing mercury speciation in Subarctic and Boreal lakes. Sci. Total Environ. **476**, 336–345 (2014)
50. Soto, D.X., Roig, R., Gacia, E., Catalan, J.: Differential accumulation of mercury and other trace metals in the food web components of a reservoir impacted by chlo-alkali plant (Flix Ebro River, Spain): implications for biomonitoring. Environ. Pollut. **159**, 1481–1489 (2011)
51. Satarug, S., Garrett, S.H., Sens, M.A., Sens, D.A.: Cadmium, environmental exposure, and health outcomes. Environ. Health Perspect. **118**(2), 82–190 (2010)
52. Brzoska, M.M., Moniuszko-Jakoniuk, J.: Interaction between cadmium and zinc in the organism. Food Chem. Toxicol. **39**, 967–980 (2001)
53. McGeer, J.C., Szebedinsky, C., McDonald, D.G., Wood, C.M.: Effects of chronic sublethal exposure to water-borne Cu, Cd or Zn in rainbow trout 2: tissue specific metal accumulation. Aquat. Toxicol. **50**, 245–256 (2000)
54. Annabi, A., Said, K., Messaoudi, I.: Cadmium: bioaccumulation, histopathology and detoxifying mechanisms in fish. Am. J. Res. Com. **1**, 60–79 (2013)
55. Li, J., Miao, X., Hao, Y., Xie, Z., Zou, S., Zhou, C.: Health risk assessment of metals (Cu, Pb, Zn, Cr, Cd, As, Hg, Se) in angling fish with different lengths collected from Liuzhou, China. Int. J. Environ. Res. Public Health **17**(7), 2192 (2020)
56. Li, Q., Nishijo, M., Nakagawa, H., Morikawa, Y., Sakurai, M., Nakamura, K., Kido, T., Nogawa, K., Dai, M.: Relationship between urinary cadmium and mortality in habitants of a cadmium-polluted area: a 22-year follow-up study in Japan. Chin. Med. J. **124**(21), 3504–3509 (2011)
57. Sigel, A, Helmut Sige, H, Sigel, R.: Cadmium: From Toxicity to Essentiality. Springer, p. 560 (2013)
58. Perez, E., Hoang, T.: Chronic toxicity of binary-metal mixtures of cadmium and zinc to Daphnia magna. Environ. Toxicol. Chem. **99**, 1–11 (2017)
59. Griffith, M.B.: Toxicological perspective on the osmoregulation and ionoregulation physiology of major ions by freshwater

animals: teleost fish, crustacea, aquatic insects, and Mollusca. Environ. Toxicol. Chem. **36**(3), 576–600 (2017)
60. Balbus, J.M., Boxall, A.B.A., Fenske, R.A., McKone, T.E., Zeise, L.: Implications of global climate change for the assessment and management of human health risks of chemicals in the natural environment. Environ. Toxicol. Chem. **32**, 62–78 (2013)
61. Landis, W.G., Durda, J.L., Brooks, M.L., Chapman, P.M., Menzie, C.A., Stahl, R.G., Jr., Stauber, J.L.: Ecological risk assessment in the context of global climate change. Environ. Toxicol. Chem. **32**, 79–92 (2013)
62. Stern, G.A., Macdonald, R.W., Outridge, P.M., Wilson, S., Chételat, J., Cole, A., Hintelmann, H., Loseto, L.L., Steffen, A., Wang, F., Zdanowicz, C.: How does climate change influence Arctic mercury? Sci. Total Environ. **414**, 22–42 (2012)
63. Lan, W.R., Huang, X.G., Lin, L.X., Li, S.X., Liu, F.J.: Thermal discharge influences the bioaccumulation and bioavailability of metals in oysters: Implications of ocean warming. Environ. Pollut. **259**, 113821 (2020)
64. Nardi, A., Mincarelli, L.F., Benedetti, M., Fattorini, D., d'Errico, G., Regoli, F.: Indirect effects of climate changes on cadmium bioavailability and biological effects in the Mediterranean mussel Mytilus galloprovincialis. Chemosphere **169**, 493–502 (2017)
65. Ahonen, S.A., Hayden, B., Leppänen, J.J., Kahilainen, K.K.: Climate and productivity affect total mercury concentration and bioaccumulation rate of fish along a spatial gradient of subarctic lakes. Sci. Total Environ. **637–638**, 1586–1596 (2018)

Peculiarities of the Geochemical Organization of the Modern Noosphere and Methods of Its Study for Detection of Endemic Diseases of Geochemical Nature

E. M. Korobova

1 Introduction

At present, there is a sharp worldwide increase in interest in the problems of geochemical ecology [1]. In particular, the works discuss the risk of diseases caused by increasing environmental pollution. This interest is instigated by a considerable growth of patients and specific endemic diseases (berylliosis, mercurialism, chromic pneumosclerosis, Itai-Itai etc.) occurring due to technogenic accidents and involvement in the biological cycle of large volumes of elements and compounds not peculiar to the natural environment. Prevention of such diseases requires strict control of food quality and the consistent implementation of environmental measures. At the same time, there is a growing need to develop new methods for assessing the risk of appearance of the provoked diseases for organisms living in various natural conditions since local food sources often differ significantly in the content of chemical elements.

During evolution, organisms have directly adapted to environmental changes and, on the other hand, have improved the conditions of this environment by creating bioinert [2] formations—soils and surface waters used as a substrate and a source of nutrients. Such an ongoing bilateral process led to complication and improvement of interaction between the living matter (according to Vernadsky) and the environment. At the same time due to the most severe competition between species in struggle for the light, space, and resources, all stable biocenoses should have existed in precisely optimal geochemical conditions. Otherwise, following the law of obligatory filling of ecological niches [3–6] and others, they would be almost immediately replaced by more viable communities. By conditions this situation excluded durable existence of endemic zones and the endemic diseases proper.

Nevertheless, people have known the spread of such endemic diseases since ancient times. Among the most common there are endemic goitre and the resulting cretinism. Such diseases mention written sources of ancient China, India, Egypt, Greece, the Roman Empire, and their symptoms were found 2000 years ago in America [7]. By the early 1950s, deficiency or excess of more than 25 chemical elements (B, Be, F, I, Se, As, Mo, Ca, Sr, Ba, Mn, Cr, Co, Ni, Cu, Zn, and others) were described as numerous biogeochemical provinces (according to [33]). The following studies continued revealing endemic diseases in animals and humans related to excess and deficiency of trace elements in different countries [8–24]. These facts proved that ecological and geochemical living conditions in such cases were far from optimum.

The search for the causes of the apparent paradox has led to creating the concept of the modern noosphere and developing a new methodological approach to detecting and preventing endemic diseases of geochemical nature.

2 Specifics of the Structural Organization of the Modern Noosphere

Analysis of the observed biogeochemical endemics showed that all of them are peculiar to either humans or cultivated plants and animals [25]. On the contrary, no stable endemic diseases were recorded among wild animals and native plants. Moreover, anthropological studies of ancient people also did not reveal any signs of such diseases [26]. These facts led to conclusion that such diseases occurred after the emergence of *Homo* sapiens as a species that turned out to be able to survive in unfavourable conditions, including geochemical ones.

Indeed, the geochemical structure of the primary biosphere has formed over billions of years. Over time, life has

E. M. Korobova (✉)
Vernadsky Institute of Geochemistry and Analytical Chemistry, Russian Academy of Sciences, 19, Kosygin St., Moscow, 119991, Russia
e-mail: korobova@geokhi.ru

V. P. Kolotov and N. S. Bezaeva (eds.), *Advances in Geochemistry, Analytical Chemistry, and Planetary Sciences*,
https://doi.org/10.1007/978-3-031-09883-3_26

covered the entire planet, and the exchange of matter between organisms and the environment occurred in the entire range of sharply different geochemical environments. This variety led to the formation of distinctive flora and fauna of individual regions. It is this variety which A. P. Vinogradov probably meant when he linked geographical variability of organisms to their biological responses to changes in geochemical environments of two types: (1) natural selection of local flora and fauna under the influence of the environment and (2) biological variability associated with the appearance of races, species, and subspecies [27].

It has already been said that the ideal correspondence of all species to the parameters of their ecological niche under conditions of highly rigorous natural selection (competition) made it practically impossible to have stable endemic diseases. Intelligence in one universally adaptable species turned out to be not only a decisive competitive advantage providing for its almost undivided dominance but also a factor of qualitative modification of the entire environment. In this new state, the biosphere ceased to be an entirely self-organizing and self-regulating system.

The concept of "noosphere" as a new stage of the biosphere evolution was first formulated by V. I. Vernadsky. Having borrowed the term from the French mathematician and philosopher E. Le Roy, he considered the noosphere a material object of biogeochemical study. Noting the qualitative differences of the two states of the system, he wrote: "With the appearance on our planet of an intellectually gifted living being, the planet transits into a new stage of its history" [28, p. 258]. Further developing the idea, Vernadsky emphasized: "… greater independence [of man], than all other organisms, from its conditions is the main factor which, in the end, emerged in the geological evolutionary process of creation of the noosphere" [29, p.42].

However, even after becoming intelligent, man has not ceased to be part of a system from which he "cannot be free for a second". His metabolism results from the entire long history of the evolution of life and is fixed by genetic mechanisms that guarantee survival. Vernadsky underlined that the absence of traces of abiogenesis and azoic (devoid of life) geological epochs witnesses the following. "…firstly, the modern living matter is genetically related to the living matter of all past geological epochs; and secondly, that during all that time conditions of the terrestrial environment were available for its existence, that is, were continuously close to modern" [30, p. 20]. The obligate consequence is that finding themselves in a geochemical environment that did not correspond to the genetically fixed conditions that existed in the places of their formation, any of the migrating species must either suffer from this mismatch and disappear quickly or adapt just as quickly. *Homo sapiens*, however, appeared to be an exception to the general rule—thanks to a decisive competitive advantage, he could survive for a long time in suboptimal conditions and rapidly populated almost the entire planet available to him. Which, however, did not mean that such colonization caused no adverse consequences.

In our opinion, this is the reason why biogeochemical endemic diseases have a pronounced spatial localization, i.e., they strictly appear in areas characterized by the specific chemical composition of the soil, water, and/or vegetation. It is worth mentioning that biogeochemical endemic diseases associated with biogeochemical provinces could be narrowly localized (azonal) or occupy entire natural zones, with azonal biogeochemical provinces closely related to geochemical provinces [31–33].

The above provisions allow concluding that, firstly, there exists a geochemical optimum for *Homo sapiens* similar to any other creature. It is a complex of geochemical conditions of the environment in which man has formed as a species. Secondly, a significant difference from this optimum geochemical background concerning chemical elements present in the environment is a sign of biogeochemical province.

In this respect, considering the process of human evolution as a species, we can state that the first stable endemic diseases of geochemical nature could appear only among *Homo sapiens* and those species of domesticated plants and domesticated animals, which accompanied him in the development of new places of residence. That is, it emerged at an early stage of civilization development and had a purely natural genesis.

The next stage in forming noosphere geochemical provinces emerged as civilization developed and corresponded to the beginning of the industrial revolution. This new factor in the geochemical transformation of the noosphere led to the entry into the biogeochemical cycle of a significant number of non-biosphere substances and compounds. These new elements and substances such as PAHs or artificial radionuclides provoked the appearance of previously unknown diseases. A characteristic structural feature of such provinces is their confinement to physical (point, less often linear) sources of release, which leads to the formation of geochemical anomalies of peculiar mono- and polycentric structure, usually well suited to modelling and mapping. However, studying the effects of the formation of such anomalies should also pay attention to the fact that the flow of matter from anthropogenic sources takes place in the background of pre-existing geochemical heterogeneity. As a result, both introduced and aboriginal species can suffer from negative geochemical impact, which significantly complicates the analysis of the causes of the prevalence of a set of modern diseases.

As there are almost no territories unaffected by anthropogenic geochemical influence, we can make a generalizing conclusion that the geochemical structure of the modern noosphere is genetically two-layered. It contains a relatively

thin (and often heterogeneous) layer of artificial origin that overlays the initial natural geochemical heterogeneity. Anthropogenic substances, penetrating the stable biogeochemical cycles, begin to noticeably change the ecological-geochemical situation since anthropogenic input can exceed the natural concentrations of individual elements and often contains many elements' isotopes and compounds alien to the biosphere.

3 Concerning Specificity of the Mechanism of Adaptation to Geochemical Environmental Conditions

The ability of organisms to occupy a wide variety of ecological niches is presented by many examples of their adaptation to even the most complicated geochemical environments. However, the mechanism of this adaptation has not yet been fully disclosed.

Millions of experiments carried out with experimental animals and plants using different doses of macro-and micronutrients have demonstrated the presence of individuals capable of surviving and recovering in extreme geochemical conditions. Currently, there are two main hypotheses for the formation of the species survival mechanism: (1) random mutations of individuals with a positive outcome followed by genetic fixation, and (2) the presence in species or races of a hereditarily fixed ability to survive specifically in extreme conditions. Results of experiments and the direction of preceding evolution allow a logical inference that the safety mechanism for protection of not individuals, but populations proper was in due time "on-demand" genetically fixed as "sleeping genes" which are activated randomly only in the sufficient minimum of individuals of a population. We know that the volume of inherited (genetic) information in each specimen is enormous. At the same time, a considerable part of information is preserved in "sleeping" (inactive) genes, which give the possibility, in case of emergencies, for example, to one individual out of a thousand (the one having necessary gene being active) to survive and give viable offspring in the form of stable morph capable of quick recovery of the whole population. The action of just such a mechanism was explicitly shown, for example, in the experiments of Prat [34], Bradshaw [35, 36] and others. They demonstrated that such a mechanism of protection against external influences reliably works only when in every individual of a population a different set of "dormant" genes is activated, because of which the complete set of active genes in the individual is specific. This mechanism demands the existence in any local population of a small but a sufficient number of individuals possessing safety mechanisms for an immediate response to almost the entire range of possible extreme influences. Thus, the population remains reliably protected even in the case of the death of more than 99% of population members. This mechanism not only provides an immediate response to changes in the environment but is also the most effective since experience shows that it ensures the safety of existing species and biocenoses in the case of extreme (including infectious) influences capable, under other conditions, of irrevocably destroying them. This hypothesis is also confirmed by the scientific facts related, for example, to the use of insecticides against the Colorado potato beetle. Recently, subspecies were found to tolerate insecticide treatment differently in their evolutionary tree [37].

Such inherited mechanisms appear to exist in all living organisms, including humans. We believe that consideration of this hypothesis should be a priority for geneticists since even an accidental result of an external (artificial) impact, which natural protective mechanisms cannot counter, may turn out to be catastrophic.

The geochemical concept of the modern noosphere can be briefly outlined as follows.

1. The main problem of the ecological branch of biogeochemistry is the establishment of existing regularly formed links between the geochemical parameters of the habitat and the state of living organisms living in this environment. The practical solution to the problem is to reveal regularities in the spatial distribution of endemic diseases of geochemical origin.
2. The geochemical heterogeneity of the biosphere has evolved under two complementary processes. On the one hand, the living organisms targetedly adapted to the changing environment. On the other hand, they improved the environment by forming bioinert matters used as substrates and sources of nutrients. Thus, these processes in the primary biosphere brought into being a regular concordance between all living organisms and their environments, and all biogeocenoses ideally corresponded to the whole complex of their environmental parameters.
3. The stable biogeochemical endemic diseases result from the appearance in the biosphere of the intelligence species *Homo sapiens* that has caused the biosphere's transition to the noosphere. At that, the first geochemical endemic diseases had a purely natural origin. A complete absence of these diseases in the indigenous species is their peculiar feature.
4. With the development of civilization, industry and agriculture, technogenic biogeochemical provinces and endemic diseases caused by local and sometimes global pollution of almost all environmental objects came into being and spread. Their difference from the natural is that

(1) they have other spatial structure (mono-or polycentric anomaly in the zones of technogenic pollution around the sources of contamination); (2) they affect practically all organisms living in the contaminated areas, including indigenous, and (3) they always exist in the initially natural geochemical background, including environmentally unfavourable.

Thus, it is reasonable to distinguish between endemic biogeochemical diseases of three types: (1) natural, (2) technogenic, (3) combined natural and technogenic. Accordingly, the structure of modern geochemical provinces can be mapped and accounted of in biogeochemical zoning and the construction of maps of the geochemical risk of endemic diseases.

4 Methodological Approaches to Biogeochemical Zoning of the Noosphere

Like any other zoning, biogeochemical zoning is nothing more than a tool for schematizing existing ideas about the continuous environment, suitable for solving a particular class of problems with certain accuracy and detail. One should note that, despite many attempts, there is no universal zoning and cannot be as the approaches and methods of zoning must be consistent with the parameters of the problem. The purpose and the spatial and temporal scale of the study define the optimal decision.

To date, there are two qualitatively different principles of biogeochemical zoning. The first one is the spatial division of the area according to the variability of the basic biogeochemical properties of the environment (the biogeochemical zoning proper). The second is spatial mapping distribution of the biological effects due to the interaction of certain species with the environment (e.g. maps of the specific diseases distribution or the risk of their appearance).

Zoning can be based on the integrated approach (taking into account the main geochemical components) and the particular (based on the analysis of changes in the concentration of a single element).

At the same time, an important issue is the selection of primary cartographic layers corresponding to both the natural differentiation of the area and the level of anthropogenic loads.

The integral result of the interaction of all living organisms with the environment is reflected by the structure and chemical composition of the soil cover. In this sense, M. M. Kamshilov called the soil the "ecologically optimized substrate" [38, p. 152]. The modern high level of chemical exploration of the soil cover and the stability of its composition shown by [39, 40] and others allows using soil maps as fundamental in assessing natural biogeochemical differentiation of the area [24].

Technogenic pollution is formed due to deposition of contaminants from the atmosphere, pollutant discharge into the river system, ameliorants application, etc. Its structure is well identified by the source and composition of pollutants that form characteristic mono- or polycentric anomalies of the corresponding chemical elements and compounds.

Basing on the proposed approach, the algorithm for building risk maps reduces to the following sequence of operations:

(1) construction of a natural risk map based on the soil map with the ranking of soil cover in terms of the potential abundance of the studied chemical element or group of elements.
(2) construction of a map of technogenic risk by ranking the area according to the degree of contamination with the studied chemical element or group of elements.
(3) overlay operation and constructing a map of combined (natural and technogenic) risk with the ranking of separated areas by the level of total risk.
(4) spatial comparison of the constructed risk maps with medical data on the prevalence of various diseases.

5 Example of Building Thyroid Disease Risk Maps

As mentioned above, endemic thyroid diseases have been known for over 3,000 years, and methods of prevention are also known. Nevertheless, according to the International Agency for Research on Cancer (IARC), the incidence of thyroid disease is increasing worldwide, with the prevalence of this disease over the past five years being highest in the developed and developing countries: the United States and Canada, Australia, China, etc. (Fig. 1).

In 2020, thyroid cancer (ThC) was included in the top 20 diseases in terms of mortality among women, with the lowest mortality from ThC in Central and Southern Africa (Fig. 2).

Without disputing the connection between disease prevalence and the level of population surveys and mortality with the level of medical care, which are certainly lower in countries with lower incomes, it should be noted that the developed countries are not characterized by minimum values of the level of morbidity. In our view, this is in part due to the lack of study of the relationship between diseases and geochemical environmental conditions. In this respect, we studied the peculiarities of the prevalence of thyroid diseases among the population of the regions affected by the

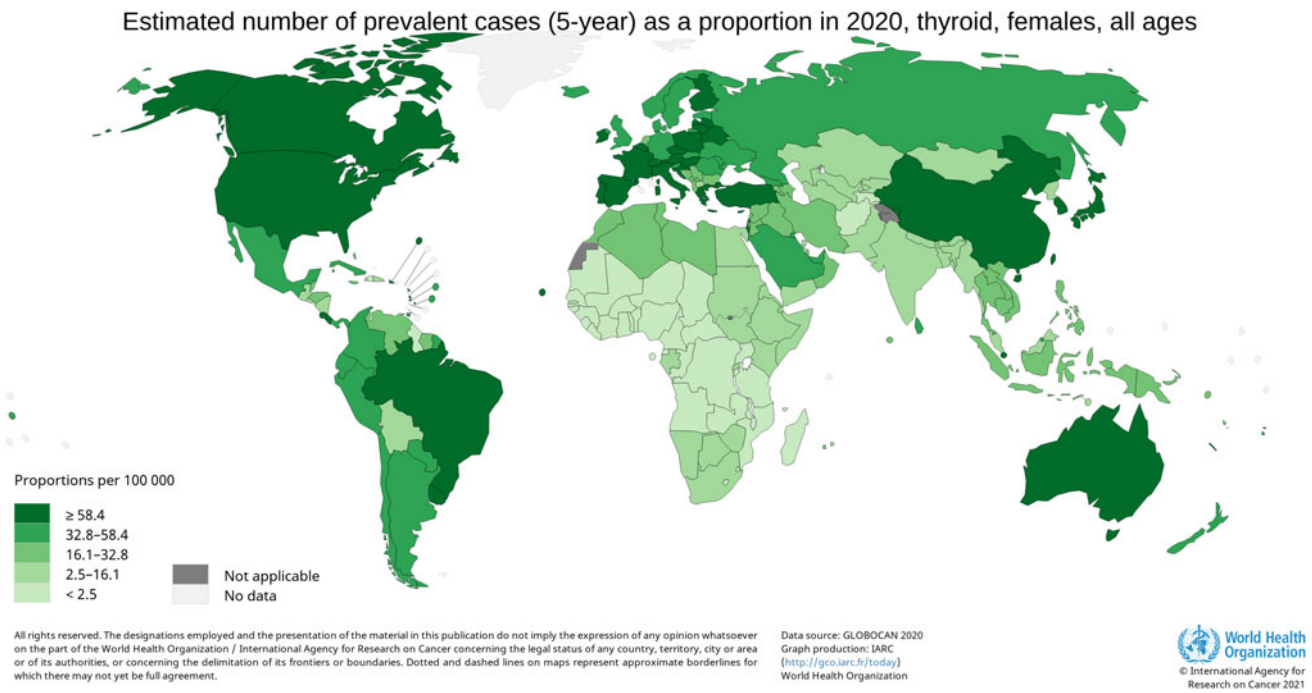

Fig. 1 Number of ThC cases among women of all ages over 5 years (2016–2020), IARC data [41]

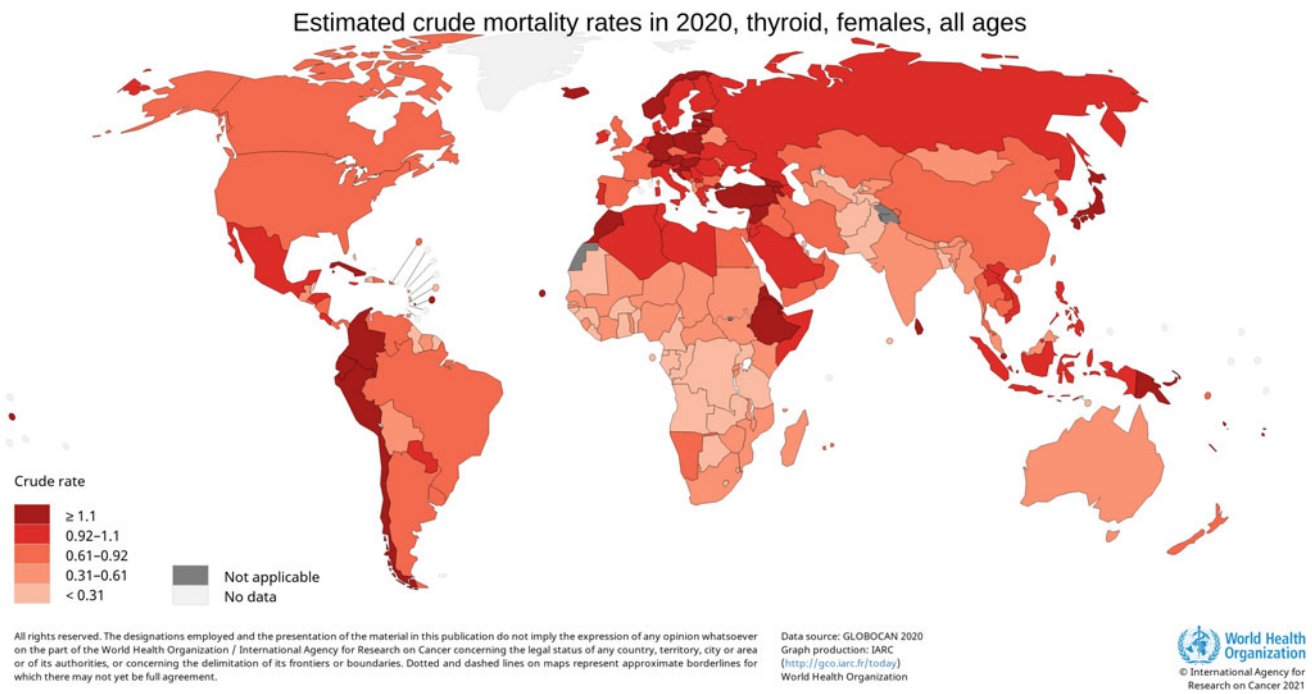

Fig. 2 The mortality rate of women of all ages from ThC in 2020 (IARC data, [42])

Chernobyl catastrophe. The principal point was that a significant amount of radioactive ^{131}I entered local food chains, which led to the so-called "iodine attack" that is the enhanced irradiation of the thyroid gland functionally concentrating iodine. Thereby, soils of the affected territories differed in stable iodine soil supply in places by ten times, and the level of contamination with ^{131}I varied by orders of magnitude.

Figure 3 shows an example of the construction of a thyroid disease risk map for the four regions of the Russian

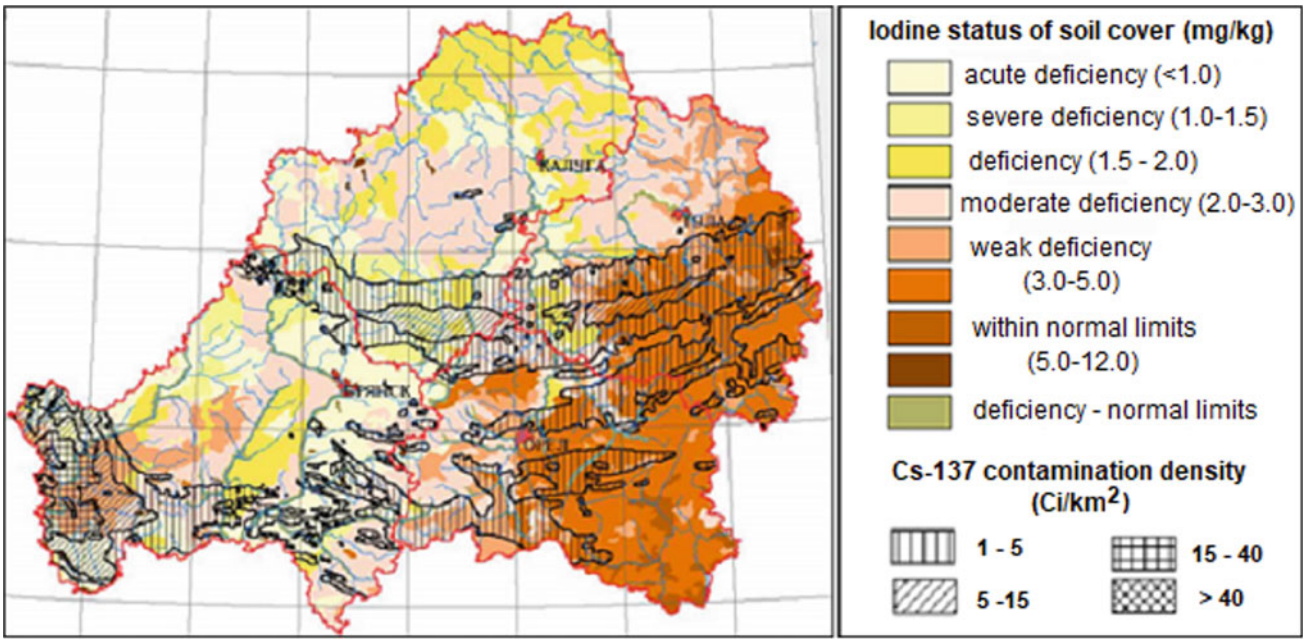

Fig. 3 Superposition of iodine availability in soil and contamination of the territory with radioactive isotopes ^{137}Cs (after [42, 43]). Note that the density of ^{131}I fallout was evaluated by using equation in [43], another estimate is proposed in [44]

Federation affected by the Chernobyl accident. At this stage of work, we used a ^{137}Cs contamination map to show the distribution of radionuclide contamination without recalculations from ^{137}Cs to ^{131}I.

The quantitative estimate of stable iodine status of the soil cover around the affected settlements was used in a population-based case—control study within the IARC international project for evaluating the risk of thyroid cancer [45]. The results showed that the level of iodine deficiency appeared sufficient to provoke almost a three-fold increase in the risk of thyroid cancer among children living in the most affected areas of Russia and Belarus irrespective of consumption of potassium iodide (Table 1).

The construction of a combined risk map accounting for both the "iodine attack" and iodine deficiency demanded the development of a particular methodology to rank the contaminated settlements according to the supply of stable iodine and construct a map of ^{131}I deposition density. This was based on the values of parameters established in ^{131}I/^{137}Cs equation proposed by Zvonova [47]. The other electronic variant of the combined natural and technogenic risk map was constructed utilizing specialized GIS [48]. This map was overlaid with a grid of administrative districts (Fig. 4). The procedure made it possible to compare the assessed risk levels with the medical data available per district. Thanks to cooperation with the Bryansk Clinical Diagnostic Center, it was also possible to compare the incidence of thyroid cancer among the population of rural and urban settlements of the region (Fig. 5).

The obtained risk map estimates showed not only satisfactory similarity with the observed pattern of disease incidence but also revealed differences in the level (Fig. 5) and dynamics (Fig. 6) of the spread of thyroid cancer among the rural and urban populations.

Thus, the basic applicability of the proposed concept and the representativeness of the used methodological approaches were tested experimentally and confirmed statistically.

Table 1 Estimated risk of developing thyroid cancer after a radiation dose of 1 Gy, by level of soil iodine in the settlement of residence at the time of the accident and by potassium iodide (i.e., antistrumin) consumption status (subjects with radiation doses to the thyroid of less than 2 Gy) (after [45] with soil levels shown in [46]

Consumption of potassium iodide	Odds ratio at 1 Gy compared with no exposure 95% confidence interval	
	Highest two tertiles of soil iodine (> 2.5 mg/dm^3)	Lowest tertile of soil iodine (< 2.5 mg/dm^3)
No	3.5 (1.8–7.0)	10.8 (5.6–20.8)
Yes	1.1 (0.3–3.6)	3.3 (1.0–10.6)

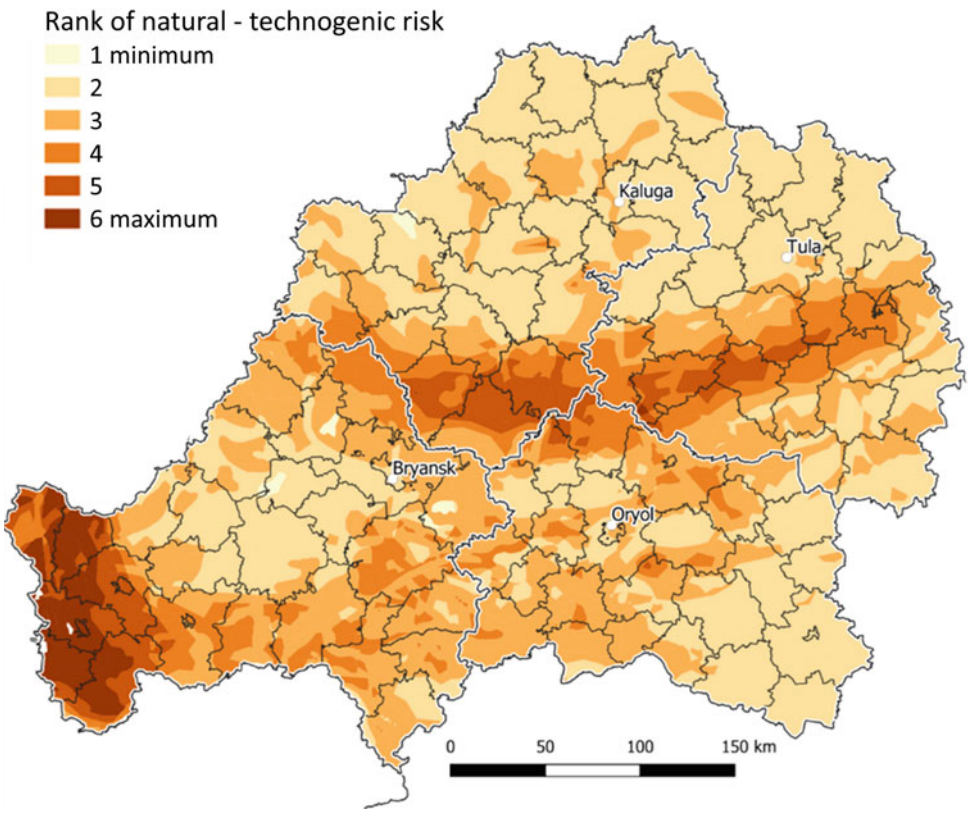

Fig. 4 Ranking of the four regions of the Russian Federation affected by the Chernobyl accident in terms of thyroid disease risk due to a combination of iodine deficiency level and exposure to radioactive iodine isotopes (in the absence of preventive measures)

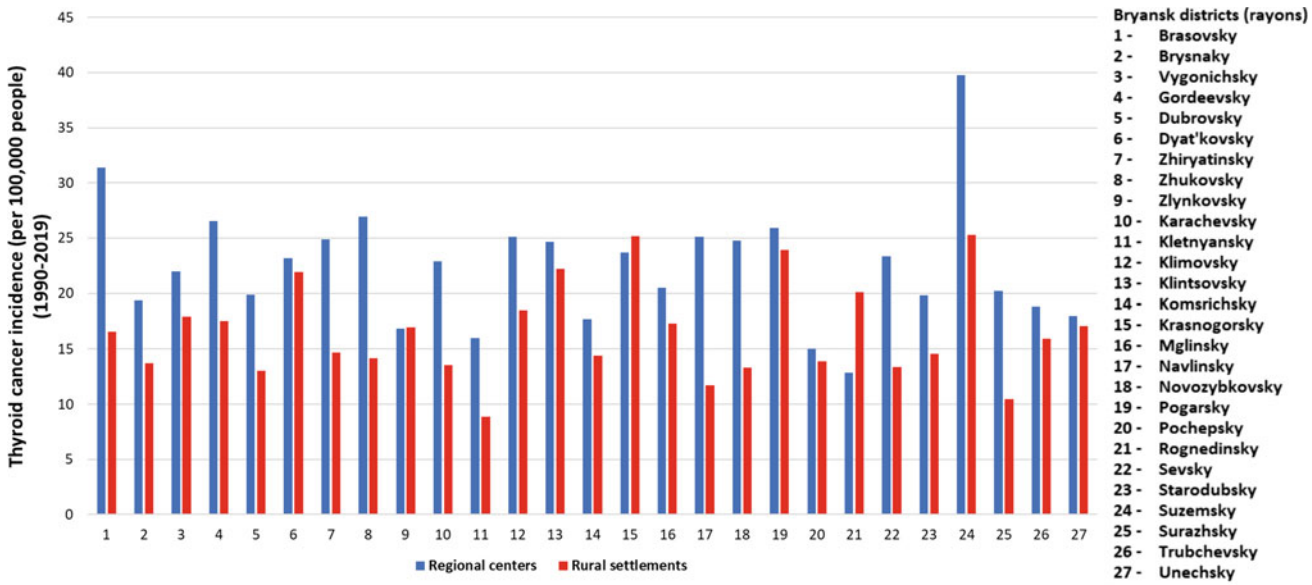

Fig. 5 The number of thyroid cancer cases among the residents of urban and rural settlements of the Bryansk region for five-year periods after the Chernobyl accident for period from 1990 to 2019 (according to the data of the Bryansk Clinical Diagnostic Center)

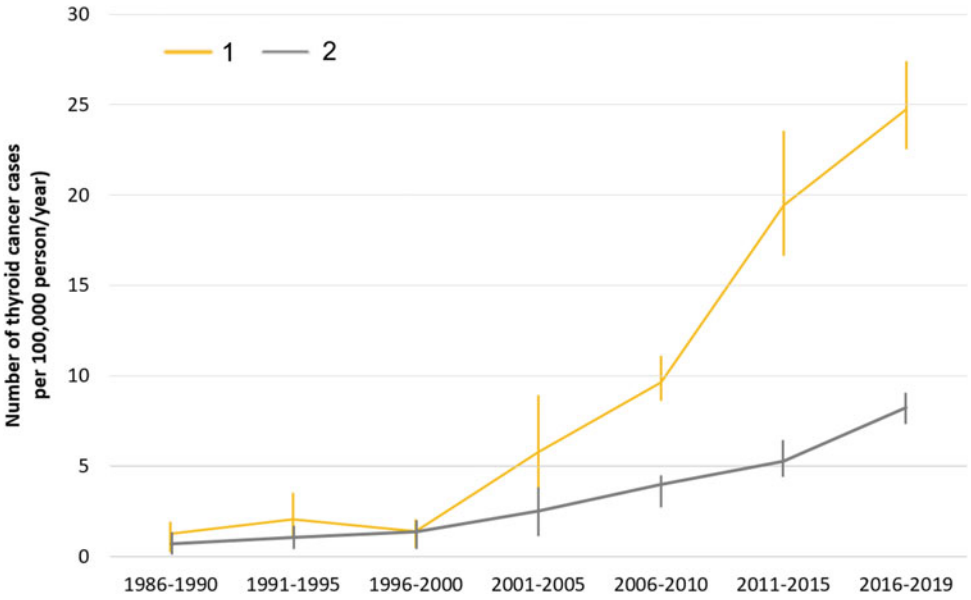

Fig. 6 The dynamics of thyroid cancer growth among the residents of urban (1) and rural (2) settlements of the Bryansk region for five years after the Chernobyl accident (after [49])

6 Conclusions

1. With the appearance of Homo sapiens, the primary biosphere has undergone a radical qualitative change, passing to the noosphere. With the further development of civilization, its geochemical structure began to change. The modern noosphere is now a two-layer geochemical system formed by a superposition of geochemical fields of natural and anthropogenic genesis.
2. The regular structural ordering of the natural and anthropogenic layers of the noosphere can be mapped by a priori means in the form of an appropriate cartographic surface.
3. The geochemical structure of intact soil cover can mark the natural geochemical background. At the same time, the anthropogenic component of the modern noosphere in most cases is a set of superimposed geochemical anomalies of mono- or polycentric type. Hence, its contribution is relatively easy to quantify.
4. The essential task of geochemical ecology in assessing the comfort of the geochemical environment can be theoretically correctly solved by analyzing the interference picture obtained by the cartographic combination of natural and anthropogenic geochemical structures, which can be interpreted as a risk map, comprehensively characterizing the combined environmental geochemical impact on all ecosystem components, including animals and humans.

Acknowledgements I thank my colleagues Victor Berezkin, Lyudmila Kolmykova and Vladimir Baranchukov for assistance in field and laboratory work and data handling. I am grateful to Boris Ryzhenko and Sergey Romanov for productive discussion and Ivan Kryshev for valuable comments. The work is conducted under the GEOKHI RAS state assignment. This work was partly funded by the Russian Foundation for Basic Research and Belorussian Republican Foundation for Basic Research (grant #20-55-00012).

References

1. Kovalsky, V.: Geochemical Ecology. Nauka, Moscow (1974)
2. Vernadsky, V.: Biosphere. Thoughts and Sketches. Collection of Scientific Works by V.I. Vernadsky. Publishing House "Noosphere", Moscow (2001)
3. Darwin, C.: The Origin of Species by Means of Natural Selection: Collected Works in 9 vols, vol. 3. Moscow, Leningrad (1939)
4. Gause, A.: Ecology and Evolutionary Theory. Nauka, Leningrad (1984)
5. Shvarts, S.: Influence of microelements on animals in natural conditions of ore field. Tr. Biogeochem. Lab. **10**, 76–81 (1954)
6. Shvarts, S.: Ecological Regularities of Evolution. Nauka, Moscow (1980)
7. Bauduera, F., Tankersley, K.: Evidence of an ancient (2000 years ago) goitre attributed to iodine deficiency in North America. Med. Hypotheses **118**, 6–8 (2018)
8. Shoshin, A.: Fundamentals of Medical Geography. Publishing House of USSR Academy of Sciences, Leningrad (1962)
9. Avtsyn, A., Zhavoronkov, A., Rish, M., Strochkova, L.: Microelement Diseases of Man. Meditsina, Moscow (1991)
10. Avtsyn, A.: Introduction to Geographical Pathology. Meditsina, Moscow (1972)
11. Shkolnik, M.: Micronutrients in Plant. Nauka, Leningrad (1974)
12. Shkolnik, M., Makarova, N.: Microelements in Agriculture. Publishing House of USSR Academy of Sciences, Moscow, Leningrad (1957)
13. Zhavoronkov, A., Mikhaleva, L., Avtsyn, A.: Microelementosis—a new class of human, animal and plant diseases. In: Proceedings of Biogeochemical Laboratory, vol. 23. Nauka, Moscow (1999)
14. Fuge, R., Johnson, C.: The geochemistry of iodine—a review. Environ. Geochem. Health **8**, 31–54 (1986)

15. Fuge, R., Johnson, C.: Iodine and human health, the role of environmental geochemistry and diet, a review. Appl. Geochem. **63**, 282–302 (2015)
16. Islam, M., Lahermo, P., Salmanin, R., Rojestaczer, S., Peuroniami, V.: Lake and reservoir water quality affected by metals leaching from tropical soil Sri Lanka. Environ. Geochem. **39**(10), 31–35 (2000)
17. Johnson, C.: The Geochemistry of Iodine and its Application to Environmental Strategies for Reducing the Risks from Iodine Deficiency Disorders (IDD). CR/03/057N (2003)
18. Guyot, H, Saegerman, C., Lebreton, P., Sandersen, C., Rollin F.: Epidemiology of trace elements deficiencies in Belgian beef and dairy cattle herds. J. Trace Elements Med. Biol. **23**, 116–123
19. Watts, M., Mitchell, C.: A pilot study on iodine in soils of Greater Kabul and Nangarhar provinces of Afghanistan. Environ. Geochem. Health **31**, 503–509 (2009)
20. Yu, H., Zhang, K.: Links between environmental geochemistry and rate of birth defects: Shanxi Province, China. Sci. Total Environ. **409**, 447–451 (2011)
21. Axelson, U., Söderström, M., Jonsson, A.: Risk assessment of high concentrations of molybdenum in forage. Environ. Geochem. Health **40**, 2685–2694 (2018)
22. Pi, K., Wang, Y., Xie, X., Su, C., Junxia, L.: Hydrogeochemistry of co-occurring geogenic arsenic, fluoride and iodine in groundwater at Datong Basin, northern China. J. Hazard. Mater. **300**, 652–661 (2015)
23. Jemal, A.: Trace elements geochemistry in high-incidence areas of liver-related diseases, northwestern Ethiopia. Environ. Geochem. Health. (2019). https://doi.org/10.1007/s10653-019-00387-3
24. Kolmykova, L., Korobova, E., Gromyak, I., Korsakova, N., Danilova, V.: Ecological and geochemical assessment of the chemical composition of drinking water of the Bryansk region in connection with an increased risk of thyroid disease. Geochemistry **65**(1), 64–76 (2020)
25. Korobova, E.: Genesis and regularities of spatial organization of modern biogeochemical provinces. D. thesis for the degree of Doctor of Geology and Mineralogy. GEOKHI RAS, Moscow (2016)
26. Buzhilova, A.: Adaptive processes in the ancient population of Eastern Europe: according to the data of paleopathology: doctoral thesis. Moscow (2001)
27. Vinogradov, A.: Biogeochemical provinces and endemies. Doklady AS USSR 1 1963. № 3. C. 199–213 (1963)
28. Vernadsky, V.: The study of life phenomena and new physics. Works on soil geochemistry and biogeochemistry (after 1910). In: Galimov, E.M. (ed.) Collected Works, vol. 7 (2013)
29. Vernadsky, V.: Philosophical Thoughts of a Naturalist. Nauka, Moscow (1988)
30. Vernadsky, V.: Biosphere and the Noosphere. Nauka, Moscow (1989)
31. Vinogradov, A.: Fluorine in Nature: to the question of fluorine as a cause of so-called mottling of enamel. Hygiene Sanitation **3**, 11–25 (1937)
32. Vinogradov, A.: Biogeochemical provinces and endemic diseases. Rep. USSR Acad. Sci. **18**, 4–5 (1938)
33. Vinogradov, A.: Basic regularities in the distribution of trace elements between plants and the environment. In: Proceedings of the Conference on Trace Elements March 15–19, 1950, pp. 7–20. Publishing House of the Academy of Sciences of the USSR, Moscow (1952)
34. Prat. S.: Die erblichkeit der Resistenz gegen Kupfer. Ber. Dtsch. bot. Ges. L, 65–67 (1934)
35. Bradshaw, A.: Populations of Agrostis tenuis resistant to lead and zinc poisoning. Nature **169**, 28 (1952)
36. Bradshaw, A.: Plant evolution in extreme. In: Ecological Genetic and Evolution, pp. 79–93. Oxford, Edinburgh (1971)
37. Brevik, K., Bueno, E., McKay, S., Schoville, S., Chen, Y.: Insecticide exposure affects intergenerational patterns of DNA methylation in the Colorado potato beetle, *Leptinotarsa decemlineata*. Evolut. Appl. (2020). https://doi.org/10.1111/eva.13153
38. Kamshilov, M.: Evolution of the Biosphere. Nauka, Moscow (1974)
39. Gennadyev, A.: Soils and Time: Models of Development. Moscow State University Press, Moscow (1990)
40. Romanova, T.: Diagnostics of Soils of Belarus and Their Classification in FAO-WRB System. RUP "Institute for Soil Science and Agrochemistry", Minsk (2004)
41. International Agency for Research on Cancer (IARC), World Health Organization (WHO): Cancer today. Estimated number of prevalent cases (5-year) as a proportion in 2020, thyroid, females, all ages. https://gco.iarc.fr/today/online-analysis-map?v=2020&mode=population&mode_population=continents&population=900&populations=900&key=crude_rate&sex=2&cancer=32&type=2&statistic=5&prevalence=1&population_group=0&ages_group%5B%5D=0&ages_group%5B%5D=17&nb_items=10&group_cancer=1&include_nmsc=1&include_nmsc_other=1&projection=natural-earth&color_palette=default&map_scale=quantile&map_nb_colors=5&continent=0&show_ranking=0&rotate=%255B10%252C0%255D. Last accessed 2021/09/30
42. Korobova, E., Kuvylin, A.: To estimate iodine status of territories affected by radioisotope iodine deposition as a result of the Chernobyl accident Radioactivity after nuclear explosions and accidents. In: Izrael, Y. (ed.) International CONFERENCE 2005, vol. 3, pp. 202–206. Hydrometeoizdat, Moscowx (2006)
43. Mahonko, K., Kozłowa, E., Volokitin, A.: Radioiodine accumulation on soil and reconstruction of doses from iodine exposure on the territory contaminated after the Chernobyl accident. Radiation Risk **7**, 90–142 (1996)
44. Gavrilin, Y., Volkov, V., Makarenkova, I.: Retrospective reconstruction of the integral exposures of iodine—131 for the settlements of the Bryansk region of Russia based on the results of determination in 2008 of iodine-129 content in soil. Radiation Hygiene **2–3**, 38–44 (2009)
45. Cardis, E., Kesminiene, A., Ivanov, V., et al.: Risk of thyroid cancer after exposure to ^{131}I in childhood. J. Nat. Cancer Inst. **97**, 10 (2005)
46. Korobova, E., Anoshko, Y., Kesminiene, A., Kouvyline, A.: Evaluation of stable iodine status of the areas affected by the Chernobyl accident in an epidemiological study in Belarus and the Russian Federation. J. Geochem. Explor. **107**, 123–134 (2010)
47. Korobova, E.: Ecological and Geochemical Problems of the Modern Noosphere. RAS, Moscow (2019)
48. Baranchukov, V., Korobova, E., Romanov, S.: Application of geoinformation technologies for minimization of thyroid gland diseases in the impact areas of the radioiodine fallout, EGU General Assembly 2020, Online, 4–8 May 2020, EGU2020-9000. https://doi.org/10.5194/egusphere-egu2020-9000 (2020)
49. Korobova, E., Baranchukov, V., Kurnosova, I., Silenok, A.: Spatial geochemical differentiation of the iodine-induced health risk and distribution of thyroid cancer among urban and rural population of the Central Russian Plain affected by the Chernobyl NPP accident. J Environ. Geochem. Health (2021) (in press)

Geochemical Ecology of Organisms in the Biosphere Technogenesis: Analytical Review and Some Results

V. A. Safonov

1 Geochemical Ecology and Biosphere Taxons

Living organisms are spread all over the world. They inhabit the hydrosphere, upper part of the lithosphere, and the lower layers of the atmosphere, forming the biosphere. The biosphere is characterized by significant heterogeneity associated with the diversity of lithosphere structure and geological materials. The chemical composition of organisms significantly affects the processes of soil formation, enrichment of soils with mineral elements, its structure, and physicochemical peculiarities. The formed variety of soils is one of the determining factors of the biological diversity of ecological communities of microorganisms, plants, and animals. In general, the biosphere is a unique, integrated, and well-coordinated ecological system that is relatively balanced and dynamically changing. Within this system, the organisms are closely associated with each other and with surrounding non-organic biogeochemical feeding chains. They are involved in the biogenic pathways of migration of chemical elements via organic matter and geochemical medium [1, 2].

Within the boundaries of the biosphere, living systems absorb atoms from the surrounding space and use them in the processes of biogenic migration, create cycles of chemical elements, accumulate, and diffuse them. Living matter extracts elements from some molecules and includes them in the composition of other molecules, forming new chemical compounds with peculiar properties. Biochemical reactions would be impossible without the presence of mineral elements. Their fundamental functions include the formation of cells and tissues, production of energy, work of cellular membranes, maintenance of homeostasis, activation of biochemical reactions within enzymatic systems, and transfer of inherited information [1, 3, 4].

The normal functioning of all living organisms occurs within the range of the optimal number of biogenic and toxic elements and their compounds. At the same time, nearly any biogenic element becomes toxic in certain conditions. The limiting upper and lower boundaries of the optimal ranges are called “threshold concentrations”. The capability to regulate metabolic processes within these threshold concentrations is determined by the genetic and phenotypic peculiarities of an organism. Threshold concentrations are limiting upper and lower boundaries of the content of chemical elements in soils, water, air, feed, food products, fluids, and organism tissues. Between them, an organism can regulate metabolic processes. The levels of elements lower than minimal and higher than maximal values lead to disturbances of physiological regulation. Plants, humans, and animals develop dysfunctions, biochemical changes in metabolism, morphological changes in organs, and endemic diseases. The threshold concentrations maintain the coordination and stability of metabolic processes but keep open the pathways for changes and evolution of organisms, ecosystems, and biosphere under the influence of extreme factors of geochemical medium [5, 6].

The levels of chemical elements that maintain living forms can vary depending on the peculiarities of biosphere taxons. Kovalsky suggested three orders of such taxons based on the principle of geographic continuity: regions of the biosphere, subregions of the biosphere, and biogeochemical anomalies or provinces. Subregions have certain biogeochemical features and run into one another with more or less evident boundaries [7]. Part of a biosphere subregions with constant elevated or decreased threshold values of chemical elements concentration is characterized by the constant manifestation of endemic biogeochemical reactions in living organisms. Another part of subregions is only potentially dangerous for the development of endemic pathologies. Still, there are areas of the subregions where only rare manifestations of certain biological reactions are possible [8].

V. A. Safonov (✉)
Vernadsky Institute of Geochemistry and Analytical Chemistry, Russian Academy of Sciences, 19 Kosygin St., Moscow, 119991, Russia
e-mail: vsafonov2020@mail.ru

V. P. Kolotov and N. S. Bezaeva (eds.), *Advances in Geochemistry, Analytical Chemistry, and Planetary Sciences*,
https://doi.org/10.1007/978-3-031-09883-3_27

Specific clinical manifestations of biological reactions are diverse. For example, zinc deficiency leads to the development of parakeratosis and local dermatoses, mucous and cartilaginous lesions, and alopecia [9, 10]. Iodine deficiency in combination with selenium deficiency impairs thyroid hormones metabolism causing endocrine disorders in humans and animals and hypothyroidism [11, 12]. Accumulation of toxic elements in animals is often manifested as toxicoses with peculiar features. Thus, the excess of lead provokes disturbances of CNS function, anemia, and posterior paralysis. The excess of nickel leads to skin lesions, eyesight impairments, gastroenteritis, and vascular thrombosis; cadmium—to osteoporosis, nephrosis, calcium, and phosphorus metabolism disorders. Besides, apart from specific signs, the violation of threshold concentrations of chemical elements leads to general functional disorders that include a decrease in agricultural animal productivity, worsening of reproductive capacity, immune reactions, organism resistance, and development of tumor diseases [13, 14]. Diselementoses in plants lead to growth inhibition, delay of phonologic phases, decrease in linear sizes of sprouts and roots, and a reduction of biomass accumulation. High levels of toxic elements in the environment lead to the damage of the root system, chlorosis, and the decay of leaves [15]. The excessive amount of heavy metals leads to a decrease in the activity of soil enzymes and crop yield, and the production of food products that do not meet the safety requirements [16]. It should be noted that in the course of evolution, many species of plants developed protective mechanisms that include concentration, deconcentration, and hyperaccumulation of chemical elements. These mechanisms allow the species to exist in biogeochemical provinces with anomalous and high levels of some chemical elements [17]. Animals also use mechanisms based on the regulation of cellular permeability, activation of enzymes of detoxication, binding of heavy metal atoms with nutrients and intracellular proteins (metallothioneins) [18, 19].

2 Technogenic Modification of the Biosphere

Anthropogenic activity significantly enhances the redistribution of biosphere substances. New biogeochemical provinces of technogenic origin appear because of an acute growth of industrial activity, mining, and processing of mineral deposits, functioning of objects of energetic complex, extensive land utilization, application of fertilizers and pesticides, war activities, and trials.

Agricultural activity exerts upscale and severe influence on the landscape, soils, hydrogeographic network, underground waters, and atmosphere. A significant part of natural ecological communities is transformed by humans into agrobiocenoses with controlled flows of organic and non-organic matter [20, 21].

In modern life, humans need not only agricultural food products but also developed industry and technologies. The term "technogenesis" proposed by the academician Fersman in 1934 reflects significant anthropogenic impact in evolution processes [22]. "Technogenesis is a combination of chemical and technical activities produced by humans that leads to the redistribution of chemical masses of the earth's crust. Technogenesis is a geochemical activity that results from the industrial activity of humans". Technogenic modifications significantly change the outlook of all biosphere.

The development of a large complex of events and geological processes that results from mining is especially evident. Technical progress allowed humans to mine ore deposits from ten to thousands of meters deep, and in some cases, more than 10 km deep [23]. Thus, in some areas, the migration of substances accelerates manifold. The quarry and further enrichment of mineral deposits lead to the formation of man-made objects. The appearance of technogenically changed soils (technosol) that include the mixture of unevenly granulometric composition of uncovering and enclosing ore deposits. Solid mining operations wastes, called tailing dumps, mix with soils and form technosols. Areas of degradation appear with reduced biodiversity, expressed worsening of soil fertility, and erosive processes [24].

The activity of humans inevitably causes biogeochemical transformation. New natural-technogenic taxons with a deficiency of essential microelements constantly appear. Along with this, biogeochemical provinces appear, wherein the content of chemical elements exceeds the upper threshold concentration, which is dangerous for the health and existence of living organisms. Thus, more and more attention is paid to the complex many-sided evaluation of the technogenic effect on the biosphere. A significant contribution is made by a relatively new scientific direction called geochemical ecology. Kovalsky defined this science as "a science that studies the interaction of organisms and their communities with the geochemical medium in the biosphere as well as organisms in populations, biocenoses, biochemical provinces, and areas as structural parts of a common organized ecological system (biosphere) (1974) [1]. Geochemical ecology provides data on the chemical composition of living organisms in a close association with the environment, biological reactions to the changes in the geochemistry of ecosystems and creates the basis for ecological monitoring and measures for technogenic pollution management.

3 Biological Reactions of Living Organisms

The excess of heavy metals associated with the appearance of natural and technology induced biogeochemical provinces provokes response changes in all groups of living organisms. Pollution of soils with heavy metals affects the structure of

cenosis of microorganisms: their number and ratio of ecologic-trophic groups. In many cases, field observations on sites with high toxic load show a reduction of the bacterial population, which is caused by the inactivation of enzymes by binding heavy metals with sulfhydryl groups of protein molecules, inhibition of protein synthesis, and impairment of bacterial cell membrane permeability. However, the study of soils in the Sverdlovsk Region, that are highly affected by technogenic load due to polymetallic dust emissions from the ore mining and processing industry, showed that aerobic and anaerobic cellulose-degrading bacterial had adaptive biological reactions. This provided an increase in the microorganism population and their activity in polluted soil [25, 26]. The development of tolerance can be explained by the passive formation of complexes with organic compounds [27]. Protective reaction, common for all living organisms, activates the transportation mechanisms of heavy metals redistribution so that they get bound with metallothionein. In response to an increase in the level of pollutants inside a cell (for example, mercury, cadmium, copper), the number of metallothioneins increases. These complexes exist for a short time and function during periods of intoxication and stress impact [28].

The binding of heavy metals with other biomolecules leads to unfavorable effects. Such complexes are often similar by their biologically active compounds, have similar geometric proportions, or distribution of charges. They compete with enzymes, hormones, and neuromediators. Complexes with heavy metals inhibit antioxidant enzymes that prevent the accumulation of excessive amounts of hydrogen peroxide (H_2O_2). In reactions of oxidation, hydrogen peroxide acts as a precursor of a highly toxic hydroxyl radical. Besides, metals with mixed valence accelerate the rate of formation of reactive oxygen intermediate (ROI). Intensification of peroxide and free-radical reactions enhance the damage of proteins, lipids, and nucleic acids. The damage of lipid bilayer of cellular membranes leads to changes in permeability and cellular death. Thus, in the condition of technogenic pollution, living organisms are also prone to oxidative stress.

Plants developed a capacity to resist intoxication by forming complexes of phytochelatins with heavy metals. This mechanism of detoxication binds up to 90% of metals and realizes within three stages: the synthesis of a peptide with a phytochelatin synthase activated by a metal ion, formation of a complex with heavy metal, and transport of the complex into the vacuole [29]. Suppression of oxidative stress occurs due to the activation of the enzymatic link of antioxidant protection. The synthesis of flavonoids, phenolcarbonic acids, and tannins enhances in plant's organs. A high rate of antioxidants production is observed in *Polygonum aviculare L.* Usually, it acts as a pioneering plant that starts growing in technogenic transformed territories [30].

The biological reaction of a plant organism on technogenic pollutants includes an accumulation of toxic elements in vegetative and reproductive organs. The accumulation of toxicants is determined by the peculiarities of functioning of physiological barriers "root-stem", "stem-leaf", and "stem-reproductive organs". As a rule, they are more expressed for highly toxic elements and less expressed for less toxic biogenic elements. The degree of accumulation significantly varies depending on the toxicant and plant's species or geni. The choice of species indicators in the ecological-geochemical studies is based on this property. For example, a birch (*Betula pendula Roth* and *Betula pubescens Ehrh.*) is used for the assessment of the ecological situation on urbanized and man-made landscapes because it is characterized by an expressed accumulation of the most toxic heavy metals in leaves: cadmium, nickel, lead, and manganese. Birch leaves contain up to 650 mg/kg of manganese (dry matter), while in other species (poplar, ash tree, linden), it varied within 100–120 mg/kg. The content of cadmium in birch samples is 2 times higher than in poplar samples and 7 times higher than in ash tree and linden) [31].

Macro and hyperconcentrations of chemical elements, often met among plants, are also observed in animals. Thus, macroconcentration is spread among invertebrates: crustaceans, arachnids, gastropods, and earthworms [32, 33].

The high intensity of free radical reactions in animals with toxic stress activates various mechanisms of antioxidant protection. Response induction of its enzymatic link is the most important protective reaction that fights oxidative stress caused by the technogenic modification of the environment. In bivalved mollusks (*Dreissena polymorpha Pallas*) that inhabit Rybinsk water storage reservoir polluted with heavy metals (lead, vanadium, chromium, nickel, zinc, and copper) coming from industrial objects of Cherepovets city, a simultaneous increase in the content of malondialdehyde (product of lipid peroxidation) and activity of catalase (an antioxidant enzyme). The same occurs also in the experimental conditions of exposure to cadmium at the dose of 34 mg/L. The activity of lactase, glutathione peroxidase, and glutathione reductase increased in water ecosystems in fish and invertebrates [34, 35]. In young bovine cattle livestock, the levels of malondialdehyde increased by 55.1–94.2%, antioxidant protein ceruloplasmin—by 1.12–2.05 times, and activity of catalase—by 1.1–1.7 times in response to an increase of mean normative concentrations of cadmium by 32.4–47.2%, lead—by 23.0–26.5%, and nickel—by 15.6–17.0%. The changes in oxidant-antioxidant status are more expressed in cases when intoxication is complicated by bronchopneumonia and gastroenteritis [36].

Intensification of free-radical oxidation in living organisms occurs not only in cases of excessive impact of toxic elements. Often, the manifestation of oxidative stress is observed in biogeochemical provinces with low levels of

separate microelements in ecosystems. Thus, some studies revealed a deficiency of selenium in soils and plants in the Kirov Region. In pregnant cows with the provision of microelements at the level of 44.2–62.5% from the level of Voronezh Region (favorable area), the accumulation of malondialdehyde was 20.2–95.5% higher in similar cows in the Voronezh Region. Apart from this, in a biogeochemical province, a deficiency of selenium leads to a reduction of activity of the glutathione antioxidant system. It was mostly revealed in down-calving cows. The levels of glutathione peroxidase were higher by 42.3% and glutathione reductase by 2.5 times [37, 38].

The condition of the environment significantly affects the spread of non-contagious pathology in animals. A long-term living in technogenically transformed conditions leads to some general changes in hemopoiesis and immune biological reactivity to an organism. Large bovine cattle are characterized by an inhibition of hemopoietic function in the Sverdlovsk Region in areas polluted with heavy metals and radionuclides. These animals have decreased levels of erythrocytes (by 17.9%), hemoglobin (by 27.1%), and color index (by 9.3%), increased levels of eosinophils, and relatively expressed monocytosis. Eosinophil count in cattle with chronic intoxication with aluminum, copper, lead, and cadmium was 3–4 times higher than in favorable regions. Early signs of impairments include changes in the functional activity of the immune system. In an unfavorable ecological situation, cattle have a decrease in the lymphocyte count, suppression of T-cells, and a synthesis of immunoglobulins. Both an increase and a decrease of parameters of phagocyte activity of neutrophils and phagocytic index can be observed. The function of humoral immunity worsens and lysozyme and bactericidal activity of the blood reduces. Xenobiotics provoke tissue damage, which is expressed as the growth of anime transferase activity [39, 40]. The study of the biogeochemical condition of the Unal crater revealed a high level of lead in local plants, which led to the intoxication of animals. In this case, a decrease in the concentration of hemoglobin and activity of dehydratase δ-aminolevulinic acid in the blood of large bovine cattle. The activity of acetylcholinesterase in the blood serum was at the minimal physiological level [41].

In iodine-deficient areas (0.012–0.093 mg/kg I in soil) of the Ryazan Region that are characterized by elevated levels of zinc, lead, cadmium, copper, arsenic, and ^{137}Cs, calves have disturbances in the development of glandular tissues and myocardium. Disorders of the myocardium lead to the pathological rhythm of blood circulation in vessels. Older animals have anomalies in the development of lacteous glands, mastitis, immune disorders, and reduced resistance to leucosis. In the unfavorable areas, 15% of calves are born with incurable hypoplasia of the thyroid gland. Under ecotoxication and iodine deficiency, there are deviances in the development of morphological structure of the glandular tissue in field voles (*Microtus arvalis Pall* and *Clethrionomys glareolus Schreb*) and their embryos have developmental disorders [42].

A significant environmental contamination of biogeochemical provinces with xenobiotics via a trophic chain "soil–plant-animal" leads to contamination of food products obtained on farms located nearby industrial objects. Because of certain peculiarities of the distribution and accumulation of heavy metals by animal organs, the consumption of subproducts (liver, kidney, and lungs) is more dangerous than meat. These organs accumulate heavy metals more actively than meat [43]. Heavy metals and other toxic elements can be detected in milk. It is important to prevent the transport of toxicants along the food chain to animals and humans by the establishment of ecological-geochemical monitoring in the biogeochemical provinces and sources of pollutants and implementation of meliorative, recultivative, and other measures.

4 Geochemical Ecology of Organisms in the Technogenic Biogeochemical Anomalies in Russia

4.1 Tyrnyauz Wolfram-Molybdenum Province

The peculiarities of biogenic migration of molybdenum and other microelements in the condition of technogenic biogeochemical province with extremely high content of wolfram and molybdenum were studied. This hypermolybdenum anomaly is located on the territory of the river Baksan basin in the Kabardino-Balkarian Republic. It appeared because of the migration of the tailing dump of the Tyrnyauz mining and processing plant. Wolfram-molybdenum deposit was discovered in 1934 and mined by an underground method since 1940 and by a combined method since 1968. Deposits of ore are classified as scheelite-molybdenum type with the content of Mo 0.03–0.2%, W—up to 0.8%, Cu—0.3%. Besides, they contain the concomitant elements: Ag, Au, Bi, Se, and Tl. For economic reasons, mining is stopped there at the moment. However, half-century activity of the plant left around 106 million tons of waste in two tailing dumps. The sources of environmental pollution include solid waste spread by wind, migration of metals from the main quarry with waters of Maliy and Bolshoy Mukulan springs, and feeding waters of Baksan. Biogeochemical studies were carried out in 2003, 2009, and 2019. The sampling of water, soil, plants, and production animal milk was performed on 32 sites of polluted and reference territories [44].

It was established that because of the interaction of Bolshoy Mukulan spring with the quarry ore, its waters got intensively enriched with minerals. The mineralization of

water was 518 mg/L. The content of calcium was 188.4 mg/L and exceeded the content of magnesium by 10 times. In the water filtered from the suspended particles, the concentration of molybdenum did not exceed 10 μg/L. The highest levels of copper were revealed in the water of the river (5.8 μg/L). The content of wolfram was 9–10 μg/L in the area of Tyrnyauz-Bylym. Besides, high content of rhenium was revealed in the area of Tyrnyauz-Bylym. In the probes of running water, its content was 0.54 μg/L; in the probes from springs and river Kamyksu, the concentration of rhenium was 0.19–0.55 μg/L, which 10–50 times exceeded the reference values. In general, the concentration of metals in the basin of river Baksan did not exceed the exiting hygienic norms for drinking water [45, 46].

The study of soil showed that the left bank of the Baksan river within the areas of Tyrnyauz and Bylym is a natural and man-induced biogeochemical province with anomalous levels of molybdenum and wolfram in the environment. Some of the obtained soil samples were enriched with lead (up to 150 mg/kg) and arsenic (up to 60–80 mg/kg). The effluent o the former Tyrnyauz plant contains high levels of wolfram (511 mg/kg), molybdenum (341 mg/kg), and in some cases, elevated levels of copper. In some samples, the concentration of metals reaches up to 1000 mg/kg, which makes effluents of Tyrnyauz wolfram-molybdenum plant meet the criteria of a man-made deposit [47].

The plants that grow in the basin of the river Baksan experience a deficiency of essential microelements I and Se in the combination with high levels of iron that reach up to 342 mg/kg. Elevated levels of molybdenum and wolfram were revealed in plants from Tyrnyuaz and Bylym (the content of Mo—up to 31 mg/kg, W—up to 12 mg/kg). The plants from meadows located nearby the tailing dump contained dangerous concentrations of some elements for farm animals (Mo—64.5 mg/kg and W—33 mg/kg). It was noted that the coefficient of biological accumulation of wolfram was lower in comparison with molybdenum. The most intensive accumulation of Mo and W by plants is observed within the mining anomaly of Tyrnyauz and Bylym. Plants that grow on the territory of Tyrnyauz deposit also accumulate rhenium.

The study of samples of milk and fat-free cream of local large bovine cattle demonstrated a transition of metals from plant feed to animal organism and animals farm products. Thus, their content in the fat-free cream increased by 5–10 times in comparison with samples provided by the farmers from the reference areas (Prokhladnyi city and Zayukovo village). In the blood and hair samples, the levels of Mo and W were also elevated in comparison with the reference areas. The study of molybdenum toxicoses in animals showed molybdenum was antagonistic to copper and sulfur. It is especially evident in cases when copper prevailed over molybdenum in the consumed feed. The revealed low provision of selenium and iodine can be associated with the risk of white-muscle disease in young livestock and hypothyroidism [48–50].

Based on the systemic studies of this subregion of the biosphere, a formation of nature and technogenic biogeochemical anomaly was revealed that is characterized by the presence of a complex of toxic pollutants resulted from the operation of Tyrnyauz wolfram-molybdenum plant and migration of its pollutants from the tailing dumps.

4.2 Technogenic Anomaly of the River Ardon Basin

A complex study of polymetallic technogenic anomalies of the Sadonsk ore field was performed. Special attention was paid to the sources of pollution of territories and migration of Pb, Zn, Cd, Cu, and As within the Ardon river basin and Unal tailing dump of the former Mizursk Mining and Processing Plant (the Republic of North Ossetia-Alania). Man-induced interventions resulted in the formation of a biogeochemical province with a critical content of toxic chemical elements in the Sadonsk polymetallic ore region. The study included the streambed of the river Ardon basin. Unal tailing dump is located nearby the village Unal on the right bank of the river Ardon in the place of the outlet of rivers Unaldon and Mairamdon. The tailing dump was formed in 1984 to store the wastes from the Mizurskiy Mining and Processing Plant. During the period of its active performance, a total of 3 million ton of tailings were accumulated [41].

In the formation of a technogenic biogeochemical anomaly, a significant contribution was made by effluent waters from the tailing dump, dust, and pulp as well movements of metals with Ardon and Unaldon streams. Filtered water from the Unaldon river contains high concentrations of zinc (447 μg/L) and cadmium (1.8 μg/L). Filtered effluents from the tailing dump contained 2.6–10.8 μg/L of lead, 0.3–95 μg/L of cadmium, 8.0–10.4 μg/L of copper, and 130–160 μg/L. The concentrations of metals in the river increase after the dump of effluents. The levels of lead increased from 0.2–0.6 to 0.8–1.6, cadmium—from 0.06–0.27 to 0.1–0.35, copper—from 1.4–2.9 to 2.2–3.7, and zinc—from 28–50 to 25–62 μg/L. In discharge waters, the concentrations of sulfate-ion and selenium were 3200 and 1.6 mg/L, respectively. A hundred meters from the area of discharge, the content of sulfate-ion decreased by 10 times, and in the river mouth, the content of sulfate-ion was 50–60 mg/L and selenium—200–330 μg/L.

High concentrations of heavy metals in the alluvium of the Ardon river were detected 12 km away. There are two anomalies of lead and copper nearby the tailing dump. One of them is associated with deflation of the tailing dump

surface. The second one appeared after the outflow of clarified water from the sedimentary reservoir.

Technogenically transformed soils around the Unal tailing dump are severely polluted with metals. Under the influence of wind erosion and deflation, the pulp of the Mizursk plant forms technosols with heavy metal-enriched upper layers. For example, the content of metals in the superficial layer 0–10 cm is 10 times higher in comparison with their content in a lower horizon > 15 cm. A similar tendency of a metal distribution is observed in soils nearly in all the studied areas. In the transformed pulp, the following concentrations of metals were detected: lead—3.54%, zinc—2.73%, and cadmium—248 mg/kg. Thus, the pulp from the tailing dump is a man-made deposit of the mentioned chemical elements. In the pulp samples, the content of arsenic was 10–15 times higher than in the reference areas. The main part of the studied heavy metals is present in technosols in a close association with organic matter and iron and manganese hydroxides. The same is true for arsenic. The largest part of mobile compounds is typical for cadmium. In soils of various degrees of contamination, the mobility of toxic elements increases. There were no significant changes revealed in the migration of chemical elements within a 20-year period of study [51].

A significant influence of the air pathway of pollution was revealed. The areas of lower terraces of the river Ardon are characterized by intensive dust sediments that vary from 74 to 304 kg/km^2 per day.

A reduction of plant species diversity and biomass harvested from 1 m^2. Some species have signs of such diseases as chlorosis and leave necrosis [52]. There are strong correlations between the levels of toxic elements in plants and soils. Thus, s strong correlation was revealed between the level of zinc in soil and birch leaves (r = + 0.892), the levels of copper and lead in the harvested hay (r = + 0.98–0.99), in birch leaves, it is less expressed (r = + 0.69–0.73). The data comparison showed that the content of arsenic decreased from 1999 to 2019. Within the borders of the Unal tailing dump, the level of As in the harvested hay decreased by 3–5 times, and in the reference areas—by 5–10 times, which indicated the mobility of arsenic in landscapes and its inclusion in biochemical cycles.

Technogenic impact on the plant cover is also manifested as dust pollution. At the distance of 1.5–2 km from the tailing dump, the leaves get significantly covered by pollutants. The water fraction of the washed-away pollutants contains around 16–40.2% of the total content of metals. In the reference areas, these values were 6.2–6.5%.

The enzymatic activity and hemoglobin levels used as bioindicators of animals reaction revealed lead intoxication in large bovine cattle in vil. Mizur and Unal. The levels of lead and arsenic were elevated in the samples of animal hair taken in vil. Mizur and Unal: 0.82–6.23 mg/L and 1.1–2.5 mg/kg, respectively. The content of cadmium was 0.73–1.31 mg/kg, zinc—91–152 mg/kg, and copper—11.4–18.6 mg/kg. The content of zinc was close to the samples from the reference areas (115 ± 5 mg/kg), the levels of other mentioned metals and arsenic exceeded the reference values by 8–10 times. High levels of lead and arsenic were also revealed in animals hair from samples taken in vil. Ramonovo. The elevated content of these chemical elements is a risk factor. Still, there were no evident biological reactions revealed in animals during the study.

The complex of biogeochemical studies in the basin of the river Ardon allowed the researchers to classify some territories as natural and technogenic biogeochemical anomalies of the primary and secondary genesis with an excessive amount of metals and selenium and iodine deficiency. Because of a high content of heavy metals and concomitant mobile forms of arsenic, the described biosphere taxons are characterized as areas of ecological risks.

4.3 Technogenic Anomalies in the Novotroitsk Gold-Arsenic Deposit

In 2019–2021, the study on geochemical ecology of natural and technogenic anomalies in the Southern Urals was continued. One of the last studies was dedicated to the content of arsenic and heavy metals in biogeocenoses formed as a result of mining of the gold-arsenic deposit located nearly the city of Plast (Chelyabinsk Region). The Novotroitsk tailing dump was formed in the city by the wastes of the mining and enrichment plant [53]. To study how the human impact affects the ecological condition of a technogenic anomaly, the researchers have gathered the samples of water, soil, technosols, plants, and animal hair on 12 sites.

A high content of arsenic is typical for water nearby the tailing dump. At a distance of 200 m from its borders, the content of the toxic element was 490 μg/L. While in a reference water reservoir nearby vil. Kichigino (> 35 km from the tailing dump), this parameter was 4 μg/L. In the running water of Plast city, the concentration of arsenic was minimal (0.3 μg/L).

The excess of the maximum allowable concentration of arsenic was revealed in technosols of the tailing dumps. The mean concentrations of the chemical element in probes were 787.7 mg/kg (tailing dump 0–20 cm deep) and 72 mg/kg (100 m from the tailing dump). The reference level was 9.6 mg/kg. At the same time, it was noted that high levels of As were detected at a closing slope of the man-made object: mean level was 1097.5 mg/kg and maximal concentration was 1360 mg/kg. On the contrary, probes from the top of the tailing dump contained 410 mg/kg of arsenic and probes from the slopes—572.3 mg/kg. Such distribution of the toxic element can be explained by the processes of migration

of chemical elements with drainage waters. A similar scheme of distribution is observed for lead. In the top of the tailing dump, the level of lead was 16.1 mg/kg, in the slopes —20.1 mg/kg, in the points of closing slopes—29.8 mg/kg. The level of copper was 23.5 mg/kg on the top of the tailing dump, 30.8 mg/kg on the slopes, and 36.2 mg/kg in the points of closing slopes. The level of zinc was 56 mg/kg on the top of the tailing dump, 72.8 mg/kg in the slopes, and 72 mg/kg in the closing points. The level of cadmium was 1.36 mg/kg on the top of the tailing dump, 1.47 mg/kg in the slopes, and 1.55 mg/kg in the points of closing slopes. Such consistencies were not revealed for nickel and strontium.

The concentration of As in technosols hundreds of times higher than the allowable (maximum allowable concentration—2.0 mg/kg) determines the accumulation of the toxic element by above and under the ground plant organs. In the sprouts of umbelliferous plants sampled in 2021 in various areas of the tailing dump, the concentration of As was 11.5–72.1 mg/kg, in the root system—10–184 mg/kg, in birch leaves—27.6 mg/kg, and pine straw—83.1 mg/kg. Birch leaves from the reference vil. Kichigino contained 3.0 mg/kg of arsenic and pine straw—1.4 mg/kg. There is a correlation between the content of As in the root system and technosol ($r = +0.76$). A moderate correlation is also observed for Zn ($r = +0.57$), Cd ($r = +0.48$), and Cu ($r = +0.47$).

The analysis of the samples of mole fur (Talpa europaea) revealed a significant degree of environmental contamination with arsenic. The mean content of the element in the samples of mole fur that inhabit the tailing dump was 212.8 mg/kg, in the samples from the reference areas—0.9 mg/kg (> 15 km, vil. Demarino, riv. Kabanka). The concentrations of some metals also exceeded the reference values: Zn—by 1.3, Cu—by 2.1, Pb—by 4.2, Hg—by 33.5 times [54].

It is known that an insignificant content of arsenic is present in living systems and the supplements with its compounds can be used in bird farming to increase the quality of eggshells. At the same time, arsenic is a potent toxicant that can block some essential compounds and enzymatic systems. Intoxication with arsenic impairs redox processes and the energetic mechanisms of cellular respiration. Thus, the Novotroitsk tailing dump and similar man-made objects negatively affect the ecological condition of biosphere taxons [32, 33, 55].

5 Conclusion

Presently, the number of technogenic anomalies is constantly increasing. Their formation is associated with waste landfilling, dumping of polluted water, emissions of industrial pollutants into the atmosphere, and agrotechnical activities. The lack of focus on these problems inevitably leads to negative consequences for the environment significantly worsening the ecological situation in the country and region. No doubt that the appearance of natural and technologenic biogeochemical anomalies leads to an increase in the rate of pathological conditions (microelementoses) [56, 57]. Considering rapidly developing technogenesis of the biosphere, it is of high importance that ecological, biogeochemical, and associated researches are focused on the study of heavy metals accumulation and migration as well as radionuclides, and other toxic pollutants.

References

1. Kovalsky, V.V.: Geochemical Ecology. Science, Moscow (1974)
2. Kovalsky, V.V.: Geochemical Environment and Life. Science, Moscow (1982)
3. Oberlis, D., Kharland, B., Skalnyi, A.: Biological Role of Macro and Microelements in Humans and Animals. Science, Saint Petersburg (2008)
4. Nieder, R., Benbi, D.K., Reichl, F.X.: Microelements and Their Role in Human Health. Soil Components and Human Health, pp. 317–374. Springer, Dordrecht (2018)
5. Kovalsky, V.V.: Threshold concentration of chemical elements in soils and possible reactions of organisms. In: Microelements in the Biosphere and Their Application in Agriculture and Medicine in Siberia and the Far East, pp. 30–39 (1973)
6. Tunakova, Yu.A., Novikova, S.V., Faizullin, R.I., Valiev, V.S.: Approximation of the dependency of trace elements concentrations in internal media upon their contents in environmental objects. BioNanoScience **8**, 288–295 (2018)
7. Kovalsky, V.V.: Regions of the biosphere are based on the biogeochemical regional patterns. In: Biosphere and Its Resources. Science, Moscow (1971)
8. Perelman, A.I.: An association between biogeochemical provinces and landscape geochemistry. In: Issues of Biogeochemistry and Geochemical Ecology, pp. 115–133. Science, Moscow (1999)
9. Naresh, R., Dwivedi, S.K., Dey, S., Swarup, D.: Zinc, copper and cobalt concentrations in blood during inflammation of the mammary gland in dairy cows. Asian Australas. J. Anim. Sci. **14**(4), 564–566 (2001)
10. López-Alonso, M., Prieto, F., Miranda, M., Castillo, C., Hernández, J., Benedito, J.L.: The role of metallothionein and zinc in hepatic copper accumulation in cattle. Vet. J. **169**(2), 262–267 (2005)
11. Vorobyov, V., Vorobyov, D., Polkovnichenko, P., Safonov, V.: Evaluation of hematological and metabolic parameters in small ruminants with trace element s deficiency under different biogeochemical conditions. World's Veterinary J. **9**(4), 311–316 (2019)
12. Vorobyev, V.I., Vorobyev, D.V., Zakharkina, N.I., Polkovnichenko, A.P., Safonov, V.A.: Physiological status of 'king' squab pigeon (Columba Livia gm. Cv. 'king') in biogeochemical conditions of low iodine, selenium and cobalt levels in the environment. Asia Life Sci. **28**(1), 99–110 (2019)
13. Ermakov, V.V., Moiseenok, A.G., Safonov, V.A., Kovalsky, Y. V.: Biogeochemistry of polyelemental microelementoses. Food Ind. Sci. Technol. **12**(3(45)), 24–30 (2019)
14. Chalaya, O.S., Chalyi, A.I.: Peculiarities of ecotoxic influence of cadmium on some biological objects of agrobiocenoses. Animal Farming Veterinary Med. **4**, 3–7 (2019)

15. Titov, A.F., Kaznin,a N.M., Talanova, V.V.: Heavy Metals and Plants: Monography. Karelia Scientific Center of the RAS, Petrozavodsk (2014)
16. Srivastava, V., Sarkar, A., Singh, S., Singh, P., de Araujo, A.S.F., Rajeev, P.: Agroecological responses of heavy metal pollution with special emphasis on soil health and plant performances. Front. Environ. Sci. **5**, 64 (2017)
17. Ufimtseva, M.D.: Consistencies in the accumulation of chemical elements by higher plants and their reactions in the abnormal biogeochemical provinces. Geochemistry **5**, 450–465 (2015)
18. Janssens, T.K.S., Roelofs, D., van Straalen, N.M.: Molecular mechanisms of heavy metal tolerance and evolution in invertebrates. Insect Sci. **16**, 3–18 (2009)
19. Gashkina, N.A., Moiseenko, T.I., Kudryavtseva, L.P.: Fish response of metal bioaccumulation to reduced toxic load on long-term contaminated Lake Imandra. Ecotoxicol. Environ. Saf. **191**, 110205 (2020)
20. Singh, N., Gupta, V.K., Kumar, A., Sharma, B.: Synergetic effects of heavy metals and pesticides in living systems. Front. Chem. **5**, 70 (2017)
21. Shurpali, N., Agarwal, A.K., Srivastava, V.K.: Greenhouse Gas Emissions. Challenges, Technologies and Solutions, 1st edn. Springer (2019)
22. Fersman, A.E.: Geochemitry, vol. 2. ONTI. Goschimizdat, Leningrad (1934)
23. Kazdym, A.A.: Modern conceptual issues of technogenesis and mineralogy of technogenesis (theory and practice). Mineral. Technogenesis **9**, 238–252 (2008)
24. Konovalov, V.E., Germanovich, Y.G.: Migration of substances during ore mining and their primary processing. J. Higher Educ. Inst. J. Min. **2**, 30–39 (2018)
25. Medvedev, I.F., Derevyagin, S.S.: Heavy Metals in the Ecosystems: Monography. Saratov (2017)
26. Litvinenko, L.V., Gordeeva, V.A.: Influence of heavy metals on the viability of cellulose-degrading bacteria in the conditions of perennial technogenic pollution of sod-meadow soils. Acute Issues Humanitarian Nat. Sci. **2–3**, 50–54 (2017)
27. Sarret, G., Manceau, A., Cuny, D., van Haluwyn, C., Deruelle, S., Hazemann, J.-L., Soldo, Y., Eybert-Burard, L., Menthonnex, J.-J.: Mechanisms of lichen resistance to metallic pollution. Environ. Sci. Technol. **32**(21), 3325–3330 (1998)
28. Shaplygina, Y.N., Kurochkina, T.F., Nasibulina, B.M.: Peculiarities of the influence of heavy metals on river bottom organisms inhabiting Volga delta. Nat. Sci. **3**(44), 51–60 (2013)
29. Cobbett, C.S.: Phytochelatins and their roles in heavy metal detoxification. Plant Physiol. **123**(3), 825–832 (2000)
30. Nemereshina, O.N., Petrova, G.V., Shaikhutdinova, A.A.: Some aspects of adaptation of *Polygonum aviculare* L. to the pollution of soils with heavy metals. Issues Orenburg State Agrarian Univ. **1**, 230–234 (2012)
31. Vetchinnikova, L.V., Kuznetsova, T.Y., Titov, A.F.: Peculiarities of the accumulation of heavy metals in the leaves of tree plants on the urbanized territories in the conditions of the North. Works Karelia Sci. Center RAS **3**, 68–73 (2013)
32. Safonov, V.A., Samburova, M.A., Salimzade, E.O.A.: The indication of chemical elemental composition in the environmental objects in the conditions of technogenic biochemical provinces. In: Biological Diversity of Natural and Anthropogenic Landscapes: Study and Protection. Collection of Materials of II International Scientific-Practical Conference, pp. 215–220 (2021)
33. Samburova, M.A., Safonov, V.A.: The content of arsenic in the soil and living organisms in the area of man-made mineral formation. The impact of the COVID-19 on the economy and the environment in the era of the fourth industrial revolution. Book of abstracts, p. 62 (2021)
34. Klimova, Y.S., Chuiko, G.M., Gapeeva, M.V., Pesnya, D.S.: Parameters of oxidative stress in *Dreissena polymorpha* (Pallas, 1771) as a biomarker for the evaluation of chronic anthropogenic pollution of different areas of the Rybinsk tailing dump. Siberian Ecol. J. **2**, 210–217 (2017)
35. Das, D., Moniruzzaman, M., Sarbajna, A., Chakraborty, S.B.: Effect of heavy metals on tissue-specific antioxidant response in Indian major carps. Environ. Sci. Pollut. Res. **24**, 18010–18024 (2017)
36. Gertman, A.M., Samsonova, T.S., Manina, E.M., Naumova, O.V., Karimova, G.A.: Lipid peroxidation—antioxidant system in calves with non-contagious pathology in the conditions of ecologically unfavorable situation and methods of its correction. In: Acute Issues of Biotechnology and Veterinary Sciences: Theory and Practice. Materials of National Scientific Conference of the Institute of veterinary medicine, pp. 26–37. Troitsk (2020)
37. Safonov, V.A.: Metabolic profile of high productive cows during pregnancy and barrenness. Agricult. Biol. **43**(4), 64–67 (2008)
38. Safonov, V.: Comparison of LPO-AOS indices and biochemical composition of animal blood in biogeochemical provinces with different levels of selenium. Biol. Trace Element Res. 1–7 (2021)
39. Shkuratova, I.A., Shushurin, A.D.: Clinical and immunobiochemical status of productive animals in the conditions of technogenic pollution. J. Orenburg State Agrarian Univ. **3–1**, 131–133 (2004)
40. Donnik, I.M., Shkuratova, I.A., Isaeva, A.G., Vereshchak, N.A., Krivonogova, A.S., Beikin, Y.B., Portnov, V.S., Barashkin, M.I., Lorets, O.G.: Physiological peculiarities of animals in the regions of technogenic pollution. Agrarian J. Urals **1**(93), 26–28 (2012)
41. Petrunina, N.S., Tyutikov, S.F., Degtyarev, A.P., Krechetova, E. V., Ermakov, V.V.: Transformation of biogeochemical anomalies of the river Ardon basin (Northern Ossetia). In: Fundamental and Innovative Aspects of Biogeochemistry, pp. 170–172. Materials of VII Biogeochemical School, Moscow (2011)
42. Nefedova, S.A.: Ecological-physiological mechanisms of adaptation of animals to anthropogenic effects (in the Ryazan Region). Abstract of thesis. Petrozavodsk (2012)
43. Baimova, S.R.: Heavy metals in the system "soil-plants-animals" in the conditions of Bashkir Trans-Urals. Abstract of thesis, Ufa (2009)
44. Ermakov, V.V., Khushvakhtova, S.D., Tyutikov, S.F., Buryak, A. K., Danilova, V.N., Pytskii, I.S., Khabarov, V.B.: Peculiarities of the accumulation of molybdenum, wolfram, copper, and rhenium in the biogeochemical food chain. J. Russian Fund Fundamental Stud. **1**(77), 34–38 (2013)
45. Safonov, V.A., Ermakov, V.V., Degtyarev, A.P., Dogadkin, N.N.: Prospects of biogeochemical method implementation in identifying rhenium anomalies. In: IOP Conference Series: Earth and Environmental science. Conference proceedings. Krasnoyarsk Science and Technology City Hall of the Russian Union of Scientific and Engineering Associations, p. 62035 (2020)
46. Moiseenko, T.I., Dinu, M.I., Gashkina, N.A., Kremleva, T.A.: Aquatic environment and anthropogenic factor effects on distribution of trace elements in surface waters of European Russia and Western Siberia. Environ. Res. Lett. **14**(6), 065010 (2019)
47. Vinokurov, S.F., Bogatikov, O.A., Gurbanov, A.G., Karaamuzov, B.S., Gazeev, V.M., Leksin, A.B., Shevchenko, A.V., Dolov, S. M., Dudarov, Z.I., Serehin, O.D., Sychkova, V.A.: Ecological Risks of the Storage of Wastes From the Tyrnyauz Wolfram-Molybdenum Plant and Issues of Their Complex Utilization. Kabardino-Balkarian University, Nalchik (2018)
48. Kolmykova, L.I., Korobova, E.M., Gromyak, I.N., Korsakova, N. V., Danilova, V.N.: Ecological and geochemical assessment of the chemical composition of drinking waters of Bryansk oblast with application to increased risk of thyroid gland diseases. Geochem. Int. **58**(1), 66–76 (2020)

49. Moiseenko, T.I.: Evolutionary processes in anthropogenic biogeochemical provinces. Geochem. Int. **56**(10), 982–991 (2018)
50. Ermakov, V., Safonov, V., Dogadkin, D.: Characteristic features of molybdenum, copper, tungsten and rhenium accumulation in the environment. Innovative Infrastruct. Solut. **6**, 104 (2021). https://doi.org/10.1007/s41062-021-00481-5
51. Degtyarev, A.P., Ermakov, V.V.: Ecological and chemical evaluation of the Ardon river basin (Northern Osetiya). Geochem. Int. **36**(1), 79–84 (1998)
52. Ermakov, V.V.: Technogenesis of the biosphere and biogeochemical transformation of its taxons. In: Ecological Monitoring of the Environment. Materials of the International School of Young Scientists, pp. 76–95. Novosibirsk State Agrarian University (2016)
53. Rylnikova, M.V., Radchenko, D.N., Tsupkina, M.V., Safonov, V. A.: The study of ecological influence of the Novotroitsk tailing dump on plants and living organisms. J. TulSU **1**, 108–120 (2020)
54. Samburova, M.A., Safonov, V.A., Rylnikova, M.V., Radchenko, D.N.: The Novotroitsk tailing dump influence on the arsenic and heavy metals accumulation in living organisms. IOP Conf. Ser. Earth Environ. Sci. AGRITECH-V-2021 **839**, 042087 (2021)
55. Bol'shakov, V.N., Moiseenko, T.I.: Anthropogenic evolution of animals: facts and their interpretation. Russ. J. Ecol. **40**(5), 305–313 (2009)
56. Avtsyn, A.P., Zhavoronkov, A.A., Rish, M.A., Strochkova, L.S.: Human Microelemenntosis: Etiology, Classification, Organopathology. Medicine, Moscow (1991)
57. Ermakov, V.V., Tyutikov, S.F., Safonov, V.A.: Biogeochemical Indication of Microelementoses. RAS, Moscow (2018)

Analytical Chemistry, Radiochemistry, and Radioecology

From the Theory of Spectra to the Theory of Chemical Reactions

L. A. Gribov, V. I. Baranov, and I. V. Mikhailov

1 Introduction

One of the first person to point out the possibility of creating a theory of chemical reactions on the basis of the theory of molecular spectra was B. I. Stepanov. Back in 1972, he noted the identity of the methods for describing chemical and spectroscopic processes, since a chemical reaction from the point of view of spectroscopy is one of the types of non-optical transition between energy levels, and in some cases even a purely optical transition is equivalent to a chemical transformation of the system [1]. The idea of B. I. Stepanov was developed in the works of employees of the Laboratory of Molecular Modeling and Spectroscopy of the Vernadsky Insitute RAS under the guidance of one of the authors of this article.

The common points of the theory of spectra and the theory of chemical reactions is the assumption that processes are transitions between discrete energy levels and their probabilities are determined by square of the matrix element of the dipole moment operator. Transitions (excitation and relaxation of the system to the state with the lowest energy) in one potential well are shown in Fig. 1a. However, if level 3 is common to two wells (Fig. 1b), then when the excited level 1 is unloading a transition from level 3 to the ground level 8 of the right well becomes possible, which is the appearance of a different structure. The transition from the left to the right well can be interpreted as a chemical reaction. It is important to note here that the descriptions of the behavior of a system with one potential well, when only optical spectra appear, and a system with two wells, when a structural transformation becomes possible, coincide. It is this analogy that suggests that it is advisable to construct the theory of chemical reactions as an extension of the theory of spectra.

It is obvious that the development of the theory of molecular spectra and the creation of a quantitative theory of intermolecular transformations are necessary conditions for achieving this goal. Both of them are briefly considered in the first two sections, while the third section presents the results of modeling real chemical (photochemical) processes.

2 Molecular Spectra

The development of the theory of molecular spectra and the creation of corresponding computer programs have been the main directions of research at the Laboratory of Molecular Modeling and Spectroscopy of the Vernadsky Institute RAS for many years. Modeling of reactions begins with the formation of adiabatic and harmonic models of molecules corresponding to the minima of the potential wells of the initial substances and reaction products. Structural-dynamic models of molecules (geometry, force constants) in ground and excited states are created using semi-empirical methods developed in the theory of vibrational and electronic-vibrational spectra of complex molecules [2–5].

The correctness of molecular models in the ground states is confirmed by the qualitative and quantitative reproduction of the frequencies and intensities of the experimental IR spectra. As an example, Figs. 2 and 3 shows the calculated and experimental dependences of the optical density ($\times\ 10^5$ cm^2/mol) on the wavenumber (cm^{-1}) for 1,2-Dimethylbenzene (o-Xylene) and Ethanol, respectively. The experimental spectra were taken from the database [6].

The semiempirical method for calculating molecular electronic-vibrational spectra [5] allows one to obtain quantitative estimates of the probabilities of intramolecular transitions between the vibrational sublevels of the ground and excited electronic states. These probabilities are the most important parameters of molecular models used in modeling

L. A. Gribov · V. I. Baranov (✉) · I. V. Mikhailov
Vernadsky Institute of Geochemistry and Analytical Chemistry, Russian Academy of Sciences, 19 Kosygin St., Moscow, 119991, Russia
e-mail: baranov_50@mail.ru

V. P. Kolotov and N. S. Bezaeva (eds.), *Advances in Geochemistry, Analytical Chemistry, and Planetary Sciences*,
https://doi.org/10.1007/978-3-031-09883-3_28

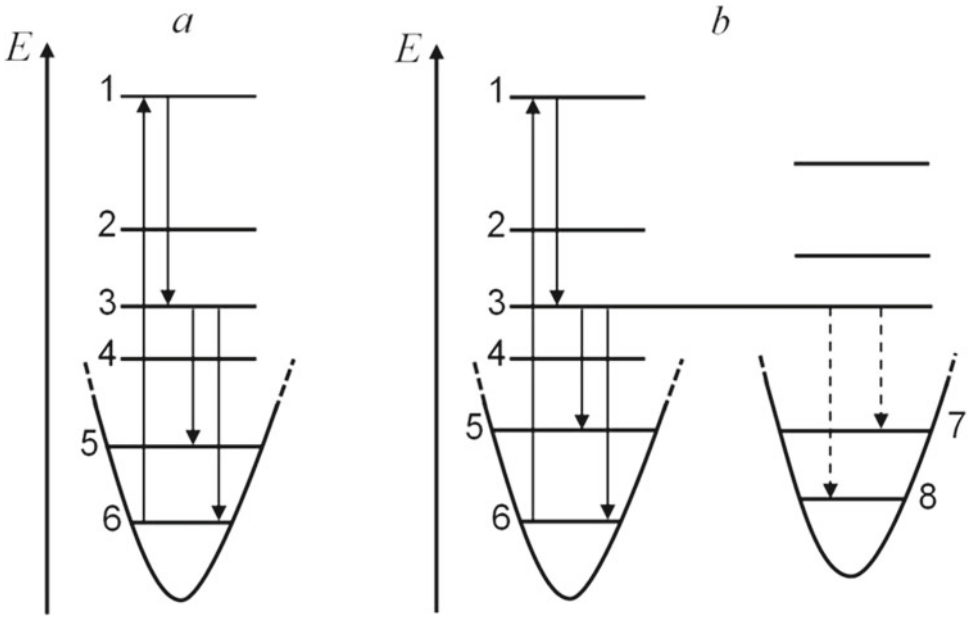

Fig. 1 Scheme of energy levels and possible transitions between them for molecular systems with one potential well (**a**) and two potential wells (**b**)

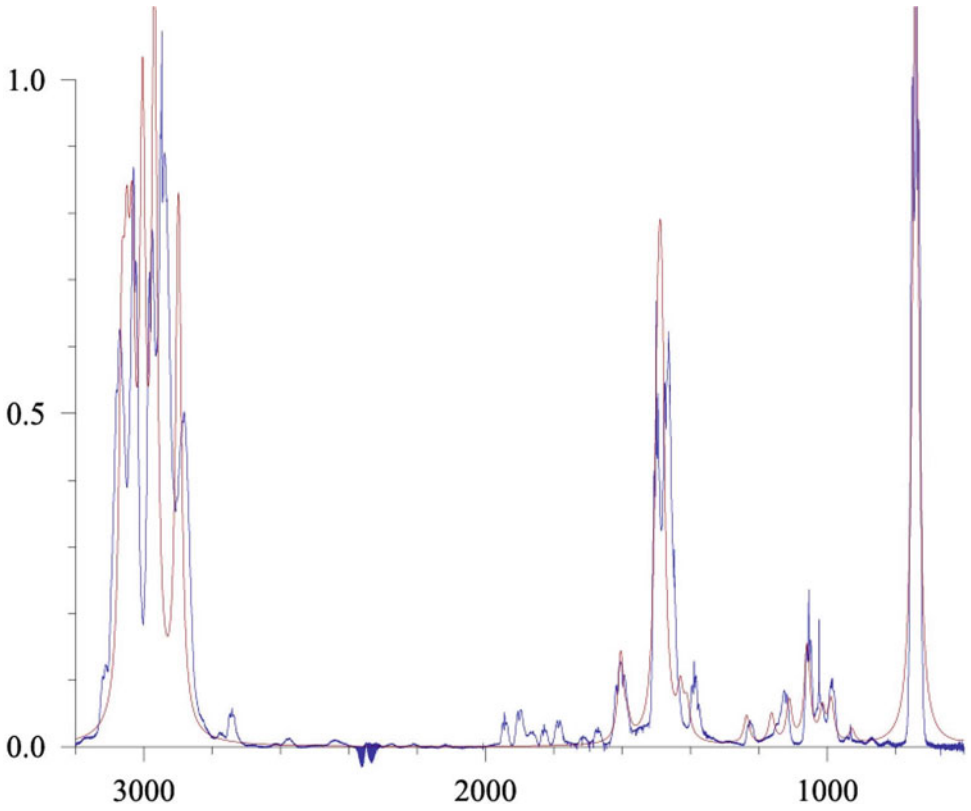

Fig. 2 Calculated (red) and experimental (blue) IR spectra of 1,2-Dimethylbenzene

reactive intermolecular transitions. Our experience of calculating the electronic-vibrational spectra of complex molecules shows that differences between the calculated values of the energies of the ground and excited electronic states (at least for the lower excited states) are on the order of the energy of a vibrational quantum, i.e. they are small corrections. This allows us to neglect their influence on the kinetics of structural transformation. The spectral expression of this property is that the most intense in the vibrational structure of the absorption and fluorescence spectra are lines corresponding to transitions between levels with the same vibrational quantum numbers v ($\Delta v = 0$) or differing by unity ($\Delta v = 1$).

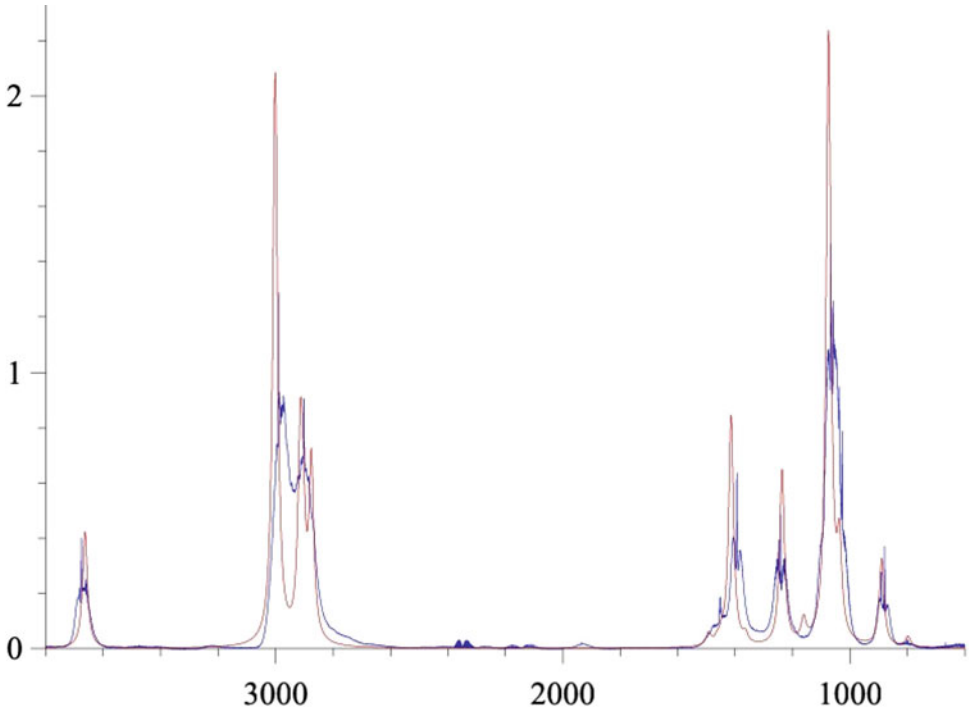

Fig. 3 Calculated (red) and experimental (blue) IR spectra of Ethanol

3 Intermolecular Transitions

According to our approach [7, 8] to the description of chemical reactions, structural transformations in molecules occur due to nonradiative transitions between resonating electronic-vibrational states of (in the simplest case) two interacting structures. The corresponding quantum beats with a frequency ω appear and the migrating without changing the energy wave packet can be written in the form.

$$\Psi(t) = \Psi_1 \cos \omega t \pm i\Psi_2 \sin \omega t,$$

where Ψ_1 and Ψ_2 are the electron-nuclear functions of stationary states of interacting structures and it is assumed that at the initial moment of time the molecular system was in a state corresponding to the initial compound $\Psi(0) = \Psi_1$. The frequency of quantum beats ω is determined by the value of the corresponding off-diagonal element of the energy matrix, which characterizes the interaction of resonating states

$$\omega = E_{\text{en}} S_{\text{en}}/\hbar$$

where $E_{\text{en}} = (E_1 + E_2)/2$ is the average value of the energy of electronic-vibrational levels of interacting structures and S_{en} is the overlap integral of the corresponding vibronic functions. It is the overlap integral S_{en} that is key value in determining the probability of a nonradiative transition, since, depending on the difference in the geometry of the interacting structures, it can vary by many orders of magnitude. On the other hand at small values of S_{en}, the value of ω may be sufficient for the reaction to proceed (nonzero product yield) due to the high excitation energy. In the adiabatic approximation, the integral S_{en} is factorized and reduced to the product of the electronic S_{el} and the vibrational S_{vib} components $S_{\text{en}} = S_{\text{el}}\, S_{\text{vib}}$. Efficient approximate procedures for removing the problem of calculating the integral S_{el} and calculating multidimensional integrals S_{vib} were developed.

The most important stages of modeling structural rearrangements during chemical transformations are determining the values of structural deformations, assessing the probability of structural rearrangements, a detailed analysis of the properties of the multidimensional surface of intersection of the potentials of interacting structures with finding a critical point with minimum energy on this surface, as well as drawing up a system of differential equations describing the kinetics of the process. For each of these problems, algorithms were developed and computer programs were created.

In the simplest case of isomeric rearrangements, to determine the transformation parameters of the normalized normal coordinates of the initial structure (column X) and the reaction product (column X')

$$X' = JX + g$$

the elements of the square matrix of rotation (entanglement) and rescaling of the normal coordinates J and the column of shift of normal coordinates (i.e. shift of the minima of the corresponding potential wells) g are calculated. The probability of a nonradiative reaction transition is determined

mainly by the magnitude of the shift in the positions of the minima of potential wells since $S_{vib} \sim \exp(-g)$.

Since the structural transformation during chemical transformation is described as a transition from one potential well to another separated from the original by a barrier the combining wells should have a pronounced asymmetry. The curvature of the potential function at the edges of the two-minimum well is significantly greater than in the middle in the area of the barrier. The nonparabolic form of the potential wells of the combining structures leads to a significant increase in the overlap integral S_{vib} and the probability of a nonradiative transition.

To take into account the asymmetry of potential wells due to the presence of a barrier, empirical parameters u_i are used that specify the magnitude of the "broadening" of the wells along all or a part of the normal coordinates. Since in the harmonic approximation the cross sections of potential energy surfaces (PES) by the coordinate planes are parabolas, u_i are, in fact, the ratios of the focal parameters of the "broadened" parabolas (p_u) and the initial ones, matched with the corresponding frequencies of the IR spectrum ($p_0 < p_u$). Figure 4 illustrates the described situation. The cross-sections of the two-minimum potential surface along the coordinates X_2 (X'_2) have a symmetric form, but for the cross-sections along the coordinates X_1 (X'_1) it is necessary to introduce "broadening" of the internal half-parabolas so that their shape is correctly transmitted in the barrier region, where the overlap of the wave functions of the combining states of molecules is maximum.

Let us consider in more detail the cross section of the two-minimum potential along the normal coordinates X_1 (X'_1). When the wells are located close enough to each other, energy levels with nonzero wave functions may arise within two wells at once (Fig. 5). It is clearly seen that when two wells with two pairs of states with very close but unequal energies approach each other, two different situations arise. For the lower pair of states with close energies, each of the two wave functions is localized only within its own well. But for the upper pair of states, the energies of which are much closer to the barrier, spreading of both wave functions over the entire region of the two-minimum potential is observed. The emerging doublet (resonance level) determines the possibility of a structural transformation—a transition from one well to another.

When considering options for taking into account the asymmetry of potential wells, it turned out to be convenient to use the concept of a broadening function $u(X_{Bi})$, which associates the value of the ith coordinate X_{Bi} of the barrier top (point X_B in Fig. 4) with the value of the ratio of focal parameters for the PES cross section along the ith normalized normal coordinate X_i. Among the large number of possible types of functional dependence $u(X_{Bi})$, of practical interest is, first of all, stepwise:

$$u(X_{Bi}) = \begin{cases} U_0, X_{Bi} > X_0 \\ 1, X_{Bi} \le X_0 \end{cases}.$$

The stepwise function has only two parameters: step height U_0 and its position X_0. On the one hand, this type of dependence can provide a significant decrease in the proportion N_D of normal coordinates for which the potential

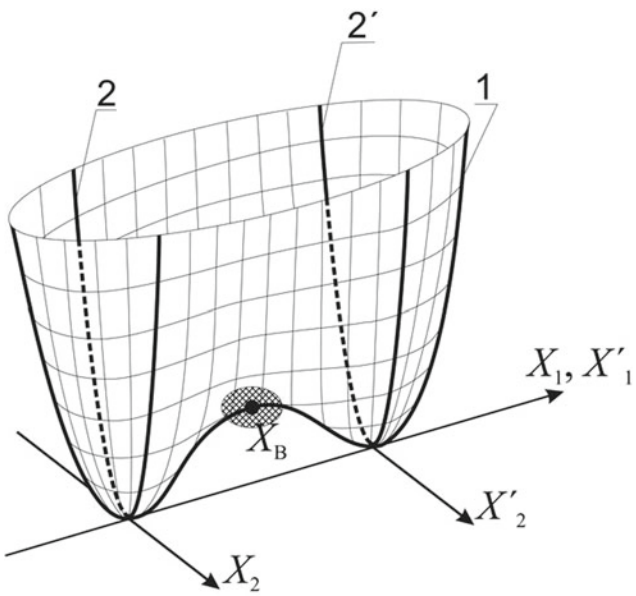

Fig. 4 Two-minimum PES and its cross sections along normal coordinates

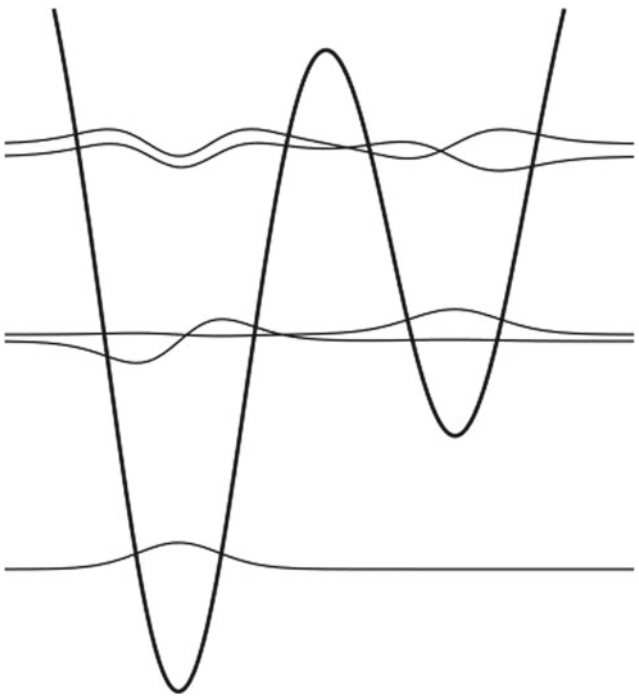

Fig. 5 Wave functions for a two-minimum potential well

surface is corrected taking into account its asymmetry, which corresponds to the well-known fact of a small number of coordinates involved in the process of structural transformation. But on the other hand, the smaller N_D, the more the shape of the potential surface is distorted, and as a result, the position of the barrier top in the space of normal coordinates shifts more strongly. This can lead to ambiguity in the definition of resonant states. To characterize the magnitude of the displacement of the top of the barrier, it is convenient to use the angle of rotation ξ of the vector directed from the minimum of the potential well to the point X_B.

In addition to simple models describing quantum beats in the case of two and three resonating states, the problems of multichannel reaction transformations were solved in general form for an arbitrary number of quasi-degenerate levels. It is shown that in this case it is also possible to construct an oscillating wave packet leading to a transition from one subsystem to another. A distinctive feature of the multilevel case from the two-level case is the non-periodic nature of the oscillations and a significant increase in the probability of a nonradiative transition.

The kinetics of the intramolecular and intermolecular processes is described by a system of differential equations

$$\frac{dn}{dt} = Pn,$$

where n is the column of the populations of the discrete energy levels of the molecular ensemble consisting of the initial structures and reaction products, and P is the matrix of probabilities of all possible (optical, nonradiative) transitions.

For an intramolecular transition between two nonresonant energy levels with populations n_1 and n_2, characterized by the probability p_{12}, the change in the populations is written in the form

$$dn_1/dt = -p_{12}n_1, dn_2/dt = p_{12}n_1.$$

In the presence of nonradiative transitions along resonating energy levels some elements of the transition probability matrix P will depend on time. Optical transitions appear between ordinary and resonating levels with probabilities determined by the squares of the matrix elements of the intramolecular dipole transitions multiplied by the oscillating factors $\cos^2\omega t$ or/and $\sin^2\omega t$. The choice of factors is determined by the initial conditions, i.e. direction of structural transformation. For transitions between energy levels of the initial structure (donor), when one of the combining states is resonating with the quantum beat frequency ω, the transition probability is multiplied by $\cos^2\omega t$

$$dn_1/dt = -p_{12}n_1 cos^2\omega t, dn_2/dt = p_{12}n_1 cos^2\omega t.$$

and for the emerging structure (acceptor), by $\sin^2\omega t$.

$$dn_1/dt = -p_{12}n_1 \sin^2\omega t, dn_2/dt = p_{12}n_1 \sin^2\omega t.$$

In the complex case of a transition between a pair of resonating levels corresponding to interactions of two or more isomeric forms, coefficients $\cos^2\omega_1 t \times \sin^2\omega_2 t$ are introduced, where ω_1 and ω_2 are the frequencies of quantum beats of different resonance levels. The frequency ω_1 corresponds to the upper resonant level in energy, and the frequency ω_2 corresponds to the lower one.

All of the above corresponds to the simplest case of chain isomerization, when the sequence of isomeric transformations under given initial conditions is uniquely determined, and, therefore, for each resonance level it is known which isomer is a donor and which is an acceptor. In more complex situations, there may be several routes of isomeric transformations, and these routes may intersect. When considering the same resonance level for one route, an isomer can be a donor, and for another, an acceptor. For example, when modeling phototransformations of molecules under constant broadband excitation it is impossible to unambiguously ascribe donor or acceptor properties to reagents. This leads to the need to derive the rules for compiling a system of kinetic equations in the general case. For this, we divide the resonating state into two (or several) formally independent states with the corresponding wave functions.

Then, for the resonance level with population r, it is necessary to write two equations—for populations r_1 and r_2, corresponding to the cases when structure 1 is a donor and structure 2 is an acceptor, and vice versa, when structure 1 is an acceptor and structure 2 is a donor. The population r for a molecular ensemble will be equal to $r_1 + r_2$. In the equations for the populations of levels to which transitions from this resonance state are possible, the terms corresponding to these transitions will appear, including the donor and acceptor components in the form $r_1 \cos^2\omega t + r_2 \sin^2\omega t$ for structure 1 and $r_1 \sin^2\omega t + r_2 \cos^2\omega t$ for structure 2. For the levels from which transitions to the resonance state occur, the terms in the corresponding equations always have a donor form, i.e. contain factors $\cos^2\omega t$ in both structure 1 and structure 2.

If, in addition to intramolecular transitions accompanied by absorption or emission of electromagnetic waves, and resonant intermolecular transitions, other reaction transformations (synthesis and decomposition) occur in the system, then the system of kinetic equations can be extended by including additional equations or terms describing these processes.

The decomposition of the initial molecule (van der Waals complex capable of decay with probability α), which was in state 1, as a result of which states 2 and 3 of the reaction products are populated, is described by a system of three equations

$$dn_1/dt = -\alpha n_1, dn_2/dt = \alpha n_1, dn_3/dt = \alpha n_1.$$

The process of the appearance of a new molecule in state 1 from the two initial ones, which were in states 2 and 3, with probability β can also be characterized by a system of three equations

$$dn_2/dt = -\beta n_2 n_3, dn_3/dt = -\beta n_2 n_3, dn_1/dt = \beta n_2 n_3.$$

4 Chemical Reactions

In the simplest case, a three-level scheme can be used to describe the chemical transformation of one object into another in the presence of a common (resonance) level and when only this state is excited: the resonance level, the main level of the initial object, and the main level of the reaction product (Fig. 6).

The corresponding system of kinetic equations has the form

$$\begin{cases} dn_I/dt = n_R w_I \cos^2 \omega t \\ dn_{II}/dt = n_R w_{II} \sin^2 \omega t \\ dn_R/dt = -n_R(w_I \cos^2 \omega t + w_{II} \sin^2 \omega t) \end{cases},$$

where n_I and n_{II} are the populations of the energy levels of the ground states of the initial structure and the reaction product, n_R is the population of the resonance level, w_I and w_{II} are the total probabilities of spontaneous transitions from the resonance level to the levels of the ground states of the initial object and the reaction product, ω is the frequency of quantum beats.

For the population of the resonance level as a function of time under the initial conditions $n_I(0) = n_{II}(0) = 0$, $n_R = 1$, we can obtain the expression

$$n_R(t) = \exp\left(-\frac{w_I + w_{II}}{2}t - \frac{w_I - w_{II}}{4\omega}\sin 2\omega t\right).$$

Then formula for the amount of product after complete unloading of the resonance level (for reaction yield φ).

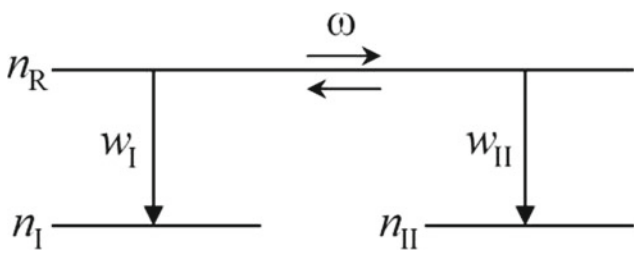

Fig. 6 Three-level scheme of molecular transformation

$$\varphi = w_{II} \int_0^\infty \exp\left(-\frac{w_I + w_{II}}{2}t - \frac{w_I - w_{II}}{4\omega}\sin 2\omega t\right) \sin^2 \omega t \, dt.$$

If the total probabilities of intramolecular optical transitions w_I and w_{II} have values close in order of magnitude, then the second term under the exponent in the integrand can be neglected and the approximate expression for φ takes the form

$$\varphi \approx \frac{w_{II}}{w_I + w_{II}} \frac{1}{1 + \left(\frac{w_I + w_{II}}{4\omega}\right)^2}.$$

It is clearly seen that the reaction yield can take values from 0 at $\omega \to 0$ to φ_{max} at $\omega \to \infty$, where

$$\varphi_{max} = w_{II}/(w_I + w_{II}).$$

Photochemical reactions of structural isomerization are the most natural object of study to test the possibilities of the proposed approach for the quantitative description of chemical transformations. Calculations were made of the kinetics and quantum yields of ten phototransformations of real molecules, divided into three groups.

The first group (I) included photochemical transformations of six molecules of the diene series into their cyclic isomers:

(1) cis-butadiene-1,3 → cyclobutene;
(2) 2-methyl-butadiene-1,3 → 1-methylcyclobutene;
(3) 2,3-dimethyl-butadiene-1,3 → dimethylcyclobutene;
(4) pentadiene-1,3 → 3-methylcyclobutene;
(5) 2,4-dimethyl-pentadiene-1,3 → trimethylcyclobutene;
(6) 1-methoxy-butadiene-1,3 → methoxycyclobutene.

The second group (II) included two reactions of structural isomerization of aromatic molecules with transfer of very large substituents (methyl, ethyl groups):

(7) *o*-diethylbenzene → *m*-diethylbenzene;
(8) *o*-xylene → *m*-xylene.

The third group (III) included two reactions of structural isomerization of aldehydes (ketones) with opening of the cyclic (cyclopropyl group) fragment:

(9) cyclopropylmethanal → 2-butenal;
(10) cyclopropylethanal → 3-pentenone-2.

The reactions of the third group are distinguished by the fact that they have a relatively high quantum yield (an order of magnitude higher than in other reactions).

In the first two columns of Table 1 the values of the total probabilities w_I and w_{II} calculated for all ten reactions are given. For all reactions except 1, 9, and 10, $w_{II} > w_I$ (for reaction 8, $w_{II} \approx w_I$). It can be noted that for almost all reactions in which ring opening or, conversely, ring formation occurs, the total probability for an isomer containing a ring is greater than for an isomer without a ring (reactions 2–6, 9, 10; the exception is reaction 1). From Table 1 it is clearly seen that the total probabilities w_I and w_{II} have, as a rule, close (in order of magnitude) values.

For the studied reactions, two situations are possible: $\varphi_{max} > \varphi_{exp}$ and $\varphi_{max} < \varphi_{exp}$. The latter situation is realized, for example, in reactions 9 and 10, for which φ_{max} is noticeably smaller than for most other reactions, and the experimental quantum yield, on the contrary, is much higher (see the last two columns of Table 1). This situation makes it impossible to determine the optimal values of the parameters of molecular models and the frequency of quantum beats corresponding to the experimental quantum yield and leaves it possible to indicate only the lower boundary of the region of maximum approximation to the experimental results. For reactions with zero quantum yield 5 and 6, you can also specify the boundary, this time the upper one, of the region where the values of the quantum yield are less than a predetermined small value.

In order for semi-empirical models of photochemical reactions to be of practical value, their parameters should have similar values in a series of similar reactions. Only in this case it is possible to quantitatively predict the course of photochemical transformations and the magnitudes of quantum yields.

In order to elucidate the dependence of the quantum yields of reactions 1–10 on the values of the model parameters U_0, X_0 and determine their optimal values for groups of similar reactions, model calculations were carried out in a wide range of values of these parameters. As typical example, Fig. 7 shows three-dimensional plots obtained for reaction 1 in coordinates (φ, U_0, X_0). A characteristic of all

Table 1 The total probabilities of spontaneous transitions from the resonance level to the levels of the ground states of the initial object (w_I, s^{-1}) and product (w_{II}, s^{-1}), as well as experimental (φ_{exp}) and the maximum possible within the framework of the model used (φ_{max}) quantum yields for photoisomerization reactions 1–10

№.	w_I	w_{II}	φ_{exp}	φ_{max}
1	2.05×10^{10}	3.08×10^{10}	0.3 (0.03)	0.60
2	1.87×10^{10}	3.16×10^{10}	0.09	0.63
3	1.17×10^{10}	1.83×10^{10}	0.12	0.61
4	2.63×10^{10}	3.14×10^{10}	0.03	0.54
5	1.92×10^{10}	2.72×10^{10}	0	0.59
6	1.47×10^{10}	7.71×10^{9}	0	0.34
7	1.74×10^{6}	3.17×10^{6}	0.03	0.65
8	1.71×10^{6}	1.73×10^{6}	0.013	0.50
9	6.00×10^{6}	1.31×10^{6}	0.35	0.18
10	3.18×10^{5}	1.21×10^{5}	0.3 (0.34)	0.28

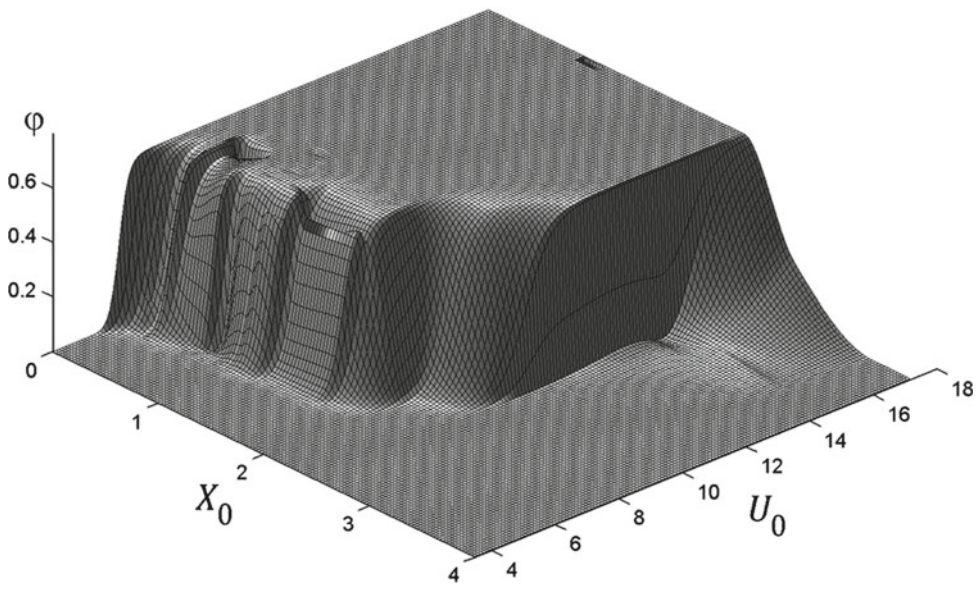

Fig. 7 Dependence $\varphi(U_0,X_0)$ for reaction 1

the considered reactions is a rather narrow band of values of the parameters U_0 and X_0 at which the quantum yield changes from the minimum ($\varphi_{min} = 0$) to the maximum possible value φ_{max}. It is these bands that are of greatest interest.

It is very important that for all the reactions considered, the experimental values of the quantum yields φ_{exp} lie in these regions or in the immediate vicinity of them (for reactions 9 and 10, the deviation is no more than $0.5 \times \varphi_{exp}$). Thus, within the framework of this model, it is possible to choose such a set of the parameters U_0 and X_0, at which agreement of the calculated quantum yields of reactions with the experimental values is achieved.

Obviously, the intersection of the obtained surfaces $\varphi(U_0, X_0)$ with the horizontal plane $\varphi = \varphi_{exp}$ (provided that $\varphi_{max} > \varphi_{exp}$) determine the curve of the optimal values of the parameters U_0 and X_0 for each reaction, and the intersection with two horizontal planes $\varphi = (1 \pm \Delta)\varphi_{exp}$, where $0 \leq \Delta < 1$, is the band of the values of the parameters U_0 and X_0 which corresponds to the deviation of the calculated quantum yield from the experimental one no more than on $\Delta \times 100\%$. Of greatest interest are the areas of approach/intersection of bands of close to optimal values of parameters U_0 and X_0 for reactions of the same type.

The common areas of such bands determine the values of the model parameters at which the calculated quantum yield deviates from the experimental value by no more than a value $\Delta \times 100\%$ for all reactions included in one of the three groups. An example for reactions of group II is shown in Fig. 8. In addition to the bands themselves obtained at $\Delta = 0.75$, for reactions 7 (bold curves) and 8 (thin curves), the boundaries corresponding to different values of the angle ξ (two colors of the curves correspond to two reactions) and a common boundary for the fraction of coordinates $N_D <$ 40% are shown.

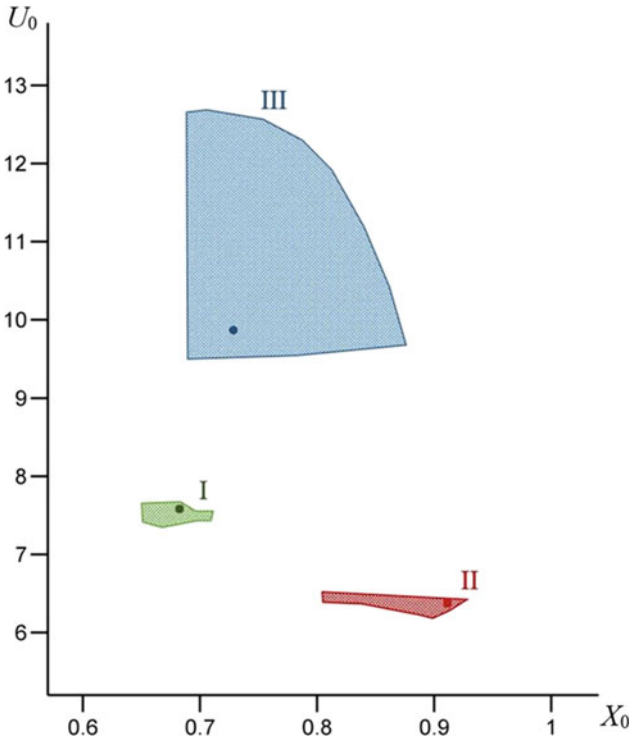

Fig. 9 Domains of values of parameters U_0 and X_0 at $\Delta = 0.5$ for three groups of reactions

The position of the regions of values of the model parameters U_0 and X_0 for all three groups of reactions, which correspond to the theoretical values of quantum yields that deviate from the experimental ones by no more than 50%, are shown in Fig. 9. The dots mark the optimal values of the parameters U_{opt} and X_{opt} for the reaction groups. Their values turned out to be as follows: 7.59 and 0.68 for group I, 6.36 and 0.92 for group II, 10.0 and 0.75 for group III. It can be seen that all reactions are clearly grouped according to

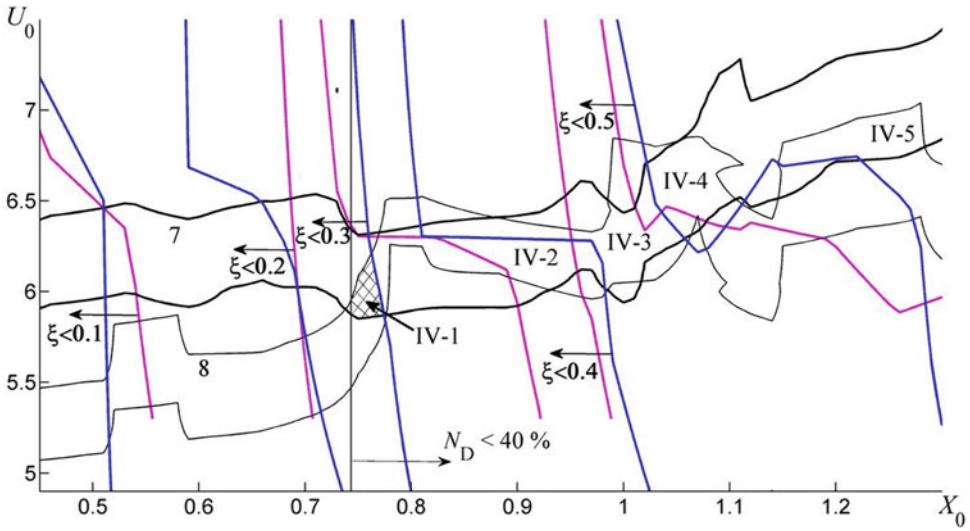

Fig. 8 Bands of values of the parameters U_0 and X_0 and the boundaries for ξ and N_D

Table 2 Theoretical quantum yields $\varphi_{calc} = \varphi(U_{opt},X_{opt})$, experimental quantum yields φ_{exp}, boundary values of angle ξ and proportion of normal coordinates N_D, as well as relative values of deviations of calculated quantum yields from experimental ones for reactions 1–10

Group	Reaction	N_D,%	ξ, rad	φ_{calc}	φ_{exp}	$\delta\varphi$,%	$\delta\varphi^*$,%	$\delta\varphi^{**}$,%
I	(1)	35	0.1	0.6	0.3	100	97	96
	(2)	42	0.2	0.072	0.09	20	72	64
	(3)	35	0.2	0.13	0.12	8	358	38
	(4)	38	0.2	0.036	0.03	20	99	23
	(5)	33	0.2	10^{-15}	0	–	–	–
	(6)	44	0.2	10^{-6}	0	–	–	–
II	(7)	32	0.3	0.032	0.03	6	93	95
	(8)	40	0.4	0.012	0.013	6	958	1104
III	(9)	50	0.3	0.18	0.35	49	–	–
	(10)	40	0.4	0.28	0.30	8	–	–

their type and the regions of parameter values corresponding to reactions of different types are strongly spaced apart.

The results of calculating quantum yields φ_{calc} at the above values U_{opt} and X_{opt} and for each group of reactions are shown in Table 2. Table 2 also contains the values of the experimental quantum yields φ_{exp} [9, 10], the relative values of the deviations of the calculated quantum yields from the experimental ones

$$\delta\varphi = \frac{\left|\varphi_{calc} - \varphi_{exp}\right|}{\varphi_{exp}} \cdot 100\%,$$

the fraction N_D of normal coordinates for which the transformation of the potential surface is carried out taking into account its asymmetry, and the values of the angles ξ. For comparison, the last two columns show the values of the relative deviations $\delta\varphi^*$ and $\delta\varphi^{**}$, obtained for a one-parameter stepwise broadening function with a fixed position of the step at $X_0 = 0$ (total broadening, $N_D = 100\%$) and $X_0 = 1/\sqrt{2}$, respectively. It should be noted that for reactions 5 and 6 which do not occur according to the experimental data $\varphi_{calc} < 10^{-5}$. Although the result obtained for reaction 1 does not satisfy the specified deviation value (50%), it can still be considered quite satisfactory, since the theoretical value correctly conveys an order of magnitude of the quantum yield, and there are very contradictory experimental data for this reaction in the literature.

Thus, it has been shown that it is possible to perform predictive calculations of the quantum yields of photochemical transformations with a satisfactory prediction accuracy, and the parameters of the chosen model have a high degree of transferability.

The approach to the construction of a physical theory of chemical reactions briefly outlined in the article is based on the idea of using of the theory of molecular spectra to describe a wide range of molecular processes, primarily chemical transformations. The efficiency of this approach is confirmed by the fact that on its basis some general rules for the course of chemical reactions are obtained which are quite consistent with experiment. There are examples of quantitative coincidences which confirms the suitability of the calculation methods created within the framework of the proposed theory for solving specific problems.

References

1. Stepanov, B.I.: On the identity of methods for describing chemical and spectroscopic processes. Vestsi, Akad. Navuk BSSR, Ser. Fiz.-Mat. Navuk **1**(3), 67–73 (1972). (in Russian)
2. Vol'kenshtein, M.V., Gribov, L.A., El'yashevich, M.A., Stepanov, B.I.: Vibrations of Molecules. Nauka, Moscow (1972)
3. Gribov, L.A., Orville-Thomas, W.J.: Theory and Methods of Calculation of Molecular Spectra. John Wiley and Sons, Chichester, New York (1988)
4. Gribov, L.A.: Molecular Vibrations. LIBROKOM, Moscow (2009).(in Russian)
5. Gribov, L.A., Baranov, V.I., Zelent'sov, D.Y.: Electronic-Vibrational Spectra of Polyatomic Molecules: Theory and Methods of Calculation. Nauka, Moscow (1997).(in Russian)
6. NIST Chemistry WebBook. https://webbook.nist.gov/chemistry. Last accessed 2021/10/15
7. Gribov, L.A., Baranov, V.I.: Theory and Methods of Calculation of Molecular Processes: Spectra, Chemical Transformations, and Molecular Logics. KomKniga, Moscow (2006).(in Russian)
8. Gribov, L.A., Baranov, V.I., Mikhailov, I.V.: Physical Theory of Chemical Reactions. Rusains, Moscow (2019).(in Russian)
9. Turro, N.J.: Molecular Photochemistry. Benjamin, New York (1965)
10. Calvert, J.G., Pitts, J.N.: Photochemistry. Wiley, New York (1966)

Method for the Selection of Polar Stationary Phases for Gas–Liquid Chromatography Based on the Theory of Intermolecular Interaction

E. A. Zaitceva and A. M. Dolgonosov

1 Introduction

Gas chromatography (GC) solves complex problems, dictated in particular by the protection of human health, where quality control of food products is required. The separation of mixtures of structural and geometric isomers is particularly challenging. Many stationary phases (SPs) of different polarities developed for such tasks are known. It is important to carry out the correct choice of experimental conditions and the key point is the exact choice of a selective stationary phase (SP).

Such methods of phase classification as Rorschneider scheme [1–3], McReynolds [4], Abraham's solvation parameters model [5–8] are known for the SP selection. In these methods, the SP characterization is represented by a large number of empirical parameters requiring their experimental determination. To reduce the number of experiments, many one-dimensional schemes [9, 10] describing SP by one parameter in the experimental system 1-octanol-water have been developed. The statistical analysis of a big data set carried out in [11] proved that two independent parameters are necessary and sufficient for a complete description of the selectivity related to the SP polarity, which indicates the redundancy of multi-parameter schemes and the insufficiency of one-dimensional classification schemes.

The listed methods have essential disadvantages—empiricism and labor intensity. To determine SP parameters, special experiments with reference substances are required, which significantly reduces their predictive ability, and the calculation of SP parameters from their structure is impossible. These drawbacks can be eliminated by applying the theory of intermolecular interactions (IMI) in the sorbate-sorbent system; however, non-empirical methods are not capable of calculating gas-chromatographic systems due to their complexity, and semi-empirical methods based on the rather crude principle of additivity of atomic-atomic potentials use a large number of fitting parameters and do not give the necessary accuracy of calculations.

The capabilities of the theory of generalized charges (TGC) [12] in the description of non-polar chromatographic systems have been demonstrated in [13–15]. TGC derives a non-empirical form of the Lennard–Jones potential and allows the adsorption of non-polar substances on non-polar SPs to be calculated. It is important to extend this approach to other types of IMIs—polar interactions and hydrogen bonds (H-bonds). The development of a theoretically justified and more accurate classification of SPs based on the proposed IMI model, taking into account all types of interactions in the gas-chromatographic system, and its application in solving the problems of increasing the selectivity of gas chromatography, is the main topic of the authors' studies [16–22].

This paper is devoted to the description of a new model for IMI and a developed on its basis method of classifying SPs in GC as well as to the solution of complicated analytical problems related to the choice of conditions for isomer separation.

2 Theoretical Part

2.1 Formulation of the Model of Intermolecular Interactions

Two molecular objects, designated by us as *i* and *sp,* are considered (hereafter, in the developed method of three-parameter characterization (TPCh), the indices *i* and *sp* denote the analyte molecule and the stationary phase, respectively). The model is based on a general form expression for the total energy of intermolecular interaction that contains three independent energy contributions:

E. A. Zaitceva (✉) · A. M. Dolgonosov
Vernadsky Institute of Geochemistry and Analytical Chemistry, Russian Academy of Sciences, 19 Kosygin St., Moscow, 119991, Russia
e-mail: lil-dante@mail.ru

V. P. Kolotov and N. S. Bezaeva (eds.), *Advances in Geochemistry, Analytical Chemistry, and Planetary Sciences*,
https://doi.org/10.1007/978-3-031-09883-3_29

$$U = U_{np} + U_{dp} + n_H E_H, \quad (1)$$

where $U_{np}(Q_i, Q_{sp}, r)$ is non-polar interaction energy, $U_{dp}(\mu_i^2, \mu_{sp}^2, r)$ is polar interaction energy, $E_H(r)$ is H-bonding energy, n_H is probability of H-bond formation [23, 24], Q is generalized charge, μ is dipole moment, r is distance between centers of interacting molecules i and sp.

The generalized charge (GC) for individual rigid molecules is calculated by the following formula [12]:

$$Q = V^{3/4}, V = N_\sigma + N_\pi\sqrt{2} - s \quad (2)$$

where V is the electron volume, N_σ, N_π are numbers of σ- and π-electrons of the rigid fragment, s is the number of screened electrons—valence electrons of the molecule lying beyond the screening horizon located at a distance r_s from the interaction site.

The screening radius is calculated through the electron energy E_1 [24]:

$$r_s = 1.710e\sqrt{a_0/E_1}, \quad (3)$$

where e is the elementary charge, a_0 is the Bohr radius. The average energy E_1 is defined as the energy of formation of a molecule divided by the number of its valence electrons.

To calculate the number of screened electrons s in the case of small molecules, a simple counting rule can be used: (1) if there are no three- and four-substituted carbon atoms in the molecule, the number of screened electrons s is 0; (2) if there are three- and/or four-substituted C atoms, s is 1 and 3, respectively, for each three- and/or four-substituted C atom. In the case of large molecules, where such an obvious calculation is difficult, the formula (3) or special programs, discussed below, are used.

If the distance is measured in nm and the energy in kJ/mol, we obtain the formula for the screening radius $r_s = 6.642E_1^{-1/2}$, according to which the values of the screening radius fall into the region of 0.3–0.4 nm. The screening radius is similar to the Wigner–Seitz radius known in atomic physics, for which the meaning is specified here and the corresponding coefficient is determined [23].

2.2 Components of Expression for Total Intermolecular Interaction Energy

(1) Non-polar interaction energy. The energy has the form of Lennard–Jones potential with theoretical coefficients derived from the TGC [12]:

$$U_{np}(r) = Q_i Q_{sp} u_b(r); u_b(r) = \frac{e^2}{a_0}\left[1.938 \cdot 10^5 (r/a_0)^{-12} - 5.115(r/a_0)^{-6}\right] \quad (4)$$

(2) Polar interaction energy. For the case of an amorphous medium, the polar energy is expressed as the sum of the Reinganum-Keesom orientation interaction [25, 26] and the Debye-Falkenhagen induction interaction [27, 28]:

$$U_{dp} = U_{or} + U_{ind} = -\left(\frac{2\mu_1^2\mu_2^2}{3k_BT} + \alpha_{sp}\mu_i^2 + \alpha_i\mu_{sp}^2\right) r^{-6}, \quad (5)$$

where $\alpha = aQ$ [11] is the electron polarizability of the molecule related to its GC: $a = 4.948a_0^3$, k_B is the Boltzmann constant, T is the temperature.

(3) Hydrogen bonding energy and probability of its formation.

The H-bond energy is presented as a quantum mechanical estimate of its lower limit [16–19, 29]:

$$U_H \approx -\frac{3e^2a_0}{16}\frac{n_H}{r^2}; \quad (6)$$

The probabilistic nature of the H-bonding process is due to the narrow directionality of the bonding, which is reflected in the potential function of the IMI as a narrow "draw-well" inside the relatively wide potential well of the van der Waals interactions. The probability being sought is expressed through the ratio of the dimensions of the draw-well and the molecules being bound. When estimating the geometric values, the GC proportional to the projection area of the molecular fragment on the plane separating the molecules is taken into account [13, 29].

$$n_H = \frac{\sqrt{Q_{(a)i}Q_{(d)sp}} + \sqrt{Q_{(d)sp}Q_{(a)sp}}}{2\left(Q_{(a)i}Q_{(d)i}\right)^{1/4}\sqrt{Q_{(mol)sp}}} \quad (7)$$

where $Q_{(a)}$ is GC of an acceptor group, $Q_{(d)}$ is GC of a donor group, $Q_{(mol)}$ is GC of a molecule.

It follows from formula (7) that if the acceptor group of a molecule i is simultaneously a donor group for H-bond, i.e., at $Q_{(a)i} = Q_{(d)i}$, expression (7) takes the form

$$n_H = \frac{\sqrt{Q_{(d)sp}} + \sqrt{Q_{(a)sp}}}{2\sqrt{Q_{(mol)sp}}}. \quad (8)$$

2.3 Equilibrium Characteristics of Intermolecular Interaction

Equating the derivative of function (1) to zero gives the equation for the distance $r = xr_b$:

$$Ax^{10} + Bx^6 - 1 = 0 \quad (9)$$

with the coefficients:

$$A = -\frac{c_H n_H}{U_0 Q_m r_b^2}, B = 1 + c\left(\frac{\mu_i^2}{Q_i} + \frac{\mu_{sp}^2}{Q_{sp}} + c_T \frac{\mu_i^2}{Q_i}\frac{\mu_{sp}^2}{Q_{sp}}\right) \quad (10)$$

where the notations $c = \frac{0.9676}{e^2 a_0^2}$, $c_T = \frac{0.1347}{a_0^3 k_B T}$ are inserted. Substituting the root of Eq. (9) ($x_{eq} \approx (A+B)^{-1/6}$ assuming $A \ll 1; B - 1 \ll 1$) in the form of $r_{eq} = r_b x_{eq}$, where $r_b = 6.505\, a_0$ [17], into (1) will give the equilibrium adsorption energy $U_{\min}$.

Dividing each term of the equilibrium energy by the contribution of the nonpolar interaction yields the reduced equilibrium energy:

$$u = \frac{U_{\min}}{U_{np}} = 1 + \frac{U_{dp}}{U_{np}} + \frac{E_H}{U_{np}} = A^2 + B \cdot A^{1/3} \quad (11)$$

The expressions of coefficients A and B in Eq. (11) contain the characteristics of interacting objects in the form of the ratio of the characteristics of dipole moment squares and the probability of H-bond formation to GC. Equation (11) is applicable to both adsorption and the general case of IMI, since the adsorbent and the molecule are described by similar parameters.

It follows from the TGC that the reduced energy can be determined from the chromatographic retention data in the form of Kovacs indices [30]:

$$u_i \approx Q_i^{-1}(0.06 I_i + 2)^{3/4}, \quad (12)$$

where I_i is the Kovacs index of the adsorbate molecule on the SP under studying.

Expression (12) is identical for normal alkanes and has an approximate character for other molecules [24, 30].

2.4 Three-Parameter Selectivity Characterization Method for Chromatographic Stationary Phases

The TPCh method is based on three key characteristics of molecules: (1) electron polarizability described by GC, (2) polarity described by electrical dipole moments, (3) ability to form H-bonds. The TPC method allows us to characterize SPs in the same way as molecules, and the quantity characterizing the adsorbate retention on SPs is the Kovacs indices. Note that the theoretical approaches underlying the method allow us to relate the result of the combined action of all intermolecular forces to the structure of interacting molecules. The chromatographic and SP characteristics are related through the reduced energy u (12).

The mathematical definitions of the required SP characteristics are as follows:

Polarity is the ratio of the dipole moment square of the SP to its GC:

$$v_{sp} = \frac{\mu_{sp}^2}{Q_{sp}}, \quad (13)$$

and *hydrophilicity* is the ratio of the probability of H-bond formation by the phase to its GC:

$$w_{sp} = \frac{n_{Hsp}}{Q_{sp}} \quad (14)$$

In formula (8), the probability of H-bond formation is considered as a characteristic of the SP. This is due to the fact that, having a sufficient number of degrees of freedom, the analyte molecule approaches the surface of the SP from the gas phase in such a way that it is always able to form an H-bond with it. Therefore, the probabilistic character arises due to the fact that the SP molecule must turn in such a way that it takes the correct position against the interfering influence of neighboring molecules.

2.5 Direct and Inverse Problems of Intermolecular Interaction Modeling for the "Stationary Phase-Adsorbate" System

The polarity and hydrophilicity characteristics are determined by formulas (15) and (16) from the structural formulas of molecules by calculating GC, dipole moments, and conditional probabilities of participation in H-bond formation. Such a theoretical, or a priori calculation solves *the direct simulation problem.*

Often, however, SPs are polymers whose structure is not disclosed by the manufacturers. In this case, the *inverse simulation problem* for obtaining selectivity characteristics from chromatographic experiment data should be solved in order to characterize the SP.

Direct simulation problem

Solving a direct problem boils down to several steps:

1. Determination of the average covalent bonding electron energy E_1 and screening radius r_s by formula (2). A fragment of the near-surface SP layer, occupying the volume of the screening hemisphere and containing functional groups, is determined. The SP site in the

screening hemisphere reflects the properties of the whole SP when interacting with a small analyte molecule;

2. Calculation of GC through the average electron energy of the covalent bond E_1 by the formula:

$$Q_{sp} = \frac{\kappa}{0.177}\left(\frac{e^2}{a_0 E_1}\right)^{3/2}, \quad (15)$$

where κ is stacking density of liquid molecules [29]. The value κ usually takes values close to 0.7 for small molecules, and for long filamentous molecules close to 0.9.

3. Determination of the dipole moment μ_{sp} of the fragment. The mathematical modeling program Chem3D [31] or reference data for the functional groups included in the selected fragment are used for the calculation;
4. Calculation of the H-bonding index n_H by formula (8), since only SP is considered;
5. Calculation of SP polarity v_{sp} by formula (13);
6. Calculation of SP hydrophilicity w_{sp} by formula (14).

Thus, from the structural formula of the SP macromolecule it is possible to find the polarity and hydrophilicity, i.e., to determine the SP coordinates in the diagram called *a selectivity map*. The presence of two coordinates coincides with the conclusions of the statistical analysis in [11], indicating the necessity and sufficiency of two independent parameters to describe the selectivity of the polar SP.

The solution of the direct problem can be considered as an example of calculating the selectivity characteristics of polyethylene glycol-based phases (PEG-SP) with different molecular weights [21]; the structural formula is HO–$[CH_2CH_2O]_N$–H.

Sequence of theoretical calculation from the structural formula of polyethylene glycol (PEG):

1. The mass of a macromolecule is related to the number of monomeric units (N) by the formula

$$M = 44\mathrm{N} + 18$$

2. Dipole moment calculation. Dependence of the average value of the dipole moment squared on the polymer mass per one oxygen atom:

$$\mu_{sp}^2 = \frac{1}{2}\left(\frac{\mathrm{N}-1}{\mathrm{N}+1}\mu_1^2 + \frac{2}{\mathrm{N}+1}\mu_2^2\right) \approx \frac{0.66M + 84.7}{M+26}\ \mathrm{D}^2$$

where μ_1^2 is the square of the dipole moment for the homogeneous polymer part, μ_2^2 is the dipole moment of the PEG end groups.

3. Calculation of generalized charge. The following dependence of GZ on the number of monomer units, taking into account formula (15), is converted into dependence on polymer mass.

$$Q_{sp} = \frac{c_0 N_b}{\sum_{i=1}^{N_b}(E_{bi}/2)^{3/2}} = \frac{c_0 \cdot (7\mathrm{N}+1)}{\mathrm{N}(E_{CC}/2)^{3/2} + 4\mathrm{N}(E_{CH}/2)^{3/2} + (2\mathrm{N}-1)(E_{CO}/2)^{3/2} + 2(E_{OH}/2)^{3/2}},$$

where $c_0 = 20213$ (kJ/mol)$^{3/2}$, N_b—number of covalent bonds in the molecule, falling into the screening sphere, E_{bi}—energy of i covalent bond: E_{CC}—energy of C–C bond, E_{CH}—energy of C–H bond, E_{CO}—energy of C–O bond, E_{OH}—energy of O–H bond.

4. Calculation of SP polarity by formula (13).
5. Calculation of H-bonding probability. Dependence of the probability of PEG participation in H-bonding with an H-bond donor adsorbate on the polymer mass:

$$n_{Hsp} = \frac{3^{3/8} + (\mathrm{N}+2)^{3/8}}{2(7\mathrm{N}+2)^{3/8}} = \frac{132^{3/8} + (M+70)^{3/8}}{2(7M-38)^{3/8}}$$

6. Calculation of hydrophilicity by formula (14).

Using the formulas listed in points 2, 3 and 5, a parametric dependence of hydrophilicity on polarity for PEG is obtained (the parameter is the polymer mass).

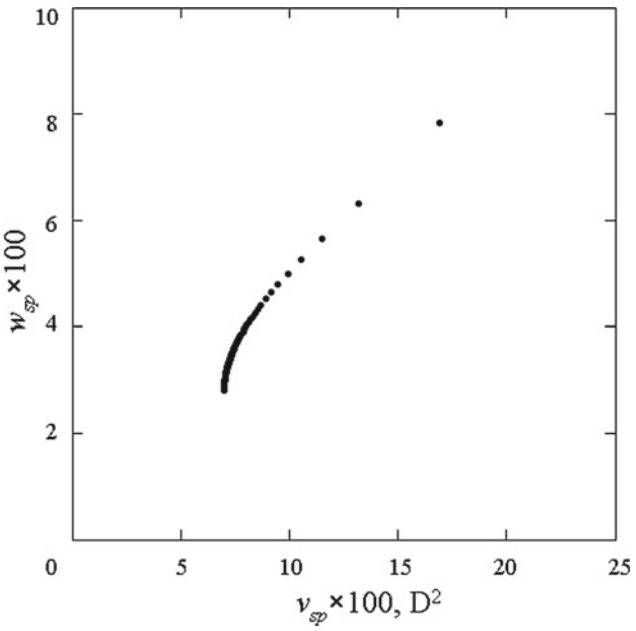

Fig. 1 Plot of polarity dependence on hydrophilicity for PEG-SP with different masses. The data of the theoretical calculation are given as a discrete curve with the molecular weight step equal to the monomer mass

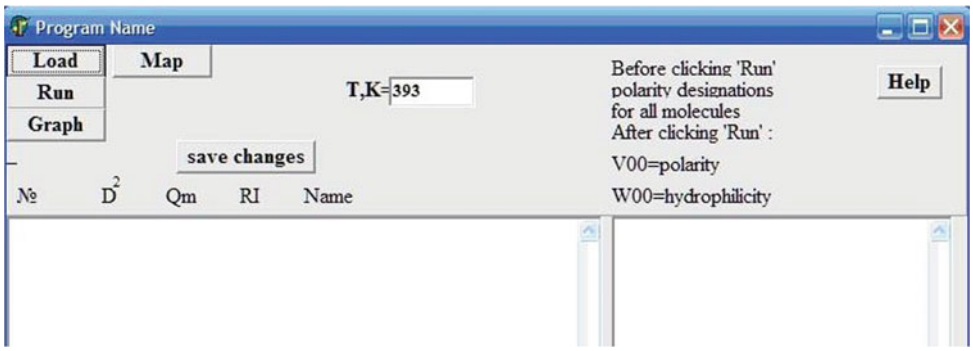

Fig. 2 STAPHMAP program functional menu

Figure 1 shows a plot in polarity-hydrophilicity coordinates for PEG-SP with different masses.

Thus, when solving the direct problem, the dependence of selectivity characteristics on the molecular weight of the polymer was found—the higher the molecular weight of PEG, the lower the values of selectivity characteristics.

Inverse simulation problem

The stages of solving the inverse problem:

(1) Obtain experimental data on the retention of polar adsorbates on the studied SP in the form of Kovacs indices. Kovacs indices for non-polar phases can be calculated using INKOVERTI program [32, 33], also literature data on Kovacs indices can be used;
(2) Calculation using the structural formula of adsorbate GC (formula (2); GEOMOL and T-HENRY programs [34]) and adsorbate dipole moment (reference data; Chem3D program [31]). Determination of polarity $v_i = \frac{\mu_i^2}{Q_i}$;
(3) Separation of adsorbates into sets M_0 and M_1. For this purpose, the characteristics of v_{0i} and S_i are calculated by the following formulas:

$$v_{0i} = \frac{\sqrt{u_i} - 1 - cv_i}{c \cdot (1 + c_T v_i)}; \tag{16}$$

$$S_i = 7.62 \cdot 10^{-3} \frac{u_i - \left[1 + c \cdot \left(v_i + v_{sp} + c_T v_i v_{sp}\right)\right]^2}{\left[1 + c \cdot \left(v_i + v_{sp} + c_T v_i v_{sp}\right)\right]^{1/3}}, \tag{17}$$

and a histogram of the distribution of values is constructed S_i. If the histogram has two maxima, then according to the peaks, the points are divided into two sets: the points of the left part belong to the set M_0, and the points of the right part belong to the set M_1. If there is one maximum on the histogram, the procedure is completed with the result according to SP polarity [v_{sp} averaged according to (18)] and zero hydrophilicity. Separation of analyte molecules into sets is possible using STAPHMAP program [34].

(4) Calculation of the SP polarity for a set M_0 molecules by the formula:

$$v_{sp} = \frac{\sum v_{0i} v_i}{\sum v_i} \tag{18}$$

(5) Calculation of SP hydrophilicity for a set M_1 molecules by the formula:

$$w_{sp} = \frac{\sum S_i}{\sum w_i} \tag{19}$$

The calculation technique allows the characteristics of the SP to be determined from the data of only two polar molecules—one of the sets M_0 and M_1.

2.6 STAPHMAP Program

The computer program STAPHMAP [34] is developed for the classification of fixed phases in gas chromatography by solving an inverse problem based on experimental data on the Kovacs indices on the characterized phases. The program allows the automatic calculation of GC SP selectivity characteristics and the separation of molecules into 2 sets based on hydrophilicity. The input data for the program operation is a table of molecule characteristics containing five columns: molecule number, dipole moment square, generalized charge, Kovacs index, and molecule name.

The interface of the *main window* (Fig. 2) represents two fields: the field of input data with the possibility to edit it and the field of calculated data obtained from the structure of analyte molecules.

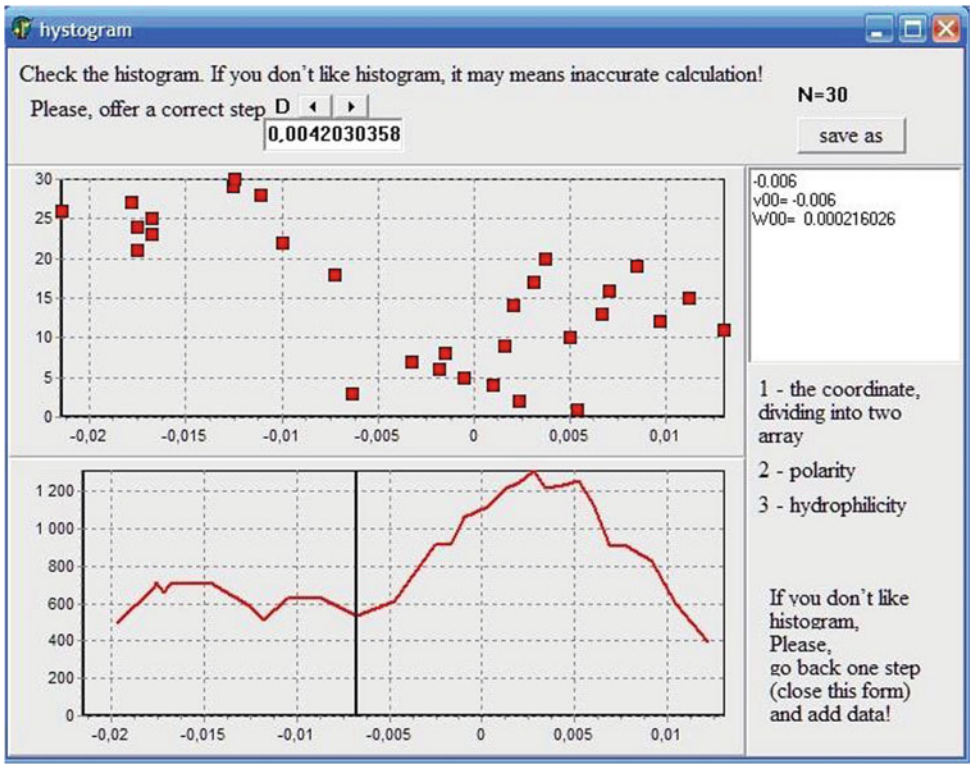

Fig. 3 STAPHMAP histogram window—Distribution graph of analyte characteristics values by sets and distribution histogram

Sequence of work with the program:

1. Creating an input data file.
2. Running the program, calculation of SP characteristics. Calculation of SP selectivity characteristics is performed by the program according to the formulas (16–19).
3. Separation of molecules into sets. The graph of the distribution of hydrophilicity values is shown in Fig. 3.
4. Creating selectivity map (see Sect. 2.6)

2.7 Selectivity Map

The found characteristics of SPs can be represented in the form of a two-dimensional map of selectivity. Figure 4 shows the selectivity map for 23 SPs based on the results of selectivity characteristics calculation from experimental data—Kovacs indices for two molecules belonging to different hydrophilicity classes on each SP. No dependence of polarity and hydrophilicity characteristics on each other is observed.

The map of selectivity can be conventionally divided into 9 regions, distinguishing levels of small, medium and strong polarity, and small, medium and strong hydrophilicity. This division is represented by the grid in Fig. 4. Phases № 1–6 fall into the P1H1 region, phase № 7 fall into the P1H2 region, phase № 8 fall into the P2H2 region, phases № 9–11 and 18–22 fall into the P3H2 region, phases № 12–13 fall into the P3H3 region, phase № 14–17 fall into the P1H3, P2H3 and P3H1 regions, while none of the phases considered falls into the P3H2 region.

Non-polar SPs, such as Squalane (№ 1) and polymethylsiloxane-based phases, fell into the P1H1 region. Squalane, which is postulated to be absolutely non-polar reference SP in the RMR method, has a small hydrophilicity. This is due to the fact that the real phase called Squalane—as opposed to the pure substance—has impurities of the detergent that was used in the preparation of the chromatography column, which gives it a slight hydrophilicity; this remark applies to all low-polarized SPs.

The P2H2 region included PEG-based phases selective to oxygen-containing compounds with medium polarity and medium hydrophilicity.

SPs with different substituents in polysiloxane (PSO-SPs) fall into the regions P1H1, P2H1, P2H2 and P3H2 (phases № 2, 3, 4, 5, 6, 8, 9, 10, 11, 13). We observe the dependence of polarity and hydrophilicity characteristics on the composition for these SPs—they increase with an increase in the number and degree of electronegativity of functional groups.

Phases with a large number of polar functional groups, providing their high polarity and hydrophilicity, fall into the region of P3H3 on the selectivity map.

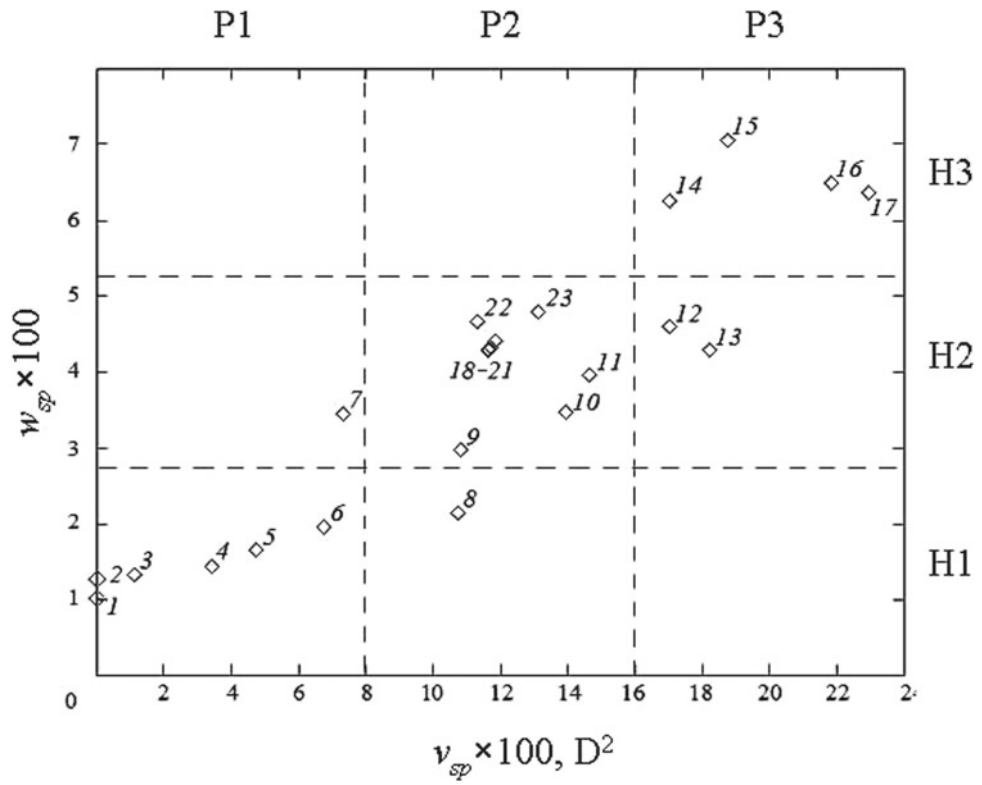

Fig. 4 Selectivity map of the chromatographic phases. Designations: 1—Squalane, 2—Apiezon L, 3—Versilub F-50, 4—OV-7, 5—DC-710, 6—OV-25, 7—Ucon 50 HB-280X, 8—OV-225, 9—XE-60, 10—Silar-5CP, 11—XF-1150, 12—Reoplex 400, 13—Silar-7CP, 14—Diglycerol, 15—THEED, 16—TCEP, 17—Cyanoethylsucrose; Block A: 18—PEG 20M, 19—PEG 20M-TPA, 20—PEG 6000, 21—PEG 4000, 22—Quadrol, 23—PEG 1000

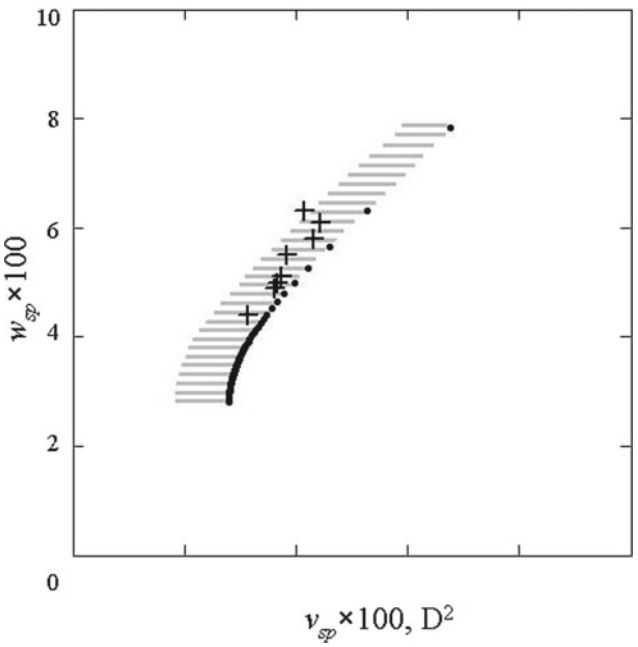

Fig. 5 Selectivity map for PEG-SP with different masses. Notations: (+)—data calculated from RMR constants, dashed curve—theoretically calculated characteristics of PEGs with different molecular masses. Shaded area of errors

A selectivity map is a fairly simple and obvious way to classify an SP. A map of selectivity can be built in the STAPHMAP program. The map is opened by pressing the **Map** button in the main program window.

3 Results and Discussion

3.1 Internal Consistency of the Applied IMI Model

To check the internal consistency of the IMI model, the results of the calculation of the SP characteristics are compared by two methods—a priori calculation from the structural formula and the calculation of the characteristics from experimental data.

The map of selectivity in the P2H2 region (Fig. 4) shows SPs based on polyethylene glycol of different molecular masses arranged in a seemingly chaotic order (phases № 18–21 and 23). Consideration of the properties of PEG depending on their molecular weight showed that these properties obey a certain regularity (see Fig. 1). The same regularity was investigated based on experimental data by solving an inverse problem.

Table 1 Approximate relationship between phase classification methods

Value	Expression	
Relation between calculation methods via incremental benchmark "e"	$\Delta I_e = x_e = 16.67 Q_e^{4/3}\left(u_e^{4/3} - 1\right)$	(20)
Calculation of dimensionless sorption energy from the increment of the standard	$u_e \approx \left(1 + 0.06 x_e Q_e^{-4/3}\right)^{3/4}$	(21)
SP polarity according to the data for the ketone molecule ($e = 3$)	$v_{sp} = \frac{\sqrt{u_3} - 1 - cv_3}{c\cdot(1 + c_T v_3)}$	(22)
Hydrophilicity of SP according to data for alcohol molecule ($e = 2$)	$w_{sp} = 7.62 \cdot 10^{-3} \frac{u_2 - \left[1 + c\cdot\left(v_2 + v_{sp} + c_T v_2 v_{sp}\right)\right]^2}{w_2\left[1 + c\cdot\left(v_2 + v_{sp} + c_T v_2 v_{sp}\right)\right]^{1/3}}$	(23)

Figure 5 shows the graph in polarity-hydrophilicity coordinates for PEG-SP with different masses. The diagram shows the characteristics of PEG-SP with polarity and hydrophilicity values calculated a priori and from experimental data in the form of Rorschneider-McReynolds (RMR) constants for molecules belonging to different hydrophilicity classes: polarity is calculated for 2-pentanone, hydrophilicity—for 1-butanol. Grey shading indicates a corridor of systematic error that includes all experimental points due to an underestimation of polarity values by a constant value in its calculation from the RMR constants. The formulas for calculating the selectivity characteristics from the RMR constants are given in Table 1.

The behavior of most of the experimental points on the graph corresponds to the theoretical dependence of the values of polarity and hydrophilicity on the PEG mass, however, the points for some SP fall out of the correct sequence, although they belong to the same curve. This can be explained by a possible error in the manufacturer's indication of the polymer molecular weight.

The comparison results show good agreement between the positions of the points of theoretical and experimental characteristics of PEGs determining their selectivity as SP. The model used for the forward and inverse problem calculations is internally consistent.

3.2 Comparison of Three-Parameter Characterization Method and Rorschneider-McReynolds Method

Both the inverse TPCh method and the RMR method use Kovacs indices to calculate SP characteristics - this allows to find the relationship between them and to calculate selectivity characteristics directly from RMR constants; this information can be more convenient than Kovacs indices since RMR constants are the passport data of the chromatographic column.

The expressions for calculating the selectivity characteristics from the RMR constants are presented in Table 1 [18]. Two reference molecules of the RMR method, 2-pentanone and 1-butanol, belonging to the sets and M_0M_1, respectively, were chosen for the calculation.

Figure 6 shows a comparison of the polarity (a) and hydrophilicity (b) values of SP calculated from Kovacs indices and from McReynolds constants x_e.

There is a shift to constant polarity values (Fig. 6a) (0.025 ± 0.005 D^2), which is due to the fact that the RMR method incorrectly uses several interrelated polarity parameters, and 2-pentanone accounts for only part of the polarity in this scheme. This indicates the redundancy of the RMR method with respect to the polarity characterization.

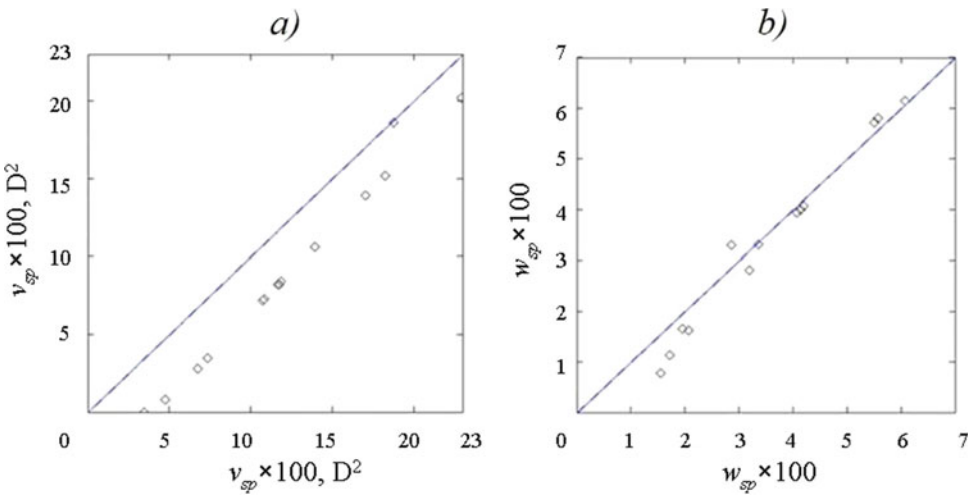

Fig. 6 Correlation of **a** polarity values, **b** hydrophilicity values, indices (TPH)—values of characteristics calculated from Kovacs indices, (RMR)—calculated from RMR constants

Comparison of the hydrophilicity values (Fig. 6b) calculated by different methods gives no shift—there is only one H-bond donor reference in the RMR scheme and there is no redistribution of the hydrophilicity characteristic among other molecules. The small discrepancy in the values at the beginning of the coordinates is due to the postulation of Squalane as a reference for nonpolar SPs in the RMR method.

The obtained correlations indicate the consistency of the TPC and RMR methods and the possibility of determining the SP selectivity characteristics from RMR constants.

3.3 Solving Complex Analytical Problems

The application of the theoretical approach developed in this work allowed solving complex analytical problems concerning not only the selection of SP in polarity and hydrophilicity, but also the consideration of more subtle points related to the inversion of selectivity to given pairs of components.

Selection of the SP by selectivity map

The developed TPC method is able not only to classify SPs, but also to solve specific analytical problems in selecting the phase most selective to the target analytes.

The choice of the SP is carried out in accordance with the empirical principle of similarity of properties. The equation for the sorption energy (1) can be represented as the scalar product of three-dimensional vectors with components proportional to the parameters of Q, μ^2 and n_H each of the interacting objects. The same refers to vectors, which characterize the SP. The increase of the sorption energy leads to the increase of SP selectivity to a molecule. Considering a set of molecules, close in their retention on the considered SP, the maximum value of the scalar product will be obtained for the molecule, the angle of which ϕ with the SP vector is zero. The condition of parallelism of the vectors characterizing the properties of substances serves as a quantitative explanation of the well-known rule in chemistry for the selection of good solvents—"like in like". The transition to polarity and hydrophilicity parameters is equivalent to projecting these vectors onto the plane of the selectivity map. It turns out that the more the SP is similar in properties to the target analytes, i.e., on the selectivity map its coordinates are as close as possible to the coordinates of the target analytes, the stronger its selectivity responds to changes in these properties. This is important in the case of separating substances in which the difference in Kovacs indices is insignificant, on the order of 10 units. By using the selectivity map and plotting the characteristics of the analytes on it, a selective SP can be selected.

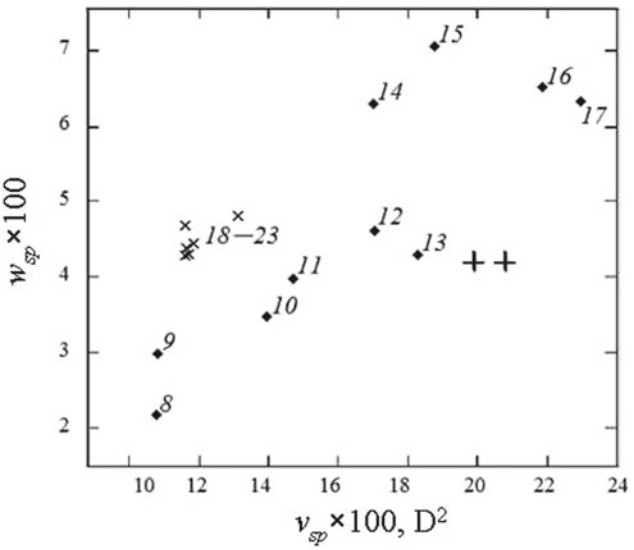

Fig. 7 SP selectivity map with target analyte characteristics marked with +. Numbering of SPs corresponds to the caption of Fig. 4

Figure 7 shows a fragment of the selectivity map (see Fig. 4) with the characteristics of a pair of analytes plotted on it. The isomers of esters, propyl acetate and ethyl propionate, are chosen as examples. The characteristics of the analytes are calculated from their structural formula as characteristics of their liquid phase. The most selective to the target analytes, is SP № 13, this choice is confirmed by data from the paper [35].

However, the selection of SPs using the selectivity map alone is not always sufficient, for example, it will be shown below that an additional criterion is responsible for the selectivity of SPs to geometric isomers.

Peculiarities of SP selection when solving the problem of separation of geometric isomers of fatty acid methyl esters

The actual task of chromatographic analysis is the determination of trans-isomers of monounsaturated fatty acids in foodstuffs. It was found that there is no safe level of consumption of industrial trans-isomers of monounsaturated fatty acids from partially hydrogenated oils, accordingly, they should be completely removed from food products. Fatty acids are determined by gas chromatography from their methyl esters (FAMEs), the analysis is difficult because of the proximity of the trans- and cis-isomers and requires special chromatographic conditions—the length of the capillary column is several times longer than standard. Two groups of SPs, PEGs and polysiloxanes with cyanopropyl groups (PSO-CPG), are described in the literature for the separation of geometric isomers of FAMEs. In food analysis,

the task is complicated by the need to identify hazardous trans-isomers in the presence of an excess of useful cis-isomers. The order of separation of the FAMEs isomers is inverse, with the trans-isomer coming out first in some systems and the cis-isomer of FAME coming out second, and the reverse order in other systems. Another problem associated with this problem is the identification of isomers, which detection fails, and the selectivity map cannot explain this inversion.

Two known sorption mechanisms—adsorption on the SP surface (A-sorption) and bulk-sorption (B-sorption)—have been considered to explain the inversion.

A-sorption is realized if the analyte has progressive degrees of freedom allowing it to move freely along the surface. If the phase surface is sufficiently flat, the trans isomer has the advantage due to the higher interaction energy, geometric isomers go in the order of cis/trans. B-sorption is achieved when the adsorbed molecule loses progressive degrees of freedom and the analyte, due to the formation of a narrow H-bond, is fixed near the SP macromolecule for long enough to form a cavity in which the analyte molecule enters. In this case, due to the smaller size of the cis-isomer has an advantage, the isomers come out in the order trans/cis.

The criterion determining the sorption mechanism of molecules is ζ [12, 21, 36]:

$$\zeta = \tau'_A/\tau_M \tag{24}$$

where τ'_A is the duration of contact of an analyte molecule with one surface molecule, τ_M is the period of rearrangement of the tangle links when an analyte molecule is surrounded by a surface macromolecule.

Thus, if the criterion is $\zeta \ll 1$, the A-sorption mechanism is implemented, and if the criterion is of order 1, the B-sorption mechanism is implemented.

B-sorption model

The surface of the polymer phase is composed by macromolecules, which are presented as a Gaussian ball. A real macromolecule can be represented as a chain of free-link units, taking Kuhn's segments for the units [22].

The interaction is characterized by the following processes: (1) phase surface adsorption; (2) the rearrangement a change in orientation of the macromolecule segments when interacting with the analyte molecule; (3) when contact time is comparable to relaxation time of the macromolecule, the ball forms a cavity around the molecule which leads to absorption of the analyte.

The system "analyte molecule—SP macromolecule" is represented as a hollow sphere or its segment formed by the macromolecule units, where the analyte molecule enters. The radius of the sphere (R_h) is determined by the following formula [22]:

$$R_h \approx R_M - r_b, \tag{25}$$

where R_M is the ball size, r_b is the half of van der Waals thickness of the links.

Note that for the B-sorption mechanism to be realized, two strict conditions must be fulfilled.

The first condition of B-sorption

In order for the analyte molecule to be fixed near the polymer macromolecule for a time sufficient for the cavity formation, it is necessary to restrict the translational degrees of freedom of motion of the analyte along the SP surface. This restriction is caused by the presence of a narrow H-bond. It is necessary to determine whether one H-bond is sufficient for analyte fixation time near the macromolecule.

The adsorption of polar molecules with the participation of the H-bond is accompanied by the fixation of the analyte molecule at the point of bond formation. The number of translational degrees of freedom of the analyte on the phase surface is directly related to the share of van der Waals interactions in the adsorption energy [22]:

$$\frac{s}{2} = \frac{E_A - E_H}{E_A}, \tag{26}$$

where E_H is hydrogen bond energy. The condition $\tau'_A \sim \tau_A$ requires that the hydrogen bond energy constitutes a significant part of the total adsorption energy. Adopting in Henry's constant an estimate of $L + r_b \approx 0.75kl_c$, where $k \sim 10$, we find:

$$\zeta \approx \zeta_0 \left(k^2/N_c\right)^{E_H/2E_A} \exp(E_H/RT) \tag{27}$$

Due to the small value $\zeta_0 \sim 10^{-2}$ for the realization of B-sorption the level of the ratio $\zeta/\zeta_0 \sim 10^{1.5}$ and above is of interest.

The ratio of adsorption energy to temperature E_A/RT can be estimated from the chromatographic conditions: to avoid too long experiments, the retention factor should not be exceed 100 on the order of magnitude [22]. By taking the logarithm of the retention factor we obtain:$E_A/RT \leq 5$. On the other hand, the logarithmizing of (27) yields a lower estimate:

$$\frac{E_H}{RT} \approx \ln\frac{\zeta}{\zeta_0} + \frac{E_H}{2E_A}\ln\frac{N_c}{k^2} \approx \ln\frac{\zeta}{\zeta_0}\left(1 + \frac{RT}{2E_A}\ln\frac{N_c}{k^2}\right) \approx 3 \tag{28}$$

Since $E_H < E_A$, taking into account the corrections we get the interval: $3 \le E_H/RT \le 4$. In [29, 35] an estimation of the molar H-bond energy through the average number of H-bonds per analyte is presented in the n_H form [22]:

$$E_H = 11.6 n_H \,(\mathrm{kJ/mol}) \tag{29}$$

where $n_H = z n_{H12}$ is the average number of H-bonds, z is the coordination number of the analyte for the H-bond with the SP, n_{H12} is the H-bond formation probability.

In [37], a general expression was derived for the lower bound of the H-bond probability:

$$n_{H12\ \min} = \frac{\sqrt{Q_{am}Q_{dM}} + \sqrt{Q_{dm}Q_{aM}}}{2\sqrt{Q_m Q_M}}, \tag{30}$$

where and Q_m and Q_M are the values of GCs of the analyte and the polymer, and Q_a and Q_d are GCs of the acceptor group and the donor group of the molecule, respectively. In the special case, when the analyte is FAME, which has no donor groups ($Q_{dm} = 0$), but has excess acceptor groups ($Q_{am}/Q_m \approx 1$), we obtain of (31)

$$n_H = z n_{H12} \approx \frac{z}{2}\left(\frac{Q_{dM}}{Q_M}\right)^{1/2} \tag{31}$$

GC of the molecules in the simple cases considered here is given by formula (2).

There are strongly hydrophilic SPs, for which the ratio Q_{dM}/Q_M is large enough to the n_H be close to the upper limit according to (32): $z/2$. If $n_H \approx z/2$ in the case of fatty acids using for themselves GC analysis the temperatures of 400–445 K, the values $E_H/RT \ge 11.6/3.7 \approx 3.1$ are reached when the analyte is coordinated with the phase by two H-bonds, i.e. at $z = 2$. Since the analyte has no donor groups, it is necessary that the SP contains pairs of donor functional groups (such as –OH, $–NH_2$ or –CN groups) located close to each other (0.4 nm).

So, for curvature of SP surface under analyte molecule in the form of spherical segment with height of order of its curvature radius ($h \approx R_h$, when $\zeta \approx 0.5$), molecule of fatty acid methyl ester must be able to form at least two H-bonds with SP [22].

The second condition of B-sorption

In B-sorption, when a cavity with a height on the surface of the phase of the order of the radius of curvature in which the molecule is placed, cis-isomer position becomes energetically more favorable than of trans-isomer position. The best separation of isomers corresponds to the parameters SP —$\frac{1}{2}L_{cs} < R_h < \frac{1}{2}L_{tr}$—the radius of the cavity is more than half the length of the cis isomer and less than half the length of the trans isomer [22].

Consideration of the mechanisms of A-sorption and B-sorption of the interaction of FAME with SP macromolecules allows us to conclude that B-sorption has a stronger effect on the selectivity of the separation of geometric isomers than A-sorption: when a cis-isomer enters the cavity, it interacts with SP by its entire surface, which significantly increases the sorption energy and, consequently, the retention. This makes the application of SPs implementing the B-sorption mechanism promising for the analysis of the content of trans-fats in food by GC method.

There are only two groups of SPs that cope with the separation of geometric isomers of FAMEs, let us consider them below.

Polyethylene glycols

PEG does not have enough donor groups to form two H-bonds with FAMEs. Therefore, the A-sorption mechanism is realized in such a system. For the most complete separation of geometric isomers of FAMEs in the cis-/trans- order, PEGs with the highest molecular weight are used, so that the surface of SP is as flat as possible. Then the trans-isomer will have an advantage and be retained stronger.

Polysiloxanes SP with cyanopropyl substituents

The presence of a large number of donor groups for the formation of H-bonds in SP based on polysiloxane with cyanopropyl groups (PSO-CPG) ensures the formation of paired H-bonds with the FAME molecule—the first condition of sorption in the cavity is satisfied. The expression for the mass of N-linked PSO-CPG polymer: $m_M = m_2 + m_1 N$, where m_1 is the mass of the monomer unit (180 Da), m_2 is the mass of end groups (162 Da). Under the conditions of the chromatographic experiment, Kuhn's segment for PSO-CPG corresponds to two monomers; its length is $l_c = 0.57$ nm.

General formula of FAME molecule:$C_nH_{2n-1}O_2CH_3$. The length of the trans-isomer of FAME in the most favorable trans-conformation is equal to $[2 \cdot 0.11 + (n+1) \cdot 0.15] \cdot \sqrt{2/3}$ nm, where n is the carbon number of the acid. Find the length of the cis-isomer by subtracting the difference in the lengths of the isomers (0.1 nm): $L_{cs} \approx 0.12\,(n+1) + 0.08$ nm. The equation for the PSO-CPG mass required for the cis-isomer FAME to fit in the cavity of the SP is derived from the equality of the cavity diameter and the length of the cis-isomer: $0.57\sqrt{(m_M - 162)/360} - 0.34 = 0.06(n+1) + 0.04$, from whence [22]:

$$m_M = 3.99(n + 7.33)^2 + 162 \tag{32}$$

Table 2 Cavity radii [22] in phases based on cyanopropylpolysiloxanes of different molecular weight [38]

Stationary phase	m_M	Rh
A (Silar 10 C)	4122	1.55
B (Silar 10 C)	10,242	2.68
C (Silar 10 C)	3402	1.37
SP 2340	2862	1.22
OV-275	2094	1.06
Silar 9 CP	3402	1.37

Table 3 PSO-CPG molecular weights

Carbon number of the acid n	Acid name	$m_M(32)$	Closest exact mass of PCO-CPG m_M and number of monomers (N)
15	Pentadecene	2152	2142 (11)
16	Palmitine	2334	2322 (12)
17	Heptadecene	2524	2502 (13)
18	Oleic, Stearic	2722	2682 (14)–2862 (15)

Table 2 shows the cavity size calculation results for a number of SPs representing PCO-CPGs of different molecular weights [22, 38].

Of the SPs presented in Table 2, the condition $L_{cs} < 2R_h < L_{tr}$ at n = 18 is best satisfied by phase OV-275 and the other phases to a lesser extent; this conclusion is confirmed by data from the literature [38] and catalogues of SP manufacturers [39]. Thus, the carbon number of the monounsaturated fatty acid can be used to predict the most selective SP for the separation of its geometric isomers [22].

Table 3 shows the theoretical prediction of the most suitable PCO-CPG in terms of masses for the separation of geometric isomers of MEGC with C15–C18 radicals [22].

According to the theoretical calculation, the optimal SPs for the determination of trans fats in the presence of cis-isomers are PSO-CPGs with masses in the range of 2500–2800 Da. Polymers with lower masses can be optimal for shorter analytes, but their selectivity for FAME with C17, C18 radicals will noticeably decrease due to the small cavity size that does not accommodate not only trans but also cis-isomers.

Thus, we can not only explain the inversion of SP selectivity with respect to geometric isomers of FAMEs and the order of isomer yield depending on the structural formula of SPs, but also predict the most efficient SPs for separating geometric isomers of FAMEs based on their structure [22].

4 Conclusion

A mathematical model of the interaction between the stationary phase and the adsorbate has been proposed which takes into account 3 types of energy contributions: non-polar, polar and hydrogen bonds. The method of three-parametric characterization of fixed phases for increasing selectivity of analytical gas–liquid chromatography has been developed. Ways of calculating selectivity characteristics have been developed: a priori by the structural formula of the stationary phase (direct simulation problem) and from experimental data on chromatographic retention (inverse simulation problem). The dependence of polarity and hydrophilicity characteristics of fixed phases on polymer mass has been found for the first time. A computer program STAPHMAP has been developed which allows adsorbate molecules to be classified into hydrophilicity classes and the selectivity characteristics of stationary phases to be calculated from experimental data using Kovacs indices. For the first time, a graphical method for classifying gas chromatographic stationary phases in the form of a selectivity map has been proposed. The selectivity map is applied to select the stationary phase most selective to the target analyte, for which the principle of similarity of properties is used. An explanation for the inversion of selectivity of stationary phases in the gas chromatographic analysis of geometrical isomers of monounsaturated fatty acids has been proposed. Quantitative criteria for realization of A-sorption and B-sorption mechanisms have been determined. The developed approach has shown the prospects of realization of mechanism of B-sorption at the analysis of the content of trans-fats in food by gas chromatography. Characteristics of cyanopropylpolysiloxanes for selective separation of geometrical isomers of monounsaturated fatty acids depending on the carbon number of acid were predicted.

References

1. Souter, P.: Calculation of Rohrschneider constants. J. Chromatogr. A **92**(2), 231–236 (1974)
2. Ashes, J.R., Haken, J.K.: Gas chromatography of homologous esters: X. Data prediction properties of a Rohrschneider-type scheme. J. Chromatogr. A **135**(1), 61–65 (1977)
3. Lukáš, J.: Modification of the Rohrschneider method for the classification of the polarity of polymeric sorbents based on methacrylic acid esters. J. Chromatogr. A **190**(1), 13–19 (1980)
4. Roth, M., Novák, J.: Correlation of two criteria of polarity for stationary phases in gas-liquid chromatography. J. Chromatogr. A **234**, 337–345 (1982)
5. Abraham, M.H., Andonian-Haftvena, J., MyDua, C., Osei-Owusua, J.P., Sakellariou, P., Shuely, W.J., Poole, C.F., Poole, S.K.: Comparison of uncorrected retention data on a capillary and a packed hexadecane column with corrected retention data on a packed squalane column. J. Chromatogr. A **688**, 125–134 (1994)
6. Tian, W., Ballantine, D.S., Jr.: Characterization of Cyano-functionalized stationary gas chromatographic phases by linear solvation energy relationships. J. Chromatogr. A **718**, 357–369 (1995)
7. Vitha, M., Carr, P.W.: The chemical interpretation and practice of linear solvation energy relationships in chromatography. J. Chromatogr. A **1126**, 143–194 (2006)
8. Tan, L., Carr, P.W.: Study of retention in reversed-phase liquid chromatography using linear solvation energy relationships: II. The mobile phase. J. Chromatogr. A **799**, 1–19 (1998)
9. Ševčik, J., Löwentap, M.S.H.: New criterion for polarity of stationary phases in gas chromatography. J. Chromatogr. A **217**, 139–150 (1981)
10. Dolgonosov, A.M., Rudakov, O.B., Surovtsev, I.S., Prudkovsky, A.G.: Column Analytical Chromatography as an Object of Mathematical Modeling. GEOCHI RAS—Voronezh GASU, Voronezh (2013)
11. Juvancz, Z., Cserhaiti, T., Markides, K.E., Bradshaw, J.S., Lee, M. L.: Characterization of some new polysiloxane stationary phases by principal component analysis. Chromatographia **38**, 227–231 (1994)
12. Dolgonosov, A.M.: An Electron Gas Model and Generalized Charge Theory for the Description of Interatomic Interactions and Adsorption. LIBROCOM, Moscow (2009)
13. Dolgonosov, A.M.: Generalized charge in the description of adsorption in the Henry region. J. Phys. Chem. **76**(6), 1107–1112 (2002)
14. Dolgonosov, A.M.: Theory of generalized charges for interatomic interactions. J. Phys. Chem. **75**(10), 1813–1820 (2001)
15. Dolgonosov, A.M., Prudkovsky, A.G.: Effects of non-ideal adsorption on a rough liquid phase surface in gas chromatography. Index of "non-freedom" and steric factor of adsorbate molecules. J. Phys. Chem. **80**(6), 1098–1103 (2006)
16. Dolgonosov, A.M., Zaitceva, E.A.: Polarity characterization of stationary phase in gas chromatography based on theoretical description of intermolecular interactions. I. The case of absence of hydrogen bonds. Sorption Chromatogr. Processes **14**(4), 578–590 (2014)
17. Dolgonosov, A.M., Zaitceva, E.A.: Polarity characterization of stationary phase in gas chromatography based on theoretical description of intermolecular interactions. II. The case of hydrogen bonds. Sorption Chromatogr. Processes **15**(3), 321–332 (2015)
18. Zaitceva, E.A., Dolgonosov, A.M.: Theoretical evaluation of selectivity characteristics of gas chromatographic fixed phases. Sorption Chromatogr. Processes **18**(5), 676–689 (2018)
19. Zaitceva, E.A., Dolgonosov, A.M.: Three-parameter model of intermolecular interactions as a basis for classification and selection of fixed phases for gas chromatography. Sorption Chromatogr. Processes **19**(5) 525–541 (2019)
20. Dolgonosov, A.M.: Polarity and hydrophilicity are fundamental independent characteristics of chromatographic fixed phases. Sorption Chromatogr. Processes **15**(3), 312–320 (2015)
21. Dolgonosov, A.M., Zaitceva, E.A.: Model of intermolecular interaction with hydrogen bond formation and its application for characterization of selectivity of chromatographic phases by example of polyethylene glycols. J. Struct. Chem. **61**(8), 1300–1311 (2020)
22. Dolgonosov, A.M., Zaitceva, E.A.: Factors determining the selectivity of stationary phases to geometric isomers of fatty acids in GLC analysis. J. Anal. Chem. **75**(12), 1119–1128 (2020)
23. Dolgonosov, A.M.: A model of hydrogen bond formation between vapor and liquid molecules. J. Struct. Chem. **61**(7), 1107–1120 (2020)
24. Dolgonosov, A.M.: The surface tension coefficients and critical temperatures of uniform nonpolar liquids from a priori calculations within the framework of the theory of generalized charges. Russ. Chem. Bull. **65**(4), 952–963 (2016)
25. Reinganum, M.: Kräfte elektrischer Doppelpunkte nach der statistischen Mechanik und Anwendung auf molekulare und Ionenwirkungen. Ann. Phys. **343**(8), 649–668 (1912)
26. Keesom, W.H.: Die van der Waalsschen Kohäsionskräfte. Physikalische Zeitschrift **22**, 129–141 (1921)
27. Debye, P.: Van der Waals cohesionforces. Physikalische Zeitschrift **21**, 178–187 (1920)
28. Falkenhagen, H.: Kohäsion und zustandsgleichung bei dipolgasen. Physikalische Zeitschrift **23**, 87–95 (1922)
29. Dolgonosov, A.M.: Representation of hydrogen bonding following from the theory of generalized charges. J. Struct. Chem. **60**(11), 1765–1774 (2019)
30. Dolgonosov, A.M.: Relationship of adsorption energy to the Kovacs index derived from the theory of generalized charges. Sorption Chromatogr. Processes **15**(2), 168–178 (2015)
31. Cambridgesoft. http://www.cambridgesoft.com. Last accessed 2021/10/08
32. Prudkovsky, A.G., Dolgonosov, A.M.: Tool for evaluation of Kovacs index by retention time of substance in gas chromatography. J. Anal. Chem. **63**(9), 935–940 (2008)
33. Dolgonosov, A.M., Prudkovsky, A.G.: Intramolecular rotation barriers by the temperature dependence of Henry's constant in the region of stiffness violation of an adsorbed molecule. J. Phys. Chem. **82**(5), 931–939 (2008)
34. Zaitceva, E.A.: Method for description of selectivity of liquid fixed phases in analytical chromatography of polar organic compounds and their isomers. Dissertation. Cand. GEOKHI RAS, Moscow. http://www.geokhi.ru/Thesis/2021/Candidate/Zaitseva/Dissertation_Zaitseva_EA.pdf. Last accessed 2021/10/08.
35. Lu, C., Guo, W., Yin, C.: Quantitative structure-retention relationship study of the gas chromatographic retention indices of saturated esters on different stationary phases using novel topological indices. Anal. Chim. Acta **561**, 96–102 (2006)
36. Dolgonosov, A.M., Prudkovsky, A.G.: Distribution mechanism in gas-liquid chromatography involving the effect of conformational rearrangement of a stationary phase macromolecule upon contact with an adsorbate molecule. Sorption Chromatogr. Processes **10**(6), 887–893 (2010)
37. Dolgonosov, A.M.: Universal ratio for the energy and length of covalent bonding following from the theory of generalized charges. J. Inorg. Chem. **62**(3), 330–336 (2017)

38. Heckers, H., Dittmar, K., Melcher, F.W., Kalinowski, H.O.: Silar 10 C, Silar 9 CP, SP-2340 and OV-275 in the gas-liquid chromatography of fatty acid methyl esters on packed columns: chromatographic characteristics and molecular structures. J. Chromarogr. **13**(5), 93–107 (1977)

39. ~Agilent chromatography fixed-phase and consumables catalog. https://www.agilent.com/en/product/gc-columns/application-specific-gc-columns/select-fame-columns. Last accessed 2021/10/08

Acid Retardation Method and Its New Variants for the Separation of Components of Complex Solutions

R. Kh. Khamizov, A. N. Krachak, N. S. Vlasovskikh, and A. N. Gruzdeva

1 Introduction

Discovered many years ago, a method for separating mixed concentrated solutions of acids and their salts on anion exchanging resin—the Acid Retardation method [1], still seems to be intriguing, obscure and is of interest from theoretical and practical points of view. Processes based on this method are very simple, do not require any reagents other than pure water for the regeneration of sorbents and the implementation of repeated working cycles of sorption–desorption. Simple or standard AR- processes consist of repetitive work cycles. At the first stage of each cycle, a mixed solution of acid and salt is passed through a bed of inert nanoporous material, for example, a hypercrosslinked polymer or gel-type anion exchanger in the anionic form equilibrated with the solution (to avoid ion exchange reactions). In this case, separation occurs: the acid remains in the column for some time, while the salt solution passes without delay through the bed of sorption material. After acid `breakthrough', water is passed through the column, and the acid solution is displaced. These processes can be used for the processing of some highly acidic technological solutions and wastewater in the metallurgical and chemical industries; they are also promising for sample preparation in analytical chemistry [2–4].

Despite the continuing great interest in the study of the AR method [4–20], there is still no common point of view on the mechanisms of separation processes. A mechanism of extraction of low molecular electrolytes on two-phase cross-linked polyelectrolytes with different distributions of components in phases was proposed in the works of Ferapontov and co-authors [4–10]. However, in these works, the reason for the selective absorption of acids in comparison with salts remained unclear. Davankov and co-authors [11–20] proposed a mechanism of ion exclusion based on the fact that, due to the size effect, hydroxonium ion can penetrate into the sorbent matrix to a greater extent than large hydrated cations of metals. This penetration is accompanied by additional exchange between the sorbent and external solution with low molecular weight anions and water to ensure electroneutrality and mechanical equilibrium. This mechanism, in principle, explains the dynamic chromatographic effects observed in the separation of components by acid retardation. However, questions remain, and they are related to the fact that, in contrast to the separation of acids and salts, practically no significant effects are observed for the separation of the salts themselves even for hydrated cations of various sizes. Moreover, it is unclear why AR processes are equally easily feasible when using practically neutral hypercrosslinked polymers and anion exchangers with a positively charged matrix, which are characterized by Donnan displacement of co-ions.

This paper presents the main results of further studies of the acid retardation method in order to further clarify the mechanisms of AR-separation of components, as well as to identify other processes at the molecular level accompanying such a separation. These researches were carried out in the laboratory of sorption methods of the Vernadsky Institute RAS in collaboration with a group of theoreticians from the Physics Department of Moscow State University. These results proved to be very important for the development and expansion of the capabilities of the acid retardation method itself. It should be noted that until now, one of the main limitations of the standard version of the AR method has been that it was applicable only when the salts separated from the acid are readily soluble. This is only possible in chloride and nitrate environments. When separating in real concentrated sulfate or phosphate media containing, as a rule, iron, alkaline earth metals and other components, standard AR processes turned out to be useless. Another

R. Kh. Khamizov (✉) · A. N. Krachak · N. S. Vlasovskikh · A. N. Gruzdeva
Vernadsky Institute of Ceochemistry and Analytical Chemistry, Russian Academy of Sciences, 19 Kosygin St., Moscow, 119991, Russia
e-mail: khamiz@mail.ru

V. P. Kolotov and N. S. Bezaeva (eds.), *Advances in Geochemistry, Analytical Chemistry, and Planetary Sciences*,
https://doi.org/10.1007/978-3-031-09883-3_30

limitation of the standard AR method is that of the original processed solution. It is also not always possible to organize a countercurrent process. In these cases, another version of the acid retardation method may turn out to be useful, which can be implemented in an anion-resin bed, in which the porosity (intergranular) space is filled with an organic liquid immiscible with water and aqueous solutions. This approach turns out to be especially successful for sample preparation from strongly acidic solutions for elemental analysis by ICP methods.

2 Simple Cyclic Processes

Figure 1 shows examples break-through curves (concentrations of components in the eluate fractions leaving the column) obtained for acid and salt separation in standard AR-process for mixed solutions of—and—$Sr(NO_3)$ with almost the same initial ratio of the components. Zones I-III correspond to successive stages of passing the concentrated mixed solution through the column with the anion exchanger in NO_3^- form in the bottom-up direction. At the stage marked by zone I, there is a displacement of water, which was initially in the free volume and porosity (interbead) space of the anion-exchange resin bed. Then the salt solution comes out of the column, separated from the acid coming out later, zone III corresponds to the onset of equilibrium, the fractions of the solution coming out of the column are close to the composition of the initial mixed solution, and they can be returned into the fed solution. Zones IV–V correspond to the successive stages of column regeneration—displacement of the acid retained by the anion exchanger with clean water flowing through the bed in the top-down direction. After the completion of the complete duty cycle, the listed operations are repeated. Flow directions in the AR-process are chosen so that there is no gravitational blurring of the shown concentration fronts, and for this purpose, the less dense solution is always above the denser one in the sorbent bed. All possible stages of the process are shown for familiarization. It is clear that after examining the yield patterns after the first cycle, it is possible to skip the operation for zone III and not obtain the corresponding eluate fractions in the next repeated separation work cycles. It is also possible to stop the process at a convenient point in zone IV and not perform the next step. As can be seen from the data presented, the presence of magnesium cation instead of strontium in the stock solution, at all other equal conditions, significantly increases the acid retention and the degree of separation of the components, as judged by the volume of solution exiting from the column until the neutral reaction ($pH > 5$) is reached. The break-through curves in the presented figures are plotted with a continuing current volume on the abscissa axis for all successive stages of a single process cycle.

Data on acid sorption obtained for almost identical (in concentrations) mixtures of nitric acid and nitrates of various metals are shown in Fig. 2. The figure compares sections of the break-through curves of HNO_3 corresponding to the sorption stage obtained in a series of experiments performed under identical conditions on the same load of strong base anion exchanger AV-17 in NO_3^- the form. In each case, after equalization of concentrations of nitric acid at the inlet and outlet of the column, sorbed components—acid and salt—were displaced by distilled water (these sections of the acid, as well as the concentration curves of the salts are not given). The data obtained show that in the presence of the accompanying cation, the character of the acid retention curve and its amount absorbed by the anion exchanger noticeably change.

From the data shown in Figs. 1 and 2 we can see that the influence of cation is the stronger the higher its charge is. For cations with the same charge there is a change in their influence on the amount of retained acid in accordance with the following series: $Q_H(\mathrm{Li}) > Q_H(\mathrm{Na}) > Q_H(\mathrm{Rb}) > Q_H(\mathrm{Cs})$; $Q_H(\mathrm{Mg}) > Q_H(\mathrm{Ca}) > Q_H(\mathrm{Sr})$; $Q_H(\mathrm{Al}) > Q_H(\mathrm{La})$. Thus, cations with smaller ionic radii and with larger charges have a stronger influence on acid absorption by the anion exchanger. This dependence is clearly demonstrated in Fig. 3, which shows the effect of the parameter equal to the ratio of the ion charge to its crystallochemical radius on the value of such a parameter as "excess" retention of nitric acid, measured under the same conditions for all salts. This parameter is defined as the difference between the equilibrium amounts of retained acid, measured under otherwise equal conditions when passing the initial mixed solution and one-component solution of acid with the same concentration of HNO_3. All obtained results lie practically on the same linear dependence. It can be seen that the nature of the metal cation which presents in the solution together with the acid in the form of its salt has a significant impact on the sorption properties of the anion exchanger in the Acid Retardation method [21, 22]. Compared to the retention of acid from its single-component solution, the presence of metal salt in it can create additional ion exchange capacity, the values of which differ by almost an order of magnitude for cations of different nature.

3 Results of Theoretical Analysis and Mechanism of Separation

The patterns shown, at first glance, correspond to the mechanism of ionic exclusion discussed above. In order to clarify the nature of selectivity to acids, a theoretical analysis [23, 24] was made in which other possible separation mechanisms were considered. They were based on the fact

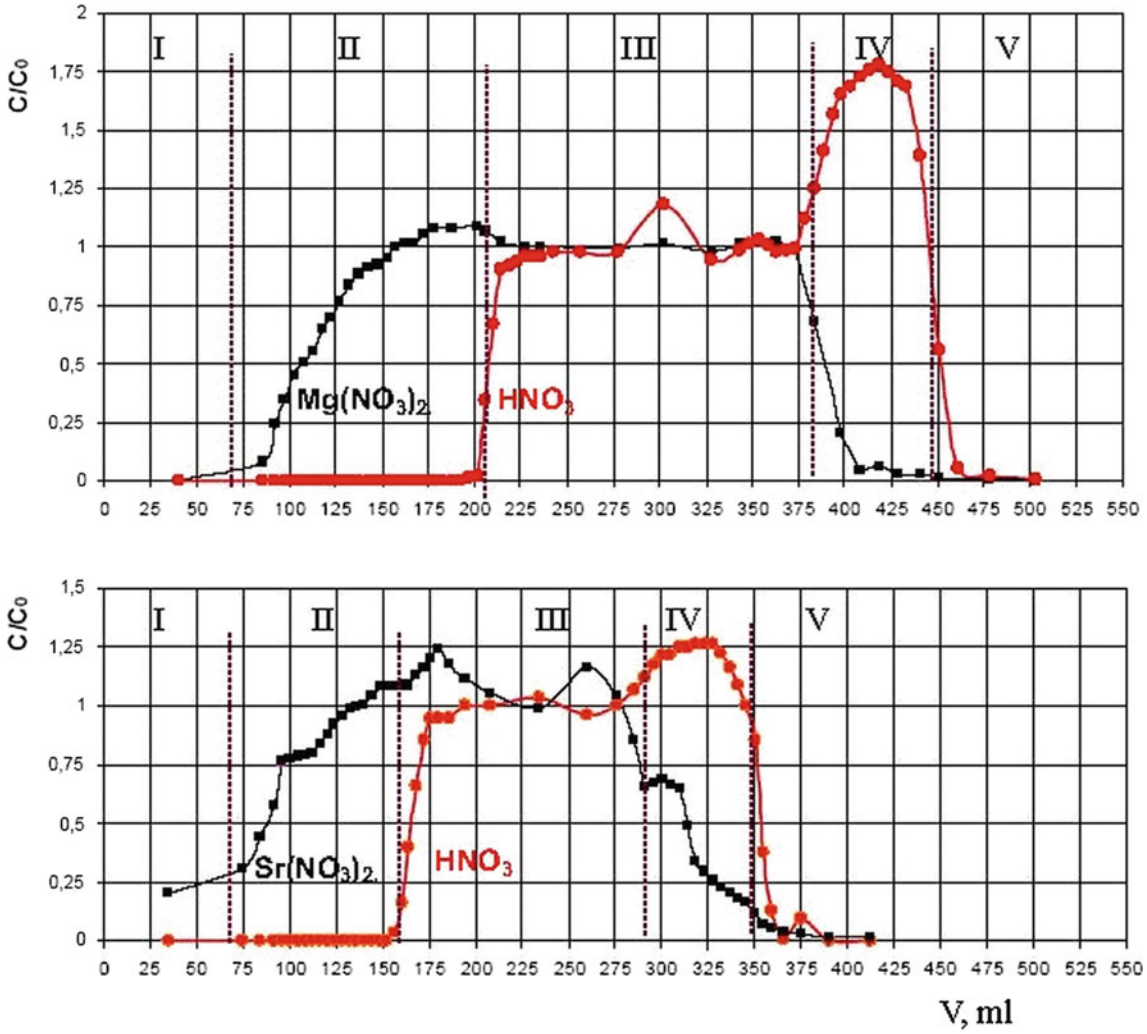

Fig. 1 Concentration histories and break-through curves of the AR-separation of components from binary mixtures: 1.33 M HNO_3—0.99 M $Mg(NO_3)_2$ and 1.4 M HNO_3—0.98 M $Sr(NO_3)_2$. Strong base anion exchanger AV-17 in the NO_3—form: bed volume—169 ml (H = 28 cm); flow rate—1 ml/min

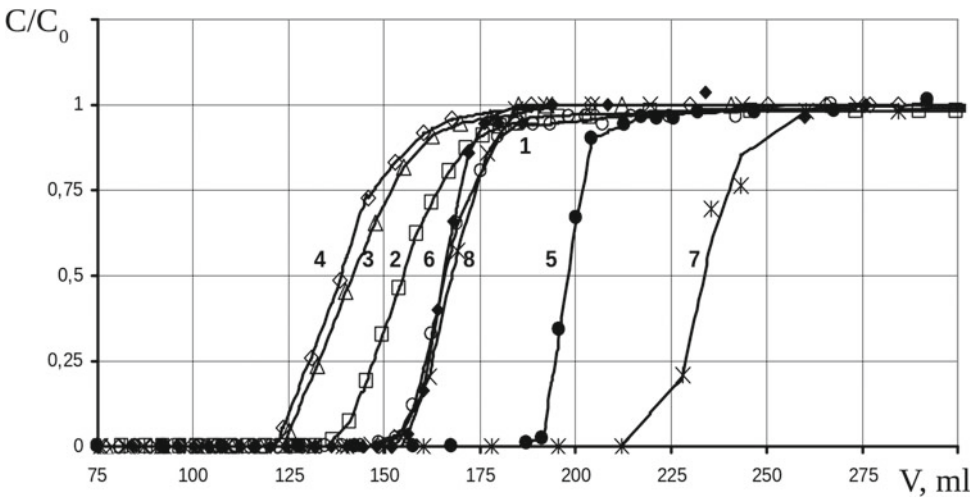

Fig.2 Concentration histories of the retention of HNO_3 in the presence of nitrate salts formed by various cations: 1-Li^+, 2-Na^+, 3-Rb^+, 4-Cs^+, 5-Mg^{2+}, 6-Sr^{2+}, 7-Al^{3+}, 8-La^{3+}

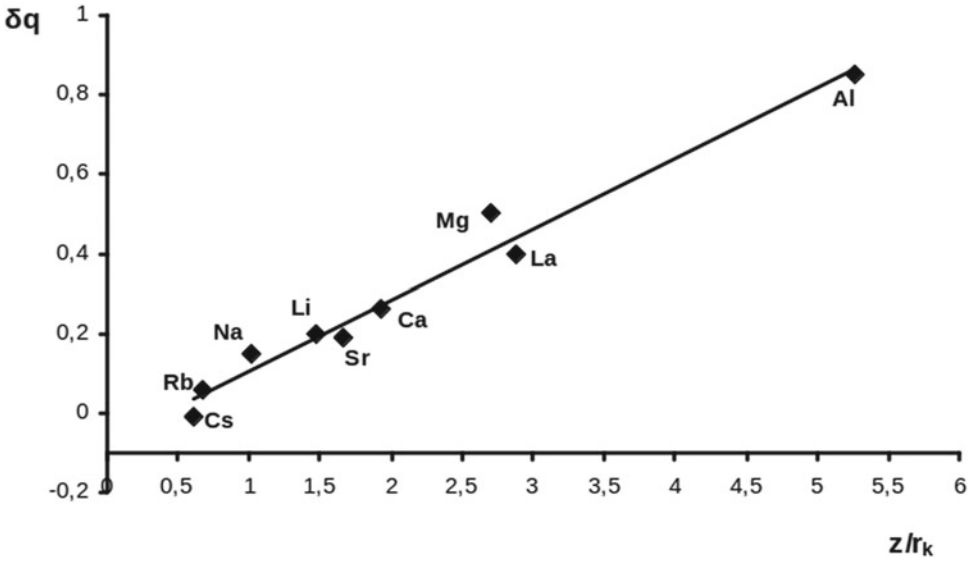

Fig. 3 The additional sorption capacity of a strongly basic anion exchanger for acid, achieved by adding metal nitrate (1 mol/l) to the initial solution of HNO_3 (1.4 mol/l)

that in concentrated solutions and in media with reduced dielectric permittivity, acids dissociate less and may exist in the form of molecules or strongly bound ionic pairs. Such components can participate equally with water in competitive solvation processes of the anion-exchanging resin matrix, which carries an excess charge, and the solvation of charged counterions in the ion-exchange resin phase. They can also easily penetrate into nanoscale pores compared to ions with a large hydrate shell, which are the ions formed during dissociation of salts in the external solution. Possible mechanisms of competitive solvation [23] and molecular sorption (retention) of acids [24] have been considered. The physical models and theoretical concepts used in these works were practically the same and were based on the new approach to calculating the activity coefficients of ions in multicomponent systems developed by Tikhonov and co-authors [25–28]. Since the aforementioned papers describe everything in sufficient detail, here we do not consider the mathematical aspects of the theory, which would occupy a large place. A two-phase physical model consisting of external and "internal" solutions is considered. The latter is a liquid phase inside a gel-type anionic resin or in nanopores of a supercross-linked copolymer. Transition energies of molecular and ionic components between the phases and their equilibrium distribution are calculated using an approach close to Debye-Hückel theory, but differing in that, the volumes occupied by the components in the respective phases are taken into account. One of the main results and criteria of correctness of the developed model is the possibility to calculate the so-called average value of dielectric permittivity in complex multicomponent aqueous media. These calculations make use of the fact that the low-frequency limit of the dielectric constant of water under normal conditions can vary from 78 in the mass of free water to 2 in the hydrate ion shell [29]. The latter is due to the fact that in the hydrate shell water molecules are already polarized, and the dipoles are already oriented by the polarizing ion so that the external electric field of such water is no longer weakened. Figure 4 shows the calculation of dependencies of averaged dielectric permittivity of the solvent (ε) on the concentration of dissolved salt in it. As can be seen from the presented curves, the calculations for concentrated one-component solutions satisfactorily coincide with the experimental results obtained by other authors under independent conditions [30]. These results confirm the adequacy of the developed model used, among others, in [23]. Modeling taking into account the characteristics of different organic monomers and the structure of sorption materials shows that in the internal solution of a neutral sorbent, e.g., super crosslinked polystyrene, the values ε may reach values from 20 to 10 depending on the concentration of the electrolytes (according to them on the upper curves). In an anion exchanger with charged functional groups and neutralizing counterions, dielectric constant values can be even lower. Figure 5 shows our calculated dependences of the nitric acid dissociation constant on the dielectric permittivity of the solvent. It can be seen that almost completely dissociated in pure water, HNO_3 becomes a weak acid in predominantly molecular form at values of $\varepsilon < 20$. The results obtained are confirmed by experimental tabulated data [31] on the dissociation constants of nitric acid in various organic solvents. The dependence of its dissociation constant on values of ε for different organic compounds has approximately the same form as the calculated theoretical curve. Thus, the mechanism of ionic exclusion proposed earlier in [11–20] should be corrected. The sieve effect responsible for the separation of acids and salts in AR method is determined by the molecular absorption of acid and the exclusion of strongly

hydrated and having large size ionic pairs of salts. In this case, electroneutrality is initially provided and the Donnan rejection of the co-ions has as little effect on the separation process in the anion exchanger as well as in the neutral nanoporous sorbent. The possibility of acid displacement by water at the regeneration stages in AR-processes is determined by competitive solvation between water and polar acid molecules. The model of sorption dynamics built with consideration of molecular retention of acid and competitive solvation [23, 24, 32] allows to adequately describe the real separation processes in columns, which is demonstrated by comparison of experimental and calculated curves in Figs. 6 and 7.

4 Complex AR Processes in Colloidal Systems

The examples of simple processes presented above were interesting to explain the mechanism of acid and salt separation. However, they are of little practical use because the acidic solutions to be processed must not contain components leading to the formation of poorly soluble compounds and associated precipitates in a neutral medium. This condition arises because the separation process itself involves the introduction of salts into the neutral solution at the acid retardation stage. In real industrial practice any process of acid leaching of valuable components from natural raw materials is connected with formation of multicomponent solution, containing iron and other components, stable only in acid medium. In addition, sulfuric acid, which forms insoluble sulphates with alkaline earth elements, is often used for ore stripping. Finally, there are very large-scale processes which lead to formation of low-stable colloidal multicomponent systems irrespective of the type of acid used for the decomposition of natural raw materials. Here are some actual examples of systems to which standard AR-processes cannot be applied, and they should be modified.

4.1 Processing of Wet Phosphoric Acid

Industrial wet process phosphoric acid (WPA) is oversaturated by a large number of impurities of low soluble phosphate and sulphate compounds which are spontaneously but slowly precipitated from it (Table 1). Due to the high level of contamination, WPA cannot be used directly for the production of some modern products, for example, soluble fertilizers of high-quality. On the other hand, depending on the initial raw material, some sorts of industrial phosphoric acids contain valuable components, in particular, up to 1 kg/t of rare-earth elements (REE). The relevance of the development of the new AR-process outlined below was due to the temptation of simultaneously solving the tasks: purification of phosphoric acid and REE extraction.

Attempts to use the standard technique of simple AR-processes described above for processing of wet phosphoric acid were unsuccessful. In all experiments, deposition of low-soluble substances in the ion-exchange resin bed took place. At room temperature such deposition occurred rather slowly and after the front of the nearly neutral salt solution reached the top of the columns. In experiments with hot WPA sedimentation occurred immediately after the beginning of acid retardation stage (temperature conditions were set by the necessity of technology development with preservation of purified acid heat for its further industrial processing). Initially, one or more small precipitation belts were formed in the lower part of the column, where the initial acid entered, which followed the flow, but with a certain delay, moved in a complex way towards the column outlet. Such behavior is almost fully consistent with theoretical ideas about percolation of multicomponent solutions and colloids with excessive content of low soluble substances [33]. At the end of the retention stage, a large amount of precipitation accumulated at the top of the column in the form of one broad belt in the ion-exchange bed. It became clear that a simple cyclic AR-process is not applicable to such a complex system as industrial phosphoric

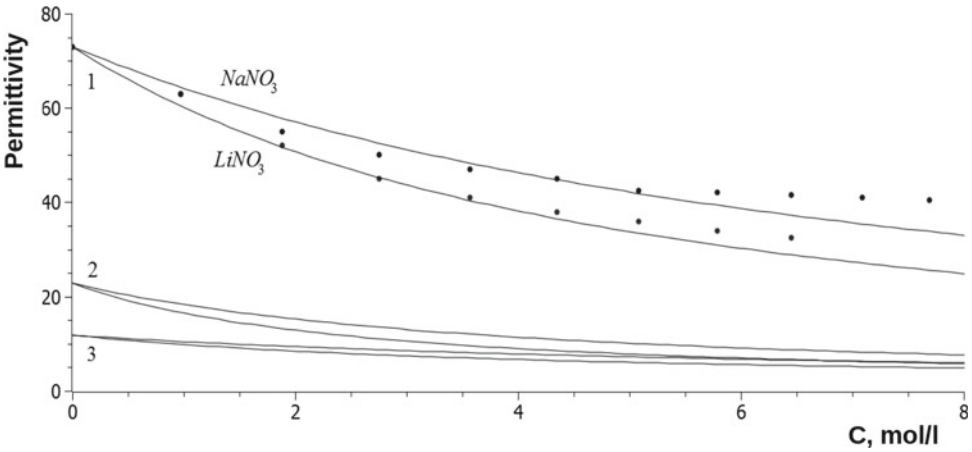

Fig. 4 Dependence of the average dielectric constant of the solvent on the concentration of the dissolved salt. 1-external solution; 2,3- internal solution in the sorbent grain in the absence (2) and the presence of charged functional groups. Solid lines are calculated data, points are experimental data

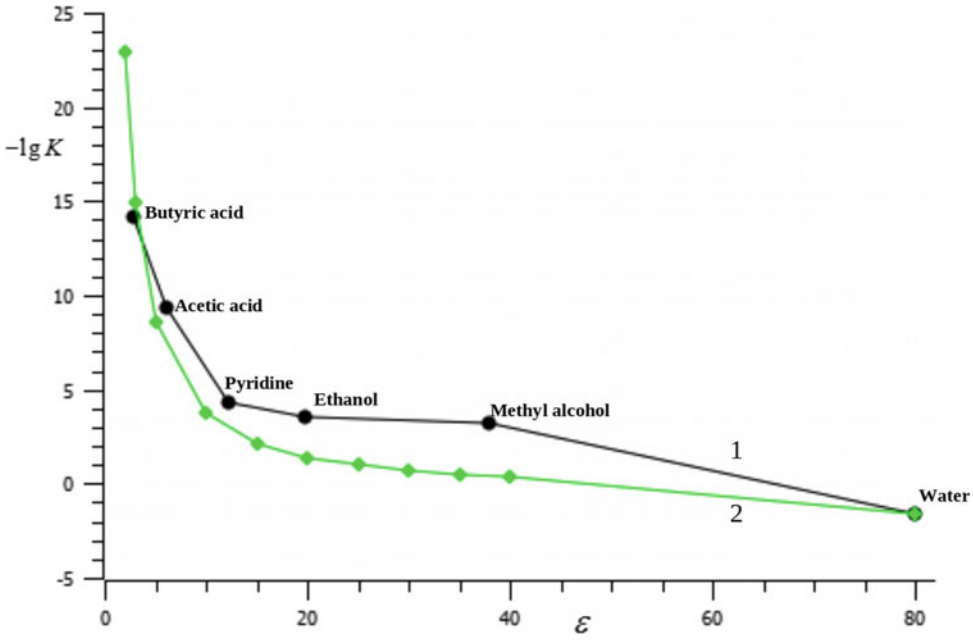

Fig. 5 Dissociation constants of nitric acid in solvents with different dielectric constants

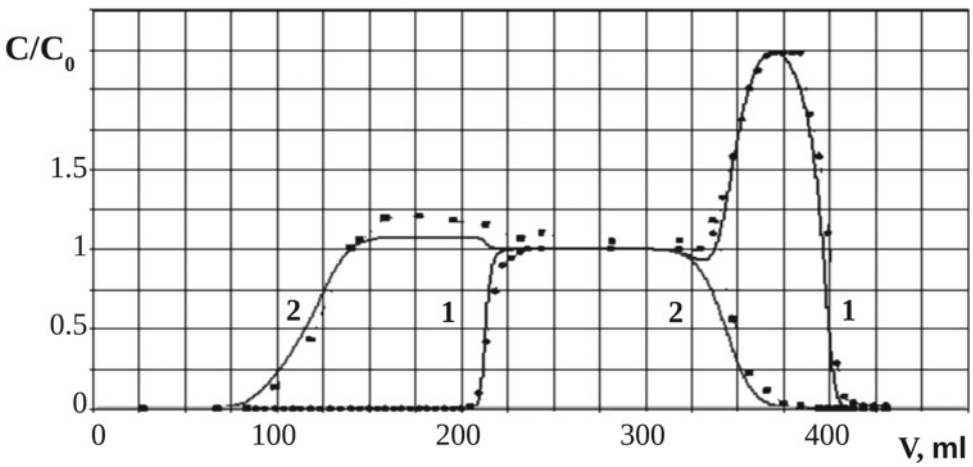

Fig. 6 Concentration histories of the components in the AR-process of separating (1) HNO_3 and (2) $NaNO_3$ from a mixed solution of 1.4 M nitric acid and 2.96 M sodium nitrate

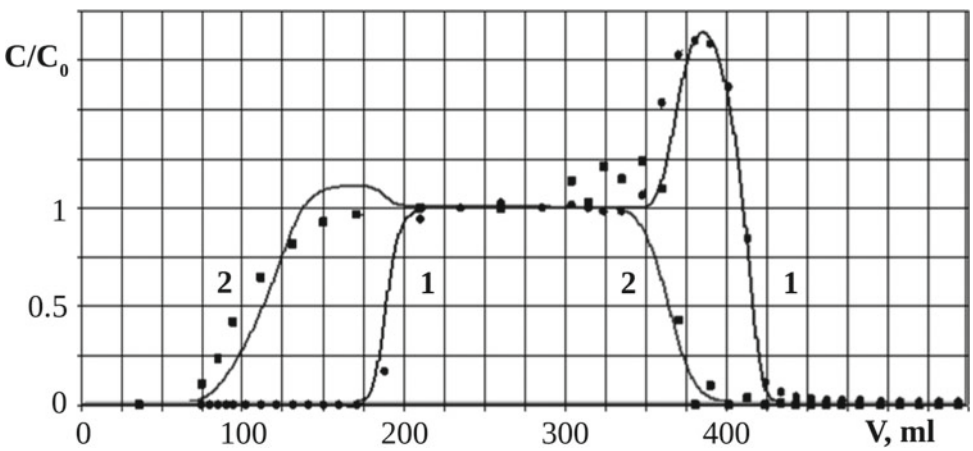

Fig. 7 Concentration histories of the components in the AR-process of separating HNO_3 (1) and $LiNO_3$ (2) from a mixed solution of nitric acid 1.4 M and lithium nitrate 2.96 M

acid. Figure 8 shows photos of the column for the initial (a) and final (b) stages of the experiment with WPA.

Any attempt to influence the wet process phosphoric acid solution itself even after its deep mechanical filtration, for example, by adding negligible amounts of alkaline agents or even by diluting water, immediately leads to the appearance of precipitation. It seems that there are practically no tools to control the process of separation of WPA components, i.e., there is no possibility to overcome the problem of sludge formation. Moreover, it seems impossible to realize repeated cycles of acid retardation in the sorbent bed with separation of salt components. However, it is necessary to distinguish the behavior of oversaturated solutions and colloidal systems in the free volume of the liquid and in the porous medium. Theory and practice of ion-exchange processes accompanied by the effect of isothermal supersaturation [34–37] were previously developed, and these developments were based on the following reasons for stabilization of supersaturated solutions in the gel ion-exchange resin bed:

- stabilization inside the nanopores is of thermodynamic character and is connected with impossibility of reaching the critical size of nucleation of crystallization by Gibbs for the most of known systems;
- stabilization in the outer bed—in the interspace volume between the sorbent grains (if we use the two-layer model described above in the theoretical analysis) has a kinetic character and is associated with the fact that due to immobilization of colloidal particles on the surface of ion-exchange grains the fastest of crystallization mechanisms, namely, the Brownian interaction of these particles, ceases to be the determining factor; a slower process related to the mechanism of single nucleate growth due to "feeding" at the molecular level starts playing a more important role. In the ion-exchange process, the isothermal supersaturation itself (IXISS effect) is related to the uniform distribution of functional groups at the molecular level, and the concentration of the resulting low-soluble substance is limited and cannot exceed the concentration of such groups. In the AR- process, there is no such limitation, and a colloidal system with an arbitrary content of substances capable of precipitation passes through the porous medium. Except for this difference, other regularities are completely the same in the system: nanoporous resin in contact with supersaturated solution (colloidal dispersion).

In the classical AR-process, the entire bed of the porous material is in a pure water medium before passing the mixed acid–salt solution. After the start of the process, the front of the salt components to be extracted from the acid immediately enters the neutral medium. Let us imagine that instead of water we will use a weak solution of the same phosphoric acid, which fill the bed. Its concentration may be negligible

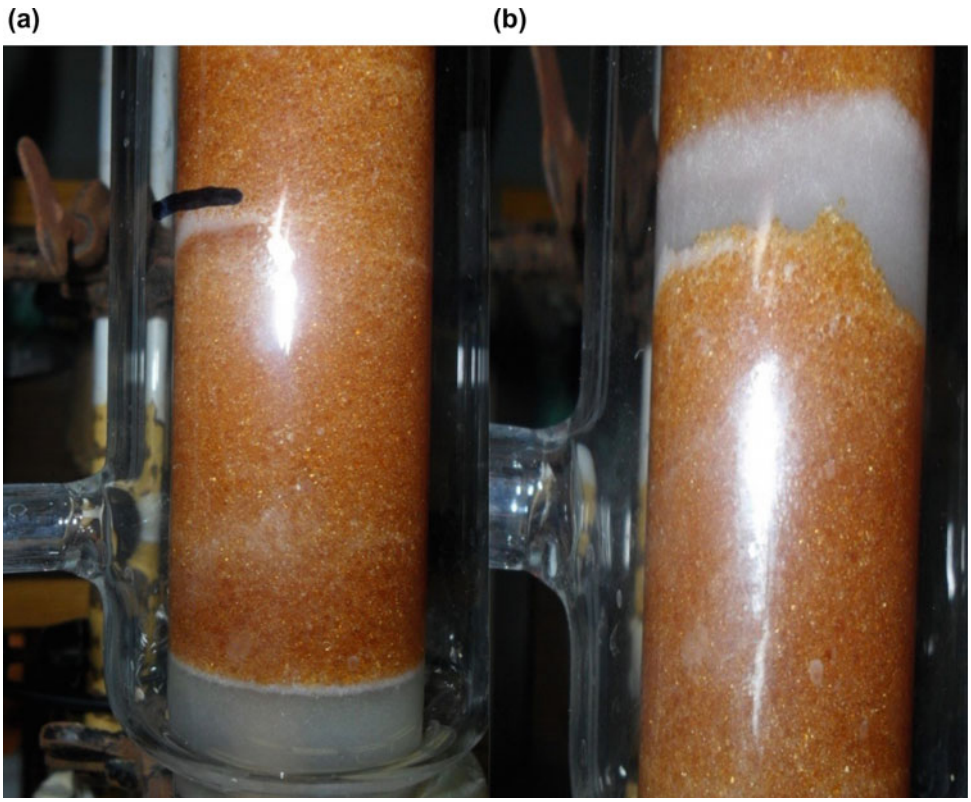

Fig. 8 Initial (**a**) and final (**b**) stages of the process of precipitation in the bed of ion exchanger in the phosphate form when passing hot EPA through a column in accordance with the technique of the standard AR-process

compared to the concentration of the processed WPA. In accordance with the mechanisms of molecular sorption and competitive solvation considered above, as soon as the front of the salt components reaches a certain point and the electrolyte concentration rises sharply, practically all the acid appears on the surface and in the phase of the sorption material, a significant part of colloidal particles also appears on the surface in accordance with the mechanism of the IXISS-effect. It turns out that the dynamic film of colloidal particles will move in the medium saturated with acid. It can be assumed that in this case, sedimentation will be substantially slowed down and AR-processes in complex systems can proceed more stably. Verification of this hypothesis for a large number of multi-component liquid acid-processed concentrates of various natural silicate and phosphate raw materials [32, 38–44], shows that it is always possible to select conditions for realization of stable separation processes by acid retardation without sedimentation in columns. As for the wet phosphoric acid, it is sufficient to use 0.1–0.4 M solutions of phosphoric acid as a desorbing agent instead of water depending on the temperature to carry out repeated modified cyclic AR separation processes [38–41].

Figures 9 and 10 show examples of concentration histories (break-through curves) of separation of industrial WPA components on laboratory columns with strongly basic anion exchangers taken in equilibrium anionic forms excluding ion-exchange processes. Vertical lines on the presented curves show the boundaries between fraction volumes corresponding to different stages of the process. Due to the coincidence of spectral analytical lines for a number of elements, including REE, some curves in the figure are given for two or three components. When WPA solution is passed through the column pre-treated with 0.4 M phosphoric acid solution, first, this solution is displaced from the porosity space and free volume, then the acid retention stage proper occurs. Then, the initial WPA solution is displaced from the column, and finally, the stage of purified phosphoric acid displacement is observed. A distinctive feature of the data presented is that a high degree of concentration of the salt components is observed, while the displaced acid is practically not concentrated. This is due to the ratio of component concentrations in the initial WPA, in which the concentration of impurities is significantly less than that of the acid itself. The concentration of acid in the desorbing agent is only a few percent of the concentration of the main component in the initial WPA. In a cyclic process, a small fraction of the purified acid from the previous cycle can be used as pure acid to prepare the desorbing agent for each subsequent cycle. The purest acid fraction is the tail one of the acid displacement stage.

Table 2 shows examples of purified acid compositions obtained by the proposed modified AR-process. Studies conducted jointly with specialists from "Professor Ya. V. Samoilov Institute, JSC NIUIF—PhosAgro", as well as from "NewChem Technology", LLC and "EuroChem Group AG" showed that the achieved level of purification of WPA allows to use the purified product in technological processes for water-soluble fertilizers. Table 3 presents data on the content of all components detected by ICP-MS in REE concentrates of different stages of processing and purification, obtained by oxalate method [32]. The resulting final product (concentrate 3) is of higher quality by the totality of parameters than industrial mixed REE concentrates (for example, at Solikamsk magnesium plant) (Table 2).

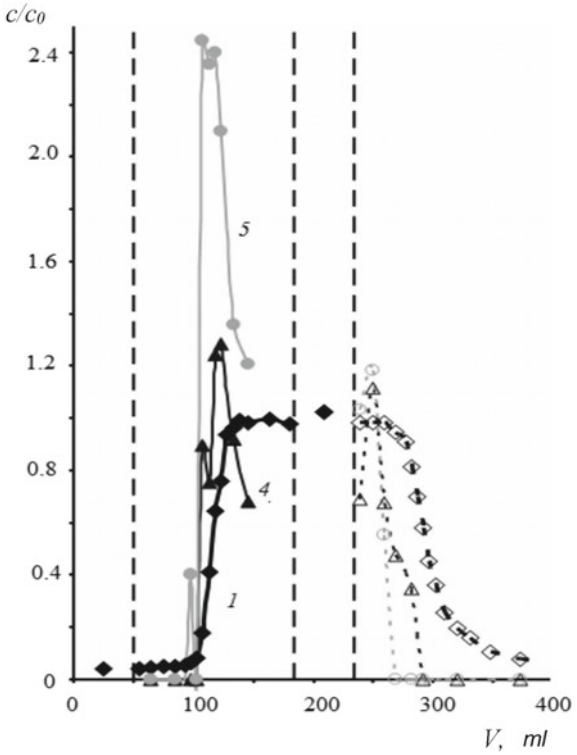

Fig. 9 Break-through curves of some components in one of the repetitive cycles of WPA processing on the LEWATIT Mono Plus M500 anion exchanger in equilibrium anionic form using a modified AR-process. Acid-1, cerium, lanthanum and titanium-4, neodymium and cerium-5. Solid lines correspond to the retention stage, dotted lines —to the acid desorption stage. Displacing agent—0.15 M H_3PO_4 solution. Temperature maintained throughout the cycle—650 °C

Figure 11 shows the results of one of the bench experiments (on larger columns with resin bed of 1 l), simulating industrial process of WPA processing. According to the curves shown in the figure, separation of filtrates into fractions takes place based on the following considerations: filtrate corresponding to fraction I is used in the stage of acid displacement in the next cycle; II is a salt solution from which REE extraction is easy; filtrate III is returned to the tank with initial WPA, IV is partially purified acid for fertilizer production. According to the chosen optimum

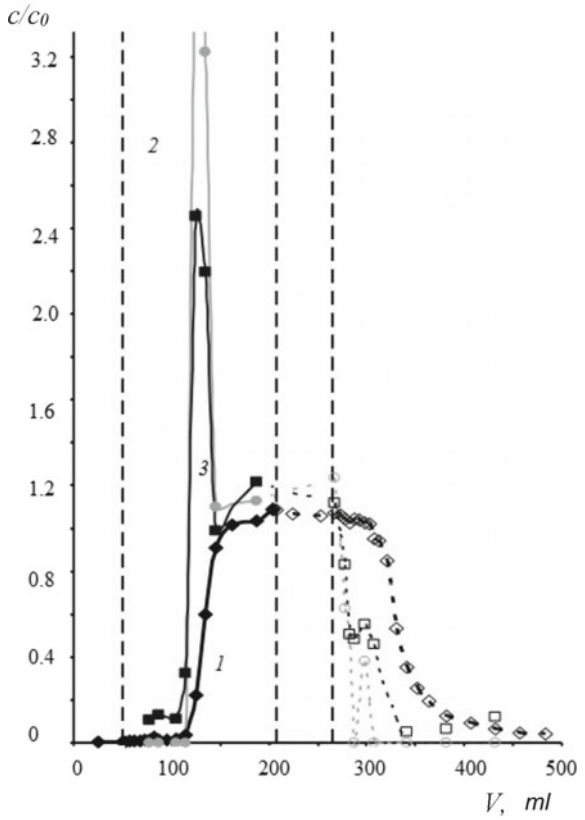

Fig. 10 Break-through curves of some components in one of the repeating cycles of EPA processing on the AV-17 anion exchanger in the modified AR-process. Acid-1, neodymium and cerium-2, cerium, lanthanum and titanium-3. Solid lines correspond to the retention stage, dotted lines—to the acid desorption stage. Displacing agent—0.15 M H_3PO_4 solution. Temperature—650 °C

Table 1 Composition of the industrial wet phosphoric acid used in experiments

Macro-components, %		Rare earth metals, mg/l	
P_2O_5	26.6	Ce	311
SO_3	2	Nd	158
F	1.8	La	128
CaO	0.1	Pr	42
Na_2O	0.06	Gd	28
K_2O	0.01	Sm	27
SiO_2	1.1	Dy	16
Al_2O_3	0.44	Eu	8.3
Fe_2O_3	0.26	Er	7
MgO	0.053	Yb	4

conditions every fifth working cycle is continued almost to equilibrium to get tail fraction V of well purified acid, which will be used for preparation of desorbing agent for next four cycles.

Pilot testing of the proposed technology for purification of wet process phosphoric acid in plant conditions was carried out jointly with specialists from some of listed profile organizations. A photograph of the pilot plant used in the tests was presented above in a short introductory article on the Laboratory of Sorption methods. Some results of pilot testing are presented in Table 4. They demonstrate a good reproducibility of work cycles of the proposed variant of AR method. The results obtained during the pilot tests were used to create a technological design for a facility under construction for the production of high-quality fertilizers from purified phosphoric acid.

4.2 Some Other Examples

The modified AR method, with the displacement of concentrated acid at the stages of regeneration in each operating cycle with using diluted and purified acid from the tail fractions of each previous cycle, allows creating stable separation processes for other systems of interest to practice. An example of such a system is acidic mixed sulfate leaching solutions obtained by processing serpentinite with concentrated sulfuric acid. Serpentinite is a raw material rich in magnesium (more than 40% MgO) due to the content of serpentine, a group of compositionally related minerals, such as lizardite: $Mg_3Si_2O_5(OH)_4$, antigorite: $(Mg, Fe)_3Si_2O_5(OH)_4$, as well as minerals of the same type, containing impurities of nickel, chromium, manganese, zinc and other metals. When decomposing serpentinite with an excess of hot concentrated sulfuric acid, an acidic solution is obtained. The pure magnesium product is isolated from this one in two stages: first, iron and other impurities are precipitated by the addition of alkaline agents. At the second stage, a solution is separated from the precipitate, after that is concentrated to crystallize magnesium sulfate, or the resulting weakly alkaline magnesium sulfate solution is additionally treated with alkali to obtain a precipitate of a more popular product —magnesium hydroxide. The processing of the original mixed solution with a high residual acid content leads to unjustified costs of alkaline agents. The preliminary separation of saline and acidic solutions by the AR method would significantly reduce the consumption of the reagent, as well as return the separated acid to the head of the technological process of the decomposition of serpentinite. However, the use of the standard AR method is impossible due to precipitation of hydroxides of iron, chromium and other impurities and colmatation of the sorption bed of the anion exchanger. Figure 12 shows an example of a working cycle for separating components using a modified acid retardation method on a column with strong base anionic resin in sulfate form, pretreated with a weak (0.02 M) solution of sulfuric acid which remains in the interspace

Table 2 Purification of phosphoric acid simultaneously with the extraction of REM by a modified AR-process

Solutions	Composition							
	H^+, eqv/l	Ca, mg/l	Ce, mg/l	Fe, mg/l	La, mg/l	Mn, mg/l	Nd, mg/l	Y, mg/l
Initial WPA	10.6	645	359.25	2277.5	123.5	183	205.75	95
Recycled regeneration solution	0.45	0.97	0.71	30.75	0.31	0.15	0.52	0.76
Poorly purified phosphoric acid	10.6	162.0	104.5	1598.7	34.13	34.5	57.6	29.08
Purified phosphoric acid	9.4	43.7	39.5	479.6	13.3	11.7	22.3	10.4

Table 3 Compositions of the obtained solid rare-earth concentrates

Element	DL*, μg/l	*C*, μg/l			Элемент	DL, μg/l	*C*, μg/l		
		1	2	3			1	2	3
Li	0.2	1.3	< DL	< DL	Cs	0.03	30.9	0.063	0.098
Be	0.1	< DL	< DL	< DL	Ba	0.7	63.2	< DL	< DL
Na	20	2918	< DL	< DL	La	0.3	40,154	60,325	112,085
Mg	7	2394	< DL	15.1	Ce	0.3	87,830	110,281	239,131
Al	945	41,553	2030	4400	Pr	0.03	10,174	15,623	34,768
K	62	6903	209	317	Nd	0.08	37,418	60,038	132,703
Ca	218	38,887	830	1800	Sm	0.02	6000	10,369	22,749
Sc	4	< DL	< DL	< DL	Eu	0.05	1721	3243	7051
TI	7	3186	< DL	< DL	Gd	0.05	5572	11,201	24,696
V	8	48.5	< DL	< DL	Tb	0.03	570	1225	2544
Cr	7	64.9	< DL	< DL	Dy	0.04	2799	6237	12,934
Mn	10	420	< DL	< DL	Ho	0.02	493	1125	2327
Fe	9	53,718	123	123	Er	0.05	1285	2445	5045
Co	0.7	1.5	< DL	< DL	Tm	0.02	137	272	476
Ni	5	42.7	< DL	< DL	Yb	0.07	618	923	1595
Cu	5	< DL	< DL	< DL	Lu	0.03	60.4	77.9	165
Zn	3	5.9	< DL	< DL	Hf	11	< DL	< 24	< 53
Rb	0.3	311	8.7	16.7	Ta	3	< DL	< 7	< 14
Sr	0.5	6833	57.1	118	W	3	< DL	< 6	< 13
Y	0.1	20,211	35,009	76,934	Re	0.1	< DL	< 0.2	< 0.6
Zr	0.7	29.4	26.7	37.3	Ir	0.1	< DL	< DL	2.8
Nb	0.1	16.4	< DL	< DL	Pt	0.1	< DL	< DL	428
Mo	0.7	1.3	< DL	< DL	Au	0.1	< DL	< DL	< DL
Rh	0.7	< DL	< DL	< DL	Hg	0.2	< DL	< DL	< DL
Pd	0.3	< DL	< DL	< DL	Tl	0.06	0.1	< DL	< DL
Ag	0.2	< DL	< DL	< 1	Pb	0.5	44.6	2	6.5
Cd	0.3	< DL	< DL	< DL	Bi	0.05	< ПО	7.9	10.2
Sn	2	2.8	< DL	< DL	Pa	0.02	1881	633	1377
Sb	0.1	2.2	1.6	3	U	0.02	0.3	0.042	0.087

1—primary concentrate, 2—oxalates and 3—REM oxides
*DL**—detection limit in the ICP-MS method

volume of the column. Part of the ferrous sulfate leaves the column together with the magnesium sulfate solution after the water has been displaced. In the technological process, this stage is completed so that the condition of pH $\geq$ 2 is met. For clarity, a laboratory experiment demonstrated the yield of an equilibrium solution at the sorption stage and the same solution at the beginning of the regeneration stage. This solution is completely identical to the original one, it

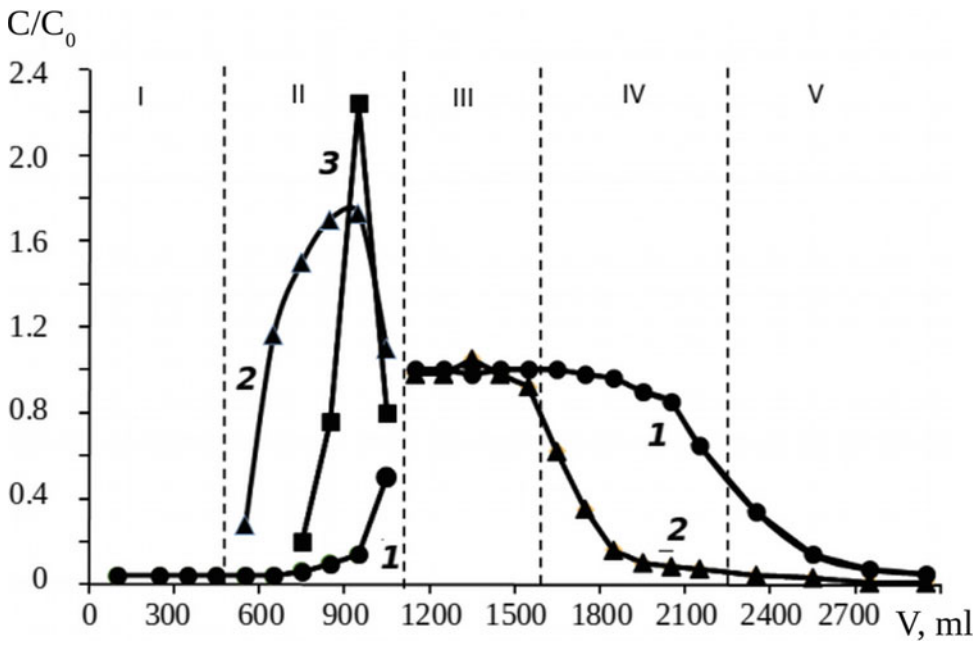

Fig. 11 Break-through curves of the components in the full cycle of the modified AR-process, simulating the technological process of processing extraction phosphoric acid on the AB-17 anion exchanger. Zones I and II correspond to the acid retention stage, III–V displacement stage. 1—phosphoric acid, 2—Ca + Mg, 3—Ce + Nd. Temperature during the process—65 °C

Table 4 Some of results on the WPA purification at pilot testing

Components, %	Initial WPA	Phosphoric acid purified in successive working cycles					
		Cycle 1	2	3	4	5	6
P_2O_5	25.4	21.84	23.02	22.49	22.02	22.67	23.01
MgO	1.01	0.09	0.08	0.11	0.07	0.06	0.06
CaO	0.47	0.03	0.03	0.04	0.01	0.02	0.02

comes back and mixes with it. Concentrated sulfuric acid with residual magnesium and iron is also returned to the head of the process to prepare the acid solution for serpentinite decomposition. The latest fractions of highly purified and dilute sulfuric acid are used to prepare the 0.02 M regeneration solution, which is used in the next cycle to displace the concentrated acid-rich solution and regenerate the resin bed. The process is completely stable, no sediments are formed in the column.

Another example of a possibly successful use of the proposed version of AR method is illustrated in Fig. 13. It is associated with the acid–salt processing of alumina-containing raw materials (low grade bauxite, nepheline) in a closed-loop process being developed at the V. I. Vernadsky Institute in collaboration with some commercial companies [42–44]. According to this acid-salt technology, the feedstock is treated with hot ammonium bisulfate solution. After all the operations of leaching, cooling and precipitation of aluminum ammonium alum (which is then redissolved in water), circulating solution of ammonium sulfate is formed. This one is subjected to evaporation and crystallization of ammonium sulfate followed by its thermal decomposition (at a temperature of 250–350 degrees) with obtaining ammonium bisulfate, which is re-dissolved for application at next stage of leaching. During the decomposition of ammonium sulfate, ammonia is formed, with the help of which operations are carried out to precipitate aluminum hydroxide from the alum solution. The same amount of bisulfate is formed and is in the cycle. The problem is that in order to increase the degree and rate of aluminum recovery, it is necessary to use an excess amount of a leaching agent—ammonium bisulfate. Therefore, in a real process, after the separation of alum, a mixed solution of ammonium sulfate and bisulfate is formed, containing impurities of iron and other contaminating components. It is necessary to extract sulfuric acid from this solution and obtain an almost neutral solution enriched with ammonium sulfate. From the latter one, as it becomes possible, iron hydroxides and other impurities can be separated with a small consumption of ammonia. The resulting and completely neutral ammonium sulfate solution (No1) is further processed as described above. The main amount of ammonia obtained during the decomposition of solid ammonium sulfate is spent on the precipitation of aluminum hydroxide from the alum solution. After separation of the hydroxide, solution No. 2 (of ammonium sulfate also) remains, which is combined with solution No. 1. The complete cycle is being closed. Theoretically, chemical reagents are not consumed here, except for alumina-containing raw

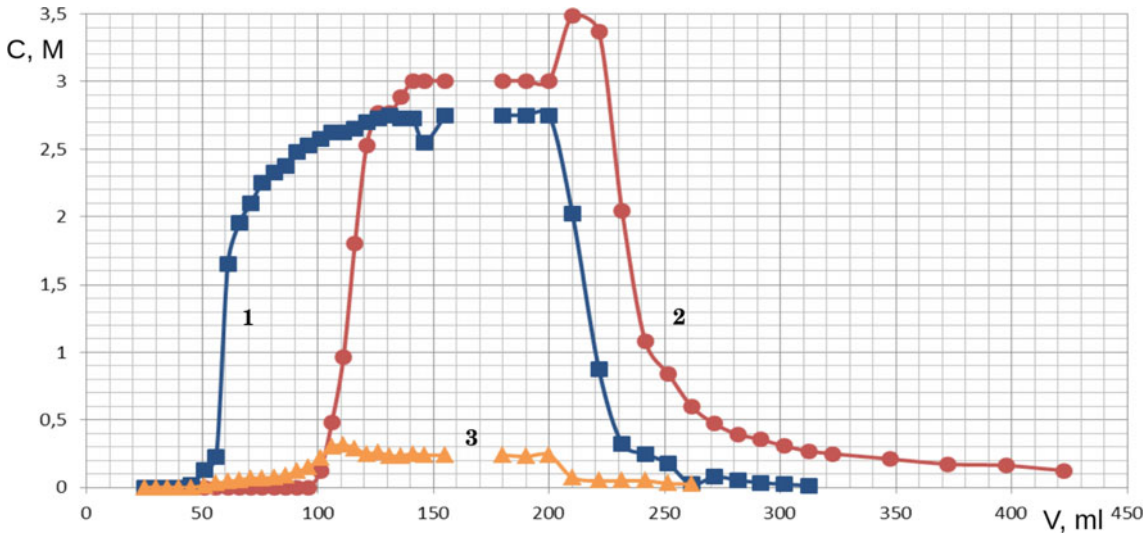

Fig. 12 Concentration histories of $MgSO_4$ (1), $FeSO_4$ and sulfuric acid (2) in the process with acidic solution of decomposition of natural serpentinite. Bed volume—85 ml, flow rate—3 ml/min

materials [44]. The proposed version of AR-method can be used for the extraction of sulfuric acid from the mixed solution of ammonium sulfate and bisulfate [43]. It is this separation process that is shown in Fig. 13. Salt solution of ammonium sulfate containing iron and residual aluminum sulfates is extracted at the sorption stage. Ammonium bisulfate admixed with sulfuric acid obtained at the displacement (regeneration) stage is recycled for preparing leaching agent. The tail fractions of diluted sulfuric acid are used for the displacement operation at a next work cycle of the stable AR-process. Thus, there are prospects for creating a new efficient technology for the production of alumina from low-grade raw materials in a circular process with the extraction and consumption of the same amount of salt reagent in each cycle. A distinctive feature of this scheme is the use of a special acid-retardation technology to return the residual amounts of acid and salt to the technological head. This can significantly reduce the consumption of reagents.

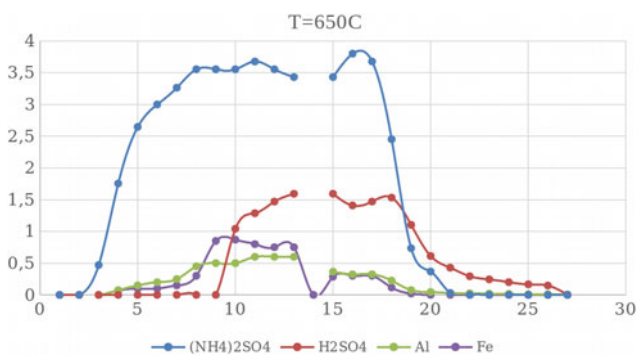

Fig. 13 Separation of the components of the washing solution for solid residues of bauxite decomposition by the bisulfate method. IEX bed volume—45 ml, flow rate—1 ml/min

5 AR Processes in Columns with Two Liquid Phases

A new approach to the separation of electrolytes with ion exchanging resins and molecular sorbents in multiphase systems has been proposed [45–48, 50]. The distinctive property of the approach is that in sorption processes, the volume of space occupied by the processed solution is significantly reduced, for which the bed of granular sorbent is filled with a certain organic liquid substance that is not miscible with aqueous solutions. A mixture of such organic substances can also be used. When solutions of ionic mixtures pass through such a layer of granular material in the absence of free space between the granules, as well as in conditions when the organic liquid repels water and aqueous solutions, the latter are introduced at the interface between the organic liquid and the hydrophilic surface of the granules, forming the thinnest stationary dynamic film enveloping each sorbent granule and flowing down the points of contact between them. In fact, this leads to an increase in the surface area of contact between the working solution and the sorbent by hundreds and thousands of times. This also leads to a significant reduction in the duration of sorption cycles and the absence of erosion effects associated with the influence of longitudinal dispersion [46, 47]. The organic liquid remains in the column during the processing of aquatic electrolyte solutions. A small amount of organic matter, which can be carried out from the sorbent bed at increased rates of solution transmission, returns due to its lower density and a specially organized connection of the bottom and top of the sorption column. Figure 14 shows a laboratory bench installation, which is provided with a

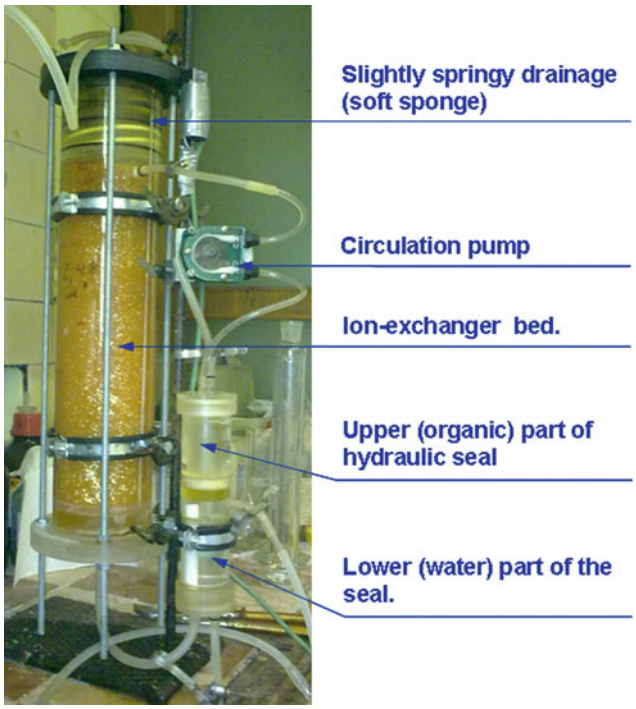

Fig. 14 Laboratory stand for separation of ionic mixtures in column with organic phase. Loading: strong base anionic resin AV-17, sulfate form; bed volume: 3150 ml, swollen in water and filled with decanol

special auxiliary column for collecting the possible leaks of organic liquid. Organic matter floats up in the free volume of the column forming the upper layer of immiscible liquid phases. The organic liquid, at a certain calculated flow rate, is returned back to the working sorption column using a small pump.

Two examples of separation of the salts and acid from the same solution are shown in Fig. 15. The solution was obtained by nitric acid leaching of aluminum salt from nepheline concentrate. Such a solution contains many components, the main of which are nitric acid (about 8%), aluminum nitrate ($\sim$ 16%) and sodium nitrate ($\sim$ 6%). The first example (top) shows the results obtained using the proposed approach in a column containing an organic phase —nonanoic acid. The second one presents the experimental results obtained with a standard column loaded the same sorption bed. The passage of the stock solution through both columns was carried out at the same flow rate in the direction from top to bottom. In each experiment, the acid desorption step was carried out with deionized water (which is quite acceptable for nitrate solutions). It can be seen that there is no need to use an upward flow of dense fed solution when using columns with an organic phase. Under the same conditions, a significant blurring of concentration fronts is observed when using a standard column in the aqueous phase. In addition, other things being equal, the proposed approach makes it possible to reduce the duration of repeated sorption–desorption cycles and increase the separation efficiency for returning acid to the technological process.

Another example of possibility of application of the suggested method is presented in Fig. 16 which shows the AR-process of separation for purification of concentrated copper electrolytes. The necessity of purification of the circulating working solution for electrolysis is caused by requirements to quality of a final product—cathode copper. In particular, the content of such impurities as arsenic and antimony is strictly limited. The acid retardation method is based on selective competitive absorption of As(V) and Sb (V) derivatives over sulfuric acid in each work cycle on strongly base anion-exchange resin in mixed anionic form equilibrium with the initial multi-component solution for electrolysis. The break-through curves shown in Fig. 16 were obtained with real working electrolyte of the Balkhash copper plant (Kazakhstan) using a laboratory stand with a column containing 4.5 L of AV-17.

An interesting feature of the shown separation processes in columns with two immiscible liquid phases, as well as other similar processes studied by us [45–48, 50], is that no significant effects of concentration of micro-components at the stages of acid retention are observed, as it was seen by examples of separation without organic liquids. One can always find a section of the break-through curves of the components which corresponds to the fractions with the content of all salt components equal to that in the original stock solution, but with significantly reduced content of the acid. This can be seen, for example, in Fig. 15a in the section of the curves corresponding to fractions of the eluate from 50 to 75 ml. This pattern is confirmed for other systems, for example, by the data on the sorption of components obtained in an experiment with a model solution of bone mineralizate are shown in Fig. 17. Here, lines 1 and 2 “cut” the area within which the salt components are contained in average concentrations, which are practically equal to the corresponding concentrations in the initial solution under analysis. The observed effect can be used for sample preparation in elemental analysis, for example, by ICP AES or ICP MS methods. It is known that in these methods the acidity of samples should be limited. At the same time, many difficult-to-decompose geological samples or biological tissues are treated with excessive amounts of concentrated acids. The resulting solutions must be diluted or should be neutralized, leading to additional mineralization and also to the need for dilution. All of these operations reduce the sensitivity of instrumental analysis. A small column with an organic phase filling the resin bed in an anionic form equilibrium with the analyzed solution can be simply used for sample preparation. In the process shown in Fig. 17, nitrates and nitric acid from a mineralizate obtained by prolonged treatment of bone tissue with 14 M nitric acid were separated, the fractions limited by lines 1 and 2 were chosen as

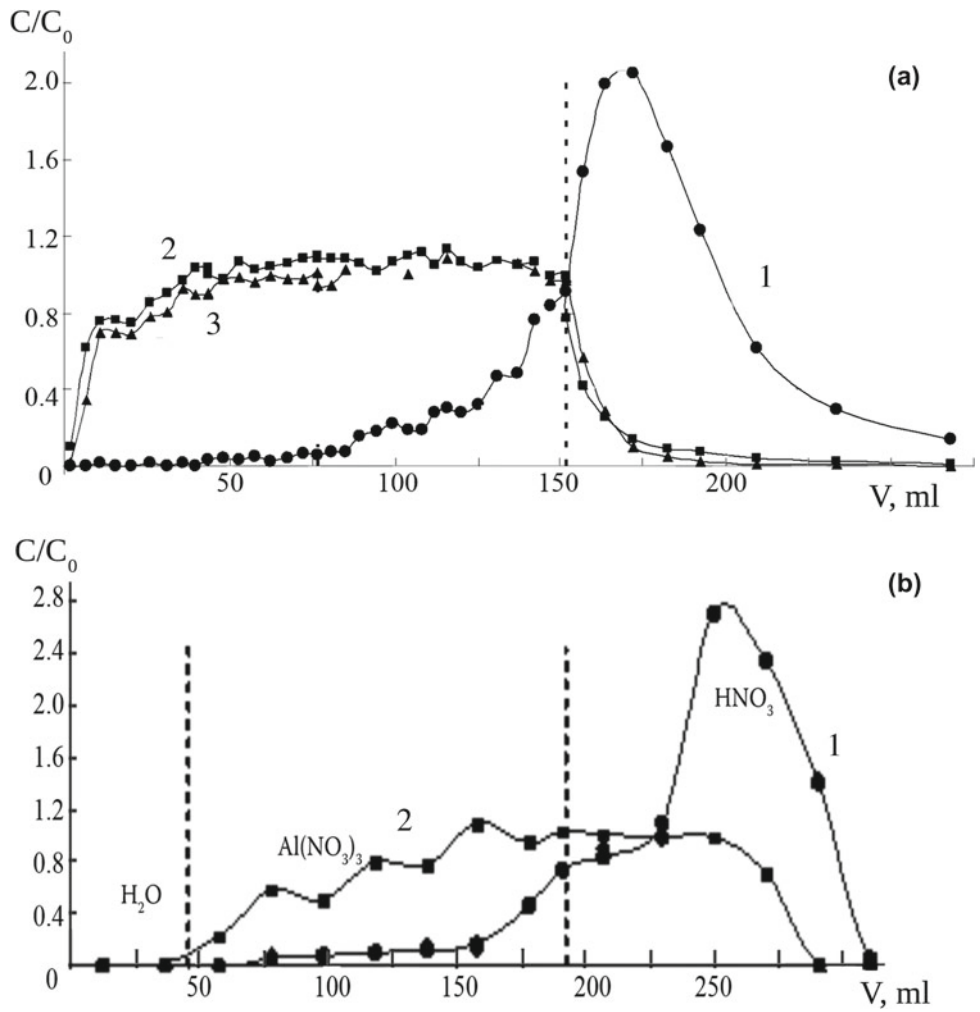

Fig. 15 Break-through curves for the separation of nitric acid and metal nitrates on a strongly basic anion exchanger in the nitrate form. bed volume: 110 ml. The flow rate of the solution and water in the direction from top to bottom is 2 column volumes (BV) per hour. A—interspace volume is filled with nonanoic acid; B—conventional ion-exchange bed with water

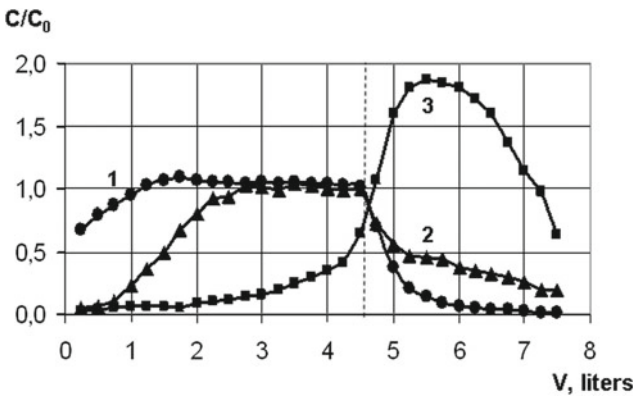

Fig. 16 Break-through curves of components in the process of arsenic removal from copper electrolyte. 1: $CuSO_4$; 2: H_2SO_4; 3: H_3AsO_3 + H_3AsO_4; Column loadings: anionic resin in initial form equilibrated with pure electrolyte, washed with water and filled after with decanol. Composition of the influent at sorption stage (/l): H_2SO_4: 220; $CuSO_4$: 105; Total As: 4.5 mg/l. Bed volume—3.15 l. Flow rate: 2 BV/h

convenient for choosing an analytical sample. Table 5 shows the data obtained by direct analysis of a sample of atomic emission with inductively coupled plasma on an IRIS Intrepid II XDL spectrometer (Thermo Electron Corp., USA). It can be seen that the difference between the values of the initial and measured concentrations for different analytes does not exceed 22.9%.

The authors of [49] used our proposed modified AR method and showed that this "technique can be successfully applied for solving specific analytical tasks … we recommend the reduction of a solution acidity prior to the introduction of the solution in plasma of ICP- MS". The authors carried out the determination of a large number of trace elements, including REE at a concentration level from fractions of ppb to tens of them. On the basis on the statistics of 6 parallel determinations, the they demonstrated good chemical-analytical statistics of the combined method.

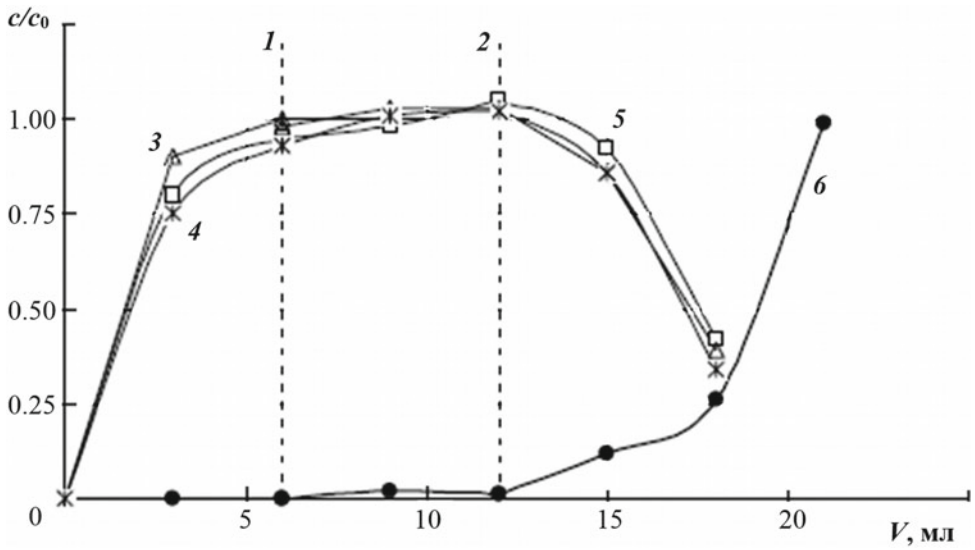

Fig. 17 Concentration history of components at passing model solution of mineralizate of bone tissue decomposition through the column filled with decanol. Bed volume—19.6 ml. Solution flow rate—0.2 ml/min

Table 5 Comparison of data on the content of meso- and micro-components in the initial solution of bone mineralizate and the solution after separation of nitric acid

Solutions	Concentration, mg/l								
	Sr	Zn	Al	B	Zr	Ti	Cu	Cd	Mo
Initial	42	51	42	3.3	0.5	0.70	0.42	0.12	0.2
Eluate fraction	36	42	33	3.5	0.6	0.54	0.50	0.10	0.2
Difference, %	− 14.3	− 17.6	− 21.4	6.1	− 20.0	− 22.9	19.0	− 16.6	0.0

Table 6 Results of spectral analysis of fractions (V = 2 ml) taken during sample preparation in the modified AR method

Element	Number of series, n	Mean value C/C_0	Standard deviation	Standard error of the mean	± Δ(0.95)
Li	5	0.990	0.060	0.035	0.111
Be	5	0.999	0.060	0.035	0.110
Na	5	1.047	0.075	0.043	0.138
Mg	5	1.021	0.079	0.045	0.145
Al	5	1.044	0.081	0.047	0.148
K	5	0.979	0.081	0.047	0.149
Ca	5	0.904	0.077	0.044	0.141
Sc	5	0.847	0.032	0.019	0.060
V	5	0.977	0.063	0.036	0.115
Cr	5	1.068	0.045	0.026	0.083
Mn	5	1.034	0.046	0.027	0.085
Fe	5	1.041	0.072	0.042	0.132
Co	5	1.018	0.053	0.031	0.097
Ni	5	0.995	0.092	0.053	0.169
Cu	5	0.953	0.009	0.005	0.017
Zn	5	1.080	0.062	0.036	0.113
As	5	0.488	0.073	0.042	0.135
Se	5	0.781	0.058	0.034	0.107
Sr	5	0.934	0.060	0.035	0.111
Mo	5	0.465	0.045	0.026	0.082
Ag	5	0.316	0.137	0.079	0.251
Sb	5	1.755	0.427	0.246	0.783
Tl	5	0.645	0.092	0.053	0.168
Pb	5	0.140	0.036	0.021	0.065

The work [50] describes the results of our experiments, the purpose of which was an attempt to expand the range of tasks to be solved for the analysis of real objects, in particular, the concentrated solutions of soil demineralization by the ICP MS method. It was demonstrated a slight difference between the "introduced" (C_0) and "found" (C) concentration values for more than 20 elements. Demineralization of the soil was carried out with 35% nitric acid obtained from distilled 70% one and deionized water. A column was used with a bed volume of strongly basic anion exchanger of 19.6 ml, filled with decanol. For sample preparation, a 2 ml of fraction with the acid content of no more than 3% was taken. The analysis was carried out using the instrument: ICP-MS 7700 × Agilent. Unsatisfactory results were obtained for elements that form anions (Se, As, Sb. Mo), which, possibly, was due to their ion-exchange sorption. With the exception of Tl, Ag and Pb, satisfactory results were obtained for all other cation-forming elements. The corresponding data of statistical analysis of the results of chemical-analytical experiments in 5 series of parallel determinations are shown in Table 6. They indicate good prospects for using the proposed method of sample preparation in instrumental elemental analysis.

The performed studies demonstrate new possibilities of the proposed versions of AR separation method for solving various technological and chemical-analytical problems using ion exchange and molecular sorption. In comparison with traditional approaches, they make it possible to separate acids from salts not only without using commercial reagents, but also without any restrictions related to the precipitation effects in sorbent beds. When using processes with isothermal supersaturation of solutions in ion exchange, as well as the processes in columns with two liquid phases, there is a significant increase in the efficiency of separation of components.

Acknowledgements the authors are grateful to: V. P. Kolotov for his help in organizing the analysis of REE concentrates; G. B. Sidelnikov (Faculty of Physics, Moscow State University) for his help in writing programs and performing calculations; M. N. Tsikin, V. V. Dolgov, V. S. Sushchev and Yu. D. Chernenko, V. V. Sokolov (NIUIF named after V. Ya. Samoilov) for help in organizing and conducting bench tests, S. Kh. Khamizov, A. N. Smirnov and all employees of NewKem Technology LLC and Scientific and Production Enterprise JSC SPE "Radiy" for the creation and provision of a bench-scale installation and for assistance in its testing.

References

1. Hatch, M.J., Dillon, J.A.: Acid retardation. A simple physical method of separation of strong acids from their salts. I&EC Process Design Dev. **2**(4), 253–263 (1963)
2. Gotzelmann, W., Hartinger, L., Gulbass, M.: Stofftrennung und Stoffruckgewinnung mit dem Retardation-Verfaren, Teil.1. Metalloberflache **41**(5), 208–212 (1987)
3. Brown, C.J.: Fluid treatment method and apparatus. Patent No. 4673507, US (1987)
4. Ferapontov, N.B., Gorshkov, V.I., Trobov, K.T., Parbuzina, L.R., Gavlina, O.T., Strusovskaya, N.L.: Reagent-free separation of electrolytes on ion exchangers. Russ. J. Phys. Chem. A **70**(5), 840–843 (1996)
5. Ferapontov, N.B., Gorshkov, V.I., Trobov, K.T., Parbuzina, L.P., Gavlina, O.T., Strusovskaya, N.L.: Sorption properties of high-basicity anionites at equilibrium with solutions of electrolytes. Russ. J. Phys. Chem. A **70**(12), 2072–2077 (1996)
6. Ferapontov, N.B., Gorshkov, V.I., Parbuzina, L.R., Trobov, H.T., Strusovskaya, N.L.: Heterophase model of swollen cross-linked polyelectrolyte. React. Funct. Polym. **41**(1), 213–225 (1999)
7. Ferapontov, N.B., Parbuzina, L.R., Gorshkov, V.I., Strusovskaya, N.L., Gagarin, A.N.: Interaction of cross-linked polyelectrolytes with solutions of low-molecular-weight electrolytes. React. Funct. Polym. **45**(2), 145–153 (2000)
8. Gruzdeva, A.N., Gorshkov, V.I., Gagarin, A.N., Ferapontov, N.B.: Separation of electrolytes by sorption on crosslinked poly(vinyl alcohol). Russ. J. Phys. Chem. A **79**(7), 1150–1152 (2005)
9. Ferapontov, N.B., Gorshkov, V.I., Parbuzina, L.R., Strusovskaya, N.L., Gagarin, A.N.: Thermodynamics of interphase equilibrium in system ion exchanger-solution of low molecular weight electrolyte. React. Funct. Polym. **66**(12), 1749–1756 (2006)
10. Gorshkov, V.I., Ferapontov, N.B.: Separation of strong electrolyte mixtures by sorption on ion exchangers and the determination of a single-step separation factor. Russ. J. Phys. Chem. A **81**(8), 1314–1319 (2007)
11. Tsyurupa, M.P., Tarabaeva, O.G., Pastukhov, A.V., Davankov, V. A.: Sorption of ions of heavy metals by neutral hypercrosslinked polystyrene. Int. J. Polym. Mater. **52**(5), 403–414 (2003)
12. Davankov, V.A., Tsyurupa, M.P., Alexienko, N.N.: Selectivity in preparative separations of inorganic electrolytes by size-exclusion chromatography on hypercrosslinked polystyrene and microporous carbons. J. Chromatogr. A **1100**(1), 32–39 (2005)
13. Davankov, V., Tsyurupa, M.: Chromatographic resolution of a salt into its parent acid and base constituents. J. Chromatogr. A **1136** (1), 118–122 (2006)
14. Laatikainen, M., Sainio, T., Paatero, E., Davankov, V., Tsyurupa, M., Blinnikova, Z.: Modeling of size-exclusion chromatography of electrolytes on non-ionic nanoporous adsorbents. J. Chromatogr. A **1149**(2), 245–253 (2007)
15. Laatikainen, M., Sainio, T., Paatero, E., Davankov, V., Tsyurupa, M., Blinnikova, Z.: Chromatographic separation of a concentrated HCL-$CaCL_2$ solution on non-ionic hypercrosslinked polystyrene. Reactive Functional Polym. **67**(12), 1589–1598 (2007)
16. Davankov, V.A., Tsyurupa, M.P., Blinnikova, Z.K.: Separation of a $CaCl_2$-HCl model mixture on neutral nanoporous hypercrosslinked polystyrene under static and dynamic conditions. Russ. J. Phys. Chem. A **82**(3), 434–438 (2008)
17. Pastukhov, A.V., Davankov, V.A., Tsyurupa, M.P., Blinnikova, Z. K., Kavalerskaya, N.E.: The contraction of granules of nanoporous super-cross-linked polystyrene sorbents as a result of the exclusion of large-sized mineral electrolyte ions from the polymer phase. Russ. J. Phys. Chem. A **83**(3), 457–464 (2009)
18. Blinnikova, Z.K., Maerle, K.V., Tsyurupa, M.P., Davankov, V.A.: Pecularities of the separation of mineral salts by means of size exclusion chromatography on the neutral nanoporous polystyrene sorbents. Sorbtsionnye I Chromatograficheskie Pprocessy **9**(3), 323–331 (2009). (in Russian)
19. Davankov, V., Tsyurupa, M., Blinnikova, Z., Pavlova, L.: Self-concentration effects in preparative SEC of mineral electrolytes using nanoporous neutral polymeric sorbents. J. Sep. Sci. **32**(1), 64–73 (2009)

20. Tsyurupa, M.P., Blinnikova, Z.K., Davankov, V.A.: Size exclusion chromatography of mineral electrolytes on neutral nanoporous hypercrosslinked polystyrene: mechanism of acid retardation, salt retardation, base retardation. Sorbtsionnye I Chromatograficheskie Processy **13**(5), 541–552 (2013). (in Russian)
21. Krachak, A.N., Khamizov, R.K., Poznukhova, V.A., Podgornaya, E.B., Durnaykin, V.A.: Basic regularities of electrolyte separation in the method of acid retardation. I. Influence of cation type on the sorption of acids and their salts from binary solutions. Sorbtsionnye I Chromatograficheskie Processy **11**(1), 77–88 (2011). (in Russian)
22. Krachak, A.N., Khamizov, R.K., Dolgonosov, A.M., Malkova, L. M.: Basic regularities of electrolyte separation in the method of Acid Retardation. II. Influence of acid and salt concentration on their sorption from individual solutions. Sorbtsionnye I Chromatograficheskie Processy **14**(6) 902–911 (2014). (in Russian)
23. Sidelnikov, G.B., Tikhonov, N.A., Khamizov, R.K., Krachak, A. N.: Modeling and study of sorption and separation of acids in solution. Math. Models Comput. Simul. **5**(6), 501–510 (2013)
24. Glotova, E.A., Tikhonov, N.A., Khamizov, R.K., Krachak, A.N.: Mathematical modeling of a sorption process for the retention of acid from a solution. Moscow Univ. Phys. Bull. **68**(1), 65–70 (2013)
25. Tikhonov, N.A.: A New approach to calculating activity coefficients in a wide range of electrolyte concentration. Dokl. Math. **82** (2), 808–810 (2010)
26. Tikhonov, N.A., Sidelnikov, G.B.: Quantitative analysis of physical factors that determine the behavior of activity coefficients of electrolytes. J. Math. Chem. **51**(10), 2746–2756 (2013)
27. Tikhonov, N.A., Sidelnikov, G.B.: Modeling of physical effects governing the behavior of the activity coefficients of an electrolyte. Math. Models Comput. Simul. **7**(1), 6–12 (2015)
28. Tikhonov, N.A., Tokmachev, M.G.: Quantitative analysis of physical factors that determine activity coefficients of electrolytes. III. Mixtures of electrolytes. J. Math. Chem. **54**(2), 592–601 (2016)
29. Robinson, R.A., Stokes, R.H.: Electrolyte Solutions. Butterworth and Co, London (1970)
30. Lyashchenko, A.K., Karataeva, I.M.: The activity of water and permittivity of aqueous solutions of electrolytes. Russ. J. Phys. Chem. A **84**(2), 320–328 (2010)
31. Nikolsky, B.P. (ed.): Chemist's Handbook in 6 volumes. In: Chemistry, vol. 1, 3. Moscow, Leningrad (1963, 1964)
32. Khamizov, R.K., Krachak, A.N., Gruzdeva, A.N., Vlasovskikh, N. S., Tikhonov, N.A.: Separation of concentrated acid and salt solutions in nanoporous media as the basis for a new technology of processing of phosphorus-containing raw materials. Geochem. Int. **54**(13), 1221–1235 (2016)
33. Helfferich, F.G.: The theory of precipitation/dissolution waves. AIChE J. **35**(1), 75–87 (1989)
34. Khamizov, R.K., Myasoedov, B.F., Rudenko, B.A., Tikhonov, N. A.: General character of isothermal supersaturation in ion exchange. Doklady Phys. Chem. **356**(1–3), 310–314 (1997)
35. Muraviev, D., Khamizov, R.K., Tikhonov, N.A.: Pecularities of the dynamics of ion exchange in supersaturated solutions and colloid systems. Langmuir **19**(26), 10852–10856 (2003)
36. Muraviev, D.N., Khamizov, R.K.: Ion exchange isothermal supersaturation. Concept, problems and application. Ion Exchange Solvent Extract. Ser. Adv. **16**, 119–210 (2004)
37. Tikhonov, N.A.: On the phenomenon of isothermal supersaturation of solutions at ion exchange in porous media. J. Math. Chem. **57** (1), 315–326 (2019)
38. Vlasovskikh, N.S.,Khamizov, S.K., Khamizov, R.K., Krachak, A. N., Gruzdeva, A.N., Tsikin, M.N.,Dolgov, V.V.: Extraction of impurities: REM and other metals, from phosphoric acid. Sorbtsionnye I Chromatograficheskie Processy **13**(5), 605–617 (2013). (in Russian)
39. Khamizov, R.K., Krachak, A.N., Gruzdeva, A.N., Vlasovskikh, N. S. et al.: Method for extracting rare earth elements from wet phosphoric acid. Patent RF 2544731 (2015)
40. Khamizov, R.K., Krachak, A.N., Gruzdeva, A.N., Vlasovskikh, N. S. et al.: Method for extracting rare earth elements from wet phosphoric acid. Patent RF 2545337 (2015)
41. Kaznacheev, M.A., Tikhonov, N.A., Khamizov, R.K.: Influence of impurity components on the precipitation of calcium salts during the purification of phosphoric acid on anionite by the method of acid retardation. Sorbtsionnye I Chromatograficheskie Processy **21** (4), 547–554 (2021). (in Russian)
42. Khamizov, R.K., Vlasovskikh, N.S., Moroshkina, L.P., Krachak, A.N., Gruzdeva, A.N., Khamizov, S.K.: Acid retardation method of separation for closed-circuit processing of alumina-containing raw materials with the use of salt-acid digestion. Sorbtsionnye I Chromatograficheskie Processy **17**(6), 877–885 (2017)
43. Khamizov, R.K., Kogarko, L.N., Vlasovskikh, N.S., Krachak, A. N., Gruzdeva, A.N., Zaitsev, V.A., Moroshkina, L.P.: On the possibility of separation of ammonium bisulfate into sulfate and acid in the cyclic salt-type processing of alumina-containing raw materials. Dokl. Chem. **481**(1), 157–159 (2018)
44. Khamizov, R.K., Zaitsev, V.A., Gruzdeva, A.N., Krachak, A.N., Rarova, I.G., Vlasovskikh, N.S., Moroshkina, L.P.: Feasibility of acid–salt processing of alumina-containing raw materials in a closed-loop process. Russ. J. Appl. Chem. **93**(7), 1059–1067 (2020)
45. Khamizov, R.K., Krachak, A.N., Khamizov, S.K.: Separation of ionic mixtures in sorption columns with two liquid phases. Sorbtsionnye I Chromatograficheskie Processy **14**(1), 14–23 (2014)
46. Khamizov, R.K., Krachak, A.N., Podgornaya, E.B., Khamizov, S. K.: Method of mass transfer process. US Patent 8940175 (2015)
47. Khamizov, R.K., Krachak, A.N., Gruzdeva, A.N., Khamizov, S. K., Vlasovskikh, N.S.: Separation of concentrated ion mixtures in sorption columns with two liquid phases. Ion Exchange Solvent Extract. Ser. Adv. **22**, 147–174 (2016)
48. Podgornaya, E.B., Burova, O.I., Radilov, A.S., Khamizov, R.K.: Using sorption method of acid retardation in the systems composed of two liquid phases, to address the problems of sample preparation in ICP-MS elemental analysis. Sorbtsionnye I Chromatograficheskie Processy **13**(5), 618–622 (2013). (in Russian)
49. Seregina, I.F., Perevoznik, O.A., Bolshov, M.A.: Acid retardation method in analysis of strongly acidic solutions by inductively coupled plasma mass-spectrometry. Talanta **159**, 387–394 (2016)
50. Khamizov, R.K., Krachak, A.N., Podgornaya, E.B., Gruzdeva, A. N.: Acid retardation effect in sorption columns with two liquid phases: capabilities of application to sample preparation in elemental analysis. J. Analyt. Chem. **74**(3), 226–238 (2019)

Pulsed Atomization and Excitation Sources with Solution Electrodes for Optical Emission Spectroscopy

V. V. Yagov, A. S. Korotkov, A. A. Zhirkov, and B. K. Zuev

1 Introduction

The history of the study of electric discharges on liquid surfaces dates back almost a century and a half [1]. However, the systematic application of the corresponding sources lasts less than three decades. Significant for the development of this direction was the appearance of a monograph containing data on the physics of electric discharges with liquid electrodes [2], and pioneer works by Cherfalvi and Mezei on spectroscopy with a source based on a glow discharge with electrolyte cathode [3]. The current state of the direction can be judged from the review [4].

The most common plasma excitation source with a liquid electrode is a stationary discharge of atmospheric pressure between a metallic anode and a liquid cathode (solution-cathode glow discharge SCGD) (Fig. 1a) [4–11]. Recently, sources with reversed polarity based on solution-anode glow discharge (SAGD) [12–15] have also been studied. SCGD and SAGD are naturally combined under the name SEGD (solution-electrode glow discharge), which also includes discharges between two liquid electrodes. Exactly such systems have been proposed in our laboratory. We have investigated pulsed discharges for use in miniature, inexpensive sources suitable for sensors and adapted for detecting major metals in flow. In 1998 we published the first papers on drop-spark discharge (DSD) arising at voltage over 0.8 kV at convergence of oppositely charged droplets (Fig. 1b) [16–18]. In 2002 the first paper [19] was published on the flow boiling discharge (FBD) which occurs under the action of a high voltage pulse causing superheating and boiling of liquid in a narrow channel (see Fig. 1c). In DSD, the discharge burns between meniscuses of approaching droplets; in FBD, it burns between the receding liquid walls of a growing vapor plug. Thus, in both cases the plasma exchanges a charge with two liquid electrodes, but the burning conditions of DSD and FBD are significantly different. The duration of DSD and FBD varies from units to hundreds of milliseconds, with their properties differing little from steady-state SEGDs most of the time, as confirmed by synchronous measurements of current and light intensity [17–20]. Although steady-state SEGDs, DSDs, and FBDs are structurally executed as atmospheric pressure discharges, in the case of FBDs the pressure at the early stage of the discharge is increased. FBD occurs in an initially continuous liquid; the length of the FBD torch increases from 0 to 1–2 cm in a time of the order of 1 ms; rapid ejection of water requires overpressure of the order of 1 bar.

SEGD-based sources have an obvious advantage and an equally inherent disadvantage. The advantage is the absence of the nebulizer, which is a rather complex and capricious component in traditional atomic spectral analysis instruments. The nebulizer is subject to a "memory effect", especially when the same elements appearing alternately as major and minor component. In sources with liquid electrodes an abrupt change in the sample composition does not create major problems. A DSD-based spectrometer was used for measurements in brines and biological samples of complex phase composition [21, 22].

The disadvantage of SEGD is due to the high content of water vapor and hydrogen in plasma. Due to the thermal dissociation of water, the thermal conductivity of water vapor at 3000 K is about 6 times higher than that of air and 4 times higher than that of helium [23]. Since the discharges of interest have millimeter dimensions and located on the free surface of water, the increase in electric power of the discharge is almost entirely spent on evaporation and thermal dissociation of the enhanced vapor flow. The slopes of the temperature dependence curves of heat capacity and thermal conductivity of water in the range of 2000–3000 K are too steep for the SEGD molecular temperature of atmospheric

V. V. Yagov (✉) · A. S. Korotkov · A. A. Zhirkov · B. K. Zuev
Vernadsky Institute of Geochemistry and Analytical Chemistry, Russian Academy of Sciences, 19 Kosygin St., Moscow, 119991, Russia
e-mail: vladvy65@yandex.ru

V. P. Kolotov and N. S. Bezaeva (eds.), *Advances in Geochemistry, Analytical Chemistry, and Planetary Sciences*,
https://doi.org/10.1007/978-3-031-09883-3_31

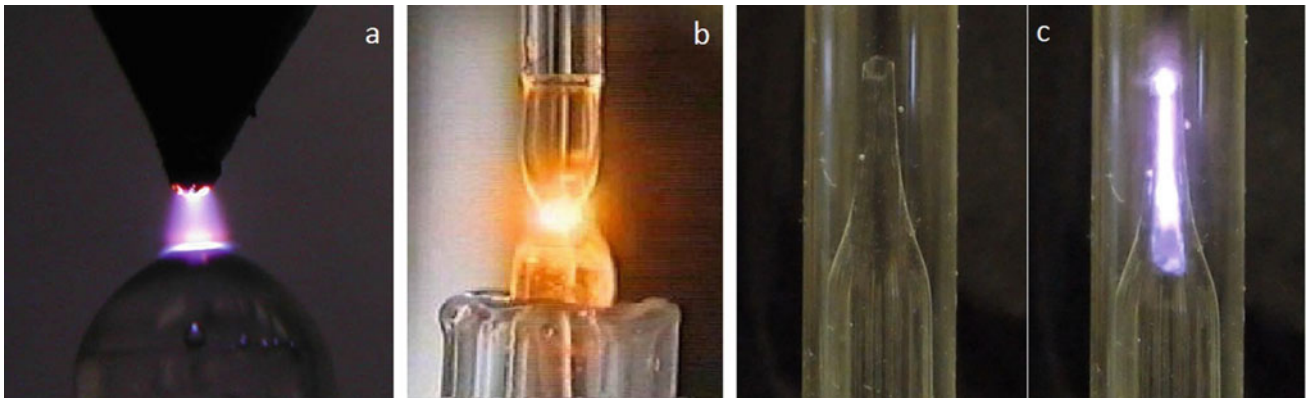

Fig. 1 Types of SEGDs. **a** SCGD with flow liquid cathode (1.2 kV). **b** DSD (1.2 kV, 1 mM Na in solution cathode). **c** FBD (2.5 kV). Supporting electrolyte was 0.2 M HNO_3 in all cases

pressure to overcome the 3000 K mark. Therefore, molecules more stable than H_2O will mostly not undergo thermal dissociation. Accordingly, to make a universal source based on SEGD, competing with inductively coupled plasma (ICP) on the diversity of analytes is hardly realistic. On the other hand, the relatively low temperature is favorable for the determination of easily ionized metals. Dissociated vapor recombines at the periphery, increasing the temperature-homogeneous volume of the torch.

For the determination of elements that are difficult to atomize and difficult to excite, stationary SEGDs are "dried" by a stream of argon or helium [4]. As water vapor is diluted with a noble gas, the temperature increase especially with a growth in the torch size. Such sources can surpass ICP-OES in sensitivity of determination of individual elements [4]. However, limitations still remain: this is indicated by the very fact of widespread use of tungsten electrode, with which one obviously cannot claim to determine tungsten. Although stationary SEGDs in an inert atmosphere provide the best analytical performance, there is a danger of losing the simplicity of design and remaining a secondary version of ICP when going down this path.

2 Plasma Instabilities and Mechanism of Electrolyte Cathode Atomization

The first question that arises when attempting to apply a discharge to the surface of an aqueous solution for its analysis is whether the discharge will burn in any way. If a pulsed discharge starting with a spark breakdown were to occur between any conductors, the ability to maintain a stationary discharge is not guaranteed in advance. It depends not only on the composition of the atmosphere and the parameters of the electric circuit, but also on the composition of the solution. It turned out that stationary SEGDs are stable only over dilute (<0.2 M) solutions of strong electrolytes, usually mineral acids (e.g., [5]). Since the burning voltage is significantly lower than the breakdown voltage, the extinguished stationary discharge does not ignite spontaneously, moreover, a very delicate thermal regime affecting, among other things, the atmospheric composition is disturbed. Therefore, it takes at least several minutes to return the installation to its operational state. The use of pulsed discharges allows to get around this difficulty to a large extent. Firstly, for the systems we used, it is sufficient that stability is maintained at times of the order of 0.01 s (instead of tens of seconds for stationary discharges). Second, even if a current surge associated with instability occurred at the n-th discharge, the corresponding spectrum is rejected by the type of the current curve, but this does not affect the $(n + 1)$-th discharge: by the beginning of the next pulse the system "forgets" all the past events (the concentration and thermal disturbances in the liquid are carried away by the flow, the atmosphere relaxes due to natural convection).

The sources of interest belong to the anomalous glow discharge. The electron temperature is significantly higher than the molecular temperature, which allows one to observe hard (up to 10 eV) lines in the emission spectrum. Various instabilities are characteristic of the glow discharge, especially significant at atmospheric pressure. First of all, it is the contraction of the positive column: a homogeneous diffuse glow splits into a hot filament and cold peripheral regions. The abnormally high thermal conductivity of thermally dissociated water vapor restrains the development of overheating instability. Another reason for SEGD stability is the low (compared to metals) electrical conductivity of the electrolyte, which limits the current density at the interface, preventing the contraction from spreading to the near-cathode region. In addition, the surface of the aqueous solution responds to the local increase in current density by enhancement of the vapor flux, cooling the hot plasma region. Thus, it turns out that the

factors limiting the temperature and, consequently, the possibility of determining the hard to atomize elements, provide the stability of SEGD.

However, for analytical applications it is still necessary to ensure that the non-volatile solution components enter the plasma. For SCGD, metals enter the discharge torch due to aerosol spraying of the electrolyte cathode. As it was shown as early as in [3] and repeatedly confirmed later, for this, firstly, a sufficient current strength should be provided. As shown in our works, a sufficiently high concentration of supporting electrolyte is also required for sputtering [24, 25]. This agrees with the data of [3] with the only difference that the authors of [3] and some other publications were limited to mineral acids and interpreted the effect of electrolyte concentration as pH influence. However, as shown by us in [24] and by the authors [6], who ignited stationary SCGD on ammonia solutions, pH does not play a special role. In [26], we showed that the sputtering of the electrolyte cathode increases with rising liquid temperature and decreases with increasing flow rate. For this purpose, we had to use a steady-state jet SCGD with a liquid velocity of several m/s, because in typical slow flow installations the solution is heated almost to boiling by the discharge itself [4]. Experiments on the influence of the cathode solution temperature on the signal in the case of DSD also confirmed the enhancement of sputtering at heating. The indicated regularities testify in favor of thermal nature of sputtering in SCGD.

Let's try to outline the qualitative mechanism of electrolyte cathode sputtering. The SCGD positive column produces one or more filaments that reach the water surface. A homogeneous torch pattern is formed from several fast running filaments. In the works of Tazmeev [27, 28], the filaments are visualized by high-speed video imaging for high-power SCGD. According to the author's estimations [27], their speed along the electrolyte cathode is about 1 m/s, and the current density is about 100 A/cm^2. A similar picture is noted by the authors [29], where high speed video imaging was carried out under typical conditions for analytical SCGD.

The thermal nature of cathodic sputtering [26] suggests a role for boiling: if a microbubble forms below the liquid surface, it will induce sputtering by crossing the interface. However, it is not easy to explain how microbubbles can form when heated on the gas side under conditions where the free surface creates almost unlimited opportunities for heat removal. It can be assumed that the cause of microbubble formation is evaporation-induced enhancement of electrolyte surface concentration combined with the movement of plasma filaments.

Let us consider a fragment of the surface of the electrolyte cathode. The dark gray band in Fig. 2a indicates that the liquid surface layer in contact with plasma is enriched with electrolyte due to evaporative concentrating and, therefore, has an increased electrical conductivity. Therefore, a microbubble is formed slightly deeper (in subsurface layer), where the current density is the same and conductivity is lower, when passing through the selected section of the plasma filament.

A certain threshold current density must be exceeded for a vapor microbubble to occur in a liquid. To reach it, the electrolyte must have a sufficient concentration. In too dilute solutions, the bundle of electric current lines simply cannot come to the surface without blurring. This seems to be the reason why the concentration of the supporting electrolyte affects sputtering. The nature of the electrolyte has no matter. Only the electrical conductivity of the solution is important, allowing the plasma filament to "continue in the liquid" and locally warm the subsurface layer to the formation of the vapor phase nucleation.

Subsequently, the bubble may continue to grow, rise to the surface, and explode, ejecting liquid particles into the plasma, as depicted in Fig. 2b. Another possibility is that the plasma filament goes away, the solution cools, and the microbubble collapses to form a cavitation jet which, if directed appropriately, can cause sputtering of the liquid (Fig. 2c). This mechanism is attracted in the discussion of ultrasonic nebulization.

Of course, the given scheme is conditional. In general, the idea is that contracting of the glow discharge causes rapid changes in the local current density on the surface of the electrolyte cathode, which is accompanied by mechanical perturbation of the interface. Bubbles are not the only option. It is possible, for example, following [29], to assume that negatively charged crests of waves caused by moving plasma filaments are disrupted by the electric field.

3 Electrolyte Anode Versus Electrolyte Cathode

The striking difference of the character of substance inflow from the electrolyte anode and the electrolyte cathode is evident from the picture of the jet SEGD (Fig. 3a). The stationary discharge was ignited between two identical jets. Nevertheless, the impression is that the left (negative) jet "burns", emitting substance, while the right (positive) jet passes through the torch without even particularly perturbing it. This picture corresponds to the physics of the process: cathode voltage drop is about 500 V [2, 3, 29], correspondingly, large power is dissipated on the surface of the cathode jet, which leads to aerosol sputtering of the liquid. Anode voltage drop is only a few tens of volts [2], so there is no sputtering of anode.

For a long time, it was believed that metals could enter the plasma only from the electrolyte cathode. However, in 2016, papers were published showing that some elements

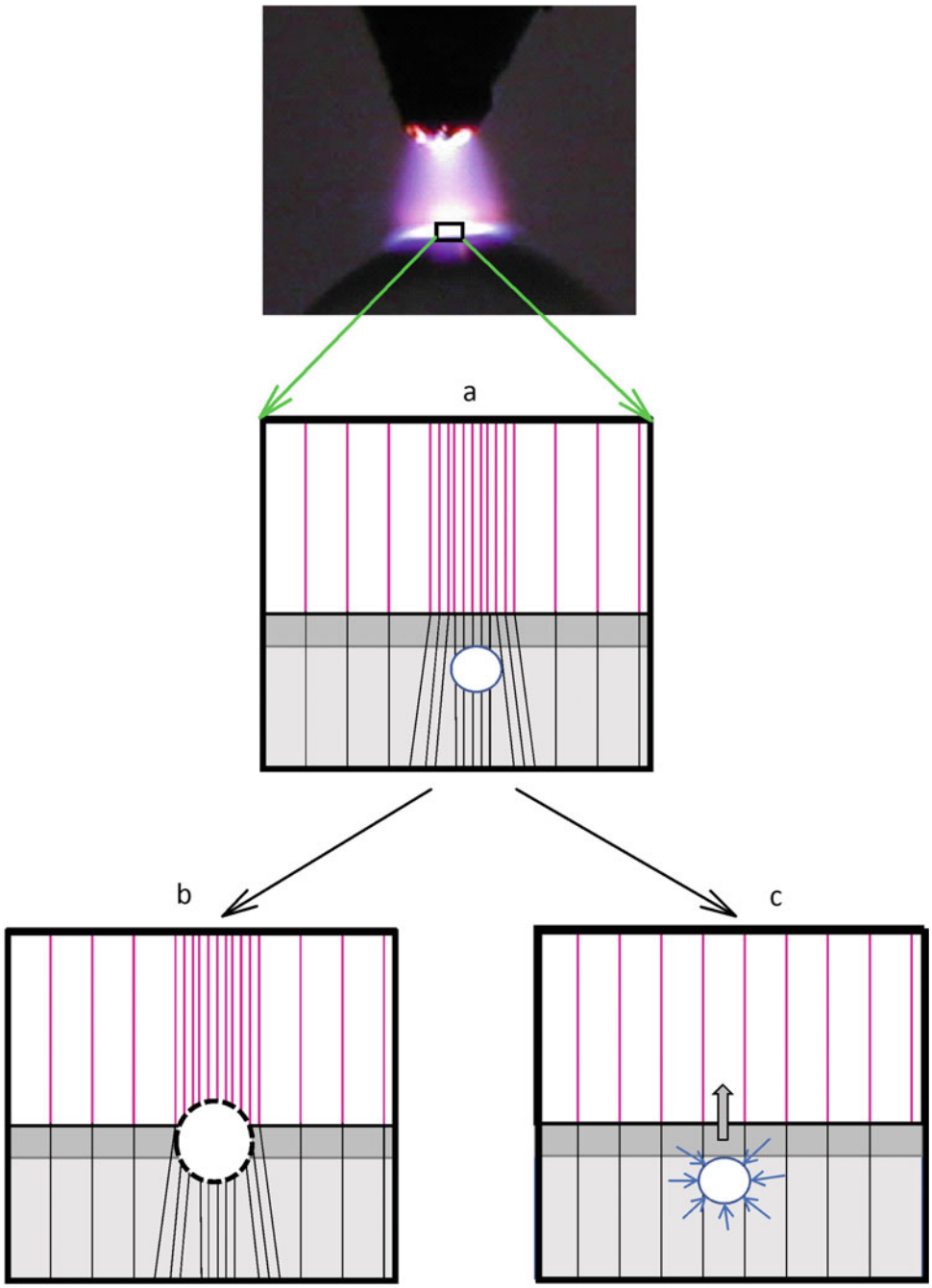

Fig. 2 Potential mechanism of filament-induced electrolyte cathode sputtering. Figure shows current lines in plasma and in liquid

enter the plasma from the electrolyte anode, in some cases even in larger amounts [12, 13]. Figure 3b illustrates this effect using thallium glow in DSD as an example. The greenish flare light in the left photo is associated with an intense Tl line of 535.0 nm, whereas the right photo shows only a faint lilac background glow. Both images were obtained for identical solutions; the only difference is that in the left photo the drop containing thallium was positively charged, while in the right one it was negatively charged. Surprising picture: thallium is more quickly transferred into the plasma from a non-sputtering electrolyte anode than from a sputtering cathode! Already 2 μM Tl in the electrolyte anode causes a glow, which significantly overlaps the background and is easily registered visually.

To date, the list of elements whose lines in the SAGD spectrum have high or at least comparable intensity with SCGD includes Ag, Zn, Cd, Hg, In, Tl, Pb, As, Bi, Hg, Sb, Se, and Te [12–15, 22]. Their transfer across the electrolyte anode/plasma boundary is selective, whereas other metals (Na, K, Ca, Al, Fe, etc.) from the electrolyte anode do not enter the plasma. All "anodic" elements have relatively volatile forms (in particular hydrides) under reducing conditions that

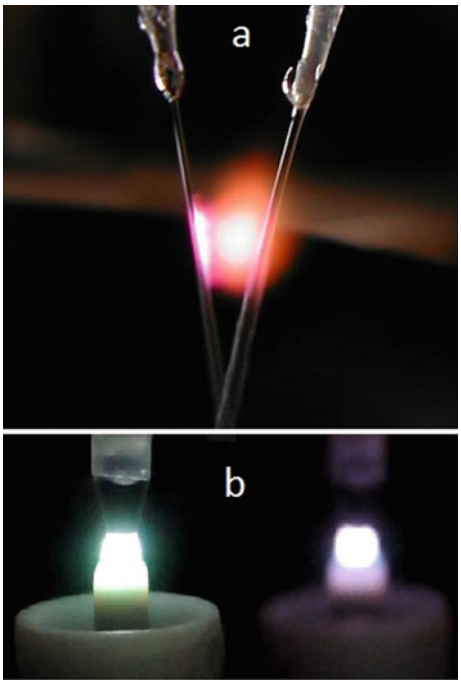

Fig. 3 The difference between the electrolyte cathode and the electrolyte anode. **a** the discharge between jets in a symmetrical system (2 kV, 0.2 M HCl). **b** DSD (2.5 kV) with the Tl solution (20 µL 2 µM Tl in 24 mM HNO_3) on the anode (left) and on the cathode (right)

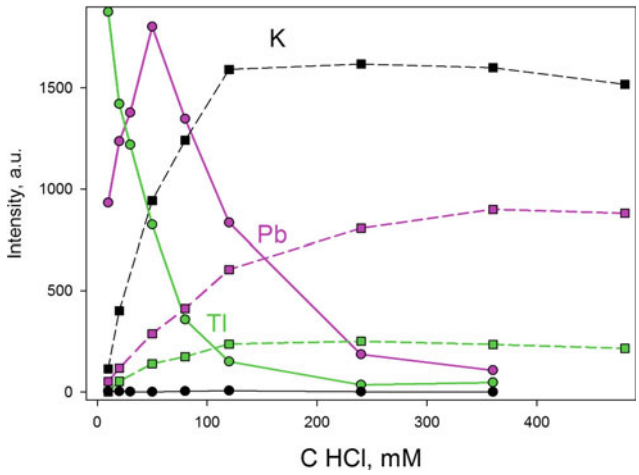

Fig. 4 Dependence of atomic line intensities of Tl 535.0 nm, K 766.5 nm and Pb 405.8 nm in the DSD spectrum on HCl concentration. The solid lines are the sample in the electrolyte anode, the dotted lines are the sample in the electrolyte cathode. Other conditions are as in [22]

can occur on the surface of an electrolyte anode undergoing electron bombardment. Therefore, the assumption of the role of volatile hydrides seems plausible [15], with some doubts related to the presence of O_2 and HNO_3.

As noted above, a characteristic feature of SCGD is the upward dependence of the signal on the concentration of the supporting electrolyte. It is interesting to compare such dependences for the electrolyte cathode and the electrolyte anode. Corresponding measurements were carried out for DSD on the setup described in [22, 30].

As can be seen from Fig. 4, the dashed curves referring to the electrolyte cathode for all three metals behave similarly: the intensity of the lines increases with increasing concentration of HCl up to a maximum in the region of 0.15–0.4 M. It was shown earlier that ascending section of the signal dependence on supporting electrolyte concentration has a similar form both for different acids and for electrolytes of other nature [24]. (We previously confirmed this pattern not only for DSD but also for steady-state SCGD [24] and FBD [25].) The possible reason for the influence of the supporting electrolyte concentration on sputtering was discussed in the previous section.

For lead the optimum concentration of HCl for the anode is 60 mM, after which the intensity begins to decrease quite rapidly. For thallium the intensity monotonically decreases with increasing concentration of hydrochloric acid, finally the lines of potassium added into the anodic electrolyte are completely absent in the DSD spectrum.

The DSD was used as an atomization and excitation source in a mockup of a portable solution analyzer created in the laboratory. The device contained a high voltage power supply (2.5 kV, 6 µF), a Maya 2000 Pro spectrometer with which spectra were recorded in the 200–1100 nm range, a current measuring and synchronization unit, and a sample input system in two versions: either with continuous solution feeding through an overflow tube or with sample application in individual drops (20 µl). The instrument features a polarity reversal option: it can be used in both SCGD [30] and SAGD [22] modes. The instrument was used in development of hydrochemical technology and for analysis of biological fluids. SCGD mode for determination of Na, K, Mg and Ca turned out to be the most demanded in practice.

In the SAGD mode, the device was used mainly to study the matrix effects [22]. The advantage of the device is the possibility to vary the chemical composition of the sample almost unlimitedly, including aggressive media, which is due to the microliter volume and the absence of open optical design elements. One of the interesting results found in the study of SAGD is that the possibility of direct determination of some heavy metals in brines with sensitivity not inferior to determination in commonly used mineral acid solutions was shown.

4 Conclusions

The aqueous electrolyte/plasma interface stabilizes the glow discharge, allowing non-equilibrium to persist up to atmospheric pressure; therefore, despite the low molecular

temperature limited by water vapor dissociation, SEGD spectra contain lines of elements with sufficiently high excitation thresholds. However, SEGDs are still significantly inferior to ICP-OES in terms of the determination of difficult-to-atomize and difficult-to-excite elements.

The fact that SCGD combines the functions of nebulizer and excitation source creates prerequisites for the creation of simple, compact and economical emission spectrometers for solution analysis. This capability is easier to implement in the case of pulsed discharges. Pulsed sources require less energy, are safer and need no cooling. They can be used in portable devices and chemical sensors.

The essential problem of SEGD is plasma stability. The positive column at atmospheric pressure is prone to filamentation. According to our conceptions, sputtering of electrolyte cathode is caused by interaction of current filaments with liquid, i.e. analytical application and filamentation are inseparably connected. The degree of contraction depends on the composition of the liquid. Introducing highly mineralized samples into the electrolyte cathode leads to rapid plasma disruption. For pulsed sources (unlike stationary sources) this is not a big problem, because instability does not have time to develop for several milliseconds of discharge burning. Therefore, pulsed sources can be used practically for any samples with ionic conductivity. Of course, with all their advantages, pulse sources are inferior to stationary sources in a number of positions, first of all, in sensitivity and reproducibility of determination of most elements in dilute mineral acids.

Nonvolatile components of electrolyte cathode enter the plasma in the form of aerosol. The transport at the electrolyte anode/plasma interface has a different character: some heavy metals enter the discharge selectively, without sputtering the matrix. In fact, this is an unconventional electrochemical reaction, which takes place in monolayer and, correspondingly, is extremely sensitive to the form of the element and the presence of surface-active impurities. The effect of selective transport of matter from the electrolyte anode into plasma discovered by the authors [12] and [13] is, in our opinion, currently underestimated; its significance goes beyond analytical emission spectroscopy. Pulsed discharges allow us to freely vary the composition of the electrolyte anode, which is useful for studying this interesting new phenomenon and ways to apply it in analysis.

References

1. Gubkin, J.: Electrolytic metal deposition on the free-surface of a salt solution (in German). Ann. Phys., Berlin (1887)
2. Gaisin, F.M., Son, E.E.: Electrophysical processes in discharges with solid and liquid electrodes. Ural'sk. Gos. Univ, Sverdlovsk (1989)
3. Cherfalvi, T., Mezei, P.: Direct solution analysis by glow discharge: electrolyte-cathode discharge spectrometry. J. Anal. At. Spectrom. **9**(3), 345–349 (1994)
4. Pohl, P., Jamroz, P., Swidereski, K., Dzimitrowicz, A., Lesniewicz, A.: Critical evaluation of recent achievements in low power glow discharge generated at atmospheric pressure between a flowing liquid cathode and a metallic anode for element analysis by optical emission spectrometry. Trends Anal. Chem. **88**, 119–133 (2017)
5. Wang, Z., Gai, R., Zhou, L., Zhang, Z.: Design modification of a solution-cathode glow discharge-atomic emission spectrometer for the determination of trace metals in titanium dioxide. J. Anal. At. Spectrom. **29**(11), 2042–2049 (2014)
6. Manjusha, R., Shekhar, R., Jaikumar, S.: Direct determination of impurities in high purity chemicals by electrolyte cathode discharge atomic emission spectrometry (ELCAD-AES). Microchem. J. **145**, 301–307 (2019)
7. Decker, C.G., Webb, M.R.: Measurements of sample and plasma properties in solution cathode glow discharge and effects of organic additives on these properties. J. Anal. At. Spectrom. **31**(1), 312–318 (2016)
8. Jamroz, P., Pohl, P., Zyrnicki, W.: An analytical performance of atmospheric pressure glow discharge generated in contact with flowing small size liquid cathode. J. Anal. At. Spectrom. **27**(6), 1032–1037 (2012)
9. Manjusha, R., Reddy, M.A., Shekhar, R., Kumar, S.J.: Determination of major to trace level elements in Zircaloys by electrolyte cathode discharge atomic emission spectrometry using formic acid. J. Anal. At. Spectrom. **28**(12), 1932–1939 (2013)
10. Doroski, T.A., King, A.M., Fritz, M.P., Webb, M.R.: Solution-cathode glow discharge - optical emission spectrometry of a new design and using a compact spectrograph. J. Anal. At. Spectrom. **28**(7), 1090–1095 (2013)
11. Schwartz, A.J., Ray, S.J., Hieftje, G.M.: Automatable on-line generation of calibration curves and standard additions in solution-cathode glow discharge optical emission spectrometry. Spectrochimica Acta B. **105**(3), 77–83 (2015)
12. Liu, X., Zhu, Z., He, D., Zheng, H., Gan, Y., Belshaw, N.S., Hu, S., Wang, Y.: Highly sensitive elemental analysis of Cd and Zn by solution anode glow discharge atomic emission spectrometry. J. Anal. At. Spectrom. **31**(5), 1089–1096 (2016)
13. Greda, K., Swiderski, K., Jamroz, P., Pohl, P.: Flowing liquid anode atmospheric pressure glow discharge as an excitation source for optical emission spectrometry with improved detectability of Ag, Cd, Hg, Pb. Tl Zn. Anal. chem. **88**(17), 8812–8820 (2016)
14. Jamroz, P., Greda, K., Dzimitrowicz, A., Swiderski, K., Pohl, P.: Sensitive determination of Cd in small-volume samples by miniaturized liquid drop anode atmospheric pressure glow discharge optical emission spectrometry. Anal. Chem. **89**(11), 5729–5733 (2017)
15. Gorska, M., Greda, K., Pohl, P.: On the coupling of hydride generation with flowing liquid anode atmospheric pressure glow discharge for determination of traces of As, Bi, Hg, Sb and Se by optical emission spectrometry. Talanta **222**(1), 121510–121520 (2021)
16. Yagov, V.V., Korotkov, A.S., Zuev, B.K.: Electric discharge in the interelectrolyte gap: prospects for creation of an atomic emission sensor. Dokl. Ross. Akad. Nauk **359**(2), 208 (1998)
17. Yagov, V.V., Korotkov, A.S., Zuev, B.K., Myasoedov, B.F.: Drop-spark discharge: an atomization and excitation source for atomic-emission sensors. Mendeleev Commun. **8**, 161–162 (1998)
18. Yagov, V.V., Getsina, M.L.: Atomic-emission determination of metals in water using a drop-spark discharge. J. Anal. Chem. **54**(8), 724–730 (1999)

19. Zuev, B.K., Yagov, V.V., Getsina, M.L., Rudenko, B.A.: Discharge on boiling in a channel as a new atomization and excitation source for the flow determination of metals by atomic emission spectrometry. J. Anal. Chem. **57**(10), 907 (2002)
20. Zuev, B.K., Yagov, V.V., Grachev, A.S.: Discharge on boiling in a channel: effect of channel geometry on the performance characteristics of determining metals in a liquid flow by atomic emission spectrometry. J. Anal. Chem. **61**(12), 1172–1176 (2006)
21. Zhirkov, A.A., Yagov, V.V., Zuev, B.K., Vlasova, A.A.: A microplasma analyzer for the determination of alkali and alkaline-earth metals in small volumes of samples of complex phase composition. J. Anal. Chem. **70**(12), 1468–1474 (2015)
22. Yagov, V.V., Zhirkov, A.A.: Analytical possibilities of the drop-spark spectrometer when introducing a sample into the electrolyte anode. J. Anal. Chem. V. 77(5), 550–554 (2022).
23. Vargaftik, N.B., Filippov, L.P., Tarzimanov, A.A., Totskii, E.E.: Handbook of thermal conductivity of liquids and gases, 1st ed. CRC Press, Boca Raton, Florida, USA (1993)
24. Yagov, V.V., Gentsina, M.L.: Effect of supporting electrolyte composition on the intensity of metal lines in electrolyte-cathode discharge spectra. J. Anal. Chem. **59**(1), 64–70 (2004)
25. Zuev, B.K., Yagov, V.V., Grachev, A.S.: Discharge in liquids as a spectral source of radiation: effect of the supporting electrolyte on the intensity of metal lines. J. Anal. Chem. **63**(6), 586–589 (2008)
26. Yagov, V.V., Getsina, M.L., Zuev, B.K.: Use of electrolyte jet cathode glow discharges as sources of emission spectra for atomic emission detectors in flow-injection analysis. J. Anal. Chem. **59** (11), 1037–1041 (2004)
27. Tazmeev, G.K., Timerkaev, B.A., Tazmeev, K.K.: Study of the binding zone of electrical discharge to the liquid cathode by high-speed visualization. J. Phys. Conf. Ser. **789**(1), 012059–012064 (2017)
28. Tazmeev, G.K., Timerkaev, B.A., Tazmeev, A.K.: The emergence and development of spark channels in the plasma column of a gas discharge between water-solution cathode and a copper anode. J. Phys. Conf. Ser. **927**, 012064–012069 (2017)
29. Orejas, J., Hazel, N., Ray, S.J.: The solution-cathode glow discharge in slow motion: characterization of glow discharge filament structure and droplet ejection using a rectangular capillary. Spectrochim. Acta Part B **181**(7), 106209–106220 (2021)
30. Yagov, V.V., Korotkov, A.S., Zhirkov, A.A., Pogonin, V.I., Zuev, B.K.: A portable atomic emission spectrometer based on a drop-spark discharge for analyzing solutions. J. Anal. Chem. **74** (3), 270–275 (2019)

Ultrasound Suspension Columns for Solid-Phase Extraction of Platinum and Palladium

R. Kh. Dzhenloda, O. B. Mokhodoeva, T. V. Danilova, V. V. Maksimova, and V. M. Shkinev

1 Introduction

Ultrasound is often used in analytical chemistry both in sample preparation and detection of dissolved analytes [1]. It is known that ultrasound can affect the kinetics of metal sorption from aqueous solutions by complexing and ion-exchange materials. Microacoustic currents arising in the ultrasonic field create the necessary conditions for accelerated sorption due to the intensification of mass transfer in the sorbate-sorbent system.

There are various kinds of ultrasound exposure. In particular, the superposition of direct and reflected waves produces standing ultrasound waves, capable of retaining sorbent particles. In contrast to the traditional application of standing ultrasound waves for separation of microobjects, we were the first to propose their use in sorption processes [2–4]. An ultrasound suspension column (USC) was developed to implement these processes. In this type of columns standing ultrasound waves can hold the sorbent grains and simultaneously intensify the sorption process due to the formation of microturbulent liquid flows. The USC uses ultrasonic fields in the non-cavitating megahertz range, that makes it possible to form layers of sorbent particles with a frequency of half the ultrasound wavelength and maintain the integrity of the sorbent particles. It has been shown that the USC can be used for preconcentration of heavy metals from solutions [3], recovery of rare earth elements from wines [4], preconcentration of DNA from environmental samples [2].

In continuation of the research we studied the possibility of sorption preconcentration of platinum group metals (PGM) under the USC conditions.

R. Kh.Dzhenloda (✉) · O. B. Mokhodoeva · T. V. Danilova · V. V.Maksimova · V. M. Shkinev
Vernadsky Institute of Geochemistry and Analytical Chemistry, Russian Academy of Sciences, 19 Kosygin St., Moscow, 119991, Russia
e-mail: dzhenloda@geokhi.ru

PGM are widely used in various industries due to their unique physical, chemical, and catalytic properties [5]. The indispensability of PGM in a number of practical applications, such as palladium and platinum in the automobile and hydrogen power engineering, determines the growing demand for these metals and, accordingly, the need to improve methods of their recovery and processing [6, 7].

The methods of analytical determination of PGM play the most important role in the processes of production of refined metals from both primary and secondary raw materials. Taking into account low concentrations of PGM, complicated matrix composition, and high salt content, direct determination of PGM in technological solutions is difficult even with the use of the modern instrumental techniqes [8, 9]. In this regard, the mandatory stage of sample preparation is the PGM preconcentration and separation of matrix components (copper, nickel, aluminum, iron, etc.). For these purposes, the use of solid-phase extraction methods is preferable.

Previously, the advantages of ionic liquid using in solid-phase extraction of PGM were demonstrated. The application of phosphonium- and imidazolium-type ionic liquids as modifying agents of solid polymeric, carbon, and magnetic supports has been studied [10–14].

In this work the method of solid-phase extraction of platinum and palladium in the USC using Cyphos®IL-101 phosphonium ionic liquid and Kromasil® 100-5-Sil microparticles is proposed. The efficiency of recovery and preconcentration of platinum and palladium from model multicomponent solutions and their subsequent determination by ICP-AES is discussed.

2 Experimental Part

2.1 Reagents and Solutions

Trihexyl(tetradecyl)phosphonium chloride (Cyphos®IL-101) (purity 95%, Sigma-Aldrich, Germany) was used as a

V. P. Kolotov and N. S. Bezaeva (eds.), *Advances in Geochemistry, Analytical Chemistry, and Planetary Sciences*,
https://doi.org/10.1007/978-3-031-09883-3_32

modifying agent. Kromasil® 100-5-Sil (average particle size 5 μm, average pore size 100 Å, Biochemmack, Russia) was used as a solid support. Model solutions for solid-phase extraction were prepared from standard solutions of platinum and palladium with concentration of 10 g/L in 10% HCl (High-Purity Standards, USA), hydrochloric acid (35%, Chimmed, Russia), chlorides of copper(II), nickel(II), iron (III) (chemical pure, Chimmed, Russia). Solutions of nitric acid (65%, Chimmed, Russia), sodium perchlorate (purity 98%, Chimmed, Russia) and thiourea (putity 99%, Vekton, Russia) were used for elution of platinum metals.

2.2 Instrumentation

The sorbent was weighed on a Highland HCV 602H electronic laboratory balance (Adam Equipment Co Ltd., UK).

An orbital shaker (SkyLine, Latvia) and an ultrasonic bath (Sapphire, Russia) were used for solid-phase extraction in a batch mode; a laboratory centrifuge SM-6M (SkyLine, Latvia) was used for separation of phases.

To carry out solid-phase extraction in a dynamic mode, a setup with a focused ultrasound emitter with a frequency of 2.65 MHz and sound intensity of 10 W/cm^2 (Institute for Analytical Instrumentation, Russian Academy of Sciences) was used (Fig. 1). A peristaltic pump of L/S MasterFlex series (Cole-Parmer, USA) was used to pass the solution through a flow sorption system.

The concentration of platinum and palladium ions in solutions before and after solid-phase extraction was determined by inductively coupled plasma atomic emission spectrometry using an ICAP-6500 Duo instrument (ThermoElectron, USA).

2.3 Preparation of the Sorbent

100–500 mg of Kromasil® 100-5-Sil sample washed with ethanol and dried to constant weight was kept in a solution of Cyphos®IL-101 in ethanol with a volume of 0.5–1 ml with ionic liquid concentration of 40–150 mg/mL in a closed vessel for 30 min in an ultrasonic bath. Then the obtained sorbent was dried in air, washed with 0.1–1 M HCl and dried again to constant weight. The ionic liquid content on silica (mmol/g) was estimated by the difference in mass before and after sorbent modification.

2.4 Solid-Phase Extraction in a Batch Mode

A 20 mg sample of sorbent was contacted with a solution of platinum metals with a volume of 5–10 mL and a metal concentration of 10–50 μg/mL in 15 mL test tubes on an orbital shaker for 5–60 min. Then the phases were separated and the sorbent was washed with 0.1–1 M HCl. For subsequent elution, the washed sorbent was contacted with a 2 mL eluent solution for 15–30 min. The aqueous phases were analyzed for metal content by inductively coupled plasma atomic emission spectrometry (ICP-AES).

2.5 Solid-Phase Extraction in the USC

A 20 mg sample of sorbent in the form of suspension in 0.1–1 M HCl with a volume of 5 mL was placed in a cylindrical flow-through chamber of the USC mounted at a distance of 20 mm from the ultrasound emitter. A 10–50 mL platinum metal solution with a metal concentration of 0.2–50 μg/mL was pumped through the chamber with the sorbent suspension in a standing ultrasound wave at a rate of 0.1–1 mL/min. The sorbent was washed in a flow mode with 0.1–1 M HCl, after that eluent with a volume of 2 mL was passed trough the sorbent. The aqueous solutions were analyzed for metal content.

3 Results and Discussion

3.1 The Features of Standing Ultrasound Waves and Selection of the Optimal Conditions of the USC Operation

In contrast to membrane filtration methods, the use of standing ultrasound waves ensures separation of particles not only by size, but also by their density and compressibility. This feature can be considered as the main advantage, providing flexibility, versatility and universality of the method. For example, it is possible to carry out fractionation according to several parameters in the case of particles with well-known or targeted properties.

Standing ultrasound waves are capable of holding solid particles in the variable pressure nodes. This effect is due to the action of several forces in the field of a standing ultrasound wave on sorbent particles in suspensions, mainly the forces of radiation pressure, Stokes, gravity [15].

According to the calculations of particle retention [14, 16] at the ultrasound frequency of 2.65 MHz, which is necessary for the formation of a standing ultrasound wave, the optimum ultrasound intensity is a value equal to 10 W/cm^2. It is shown that the method based on generation of standing ultrasound waves by means of a focusing emitter, when a particle suspension flow is carried out along axial line perpendicular to the emitter center, is applicable for retention of solid particles. To organize the method operability, the ultrasound wavelength is chosen from the ratio $\lambda \leq 2\pi a$, where λ—the ultrasound wavelength, a—the characteristic

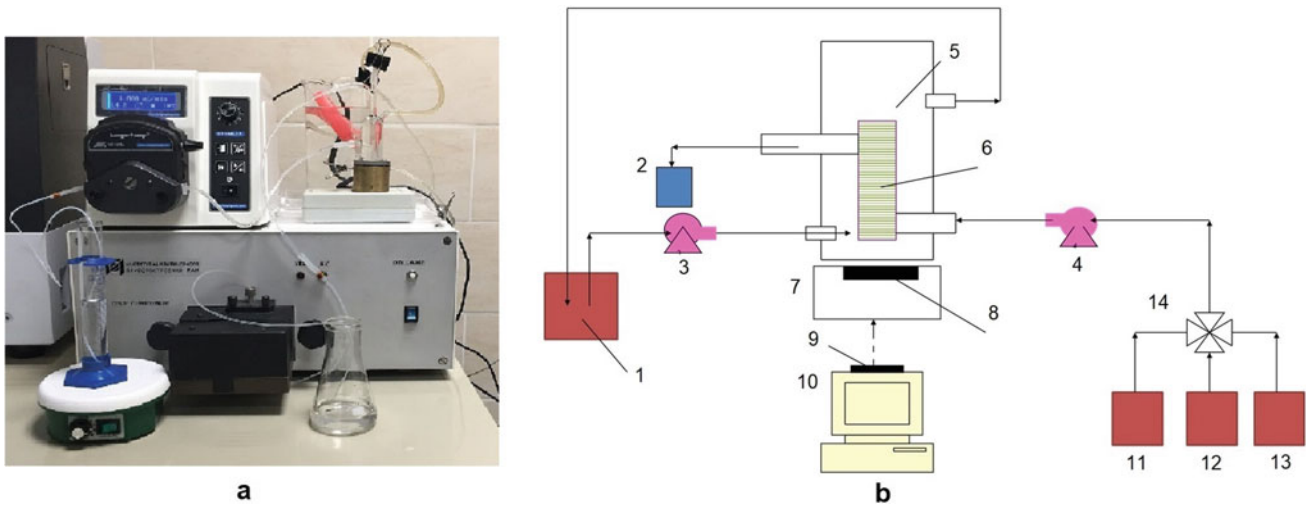

Fig. 1 Ultrasound suspension column appearance (**a**) and scheme (**b**): 1—cooling water, 2—collector for solution after solid-phase extraction and elution, 3, 4—pumps, 5—water bath, 6—column, 7—ultrasonic unit body, 8—transducer, 9—bluetooth USB adapter, 10—computer, 11—sample, 12—washing solution, 13—eluent, and 14—valve

size of the particles displaced by the field. If this condition is violated, the use of radiation force becomes ineffective and the retention of solid particles is impossible.

To realize the sorption process under the USC conditions, it is important not only to retain the sorbent particles, but also to ensure their effective contact with the solution and the necessary mass transfer. In this regard, the certain requirements are imposed on the size and density of the sorbent, as well as the design of the sorption cell. We have determined that the sorbent particles must be strictly monodisperse with a particle size of 5–6 μm and actual density ≥ 2200 kg/m^3. In order to avoid formation of stagnation zones the sorption cell of the USC must be of cylindrical shape with length not more than 50 mm and diameter of 5 mm. For such kind of the cell design the optimal sorbent mass is 20 mg.

Sorption materials based on silica, widely used in the practice of analytical chemistry and technology, meet the requirements to the sorbents. The sorbent Kromasil® 100-5-Sil with a particle size of 5 μm was chosen for this research.

Figure 2 demonstrates the dynamics of the retention of Kromasil® 100–5-Sil sorbent in the USC.

It should be noted that the selected sorbent also meets the requirements of mechanical and chemical stability required for operation in acidic, high-salt solutions under prolonged treatment with ultrasound [17]. In addition, silica-based sorbents are versatile for various types of surface modification in order to give the specified sorption capacity and selectivity.

In this work, Kromasil® 100-5-Sil was used as a solid support for solid-phase extraction of platinum metals for modification with Cyphos®IL-101.

3.2 Selection of the Optimal Conditions for Solid-Phase Extraction of Pt(IV) and Pd(II)

The main characteristics of the sorbents used for PGM preconcentration are their kinetic properties, sorption capacity in a wide range of acidity, selectivity of recovery in the presence of macrocomponents such as iron(III), copper (II), nickel(II), etc. To investigate these and other sorption properties, it was primarily important to choose the optimum content of ionic liquid on a solid support.[1] According to the obtained experimental data the optimum content of Cyphos®IL-101 on silica Kromasil® 100-5-Sil is 0.2–0.3 mmol/g (Fig. 3).

Figure 4 shows the data on the degree of recovery of platinum and palladium depending on the contact time of the phases in normal conditions and under the influence of ultrasound.

As it can be seen, to reach the equilibrium in the sorption system 5 min is enough in the case of palladium, while for platinum a longer contact of solution with the sorbent—more than 30 min—is necessary. It was found that under the influence of ultrasound on the sorption system it is possible to reduce the contact time of phases, necessary for complete recovery of both metals to 10 min.

Refining technologies for platinum-containing materials, such as hydrochlorination, cause their high acidity and high content of chloride ions. In this regard, the choice of silica as

[1] Non-modified Kromasil® 100–5-Sil has no any sorption activity towards Pt(IV) and Pd(II) ions in the studied media.

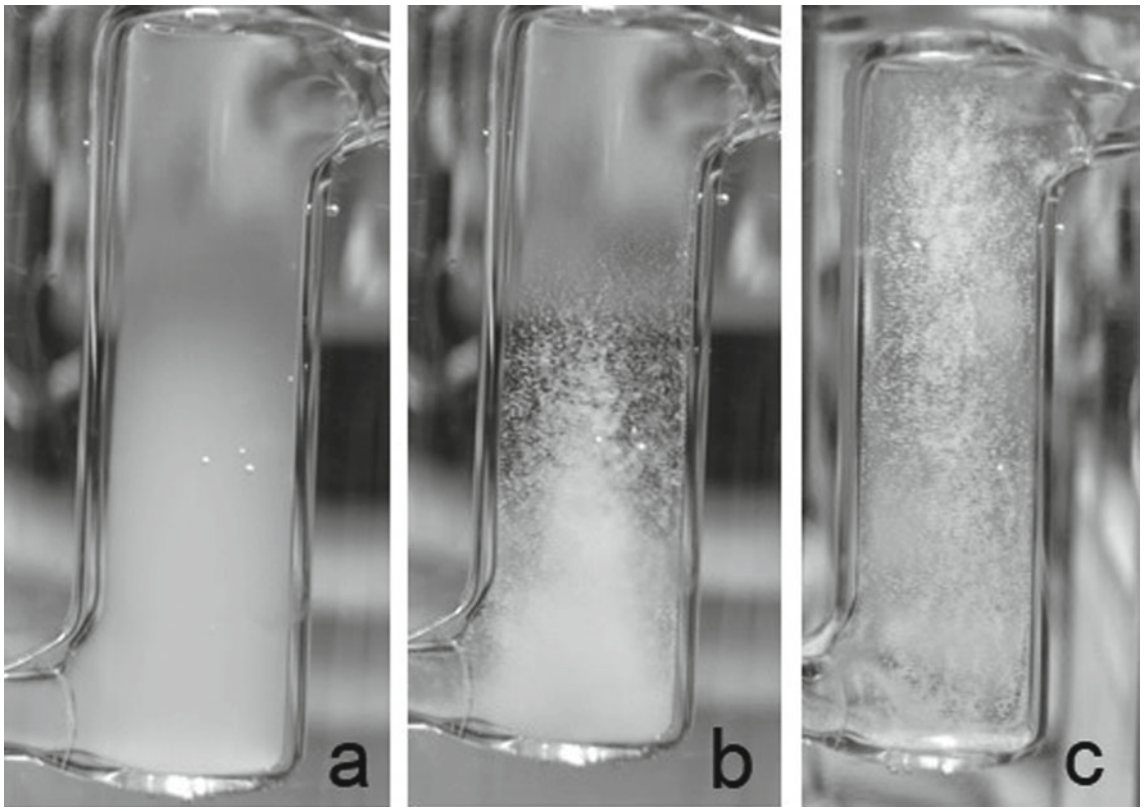

Fig. 2 Process of retention of Kromasil® 100-5-Sil particles in the sorbent cell of the USC over time: **a** 0 min; **b** 2 min; **c** 5 min

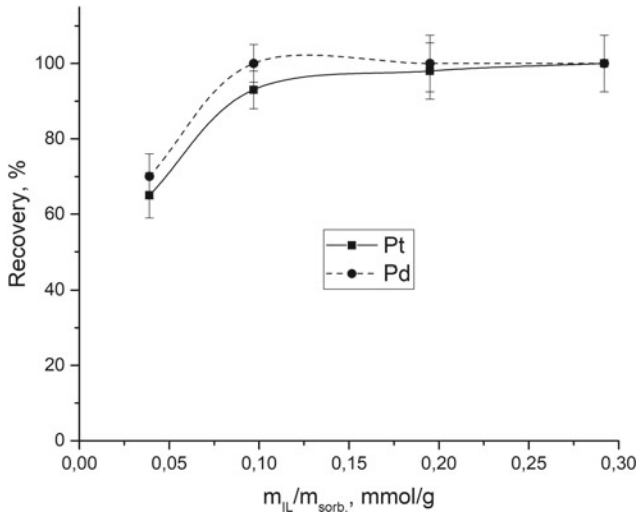

Fig. 3 The effect of ionic liquid content on Pt(IV) and Pd(II) recovery (1 M HCl, V = 5 mL, m_{sorb} = 20 mg, phase contact time 30 min)

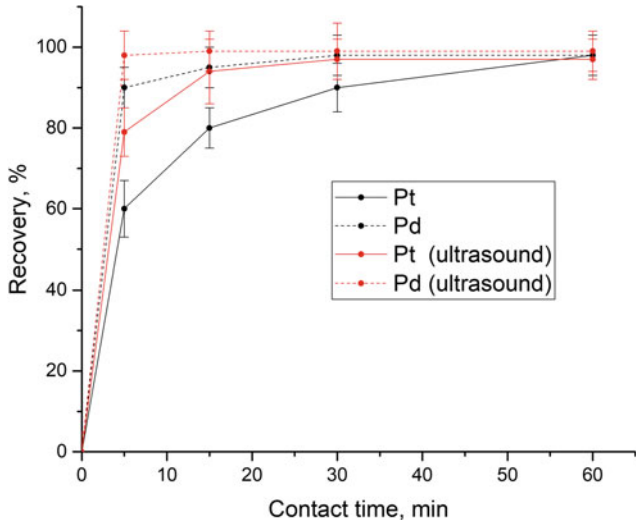

Fig. 4 The effect of phase contact time on Pt(IV) and Pd(II) recovery (1 M HCl, V = 5 mL, m_{sorb} = 20 mg, [IL] = 0.2 mmol/g)

a solid support is reasonable due to its hydrolytic stability in acidic media and non-swelling.

The sorption ability of Kromasil® 100-5-Sil modified with Cyphos®IL-101 towards Pt(IV) and Pd(II) ions was studied in the range of HCl concentration of 0.1–6 M. It was found that the sorbent is characterized by high chemical stability in the whole studied range of acidity; however, when HCl concentration is more than 3 M, the degree of platinum and palladium recovery slightly decreases. Probably, the metal extraction is realized by ion-exchange

mechanism and at a high acid concentration the competing influence of chloride ions is possible. This is consistent with the literature data on extraction of platinum metals by phosphonium ionic liquids [18, 19]. Thus, the HCl concentration of 0.1–1 M was chosen as the optimum acidity of the solution with the chloride ions content should not exceed 100 g/L.

To estimate the selectivity of the sorbent the solid-phase extraction of platinum and palladium ($n \cdot 10^{-5}$ g/L) was studied in the presence of Fe(III), Cu(II) and Ni(II) ($n \cdot 10^{-1}$–10^{-3} g/L) from 0.1 to 1 M HCl solutions. It was shown that under these conditions nonferrous metals completely remain in the aqueous phase, while platinum metals are quantitatively passed to the sorbent phase. This allows to use the sorbent for the selective recovery of platinum metals from solutions of complex composition.

3.3 Solid-Phase Extraction of Pt(IV) and Pd(II) in the USC

As it was shown above, ultrasound intensification of platinum metal recovery allows to improve kinetic characteristics of sorbent and to increase extraction efficiency. Under the USC conditions it is possible to carry out solid-phase extraction in a dynamic mode under the action of ultrasound.

The optimum flow rate and the ratio of the sorbent mass to the solution volume were determined. It was found that at a flow rate of 0.1–0.2 mL/min quantitative recovery of platinum and palladium from solutions with a volume of 2–50 mL is achieved with a sorbent mass of 20 mg; an increase in the solution flow rate to 1.0 mL/min leads to a decrease in the degree of metal recovery.

Table 1 demonstrates the data on recovery of Pt(IV) and Pd(II) in the USC under optimum conditions, as well as the data on elution of extracted metal ions by various eluents. Elution of analytes is a highly important stage, especially for platinum group metals, for which it is usually difficult. As can be seen, the obtained sorbent ensures not only efficient recovery of targeted metals, but their almost quantitative elution with the use of 2 M HNO_3, 5% thiourea solution in 0.01 M HCl and 1 M $NaClO_4$ as eluents.

Based on the experimental data the method of solid-phase extraction of platinum and palladium in the USC from the model solutions combined with their subsequent instrumental determination was developed. Table 2 shows the results of the ICP-AES determination of platinum and palladium after preconcentration in the USC by the sorbent based on Kromasil® 100–5-Sil modified with Cyphos®IL-101 and elution by 2 M HNO_3.

Good agreement of the obtained results indicates the efficiency of the USC application for selective recovery and preconcentration of Pt(IV) and Pd(II) and their subsequent ICP-AES determination.

4 Conclusion

The features of the ultrasound suspension columns in sorption processes are discussed, the optimal parameters of sorbent cell and ultrasound field are selected. Recommendations on selection of sorbents for efficient retention and solid-phase extraction in the USC are given.

The sorbent based on Kromasil® 100-5-Sil and Cyphos®IL-101 is characterized by high sorption capacity and selectivity towards platinum and palladium ions in

Table 1 Solid-phase extraction and elution of Pt(IV) and Pd(II) in the USC (n = 4; P = 0.95)

Stage	Solution/Eluent	Recovery (%)	
		Pt	Pd
Solid-phase extraction	1 M HCl	98 ± 4	99 ± 3
Elution	2 M HNO_3	95 ± 5	97 ± 8
	5% Thiourea in 0.01 M HCl	93 ± 9	94 ± 8
	1 M $NaClO_4$	93 ± 10	75 ± 9

Table 2 ICP-AES determination of Pt(IV) and Pd(II) in model solution (n = 3, P = 0.95). Solid-phase extraction: μg/mL—Pt 0.2, Pd 0.2, Fe 250, Cu 300, Ni 300; 1 M HCl, V = 25 mL, m_{sorb} = 20 mg, [IL] = 0.2 mmol/g, F = 0.2 mL/min. Elution: 2 M HNO_3, V = 2 mL, F = 0.2 mL/min.

Metal	Spiked		Recovered	
	μg/mL	μg	μg/mL	μg
Pt	0.25	5	2.47 ± 0.25	4.95 ± 0.50
Pd	0.25	5	2.50 ± 0.22	5.01 ± 0.45

hydrochloric acid solutions. The possibility of preconcentration of platinum metals using the developed sorbent in the ultrasound suspension column and subsequent determination by the ICP-AES has been demonstrated.

Acknowledgements This work is conducted under the GEOKHI RAS state assignment.

References

1. Capote, F.P., Luque de Castro, M.D.: Analytical Applications of Ultrasound, 1st edn., p. 26. Elsevier Science (2006)
2. Dzhenloda, R.Kh., Petrov, D.G., Shkinev, V.M., Spivakov, B.Ya.: DNA recovery from environmental samples on suspension columns under a combined action of ultrasound and magnetic fields followed by polymerase chain reaction detection. Mendeleev Commun. **27**(3), 302–303 (2017)
3. Spivakov, B.Y., Shkinev, V.M., Danilova, T.V., Knyazkov, N.N., Kurochkin, V.E., Karandashev, V.K.: Suspension column for recovery and separation of substances using ultrasound-assisted retention of bead sorbents. Talanta **102**, 88–92 (2012)
4. Dzhenloda, R.K., Shkinev, V.M., Danilova, T.V., Temerdashev, Z.A., Karandashev, V.K., Spivakov, B.Y.: Suspension columns with grain sorbents retained in an ultrasonic field for separation and determination of rare-earth elements in wines. J. Anal. Chem. **70**(12), 1456–1462 (2015)
5. Mudd, G., Jowitt, S., Werner, T.: Global platinum group element resources, reserves and mining—A critical assessment. Sci. Total Environ. **622–623**, 614–625 (2018)
6. Rao, C.R.M., Reddi, G.S.: Platinum group metals (PGM); occurrence, use and recent trends in their determination. Trends Anal. Chem. **19**(9), 565–586 (2000)
7. Komendova, R.: Recent advances in the preconcentration and determination of platinum group metals in environmental and biological samples. Trends Anal. Chem. **122**, 115708 (2020)
8. Grebneva-Balyuk, O.N., Kubrakova, I.V.: Determination of platinum group elements in geological samples by inductively coupled plasma mass spectrometry: possibilities and limitations. J. Anal. Chem. **75**, 275–285 (2020)
9. Myasoedova, G.V., Mokhodoeva, O.B., Kubrakova, I.V.: Trends in sorption preconcentration combined with noble metal determination. Anal. Sci. **23**(9), 1031–1039 (2007)
10. Mokhodoeva, O.B., Myasoedova, G.V., Kubrakova, I.V., Nikulin, A.V., Artyushin, O.I., Odinets, I.L.: New solid extractants for preconcentrating noble metals. J. Anal. Chem. **65**(1), 12–16 (2010)
11. Myasoedova, G.V., Molochnikova, N.P., Mokhodoeva, O.B., Myasoedov, B.F.: Application of ionic liquids for solid-phase extraction of trace elements. Anal. Sci. **24**(10), 1351–1353 (2008)
12. Mokhodoeva, O.B., Maksimova, V.V., Dzhenloda, R.K., Shkinev, V.M.: Magnetic nanoparticles modified by ionic liquids in environmental analysis. J. Anal. Chem. **76**(6), 675–684 (2021)
13. Mokhodoeva, O., Shkinev, V., Maksimova, V., Dzhenloda, R., Spivakov, B.: Recovery of platinum group metals using magnetic nanoparticles modified with ionic liquids. Sep. Purif. Technol. **248**, 117049 (2020)
14. Mokhodoeva, O.B., Nikulin, A.V., Myasoedova, G.V., Kubrakova, I.V.: A new combined ETAAS method for the determination of platinum, palladium, and gold traces in natural samples. J. Anal. Chem. **67**(6), 531–536 (2012)
15. Knyazkov, N.N., Makarova, E.D., Morev, S.A., Spivakov, B.Ya., Shkinev, V.M.: Methodological basis of the standing wave ultrasonic field application for the flow fractionation of the particles of different nature (in Russian). Sci. Instrum. **16**(2), 23–34 (2006).
16. Dzhenloda, R.Kh., Knyazkov, N.N., Makarova, E.D., Sharfarets, B.P., Shkinev, V.M.: Some grounding in theory of particle trapping in ultrasonic suspension column (in Russian). Sci. Instrum. **23**, 44–55 (2013)
17. Konshina, D.N., Konshin, V.V., Dzhenloda, R.H., Shkinev, V.M., Danilova, T.V., Karandashev, V.K.: Synthesis and characterization of silica covalently immobilized with azohydrazon (formazan) groups for recovery of noble metals (in Russian). Sorption Chromatogr. Process. **14**(3), 485–493 (2014)
18. Rzelewska-Piekut, M., Regel-Rosocka, M.: Separation of Pt(IV), Pd(II), Ru(III) and Rh(III) from model chloride solutions by liquid-liquid extraction with phosphonium ionic liquids. Sep. Purif. Technol. **212**, 791–801 (2019)
19. Papaiconomou, N., Svecova, L., Bonnaud, C., Cathelin, L., Billard, I.: Chainet E: Possibilities and limitations in separating Pt(IV) from Pd(II) combining imidazolium and phosphonium ionic liquids. Dalton Trans. **44**(46), 20131–20138 (2015)

Sorption-Spectrometric Determination of Organic Acids on the Solid-Phase of Fibrous Filled Sorbents

V. P. Dedkova, O. P. Shvoeva, and A. A. Grechnikov

1 Introduction

The sorption-spectrometric method of analysis based on concentration, complexation of metal ions with organic ligands and subsequent registration of the analytical signal directly from the solid phase belongs to the most effective and universal methods of analysis. Compared to conventional spectrophotometry, solid-phase spectrometry can significantly increase the sensitivity, selectivity of determination, as well as reduce the analysis time and reduce the possible losses in the process of sample preparation [1, 2].

Various materials such as paper, silica, foamed polyurethanes, sorbents based on polystyrene and polyvinyl chloride, ion exchange resins, etc. are used as solid phases in sorption spectrometry [3, 4]. Modified ion-exchange materials prepared from ion-exchangers by sorption of organic analytical reagents occupy an important place among various sorbents [2, 5, 6]. They possess high sorption capacity, good kinetic characteristics (high rates of sorption and filtration), mechanical and chemical stability. This allows their application in conditions of high acidity or basicity of medium as well as in the presence of oxidizing and reducing agents that are used to reduce the influence of interfering components. A convenient and inexpensive carrier of ion-exchange materials is porous polyacrylonitrile fiber (**PANF**). Such a fiber allows varying the filler, which can be used cation- and anion-exchangers with different ion-exchange groups. The use of solid-phase fibrous filled materials allows for simultaneous increase in sensitivity and selectivity of the sorption-spectroscopic determination technique. PANF fibrous materials filled with ion-exchangers have proved to be good for determination of metal cations by color reactions with organic reagents on a solid phase [7, 8]. Determination can be performed in various ways, including sorption of the complex obtained in solution, sorption of the metal ion with subsequent reaction with an organic reagent, sorption of the organic reagent with subsequent reaction with metal cation on a solid phase.

In this work the capabilities of fibrous materials filled with ion exchanger for sorption-spectrometric determination of salicylic, malonic, ascorbic acids in the form of their complexes with metal cations are investigated. Wide application of these organic acids in various branches causes urgency of development of simple express methods of their determination for use in ecological monitoring, in medical practice, in a pharmaceutical industry, for the analysis of foodstuffs and other areas.

2 Experimental

Polyacrylonitrile fiber filled with strongly basic fine-dispersed anion-exchanger AB-17 (Research Institute of Synthetic Fiber, Russia) was used as solid-phase sorbent. The degree of filling was 50 wt.%. PANF—AB-17 sorbents in the form of disks 20 mm in diameter and ~10 mg mass of dry disk were used in the swollen state. For this purpose, they were kept in distilled water during one day. After swelling, the sorbent was successively washed with 1 M HCl and water, and then stored in distilled water.

All reagents used in the work were of chemically pure or analytical grade. The stock 0.1 M solution of salicylic acid was prepared by dissolving 0.138 g of the analyte in 10 ml of ethanol. Working solutions were prepared by dilution of the stock solution with distilled water. A 0.1 M solution of $FeCl_3$ in 0.05 M HCl was prepared by dissolving 2.70 g of $FeCl_3 \cdot 6H_2O$ in 100 ml of 0.05 M HCl. The necessary values of acidity were set by adding 0.01–1 M solutions of HCl and NaOH.

The stock solution of titanium(IV) (1 mg/ml) was prepared by diluting 0.23 ml of $TiCl_4$ preparation (density

V. P. Dedkova (✉) · O. P. Shvoeva · A. A. Grechnikov
Vernadsky Institute of Geochemistry and Analytical Chemistry, Russian Academy of Sciences, 19 Kosygin St., Moscow, 119991, Russia
e-mail: Dedva@yandex.ru

V. P. Kolotov and N. S. Bezaeva (eds.), *Advances in Geochemistry, Analytical Chemistry, and Planetary Sciences*,
https://doi.org/10.1007/978-3-031-09883-3_33

1.73 g/ml) to 100 ml of 6 M HCl. Working solutions of titanium (IV) were prepared by diluting the stock solution in 0.1 M HCl. The working solutions of malonic acid were prepared by dissolving the corresponding amount of the analyte in water. 0.05% solution of phenylfluorone was obtained by dissolving 5 mg of the reagent in 10 ml of ethanol under heating in a boiling water bath.

Vanadium working solutions were prepared by dissolving $NaVO_3 \cdot H_2O$ in water. A solution of 8-hydroxyquinoline-5-sulfonic acid (0.1%) was prepared by dissolving 50 mg of the reagent in 50 ml of water, adding 0.2 ml of 1 M NaOH solution, and heating in a water bath; after cooling to room temperature, it was diluted with water. Ascorbic acid solutions were prepared by dissolving the corresponding amount of the analyte in water. To produce the necessary acidity of the solutions, 0.1 and 0.01 M solutions of HCl and NaOH were used.

Diffuse reflectance parameters were recorded using a Pulsar spectrocolorimeter (Khimavtomatika, Uzbekistan). The difference between the diffuse reflectance coefficients of discs ($\Delta R = R_0 - R_{Me}$) after the sorption of an organic acid and its reaction with ions sorbed from control and analyzed solutions was taken as an analytical signal. The control solution contained all components of the reaction except for the component whose action was studied; it was passed through all operations as the test solution. The acidity of solutions was controlled with a glass electrode (potentiometer pH-673 M). The influence of various factors on sorption and analytical signals were studied at room temperature in static and dynamic modes. In static mode 20–200 ml of solutions containing various amounts of the compound being determined were stirred with PANF—AB-17 disks for 15 min. The disks were removed, the reaction was carried out and the diffuse reflectance coefficient was measured. In dynamic mode, PANF—AB-17 disks were placed in flow cells and solutions were pumped through cells with a peristaltic pump PP-2-15 (Zalimp, Poland) at a rate of 5 ml/min followed by measurement of the analytical signal.

3 Results and Discussion

3.1 Determination of Salicylic Acid

Salicylic acid forms coloured complexes when interacting with Fe(III) ions, which was the basis for developing the technique of its sorption-spectrometric determination.

The influence of pH during salicylic acid sorption on PANF—AB-17 is illustrated in Fig. 1. It can be seen that the analytical signal increases when the pH increases from 1 to 3, and in the pH range of 3–9 the increase in the analytical signal is insignificant. For sorption of salicylic acid a pH value of 3.0 + 0.1 was chosen.

Figure 2 shows diffuse reflectance spectra obtained by sorption on PANV - AB-17 disks from 20 ml of control solution (1) and $2.5.10^{-5}$ M salicylic acid solution (2). The maximum analytical signal is recorded at a wavelength of 600 nm in 1–2 min after the application of $FeCl_3$ solution on the disk.

The effect of salicylic acid sorption mode on the analytical signals of complexes with iron ions was studied by contacting 20–200 ml solutions containing 70 μg of salicylic acid with PANF—AB-17 disks under static and dynamic conditions. The results are presented in Fig. 3. Increase of solution volume from 20 to 200 ml practically does not influence on analytical signal change in dynamic variant of sorption, but leads to 2, 2 times decrease of signal at contact of solutions with PANF—AB-17 disks for 15 min. When developing the technique for determination of salicylic acid sorption was performed in the dynamic variant by pumping 100 ml of solution through the PANF—AB-17 disk at a flow rate of 5 ml/min.

Dependences of analytical signals on salicylic acid concentration were studied in static (volume 20 ml) and dynamic (volume 100 ml) variants of sorption from solutions with pH3. The calibration graphs are linear in the concentration ranges of salicylic acid (0.25–2) $\times$ 10^{-5} M and (0.5–4) $\times$ 10^{-6} M and are described, respectively, for the static and dynamic sorption variants by the following equations:

$$C(M) = (\Delta R_{600} - 0.07)/0.19 \quad (1)$$

$$C(M) = (\Delta R_{600} - 0.06)/0.12 \quad (2)$$

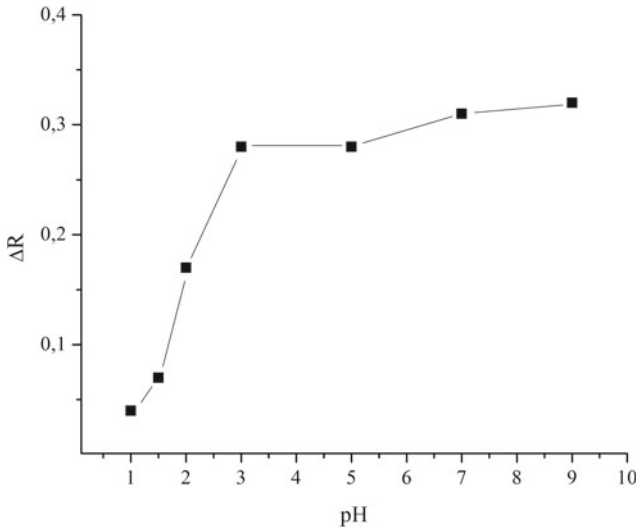

Fig. 1 Dependences of analytical signals of Fe(III) complexes with salicylic acid on pH of solutions at sorption on PANF—AB-17. $C_{salicylic\ acid}$ = 1.5•10^{-5} M; C_{Fe} = 3•10^{-2} M

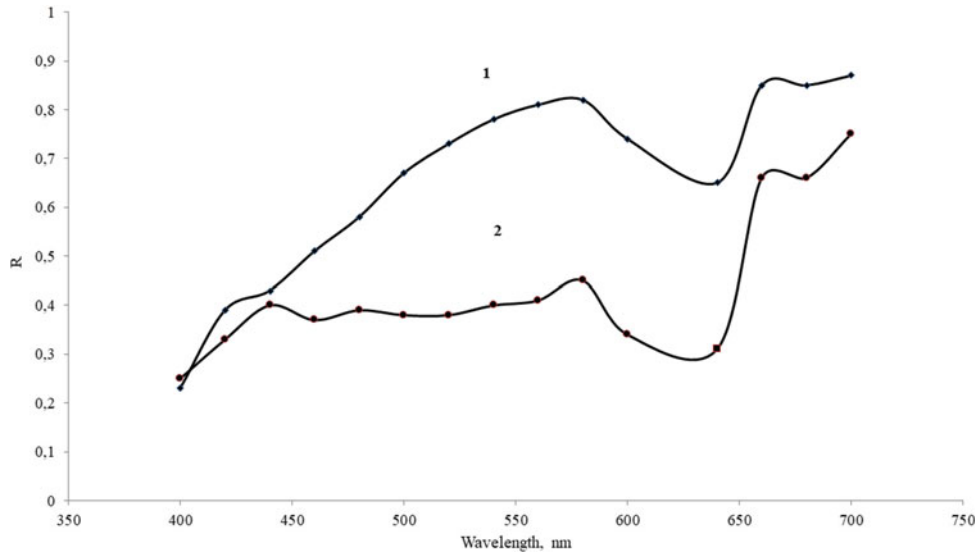

Fig. 2 Diffuse reflectance spectra of PANF—AB-17 disks after contact with control solution (1) and 2.5×10^{-5} M salicylic acid solution (2) and subsequent treatment with 0.05 ml of 0.1 M $FeCl_3$ solution in 0.05 M HCl

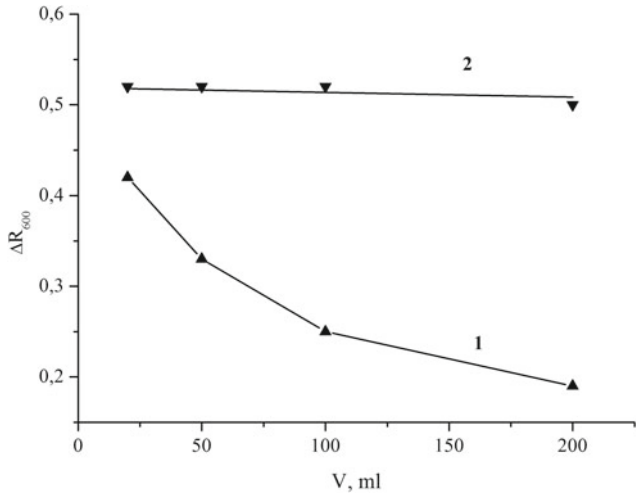

Fig. 3 Dependence of analytical signals of Fe(III) complexes with salicylic acid on analyzed solution volume: (1)—stirring of solutions during 15 min, (2)—pumping solutions through the disks at a rate of 5 ml/min

where $\Delta R_{600} = R_0 - R_1$ after sorption of salicylic acid from control and analyzed solutions and interaction with Fe(III).

The results obtained were used to develop a procedure for analyzing various waters for salicylic acid content. The procedure is as follows. The analyzed sample is placed in a beaker and pH3 is produced using 1 M and 0.1 M HCl. PANF—AB-17 disc swollen in distilled water is placed in flow cells and the analyzed solution is pumped at the rate of 5 ml/min. Disc is removed, the excess of liquid is removed with filter paper. Then the disc is placed on the bottom of beaker, 2 drops of 0.1 M $FeCl_3$ solution in 0.05 M HCl are added and after 1–2 min, the diffuse reflectance coefficients of the control disk and the analyzed disk are measured at 600 nm. The salicylic acid content is calculated by Formula (2). When using the test-method under visual observation, the disc colour is compared with the colour scale obtained similarly for 10, 20, 30, 40 and 50 μg salicylic acid. The coloration of the discs varies from pale lilac to purple.

The procedure was tested in the analysis of tap (Moscow) and well (Moscow region) water. Correctness of the results was evaluated by the "spike-recovery" method. The results are presented in Table 1. The relative standard deviation does not exceed 0.1. Analysis of 5–6 samples takes not more than 30 min.

3.2 Determination of Malonic Acid

The method of titanium determination based on sorption of malonate complexes of Ti(IV) and subsequent formation of

Table 1 Determination of salicylic acid in waters ($n = 3$, $P = 0.95$)

Water	Introduced (μg)	Found (μg)	Relative standard deviation
Tape (Moscow)	– 11.9 31.7	<2.0 15.0 + 3.1 30.6 + 1.4	 0.09 0.02
Well (Moscow region)	– 18.9 43.5	<2.0 21.8 + 3.0 43.1 + 1.8	 0.06 0.02

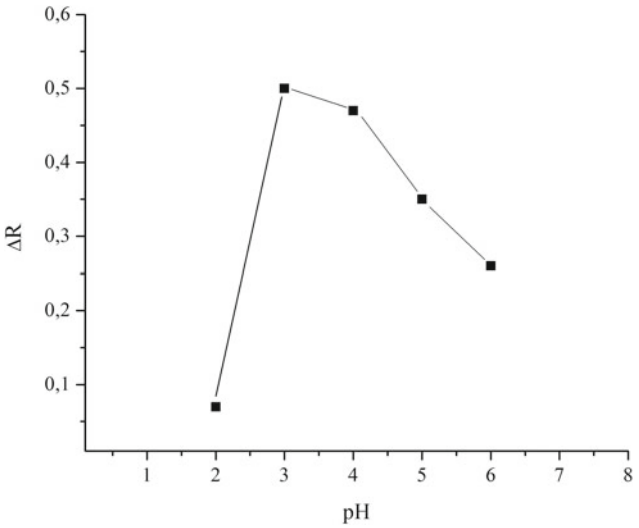

Fig. 4 Dependence of analytical signals of complexes Ti(IV) with malonic acid and phenylfluorane on pH of solutions at sorption on PANF-AB-17. $C_{malonic\ acid} = 0.2 \times 10^{-4}$ M; $C_{Ti} = 0.2 \times 10^{-5}$ M

coloured complexes of titanium with phenylfluoron on the solid phase of fibrous material PANF—AB-17 has been developed earlier [9]. In this paper the system Ti(IV)—malonic acid—(PANF—AB-17)—phenylfluoron has been studied for determination of malonic acid.

The influence of pH on the sorption of malonic titanium complexes on PANF—AB-17 was studied for the solutions containing 2–10 μg of Ti(IV) and 10–70 μg of malonic acid in 20 ml solution, in the pH range 2–6. The results obtained are shown in Fig. 4. It can be seen that the optimal pH value is 3. It was also found from diffuse reflectance spectra that the maximum analytical signal is achieved at a wavelength of 600 nm.

The dependence of analytical signals on the concentration of malonic acid was studied at the found optimum conditions of sorption of malonic titanium complexes on solid phase PANV—AB-17: solution volume 20 ml, pH 3, Ti concentration 0.25 μg/ml, time of solution stirring with disks 15 min, amount of 0.05% phenylfluoroic solution 4 drops. The calibration graph is linear in the concentration range of malonic acid 0.5–5.0 μg/ml and is described by the equation:

$$C(\mu g/ml) = (\Delta R_{600} - 0.04)/0.1 \quad (3)$$

The procedure of malonic acid determination in various waters is as follows. To 20 ml of the analyzed sample 0.25 ml of titanium solution with the concentration of 20 μg/ml is added, pH 3 is adjusted with 0.1 M NaOH solution, PANF—AB-17 is introduced and the disk is stirred for 15 min. The disk is taken out, blotted with filter paper, 4 drops of 0.05% phenylfluoroic solution is applied and after 3 min the diffuse reflectance coefficients of the control disk and the analyzed disk are measured at 600 nm. The malonic acid concentration is calculated by Formula (3).

3.3 Determination of Ascorbic Acid

To determine ascorbic acid, the known system V(V)—8-hydroxyquinoline-5-sulfonic acid—HCl was studied [10]. When vanadium(V) interacts with 8-hydroxyquinoline-5-sulfonic acid sorbed on PANF-AV-17, a yellowish-green complex compound is formed, which changes the color to almost black with a maximum signal at wavelength 640 nm after treatment with HCl solution. Upon further application of ascorbic acid to the disk with the formed complex compound, the coloration changes from black to green [11]. This phenomenon was used to develop a technique for sorption-spectrometric determination of ascorbic acid.

Study of conditions of vanadium complex formation with 8-hydroxyquinoline-5-sulfonic acid sorbed on PANF—AB-17 showed that the optimum pH value is 5.0 + 0.5. The maximum analytical signal calculated from the difference of diffuse reflectance coefficients of complex V(V)—8-hydroxyquinoline-5-sulfonic acid—HCl before and after exposure to ascorbic acid is observed at a wavelength of 500 nm. It was found that the dependence of the analytical signal on ascorbic acid concentration is linear in the range of 0.1–1 mg/ml, and the calibration graph is described by the equation:

$$C(mg/ml) = (\Delta R_{500} - 0.03)/0.32 \quad (4)$$

The procedure of ascorbic acid determination is as follows. Two drops of a 0.1% solution of 8-hydroxyquinoline-5-sulfonic acid in water, 1 drop of a 0.01 M $NaVO_3$ solution in water, 2 drops of 0.1 M HCl and 2 drops of the test solution are applied on PANF-AB-17 discs successively at an interval of about 30 s. The diffuse reflectance coefficients of the control disk (and the analyzed disk are measured at 500 nm and the concentration of ascorbic acid in the analyzed solution is calculated according to the Formula (4). To determine ascorbic acid using the test-method the coloring of discs is compared with a color scale containing 2, 5, 10 and 30 μg of ascorbic acid.

Acknowledgements This work is conducted under the GEOKHI RAS state assignment.

References

1. Zolotov, Yu.A., Tsizin, G.I., Dmitrienko, S.G., Morosanova, E.I.: Adsorption preconcentration of trace components from solutions: application in inorganic analysis. Nauka, Moscow (2007).(in Russian)
2. Brykina, G.D., Marchenko, D.Y., Shpigun, O.A.: Solid-phase spectrophotometry. J. Anal. Chem. **50**(5), 440–446 (1995)
3. Savvin, S.B., Dedkova, V.P., Shvoeva, O.P.: Sorption-spectroscopic and test methods for the determination of metal

ions on the solid-phase of ion-exchange materials. Russ. Chem. Rev. **69**(3), 187–200 (2000)
4. Tsysin, G.I.: Methods of the preconcentration of trace components: development in Russia (1991–2010). J. Anal. Chem. **66**(11), 1020–1028 (2011)
5. Zaporozhets, O.A., Gaver, O.M., Sukhan, V.V.: Immobilisation of analytical reagents on support surfaces. Russ. Chem. Rev. **66**(7), 637–646 (1997)
6. Matsuoka, S., Yoshimura, K.: Recent trends in solid phase spectrometry: 2003–2009. Rev. Anal. Chim. Acta. **664**(1), 1–18 (2010)
7. Shvoeva, O.P., Dedkova, V.P., Savvin, S.B.: Sorption-spectroscopy and test determination of uranium (VI) and iron (III) from a single sample on the solid phase of fiber materials filled with an AB-17 ion exchanger. J. Anal. Chem. **68**(10), 880–884 (2013)
8. Dedkova, V.P., Shvoeva, O.P., Grechnikov, A.A.: Organic reagents and double-layer supports in the sequential sorption-spectroscopic determination of Ti(IV), V(V), Mo(VI) and Ni(II) from one sample. J. Anal. Chem. **74**(2), 108–113 (2019)
9. Dedkova, V.P., Shvoeva, O.P., Grechnikov, A.A.: Complexation of titanium(IV) malonates with phenylflyorone and 2,7-dichlorochromotropic acid on a solid phase of PANV - AV-17. J. Anal. Chem. **70**(12), 1463–1467 (2015)
10. Korenman, I.M.: Organic reagents in inorganic analysis. Khimiya, Moscow (1980).(in Russian)
11. Dedkova, V.P., Shvoeva, O.P., Savvin, S.B.: Determination of vanadium (V) and chromium (VI) in a single sample on a fibrous ion exchanger disk. J. Anal. Chem. **64**(4), 350–353 (2009)

Extraction Method of Crude Oil Sample Preparation for Determination of Mobile Forms of Trace Elements

T. A. Maryutina, E. Yu. Savonina, O. N. Katasonova, and B. Y. Spivakov

1 Introduction

Metals in crude oil are present in a variety of forms (from strong coordinated organic compounds to water-soluble salts) [1]. Information on the forms of metals in oil is important both for selecting methods of oil processing and in studying its morphology.

Practically there are no works on research of forms of metal presence in samples of crude oils of various fields due to methodological difficulties. The majority of the published works are devoted to studying porphyrin complexes of vanadium and nickel in connection with their high concentration in oil, strategic value of the metals and their negative influence on activity of expensive processing catalysts. The information on the forms of other metals present in oil is only speculative.

Any of modern methods of determination of the content of elements in oil demands use of a preliminary stage of sample preparation [2]. Among methods of sample preparation of oil raw materials (oils and oil products), extraction takes a separate place due to the possibility of simultaneous solution of at least two tasks: extraction of an analyte into a simpler matrix for analysis and obtaining a solution of target components for further use. For realization of the extraction process of components extraction from oil raw materials under laboratory conditions, there are many variants available: from the classical batch extraction in a test tube to the hardware version, for example in a centrifugal extractor. A separate place among extraction methods occupies supercritical fluid extraction, allowing to allocate elements in one of products (asphalt) of process.

T. A. Maryutina (✉) · E. Yu.Savonina · O. N. Katasonova · B. Y. Spivakov
Vernadsky Institute of Geochemistry and Analytical Chemistry, Russian Academy of Sciences, 19 Kosygin St, Moscow, 119991, Russia
e-mail: t_maryutina@mail.ru

An integrated approach for determining the trace amounts of elements, namely rare and rare-earth elements (RE and REE) in oil and oil products samples was developed in 2016, in the Concentration Laboratory of Vernadsky Institute [3, 4]. Estimation of the content of a number of RE and REE in oils is difficult because of their low concentrations, the determination of which requires the use of highly sensitive instrumental methods of analysis or methods of preliminary sample preparation, allowing to concentrate REE [4].

In the present work, features of application of extraction concentration of trace quantities of mobile forms of RE and REE from oil in a rotating coiled column (RCC) with the use of nitric acid as a stationary phase (the priority matrix for the subsequent ICP-MS determination of isolated elements) are described. A photo of a planetary centrifuge equipped with a specially designed RCC is shown in Fig. 1. The RCC is a tube (Teflon capillary) wound as a single- or multilayer spiral on a rigid or flexible core, which rotates around its axis and simultaneously around the central axis of the device by analogy of motion of the Moon around the Earth [4]. The fixed phase (nitric acid solution in our case) is held in RCC due to the field of mass forces arising during planetary rotation of the column, while the analyzed sample of oil or oil product (mobile phase) is pumped through RCC by a peristaltic pump. When retaining certain volume (usually about 50% of total column volume), which is equal to 10 ml of mineral acid solution in RCC and pumping significant volumes of oil sample (100 ml and more), we can concentrate elements from oil into water phase by 10 and more times (depending on a ratio of retained acid volume to pumped oil volume). Extraction concentration expands the possibilities of oil analysis to determine the content of rare and rare-earth elements in them.

The present work shows the possibility of extraction concentration of mobile forms of RE, REE, and PGM from crude oil samples of Timan-Pechora basin in RCC for the subsequent analysis of the extracts obtained by ICP-MS.

V. P. Kolotov and N. S. Bezaeva (eds.), *Advances in Geochemistry, Analytical Chemistry, and Planetary Sciences*,
https://doi.org/10.1007/978-3-031-09883-3_34

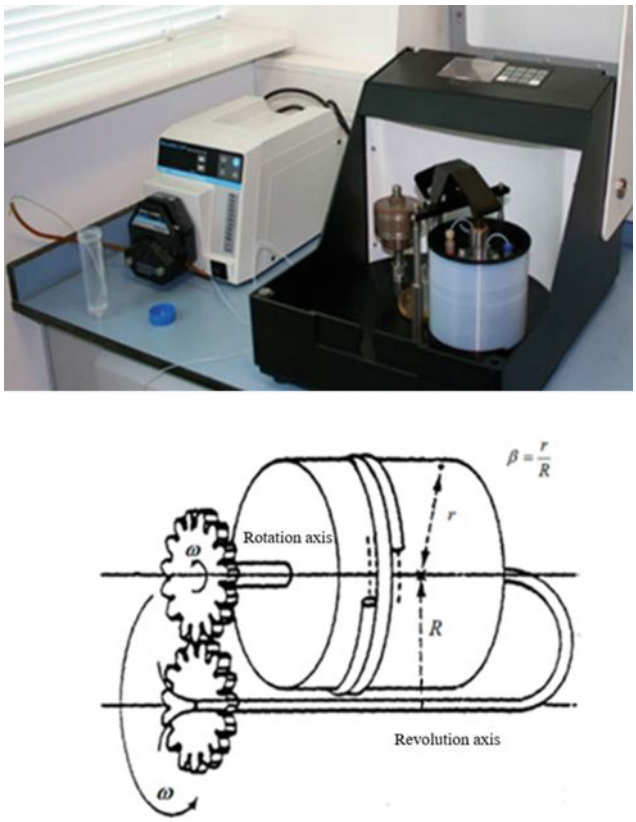

Fig. 1 The photo and diagram of the planetary centrifuge with RCC

The content of mobile forms of metals in various fields of the Timan-Pechora oil and gas bearing province was estimated.

2 Experimental Part

Samples of six different oils, selected from the fields of Timan-Pechora basin, differing in the conditions of occurrence and in physical and chemical parameters were studied. The characteristics of oils are given in Table 1.

Concentration of REE was carried out in a planetary centrifuge equipped with a rotating coiled column (Institute of Analytical Instrumentation, Russian Academy of Sciences) in the flow mode. The volume of extractant was 10 ml, the volume of oil was 100 ml. The parameters of RCC operation are presented in Table 2.

0.5 M aqueous solution of nitric acid (*A.C.S. reagent*, Himmed, Russia) was used as an extractant (stationary phase). Toluene (*A.C.S. reagent*, Component-reactive, Russia) was used to dilute oils in order to achieve the necessary values of density and viscosity, allowing to retain the extractant in RCC and conduct extraction in the system 0.5 M HNO_3—oil, [5]. Standard solutions of trace elements (1000 mg/L) in 2% HNO_3 (High Purity Standarts, USA) were used for ICP-MS analysis.

An Agilent 7900 spectrometer (Agilent Technologies) was used to determine REE by inductively coupled plasma mass spectrometry. The parameters of the spectrometer operation were selected earlier [5].

3 Results and Discussion

All investigated oil samples are selected from a number of fields of Timan-Pechora oil-and-gas province, differing by tectonic zoning, time of formation, depth of occurrence of productive strata. Oil samples according to their classification accepted at XII International Petroleum Congress in Houston (USA) in 1987 г. [6] belong to medium-viscous and extra-viscous, their density values vary in a range from 871 to 947 kg/m^3.

The Timan-Pechora oil and gas bearing province is characterized by a variety of structural and tectonic elements. In addition to vanadium, nickel, chromium, cobalt, copper, zinc, and lead, the oils of the Timan-Pechora basin are enriched with selenium, strontium, rhenium, zirconium, titanium, uranium, and REE, however, this distribution is uneven and depends on geochemical and evolutionary features of oil formation.

Table 1 General description of the studied oils

Oil and gas bearing province	The field	Tectonic element of the area [8, 13, 14]	Age of the breed [8, 13, 14]	Dynamic viscosity, CPS	Density (kg/cm^3)
Timan-Pechora	Varandey	Varandey-Adzvinsky structural zone	MZ_ T2, T1; Pz_P1	35,3	905
	West Tebuk	Izhma-Pechora Depression	Pz_D3	8,4	871
	Laboganskoe	Val Sorokina	MZ_T1; Pz_P2, P1, C1	328	947
	Tobojskoye	Varandey-Adzvinsky structural zone	Pz_C1t, D3f	239,2	913
	North Saremboy	Varandey-Adzvinsky structural zone	Pz_D1l	68,7	884
	Yaregskoe	Izhma-Pechora Depression	Pz_D3, D2	2750	944

Table 1 to the article by Maryutina T. A., Savonina E. Yu., Katasonova O.N. Extraction method of crude oil samples preparation for determination of mobile forms of microelements

Table 2 Design and working parameters of planetary centrifuge

Column volume (V_C, cm^3)	Retained volume of stationary phase (V_S, cm^3)	Column rotation rate ω (r/min)	Ratio of column rotation and revolution radius, β = r/R	Rate of passing the mobile phase F (ml/min)	Internal column diameter d (mm)
20	10	600	0.65	0.5–1	2

Table 2 to the article by Maryutina T. A., Savonina E. Yu., Katasonova O. N. Extraction method of crude oil samples preparation for determination of mobile forms of microelements

The contents of the overwhelming majority of RE and REE were below limits of detection (LD). In the use of classical sample preparation—acid microwave decomposition of samples of oil with the subsequent ICP-MS analysis. In spite of the fact that only water- and acid-soluble forms of elements are concentrated in 0.5–1 M aqueous solutions of nitric acid in RCC, this approach is simple in execution and gives an opportunity to conduct ICP-MS determination of RE and REE for preliminary evaluation of their presence in oils as well as mobile forms of other elements.

Tables 3 and 5 show the results of determination of REE and rare metals in samples of crude oils after their concentration in RCC. In samples of investigated samples, except for oil of Yaregskoye field, concentration of mobile forms of REE does not exceed 0.31 μg/kg and as a whole is from 0.01 to 0.1% of the total contents of these elements in asphaltenes [7, 8]. Such low values confirm once more the assumption that REE are in the viscous oil as complexes with complex heterocyclic and aromatic ligands. Especially stable are the compounds in which REE interact with organic substances via oxygen [8]. However, the content of mobile forms of REE in the oil of the Yaregskoye field differs significantly from the generally accepted standards. Based on the ratio of the total REE concentration in the tarry-asphaltene fraction (290 μg/kg) [7] and crude oil, one can suppose that the oil of the Yaregskoye field is also unique in the presence of more than 20% of REE in the mobile form. This anomaly is most likely associated with the presence of oil-titanium ore located above the productive strata of the Yaregskoye field, which is enriched with uranium (50% of Russian deposits) [8]. This assumption confirms the increased content of mobile forms not only for REE, but also for a number of rare metals, which are satellites of minerals of ore (Zr, Nb, Ti, Hf, Tl, Ga) and also uranium in oil Yaregskoe field in comparison with other fields of Timan-Pechora basin. The asphaltenes which are more rich in these elements [7, 9].

The specialization of oils in relation to platinum metals is formed on the basis of Ru/Ir relations. The oils of Timan-Pechora basin refer to oils of mixed Ru-Ir type. The determination of platinum group of metals has also become possible due to concentration in RCC. Maximum degrees of extracting the mobile forms for ruthenium and iridium make 0.8 and 0.5%, respectively, and 6.7% for rhodium in the oils of the Varandey and Yaregskoye fields (Table 4). In asphaltenes, the average content of platinum metals is in times less in relation to REE and does not exceed 0.5–4 μg/kg for each element [10].

In spite of the fact that the oil of Labagan field is characterized by the highest concentrations of RE, REE, nonferrous metals, by mobile forms of "macrocomponents" it is comparable with other fields of oil-and-gas platform (Tables 3–5). As a rule such elements as vanadium, nickel, zinc, copper, chrome, cobalt are in oil in the form of porphyrin complexes, metals content in mobile form was less than 1% for all investigated oil samples [11]. The oil of the Labagan field is significantly inferior to the oils of the other three fields of the Varandey-Adzvinsky structural zone by the content of mobile forms of alkali and alkaline earth metals, but is enriched with rhenium, hafnium, zirconium and uranium. Formation water is the source of alkali and alkaline earth metals. They are represented as salts of inorganic acids, phenolates, thiophenolates is particularly rich in alkali and alkaline earth metals [11]. The oil of the Varandey field is located directly on the shore of the Barents Sea.

There is an increased content of mobile forms of zinc, titanium, selenium in the oils of the Varandey and North Saremboy fields, cadmium and chromium in the oils of the Varandey field (Table 5).

The low content of mobile forms of metals in oil (from 0.01 to 1%) confirms the assumptions of Gottich and coauthors [12] about their organoelement nature. According to the theory proposed by the authors of the works [8, 12], migration of elements from parental rocks was carried out by hydrothermal carbonic fluids mainly in the form of carbonyl compounds. These fluids were also not only media for synthesis but also excellent solvent for organic matters of any nature. In course of time after decomposition of carbonyl compounds the main part of metals accumulated in stable organometallic complexes.

Thus, extraction concentration with the use of RCC provides an opportunity to obtain information about the content of mobile forms of RE, REE and platinum group metals in oils. In addition, RCC allows the use of a wide range of two-phase systems, which will expand the information on the forms of the elements in the oil.

Table 3 Results of mobile forms of REE determination in crude oils (ng/kg)

The field	La	Ce	Pr	Nd	Sm	Eu	Gd	Tb	Dy	Ho	Er	Tm	Yb	Lu	∑Ln
Varandey	30.1	60.0	7.05	20.0	10.1	0.03	7.01	1.12	6.14	2.04	7.11	1.05	8.22	2.14	162
West Tebuk	0.32	0.51	0.05	0.34	0.31	0.04	0.06	0.04	0.13	0.01	0.61	0.04	0.33	0.50	3.29
Laboganskoe	50.3	60.6	22.2	91.2	20.4	6.21	21.1	3.43	10.4	3.15	10.8	1.43	3.45	0.74	305
Tobojskoye	6.05	10.1	1.11	4.07	2.32	0.36	0.08	1.01	0.24	0.15	1.14	0.05	0.33	0.71	27.7
North Saremboy	7.12	10.2	2.24	5.05	1.07	0.23	0.08	1.41	0.52	0.23	2.12	0.04	0.41	0.22	30.9
Yaregskoe*	4.21	14.9	2.47	13.2	3.13	0.81	5.42	1.10	7.41	1.72	5.30	0.73	3.71	0.53	64.6

*Concentration in μg/kg

Table 3 to the article by Maryutina T.A., Savonina E.Yu., Katasonova O.N. Extraction method of crude oil samples preparation for determination of mobile forms of microelements

Table 4 Results of mobile forms of precious and disseminated metals determination in crude oils

The field	Precious metals (ng/kg)					Disseminated metals							
						µg/kg				ng/kg			
	Ru	Rh	Ag	Ir	Pt	Ga	Se	Rb	Cd	Te	Re	Hf	Tl
Varandey	9.33	29.5	8.31	0.66	0.33	0.09	1.16	3.03	2.52	2.19	15.2	2.19	11.5
West Tebuk	0.09	0.13	1.15	0.06	0.13	n.d	0.64	0.01	0.002	0.51	2.05	0.38	1.95
Laboganskoe	0.12	0.18	6.23	0.09	0.18	0.03	0.34	0.03	0.08	0.71	27.4	2.85	11.2
Tobojskoye	0.12	1.81	1.48	0.08	0.16	0.02	0.91	0.10	0.01	0.96	3.15	0.49	26.8
North Saremboy	2.84	4.43	3.19	0.27	0.13	0.01	5.76	1.68	0.06	0.99	2.41	0.89	0.44
Yaregskoe	1.53	4.73	27.8	4.87	1.39	0.41	10.4	1.74	0.08	3.61	4.13	110	306

Table 4 to the article by Maryutina T.A., Savonina E.Yu., Katasonova O.N. Extraction method of crude oil samples preparation for determination of mobile forms of microelements

Table 5 Results of mobile forms of rare, non-ferrous metals and other elements determination in crude oils

The field	Rare metals						Non-ferrous metals and other elements									
	ng/kg				µg/kg		ng/kg		µg/kg							
	Be	Cs	Zr	Nb	Li	Sr	U	Sb	Ti	V	Cr	Co	Ni	Zn	Pb	Cu
Varandey	15.3	328	9.24	16.3	43.8	963	9.14	109	0.77	10.9	29.5	0.73	8.02	274	2.67	11.1
West Tebuk	0.51	1.28	8.15	3.15	0.13	0.64	0.42	19.2	0.06	3.25	0.28	11.1	0.99	4.63	0.51	0.65
Laboganskoe	1.62	3.71	64.1	12.1	0.21	2.67	41.4	9.21	0.23	7.46	0.71	0.69	16.2	89.3	5.32	4.08
Tobojskoye	1.14	26.4	10.4	3.32	0.89	26.4	2.12	4.29	0.13	5.48	0.89	10.5	4.77	33.0	1.63	1.47
North Saremboy	1.34	248	12.2	3.10	17.7	173	9.30	22.2	0.97	0.08	1.41	0.04	0.59	363	1.79	15.5
Yaregskoe*	1.36	1.18	3.48	0.03	1.77	89.0	1.02	1.42	16.1	51.4	7.74	10.7	16.0	41.7	17.4	32.7

*Concentration in µg/kg

Table 5 to the article by Maryutina T.A., Savonina E.Yu., Katasonova O.N. Extraction method of oil samples preparation for determination of mobile forms of microelements

4 Conclusions

The results obtained show the possibility of extraction concentration of RE, REE and platinum group metals from crude oils in RCC to assess the presence of mobile forms of elements in oils. Abnormally high content of mobile forms of REE, as well as uranium, zirconium, niobium, titanium, thallium, hafnium, gallium in the oil of Yaregskoe field confirms that their source are minerals of oil-titanium ore. The low content of mobile forms of metals in oils of other fields of the Timan-Pechora basin is consistent with the theory of their occurrence in the form of strong organoelement compounds.

Acknowledgements This work is conducted under the GEOKHI RAS state assignment.

References

1. Maryutina, T.A., Timerbaev, A.R.: Metal speciation analysis of petroleum: Myth or reality? Analytica Chimica Acta **991**, 1–8 (2017)
2. Maryutina, T.A., Katasonova, O.N., Savonina, E.Y., Spivakov, B. Y.: Present-day methods for the determination of trace elements in oil and its fractions. J. Anal. Anal. Chem. **72**, 490–509 (2017)
3. Maryutina, T.A., Savonina, E.Y., Katasonova, O.N.: A combined method of sample preparation for the determination of the total element composition of oils. J. Anal. Chem. **71**(11), 1126–1130 (2016)
4. Soin, A., Maryutina, T., Musina, N., Soin, A.: New possibility for REE determination in oil. Int. J. Spectroscopy. 1 (2012)
5. Savonina, E.Y., Maryutina, T.A., Katasonova, O.N.: Determination of microelements in oil by combined sample preparation technique. Inorg. Mater. **53**(14), 1448–1453 (2017)
6. Sukhanov, A.A., Petrova, U.E.: Resource base of associated components of heavy oils of Russia. Oil Gas Geol. Theory Practice **3**, 1–11 (2008)

7. Vinokurov, S.F., Gottikh, R.P., Pisotsky, B.I.: Features of lanthanides distribution in resin-asphaltene fractions one of geochemical criteria of microelement sources in oil. Geochemistry **4**, 377–389 (2010)
8. Kalinina, A.A., Kalinin, E.P.: Geological and economic evaluation of integrated use of Yareg heavy oil. Izvestiya Komi Scientific Centre, Ural RAS Department T.3, No. 15, pp. 110–117 (2013)
9. Gottikh, R.P., Pisotsky, B.I., Malinina, S.S., Chernenkova, A.I.: The role of deep processes in the formation of hydrocarbon accumulations of the Timan-Pechora oil and gas province. Geol. Oil Gas **3**, 86–100 (2016)
10. Marakushev, A.A., Pisotsky, B.I., Paneyakh, N.A., Gottikh, R.P.: Geochemical specificity of oil and origin of its deposits. Rep. Acad. Sci. **398**(6), 795–799 (2004)
11. Batueva, I.Yu., Gaile, A.A., Pokonova, Yu.V.: Chemistry of crude oil. L. Chemistry 360 (1984)
12. Gottikh, R.P., Pisotsky, B.I., Mokhov, A.V.: Conditions of bitumen formation in the Timan-Pechora province (based on the results of geochemical studies). Rep. Acad. Sci. **456**(3), 326–331 (2014)
13. Klimenko, S.S., Anischenko, L.A.: Features of naphthidogenesis in the Timan-Pechersk oil-and-gas bearing basin. Izvestiya Komi Scientific Center, URO RAS, No. 2, pp. 61–69 (2020)
14. Stupakova, A.V.: Timan-Pechora basin. Structure and main stages of development. Georesources. Special issue, Chap.1, pp. 56–64 (2017)

Identification of Spectral and Non-spectral Interferences in Trace Elements Determination by Inductively Coupled Plasma Methods

O. N. Grebneva-Balyuk, O. A. Tyutyunnik, and I. V. Kubrakova

1 Introduction

The main trend in the development of analytical chemistry is the determination of lower and lower concentrations of analyte in samples of with complex matrix (geochronology, semiconductors, nanomaterials, forensic science, environmental, etc.).

The analyst should remember that the smaller the concentration of analyte, the greater the uncertainty of the final result. This is usually a result of the following factors: (1) large excess of other components in the sample; (2) use of multistep analytical procedures; (3) possibility of positive errors because of contamination of the object studied; (4) possibility of loss of analyte, for example as a result of adsorption or degradation; (5) interference caused by the presence of other components; (6) low precision of instrumental measurements compared with chemical measurements for determination of large amounts (high concentrations) [1].

For several decades, ICP methods have played an important role in elemental analysis due to unique properties of plasma. Argon inductively coupled plasma is a high-temperature source (6000–10000 K), and is characterized by a high concentration of electrons ($\sim 10^{20}$–10^{22} cm^{-3}) and argon ions. Almost complete atomization/ionization of easily ionized elements and partial atomization/ ionization of other elements occur in plasma. On the one hand, this allows the multielement determination of analytes at the ppb level for ICP-AES and at the ppt level for ICP-MS, on the other hand, it contributes to the appearance of interferences of various origins.

There are many reasons for the appearance of interferences—argon plasma, matrix components of the sample, water, acids, accompanying elements in the sample, oxygen/nitrogen/carbon from air. Experts have divided interferences into spectral, non-spectral and physical-based [2–4].

An example of spectral and non-spectral interferences in ICP-AES is the large number of spectral lines emitted by each element, the plasma gas supporting the plasma, the sample matrix components, and the atmospheric components entering the plasma.

In ICP-MS, spectral and non-spectral interferences are more pronounced. Spectral interferences include the formation of polyatomic, doubly charged, and isobaric ions. Non-spectral (matrix) interferences are associated with the effect of sample transport and the physical suppression of the analyte signal due to changes in aerosol characteristics (formation and size of droplets), as well as the influence of the matrix on ionization conditions. Plasma ionization conditions are so fragile that high concentrations of acids and matrix elements severely suppress the analytical signal. Space charge interference is also referred to as matrix interference.

As an example of physical-based influences, we can consider the data published in work [5], where the authors write about the existence of "virtual" lines that arise due to the illumination of the detector from intense spectral lines at neighboring scattering orders.

To ensure the quality of the results obtained, it is important to identify the interferences of any origin and to choose the optimal-compromise instrumental parameters under the conditions of multielement analysis.

Table 1 lists ways to identify and account for spectral and non-spectral interferences. The first two methods are generally accepted in analytical practice.

The variety of analytical tasks and the need to develop new methods of analysis dictate the creation of a universal method for detecting interference of various origins.

Our proposed method is based on calculation the experimental value of limit of quantitation (eLOQ). In this case

O. N. Grebneva-Balyuk (✉) · O. A. Tyutyunnik · I. V. Kubrakova
Vernadsky Institute of Geochemistry and Analytical Chemistry, Russian Academy of Sciences, 19 Kosygin St., Moscow, 119991, Russia
e-mail: grebneva@geokhi.ru

V. P. Kolotov and N. S. Bezaeva (eds.), *Advances in Geochemistry, Analytical Chemistry, and Planetary Sciences*,
https://doi.org/10.1007/978-3-031-09883-3_35

Table 1 Methods for searching and accounting for interferences

Method	Reference	Comments
Working with libraries of spectral lines or isotopes	Any ICP-spectrometer	Libraries do not always contain all the information
Analysis of single-element and / or multi-element solutions simulating the composition of the future analyzed sample and then calculation the coefficients of interelement correction	[6]	Coefficients of interelement correction are not suitable for changing chemical composition of the matrix
Identification and correction of interferences due to the introduction of an interferent into the analyzed sample	[7, 8]	Interelement correction does not sufficiently improve the results and requires additional instrumental techniques to remove interferences, in particular, the additional use of dynamic reaction cell (DRC)
Determination of detection/quantification limits by plotting the RSD of the pure signal on the analyte concentration	[9]	At low analyte concentrations, using of dependence of RSD on element concentration proved to be convenient and reliable both for calculation limits of detection and quantification, and for method validation
Comparison of slope angles of calibration curves for solutions differing in composition	[10]	The proposed method made it possible to compare different methods of calibrating the spectrometer. The authors preferred calibration by the standard addition method. The proposed method has been tested on only one type of samples
Calculation of mutual interference coefficients and compilation of an interference matrix	[4]	This method to identifying and taking into account mutual interferences gives a large determination error at low concentrations of elements and significant spectral interferences

eLOQ is the lowest concentration on the calibration graph, measured under the selected instrumental conditions, taking into account the purity of the reagents [11, 12]. The formula for calculating the experimentally obtained value of eLOQ can be represented as follows

$$eLOQ = (I_B \cdot C_A)/I_A \quad (1)$$

where I_B is the raw intensity of blank, C_A is the known concentration of the analyte, I_A is the raw intensity of the signal of the analyte. For calculations, we suggest using raw intensity, i.e. intensity value without mathematical processing. This is done to exclude possible assumptions, limitations, and other operations of the mathematical apparatus incorporated in the software of a modern spectrometer.

Model experiments were carried out on systems simulating the composition of technological, biological and natural objects, the elemental composition of which is characterized by spectral and non-spectral interferences.

ICP-AES studies were carried out using aqueous solutions and solutions with a matrix zirconium content of 1 mg/ml. Zirconium has a rich set of spectral lines which, at high concentrations, affects the spectral lines of most elements of the Periodic Table. Searching and taking into account the interferences is important when determining impurities in technological objects, in particular, in zirconium oxide and zirconium alloys.

ICP-MS studies were carried out using the aqueous solutions and solutions containing organic carbon. The presence of carbon in the analyzed solutions, even after decomposition and concentration, is common for various sample preparation schemes for natural and biological objects. Previously, we have shown that residual carbon in solutions after the decomposition of oil of different viscosity influences the formation of analytical signals of ICP-MS [13]. In this regard, it is important to identify and take into account the degree of carbon influence when determining elements at the level of ultra-trace concentrations.

2 Experimental

An IRIS Intrepid II DUO spectrometer (Thermo Electron Corp., USA) with a semiconductor CID detector was used for ICP-AES measurements. The spectral range is 165–1050 nm. Operating conditions: RF power—1150 W; plasma argon flow rate—15.0 l/min, auxiliary argon flow rate—0.5 l/min and nebulizer flow rate—0.73 l/min.

ICP-MS measurements were performed on an ELEMENT XR high-resolution double focusing spectrometer (Finnigan MAT., Germany). Operating conditions: RF power—1200 W; spray chamber—cyclonic; nebulizer—MicroMist (conical); plasma argon flow rate—16.0 l/min,

auxiliary argon flow rate—0.9 l/min and nebulizer flow rate —1.010 l/min.

In order to improve the quality of the determination of trace and ultra-trace concentrations, double-distilled water and concentrated nitric acid (high pure grade, Khimmed, Russia) were additionally purified using a BSB-939-IR non-boiling distillation system (Berghof, Germany).

Working solutions were prepared by serial weight dilution using standard multielement solutions with a content of 100 ppm of each element (High-Purity Standards, USA).

To prepare model solutions containing zirconium and chromium as a matrix elements, a single-element solution of zirconium and chromium 10 mg/ml was used (Inorganic Ventures, USA).

Citric acid of chemically pure grade was used as a carbon source for the preparation of model solutions containing an organic matrix (LenReaktiv, Russia).

All calculations were performed using Excel software.

3 Results and Discussion

ICP methods are relative methods of analysis. Therefore, the calibration stage of the spectrometer is always important. The generally accepted empirical approach is to construct a dependence in the form of signals for known analyte concentrations in standard solutions (i.e., for solutions with a known analyte concentration). However, the problem is that in the presence of spectral and non-spectral influences, the calibration dependence is not a direct characteristic of the analyte, which ultimately leads to an inaccurate analytical result.

An increase in the number of sample components and large variations in the concentrations of analyte-interferent potentially lead to large analytical errors in the determination of trace elements.

Therefore, the analyst should take this into account during the analytical procedure and, if necessary, various methods of detecting spectral and non-spectral interference are used.

The presence of spectral and non-spectral interference leads to the fact that the calibration dependence in the range of low concentrations is not linear. In such a case, it is proposed to take the beginning of the linear part as the limit of quantification. This is based on the assumption that, from this point onward, the accuracy is sufficient for quantification.

Our proposed method for searching interferences includes analysis of at least three solutions with known analyte concentrations plus analysis of a blank solution. Further, according to the Formula (1), the eLOQ value is calculated for solutions with known concentrations. It is important to take into account that the calculation should be carried out only using raw intensity values. Then, the results are processed. If the eLOQ values are the close or have minor discrepancies, then one can draw conclusions about the absence of spectral interferences. If the eLOQ values have significant discrepancies, then this indicates the presence of interferences, and, therefore, a decision is made about using the spectral line or isotope. If it is not possible to exclude a spectral line or an isotope from the analysis, then the detected interference must be taken into account by mathematical correction (preferably) or an interfering element must be excluded by concentration.

The proposed calculation method is invariant, i.e. eLOQ can be calculated using a constant analyte concentration by varying the concentration of the expected interferent or matrix.

Table 2 shows the raw intensities of the ICP-AES and the eLOQ values calculated by (1). If the three obtained values of eLOQ are the close, then it can be concluded that (1) the spectral line is free from interference and can be successfully used to determine the element in the analyzed matrix; (2) all three obtained values are close to the true experimentally found value of eLOQ under the selected experimental conditions.

If the values obtained differ, then this indicates the presence of spectral or non-spectral interference.

eLOQs obtained for solutions containing 1 mg/ml zirconium indicate that zirconium affects almost all selected spectral lines of the analyzed elements (Table 2). Consider the eLOQ values for the spectral lines Cd 214.4 nm and Cd 228.8 nm, Cu 224.7 nm and Cu 327.3 nm in the presence of zirconium. From Table 2 it can be seen that the eLOQ values change with changing concentrations of cadmium and copper. Following our proposed method, a change in eLOQ with a change in concentration indicates the presence of interferences.

To understand the processes occurring in plasma and to explain the increase in eLOQ values in the presence of zirconium, we used the Saha ionization equation and Boltzmann distribution law [14]. The calculations were done using the resource www.physics.nist.gov [15].

Tables 3 and 4, Figs. 1 and 2 show the calculated intensities for the spectral lines Cu 224.7 and Cu 327.3 nm, Cd 214.4 and Cd 228.8 nm under different analyte concentrations. From Tables 3 and 4 it can be seen that the total intensities of the spectral lines of copper and zirconium, cadmium and zirconium do not have a linear relationship with a change in the concentration ratio of copper and zirconium, cadmium and zirconium. This has been confirmed experimentally (Table 2).

Figures 3 and 4 show the theoretical spectra near the analytical line Cu 224.7 nm and analytical line Cd 214.4 nm with varying the ratio of the concentrations of Cu: Zr and Cd: Zr. It is shown that an increase in the concentration of

Table 2 Experimentally obtained values of eLOQ by ICP-AES

Element/λ (nm)	Model solutions without matrix element		Model solutions, containing 1 mg/ml zirconium (including blank)		Possible interference from zirconium
	I, counts/s blank 0.1 ppm 1 ppm 10 ppm	eLOQ (ppm)	I, counts/s blank 0.01 ppm 0.1 ppm 1 ppm	eLOQ (ppm)	λ (nm)
Al396.1	0.0113 0.1027 0.8801 11.03	0.01 0.01 0.01	10.65 10.86 14.88 57.14	0.01 0.07 0.19	396.3
Ba455.4	0.0008 0.0931 0.9306 8.936	0.0009 0.0009 0.0009	14.43 26.83 155.7 1431	0.005 0.009 0.01	456.1
Cd214.4	0.1339 5.541 61.1 603.1	0.002 0.002 0.002	3.539 4.528 13.39 104.9	0.008 0.03 0.03	214.4
Cd228.8	0.0018 0.0888 0.984 8.878	0.002 0.002 0.002	6.945 8.401 21.95 162.9	0.008 0.03 0.04	227.6 228.3
Ce413.3	0.0168 0.1033 0.8257 8.666	0.02 0.02 0.02	54.56 54.78 59.24 99.05	0.01 0.09 0.55	413.2
Ce446.0	0.2622 2.748 22.51 226.4	0.01 0.01 0.01	76.92 77.33 81.39 118.4	0.01 0.09 0.65	445.7 446.6
Cr267.7	0.1218 3.522 29.61 280.1	0.004 0.004 0.004	11.41 11.92 16.81 64.11	0.01 0.07 5.5	267.7
Cr357.8	0.0044 0.1012 0.8966 10.26	0.004 0.005 0.004	11.03 11.54 16.37 67.73	0.01 0.08 0.16	358.5
Cu224.7	0.1521 0.7933 7.405 81.21	0.02 0.02 0.02	2.757 2.863 3.976 15.99	0.01 0.07 0.17	224.7
Cu327.3	0.055 6.126 62.59 661.5	0.0009 0.0009 0.0008	31.44 32.32 41.45 135.2	0.01 0.08 0.2	327.9
Fe240.4	0.0522 1.127 7.357 65.52	0.005 0.007 0.008	7.125 7.361 9.024 25.03	0.01 0.08 0.28	240.5
Fe259.9	0.022 0.1582 0.999 8.802	0.01 0.02 0.03	6.327 7.345 14.46 83.33	0.009 0.04 0.08	259.4

(continued)

Table 2 (continued)

Element/λ (nm)	Model solutions without matrix element		Model solutions, containing 1 mg/ml zirconium (including blank)		Possible interference from zirconium
	I, counts/s blank 0.1 ppm 1 ppm 10 ppm	eLOQ (ppm)	I, counts/s blank 0.01 ppm 0.1 ppm 1 ppm	eLOQ (ppm)	λ (nm)
Ge206.8	0.0345 0.1284 1.071 10.94	0.03 0.03 0.03	6.789 6.925 8.29 22.71	0.01 0.08 0.3	206.9
Hf232.2	0.0065 0.0859 0.796 7.775	0.008 0.008 0.008	4.254 4.356 5.369 15.41	0.01 0.08 0.27	230.8
Hf263.8	0.0153 0.1451 1.266 12.57	0.01 0.01 0.01	8.338 8.653 11.81 42.05	0.009 0.07 0.2	262.8 264.4
Mg285.2	0.0618 0.1419 0.884 8.533	0.04 0.07 0.07	15.54 16.54 30.59 173.0	0.009 0.05 0.09	
Mn257.6	0.0005 0.0842 0.8037 7.752	0.0006 0.0006 0.0006	8.804 11.72 39.95 320.3	0.008 0.02 0.03	
Mn259.3	0.1732 15.17 143.8 1388	0.001 0.001 0.001	10.18 12.66 36.86 277	0.008 0.03 0.04	259.4
Mo202.0	0.0273 0.2293 2.671 18.04	0.01 0.01 0.015	6.445 7.186 14.18 85.91	0.009 0.05 0.08	201.7 202.6
Pb261.4	0.0111 1.497 14.53 163.3	0.0007 0.0008 0.0007	9.17 11.27 31.97 237.6	0.008 0.03 0.04	262.0
Sc361.3	0.0003 0.0995 0.9919 9.471	0.0003 0.0003 0.0003	15.93 26.31 132.4 1172	0.006 0.01 0.01	
Ti334.9	0.0027 0.0991 0.9588 8.414	0.003 0.003 0.003	30.36 34.78 79.54 476.6	0.009 0.04 0.06	
Ti337.2	0.8354 19.98 185.2 1516	0.004 0.0045 0.0055	38.84 41.85 73.2 315.9	0.01 0.05 0.1	
W207.9	1.044 2.249 14.05 131.4	0.05 0.07 0.08	6.351 6.576 8.579 28.51	0.01 0.07 0.2	207.7 208.7

zirconium has a significant effect on obtaining information on the intensities of the analytical lines of copper and cadmium. When the concentration ratios are 0.001:99.999 for Cu:Zr and 0.0001:99.9999 for Cd:Zr, the registration of analytical signals (intensities) on Cu 224.7 nm and Cd 214.4 nm is not possible.

The results presented in Tables 2, 3 and 4, as well as in Figs. 1, 2, 3 and 4, indicate that almost any corrections for the interelement and matrix interferences are applicable within the same order, and at high concentrations of matrix and interfering elements cannot be used. As a solution to this problem, the separation of the matrix, complete or partially controlled, can be proposed. This procedure will allow for the correct determination of impurities in samples such as zirconium alloys, zirconium oxide, natural and technological objects with a high zirconium content.

The experimental data for high-resolution ICP-MS are shown in Table 5. Since high-resolution mass spectrometers are equipped with highly sensitive detectors, the cleanliness of the labware, reagents, room, etc. used in trace and ultra-trace analysis is important [16]. It is also important to completely eliminate the memory effect, which introduces a significant error in the calculation of the LOQ [17]. From Table 5 it follows that our proposed method for detecting interference through the calculation eLOQ is applicable to ICP-MS.

Consider the values obtained for $^{55}Mn^+$ and $^{75}As^+$ (Table 5). Manganese and arsenic are commonly present as impurities in high purity nitric acid used as a reagent, and our working solutions are prepared using this reagent. For the selected isotopes in the analyzed solutions, the following polyatomic interferences are possible:

$$^{55}Mn^+ : {}^{40}Ar^{14}N^1H^+, {}^{39}K^{16}O^+, {}^{37}Co^{18}O^+, {}^{40}Ar^{15}N^+, {}^{38}Ar^{17}O^+, {}^{36}Ar^{18}O^1H^+, {}^{38}Ar^{16}O^1H^+,$$

$$^{75}As^+ : {}^{59}Co^{16}O^+, {}^{36}Ar^{38}Ar^1H^+, {}^{36}Ar^{39}K^+, {}^{43}Ar^{16}O_2^+$$

which can be eliminated using a reaction/collision cell of quadrupole mass spectrometer (Q-ICP-MS) or with a high resolution mass spectrometer (HR-ICP-MS).

It was found that eLOQ of $^{55}Mn^+$ is 0.04 ppb (medium resolution) and eLOQ of $^{75}As^+$ is 0.05 ppb (high resolution) for aqueous model solutions. Three identical eLOQ values for $^{55}Mn^+$ and three close ones for $^{75}As^+$ indicate the absence of the interferences of the above polyatomic ions on the analytical signals of manganese and arsenic.

One of the common components of the analyzed objects is carbon, which is included in the composition of the initial samples, reagents, air, etc. We have shown that the carbon contained in the analyzed solutions affects the formation of the analytical signal, both in ICP-AES and ICP-MS [10]. Moreover, the effects in ICP-MS are more pronounced due to the sensitivity of the detector. Table 5 presents the eLOQ values obtained for solutions containing organic carbon at a concentration of 520 ppm carbon (citric acid). It can be seen that the presence of carbon degrades the eLOQ of most of the isotopes studied. This observation should be taken into account when analyzing objects where low eLOQs are required (biological and natural objects, as well as high purity substances).

The proposed method is invariant, i.e. it can be used to calculate eLOQ where the analyte concentration is constant and the concentration of the interferent or matrix changes. As an example, we present the experimental data obtained for the rhodium-chromium pair. It was previously shown that chromium oxides have a significant effect on Q-ICP-MS determination of rhodium monoisotope ($^{103}Rh^+$) [18]. Cr based interference can be expected not only in combination with ^{53}Cr, but also with the most abundant ^{52}Cr, possibly forming $^{16}O_2{}^{18}O^{52}Cr^+$ (101.9295) and $^2H^{16}O_3{}^{52}Cr$ (101.9409), which can introduce a significant error in the determination of rhodium in geological samples, for example, in chromites and peridotites. We investigated the effect of excess chromium by HR-ICP-MS determination of rhodium [19]. Table 6 shows the values of analytical signals for

Table 3 Theoretical values of the intensities of spectral lines of copper and zirconium, calculated using the Saha-Boltzmann equations. $T_e = 1$ eV, $N_e = 1 \times 10^{17}$e/cm^3

Ratio of Cu:Zr (%)	I on λ 224.7 nm, a.e		∑I	I on λ 327.3 nm, a.e		∑I
	Cu II	Zr III	Cu II + Zr III	Cu I	Zr III	Cu I + Zr III
1: 99	4752	3.2	4755	1736	45.5	1782
0.1: 99.9	478	3.9	482	173.6	72.6	246.4
0.01: 99.99	47.8	4.3	52	16.9	57.3	74.2
0.001: 99.999	4.8	3.7	8.5	1.6	48.5	50.3
0.0001: 99.9999	0.48	3.2	3.7			

Table 4 Theoretical values of the intensities of the spectral lines of cadmium and zirconium, calculated using the Saha-Boltzmann equations. T_e = 1 eV, $N_e = 1 \times 10^{17}$e/cm^3

Ratio of Cd:Zr, %	I on λ 214.4 nm, a.e.		∑I	I on λ 228.8 nm, a.e.		∑I
	Cd II	Zr III	Cd II+ Zr III	Cd I	Zr III	Cd I+ Zr III
0.01:99.99	553.1	4.43	557.53	105.39	0.08	105.47
0.001:99.999	55.3	4.35	59.65	10.46	0.09	10.57
0.0001:99.9999	5.53	4.43	9.96	1.05	0.08	1.13
0.00001:99.99999	0.553	4.39	4.95	0.1	0.03	0.13

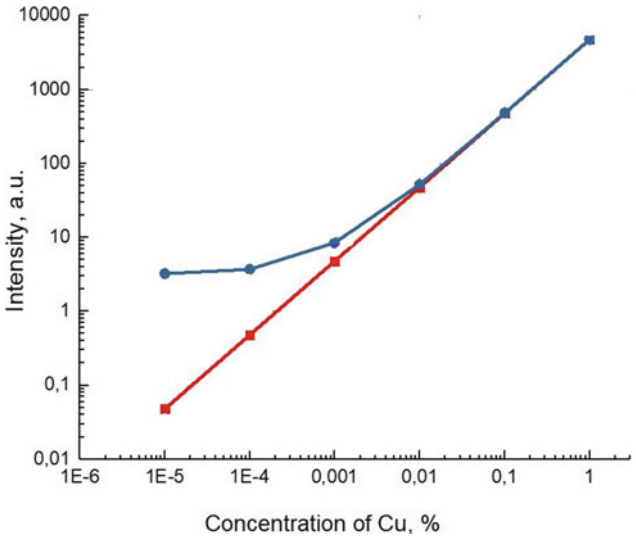

Fig. 1 Dependence of ∑I of Cu II and Zr III (blue) and I of Cu II (red) 224.7 nm on the concentration of copper in the presence of zirconium

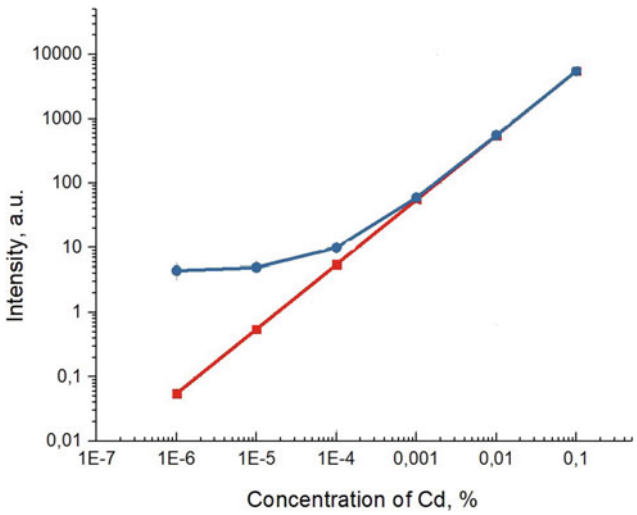

Fig. 2 Dependence of ∑I of Cd II and Zr III (blue) and I of Cd II (red) 214.4 nm on the concentration of cadmium in the presence of zirconium

$^{103}Rh^+$ in model solutions containing the analyte and the interferent at different concentrations. Table 6 shows that even 2500 excess chromium does not affect eLOQ, and therefore the use of HR-ICP-MS can eliminate the interference of polyatomic ions of chromium oxide, which cannot be provided by Q-ICP-MS. The eLOQ values obtained for different resolutions of the HR-ICP-MS spectrometer also confirm the fact that with increasing resolution the sensitivity decreases and, as a consequence, the eLOQ becomes worse.

4 Conclusion

To ensure the quality of the analytical information obtained, we have proposed a new method for searching spectral and non-spectral interferences, which consists of calculating the eLOQ at different concentrations of analyte. The proposed method was tested on ICP-AES and ICP-MS analysis of multielement aqueous solutions and solutions containing an inorganic or organic matrix. It is shown that

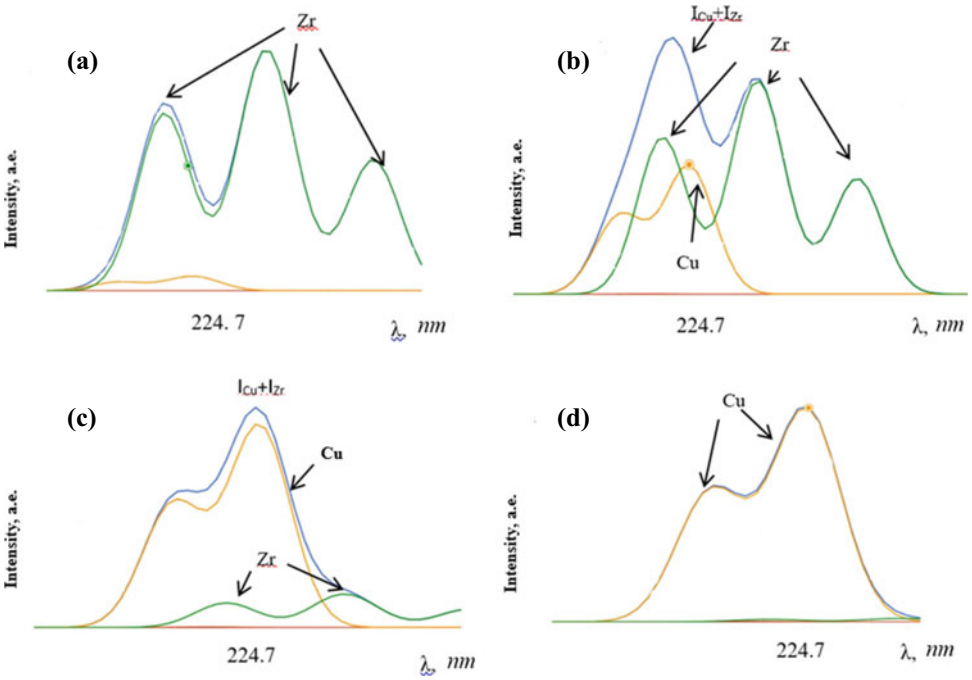

Fig. 3 Spectra near the analytical line of Cu 224.7 nm with varying concentration ratio Cu:Zr **a** 0.0001:99.9999; **b** 0.001:99.999; **c** 0.01:99.99; **d** 0.1:99.9

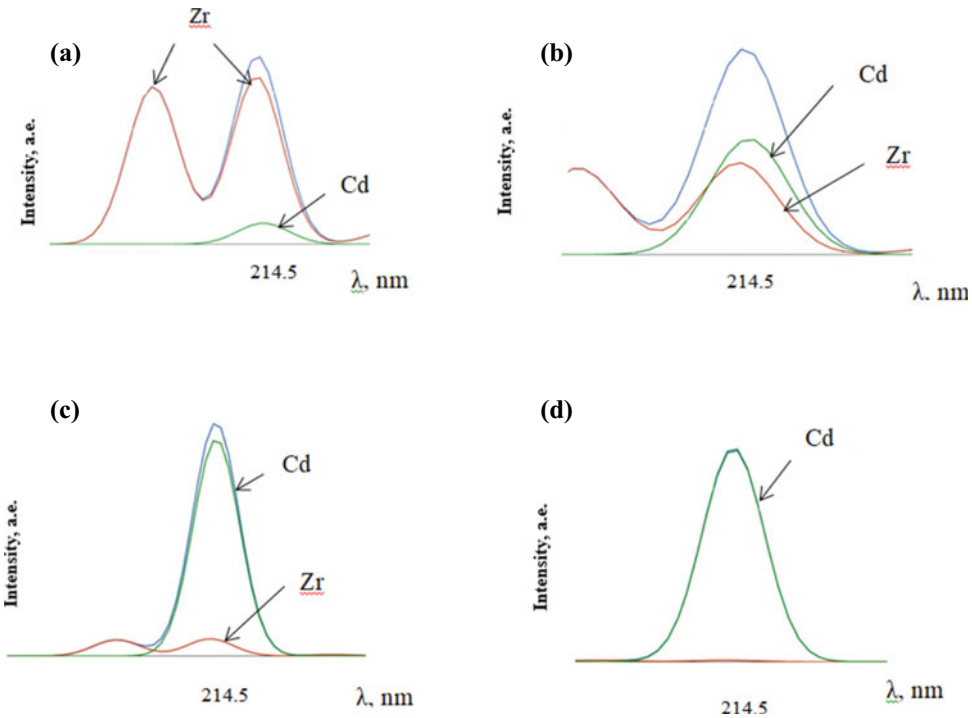

Fig. 4 Spectra near the analytical line of Cd 214.4 nm with varying concentration ratio Cd:Zr **a** 0.00001:99.99999; **b** 0.0001:99.9999; **c** 0.001:99.999; **d** 0.01:99.99

Table 5 Experimentally obtained values of eLOQ by ICP-MS

Isotope	Model solutions without matrix element		Model solutions, containing 520 mg/ml carbon (including blank)	
	I, counts/s blank 0.1 ppb 1.0 ppb 10 ppb	eLOQ, ppb	I, counts/s blank 0.1 ppb 1.0 ppb	eLOQ, ppb
$^{89}Y^{+}$ (LR)	572 194747 1929794 19066578	0.0003 0.0003 0.0003	1922 244698 2184714	0.0008 0.0009
$^{139}La^{+}$ (LR)	913 203958 2066825 22825000	0.0004 0.0004 0.0004	3464 283191 2513923	0.001 0.001
$^{140}Ce^{+}$ (LR)	748 77514 769756 7847423	0.001 0.001 0.001	2131 65233 675421	0.003 0.003
$^{141}Pr^{+}$ (LR)	264 231804 2312848 24408035	0.0001 0.0001 0.0001	1091 328552 2903756	0.0003 0.0004
$^{143}Nd^{+}$ (LR)	135 26569 260487 2700038	0.0005 0.0005 0.0005	426 38783 323511	0.001 0.001
$^{147}Sm^{+}$ (LR)	54 30291 299621 2732970	0.0002 0.0002 0.0002	150 44073 378159	0.0003 0.0004
$^{151}Eu^{+}$ (LR)	89 90184 900154 8964390	0.0001 0.0001 0.0001	309 138396 1180331	0.0002 0.0003
$^{157}Gd^{+}$ (LR)	40 31625 301284 3953201	0.0001 0.0001 0.0001	123 48006 403879	0.0003 0.0003
$^{159}Tb^{+}$ (LR)	75 159952 1599013 16016750	0.00005 0.00005 0.00005	332 260497 2257719	0.0001 0.0001
$^{161}Dy^{+}$ (LR)	42 48258 481951 4794708	0.0001 0.0001 0.0001	117 72872 626324	0.0002 0.0002
$^{165}Ho^{+}$ (LR)	106 249624 2504921 26589003	0.00004 0.00004 0.00004	400 381956 3431097	0.0001 0.0001
$^{166}Er^{+}$ (LR)	79 78774 791002 7905443	0.0001 0.0001 0.0001	208 122904 1062628	0.0002 0.0002
$^{169}Tm^{+}$ (LR)	69 230991 2401725	0.00003 0.00003 0.00003	338 369463 3289687	0.0001 0.0001

(continued)

Table 5 (continued)

Isotope	Model solutions without matrix element		Model solutions, containing 520 mg/ml carbon (including blank)	
	23007491			
$^{172}Yb^{+}$ (LR)	19 53338 503439 5129780	0.00004 0.00004 0.00004	97 80660 684741	0.0001 0.0001
$^{175}Lu^{+}$ (LR)	503 202753 2115302 25157030	0.0002 0.0002 0.0002	1085 337353 2981497	0.0003 0.0003
$^{45}Sc^{+}$ (MR)	29 7472 70650	0.0004 0.0004	44 7772 66895	0.0006 0.0007
$^{51}V^{+}$ (MR)	86 1358 13029 143587	0.006 0.006 0.006	93 1528 13813	0.007 0.007
$^{55}Mn^{+}$ (MR)	989 2486 22959 225270	0.04 0.04 0.04	2607 3300 15804	0.08 0.16
$^{75}As^{+}$ (HR)	23 71 469 4932	0.03 0.05 0.05	182 - 1993 12504	0.2 0.3

*LR—Low Resolution, MR—Middle Resolution, HR—High Resolution

Table 6 Experimentally obtained values of $^{103}Rh^{+}$ in the presence of chromium

Rh: Cr, ppb	LR*		MR		HR	
	I, counts/s	eLOQ, ppb	I, counts/s	eLOQ, ppb	I, counts/s	eLOQ, ppb
Blank	80		20		24	
1,2: 210	66,236	0,0001	61,448	0,0003	6012	0,004
1,07: 810	711,022	0,0001	63,506	0,0003	6371	0,004
1,44: 2500	909,513	0,0001	83,867	0,0003	7630	0,005

*LR—Low Resolution, MR—Middle Resolution, HR—High Resolution

the coefficients of interelement correction should be calculated and used only within the one order of analyte concentrations.

The method proposed is useful in the development of analytical analysis schemes for the trace element determination.

Acknowledgements This work is conducted under the GEOKHI RAS state assignment.

References

1. Baranowska, I. (ed.): Handbook of Trace Analysis. Fundamentals and applications. Springer. Switzerland (2016)
2. Thomas, R.: Practical Guide to ICP-MS. Marcel Dekker, Inc., Basel, New York (2003)
3. Todoli, J.L, Mermet, J.-M.: Encyclopedia of Analytical Chemistry. Wiley Ltd. (2006–2011)
4. Agatemor, C., Beauchemin, D.: Matrix effects in inductively coupled plasma mass spectrometry: a review. Anal. Chim. Acta **706**, 66–83 (2011)
5. Zybinsky, A.M., Kolotov, V.P., Karandashev, V.K., Kordyukov, S.V.: Determination of rare-earth and accompanying elements in niobium−rare-earth ores by inductively coupled plasma atomic emission spectrometry using model calibration and a mathematical approach for resolving spectral interferences. J. Anal. Chem. **74**(3), 213–225 (2019)
6. Golloch, A. (ed.) Handbook of Rare Earth Elements: Analytics. Walter de Gruyter GmBH, Berlin/Boston (2017)
7. Alekseev, A.V., Yakimovich, P.V., Min, P.S.: Determination of impurities in an Nb-based alloy by ICP-MS. Trudy VIAM **6**, 29–37 (2015)
8. Pupyshev, A.A., Danilova, D.A.: The use of inductively coupled plasma atomic emission spectrometry for the analysis of materials and products of ferrous metallurgy. Analytica i Control **11**(2–3), 131–218 (2007)

9. Bonnefoy, C., Menudier, A., Moesch, C., Lachaˆtrea, G., Mermet, J.-M.: Validation of the determination of lead in whole blood by ICP-MS. J. Anal. At. Spectrom. **17**, 1161–1165 (2002)
10. Bonnefoy, C., Menudier, A., Moesch, C., Lachatre, G., Mermet, J.-M.: Determination of chromium in whole blood by DRC–ICP–MS: spectral and non-spectral interferences. Anal Bioanal Chem. **383**, 167–173 (2005)
11. Guide to Quality in Analytical Chemistry. An Aid to Accreditation, 3rd ed. (2016). http://www.eurachem.org. Accessed 07 Aug 2021
12. Mermet, J.-M., Granier, G., Fichet, P.: A logical way through the limits of quantitation in inductively coupled plasma spectrochemistry. Spectrochim. Acta Part B **76**, 221–225 (2012)
13. Grebneva-Balyuk, O.N., Kubrakova, I.V., Tyutyunnik, O.A., Lapshin, S.Yu., Pryazhnikov, D.V.: Multielement analysis of oil by ICP–AES and ICP–MS with microwave-assisted sample preparation. J. Anal. Chem. **76**(3), 304–312 (2021)
14. Chen, F.F.: Introduction to Plasma Physics. Translated from English. Mir, Moscow (1987)
15. http://www.physics.nist.gov. Accessed 20 Sept 2021
16. Dean, J.R.: Practical Inductively Coupled Plasma Spectroscopy. Wiley Ltd., England (2005)
17. Rodushkin, I., Engström, E., Baxter, D.C.: Sources of contamination and remedial strategies in the multi-elemental trace analysis laboratory. Anal. Bioanal. Chem. 396, 365–377 (2010)
18. Krushevska, A.P., Zhou, Y., Ravikumar, V., Kim, Y.-J., Hinrichs, J.: Chromium based polyatomic interferences on rhodium in ICP-MS. J. Anal. Atom. Spectrom. **21**, 847–855 (2006)
19. Tyutyunnik, O.A., Nabiullina, S.N., Anosova, M.O., Kubrakova, I. V.: Determination of trace amounts of platinum group elements and gold in ultrabasic rocks by inductively coupled plasma mass spectrometry using AG-X8 and LN-resin sorbents. J. Anal. Chem. **75**(6), 769–777 (2020)

iPlasmaProQuad: A Computer System Based on a Relational DBMS for Processing and Monitoring the Results of Routine Analysis by the ICP-MS Method

V. P. Kolotov, A. V. Zhilkina, and A. O. Khludneva

1 Introduction

Obtaining qualitatively new results in geochemistry, biology, medicine, and other disciplines is determined by how accurate and complete information the researcher has about the chemical composition of the studied object. Today Quadrupole Mass Spectrometry with Inductively Coupled Plasma (ICP-QMS) is the leading method for the determination of ultra-low concentrations of elements in various samples [1, 2]. Improving the accuracy of quadrupole inductively coupled plasma mass spectrometry depends on several steps in the analysis procedure, of which acid mineralization of samples, measurement of mass spectra, and processing mass spectrometric information are decisive.

Sample preparation is a critical step in ICP-QMS analysis that determines its success. Many approaches have been developed and used [3–5]. To improve the reproducibility of acid mineralization of many geological samples simultaneously, an ingeniously designed apparatus has been developed [6]. It allows the acid decomposition of geological samples of different classes (from mafic to ultramafic rocks).

Hardware in several designs (including acid distillation in a gas stream) is intended for simultaneous processing of up to 24 samples at full control of decomposition conditions. The developed hardware is based on the principle of maximum formalization of the description of operations that make up the decomposition procedure for samples of a different type. This principle improves the reproducibility of the decomposition procedure (and, under certain conditions, the accuracy of the analysis).

A significant point is that data processing is an analysis bottleneck that significantly reduces productivity. For example, measuring a batch of 20–30 samples takes less than one working day, while data processing can take two or three days, and sometimes more. It is due to the introduction of various kinds of corrections for matrix effects, spectral interference, spectrometer sensitivity drift over time, integration of results for individual isotopes, and many other factors. In many laboratories, spreadsheets are used for this purpose. The manipulation of spreadsheets requires a clear understanding of the algorithm of action and is usually a sequence of several (usually manual due to variable size) operations on data sets. This is where subjective errors can arise, due to the so-called human factor. In addition, neither the in-house mass spectrometer software nor the subsequent additional calculations in a spreadsheet make it possible to assess the accumulation of error in the calculations and evaluate the most critical stage of the mass spectrometric measurement and calculation of concentration. It is also difficult to document all input corrections, which breaks the chain of traceability of the formation of analysis results.

That is why developing a program for mass spectrometric information processing remains an important task. There are a few publications in the literature devoted to the development of software for such tasks. For example, the article by Tharaud et al. [7] presents the uFREASI software for the processing of elemental analysis data from ICP-MS spectrometers. The software provides concentration calculations, various data correction options, error accumulation evaluation, etc. The software is written in C++ and is freely distributable. Another freeware package is Iolite [8]. It is based on the Igor Pro package with its programming language (Wavemetrics Incorporated). The package includes advanced graphics and many useful options. The Iolite program works with primary spectra of any origin with time-resolved output. The program provides in particular laser ablation (LA ICP-MS) data processing and is aimed at advanced users who develop analysis methodology. The user-oriented package ADE [9] is positioned by the authors for routine ICP-MS analyses. The IsotopeMaker [10] builds on the well-known MATLAB package and is aimed

V. P. Kolotov (✉) · A. V. Zhilkina · A. O. Khludneva
Vernadsky Institute of Geochemistry and Analytical Chemistry, Russian Academy of Sciences, 19 Kosygin St., Moscow, 119991, Russia
e-mail: kolotov@geokhi.ru

V. P. Kolotov and N. S. Bezaeva (eds.), *Advances in Geochemistry, Analytical Chemistry, and Planetary Sciences*,
https://doi.org/10.1007/978-3-031-09883-3_36

primarily at isotopic analysis, including the LA ICP-MS version. Information is available on programs focused exclusively on LA ICP-MS data processing [11, 12].

2 Experimental Part

2.1 Equipment

An X Series II quadrupole inductively coupled plasma mass spectrometer (Thermo Scientific) equipped with a concentric atomizer and a quartz cyclone atomization chamber cooled by a Peltier element (2 °C) was used. Parameters of the measurement: generator output power 1400 W, plasma gas (Ar) flow rate 13 l/min, auxiliary 0.95 l/min, Ar flow rate through the nebulizer 0.87 l/min, sample flow rate 0.8 ml/min. The mass spectra were measured using two scanning modes: Survey Scan with 5 passes from 5 to 240 m/z and Peak Jumping with 1 channel per mass, integration time 20 ms, and 25 passes. All measurements were performed with PlasmaScreen software. If all device settings are observed, the level of oxide ions CeO^+/Ce^+ is not more than 2%, the level of double-charged ions (Ba^{2+}/Ba^+) is not over 3%.

2.2 Reagents

To prepare calibration solutions and for decomposition**,** we used the listed chemical substances: deionized water distilled without boiling in PTFE Subboiler ECO IR Maassen (Germany) water and acid treatment system; acids produced by Merck (Germany): HF (40% for analysis), HNO_3 (65% for analysis, max 0.005 ppm Hg), $HClO_4$ (70–72% for analysis), H_3BO_3 (for analysis), as well as HCl (GOST 3118-77), distilled (27%) without boiling in the PTFE Subboiler ECO IR system. ICP-MS-68 multi-element standard calibration solutions (Solution A and Solution B) produced by High purity standards (USA), single element solutions of REE with a concentration of each element 1000 µg/ml (Merk, Germany).

Working calibration solutions for ICP-MS were prepared by successive dilution of initial solutions of multi-element standard solutions ICP-MS-68 to concentrations of 10 µg/L for solution A and 5 and 10 µg/L for solution B. A multi-element standard solution for REE group with a concentration of each element of 10 µg/L was prepared by mixing solutions of individual REE standards. In all cases, 2% solution of HNO_3 was used as diluent. A solution of In (10 µg/L in 2% HNO3) was used as an internal standard. Solutions were diluted in 10 ml disposable polyethylene tubes (Litaplast-Med, Republic of Belarus) or 50 ml (Cititest Labware Manufacturing Co., Ltd., China) before measurement. The gravimetric method was used to control the dilution degree.

3 Results and Discussion

To automate the processing of the mass spectra, a computer software iPlasmaProQuad has been developed. The mass spectrometer is used only as a detector for the mass spectra, providing the corresponding peak areas and the meta-information about the measurement conditions. All other necessary calculations are performed by the computer program itself. The architecture of the iPlasmaProQuad software is based on an entirely different concept compared to the programs mentioned in the Introduction. All calculation operations are based on the system of consecutive queries, the results of which can be seen immediately using MS Access. Query compilation takes place in an interactive environment, so knowledge of the SQL language is usually not required. Learning how to create queries in MS Access using the available constructor is not difficult. This means that users can easily modify and extend the functionality of the program. Another advantage of the developed architecture is that the management of a query sequence can be entrusted to an external program written in a high-level programming language, such as C#. This is exactly how iPlasmaProQuad is implemented, where the interface with the user is written in this language. The task of the interface shell is to request the name of a file containing the results of a batch of samples measured on a mass spectrometer, import the information into database tables, check the integrity of the received information (query calls) and then run a sequence of queries that perform the calculations.

The approach implemented relies, for the most part, on the experience of using relational databases to process information in neutron activation analysis [13, 14]. At that time, desktop DBMSs had relatively limited capabilities. Therefore, they were mainly tasked with storing structured information and generating various types of reports. The progress of the development of desktop database management systems and their convergence in functionality with industrial SQL systems allow today to solve significantly more complex tasks. The first version of the iPlasmaProQuad software was presented at the Euroanalysis 2019 conference [15].

The database currently includes over 50 tables and more than 110 queries. The tables store different data. The tables are prefixed, depending on their purpose, for ease of use:

c_—service user's control data; sample/calibration solution measurement data, batch processing algorithm control

parameters, batch data for each sample (mass, dilution, etc.). The parameters controlling the processing can be changed via the software interface;

h_—handbook data: isotope abundances, recommended contents of elements in standard samples (solutions and solids), statistical tables, relationships of different units, constants, etc.;

t_—temporary/imported data: temporary tables for importing mass spectra measurement results, checking their integrity;

x_—experimental data: copying of validated data from temporary import tables of measurement results and converting them to a standard format;

r_—results data: results of calibrations, calculation of isotope concentrations, isotope consolidation, results of introducing various corrections (matrix effect, calibration drift, interference, etc.);

aux_—auxiliary tables: auxiliary tables for intermediate calculations/data.

All working tables (t_, x_, r_, aux_) are initially present in the database (without records) for their inclusion in the data relational scheme and for correct query execution.

The main window is a system of 5 menu items, the functionality of which follows the name: File (select the file with the measurement data to be processed), Import (enter the measurement results of mass spectra into the database), ControlPanel (control panel for data processing, sets the control table data), Tools (set of functions controlling the database: clearing temporary tables, compacting the database, etc.). In addition, the main screen of the program has 5 tabs, which are accessed according to the current context of the program. The tabs are used to display various reports, manage the list of isotopes involved in the calculation of element concentrations and other tasks. The lower part of the window has a log-file output panel (indicating the status of the program at different stages of its operation). The windows look and what they do is described in the Operator's Manual (F1). Here are two examples. Figure 1 shows a fragment of a window with a list of measured batch samples received after data import into the database and a pop-up window for setting some parameters to control further data processing.

3.1 Data Integrity Check

Once the primary data from the mass spectrometer have been entered into the t_tables, they are supplemented with several reference data and checked for consistency using a query system. The result is a working x_tables, which does not change during processing to ensure that repeated processing cycles can be called with different parameters.

3.2 Codification of Samples

Codification is an important part of determining the correctness and unambiguity of possible mathematical operations in sample lot processing. A set of codification rules has been developed to identify the sample batch and the customer, parallel samples and parallel measurements of the same sample, the presence of an internal standard in the sample, the sample dilution factor, and other data to process them properly.

3.3 Calibration Procedure

It is common practice in ICP-MS analysis to measure in blocks: first, the calibration solutions are measured, then several samples are analysed (10–15, depending on sample type, variation in sensitivity, etc.), then calibration is performed again, and so on. The instrument's in-house software provides a calibration that opens a block of samples. The iPlasmaProQuad software is more powerful in this area: the concentration can be calculated by both opening and closing calibrations or by interpolating calibrations (between the preceding and closing calibrations, depending on the time of measurement) and by combined calibrations (for all blocks).

During the calibration process, an auxiliary table is first generated, containing the data for the standard solutions necessary to calculate the linear regression parameters for each isotope. The sums Σx^2, Σy^2, Σxy, and linear regression parameters for each isotope are calculated for each calibration block separately, including for the union of all blocks ($Y = b * x$). These parameters also include the values of standard deviations of the linear coefficient (b) and the calibration model (Y) to allow for the uncertainty introduced by the calibration in the concentration results. Two calibration tables are generated in which the concentrations of the elements are expressed in both ppb and nanomoles.

There are two models of calibration available to the user. One generally accepted mathematical model of calibration is based on the assumption of homoscedasticity (relative stability, homogeneity of the variance of the random error) of the observed Y values (model 1). This is a prerequisite for the application of the least squares method. Statistical analysis shows, however, that the variance of observed Y values is not constant but is approximately proportional to the square of the measurand. Then the logarithm of Y values will satisfy the homoscedasticity condition (model 2). In this

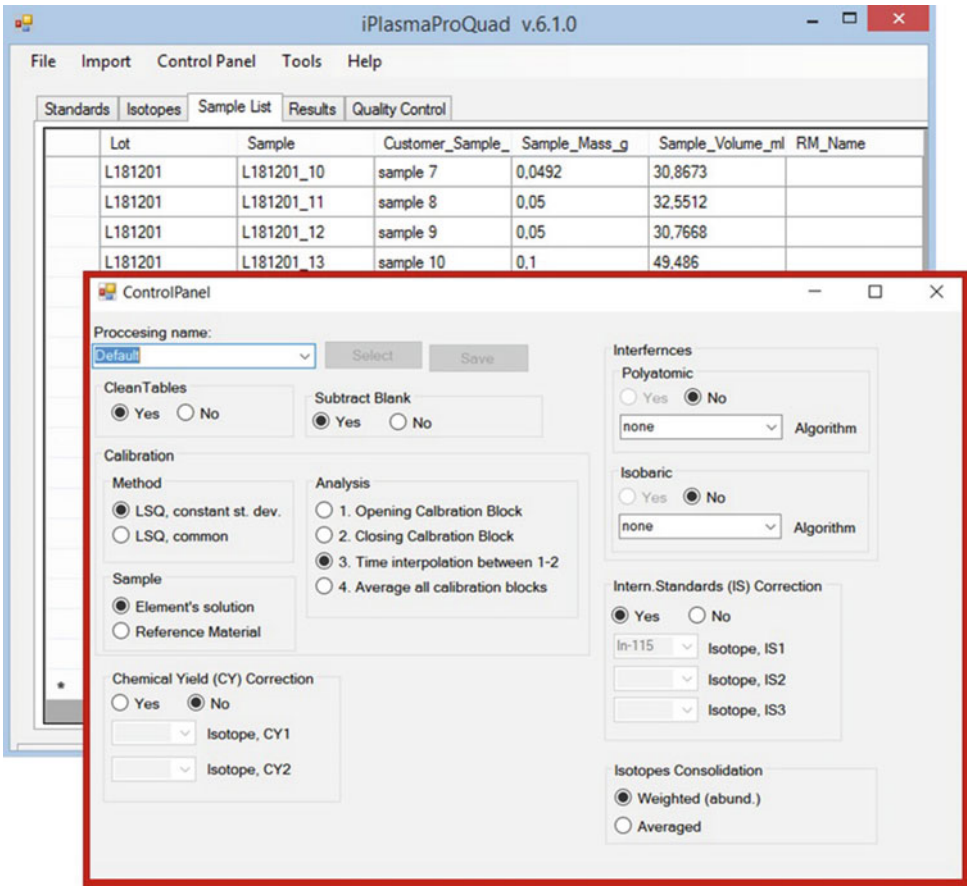

Fig. 1 Fragment of the main program window after entering data from the mass spectrometer and an example of the dialog box (framed) opened by calling the ControlPanel menu item

case, the error of the logarithm will correspond to the relative error of the measured quantity Y. By default, the program uses the latest calibration model (model 1 can be plugged in if desired). An important feature of the program is that it implements two branches using both homo- and heteroscedastic calibration curves to calculate the concentration.

3.4 Computation of Concentrations in a Series of Analyzing Solutions

Once the linear regression parameters ***Y=b*x*** are calculated for each isotope for each calibration block, they can calculate concentrations in the series of the analyzed solutions. The iPlasmaProQuad software defaults to the sensitivity coefficient ***b*** obtained by linear time interpolation between the opening and closing calibration block. Error estimates (variance) are calculated from the combined calibration as relative standard deviation value (1) and absolute standard deviation value (2).

$$\mathrm{dC} = \mathrm{Sqr}([\mathrm{dY0}]^2 + [\mathrm{db0}]^2) \quad (1)$$

where dY0 is the relative standard deviation of Y, db0 is the relative standard deviation of the coefficient b (when all calibration blocks are combined).

$$\mathrm{sC} = \mathrm{dC} * [\mathrm{Conc\_ppb}] \quad (2)$$

where [Conc_ppb] is the field containing the concentration of the isotope.

3.5 Correction for the Internal Standard

The concentration values calculated in the previous step can be refined by multiplying by a correction factor to account for changes in the sensitivity of the registration system. For this purpose, an internal standard (usually indium) of known concentration (e.g. 10 ppb) is added to the analysed solutions. The composition of the internal standard used is stored in table h_InternalStandards. Similarly, the standard deviation of the concentration of the internal standard is estimated, which is used to estimate the total uncertainty of the results when making sensitivity corrections to the registration system.

3.6 Accounting for Spectral Interferences

The problem of spectral interference in quadrupole mass spectrometry is solved either by using reaction (collision) cells or by a computation method. The latter method somehow relies on experimental results of determining the apparent concentrations of isotopes-analytes and mathematical methods for solving a system of equations.

The database includes a table of potential polyatomic interferences containing about 1 thousand records. The record contains the analysed isotope and the isotope fields composing the polyatomic components. The record includes a field with the apparent concentration of the analysed isotope. The value of the apparent concentration is determined during the analysis, based on the measurement results of various type samples. Among them are blank samples, solutions of standard samples, or solutions of model mixtures. When assessing the correction value for polyatomic interferences involving main elements (which are usually not determined by the ICP-MS method), it is necessary to have information about their concentration (for example, according to ICP-AES data or others).

3.7 Estimation of Detection Limits and Subtraction of Blank Test Results

The isotope concentrations are corrected for the content of analysed elements detected in the blank samples. For this purpose, the mean values and errors of blank samples for different dilutions are computed and entered in an auxiliary table by the correspondent queries. Then the software calculates the detection limits for each isotope for blank samples (DL_Lb) at different dilutions using the Student's t-distribution (table h_t_Student).

$$\mathrm{DL\_Lb} = \mathrm{sC\_Lb} * \mathrm{t\_95(n\_Lb)}, \quad (3)$$

where sC_Lb is the standard deviation of the element concentration (ppb) in the blank sample (Lb), t_95(n_Lb)- data from the Student's table.

Calculate the lower (Lci) and upper (Uci) limits of the confidence interval for the element concentration after background subtraction:

$$\mathrm{Lci} = [\mathrm{C}] - \mathrm{Sqr}(([\mathrm{C\_corr\_In}] * (1 - 1/[\mathrm{Err\_Factor\_corr\_In}]))^2 + [\mathrm{CI\_lb}]^2) \quad (4)$$

$$\mathrm{Uci} = [\mathrm{C}] + \mathrm{Sqr}(([\mathrm{C\_corr\_In}] * ([\mathrm{Err\_Factor\_corr\_In}] - 1))^2 + [\mathrm{CI\_lb}]^2) \quad (5)$$

where CI_Lb= CI_Lb = sC_Lb * t_95(n_Lb) / sqrt(n_Lb) the confidence interval for determining the mean value of the element concentration.

Next, the significance of the concentration found compared to the detection limit value is determined. At this stage, three logical fields are generated for the analyst to characterize the three levels of reliability of the found concentration values of the isotope of the element being determined (Table 1).

This produces three qualitative attributes characterizing the analysis result: “confident” when criterion 3 is met; “acceptable” when criterion 2 is met, but criterion 3 is not; “semi-quantitative” when the analysis result is close to the detection limit, i.e., criterion 1 is met, but criterion 2 is not.

3.8 Determining Elemental Concentrations

The iPlasmaProQuad software has sufficient functionality related to the processing of analysis data by individual isotopes to determine element content. The user can select weight functions (isotope abundance, the uncertainty of analysis results, etc.) to calculate element concentrations in samples considering all dilutions and sample mass. It is also possible to exclude certain isotopes (e.g. in the case of spectral interference) when calculating the concentration of an element.

Furthermore, the software identifies parallel samples from the sample code and can consolidate the data in a statistically sound manner. This also applies to parallel measurements of the same sample, e.g. at different dilutions.

3.9 Estimating the Uncertainty of the Concentration Measurement

Ultimately, the software calculates the overall uncertainty of the element concentration measurement in the sample using the partial uncertainty values estimated at each step. They are sample (peak) measurement, calibration, the introduction of correction for changes in sensitivity of the measuring system over time, consideration of matrix effects, the introduction of correction by spectral interference (not yet fully implemented), determination of element concentration by isotope (for multi-isotopic elements), and some other factors.

3.10 Quality Control of the Analysis Results

A special feature of the software is the possibility to carry out quality control of the obtained data. The database contains information for over 30 geological reference materials

Table 1 Reliability criteria for the analysis results

Case	Field name	Status	Criterion
1	Over DL	"Yes"	(1) if C > DL, i.e., the element concentration found is above the detection limit
2	Sign	"Yes"	(2) if Lci > 0, i.e., the lower limit of the 95% confidence interval of the concentration is above zero
3	Sure	"Yes"	(3) if Lci > DL, i.e., confident determination

of different origins used in the lab. The user can extend this list by editing the data in the table h_RMs_SolidList.

If a reference material(s) has been included in the batch of samples analysed, the software automatically provides a report comparing the analysis results obtained with the certified values, including the confidence interval and the relative deviation from the certificate. The results are placed on the Quality Control tab.

3.11 Reporting and Quality Control of Analysis Results

iPlasmaProQuad software is arranged in such a way that initially, the database contains results *of all* (!) calculation variants. The formation of reports is determined by the customer depending on the tasks of the investigation, for which the analysis was carried out. This choice is determined by the parameters set in the control panel of the program. The results are accessible for viewing in a window of the program, tab Results. Simultaneously, the software creates an export file in MS Excel spreadsheet format.

A series of tabs representing similar data sets (Sample element) is placed in the file, which can be seen as a metaphor for a multidimensional array (Fig. 2).

The arrays contain the following data:

- results of the analysis (no data is available if the element is below the detection limit);
- the uncertainty of the measurement results, the detection limit for each element in each sample;

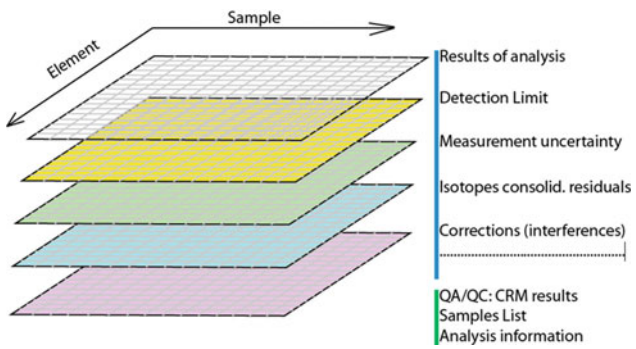

Fig. 2 Diagram of a multidimensional array of analysis results that are exported to MS Excel tabs

- three tabs containing logical information about the reliability of the measurement results according to the criteria given in Table 1;
- the standard deviation of the results of the analysis of the parallel samples (if they were presented in a batch);
- is the standard deviation of the results of parallel measurements of the same sample, including at different dilutions;
- quality control of the analysis (degree of deviation from certificate data) of the reference sample composition (if it/they were present in the sample lot);
- convergence of isotope analysis data when determining an element (for multi-isotopic elements);
- normalized concentrations (e.g. relative to chondrites, basalts-MORB) and several other data.

In this way, the array index (i, j) can operate with related data when performing intelligent data processing, constructing dependencies concerning the uncertainty of the analysis results when solving problems in the subject area.

Moreover, macros have been prepared in the template of the MS Excel file where the above information is uploaded. The macros can mark the degree of reliability of the data by highlighting them with the background color of the cell on the tab with the analysis results (red, yellow for cases 1 and 2 indicated in Table 1), as well as indicate by font type the results of the analysis of parallel samples (bold) and parallel measurements (italics).

3.12 Use of Concentration Measurement Uncertainty Data When Analysing a Single Sample

It is common practice for geological samples to be collected in the field, in the study area, with reference to the sampling location (coordinates, petrological/mineralogical characteristics, etc.). The laboratory then determines a geochemically representative batch of samples based on the results of the preliminary study, requiring detailed elemental analysis, including the determination of trace elements. At this stage, each sample is represented by a single sample, assuming that the analytical methodology used is well established and its metrological characteristics have been determined. Usually, one or more reference materials of a similar type are added

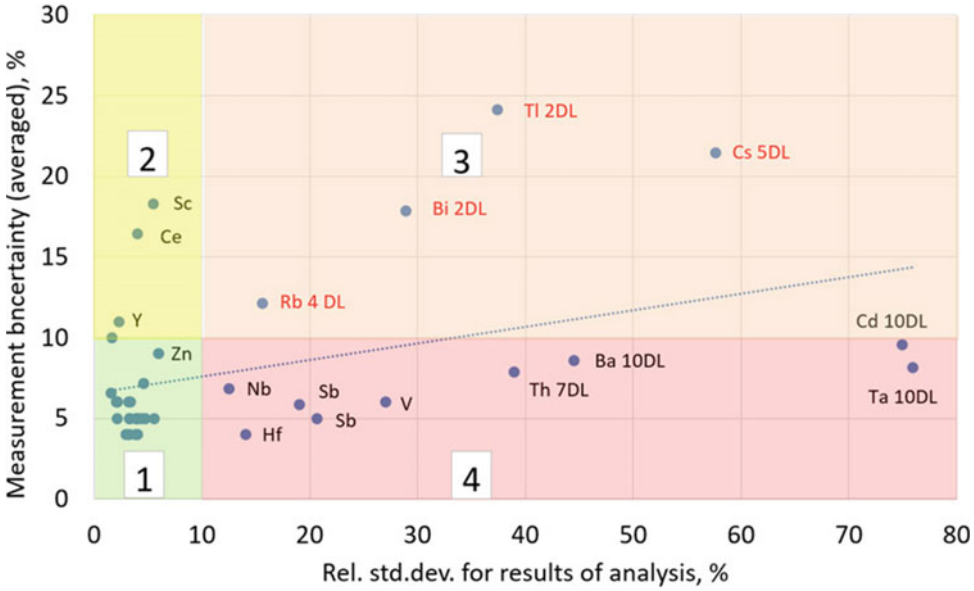

Fig. 3 Results of the analysis of the BIR-1 standard sample. Seven parallel samples, the elements are plotted in the coordinates mean concentration measurement uncertainty (%) and relative standard deviation of experimental results and certificate (%). The designation nDL (next to the element designation) indicates the excess of the concentration found over the detection limit (DL)

to the batch of samples to control the quality of sample preparation. If reliable and highly reproducible decomposition methods are relied upon, then the uncertainty values obtained in sample measurement can provide useful information in interpreting the data and reveal some problems.

A series of experiments were carried out to illustrate this point. In one of them, a set of seven parallel samples of a well-certified basalt reference material BIR-1 (USGS) was analysed. The decomposition methodology is presented in Ref. [5]. Using iPlasmaProQuad software, processing of samples, including estimation of uncertainty of concentration measurements and calculation of deviation of mean values of certain concentrations from the certificate, were performed. The results of comparison of the relative standard deviation of the analysis results from the certificate and the mean value of uncertainty of concentration measurement for all samples are presented in Fig.3. Assuming that the uncertainty of acceptable quality results should not exceed a threshold of 10%, several zones can then be distinguished.

Zone 1—no problems were found with the results. Interestingly, the uncertainty of the single measurement corresponds to the relative standard deviation of the analysis results from the certificate;

Zone 2—exceeds the threshold of 10% for the uncertainty value of a single sample concentration measurement due to calibration problems;

Zone 3—high uncertainty in measuring sample concentrations correlates with the relative standard deviation data with the certificate. This is explained by the fact that the content of the elements in this zone is close to the detection limit;

Zone 4—problems with the determination of elements in this zone are either due to problems with sample preparation (sample decomposition) or (less likely) due to the inaccuracy of the certificate.

4 Conclusion

When carrying out mass spectrometric analysis of a series of samples, the device generates large arrays of homogeneous data. A relational database management system (MS Access) is an off-the-shelf solution for handling arrays of homogeneous data. It is shown that the mathematical capabilities of modern relational data management systems (MS Access) are sufficient to process data in a quadrupole ICP-MS. The processing algorithm can be transferred to a network database environment MS SQL, which is easily scalable and is now an industry standard. Users of the developed program receive analysis results in a qualitatively new form (a multidimensional array of structured information), which, in turn, provides an increase in the level of research in the subject area.

Acknowledgements This work is conducted under the GEOKHI RAS state assignment and supported in part by RFBR grant 19-03-00953. The authors are grateful to E. I. Bozhenko and A. M. Zybinsky for their contributions to the development of the software.

References

1. Linge, K.L., Jarvis, K.E.: Quadrupole ICP-MS: introduction to instrumentation, measurement techniques and analytical capabilities. Geostand. Geoanal. Res. **33**(4), 445–467 (2009). https://doi.org/10.1111/j.1751-908X.2009.00039.x

2. Balaram, V.: Current and emerging analytical techniques for geochemical and geochronological studies. Geol. J. **56**(5), 2300–2359 (2021). https://doi.org/10.1002/gj.4005
3. Cotta, A.J.B., Enzweiler, J.: Classical and new procedures of whole rock dissolution for trace element determination by ICP-MS. Geostand. Geoanal. Res. **36**(1), 27–50 (2012). https://doi.org/10.1111/j.1751-908X.2011.00115.x
4. Matusiewicz, H.: Sample preparation for inorganic trace element analysis. Phys. Sci. Rev. **2**(5) (2017). https://doi.org/10.1515/psr-2017-8001
5. Karandashev, V.K., Khvostikov, V.A., Nosenko, S.V., Burmii, Z. P.: Stable highly enriched isotopes in routine analysis of rocks, soils, grounds, and sediments by ICP-MS. Inorg. Mater. **53**(14), 1432–1441 (2017). https://doi.org/10.1134/s0020168517140084
6. Kolotov, V.P., Zhilkina, A.V., Shirokova, V.I., Dogadkin, N.N., Gromyak, I.N., Dogadkin, D.N., Zybinsky, A.M., Tyurin, D.A.: A new approach to sample mineralization in an open system for the analysis of geological samples by inductively coupled plasma mass spectrometry with improved performance characteristics. J. Anal. Chem. **75**(5), 569–581 (2020). https://doi.org/10.1134/S1061934820050081
7. Tharaud, M., Gardoll, S., Khelifi, O., Benedetti, M.F., Sivry, Y.: uFREASI: user-FRiendly Elemental dAta procesSIng. A free and easy-to-use tool for elemental data treatment. Microchem. J. **121**, 32–40 (2015). https://doi.org/10.1016/j.microc.2015.01.011
8. Paton, C., Hellstrom, J., Paul, B., Woodhead, J., Hergt, J.: Iolite: freeware for the visualisation and processing of mass spectrometric data. J. Anal. At. Spectrom. **26**(12), 2508–2518 (2011). https://doi.org/10.1039/c1ja10172b
9. Fleischer, H., Adam, M., Thurow, K., IEEE: Flexible Software solution for rapid manual and automated data evaluation in ICP-MS. In: 2015 IEEE International Instrumentation and Measurement Technology Conference (I2mtc), pp. 1602–1607 (2015)
10. Zhang, L., Ren, Z.Y., Xia, X.P., Li, J., Zhang, Z.F.: IsotopeMaker: a Matlab program for isotopic data reduction. Int. J. Mass Spectrom. **392**, 118–124 (2015). https://doi.org/10.1016/j.ijms.2015.09.019
11. Lopez-Fernandez, H., Pessoa, G.D., Arruda, M.A.Z., Capelo-Martinez, J.L., Fdez-Riverola, F., Glez-Pena, D., Reboiro-Jato, M.: LA-iMageS: a software for elemental distribution bioimaging using LA-ICP-MS data. J. Cheminform. **8**,(2016). https://doi.org/10.1186/s13321-016-0178-7
12. Lugli, F., Weber, M., Giovanardi, T., Arrighi, S., Bortolini, E., Figus, C., Marciani, G., Oxilia, G., Romandini, M., Silvestrini, S., Jochum, K.P., Benazzi, S., Cipriani, A.: Fast offline data reduction of laser ablation MC-ICP-MS Sr isotope measurements via an interactive Excel-based spreadsheet "SrDR." J. Anal. At. Spectrom. **35**(5), 852–862 (2020). https://doi.org/10.1039/c9ja00424f
13. Kolotov, V.P., Atrashkevich, V.V.: Software Aspro-Nuc—gamma-ray spectrometry, routine Naa, isotope identification and data management. J. Radioan. Nucl. Ch. Ar. **193**(2), 195–206 (1995). https://doi.org/10.1007/Bf02039875
14. Kolotov, V.P., Atrashkevich, V.V.: Data-processing in routine neutron-activation analysis using a data-base management-system. J. Anal. Chem. **49**(1), 95–99 (1994)
15. Kolotov, V.P., Zybinsky, A.M., Zhilkina, A.V: Methodology and software for comprehensive ICP-QMS data processing using advanced capabilities of relational data base management system. In: XX Euroanalysis-2019 Conference, Istanbul University, Turkey, September 1–5, pp. 145–147 (2019)

Statistical Methods in Analytical Chemistry

V. A. Dementiev

1 Introduction

Several years ago, the author searched Scopus for keywords combination *Analytical Chemistry* AND *Mathematical Statistics* and received a list of 650 articles. Most of these articles were related to the activities of industrial laboratories, research on environmental pollution and food quality, medicine and pharmacology. What was the place of statistical methods in these papers? There were four categories: (a) references of the authors, what methods of statistics they used when conducting specific analyzes, for example [1]; (b) reports on the search for new statistical techniques, if well-known ones do not give acceptable results, for example [2]; (c) recommendations of higher organizations, societies and committees, for example [3]; (d) educational literature for industrial workers, for example [4]. It seemed to me that such articles is not interesting for those who are engaged in fundamental research in analytical chemistry.

The set of articles on the use of chemometric methods in analytical chemistry stands apart. These methods cannot be regarded in the strict sense as methods of mathematical statistics, although they, of course, rely on it. Mathematical statistics deals with relatively simple situations in which randomness manifests itself. There are not so many such typical situations in analytical practice. But in connection with the influx of complex instrumental methods of research, which give huge arrays of data of a complex structure, it became necessary to somehow understand this structure in order to highlight clear analytical signals. And since mathematical statistics cannot offer systematic recipes here, researchers are trying to invent various heuristic approaches to separating useful analytical signals from useless information noise. It is these attempts that constitute a new branch of the art of primary processing of experimental data. It is clear that this approach is not typical for research in fundamental analytical chemistry. Like any fundamental science, this branch of chemistry tries to simplify the studied natural and laboratory situations, and not complicate them.

Then I limited my search Scopus for keywords combination *Analytical Chemistry* AND *Mathematical Statistics* only by journals Analytical Chemistry and Analytica Chimica Acta and received a list of 23 articles. Why so little? Why is analytical chemistry so little interested in this data processing tool? Let me repeat once more what was said above in other words. Fundamental science is looking for either new natural laws or means of a breakthrough in solving long-standing and unsolved problems. Such searches require the utmost possible simplification of situations. This can be achieved either through a sophisticated experiment that eliminates all unimportant factors, or through deeply thought-out theoretical models. These funds eliminate the sources of accidents in advance, leaving only some unavoidable minimum of them. And then the researcher does not need complex statistical methods and uses simple standard ones.

There is another important reason for the weak interest of an analytical chemist in the methods of mathematical statistics. The fact is that by working hard on a complex problem, at the forefront of a narrow field of knowledge, the researcher is very deeply immersed in the essence of the data obtained. No one knows the behavior of this data better than the researcher himself. In particular, no specialist in the methods of mathematical statistics can as deeply know the nature of these data. Therefore, for a researcher of a complex problem, the simplest means of representative statistics are usually sufficient to present their results so that colleagues can unambiguously understand the data obtained by the author, try to reproduce the new results and compare them with the author's results. Of course, such a comparison requires an objective assessment of the accuracy of the data obtained by different authors in not quite the same laboratory

V. A. Dementiev (✉)
Vernadsky Institute of Geochemistry and Analytical Chemistry, Russian Academy of Sciences, 19 Kosygin St., Moscow, 119991, Russia
e-mail: d_vasily@mail.ru

V. P. Kolotov and N. S. Bezaeva (eds.), *Advances in Geochemistry, Analytical Chemistry, and Planetary Sciences*,
https://doi.org/10.1007/978-3-031-09883-3_37

or natural conditions. This is where information about the statistical properties of the data obtained helps, and it is enough to express this information in a simple form of confidence intervals with their declared reliability. But when, on the basis of a breakthrough in solving a problem (for example, a sharp decrease in the detection limit of a substance in a sample), new analytical methods are built, one has to deal with additional factors of an unclear statistical nature. Then it is necessary to select adequate statistical recipes, or to develop new chemometric methods of data processing.

Based on the foregoing, the author sets himself the task of identifying which statistical methods may be useful in the research, and not in the production activities of the analytical chemist.

2 Univariate Statistics

When studying even very complex phenomena, we want to represent our final understanding with one number. Unfortunately, our views are always somewhat vague. Therefore, a conscientious researcher needs a means to present the main result in the form of a confidence interval. He finds such means in one-dimensional mathematical statistics. This is the main section of statistics for any researcher. One-dimensional statistics attempts to describe the behavior of the measurement result of a single characteristic x of an object under such constant conditions when repeated measurements give different values. Such behavior is considered fully described if it can be formulated in the form of a distribution law for the values of x. Such a law can be formulated in various ways.

In manuals on statistics, the distribution law of x is most often given by a mathematical formula. Using this formula, you can calculate either the probability of an exact value of x occurring, or the probability of a value of x falling within the interval from x to $x + dx$. In the first case, the law is given by the formula

$$W = W(x, a), \tag{1}$$

where a is a vector of parameters characterizing the measurement conditions. In the second case, the law is given by the formula

$$w = w(x, a), \tag{2}$$

where w is the probability density, which is then used to calculate the probability

$$W(x, dx) = w(x, a)dx.$$

I do not know of examples of works where the researcher who carried out the measurements would specify the forms of laws (1) or (2) established by him as a report to the scientific community. It is the responsibility of the researcher to establish one of these laws. It comes down to choosing a specific formula and determining the vector of parameters a characterizing the experimental conditions. After that, on the basis of the established specific law, various derived quantities are calculated, which briefly and clearly describe the behavior of the object. Typically, these are the mean x_{av}, the standard deviation Δx, and the reliability Q of the confidence interval $x = x_{av} \pm \Delta x$. If you follow the rules of good manners, then it is necessary to mention the name of the law on the basis of which the confidence interval was obtained. This is usually not done. The law is simply implied. In radiometric studies, each detector count is considered a rare event. Then (1) is Poisson's law. From it follow the formulas for calculating the values of x_{av}, Δx and Q. The researcher needs to determine the value of the only parameter $a = \lambda$ from the results of the experiment. This is the average rate of arrival of pulses during one measurement. If not a discrete, but a continuous characteristic of an object is measured, then it is usually assumed that (2) is a normal distribution law with two parameters: the mathematical expectation μ and the variance σ^2. All values included in the expression for the confidence interval are easy to calculate. It remains for the researcher to determine the values of the parameters μ and σ^2 from the results of the experiment. All these positions and computational recipes are well known. There are also known troubles associated with the application of these recipes in practice. Let us be absolutely sure that in the experiment we are dealing with the manifestation of the normal distribution law. Very good. The trouble is that we never know and will never know the specific values of the parameters of this law μ and σ^2. We have to be content with empirical estimates of these parameters. Instead of μ, we, according to the experimental data, find the average value

$$x_{av} = \frac{1}{n}\sum_{i=1}^{n} x_i, \tag{3}$$

where i is the number of the measurement; n is the number of measurements. Instead of σ^2, we, according to the experimental data, find an empirical estimate of the variance

$$s^2 = \frac{1}{n-1}\sum_{i=1}^{n} (x_{av} - x_i)^2. \tag{4}$$

Usually we are interested in the statistical properties not of the results of measurements x_i, but of the random variable x_{av}. With its mathematical expectation everything is in order, it is also equal to μ, regardless of the number of dimensions. But the variance behaves worse, it is equal to s^2/n, that is, it depends on the number of measurements. Note that the sum

in (4) is supposed to be divided not by n, but by the number of degrees of freedom $k = n - 1$. This is a payment for the fact that in (4) we use not the theoretical value of μ, but its estimate x_{av}, which connects all the values x_i by a linear dependence. A nuisance arises—we claim that we firmly know the distribution law manifested in the experiment, but we do not know the exact parameters of this law.

There is still a nuisance. If we knew the exact form of the normal law that manifested itself, then we could use its consequence that the normalized random variable

$$Z = \frac{\mu - X}{\sigma}$$

is also distributed according to the normal law with parameters 0, 1. This would be very convenient when constructing a confidence interval $x = x_{av} \pm \Delta x$ for a separate measurement result. We could write $\Delta x = t\sigma$ with the reliability Q, which would be found from the tables of the normal distribution, depending on the chosen coefficient t. Or, on the contrary, to set the reliability Q, and this would automatically lead to the choice of the coefficient t. However, it turns out that just from the normal distribution for the random variable x_{av} of interest to us, a consequence is obtained: the normalized random variable

$$z = \frac{\mu - x_{av}}{s/\sqrt{n}}$$

is no longer distributed according to the normal law, but according to the Student's law. With the help of this law, the confidence interval is constructed in the same form

$$\Delta x_{av} = t\frac{s}{\sqrt{n}},$$

but with the same value of reliability Q, the coefficient t turns out to be increased. And it is the larger, the smaller the number of degrees of freedom k. We were lucky only in that for very large k, the Student's distribution quickly approaches the normal distribution. However, if we have no time to carry out hundreds of measurements of the same quantity and we only make three measurements, then

$$\Delta x_{av} = \frac{s}{\sqrt{3}}$$

and x_{av} lies in the interval $x = x_{av} \pm \Delta x_{av}$ with reliability $Q = 57.7\%$.

However, these are far from the main troubles. Let's turn to law (2). This law in its own specific language describes the conditions of the experiment. The manners and customs of natural science require the researcher to have comprehensive information about the conditions of his experiment. Consequently, he is obliged not only to mention in the report which distribution law commands the behavior of the measured quantity, but also to independently establish the form of this law. Nobody, as a rule, does this, since two geniuses—Gauss and Chebyshev—have already figured out and explained to us two important points.

1. *The Gaussian normal distribution law is extremely convenient for deriving formulas for all computational recipes used in the practice of processing measurement results. There is simply no other law so convenient in its form.*
2. *If Nature supplies to the input of the measuring device a quantity distorted by an infinite number of small random factors, and the researcher carries out an infinite number of measurements of this quantity, then at the output of the device there is a number of random numbers obeying the normal distribution law. This follows from Chebyshev's law of large numbers and from Lyapunov's theorem.*

We all understood this and got used to using it. But scientific thought does not stand still, bewilderment and discontent arise. This grumbling of discontent can be seen in the set of texts that I received from the Scopus system. This means that the analysts were among the dissatisfied.

It is clear who is to blame—Gauss and Chebyshev. What to do is also more or less clear—it is nevertheless necessary to clarify the conditions of the experiment including the distribution law of the measured quantity, since we use this law. Here is the third cardinal question—how are we going to do this—for some reason it is not customary to ask. Of course, experts in the methods of mathematical statistics asked this question, but they did not report very loudly what they had gotten with the answer. And it turned out that the most difficult task of statistics, practically not solvable in practice, consists precisely in establishing the specific form of the law (2) or at least in testing the hypothesis that the results of a series of measurements agree with the normal law.

Why do we have the right to be unhappy with Gauss's law? Everything is fine in this law

$$w(x) = \frac{1}{\sigma\sqrt{2\pi}}\exp\left(-\frac{(x-\mu)^2}{2\sigma^2}\right), \tag{5}$$

except for the difficulties with the physical interpretation of those predictions that it gives on its edges, where $|x - \mu| \gg \sigma$. The law predicts an extremely low probability of detecting such a value of x in an experiment. But this probability is not zero. This means that we have the opportunity to observe at least a few such cases, if we have patience and carry out these measurements millions and billions of times. However, any experimenter in an informal setting will say: *This can never be*. The author can justify this *never* by the laws of physics. But this can also be done

mathematically. Pay attention to the prerequisite for the practical feasibility of the normal law—an *infinite* number of measurements and an *infinite* number of random extraneous influences are required for the real distribution law to converge to the normal one. And we know that if *infinite* appears in physical reasoning and conclusions, then this is a reliable sign that the physicist does not understand something here. A mathematician has the right to imagine infinity and investigate its manifestations in mathematical objects. But we are investigating physical reality, natural objects, where infinity has no place.

So, we should understand that law (5) is not a law of Nature, but our model idea of a law unknown to us. It can be conveniently used, but with an eye to the limits of its applicability. We do this with those empirical laws that we discover and formulate in natural science. Why should law (5) be an exception? If we do not remember that these are our model concepts of the behavior of the measured quantities, and take it especially seriously, then very gross errors in the interpretation of experimental results are possible. Hence, dissatisfaction with this law arose. It is possible to predict with confidence the further development of this unpleasant situation: since all computational recipes for one-dimensional statistics are derived from law (5), then over time there will be dissatisfaction with other formulas of mathematical statistics.

Here the author must say a few words to justify the entire glorious cohort of specialists who developed the initial ideas of Gauss and Chebyshev. The point is that mathematical statistics is not a science. It is not even part of mathematics. I will refer to the private communication of the professional mathematician V.M. Imaykin, a pupil of the Kolmogorov school: *Kolmogorov, in the end, found the mathematical foundations of the theory of probability. But even he could not find the mathematical foundations of statistics*. The author is not a mathematician and does not understand what the mathematical foundations of any branch of mathematics are. However, there is something useful in this statement for understanding our relationship with mathematical statistics. So, now we understand that Gauss and Chebyshev are not to blame, but natural scientists. This can be seen from the stages in the development of mathematical statistics.

1. In geodesy, a practical difficult problem has arisen to prevent the uncontrolled accumulation of measurement errors, when, moving from benchmark to benchmark, surveyors add one to the other the values of the changed and calculated distances. It took the genius of Gauss to guess the correct form of the one-dimensional law of distribution of errors and come up with a least squares method for uniformly spreading all errors over all geodesic reference points.
2. The explosion in productivity in US agriculture posed new, already multidimensional, statistical challenges. Specialists from Europe was attracted. They solved these problems and left their names in history. Very soon, similar tasks were realized in medicine. Medical data processing standards were formulated based on methods developed for agriculture. These standards are used by the whole world today.
3. The explosion of world banking has demanded new methods for analyzing very complex data from practical psychology. The diversity of these data suggested their statistical nature. The names of people who developed new methods of multivariate statistics appeared in statistics. It turned out that these methods can only be implemented using powerful computing technology. But by that time, computers had already appeared. And now chemometry is adapting these methods (factor analysis, principal component analysis) to the problems of processing large amounts of experimental data.

We, workers in the fundamental branches of natural science, do not set such acute tasks for specialists. Therefore, we ourselves are to blame for some of our statistical troubles. The rescue of drowning people is the work of the drowning people themselves.

3 Multivariate Statistics

The simplest case of multivariate statistics is known to almost everyone who measures two quantities at the same time in order to find out how one quantity depends on the other. This dependence, when it has already been identified, is best expressed by some kind of analytical function, the parameters of which are determined just from the measurements. However, there is a long way to go if such measurements are taken for the first time. Due to the fact that both quantities are measured with errors, the functional dependence is obscured. First of all, it is necessary to find out whether there is any relationship between the two quantities, how close it is. The simplest assumption is made that the dependence is similar to linear. This can always be plausible if both values vary within small limits. To assess the degree of closeness of dependence to a linear one, it is customary to calculate the correlation coefficient. Such a characteristic of the phenomenon under study is a parameter of the two-dimensional distribution density of the simultaneous appearance of two measured quantities. Let us focus on this simplest case of multidimensional statistics, since it allows us to quite clearly consider all the advantages and all the difficulties of the general case of simultaneous measurement of many quantities.

Let me remind you how the idea of the correlation coefficient between two random variables Y and X arises. Let these values obey each separately their normal distribution with the parameters μ_Y, σ_Y and μ_X, σ_X. Then the joint distribution of these quantities, that is, the probability density of detecting simultaneously the quantity Y in the vicinity of a particular value of y and the quantity X in the vicinity of a particular value of x, is determined by the two-dimensional normal distribution

$$w(y,x) = \frac{1}{2\pi\sigma_Y\sigma_X\sqrt{1-\rho^2}} \exp\left(-\frac{1}{2(1-\rho^2)}\left[\frac{(y-\mu_Y)^2}{\sigma_Y^2} + \frac{(x-\mu_X)^2}{\sigma_X^2} - 2\rho\frac{(y-\mu_Y)(x-\mu_X)}{\sigma_Y\sigma_X}\right]\right). \quad (6)$$

Theoretically, the relationship between Y and X is characterized by the covariance value cov(YX), which is an analogue of variance. This is the expected value of the product

$$(Y-\mu_Y)(X-\mu_X).$$

The correlation coefficient

$$\rho = \frac{\mathrm{cov}(YX)}{\sigma_Y\sigma_X}$$

also characterizes the relationship between the quantities Y and X, but in practice it is more convenient than covariance, since ρ is a dimensionless quantity. The structure of the cumbersome formula (6) is easy to understand by examining the special cases of the degree of dependence between Y and X.

If Y and X are statistically independent, that is, $\rho = 0$, then the right-hand side of (6) turns into the product of two normal densities.

If Y and X are related by an exact linear relationship $Y = aX + b$, then on the right-hand side of (6) there appears an uncertainty $0 \times \infty$. And we know—as soon as infinity appeared in the reasoning, it means that someone does not understand something. If Y and X are connected by exact functional dependence, then there is nothing to talk about probabilities and explore the structure of formula (6). Still, thanks to mathematics, which gives us in difficult cases an understanding of the degree of our misunderstanding.

If $-1 < \rho < 1$ and $\rho \neq 0$ then there is a linear regression relationship between Y and X

$$y - \mu_Y = \rho\frac{\sigma_Y}{\sigma_X}(x-\mu_X). \quad (7)$$

So we see that the correlation coefficient is the most useful thing. However, we are in trouble again. This time they are quite large. Compare the construction (6) with the simple construction (5), taking into account also the construction for ρ. It is clear that we are in for even bigger troubles than those described in the section on univariate statistics. How to find in practice the value of r, which is an empirical estimate of the theoretical value of ρ? It's not that hard. We will proceed as in one-dimensional statistics—we will replace all theoretical values in the definition of ρ with their empirical estimates. But what are the statistical properties of r? Here is the trouble:

1. The value of r approaches ρ only for a huge set of pairs of measurements y_i, x_i. Moreover, it always remains less than ρ.
2. The variance r depends not only on the number of measured pairs, but also on the value of the correlation coefficient itself.

The latter is especially unpleasant when the theoretical value $\rho \approx 0$. Then the empirical value of r can turn out to be practically anything you like, even with a large number n. This can be seen from the approximate formula

$$\sigma_r \approx \frac{1-\rho^2}{\sqrt{n}}. \quad (8)$$

We are already prepared for the fact that theoretical variances are always less than their empirical estimates. Consequently, the confidence interval for r calculated using (8) will be greatly narrowed. Let it be known from somewhere that under specific conditions $\rho = 0$. Let us make three measurements of the pairs y_i, x_i and calculate the value of r. With high reliability, we can expect that r will be in the range from -0.58 to 0.58. Most likely, these limits can be even wider. And we tend to think that the correlation coefficient $r = 0.6$ is quite decent. It turns out indecent.

Everything that has been said above about the troubles in finding the correlation coefficient refers to the hypothetical case of two quantities Y and X following the two-dimensional normal distribution law. But if we know that in one-dimensional dimensions we have little chance of observing manifestations of law (5), then what are the chances of observing manifestations of law (6) in two-dimensional dimensions? A sad conclusion follows—since all complex formulas of mathematical statistics are derived only from law (5), then in practice statistics cannot tell us anything about the properties of the correlation coefficients we measure.

Fundamental methodological difficulties in the search for correlations between experimental data arise when we simultaneously measure a set of quantities between which mutual influences can appear. The most common case is the calibration of a device that measures the concentrations of

the components of a mixture of substances by spectral characteristics. Some substances here tend to suppress the spectral manifestations of other substances. And it is clear that the search for pairwise correlations, described above, cannot be dispensed with here. There are multiple correlations. We simply cannot measure multiple correlations. But multivariate mathematical statistics can describe multiple correlations based on the multivariate normal distribution of the joint manifestation of random variables X. Here $X = [X_1, X_2, \ldots, X_N]$ is a row matrix, and its elements are random variables. The formula for the multivariate distribution law is a generalization of (6) to the N-dimensional case. The difference is that in this case, to describe the relationships between random variables, they use not the correlation coefficients, but pair covariance. The expression of this law includes a square matrix C, the off-diagonal elements of which are paired covariance $\mathrm{cov}(X_iX_j)$ and diagonal elements $\mathrm{cov}(X_iX_i) = \sigma_i^2$ are one-dimensional variances.

Matrix C is the main object of research in multivariate statistics. Some of these research methods may interest us professionally.

In the method of principal components, the matrix C or its empirical estimate based on experimental data is investigated. It is diagonalized and its eigenvalues are sorted in descending order and its eigenvectors are rearranged accordingly. Formally, this is a transition from random variables X to other random variables Y. The transition is made just with the help of the matrix of eigenvectors. Each new random variable in the Y matrix is a linear combination of all values from X with coefficients equal to the elements of the appropriate column of the eigenvector matrix.

It turns out that the results of this conversion are extremely useful. The eigenvalues of the matrix C are one-dimensional variances of new, already statistically independent random variables Y. The variables Y have very different statistical properties. Large variances are the first. This means that these linear combinations of the initial random variables are subject to the greatest fluctuations and variations in this experiment. They influence each other the most. Such combinations are called main components. It may well turn out that in the column of the eigenvector of the first element of Y, some elements are equal to zero or close to zero. This means that the corresponding elements of the X matrix do not affect the variability of this new Y_1 value. Thus, it becomes clear between which X there is the strongest mutual influence. They are what you need to pay close attention to when developing an analytical method.

Among the eigenvalues of the matrix C, there may be zero or almost zero values. This means that some linear combinations of the original quantities do not vary at all and behave like constants. You should not rely on them at all when developing an analytical method. Thus, there is a reduction in the number of random variables in this experiment.

I am not sure that it is so easy for analysts immersed in the fundamental problems of their science to master and apply the principal component method in their research routine. I am not sure that physicists are ready to give analysts specific methodological advice related to statistics. But I am sure that it would be useful to start joint work in which we would find out which of the methods of mathematical statistics we know are adequate to the research routine of analysts. However, such searches have already begun relatively long ago [5–7]. Attempts of mathematicians to take part in this process are visible [8]. There is a work that directly illustrates the meaning of my proposal [9].

4 How to Overcome All the Noted Statistical Difficulties

The author sees the only available way: to rely not on model ideas about the distribution laws of our experimental data and not on the derivation of formulas for calculating the statistical properties of our complex functions from these data, but on these data themselves and on those statistical properties that they themselves exhibit in this particular experiment. If we need some functions from our data, then we will calculate these functions, while examining their statistical properties.

This idea is in perfect agreement with the methodology of natural science. The main thing in natural science is observations, necessarily repeated. This is followed by reflections and attempts to quantify the observations. Let's start again with the case of one-dimensional statistics. Suppose we measured the same value several times with one device, received a series of slightly different numbers, looked closely at them and saw that they exhibit some statistical properties—similarity and spread. Our understanding of these properties must be expressed quantitatively and preferably in a form familiar to the scientific community. We can calculate all the usual indicators of the so-called representative statistics: mean value, standard deviation. There are familiar definitions and formulas for this. They do not depend on the distribution law of the measured random variable. Various recipes for constructing the confidence interval for the mean value of the measured value depend on this law. But the series of numbers we have received somehow manifests its inherent distribution law, albeit not very clearly.

Let's try to simulate the behavior of the measurement results, remembering that these results are random. Let's take the first number from our experimental sample of numbers. Could it not have appeared during the

measurements? It could very well. Could the adjacent number appear twice in a row? It could very well. These are perfectly legitimate assumptions. Let's use this and prepare a new sample by removing the first number from the experimental sample and duplicating the second. Such a new sample could well be realized in our measurement process. Let's calculate again the average value. It will be slightly different from the first. And this is very good, since the average value itself begins to show us its statistical properties.

We will repeat this simulation process many times, each time assigning the number of the discarded number from the original sample using a random number generator. Each time from a new artificial sample we will calculate the average value. These samples are only slightly artificial. Basically, they carry all the features of our only experimental sample. The size n of each sample is the same, the composition of the numbers in the sample is almost the same, since we did not commit too much violence on the sample. We accidentally cut out one number, but added another from the same company (that's why such a simulation method, when each time we simply cut out one random value from the original sample, is called jack-knife, and we showed it in a slightly modified form so as not to change n). Each time we calculate the average value from the simulated sample. So we can collect a very large number M of averages values and build a histogram that will tell us a lot about the statistical law, which is no longer subject to the measured value, but its average value. After all, nobody canceled Chebyshev's law of large numbers. Its manifestations do not depend on the distribution law of a random variable. It only asserts that with an increase in M, the average value of the average values approaches the expected value of a random variable. How close? We will immediately see this from the histogram of average values. Having set the reliability Q, we directly determine the boundaries of the corresponding confidence interval by the wings of the histogram. A report for the scientific community is ready. Here is the confidence interval. Here is the reliability that the unknown expected value of the measurement result falls within this interval. It turned out that it is not even necessary to calculate an empirical estimate of the variance. It is clear that in the same way it is possible to obtain the confidence interval and its reliability for any other function from the experimental sample, and not just for the average value.

5 Bootstrap Method for Finding Complex Statistical Functions from Small Samples

Let us show how different the interpretations of the results obtained by the methods of classical statistics and the bootstrap method [10], which is very similar to the jack-knife method, can be. To do this, we will use the data of biochemical analysis, known to us from a private communication of colleagues. In several age groups of patients during the examinations, the activity of a certain enzyme was analyzed. It was necessary to find out whether this activity depends on age. All groups were small (no more than 15 patients), but a certain age group of 6 patients was especially small. In the same group, the enzyme activity in the analyzes was the lowest. It is represented by the following set of values:

$$a_e = \{0 \quad 0 \quad 0 \quad 0.04 \quad 0.14 \quad 0\} \tag{9}$$

In order to compare the indicators of this group with others, it is necessary to find the confidence interval in which the average value of the random variable A in this group falls. We require that the reliability is 95%.

Classical statistics give the following results. The mean is 0.03; the standard deviation of the mean is 0.025; Student's coefficient for reliability 0.95 and the number of degrees of freedom 5 is 2.57. From here we get the conclusion: the average value with 95% reliability lies in the range from −0.035 to +0.095. This is an absurd conclusion, since the biochemical meaning of the random variable A excludes the possibility of taking negative values.

Bootstrap leads to a different conclusion. In the sample of means there are no and cannot be negative values. There are zero ones since it is quite possible that random bootstrap samples will be formed, which include six zero experimental values of A. This is clearly seen on the histogram constructed from 1000 bootstrap samples (Fig. 1).

If we discard the 5% tail from the side of high values in this histogram, then the average value of A with 95% reliability will lie in the range from 0.0 to + 0.07. This conclusion is quite acceptable for a specialist. It is also pleasant

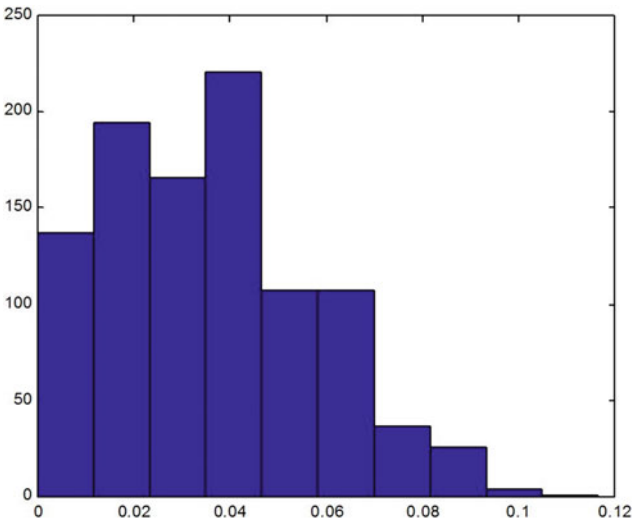

Fig. 1 Histogram constructed from 1000 bootstrap samples for set of measured values (9)

that the width of the confidence interval according to the bootstrap turns out to be smaller than according to the classical recipe. This makes it possible to reliably record a smaller difference between the enzyme activities in two close age groups.

Let us explain why the classic recipes led to an unacceptable result. The fact is that in this case the researcher must rely on the hypothesis that the measured values follow a normal distribution with sample estimates: expected value 0.03; standard deviation 0.056. This means that, with a 95% probability enzyme activity values from −0.082 to + 0.14 can be found in this group of patients. We see that according to this criterion, we cannot reject any of the experimental values of the enzyme activity. Therefore, accepting this hypothesis, the researcher introduces disinformation into his results. Therefore, he receives artifacts in the final results and is forced to give them the wrong interpretation.

How does a specialist act in such cases? Most likely, he is guided by his rich experience and concludes that one-dimensional mathematical statistics is not able to see in this experimental material anything that he would not see with the naked eye. The statistics can only give numerical estimates of the parameters for interpretation of the observed facts. If classical statistics, tightly tied to the law of normal distribution, gives an absurd estimate of the parameters then the specialist have to select other recipes that will give more reasonable estimates.

Bootstrap is another recipe. It is not tied not only to the law of normal distribution, but also to any previously assumed distribution of the investigated random variable. Bootstrap tries to probe the distribution of this random variable directly in the course of calculations. He examines the primary material so thoroughly and in detail that literally every single result from the experimental sample makes its significant contribution to the formation of the final result and its interpretation. Bootstrap literally emphasizes all the statistical features of the primary material, and classical statistics smooths out these features.

Let us illustrate what has been said with one more example. The material presented below arose when processing the personal data of a group of patients who were asked to subjectively assess their quality of life Q before undergoing treatment. In a group of 17 people, the following results were obtained

$$\{100\ 100\ 100\ 78.64\ 89.21\ 78.01\ 0\ 88.8\ 78.01\ 100\ 100\ 77.67\ 100\ 89.21\ 100\ 65.47\ 78.64\} \quad (10)$$

We want to find out what happens to the Qs in this group after the course of treatment. We will compare the confidence intervals for the mean in two samples obtained at different points in time. Now let's form the confidence interval for the given sample.

Classical statistics give the following results: mean value 83.7; standard deviation 6.1; Student's coefficient 2.12 for reliability 0.95 and the number of degrees of freedom 16. Hence, we obtain a conclusion based on the assumption of the applicability of the normal distribution: the average value of Q with a reliability of 95% lies in the range from 70.9 to 96.6. As if everything is in order. But the presence of the zero value in the sample is embarrassing. Does this value agree with the normal distribution? If we apply 3σ criterion to this value then there cannot be values less than 10.8 with a probability of almost 100%. But seventh element is significantly less than this limiting value. And the recipes for classical statistics require that we discard this observation as clearly erroneous, and process a new vector with 16 elements.

For this sample, we get the following results: mean value 88.9; standard deviation 3; Student's coefficient 2.13 for reliability 0.95 and the number of degrees of freedom 15. Hence, we obtain a conclusion based on the assumption of the applicability of the normal distribution to a truncated sample: the average value of Q with a reliability of 95% lies in the range from 82.7 to 95.3. It can be seen that the application of the 3σ criterion significantly influenced the result. The quality of life indicator noticeably shifted upwards, and the confidence interval narrowed very noticeably. The latter increases the chances of the researcher to notice the effect of the treatment on the change in this indicator in this group. It remains only to anticipate the success of the chosen therapy.

However let us ask ourselves a question: how justified is the application of 3σ criterion? Exactly to the extent that the assumption that the given samples obey the normal distribution is justified. It is irrational to solve this issue by statistical methods. It is better to ask a specialist what properties of his patients could lead to the appearance of a zero subjective assessment of the quality of life. Or such an assessment could have appeared as a result of the patient's inability to handle the questionnaires. Here it turns out that among patients there are often individuals who are inclined to greatly underestimate their assessment of the quality of life before the course of treatment. If a specialist wants to conduct a questionnaire taking into account this possibility, then there is no reason to apply 3σ criterion, since the preliminary filtering in this study can only be carried out on a meaningful, and not on a formal level.

After performing bootstrap processing of the original sample, we get a histogram of 1000 means for this sample, shown in Fig. 2.

Attention is drawn to the asymmetry of the histogram. It seems that a large sample of means does not follow a normal distribution. This is not surprising, since the initial experimental sample clearly does not obey this law, if we are also interested in patients who tend to underestimate their

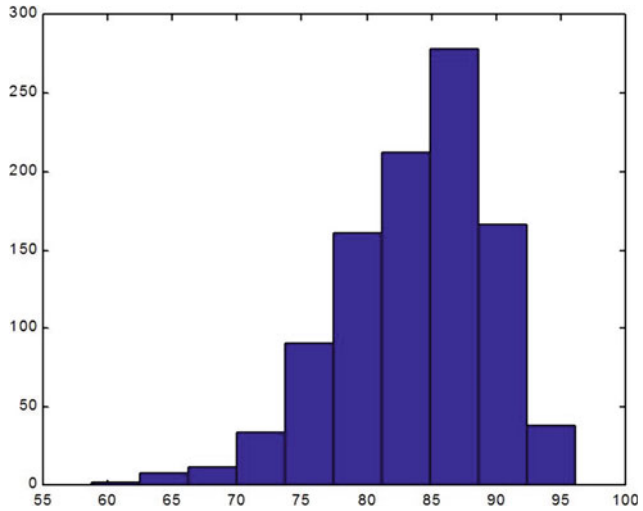

Fig. 2 Histogram constructed from 1000 bootstrap samples for set of measured values (10)

indicators. We don't know which law governs the distribution of our raw data. We didn't even try to recognize it. But we are convinced that the bootstrap sensibly gropes for the consequences of this law in the distribution of such a function of the initial data as their mean. And nothing prevents us from directly on the histogram to note such a tail of low means, the number of which is 5% of the entire 1000 values formed by the bootstrap. From here we get the confidence interval for the average indicator of the quality of life in this group from 74 to 96. The average value of the means is 83.7. The bootstrap method gives results very close to classical ones. The difference is that classical statistics force us to replace the original sample with a truncated one, and we would not like to do this.

The analysis of the above two examples allows us to draw two generalizing conclusions that were not noticed by the authors of this method.

1. Bootstrap allows you to calculate various functions from the experimental sample and directly evaluate the statistical properties of these functions, without relying on any distribution laws of both the arguments and the functions themselves.
2. Bootstrap allows you to estimate the parameters of those unknown and complex distribution laws, which are followed by the results of observations of the complex behavior of natural objects.

The multidimensional case does not introduce anything new in the particular application of imitation methods of statistics based on the use of computer technology. Only the computation of functions from the initial samples becomes more complicated. So, when studying pairwise correlations, the sample contains pairs of measurement results. And at each iteration of the bootstrap loop, here it is necessary to calculate the value of the correlation coefficient. Then you need to build a histogram of the coefficient values. The algorithm is slightly more complex than the examples above. When studying multiple correlations, vectors of measurement results are in the sample. And at each bootstrap loop iteration, here it is necessary to calculate the eigenvalues and eigenvectors of the random covariance matrix.

6 Conclusion

Complex recipes for one-dimensional mathematical statistics are not very necessary in the research routine of an analytical chemist. He understands the statistical properties of his experimental material better than any mathematical statistician.

Simple recipes for one-dimensional mathematical statistics are very necessary in the research routine of the analytical chemist. Using them requires a very deep understanding of the statistical implications of these recipes. Otherwise, annoying mistakes are possible when presenting the results to the scientific community.

Recipes for multivariate statistics can be extremely useful precisely in the research activities of the analytical chemist. The search for methods of this statistics that are adequate for analytical chemistry may require the organization of joint work with the participation of both chemists and specialists in the field of mathematical statistics.

Methods of imitation statistics, based on the intensive use of computer technology, are able to save the researcher from any difficulties associated with the fundamental methodological shortcomings of mathematical statistics itself.

References

1. Brown, R.J.C., Goddard, S.L., Brown, A.S.: Using principal component analysis to detect outliers in ambient air monitoring studies. Int. J. Environ. Anal. Chem. **90**(10), 761–772 (2010)
2. Lozano, V.A., Ibañez, G.A., Olivieri, A.C.: Experimental design for the study and optimization of the effect of different surfactants on the spectrophotometric determination of sulfide based on phenothiazine dye production. Anal. Chem. **82**(11), 4510–4519 (2010)
3. Hubert, P., Nguyen-Huu, J.-J., Boulanger, B., Chapuzet, E., Cohen, N., Compagnon, P.-A., Dewé, W., Feinberg, M., Laurentie, M., Mercier, N., Muzard, G., Valat, L., Rozet, E.: Harmonization of strategies for the validation of quantitative analytical procedures: a SFSTP proposal. Part IV. Examples of application. J. Pharm. Biomed. Anal. **48**(3), 760–771 (2008)
4. Coleman, D., Vanatta, L.: Statistics in analytical chemistry: Part 32-detection limits via 3-sigma. Am. Lab. **40**(20), 60–62 (2008)
5. Frank, I.E., Pungor, E., Veress, G.E.: Statistical decision theory applied to analytical chemistry. Part 1. The statistical decision model and its relation to branches of mathematical statistics. Anal. Chim. Acta. **133**(3), 433–441 (1981)

6. McFarren, E.F., Lishka, R.J., Parker, J.H.: Criterion for judging acceptability of analytical methods. Anal. Chem. **42**(3), 358–365 (1970)
7. Sarbu, C.: Application of informational analysis of variance in analytical chemistry. Anal. Chim. Acta. **271**(2), 269–274 (1993)
8. Faber, N.M., Buydens, L.M.C., Kateman, G.: Aspects of pseudo-rank estimation methods based on an estimate of the size of the measurement error. Anal. Chim. Acta. **296**(1), 1–20 (1994)
9. Rao, R., Lakshminarayanan, S.: Variable interaction network based variable selection for multivariate calibration. Anal. Chim. Acta. **599**(1), 24–35 (2007)
10. Efron, B., Tibshirani, R.: An Introduction to the Bootstrap. Chapman & Hall/CRC, Boca Raton (1993)

A New Development in Theory of Multielectron Systems

B. K. Novosadov

1 Introduction

A system of many particles interacting with pair potentials is a subject of theoretical investigations in quantum chemistry and nuclear physics. The most popular approaches in solving corresponding Schroedinger equations are one-particle (orbital) representations and based on them the Hartree–Fock equations. A more explicit approaches consist in a rather complex algorithms of "r12" approximations for a wave function [1–4], which can be employed for a system of few particles with a small number of electrons. Therefore, the approaches should be added by a more convenient mathematical tools to provide a wider field of applications in computational chemistry. Some suggestions are of subject of this paper. Note that some approaches in atomic and molecular physics need in a clearer physical setting and understanding. For example, a problem of separation of rotations and inner movements in a free system of few particles is discussed for decades but did not find a fully satisfactory representation in atomic and molecular theory. To this connection, there did not exist a few-particle Hamiltonian expression in which the rotation of the system as a whole would be represented in accordance with the conservation law for the angular momentum. This problem is considered in this publication, too. A method of two-electron representation of multielectron wave functions is pointed out which could serve as a new development of quantum chemistry tools for large molecular systems. So, we give an attention to precise solving two-electron equations for helium-like atoms.

2 On a Separation of Rotation of Atomic Electrons as a Whole in the Hamiltonian

In literature it is known the expression of kinetic energy of one particle in a central field through the angular momentum. This representation allows one to use the angular momentum conservative law to classify the spectrum and states of the particle by rotational series. The same problem may be settled for a multiparticle system like an atom or a molecule. But a corresponding general explicit formula for kinetic energy of a system of particles was absent to separate the rotation of the system as a whole. It is obvious that a free atom rotates and possesses the angular momentum conservation law which is characterized by integer eigenvalues. The latter may be used to classify atomic spectra by rotational series. Those quantum numbers may be included into wave equations for describing inner movements of atomic electrons. Mathematical methods in which the conservation laws are employed are called as conservative ones. These methods are of importance when interpretating interstellar chemical objects more precisely then without characterizing rotational states. It is well known that the rotational energy does not conserve as a moment of inertia of an atom depends on electronic coordinates. But inner movements of electrons and energy eigenvalues are dependent parametrically on angular momentum quantum numbers. The kinetic energy operator may be transformed into a necessary form as follows below.

Write down a nonrelativistic expression of the kinetic energy for a system of particles

$$T = \sum_{i=1}^{n} \frac{\mathbf{p}_i^2}{2m_i}, \tag{2.1}$$

where $\mathbf{p}_i$, m_i are momentum and mass of a particle. By the definition the full moment of momentum operator is a vector sum of vector products of radius-vectors and particle momentum operators

B. K. Novosadov (✉)
Vernadsky Institute of Geochemistry and Analytical Chemistry, Russian Academy of Sciences, 19 Kosygin St., Moscow, 119991, Russia
e-mail: bk.novosadov@mail.ru

V. P. Kolotov and N. S. Bezaeva (eds.), *Advances in Geochemistry, Analytical Chemistry, and Planetary Sciences*,
https://doi.org/10.1007/978-3-031-09883-3_38

$$\mathbf{L} = \sum_{i=1}^{n} \mathbf{L}_i = \sum_{i=1}^{n} \mathbf{r}_i \times \mathbf{p}_i. \tag{2.2}$$

Then one obtains square of the moment of momentum operator (2.2),

$$\mathbf{L}^2 = \left(\sum_{i=1}^{n} \mathbf{L}_i \right)^2 = \sum_{i=1}^{n} \mathbf{L}_i^2 + \sum_{i=1, i\neq j}^{n} \sum_{j=1}^{n} \mathbf{L}_i \mathbf{L}_j. \tag{2.3}$$

With the Lagrange identity taking into account differential property of the momentum

$$[\mathbf{rp}][\mathbf{rp}] = r^2 p^2 - (\mathbf{rp})^2 + i\hbar(\mathbf{rp}), \tag{2.4}$$

transform the squares of angular momenta of particles:

$$\sum_{i=1}^{n} \mathbf{L}_i^2 = \sum_{i=1}^{n} \left[r_i^2 p_i^2 - (\mathbf{r}_i \mathbf{p}_i)^2 + i\hbar(\mathbf{r}_i \mathbf{p}_i) \right]. \tag{2.5}$$

In the square brackets in the r.h.s. of the equality consider the first term and make an algebraic identity transformation with it

$$\sum_{i=1}^{n} r_i^2 p_i^2 = \sum_{i=1}^{n} m_i r_i^2 \frac{p_i^2}{m_i} = \sum_{i=1}^{n} (J - J_i) \frac{p_i^2}{m_i} \tag{2.6}$$

where moments of inertia of the particle system are introduced

$$J = \sum_{i=1}^{n} m_i r_i^2, J_i = J - m_i r_i^2. \tag{2.7}$$

Taking into consideration that the full moment of inertia does not depend on the sum index one can carry out its quantity out of the sum sign then a doubled kinetic energy of the particle system proved to be in the sum

$$\sum_{i=1}^{n} r_i^2 p_i^2 = 2J \cdot T - \sum_{i=1}^{n} J_i \frac{p_i^2}{m_i}, \tag{2.8}$$

where T is given by (2.1). Substituting this expression into the formulae (2.5) and (2.3) one obtains a general expression of the kinetic energy T via the squared angular momentum of a multiparticle system as follows

$$T = \frac{L^2}{2J} + \sum_{i=1}^{n} \frac{J_i}{J} \frac{p_i^2}{2m_i} + \frac{1}{2J} \sum_{i=1}^{n} \left[-(\mathbf{r}_i \mathbf{p}_i)^2 + i\hbar(\mathbf{r}_i \mathbf{p}_i) \right] - \frac{1}{2J} \sum_{i=1, i\neq j}^{n} \sum_{j=1}^{n} \mathbf{L}_i \mathbf{L}_j. \tag{2.9}$$

Now we can analyze the new kinetic energy operator. The first term in the r.h.s. is the rotation energy of the particle system as a whole. Thus, one obtains a clear representation on how the rotational part of the full energy of a multiparticle system enters the kinetic energy operator. For a closed system of particles, the angular momentum is conserved and its eigenvalues are integer numbers. Being dependent on particles' coordinates, this yield is a repulsive potential of particles during rotation of the system as a whole. The sum of the next terms of the expression (2.9) is an inner energy of the system. We see that the rotation energy part does not conserve, but it provides a rotational state of the system marked by the quantum number L. Note that the eigenfunction system of the angular momentum of a free particle system is distinguished of that for a rotator or a solid by a *multipole* degeneration. It gives some features to the theory of structures of atomic and molecular systems. The eigenvalue and eigenfunction problem for the angular momentum of a system of particles may be reduced to solving an equation with the operator of the squared angular momentum (here we neglect by spin momenta of particles)

$$L^2 \chi = \lambda \chi. \tag{2.10}$$

Solutions of this equation are multipolar spherical harmonics [5] which may be represented in the form of linear combinations of products of usual spherical harmonics of angular coordinates of particle radius-vectors of a system center-of-mass or a force center. In the cited monograph a tensor representation of the named harmonics is given in the form of different schemes of angular momenta coupling of different particles. The angular momentum eigenvalues prove to be nonnegative integers and may be calculated by a simple algorithm [5] which is formulated as follows.

The additivity of particle angular moments allows one to represent a solution as a linear combination of products of spherical functions in angular variables of the particle radius-vectors. Substitute it into the Eq. (2.10), then multiply the equation to the left by one of the functions of the linear combination, and integrate over the angular coordinates. An eigenvalue matrix equation for the moment of momentum will be obtained, which allows one to calculate linear combination coefficients. Though the obtained matrix has infinite order, however it breaks onto blocks of finite orders due to the rules of acting the partial angular moment operators and because of the orthogonality of the basis functions. For a system of particles solutions of the Eq. (2.10) are a degenerated set of the eigenvalues at each value of the moment of momentum and its projection. These sets are countable, and the degenerated eigenfunctions can be numbered with positive integers. Thus, the rotational states are put in order by the eigenvalue of the angular moment and by an index in a series of degenerated functions at a given value of the full moment and values of particle moments. According to what has been said the kinetic energy shall contain some centrifugal yields depending on a given rotational state of the atom that are defined not only by the first term in the r.h.s. of

the Eq. (2.9) but by the last sum of that relationship, also. So even at the zero value of the full angular moment different rotational states shall give different yields into centrifugal energy which are calculated from the last operator sum in the kinetic operator (2.9). To see this property, we give three first rotational functions of degenerated eigenfunctions at $L = 0$ for systems of two particles in a central field $(\omega \equiv \theta, \varphi)$ –

$$\chi_1(\omega_1, \omega_2) = Y_{00}(\omega_1) Y_{00}(\omega_2),$$

$$\chi_2(\omega_1, \omega_2) = 3^{-1/2}(Y_{10}(\omega_1) Y_{10}(\omega_2) + Y_{11}(\omega_1) Y_{1-1}(\omega_2) + Y_{1-1}(\omega_1) Y_{11}(\omega_2)),$$

$$\chi_3(\omega_1, \omega_2) = 5^{-1/2} \sum_{a+b=0} Y_{2a}(\omega_1) Y_{2b}(\omega_2); \quad |a|, |b| \le 2.$$

Analogously, one can consider rotational states of systems with more than two particles.

3 A System of Two Electrons

Consider a system of two electrons in a central field. The importance of two-electron systems is connected with that it gives the simplest system with pair interaction potential and can explain electron correlation effects in atoms. Below we give another argument of importance the two-electron states for the theory of atoms and molecules.

The theory of two-electron atoms was considered in the first applications of quantum mechanics by Heisenberg, Hylleraas, Fock et al. [6–8]. In Fock works there were formulated correct mathematical methods of constructing two-electron functions for the ground state of helium. That time he did not used the conservative expression for the helium Hamiltonian, so here we present an application of our approach to the helium problem.

The correlation problem is of importance for a necessity of taking into consideration more precisely two-electron states in atoms and molecules to obtain an accuracy of about 1 kcal/mole in the energy of a system. The usage of energy basis functions needs in eigenfunctions of both discrete, and continuum spectra of a system. But it is well known that series of solutions of the corresponding Schroedinger equations converge faster to an exact value when one uses a Sturmian basis set. In some works [5, 9–11] it was shown that orthogonal with a weight like one-electron potential functions are much better approximate wave functions of atoms then Hartree–Fock approximations. We can go farther on employing a Sturmian representation if we take interelectron potential as a weight function of orthogonality for basis functions. For this purpose, consider a new representation of interelectron potential in a four-dimensional space.

The Coulombic potential function is the inverse distance between charges $Z_1 e$ and $Z_2 e$ localized in points with Cartesian coordinates $\mathbf{r}_1$ and $\mathbf{r}_2$, namely

$$V = Z_1 Z_2 e^2 r_{12}^{-1}, \qquad r_{12} = |\mathbf{r}_1 - \mathbf{r}_2|. \tag{3.1}$$

Due to the spherical symmetry of this function, it may be expressed in the spherical coordinates of the particles, r, θ, φ,

$$r_{12}^2 = r_1^2 + r_2^2 - 2 r_1 r_2 \cos\ \omega,$$

with

$$\cos\omega = \cos\theta_1 \cos\theta_2 + \sin\theta_1 \sin\theta_2 \cos(\varphi_1 - \varphi_2).$$

The potential (3.1), as is well known, may be expanded in a series over Legendre polynomials of the argument ω, that is

$$r_{12}^{-1} = \sum_{l=0}^{\infty} 2^{-l-1/2} (r_1 r_2)^{-l-1} \left(r_1^2 + r_2^2 - |r_1^2 - r_2^2|\right)^{l+1/2} P_l(\cos\omega). \tag{3.2}$$

A further algebra for an application of this formula, as it may be seen, is not simple because of the complicated radial dependence. To overcome this problem, we introduce a trigonometric change of radii by a stereographic projection

$$r = a_0 \tan(\alpha/2), \tag{3.3}$$

where $a_0 = m^{-1} e^{-2} \hbar^2$ is the Bohr's radius.

Use the atomic units $e = m = \hbar = 1$, and $a_0 = 1$. After simple trigonometric transformations one has obtained

$$|\mathbf{r}_1 - \mathbf{r}_2|^{-1} = 2\cos(\alpha_1/2)\cos(\alpha_2/2)(2 - 2\cos\tilde{\omega})^{-1/2}, \tag{3.4}$$

with $\tilde{\omega}$ being the arc length of the large circle between two points on the surface of a unit O(4) sphere

$$\cos\tilde{\omega} = \cos\alpha_1 \cos\alpha_2 + \sin\alpha_1 \sin\alpha_2 \cos\omega.$$

The next step is in finding a series for the fraction (3.4) over O(4) spherical harmonics which can serve as basis elements when solving the wave equation.

The series (3.2) over Legendre polynomials does not suit for this purpose. We should use a series by Gegenbauer polynomials as follows

$$\left(r_1^2 + r_2^2 - 2 r_1 r_2 x\right)^{-\lambda} = \sum_{n=1}^{\infty} 2^{-n-\lambda+1} (r_1 r_2)^{-n-2\lambda+1} \left(r_1^2 + r_2^2 - |r_1^2 - r_2^2|\right)^{n+\lambda-1} C_{n-1}^{\lambda}(x), \tag{3.5}$$

and then the bilinear series over normalized to 1 harmonics O(4):

$$C^1_{n-1}(\cos\tilde{\omega}) = n^{-1}\sum_{lm}\Psi_{nlm}(\Omega_1)\Psi^*_{nlm}(\Omega_2),\quad \Omega \equiv (\alpha,\theta,\varphi). \tag{3.6}$$

But in our case $\lambda = 1/2$ and we come to (3.2) (remind that $P_l(x) = C_l^{1/2}(x)$). So, we need in a series of the following kind

$$(2-2x)^{-1/2} = \sum_{n=1}^{\infty} a_{n-1}C^1_{n-1}(x). \tag{3.7}$$

The coefficients a_n are calculated by the formula [12]

$$a_{n-1} = 8n\left[\left(4n^2-1\right)\pi\right]^{-1},$$

and one arrives at a bilinear series seeked over O(4) harmonics

$$(2-2\cos\tilde{\omega})^{-1/2} = \sum_{n=1}^{\infty}\sum_{l<n,|m|\le l} n^{-1}a_{n-1}\Psi_{nlm}(\Omega_1)\Psi^*_{nlm}(\Omega_2). \tag{3.8}$$

We can notice that the products of the spherical harmonics in (3.6) are bipolar harmonics in R^4, so the set of bipolar harmonics can serve a basis set in two-electron problem and in constructing orthogonal set with the weight r_{12}^{-1}, and also the integrals with this potential are reduced to Wigner coefficients.

A behavior of the two-electron wave function at the origin is regular and provided by the spherical harmonics. However, when radial variables tend to infinity the asymptotic behavior has an exponential form as a function of radii of the two electrons. To provide this function with a model of independent particles (when neglecting by their interaction) one ought to introduce the full energy of the particles onto the exponent as follows (we give a generalized expression for n particles)

$$f_\infty = exp\left(-\sqrt{\frac{-2E}{\sum_{k=1}^n \zeta_k^2}}\sum_{k=1}^n \zeta_k r_k\right). \tag{3.9}$$

So, this function reflects, as it may be seen, the proper wave function asymptotics at the infinite radii in the model of independent particles. The exponential parameters ζ_k are usual Slater exponents of atomic orbitals. It is clear, the full energy diminishes the exponents of the independent particles because the fraction under the radical is less then unity. We seek for a solution of the Schroedinger equation in the form as follows

$$\psi(r_1,r_2) = f_\infty\phi(r_1,r_2). \tag{3.10}$$

Note that here the asymptotics serves as a weight function in an orthogonal set of eigenfunctions of the Schroedinger equation if one uses the spherical coordinates for particles and the function $\phi(r_1,r_2)$ is constructed as a series by powers of the electron radii. This representation was used by Fock et al. in the theory of helium [8, 9, 13]. But we can omit the exponentials and after having transferred to a system of angular variables solve the eigenvalue problem in angular coordinates using orthogonality relations of a system of special spherical basis function. This calculation may be organized as follows.

Substitute (3.10) into the Schroedinger equation and consider acting of the Laplacians on the product of functions. One obtains

$$\begin{aligned}&(\Delta_1+\Delta_2)e^{-a\zeta_1 r_1 - a\zeta_2 r_2}\phi(\mathbf{r}_1,\mathbf{r}_2)\\ &= \{(\Delta_1+\Delta_2)\phi - 2a\left(\zeta_1\frac{\partial\phi}{\partial r_1}+\zeta_2\frac{\partial\phi}{\partial r_2}\right)\\ &+ \left[a^2\left(\zeta_1^2+\zeta_2^2\right) + -2a\left(\zeta_1 r_1^{-1}+\zeta_2 r_2^{-1}\right)\phi\right]\}e^{-a\zeta_1 r_1 - a\zeta_2 r_2}.\end{aligned} \tag{3.11}$$

The sum of the Laplacians may be expressed via the angular momentum according to the Eq. (2.9), it gives a possibility to use the conservative law of the angular momentum of the system. Thus, the Schroedinger equation for the two-electron function ϕ may be written as follows

$$\begin{aligned}&\left(\frac{\mathbf{L}^2}{2J}+\sum_{i=1}^2\frac{J_i}{2J}\mathbf{p}_i^2+\frac{1}{2J}\sum_{i=1}^2\left[-(\mathbf{r}_i\mathbf{p}_i)^2+i\hbar(\mathbf{r}_i\mathbf{p}_i)\right]-\frac{1}{J}\mathbf{L}_1\mathbf{L}_2\right)\phi\\ &-2a\left(\zeta_1\frac{\partial\phi}{\partial r_1}+\zeta_2\frac{\partial\phi}{\partial r_2}\right)+\left[a^2\left(\zeta_1^2+\zeta_2^2\right)-2a\left(\zeta_1 r_1^{-1}+\zeta_2 r_2^{-1}\right)\right]\phi\\ &-\frac{Z}{r_1}\phi-\frac{Z}{r_2}\phi+\frac{1}{r_{12}}\phi = E\phi,\end{aligned} \tag{3.12}$$

where the asymptotical function is omitted in the equation. For the closed system the angular momentum operator has integer eigenvalues and one can replace the operator by its eigen-number $\mathbf{L}^2 = L(L+1)$. In such a way one can consider a set of two-electronic states in a given rotational state of the system as a whole. If we put $L = 0$, then the two-electronic states correspond to the absence of the rotation of the system as a whole. Nevertheless, it does not mean the absence of the rotational movement of the particles as it has been stated in Sect. 2. The yields in the kinetic part of the Hamiltonian may be divided by kinetic energy and centrifugal potentials due to rotations of particles round the nucleus, provided the electronic kinetic energy yields being modified by the rotational movement of the atom as whole. Thus, the atomic energy spectrum consists in series by the atomic angular momentum and countable set of the rotational states belonging to the quantum number of this momentum. It is obvious that for atomic systems with a large number of electrons the rotational series in energy spectra

should be very close to each other giving a diffusion of spectral lines in experimental atomic spectra. To facilitate an analytical and computational research, one can consider the rotational potentials like perturbation of a repulsive type, so the corrections may be easily calculated because the perturbation potential contains the electronic variables in a factorized form.

The Eq. (3.12) might be solved by the Fock method expanding the wave function by powers of radii. But having in mind the variational method of calculation the energy spectrum, we prefer to transfer to angle variables and use Fourier series by polyspherical functions in R^4. Our idea is in the usage of bipolar function which should produce an orthogonal set with the weight r_{12}^{-1}. The parameters ζ_k can serve as variational quantities. This is a new representation in the atomic theory that can simplify computations when analyzing spectral properties of atoms. In the next Section we shall show that it is sufficient to consider the problem of two particles bearing in mind the two-particle form of atomic and molecular potential functions in Schroedinger equations. A more detailed consideration of the suggested method will be done elsewhere.

4 A Two-Electron Decomposition Method for Many-Electron Systems

In electronic systems there take place pair interactions like pair attraction of nuclei and electrons and pair repulsions in nuclear and electronic subsystems. Here we consider atomic systems.

A direct solving a many-electron Schroedinger equation does not turn out well since the potential function does not admit a separation of variables by electron coordinates. Methods of incomplete separation of variables in such equations prove to be labor-consuming and does not reduce suitable approach for numerical calculations of wave functions and spectra of many-electron systems. One has to use roundabout ways to overcome computational difficulties in this almost unsolvable mathematical problem of the theory of many interacting bodies movement. Here we suggest to use an auxiliary equation and a passage to the limit in the auxiliary wave function which allow to represent a solution of initial problem of many bodies via a solution of the problem on movement two interacting bodies in an external field.

Consider the Schroedinger equation for a system of n particles in an external field interacting by pair potentials

$$\sum_{i=1}^{n} T_i\Psi + \sum_{i=1}^{n} V_i\Psi + \sum_{i>j=1}^{n} W_{ij}\Psi = E\Psi, \tag{4.1}$$

where $T_i = -\frac{1}{2m_i}\Delta_i$, V_i are external field potentials, W_{ij} are interaction potentials between particles which are Coulombic potentials in atomic and molecular problems. The pair character of the potential function of the equation suggests itself a description with basis functions depending on coordinates of two particles, that is, biorbitals. However, in contrast to orbital approaches the use of biorbital representations reduces to complicated analytical expressions not giving simplification in numerical calculations. To overcome this problem, consider an auxiliary wave equation for an artificial system of interacting particles which is connected with the initial system of particles by a passage to the limit with decreasing particles number up to the initial number. For clearness of reasoning consider a system of three particles. A generalization of the method can be easily made.

Write down the Hamiltonian as follows

$$H = T_1 + V_1 + T_2 + V_2 + T_3 + V_3 + W_{12} + W_{13} + W_{23} \tag{4.2}$$

Represent the Hamiltonian as a sum of Hamiltonians by pairs of particles. Have

$$H = H_{12} + H_{13} + H_{23}, \tag{4.3}$$

where

$$H_{12} = \frac{1}{2}(T_1 + V_1 + T_2 + V_2) + W_{12}, \text{etc.} \tag{4.4}$$

Suppose that eigen-solutions of these operators are known

$$H_{ij}\varphi_{ij} = E_{ij}\varphi_{ij}. \tag{4.5}$$

Consider a system of particles with twice number of particles than the initial system with the Hamiltonian of kind

$$H' = H_{12} + H_{34} + H_{56}, \tag{4.6}$$

where the indices answer to particles' numbers. In this Hamiltonian the variables are obviously separated by pairs of particle coordinates. Thus, solutions of the wave equation with this Hamiltonian may be represented as a product of biorbitals (bispinorbital or bispinal)

$$\varphi = \varphi_{12}\varphi_{34}\varphi_{56}. \tag{4.7}$$

The energy of this system is calculated as the sum of biorbital energies

$$E' = E_{12} + E_{34} + E_{56}. \tag{4.8}$$

For obtaining a solution of the initial wave equation for the three particles one has to make the passage to the limit by

diminishing the number of the particles of auxiliary problem to initial number posing the next equality of the coordinates: $4 \rightarrow 1$, $5 \rightarrow 2$, $6 \rightarrow 3$. Thus, one obtains an expression for the energy of the three particles as a sum of the biorbital energies.

$$E = E_{12} + E_{13} + E_{23}. \tag{4.9}$$

The wave function of the system is represented in factorized form through biorbital wave functions

$$\Psi = \varphi_{12}\varphi_{13}\varphi_{23}. \tag{4.10}$$

It remains to solve a Schroedinger equation for a pair of interacting particles. Above we have considered biorbital problem for an atomic system. The problem for molecules will be stated elsewhere. An algorithm of solving the problem for n particles reduces to an auxiliary problem on a movement of $n(n-1)$ particles and the system energy is calculated as follows

$$E = \sum_{i>j=1}^{n} E_{ij}. \tag{4.11}$$

Correspondingly the wave function for a system of n particles is represented by the product of $n(n-1)/2$ biorbitals

$$\Psi = \prod_{i>j=1}^{n} \varphi_{ij}. \tag{4.12}$$

The biorbital Hamiltonian takes the form

$$H_{ij} = \frac{1}{n-1}\left(T_i + V_i + T_j + V_j\right) + W_{ij}. \tag{4.13}$$

In the suggested approach a fundamental problem is put forth on solving the Schroedinger equation for a system of two particles that simplifies substantially a general statement of the quantum mechanical and quantum chemistry problem on calculation of states for multielectron or another multiparticle systems (for example, nuclear systems) with pair interactions of particles.

References

1. Ten-no, S.: Initiation of explicitly correlated Slater-type geminal theory. Chem. Phys. Lett. **398**, 56–61 (2004)
2. Sherrill, C.D.: Frontiers in electronic structure theory. J. Chem Phys. **132**, 110902 (2010)
3. Noga, J.: Introducing explicitly correlated coupled cluster approaches into the world of astrophysics. EPJ Web of Conferencies, vol. 34, p. 02001 (2012). https://doi.org/10.1051/20123402001
4. Bokhan, D., Ten-no, S., Noga, J.: Implementation of the CCSD (T)-F12 method using cusp conditions. Phys. Chem. Chem. Phys. **10**, 3320–3326 (2008)
5. Novosadov, B.K.: Analytical Theory of Atom. Analiticheskaya teoriya atoma, p. 322. Kniga po trebovaniyu, (in Russian) Moscow (2014)
6. Heisenberg, W.: Z. Phys. **39**, 499 (1927)
7. Hylleraas, E.A.: Norske Vidensk. Akad. Skrift., Mat.-Naturv. Kl. No 6 (Oslo) (1932)
8. Fock, V.A.: Izv. AN SSSR. Ser. Fiz. **18**, 161 (1954)
9. Avery, J., Hansen, T.B.: Int. J. Quantum Chem. **60**, 201 (1996)
10. Novosadov, B.K.: Intern. J. Quant. Chem. **24**, 1–18 (1983)
11. Mardoyan, L.G., Sissakian, A.N.: J. Nucl. Phys. **55**(9), 2458 (1992)
12. Brychkov, Y.A., Marichev, O.I.: Integrals and Series. Special Functions. Nauka, Moscow (1983). Formula 5.13.1.6
13. Demkov, Y.N., Yermolayev, A.M.: JETF. **36**(3), 896 (1959)

New Methods and Materials in Nuclear Fuel Fabrication and Spent Nuclear Fuel and Radioactive Waste Management

S. E. Vinokurov, S. A. Kulikova, A. V. Frolova, S. S. Danilov, K. Y. Belova, A. A. Rodionova, and B. F. Myasoedov

1 Introduction

The closed nuclear fuel cycle (NFC) within the framework of the two-component nuclear energy concept developed in Russia includes uranium mining, nuclear fuel fabrication, spent nuclear fuel (SNF) reprocessing to return fissile nuclides into the cycle, fractionation of generated high-level waste (HLW) for removal and separate management of radioactive waste (RW) components of various hazard levels, including immobilization of the resulting removed waste into preservating matrices for environmentally safe temporary storage or final disposal in RW facilities. In Russia solidified HLW and long-lived waste have to be placed in underground repository. Safety for the final disposal of waste is ensured by a complex of engineering and natural barriers. In this regard, a separate actual task is also to justify the effectiveness of host rocks in preventing the penetration of radionuclides into the environment.

In recent years, the researches in the mentioned scientific directions have been carried out in Vernadsky Institute RAS in order to justify the effectiveness and radiation safety of the realized concept of closed NFC using thermal and fast neutron reactors. This article presents and summarizes the results of the following works:

- determination of the possibility of using microwave radiation in the processes of oxide (or nitride) nuclear fuel fabrication from the production of initial mixtures based on uranium dioxide (or mixed fuel) to the sintering of fuel pellets;
- a new technology for nuclear fuel regeneration by separation of fissile components and fractionation of formed HLW using a single extractant—tributyl phosphate (TBP);
- immobilization of RW generated during SNF reprocessing into preservating matrices depending on waste hazard and the order of their storage or disposal in near-surface or deep storage facilities;
- study of radionuclide distribution on rock minerals of natural safety barriers of the Nizhnekansky granitoid massif as a site for underground disposal of solidified RW.

2 Nuclear Fuel Fabrication Using Microwave Radiation

Currently, the final product of reprocessing both uranium ores and SNF is solution of uranyl nitrate, from which uranium is precipitated in the form of ammonium uranyl tricarbonate, ammonium diuranate, and a number of other compounds–precursors. These precursors are calcined in electric resistance furnaces to produce a ceramic grade UO_2 powder. Then the powder is pressed in appropriate molds and sintered in convection electric furnaces into ceramic fuel pellets. The above procedures have a number of significant drawbacks, first of all, the multistage deposition processes, the formation of large amounts of liquid RW (LRW), as well as the duration of calcination and sintering processes in resistance furnaces, requiring high energy consumption. At the same time, microwave radiation is widely used in chemical synthesis, catalysis, sintering of ceramics, sample preparation and other processes, which ensures rapid, selective, voluminous and homogeneous heating, as well as significantly lower energy consumption. Earlier in our work [1] we described the following developed methods using microwave radiation: obtaining uranium oxides from its compounds; reprocessing of unconditioned ceramic pellets of oxide uranium fuel; preparing powders of actinide oxides

S. E. Vinokurov (✉) · S. A. Kulikova · A. V. Frolova · S. S. Danilov · K. Y. Belova · A. A. Rodionova · B. F. Myasoedov
Vernadsky Institute of Geochemistry and Analytical Chemistry, Russian Academy of Sciences, 19 Kosygin St., Moscow, 119991, Russia
e-mail: vinokurov@geokhi.ru

A. A. Rodionova
Lomonosov Moscow State University, Leninskie Gory St., 1 Bld. 3, Moscow, 119991, Russia

V. P. Kolotov and N. S. Bezaeva (eds.), *Advances in Geochemistry, Analytical Chemistry, and Planetary Sciences*,
https://doi.org/10.1007/978-3-031-09883-3_39

by thermal denitration of U, Np, Pu nitrates solutions in the presence of hydrazine hydrate. The results of the development of our research in order to create a scientific basis for a new technology of nuclear fuel production, including regenerated fuel, using microwave radiation is represented in this chapter. The possibilities of using microwave radiation to obtain conditioned uranium dioxide powder from nitrate solutions and from uranium trioxide powder in reducing and inert atmospheres and in air were investigated [2], including in the presence of organic reducing agents (carbohydrazide ($OC(NHNH_2)_2$), acetohydroxamic ($CH_3CONHOH$) and aminoacetic acid (glycine, NH_2CH_2COOH)) contained in the reextracts during the extraction reprocessing of SNF from BREST-300 reactor. It was important to investigate the possibility of using microwave radiation for thermal denitration of nitric acid solutions of uranium to obtain UO_2 powder. Description of the experimental setup is given in [3].

It was found that the effect of microwave radiation on nitrate solutions is intense release of nitrogen oxides, water vapor and the formation of uranium compounds in the form of dark orange mass, both in air and in an atmosphere of reducing gas mixture (RGM) of argon with 10 vol% hydrogen [3]. According to spectrophotometric (Unicam UV-300, Unicam Instruments, UK) and radiometric methods (alpha spectrometer Alpha Analyst, Canberra, USA), it was shown that the resulting compound is UO_3. In this case, further exposure to radiation doesn't lead to changes in the obtained UO_3 powder. At the same time, it was shown that when the solutions-imitators containing organic reducing agents are reacted, U(IV) is formed in them due to partial reduction of U(VI). At the same time mixed uranium oxide UO_x powders with U(VI) content from 73 to 84% and U(IV) content from 27 to 16% respectively are obtained. Further thermal impact of 180 W microwave radiation on UO_x resulted in powders heating up to ~ 700 °C and in an atmosphere of RGM to the quantitative obtaining of UO_2 powder, which was confirmed by X-ray diffractometry (ULTIMA-IV, Rigaku, Japan): uraninite, card 65–0285 [4].

Also, the possibility of obtaining UO_2 directly from UO_3 in the presence of organic reducing agents was investigated. Studies were carried out using a microwave system Discover (SP-D, CEM Corp., USA). It was shown that when exposed to microwave radiation on mixtures of UO_3 and carbohydrazide or acetohydroxamic acid at their molar ratio of 1:1, the content of U(IV) is about 33–34%, which corresponds to its content in U_3O_8. Obviously, hydrazine and CO obtained from carbohydrazide and acetohydroxamic acid by reactions (1) and (2), respectively, partially reduce UO_3 to UO_2 by reactions (3) and (4), respectively. The resulting UO_2 absorbs microwave energy and rapidly heats the reaction mass to a temperature at which oxygen begins to detach from UO_3 to form U_3O_8, which also absorbs radiation energy, causing additional heating in the reaction mass.

$$(N_2H_3)_2CO + H_2O \rightarrow 2N_2H_4 + CO_2 \quad (1)$$

$$CH_3CONHOH \rightarrow CH_3NHOH + CO \quad (2)$$

$$2UO_3 + N_2H_4 \rightarrow 2UO_2 + N_2 + H_2O \quad (3)$$

$$UO_3 + CO \rightarrow UO_2 + CO_2 \quad (4)$$

At the same time, UO_3 in a mixture with carbohydrazide or acetohydroxamic acid taken in 1.5 molar excess relative to UO_3 almost quantitatively changes into UO_2. This is due to the fact that the gases formed in the decomposition of carbohydrazide and acetohydroxamic acid (N_2 and CO_2 or CH_3NOH + CO), the volume of which is much greater than the internal volume of the reactor, displaces the air in the reactor. Thus, a reducing atmosphere is created in the reactor, which leads to the generation of UO_2.

The data on the granulometric composition and physical characteristics of the obtained UO_2 powders are given in Table 1. The mass fraction of uranium and, accordingly, the fullness of its recovery in the obtained powders were determined by spectrophotometry, radiometry, thermogravimetric (TG) analysis and differential scanning calorimetry (DSC) (synchronous thermal analyzer STA 409 PC Luxx, Netzsch, Germany), as well as by powder X-ray diffractometry. The particle size distribution of powders was studied using a Hsiangtai LS-300 (Taiwan) vibration sieve analyzer at a rotation speed of 3000 rpm for 15 min. Specific surface area of the powder was determined using Quadrasorb SI/Kr; bulk density with shrinkage—according to the technique [5]. The moisture content in the powder was also evaluated by TG/DSC with gas phase mass spectrometry. The data in Table 1 shows that the physical characteristics of the investigated powders satisfy the regulatory requirements [6] for ceramic-quality UO_2 powder used in the industrial fabrication of oxide nuclear fuel for nuclear power plants.

The influence of pressing and sintering conditions of the obtained uranium dioxide powder under microwave radiation on the quality of fuel pellets was studied. UO_2 powder for next pressing and sintering of fuel pellets was prepared by exposure to microwave radiation on the uranyl nitrate solution containing 400 g/L of uranium; characteristics of the powder are given in Table 1. Uranium dioxide pellets were obtained by pressing in the hydraulic press PGR (LAB TOOLS) with a matrix and punch diameter of 10 mm; the surface of the mold was coated with glycerol. When pressing the pellets, the mass of pressed powder, pressure (from 2 to 6 tf/cm^2) and pressing method (single- or double-sided) were varied. Before sintering, the obtained tablets were dried at 90 °C to a residual moisture of not more than 1 wt%.

Table 1 Characteristics of UO_2 powders obtained from uranyl nitrate solutions by their thermochemical denitration using microwave radiation in an atmosphere of RGM (n.d.–not determined)

Characteristics of prepared UO_2 powders	UO_2 powders obtained under different conditions when exposed to microwave radiation				Regulatory requirements [6]
	From nitrate solutions–surrogate reextracts in an atmosphere of RGM	From UO_3 powder in the presence of carbohydrazide	From UO_3 powder in the presence of acetohydroxamic acid	From a solution of uranyl nitrate with a uranium concentration of 400 g/L in an atmosphere of RGM	
1	2	3	4	5	6
Granulometric composition, microns (share of separate fraction in the sample, %)	From 25 to 400–no less than 99.6%	x > 400 (1.4) 125 < x < 400 (65.8) 50 < x < 125 (17.8) 25 < x < 50 (12.0) x < 25 (3.1)	x > 400 (2.1) 125 < x < 400 (60.3) 50 < x < 125 (19.4) 25 < x < 50 (15.9) x < 25 (2.3)	x > 400 (0.3) 125 < x < 400 (46.5) 50 < x < 125 (28.1) 25 < x < 50 (25.0) x < 25 (0.1)	No regulated
Mass fraction of uranium in the powder, %	No less than 88.1	88.0	88.0	88.1	No less than 87.4
Bulk density with shrinkage, g/cm^3	2.35–2.43	2.6	2.7	2.4	No less than 1.8
Specific surface area, m^2/g	2.15–2.40	3.2	2.1	2.7	2.0–3.5
Mass fraction of moisture, %	n.d	No more than 0.1	No more than 0.1	~ 0.1	No more than 0.4

Schematic of the microwave sintering system for pressed tablets is shown in Fig. 1. For sintering, a microwave furnace KOCATEQ MWO2100/34 E (South Korea) with a power of up to 2.1 kW and a frequency of 2.45 GHz with two dissectors for uniform distribution of microwaves in the furnace chamber was used. The pellets were placed in a hermetically sealed reactor located in the furnace chamber and consisting of an alundum tube 400 mm long, 32 mm in diameter and 2 mm thick, into which quartz plugs were inserted at both ends, ground to its inner surface, with nozzles for the reactor inlet and outlet of RGM through a trap to atmosphere, which excluded the entry of atmospheric air into the reactor. The reactor was placed in a thermoprotective vessel made of lightweight fibrous ceramic composite (LWFC).

It was found that achieving the desired density of sintered pellets about 10.40 g/cm^3 (95% of the theoretical density of UO_2, equal to 10.97 g/cm^3) occurs in the temperature regime that includes an exposure at 1650 ± 20 °C for at least 4 h. The open porosity of such pellets is about 0.25 vol%, which corresponds to the permissible limit—not more than 1 vol%. It was noted that the density of obtained tablets practically does not depend on the mass of sintered pellets in the range from 2 to 6 g, as well as on the pressure of pressing pellets or the method of pressing.

3 New Technologies for SNF Reprocessing and RW Fractionation

Vernadsky Institute RAS is developing a new extraction process for SNF reprocessing using a single extractant—TBP, including: separation of uranium and plutonium (possibly also neptunium) from head-cycle raffinate, followed by purification of fissile nuclides from fission products (FP), production of uranium dioxide powder (or mixed actinide dioxide solution) and fabrication of fuel pellets; fractionation of head-cycle raffinate to remove separate fractions, including cesium-strontium fraction, rare earth elements (REE) fraction and minor actinides, Am and Cm; quantitative extraction of americium for following transmutation in heterogeneous or homogeneous fast reactors; immobilization of generated waste in effective preservating matrices depending on waste hazard and order of its storage or burial; controlled storage of certain types of solidified RW or their final disposal in deep storage facilities. This section presents the results of the development of individual technological processes.

Earlier, we developed a method for dissolving oxide SNF in weakly acidic solutions of Fe(III) nitrate [7–12]. In these papers it was shown that when unirradiated ceramic UO_2

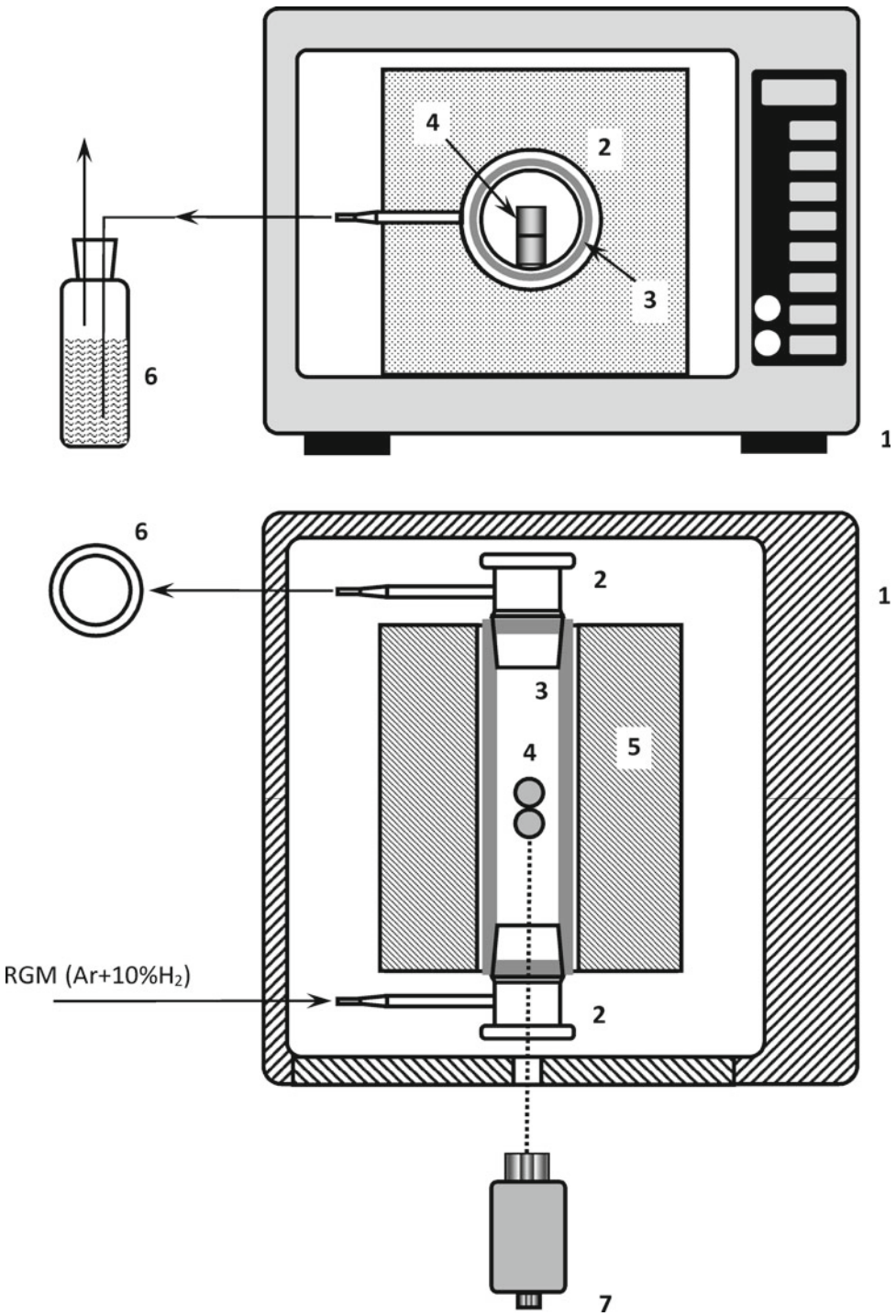

Fig. 1 Schematic diagram of an installation for sintering of UO_2 pellets under microwave radiation (top and bottom–side and top views, respectively): 1—microwave oven; 2—polished quartz plug with a pipe for RGM supply or outlet; 3—alundum tube with slits; 4—pellets of UO_2; 5—thermal protection cover of LWFC; 6—trap-hydro trap with water; 7—visual pyrometer

pellets or model SNF are dissolved in a weakly acidic solution at a molar ratio of Fe(III): U $\geq$ 2.0 fissile nuclides —U and Pu—pass into solution together with the FP—Cs, Sr, Ba, Y, La and Ce, whereas Ru, Mo, Tc ($\sim$95%), Zr ($\sim$50%), and Pd ($\sim$50%) appear in a precipitate with Fe, partially ($\sim$50%) separated as the main salt, Fe dihydroxonitrate. It was also shown that uranium and plutonium can be removed from the resulting weakly acidic solution in the presence of iron nitrate as a desalting agent by extraction with 30% TBP solutions in isoparaffin diluent Isopar M.

The developed method has been tested on real samples of WWER-1000 reactor SNF [13]. In the experiments we used a spill of SNF with a burnup of 60 GW·d/ton of U with 7–8 years of holding. The molar ratio SNF:Fe was 1:2.2, the time of complete dissolution was 1 h at a dissolution temperature of about 95 °C without stirring in the absence of

nitric acid. During dissolution, iron nitrate partially was hydrolyzed and precipitated, which took up FP, as we showed earlier on imitators. At the same time, the resulting precipitate of the basic iron salt also trapped several percent of the plutonium, which is unacceptable. Thus, optimization of the SNF dissolution process should be aimed at quantitative transfer of SNF into solution while avoiding formation of the precipitate of the main iron salt.

One of the important goals of the technology under development is to produce plutonium–uranium fuel for thermal or fast reactors, which will allow efficient use of fissile nuclides contained in SNF. In obtaining uranium–plutonium oxide MOX (or REMIX) fuel there are two possible ways of obtaining the mixture: (1) mixing individual powders of uranium and plutonium oxides, but there are difficulties because of plutonium dioxide dissolution during the following SNF reprocessing, and (2) obtaining the solid solution of U and Pu from solution by their precipitation, which seems to be the most promising way. We have shown that precipitation of uranium and plutonium from solutions with production of peroxides has a number of significant advantages [7, 12, 13]. Thus, uranium and plutonium peroxides with a purification factor of more than 30 from REE, transplutonium elements (TPE) and cesium were obtained on simulated and real SNF. It can be noted that the advantage of this method is uniform and "soft" deposition of uranium and plutonium, in contrast to "hard" ammonia deposition, as well as the absence of secondary waste. In addition, the precipitation of uranium and plutonium peroxides can leave neptunium in the solution, which in the case of using recovered fuel in thermal reactors will lead to the formation of ^{238}Pu and deterioration of plutonium properties in the following fuel recycling.

Extraction of TPE and REE from weak acid solutions with a single extractant—30% TBP—using iron nitrate as a desalting agent is the key process for realization of the new technology of SNF reprocessing. Thus, we previously obtained data on the leaching of americium and europium by iron nitrate during extraction in 30% TBP (Table 2) [13]. It was found that the presence of the desalting agent, iron nitrate, at a concentration of 1 mol/L in solution significantly increases the extraction of americium and europium, while with increasing nitric acid concentration the desalting effect is reduced, with the acid itself having a much weaker desalting effect than iron nitrate. In another experiment, it was confirmed that in the absence of iron in the solution, neodymium is practically not extracted by 30% TBP. With increasing concentrations of iron nitrate, the extraction of neodymium increases sharply, reaching a neodymium distribution coefficient of up to 12 at a concentration of iron nitrate of 2.1 mol/L. Thus, in the presence of iron nitrate 30% TBP along with uranium and plutonium effectively extracts TPE and REE.

Separation into a separate Am stream for transmutation in a fast reactor (for example, liquid-salt burner) would radically reduce the volume of HLW for deep disposal. The isotopes ^{243}Cm and ^{244}Cm contained in WWER SNF are short-lived isotopes with half-lives of 29.1 and 18.1 years, respectively; their decay produces daughter isotopes ^{239}Pu and ^{240}Pu, which can be sent to any type of reactor after Cm isotope holding. On the other hand, both Am isotopes are long-lived and require postburning in fast or liquid-salt reactors. Therefore, it is advisable to obtain separately the Cm and REE fractions for holding and the Am fraction for transmutation in fast reactors.

As part of the developed SNF reprocessing technology, selective separation of Am is possible when americium is converted to higher oxidation states [14]. Thus, we have shown that this is achieved by stabilizing Am(V), not extractable by 30% TBP in the presence of desalting agents, while Cm and REE under such conditions are extracted in the organic phase. Am(V) can be obtained by oxidation of Am(III) to Am(VI), which is very unstable and gradually transferred to Am(V), which is more stable under these conditions. It is noted that the presence of the NH_4NO_3 as a desalting agent does not affect the stability of Am(V) and Am(III) in 0.1 mol/L HNO_3 [14]. The separation of Am(V) and Cm(III) in 8 mol/L NH_4NO_3 with 0.1 mol/L HNO_3 using 30% TBP in Isopar M was performed by oxidation of Am(III) to Am(VI) and its following reduction to Am(V) according to reactions (5) and (6). The obtained Am(VI) was reduced to Am(V) by addition of H_2O_2 before extraction from 0.1 mol/L HNO_3 in the presence of 8 mol/L NH_4NO_3.

Table 2 Extraction of Am and Eu with 30% TBP from dilute solutions of nitric acid, Eu content in the initial solution of 3 g/L

HNO_3 concentration, mol/L	Desalting agent	D_{Am}	D_{Eu}	Separation factor
0.05	–	< 0.001	< 0.001	
0.2		0.004	< 0.001	
0.5		0.01	0.026	
1		0.02	0.03	
0.05	$Fe(NO_3)_3$ 1 mol/L	1.07	2.1	2.0
0.1		1.04	2.06	2.0
0.2		0.82	1.2	1.5

Table 3 Results of separation of americium and curium by extraction of 30% TBP from 0.1 mol/L HNO_3 in the presence of 8 mol/L NH_4NO_3

Solution		Concentration, mol/L			Distribution coefficient		Sorption degree %		Separation factor
		Am(V)	Am(III)	Cm(III)	Am	Cm	Am	Cm	$S_{Am/Cm}$
Initial		$2.9 \cdot 10^{-4}$	–	$2.2 \cdot 10^{-6}$	0.46	30.7	31.4	96.9	67.3
After extraction	Raffinate	$2.0 \cdot 10^{-4}$	–	$7.0 \cdot 10^{-8}$					
	Extract	–	$0.9 \cdot 10^{-4}$	$2.2 \cdot 10^{-6}$					

$$2\ Am^{3+} + 3\ S_2O_8^{2-} + 4\ H_2O \rightarrow 2\ AmO_2^{2+} + 6\ SO_4^{2-} + 8\ H^+ \quad (5)$$

$$AmO_2^{2+} + H_2O_2 + 2\ H^+ \rightarrow AmO_2^{+} + 2\ H_2O \quad (6)$$

The results on separation of americium and curium in the presence of desalting agent are presented in Table 3. As a result of the extraction, up to 97% of Cm(III) and 31% of Am(III) are transferred from the aqueous phase to the organic phase in one contact. The Am(V) remaining in the aqueous phase after extraction (70%) contains about 31 times less Cm compared to the initial solution, only 3%. Obviously, a more effective separation of americium and curium can be obtained by repeated contacts in the countercurrent extraction process.

4 Immobilization of RW into New Preserving Matrices

The problem of RW management is a key one in the atomic energy development. Approaches to RW management require optimization and selection of the most effective technologies to comply with the ambitious concept of the industry—the absence of RW discharges into an open body of water, the gradual abandonment of underground waste injection, conditioning of all types of waste generated, solving the problems of accumulated waste from past defense activities, withdrawal from operation of nuclear legacy facilities.

According to the rules and regulations in force in Russia [15], cement and glass-like matrices are used to immobilize long-lived intermediate-level waste (ILW) and HLW. At the same time, it should be noted that the use of these matrices does not allow for the effective solidification of some types of RW that are new for the NFC (for example, solutions with a high content of salts, including sulfates and chlorides), as well as waste, which must be handled during decommissioning of radiation hazardous facilities (for example, sludge deposits of industrial reservoirs or irradiated graphite of uranium-graphite reactors). It should be especially noted that there is a regulatory prohibition on the management of certain types of RW (for example, containing ammonium or radiocarbon formed from nitrogen in nitride fuel) using standard methods.

This article presents the results of research on the selection and substantiation of sodium aluminum iron phosphate glass in the Na_2O-Al_2O_3-Fe_2O_3-P_2O_5 system (NAFP glass), including the selection of the composition and study of the effect on the properties of this glass of various elements-imitating RW, in particular, REE, uranium, transuranium elements (TRU) and corrosion products.

Mineral-like matrices are considered as an alternative to cement and glass for RW immobilization. High-temperature methods for the synthesis of such matrices include a preliminary radiation-hazardous stage of waste calcination, are extremely demanding on the quality of the matrix-forming mixture and can lead to environmental pollution with volatile radionuclides. Thus, a mineral-like magnesium potassium phosphate (MPP) matrix obtained at room temperature seems promising.

Below are the main results on the development of new preservating matrices for RW disposal.

4.1 Glass-Like Sodium Aluminum Iron Phosphate (NAFP) Matrix

According to the multi-barrier concept for HLW management, the first barrier should be a preservating matrix with high hardness, mechanical strength, chemical and radiation stability, and meet the requirements throughout the entire life of the storage facility. The only matrix used in industry for HLW management today is glass. Borosilicate glass is used for the immobilization of HLW in France, Great Britain, Germany, Japan, India and South Korea, and aluminophosphate glass—in Russia [16].

As a matrix for high-iron RW, we proposed system, mol %: 40 Na_2O, 10 Al_2O_3, 10 Fe_2O_3, 40 P_2O_5. The composition of the glass, lying between the ortho- and pyrophosphate compositions, was chosen close to the base alumophosphate glass (used at Mayak Production Association, Russia), mol %: 40 Na_2O, 20 Al_2O_3, 40 P_2O_5 [17, 18]. In the selected system Al_2O_3 was equimolarly replaced by Fe_2O_3. Glasses were synthesized from charges prepared from dry reagents (sodium metaphosphate, aluminum oxide and iron oxide).

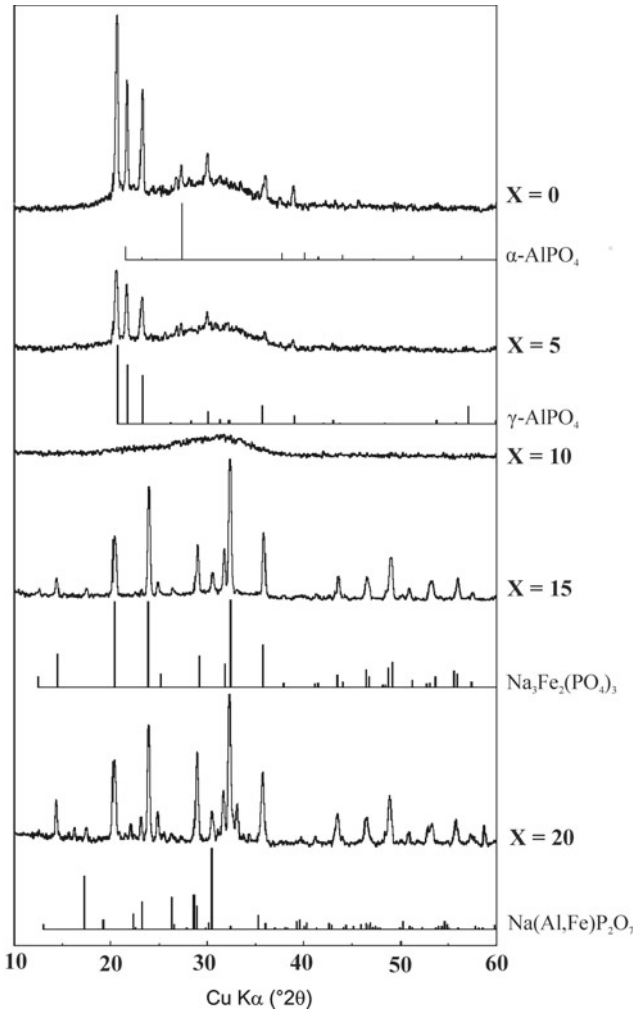

Fig. 2 X-ray diffraction patterns of the synthesized annealed samples of NAFP glass in the system, mol%: 40 Na_2O, (20-x) Al_2O_3, x Fe_2O_3, 40 P_2O_5

The charges were heated in quartz or corundum crucibles for 4 h, followed by isothermal holding for 30–120 min. After that, part of the melt was poured onto a metal tray for rapid cooling in air, and part of the melt in crucibles was annealed in a switched off furnace to room temperature. It is shown in [19], that at 10 mol% substitution of Al_2O_3 for Fe_2O_3 he crystallization stability of glass increases, including during annealing. The Fig. 2 shows that this glass is homogeneous and X-ray amorphous, while the rest of the annealed samples have a tendency to crystallize.

The chemical stability of glasses increases when 10 mol % Al_2O_3 is replaced by Fe_2O_3. At the same time, with a further increase in the content of Fe_2O_3, the chemical stability begins to decrease [18]. It was found that irradiation of quenched glass samples of the selected composition (with 10 mol% replacement of Al_2O_3 by Fe_2O_3) with accelerated electrons with an energy of 8 meV until an absorbed dose of 1 MGy is reached does not lead to noticeable changes in the structure of the glasses. There are some changes in the infrared spectra, which can be caused by variations in the coordination state of aluminum, as well as the accumulation of radiolysis products of absorbed water in glasses [20].

To study the influence of individual components of HLW on the structure and properties of NAFP glass, samples were synthesized containing weight amounts of simulators of RW, such as U, Pu, Np, REE, Re as a simulator of technetium, Mo, Zr (Table 4). REE oxides were introduced in the form of elements in various oxidation states (II, III, IV) in order to cover the spectrum of possible oxidation states of lanthanides and TRU in HLW. It was found that all the samples of quenched glasses were amorphous, while in the annealed samples, precipitation of the phases of monazite and $Na_3(Fe, Al)_2(PO_4)_3$ was observed. The chemical stability of quenched samples does not deteriorate in comparison with blank samples and is $(1–8)\cdot10^{-7}$ g/(cm^2•day) for all components, while in annealed samples it deteriorates 2–40 times, but at the same time, the leaching rate of the REE themselves remain low, which can be explained by the inclusion of REE in the crystalline phases of monazite [21].

Addition of uranium oxides up to 50 wt% made it possible to study in detail the behavior of uranium in a selected glass composition. The oxidation state of uranium in the obtained samples was determined. It was found that uranium is in the form of a complex oxide UO_{2+x} with the following composition, at%: 0.3 U^{4+}; ~ 68 U^{5+}; ~ 31 U^{6+}, t can be concluded that uranium is present in NAFP glasses in the form of clusters $\left[UO_2^{n+}O_m\right]^{k-}$, where n = 1 or 2, m = 4.5 or 6 [22]. It was found that the leachability parameters depend, among other things, on the form of the introduced uranium oxide and its amount, and the dependence of the normalized weight loss and the rate of leaching of sodium and other

Table 4 Compositions of synthesized NAFP glasses containing weight amounts of elements–HLW components

Name of samples of NAFP glass	Content of components of HLW
NAFP-REE	Up to 10 wt% REE oxides—Ce, La, Eu, Pr, Nd, Sm, Gd, Tb, Dy, Ho, Er, Yb, Y
NAFP-U	Up to 50 wt% U
NAFP-Re, Tc	Up to 6 wt% Re, Tc
NAFP-Mo, Zr	Up to 5 wt% Mo, Zr oxides
NAFP-Np, Pu	0.5 wt% Np, Pu

elements on the oxidation state and uranium content in glasses have a complex character, which is due to structural rearrangements in the anionic matrix of the glass network, especially at high concentrations of uranium introduced into the initial charge in the form of uranyl nitrate [23].

It was found that when 0.5 wt% neptunium is included in glass, it is present mainly in the form of Np^{4+} ions (70–80% of the total content) and a smaller amount of Np(V) in the form of neptunoyl NpO_2^+ ions, while plutonium added in the same amount is in the form of Pu(IV) and Pu(III) in the form of Pu^{4+} and Pu^{3+} ions in an oxygen environment with N ~ 6–8 and, probably, Pu(V) in the form of plutonoyl PuO_2^+ with N ~ 5.5–6.0. The values of the normalized leaching rate of Np and Pu differ by about an order of magnitude: 10^{-8} and 10^{-9} g/(cm^2•day), respectively, which can be explained by the difference in the preferred oxidation states.

With the inclusion of Re as a simulator of Tc, it was shown that its inclusion is up to 70% of the introduced amount, which is due to the volatility of perrhenates and pertechnetates, respectively. It was found that the leaching rate of structure-forming elements does not depend on the amount of immobilized rhenium and is about 10^{-6} g/(cm^2•day), which corresponds to the rate of leaching of components from glass of basic composition. The predominant oxidation state is Re(VII) [24]. Technetium is immobilized similarly to Re with the inclusion of up to 70% of the introduced amount, has a similar order of leaching of components, but its predominant oxidation state Tc(IV) [24].

The effect of transition metals was considered using the example of nickel. It has been found that the addition of nickel oxide in excess of the added iron oxide negatively affects the crystallization stability of the glass. It was assumed that for the immobilization of transition metals, a proportional equimolar replacement of Fe_2O_3 with transition metal oxides is required. It has been shown that the inclusion of up to 5 wt% MoO_3 and up to 1 wt% ZrO_2 in NAFP glass does not lead to the formation of independent crystalline phases. Glasses containing such amounts of Mo and Zr have an amorphous structure and low leaching rate of elements—at the level of 10^{-6} g/(cm^2•day).

Thus, we have established the optimal composition of NAFP glass in the system, mol%: 40 Na_2O, 10 Al_2O_3, 10 Fe_2O_3, which is promising for use as a matrix for HLW immobilization.

4.2 Low-Temperature Mineral-Like Magnesium Potassium Phosphate (MPP) Matrix

Mineral-like MPP matrix is formed at room temperature in an aqueous solution according to the reaction (7). It should be noted that the practical use of the MPP matrix for ILW and HLW immobilization will make it possible to avoid, unlike glass or ceramics, the creation of expensive high-temperature melters, the elimination of which after the end of the service life presents a special radioecological problem and is currently not carried out. The interest in this matrix in recent years in various countries of the world (USA, China, Korea, France, etc.) had been constantly increasing, which is reflected in the constantly growing number of publications.

$$MgO + KH_2PO_4 + 5H_2O \rightarrow MgKPO_4 \cdot 6H_2O \quad (7)$$

This article presents the results of the studies performed on the use of the MPP matrix for the immobilization of RW of various origins, activity level, state of aggregation, chemical and radionuclide composition.

Magnesium oxide (MgO) is a necessary binder reagent for reaction (7) for the synthesis of MPP matrix; it is usually produced by firing carbonate minerals—magnesite ($MgCO_3$) and dolomite ($CaMg(CO_3)_2$) at 700–800 °C. Thus, when testing several commercial MgO samples obtained from magnesite, it was shown that the composition and structure of MgO powders affect the quality of the resulting compound. We have shown that to obtain a homogeneous MPP compound with a compressive strength of about 15 MPa (requirement for the cement compound is no less than 4.9 MPa [15]) it is necessary to use MgO powder with a particle size of no more than 50 μm, with an average crystallite size no less than 40 nm. It was noted that impurities in the MgO powder of metal compounds (silicon, calcium and iron) do not have a significant effect on the synthesis conditions and the mechanical strength of the compound [25].

MgO presented on the market with a purity of at least 99 wt% has a high cost-up to $5000 per ton. At the same time, it is obvious that for the competitiveness of the technology of solidification of RW using the MPP matrix, cheaper raw materials should be used, for example, so that the cost of MgO is at the level of the cost of Portland cement ($300–400 per ton). For this, we have proposed a practically waste-free and economically viable method for producing MgO from the widely available natural mineral serpentinite [26]. The advantage of the bisulfate method of processing serpentinite is the possibility of creating a closed-loop technological process, in which all reagents are recovered, thereby ensuring the above-mentioned cost of MgO. The obtained MgO sample, in addition to the target periclase phase, also contained impurities $Mg(OH)_2$ (brucite) and $Mg_5(CO_3)_4(OH)_2{\cdot}4H_2O$ (hydromagnesite) and had a large specific surface area (64.5 m^2/g), apparently, due to the layered structure, which led to an unacceptable increase in the rate of reaction (7) and the production of an inhomogeneous compound with low strength. Earlier in the paper [25], it was noted that preliminary high-temperature heat

treatment of MgO powder at 1300 °C for 3 h reduces its chemical activity (specific surface area decreases to 5.4 m^2/g) and, as a consequence, optimizes the reaction (7) rate. In this case, the calcined MgO sample consists of a target phase with a periclase structure with an average crystallite size of at least 62 nm, an MgO content of at least 99.7 wt% and a particle size of about 55 μm, which corresponds to the previously obtained data for commercial MgO powder [25]. The composition (Fig. 3) and properties of the MPP matrix samples made using pre-calcined MgO powder obtained from serpentinite correspond to the matrix obtained using commercial MgO powder. The high chemical stability of the MPP matrix is shown: the differential leaching rate of magnesium, potassium and phosphorus from the sample on the 91st day of contact with water does not exceed $1.6 \cdot 10^{-5}$, $4.7 \cdot 10^{-4}$ and $8.9 \cdot 10^{-5}$ g/(cm^2·day), respectively [26].

In the papers [27–30], samples of the MPP compound were synthesized during the immobilization of nitrate solutions of uranium, cesium, strontium, sodium, ammonium, lanthanum and iron as imitators of LRW. The study of the phase composition and structure of the compounds has shown that the main crystalline phase of the studied samples is $MgKPO_4 \cdot 6H_2O$—an analogue of the natural mineral K-struvite, and the components of the waste are contained in stable low-soluble phosphate compounds. For example, cesium is in the composition in $MgCsPO_4 \cdot 6H_2O$, strontium —$Sr_3(PO_4)_2$, sodium—$MgNaPO_4 \cdot 6H_2O$ and Na_3PO_4 (olympite), ammonium—$MgNH_4PO_4 \cdot 6H_2O$ (struvite), lanthanum—$LaPO_4 \cdot 0.5H_2O$ (rhabdofan-(La)), uranium—$K(UO_2)PO_4 \cdot 3H_2O$ (metaancoleitis). It is shown that the mechanical (15 ± 3 MPa), thermal (up to 450 °C) and radiation (absorbed dose of 1 MGy) stability of the compounds corresponds to the current regulatory requirements [15]. The high chemical stability of the samples was established: the differential leaching rate of uranium, ^{239}Pu and ^{152}Eu on the 28th day was $1.7 \cdot 10^{-6}$, $2.1 \cdot 10^{-6}$ and $1.4 \cdot 10^{-4}$ g/(cm^2·day), respectively. It is noted that the introduction of a mineral additive—wollastonite—into the compound leads to a decrease in the leaching rate of radionuclides by up to 5 times.

In our research [27, 29] we proposed the MPP matrix for solidification of a high-salt simulator of actinide-containing ILW of complex radionuclide and chemical composition, containing a significant amount of corrosive components (nitric and sulfuric acids, iron) and ammonium ions. Since such ILW cannot be cured into a cementitious compound due to the high content of ammonium nitrate according to [15] and the high specific activity of long-lived alpha-containing nuclides, and the sulfates present in the waste negatively affect the quality of the glass-like compound. The obtained samples of the MPP compound with an immobilized strongly acidic solution simulating one stripped off raffinate of extraction refining of plutonium and neptunium had high compressive strength (10–15 MPa), including after their irradiation with an electron beam and a ^{137}Cs source (absorbed dose 1 and 0.12 MGy, respectively), after 30 freeze / thaw cycles (−40… + 40 °C), as well as after a 90-day immersion in water. The differential leaching rate of radionuclides from the MPP compound on the 28th day was (Fig. 4): ^{137}Cs–$1.6 \cdot 10^{-4}$ g/(cm^2·day), ^{90}Sr–$6.9 \cdot 10^{-6}$ g/(cm^2·day), which is below the permissible limit for a cement compound—no more than 10^{-3} g/(cm^2·day) [15]; ^{239}Pu–$4.3 \cdot 10^{-7}$ g/(cm^2·day) and ^{241}Am–$1.8 \cdot 10^{-6}$ g/(cm^2·day). It has been shown that the leaching of the compound components is controlled by various mechanisms, for example, the leaching of ^{90}Sr, ^{239}Pu and ^{241}Am in the first 7 days is generally similar and occurs due to their leaching from the surface of the compound. As the time of contact with water increases, the mechanisms of leaching of these radionuclides differ: for ^{90}Sr leaching from the surface continues; for ^{239}Pu–depletion of the surface layer; ^{241}Am–diffusion, probably from chemically stable Am(III) orthophosphate, which is analogous to monazite [29].

Our research [3–34] was aimed at the development of a new technology for immobilization of HLW using the MPP matrix as an alternative to vitrification. It was shown that the MPP compound, containing multicomponent HLW simulator, consists of a basic phosphate phase of the average composition $Mg_{1.1}Na_{0.35}K_{0.45}PO_4 \cdot (4–6)H_2O$ and a cesium-enriched phase of $MgCs_{0.5}Na_{0.2}K_{0.3}PO_4 \cdot (5–6)H_2O$ [32]. The

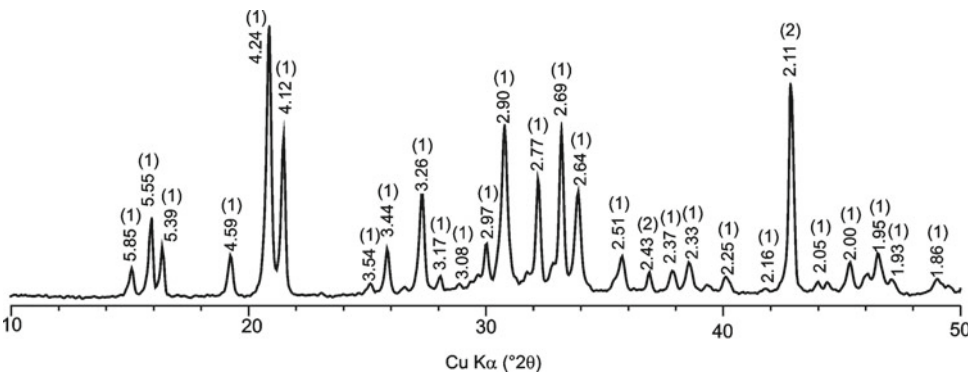

Fig. 3 X-ray diffraction pattern of the MPP matrix

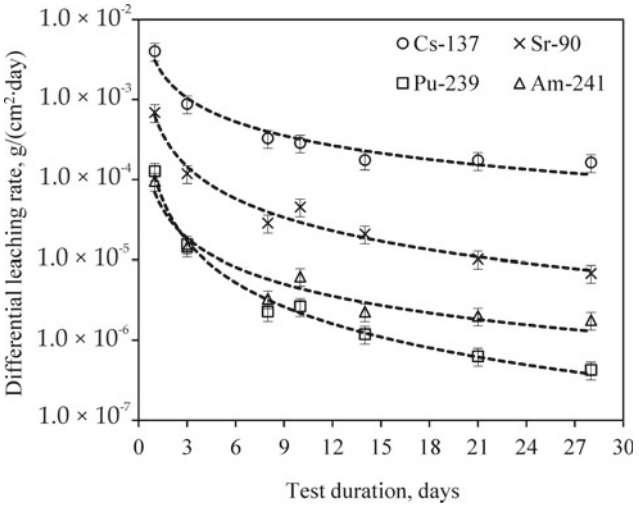

Fig. 4 Kinetic curves of leaching of radionuclides from MPP compound with immobilized ILW simulator

leaching rate of ^{239}Pu is the main criterion for assessing the quality of the matrix for HLW immobilization. It has been shown that the differential leaching rate of ^{239}Pu and ^{241}Am from the MPP compound on the 28th day of contact with water is $3.5 \cdot 10^{-7}$ and $5.3 \cdot 10^{-7}$ g/(cm^2•day), respectively [30], which meets the requirements for glass-like compound (no more than $1 \cdot 10^{-7}$ g/(cm^2•day)) [15]. It was found that when the MPP of the compound is heated, the matrix dehydrates and the quantitative removal of water from the samples is achieved at 180 °C in 6 h. One of the requirements for vitrified HLW is the thermal stability of the compound up to 450 °C [15], at which its dehydration will inevitably occur. Thus, the use of the dehydrated MPP compound for disposal of HLW radionuclides will not lead to the formation of explosive radiolytic hydrogen. It should also be noted that we previously established an extremely low chemical yield of hydrogen (0.004 H_2 molecules/100 eV) from the MPP compound after immobilization the simulator of high-salt HLW [27]. It has been shown that the introduction of mineral fillers—wollastonite [32] and zeolite [33]—increases the mechanical, thermal, and chemical stability of the MPP compound, including after its dehydration and heat treatment up to 450 °C. The compound containing 23 wt% wollastonite or 28.6 wt% zeolite retains high compressive strength (at least 9.0 MPa) even after heat treatment at 450 °C. Thermophysical indicators of the quality of the MPP of the compound were determined: the coefficient of thermal expansion of the compound in the range 250–550 °C was $(11.6 \pm 0.3) \cdot 10^{-6} \cdot 1/°C$, and the coefficient of thermal conductivity in the range 20–500 °C—about 0.5 W/(m K) [32]. It was found that the differential leaching rate of the components of the compound containing 23 wt% wollastonite on the 90th day of contact with water is g/(cm^2•day): Mg–$6.7 \cdot 10^{-6}$, K–$3.0 \cdot 10^{-4}$, P–$1.2 \cdot 10^{-4}$, ^{137}Cs–$4.6 \cdot 10^{-7}$, ^{90}Sr–$9.6 \cdot 10^{-7}$, ^{239}Pu–$3.7 \cdot 10^{-9}$, ^{241}Am–$9.6 \cdot 10^{-10}$ (Fig. 5) [31]. It was shown that leaching of radionuclides from compounds in the first 1–2 weeks of the test occurs due to dissolution (^{137}Cs) or washing (^{90}Sr) of the surface layer or diffusion from the inner layers (^{239}Pu and ^{241}Am), and during the continuation of the test, due to depletion of the surface layer. The differential leaching rate of radionuclides from a compound containing 28.6 wt% zeolite is: ^{137}Cs–$2.6 \cdot 10^{-7}$, ^{90}Sr–$2.9 \cdot 10^{-6}$, ^{239}Pu–$1.7 \cdot 10^{-9}$ and ^{241}Am–$2.9 \cdot 10^{-9}$ g/(cm^2•day) [33]. Thus, the chemical stability of the MPP compound meets the requirements for a glass-like compound: the permissible leaching rate of ^{137}Cs is no more than $1 \cdot 10^{-5}$ g/(cm^2•day), ^{90}Sr–is no more than $1 \cdot 10^{-6}$ g/(cm^2•day), ^{239}Pu–$1 \cdot 10^{-7}$ g/(cm^2•day) [15].

It is noted that the differential leaching rate of radionuclides from a compound containing 23 wt% wollastonite increases by almost an order of magnitude after heat treatment of the compound at 450 °C, g/(cm^2•day): ^{239}Pu–$7.8 \cdot 10^{-9}$, ^{152}Eu–$1.7 \cdot 10^{-7}$ and ^{90}Sr–$8.8 \cdot 10^{-6}$, however, the speed remains in line with regulatory requirements [15].

Immobilization of mobile cesium isotopes, the activity of which makes the main contribution to the total activity of HLW, is an important task in the solidification of HLW in the MPP compound. In addition, the resulting compound containing heat-generating radionuclides can be significantly heated, which sharply raises the question of its thermal stability. The research [35] was aimed at assessing the effect of various methodological approaches to HLW solidification using various sorbents for binding cesium isotopes and/or mineral modifiers on the thermal stability of the MPP compound, which was evaluated by the mechanical strength of the compound and its resistance to cesium leaching. Various sorbents were used to bind cesium in a

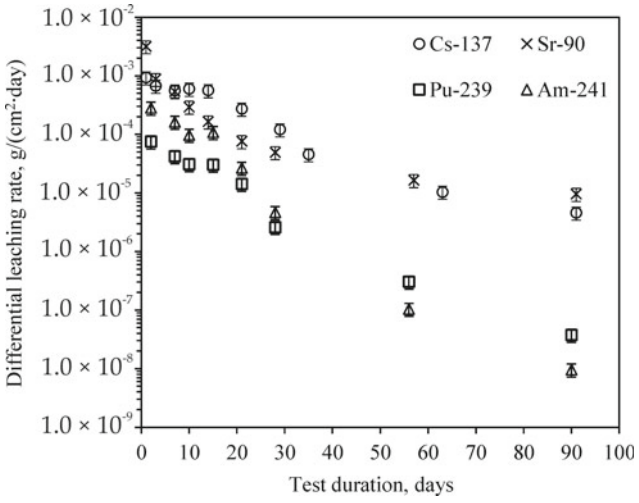

Fig. 5 Kinetic curves of leaching rate of radionuclides from the MPP compound with the immobilized HLW simulator and containing 23 wt% wollastonite

multicomponent high-salt solution-simulator of HLW: potassium-nickel ferrocyanide (PNF), natural zeolite, synthetic zeolite Na-mordenite and silicotungstic acid (STA). In the case of using zeolites, they also played the role of a mineral modifier, while when using PNF and STA, wollastonite and natural zeolite were added to the compound, respectively. It has been shown that heat treatment of a compound containing PNF and wollastonite to 450 °C has practically no effect on its compressive strength (about 12–19 MPa), and in the case of compounds containing natural zeolite, Na-mordenite and STA, it leads to a decrease in their high mechanical strength from 40 to 50 MPa on average 2–3 times. It was noted that the differential leaching rate of ^{137}Cs on the 28th day from the MPP of the compound with natural zeolite, Na-mordenite or STA was $(2.9–11.0) \cdot 10^{-5}$ g/(cm^2•day), and the dependence on the temperature of heat treatment of the compound was insignificant. Whereas the differential leaching rate of ^{137}Cs from the MPP compound containing PNF and 23.3 wt% wollastonite was $2.7 \cdot 10^{-6}$ g/(cm^2•day) and depended on the temperature of the compound heat treatment. At the same time, the leaching rate of ^{137}Cs only from the compound containing PNF and wollastonite meets the regulatory requirements for vitrified HLW [15]. It has been shown that the differential rate of ^{137}Cs leaching on day 28th from a compound containing PNF and wollastonite after heating to 250 °C was $5.3 \cdot 10^{-6}$ g/(cm^2•day). Whereas at a higher temperature, the ^{137}Cs leaching rate increased by a factor of 20 or more and amounted to $(1.2–3.3) \cdot 10^{-4}$ g/(cm^2•day) (Fig. 6), which was related to the decomposition of PNF.

Earlier it was noted that at present the Russian nuclear industry is focused on NFC closure using both thermal and fast neutron reactors. At the same time, during the combined

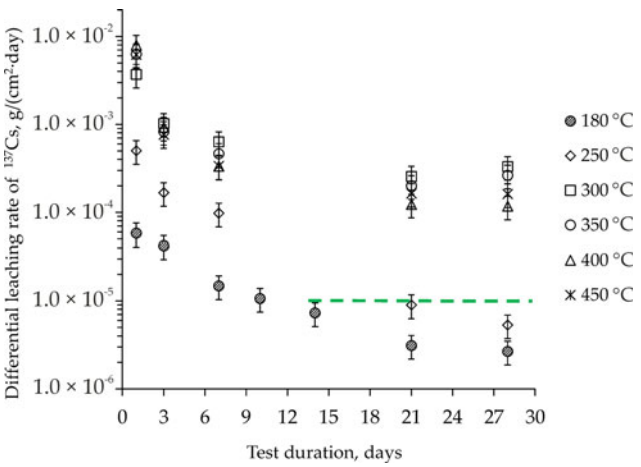

Fig. 6 Kinetic curves of the ^{137}Cs leaching rate from MPP compound samples, containing PNF and wollastonite, in dependence on the temperature of their heat treatment (green line is the upper limit of the ^{137}Cs leaching rate requirements for vitrified HLW)

pyrochemical and hydrometallurgical processing of mixed uranium–plutonium nitride (MNUP) SNF of the BREST-OD-300 reactor with lead coolant, new types of waste are generated [36]. Thus, RW during hydrometallurgical processing of MNUP SNF is containing ^{14}C in the form of $CaCO_3$ [37–39], and during pyrochemical processing—spent electrolyte [39, 40], which must be immobilized into stable forms.

In papers [37–39] we have investigated the possibility of using the MPP matrix to solve the problem of immobilization of RW containing radiocarbon (^{14}C). The study of the phase composition of the samples containing $CaCO_3$ showed that all the obtained compounds consist of the phases $MgKPO_4$•$6H_2O$, MgO and $CaCO_3$ including those after irradiation with a dose of 10^7 Gy. At the same time, with an increase in the irradiation dose of compounds containing 40 wt% $CaCO_3$ to a dose of 10^8 Gy the diffraction reflections of the $MgKPO_4 \cdot 6H_2O$ phase were not identified, apparently due to the radiolysis of crystallization water. It was found that the irradiated samples are composed of the phases of trigonal $CaCO_3$, cubic MgO, monoclinic magnesium pyrophosphate $Mg_2P_2O_7$ and the minor phase $K_6P_6O_{18}$•$3H_2O$ [38, 39]. In the study of the mechanical strength of the compound, it was found that the compressive strength of the samples obtained is 22 ± 5 MPa [37], which meets the regulatory requirements (no less than 4.9 MPa) [15]. The content of released CO_2 from the MPP compound with immobilized $CaCO_3$ during the synthesis and holding of the samples in the air atmosphere of a sealed box became constant after 7–9 days of holding the compound and did not change until the end of the curing time (14 days), and its fraction did not exceed 2% of the introduced CO_2 in the original calcium carbonate [39]. In this case, the rate of leaching of the carbonate ion from the compounds, including after irradiation with a dose of 10^8 Gy, on the 28th day of contact with water was no more than 2.8 and $4.3 \cdot 10^{-3}$ g/(cm^2•day), respectively [38, 39].

During immobilization of the spent electrolyte simulator LiCl-KCl-CsCl in the MPP matrix, it was found that the matrix is successfully formed, and cesium is contained in $MgCsPO_4$•$6H_2O$ or CsH_2PO_4 due to the replacement of potassium ions with cesium in the matrix structure or in the initial potassium dihydrogen phosphate, respectively. It was found that the compressive strength of the samples of the compound containing the LiCl-KCl-CsCl solution is (9.1 ± 0.4) MPa. As previously noted the introduction of zeolite, which, among other things, was a sorbent for the preliminary binding of cesium, in the composition of the MPP compound leads to a significant increase in both the mechanical strength and its thermal stability. The compressive strength of the compound increases 2–3 times: (17–26) MPa, and after heat treatment at 180 and 450 °C–(16–20) and (9–13) MPa, respectively. The differential rate of

^{137}Cs leaching from the compound containing the spent electrolyte simulator on the 90th day of contact with water is (5–11) · 10^{-5} g/(cm^2•day). Heat treatment of compounds at 450 °C practically does not lead to a change in the leaching rate, which is (7–11) · 10^{-5} g/(cm^2•day) [39, 40].

Thus, as a result of our work, it has been shown that a low-temperature MPP matrix can become a universal material, the use of which will make a significant contribution to solving the problem of RW management.

5 Distribution of Radionuclides on Minerals of Rocks of the Nizhnekansky Granitoid Massif Under Conditions of HLW Underground Disposal

The concept of a multi-barrier protection system for HLW disposal involves both engineering and natural barriers [35]. A natural barrier that prevents penetration of radionuclides into the environment is the host rock surrounding the HLW underground repository. At the present time all over the world there is a search for sites with different geology suitable for HLW location [41–43]. In Russia, as in most countries, crystalline rocks are being considered. As the investigated object for location of the future repository of HLW was selected "Yeniseisky" site in the zone of exocontact of the Nizhnekansky granitoid massif in 60 km from Krasnoyarsk city [44]. To justify the safety of the repository at the selected site, it is initially planned to create an underground research laboratory, in which, along with geochemical and hydrogeological studies, it is planned to study the migration of radionuclides in fractured waters [45, 46]. One of the key processes controlling the behavior of radionuclides in the conditions of underground disposal are the processes of sorption/desorption; therefore, special attention is paid to studying the sorption properties of crystalline rocks forming the site of future disposal.

Retention properties of crystalline rocks of the "Yeniseisky" site, including fractured rocks, with respect to various radionuclides were considered in papers [47–52]. In addition to establish the main parameters characterizing the sorption–diffusion of radionuclides under varying parameters of the groundwater environment, many authors note that the mineral composition of rock samples can have a significant influence on radionuclide retention. Based on data on the microdistribution of radionuclides on the sample surface, it was shown that the sorption of a particular radionuclide can be controlled by individual mineral phases [48, 52, 53]. The rocks of the "Yeniseisky" site, represented mainly by plagio and granite-gneisses, are heterogeneous in their composition, which is caused by the presence of mineralized fractures and dyke vein formations [54]. Therefore, the study of general regularities of radionuclide sorption by rocks should be completed by understanding the role of separate mineral phases in retention of mobilized waste components. Such information will help to conduct more detailed modeling of radionuclide migration in the area of future HLW disposal.

To determine a quantitative assessment of the sorption efficiency of individual minerals phases the technique to determine the parameter of relative sorption efficiency (RSE) characterizing the contribution of each mineral phase of a heterogeneous system to the sorption of various radionuclides (Cs, Sr, Am, Pu, Np, U) was developed in [55–57]. The RSE parameter was calculated as the ratio of the proportion of sorption on an individual mineral phase to the proportion of the surface area occupied by this phase. The method for determining the RSE parameter is based on a comparative analysis of the radiogram, which characterizes the micro-distribution of radionuclides over the surface of the rock sample, with the SEM image, in which the mineral phases were identified. To simplify the analysis of the radiogram and its comparison with the SEM image, the black-and-white radiogram was previously converted into a pseudo-color image using the ImageJ program (Fig. 7) [57]. The photostimulated luminescence (PSL) intensities of the pseudo-color image were correlated with the different mineral phases on the surface of the rock sample. As a result of histogram construction in ImageJ program, where PSL intensity is proportional to activity of sorbed radionuclide, and number of pixels is proportional to area occupied by mineral phase, RSE parameters were determined.

To study radionuclide microdistribution, intact rock samples of the "Yeniseisky" site of the exocontact zone of the Nizhnekansky granitoid massif from borehole R-12 were considered. The most important mineral phases for cesium sorption are layered silicates (biotite, muscovite), because for them the RSE parameters reach of 1.8. Other mineral phases such as quartz, feldspars, calcite with apatite have no significant influence on cesium sorption [57].

For radium, as in the case of cesium, the effective mineral phase is muscovite (RSE = 2.0), which is explained by the mechanism of ion exchange, which is typical for the sorption of single- and double-charged elements on layered silicates [58, 59]. Zeolite with clays also showed a high RSE value of about 2. The RSE values of radium on magnetite and plagioclase were less than one, indicating low efficiency [57].

In the case of americium sorption, the most preferable mineral phase is apatite (RSE = 2.0), followed by chlorite and Fe-containing mineral phases (magnetite with ilmenite) with RSE equal to 1.8 and 1.5, respectively [56]. The remaining mineral phases have average sorption efficiency (RSE ~ 1). In this case, the obtained RSE values give a more clear division of minerals by efficiency in contrast to the values of distribution coefficients of americium on different minerals in the work [60].

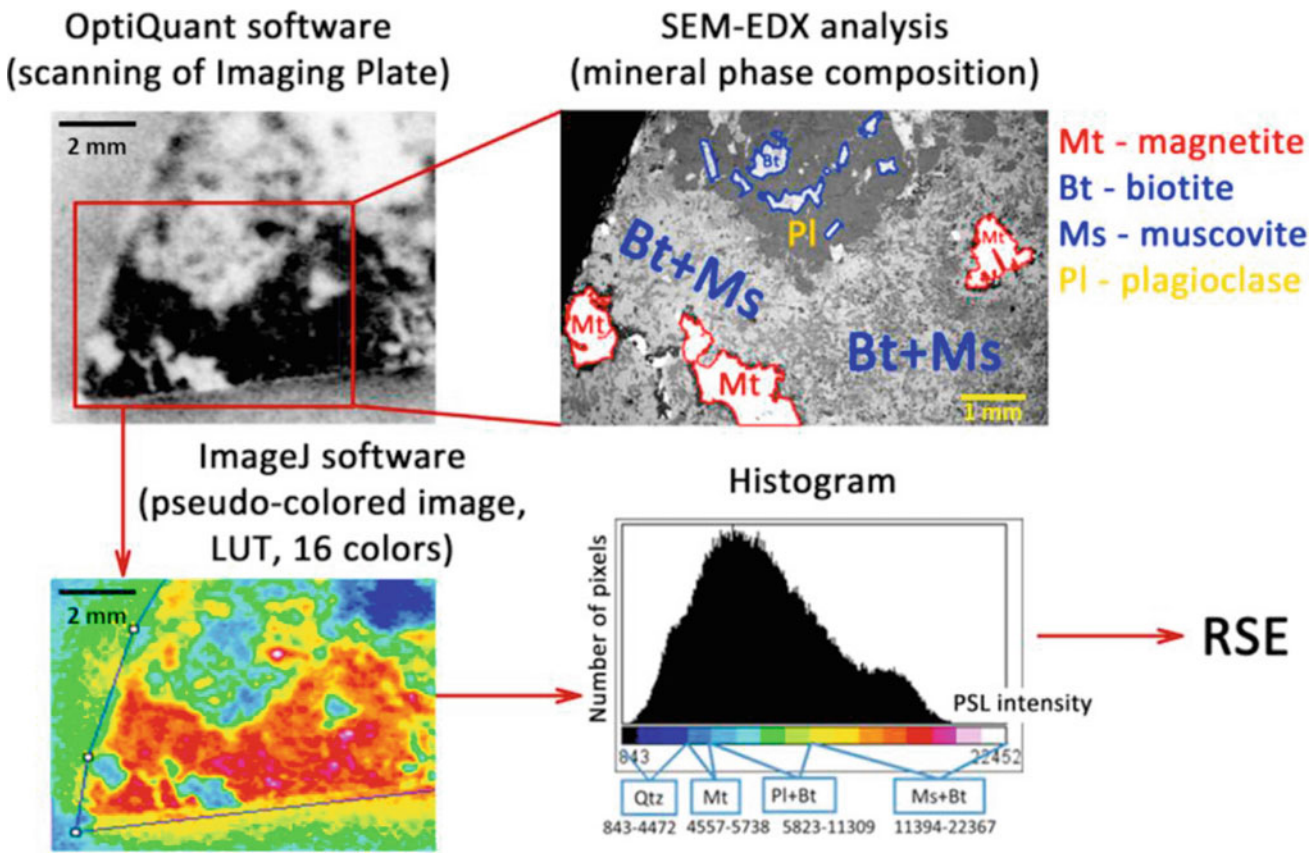

Fig. 7 Calculation scheme for relative sorption efficiency determination

Neptunium was predominantly sorbed on monazite phosphate (RSE = 2.5). Another mineral phase (association), having high sorption efficiency in relation to neptunium is magnetite with an impurity of quartz [57]. Obviously, in this case, magnetite takes the main role in the retention of neptunium, since the Fe(II) in its composition reduces neptunium, thereby increasing its sorption [61]. Among the layered silicates was identified biotite, which has average sorption properties (RSE = 1.4), which is probably due to the fact that this mineral also contains Fe(II).

As in the cases of americium and neptunium, plutonium is characterized by the formation of inner-sphere complexes on the surface of minerals, so it showed good sorption on apatite (RSE = 1.8). Other preferable mineral phases for plutonium were magnetite with an impurity of Al_2O_3 as well as chlorite with RSE values equal to 1.6 and 1.9, respectively [57]. Thus, the high sorption capacity on these minerals can be explained by the presence of Fe(II) in their composition.

For uranium, the most effective mineral phases are the layered aluminosilicates muscovite and biotite with an RSE of 1.5 and 1.7, respectively [57]. In the work [62] was noted that the main mechanism of uranium sorption on layered silicates is complexation through the formation of triple uranyl carbonate complexes at the edge sites.

Thus, the study of sorption properties of host rocks of the Nizhnekansky granitoid massif zone should take into account the role of individual mineral phases, represented by a heterogeneous system, in retention of mobilized waste components. We obtained data on the relative sorption efficiency of radionuclides and established the preferential phases of sorption for each radionuclide. For Cs(I) and Sr(II) the most effective are layered aluminosilicates (muscovite, biotite, clays); for Am(III), Pu(IV), Np(V)—phosphates (monazite, apatite), carbonates (calcite), Fe containing mineral (magnetite); for U(VI)—layered aluminosilicates (muscovite and biotite).

6 Conclusion

The presented results of laboratory studies have demonstrated the prospects of industrial application of newly developed methods and materials in the technological processes of nuclear fuel fabrication and SNF and RW management. The most important stage of pilot tests of the

proposed solutions for scientific and practical justification of their efficiency, radiation safety, technological feasibility, as well as technical and economic justification is expected in the future.

Acknowledgements This work is conducted under the GEOKHI RAS state assignment.

References

1. Kulyako, Y.M., Trofimov, T.I., Perevalov, S.A., Malikov, D.A., Samsonov, M.D., Vinokurov, S.E., Myasoedov, B.F.: Obtaining and reprocessing oxide nuclear fuel: new approaches and methods. Voprosy Radiacionnoi. Bezopasnosti. **3**, 13–22 (2015). (in Russian)
2. Kulyako, Y.M., Trofimov, T.I., Pilyshenko, K.S.: Preparation of mixed actinide dioxide powders by thermal reduction denitration using microwave radiation. Nuclear Phys. Eng. **9**(5), 425–428 (2018)
3. Kulyako, Y., Trofimov, T., Pilyushenko, K., Malikov, D., Perevalov, S., Vinokurov, S., Savel'ev, B., Myasoedov, B.: Preparation of powdered uranium oxides by denitration of nitric acid uranium solutions using uhf radiation. Radiochemistry **61**(1), 1–4 (2019)
4. JCPDS-Int. Centre Diffraction Data. PCPDFWIN **2**(2) (1999)
5. OI 001.350-2004. Poroshki oksidov urana. Metodika ispitanii dlya opredelenia nasipnoy plotnosti s ispol'zovaniem utryaski (in Russian)
6. TU 95414–2005. Poroshok dioksida urana keramicheskogo sorta s soderzhaniem isotope uran-235 menee 5.0%. Tehnicheskie uslovia (in Russian)
7. Kulyako, Y.M., Perevalov, S.A., Trofimov, T.I., Malikov, D.A., Samsonov, M.D., Vinokurov, S.E., Myasoedov, B.F.: Behavior of fission products in the course of dissolution of simulated spent nuclear fuel in iron nitrate solutions and of recovery of uranium and plutonium from the resulting solutions. Radiochemistry **53**(6), 608–611 (2011)
8. Kulyako, Y.M., Perevalov, S.A., Trofimov, T.I., Samsonov, M.D., Vinokurov, S.E., Malikov, D.A., Myasoedov, B.F.: Factors governing the efficiency of dissolution of UO_2 ceramic pellets in aqueous solutions of iron nitrate. Radiochemistry **56**(3), 247–251 (2014)
9. Myasoedov, B.F., Kulyako, Y.M.: New approaches to reprocessing of oxide nuclear fuel. J. Radioanal. Nucl. Chem. **296**(2), 1127–1131 (2013)
10. Myasoedov, B.F., Kalmykov, S.N., Kulyako, Y.M., Vinokurov, S. E.: Nuclear fuel cycle and its impact on the environment. Geochem. Int. **54**(13), 1156–1167 (2016)
11. Kulyako, Y.M., Trofimov, T.I., Ilin, E.G., Myasoedov, B.F.: New approaches to processing and fabrication of oxide nuclear fuels. Russ. J. Gen. Chem. **81**(9), 1960–1965 (2011)
12. Kulyako, Y.M., Trofimov, T.I., Malikov, D.A., Perevalov, S.A., Samsonov, M.D., Vinokurov, S.E., Myasoedov, B.F., Shadrin, A. Y.: New approaches to reprocessing of oxide nuclear fuel. Radiochemistry **52**(4), 344–349 (2010)
13. Fedorov, Y.S., Kulyako, Y.M., Blazheva, I.V., Goletskii, N.D., Ziberman, B.Y., Metalidi, M.M., Petrov, Y.Y., Ryabkova, N.V., Vinokurov, S.E., Trofimov, T.I., Myasoedov, B.F.: Dissolution of WWER-1000 spent nuclear fuel in a weakly acidic solution of iron nitrate and recovery of actinides and rare earth elements with TBP solutions. Radiochemistry **58**(3), 265–270 (2016)
14. Kulyako, Y.M., Malikov, D.A., Trofimov, T.I., Vinokurov, S.E., Pilyshenko, K.S., Zevakin, E.A., Myasoedov, B.F.: Separation of Am and Cm by extraction from weakly acidic nitrate solution with tributyl phosphate in isoparaffin diluent. Radiochemistry **60**(1), 18–22 (2018)
15. Federal norms and rules in the field of atomic energy use "Collection, processing, storage and conditioning of liquid radioactive waste. Safety Requirements" (NP-019-15), pp. 1–22. Rostekhnadzor, Russia (2015)
16. Donald, I.: Waste Immobilization in Glass and Ceramic Based Hosts: Radioactive, Toxic and Hazardous Wastes. Wiley, United Kingdom (2010)
17. Stefanovsky, S., Stefanovskaya, O., Vinokurov, S., Danilov, S., Myasoedov, B.: Phase composition, structure, and hydrolytic durability of glasses in the Na_2O-Al_2O_3-(Fe_2O_3)-P_2O_5 system at replacement of Al_2O_3 by Fe_2O_3. Radiochemistry **57**(4), 348–355 (2015)
18. Stefanovsky, S., Stefanovskaya, O., Kadyko, M., Myasoedov, B., Nikonov, B., Vinokurov, S., Danilov, S.: Effect of synthesis conditions on the phase composition and structure of sodium-aluminum-iron-phosphate glasses. Voprosy Radiacionnoi Bezopasnosti **3**, 56–66 (2015). (in Russian)
19. Stefanovsky, S., Stefanovsky, O., Kadyko, M., Presniakov, I., Myasoedov, B.: The effect of Fe_2O_3 substitution for Al_2O_3 on the phase composition and structure of sodium–aluminum–iron phosphate glasses. J. Non-Cryst. Solids **425**, 138–145 (2015)
20. Stefanovsky, S., Presniakov, I., Sobolev, A., Kadyko, M., Stefanovskya, O.: Effect of emission by accelerated electrons on the iron oxidation state and structure of sodium-aluminum-iron-phosphate glasses. Phys. Chem. Mater. Treat. **6**, 25–41 (2016)
21. Danilov, S., Stefanovsky, S., Stefanovskaya, O., Vinokurov, S., Myasoedov, B., Teterin, Y.: Aluminum (Iron) phosphate glasses containing rare earth and transuranium elements: phase composition, oxidation state of Np and Pu, and hydrolytic durability. Radiochemistry **60**(4), 434–439 (2018)
22. Maslakov, K., Teterin, Y., Stefanovsky, S., Kalmykov, S., Teterin, A., Ivanov, K.: XPS study of uranium-containing sodium-aluminum-iron-phosphate glasses. J. Alloy. Compd. **712**, 36–43 (2017)
23. Danilov, S., Vinokurov, S., Myasoedov, B., Stefanovsky, S.: Hydrolytic durability of uranium-containing sodium aluminum (iron) phosphate glasses. Radiochemistry **59**(3), 259–263 (2017)
24. Danilov, S., Frolova, A., Teterin, A., Maslakov, K., Teterin, Y., Vinokurov, S.: Immobilization of rhenium as a technetium surrogate in aluminum iron phosphate glass. Radiochemistry **63**(1), 99–106 (2021)
25. Vinokurov, S.E., Kulikova, S.A., Krupskaya, V.V., Tyupina, E.A.: Effect of characteristics of magnesium oxide powder on composition and strength of magnesium potassium phosphate compound for solidifying radioactive waste. Russ. J. Appl. Chem. **92**(4), 490–497 (2019)
26. Kulikova, S.A., Vinokurov, S.E., Khamizov, R.K., Vlasovskikh, N.S., Belova, K.Y., Dzhenloda, R.K., Konov, M.A., Myasoedov, B.F.: The use of MgO obtained from serpentinite in the synthesis of a magnesium potassium phosphate matrix for radioactive waste immobilization. Appl. Sci. **11**, 220 (2021)
27. Vinokurov, S.E., Kulikova, S.A., Krupskaya, V.V., Myasoedov, B.F.: Magnesium potassium phosphate compound for radioactive waste immobilization: phase composition, structure, and physicochemical and hydrolytic durability. Radiochemistry **60**(1), 70–78 (2018)
28. Vinokurov, S.E., Kulikova, S.A., Belova, K.Y., Rodionova, A.A., Myasoedov, B.F.: Phase composition, structure, and hydrolytic durability of a uranium-containing magnesium potassium phosphate compound. Radiochemistry **60**(6), 644–647 (2018)

29. Vinokurov, S.E., Kulikova, S.A., Krupskaya, V.V., Danilov, S.S., Gromyak, I.N., Myasoedov, B.F.: Investigation of the leaching behavior of components of the magnesium potassium phosphate matrix after high salt radioactive waste immobilization. J. Radioanal. Nucl. Chem. **315**(3), 481–486 (2018)
30. Vinokurov, S.E., Kulikova, S.A., Myasoedov, B.F.: Magnesium potassium phosphate compound for immobilization of radioactive waste containing actinide and rare earth elements. Materials **11**, 976 (2018)
31. Vinokurov, S.E., Kulikova, S.A., Myasoedov, B.F.: Solidification of high level waste using magnesium potassium phosphate compound. Nucl. Eng. Technol. **51**(3), 755–760 (2019)
32. Vinokurov, S.E., Kulikova, S.A., Myasoedov, B.F.: Hydrolytic and thermal stability of magnesium potassium phosphate compound for immobilization of high level waste. J. Radioanal. Nucl. Chem. **318**(3), 2401–2405 (2018)
33. Kulikova, S.A., Vinokurov, S.E.: The influence of zeolite (Sokyrnytsya deposit) on the physical and chemical resistance of a magnesium potassium phosphate compound for the immobilization of high-level waste. Molecules **24**(19), 3421 (2019)
34. Kulikova, S.A., Danilov, S.S., Belova, K.Y., Rodionova, A.A., Vinokurov, S.E.: Optimization of the solidification method of high-level waste for increasing the thermal stability of the magnesium potassium phosphate compound. Energies **13**(15), 3789 (2020)
35. IAEA. Geological Disposal Facilities for Radioactive Waste Specific Safety Guide. IAEA, pp. 124 (2011)
36. Shadrin, A.Y., Dvoeglazov, K.N., Maslennikov, A.G., Kashcheev, V.A., Tret'yakova, S.G., Shmidt, O.V., Vidanov, V.L., Ustinov, O.A., Volk, V.I., Veselov, S.N., Ishunin, V.S.: PH process as a technology for reprocessing mixed uranium-plutonium fuel from BREST-OD-300 reactor. Radiochemistry **58**, 271–279 (2016)
37. Dmitrieva, A.V., Kalenova, M.Y., Kulikova, S.A., Kuznetsov, I. V., Koshcheev, A.M., Vinokurov, S.E.: Magnesium-potassium phosphate matrix for immobilization of 14C. Russ. J. Appl. Chem. **91**(4), 641–646 (2018)
38. Lizin, A.A., Yandaev, D.M., Shadrin, A.Y., Kalenova, M.Y., Dmitrieva, A.V., Tomilin, S.V., Golubenko, I.S., Khamdeev, M.I., Momotov, V.N., Tikhonova, D.E., Dmitrieva, O.S., Kolobova, A. A., Poglyad, S.S., Dodonova, M.V., Vinokurov, S.E., Myasoedov, B.F.: Radiation and chemical stability of a magnesium-phosphate matrix for ^{14}C immobilization. Radiochemistry **62**(1), 131–137 (2020)
39. Vinokurov, S.E., Kulikova, S.A.: Magnesium potassium phosphate matrix for the immobilization of radioactive waste generated during the reprocessing of mixed uranium plutonium nitride spent nuclear fuel. RAD Conf. Proc. **4**, 11–17 (2020)
40. Kulikova, S.A., Belova, K.Y., Tyupina, E.A., Vinokurov, S.E.: Conditioning of spent electrolyte surrogate LiCl-KCl-CsCl using magnesium potassium phosphate compound. Energies **13**(8), 1963 (2020)
41. McKinley, I.G., Alexander, R.W., Blaser, P.C.: Development of geological disposal concepts. Radioact. Environ. **9**(6), 41–76 (2007)
42. Stephens, M.B.: Forsmark site investigation. Bedrock geology—overview and excursion guide. SKB Rep. 52 (2010)
43. Alexander, W.R., McKinley, I.G., Vomvoris, S.: Nagra's Grimsel URL: from underground testing to the demonstration of disposal systems. Proceedings—10th International Conference Environmental Remediation Radioactivity Waste Management ICEM'05, vol. 2005, pp. 1678–1683 (2005)
44. Anderson, E.B., et al.: Underground Isolation of Radioactive Waste, p. 592. Mining Book, Moscow, (2011) (in Russian)
45. Abramov, A.A., Bolshov, L.A., Dorofeev, A.N., Igin, I.M., Kazakov, K.S., Krasilnikov, V.Y., Linge, I.I., Trokhov, N.N., Utkin, S.S.: Underground research laboratory in the nizhnekanskiy massif: evolutionary design study. Radioact. Waste **10**(1), 9–21 (2020)
46. Gupalo, V.S.: Spatial characterization of the physical process parameters in rock mass during construction of the underground facility for the RW disposal. Russ. J. Earth Sci. **19**(6), 1–13 (2019)
47. Petrov, V.G., Vlasova, I.E., Kuzmenkova, N.V., Kalmykov, S.N.: Sorption characteristics of rocks in the Yenisei site of Nizhnekansky granitoid massif. Gorn. Zhurnal **10**, 84–88 (2015)
48. Vlasova, I., Petrov, V., Kuzmenkova, N., Kashtanov, A., Petrov, V., Poluektov, V., Kalmykov, S., Hammer, J.: Sorption of radionuclides on the rocks of the exocontact zone of Nizhnekansky granitoid massif. MRS Adv. **1**(61), 4061–4067 (2016)
49. Martynov, K.V., Konevnik, Y.V., Zakharova, E.V.: Barrier properties of crystalline rocks in radionuclide migration. Radiochemistry **59**(4), 425–433 (2017)
50. Konevnik, Y.V., Zakharova, E.V., Martynov, K.V., Shiryaev, A. A.: Influence of temperature on the speciation of radionuclides sorbed onto rocks from the Nizhnekansky massif. Radiochemistry **59**(3), 320–325 (2017)
51. Konevnik, Yu.V., Zakharova, E.V., Martynov, K.V., Andryushchenko, N.D., Proshin, I.M.: Influence of temperature on the sorption properties of rocks from the Nizhnekansky massif. Radiochemistry **59**(3), 313–319 (2017)
52. Rozov, K.B., Rumynin, V.G., Nikulenkov, A.M., Leskova, P.G.: Sorption of 137Cs, 90Sr, Se, 99Tc, 152(154)Eu, 239(240)Pu on fractured rocks of the Yeniseysky site (Nizhne-Kansky massif, Krasnoyarsk region, Russia). J. Environ. Radioact. **192**, 513–523 (2018)
53. Konevnik, Yu.V., Zakharova, E.V., Shiryaev, A.A., Olds, T.A., Burns, P.C.: Mineral-specific heterogeneous neptunium sorption onto geological repository rocks in oxic and anoxic conditions and various temperatures. Chem. Geol. **545**, 119654 (2020)
54. Petrov, V.A., Poluektov, V.V., Hammer, J.R., Zulauf, G.: Analysis of mineralogical and deformation-induced transformations of Nizhnekansky Massif rocks to estimate their retention capacity in geological disposal and isolation of radioactive waste. Gorn. Zhurnal **10**, 67–72 (2015)
55. Rodionova, A.A., Petrov, V.G., Vlasova, I.E., Kalmykov, S.N., Petrov, V.A., Poluektov, V.V., Hammer, J.: The radionuclide distribution onto different mineral phases of the rocks of the exocontact zone of Nizhnekansky granitoid massif. Perspect. Sci. **12**, 100406 (2019)
56. Rodionova, A.A., Petrov, V.G., Vlasova, I.E., Yapuskurt, V.O., Petrov, V.A., Poluektov, V.V., Hammer, J., Kalmykov, S.N.: Digital radiography for evaluating the relative efficiency of radionuclide sorption onto various rock minerals. Radiochemistry **61**(1), 37–43 (2019)
57. Petrov, V.G., Vlasova, I.E., Rodionova, A.A., Yapaskurt, V.O., Korolev, V.V., Petrov, V.A., Poluektov, V.V., Hammer, J., Kalmykov, S.N.: Preferential sorption of radionuclides on different mineral phases typical for host rocks at the site of the future Russian high level waste repository. Appl. Geochem. **100**, 90–95 (2019)
58. McKinley, J.P., Zachara, J.M., Heald, S.M., Dohnalkova, A., Newville, M.G., Sutton, S.R.: Microscale distribution of cesium sorbed to biotite and muscovite. Environ. Sci. Technol. **38**(4), 1017–1023 (2004)
59. Ames, L.L., McGarrah, J.E., Walker, B.A.: Sorption of uranium and radium by biotite, muscovite and phlogopite. Clays Clay Miner. **31**(5), 343–351 (1983)
60. Allard, B., Beall, G.W.: Sorption of americium on geologic media. J. Environ. Sci. Heal. Part A Environ. Sci. Eng. **14**(6), 507–518 (1979)

61. Nakata, K., Nagasaki, S., Tanaka, S., Sakamoto, Y., Tanaka, T., Ogawa, H.: Sorption and reduction of neptunium(V) on the surface of iron oxides. Radiochim. Acta. **90**(9), 665–669 (2002)
62. Arnold, T., Utsunomiya, S., Gerhard, G., Ewing, R.C., Baumann, N., Brendler, V.: Adsorbed U(VI) surface species on muscovite identified by laser fluorescence spectroscopy and transmission electron microscopy. Environ. Sci. Technol. **40**(15), 4646–4652 (2006)

Prototypes of New Radiopharmaceuticals Based on Carbon Nanomaterials: Nanodiamonds Versus Nanotubes

A. G. Kazakov, J. S. Babenya, T. Y. Ekatova, S. E. Vinokurov, and B. F. Myasoedov

1 Introduction

Nuclear medicine is the field of medicine that uses short-lived radioactive isotopes as a basis for pharmaceuticals (RPs) for diagnostics and therapy. Besides a radionuclide, RPs can also include carrier, chelator, vector, linker, and other differently functioning components, which in conjunction should provide targeted delivery of RPs to affected organs and tissues.

Nowadays nanomaterials are actively being studied as isotope carriers for RPs, with carbon nanomaterials (CNs) being the promising ones. The main advantages of such material include significant surface area and the possibility of its targeted functionalization by different groups or substances [1, 2]. The listed properties of CNs allow to directionally create nanomaterials for different tasks [3–5], in particular, the possibility of binding cations of metals to the surface of CNs allows to consider CNs as a basis for RPs [6, 7]. There are works presenting studies on properties of RPs based on CNs such as nanodiamonds (NDs) [8, 9], graphene and its oxide [10–15], carbon nanotubes (CNTs) [16–22], and others. The investigation of conditions in which radionuclide successfully binds with CNs is the first step towards creating these RPs.

The results of our recent studies on CNs as carriers of medical radionuclides for further creation of RPs are presented in this work. We investigated the sorption of isotopes of the following elements: Tc [23, 24], Y [23, 25, 26], Ga [27], Bi [23, 28], Ac [29], and Ra [23], which have isotopes for therapy and diagnostics in nuclear medicine, onto NDs and multi-walled CNTs (MWCNTs). After generalization and comparison of results of conducted experiments, the optimal carriers for each radionuclide are suggested to help to create RPs on their basis in the future.

2 Preparation of CNs and Their Characterization

The commercial samples of the following CNs were used in our research: ND powder (SKTB «Technolog», Russia, trade mark UDA-TAN) and MWCNT powder («Nano-TekhTsentr» Ltd., Tambov, Russia). All chemical reagents used in this study were chemically pure.

Physico-chemical properties of used CNs were determined using the following methods: high-resolution TEM (JEOL JEM-2100F/Cs/GIF (200 kV, 0.8 A), Tokyo, Japan), ICP-MS (X Series 2, Thermo Scientific, USA), XPS (Kratos Axis Ultra DLD, Great Britain), DLC (ZetaSizer Nano ZS analyzer (633 nm) ZEN 3600, Great Britain), BET and potentiometric titration. The determined physico-chemical properties are presented in Table 1.

3 Sorption and Desorption Experiments

Sorption of chosen radionuclides was studied in water solutions with different pH made by addition of HCl or NH_3 to double distilled water (DDW), in 0.9% NaCl, in phosphate buffered saline with pH 7.3 (PBS) using suspensions of 1 mg/mL CNs. The solution of selected media was added into Eppendorf test-tubes, then the aliquot of CNs suspension and radioactive tracer were added to such an extent that the volume of the solution became 1 mL and CNs content was 100 μg/mL. Experiments were conducted at 25 or 37 °C (25 °C by default unless otherwise stated), controlled by thermal shaker attachment (TS-100 m Biosan, Latvia). After shaking at speed of 1100 rpm, phases were separated by centrifuging for 20 min at 18,000 g (centrifuge CM-50,

A. G. Kazakov (✉) · J. S. Babenya · T. Y. Ekatova · S. E. Vinokurov · B. F. Myasoedov
Vernadsky Institute of Geochemistry and Analytical Chemistry, Russian Academy of Sciences, 19 Kosygin St, Moscow, 119991, Russia
e-mail: adeptak92@mail.ru

V. P. Kolotov and N. S. Bezaeva (eds.), *Advances in Geochemistry, Analytical Chemistry, and Planetary Sciences*,
https://doi.org/10.1007/978-3-031-09883-3_40

Table 1 Characterized properties of used CNs [23]

Characteristics	ND	MWCNT
Shapes and sizes of initial particles	Spherical particles, 3–10 nm	Length > $2 \cdot 10^4$ nm; diameter 30 nm; wall thickness 5–10 nm
Elemental composition of surface according to XPS, %	C (sp^3)–92.3 O–7.7	C (sp^2)–99.0 O–1.0
Amount of impurities according to ICP-MS, mg/g	1.4	14.0
Main impurities (more than 0.1 mg/g) and their amount, mg/g	Fe–0.538 Ti–0.459 K–0.156	Mo–6.880 Co–5.830 Al–0.635 Ni–0.156
Specific surface area, m^2/g	240	160
Size of particles and their aggregates in hydrosols according to DLC, nm	100	n/d[1]
Number of carboxyl groups on the surface, μmol/g	330	–

[1]Linear size of particles exceeds 10^3 nm at least in one direction

Eppendorf, USA), aliquot of the obtained solution was taken, and its gamma- or beta-spectrum was registered [23].

Stability of radionuclides sorbed onto CNs was studied by determination of desorption in model biological solutions: 0.9% NaCl, PBS, 40 g/L of bovine serum albumin (BSA) in PBS, and fetal bovine serum (FBS). The solution in the test-tube was agitated, placed on a shaker, then centrifuged again, and the 0.5 mL of supernatant were separated for measurement.

Data on medical isotopes of Tc, Y, Ga, Bi, Ac, and Ra, isotopes used in the experiments, and also on methods of their production is presented in Table 2. Content of ^{90}Y in experiments was determined by liquid scintillation spectrometry (LS-spectrometer GreenStar, Russia) using LS-cocktail UltimaGold (PerkinElmer Inc., USA). Determination of all other radionuclide contents was conducted using gamma-ray spectrometer with high-purity germanium detector GC 1020 (Canberra Inc., USA).

Table 2 Medical isotopes, isotopes used in our experiments and ways of their production

Nuclear medicine isotope and its application	Isotope used in experiments	$T_{1/2}$ of used isotopes	Most intensive gamma-rays, keV, (p, %)	Manufacturer and/or way of production
^{99m}Tc, SPECT[1]	^{99m}Tc	6.01 h	140.5 (89)	Karpov Institute of Physical Chemistry (Obninsk, Russia), separation from commercial $^{99}Mo/^{99m}Tc$ generator
^{90}Y, β-therapy	^{90}Y	64.00 h	–	Separation from parent ^{90}Sr solution using method [26]
^{68}Ga, PET[2]	^{68}Ga	67.63 min	1077.4 (3)	Cyclotron Co., Ltd., (Obninsk), separation from parent ^{68}Ge solution using method [27]
$^{212,213}Bi$, α-therapy	^{207}Bi	31.55 y	569.7 (97) 1063.7 (74)	Cyclotron Co., Ltd., (Obninsk)
^{225}Ac, α-therapy	^{228}Ac	6.15 h	338.3 (11) 911.2 (26)	Separation from parent ^{228}Ra solution separated from $^{232}Th(NO_3)_4$ (sample age was 60 years) using method [29]
^{223}Ra, α-therapy	^{226}Ra	1600 y	186.2 (4)	Dissolving of $^{226}RaBr_2$ and using aliquots of obtained solution

[1]Single-photon emission computed tomography
[2]Positron emission tomography

3.1 Nanodiamonds

Sorption of Tc(VII) milked from ^{99}Mo/^{99m}Tc generator in form of $^{99m}TcO_4^-$ was carried out in a DDW. It was determined that sorption of Tc(VII) onto NDs was 50% for 5 min and the equilibrium is achieved within 5 min [23, 24]. It was shown that 0.9% NaCl, PBS and BSA in PBS quantitatively desorbed Tc(VII) from NDs after 30 min. Moreover, it was established that no sorption onto these samples could be observed in the presence of 0.9% NaCl in 1 h. For this reason in all further experiments Tc(VII) was reduced to Tc(IV) by tin(II) chloride using well-known method [30]. To fixate pH of solution after the reduction, the sorption was conducted in PBS. It was determined that NDs sorbed about 90% of Tc(IV), and the sorption process occurred quickly – equilibrium was attained after 5 min. The stability of obtained conjugate if Tc(IV)@ND was studied in BSA in PBS media. It was shown that Tc(IV) desorption did not exceed 5% at 37 ˚C after 24 h. Thus, the study showed that Tc(IV)@ND would likely be stable after being injected into bloodstream, and corresponding in vivo experiments were conducted to prove this suggestion (Sect. 5).

Sorption of Y(III) was studied in PBS for 24 h, it was determined that after 15 min 85% of Y(III) was sorbed onto NDs, and then sorption equilibrium was gradually established over 24 h [23]. Sorption of Y(III) onto NDs in aqueous solutions was also studied in detail at pH 3 to 7, in 0.9% NaCl and in PBS [25]. No sorption was observed at pH 3 in 1 h. At pH 4 NDs sorbed 45% Y(III) in 2 h, at pH 4.5 sorption increased up to 60% in the same time, pH increasing to 5 led to the quantitative sorption (Fig. 1). The sorption equilibrium was achieved in the first 15 min in the whole studied range of pH. Thus, it was shown that increase in acidity of solution resulted in decrease in sorption. To determine the influence of salt content on the sorption of Y (III), sorption in aqueous solution with pH 7, in 0.9% NaCl, and in PBS was studied. The results demonstrated that the presence of salts caused no significant change in sorption of Y(III). Thus, sorption in aqueous solutions and in PBS reached 90%, and in 0.9% NaCl insignificantly decreased to 84% in 2 h. To determine the stability of Y(III)@ND conjugate, its stability in FBS at 37 °C was studied; it was established that desorption reached 10% in 1 h, then gradually rose up to 25% in 24 h.

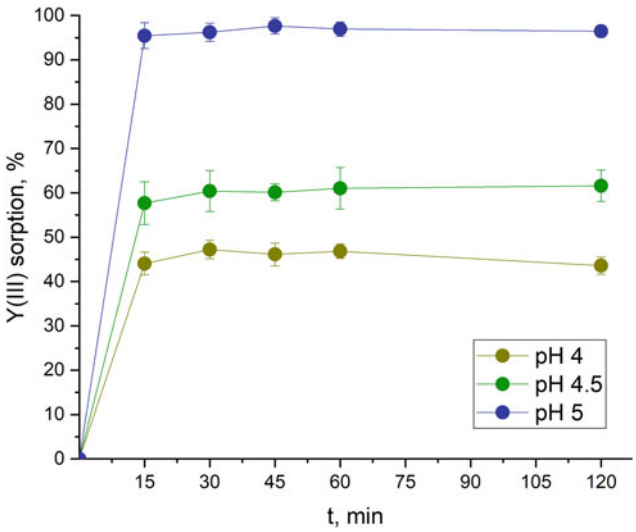

Fig. 1 Sorption of Y(III) onto NDs in water solutions at 25 °C

The influence of sizes of NDs aggregates in hydrosols and ζ-potential of their surface on sorption of Y(III) was studied [26]. NDs from different manufacturers were used for this purpose; Table 3 presents their properties and obtained equilibrium values of sorption and desorption.

Obtained data showed that the values of sorption and desorption did not depend on elemental composition of surface, but correlated with aggregate sizes and ζ-potential. Thus, the decrease in aggregate sizes from 600 to 80 nm (and increase in ζ-potential from 5 to 30 mV accordingly) resulted in increase in sorption by 15% and decrease in desorption by 5%. As a result, future use of NDs as ^{90}Y carriers in RPs requires controlling sizes of NDs aggregates.

We investigated sorption kinetics of Ga(III) onto NDs in DDW [27]. It was shown that sorption equilibrium was achieved in 5 min, with ND sorbing 80% of Ga(III). Dependence of Ga(III) sorption on pH was also investigated (Fig. 2). It was demonstrated that decreasing pH to 5 resulted in the slight decrease (by 5%) of Ga(III) sorption (compared to pH 7), while at pH 3 there was a significant decrease in sorption of Ga(III) to 25% in 120 min. In addition, sorption at pH 3 slowed down, and equilibrium was achieved in 45 min, while at pH 5 and 7—in 5 min. At pH 1, as shown by our studies, Ga(III) sorption was not observed for 120 min. Examination of stability of Ga(III) @ND in BSA in PBS showed that only 20% of Ga(III) were desorbed after 90 min. Study of Ga(III) desorption from ND at 37 °C demonstrated that desorption increased insignificantly—up to 35% in 90 min.

Study on sorption of Bi(III) indicated that sorption in DDW was close to quantitative, and equilibrium was achieved in 5 min [23]. Dependence on pH was studied in detail; the absence of sorption was observed in 60 min at pH 1 [28]. With increasing pH, the sorption increased too (Fig. 3). Thus, sorption was 40% at pH 2; with an increase in pH to 3 sorption became more than 80%. At pH in the range of 5 to 7, the maximum sorption of Bi(III) was observed (> 95%). It is also noticeable that the sorption of Bi(III) in all cases was characterized by fast kinetics-equilibrium occurred in 5–15 min. Desorption studies in BSA in PBS demonstrated that no more than 5% of Bi(III) was desorbed in 5 h. This value did not change while examining Bi(III)

Table 3 The results of the study on sorption and desorption of Y(III) onto commercial NDs from different manufacturers

Sample	According to XPS			According to DLS		Sorption of Y (III) in PBS in 0.5 h, %	Desorption of Y (III) in solution of BSA in PBS in 15 min, %
	C, at. %	O, at. %	N, at. %	ζ-potential, mV	Average size of aggregates, nm		
UDA-TAN (SKTB «Technolog», Russia)	91.0	7.7	1.3	+34 ± 5	70	98.6 ± 0.5	19.2 ± 1.8
PL-SDND («PlasmaChem», Germany)	82.3	15.8	1.9	−42 ± 11	50	95.6 ± 1.0	21.9 ± 3.2
PL-D-G01 («PlasmaChem», Germany)	86.2	12.2	1.6	−4 ± 3	600	80.5 ± 1.8	27.1 ± 3.9
StaNDsart ND («Adamas nanotechnologies», USA)	90.2	8.5	1.3	−11 ± 5	550	79.2 ± 2.4	24.7 ± 4.3
Ray ND («Ray techniques Ltd.», Israel)	90.3	8.0	1.7	+29 ± 5	80	93.5 ± 1.1	20.4 ± 2.8

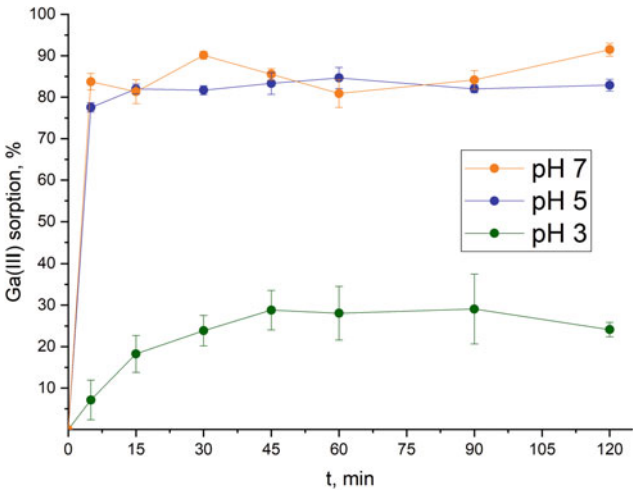

Fig. 2 Sorption of Ga(III) onto NDs in water solutions at 25 °C

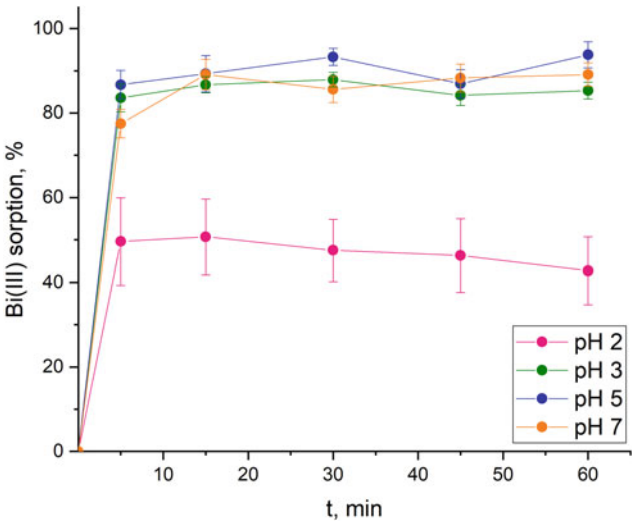

Fig. 3 Sorption of Bi(III) onto NDs in water solutions at 25 °C

desorption in the same media at 37 °C for 5 h. Additionally, desorption of Bi(III) in FBS at 37 °C was investigated, and its value in 120 min was 19%.

Sorption of Ac(III) was studied in PBS and was close to quantitative (no less than 95%) with equilibrium being achieved in 30 min [29]. Desorption of Ac(III) in BSA in PBS media was 35% in 30 min, and the desorption value did not significantly change in the following 3 h.

Sorption of Ra(II) in aqueous solutions was not observed in 1 h [23].

3.2 Carbon Nanotubes

Sorption of Tc(VII) onto MWCNTs in DDW reached 70%, and the equilibrium was achieved in 5 min [23]. However, as in the case of NDs, increase in salt content led to quantitative desorption, and Tc(VII) was reduced to Tc(IV) in the further experiments. It was determined that sorption of Tc (IV) onto MWCNTs did not exceed 10% in 60 min, so MWCNTs cannot be considered to be a promising carrier of ^{99m}Tc.

The study of Y(III) sorption in PBS found that MWCNTs showed a weak ability to sorb Y(III)–45% was sorbed after 30 min, after which equilibrium was observed at 24 h [23]. The study of desorption in BSA in PBS showed that desorption of Y(III) from MWCNTs was 20% in 15 min, and this value did not change in 1 h. Obtained values of sorption and desorption indicate difficulties in using MWCNTs as carrier of Y(III).

Sorption of Ga(III) onto MWCNTs in DDW did not exceed 30% in 120 min, while quantitative desorption in BSA in PBS was observed in 15 min, so the impossibility of using MWCNTs as a carrier of Ga(III) without their additional modification can be concluded [27].

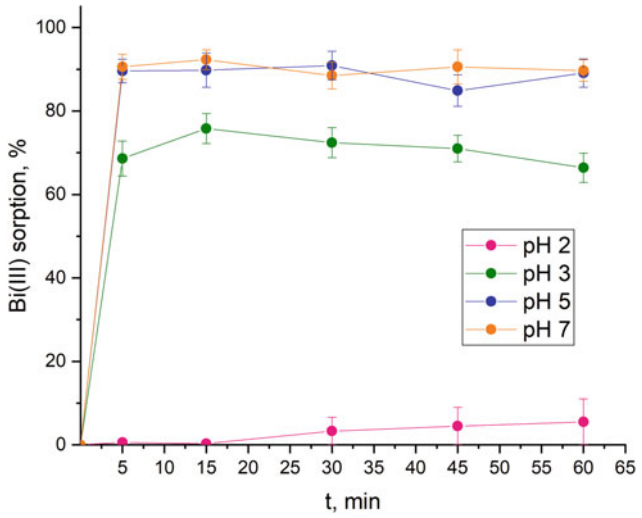

Fig. 4 Sorption of Bi(III) onto MWCNTs in water solutions at 25 °C

Sorption of Bi(III) in DDW had value of 90%, and equilibrium was achieved in 5 min [23]. While studying its sorption in aqueous solutions with lower pH, it was found that no sorption was observed for 60 min at pH 1 and 2 [28]. As in case of NDs, the sorption value increased with increasing pH, and sorption was 70% at pH 3 and 90% at pH 5–7 (Fig. 4). Desorption of Bi(III) was 30% in PBS in BSA in 5 h and 50% in FBS in 2 h, thus, MWCNTs showed less binding of Bi(III) in comparison to NDs.

Sorption values of Ac(III) onto MWCNTs coincided with ones for NDs: sorption in PBS was close to quantitative, but after adding BSA in the solution about 35% of Ac(III) desorbed in 30 min [29].

Like NDs, MWCNTs did not sorb Ra(II) in aqueous solutions [23].

4 The Comparison of Sorption Properties of NDs and MWCNTs

Sorption of medical radionuclides with different sizes, valences, and chemical properties onto NDs and MWCNT with various forms, sizes, compositions, and other physico-chemical properties was studied in our works. Obtained data is systematized and presented in Table 4 for comparison.

It can be concluded from the obtained data that NDs proved to be significantly more promising carrier of medical radionuclides than MWCNTs. Based on the structure of studied CNs surface, we can assume that the main mechanism of binding is the interaction of cations of examined elements with carboxyl groups. For this reason, MWCNTs demonstrated less sorption efficiency and stability compared to NDs. According to the obtained data, NDs are optimal carriers of Tc(IV), Y(III), Bi(III). In case of Ga(III) and Ac (III), desorption was significant, and additional modification of the surface of NDs is required to decrease it; in particular, oxidation of the surface can be used [27, 29]. As for MWCNTs, minimal desorption was 20% for Y(III), which is a promising result, but without the additional modification of the surface further studies can be difficult. At the same time, neither NDs nor MWCNTs cannot be considered to be a promising carrier of Tc(VII) and Ra(II).

5 Stability of Tc(IV)@ND in Blood In Vivo

To determine stability of radionuclides sorbed onto CNs in blood in vivo, Tc(IV)@ND conjugate was selected. This conjugate was injected intravenously in tail vein of laboratory mice (CD-1); comparison sample with the same activity of Tc(IV) without NDs was also injected.

To create Tc(IV)@ND, sorption of Tc(IV) onto NDs in PBS media was conducted. The samples were then centrifuged, supernatant was removed (to dispose of unsorbed Tc(IV)), the precipitate was once again suspended in PBS. 150 µL of obtained suspensions containing 100 µg/mL of NDs were injected in tail vein. To study kinetics of conjugate distribution in blood, blood from facial vein of mice was taken after 5 and 20 min of injection, and also after 60 min by cardiac puncture with the following euthanasia. 5 min after the injection time, when the injected sample already distributed in blood, was chosen as the starting point to determine the elimination rate of Tc(IV)@ND; the results of the experiment are presented in Table 5. Quick

Table 4 Comparison of sorption and desorption of studied radionuclides onto NDs and MWCNTs

Element	Maximum sorption onto NDs, %	Minimum desorption from NDs, %	Maximum sorption onto MWCNTs, %	Minimum desorption from MWCNTs, %
Tc(VII)	50 in DDW	100 in 0.9% NaCl, PBS, BSA in PBS	70 in DDW	100 in 0.9% NaCl, PBS, BSA in PBS
Tc(IV)	90 in PBS	5 in BSA in PBS	10 in PBS	-
Y(III)	> 95 at pH 5–7 and in PBS	10 in FBS	45 in PBS	20 in BSA in PBS
Ga(III)	80 at pH 7	35 in BSA in PBS	30 at pH 7	100 in BSA in PBS
Bi(III)	> 95 at pH 7	5 in BSA in PBS	90 at pH 7	30 in BSA in PBS
Ac(III)	> 95 in PBS	35 in BSA in PBS	> 95 in PBS	35 in BSA in PBS
Ra(II)	0	–	0	–

Table 5 Dependence of content of Tc(IV) sorbed on NDs in blood on time compared to Tc(IV) without NDs

Time, min	% of injected activity of Tc in	
	Tc(IV) without NDs	Tc(IV)@ND
5	100.0 ± 13.3	100.0 ± 9.7
20	18.9 ± 2.6	16.4 ± 2.1
60	4.9 ± 0.6	0.5 ± 0.1

elimination of Tc(IV)@ND regarding the comparison sample was observed: after 1 h blood contained 5 and 0.5% of injected activity of Tc(IV) and Tc(IV)@ND correspondingly. The different behavior of conjugate with sorbed Tc (IV) and conjugate with Tc(IV) without nanoparticles indicated the stability of these conjugates in such conditions, and also demonstrated that the behavior of bound Tc(IV) depended not on its chemical properties, but on the behavior of nanocarrier.

6 Conclusion

A short review of our works dedicated to investigating the conditions of NDs and MWCNTs use as carriers for nuclear medicine. The sorption behavior of Tc(VII), Tc(IV), Y(III), Ga(III), Bi(III), Ac(III) and Ra(II) onto commercial samples of NDs and MWCNTs was studied. It was established that NDs are optimal carriers for all studied radionuclides except Tc(VII) and Ra(II), which allows to assume the main mechanism of interaction of radionuclide cations with CNs to be an interaction with carboxyl groups on the surface. It was shown that the additional modification of CNs surface is required to bind Tc(VII) and Ra(II), thus, further studies are necessary. Sorption of radionuclides depends on the sizes of NDs aggregates and ζ-potential of their surface, so smaller aggregates with large ζ-potential are needed for further creation of RPs. On the example of Tc(IV)@ND, stability of obtained conjugates in blood in vivo was demonstrated. Obtained data allows to conclude that NDs and MWCNTs are promising carriers of medical radionuclides, and further studies can result in RPs based on these nanomaterials.

Acknowledgements Characterization of NDs was funded by Russian Science Foundation (project 21-13-00449).

References

1. Escorcia, F.E., McDevitt, M.R., Villa, C.H., Scheinberg, D.A.: Targeted nanomaterials for radiotherapy. Nanomedicine **2**, 805–815 (2007)
2. Abd Elkodous, M., El-Sayyad, G.S., Abdelrahman, I.Y., El-Bastawisy, H.S., Mohamed, A.E., Mosallam, F.M., Nasser, H. A., Gobara, M., Baraka, A., Elsayed, M.A., El-Batal, A.I.: Therapeutic and diagnostic potential of nanomaterials for enhanced biomedical applications. Colloids Surf. B. **180**, 411–428 (2019)
3. Raju, G.S.R., Benton, L., Pavitra, E., Yu, J.S.: Multifunctional nanoparticles: recent progress in cancer therapeutics. Chem. Commun. **51**, 13248–13259 (2015)
4. Lee, D.-E., Koo, H., Sun, I.-C., Ryu, J.H., Kim, K., Kwon, I.C.: Multifunctional nanoparticles for multimodal imaging and theragnosis. Chem. Soc. Rev. **41**, 2656–2672 (2012)
5. Varani, M., Galli, F., Auletta, S., Signore, A.: Radiolabelled nanoparticles for cancer diagnosis. Clin. Transl. Imaging. **6**, 271–292 (2018)
6. Grimaldi, A.M., Incoronato, M., Salvatore, M., Soricelli, A.: Nanoparticle-based strategies for cancer immunotherapy and immunodiagnostics. Nanomedicine **12**, 2349–2365 (2017)
7. Ge, J., Zhang, Q., Zeng, J., Gu, Z., Gao, M.: Radiolabeling nanomaterials for multimodality imaging: new insights into nuclear medicine and cancer diagnosis. Biomaterials **228** (2020)
8. Kateb, B., Chiu, K., Black, K.L., Yamamoto, V., Khalsa, B., Ljubimova, J.Y., Ding, H., Patil, R., Portilla-Arias, J.A., Modo, M., Moore, D.F., Farahani, K., Okun, M.S., Prakash, N., Neman, J., Ahdoot, D., Grundfest, W., Nikzad, S., Heiss, J.D.: Nanoplatforms for constructing new approaches to cancer treatment, imaging, and drug delivery: what should be the policy?. Neuroimage. **54**, S106–S124 (2011)
9. Rojas, S., Gispert, J.D., Martín, R., Abad, S., Menchón, C., Pareto, D., Víctor, V.M., Álvaro, M., García, H., Herance, J.R.: Biodistribution of amino-functionalized diamond nanoparticles. In vivo studies based on ^{18}F radionuclide emission. ACS Nano. **5**, 5552–5559 (2011)
10. Chen, L., Zhong, X., Yi, X., Huang, M., Ning, P., Liu, T., Ge, C., Chai, Z., Liu, Z., Yang, K.: Radionuclide ^{131}I labeled reduced graphene oxide for nuclear imaging guided combined radio- and photothermal therapy of cancer. Biomaterials **66**, 21–28 (2015)
11. Suri, G.S., Kaur, A., Sen, T.: A recent trend of drug-nanoparticles in suspension for the application in drug delivery. Nanomedicine. **11**(21) (2016)
12. Goel, S., England, C.G., Chen, F., Cai, W.: Positron emission tomography and nanotechnology: a dynamic duo for cancer theranostics. Adv. Drug Deliv. Rev. **113**, 157–176 (2017)
13. Hong, H., Zhang, Y., Engle, J.W., Nayak, T.R., Theuer, C.P., Nickles, R.J., Barnhart, T.E., Cai, W.: In vivo targeting and positron emission tomography imaging of tumor vasculature with ^{66}Ga-labeled nano-graphene. Biomaterials **33**, 4147–4156 (2012)
14. Yang, K., Feng, L., Hong, H., Cai, W., Liu, Z.: Preparation and functionalization of graphene nanocomposites for biomedical applications. Nat. Protoc. **8**, 2392–2403 (2013)
15. Shi, S., Xu, C., Yang, K., Goel, S., Valdovinos, H.F., Luo, H., Ehlerding, E.B., England, C.G., Cheng, L., Chen, F., Nickles, R.J., Liu, Z., Cai, W.: Chelator-free radiolabeling of nanographene: breaking the stereotype of chelation. Angew. Chemie Int. Ed. **56**, 2889–2892 (2017)
16. McDevitt, M.R., Chattopadhyay, D., Kappel, B.J., Jaggi, J.S., Schiffman, S.R., Antczak, C., Njardarson, J.T., Brentjens, R., Scheinberg, D.A.: Tumor targeting with antibody-functionalized, radiolabeled carbon nanotubes. J. Nucl. Med. **48**, 1180–1189 (2007)
17. Swierczewska, M., Choi, K.Y., Mertz, E.L., Huang, X., Zhang, F., Zhu, L., Yoon, H.Y., Park, J.H., Bhirde, A., Lee, S., Chen, X.: A facile, one-step nanocarbon functionalization for biomedical applications. Nano Lett. **12**, 3613–3620 (2012)
18. Hong, S.Y., Tobias, G., Al-Jamal, K.T., Ballesteros, B., Ali-Boucetta, H., Lozano-Perez, S., Nellist, P.D., Sim, R.B., Finucane, C., Mather, S.J., Green, M.L.H., Kostarelos, K., Davis,

B.G.: Filled and glycosylated carbon nanotubes for in vivo radioemitter localization and imaging. Nat. Mater. **9**, 485–490 (2010)
19. McDevitt, M., McDevitt, M., Ruggiero, A., Villa, C.H., Holland, J. P., Sprinkle, S.R., May, C., Lewis, J., Scheinberg, D.: Imaging and treating tumor vasculature with targeted radiolabeled carbon nanotubes. Int. J. Nanomedicine. **5**, 783–802 (2010)
20. Cisneros, B.T., Law, J.J., Matson, M.L., Azhdarinia, A., Sevick-Muraca, E.M., Wilson, L.J.: Stable confinement of positron emission tomography and magnetic resonance agents within carbon nanotubes for bimodal imaging. Nanomedicine **9**, 2499–2509 (2014)
21. Matson, M.L., Villa, C.H., Ananta, J.S., Law, J.J., Scheinberg, D. A., Wilson, L.J.: Encapsulation of α-particle-emitting $^{225}Ac^{3+}$ ions within carbon nanotubes. J. Nucl. Med. **56**, 897–900 (2015)
22. Zhao, H., Chao, Y., Liu, J., Huang, J., Pan, J., Guo, W., Wu, J., Sheng, M., Yang, K., Wang, J., Liu, Z.: Polydopamine coated single-walled carbon nanotubes as a versatile platform with radionuclide labeling for multimodal tumor imaging and therapy. Theranostics **6**, 1833–1843 (2016)
23. Kazakov, A.G., Garashchenko, B.L., Yakovlev, R.Y., Vinokurov, S.E., Kalmykov, S.N., Myasoedov, B.F.: An experimental study of sorption/desorption of selected radionuclides on carbon nanomaterials: a quest for possible applications in future nuclear medicine. Diam. Relat. Mater. **104**, 107752 (2020)
24. Kazakov, A.G., Garashchenko, B.L., Yakovlev, R.Y., Vinokurov, S.E., Myasoedov, B.F.: Study of technetium sorption behavior on nanodiamonds using ^{99,99m}Tc isotopes. Radiochemistry **62**, 752–758 (2020)
25. Kazakov, A.G., Babenya, J.S., Ivanova, M.K., Vinokurov, S.E., Myasoedov, B.F.: Study of ^{90}Y sorption by nanodiamonds as potential carriers in RPs. In press, Radiochemistry (2022)
26. Babenya, J.S., Kazakov, A.G., Ekatova, T.Y., Yakovlev, R.Y.: The dependence of ^{90}Y sorption on nanodiamonds on sizes of their aggregates in water solutions. J. Radioanal. Nucl. Chem. **329**, 1027–1031 (2021)
27. Kazakov, A.G., Garashchenko, B.L., Ivanova, M.K., Vinokurov, S.E., Myasoedov, B.F.: Carbon nanomaterials for sorption of ^{68}Ga for potential using in positron emission tomography. Nanomaterials **10**, 1090 (2020)
28. Kazakov, A.G., Garashchenko, B.L., Babenya, J.S., Ivanova, M. K., Vinokurov, S.E., Myasoedov, B.F.: Nanodiamonds and carbon nanotubes as perspective carriers of bismuth isotopes for nuclear medicine. In: 8th International Conference on Radiation in Various Fields of Research (RAD 2020), pp. 1–6. RAD Centre, Virtual, Online (2020)
29. Kazakov, A.G., Garashchenko, B.L., Yakovlev, R.Y., Vinokurov, S.E., Kalmykov, S.N., Myasoedov, B.F.: Generator of actinium-228 and a study of the sorption of actinium by carbon nanomaterials. Radiochemistry **62**, 592–598 (2020)
30. Motaleb, M.A.: Preparation and biodistribution of ^{99m}Tc-lomefloxacin and ^{99m}Tc-ofloxacin complexes. J. Radioanal. Nucl. Chem. **272**, 95–99 (2007)

GIS in Radioecology: History and Prospects of Data Processing

V. G. Linnik, O. M. Ivanitsky, and A. V. Sokolov

1 Introduction

As a result of the Chernobyl accident, huge territories both in the USSR and in Europe were subjected to radiation contamination. The effective solution of long-term consequences of radioactive contamination required the development of new methods based on the principles of spatial radioecological analysis to assess the long-term consequences of radioactive contamination. New computer technologies, which included the creation and use of geoinformation systems with databases and modelling systems, met such requirements well. The modeling results became an obligatory element of the decision-making system for choosing the most effective countermeasures.

GIS-technologies initially focused on the tasks of organizing databases of spatially coordinated information with subsequent possibilities of processing and analysing geographical data in a cartographic form. The physical and mathematical modeling of migration processes in the structure of GIS was not initially considered. However, since the mid-1980s the tendency to integrate GIS with mathematical modeling systems has become evident [1].

In the USSR, in a very short period of time, a GIS designed to simulate radionuclide migration in the 30-km ChNPP zone was developed at the Special Design Bureau of Mathematical Machines and Systems of Glushkov Institute of Cybernetics NAS of Ukraine (IC SDB MMS) in 1986 [2]. The first version of the system was built on the basis of a specialized computer complex (SCC) "DELTA" [3]. The GIS included the following blocks: (1) information; (2) conceptual and mathematical models; (3) scenarios, preparation and design of recommendations for decision-making [3, 4].

For radio-ecological modeling a cartographic data bank was created with data processing performed in a raster format. For this purpose, the necessary software was developed. A landscape map of the Kyiv region was used as a base map [5]. That made it possible to significantly save time for creating the cartographic data bank: an alternative would have been to digitize maps of individual components of the landscape (soil, vegetation, etc.), which at that time would have required much additional time.

The modeling block included a system of visualization and automated mapping, as well as algorithms for construction of estimated and predicted radioecological maps in expert mode based on landscape borders. Mathematical models were designed to perform calculations of radionuclide migration with surface runoff as well as infiltration into groundwater [6].

Among the radioecological tasks solved in the SCC "DELTA" were the following ones: in December 1986 the maps of groundwater protection in three regions of Ukraine (Kiev, Zhitomir and Chernigov) were constructed using the models of vertical radionuclide migration, which allowed to assess the risk of groundwater contamination. In the spring of 1987, prior to the flooding of the Pripyat River, a forecast of surface washout of radionuclides from the 30-km zone was performed [7, 8]. In March–April 1987 research was mostly concerned with substantiation and design of reference network of radiation monitoring of the 60-km ChNPP zone taking into account its landscape structure [9]. According to the results of measurement of the density of radioactive contamination of soil samples taken by the reference network [10], contamination maps of the 60-km ChNPP zone were drawn.

Analysis of studies dedicated to forecasting the radio-ecological situation in the landscapes of the Chernobyl zone indicated critical importance of information support of

V. G. Linnik (✉) · O. M. Ivanitsky · A. V. Sokolov
Vernadsky Institute of Geochemistry and Analytical Chemistry, Russian Academy of Sciences, 19 Kosygin St., Moscow, 119991, Russia
e-mail: vlinnik_53@mail.ru

A. V. Sokolov
Institute for Information Transmission Problems of the Russian Academy of Sciences (Kharkevich Institute), 19 Bol'shoi Karetnyi Per., Moscow, 127051, Russia

V. P. Kolotov and N. S. Bezaeva (eds.), *Advances in Geochemistry, Analytical Chemistry, and Planetary Sciences*,
https://doi.org/10.1007/978-3-031-09883-3_41

the modeling system. The requirements of information support for modeling tasks were guided for the organization of the radiation monitoring network of the 60-km ChNPP zone, the purpose of which was to organize a test site for identifying the parameters of radioecological models taking into account the landscape diversity of conditions of migration of man-made radionuclides [9].

The relevance of considering landscape factors in radioecology was first demonstrated when substantiating the rehabilitation measures in the 30-km ChNPP zone: landscape criteria for rehabilitation measures were proposed [11], and assessment of vertical migration for individual landscapes of the Chernobyl exclusion zone was carried out (cm/year) Cs-137 [12].

The experience of 'Chernobyl' research on GIS organization on the landscape basis was summarized in a series of publications [13–16].

In autumn 1989 a scientific group organized for the purpose of conducting research on radioecological and landscape-geochemical mapping (RADLAN project [2, 17–19] was formed in the laboratory headed by L.M. Khitrov (Vernadsky Institute of Geochemistry and Analytical Chemistry of the Russian Academy of Sciences). Its purpose was to perform regional assessment of ecological situations, to analyse ways of optimal use of the areas contaminated with artificial radionuclides during the Chernobyl accident on the basis of geoinformation technologies, and provide *scientific* and technical advice to support government decision makers. The result of these studies was the development of methodology and implementation of the methodology of information support of radioecological GIS-modeling, which was later pursued in other projects.

Geoinformation studies were strongly supported by the GoskomChernobyl management and were aimed at a number of different tasks. In order to inform the GoskomChernobyl management of analyses of long-term consequences of the Chernobyl accident, a GIS at the level of selected areas on radioactive contamination was developed at IBRAE [20].

At Roshydromet, which was entrusted with the functions of radiation monitoring of the environment, geoinformation issues were of special interest. Mathematical support and software including GIS functions for the analysis and assessment of accidental radioactive contamination of the environment was created in Roshydromet's Research and Production Association "Typhoon" (RPA"Typhoon") [21]. Later, some elements of this system using the capabilities of geoinformation modelling were incorporated into the decision support system for nuclear accidents (RODOS) created under the auspices of the European Commission [22].

A radioecological GIS was designed at the Institute of Global Climate and Ecology for creating the Atlas of radioactive contamination of Russia, Belarus and Ukraine after the Chernobyl accident [23–25]. The importance of including landscape information as a separate information layer for the radioecological assessment of the contaminated territories was noted in [26]. The Atlas on Caesium Contamination of Europe after the Chernobyl Nuclear Plant Accident [27] has become possible as a result of collaboration with experts of the European Commission and colleagues from European research community on using geoinformation technologies.

Producing the European Atlas of Pollution required special procedures for data harmonization, since 30 countries were involved in the project, researchers using different monitoring methods and dealing with significant non-homogeneity of radioactive contamination. While developing the Atlas, robust interpolation algorithms embedded in the GIS structure were tested [28].

Extensive geoinformation research on creation of multiscale radioecological GIS taking into account landscape structure of contaminated territories was conducted in Russian Scientific-Practical and Expert-Analytical Centre (RSPEAC) at the Department of Geoinformation Investigations from 1992 till 1995 and starting with March 1995 the investigation was continued in the "Regional geoinformation analysis" laboratory organized at Vernadsky Institute RAS.

The first version of the radioecological GIS created at the RSPEAC in 1992 included two scale levels: (1) the level of monitoring sites (1:200 scale) and (2) collective farms of the Novozybkov district (Bryansk Region) (1:25,000 and 1:50,000 scale) [29].

Data on radioactive contamination of settlements were collected at RPA "Typhoon", close cooperation with which permitted to produce the RadGIS "Bryansk" in the RSPEAC.

2 Decision Support Systems (DSS) in Radioecology

Radioecology traditionally uses different mathematical models [30–33], which usually investigate the processes of radionuclide transfer between separate blocks (compartments) of ecosystem, without taking into account the features of the spatial structure of ecosystems. These models are effective for ecological modeling of transition of chemical elements along food chains and in general for biogeochemical migration. Mathematical calculations (modeling) are performed for a single pixel (raster technology) or a single contour (vector technology), which by default is assumed to be homogeneous (this is one-dimensional modeling). In contrast, GIS modeling allows taking into account heterogeneity of spatial structure of ecosystems, thereby transitioning from a point to a spatially distributed radioecological model is achieved.

Table 1 Spatial resolution of radioecological GIS modelling [34]

Radioecological risk assessment maps	SAVE	RESTORE	CESER
Region	15 countries in Europe	Contaminated areas, Ukraine, Belarus, Russian federation	9 river basins in Scotland
Resolution	5 × 5 km	1 × 1 km	10 × 10 m

The apparent effectiveness of geographic information modelling in radioecology, enabling the processing of thematic maps for spatial analysis and forecasting of the radioecological situation, has prompted the European Commission to fund a number of radioecological projects in which Geographic Information Systems (GIS) have played a key role [34].

The radioecological GIS is constructed as a system including data on the factors determining radionuclide migration capability and radiation dose formation (soils, landscapes, vegetation cover, relief, land use) and radionuclide contamination data. The use of the topographic basis for the construction of predictive radioecological maps without taking into account the landscape structure and the character of land use could not provide the possibility of verification of the predictions themselves.

Methodological and theoretical generalizations in terms of integration of GIS with mathematical models began to appear in the late 1980s and early 1990s. One of the first successful experiments was the creation of the specialized package PcRaster [35, 36], which simulated moisture transport in the landscape. The developed specialized dynamic modeling language allowed carrying out calculations in raster form where separate thematic layers (maps) such as topography, soil, vegetation, etc. were used as model input parameters.

Integration of mathematical modeling systems with GIS-systems was carried out in the following ways [36]: (1) Mathematical modeling is performed separately, then the modeling results are exported and included as a separate layer in the GIS; (2) Mathematical models are directly included in the GIS structure. The second approach was implemented in the PcRaster package.

Practical work on creation of radioecological GIS in the Russian Federation was started in 1992; already in 1993–1994 the first rather simple GIS was created. These GIS supported functions of storage, primary processing and visualization of data on radionuclide contamination in cartographic form [37].

The first GIS with modeling functions for decision-making was implemented at the level of a collective farm (Kolkhoz "Reshitel'ny") [29], where electronic maps of milk radionuclide pollution were constructed based on the *soil–plant transfer coefficient* of Cs-137. A vector map with the boundaries of land use and soil units was used. The map attributes included the following parameters: soil type, density of cesium-137 contamination, as well as agrochemical parameters. Modeling of agricultural products contamination, evaluation of the *efficiency of countermeasures* undertaken during a post-accident period after the Chernobyl NPP accident were performed for separate contours of fields, hayfields and pastures.

In a rather short time, decision support systems (DSS) in radioecology were created in Europe [34], among them SAVE [38]—raster GIS for predicting fluxes of radiocaesium (Cs-137) into European foods; RESTORE [39–41]—raster GIS for CIS countries (with ideas close to SAVE); CESER [42]—evaluation of countermeasure efficiency, RODOS [43]—evaluation of consequences after radiation accidents.

Those projects had much in common, all of them using raster technology convenient for GIS modelling. The spatial data sets include the following information layers (digital thematic maps): (1) levels of radioactive pollution; (2) soil types, and (3) land use. However, non-identical sources (different scales) for generating GIS map databases may have caused digital map data to vary significantly in accuracy and uncertainty.

SAVE (Western Europe) is based on the maps on the scale 1:1,000,000, whereas CESER (Scotland) is based on 1:25,000 to 1:50,000 scale; RESTORE is based on 1:10,000 to 1:200,000 scale maps.

As a result, GIS modeling was carried out by a raster method with different spatial resolutions (Table 1).

2.1 RadGIS "Bryansk" and Models of Radionuclide Migration in Soil–Plant System

Modelling approach for the transfer of radionuclides to agricultural products uses transfer factors (TF), which are determined experimentally. Since the transfer of radionuclides is influenced by many factors, TF can vary by the value equal to 2 or 3 orders of magnitude. For more reliable results, the dynamic semi-physical model developed by [44] is used. This model requires the following soil parameters: organic matter content, pH value, cation exchange capacity (CEC) and clay percentage. However, the currently limited experimental data on the type of relation between the

physicochemical properties of soils and the bioavailability of radionuclides make the task of accounting for this factor in mathematical models very difficult [45].

Consequently, GIS databases need maps of the spatial distribution of these parameters. For the territory of Europe, radioecological modeling was performed using the model of Absalom et al. (2001) on a 5 × 5 km grid.

The first version of Radioecological GIS of the Bryansk region (RadGIS "Bryansk") was created as a vector GIS, topographic maps of 1:200,000 scale were used for digitization, land use plans for individual farms were digitized according to 1:25,000 scale schemes. Necessary information on the soil cover structure was drawn from a paper landscape map of 1:200,000 scale created by MSU geographers specifically for GIS organization [46].

After the aerial gamma survey (AG) conducted in 1993, an AG raster layer (pixel size 100 × 100 m) was incorporated into the RadGIS "Bryansk". In order to process both vector and raster layers simultaneously, raster-vector processing of map data was required. As a result, already in 1994 the first version of vector-raster RadGIS "Bryansk", which included information on 4 topographic sheets of scale 1:200,000 of the most Cs-137 contaminated western areas of the Bryansk region, was completed. By that time, a landscape map of 1:200,000 scale in a vector format was created for the same area, which was converted to a raster format (pixel size 100 m) for radioecological modeling. A fragment of the vector-raster RadGIS "Bryansk" is shown in Fig. 1. Vector layers were represented by elements of topographic map of 1:200,000 scale (settlements) and landuse map (scale 1:50,000).

For some districts of the Bryansk region with high density of contamination (more than 40 Ci/km^2) in the initial post-accident period (1986–1988) measurements of agricultural products contamination were irregular. For such a resettlement zone (village Zaborye) in the Krasnogorsk district of the Bryansk region, whose residents had already been resettled by 1992, the reconstruction of possible levels of radioactive contamination of agricultural products for 1987, using RadGIS "Bryansk", was carried out. Since 1987, the radioactive contamination of crop products had been formed as a result of the root intake of radionuclides, so the models based on the transfer factors became effective. Figure 1 shows the model result for 1987 contamination of oats (grain), with contamination levels presented in permissible levels (PL) for convenience. In Fig. 1 the "trace" of radioactive contamination in the northeastern direction from the village of Zaborje with excess of permissible levels of radioactive contamination is clearly traced.

2.2 GIS Modelling of Agricultural Pollution

The interest in GIS-technologies demonstrated by the EU stimulated joint Russian–European projects concerning the organization of RadGIS for the areas contaminated with radionuclides due to the Chernobyl accident. The RESTORE project served as an "umbrella" for a number of projects carried out in Russia, Ukraine and Belarus.

In Russia, two EDSS projects have been developed under the auspices of the RESTORE project on (western districts

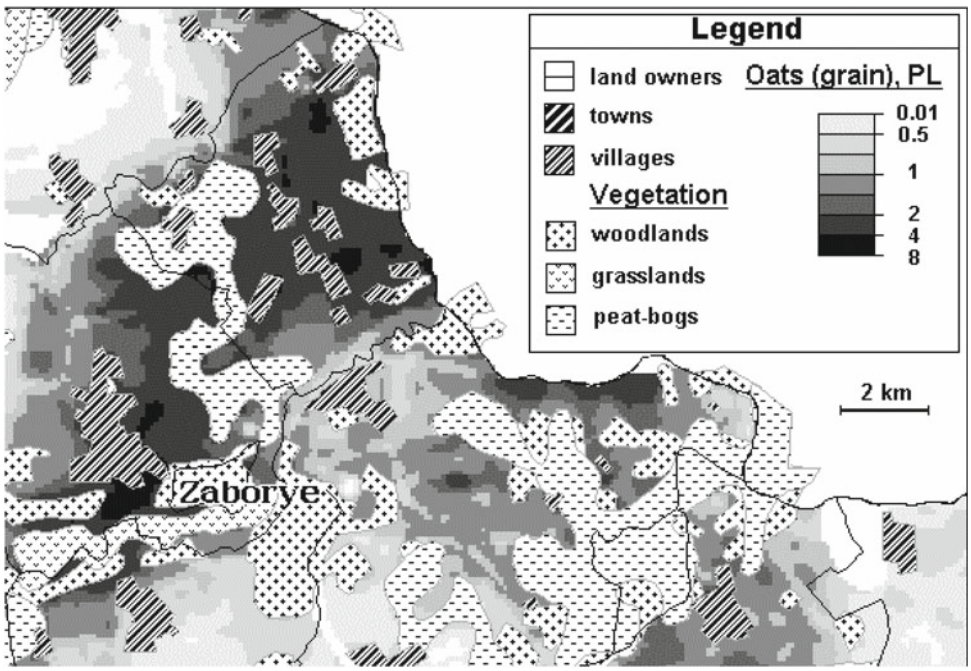

Fig. 1 Vector-raster RadGIS "Bryansk". Modelling radionuclide contamination of agricultural products—oats (grain) (Zabor'e village, Krasnogorsk district of the Bryansk region) in 1987 (in values of the permissible level—PL)

of the Bryansk region): (1) PRANA [47, 48] and (2) STRESS [49–51].

Having the same study area (western districts of the Bryansk region), the two projects still differed significantly. In the PRANA project, the main emphasis was put on the calculation of doses, effectiveness of countermeasures in agriculture, whereas in STRESS the focus was on the application scope of landscape principles of RadGIS organization for radioecological assessment of the territory.

The cartographic databases formation in the two projects was also different. In the PRANA project, the "radioactive contamination" layer took into account the results of radiation survey of Bryansk Agrohimradiology, data of radionuclide contamination RPA "Typhoon" on settlements areas, and data on radioactive contamination of forests (Leskhoz data). The STRESS project was based both on aerial gamma survey (AG) and the RPA "Typhoon" data on radioactive contamination of settlements.

The working scale in the PRANA project was 1:50,000, with all layers were presented in vector format, the "soil" layer was digitized from a specially prepared soil map, whereas in the STRESS project the "soil" layer was obtained from a 1:200,000 landscape map.

The PRANA project is organized according to a vector principle, where all calculations were performed autonomously, referring to the database, then the obtained results were displayed on the computer map. The STRESS project used a raster model technology, where information is "read out" from individual information layers.

Therefore, in the STRESS project, uncertainty in the cartographic information may have been critical, significantly distorting the results of spatial radioecological modeling.

The objective of the STRESS project was to develop a GIS-based radioecological model adopted to assess the environmental transfer of Chernobyl-derived Cs-137 to cow's milk in the Novozybkov district.

GIS-modelling of agricultural products contamination, including milk contamination, is based on the use of the following maps-parameters of radioecological model: 1—soil types (with indication of mechanical composition), 2—land use, 3—maps of Cs-137 soil contamination. The initial information to be included into GIS was presented in the following form and format:

1. Landscape map in a paper form (scale 1:200,000)
2. Land Use Schemes in a paper form (scale 1:25,000)
3. Aerial gamma survey data (raster format, 100 × 100 m grid, approximate scale 1:25,000) (Fig. 2a).

Cartographic forecast enables territorial differentiation of radio-ecological assessments depending on the character of factors change (soil type, radionuclide contamination), influencing radionuclides inflow to cultivated crops. However, the accuracy and reliability of forecasting the contamination of agricultural products with radionuclides largely depends on the accuracy of mapping information. In schematic representations of land use (scale 1:25,000) the structure of soil cover had been indicated within agricultural lands. Outside those (settlements, forested lands) information on soil character was absent. Soil data for such areas were taken from the landscape map of scale 1:200,000.

Significant difference in cartographic scales was the reason why the landscape map of scale 1:200,000 was characterized by the highest uncertainty. According to the rules of cartographic generalization, the map of 1:200,000 scale

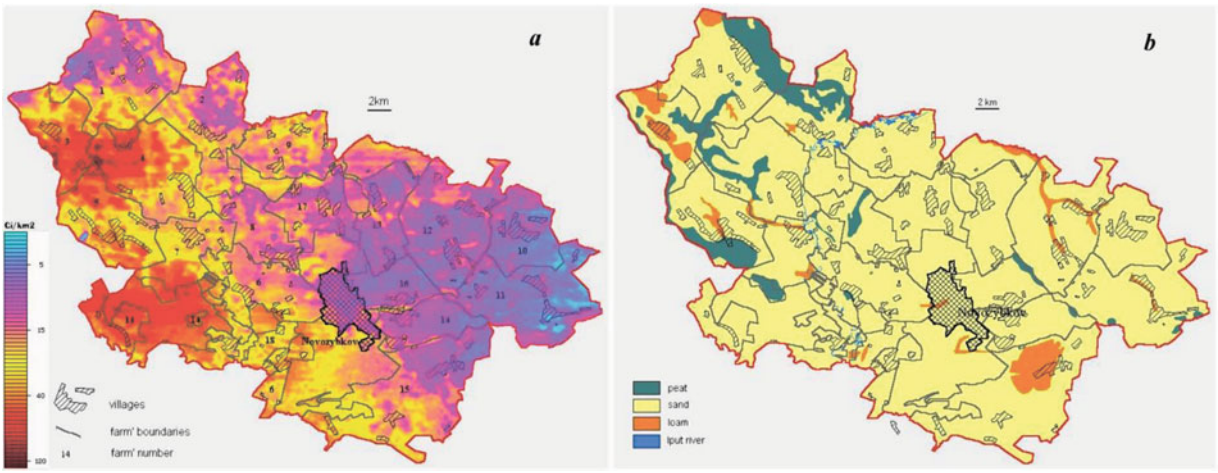

Fig. 2 **a** Cs-137 contamination of Novozybkov district, Bryansk region, Russia; **b** Soil map of the Novozybkov district project based on the landscape map (1:200,000)

does not show individual objects with linear dimensions less than 3 × 3 mm, which corresponds to an object on the ground of 600 × 600 m (one object area of 36 ha). Thus, the soil information taken from the landscape map could underestimate (due to generalization) small contours with hydromorphic (gleyey, peaty) soils that are of critical radioecological significance.

For a generalized radio-ecological assessment within the Novozybkovsky district soils from the landscape map (12 different landscapes were selected) were grouped into three classes: peat, sand, loam (Fig. 2b, soils with clay composition were not mapped due to generalization) and converted into a raster format with a pixel size 100 m. The radio-ecological forecast for the village Zaborje (Fig. 1) was made according to the raster layer "Landscapes" with a grid size of 100 × 100 m.

All the data necessary for GIS modeling were converted into PCRaster format. For modeling on the district level a grid of 100 × 100 m was used, for modeling on the farm level which needs calculation of higher accuracy a grid of 50 × 50 m was chosen.

For radio-ecological assessment within collective farms, agricultural lands were grouped into the following four gradations: arable lands, gardens, lands for haying and pastures. The data on soils were taken from the land-use maps, in some cases they were specified by the data of soil maps of the scale 1:10,000. For radio-ecological assessment, all soils within individual farms (pixel size 50 m) were grouped into four classes: peat, sand, loam, clay.

To assess the accuracy of the cartographic data on the "land use" layer, the original cartographic data after vectorization using the KAVRIN package (author A.V. Sokolov) were converted into raster format PCRaster [35, 36], using ASCII formatted data. The areas were calculated in a vector format separately by types of land use for 18 farms of Novozybkov district (Table 1), which were then compared with the statistic tabulated data of land use plans.

While creating the data bank, it was found that land use plans of scale 1:25,000 were characterized by the lowest cartographic accuracy. Their conversion into digital form (obtaining transformed bit-map images in geographic coordinates) revealed large errors (up to 30 m for linear objects) due to significant distortions of the paper copies themselves and a complete absence of reliable reference points.

An example of misalignment of information layer elements (topographic map and land use scheme) for a settlement boundary due to low georeferencing accuracy is shown in Fig. 3.

In the 1980–1990s the formation of GIS on land resources, created by manual digitizing, was challenged by reliability of digital maps, due to errors in the vectorization of traditional paper soil maps. P. Burrough in his seminal

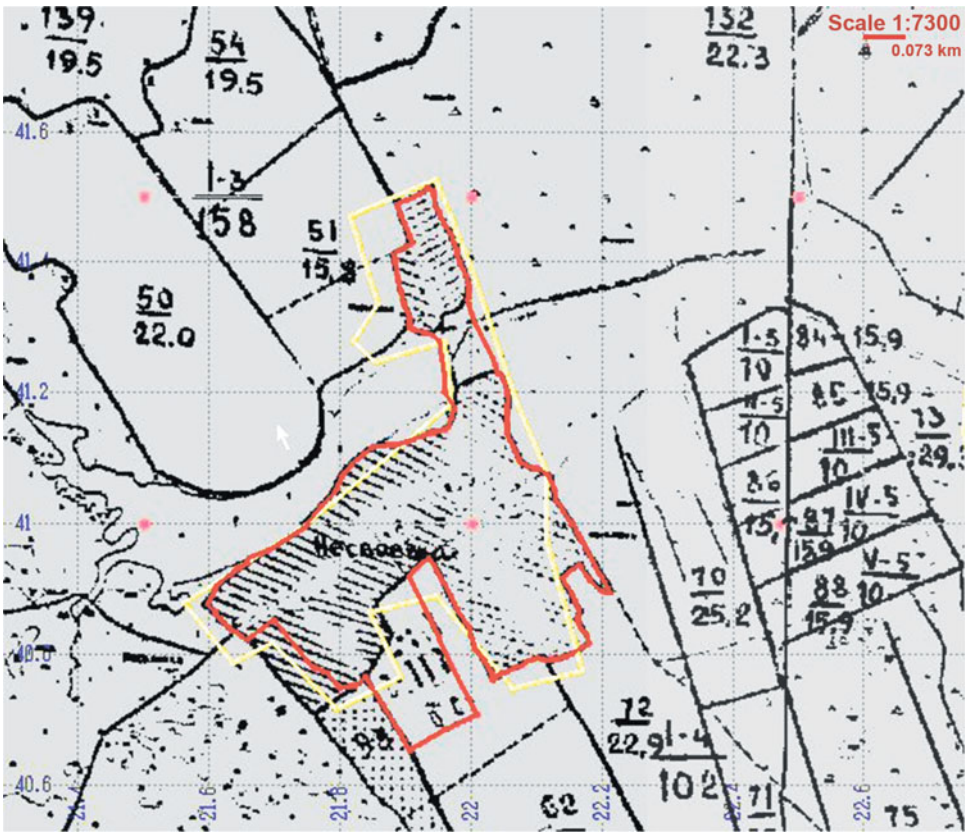

Fig. 3 Identified errors in the formation of the vector layer "land use". The yellow color indicates the boundaries of a settlement obtained from a 1:50,000 topographic map, the red one is a vectorized boundary of the 1:25,000 land use scheme

textbook in geoinformatics [52] (first edition) devoted a whole section to the discussion of the problems of uncertainty of spatial data of soil information. Due to recent advances in digital soil mapping and manual digitizing becoming obsolete, this research topic has now lost its relevance [53]. However, it is still important if there is a need to assess the reliability of digital data obtained by vectorization of "paper" soil maps, which were produced by traditional soil mapping methods adopted in the "pre-digital" era [54].

When the first radioecological databases were set up in the mid-1990s, it was quite a hot topic, as errors or uncertainties in spatially distributed data were likely to lead to similar or identical uncertainties in radioecological GIS modelling. To that end, a special study was conducted for discrepancies in squares of pastures (land registry and land use schemes). The divergence of the agricultural land area calculated for the digitized vector maps with the official land cadastral data was assessed (Table 2).

The most reliable digital map data on land use after digitization were obtained for arable land and perennial plantations. As a rule, the relative error in statistical data and calculated vector values of arable land area did not exceed 2–3%; a separate case is the farm Im. XXII S'ezda, here the relative error in arable area reached 14%.

Thus, the cartographic forecast for different crops cultivated on arable lands in terms of area (for modelling radionuclide fluxes in food chains in absolute amounts) was identical with the radioecological forecast obtained by the traditional method based on the statistic data on the distribution of arable lands within a farm.

The situation was quite different for hayfields and pastures. Table 2 shows results obtained only for pastures. The biggest inconsistencies between the cadastral data and the vectorized data of land use plans are highlighted in grey. The disagreements in data were due to a number of reasons. In a significant number of cases, boundaries of hayfields and pastures were not clearly marked on schemes or were too coarse, which led to arbitrary variation of boundaries during digitization. In some cases, when reclaimed land was available, it was not possible to separate land belonging to the farm from other land users (e.g., peat extraction). That case was typical for the farm Im. XXII S'ezda (ID = 5). In addition, some hayfield contours were not digitised as they were outside the farm boundaries, although they were accounted in the cadastre.

Thus, it is necessary to emphasize significant inconsistencies in the areas of hayfields and pastures according to statistical data and data of cartographic calculations, which must be taken into account when forecasting estimates of milk contamination, particularly with regard of the volume of contaminated milk production on collective farms.

To assess the accuracy of raster representation of map data compared to the original vector data, the effect of grid cells size on the accuracy of area objects (contours) was investigated. For this purpose, three different variants of raster resolution were chosen: 100 × 100 m, 50 × 50 m

Table 2 Pasture distribution in collective farms of the Novozybkov district and their area (in ha)

ID	Name	Landuse registry	Vector map	Grid cell size (m)		
				100 × 100	50 × 50	25 × 25
1	Rossiya	1586	1261.17	1259.0	1254.5	1255.44
2	Lenina	1263	1256.8	1257.0	1254.75	1252.44
3	Komsomolets	936	767.11	759	764.5	767.25
4	Reshilel'ny	–	573.04	568.0	573.5	573.31
5	Im. XXII S'ezda	663	1058.64	1055.0	1050.75	1050.56
6	Volna Revolyutsii	659	492.38	486	492.75	492.44
7	Krasnaya Iput'	382	198.06	122	124.75	125
8	Rodina	329	342.92	340	343.75	342.19
9	Kommunar	534	494.89	487	494.25	495.88
10	Udarnik	284	225.34	220	220.75	218.88
11	Novaya Zhiznn'	758	573.08	559	566.25	570.63
12	Vpered	703	428.99	433	427.75	429.38
13	Krutoberiozka	366	309.26	305	312	308.94
14	Novozybkovsky	679	376.25	379	377	371.13
15	Pamyat' Lenina	834	601.27	611	597	599.13
16	Boevik	284	250.99	240	251.5	251.19
17	Kirova	652	729.33	730	732.75	727.13
18	VIUA	84	85.73	86	84.75	84.44

and 25 × 25 m. The calculation was carried out for all farms of the Novozybkov region for pastures. The results obtained are summarized in Table 2.

Comparison of object areas for different sizes of grid cells and vector object storage does not reveal an increase in accuracy when the raster size is reduced, which is most likely due to the small contour of the objects on the map and tortuous boundaries. Consequently, the raster size was not of fundamental importance in the cartographic modeling in terms of increasing accuracy of the predictive estimates. Therefore, for convenience of calculations in radioecological modeling, a raster size of 50 m was chosen.

2.3 Comparative Analysis of Air-Gamma Survey and Ground-Based Soil Sampling of Settlements

The database on radionuclide contamination of the model area included airborne gamma survey (AG) data from the western part of the Bryansk region in summer-autumn of 1993, as well as the ground-based observation database for the settlements of the RPA "Typhoon".

The database of RPA "Typhoon" did not contain the primary data and presented only statistical parameters of the processed samples for individual isotopes–minimum, median and maximum values, as well as the number of samples taken within the boundaries of the settlement. Thus, the RPA "Typhoon" database characterized a settlement area (within the boundaries of a settlement). The analysis of two different layers of information on radionuclide contamination of the territories (AG and data base of RPA "Typhoon") could be performed by comparing only the same parameters.

Therefore, for each settlement of the Novozybkovsky region, for which there was information in the database of RPA "Typhoon", the statistical parameters of AG survey data were determined (Fig. 4).

Initial AG data are presented on a 100 × 100 m grid. Vectorized boundaries of settlements were overlaid on the "AG" GIS layer, then additional grids of 50 × 50 m and 25 × 25 m were obtained using a resample procedure (Fig. 4). For all grid cells of the "AG" layer included in the settlement boundaries, a data array was formed in which the maximum, minimum, median and arithmetic mean values were calculated for all three grids.

A histogram of cesium-137 distribution was constructed for 50 × 50 m grid on which minimum, maximum and median were marked by red straight lines (Fig. 4). Besides, during the calculation, the area of the settlement was determined using vector (AreaVec) and raster maps (Area) for three grid sizes (100 × 100, 50 × 50, 25 × 25 m), as well as the stock of cesium-137 in three different grids (Sum_Cs-137). In that example, it was found that the difference in the stock of cesium-137 for different grids was insignificant.

The verification of the airborne gamma survey data by ground investigation (217 settlements) showed that in the Cs-137 contamination density range of 4 to 70 Ci/km^2 a correlation coefficient r^2 = 0,948 for the median values, and in the range of 4–20 Ci/km^2 maximum agreement between the airborne survey data and the results of ground investigation was observed. Starting with the Cs-137 contamination level that exceeded 50 Ci/km^2, overestimation in the aerial survey data occurred approximately 1.3–1.8 times more often as compared with the results of the ground survey. That might have had a bearing on the results of GIS-modelling of food contamination by overestimating the latter [2].

2.4 Dynamic Models of Agricultural Radionuclide Pollution

In the mid-1990s, dynamic models of the transfer factors (TF) of radionuclides migration in the soil–plant system were proposed, which made it possible to take into account its temporal dynamics [55, 56]. For this purpose, the notion of "half-life" or "half-decay period—T1/2" was introduced by analogy with the physical notion of "half-decay period", i.e. to denote the time period during which the intensity of a simulated process decreases by 2 times.

In the STRESS project, the implemented model accounted for the decrease of TF over time using a two-exponential model of the form [57, 58].

$$T_f(t) = \begin{cases} T_{f_1}(0) * e^{-\lambda_1 t} & t \le 3.3 \text{ years} \\ T_{f_2}(0) * e^{-\lambda_2 t} & t > 3.3 \text{ years} \end{cases} \quad (1)$$

where $T_f(t)$—is the soil–plant TF value at time t; $T_f(0)$—is the TF value at the initial time moment (t = 0), λ_1, λ_2 are the ecological periods of half-reduction. $\left(T_{\downarrow}(f_{\downarrow}1), T_{\downarrow}(f_{\downarrow}2)\right)$ are calculated separately for the selected periods of TF dynamics for the following soil groups: (1) peaty; (2) sandy (sandy loam); (3) light loam; (4) clay.

Ecological periods of Cs-137 half-decay period and values of model parameters according to the results were taken from [58].

Milk contamination was calculated using the model of temporal dynamics of the TF system "soil–plant" for the period 1987–2005. As was shown above, the accuracy and reliability of radio-ecological forecasting of milk contamination depend to a great extent on the reliability of cartographic information. In traditional radio-ecological models, coefficients on separate links of food chains were used without considering their spatial variation. With using cartographic forecasting, there appears a possibility to take into

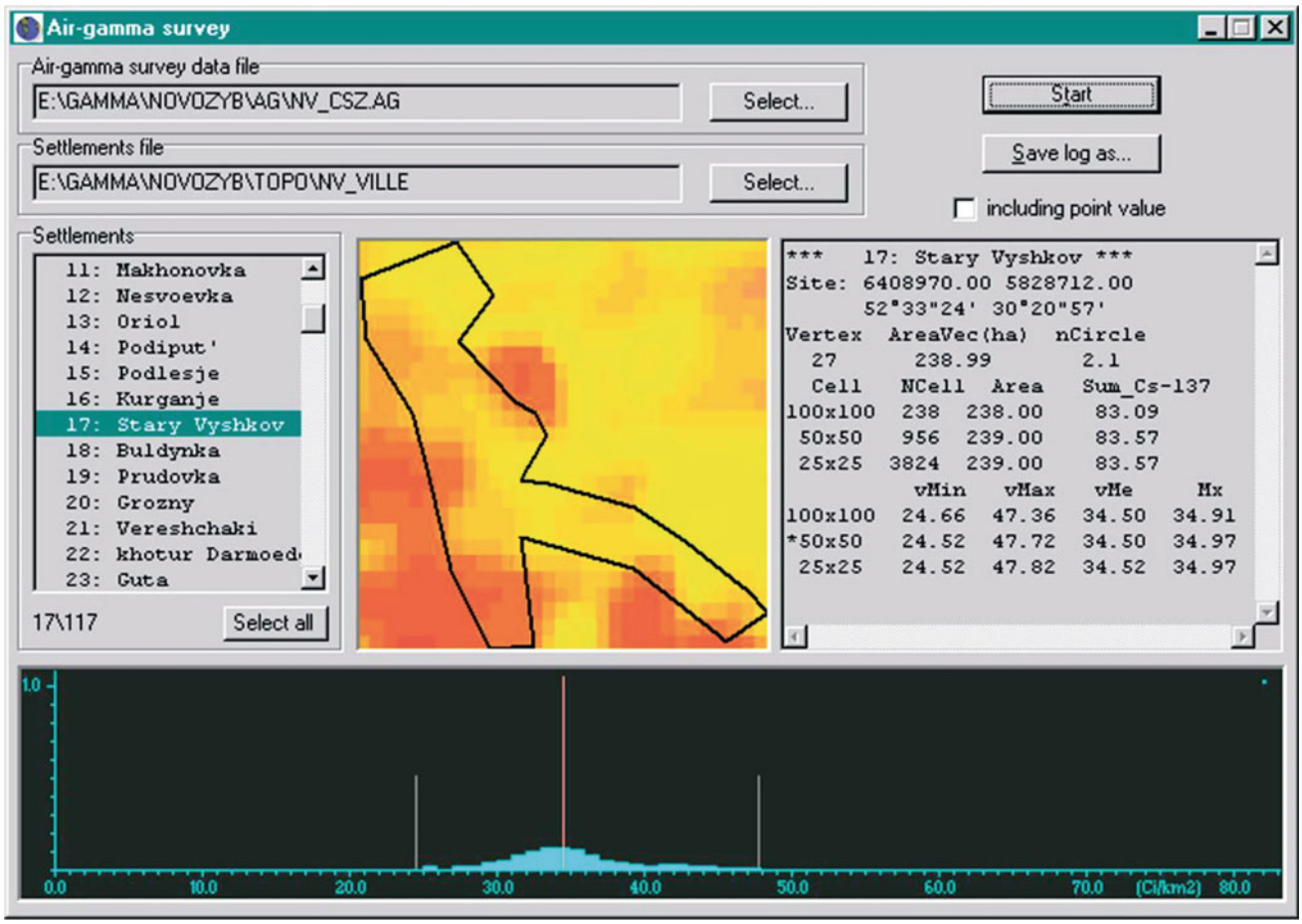

Fig. 4 Results of calculation of statistical parameters of airborne gamma (AG) survey within a settlement by different grids

account the spatial heterogeneity (soil, radionuclide contamination), which control the intensity of radionuclide inflow from soil to plants.

Because of essential uncertainty of radioecological forecasts in [59], it was proposed to use stochastic modelling methods. However, a significant limitation of the practical use of the probabilistic approach was the lack of the necessary amount of experimental data on TF. Therefore, for the stochastic modeling performed in the STRESS project, a method was suggested to generate a random sample for the assumed distribution function of the TF parameter, based on experimental values of the minimum and maximum TF values. For stochastic modeling, the normal, lognormal, and uniform distribution types of the random variable modeling the distribution of the TF parameter were used [2].

The earlier studies [59–61] showed that the Cs-137 distribution in soil, vegetation, as well as in milk, can be approximated by the lognormal law of distribution, and the obtained parameters can be appliedfor forecasting estimates of contamination of meadow and forest products [2]. The study [62], which used new experimental data on TF, showed that radioecological modeling allowed to make *longer-term* predictions (up to 2010).

Simulation modeling (Monte Carlo method) of milk was performed according to the following algorithm. A point was randomly thrown into the contour of the collective farm; if the point belonged to the contour selected for modeling (hayfield or pastureland), then grass or milk pollution was calculated for the period from 1987 to 2010 [2]. If the point did not belong to the desired type of contour, the procedure was repeated. The calculation was completed with the total number of calculations N = 10,000.

The land-use map was used as a mask for calculation (contour belonging–YES, NO), the contamination density was determined by the Cs-137 contamination map, the soil particle size distribution was determined by the landscape map, using which the "soil-vegetation" parameter TF was calculated by the model (6.4).

A linear species model was used to determine Cs-137 contamination of the plant variable:

$$GRASS_{Cs} = T_f(t) * Cs_{ag} \quad (2)$$

where -$GRASS_{Cs}$-Cs-137 concentration in agricultural products (Bq/kg), $T_f(t)$—soil–plant TF at time t (Bq/kg)/(kBq/m^2), Cs_{ag}—density of Cs-137 contamination of soil (kBq/m^2).

In case of stochastic modeling the following scenarios of getting statistical parameters of milk contamination are possible: (1) the grass contamination is modeled by the lognormal law of distribution, the grass-milk transfer factor is taken as constant (by default 1% of cesium transfer from grass into milk, grass consumption by cow is 10 kg); (2) under the lognormal law of grass contamination the grass-milk transfer factor is modeled by the uniform law of distribution in the range from 0.4% to 1.2% [39].

The difference in the results of GIS-modeling can be most clearly seen in Fig. 5, which shows the results of estimated milk contamination in 1989 in the farm named after Lenin. This farm was characterized by average density of contamination with Cs-137 equal to 16 Ci/km^2 (maximum contamination density reached 60 Ci/km^2). Soils in pastures were represented by peatlands with maximum values of TF in the "soil–plant" system.

The average measured value of milk contamination in 1989 in the farm named after Lenin (Fig. 5) was 670 Bq/l with permissible contamination level (APL) equal to 370 Bq/l. Deterministic simulation gave the following results: contamination level was: average–1168 Bq/l, median–902 Bq/l, in 98% of cases there was excess of APL. Stochastic prediction gave the following results for milk contamination levels: average–976 Bq/l, median–768 Bq/l, exceeding APL was found in 84% of cases. Thus, stochastic prediction demonstrates closer values in relation to measured values.

For the deterministic forecast (Fig. 5a) the maximum possible level of milk contamination with Cs-137 could reach the value of 3318 Bq/l, while the stochastic forecast (Fig. 5b) gave the result of 6220 Bq/l. It is interesting to note the following fact: the histogram of stochastic modelling is more "smooth" and is close to lognormal distribution, for deterministic prediction the histogram of milk contamination has two maxima. This indicates that there are two groups of soils in this farm, which differ by the TF parameter.

Hence, stochastic prediction according to 100 × 100 grid looks more plausible. In the process of cows moving through the pasture, they eat both "dirty" and "cleaner" grass, thereby averaging the level of radioactive contamination of the produced milk.

In the simulation system PcRGen-PerGrass of radioecological GIS-modeling (Fig. 6) the possibility of forecasting milk contamination separately for hayfields and pastures for 18 farms of Novozybkovsky and 20 farms of Klintsovsky district of Bryansk region was implemented.

The modeling system is based on three models that were used in the 1990s by different organizations for predictive assessments of modeling contamination of agricultural products: (1) Institute of Radiation Hygiene model (IRH, St.-Peterburg); (2) Russian Institute of Agricultural Radiology and Agroecology (RIARA, VASHNIL-2exp); (3) European Commission model (RESTORE EDSS) [2].

Modelling was performed over the time interval 1987–2005, with the a modelling step equal to one year. Two operation modes of the RIARA model (VASHNIL-2exp)—deterministic and stochastic forecast—were realized in the

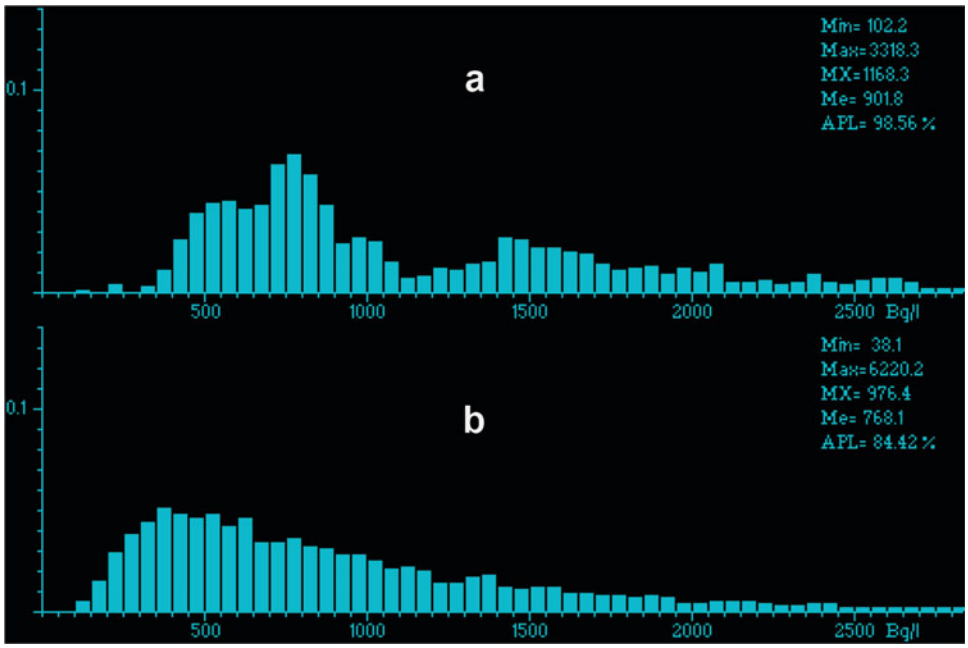

Fig. 5 Deterministic **a** and stochastic **b** distribution obtained for contamination of milk produced in the farm named after Lenin in 1989 (predicted on the basis of the Tf(t) model)

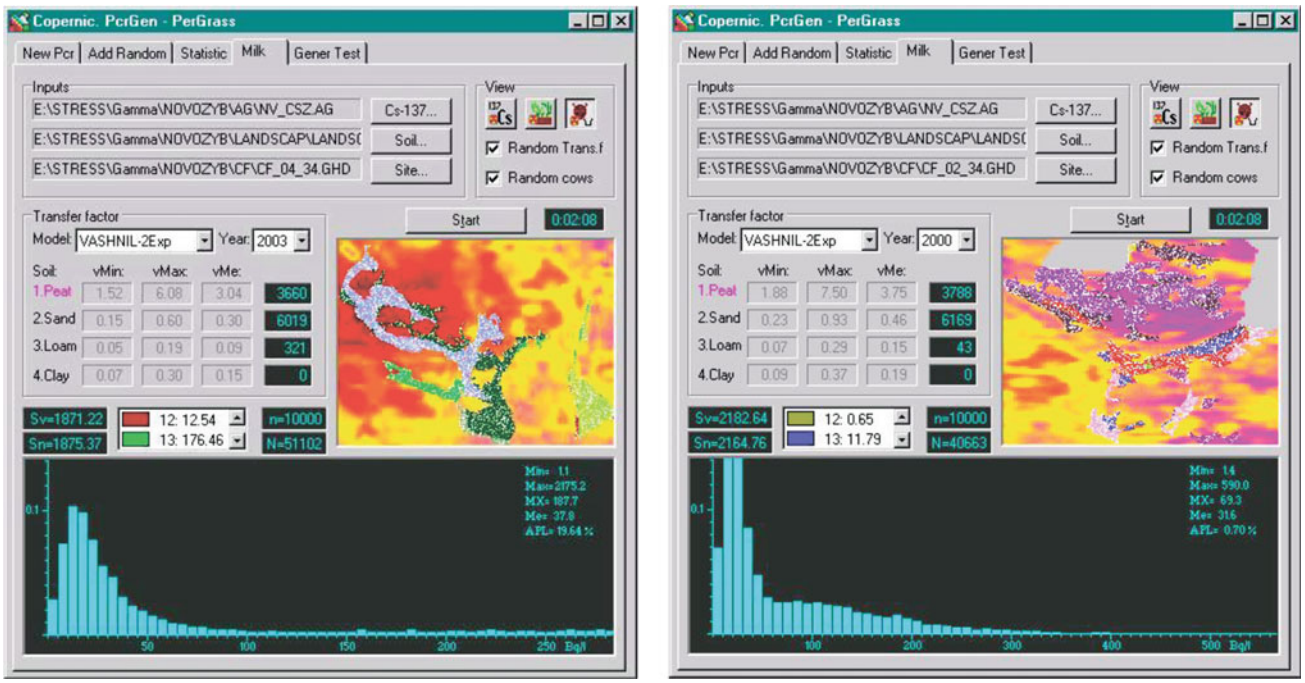

Fig. 6 Kolkhoz Reschitelny, predicted milk contamination for 2003 derived from peat soils (left) and Kolkhoz im. Lenin (right), predicted milk contamination for 2000

system [37–39]. The input parameters of the VASHNIL-2exp model were set according to the Fesenko model [58].

Figure 6 illustrates the results of stochastic modelling according to VASHNIL-2exp model for the collective farms 'Kolkhoz Reschitelny' for 2003 and 'Kolkhoz im. Lenina' for 2000. It is noteworthy, that in the collective farm 'Kolkhoz Reschitelny', excess of the permissible Cs-137 content was predicted in the area covering 19.6% of pastures while in the 'Kolkhoz im. Lenina' it was 0.7%. Consequently, in the latter since 1989 (Fig. 5) the share of contaminated milk reduced more than 100 times.

3 GIS of the Yenisei River Valley

Radioactive contamination of the floodplain of the Yenisei River resulted from technological discharges of radioactive waste from the Krasnoyarsk Mining-Chemical Combine (KMCC) in 1960–1992. At present, the rehabilitation of contaminated areas of the Yenissei floodplain has become an urgent problem for the impact zone of the KMCC. A proper choice of remediation strategy and technologies requires information on the localization of contamination, its scopes and distribution of radionuclides in the natural environment. All the obtained data can be brought together into a unified GIS included in the Decision Support System (DSS), which is created for information support on the radiation safety of population on the contaminated areas [63].

GIS creation for the Yenisei River valley in the area of discharge impact was carried out during ISTC Project # 2097 'RADLEG-RADINFO' [63–67], which in fact continued research and essentially extended the information system RadGIS-Enisei_River, built up during the preceding period within the ISTC Project #245 RADLEG, which developed databases and GIS for analysis of environmental effects of radiation.

The result of the studies was presented in the form of radioecological database organized in the form of GIS, which allows, using GIS-modeling technology to assess the radiation situation in the floodplain area of the Yenisei River contaminated due to of discharges from the Mining-Chemical Combine.

The program is implemented as a shell of the DSS "Yenisei GHK-Strelka" designed for automated processing and visualization of information required in preparation of decision-making and evaluation of environmental policy in the impact zone of the MCC. The methodology of radiation hazard evaluation using GIS modeling of technogenic radionuclides distribution in the Yenissei river floodplain is presented in Fig. 7.

The DSS is built as an information and reference system, including in some cases elements of hydrological modeling (BOSS SMS model), focusing not on the models' conceptual

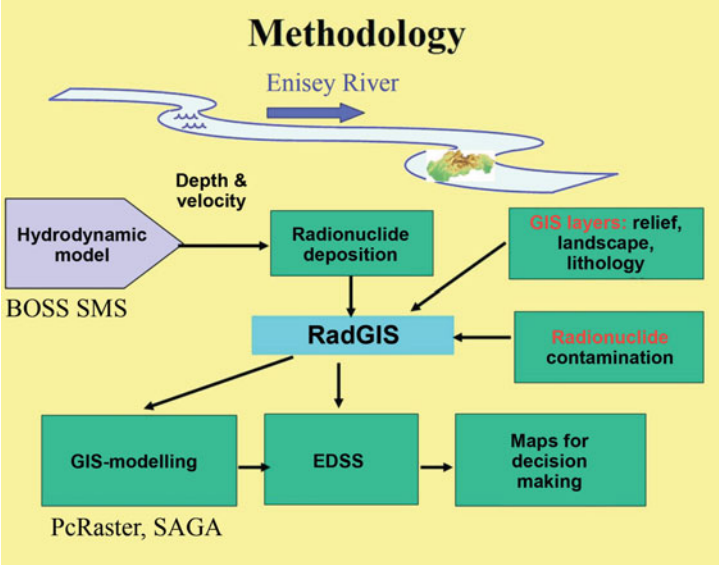

Fig. 7 GIS modeling methodology flow-chart of radiation hazard evaluation of technogenic radionuclides distribution in the Yenisei river floodplain

features but the modeling results obtained in advance according to selected scenarios, using various software tools not integrated into the DSS structure.

The basis of the "Yenisei KMCC-Strelka" was formed by the data obtained during the research conducted in August 2000 as part of the International STREAM Expedition (COPERNICUS grant). The database development included collection and expert evaluation of all available experimental data obtained during the study of radionuclide contamination of soils, sediments, and water in the floodplain of the Yenissei River over the period from 1991 through 2000 have been provided by a number of organizations including the KMCC Radioecological Center, V.G. Khlopin Radium Institute, State Institute of Applied Ecology (GIPE), Sobolev Institute of Geology and Mineralogy SB RAS, Vernadsky Institute RAS, RPA "Typhoon". The databases contain the results of determining specific activities Cs-137, Eu-152,154,155 and Co-60 in 1991, 1994, 1997, 1998, and 2000. In addition, data describing flood duration in the studied areas of the Yenissei River (from MCC to Strelka, a place of confluence of the Yenissei and Angara rivers) were also collected.

3.1 Decision Support System (DSS) "KMCC-Strelka"

In the DSS "KMCC-Strelka" (Fig. 8, Table 3) all information is presented by 9 test sites. The DSS supports access to thematic map layers with sampling points on the map and data sampling from the database using the map as a pointer. Data sampling was performed both by a site name and by georeference to, where the distance from the Krasnoyarsk hydropower station dam is used as georeference.

All information in the DSS is organized into four sections, one of which is a description of the system (DSS menu) the other three support certain capabilities of information support of decision-making procedures in the evaluation of radiation situation in the Yenisei River floodplain:

1. **DSS (system menu)**
2. **Yenisei (KMCC-Strelka)—map layers**
3. **Data bases**
4. **Models**.

The following maps were prepared for KMCC-Strelka site (in floodplain part of the Yenisei River) using manual interpretation of CORONA High-Resolution Satellite imageries: landscape map, soil types, elevation levels at 1:200,0000 scale (Table 3). The thematic maps were vectorized and presented in MapInfo format in order to organize radioecological cadastre.

Detailed lithological maps (scale 1:25,000) were prepared based on CORONA High-Resolution Satellite imageries for two sections of the Yenisei floodplain (1-Berezovy and Atamanovsky islands and 2-Kazachinsky Island), which were converted into a raster format after vectorization.

Based on the results of cartometric calculations for all 9 sites to assess the distribution of technogenic radionuclides databases of area distribution of different landscapes (14 types), soils (9 gradations) and altitude levels of both the river channel part of the Yenisei River and its floodplain part by the following gradations of altitude levels are presented: < -7 m, -3–7, -3–0, 0–1.5, 1.5–3.5, 3.5–6, 6–8, 8–11, 11–15, > 15 m.

The elevation data allows the duration and probability of flooding at each elevation to be calculated and a floodplain inundation pattern to be constructed.

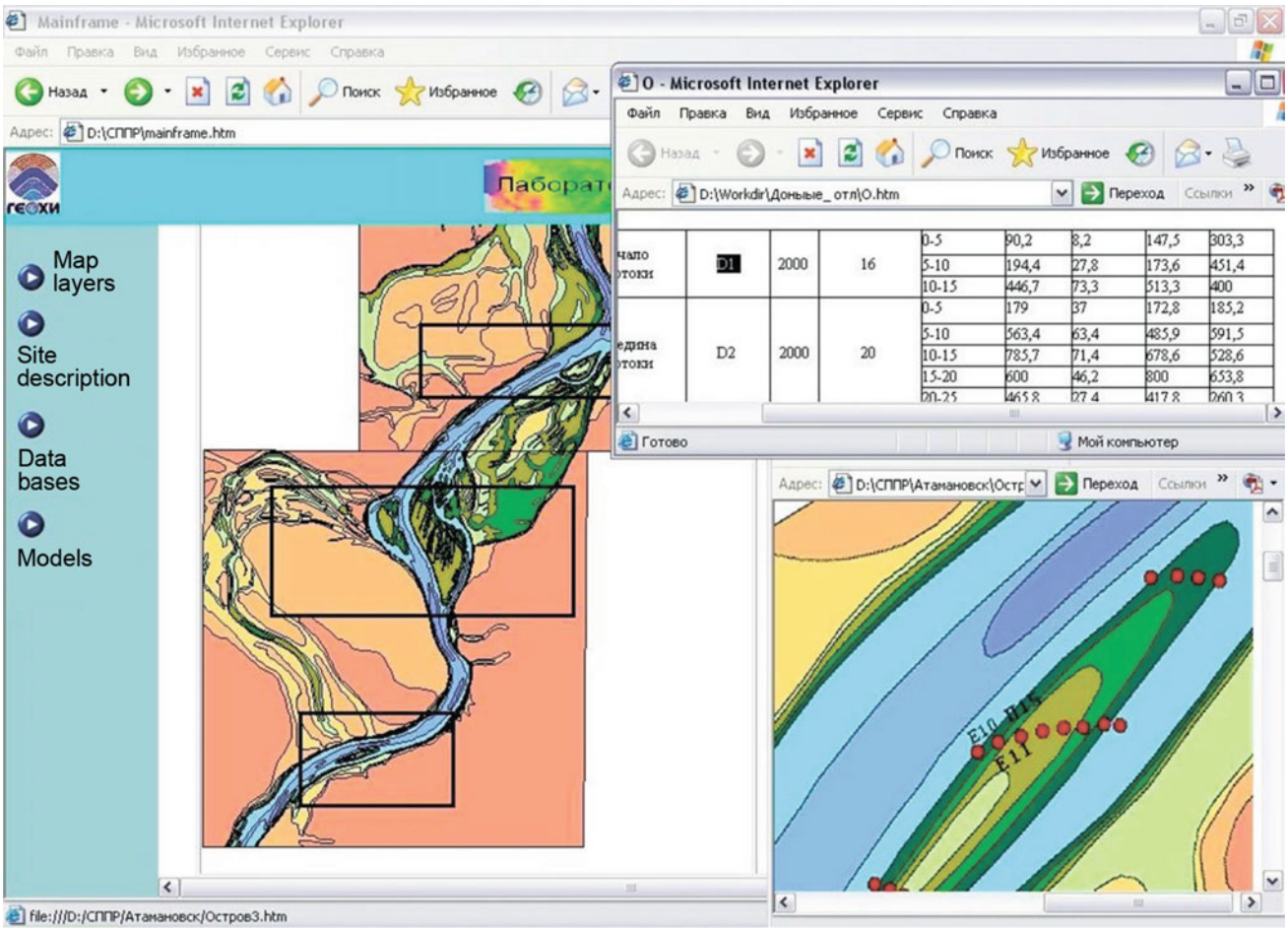

Fig. 8 User interface DSS "KMCC-Strelka" for evaluation of Yenisei River radionuclide contamination

Table 3 Fragment of data management of the DSS "Yenisei KMCC-Strelka" in site 1 (cartographic layers and line-transected data collected on landscape- radiometric survey)

No site	Landscape survey and sampling sites	Map layers + Radionuclide data base (RnDB)	Sampling sites from Krasnoyarsk (in km)	Site description	Layer statistics	Landscape-radiometric line-transected data
1–9	KMCC–Strelka	Overview	80–332		Yes	
1	Berezovy Island	Relief + DnDB	80–102	Yes	Yes	BP0, BP1, BP2, BP4
		Landscape				
		Lithology				
		Relief + RnDB	80–92			
		Relief + RnDB	88			
		Relief + RnDB	94–102			
		Relief + RnDB	96	Yes		BP-0, BP1, BP2
		Landscape	96			
		Relief + RnDB	99	Yes		BP-4
		Landscape	99			

All cartometric information is calculated for the right bank, the left bank and the island floodplain. It is essential for the area analysis of radiation situation, because in the near zone of the site the left bank was practically not exposed to radiation contamination, as the site of KMCC discharge is located on the right bank of the Yenissei river. These data are necessary for modeling radionuclide contamination spreading and dose load estimation.

After construction of the Krasnoyarsk hydroelectric power station floodplain areas above 6 m were not flooded, radionuclide contamination was formed in the 1960s. Floodplain areas in the height interval of 0–1.5 m are subjected to almost annual flooding and presently are a zone of radionuclide deposition (erosion).

The section "Databases" is of great importance in the DSS, as it contains all primary information on radioactive contamination of floodplain landscapes of the Yenisei River. The database in EXCEL format contains information on the following parameters:

1. Specific activities of artificial (Cs-137, Eu-152,154,155, Co-60) and natural (K-40, Ra-226, Th-232) radionuclides in soils of floodplain sections
2. Specific activity of artificial radionuclides (Cs-137, Eu-152,154,155, Co-60) in water and bottom sediments of the Yenissei river
3. Specific activity of artificial radionuclides (Cs-137, Eu-152,154,155, Co-60) in granulometric fractions of the floodplain soils
4. Granulometric composition of the floodplain and bottom sediment samples
5. Mineralogical composition of the floodplain soils
6. Composition of clay minerals of fine fractions
7. Specific activity of Cs-137 in clay fractions of the floodplain sediments
8. Duration of flooding of the floodplain areas in the middle reaches of the Yenisei River from 1960 to 2000.

The database contains information on mineralogical and granulometric composition of particles—carriers of radionuclides, necessary for choosing technology of rehabilitation of contaminated floodplain sediments [63]. Maximum Cs-137 sorption is characteristic of loams and silts.

Cartometric operations with separate layers allow to carry out zoning of the territory according to the degree of a risk of technogenic radionuclides contamination and the need for remediation measures. A separate block of DSS "Models" supports analytical capabilities of DSS "KMCC-Strelka".

GIS modeling was carried out in raster format. To do this, vector maps were converted to raster format using SAGA. GIS modeling of anthropogenic radionuclide distribution in the Yenisei floodplain in the DSS is performed using the functions of the PCRaster package [35, 36] (Table 4).

The section of model block "Hydrology of the Yenissei River" presents the results of hydrodynamic modeling of the flow velocity field of the Yenissei River for reconstruction of radionuclide contamination conditions in 1960–1980s when the maximum contamination of bottom sediments and floodplain soils took place due to deposition of suspended sediments contaminated with radionuclides. Deposition of radionuclides on suspended sediments depends on the size of a fraction. The finest fraction, which is the most contaminated with radionuclides, is deposited at flow velocities of less than 0.2 m/s in the Yenisei River [2, 67]. Therefore, hydrodynamic modeling allows to calculate the field of flow velocities and to single out zones where radionuclides accumulate. The hydrodynamic calculations were performed using the BOSS SMS distributed parameter simulation system [68].

An example of hydrodynamic calculations performed for two dates in 1966 (period of extreme flooding when maximum radioactive contamination of the Yenissei river valley occurred) is shown in Fig. 9.

The maximum flood in 1966 is dated to 17 June, during the period of high water recession (5 August 1966), when deposition of suspended sediments contaminated with radionuclides took place. During a period of the maximum flood (June 17, 1966), the model site on Atamanovsky Island (located in the northern part of the island) was exposed to radionuclide-contaminated sediments. During the maximum flood (June 17, 1966), the model plot Atamanovsky (located at a distance of 6 km from the site of KMCC dumping) was completely flooded. The current velocity in the river channel, according to the simulation results, was in the range of 1.5–1.8 m/s. At such velocity all fine fraction of suspended sediments contaminated with radionuclides was not deposited but was carried further downstream. During the August 5 flood, when the level of the Yenisei River dropped by approximately 6.5 m relative to its maximum value, Atamanovsky Island practically exited the river. Atamanovsky was practically out of flooding, with only the top and the mouth of the island remaining flooded. In these areas the water velocity may have been 0.25 m/s or less, at which time fine sediments could have been deposited on the floodplain surface.

The calculation of the floodplain area of the Yenisei River, where radionuclide deposition could occur, was performed also on the basis of the scheme of elevation levels, presented in a vector format MapInfo. The systematized results of these calculations were entered into SPR both in the form of database (Exel) and in the graphical form. Thus, it can be argued that the total floodplain area of the Yenisei River at the KMCC-Strelka site, where radionuclide

Table 4 GIS modeling in the DSS "Yenisei GHK-Strelka"

Model name	Research area	Isotope	Year (calculation)
Hydrology of the Yenisei River (V m/s)	Atamanovo		SELECT
Raster maps of the area	Kazachinskoye		Литология
Pollution density	Kazachinskoye	Cs-137, Eu-152-54, Co-60	SELECT
Reconstruction of dose rate and contamination density	Kazachinskoye	Cs-137	SELECT
Radionuclide contamination density	Atamanovsky Island	Cs-137	SELECT
		Co-60	SELECT
		Eu -152	SELECT
		Eu-154	SELECT
		The sum of all isotopes	SELECT
Dose rate reconstruction	Atamanovsky Island	Cs-137	SELECT
		Co-60	SELECT
		Eu-152	SELECT
		Eu-154	SELECT

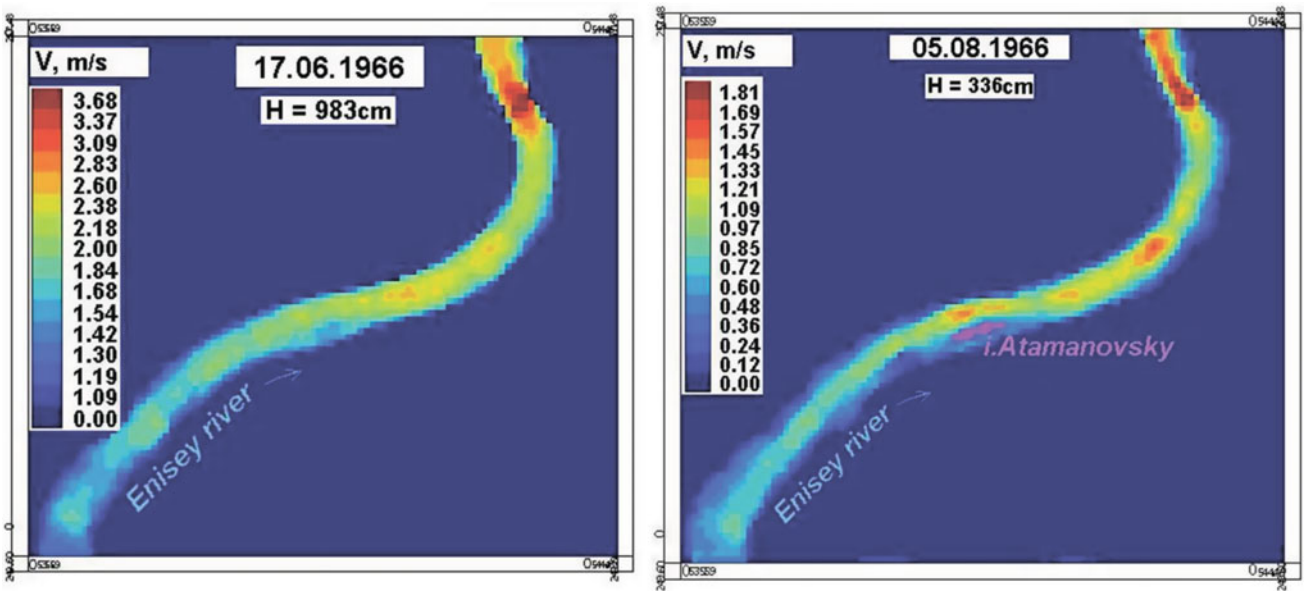

Fig. 9 Calculated current velocity in the Yenisei River in 1966: June 17 (h = 983 cm), (Q = 22,400 m^3), August 5 (h = 336 cm, Q = 6330 m^3)

deposition might have happened, is < 6 m–99.2 km^2; < 3.5 m–58.9 km^2.

A map of flooding of the Yenisei River floodplain for June 17 (flood peak) and August 5 (flood recession) is plotted in Fig. 10 using data from the "high water levels" layer.

During the period of the maximum flooding Berezovy and Atamanovsky islands were completely flooded, on

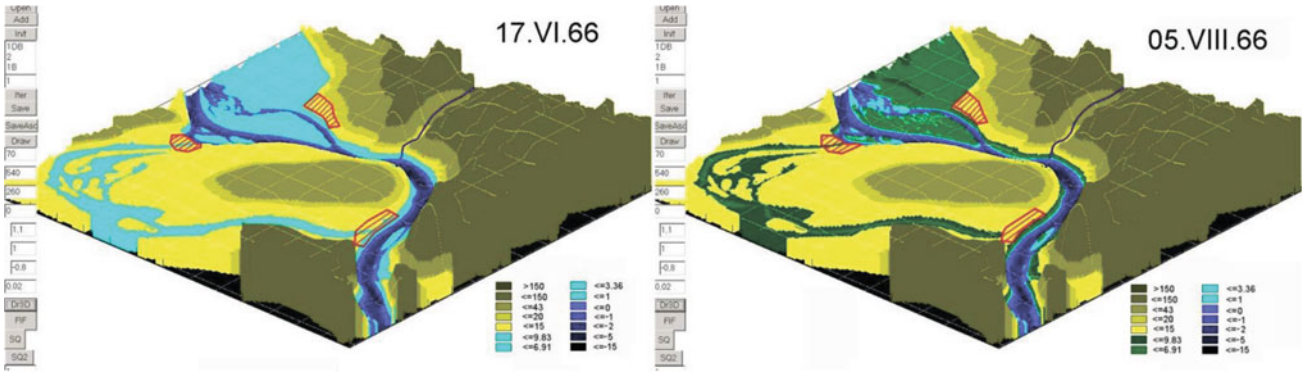

Fig. 10 Floodplain inundation pattern of the Yenisei River for June 17 (flood peak) and August 5 (flood recession)

August, 5 the low floodplain on Berezovy and Kazachiy islands was flooded, where deposition of suspended sediments contaminated with radionuclides took place.

Cartometric operations with separate layers allow to assess a risk of technogenic radionuclide contamination and the need for remediation measures. Thus, the maximum deposition of radionuclides can be observed in places of deposition of silty or sandy-silty fraction (a potential zone of remediation), while pebbles represent zones of radionuclides transit and eventually do not require specific remediation.

3.2 Distribution of Man-Made Radionuclide Contamination Density and Dose Rate Reconstruction

In [69, 70] a method of dose rate assessment was developed based on the surface activity of radionuclides in the upper soil layer up to 3 free path lengths thick, to estimate the thickness of the clean layer and to determine the thickness of a layer with 80–100% of all radionuclide activity [71]. A simplified model [72] that uses information on radionuclide activity distribution in soil was applied to calculate the external exposure dose.

After a shutdown of the direct flux reactors of the KMCC in 1992 and a sharp decrease in radionuclide flow into the Yenissei River, the upper horizons of the soil became buried by 'cleaner' sediments, whereas the maximum contamination by technogenic radionuclides was observed at a depth of 15–20 cm [73].

With regard of specific features of radioactive contamination of the Yenissei floodplain, a method of DER calculation was developed to take into account both the thickness and activity of a contaminated layer and its overlapping with clean alluvial deposits, and the contribution of radionuclides Co-60 and Eu-152,154 to the exposure dose rate besides Cs-137 [74]. According to the methodology developed for dose rate calculation, two layers of L and Z thickness are differentiated in the soil, the former of which is considered to be clean (i.e., it does not contain radionuclides), and the latter contains radionuclides with uniform distribution.

Using this methodology, doses for the year 2000 were calculated for Berezovy Island. For dose rate calculation on Berezovy Island (Fig. 11) a grid with 25 × 25 m spacing was used. For each grid node on the basis of landscape survey data, duration and frequency of flooding by reference points, the Cs-137, Co-60, Eu-152, 154 distribution parameters, as well as Z and L values were obtained.

The Atamanovskiy Island radionuclide contamination database was constructed based on the results of a survey conducted by the staff of the Institute of Geology, Geophysics and Geochemistry of the Siberian Branch of the Russian Academy of Sciences [75]. In order to identify zones of potential radionuclide deposition on Kazachy Island associated with the granulometric composition of

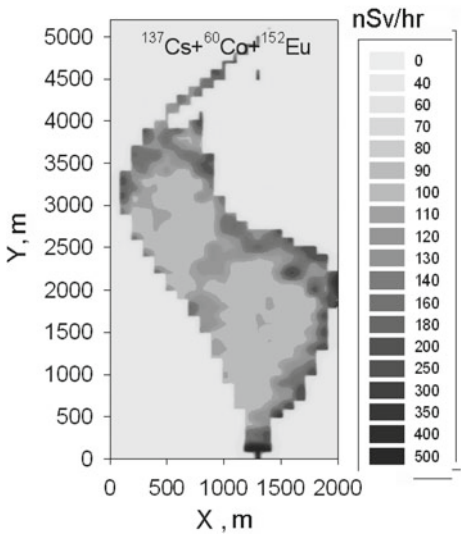

Fig. 11 Dose rate (nSv/h) generated by anthropogenic (Cs-137, Co-60, Eu-152,154) and natural radionuclides (U-238, Th-232, K-40) on Berezovy Island (2000)

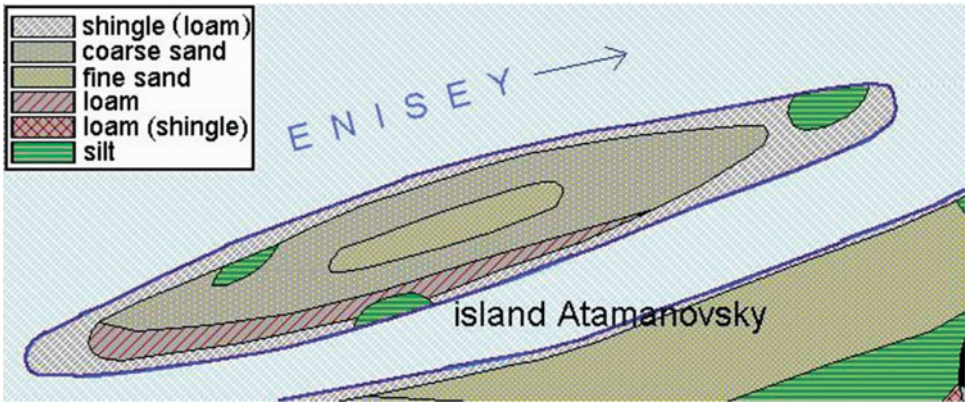

Fig. 12 Lithology of Atamanovsky Island

suspended sediments, a map of lithological composition was constructed (Fig. 12).

A simplified model [72] was used to reconstruct dose loads during the initial period of KMCC operation. Using data on Eu-152,154 isotope ratios [76], the dating of buried layers was performed at the first stage. With regard of the date of the layer formation (1966, 1992), this layer was considered "surface". The buried layers Cs-137 (Fig. 13, left) and Co-60 contamination maps for 1966, 1992 and 2000 (Fig. 13, right) were plotted for Atamanovskiy Island. The simulations were performed in the PCRaster envelope on a 10 × 10 m grid.

At the second stage, the reconstruction of the dose rate (Fig. 14) generated by Cs-137, Co-60 isotopes on a 10 × 10 m grid for 1966 took place. The suggested methodology proves to be productive for simulating changes in the radiation situation when contaminated soil layers are buried or, conversely, when they erode and reach the day surface.

GIS modeling of radionuclide spatial distribution was realized using the capabilities of the PcRaster dynamic modeling package [35]. The Information basis [block] of GIS, as a rule, consists of topographic maps, whereas PcRaster technology implements the ideology of landscape-ecological modeling, which envisages allocation of territorial units similar in radionuclide migration conditions [2].

When modeling radionuclide distribution, altitude position, lithology and landscape were taken into account. Initial vector maps were transformed into raster maps, raster modeling step was 50 × 50 m. On the basis of connection of radionuclide contamination with parameters of the landscape structure of the Yenissei river floodplain, maps of the density of contamination by man-made radionuclides on Kazachiy Island were built (Fig. 15).

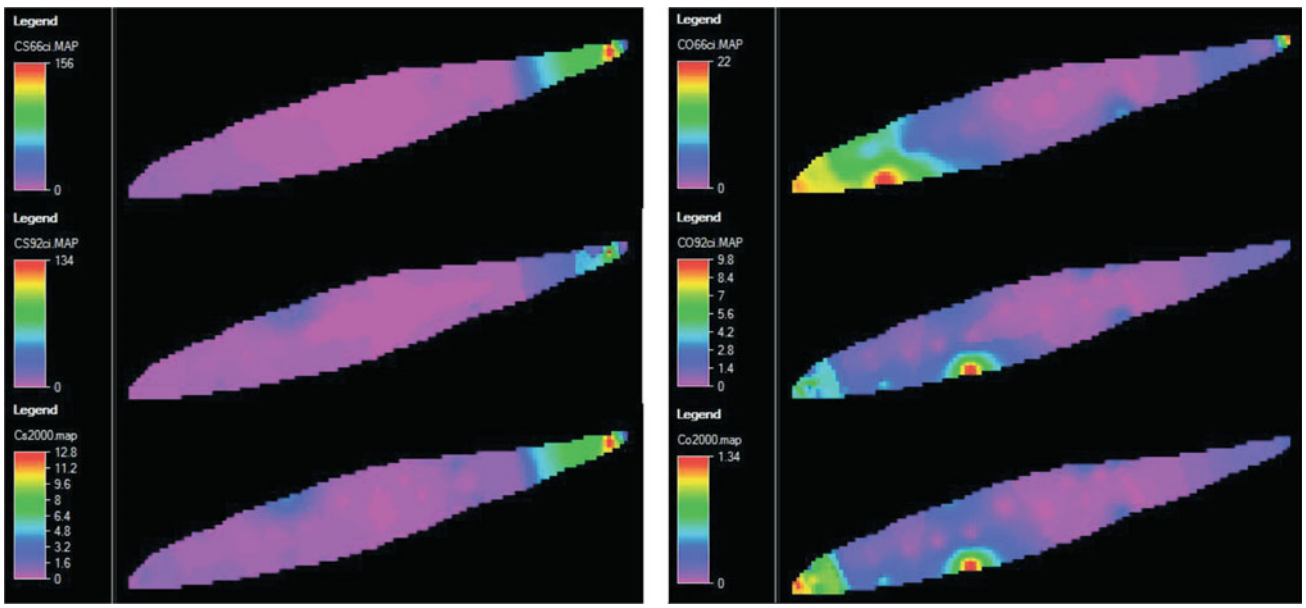

Fig. 13 Reconstruction of Cs-137 (left) and Co-60 (right) contamination densities (kBq/m^2) for 1966, 1992 and 2000 on Atamanovskiy Island

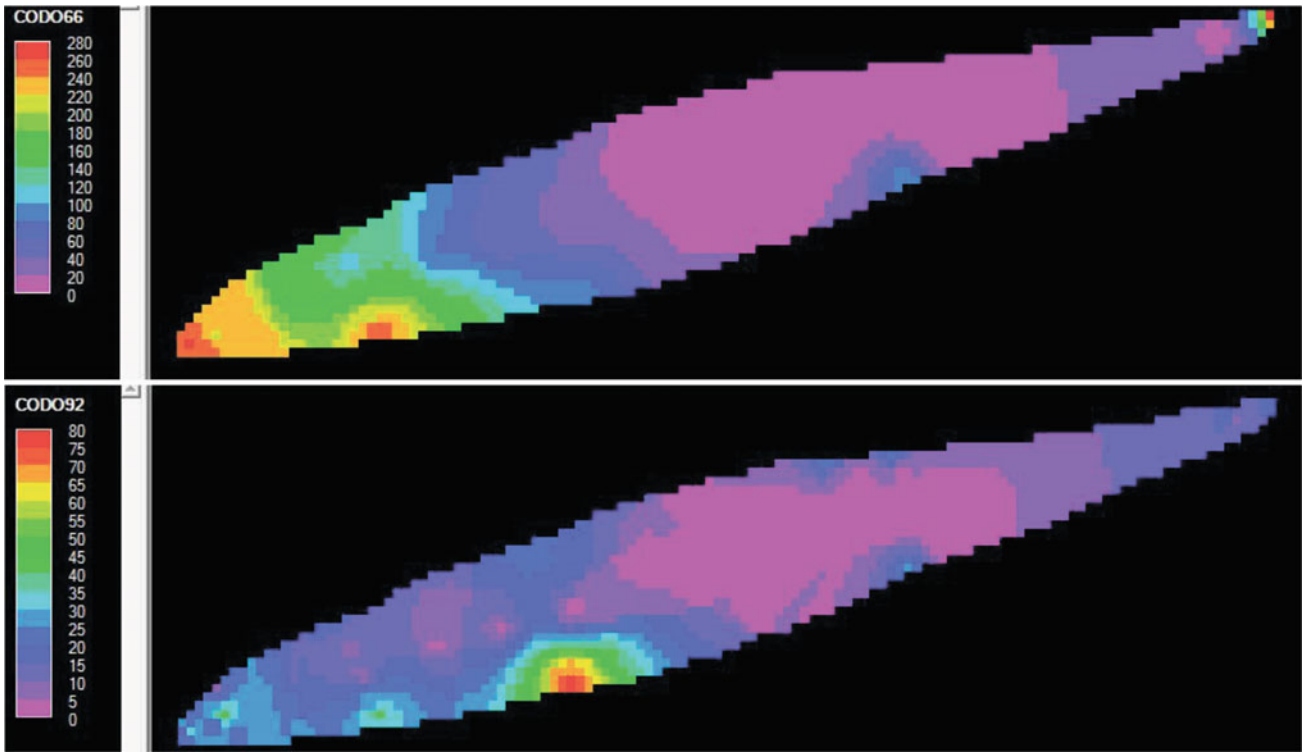

Fig. 14 Reconstruction of dose rate (nSv/h) generated by Co-60 for 1966 and 1992 on Atamanovskiy Island

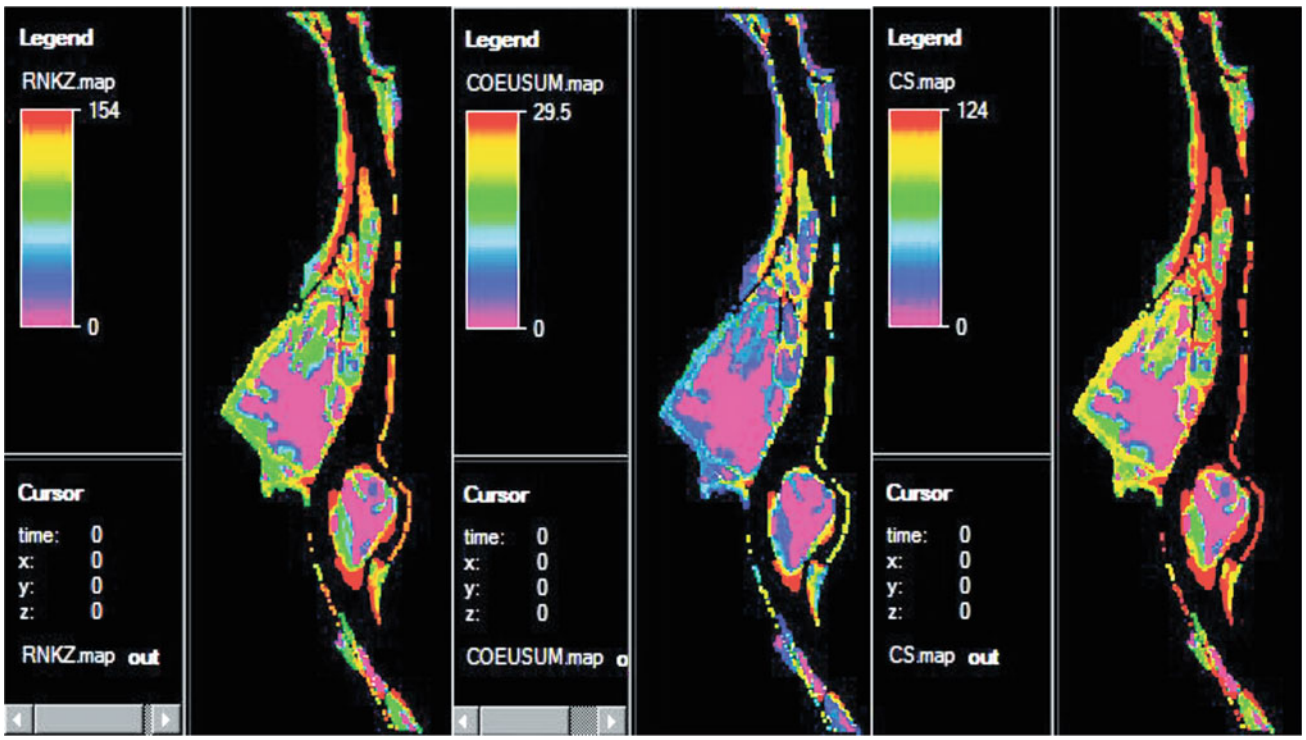

Fig. 15 Distribution of anthropogenic radionuclides at the Kazachinskiy site based on GIS modeling results. Left—the sum of ERN + sum of Co-60, Eu152,154 + Cs-137, center—the sum of Co-60, Eu-152,154, right—Cs-137 (kBq/m^2)

Incorporation of information on the total Cs-137 discharge into the DSS database as well as the estimated Cs-137 stock and area at 6 test sections of the Yenissei flood plain on the basis of experimental studies carried out in 2000 allowed to make up the balance of man-made radionuclides (estimated stock from total discharges within the allocated sections in the 200-km zone of the KMCC). According to the data of raster modeling on 50 × 50 m grid at "Kazachinskoye" site total area of contamination is equal to 15,56 km2, stock of Cs-137 is 1075 GBq (29 Ci). If this value is compared with the data on the total Cs-137 discharge [77] for the period from 1976 till 2000 (19,635 GBq or 29 Ci), the total Cs-137 stock is estimated to be Cs-137 (19,635 GBq or 530 Ci), in this site 5.5% of the total Cs-137 release for the period 1976–2000 was deposited [2].

4 Multi-Scale Levels of Landscape-Radioecological Monitoring in the Bryansk Region

Development of methods for spatial and temporal analysis of technogenic radionuclides distribution is of fundamental importance for long-term planning of radioecological situation on contaminated territories. To this end, in the most contaminated western part of the Bryansk region in 1992–1993 the landscape-radioecological monitoring network of the RSPEAC was organized to reveal the relation of radionuclide contamination to the landscape structure of the territory [2, 29, 78, 79].

Besides identification of parameters of the models of radionuclides vertical migration in soil, their transfer to vegetation as traditional tasks of radioecology, the main goal shifted to the study of the radionuclides field transformation depending on landscape conditions. For this purpose, three different scale levels of objects were chosen (Fig. 16) [2]: (1) Experimental site -is a single-type plot of landscape with a size about 100 × 100 m, occupying one element of mesoform of relief (for example, a slope), approximately homogeneous by contamination density and landscape-geochemical conditions of radionuclide migration and transformation; (2) Landscape-radiation catenary—is conjugate series of experimental sites located at different geomorphological levels (from the watershed to the bottom of the watercourse) and characterizing influence of different landscape conditions on radionuclide migration ability within elementary basins. (3) Radioecological test site—is an area of territory used for different economic purposes, including all zones of radionuclide contamination within the most typical landscapes to assess the effectiveness of countermeasures.

In 1993, after performing AG on radionuclide-contaminated areas in the western part of the Bryansk region, RadGIS "Bryansk" was supplemented with an additional raster layer (Fig. 16). In addition, information on radioactive contamination of the monitoring sites was obtained as a result of field spectrometric survey [71, 72]. Thus, the information on the radioactive contamination incorporated into the data bank embraced three scale levels differing significantly by the area of detection S [2]: (1) sampling–S $\approx$ 0.01 m^2; (2) measurement with radiometer CORAD–S = 2 m^2; AG measurements–S = 10^4 m. Consequently, there is an opportunity to study the scaling effects at transition from a microlandscape level (sampling) to a landscape level (AG).

Organization of GIS of radioecological information at the monitoring sites was also undertaken by other organizations [80]. The first experience of AG application during the elimination of the Chernobyl accident consequences dates back to 1986. For the Chernobyl zone [81] a combined approach was used, when the AG results were corrected by ground-based sampling data. However, AG data for the area around the Chernobyl nuclear power plant for the period 1986–1988 have not been preserved [82]; a new AG study of contaminated areas was required and was carried out in the 1990s. The first data of radioecological monitoring of the 60-km reference network of radioecological monitoring [81] for the period 1987–1989 were also irretrievable. The GIS of the radioecological observatory, as the exclusion zone of ChNPP is now called, includes part of the results of the ground survey on the 60-km reference network of radioecological monitoring carried out in 1987 [82].

Assessment of landscape influence to explain some shape and location characteristics of heavily contaminated areas in the 30-km zone of the Chernobyl zone is presented in papers [83]. New geoinformation technologies used by the authors made it possible to identify the impact of landscape factors on the formation of the pollution structure. On the basis of the landscape approach, an explanation of the shape and location features of heavily polluted territories in the near zone of influence of the Chernobyl NPP is given [84].

4.1 Modeling of Cs-137 Distribution at the Micro-Landscape Level

The first studies of the distribution of Cs-137 at the micro-landscape level were initiated at the RSPEAC. A detailed description of the data bank on the experimental sites of the RSPEAC is given in [2, 29]. In 1992, it was a new trend in radioecology to build a high-resolution DEM (20 cm) to account for the influence of microrelief on the

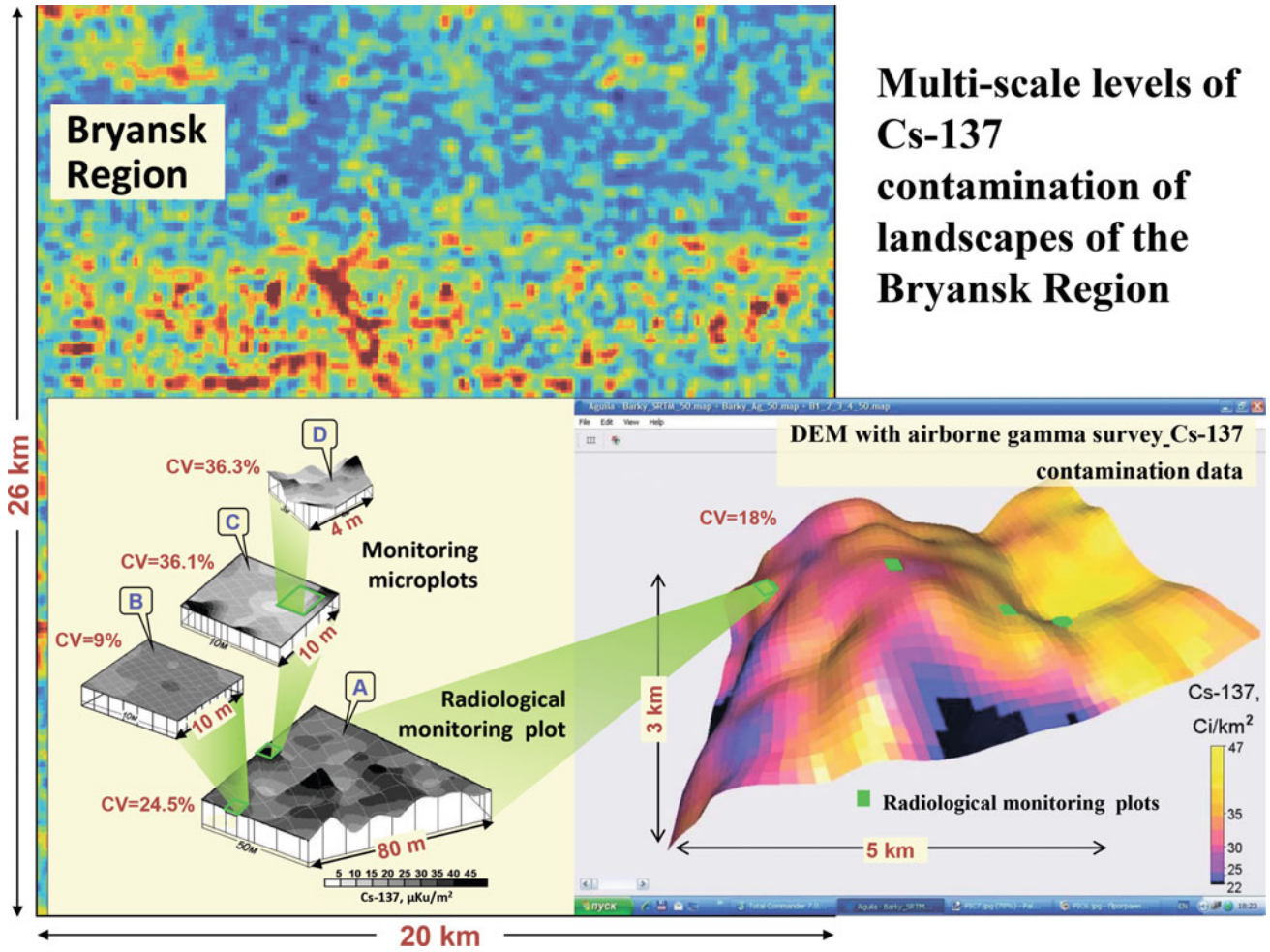

Fig. 16 Multi-scale levels of landscape-radioecological monitoring organization in the Bryansk region

nature of spatial distribution of Cs-137. The geostatistical analysis of the Cs-137 distribution made it possible to distinguish a scale hierarchy of microspot-like Cs-137 distribution [85–87], while the separation of divergence/convergence zones according to DEM processing data allowed to find out a possible structure of lateral migration flows within several meters and their relation to Cs-137 redistribution [2]. Combination of the results of field spectrometric survey with DEM data gave impetus to study the statistical structure of Cs-137 contamination at the microlandscape level and, consequently, to reveal nonlinearity of Cs-137 distribution dependence on DEM derivatives of the microrelief [2, 85–87].

Analysis of the radiometric survey results showed that the variability (CV) of Cs-137 is scale dependent, it can vary depending on the size of a sampling area, and the size of a detected sample. In Fig. 16, the CV of Cs-137 varies from 24.5% for the entire 50 × 80 m area (10 m sampling step), varying from 9% to 36.1% at 10 × 10 m (2 m sampling step), rising to the value of 36.3% at 3 × 4 m (0.5 m sampling step). Therefore, extrapolation of these results from 100 × 100 m sites, even to a 3 × 5 km area (location of the sites in the landscape) becomes a non-trivial task.

A more complicated situation is seen when moving to larger landscape objects, such as basins (size 20 × 25 km, Fig. 16). In this case, the structure of the Cs-137 contamination field is already controlled by another set of landscape factors, which cannot be clearly obtained from studies at the local level (at the site). This is one of the mysteries of the Cs-137 contamination field multiscale, associated with its multifractality.

4.2 Perspectives of Landscape-Radioecological Modeling

The experience of radioecological investigations after the Fukushima accident (2011) clearly demonstrated insufficient predictive reliability of most radioecological models. Therefore, one of the urgent task of radioecology for the

nearest future should be the development of transport and radiation impact models including physical, chemical and biological interactions that could improve making spatial and temporal predictions. The modelling of radionuclide transport and calculation of dose loads at the landscape or global environmental level, with due consideration of the degree of uncertainty, is declared to be an important task. The implementation of spatial and temporal forecasts is hardly possible without geoinformation modelling for mapping zones of transport and impact of radionuclides at the landscape level for 'identification of radiosensitive ecological zones' [88].

A revised programme for radioecological research known as the ALLIANCE Strategic Research Agenda (SRA) [89] and its update [90] state as their goal "to produce transport and impact maps of radionuclides at different scales based on thematic maps, including spatial and temporal variability, using recently developed process based models". Given the heterogeneous geographical distribution of radionuclides, it is proposed that particular attention should be paid to the detailed description of radionuclide transport processes at different scales, so that transport can be mapped at the landscape level.

Recently at the Vernadsky Institute RAS, research has been carried out with respect of landscape differentiation of Cs-137, mapping of Cs-137 patterns (Fig. 17) modeling their spatial structure in different landscapes [91].

An important direction of research is to identify causes of heterogeneity in the intensity of lateral fluxes of Cs-137 on arable soils, their relationship with landscape factors (Fig. 18). Landscape-biogeochemical factors of transformation of contamination field of two sites (Brakhlov and Kostitsa) are considered in [92].

Modern possibilities of GIS-technologies allow to make overlay of information layers, using Google Earth data to build actually a 3D model of the earth surface where road network is clearly seen, all fields, ponds are clearly visible. The highlighted Cs-137 contamination density isolines clearly identify areas of Cs-137 washout in the watershed (limited by the isoline 10 kBq/m^2) and accumulation areas in the lowlands (gully-beam network with pond, outlined by the isolines 15–20 kBq/m^2).

An important aspect of recent studies considering the landscape structure (Fig. 19, is the mathematical modeling of lateral fluxes of Cs-137.The results of modeling of lateral fluxes are presented in [93, 94], in which connection of Cs-137 distribution with different DEM derivatives is investigated, statistical models (such as GAM, GLM) are built to obtain an estimate of lateral fluxes intensity. The principal non-linearity of erosion processes in different parts of the landscape has been found; at the same time, the modeling makes it possible to classify an agrolandscape according to the risk of Cs-137 accumulation zones formation, thus solving the problem of "identification of radio-sensitive ecological zones" [88, p.76].

Along with statistical models of lateral transport, the transformation of Cs-137 patterns resulting from the divergence/convergence process of lateral fluxes is investigated [94, Fig. 19].

5 Conclusion

The radio-ecological GIS were created many years ago, and at present they do not lose their relevance. Recently, new possibilities of GIS-modeling that have included many functions of modeling morphometric parameters of relief, and new methods of physical–mathematical and statistical modeling (such as General Additive Models–GAM have provided an opportunity to obtain fundamentally new results. The 30-year experience of using geoinformation technologies in radioecology strongly confirms that

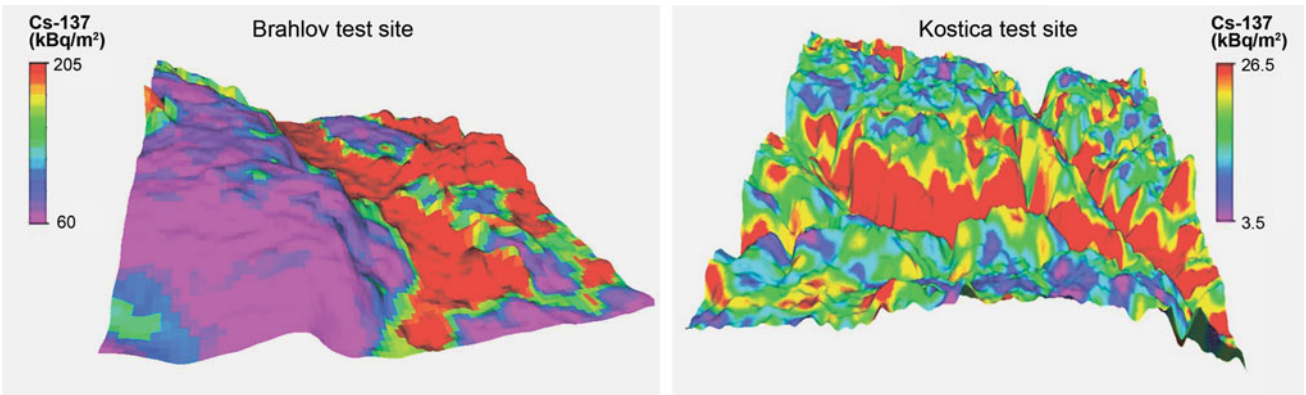

Fig. 17 Examples of Cs-137 patterns in different landscapes of the Bryansk region. Left—landscape of Brakhlov, right—landscape of Kostitsa river basin

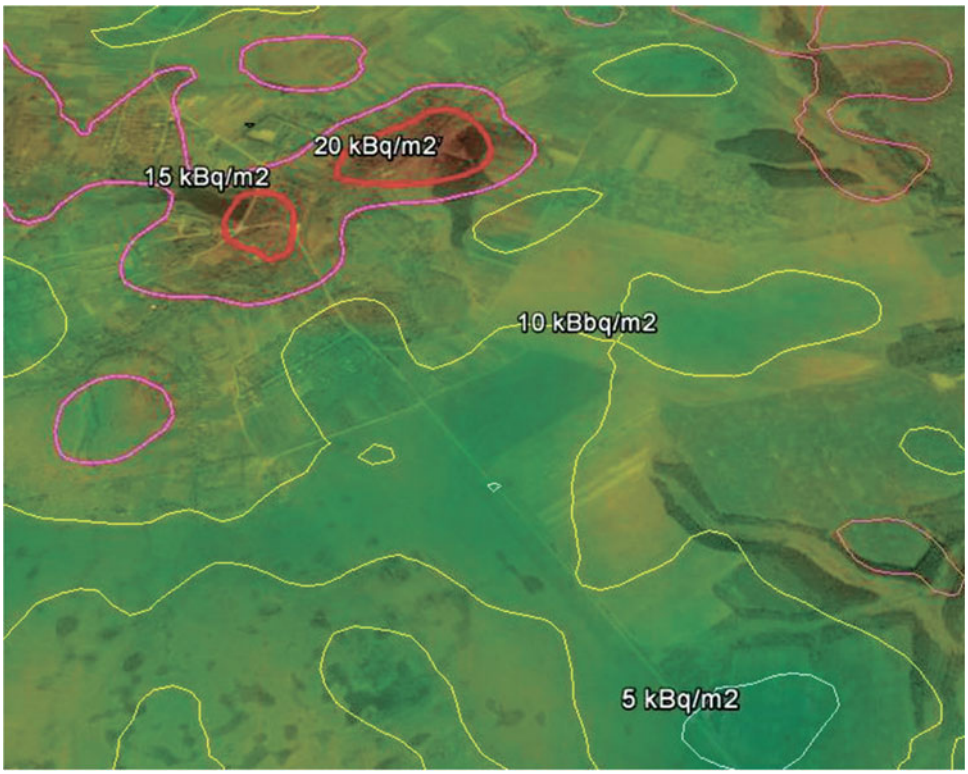

Fig. 18 Large-scale structure of Cs-137 contamination in agrocenoses of the Kostitsa river basin

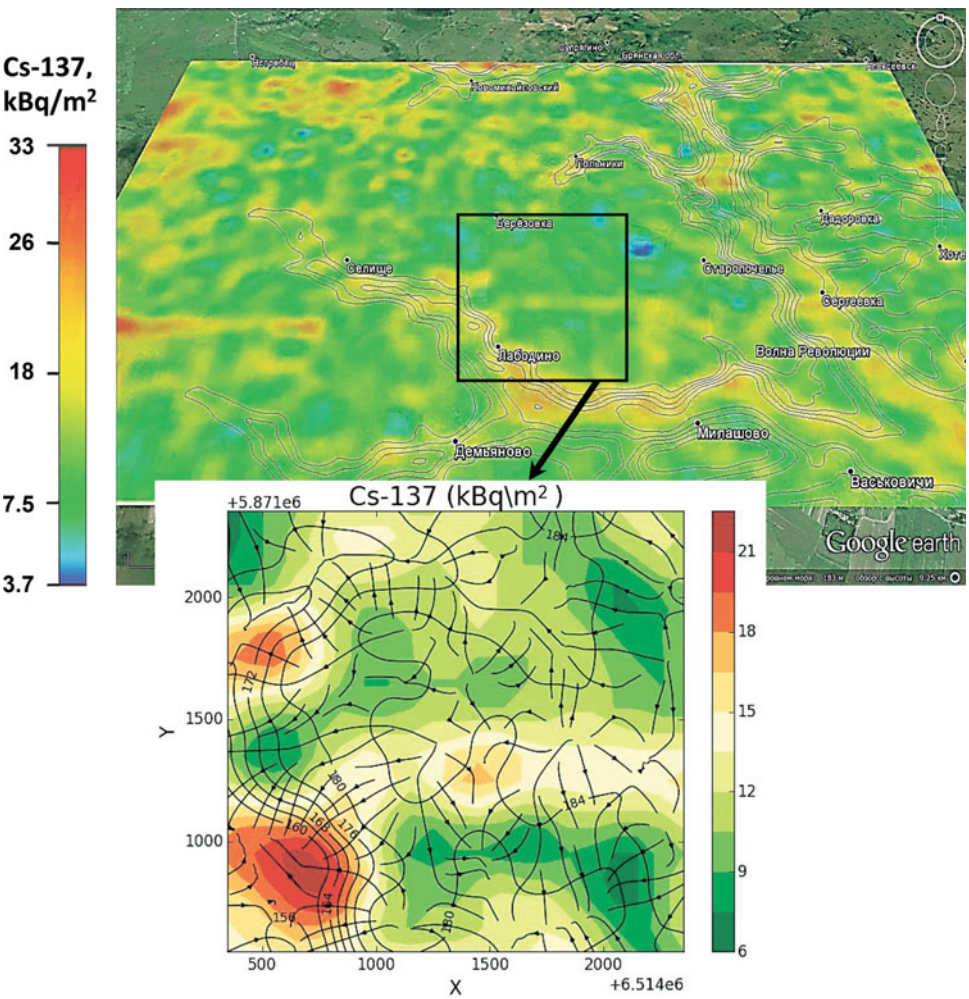

Fig. 19 RadGIS Kostica and modelling of Cs-137 lateral fluxes

modeling technologies can change, improve, but primary data always remain an invaluable source of new knowledge and results.

The experience of geoinformation modeling and creation of decision-making support systems to help eliminate the Chernobyl accident consequences is recognized as worthy of attention and further development in view of fundamentally new opportunities in the era of global digitalization and wide distribution of spatially distributed data banks of environmental and geographic information.

Acknowledgements This work is conducted under the GEOKHI RAS state assignment.

References

1. Burrough, P., McDonnel, R.: Principles of Geographical Information Systems, 2nd edn., p. 356. Oxford University Press, UK (1998)
2. Linnik, V.G.: Landscape Differentiation of Technogenic Radionuclides, p. 372. RAS, Moscow (2018)
3. Dianov, V.I.: Creation of modern computing systems for complex ecological research. Control Systems and Machines, vol. 3, pp. 83–85. Institute of Cybernetics of the Ukraine's Academy of Science, Kiev (in Russian) (1988)
4. Linnik, V.G., Chepurnoi, N.D.: The creation of a system of appraisal and forecast of radionuclide migration to the area of the Chernobyl atomic power plant accident. The Eurochernobyl Project. Report 1 Based on the first Eurochernobyl International Seminar, pp. 101–112. Kiev, April 1989. Moscow, USSR (1989)
5. Davydchuk, V.S., Zarudnaya, R.F., Mikheli, S.V., Petrov, M.F., Sorokina, L.Y., Tkachenko, A.N.: Landscapes of the Chernobyl zone and their assessment by radionuclide migration conditions. In: Marinich, A.M. (ed.) p. 112. Kiev, Naukova, Dumka (in Russian) (1994)
6. Morozov, A.A. (ed).: System Analysis and methods of Mathematical Modeling in Ecology, p. 88. V. Glushkov Institute of Cybernetics, Kiev (in Russian) (1990)
7. Davydchuk, V.S., Linnik, V.G., Chepurnoy, N.D.: Modeling of Radionuclide Migration on the Basis of Landscape Approach, vol. 2, pp. 261–274. Chernobyl'-88. Reports of the 1. All-Union scientific and technical meeting on results of accident effect elimination at the Chernobyl' NPP. Chernobyl, (in Russian) (1988)
8. Davydchuk, V.S., Linnik, V.G., Chepurnoy, N.D.: Modelling and Forecast of Radionuclide Migration in 30-km ChNPP Zone on the Basis of Landscape Approach. Chernobyl'-88, vol. 1, pp. 188–202. Reports of the 1. All-Union scientific and technical meeting on results of accident effect elimination at the Chernobyl' NPP. Migration and State of Radionuclides in the environment. Chernobyl (in Russian) (1989)
9. Davydchuk, V.S., Linnik, V.G.: Substantiation of reference network of radioecological monitoring of 60-km zone of Chernobyl NPP. In the book "Proceedings of the 1. All-Union Scientific and Technical Meeting on Results of Accident Effect Elimination at the Chernobyl' NPP, p. 75. Chernobyl (in Russian) (1988)
10. Linnik, V.G., Linnik, N.I., Lyashenko, G.B.: Software tools for display and analysis of radionuclide contamination fields for Chernobyl accident area. In: Morozov, A.A. (ed.) System Analysis and Methods of Mathematical Modeling in Ecology, pp. 20–28. V. Glushkov Institute of Cybernetics, Kiev (in Russian) (1990)
11. Davydchuk, V., Arapis, G.: Evaluation of Cs-137 in Chernobyl landscapes: mapping surface balances as background for application of rehabilitation technologies. J. Radioecol. **3**(1), 7–13 (1995)
12. Sadolko, I., Arapis, G., Davydchuk, V.: Migration velocity of Cs-137 in the soils Chernobyl area. J. Radioecol. **3**(2), 7–13 (1995)
13. Davydchuk, V.S., Linnik, V.G., Chepurnoy, N.D.: Organization of geoinformation systems for modeling of anthropogenic disturbances of the natural environment of large regions. Proc. All-Russian Res. Inst. Syst. Res. **5**, 163–167 (1988). (in Russian)
14. Davydchuk, V.S., Linnik, V.G.: Landscape block of geoinformation system. Vestn. Moscow Univ. Ser. Geogr. **5**, 25–32 (1989). (in Russian)
15. Davydchuk, V.S.: Landscape approach to the GIS organization. In: Environmental Changes and GIS. International Symposium at Asahikawa, Japan, vol. I, pp. 147–152 (Aug 1991)
16. Linnik, V.G.: GIS strategy in the landscape-geochemical and radioecological mapping of radionuclides contaminated territory. In: Environmental Changes and GIS. International Symposium at Asahikawa, Japan, August 1991, vol. 1, pp. 111–114. Asahikawa, Japan (1991)
17. Linnik, V.G., Khitrov, L.M., Korobova, E.M.: Principles of Landscape-Geochemical and Radio-Ecological Mapping of the Territories, Contaminated by Radionuclides as a Result of the Chernobyl' NPP Disaster (RADLAN project), p. 50. Vernadsky Institute, Moscow (in Russian) (1991)
18. Korobova, E.M., Linnik, V.G., Khitrov, L.M.: Landscape-geochemical and radioecological mapping of the contaminated areas. Geochem. Int. **7**, 1020–1029 (1993) (in Russian)
19. Korobova, E.M., Linnik, V.G.: Geochemical landscape strategy in monitoring the areas contaminated by the Chernobyl radionuclides. Landscape Urban Plann. **27**(1), 91–96 (1993)
20. Arutyunyan, R.V., Bolshov, L.A., Demianov, V.V., Glushko, A. V., Kabalevski, S.A., Kanevsky, M.F., Kiselev, V.P., Koptelova, N.A., Krylov, S.F., Linge, I.I., Martynenko, E.D., Pechenova, O.I., Savelieva, E.A., Serov, A.N., Haas, T., Maignan, M.: Environmental decision support system on the basis of geoinformational technologies for the analysis of nuclear accident consequences. In: The radiological Consequences of the Chernobyl Accident, pp. 539–542. EUR 16544 EN, EC (1996)
21. Shershakov, V.M., Kosykh, V.S., Borodin, R.V.: Radioecological analysis support system (RECASS). Radiat. Prot. Dosim. **50**(2–4), 181–184 (1993)
22. Shershakov, V.M., Trakhtengerts, E.A.: Development of the RODOS/RECASS system as a distributed, decision-making support system in an emergency. Radiat. Prot. Dosim. **64**(1, 2), 143–147 (1996)
23. Izrael, Y.A., Kvasnikova, E.V., Linnik, V.G.: Radioactive contamination of the territory of Russia. In: Kotlyakov, V.M., Lyuri, D.I. (eds.) The book: Changing the Natural Environment in the XX Century, pp. 202–220. Publishing House Molnet, Moscow (in Russia)
24. Atlas of radioactive pollution of European Russia, Belarus and Ukraine, p. 143. M.: Federal. Service of Geodesy and Cartography of Russia (in Russian) (1998)
25. Kvasnikova, E.V.: Theory and Practice of Radioactive Contamination Mapping. Proceedings of International Conference "Radioactivity in Nuclear Explosions and Accidents. 24–26 April 2000, vol. 1, pp. 153–159, Gidrometeoizdat, Moscow, St.-Petersburg (in Russian) (2000)
26. Izrael, Y.A., Kvasnikova, E.V.: Collection of geographical images of radioactive contamination fields. Izvestiya RAN. Ser. Geograficheskaya. (5), 7–17 (2007) (in Russian)
27. De Cort, M., Dubois, G., Fridman, S., Germenchuk, M., Izrael, Y., Janssens, A., Jones, A., Kelly, G., Knaviskova, E., Matveenko, I., Nazarov, I., Pokumeiko, Y., Sitak, V., Stukin, E., Tabachny, L.,

Tsaturov, Y., Avdyushin, S.: Atlas of Caesium 137 Deposition on Europe after the Chernobyl Accident, p. 176. IN EUR 16733 EN/EN/RU, EC (1998)
28. Dubois, G., Bossew, P.: Spatial analysis of Cs-137 in the environment: an overview on the current experience. In: Dubois, G., Malczewski, J., De Cort, M. (eds.) Mapping Radioactivity in the Environment, pp. 21–36. Spatial Interpolation Comparison 1997. EUR 20667 EN, EC (2003)
29. Linnik, V.G., Kuvylin, A.I., Kuzmichev, V.N., Korobova, E.M.: Organization of data of radioecological information on the territory of experimental polygon in Bryansk Region. Radiation and Risk, vol. 3, pp. 121–128 (in Russian) (1993)
30. Calmon, P., Thiry, Y., Zibold, G., et al.: Radionuclide Transfer in Forest Ecosystems. Quantification of Radionuclide Transfer in Terrestrial and Freshwater Environments for Radiological Assessments, vol. 2009, pp. 333–380. IAEA, Vienna (2009)
31. Diener, A., Hartmann, P., Urso, L. et al.: Approaches to modelling radioactive contaminations in forests—overview and guidance. J. Environ. Environ. Radioact. **178–179**, 203–211 (2017)
32. Mamikhin, S.V., Lipatov, D.N., Manakhov, D.V., Paramonova, T. A., Stolbova, V.V., Shcheglov, A.I.: Simulation model of the dynamics Cs-137 content in food chain components of land ecosystems. Moscow Univ. Soil Sci. Bull. **75**(2), 86–92 (2020). © Allerton Press, Inc
33. Mamikhin, S.V., Badawy, W.M., Lipatov, D.N., Manakhov, D.V., Paramonova, T.A., Stolbova, V.V., Shcheglov, A.I.: Simulation model of Cs-137 daily dynamics in the food web of the deciduous forest ecosystem. Moscow Univ. Soil Sci. Bull. **76**(2), 70–77 (2021). © Allerton Press, Inc
34. Dubois, G., Tollefsen, T., Bossew, P., De Cort, M.: GIS and radioecology: a data perspective. In: Proceedings of the 10th EC-GI & GIS Workshop, ESDI State of the Art, pp. 23–25. Warsaw, Poland (2004)
35. Van Deursen, W.P.A., Wesseling, C.G.: The PCRaster package. Technical report of the Department of Physical Geography, University of Utrecht, The Netherlands (1992)
36. Wesseling, C.G., Karssenberg, D., Van Deursen, W.P.A., Burrough, P.A.: Integrating dynamic environmental models in GIS: the development of a dynamic modelling language. Trans. GIS **1**, 40–48 (1996)
37. Linnik, V.G., Korobova, E.M., Kogan, D.L., Kuvylin, A.I.: GIS technology in education for agro-landscape optimal organization in conditions of radionuclide contamination managing change in the food-chain and environment. In: Proceedings of the Second European Scientific Conference on Higher Education in Agriculture, pp. 151–155. Foundation for European Conference on Higher Agricultural Education, Goedoelloe, Hungary (1994)
38. Howard, B.J., Wright, S.M., Barnett, C.L.: Spatial analysis of vulnerable ecosystems in Europe: spatial and dynamic prediction of radiocaesium fluxes into European foods (SAVE). Final report. Commission of the European Communities, p. 65. Grange-over-Sands: Institute of Terrestrial Ecology (1999)
39. van der Perk, M., Burema, J.K. Gillet, A.J., De Jong, K., van der Meer, M.B.: Wesseling G.G. Restore. Environmental decision support system. A deliverable for the RESTORE project (EC Contract # F24CT950021c) Utrecht university. CD-ROM (1999)
40. Van der Perk, M., Lev, T., Gillett, A., Absalom, J.P., Burrough, P. A., Crout, N.M.J., Garger, E.K., Semiochkina, N., Stephanishin, Y.V., Voigt, G.: Spatial modelling of transfer of long-lived radionuclides from soil to agricultural products in the Chernigov region, Ukraine. Ecol. Model. **128**, 35–50 (2000)
41. van der Perk, M., Burema, J.R., Burrough, P.A., Gillett, A.G., van der Meer, M.B.: A GIS-based environmental decision support system to assess the transfer of long-lived radiocaesium through food chains in areas contaminated by the Chernobyl accident. Int. J. Geogr. Inf. Sci. **15**(1), 43–64 (2001)
42. Salt, C.A., Culligan Dunsmore M.: Development of a spatial decision support system for post-emergency management of radioactively contaminated land. J. Environ. Manage. **58**(3), 169–178 (2000)
43. Ehrhard, J., Brown, J., French, S., Kelly, G.N., Mikkelsen, T., Müller, H.: RODOS: decision-making support for off-site emergency management after nuclear accidents. Kerntechnik **62**(2–3), 122–128 (1997)
44. Absalom, J.P., Young, S.D., Crout, N.M.J., Sanchez, A., Wright, S.M., Smolders, E., Nisbet, A.F., Gillett, A.G.: Predicting the transfer of radiocaesium from organic soils to plants using soil characteristics. J. Environ. Radioact. **52**(1), 31–43 (2001)
45. Mamikhin, S.V.: Biological availability of radionuclides of soils and reproduction of its dynamics in simulation models of terrestrial ecosystems. Bulletin of Moscow University. Series 17: Soil Science, vol. 2, pp. 16–21. Moscow University Publisher (2004)
46. Zhuchkova, V.K., Volkova, N.I.: Landscape Map of the Bryansk Region. Moscow State University, Moscow (1992)
47. Yatsalo, B., Mirzeabassov, O., Okhrimenko, I., Pichugina, I., Kulagin, B.: PRANA—decision support system for assessment of countermeasure strategy in the long term period of liquidation of the consequences of a nuclear accident (Agrosphere). Radiat. Prot. Dosim. **73**(1–4), 291–294 (1997)
48. Yatsalo, B., Mirzeabassov, O., Okhrimenko, I., Pichugina, I., Lisyansky, B.: PRANA: geoinformation decision support system for protection and rehabilitation of agrosphere after nuclear accident. J. Hazard. Mater. **61**(1–3), 381–384 (1998)
49. Linnik, V., Kuvylin, A., Korobova, E., Teplyakov, A., Sokolov, R.: In: van der Perk, M. (ed.) Spatial and Temporal Radioecological Survey Systems, pp. 103–126. Final report. EC Contract No. IC15-CT96-0215. Utrecht University. Utrecht. The Netherlands (1999)
50. Linnik, V., Korobova, E., Kuvylin A., van der Perk, M., Burrough, P.: GIS modelling for training in decision-making on safe production in contaminated areas (Novozybkov case study). In: Williams, E. (ed.) 5th Europrean Conference on Higher Education. Conference Proceedings, p. 202. University of Plymouth. United Kingdom (2000)
51. Linnik, V., Korobova, E., Kuvylin, A., Van der Perk, M., Burrough, P.: Regional Geoinformation System for the Spatial Assessment of Environmental Transfer of Cs-137 to Cow's Milk in the Novozybkov District, Russia. Abstracts of Fifth International Symposium and Exibition on Environmental Contamination in Central and Eastern Europe, p. 166. Prague (2000)
52. Burrough, P.A.: Principles of Geographical Information Systems for Land Resources Assessments. Oxford University Press, Oxford (1986)
53. Goodchild, M.F., Burrough, P.: A research appreciation. Trans. GIS **13**(3), 247–252 (2009)
54. Global Soil Map 2017. Materials of International Conference, Moscow, Russia, July 4–6, 2017 Conference. Abstracts. Moscow Publishing House, Russia (2017)
55. Fesenko, S.V., Alexakhin, R.M., Spiridonov, S.I., Sanzharova, N. I.: Dynamics of Cs-137 concentration in agricultural products in areas of Russia contaminated as a result of the accident at the Chernobyl nuclear power plant. Radiat. Prot. Dosim. **60**(2), 155–166 (1995)
56. Fesenko, S.V., Spiridonov, S.I., Sanzharova, N.I., Alexakhin, R. M.: Dynamics of Cs-137 bioavailability in a soil-plant system in areas of the Chernobyl nuclear power plant accident zone with a different physico-chemical composition of radioactive fallout. J. Environ. Radioact. **34**(3), 287–313 (1997)

57. Fesenko, S.V., Spiridonov, S.I., Sanzharova, N.I., Aleksakhin, R. M.: Modeling of Cs-137 bioavailability in soils subjected to contamination after Chernobyl accident. Radiat. Biol. Radioecol. **36**(4), 479–487 (1996) (in Russian)
58. Fesenko, S.V., Spiridonov, S.I., Sanzharova, N.I., Aleksakhin, R. M.: Evaluation of periods of Cs-137 content semi-reduction in the root-inhabited layer of soils of meadow ecosystems. Radiat. Biol. Radioecol. **37**(2), 267–280 (1997) (in Russian)
59. Fesenko, S.V., Chernyaeva, N.I., Sanzharova, N.I., Aleksakhin, R. M.: Probability approach towards prediction of radioactive contamination of agricultural production. At. Energy. **74**(6), 507–513 (1993) (in Russian)
60. Yatsalo, B., Mirzeabasov, O., Ohrimenko, I., Pichugina, I.: Use of probabilistic methods in radiological studies. At. Energy. **77–1**, pp. 72–78, (1994) (in Russian)
61. Khomutinin, Y.V., Kashparov, V.A., Zhebrovskaya, E.I.: Optimization of sampling and measurements at radioecological monitoring. Kiev: VlPOL. 160 (2001) (in Russian)
62. Linnik, V.G.: Landscape differentiation of technogenic radionuclides: geoinformation systems and models. In: Linnik, V.G. (ed.) Extended Abstract of Doctoral Dissertation in Geography, p. 40. Moscow State University, Moscow (in Russian) (2008)
63. Linnik, V.G., Volosov, A.G., Potapov, V.N., Saveliev, A.A., Sokolov, A.V., Sokolov, P.V., Surkov, V.V.: Landscape principles of rehabilitation of radiation contaminated territories. Creation of Decision Support System for Rehabilitation Measures. In: Abstracts. International Seminar "Problems of Cleanup and Rehabilitation of Areas Contaminated by Radioactive Materials". Moscow., June 04–06, 2007, pp. 72–77. Geocenter Group Ltd, M (in Russian) (2007)
64. Iskra, A.A., Kvasnikova, E.V., Linnik, V.G., Popov, V.K., Savkin, M.N.: Radioecological meta-database on the Yenisei river Catchment and Valley. Conference ECORAD 2004—the scientific basis for environment protection against radioactivity. Abstracts. Aix-en-Provence (France); 6–10 Sep 2004, p. 259 (2004)
65. Linnik, V.G., Volosov, A.G., Potapov, V.N., Sokolov, A.V., Surkov, V.V., Andryushina, S.B.: Development of radioecological Cadastre for radiation assessment contamination and reconstruction of dose loads in the zone of KMCC impact. In: Radioactivity and Radioactive Elements in Human Habitat: Materials of the 2nd International Conference, pp. 322–325. Tomsk, Tomsk, Tandem-Art. (in Russian) (2004)
66. Linnik, V.G., Volosov, A.G., Sokolov, A.V., Sokolov, P.V., Surkov, V.V.: Experience in development of geoinformation radioecological Cadastre databases for the Yenissei River Valley. In: Book of Abstracts of the International Conference "Modeling of Radionuclide Transfer in the Environment and the Development of Metadata Systems on Radiation-Hazardous Objects of the FSU Nuclear Complex" (RADLEG-RADINFO-2005), p. 31. Moscow (in Russian) (2005)
67. Linnik, V.G., Volosov, A.G., Lutkovsky, V.V., Potapov, V.N., Sokolov, A.V., Sokolov, P.V., Surkov, V.V.: The development of geo-information systems on radioecological conditions in the Yenisei river valley as a basis for the remediation decision-making system. In: Book of Abstracts of the International Conference "Modeling of Radionuclide Transfer in the Environment and the Development of Metadata Systems on Radiation-Hazardous Objects of the FSU Nuclear Complex" (RADLEG-RADINFO-2005), p. 34. Moscow (in Russian) (2005)
68. Lutkovsky, V.V., Linnik, V.G., Voytsekhovich, O.V.: Assessment of floodplain processes Cs-137 migration by water flow in the input river using the hydrodynamic BOSS SMS two-dimensional modeling. In: Proceedings of the UkrNIGMI. vol. 249, pp. 211–220. Kiev (in Russian) (2001)
69. Ivanov, O.P., Potapov, V.N., Shcherbak, S.B.: Calculation of gamma-radiation exposure dose rate over a flat surface with non-uniformly distributed radionuclide activity. At. Energ. **2–79**, 130–134 (1995) (in Russian)
70. Chesnokov, A.V., Govorun, A.P., Fedin, V.N., Ivanov, O.P., Liksonov, V.L., Potapov, V.N., Shcherbak, S.B., Smirnov, S.V., Urutskoev, L.I.: Method and device to measure Cs-137 soil contamination in-situ. Nucl. Instr. and Meth. A. **420**(1–2), 336–344 (1999)
71. Chesnokov, A.V., Fedin, V.I., Govorun, A.P., Ivanov, O.P., Liksonov, V.I., Potapov, V.N., Smirnov, S.V., Shcherbak, S.B., Urutskoev, L.I.: Collimated detector technique for measuring a Cs-137 deposit in soil under a clean protected layer. Appl. Radiat. Isot. **48**(9), 1265–1272 (1997)
72. Potapov, V.N.: Development of radiometric systems and methods of field and remote measurements of radioactive contamination. In: Author's Abstract of Doctoral Dissertation, p. 47. M. (2010) (in Russian)
73. Linnik, V.G., Brown, J.E., Dowdall, M., Potapov, V.N., Surkov, V.V., Korobova, E.M., Volosov, A.G., Vakulovsky, S.M., Tertyshnik, E.G.: Radioactive contamination of the Balchug (Upper Enisey) floodplain, Russia in relation to sedimentation processes and geomorphology. Sci. Total Environ. **339**(1–3), 233–251 (1 March 2005)
74. Potapov, V.N., Sokolov, A.V., Linnik, V.G., Surkov, V.V.: Estimation of radiation contamination and reconstruction of dose loads in the zone of impact of KMCC using GIS-technologies. In: Book of Abstracts of the International Conference "Modeling of Radionuclide Transfer in the Environment and the Development of Metadata Systems on Radiation-Hazardous Objects of the FSU Nuclear Complex" (RADLEG-RADINFO-2005), p. 16. Moscow (in Russian) (2005)
75. Sukhorukov, F.V., Degermendzhy, A.G., Belolipetsky, V., Bolsunovsky, A.Y., Kovalev, S.I., Kosolapova, L.G. et al.: Distribution and Migration of Radionuclides in the Yenisei Plain, p. 286. Publication, House of SB RAS, Department "Geo", Novosibirsk (in Russian) (2004)
76. Volosov, A.G., Linnik, V.G., Sokolov, A.V.: Dating of recent alluvial deposits of the Yenisei River floodplain by the ratio of europium radioisotopes. Isotopic dating of ore formation, magmatism, sedimentation, and metamorphism. In: Proceedings of the III Russian Conference on Isotope Geochronology. IGEM RAS, vol. 1, pp. 160–164. GEOS, Moscow (in Russian) (2006)
77. Vakulovsky, S.M., Tertyshnik, E.G., Borodina, T.S.: Migration of Radioactive Contaminants Discharged into the Yenisei River by the Krasnoyarsk Mining and Chemical Complex. In: Proceedings of the Ecorad 2001 Conference, vol. 2, pp. 673–676. Aix-en-Provence, France, (2001).
78. Korobova, E., Linnik, V., Gordeev, S., Ter-Saakov, A., Yermakov, A., Khilov, A., Kuvylin, A., Brodsky, S., Glebov, M.: Radioecological Monitoring in Bryansk Region Contaminated after the Chernobyl Accident. Um-weltradioaktivitat Radiologie Strahlenwirkungen. Band I. 25. Jahrestagung Binz auf Rugen, 25–30, pp. 248–251 (Sept 1993)
79. Linnik, V., Korobova, E., Vakulovsky, S.: Organization of radio-ecological monitoring of the areas of the Russian Federation contaminated due to the accident at the Chernobyl NPP (on example of the Bryansk region). EGU General Assembly, held 7–12 April, 2013 in Vienna, Austria, vol. 15, id. EGU2013-1742
80. Kashparov, V., Levchuk, S., Zhurba, M., Protsak, V., Khomutinin, Y., et al.: Spatial datasets of radionuclide contamination in the Ukrainian Chernobyl Exclusion Zone. Earth Syst. Sci. Data **10**, 339–353 (2018)

81. Stukin, E.D.: Characteristics of primary and secondary caesium-radionuclide contamination of the countryside following the Chernobyl NPP accident. In: Proceedings of Seminar on Comparative Assessment of the Environmental Impact of Radionuclides Released during Three Major Nuclear Accidents: 1991 Kyshtym, Windscale, Chernobyl Luxembourg, vol. I, pp. 255–300 (1–5 Oct 1990)
82. Kashparov, V., Levchuk, S., Zhurba, M., Protsak, V., Beresford, N., Chaplow, J.S.: Spatial radionuclide deposition data from the 60 km radial area around the Chernobyl nuclear power plant: results from a sampling survey in 1987. SEarth Syst. Sci. Data **12**, 1861–1875 (2020)
83. Gaidar, A.V., Tabachny, L.Y. Foursat, A.D. Chornomorets, N.F.: Effect of landscape on the formation of the contamination structure on adjacent to ChNPP territory. In: Buleten ekologichnogo stanu zoni vidchudgennya ta zoni bezumovnogo (obov'yaskovogo) vidselenya, N15, pp. 58–61 (in Ukr.) (2000)
84. Gaydar, A., Nasvit, O.: Analysis of radioactive contamination in the near zone of Chernobyl NPP. In: Recent Research Activities About the Chernobyl NPP Accident in Belarus, Ukraine and Russia, vol. 79, pp. 59–73. Research Reactor Institute, Kyoto University (2002)
85. Linnik, V.G., Saveliev, A.A., Govorun, A.P., Ivanitsky, O.M., Sokolov, A.V.: Spatial variability and topographic factors of Cs-137 soil contamination at a field scale. Int. J. Ecol. Dev. **8**(7), 8–25 (2007)
86. Linnik, V.G., Saveliev, A.A., Sokolov, A.V.: Transformation of the chernobyl Cs-137 contamination patterns at the microlandscape level as an indicator of stochastic landscape organization. In: Khoroshev, A., Dyakonov, K. (eds.) Landscape Patterns in a Range of Spatio-Temporal Scales. Landscape Series, vol. 26, pp. 77–89. Springer (2020). https://doi.org/10.1007/978-3-030-31185-8_5
87. Linnik, V.G., Saveliev, A.A., Govorun, A.P., Sokolov, A.V.: Spatial analysis and modeling of Cs-137 distribution at the microlandscape level (the Bryansk region). In: Dyakonov, K.N., Kasimov, N.S., Khoroshev, A.V., Kushlin, A.V. (ed.) Landscape Analysis for Sustainable Development. Theory and Applications of Landscape Science in Russia, pp. 190–199. Moscow (2007)
88. Hinton, T.G., Garnier-Laplace, J., Vandenhove, H.: An invitation to contribute to a strategic research agenda in radioecology. J. Environ. Radioact. **115**, 73–82 (2013)
89. Strategic Research Agenda for Radioecology 3rd version [DRAFT] 30/11/2019. p. 63
90. Gilbin, R., Arnold, T., Beresford, N.A., Berthomieu, C., Brown, J. E., de With, G., Vives, I., Batlle, J.: An updated strategic research agenda for the integration of radioecology in the European radiation protection research. J. Environ. Radioact. **237**, 106697 (2021) https://doi.org/10.1016/j.jenvrad.2021.106
91. Linnik, V.G., Sokolov, A.V., Mironenko, I.V.: Cs-137 patterns and their transformation in the landscapes of the Bryansk region. Nawaday trends in the development of biogeochemistry. In: Proceedings of the Biogeochemical Laboratory, vol. 25, pp. 423–434. GEOKHI RAS, Moscow (In Russian) (2016)
92. Linnik, V.G., Mironenko, I.V., Volkova, N.I., Sokolov, A.V.: Landscape-biogeochemical factors of transformation of the Cs-137 contamination field in the Bryansk region. Geochem. Int. **55**(10), 887–901 (2017)
93. Linnik, V.G., Sokolov, A.V., Saveliev, A.A., Mironenko, I.V., Volkova, N.I.: Landscape-scale modelling to predict soil lateral migration using Cs-137 on the Bryansk Opolje region (Russia). In: Book: GlobalSoilMap-Digital Soil Mapping from Country to Globe, pp. 159–164. CRC Press (2017). ISBN 9780815375487
94. Linnik, V., Sokolov, A., Ivanitsky, O., Saveliev, A.: Modelling the Extent of Cs-137 Soil Contamination Patterns at the Kostica River Basin (Bryansk Region, Russia)—EGU General Assembly Conference Abstracts, (May 2020)

Speciation of Actinides in the Environment

A. P. Novikov, T. A. Goryachenkova, A. V. Travkina, and I. Yu. Myasnikov

1 Introduction

Currently available significant amount of data on the content and distribution in different ecosystems of radionuclides that entered the biosphere with global radioactive fallout and emission products from the Chernobyl accident, as well as limited data for the impact zones of other nuclear fuel cycle (NFC) enterprises showed that radionuclides are included into the biogeochemical cycles of migration. The latter processes are accompanied by redistribution of radionuclides in terrestrial and aquatic ecosystems with formation of zones of their removal and secondary accumulation in geochemical barriers [1, 2]. Direction, intensity and mechanisms of radionuclide migration are mainly determined by the species of their ingress and residence in ecosystems as well as by those natural conditions in which they get: landscape-geochemical for terrestrial ecosystems (types of soils and vegetation, geomorphological and hydrometeorological conditions, etc.) and physical and chemical properties of water, bottom sediments and suspensions, and hydrochemical regime and hydrological conditions in aquatic ecosystems.

As a new component of the biosphere the radionuclides requires study of their geochemistry. Artificial radionuclides in contradistinction to stable isotopes and element-analogues have another origin, extremely low concentration and residence time in ecosystems. Also, there are no stable isotopes of transuranic elements in environment at all. Meanwhile, it was previously established that radionuclides are characterized by greater migration ability than their stable isotopes and element-analogues [3, 4].

Therefore, before discussing our data on the speciation of radionuclide presence and dynamics of their migration in specific areas of NFC enterprises, it is necessary to analyze the available data on the speciation of radionuclide presence in emissions from various sources of radioactive contamination. This is explained by the fact that the same study area can be contaminated by different sources.

2 Methods for Determining the Content and Speciation of Actinides in Natural Objects

The main difficulties in radiochemical analysis of environmental objects are that the mass concentration of man-made actinides in them is extremely low, and most of these most dangerous alpha emitters have no isotopic carriers (except for uranium). As a consequence, radiochemical techniques for determining actinides involve very laborious operations of separation from the large mass matrix of the analyzed sample. In addition, due to close emission energies of radionuclides and also significant activity of natural isotopes there are requirements for thorough separation of nuclides for existing detection methods.

Data of total amount of radionuclides not enough for modeling their behavior in the environment. To predict of their mobility and bioavailability information about radionuclides physicochemical speciation is required. The concept of physicochemical speciation includes:

1. particle size dependence of binding;
2. distribution by geochemical fractions (exchangeable, oxidizable, reducing, sulfide, etc.);
3. presence in cationic, anionic or neutral forms;
4. chemical form of the radionuclide (which compound it is a part of, nearest ligand environment, oxidation degree, etc.).

The methods for determining the physicochemical species of radionuclides can be divided into indirect and direct

A. P. Novikov · T. A. Goryachenkova · A. V. Travkina · I. Yu. Myasnikov (✉)
Vernadsky Institute of Geochemistry and Analytical Chemistry, Russian Academy of Sciences, 19 Kosygin St., Moscow, 119991, Russia
e-mail: myasnikov@geokhi.ru

V. P. Kolotov and N. S. Bezaeva (eds.), *Advances in Geochemistry, Analytical Chemistry, and Planetary Sciences*,
https://doi.org/10.1007/978-3-031-09883-3_42

(spectral). Indirect methods include preliminary isolation (extraction, sorption, filtration, etc.) of some species or fractions with further determination of radionuclides in them by available methods. Due to their highly sensitive indirect methods are widely used to determine the physicochemical species of radionuclides in the environment. These methods include preliminary isolation of certain species or fractions. It should be notice that mentioned processes could affect to the equilibrium distribution of the species therefore obtained results have an estimated nature.

Direct methods provide information on the speciation of radionuclides without chemical action on the sample. They have substantially greater informativity than indirect methods, but their overall sensitivity is much lower.

To determine the content in different objects of the natural environment and solutions after chemical fractionation, the scheme of radiochemical and elemental analysis of environmental objects developed in Vernadsky Institute RAS [5] was applied in the present work. This technique makes it possible to determine the content of all radionuclides in one sample, which reduces by several times the time required for sample preparation and transfer of radionuclides into a solution.

Separation and determination of neptunium is even more difficult than that of plutonium and americium due to its lower specific activity. The developed express method is based on the extraction of this radionuclide with potassium phosphorovolphramate and subsequent sorption on a porous Teflon membrane impregnated with 0.5 M solution of trioctylammonium nitrate (TOMAN) in toluene [6]. In this work a membrane with neptunium and CaF_2 extracted on it were calcined at 900ºC to activate crystal phosphor by corresponding actinide element and its luminescence signal was measured on developed in Vernadsky Institute RAS analyzer LLF-5 [7]. CaF_2, $PbMoO_4$, and $NaBi(WO_3)_2$ were used as crystallophosphors for the determination of uranium-neptunium, plutonium-neptunium, and neptunium-americium pairs, respectively.

Other physico-chemical methods (neutron-activation, atomic absorption, mass spectrometry with inductively coupled plasma, gas chromatography and elemental-organic analysis) were also applied to determine the content of chemical elements.

Methods of fractionation of physico-chemical species of radionuclides (partitioning).

To determine the species of occurrence by fractionation methods, schemes of selective sequential leaching with selective reagents and fractionation by organic matter groups were applied [8, 9]. The first method makes it possible to estimate geochemical speciation of radionuclide mobility (water-soluble, exchangeable, mobile, acid-soluble and hardly soluble). The second method makes it possible to determine the radionuclide content in different groups of organic matter of soils, bottom sediments, suspended and colloidal matter of natural waters.

Sometimes also separately define the amorphous species. The amorphous species of chemical elements and radionuclides is represented mainly by compounds, tearing in the form of films a mineral particle. The uppermost film is consist mostly of organic acids and their salts with Fe, Al, Ca and other elements. The next film is from Fe and Al hydroxides. These compounds could be soluble and may affect included radionuclides and other elements behavior. According to our earlier data, soils contain up to 90% of plutonium. For separation of amorphous species of radionuclides the solution (28.4 g $(NH4)_2C_2O_4$ and 12,6 g $H_2C_2O_4$ in 1 L) is applied.

Most often to understand the processes taking place in ecosystems and the role of separate groups of compounds in radionuclides migration it is necessary to know their distribution between organic and inorganic compounds. Extraction of organic components is carried out by repeated treatment with 0.1 M NaOH and 0.5 M $Na_2C_2O_4$ solutions. Residue of reagent washed out by distilled water. Then inorganic components repeatedly separated by a 28.4 g $(NH_4)_2C_2O_4$ and 12.6 g $H_2C_2O_4$ in 1 L until negative reaction by potassium rhodanide for iron, also ammonium rhodanide can be used.

Radionuclide migration affected by organic matter. Thus, humic acids strongly connected with solid phase, on the contrary fulvic acids and nonspecific organic matter (polysaccharides, amino acids, low molecular weight acids, etc.) are more mobile. The scheme of studying possible connections of radionuclides with separate fractions of fulvic and humic acids is given in works [10, 11].

To fractionate actinides by oxidation species, extraction [12] or complex ultrafiltration [13] methods are usually used. At the same time, the most accurate results are obtained by those methods, the application of which minimizes the influence of the used reagents on the redox reactions of actinides. In our work, we used an original method - luminescence on actinide-activated crystal phosphors (see above). Since actinides in different oxidation states form different compounds with crystallophosphors, which give a luminescence signal in different spectral regions, it is possible to analyze the solution on the speciation of actinide oxidation [14]. However, in some cases it is required to perform calcination of crystallophosphors in an inert gas atmosphere after complete removal of oxygen impurities.

Methods of determination of physical-chemical speciation of radionuclides.

The following methods are currently used to investigate the speciation of radionuclides: alpha-track analysis [11, 15, 16], X-ray electron spectroscopy [17, 18], laser spectroscopy

(laser fluorescence spectroscopy with time resolution, emission spectroscopy with laser-induced breakdown [19, 20]); mass spectrometry (secondary ion mass spectrometry [21, 22]); methods based on synchrotron radiation (XANES and EXAFS) [23–26]; scanning electron microscopy [15, 16, 27] including energy electron loss spectrometry (EELS) [28].

However, all specified methods (except alpha-tracking analysis) have insufficient detection limits for study of natural objects. Therefore, they are applied in model experiments.

3 Sources of Man-Made Radionuclide Contamination of Russian Territory

Sources of local radioactive contamination of the environment include nuclear fuel cycle enterprises, such as the Siberian Chemical Combine in the Tomsk Region (SCK), the Mining-Chemical Combine in the Krasnoyarsk Region, and "Mayak" in the Chelyabinsk Region. However, majority of leaked artificial radionuclides in the environment in Russian Federation origins from the "Mayak" [29]. Chemical explosion of waste storage facility at radiochemical plant led to accident of September 29, 1957 which was known as East-Urals Radioactive Trace (EURT) or Kyshtym disaster. [30]. The tank contained 70–80 tons of highly radioactive waste, mostly in the species of nitrate-acetate compounds. The 250–300 m^3 liquid radioactive substances were raised to a height of 1–2 km. The products of the explosion lifted into the air were fragments of structures, soil, dust, coarse aerosols and radioactive substances. A total of 20 MCi of radionuclides was released, of which about 90% were deposited on site and 10% dispersed into the environment in the form of a radioactive cloud. The fallout from moving northeastward cloud covered Chelyabinsk, Sverdlovsk and Tyumen with radionuclides spreading. The trace (EURT) was formed in 11 h and resulted distance was 350 km. Plutonium contamination at a distance of about 4 km from the epicentre and 0.5–1 km from the axis of the trace was studied by The team of Vernadsky Institute RAS [31]. According to obtain data in 1980–1982 activity of forest and grassland biocenoses was 10,566–12,794 10,566–12,794 Bq/m^2.

The plutonium migrates along the soil profile similarly to other artificial radionuclides reaching the ground surface. As the results of radio-ecological monitoring showed, the main part of plutonium continues to remain in 0–10 cm layer in turf, litter and upper part of humus horizon if the first two are low-powerful. At the same time its quantity is maximal in leached horizon under motley grass vegetation, minimal - in hydromorphic meadow-chernozem soil. Radionuclide intake, including transuranic elements, in mobile species contributed to the scientific research carried out in the territory of EURT. Plutonium distribution by soil profiles and the influence to this proccess of soil type and genetic structure discusses in Chap. 4.

At SCC for disposal of liquid radioactive waste (LRW) their burial in deeply buried layers of sedimentary rocks is applied [32]. The review [11] provides data on the chemical and radionuclide composition of waters sampled from observation wells. It is established that lateral and vertical migration of radionuclides and, in particular, the most dangerous alpha-emitting, long-lived actinides in the reservoir reservoir is not more than a few tens of meters from the injection well [33]. Causes of geochemical antimigration barrier may be sorption on the host rocks, colloid formation, microbiological transformation and bioaccumulation. The influence of the latter two factors on the physicochemical speciation of actinides was the aim of the present work (see Chap. 5).

Due to nuclear weapons testing, nuclear fuel cycle (NFC) facilities, including radioactive waste disposal, and the accessibility of these waters to European sea currents Arctic radioactive contamination studies are extremely interests.

Liquid (with a total activity of 0.75 PBq) and solid (with a total activity of 83.6 PBq) radioactive waste disposed of in the Kara and Barents Seas between the late 1950s and 1992 are potentially dangerous. Seven nuclear reactors with spent nuclear fuel, including partially defueled in the special disposal cask from nuclear icebreaker Lenin was dumped in the Kara Sea. Total number of burried nuclears reactors in this region reaches seventeen.

To ensure the safety of geological isolation of radioactive materials, knowledge of the basic regularities of radionuclide migration in the natural environment is necessary. Without this information, a correct assessment of the radiation situation, its forecasting and development of measures for rehabilitation of already contaminated territories are impossible.

The aim of the work is to study the distribution of radionuclides over the components of marine areas (bottom sediments, suspended matter, seawater, benthos) and to determine the radionuclide distribution in these components (see Chap. 6).

4 Species of Artificial Actinides Presence in Soils by the Example of East-Ural Radioactive Trace

Studying of intensity of migration and speciation of radionuclides of "global" deposition in surface landscapes is rather difficult task because of low weight content of these radionuclides being in the state of significant dispersion. Therefore, let us consider the results of our radio-ecological investigations of EURT soils.

Table 1 Content of ^{237Np} in soil and vegetation samples taken in the EURT area

No sample	Sample name	^{237}Np, Bq/kg air-dry sample
B-1	Forest litter from de-The Kyzyl-Tash lake	4.3
B-2	Bottom sediments. Lake Kyzyl-Tash	Not detected
B-3	The coastal area. Lake Kyzyl-Tash	Not detected
B-4	Bedding, EURT axis,depth 5–7 cm, 10 km from the epicenter	5.6
B-5	Soil, EURT axis, depth 5–7 cm, 10 km from the epicenter	5.2
B-6-1	Reed (leaves), Kyzyl-Tash lake	14.6
B-6-2	Reed (roots), Kyzyl-Tash lake	7.5
B-7-1	Cattail (leaves), Kyzyl-Tash lake	32
B-7-2	Cattail (roots), Kyzyl-Tash lake	13.2

Soil sections in the EURT territory were laid in forest biocenoses under birch and birch-coniferous forests to the depth of 100–126 cm. The humus thickness of the humus horizon of sod-podzol soils does not exceed 10 cm; below it there is an eluvial horizon A2, about 8 cm thick, which gradually transitions to the illuvial horizon B. The black earth has a shortened humus horizon A as compared with typical black earths of the middle belt of Russia (to 35–40 cm). Transitional humus-illuvial horizon AB appears from 40–45 cm. From the depth of 83 cm and below, the carbonate illuvial horizon B begins, where weak boiling was observed when treating the soil with concentrated HCl. Sod podzols soils are formed on yellow–brown clays, chernozems - on carbonate loams.

Fractionation of organic matter of EURT soils has shown that plutonium is predominantly related to humic substances and organomineral part (up to 80%), which ensures its low migration mobility and accumulation in the upper soil horizons. Americium is more connected with fractions of mobile fulvic and low-molecular acids (up to 80% in sod podzols and 40% in leached chernozem). The content of neptunium in all horizons of the above mentioned soils turned out to be below the detection limit. Therefore, further experiments with neptunium were performed with ^{237}Np.

In the present work, the distribution of neptunium, plutonium, and americium between specific and nonspecific components of different groups of soil organic matter was studied. It is known [8] that the composition of fulvic acid solution obtained directly after separation of humic acids is heterogeneous and represents a mixture of nonspecific low molecular weight compounds (amino acids, carboxylic and oxycarboxylic acids, polysaccharides, etc.) and specific compounds - fulvic acids proper. Separation of nonspecific compounds and fulvic acids proper was performed according to Forsythe method [34]. The content of low molecular weight nonspecific compounds in soils increases in the series $Np > Am > C_{org} > Pu$ for both chernozem and soddy-podzolic soils. The higher content of Np and Am as compared to Pu in the composition of low molecular weight nonspecific compounds causes their greater migration mobility as compared to Pu in the environment.

The obtained data allow to explain high solubility of neptunium in soil solution (up to 14% in aqueous extract of content in soil). Thus, the water-soluble species contains less than 2% of americium and tenths of a percent of plutonium. The association of neptunium with low-molecular-weight organic matter not only explains its high mobility in soils, but also the relatively high accumulation of this artificial radionuclide by vegetation (Table 1).

5 Speciation of Actinides Presence in Industrial Water Bodies and Groundwater of Radioactive Waste Collector Beds (Influence of Biological Factors)

Contamination of groundwater aquifers with actinides and macrocomponents of radioactive waste when buried in deep geological formations requires the development of multi-parameter models that take into account the consequences of technogenic impact on the geological and geochemical state of the underground system (water, rocks) as well as the recently actively studied biogeochemical processes. Of particular interest are the mechanisms of colloidal and pseudocolloidal transport of actinides in various geochemical conditions [27, 35, 36]. It is worth noting that based on a large number of works, the latter factor may play a key role in plutonium and uranium spreading, both as true colloidal particles and in the form of complex particles

Table 2 Scheme of selective desorption of radionuclides from suspended matter

No	Fraction	Leaching solution	pH, aqueous phase volume
1	Exchange	1M NH_4HCOO	pH = 7.0, V = 100 ml
2	Mobile (carbonates)	1M CH_3COOH	pH = 7.0, V = 100 ml
3	Fe/Mn oxides	0.4M NH_2OH HCl in 25% CH_3COOH	pH = 1.0, V = 100 ml
4	Organic matter	30% H_2O_2 then NH_4HCOO in 20% HNO_3	pH = 2.0, V = 100 ml
5	Remainder	HF + H_2SO_4	pH = 0

within ferrous, clayey minerals, or organic complexes [22, 27, 37–39]. In [11], when studying the rate of vertical and lateral spreading of radionuclides in underground ecosystems, it was noted that actinides can be sorbed and transported under oxidizing conditions on clay, iron and titanium particles, and under reducing conditions as aggregates on uranium dioxide surface [16].

The aim of this work is to investigate pseudocolloidal species of actinides in groundwater of different genesis and to evaluate the role of biogenic factors in pseudocolloid formation and stability.

Groundwater sampling was carried out by SCC personnel from observation wells after pumping water in the volume of one and a half wellbore. Water from the sampling hose is fed through an adapter with a glass fiber filter with pore diameter of 500–600 nm into sealed glass containers pre-filled with nitrogen. At the sampling site the pH, Eh and salt content are determined, the samples are preserved and sent for radiochemical and chemical analysis.

For filtration experiments, water samples in sealed glass vessels purged with nitrogen were sequentially filtered in the laboratory in a nitrogen atmosphere through filters with pore diameters of 5, 50, 100, 200, 400 nm with intermediate sampling for radiochemical studies. In this work, lavsan nuclear filters and standard filtration modules at a constant pressure (N_2) of about 300 kPa were used [13].

To assess the bond strength of actinides with different suspended matter fractions on filters, the selective leaching method was used (see item 2), and the parameter characterizing the bond strength, by analogy with the complexation ultrafiltration method, can be taken as the retention degree calculated by the equation:

$$Kd = (A_s/A_v)a_i,$$

where A_s—initial activity of nuclide per unit area of the filter, A_v—concentration of nuclide in the washing solution after washing, a_i—specific surface of the washed membrane equal to the ratio of the membrane area and the volume of the washing solution S/V.

Leaching experiments were performed on standard filter cells with a 4-inch diameter membrane, onto which a compactly folded initial filter with colloidal or suspended matter was placed.

Table 2. The composition of leaching solutions and treatment mode of suspended matter during selective desorption is given [40].

When studying the suspended matter retained during filtration of natural waters on filters 5–400 nm using electron microscopy it was found that for samples from the upper horizon (wells B-2-32 and B-2-38) the content of colloidal matter on filters decreases with decreasing pore size from 400 to 5 nm. On 100–400 nm filters a lot of ferruginous-clay material in which numerous uranium-bearing particles are found (Fig. 1). Uranium particles are more in sample B-2-38 than in sample B-2-32 that coincides with specific radioactivity of waters of these wells.

Heavy particles of different morphology and composition containing Ce and Zn and particles of Au–Ag–Cu composition were also found in water samples from well B-2-38 (Fig. 2).

In waters of samples from middle deep horizon (A3 and P-21 wells) there was less colloidal material than in waters of upper horizon. Especially it concerns well A3, where separate scales of kaolinite were found on filters. A group of uranium particles and Pt–Rh particle was detected. The composition and morphology of particles from well P-21 were much more diverse. Clay particles, calcium sulfate, iron oxides were found. Uranium particles and aggregates of thorium particles were found (Fig. 3). Thorium particles do not contain uranium. Whereas uranium particles extracted from the upper horizon waters contain 0.2–0.3 atomic per cent of phosphate, the particles from well R-21 contain considerably less phosphate (<0.05 at. %).

In the colloidal matter from wells C-37 and C-50 of the lower depth horizon many particles containing uranium and cerium were found. Uranium content in such particles was 0.2–0.5 at. %. But also many uranium particles without cerium and cerium particles without uranium are observed. Gold-containing particles on calcium carbonate were found. For wells of any horizon no uranium was detected in particles containing noble metals.

Uranium-containing particles are found mainly on large filters. Clay minerals and iron oxyhydroxides are present in sediments. Probably, these are associative colloids consisting of agglomerates of small particles of different composition.

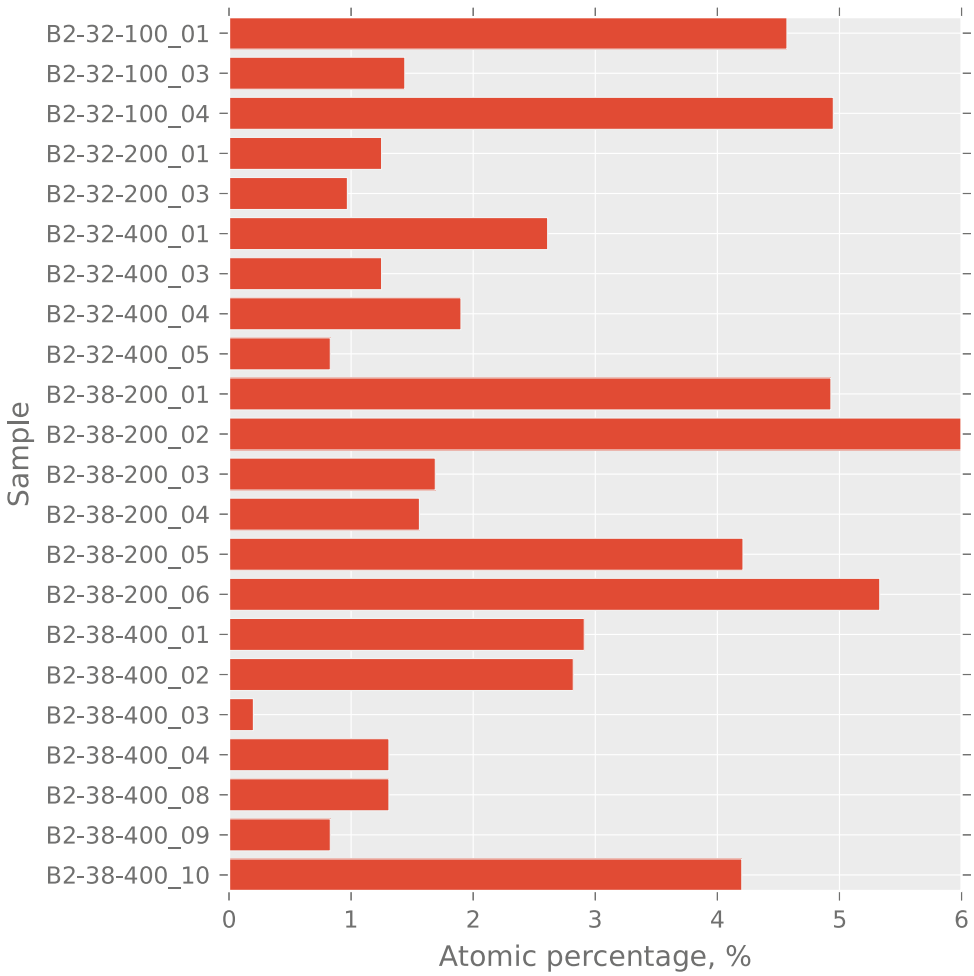

Fig. 1 Uranium content in some heavy particles, atomic %. In the particle name the first four symbols are the well number, the second three digits are the filter pore diameter in nm, the last two digits are the particle number on SEM photo

As the ultrafiltration data for waters from all horizons showed, aluminum and silicon content on the filter decreases with decreasing pore size, and iron content on the contrary increases. The content of alkaline and alkaline-earth elements is higher on the 400 nm filter, and on the rest-less, and does not change with decreasing pore diameter. Mainly calcite and barite particles are present on the filter.

Based on the results of determination of plutonium and uranium in filtrates it was established that in the lower horizon about 35% of plutonium passed through the filter with pore diameter of 5 nm—that is, it is in dissolved species, about 25% is in colloidal species (100–5 nm), and about 40% is present as larger aggregates (>100 nm). In the upper horizon, the fraction of dissolved plutonium was about 25%, about 25% was also in colloidal phase and about 50% was in large aggregates, with the fraction of the largest fraction over 400 nm being 2 times larger than for samples from the deep horizon.

For uranium in the lower horizon, about 60% was the dissolved fraction 30 was the colloidal fraction and only less than 10 were large aggregates. In the upper horizon the fraction of dissolved fraction was about 80%, colloidal about 20, the fraction of large aggregates was minimal.

The increase in the dissolved actinide fraction in the upper horizon can be explained by more oxidative conditions in the presence of a high nitrate background. At the same time, in all cases the content of colloidal fraction of 100–5 nm particles around 20–30% was observed.

Dissolved species include associative colloids. The suspended and colloidal matter extracted from water samples of lower horizons on filters with pore diameters of 200 and 50 nm were analyzed according to the scheme of selective desorption (Table 2) The results of sequential leaching of material are presented in Tables 3 and 4 as the degree of $E = 1/(1 + Kd)$ actinides recovery by selective solutions.

Based on the leaching data, it can be said that, in general, actinides are quite strongly bound to the colloidal material: for large colloids in the residue, 30 to 40%, in small ones, 50 to 60%. The residue is the fraction in which the radionuclides are very strongly bound to the colloidal material. Surprisingly, for all actinides the content in this fraction is approximately the same. This indirectly suggests that they

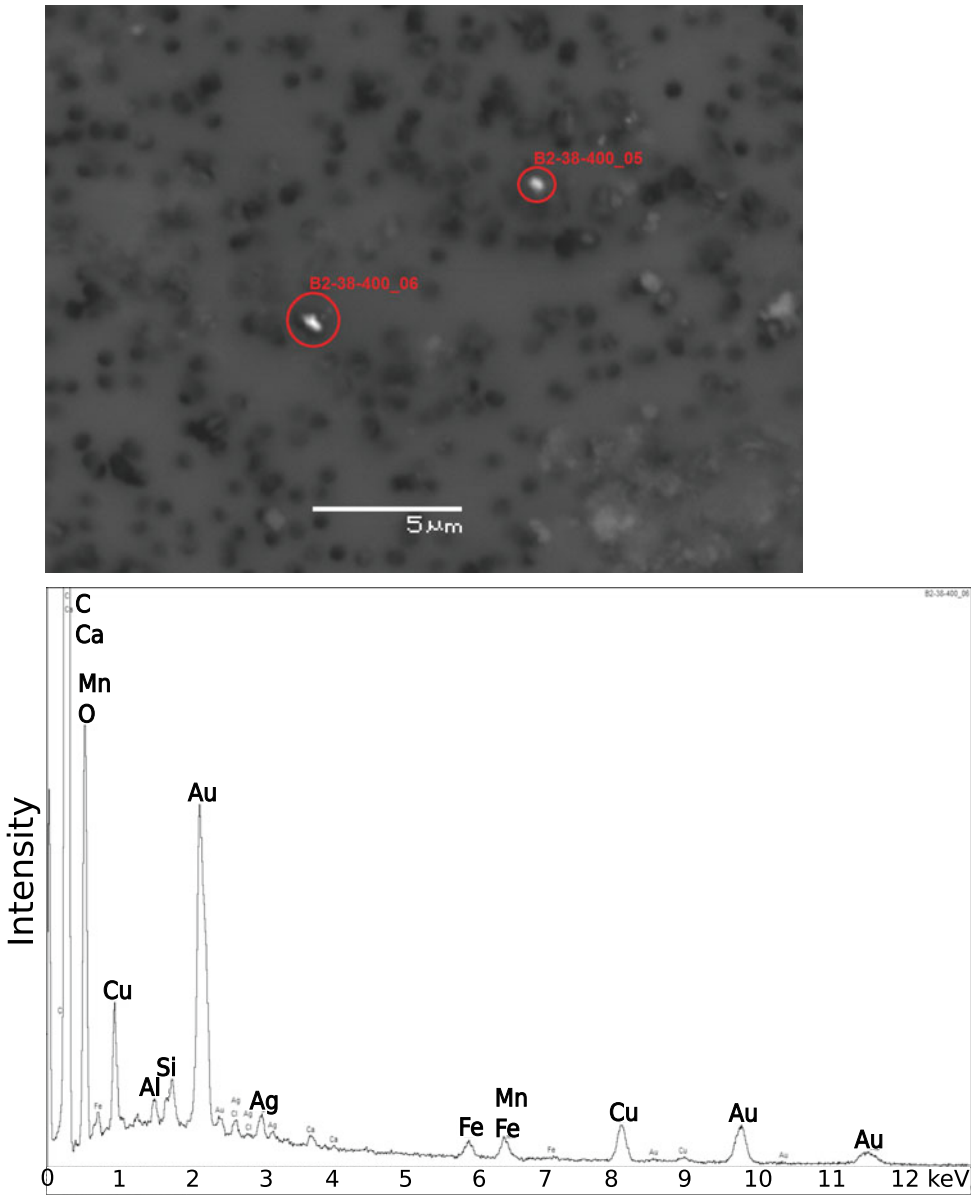

Fig. 2 SEM photo and SEM spectrum of the particle B-2-38-400-06

have close oxidation states. If we compare with other similar data, for example, obtained in the oxidative conditions of groundwater of the Karachayevskoye pollution halo ("Mayak"), the strength of binding of actinides to the colloidal matter in them is much lower [11].

In the exchange and mobile fractions, a sufficiently large amount of actinides was detected, while their total content was lower than in the residue. This testifies to their relative mobility in these systems and the risk of possible transfer by the colloidal transport mechanism [27]. The relative content of actinides in mobile fractions decreases with the decrease in the size of colloidal particles and the increase in the depth of groundwater horizon.

The most significant part of actinides (excluding residue fraction) is associated with iron, manganese and other oxides. Thus for groundwater clay and iron minerals play significant role in formation of pseudocolloids with actinides participation.

As one would expect, organic matter plays a markedly lower role in actinide accumulation by groundwater colloidal matter compared to soils, bottom sediments, and surface water suspensions. For soils and bottom sediments, the maximum amount of actinides is found in this fraction - 60–70% [11]. Interestingly, the distribution of uranium, neptunium, and plutonium across the fractions is almost identical. For soils and bottom sediments, the association with colloidal matter decreases in the series: Pu $\gg$ U $\gg$ Np [11].

Biofilms are bacterial populations attached to or between surfaces, forming a common extracellular matrix and most

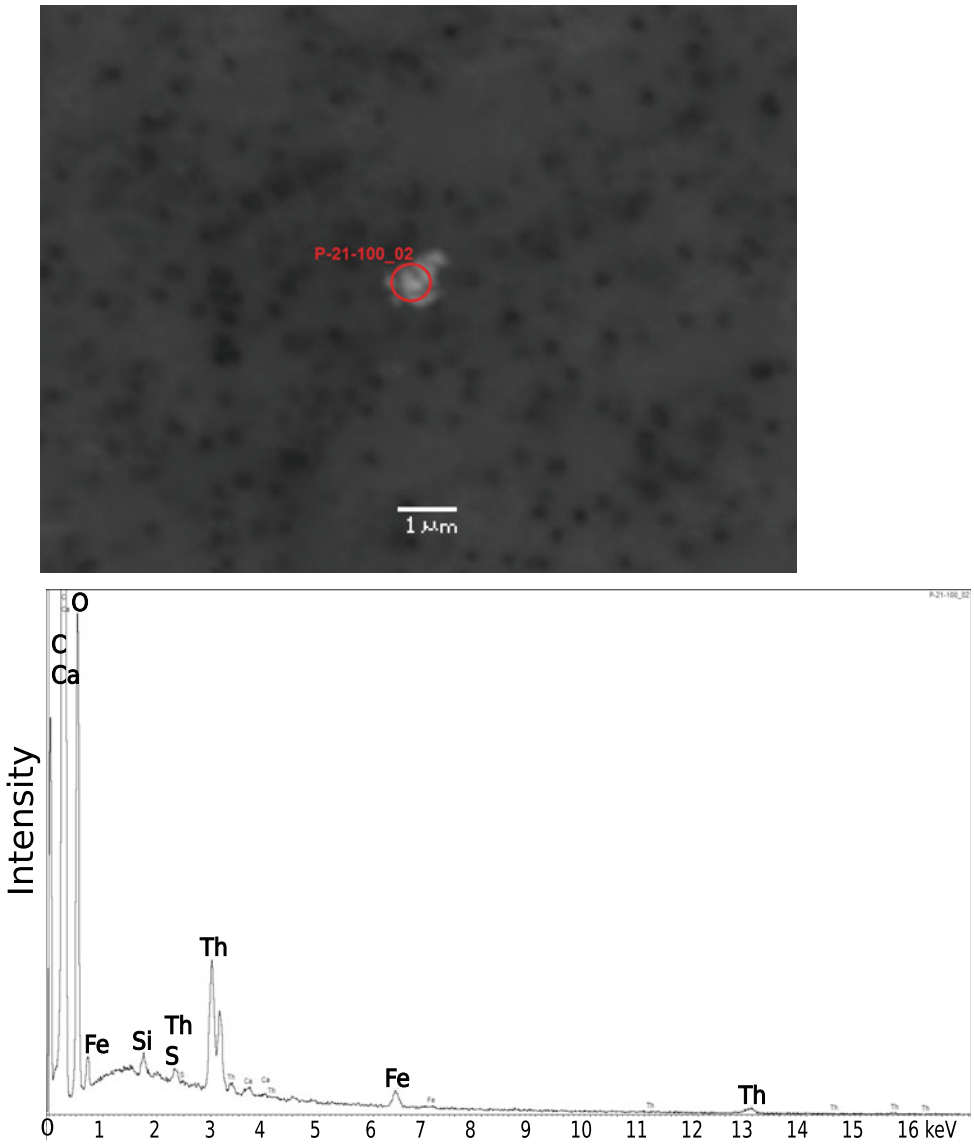

Fig. 3 SEM photo and SEM spectrum of the particle P-21-100-02

Table 3 Suspended matter fractionation as % of total radionuclide activity, 200 nm filter

Sample from the well	1			4			6		
Fraction	U	Pu	Np	U	Pu	Np	U	Pu	Np
Exchange	3.1	2.9	4.2	4.5	3.2	5.1	6.2	7.0	7.5
Movable	12.3	14.5	14.8	16.7	15.9	15.8	17.3	17.1	17.8
Fe/Mn oxides	33.8	35.9	27.7	41.4	34.7	37.8	35.4	32.3	33.4
Organic	10.0	12.7	8.6	5.8	9.0	7.2	11.2	2.3	7.0
Remainder	40.8	34.0	44.7	31.6	37.2	34.1	29.9	41.3	34.3

commonly found in porous media. According to researchers [41], bacteria form biofilms in any aqueous media with suitable conditions and sufficient nutrients. Thus, the biofilm form is the most convenient (thermodynamically stable) form of biofilm existence in the environment. Biofilms are ubiquitous in nature. It has been established that over 95% of bacteria existing in nature are in biofilms [42]. The role of biofilms in the transformation of rock minerals and the formation of secondary minerals and phases has been considered for a number of natural systems: water–rock [43–45].

Table 4 Fractionation of colloidal matter, 50 nm filter

Sample from the well	1			4			6		
Fraction	U	Pu	Np	U	Pu	Np	U	Pu	Np
Exchange	3.8	2.9	4.2	2.0	1.5	2.1	3.1	2.7	3.5
Movable	11.9	12.8	12.7	13.3	10.9	12.5	14.1	15.9	17.0
Fe/Mn oxides	27.1	28.1	24	25.7	22.9	24.6	25.2	22.2	26.4
Organic	3.9	5.8	6.3	1.6	0.8	1.7	1.9	1.7	2.3
Remainder	53.3	50.4	52.8	57.4	63.9	59.1	55.7	57.5	50.8

Sandy loam rocks of the lower horizon were sampled:

1. C-160 sampling depth 328 m
2. C-160 sampling depth 333.6 m
3. C-161 sampling depth 334.8 m
4. C-162 sampling depth 330.5 m
5. C-162 sampling depth 335 m.

which were sandy loam with clay fraction content of 10–20%. These solid phases were biogenically transformed by culturing them for two months with glucose as a carbon source in the aqueous medium of the corresponding lower horizon.

Biodiversity of microbial communities in samples of radionuclide-contaminated groundwater from the upper and lower aquifers in the area of the radioactive waste repository, as well as characterization of samples of loams subjected to biogenic transformation was performed by employees of the Federal Research Center "Fundamental Bases of Biotechnology" RAS and Institute of Physical Chemistry and Electrochemistry RAS. The information is given in issues of the Genome announcement series journals [46, 47].

Formation water samples filtered through a 0.22 μm filter were used as the aqueous phase in the sorption experiment.

In sorption experiments with treated loams, the two-phase systems were placed in penicillin vials preblown with argon and sealed. The solution with radionuclides ^{233}U, ^{237}Np, ^{239}Pu and ^{241}Am was injected with an insulin syringe. The concentrations of all radionuclides were approximately 10^{-7} M. Sorption of radionuclides was carried out in anaerobic conditions in the model solutions imitating chemical composition of waters of the bottom horizon, but differing in the content of sodium nitrate. The first solution did not contain it, in the second one its concentration reached 10,000 mg/l. Time of sorption experiments was 58 days with sampling in 7 days. Phase ratio in the sorption experiments was 0.1 g/ml.

Figures 4 and 5 show the results of the sorption experiment on sandy loam rocks of the lower horizon, which were subjected to biogenic transformation (systems 1–5) and initial (systems 6–10).

Quasi-equilibrium was established for plutonium in 5 days, americium in 10 days, uranium in 15 days, and neptunium in 50 days. Figure 4 shows degrees of radionuclides sorption from slightly mineralized solution 1 while Fig. 5 from highly mineralized solution 2.

Plutonium was quantitatively sorbed from both solutions on all samples, both those subjected to microbial growth and those without microbiota. Uranium sorption was higher from solution 1, with samples 1–5 significantly higher than samples 6–10 (not subject to biotransformation). This may indicate a redox conversion of uranium oxidation species. The sorption behavior of neptunium is similar to that of

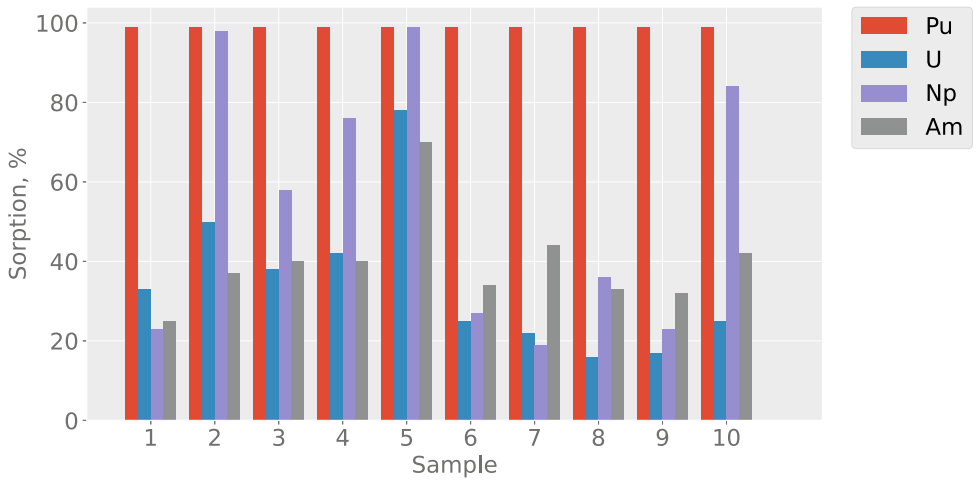

Fig. 4 Degree of radionuclide sorption from solution 1, %

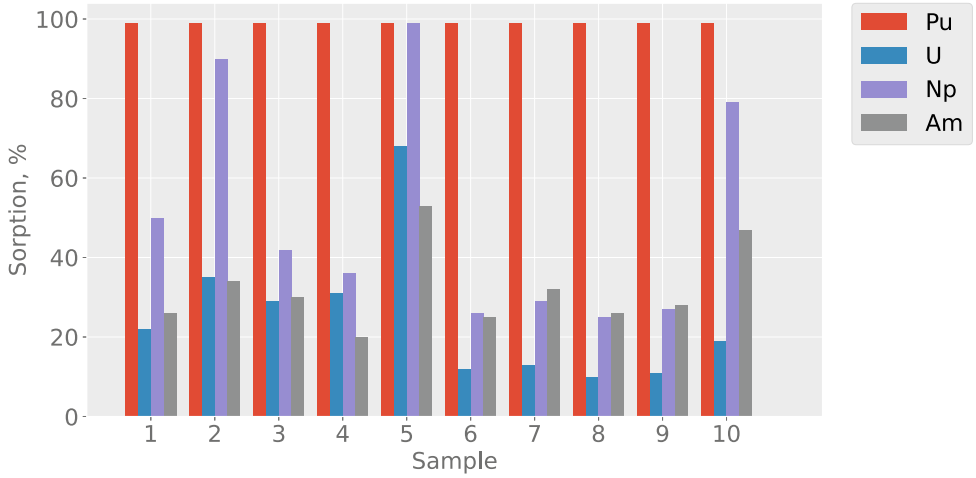

Fig. 5 Degree of radionuclide sorption from solution 2, %

uranium, but unexpectedly the sorption rates of neptunium were higher than those of uranium. Since Np(V) is the weakest sorbed species, this also indicates a possible reduction of neptunium to Np(IV) on biofilm. Neptunium, like uranium, is much more efficiently sorbed on rocks subject to bioaccumulation. Amerisium is not fully and equally sorbed on biogenic and abiogenic samples (on rock 5 the most, from solution 1 almost quantitatively). Americium is not a redox-sensitive element under natural conditions and its main oxidation state is +3. Neptunium and uranium are extracted from weakly mineralized solution to a greater extent than from highly mineralized solution.

Thus the carried out researches show high sorption efficiency of biogenic minerals.

6 Speciation of Actinides in the Marine Environment

The Arctic regions perform an important function in stabilizing biospheric processes and climate on the planet. It is known that the nature of the Arctic zone is extremely vulnerable to anthropogenic interference due to the slowdown of mass and energy exchange levels in cold latitudes. One of the main sources of pollution in the Arctic basin is buried nuclear objects and solid radioactive waste (SRW). Submerged solid radioactive waste on the bottom of the Arctic basin poses a potential hazard and this hazard has been growing every year [48]. Sources of radioactive contamination of the aquatic environment in the Arctic basin also include atmospheric fallout from the Chernobyl accident, transport of radionuclides by marine currents from Western European radiochemical plants, and transport by the Ob and Yenisei rivers of products of the nuclear power complexes located in the Urals and Siberia (primarily the "Mayak" Scientific Production Association and the Krasnoyarsk Mining and Chemical Plant). The most relevant direction of modern radioecological research in the Arctic region remains the study of regularities of man-made radionuclides inflow, assessment of migration ability of the latter and their accumulation in the shelf zone.

Among the seas of the Russian Arctic region, the Kara Sea is the most studied one [49–51]. At present, the radiation ecology of the Laptev Sea is insufficiently studied, there are practically no data on ^{239}Pu content in water and bottom sediments of this sea, and no studies have been conducted to assess the species of radionuclide occurrence.

The Laptev Sea is characterized by harsh climatic conditions. Among all the marginal Arctic seas, the Laptev Sea is minimally affected by warm Pacific and Atlantic currents [52]. Negative air temperatures persist in the Laptev Sea for 11 months and reach −28–34 ºC in its northern part. The Laptev Sea has a vast shelf and abundant river water, mainly from the Lena River (up to 700 km^3 /year) and the Khatanga River. In winter, the Laptev Sea water has a minimum biomass value (up to 0.8 µg C/l); in autumn, microplankton biomass reaches 5.7 µg C/l in the coastal zone of the Lena River delta [53].

Radionuclide intake into waters and bottom sediments of the Arctic region seas occurs from several sources: by water with runoff from rivers flowing through the contaminated territories and flowing into the Arctic seas; with sea currents contaminated with liquid and solid radioactive waste in places of their discharge and burial, and also by air transfer as part of aerosols. Earlier it was established that the main source of mineral particles and organic particles of aerosols entering the Arctic seas are metallurgical enterprises of the North, forest fires, distant transfer of substance from mid-latitudinal regions of the continent, with aerosol substance flows to the Arctic seas surface with their further concentration in bottom sediments and biota of seas, making about 570 mg/m^2 a year [54, 55].

In work [56] the activity of ^{137}Cs in the sea water of the Kara Sea and the Laptev Sea is 1.98 and 1.19 Bq/m^3, and

also the tendency of decrease in the contamination of the marine environment from west to east has been noted.

The purpose of this study is to assess the species of plutonium residence in the bottom sediments of the Laptev Sea.

Figure 6 presents a map of sea water and bottom sediment sampling stations during the expedition onboard the R/V "Akademik Keldysh" in 2020.

Water filtration to determine the volumetric activity of ^{137}Cs was carried out using a submersible pump type "Malysh". A water sample of 120 L was taken from the surface into a plastic barrel equipped with a spigot at the bottom to which a sorption column was connected. The column Ø50 mm, length 75 mm is filled with a sorbent based on cobalt ferricyanide on a fibrous cellulose carrier in an amount of 9–10 g. The filtration speed is controlled by a tap mounted at the column outlet. Optimal rate values are 150–200 ml/min. The activity of the sorbent in the obtained samples was determined in the laboratory of GEOKHI RAS by direct gamma spectrometry on HPGE-detector (Cambera).

For determination of $^{238-240}$Pu content water samples were also taken in plastic barrels of 120 l volume. Into the selected sample 0.8 g $KMnO_4$ (one ampoule of $KMnO_4$ standard titer at 0.1 M) was added, then 5 g $MnCl_2$ (manganese (II) chloride 4-water) was added and the sample was thoroughly mixed. The result was a solution with approximately pH = 6. Then, NaOH in the form of concentrated solution (arbitrary concentration) was added to the water to adjust the pH to a value within 8–9, the water was kept for about one day to form a layer of sediment, which was concentrated to a volume of 1.5 l and as a liquid concentrate and taken to the laboratory for radiochemical analysis.

Bottom sediments were sampled using a sidescratcher. Columns were cut from the sediment block lifted by the sidescraper using a plastic tube with a sharpened edge, slowly pushing it perpendicularly to the sediment layer. The columns were cut sequentially into 2 cm thick layers. In the laboratory samples were dried in the desiccator at 80–100 ºC to constant weight, weighed and ground in a mortar, sieved through a 1 mm sieve. The activity of ^{137}Cs (at 662 keV) and ^{210}Pb (at 46 keV) was determined in each column layer by gamma spectrometry on an HPGE detector (Canberra).

Extraction of $^{238-240}$Pu from bottom sediment samples was performed as from soils according to the method [11, 50] followed by isotope measurements on an Analyst alpha spectrometer (Cambera). The errors of ^{239,240}Pu measurement did not exceed 10–15%. Determination of chemical elements in bottom sediments was carried out by X-ray spectral fluorescence method.

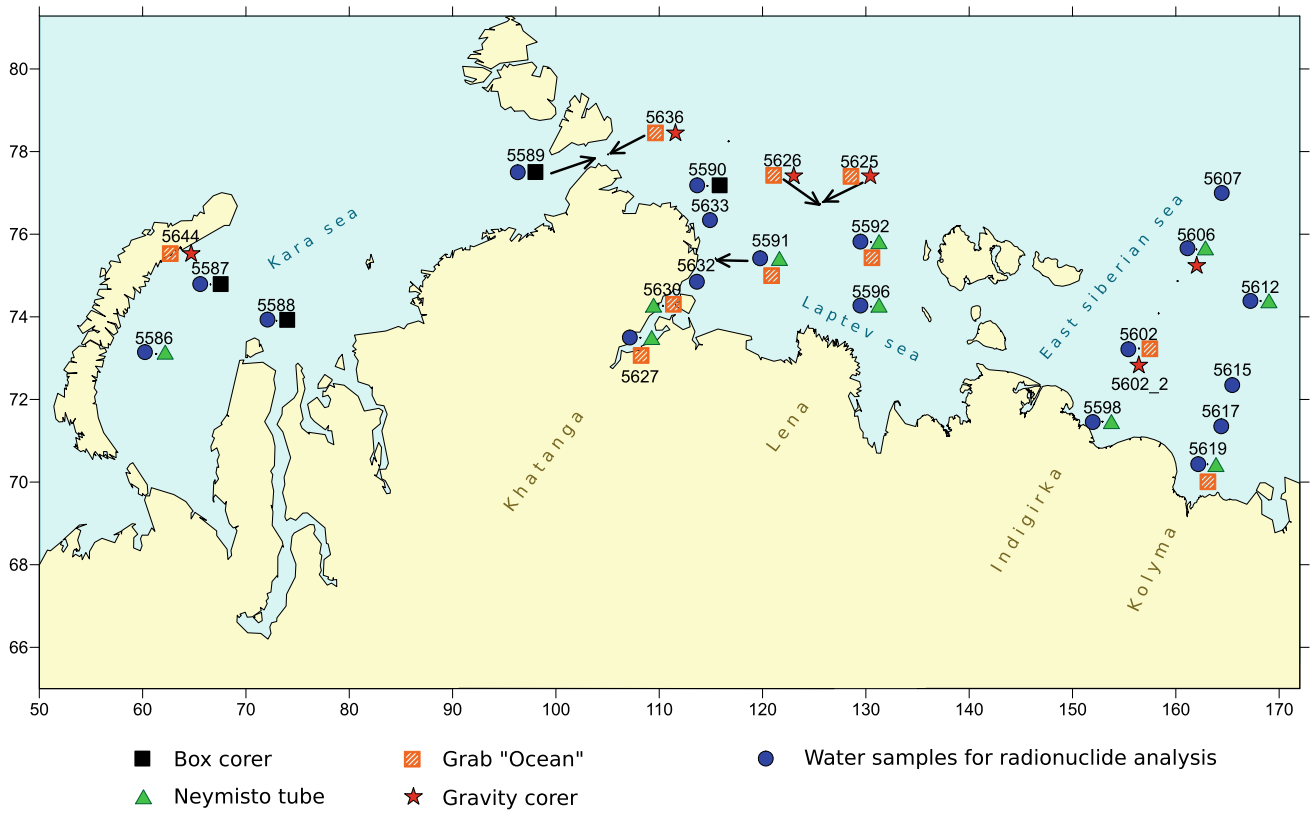

Fig. 6 Map of water and sediment sampling

Radionuclide content in water and bottom sediments of the Laptev Sea

Table 5 presents the results on the measurement of ^{137}Cs and ^{239,240}Pu activity in the Laptev Sea sea water.

Activity of ^{239,240}Pu in seawater is 0.024–0.097 Bq/m^3, which corresponds to the values determined by the global levels of ^{239,240}Pu activity in seawater of the Northern region. Activity of ^{239,240}Pu in seawater of the Kara Sea is within the same limits and is 0.02–0.10 Bq/m^3. Activity of ^{137}Cs in the sea water of the Laptev Sea is also at a level of global background (0.3–0.8 Bq/m^3). In the Kara Sea the activity of ^{137}Cs is slightly higher and varies in the range 0.8–1.2 Bq/m^3, which is connected with the place of sampling of sea water, confined to the bays of Novaya Zemlya island [50, 51]. According to literature data, activity of ^{239,240}Pu and ^{137}Cs in the water of the seas and oceans of the Northern latitudes varies within a wide range and makes 0.01–0.052 and < 1.0 Bq/m^3, respectively.

Total activity of $^{238-240}$Pu in bottom sediments of the Laptev Sea, sampled from upper horizons (0–2 cm), was found to be 0.08–0.46 Bq/kg, with maximum values confined to the mouth of the Khatanga River and Vilkitsky Strait. The isotope ratio of ^{238}Pu/^{239,240}Pu is 0.07–0.15, which corresponds to their ratio in the products of global fallout. In comparison with ^{239,240}Pu content in bottom sediments of Laptev Sea, isotope activity of ^{238}Pu is higher in bottom sediments of Kara Sea, it changes within a wide range depending on sampling location and makes 0.2–3.8 Bq/kg. The activity of ^{137}Cs in the bottom samples of the Kara Sea is also higher than the global values (1.2–21.1 Bq/kg), and the maximum activity of ^{137}Cs and $^{238-240}$Pu was found in the mouth of the Yenisei River [50].

For two transects the distribution of ^{239,240}Pu and ^{137}Cs isotope activity and chemical elements by depth of bottom sediments (stations 5591 and 5596) was studied. The total activity of ^{137}Cs in bottom sediments at station 5591 is higher than at station 5596 (38.7 and 12.6 Bq/kg, respectively), which is probably conditioned by the influence of the Khatanga river discharge and also by the proximity of continental aerosol inflows to the water area of sampling at station 5591. The total activity ^{of} ^{238}Pu/^{239,240}Pu in the samples of station 5591 is insignificantly higher than at station 5596. Main activity of ^{of} ^{238}Pu/^{239,240}Pu and ^{137}Cs in bottom sediments of station 5596 is concentrated in 0–8 cm layer (up to 80%). The ^{238}Pu/^{239,240}Pu isotope ratio in bottom sediments was found to be 0.2–0.8, with maximum values occurring in the 2–6 cm horizon of station 5591. The increased ^{238}Pu content does not correspond to the global levels of radioactive fallout and can be explained by removal from the territories contaminated as a result of accidental underground nuclear explosions in the Republic of Sakha (Yakutia) [57].

Distribution of ^{137}Cs and ^{210}Pb over depth of bottom sediments of stations 5591 and 5596 in the Laptev Sea was studied. Isotope ^{210}Pb is a product of radioactive decay of ^{238}U and enters the atmosphere from the ground surface, practically immediately captured by aerosol and dust particles and deposited on the ground surface in their composition. In modern studies the values of "atmospheric" ^{210}Pb are used as an indicator of various natural processes, including rates of sea precipitation formation, studies of aerosol particles transport in the atmosphere, etc. The results of ^{137}Cs vertical distribution in bottom sediments are also used to estimate sedimentation rates of marine sediments. According to the results of gamma spectrometric analysis of ^{210}Pb the sedimentation rate is 0.20 ± 0.04 cm/year and according to the data of spectrometry of man-made ^{137}Cs–0.16 ± 0.02 cm/year.

The content of chemical elements in the bottom sediments of cores 5591 and 5596 is different. Content of Fe, V, Cr, Co, Ni, Pb and some other chemical elements in bottom sediments of station 5591 is higher than in samples of station 5596 remote from the Laptev Sea shoreline. This most likely indicates a more active contribution of river continental sediments from the Khatanga River influencing the accumulation of chemical elements in bottom sediments of the

Table 5 Radionuclide content in Laptev Sea seawater samples, Bq/m^3

N. n/a	Station number	Place of selection	Station coordinates		^{137}Cs	$^{239.240}$Pu
1	5590	Near the Taimyr Peninsula	77,017'.00	114,066'.67	0.6 ± 0.2	0.024 ± 0.008
2	5591	Laptev Sea	75,041'.22	115,045'.55	0.5 ± 0.1	0.033 ± 0.006
3	5592	Same	75,080'.83	130,049'.67	0.3 ± 0.1	0.044 ± 0.005
4	5596	Same	74,025'.00	130,049'. 83	0.8 ± 0.1	0.052 ± 0.007
5	5627	Mouth of the Khatanga River	73,049'.43	108,017'.82	0.7 ± 0.2	0.097 ± 0.010
6	5632	Mouth of the Khatanga River	74,084'.67	113,080'. 83	0.6 ± 0.1	0.043 ± 0.006
7	5633	Laptev Sea	76,035'.83	114,096'.67	0.7 ± 0.3	0.060 ± 0.006

area of station 5591. The C_{org} content in the 2–4 cm layer of bottom sediments of station 5591, similarly to chemical elements, is higher than in sample 5596 at 11.0 and 7.8 mg/g, respectively.

Speciation of ^{239}Pu in bottom sediments of the Laptev Sea

In order to predict migration processes based on the degree of radionuclide mobility in samples of the natural environment, it is important to know not only the total content of radionuclides but also the species of their presence in the biosphere. The strength of radionuclide binding to various components of the marine environment determines the direction and intensity of their migration in the seawater-bottom sediment system.

Tables 6, 7 and 8 present the results of study of the speciation of ^{239}Pu occurrence in the Laptev Sea bottom sediment samples under laboratory conditions, since the content of this radionuclide is insufficient to estimate its speciation of occurrence under native conditions.

Table 6 Forms of ^{239}Pu in bottom sediment samples from the Laptev Sea, % of the total content in the sample

Form	Station	
	5591	5596
Exchange	7.6	10.0
Movable	39.0	36.2
Acid soluble	47.4	44.0
Remainder	10.2	10.0

Table 7 Forms of ^{239}Pu in bottom sediments, % of total content in the sample [40]

Form	Station	
	5591	5596
Exchange	N/A	N/A
Carbonate	1.8	3.1
Fe/Mn oxides	20.4	32.1
Related to organics	29.6	39.4
Remainder	48.2	25.2

The results given in Table 6 showed that 8–10% of ^{239Pu} in bottom sediments of the Laptev Sea were found as a part of the exchange species, which includes mobile organic substances in addition to easily soluble chemical compounds. With the group of relatively mobile compounds including Fe/Mn oxides 36.2 and 39.0% of ^{239}Pu is associated, the main activity of ^{239}Pu is found in the composition of hardly soluble compounds (acid soluble in 6 M HCl and residue) 54 and 58%.

When using the Tessier method, which has recently been frequently used to study the speciation of radionuclides and chemical elements in soils or bottom sediments of natural environments, it is possible to estimate the relations of the studied elements with both inorganic and organic components of natural samples (Table 7). Rather high content of ^{239}Pu was found in organic matter of bottom sediments (30.0 and 39.4% for stations 5591 and 5596 respectively).

The results obtained by the Tessier method showed that more than 30% of ^{239}Pu is in organic matter; therefore, a further study of ^{239}Pu and C_{org} bonds with different groups of organic substances of bottom sediments was carried out (Table 8). In decalcinate, where mainly mobile fulvic and low molecular weight acids, free and bound with mobile Fe/Mn compounds, and readily soluble mineral compounds are transferred, 14.3 (station 5591) and 10.1 (station 5596) % ^{239}Pu, as well as 16 and 24.4% C_{org} are bound. 11.0–15.2% ^{239}Pu is associated with GC and FA groups, and a significantly greater amount of $C_{org\ is\ associated}$, totaling 56.8 and 62.8% for GC and FA, with the main C_{org} content associated with GC. Up to 63% of ^{239}Pu remains in the residue, which includes insoluble organic matter (humins) and mineral compounds. The activity of ^{239}Pu found in the composition of organic matter using the Tessier method (Table 7) and the Orlov D.S. method. (Table 8) agree quite well with each other. Thus, 29.6 and 39.4% of ^{239}Pu (Tessier method, Table 7) are associated with organic matter, while the method of Orlov, D.S., amounts to 36.9–37.4% of ^{239}Pu (Table 8).

Acknowledgements This research is conducted under the GEOKHI RAS state assignment. The actinide luminescence research was supported by the grant of the Russian Science Foundation (project No 20-77-00092).

Table 8 Distribution of ^{239}Pu and Sorg. by groups of organic matter in the Laptev Sea bottom sediment samples, % of the total content in the sample

Form	Station			
	5591		5596	
	^{239}Pu	Sorg	^{239}Pu	Sorg
Decalcinate	14.3	16.2	10.1	24.4
Fulvic acids	11.0	19.8	15.2	24.3
Humic acids	12.1	37.0	11.6	38.5
Remainder	62.6	27.0	63.1	12.8

References

1. Pavlotskaya, F.I., Tyuryukanova, E.B., Baranov, V.I.: Global Distribution of Radioactive Strontium over the Earth's Surface. Nauka, Moscow (1970)
2. Pavlotskaya, F.I.: Migration of Radioactive Products of Global Deposition in Soils. Atomizdat, Moscow (1974)
3. Pavlotskaya, F.I.: Forms of residence and migration of radioactive products of global deposition in soils. D. thesis for the degree of Doctor of Chemistry, Geochemistry Institute, USSR Academy of Sciences, Moscow (1981).
4. Pavlotskaya, F.I.: Modern Problems of Radiogeochemistry and Cosmochemistry. Nauka, Moscow (1992)
5. Myasoedov, B.F., Novikov, A.P., Pavlotskaya, F.I.: Problems of analysis of natural objects in determining the content and forms of occurrence. J. Anal. Chem. **51**(1), 124–130 (1996)
6. Novikov, A.P., Mikheeva, M.N., Ivanova, S.A., Myasoedov, B.F.: Avt.evid. no. 5146273/27, (1992).
7. Novikov, A.P., Fabelinsky, Y.I., Lavrinovich, E.A., Goryachenkova, T.A., Grechnikov, A.A.: Speciation and determination of actinides in the environment. Geochem. Int. **54**(13), 1196–1209 (2016)
8. Orlov, D.S.: Soil Chemistry. Moscow State University Press, Moscow (1992)
9. Orlov, D.S.: Humic acids of soils and general theory of humification. Moscow State University Press, Moscow (1990)
10. Novikov, A.P., Myasoedov, B.F.: Radiochemical procedures for speciation of actinides in the Environment. Environment Protection against Radioactive pollution 147–154 (2003).
11. Novikov, A.P.: Migration of Radioniclides in the Environment. Geochem. Int. **48**(13), 1285–1398 (2010)
12. Saito, A., Choppin, G.R.: Separation of actinides in different oxidation states from neutral solutions by solvent extraction. Anal. Chem. **55**, 2454–2560 (1983)
13. Novikov, A.P., Shkinev, V.M., Spivakov, B.Ya., Myasoedov, B. F., Gekkeler, K.E., Bayer, E.: Separation and Preconcentration of Actinides by a water-soluble Oxine Polymer using membrane filtration. Radiochimica Acta 4, 481 (1988).
14. Novikov, A.P., Safonov, A.V., Babichc, T.L., Boldyrev, K.A., Kryuchkov, D.V., Lavrinovich, E.A., Kuzovkina, E.V., Emel'yanov, A.M., Goryachenkova, T.A.: Biotransformation of Neptunium in Model Groundwaters. Geochem. Int. **65**(2), 145–152 (2020)
15. Vlasova, I.E., Kalmykov, S.N., Sapozhnikov, Y.A., Simakin, S.G., Anokhin, A.Y., Aliev, R.A., Tsarev, D.A.: Radiography and local microanalysis for detection and study of actinide-containing microparticles. Radiochemistry **48**(6), 551–556 (2006)
16. Novikov, A.P., Vlasova, I.E., Safonov, A.V., Ermolaev, V.M., Zakharova, E.V., Kalmykov, S.N.: Speciation of actinides in groundwater samples collected near deep nuclear waste repositories. J. Environ. Radioact. **192**, 334–341 (2018)
17. Teterin, Y.A., Kalmykov, S.N., Novikov, A.P., Sapozhnikov, Y. A., Vukchevich, L.J., Teterin, A.Y., Maslakov, K.I., Utkin, I.O., Khasanova, A.B., Shcherbina, N.S.: Study of interaction of neptunoyl with goethite (α-FeOOH) in water medium by RPS method. Radiochemistry **46**(6), 503–509 (2004)
18. Fuggle, J.C., Burr, A.F., Lang, W., Watson, L.M., Fabian, D.Y.: X-ray photoelectron studies of thorium and uranium. J. Phys. F: Metal. Phys. **4**(2), 335 (1974)
19. Zubavicius, J.V., Slovkhotov, Y.L.: X-ray synchrotron radiation in physico-chemical studies. Advances in Chemistry **70**, 429–463 (2001)
20. Aksenov, V.A., Tyutyunnikov, S.I., Kuzmin, A.Y., Puras, Y.: EXAFS—spectroscopy on synchrotron radiation beams. Physics of elementary particles and atomic nuclei **32**(6), 1300–1350 (2001)
21. Denecke, M.A.: Actinide speciation using X-ray absorption fine structure spectroscopy. Coord. Chem. Rev. **250**, 730–754 (2006)
22. Novikov, A.P., Kalmykov, S.N., Utsunomiya, S., Ewing, R.C., Horreard, F., Merkulov, A., Clark, S.B., Tkachev, V.V., Myasoedov, B.F.: Colloid Transport of Plutonium in the Far-Field of the Mayak Production Association. Russia. Science **314**, 638–641 (2006)
23. Proceedings of the OECD-NEA Workshop on Speciation Techniques and Facilities for Radioactive Materials at Synchrotron Light Sources. Grenoble, France (1998).
24. Proceedings of the Second OECD-NEA Workshop on Speciation Techniques and Facilities for Radioactive Materials at Synchrotron Light Sources. Grenoble, France (2000).
25. Proceedings of the Third Workshop on Speciation, Techniques and Facilities for Radioactive Materials at Synchrotron Light Sources. Berkeley, CA, USA (2004).
26. Proceedings of the Fourth Workshop on Speciation, Techniques and Facilities for Radioactive Materials at Synchrotron Light Sources. Karlsruhe, Germany (2006).
27. Kersting, A.B., Efurd, D.W., Finnegan, D.L., Rokop, D.J., Smith, D.K., Thompson, J.L.: Migration of plutonium in ground water at the Nevada Test Site. Nature **397**, 56–59 (1999)
28. Colella, M., Lumpkin, G.R., Zhang, Z., Buck, E.C., Smith, K.L.: Determination of the uranium valence state in the brannerite structure using EELS, XPS, and EDX. Phys Chem Minerals **32**, 52–64 (2005)
29. Radiation Situation on the Territory of Russia and Neighboring Countries in 2019. Yearbook. Edited by K.P. Makhonko. Gidrometeoizdat, Saint Petersburg (2020).
30. Myasoedov, B.F., Drozko, E.G.: Up-to-date radioecological situation around the `Mayak' nuclear facility. J. of Alloys and Compounds **271**(273), 216–220 (1998)
31. Pavlotskaya, F.I., Goryachenkova, T.A., Emelyanov, V.V., Fedorova, Z.M., Myasoedov, B.F.: Behavior of 239 Pu and 240 Pu soil traces after accident in southern urals in 1957. At. Energ. **73**(1), 32–36 (1992)
32. Rybalchenko, A.I., Pimenov, M.K., Kostin, P.P., et al.: Deep Disposal of Liquid Radioactive Waste. Izdat, Moscow (1994)
33. Zubkov, A.A., Makarova, O.V., Danilov, V.V., et al.: Technogenic geochemical processes in sandy reservoir beds in the disposal of liquid radioactive wastes. Geoecology **2**, 133–144 (2002)
34. Forsyth, W.: Studies on the more soluble complexes of soil organic matter: 1. A method of fractionation. Biochemical Journal **41**(2), 176 (1947)
35. Avogadro, A., DeMarsily, G.. In: The role of colloids in nuclear waste disposal. Env.Sci.Techn. 23(5), 496–502 (1989).
36. Ryan, J.N., Elimelech, M.: Colloid mobilization and transport in groundwater. Colloids Surf., A **107**, 1–56 (1996)
37. McCarthy, J.F., Zachara, J.M.: Subsurface transport of contaminants. Environ. Sei. Technol. **23**, 496–502 (1989)
38. Smith, P.A., Degueldre, C.: Colloid-facilitated transport of radionuclides through fractured media. J. of Contaminant Hydrology **13**, 143–166 (1993)
39. Kurosawa, S., Ueta, S.: Effect of colloids on radionuclide migration for performance assessment of HLW disposal in Japan. Pure Appl. Chem. **73**(12), 2027–2037 (2001)
40. Tessier, A., Campbell, P.G.C., Bisson, M.: Sequential extraction procedure for the speciation of particulate trace metals. Anal. Chem. **51**(7), 844–851 (1979)
41. Costerton, J.W., Cheng, K.-J., Geesey, G.G., Ladd, T.I., Nickel, J. C., Dasgupta, M., Marrie, T.J.: Bacterial biofilms in nature and disease. Ann. Rev. Microbiol. **41**, 435–464 (1987)
42. Dworkin, M.: Microbial Cell-Cell Interactions. American Society for Microbiology, Washington (1991)

43. Amann, R.I., Stromley, J., Devereux, R., Key, R., Stahl, D.A.: Molecular and microscopic identification of sulfate-reducing bacteria in multispecies biofilms. Appl. Environ. Microbiol. **58**, 614–623 (1992)
44. Bryers, J.D.: Modelling biofilm accumulation. in Bazin, M.J., and Prosser, J.I.: Physiological Models in Microbiology. CRC Press, Boca Raton (1988).
45. Parfenova, V.V., Malnik, V.V., Boyko, S.M., Sheveleva, N.G., Logacheva, N.F., Evstigneeva, T.D., Suturin, A.N., Timoshkin, O. A.: Hydrobiota communities developing at the phase interface: water - rocks in Lake Baikal. Ecology **3**, 211–216 (2008)
46. Grouzdev, D.S., Safonov, A.V., Babich, T.L., Tourova, T.P., Krutkina, M.S., Nazina, T.N.: Draft genome sequence of a dissimilatory U(VI)-reducing bacterium, Shewanella xiamenensis strain DCB2-1, isolated from nitrate- and radionuclide-contaminated groundwater in Russia. Genome Announc **6**(25), e00555-e618 (2018)
47. Grouzdev, D.S., Babich, T.L., Tourova, T.P., Sokolova, D.S., Abdullin, R.R., Poltaraus, A.B., Schevchenko, M.A., Toshchakov, S.V., Nazina, T.N.: Draft genome sequence of Roseomonas aestuarii strain JR1/69-1-13 isolated from nitrate- and radionuclide-contaminated groundwater in Russia. Genome Announc **6**(25), e00583-e618 (2018)
48. Salbu, B., Nikitin, A., Strand, P., Christensen, G., Chumichev, V., Lind, B., Fjelldal, H., Bergan, T., Rudjord, A., Sickel, M., Valetova, N., Foyn, L.: Radioactive contamination from dumped nuclear waste in the Kara Sea-results from joint Russian-Norwegian expeditions in 1992–1994. The Science of the Total Environment **202**, 185–198 (1997)
49. Goryachenkova, T.A., Emelyanov, V.V., Kazinskaya, I.E., Barsukova, K.V., Stepanets, O.V., Myasoedov, B.F.: Plutonium content in water and bottom sediments of the Kara Sea. Radiochemistry **42**(3), 264–268 (2000)
50. Goryachenkova, T.A., Borisov, A.P., Solovyova, G.Y., Lavrinovich, E.A., Kazinskaya, I.E., Ligaev, A.N., Travkina, A.V., Novikov, A.P.: Content of man-made radionuclides in water, bottom sediments and benthos of Kara Sea and shallow bays of the archipelago New Land. Geochemistry **64**(12), 1261–1268 (2019)
51. Travkina, A.V., Goryachenkova, T.A., Borisov, A.P., Solovieva, G. Y., Ligaev, A.N., Novikov, A.P.: Monitoring of environmental contamination of Kara Sea and shallow bays of Novaya Zemlya. J. Radioanal. Nucl. Chem. **311**(3), 1673–1680 (2017)
52. Druzhkova, E.I., Makarevich, P.R.: Study of phytoplankton of the Laptev Sea: history and modernity. Proceedings of the Kola Scientific Center of the Russian Academy of Sciences 1(14), (2013).
53. Vetrov, A.A., Romankevich, E.A., Belyaev, N.A.: Chlorophyll, primary production, fluxes and balance of organic carbon in the Laptev Sea. Geochemistry **10**, 1122–1130 (2008)
54. Astakhov, A.S., Semiletov, I.P., Sattarova, V V , Shi Xuefa, Hu Limin, Aksentov, K.I., Vasilenko, Y.P., Ivanov, M.V.: Rare earth elements in bottom sediments of Russian East Arctic seas as indicators of terrigenous drift. Reports of the Academy of Sciences 482(4), 451–455 (2018).
55. Kuptsov, V.M., Lisitsyn, A.P., Shevchenko, V.P., Burenkov, V.I.: Suspended matter fluxes into bottom sediments of the Laptev Sea. Oceanology **39**(4), 597–604 (1999)
56. Matishov, G.G., Kasatkina, N.G., Usyagina, I.S.: Technogenic radioactivity of waters of the central polar basin and adjacent Arctic water areas. Proceedings of the Academy of Sciences **485** (1), 93–98 (2019)
57. Gedeonov, A.D., Petrov, E.R., Alexeev, V.G., et al.: Residual radioactive contamination at the peaceful underground nuclear explosion sites “Craton-3” and “ Crystal” in the Republic of Sakha (Yakutia). J. Environ. Radioact. **60**(1–2), 221–234 (2002)

Annex I

In memory of late scientists, who made major contributions to the formation and development of the Vernadsky Institute

V. P. Kolotov and N. S. Bezaeva (eds.), *Advances in Geochemistry, Analytical Chemistry, and Planetary Sciences*,
https://doi.org/10.1007/978-3-031-09883-3

Summary

In the first part of this annex, there is an article on the scientific biography of Academician Vladimir I. Vernadsky, followed by the description of the activities of the research group of the institute named "Scientific Heritage of V. I. Vernadsky and his school" together with a description of Memorial Cabinet-Museum of V. I. Vernadsky located in the main building of the Vernadsky Institute. Then there is an article on the scientific biography of Academician Alexander P. Vinogradov, founder of the Vernadsky Institute, followed by the description of his Memorial Cabinet-Museum. And in the second part of this annex, there are portrait photos and short scientific biographies of late scientists of the Vernadsky Institute, who made major contributions to the formation and development of the institute.

Vladimir I. Vernadsky
Academician of the USSR Academy of Sciences
Doctor of Geognosy and Mineralogy
(1863–1945)

Vladimir I. Vernadsky was born on 12 March 1863 in St. Petersburg.[1]

His father, Ivan V. Vernadsky, was a professor of political economy and statistics, and his mother, Olga P. Vernadskaya (née Konstantinovich), was a housewife. V. I. Vernadsky grew up in a highly sophisticated and intellectual environment. The family's social circle included many well-known cultural figures like P. V. Annenkov, A. A. Bakunin, N. S. Leskov, V. G. Korolenko. Vladimir Vernadsky spent his childhood in St. Petersburg and his adolescence in Kharkov (currently Ukraine).

In 1881 he enrolled in the St. Petersburg University at the Faculty of Physics and Mathematics. During this time, stalwarts of Russian science like A. M. Butlerov, D. I. Mendeleev, A. N. Beketov, I. M. Sechenov, V. V. Dokuchaev taught at the university.

Throughout his life, he kept a diary. As a 4th-year student, V. I. Vernadsky wrote in his diary: "*Science brings*

[1]This article was prepared using the book of academician E. M. Galimov «About Academician V. I. Vernadsky: to the 150th anniversary of his birth» and its chapter "Vernadsky—Scientist, Citizen, Thinker" (Nauka edition, 2013, 230 pp, in Russian). The book is freely available using the following link: http://www.geokhi.ru/DocLib5/publications/Galimov_O%20Vernadskom.pdf.

such pleasure, such great benefit, that it would seem possible to remain a figure of pure science alone… but you understand, everything that is done in the state and society, one way or another, falls on you, and you come to the need to be a figure in this state and society…" (excerpt from the diary, dated May 11, 1884). This civic position, which he determined for himself as a young man in his twenties, he held steadfastly throughout his life.

In 1891, a poor harvest in Central Russia, including the Tambov region where his estate, Vernadovka, was located, brought the peasantry to the brink of famine. Vernadsky and his friends managed to organize in some districts of the Tambov region a system of canteens ("*119 canteens, where up to 5700 people are fed*", noted Vernadsky in his letter to his wife on May 1, 1892), which supported people for almost 7 months, from autumn 1891 to summer 1892. Vernadsky was only 29 years old when he organized this canteen system.

From 1888 to 1889, he took up an internship in Munich at the Mineralogical Department under the guidance of the renowned mineralogist Prof. P. Groth. On his return from his trip abroad, he accepted an invitation to join the Moscow State University. For the next twenty years up to 1911, he taught mineralogy and crystallography at the university. During these years, Vernadsky became one of the most authoritative mineralogists of his time.

He produced fundamental works on crystallography and mineralogy. For these works, he was elected a full member of the Russian Academy of Sciences by 1911. His books, such as "Experience of Descriptive Mineralogy" and "History of Minerals of the Earth's Crust", occupy four volumes of five hundred pages each in his collected works. He followed in the footsteps of V. M. Severgin from the eighteenth century, N. I. Koksharov and E. S. Fyodorov from the nineteenth century in completing the construction of the excellent Russian school of mineralogy at the beginning of the twentieth century. This alone would have ensured his rightful place in the history of science, but this turned out to be only a small fraction of what he managed to accomplish.

V. I. Vernadsky's most significant contribution to science was connected with the notion of the geological role of living matter and the creation of the doctrine of the biosphere and the noosphere. The prerequisites for this were already established during his university days. Vernadsky's direct supervisor and teacher of mineralogy at the university was Professor Vasily V. Dokuchaev, the founder of modern soil science. As a student, Vernadsky took part in soil science expeditions organised by Dokuchaev.

Vernadsky's involvement in soil research, although sporadic, left a deep mark on his scientific experience. At Moscow State University, Vernadsky rearranged the teaching of crystallography and mineralogy. He viewed mineralogy as the science of chemical processes in the Earth's crust. This was an entirely new understanding of mineralogy. In fact, it was the beginning of geochemistry.

His understanding of the role of living matter in the chemistry of the mineral environment, also stemming from his experience of soil research, led him to a new concept in geology, which he subsequently formulated as the biosphere doctrine. Incidentally, the concept of living matter was first outlined by him in an article on the role of organisms in soil formation. The article—"On the participation of living matter in the creation of soils" was written by him in 1919.

Having become acquainted with the discovery of radioactivity by Henri Becquerel and the works of Pierre Curie and Marie Curie-Skladowska, Vernadsky was extremely fascinated by the prospects of using radioactivity as an energy source.

In 1910 V. I. Vernadsky spoke at the meeting of the Academy of Sciences, where he delivered the speech "Tasks of the day in the field of radium". He recited prophetic words: "*… In the matter of radium, no state and society can be indifferent to how, in what way, by whom and when the sources of radiant energy in its possession will be used and studied. The possession of large stocks of radium gives its owners power and authority before which the same power, which owners of gold, land, and capital receive, pales… The sources of atomic energy, millions of times greater than all those sources of forces, which were drawn to human imagination, are opened before us in the phenomena of radioactivity*".

This was articulated more than 100 years ago when the physical basis for such a prediction was still unclear to the founders of new physics, A. Einstein, E. Rutherford, and others.

With the outbreak of the war in 1914–1918, when the unpreparedness of Russia's raw material base became apparent, Vernadsky took the initiative of setting up a Commission for the Study of Russia's Natural Productive Forces (Russian abbreviation: KEPS) at the Academy of Sciences.

In the spring of 1921, Vernadsky returned to Petrograd (currently St. Petersburg) and continued his scientific work. He conceived of a fundamental monograph on living matter, by which time the first five of the 13 conceived chapters were almost ready.

In his view of living matter, Vernadsky thought that it is important to abstract from the biological definition of life. He wrote: "*In the form of living matter we do not study a biological process, but a geochemical one … we study a mass phenomenon, we go by the statistical method, in this case, the randomness is compensated, and we get an idea of an average phenomenon*".

The concept of living matter was the forerunner and basis of his most fundamental work—the doctrine of the biosphere. Vernadsky defined the biosphere as the geological shell of the Earth containing living matter.

The term "biosphere" itself was introduced into science by the German geologist Süss. Vernadsky avoided inventing new terms and usually took a term that already existed in the

literature, and if he found it relevant, he filled it with new content. Similarly, he later used the term "noosphere" introduced earlier by Frenchman Le Roy. Vernadsky showed that, with relatively little mass, living matter determines processes on a planetary scale: the emergence of granite masses in the Earth's crust; the oxygen composition of the Earth's atmosphere. Through photosynthesis and reduced carbon production, the redox cycle in the Earth's crust is started. Global processes of ore formation are linked to this cycle. Living matter transforms the properties of the geological environment, something it would not have had in the absence of life. Living matter generates chemical processes that proceed at an unusually high rate in an unusual direction.

The main thesis of Vernadsky's conception of the biosphere was the consideration of the living matter in its unity with the environment. He wrote: "*Living matter is not an accidental but a necessary factor in many geochemical reactions, in the history of all chemical elements. All these processes would proceed very differently if there was no living matter*".

The doctrine of the biosphere has had a great influence on the development of national research into the geochemistry of natural waters, gases, liquid hydrocarbons, and the role of organic matter. This wasn't accepted by the West for a long time. In the 1970s, the "Gaia hypothesis" put forward by James Lovelock became popular in the West. Its essence is that the Earth and Life constitute, supposedly, a single self-regulating organism. In Vernadsky's doctrine of the biosphere, the concept of self-regulation and feedback is also a natural component. Lovelock was not familiar with Vernadsky's work when he first published his ideas in the 1970s.[2] However, to give him credit, he later acknowledged Vernadsky's work by stating: "*we discovered him to be our most illustrious predecessor*".[3]

Another classic work by V. I. Vernadsky, "Essays on Geochemistry" was first published in 1924. Vernadsky is one of the founders of geochemistry. His predecessor was an American called F. Clark, who systematized information about the chemical composition of rocks and put them together in his work "Data of Geochemistry", published in 1908. His contemporary was the Norwegian W. Goldschmidt, who proposed the geochemical classification of elements (lithophile, chalcophile, siderophile, and atmophile), which is still in use today. Vernadsky turned to the chemical interpretation of natural processes more than once in his work as a crystallographer and mineralogist. From 1923 to 1924, he lectured on geochemistry at the Sorbonne in Paris and published it as "La Géochimie" in French. In 1927 his work "Essays on Geochemistry" was published in Russian.

The works of his predecessors and his contemporaries were more about the application of chemistry and chemical approaches to the study of the geological environment. In Vernadsky's opinion, geochemistry is the science of the history of atoms, processes, and chemical transformations. He revealed the role of factors, which were seemingly not directly related to the composition of the rocks. These include, above all, the special role of carbon and living matter. The chapter Carbon and living matter in the Earth's crust is central to Essays on Geochemistry.

Moreover, Vernadsky's geochemistry is not limited to terrestrial geology. It includes cosmochemistry. Vernadsky was the first to consider the geology of the Earth in the context of its history as a planet of the Solar System. He spoke of the fact that the Earth cannot be considered outside its relationship with the cosmos. At the time, geology was predominantly regional, with geological surveys covering only the uppermost layer of the Earth's crust. There was no data on the deep structure of the Earth, the composition of the mantle, and the core. There was no data on the structure of the oceanic crust. Therefore, the approach to the global study of the Earth in comparison with other planets in the Solar System was unusual.

V. I. Vernadsky considered the study of the Moon as a geological body and the economic development of the Moon as an urgent task. In November 1930, in his diary, he wrote down: "*We now see as a clear and achievable task of the near future the capture by the man of the Moon and planets*".

V. I. Vernadsky, of course, realised that the matter from other planets, necessary for comparative planetary analysis, would not be available in the hands of researchers in the near future. But there was another way—the extensive study of meteoritic matter. Meteorites are fragments of Solar System bodies that have fallen to Earth. Vernadsky organised the collection and description of meteorites and made efforts to expand the state collection. In the 1920s and 1930s, regular scientific expeditions were organised to places where meteorites fell. In 1935 the Meteorite Commission was established and later in 1939 transformed into the Committee on Meteorites of the USSR Academy of Sciences (Russian abbreviation: KMET). The Chairman of the Committee on Meteorites was V. I. Vernadsky. In 1941 the journal "Meteoritika" (Meteoritics in Russian) began to be published.

Vernadsky's concept of studying the Earth in the context of studying the planets of the Solar System, which may once have seemed exotic, is now well accepted, understood, and is a working concept of the international scientific community. The problems of the origin of planetary atmospheres, the origin of the ocean on Earth, the mechanism of the formation of planetary nuclei, are further problems that cannot in principle be solved by studying the Earth alone.

He showed remarkable foresight regarding the future of atomic energy, as already mentioned above. In 1922,

[2]J. Lovelock, 1972; J. Lovelock and L. Margulis, 1974.

[3]J. Lovelock. The Biosphere. New scientist, 1986, p. 51.

V. I. Vernadsky wrote: "*We are approaching a great revolution in the life of mankind, which cannot be compared with any of his earlier experiences. The time is not far off when man will get into his hands the atomic energy, such a source of power, which would give him the opportunity to build his life as he wishes. It may happen in the coming years, may happen in a century. But clearly, it has to be*." Atomic energy was not perceived as a practical possibility at the time, so these words were overlooked.

Nevertheless, Vernadsky took practical steps. He searched for and investigated radioactive minerals. He organised work on radiochemistry. By 1921, with the help of his student V. G. Khlopin, he managed to organise the production of pure radium preparation in Russia. The following year the Radium Institute was established, the centenary of which will soon be celebrated.

At the same time, as a humanist, the anticipation of the atomic age worried him. In 1922, he wrote: "*Will man be able to use this power, to direct it to the good, not to self-destruction? Has he grown to know how to use the power that science must inevitably give him? Scientists should not close their eyes to the possible consequences of their scientific work, scientific progress. They should feel responsible for all the consequences of their discoveries*." It would be more than 15 years before the discovery of the uranium fission chain reaction, which gave the key to the extraction of nuclear energy, and 23 years before the atomic bombs, which exploded over Hiroshima and Nagasaki.

In 1928, the Biogeochemical Department of KEPS was reorganised into the Biogeochemical Laboratory (also known as BIOGEL) of the Academy of Sciences. V. I. Vernadsky remained the director of the laboratory until his death. In 1934 the laboratory, together with other academic institutions, was transferred from Leningrad (currently St. Petersburg) to Moscow. In 1947 the Vernadsky Institute of Geochemistry and Analytical Chemistry was established on the basis of this laboratory.

During his lifetime, Vernadsky established 26 scientific institutions, including the Ukrainian Academy of Sciences.

As a great scientist, Vernadsky deeply understood the essence of science and the mechanism of scientific creativity. He wrote: "*Scientists are the same as dreamers and artists; they are not free from their ideas; they can work well, work long hours only on their thoughts, what their feeling draws them to. Their ideas change; the most impossible, often crazy ones appear; they swarm, swirl, merge, and overflow. And among such ideas they live and for such ideas they work… I hate all fetters of my thought, I cannot and do not want to make it go on the path practically important, the path that will not allow me to understand at least somewhat more those questions that torment me…*".

In the pre-war years, Vernadsky worked passionately on the problems of space–time and symmetry related to living organisms. The state of space–time, according to Vernadsky, was determined by its symmetry properties. In the biochemical processes of living organisms, there is always a predominance of left-hand or right-hand isomers. He called this phenomenon dissymmetry and regarded it as a fundamental difference between living and non-living matter.

This fundamental difference makes abiogenesis, i.e., the emergence of living matter in non-living nature impossible, "*a dissymmetric phenomenon is caused by the same dissymmetric cause. Based on this principle (we may call it the Curie principle), it follows that the special state of living space has a special geometry, which is not the usual Euclidean geometry*".

From the same perspective, Vernadsky considered the isotopic composition of living matter. In a paper published in 1926 under the title "Isotopes and living matter", Vernadsky suggested that "*living organisms are capable of selecting certain isotopes from their mixtures, which are elements present in our environment*".

To appreciate the course of Vernadsky's vision, it is necessary to recall that in 1926, not only did the concept of isotope fractionation not exist but the isotopes of many elements, which are key in modern isotope geochemistry, were not yet known. The heavy carbon isotope ^{13}C, the nitrogen isotope ^{15}N, the oxygen isotopes ^{18}O and ^{17}O were discovered in optical spectra in 1927–1929. It was not until 1932 that the heavy isotope of hydrogen, deuterium, would be discovered, and only 10–15 years later would the first measurements of the isotopic composition of elements in natural substances appear. It was believed that the isotopes were chemically identical. Therefore, what was Vernadsky's starting point?

Tracing back to the original idea of Vernadsky, the fractionation of isotopes in living organisms has a fundamental and profound peculiarity due to the enzymatic character of the biosynthetic processes, or, if you will, to the special chemical space of the living.

This also explains the phenomenon of dissymmetry, which is characteristic of living things. Reproducible three-dimensional structures of proteins and nucleotides can only be constructed from enantiomers. Therefore, Vernadsky's conviction of the peculiarity of the chemical space of living things proved to be correct.

Vernadsky created his work "**The Chemical Structure of the Earth's Biosphere and its Environment**" (see below*) when he was about eighty years old. He called it his most significant work, saying it was "*my main book*", "*the book of life*". It is indeed a conceptual synthesis of doctrines on the biosphere, biogeochemistry, and geochemistry he created. Periods of personal bloom and creative insight in different people occur at different ages. Poets, mathematicians, and military leaders reach this bloom more often at a young age. Encyclopedic thinkers create it in their second half of life. Vernadsky expressed his most influential ideas when he was over sixty.

In the 1930s, Vernadsky created a profound philosophical work: "**Scientific thought as a planetary phenomenon**" (see below*). Planetary phenomena are mountain building, ocean movement, volcanism—and suddenly, scientific thought was in the mix. The evolution of the biosphere, according to Vernadsky, was directed towards an increase in the rate of biogenic migration of atoms. Human activity, by means of scientific thought, contributed to the acceleration of the migration of chemical elements, hence substantiating the idea of scientific thought as a natural force of evolution in the era of the biosphere's transformation into the noosphere.

In his final stage, V. I. Vernadsky came to a rigorous and concluding formulation of his doctrine of the noosphere. He considered the inclusion of man in the biosphere not simply as a conflict between nature and man but as a new stage in the development of the biosphere. "*The noosphere is a new geological phenomenon on our planet. In it, man, for the first time, becomes a major geological force*". The idea of the increasing role of man and reason in nature had been expressed earlier in scientific philosophy. As early as the nineteenth century, North American geologist and biologist D. Dana (1813–1895) introduced the term cephalization to describe the directional movement of biological evolution towards the development of nervous systems and sophisticated, intelligent behavior in organisms. Le Comte (1823–1901) associated the same phenomenon with the advent of a particular psychozoic era. The term noosphere itself was introduced by Le Roy (1926). The generalization put forward by V. I. Vernadsky as a doctrine of the noosphere contained two main points; the first was that human activity has taken on a geological scale. A *new state* is being created *when the geological role of man begins to dominate the biosphere;* the other was that before the advent of man, evolution was a spontaneous process. With the emergence of reason, a new organising factor in the biosphere has emerged.

Vernadsky's concept of the noosphere is closely intertwined with his conception of scientific thought as a planetary phenomenon. The noosphere is presented as a stage in the development of the biosphere in which human activity becomes a geological force. Yes, but here is the important thing! Vernadsky did not refer to productive activity but intellectual activity. That is why he used the term "*noos*"—mind. The main component in the development of the noosphere is the expansion of knowledge. He wrote in his work Scientific thought as a planetary phenomenon: "*...the main geological force creating the noosphere is the growth of scientific knowledge*". Vernadsky considered transition to noosphere as a creative reasonable process, one might say a moral process. Anything that contradicted this natural course of development was ultimately doomed.

To summarise, the following key points should be noted.

Vladimir I. Vernadsky was an exceptional scientist. He created new directions in science: geochemistry, the doctrine of living matter and the biosphere, radiogeology, and he made enormous contributions to the development of mineralogy and crystallography. He had original philosophical ideas in understanding problems of symmetry, the space–time of living organisms, and scientific thought as a planetary phenomenon. He created the doctrine of the noosphere.

As a thinker, Vernadsky was remarkably perceptive. Some of his foresight, such as the future role of atomic energy, the importance of lunar and planetary exploration, and the emergence of ecological problems, were unheard of and only now fully appreciated.

And above all, Vernadsky was a great humanist. Despite, or perhaps because of, his critical mind, his attitude towards history and the future of humanity was deeply optimistic. His doctrine of the noosphere was imbued with faith in the triumph of reason.

* Vernadsky Institute RAS is currently preparing a new, improved English translation of *Scientific thought as a planetary phenomenon* and an English translation of *The Chemical Structure of the Earth's Biosphere and its Environment*, which has never been published in English before. Both books by academician V. I. Vernadsky will be published by Springer Nature in Open Access mode.

If you have any questions, suggestions, or comments or if you wish to receive an alert upon publication, please contact Dr. Natalia S. Bezaeva at bezaeva@geokhi.ru.

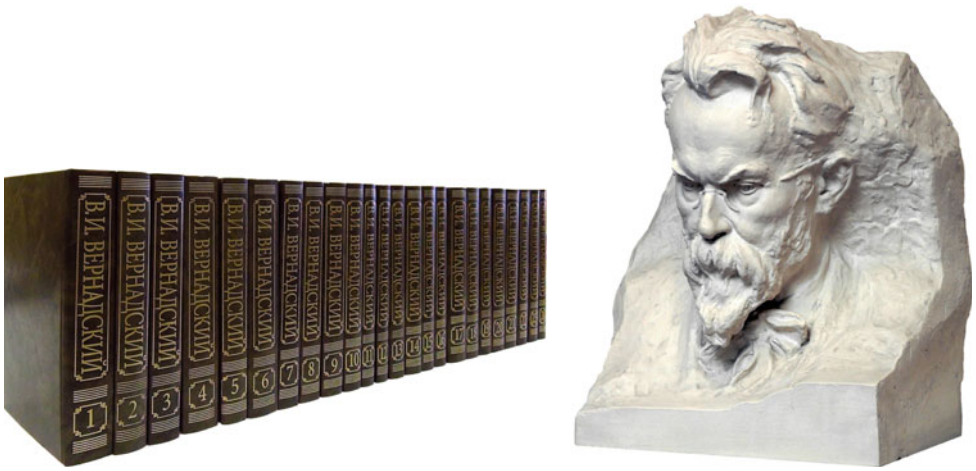

Group "Scientific heritage of V. I. Vernadsky and his school"

Head of the Group
Evgeny P. Yanin
Ph.D. in Geological and Mineralogical Sciences
Email: yanin@geokhi.ru
Website: portal.geokhi.ru/eng/vernadsky

A brief biography and the main scientific ideas of Vladimir I. Vernadsky are presented in the previous article. The creative heritage of Academician V. I. Vernadsky, his students, and followers, the documents relating to their lives and activities, have an unrivaled scientific, applied, educational, and cognitive value. They are vital for understanding the current state and further development of various branches of geological science, analytical chemistry, and natural sciences. They also help understand the history of the development of the world and domestic scientific thought, as well as for organizing scientific research, higher education, public education, for substantiation of principles of rational use of natural resources, and assess the transformation of the biosphere in modern conditions.

That is why in 1993, Vernadsky Institute organized the sector entitled The scientific heritage of V. I. Vernadsky and his school. In 1998, it was transformed into the group The scientific heritage of V. I. Vernadsky and his school, which is currently headed by E. P. Yanin, Ph.D. This group has a status of a separate research unit of the Vernadsky Institute. At different periods, this group included Doctors of Geological and Mineralogical Sciences S. M. Alexandrov and V. P. Volkov (see below for details on Dr. Volkov's bio), Ph.D. in Geological and Mineralogical SciencesA. P. Zhidikova, Ph.D. in Economy V. S. Chesnokov, Doctor of Philosophical Sciences F. T. Yanshina. Between 1999 and 2020, the Scientific Head of the Group was Academician E. M. Galimov (see below for details of Acad. Galimov). Currently, the group has 6 employees, including 4 Ph.D.'s.

The main goal and the most important tasks of the research are the studies of the creative heritage of Vernadsky and his students, the search and analysis of archival (unpublished), and little known materials and documents of scientific, scientific organizational, journalistic, epistolary, diary, and biographical nature. Their systematization, processing, providing with the necessary information and reference data, preparation for introduction into the scientific, cultural and public discourse is also done. The popularization of the creative heritage of V. I. Vernadsky and representatives of his school is also of great importance. To date, research findings have been reported in numerous articles (mostly in Russian language).

Memorial Cabinet-Museum of Academician V. I. Vernadsky

Curator of the Cabinet-Museum of Academician V. I. Vernadsky
Irina N. Ivanovskaya
Ph.D. in Geological and Mineralogical Sciences

Vernadsky Institute also possesses a Memorial Cabinet-Museum of Academician Vernadsky open to the public by appointment. This museum has a status of a separate research unit of the Vernadsky Institute but adjacent to the Group Scientific heritage of V. I. Vernadsky and his school. It is located in the main building (room 27).

A room for a cabinet-museum of Academician Vernadsky was included in the architectural plan of the main building of Vernadsky Institute according to the order of the Presidium of the USSR Academy of Sciences dated October 5, 1945, No.504, with the purpose to perpetuate the memory of the scientific, organizational, social and political activities of Academician V. I. Vernadsky. It replicated the layout of the home office from the apartment of V. I. Vernadsky in Moscow, Durnovsky Lane, where he spent the last 10 years of life. The opening of the memorial cabinet-museum took place on May 20, 1953, and was timed to the 90th anniversary of Vernadsky's birth. A visit to the museum is a journey back in time to the working environment of the scientist's office room of the late nineteenth century. The visitors cherish a part of history by simply visiting the museum and getting in the atmosphere of that time—antique furniture, a library with over 7000 titles, pictures and portraits of his family members, relatives, friends, and colleagues. Everything is placed and hung in the museum, as it was in the last home office of Vernadsky.

The main direction of the current museum's activities is the popularization of Vernadsky's ideological heritage, coverage of different stages of his life, and familiarization with his organizational, social, and political activities. About 300 people visit the museum each year. Among the visitors were scientists from the USA, China, Japan, Poland, Czech Republic, Germany, France, and other countries. The museum's tradition includes systematic excursions for graduate students of natural science and higher educational institutions and the introduction of materials reflecting the life, scientific and socio-political activities of Academician V. I. Vernadsky into their curricula. The museum organizes visiting exhibitions dedicated to Vernadsky in various cities in Russia and abroad (Figs. A.1, A.2, A.3 and A.4).

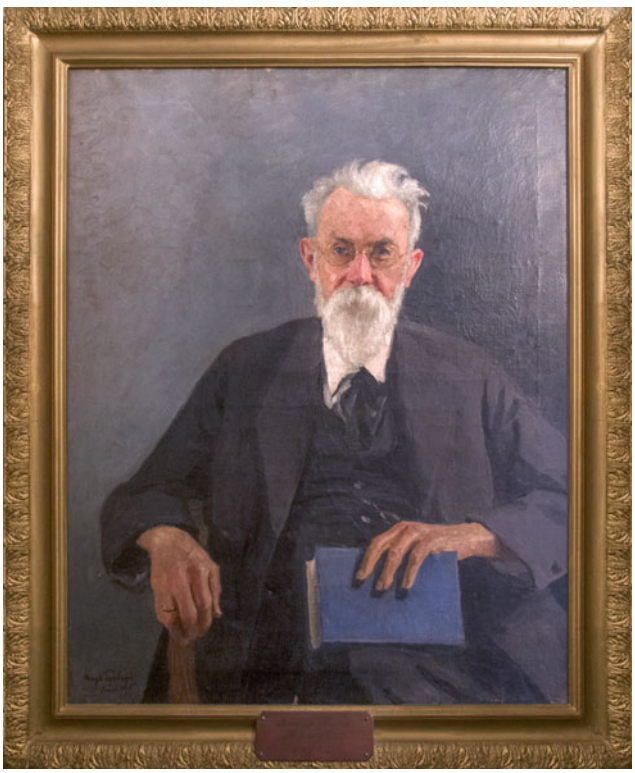

Fig. A.1 Portrait of academician V. I. Vernadsky by Igor Grabar (1934). The original portrait is kept at the Cabinet-Museum of academician Vernadsky. Igor Grabar is a famous Russian post-impressionist painter (1871–1960): https://en.wikipedia.org/wiki/Igor_Grabar

Fig. A.2 Interiors of the Cabinet-Museum of academician V. I. Vernadsky

Fig. A.3 Work table of V. I. Vernadsky

Fig. A.4 Part of the big personal library of academician V. I. Vernadsky

Alexander P. Vinogradov (1895–1975). Academician of the USSR Academy of Sciences. Founder and first Director of the Vernadsky Institute. Doctor of Chemistry (photographed 1960)

Alexander P. Vinogradov, the founder of the Vernadsky Institute RAS, was born in 1895 in St. Petersburg (Imperial Russia).[4] In 1918, he was enrolled in the Military Medical Academy. And in 1919 he was also enrolled in the Department of Chemistry of the Physics and Mathematics Faculty of the Petrograd State University (currently St. Petersburg State University). He graduated from the academy and from the university in 1924.

Vinogradov started his scientific activity with V. I. Vernadsky in 1926. A. P. Vinogradov purposefully studied the chemical elemental composition of marine organisms, plants, soils, waters, rocks, etc. As a result, a vast amount of quantitative data was accumulated based on which the basic laws of biogeochemistry were formulated, which were generalized and published in his conceptual 3-volume monograph Chemical Elemental Composition of Marine Organisms (1935–1944). This work was the first to lay down the principles of chemical ecology.

In 1937, based on the results of comprehensive studies of the chemical composition of natural objects in various regions where specific human and animal diseases were

[4]This article was prepared using the following publication (in Russian): L. D. Vinogradova (2020), To the 125th Anniversary of Academician A. P. Vinogradov: a brief scientific biography, In *Biogeochemical Innovations under the Conditions of the Biosphere Technogenesis Correction: Proceedings of the International Biogeochemical Symposium devoted to the 125th anniversary of Academician A. P. Vinogradov's birth and the 90th anniversary of Shevchenko State University of Pridnestrovie (Shevchenko State University, Tiraspol, November 5–7, 2020)*, Vol. I, p. 10–24.

observed, A. P. Vinogradov introduced the new concept of biogeochemical provinces and described the associated biogeochemical endemics—diseases caused by abnormal content of chemical elements in the habitat. This discovery was of great practical importance for medicine and agriculture.

From 1930 to 1940, A. P. Vinogradov did much to form and develop the analytical base of the Biogeochemical Laboratory of the USSR Academy of Sciences (also known as BIOGEL). The laboratory developed new analytical methods for determining small quantities of elements, including rare elements. In 1938, A. P. Vinogradov, together with I. P. Alimarin (biography presented below in this section), formulated the main trends in the development of analytical chemistry, i.e., creation of new highly sensitive methods for determination of chemical elements, development of physical and chemical methods of concentration (coprecipitation, extraction, evaporation, electrochemical, etc.), and methods of chemical phase analysis. A. P. Vinogradov introduced the polarography method into the practice of the Biochemical Laboratory of the USSR Academy of Sciences. In 1953, he initiated work on the application of the radioactivation method, one of the most sensitive multielement methods of analysis in the USSR. In 1946, A. P. Vinogradov founded the Journal of Analytical Chemistry and became its editor-in-chief.[5]

Since 1933, at the suggestion of V. I. Vernadsky, A. P. Vinogradov started isotope studies. Of particular importance in the pre-war period was the work carried out jointly with R. V. Theis to determine the isotopic composition of oxygen released during photosynthesis, which led to an important discovery that changed previous ideas about the mechanism of this process. The authors of the discovery showed that atmospheric oxygen is produced by the decomposition of water, not carbon dioxide, as previously thought.

In 1940, A. P. Vinogradov, together with the greatest physicists in the country, was included in the Commission on Uranium Problems created by the USSR Academy of Sciences on the proposal of Academicians V. I. Vernadsky and V. G. Khlopin. This was preceded, starting from 1938, by the work of A. P. Vinogradov on the development of the thermodiffusion method of uranium isotope separation. He set out his proposals on the method of uranium isotope separation and on the complex solution of the uranium problem in two documents: a letter to V. I. Vernadsky and a letter to the Presidium of the USSR Academy of Sciences.

In May 1945, A. P. Vinogradov, an outstanding chemist-analyst and scientist involved in isotope research, was brought into the so-called Soviet Atom Project, where he led the creation and development of analytical control of uranium and plutonium production in the USSR.

In the 1950s, Vinogradov worked actively in the Soviet Peace Committee and the Soviet Peace Foundation and became one of the most active participants in the International Pugwash Movement of scientists who advocated the prevention of the threat of nuclear war.

A. P. Vinogradov called for an immediate cessation of nuclear tests, which resulted in a 30% increase in the atmospheric concentration of ^{14}C between 1955 and 1960. Together with V. I. Baranov and F. I. Pavlotskaya (both biographies are presented below in this section), the results on radioactive strontium contaminating the Soviet Union territory were first obtained, and the work on the investigation of the migration mechanism of radioactive products in soil and vegetation complex of various natural zones was started. As a result of these studies, valuable data was acquired regarding the radioactive contamination of the Earth's surface caused by the products of nuclear tests.

In the postwar years, continuing his research in isotopes, Vinogradov proved to be the founder of isotope geochemistry in the USSR. He was one of the first to understand the importance of isotopic methods for solving geochemical and cosmochemical problems. In 1949, A. P. Vinogradov organized the first Laboratory of Isotope Geochemistry and Geochronology at the Vernadsky Institute to study the behavior of isotopes in natural processes and headed the laboratory from 1954 to 1975, where he raised a large school of talented isotope geochemists.

The laboratory under his leadership firstly developed the work on determining the isotopic composition of waters in metamorphic rocks and minerals, starting in the pre-war years with V. I. Vernadsky. Classical works on the geochemistry of light (hydrogen, carbon, nitrogen, oxygen, sulfur, and potassium) and heavy (lead) isotopes were carried out. Significant contributions were made to the theory of isotope effects and the creation of new methods of isotope geochronology (potassium-argon, uranium-lead, lead-lead, rubidium-strontium, and radiocarbon).

A. P. Vinogradov was paying great attention to the training of young scientists. He created the Department of Geochemistry at the Faculty of Geology of Lomonosov Moscow State and was its head between 1952 and 1975.

Since the late 1960s, the zircon dating method has been developed, and relevant geochronological maps of the shields have been constructed. In 1968, a draft geochronological scale for the Precambrian was presented at the XXIII Session of the International Geological Congress. In 1974, the rubidium-strontium method was successfully applied to determine the absolute age of lunar regolith soil. The isotope studies carried out under the leadership of A. P. Vinogradov

[5]Currently, the journal publishes articles in both Russian and English languages and welcomes submissions by international authors in English. The journal is indexed in both Scopus and Web of Sciences. For more details about the journal, see Introduction.

Main building of the Vernadsky Institute in 1950s

were of great importance for isotope geology in the USSR. They were the key to the discovery of several geological concepts and regularities. Problems of the genesis of rocks and ores, the age of their formation, including the main stages in the evolution of the Earth and the planets of the Solar System, and their dating on a geological scale, were investigated.

Since the 1950s, the Vernadsky Institute has been gradually incorporating research into the geochemistry of the Earth's crust and upper mantle, the geochemistry of ore-forming processes, biogeochemistry and organic geochemistry, radiogeochemistry, cosmochemistry and comparative planetology, isotope geochemistry and geochronology, crystal chemistry and solid-state geochemistry, and applied geochemistry.

In 1960, A. P. Vinogradov edited the 2 volumes of Atlas of lithological and paleogeographical maps of the Russian platform and its geosynclinal frame and the 4 volumes of Atlas of lithological and paleogeographical maps of the USSR. A large team of geologists (over 1000 people) took part in this work. Later, A. P. Vinogradov researched the geochemistry of individual elements; he studied the average chemical composition of the Earth's crust. In 1956 and later in 1962, he published new tables of Clarks of the Sun, meteorites, and terrestrial rocks, showing the average distribution of chemical elements.

Due to the rapid development of geochemistry in the mid-50 s, in 1956, A. P. Vinogradov founded the journal Geochemistry[6] and became its editor-in-chief.

The love of the ocean and the study of problems related to the ocean ran a red thread through all the scientific activities of Vinogradov. Based on these studies, he posed a profound scientific problem on the evolution of the composition of the water of the World Ocean during the geological history of the Earth. In 1966, A. P. Vinogradov organized and held the II International Oceanographic Congress in Moscow while being its elected President. His report at the plenary session contained conceptual foundations for ocean research. Using factual data, he compared the interaction of mantle and crustal processes during the formation of the lithosphere with similar processes during the formation of continents. In 1967, another monograph by A. P. Vinogradov, Introduction to ocean geochemistry, was published. Based on experimental data, he showed that the formation of the lithosphere and hydrosphere is a single geological process. In 1971, the preparation of the International Geological—Geophysical Atlas of the World Ocean published by the Intergovernmental Oceanographic Commission (IOC) under the auspices of UNESCO (G. B. Udintsev was the editor-in-chief) was started with the most active support from A. P. Vinogradov. In 1975, the Indian Ocean Atlas was published, then in 1990, the Atlantic Ocean Atlas, and in 2003, the Pacific Ocean Atlas was published.

A. P. Vinogradov is rightly considered to be the founder of cosmochemical research in the USSR. He played a leading role in the development of a national scientific strategy to study the bodies of the Solar System: their

[6]Currently, the journal publishes articles in both Russian and English languages and welcomes submissions by international authors in English. The English version of the journal is published under the

(Footnote 6 continued)
"Geochemistry International" title. The journal is indexed in both Scopus and Web of Sciences. For more details about the journal, see Introduction.

Bas relief of famous Russian sculptor S. T. Konenkov installed at the entrance to the conference hall of the Vernadsky Institute

composition and structure. This enormous and significant field of knowledge began with the study of the Moon. Under the leadership of A. P. Vinogradov, the institute developed special instruments for studying extraterrestrial matter (gamma-, X-ray-, mass-spectrometers, neutron detectors, gas analyzers, etc.), which were installed on space stations sent to the Moon, Venus, and Mars, which then brought the first data on their material composition. The data obtained on the content of natural radioactive elements (K, U, Th) in the rocks of the Moon fully confirmed Vinogradov's hypothesis of a predominantly basaltic composition of its surface, which he had put forward earlier. Lunar soil samples were delivered to Earth from various regions of the Moon by the automatic interplanetary stations Luna 16 (1970), Luna 20 (1972), and, later, after A. P. Vinogradov passed away, Luna 24 became a genuine triumph of the Soviet astronautics.

A comprehensive study of the regolith delivered by lunar expeditions in 1970 from the Sea of Fertility (from Latin *Mare Fecunditatis*) turned out to be of basaltoid composition, and in 1972 from the continental region turned out to be of anorthosite composition. This showed their non-identity, indicating different geochronology of the processes that formed the basalt and anorthosite lunar rocks.

The lack of an atmosphere and hydrosphere on the Moon explained the constancy in the composition of the Lunar rocks since their formation and made it possible to approach the understanding of the origin of the Earth and explain its early geological history.

Venus and Mars were also studied under the direct supervision of A. P. Vinogradov at the Vernadsky Institute of the USSR Academy of Science using interplanetary space stations and descent vehicles, in parallel with the study of the Moon. From 1967 to 1973, data on the radioactivity of surface rocks of Venus and the chemical composition of its atmosphere, which turned out to be composed of 97% carbon dioxide and a small amount of nitrogen, water vapour with traces of oxygen, and ammonia, were obtained. In his report Atmospheres of the Planets of the Solar System (MSU, 1969), A. P. Vinogradov stressed that the history of the atmosphere of Venus should be primarily determined by the greenhouse effect and the degree of atmospheric dissipation (loss of helium, hydrogen, and water). A month before he passed away, Vinogradov was able to see the first television images of the surface of Venus transmitted by the automatic interplanetary stations Venera-9 and Venera-10. The interpretation of these panoramas became Vinogradov's final research work.

In 1973, the automatic interplanetary station Mars-5, for the first time, measured the content of naturally occurring radioactive elements in rocks on the surface of Mars. Rocks in areas of ancient crust and in younger regions of volcanic origin were identified.

At the suggestion of Soviet planetary scientists, the International Astronomical Union named a mountain range on the Moon and a crater on Mars in recognition of Vinogradov.

The USSR Academy of Sciences commemorated the memory of Academician A. P. Vinogradov by naming the Institute of Geochemistry of the Siberian Branch of the USSR Academy of Sciences and the research vessel of the Far Eastern Scientific Center of the USSR Academy of Sciences after him. A. P. Vinogradov garnered a well-deserved reputation among the foreign community of scientists as an outstanding naturalist, brilliant organizer of science, and public figure.

Memorial Cabinet-Museum of Academician A. P. Vinogradov

Organizer and Curator
Loriana D. Vinogradova
Senior Researcher at Vernadsky Institute RAS
E-mail: loriana.vinogradova@mail.ru
Website: portal.geokhi.ru/eng/vinogradov

The Memorial Cabinet-Museum of Academician Alexander P. Vinogradov was established by the decree of the Presidium of the USSR Academy of Sciences No.905 dated December 25, 1975, to perpetuate the memory of the outstanding scientist-naturalist.

The Memorial Cabinet-Museum is in two rooms of the main building of the Vernadsky Institute and is part of the structure of the institute as a research unit. The task of the museum is the study, analysis, and popularization of the scientific heritage of A. P. Vinogradov, publication of works, books, publication of articles in scientific periodicals, presentations at conferences and symposiums, participation in exhibitions, creation of thematic stands, excursions, replenishment of funds with materials about the life, scientific and organizational activities of A. P. Vinogradov.

The first visitors of the cabinet-museum were participants of the XXVII session of the International Geological Congress (Moscow, August 1984), and its official opening took place on November 14, 1985, on the occasion of the 90th anniversary of A. P. Vinogradov.

The exposition is based on the home office of A. P. Vinogradov; it fully reproduces the setting and atmosphere of the scientist's work at home with furniture, scientific library, and belongings of A. P. Vinogradov, which the family donated to the institute for the organization of the Memorial Cabinet-Museum.

In another room, the memorial space is filled with a wall exposition reflecting both the outstanding role of A. P. Vinogradov in the organization of the Vernadsky Institute and his multifaceted activities. It is supplemented by diplomas on A. P. Vinogradov's election as a foreign member of foreign academies of sciences and scientific societies, diplomas on being awarded gold medals of Vernadsky and Lomonosov, diploma on receiving a gold medal from the Czechoslovak Academy of Sciences for services to humanity, stand with photos of government awards and awards of other countries which he was awarded, pictures, portraits, and some other diplomas.

The museum's funds included materials of the personal archive, including documents, photographic materials, Vernadsky's letters (to A. P. Vinogradov) and correspondence with his colleagues and wife, addresses and congratulations, periodical press materials, certificates, gifts, video, and sound recordings, including individual personal items. From 2017 to 2019 the materials of the personal archive were transferred to complete the personal fund of Academician A. P. Vinogradov No. 1691 in the Archive of the Russian Academy of Sciences, and according to the Archive staff, the A. P. Vinogradov fund is one of the most interesting in the archives of the Academy of Sciences. The museum has done a great job for the past. Apart from the excursions for those who are interested in the history of Russian science and in the unique personality of A. P. Vinogradov as an outstanding scientist, organizer, teacher, and citizen, 5 monographs and over 30 articles about the life and comprehensive scientific and organizational activities of A. P. Vinogradov have been published. One more monograph, "Multifaceted Activity of Academician A. P. Vinogradov in Documents", is ready for publication. The cabinet-museum also participated in different conferences and symposiums; the wall exposition was made; the literature of the two shelves of the three scientific libraries was described to make a card file, etc.

At the end of the 1990s and the beginning of the 2000s in the Yaroslavl region, the cabinet-museum conducted numerous memorialization activities of the Vinogradov family. The Memorial board on the patrimonial house in Petretsovo was made in memory of the father of A. P. Vinogradov—Pavel S. Vinogradov (1869–1941). The opening of the memorial plaque took place in August 2001. Deputy Head of the Administration of Tutaevsky municipal district N. N. Smirnova took

part in the opening of the memorial plaque. This was done using the data from the genealogy of Vinogradov's family tree in the Yaroslavl State Regional Archive. The work of the cabinet-museum in the Yaroslavl Region to perpetuate the memory of the Vinogradov family continues.

Currently, the museum is preparing the complete collection of A. P. Vinogradov's works as a collection of 18 volumes and has started transcribing unpublished handwritten materials for Volumes 17 and 18 from the collection No 1691 of the Archive of RAS, as well as working in the Archive reading room to find transcripts of A. P. Vinogradov's speeches at the meetings of the RAS and the Presidium of the USSR Academy of Sciences for Volume 16 (Figs. A.5, A.6 and A.7).

Fig. A.5 General view of the cabinet-museum of A. P. Vinogradov

Fig. A.6 Interiors of the cabinet-museum

Fig. A.7 Work table of A. P. Vinogradov

Ilya S. Abramson
(1910–1983)
Doctor of Technical Sciences

I. S. Abramson started working at the Vernadsky Institute of the USSR Academy of Sciences in 1969. In 1973, he founded the Laboratory of Precision Analytical Instrumentation. He designed several spectral devices, including a high-speed spectrophotometer, a precision coulometric instrument for atomic absorption, and fluorescence spectra. In 1947, he was awarded the State Prize for the development of the nighttime aerial survey method.

Igor V. Aleksandrov
(1924–1994)
Doctor of Geological and Mineralogical Sciences

I. V. Alexandrov identified the first complex carbonate compounds of niobium and tantalum and explained their transfer and separation in carbonatite and tin deposits. He also explained the main geochemical features of the behavior of tantalum and niobium, established the physico-chemical conditions for the formation and accumulation of rare elements in granitoids and granitic pegmatites, and proposed methods for assessing the productivity of tantalum mineralization.

Ivan P. Alimarin
(1903–1989)
Academician of the USSR Academy of Sciences, Doctor of Chemistry

I. P. Alimarin was an outstanding analytical chemist and winner of the USSR State Prize. For many years he was the leading authority on analytical chemistry in Russia, headed the Scientific Council of the USSR Academy of Sciences on Analytical Chemistry and the Department of Analytical Chemistry at Moscow University. He was also the editor-in-chief of the Journal of Analytical Chemistry. He contributed to the formulation and development of new methods, such as micro- and ultramicroanalysis, neutron activation analysis and other radioanalytical methods, voltammetry, methods of element concentration (coprecipitation, extraction, etc.), and numerous methods of mineral analysis. He developed analytical chemistry for rare and trace elements and methods of analysis for high purity substances.

Vladimir I. Baranov
(1892–1972)
Doctor of Physics and Mathematics, Professor

V. I. Baranov was head of the Radiological Laboratory, and from 1946 to 1962, he was the deputy director of the institute. His areas of interest were natural radioactivity of the Earth's crust, determination of the age of rocks, ocean sediments, meteorites, etc. He measured the content of several radioactive elements in rocks, identified the regularities of radioactive element distribution in the main types of soils of the USSR, determined the radioactivity of waters in oil-bearing areas and found geochemical features of radioactive contamination of the environment.

Valery L. Barsukov
(1928–1992)
Academician of the USSR Academy of Sciences, Doctor of Geological and Mineralogical Sciences, Former Director of the Vernadsky Institute

V. L. Barsukov joined the Vernadsky Institute in 1954 and became director of the institute in 1976. His research was devoted to the study of problems of ore formation, from the mechanisms of mobilisation, conditions of transport, and deposition of ore matter to the creation of original methods of prospecting and forecasting of ore deposits. He organised and led a comprehensive study of the structure and composition of the atmosphere and rocks on the surface of the planet Venus using spacecraft.

Elena V. Bibikova
(1934–2016)
Doctor of Geological and Mineralogical Sciences

E. V. Bibikova started working at the Vernadsky Institute in 1957. She developed a methodology for isotopic dating of accessory zircons (zirconometry). She conducted research in the field of isotopic dating of the oldest formations of our planet and studied the role of isotopic geochronology in solving the problems of cgeodynamics in the early Precambrian.

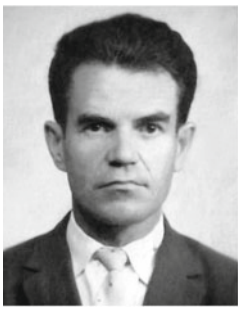

Mikhail S. Chupakhin
(1920–1991)
Doctor of Technical Sciences

M. S. Chupakhin joined the Vernadsky Institute after graduation from the Bauman Moscow State Technical University in 1952. Based on an industrial mass spectrometer, he created a facility for recording isotopic shifts of light chemical elements and isotopic differences for paleotemperature purposes. He developed mass-spectral methods for the analysis of high-purity substances.

Leonid V. Dmitriev
(1927–2005)
Doctor of Geological and Mineralogical Sciences, Professor

L. V. Dmitriev joined the Vernadsky Institute after graduating in 1951. From 1980 he headed the Laboratory of Geochemistry of Magmatic and Metamorphic Rocks. He was the first to produce the petrological maps of the Indian and Atlantic Oceans for the International Atlases. He developed quantitative geodynamic models of mantle-crustal interaction using key oceanic and continental regions.

Anatoly N. Ermakov
(1926–1994)
Doctor of Chemistry, Professor

A. N. Ermakov started and flourished at the institute, using physical methods to study the structure of matter: methods of electron paramagnetic resonance, nuclear magnetic resonance, gamma-resonance spectroscopy. He obtained critical results in radiochemistry, analytical and inorganic chemistry of rare elements, and created new directions in the study of the chemistry of complex compounds.

Kirill P. Florensky
(1915–1982)
Ph.D. in Geological and Mineralogical Sciences

K. P. Florensky started working at the Vernadsky Institute in 1947. He founded and headed the Laboratory of Comparative Planetology (1975). He substantiated the concept of the appearance of planetary atmospheres as a result of shock-explosive processes at the pregeological stage of the formation of planetary bodies. He is famous for the complex study of meteorite craters on Earth and other planets, the Tunguska event, lunar soil samples, and the selection of locations for Soviet spacecraft landings on the surface of the Moon and planets.

Erik M. Galimov
(1936–2020)
Academician of the Russian Academy of Sciences, Doctor of Geological and Mineralogical Sciences, Former Director of the Vernadsky Institute

In 1973, E. M. Galimov established and headed the Laboratory of Carbon Geochemistry at the Vernadsky Institute. In 1994, he became director of the institute. He made major contributions to the development of several major scientific areas, such as organic geochemistry, petroleum geochemistry, and hydrocarbon gases. He undertook studies like isotope geochemistry, carbon's behaviour in the planetary cycle, including the origin of the Moon and the early history of the Earth, conditions of the biosphere formation, and the formation of diamonds.

Vasily V. Gerasimovky
(1907–1979)
Doctor of Geological and Mineralogical Sciences, Professor

V. V. Gerasimovsky started working at the Vernadsky Institute in 1949. He headed the Laboratory of Magmatic and Metamorphic Rocks and carried out research on alkaline magmatism of the Earth and associated mineralization, including the study of rift zones of the World Ocean. He majorly contributed to the geological and geochemical study of alkaline provinces of the world and participated in expeditions to Greenland and East Africa.

Lev A. Gribov
(1933–2021)
Corresponding Member of the Russian Academy of Sciences, Doctor of Physics and Mathematics

L. A. Gribov created methods for calculating optical molecular spectra in the range from the far-infrared to the UV, proposed a theory of chemical reactions, laid the foundations of molecular logic, developed the theory of expert systems and approach for analysis of substances by their spectra only, without standards. He is one of the founders of mathematical chemistry. In 1975, he established and headed the Laboratory of Molecular Modelling and Spectroscopy; 1998–2008, he was Deputy Director of the Vernadsky Institute. He was awarded the State Prize.

Arnold A. Kadik
(1933–2016)
Doctor of Geological and Mineralogical Sciences, Professor

A. A. Kadik started working at the Vernadsky Institute in 1961. From 1985 he headed the Laboratory of Geochemistry of the Earth's Mantle. He contributed to the development of the Russian school of experimental studies of geochemical processes in the Earth's interior. He was one of the founders of a new direction in geochemistry related to the study of peculiarities of evolution of redox state of mantle matter during its chemical differentiation.

Arkadiy V. Karyakin
(1918–1986)
Doctor of Physics and Mathematics

A. V. Karyakin engaged in the field of spectroscopy. In 1960, he headed the Laboratory of Spectral Methods of Analysis. He had proposed new methods for increasing the sensitivity of emission spectroscopy in the analysis of ultra-pure substances with complex composition and developed new methods of analysis by molecular spectroscopy, luminescence, and photochemistry.

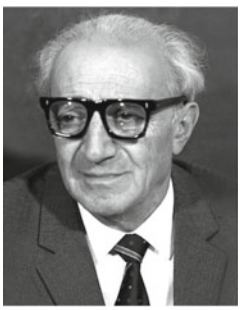

Nikolai I. Khitarov
(1903–1985)
Corresponding Member of the USSR Academy of Sciences, Doctor of Geological and Mineralogical Sciences

In 1953 N. I. Khitarov became head of the Laboratory of Magmatic Processes at the Vernadsky Institute, and from 1963 to 1970 was deputy director of the institute. A geochemist-experimentalist, he prominently contributed to the study of problems of ore formation, the solubility of water in magmatic melts, and evaluation of the role of water, the main volatile component, in the transformation of rocks and minerals at elevated temperatures and pressures.

Lev M. Khitrov
(1933–1998)
Ph.D. in Chemistry

L. M. Khitrov started working at the Vernadsky Institute in 1956. From 1977 he headed the Ocean Geochemistry Laboratory. He designed special marine instrumentation and developed methodologies for studies of radionuclide migration in water, soil, atmosphere, living organisms, and plants. He studied the consequences of nuclear explosions, the bombing of Hiroshima and Nagasaki, Chernobyl disaster.

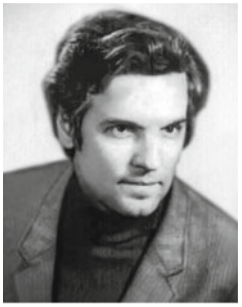

Igor L. Khodakovsky
(1941–2012)
Doctor of Chemistry, Professor

I. L. Khodakovsky started working at the Vernadsky Institute in 1963. In 1977, he established the Laboratory of Thermodynamics of Natural Processes. He contributed significantly to experimental and theoretical studies of the thermodynamics of minerals of hydrothermal ore-forming systems, to the development of physicochemical models of processes governing the composition of planetary atmospheres and their surface rocks, to the study of meteoritic matter formation processes.

Victor V. Kovalsky
(1899–1984)
Corresponding Member of Soviet Academy of Agricultural Sciences, Doctor of Biology, Professor

V. V. Kovalsky started working at the Vernadsky Institute in 1954. He studied the problem of biochemistry and biogeochemistry of trace elements in living organisms. He organised about 60 expeditions to study biogeochemical provinces and reactions of plants, animals, and humans to the lack or excess of certain trace elements in the environment.

Evgeny L. Krinov
(1906–1984)
Doctor of Geological and Mineralogical Sciences

E. L. Krinov was one of the founders of meteoritics in Russia and was the chairman of the Committee on Meteorites of the USSR Academy of Sciences from 1972. From 1979, he headed the Laboratory of Meteoritics at the Vernadsky Institute. He participated in the study of the largest meteorite falls—Tunguska and Sikhote-Alin. He received the Leonard Medal from the Meteoritical Society (1971). He was the first to publish Meteoritical Bulletin (1957–1970). Asteroid 2887 and a new meteorite mineral krinovite ($NaMg_2CrSi_3O_{10}$) are named after Krinov.

Lev L. Kunin
(1920–1990)
Doctor of Technical Sciences

L. L. Kunin obtained fundamental results in analytical and physicochemical research of metals. He authored dozens of patents. From 1967 to 1988, he worked at the Vernadsky Institute, where in 1968, he headed the Laboratory for the Determination of Gas-Forming Impurities. He was an expert in the determination of gases (oxygen, nitrogen, hydrogen) in metals and alloys using different methods (electrochemical cells, gamma-activation analysis, etc.).

Nikolay M. Kuz'min
(1936–1998)
Doctor of Chemistry, Professor

N. M. Kuz'min made a significant contribution to the development of theoretical foundations and methods of preliminary concentration of traces of inorganic and organic substances, to the development of combined and hybrid methods of analysis, to the solution of issues of intensification of sample preparation in the microwave system, to the formulation of principles and content of forensic analytical chemistry, to the creation of the concept of ecoanalytical control in Russia.

Vitaliy I. Kuznetsov
(1909–1987)
Doctor of Chemistry, Professor

V. I. Kuznetsov specialized in organic and analytical chemistry and synthesised new organic reagents selective for various elements. He started working at the Vernadsky Institute in 1949. In 1952, he became the head of the Laboratory of Organic Compounds. He had carried out the extraction separation of elements and developed a theoretical basis for colour reactions of organic reagents with inorganic ions. He developed a new method for ultra-small quantities of over 30 elements co-precipitation using organic co-precipitators and a method of thermo spectrophotometry.

Avgusta K. Lavrukhina
(1919–2006)
Doctor of Chemistry, Professor

A. K. Lavrukhina started working at the Vernadsky Institute in 1947. From 1964 to 1989, she headed the Laboratory of Cosmochemistry. Based on experimental and theoretical investigations of nuclear reactions under the action of high-energy particles, she founded a new scientific discipline—nuclear cosmochemistry. She created a quantitative model of the deep distribution of active nuclear particles and cosmogenic isotopes in cosmic bodies.

Evgeny S. Makarov
(1911–1994)
Doctor of Chemistry

E. S. Makarov started working at the institute in 1956, where he created and headed the Laboratory of Crystal Chemistry. He was a well-known scientist in the field of crystal chemistry of inorganic compounds, intermetallic compounds, and minerals. For the first time in the country, he began a theoretical and experimental study of the atomic structure of crystals with a variable number of atoms in a unit cell, determined the atomic structure of crystals of many intermetallic phases of the Daltonoid and Bertholloid type, and for the first time developed a single structural-crystal-chemical theory for phases of variable composition.

Igor N. Marov
(1933–1997)
Doctor of Chemistry, Professor

I. N. Marov was a well-known specialist in the field of chemistry of complex compounds and the mechanism of analytically important reactions using the methods of electron paramagnetic resonance and nuclear magnetic resonance. He carried out a series of works on the study of the complex formation of rare elements, including molybdenum, chromium, tungsten, silver, etc. in solutions. He contributed to understanding the mechanism of extraction of coordination compounds and the mechanism of sorption of metals by sorbents of various nature.

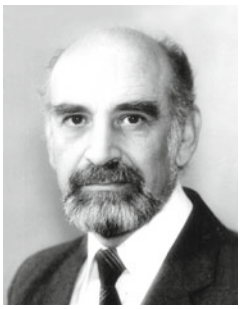

Areg A. Migdisov
(1936–2003)
Ph.D. in Geological and Mineralogical Sciences
In 1956, Areg A. Migdisov graduated from the Faculty of Geology (Department of Geochemistry), M. V. Lomonosov Moscow State University. In 1956, he started his Ph.D. program at the Vernadsky Institute. After completing his Ph.D., he was employed by the Laboratory of Sedimentary Geochemistry, and became its head in 1985. His main direction of research was the quantitative description of the geochemical regularities of the formation and evolution of the Earth's sedimentary shell. He developed methods of isotope geochemistry, which he applied to the solution of problems of regional and global sedimentology and tectonics.

Georgy B. Naumov
(1929–2019)
Doctor of Geological and Mineralogical Sciences, Professor

G. B. Naumov started to work at the Vernadsky Institute in 1953. He contributed significantly to the geochemistry of ore-forming processes. He formulated statements on complex forms of element transfer in hydrothermal solutions, the role of degassing processes, and the importance of pre-mining events in the accumulation of potential metal reserves and their conversion into potentially mobile forms.

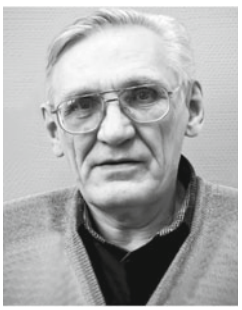

Mikhail A. Nazarov
(1949–2016)
Doctor of Geological and Mineralogical Sciences

M. A. Nazarov joined the Vernadsky Institute in 1972, and from 1989 he was head of the Department for the Study of Extraterrestrial Matter and Meteoritics and later head of Meteoritics Laboratory. Under his leadership, works on the study of geochemistry and mineralogy of lunar soil and meteorites, search and study of cosmochemical anomalies on stratigraphic boundaries, the study of impact craters have been carried out. He proposed a mineralogical interpretation of the results of the dust fraction of Halley's comet. A new mineral, nazarovite ($Ni_{12}P_5$), was named in his honour.

Petr N. Paley
(1900–1975)
Doctor of Chemistry, Professor

P. N. Paley was a participant in the Soviet atomic project on methods of analytical chemistry of uranium and plutonium. He started to work at the Vernadsky Institute in 1945, and in 1949 he became the head of Radiochemistry Laboratory. In 1965, he was promoted to the post of Deputy Director of the Vernadsky Institute. He authored methods for the precise determination of small quantities of substances required for the analysis and control of fissile materials. He received state awards and prizes for his scientific work.

Fannie I. Pavlotskaya
(1922–2006)
Doctor of Chemistry

F. I. Pavlotskaya joined the Geochemical Problems Laboratory of the Vernadsky Institute in 1947. She became the founder of a new scientific field—the geochemistry of artificial radionuclides. She was head of the group for the study of the distribution and behaviour of fission elements on the surface of the Earth. In 1979, she moved to the Radiochemistry Laboratory and headed the radioecological studies of the behaviour of actinides in environmental objects.

Alexander B. Ronov
(1913–1996)
Academician of the Russian Academy of Sciences, Doctor of Geological and Mineralogical Sciences

A. B. Ronov was a polymath who made important contributions to geology, geochemistry, palaeogeography and was one of the founders of evolutionary geochemistry, global lithology, and geochemistry. He authored the volumetric method of stratosphere research and formulated the basic law of carbonate accumulation and the geochemical principle of the preservation of life, which linked the accumulation of carbonates and living matter with the volcanic activity of the Earth.

Dmitry I. Ryabchikov
(1904–1965)
Corresponding Member of the USSR Academy of Sciences, Doctor of Chemistry

D. I. Ryabchikov was a famous analytical chemist. From 1944, he worked at the Laboratory of Geochemical Problems, which got reorganized into the Vernadsky Institute in 1947. He became the Scientific Secretary and later was promoted to the post of the Deputy Director of the institute until 1956. From 1962 to 1964, he was head of the Laboratory of Analytical Chemistry of Rare Elements. He was widely known for his research in chemistry and analytical chemistry of rare elements, platinum metals, uranium, and thorium. He received numerous government awards.

Sergey B. Savvin
(1931–2014)
Doctor of Chemistry, Professor

S. B. Savvin was a renowned scientist in the field of synthesis of organic reagents (OR), theory, and practice of their application in inorganic analysis. His main areas of activity were OR in inorganic analysis, modified and immobilized forms of OR for separation, concentration, and determination of inorganic substances. He synthesized the well-known reagent arsenazo III from a new class of bisazo-substituted chromotropic acid. He worked in IUPAC and editorial offices of scientific journals and oversaw the Laboratory of Organic Reagents.

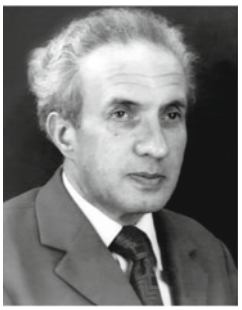

Mark M. Senyavin
(1917–1989)
Doctor of Chemistry, Professor

M. M. Senyavin was a well-known scientist in the theory and practice of ion exchange and received the USSR State Prize and the RSFSR State Prize. From 1949 he worked at the Vernadsky Institute. He was the founder of the Laboratory of Sorption Methods. He contributed considerably to the development of the Russian industry of rare-earth elements and the solution of large-scale problems of surface water treatment, including those connected with the elimination of consequences of the Chernobyl disaster.

Vladimir V. Shcherbina
(1907–1978)
Doctor of Geological and Mineralogical Sciences, Professor

From 1948 V. V. Shcherbina headed the Laboratory of Geochemistry of Single Elements at the Vernadsky Institute. Between 1972 and 1976, he was the Vice President of the International Association of Geochemistry and Cosmochemistry. He was one of the leading specialists in the field of the geochemistry of radioactive elements. He established a scientific trend—geochemistry of elements in the hypergenesis zone of ore deposits.

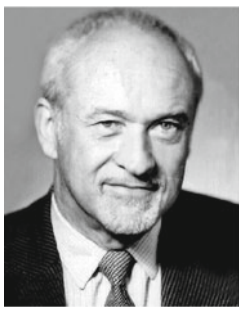

Yuri A. Shukolyukov
(1929–2013)
Doctor of Chemistry, Professor

From 1979 Yu. A. Shukolyukov headed the Laboratory of Isotope Geochemistry and Geochronology of the Vernadsky Institute, and from 1981 to 1989, he was deputy director of the institute. He made a significant contribution to the study of the behaviour of isotope systems under various physical and chemical conditions and the development of new methods of isotope geochronology, including the ones for isotopic dating of uranium and gold deposits.

Boris Ya. Spivakov
(1941–2022)
Corresponding Member of the Russian Academy of Sciences, Doctor of Chemistry, Professor B.Ya. Spivakov started working at the Vernadsky Institute in 1963. His fundamental scientific research was associated with the development of extraction, chromatographic, membrane and other modern methods of separation of substances. He proposed a general theory of exchange extraction of chelates and contributed to the theory of extraction of metal complexes from the standpoint of coordination chemistry. He was a member of the editorial boards of the journals Talanta, Fresenius J. of Analytical Chemistry, Pure and Applied Chemistry. He was a titular member of the Analytical Chemistry Division (ACD) of the IUPAC and a member of the EuCheMS (ACD).

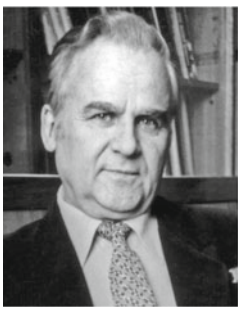

Yuri A. Surkov
(1926–2005)
Doctor of Physics and Mathematics, Professor

Yu. A. Surkov started to work at the Vernadsky Institute in 1952. His main area of research was the study of the chemical composition and physical parameters of the surfaces of Mars, Venus, the Moon, and the atmosphere of Venus. He developed experimental methods and onboard equipment of automatic interplanetary stations to study the composition, structure, and properties of the substance of the planets and interplanetary space.

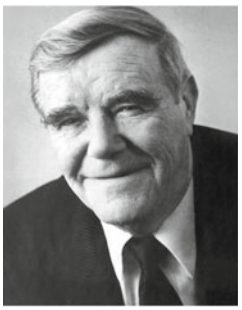

Lev V. Tauson
(1917–1989)
Academician of the USSR Academy of Sciences, Doctor of Geological and Mineralogical Sciences

L. V. Tauson worked at the Vernadsky Institute from 1947 to 1957. He then became the director of the Institute of Geochemistry in Irkutsk, Russia (currently Vinogradov Institute of Geochemistry SB RAS). He was the first to systematically study the geochemistry of disseminated and orogenic rare elements in a genetically related series of igneous rocks. He formulated the main regularities in behaviour of rare elements in the differentiation and crystallisation processes of magmatic melts.

Alexei I. Tugarinov
(1917–1977)
Corresponding Member of the USSR Academy of Sciences, Doctor of Geological and Mineralogical Sciences

A. I. Tugarinov started to work at the Vernadsky Institute in 1949. In 1965 he organised and headed the Laboratory of Rare Elements. He studied the problems of the evolution of ore formation in the Earth's history. He has shown that the formation of ore provinces and their specialisation for particular metals begins with the differentiation of crustal matter during the formation of productive sedimentary formations. He contributed majorly to the geochemistry of uranium.

Gleb B. Udintsev
(1923–2017)
Corresponding Member of the Russian Academy of Sciences, Doctor of Geography

G. B. Udintsev started working at the Vernadsky Institute in 1992. He specialised in marine geology and geophysics and carried out many years of research into the topography and structure of the bottom of the Far East seas and the Pacific Ocean. He produced several bathymetric, geomorphological, and tectonic maps. The giant fault on the bottom of the Pacific Ocean bears his name.

Vadim S. Urusov
(1936–2015)
Academician of the Russian Academy of Sciences, Doctor of Chemistry

V. S. Urusov started to work at the Vernadsky Institute in 1961, and from 1979 he headed the Laboratory of Crystal Chemistry. He created a new section of mineral crystallochemistry, energetic crystallochemistry, which allows us to analyse the relationship between the structure and properties of crystals and the energy of interatomic interactions. He proposed the concept of atomisation energy as a universal characteristic of chemical bonding energy.

Galina M. Varshal
(1932–2001)
Doctor of Chemistry

G. M. Varshal researched the role of humus substances in the processes of dispersion and accumulation of heavy metals in the hypergenesis zone. She studied the mechanism of noble metal deposit formation in sedimentary-metamorphic black-shale complexes and developed a set of highly sensitive methods for determining these metals in carbon-bearing rocks. She significantly contributed to the analytical chemistry of rare-earth elements and mercury and the analysis of mineral raw materials and natural waters.

Vladislav P. Volkov
(1934–2012)
Doctor of Geological and Mineralogical Sciences

V. P. Volkov joined the Vernadsky Institute in 1956 and conducted research related to geochemistry and petrology of igneous rocks of the Kola Peninsula. His works in thermodynamic modelling of processes of interaction of rocks of surface and atmosphere of the planet Venus are summarised in chapters of his monograph "Chemistry and physics of terrestrial planets" (1986). He contributed significantly to the scientific heritage of Academician V. I. Vernadsky.

Yury V. Yakovlev
(1928–2014)
Ph.D. in Chemistry

Yu. V. Yakovlev received the State Prize of the USSR and performed the first works at the Vernadsky Institute and the USSR on neutron activation analysis. Tasks: controlling ultra-low impurity element contents in nuclear materials, high purity substances, and semiconductors, including matrices with high cross-section self-absorption of thermal and resonant neutrons. He carried out pioneering works on the analysis of unique lunar soil samples.

Aleksey A. Yaroshevsky
(1934–2017)
Doctor of Geological and Mineralogical Sciences, Professor

A. A. Yaroshevsky specialized in the physical and chemical modelling of geochemical processes. He made significant contributions to the development of general geochemistry, geochemistry of the biosphere, and cosmochemistry. He established the regularities of the geochemical balance of the Earth's crust substance and developed the model of its formation and evolution. He proposed a physicochemical theory of the dynamics of the magmatic process, and based on this, he studied the mechanism of formation of differentiated magmatic complexes of basic and ultrabasic rocks and associated mineralization.